BRAIN IMAGING METHODS EDITOR'S PICK 2021

EDITED BY: Vince D. Calhoun

PUBLISHED IN: Frontiers in Neuroscience

frontiers Research Topics

frontiers

Frontiers eBook Copyright Statement

The copyright in the text of individual articles in this eBook is the property of their respective authors or their respective institutions or funders. The copyright in graphics and images within each article may be subject to copyright of other parties. In both cases this is subject to a license granted to Frontiers.

The compilation of articles constituting this eBook is the property of Frontiers.

Each article within this eBook, and the eBook itself, are published under the most recent version of the Creative Commons CC-BY licence. The version current at the date of publication of this eBook is CC-BY 4.0. If the CC-BY licence is updated, the licence granted by Frontiers is automatically updated to the new version.

When exercising any right under the CC-BY licence, Frontiers must be attributed as the original publisher of the article or eBook, as applicable.

Authors have the responsibility of ensuring that any graphics or other materials which are the property of others may be included in the CC-BY licence, but this should be checked before relying on the CC-BY licence to reproduce those materials. Any copyright notices relating to those materials must be complied with.

Copyright and source acknowledgement notices may not be removed and must be displayed in any copy, derivative work or partial copy which includes the elements in question.

All copyright, and all rights therein, are protected by national and international copyright laws. The above represents a summary only. For further information please read Frontiers' Conditions for Website Use and Copyright Statement, and the applicable CC-BY licence.

ISSN 1664-8714
ISBN 978-2-88966-965-3
DOI 10.3389/978-2-88966-965-3

About Frontiers

Frontiers is more than just an open-access publisher of scholarly articles: it is a pioneering approach to the world of academia, radically improving the way scholarly research is managed. The grand vision of Frontiers is a world where all people have an equal opportunity to seek, share and generate knowledge. Frontiers provides immediate and permanent online open access to all its publications, but this alone is not enough to realize our grand goals.

Frontiers Journal Series

The Frontiers Journal Series is a multi-tier and interdisciplinary set of open-access, online journals, promising a paradigm shift from the current review, selection and dissemination processes in academic publishing. All Frontiers journals are driven by researchers for researchers; therefore, they constitute a service to the scholarly community. At the same time, the Frontiers Journal Series operates on a revolutionary invention, the tiered publishing system, initially addressing specific communities of scholars, and gradually climbing up to broader public understanding, thus serving the interests of the lay society, too.

Dedication to Quality

Each Frontiers article is a landmark of the highest quality, thanks to genuinely collaborative interactions between authors and review editors, who include some of the world's best academicians. Research must be certified by peers before entering a stream of knowledge that may eventually reach the public - and shape society; therefore, Frontiers only applies the most rigorous and unbiased reviews.
Frontiers revolutionizes research publishing by freely delivering the most outstanding research, evaluated with no bias from both the academic and social point of view. By applying the most advanced information technologies, Frontiers is catapulting scholarly publishing into a new generation.

What are Frontiers Research Topics?

Frontiers Research Topics are very popular trademarks of the Frontiers Journals Series: they are collections of at least ten articles, all centered on a particular subject. With their unique mix of varied contributions from Original Research to Review Articles, Frontiers Research Topics unify the most influential researchers, the latest key findings and historical advances in a hot research area! Find out more on how to host your own Frontiers Research Topic or contribute to one as an author by contacting the Frontiers Editorial Office: frontiersin.org/about/contact

BRAIN IMAGING METHODS EDITOR'S PICK 2021

Topic Editor:
Vince D. Calhoun, Georgia State University, United States

Citation: Calhoun, V. D., ed. (2021). Brain Imaging Methods Editor's Pick 2021. Lausanne: Frontiers Media SA. doi: 10.3389/978-2-88966-965-3

Table of Contents

06 ***Correlated MRI and Ultramicroscopy (MR-UM) of Brain Tumors Reveals Vast Heterogeneity of Tumor Infiltration and Neoangiogenesis in Preclinical Models and Human Disease***
Michael O. Breckwoldt, Julia Bode, Felix Sahm, Thomas Krüwel, Gergely Solecki, Artur Hahn, Peter Wirthschaft, Anna S. Berghoff, Maximilian Haas, Varun Venkataramani, Andreas von Deimling, Wolfgang Wick, Christel Herold-Mende, Sabine Heiland, Michael Platten, Martin Bendszus, Felix T. Kurz, Frank Winkler and Björn Tews

16 ***Clinical Value of Machine Learning in the Automated Detection of Focal Cortical Dysplasia Using Quantitative Multimodal Surface-Based Features***
Jia-Jie Mo, Jian-Guo Zhang, Wen-Ling Li, Chao Chen, Na-Jing Zhou, Wen-Han Hu, Chao Zhang, Yao Wang, Xiu Wang, Chang Liu, Bao-Tian Zhao, Jun-Jian Zhou and Kai Zhang

27 ***Tracking Neural Progenitor Cell Migration in the Rodent Brain Using Magnetic Resonance Imaging***
Christiane L. Mallett, Dorela D. Shuboni-Mulligan and Erik M. Shapiro

46 ***Brain Vital Signs: Expanding From the Auditory to Visual Modality***
Gabriela M. Pawlowski, Sujoy Ghosh-Hajra, Shaun D. Fickling, Careesa C. Liu, Xiaowei Song, Stephen Robinovitch, Sam M. Doesburg and Ryan C. N. D'Arcy

59 ***The Local Brain Abnormalities in Patients With Transient Ischemic Attack: A Resting-State fMRI Study***
Yating Lv, Lingyu Li, Yulin Song, Yu Han, Chengshu Zhou, Dan Zhou, Fuding Zhang, Qiming Xue, Jinling Liu, Lijuan Zhao, Cairong Zhang and Xiujie Han

66 ***Clinical Applications for Diffusion MRI and Tractography of Cranial Nerves Within the Posterior Fossa: A Systematic Review***
Jonathan Shapey, Sjoerd B. Vos, Tom Vercauteren, Robert Bradford, Shakeel R. Saeed, Sotirios Bisdas and Sebastien Ourselin

87 ***An Information-Theoretic Approach to Quantitative Analysis of the Correspondence Between Skin Blood Flow and Functional Near-Infrared Spectroscopy Measurement in Prefrontal Cortex Activity***
Soheil Keshmiri, Hidenobu Sumioka, Masataka Okubo and Hiroshi Ishiguro

108 ***Detecting Microglial Density With Quantitative Multi-Compartment Diffusion MRI***
Sue Y. Yi, Brian R. Barnett, Maribel Torres-Velázquez, Yuxin Zhang, Samuel A. Hurley, Paul A. Rowley, Diego Hernando and John-Paul J. Yu

117 ***Brain Connectivity and Information-Flow Breakdown Revealed by a Minimum Spanning Tree-Based Analysis of MRI Data in Behavioral Variant Frontotemporal Dementia***
Valentina Saba, Enrico Premi, Viviana Cristillo, Stefano Gazzina, Fernando Palluzzi, Orazio Zanetti, Roberto Gasparotti, Alessandro Padovani, Barbara Borroni and Mario Grassi

133 ***Multilevel Mapping of Sexual Dimorphism in Intrinsic Functional Brain Networks***
Nina de Lacy, Elizabeth McCauley, J. Nathan Kutz and Vince D. Calhoun

152 ***Effects of Hemodynamic Response Function Selection on Rat fMRI Statistical Analyses***
Shin-Lei Peng, Chun-Ming Chen, Chen-You Huang, Cheng-Ting Shih, Chiun-Wei Huang, Shao-Chieh Chiu and Wu-Chung Shen

159 ***Quantification of Phase-Amplitude Coupling in Neuronal Oscillations: Comparison of Phase-Locking Value, Mean Vector Length, Modulation Index and Generalized-Linear-Modeling-Cross-Frequency-Coupling***
Mareike J. Hülsemann, Ewald Naumann and Björn Rasch

174 ***Diffusion MRI: Assessment of the Impact of Acquisition and Preprocessing Methods Using the BrainVISA-Diffuse Toolbox***
Lucile Brun, Alexandre Pron, Julien Sein, Christine Deruelle and Olivier Coulon

194 ***Objective and Automated Detection of Diffuse White Matter Abnormality in Preterm Infants Using Deep Convolutional Neural Networks***
Hailong Li, Nehal A. Parikh, Jinghua Wang, Stephanie Merhar, Ming Chen, Milan Parikh, Scott Holland and Lili He

206 ***Impaired Motor Skill Acquisition Using Mirror Visual Feedback Improved by Transcranial Direct Current Stimulation (tDCS) in Patients With Parkinson's Disease***
Mitsuya Horiba, Yoshino Ueki, Ippei Nojima, Yoko Shimizu, Kento Sahashi, Shogo Itamoto, Ayuko Suzuki, Gohei Yamada, Noriyuki Matsukawa and Ikuo Wada

217 ***An Integrative Way for Studying Neural Basis of Basic Emotions With fMRI***
Simeng Gu, Fushun Wang, Caiyun Cao, Erxi Wu, Yi-Yuan Tang and Jason H. Huang

229 ***Enhanced Regional Homogeneity and Functional Connectivity in Subjects With White Matter Hyperintensities and Cognitive Impairment***
Qing Ye, Xin Chen, Ruomeng Qin, Lili Huang, Dan Yang, Renyuan Liu, Bing Zhang, Feng Bai and Yun Xu

239 ***Performing Sparse Regularization and Dimension Reduction Simultaneously in Multimodal Data Fusion***
Zhengshi Yang, Xiaowei Zhuang, Christopher Bird, Karthik Sreenivasan, Virendra Mishra, Sarah Banks, Dietmar Cordes and the Alzheimer's Disease Neuroimaging Initiative

254 ***The Effects of Stimulator, Waveform and Current Direction on Intracortical Inhibition and Facilitation: A TMS Comparison Study***
Maximilian J. Wessel, Laurijn R. Draaisma, Takuya Morishita and Friedhelm C. Hummel

263 ***Transcranial Recording of Electrophysiological Neural Activity in the Rodent Brain* in vivo *Using Functional Photoacoustic Imaging of Near-Infrared Voltage-Sensitive Dye***
Jeeun Kang, Haichong K. Zhang, Shilpa D. Kadam, Julie Fedorko, Heather Valentine, Adarsha P. Malla, Ping Yan, Maged M. Harraz, Jin U. Kang, Arman Rahmim, Albert Gjedde, Leslie M. Loew, Dean F. Wong and Emad M. Boctor

277 ***A Novel Approach for Manual Segmentation of the Amygdala and Hippocampus in Neonate MRI***
Niloofar Hashempour, Jetro J. Tuulari, Harri Merisaari, Kristian Lidauer, Iiris Luukkonen, Jani Saunavaara, Riitta Parkkola, Tuire Lähdesmäki, Satu J. Lehtola, Maria Keskinen, John D. Lewis, Noora M. Scheinin, Linnea Karlsson and Hasse Karlsson

292 ***White Matter fMRI Activation Cannot Be Treated as a Nuisance Regressor: Overcoming a Historical Blind Spot***
Lukas A. Grajauskas, Tory Frizzell, Xiaowei Song and Ryan C. N. D'Arcy

296 ***Deep Learning-Based Deep Brain Stimulation Targeting and Clinical Applications***
Seong-Cheol Park, Joon Hyuk Cha, Seonhwa Lee, Wooyoung Jang, Chong Sik Lee and Jung Kyo Lee

310 ***More Reliable EEG Electrode Digitizing Methods Can Reduce Source Estimation Uncertainty, but Current Methods Already Accurately Identify Brodmann Areas***
Seyed Yahya Shirazi and Helen J. Huang

324 ***A Parallel Multiscale Filter Bank Convolutional Neural Networks for Motor Imagery EEG Classification***
Hao Wu, Yi Niu, Fu Li, Yuchen Li, Boxun Fu, Guangming Shi and Minghao Dong

333 ***Partial Least Squares Regression Performs Well in MRI-Based Individualized Estimations***
Chen Chen, Xuyu Cao and Lixia Tian

350 ***Differential tDCS and tACS Effects on Working Memory-Related Neural Activity and Resting-State Connectivity***
Kilian Abellaneda-Pérez, Lídia Vaqué-Alcázar, Ruben Perellón-Alfonso, Núria Bargalló, Min-Fang Kuo, Alvaro Pascual-Leone, Michael A. Nitsche and David Bartrés-Faz

364 ***Using Mobile EEG to Investigate Alpha and Beta Asymmetries During Hand and Foot Use***
Julian Packheiser, Judith Schmitz, Yaolu Pan, Yasmin El Basbasse, Patrick Friedrich, Onur Güntürkün and Sebastian Ocklenburg

377 ***fMRI-Targeted High-Angular Resolution Diffusion MR Tractography to Identify Functional Language Tracts in Healthy Controls and Glioma Patients***
Francesco Sanvito, Eduardo Caverzasi, Marco Riva, Kesshi M. Jordan, Valeria Blasi, Paola Scifo, Antonella Iadanza, Sofia Allegra Crespi, Sara Cirillo, Alessandra Casarotti, Antonella Leonetti, Guglielmo Puglisi, Marco Grimaldi, Lorenzo Bello, Maria Luisa Gorno-Tempini, Roland G. Henry, Andrea Falini and Antonella Castellano

394 ***The Potential of Functional Near-Infrared Spectroscopy-Based Neurofeedback—A Systematic Review and Recommendations for Best Practice***
Simon H. Kohl, David M. A. Mehler, Michael Lührs, Robert T. Thibault, Kerstin Konrad and Bettina Sorger

425 ***Adaptive Wavelet Based MRI Brain Image De-noising***
Noorbakhsh Amiri Golilarz, Hui Gao, Rajesh Kumar, Liaqat Ali, Yan Fu and Chun Li

frontiers in Neuroscience

ORIGINAL RESEARCH
published: 10 January 2019
doi: 10.3389/fnins.2018.01004

Check for updates

OPEN ACCESS

Edited by:
Amir Shmuel,
McGill University, Canada

Reviewed by:
Antonio Di Ieva,
Macquarie University, Australia
Dong-Hoon Lee,
University of Sydney, Australia
Helena Radbruch,
Charité Medical School, University of Berlin, Germany
Christoph Kleinschnitz,
University of Essen, Germany

***Correspondence:**
Michael O. Breckwoldt
michael.breckwoldt@med.uni-heidelberg.de
Björn Tews
b.tews@dkfz-heidelberg.de

†*These authors have contributed equally to this work*

‡**Present Address:**
Björn Tews,
AbbVie Deutschland GmbH & Co.KG, Wiesbaden, Germany

Specialty section:
This article was submitted to Brain Imaging Methods, a section of the journal Frontiers in Neuroscience

Received: *01 April 2018*
Accepted: *13 December 2018*
Published: *10 January 2019*

Citation:
Breckwoldt MO, Bode J, Sahm F, Krüwel T, Solecki G, Hahn A, Wirthschaft P, Berghoff AS, Haas M, Venkataramani V, von Deimling A, Wick W, Herold-Mende C, Heiland S, Platten M, Bendszus M, Kurz FT, Winkler F and Tews B (2019) Correlated MRI and Ultramicroscopy (MR-UM) of Brain Tumors Reveals Vast Heterogeneity of Tumor Infiltration and Neoangiogenesis in Preclinical Models and Human Disease. Front. Neurosci. 12:1004. doi: 10.3389/fnins.2018.01004

Correlated MRI and Ultramicroscopy (MR-UM) of Brain Tumors Reveals Vast Heterogeneity of Tumor Infiltration and Neoangiogenesis in Preclinical Models and Human Disease

Michael O. Breckwoldt[1,2†], Julia Bode[3†], Felix Sahm[4,5], Thomas Krüwel[3], Gergely Solecki[6], Artur Hahn[1], Peter Wirthschaft[3], Anna S. Berghoff[6], Maximilian Haas[1], Varun Venkataramani[6,7], Andreas von Deimling[4,5], Wolfgang Wick[6,8], Christel Herold-Mende[9], Sabine Heiland[1], Michael Platten[2,10], Martin Bendszus[1], Felix T. Kurz[1], Frank Winkler[6,8] and Björn Tews[3*‡]*

[1] *Neuroradiology Department, Heidelberg University Hospital, Heidelberg, Germany,* [2] *Clinical Cooperation Unit Neuroimmunology and Brain Tumor Immunology, German Cancer Research Center (DKFZ), Heidelberg, Germany,* [3] *Schaller Research Group at the University of Heidelberg and the German Cancer Research Center (DKFZ), Molecular Mechanisms of Tumor Invasion, Heidelberg, Germany,* [4] *Department of Neuropathology, Heidelberg University Hospital, Heidelberg, Germany,* [5] *Clinical Cooperation Unit Neuropathology, German Cancer Research Center (DKFZ), Heidelberg, Germany,* [6] *Clinical Cooperation Unit Neurooncology, German Cancer Consortium (DKTK) Within the DKFZ, Heidelberg, Germany,* [7] *Institute for Anatomy and Cell Biology, Heidelberg University, Heidelberg, Germany,* [8] *Neurology Clinic and National Center for Tumor Diseases, Heidelberg University Hospital, Heidelberg, Germany,* [9] *Division of Experimental Neurosurgery, Department of Neurosurgery, University of Heidelberg, Heidelberg, Germany,* [10] *Department of Neurology, University Medical Center Mannheim, University of Heidelberg, Mannheim, Germany*

Diffuse tumor infiltration into the adjacent parenchyma is an effective dissemination mechanism of brain tumors. We have previously developed correlated high field magnetic resonance imaging and ultramicroscopy (MR-UM) to study neonangiogenesis in a glioma model. In the present study we used MR-UM to investigate tumor infiltration and neoangiogenesis in a translational approach. We compare infiltration and neoangiogenesis patterns in four brain tumor models and the human disease: whereas the U87MG glioma model resembles brain metastases with an encapsulated growth and extensive neoangiogenesis, S24 experimental gliomas mimic *IDH1* wildtype glioblastomas, exhibiting infiltration into the adjacent parenchyma and along white matter tracts to the contralateral hemisphere. MR-UM resolves tumor infiltration and neoangiogenesis longitudinally based on the expression of fluorescent proteins, intravital dyes or endogenous contrasts. Our study demonstrates the huge morphological diversity of brain tumor models regarding their infiltrative and neoangiogenic capacities and further establishes MR-UM as a platform for translational neuroimaging.

Keywords: magnetic resonance microscopy, ultramicroscopy, brain tumor models, tumor invasion, brain clearing, glioblastoma

INTRODUCTION

Gliomas with their most malignant entity glioblastoma are highly malignant brain tumors with poor prognosis and a median survival of ∼15 months (Wen and Kesari, 2008). Gliomas are characterized by high cellular proliferation rates, induction of neoangiogenesis and a diffuse and infiltrative growth into the adjacent healthy brain (Furnari et al., 2007; Carmeliet and Jain, 2011). This infiltrative nature prevents more effective therapy because surgical resection and radiotherapy regimens are locally confined (Sahm et al., 2012; Osswald et al., 2015). Glioma invasion is also a challenge for treatment monitoring by magnetic resonance imaging (MRI) due to insufficient resolution (∼0.5 mm for most clinical scanners) and a lack of specific MRI sequences that can detect infiltrating glioma cells (Hyare et al., 2017; Smits and van den Bent, 2017).

So far, only very laboursome methods such as cryo-imaging that acquired thousands of physically tiled images allowed to visualize whole organs while also providing the resolution of single fluorescently labeled cells (Wilson et al., 2008; Qutaish et al., 2012). Yet, these methods lack dynamic and longitudinal imaging aspects important for monitoring tumor development and treatment response.

We have previously developed a correlated magnetic resonance imaging and ultramicroscopy approach (dubbed "MR-UM") to monitor glioma angiogenesis at single vessel resolution (Breckwoldt et al., 2016). Using an extended approach to monitor cellular infiltration and angiogenesis site by site we now map these key parameters by MRI and dual color ultramicroscopy in glioma models and compare our findings to an established model of brain metastases (Holland, 2001; Zhu et al., 2014; Osswald et al., 2015). We further use human specimen of brain metastases and resected gliomas (*IDH1* wildtype glioblastoma and *IDH1* mutant oligodendroglioma) to further advance our technique to the clinical arena.

For our analysis, we compared the conventional *IDH1* wildtype, *PTEN* mutant, *p14ARF,* and *p16* deleted U87MG model (Ishii et al., 1999; Chen et al., 2012) that has a PI3K/Akt pathway up-regulation as a result of high Akt expression (Koul et al., 2006; Radaelli et al., 2009) with a PDGFß-driven, *Ink4-Arf*-deleted, *Pten* wildtype RCAS/t-va model replication-Competent Avian Sarcoma-leukosis virus long-terminal repeat with splice acceptor (RCAS)-tumor virus A (TVA) gene delivery system (Hambardzumyan et al., 2009), the metastatic melanoma model (A2058) (Sherwin et al., 1979), and the *IDH1* wildtype (WT) S24 model kept under serum-free, stem-like conditions (Osswald et al., 2015).

We used fluorescent protein expression of tumor cells to map tumor infiltration and intravital dye labeling to assess angiogenesis by ultramicroscopy. MRI was performed longitudinally during tumor growth using advanced MRI techniques. MR-UM distinguished different infiltration patterns of single tumor cells and patterns of angiogenesis in mouse and human brain tumors. Our findings are that the conventional U87MG gliomas resemble human brain metastasis regarding their spherical growth and extensive neoangiogenesis, whereas the recently described S24 gliomas phenocopy human glioblastomas showing extensive infiltration into the adjacent parenchyma and along white matter tracts to the contralateral hemisphere.

METHODS

U87MG Glioma Model

The human glioma cell line U87MG was obtained from LGC Standards (Wesel, Germany) and cultured in Dulbecco's modified Eagle's medium (DMEM) containing 10% FBS, 100 U/ml penicillin and 100 µg/ml streptomycin (all from Sigma-Aldrich, Taufkirchen, Germany). Six to eight week old male NMRI nude mice were injected stereotactically with 50.000 U87MG-tdTomato cells in 2 µl PBS. Implantation was performed into the right hemisphere, 1 mm rostral and 2 mm lateral from the Bregma at a depth of 500 µm (n = 5 mice, Charles River, Sulzfeld, Germany) using a Hamilton syringe, driven by a fine step motor. Animals were anesthetized with ketamine/xylazine and unresponsive to stimuli during the intracranial injection. MRI was performed on day 16 and 28 post tumor cell implantation.

RCAS/t-va Model

DF-1 cells, a chicken fibroblast cell line, was obtained from LGC Standards and cultured in DMEM containing 10% FBS, 100 U/ml penicillin and 100 µg/ml streptomycin (all from Sigma-Aldrich) at 39°C. To model astrocytoma tumorigenesis, replication-competent avian leukosis virus with splice acceptor (RCAS) viral vectors containing PDGFß gene and *Discosoma* sp. red fluorescent protein (DsRed) were used for the transfection of cells. Nestin-Tv-a mice were anesthetized at postnatal days 5 to 8 with isoflurane (2%) and 40.000 DF-1 cells in a total volume of 1 µl PBS were injected into the brain. High grade gliomas developed 4.5 to 10 weeks after injection, albeit with low frequency (30%). Animals that developed hydrocephalus were sacrificed and excluded from the study (n = 4 mice were included in the study). MRI was performed weekly starting 5 weeks after inoculation.

S24 Model

The S24 cell line was derived as a primary glioblastoma culture from an IDH1 wildtype glioblastoma (Lemke et al., 2012). For the S24 glioma model, 50.000 S24 cells in 2 µl total volume were injected into the right basal ganglia (coordinates: 1 mm rostral and 2 mm lateral from the Bregma at a depth of 2 mm) in 8–10 week old male NMRI nude mice (Charles River, n=6 mice). Cells were cultivated under serum-free conditions in DMEM-F12 as sphere cultures supplemented with 2% B-27 (Thermo Fisher Scientific Inc., Waltham, MA, USA), 5 µg/ml human insulin (Sigma-Aldrich), 12.8 ng/ml heparin (Sigma-Aldrich), 0.4 ng/ml EGF (R&D Systems Inc., Minneapolis, MN, USA), and 0.4 ng/ml FGF (Thermo Fisher Scientific). MRI was performed on day 27, 48, 70, 84, 91 after tumor cell implantation.

A2058 Brain Metastasis Model

The amelanotic melanoma cell line A2058 (obtained from the ATCC-CRL-11147, 07/2011) was cultivated under standard

condition in DMEM media containing 10% FBS, 100 U/ml penicillin and 100 µg/ml streptomycin (all from Sigma-Aldrich). Cells underwent 4 *in vivo* passages to increase the brain metastatic potential as previously described (Osswald et al., 2016). A cytoplasmic RFP-tdTomato, LeGo-T2 vector (kind gift from A. Trumpp, German Cancer Research Center) was used for transfection and generation of a fluorescent cell line. 500.000 cells in 100 µl PBS were injected in the left ventricle of the mouse ($n =$ 5 mice). Animals were monitored weekly by MRI starting 2 weeks after intracardial tumor cell injection.

All cell lines were routinely tested for contamination by the multiplex cell contamination test (Schmitt and Pawlita, 2009). The test detects 28 potential cell culture contamination such as mycoplasma (14 different species), Epstein-Barr Virus and 14 possible cross contaminations with cells of human, mouse etc origin. Animal experiments were approved by the regional animal welfare committee (permit numbers: G8/14 and G189/12, Regierungspräsidium Karlsruhe, Germany).

Human Brain Metastasis Samples

Two human brain metastases samples from a lung adenocarcinoma were obtained during routine pathological autopsy and written informed consent was obtained. Brain tissue blocks (∼2 × 2 × 2 cm) included metastatic sites from the cerebellum and cortex. Tissue blocks were subjected to high resolution *ex vivo* MRI and subsequent clearing and ultramicroscopy. Additional tissue sections were stained for H&E, CD31, and cytokeratin AE1/AE3 using routine histopathological processing.

Human Glioma Samples

One glioblastoma and one oligodendroglioma tissue block were obtained during surgical resection (∼1 × 1 × 1 cm; glioblastoma: *IDH1* wildtype; oligodendroglioma: *IDH1* R132H mutation, 1p19q co-deletion). Use of patient material was approved by the Institutional Review Board at the Medical Faculty Heidelberg and written informed consent was obtained from all patients included in the study (ethics approval: 005/2003). Tissue was immediately transferred to 4% PFA and tissue blocks were subjected to high resolution *ex vivo* MRI and subsequent clearing and ultramicroscopy. MR images of the respective patient was acquired 1 day prior to surgery using routine clinical MRI sequences on a 3 Tesla MRI system (Siemens, Erlangen, Germany). Additional tissue sections were stained for H&E, CD31, and IDH1R132H using routine histopathological processing.

MR Imaging

MR imaging was performed on a 9.4 Tesla horizontal bore small animal NMR scanner (BioSpec 94/20 USR, Bruker BioSpin GmbH, Ettlingen, Germany) and performed as previously described (Breckwoldt et al., 2016). Briefly, a standard RARE T2-w and T1-w post-Gd-contrast sequence was used to monitor tumor volume (T2-w parameters: 2D sequence, TE: 33 ms, TR: 2,500 ms, flip angle: 90°, acquisition matrix: 200 x 150, number of averages: 2, slice thickness: 700 µm duration: 2 min 53 s; T1-w parameters: TE: 6 ms, 1,000 TR: ms, flip angle: 90°, acquisition matrix: 256 x 256, number of averages: 2, slice thickness: 500 µm, duration: 5 min). We also used a 3D T2-w sequence: TE 33 ms; TR: 1,800 ms; flip angle: 90°; acquisition matrix: 200 × 200; number of averages: 1; in plane resolution: 100 µm; duration: 10 min 48 s. The T1-w parameters were as follows: 3D sequence: TE: 1.9 ms; TR: 5 ms; flip angle: 60°; acquisition matrix: 128 × 128; number of averages: 4; in-plane resolution: 156 µm; duration: 5 min 28 s. To assess the tumor vasculature we used a T2*-w, gradient echo sequence (Park et al., 2008) and acquired pre- and post-contrast scans (3D sequence, 80 µm isotropic resolution, TE: 18 ms; TR: 50 ms; flip angle: 12°; number of averages: 1, acquisition matrix: 400 x 400, duration: 15 min 40 s). Pre-contrast images were used to differentiate susceptibility artifacts caused e.g., by tumor microbleedings from vessel signals that were only detectable after contrast administration. Dynamic contrast enhanced imaging (DCE) was used to assess vascular permeability (K_{trans}) (TE: 1.8 ms; TR: 16 ms; flip angle: 10°; slice thickness: 700 µm, acquisition matrix: 66 × 128, 3 slices acquired, number of averages: 1, 300 repetitions; 700 µm in plane resolution; duration: 6 min, time resolution 2 s). 0.2 mmol/kg Gd-DTPA-BMA (Omniscan, Nycomed, Ismaningen, Germany) was administered by tail vein injection for DCE and post-contrast scans. For MR imaging, animals were anesthetized with 1–2% isoflurane and kept on a heating pad. Respiration was monitored externally with a surface pad controlled by an in house developed LabView program (National Instruments Corporation, Austin, USA).

Image Processing and Analysis of MRI Data

The tumor volume was quantified in Osirix software (V.4.12, Pixmeo, Geneva, Switzerland) by manually selecting ROIs around the tumor outline on T2-w images. Segmentation of vessels was performed on T2*w images based on the typical tubular hypointense structure using AMIRA (Thermo Fisher Scientific, Hillsboro, USA). Quantification of DCE timeseries was performed in FIJI by ROI analysis of the entire tumor area. Intensity values were measured and processed in Microsoft Excel (Microsoft, USA). Signals were normalized to the time period before contrast administration (S/S_0) and displayed as "permeability" (arbitrary units, a.u.).

Labeling of the Microvasculature

For labeling of the microvasculature, animals were injected with fluorescent lectins that bind to N-acetyl-β-D-glucosamine oligomers of endothelial cells (Wälchli et al., 2015; Breckwoldt et al., 2016). Isolectin-FITC or lectin texas-red (12 mg/kg, Sigma-Aldrich or Vector Laboratories, Burlingame, CA USA) was injected iv in 100 µl PBS after the last MRI. Animals were sacrificed 5 min after lectin injection by a ketamine/xylazine overdose and transcardially perfused with 20 ml PBS followed by 20 ml 4% PFA (Histofix, Carl Roth, Karlsruhe, Germany).

Fixation and Clearing of Mouse and Human Samples

Mouse brains were fixed after perfusion with 4% PFA for 24 h and stored in PBS at 4°C in the dark. For UM-analysis whole

brains were optically cleared using the FluoClearBABB protocol (Schwarz et al., 2015; Alves et al., 2016; Breckwoldt et al., 2016). The protocol is based on benzyl alcohol/benzyl benzoate clearing in combination with a basic pH. For the dehydration of brains analytical grade alcohol (t-butanol, Sigma-Aldrich) was diluted with double-distilled water. Brains were dehydrated using t-butanols ranging from 30 to 100%. The clearing solution BABB was prepared by mixing benzyl alcohol (Merck, analytical grade) and benzyl benzoate (Sigma-Aldrich, "purissimum p.A." grade) in a 1:2 volume ratio. The pH levels of dehydration and clearing solutions were adjusted using an InLab Science electrode suited for organic solvents (Mettler-Toledo, Columbus, Ohio, United States). pH levels were adjusted with triethylamine (Sigma-Aldrich). BABB cleared samples were stable over time and showed no apparent decrease in fluorescence signal. Samples were kept in BABB at 4°C in the dark. The stability allowed re-imaging of the sample over time. Bleaching of samples was also not a major issue.

For clearing of human samples, we used the iDISCO+ protocol (Renier et al., 2014). The working distance of the objective is 1 cm. Therefore, we needed to trim human tissue blocks to the appropriate size ($\sim$0.5–1cm^3) in order to place the sample under the objective.

Acquisition and Analysis of Ultramicroscopy Data Sets

Cleared brains were scanned with a light sheet microscope (LaVision BioTec GmbH, Bielefeld, Germany). We used a magnification of 1.0x and 2.0x with a 2x objective lens and a white light laser (SuperK EXTREME 80 mHz VIS; NKT Photonics, Cologne, Germany). For lectin stained vessels, the following filters were used: lectin-FITC, excitation 470/40 nm; emission 525/50 nm; lectin-texas red excitation 545/25; emission 585/40. Z-stacks of 5 µm step size and a total range of 1,500–2,000 µm for transversal measurement of whole brains were acquired. The resolution of our light sheet microscope setup is 6 × 6 µm with a lightsheet thickness of 2 µm. In comparison to MRI this is at least a 13-fold higher resolution (our T2* sequence has an isotropic resolution of 80 µm). The method allows to image single tumor cells invading into the adjacent parenchyma or microvessels that are $\sim$5 µm in diameter. Images were exported as tagged image file (tif) and further processed in ImageJ package FIJI, version 1.49 (http://fiji.sc/Fiji). Segmentation of fluorescent tumor cells or the microvasculature in the ultramicroscopy datasets was performed with Ilastik (Haubold et al., 2016). Segmentation was done in a supervised, semiautomated fashion.

Histology

After fixation, S24-tdTomato tumor-bearing brains were coronally cut into 100 µm sections with a vibratome (Sigmann Elektronik, Hüffenhardt, Germany). Sections were permeabilized with 0.2% TX100 for 3 h, stained with DAPI (Vectorshield, Vector Laboratories) and mounted on coverslips. Images were acquired on a confocal laser-scanning microscope (Leica SP8, Leica, Germany) using a immersion oil objective with a 63-fold magnification (numeric aperture = 1.4). Images were acquired as tile scans at a pixel size of 141 and 300-nm z steps within a field of view of 655.92 × 920.07 µm.

Statistical Analysis

Data is shown as mean ± S.E.M in graphs or mean ± S.D. with 95% confidence interval (C.I.) in results section. Statistical analyses were performed in PRISM (GraphPad La Jolla, USA). Two-tailed student's *t*-tests were used to compare two groups. One-way ANOVA with Bonferroni's *post-hoc* testing was used for multiple comparisons. *p*-values < 0.05 were considered significant, $^*p < 0.05$; $^{**}p < 0.01$; $^{***}p < 0.001$.

RESULTS

U87MG Mouse Tumors Show Intratumoral Heterogeneity

To assess the capability to perform dual color MR-UM we employed the U87MG tumor model to visualize tumor cells (U87MG-tdTomato) and the microvasculature (lectin-FITC) concomitantly. We monitored U87MG tumors longitudinally by MRI and imaged mice at day 16 and 28 after tumor implantation into the right cortex. MRI after gadolinium (Gd)-contrast administration showed the expected rapid growth with blood-brain barrier disruption (BBB-D, tumor volume day 16: 1.3 µl ± 0.58 vs. day 28: 5.4 µl ± 3.0; CI: 0.92 to 7.2; $p = 0.02$; **Figures 1A,B**). Dynamic contrast-enhanced imaging showed a progressive increase of vascular permeability during the course of tumor progression, suggestive of ongoing neoangiogenesis ($p < 0.05$, **Figure 1C**). Tumor vessels were also discernible by T2*-w imaging following Gd-contrast administration as hypointense tubular structures in parts of the tumor core (**Figure 1D**).

After the completion of MR measurements animals were injected with lectin-FITC for microvasculature labeling and subjected to brain clearing using the FluoClearBABB protocol (Schwarz et al., 2015). Unexpectedly, ultramicroscopy showed intratumoral heterogeneity with areas of increased tumor cell density and pathological vascularization in some parts of the tumor, whereas adjacent tumorous areas exhibited markedly less tumor cells and only few neovessels (**Figures 1E,F**). As expected U87MG tumors grew bulky with a clear separation of the tumor from the adjacent healthy parenchyma (**Figure 1F**).

RCAS Tumors Are Highly Angiogenic and Show Multiple Intratumoral Microbleedings

To further dissect infiltration patterns in a more recently described autochthonous glioma model we used the RCAS/t-va system. RCAS tumors grew initially slow and were only visible by MRI at 3 to 4 weeks after virus transduction (**Figure 2A**). At this early timepoint no microbleedings were detectable on T2*. However, upon initial tumor detection by MRI, tumors grew rapidly with massive angiogenesis, blood-brain barrier disruption and the development of intratumoral microbleedings at the tumor-brain parenchyma border as visualized by T2* and DCE imaging (early tumor volume: 3.1 µl ± 2.2 vs late tumor volume: 23.5 µl ± 20.0; CI: −4.1 to 45; $p < 0.05$; **Figures 2B–D**). Contrary to our expectation we did not find apparent infiltrative growth

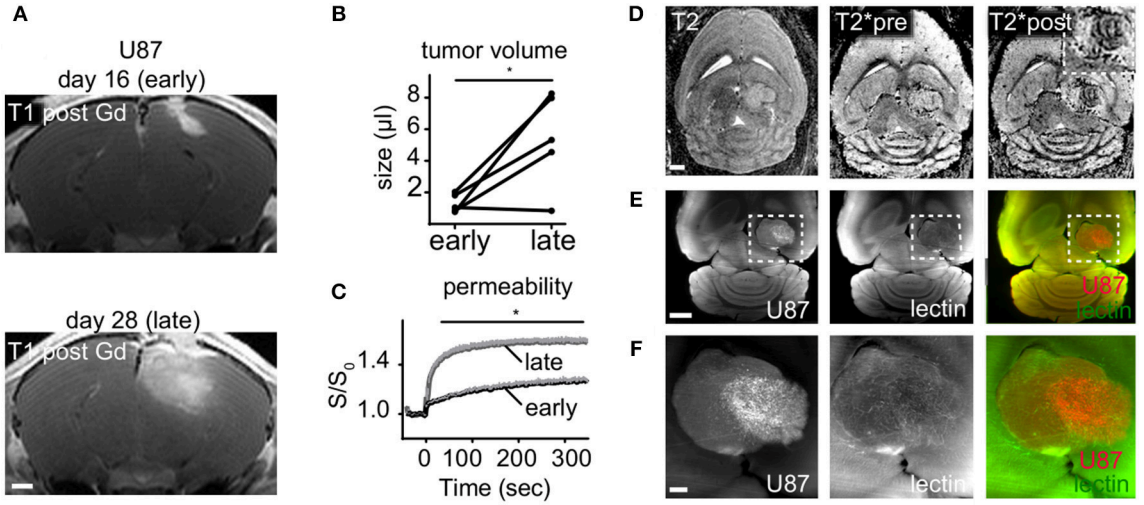

FIGURE 1 | MR-UM of U87MG shows tumor heterogeneity. T1-w images post Gd-contrast application of U87MG tumors 16 days (early) and 28 days (late) after cortical tumor inoculation ($n = 5$ mice; **A**). Tumor volume quantification **(B)**. Dynamic contrast enhanced imaging shows vascular permeability over time **(C)**. T2-w, T2* pre and after Gd-contrast application **(D)**. Inset in the upper right corner shows that only the lateral tumor compartment exhibits hypointense tubular vessels. Ultramicroscopy performed after tissue clearing of DS-red labeled U87MG tumor cells and lectin-FITC labeled vessels **(E)**. Magnified images depict two compartments of the bulk tumor **(F)**. Images in **(F)** are maximum intensity projections. Scale bars are 1 mm in **(A,D,E)**, and 100 µm in **(F)**. $^*p < 0.05$.

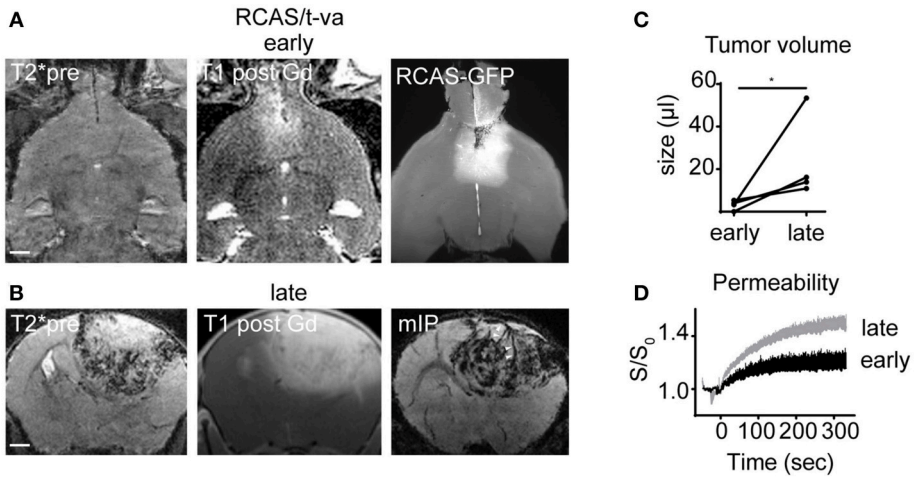

FIGURE 2 | MR-UM of RCAS/t-va tumors. Representative T2*, T1 post and ultramicroscopy image at an early tumor stage ($n = 4$ mice; **A**). Lower row shows T2*, T1 post and minimum intensity projection (mIP) at a late tumor stage **(B)**. Quantification of tumor volume **(C)** and dynamic contrast enhanced imaging **(D)**. Arrowheads in mIP indicate tumor vessels. Scale bars in **(A,B)** are 1 mm. $^*p < 0.05$.

of RCAS/t-va tumors on ultramicroscopy but rather a clearly defined tumor-parenchyma border (**Figure 2A**).

S24 Tumors Grow Slowly Over Time and Diffusely Infiltrate Into the Adjacent Brain Using White Matter Tracts as Guide Structures

S24 gliomas are patient derived, glioma stem-like cells that have been recently described by our group (Osswald et al., 2015). S24 xenografts form large networks of interconnected tumor cells that use tumor microtubes for intercellular signaling and equilibration of the network, thus mediating resistance against radiochemotherapy (Jung et al., 2017; Weil et al., 2017). We implanted S24 tumors in the midbrain and performed MRI measurements longitudinally 4, 6, 10, 12, and 13 weeks after tumor implantation. Tumors were detected by MRI around week 10 and behaved markedly different than U87MG or RCAS/t-va tumors. MRI changes were only apparent on T2w imaging with subtle T2 hyperintensity and a progressing mass effect, whereas there was no obvious neoangiogenesis nor intratumoral microbleedings and only marginal blood-brain barrier disruption, (**Figures 3A–E**). After brain clearing, however, the full extent of diffuse tumor

infiltration became apparent. Defined tumor-brain parenchyma borders were missing and infiltration followed white matter structures, such as the corpus callosum or the posterior commissure (**Figures 3F,G**, **Supplementary Movies 1–3**). There was also profound infiltration into the basal ganglia and to the contralateral hemisphere, showing a mass effect and increased fluorescence intensity caused by tdTomato expressing S24 cells in the basal ganglia and cortex (**Figures 3H,I**). To further visualize tumor microtubes and interconnected tumor cells, we performed confocal microscopy of S24 vibratome sections which confirmed the spread of tdTomato-labeled S24 cells throughout the entire hemisphere (**Figure 3J**).

The Melanoma Brain Metastasis Model A2058 Shows Rapid, Encapsulated Growth Without Infiltration

To further complete the picture of brain tumor lesions, we performed experiments in a mouse melanoma metastasis model. After intracardial injection of A2058 melanoma cells, metastases developed in a seemingly random fashion mainly in cerebral hemispheres and at the basal entry points of the large brain supplying arterial vessels (**Supplementary Figures 1A,B**). Metastases grew agressively within 1 week after the first detection by MRI with severe BBB-D and neovessel formation, as depicted by T2* imaging and ultramicroscopy after lectin-FITC injection (early tumor volume: 1.3 µl ± 1.2 vs. late tumor volume: 18.3 µl ± 15.3; CI: −1.4 to 35.3; $p = 0.03$; **Supplementary Figures 1C–E**). The growth pattern was restricted to an encapsulated form without apparent infiltration.

Human Brain Metastasis Show an Encapsulated Growth Pattern

To investigate the translatability of the MR-UM approach we obtained autopsy material from a patient with a lung adenocarcinoma that had formed several cerebral metastases. We performed MRI of two excised tissue blocks (∼2 cm^3) from the cerebellum and cortex that showed the presence of subcortical metastases within the subcortical white matter (**Figures 4A,B**). Metastases had a sharp demarcation from the surrounding healthy tissue on MRI and ultramicroscopy (**Supplementary Figures 2A,B**) and stained positive for cytokeratin AE1/AE3 by immunohistochemistry (**Supplementary Figures 2C,D**).

Human Glioblastoma Shows an Invasive Growth Without Clear Separation From the Healthy Parenchyma and Is Highly Angiogenic

We further employed the MR-UM approach to investigate intraoperatively obtained resection material from two glioma patients, one with a glioblastoma (WHO grade IV, *IDH1* wildtype) and one with an oligodendroglioma (WHO grade II, *IDH1* mutant). The glioblastoma showed prominent neoangiogenesis which was already apparent as tubular hypointensities on SWI images acquired before resection (**Figure 4C**). The high amount of angiogenesis was confirmed by *ex vivo* MRI of the resected specimen (**Figure 4D**). For correlative ultramicroscopy we relied on endogenous tissue contrast. Interestingly, the pathological blood vessel network of glioblastoma could be visualized by fluorescent, intravascular erythrocytes within tumor blood vessels (**Figures 4E,F**). Tumor vessels could also be easily segmented both from *ex vivo* MRI based on tubular T2* hypointense structures as well as from form ultramicroscopy data (**Figure 4G**, **Supplementary Movie 4**). H&E histology showed the typical morphology of glioblastoma and confirmed multiple pathological neovessels on CD31 immunohistochemistry (**Figure 4H**).

In contrast, neoangiogenesis was not apparent in an *IDH1* mutant oligodendroglioma specimen. Before resection, MRI showed T2 hyperintense areas but no Gd-contrast enhancement nor intratumoral susceptibility signals (**Supplementary Figure 3A**). The less aggressive phenotype was also confirmed by *ex vivo* MRI, ultramicroscopy and immunohistochemistry that did not detect pathological neovessels (**Supplementary Figures 3B–D**).

DISCUSSION

Glioblastoma is characterized by diffuse tumor infiltration into the adjacent healthy parenchyma and the formation of pathological neovessels. In order to assess these key features, we extended our recently established correlated magnetic resonance and ultramicroscopy (MR-UM) approach to now visualize angiogenesis and tumor invasion concomitantly. We further show as a proof of concept the applicability of our platform to clinical samples. We employed different brain tumor models as well as human glioma and brain metastases samples and find major heterogeneity regarding their degree of neoangiogenesis and growth pattern. MR-UM uses the strength of MRI and ultramicroscopy, namely longitudinal *in vivo* imaging by MRI and the high resolution of ultramicroscopy combined with fluorescent genetic and intravital dye labeling. Additionally, both techniques result in 3D datasets of the entire, intact organ. Spatial information and growth dynamics are important aspects of tumor biology that get lost in the plethora of genetic and epigenetic studies that are currently revolutionizing the field (Jones et al., 2012; Plaisier et al., 2016; Northcott et al., 2017). By applying MR-UM we are able to compare established preclinical models of glioma and brain metastases with the human diseases to determine different biological features of the model. We find that the S24 tumor model showed a highly invasive growth without apparent ongoing neoangiogenesis. In contrast to classical glioma models like Gl261 or U87MG which behave more like brain metastasis, S24 tumors grow slowly and much less angiogenic. Thus, S24 could enable investigations into the infiltrative nature of the disease, a feature that conventional glioma models show only to a limited degree.

We further establish MR-UM on clinical samples. *IDH1* WT glioblastomas display an aggressive behavior with tumor infiltration along white matter structures and the formation of neovessels (Chen et al., 2012). Both aspects can be visualized by MR-UM. We made use of the endogenous contrast of red blood cells to visualize the vascularization, a feature that was also apparent by T2*-w MRI. In contrast, brain metastasis in a preclinical model and human metastases specimen showed an

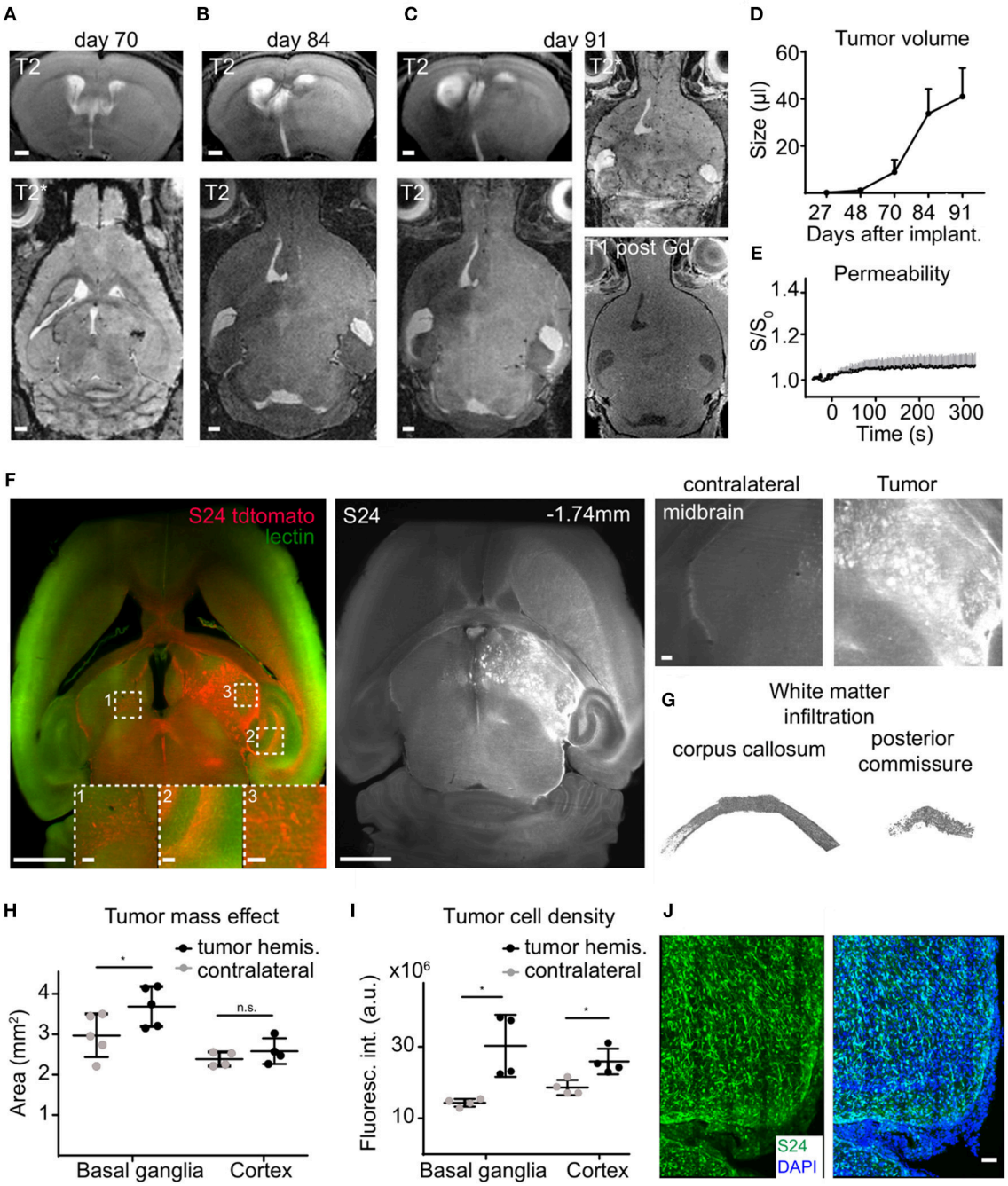

FIGURE 3 | S24 tumors show a diffuse infiltration in the adjacent brain parenchyma. Longitudinal T2w images of S24 tumors at day 70 **(A)**, 84 **(B)**, and 91 **(C)** after tumor cell implantation into the midbrain ($n = 6$ mice). S24 tumors do not show intratumoral susceptibility changes nor Gd-contrast enhancement **(C)**. Quantification of tumor size based on T2 hyperintense areas **(D)** and vascular permeability as assessed by DCE MRI **(E)**. Ultramicroscopy image of S24 tdTomato cells labeled with lectin FITC **(F)**. S24 tumor spread occurs throughout the injected hemisphere and to the contralateral site. Magnified images of the midbrain, hippocampus, and contralateral hemisphere illustrate tumor cell invasion. Segmentation of single S24 tumor cells (depicted in gray) in the corpus callosum and in the posterior commissure **(G)**. Quantification of the total area **(H)** and fluorescence intensity **(I)** of the basal ganglia and the cortex illustrates the mass effect and volume increase caused by the tumor. Confocal micrograph (recorded as composite image, tile scan) of an S24 tumor section **(J)**. Scale bars are 1 mm in **(A–C)**, 50 µm in **(J)** and 1 mm in **(F)** (100 µm in magnified images). *$p < 0.05$.

encapsulated growth and strong angiogenesis similar to U87MG glioma cells.

Our study builds on existing work that has demonstrated the importance of neoangiogenesis in glioblastoma and its association with overall survival (Birner et al., 2003; Jain et al., 2007; Plate et al., 2012). Also, previous techniques were developed to automatically quantify the microvessel architecture of glioblastoma using fractal-based histopathology (Di Ieva

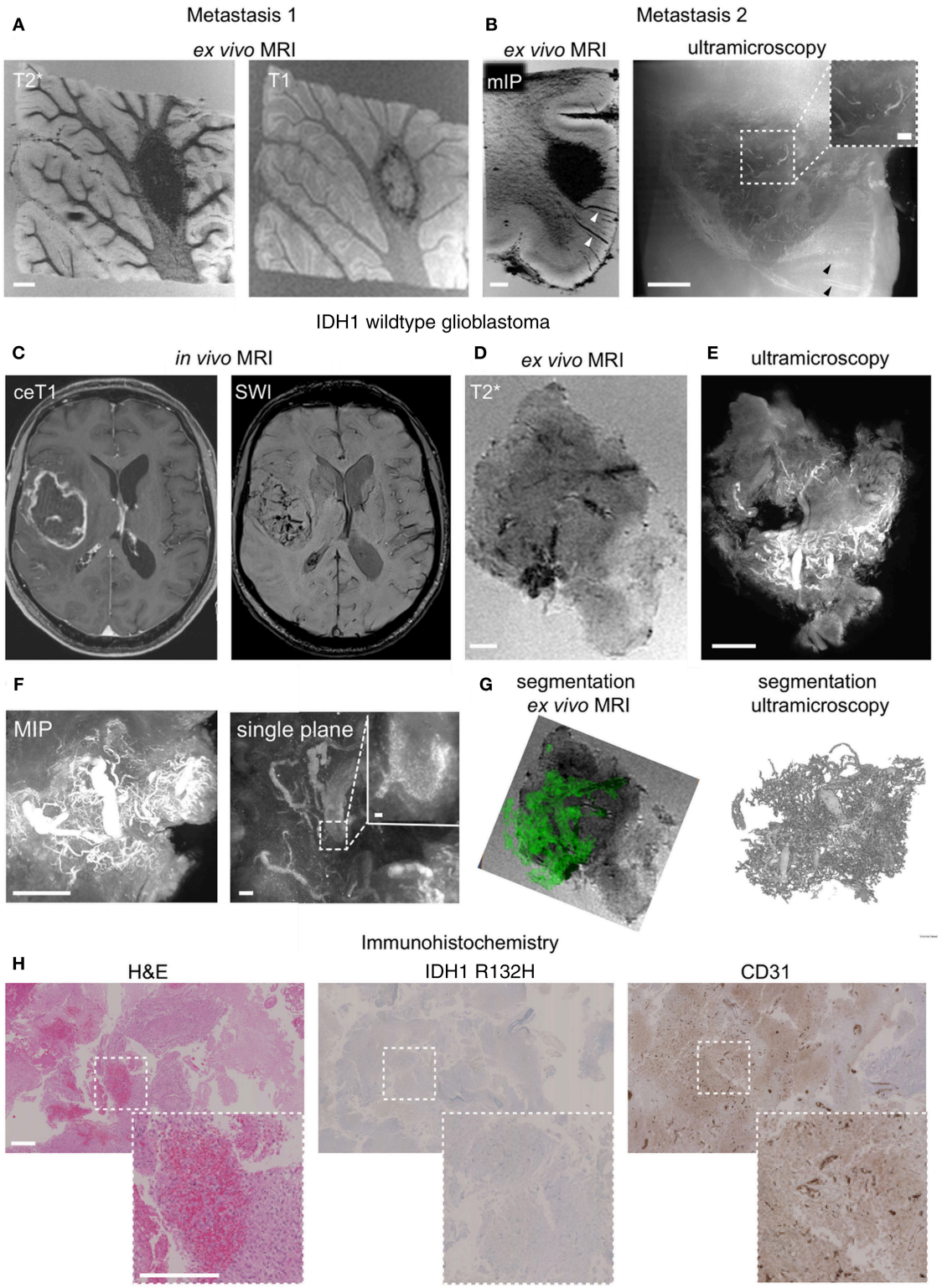

FIGURE 4 | MR-UM of human brain metastasis and glioblastoma. T2* and T1-w images of a human brain metastasis in the cerebellar white matter **(A)**. Depiction of a subcortical metastasis by T2*, shown as minimum intensity projection, mIP to illustrate hypointense tumor draining vessels (arrowhead) and ultramicroscopy **(B)**. *In vivo* MRI of human glioblastoma (*IDH1* wildtype) patient and after specimen resection **(C,D)**. Ultramicroscopy shows the Tortuous tumor vessel network **(E)**. Magnified image shows single, autofluorescent erythrocytes recorded in the red channel as the source of vascular contrast **(F)**. Segmentation of tumor vessels from *ex vivo* MRI and ultramicroscopy **(G)**. H&E staining of paraffin section, IDH1R132H and CD31 immunohistochemistry **(H)**. MIP: maximum intensity projection. Scale bars are 1 mm in **(A–E,H)**, and 50 μm in **(F)** (200 μm in inset in **B** and 10 μm in inset in **F**).

et al., 2011). However, such analyses were restricted to tissue sections, thus loosing the inherent complex 3D-architecture of microvessels. Elegant *in vivo* imaging approaches for vasculature mapping and therapeutic response assessment have involved MR imaging (de Oliveira et al., 2017), optical frequency domain imaging (Vakoc et al., 2009) and intravital microscopy (Farrar et al., 2010; Fukumura et al., 2010). Such techniques are powerful to dissect dynamic processes in the tumor microenvironment and can e.g., delineate treatment effects and elucidate underlying mechanisms. Intravital imaging is however restricted to a depth penetration of ∼1 mm below the cortical surface. In contrast optical clearing can assess alterations in the microvasculature and tumor cell invasion in the entire unsectioned brain (Breckwoldt et al., 2016; Lagerweij et al., 2017).

Limitation of our study include the following: human brain tumor samples that are obtained from resections are difficult to register to pre-surgical imaging. This would be possible in stereotactic interventions. However, the tissue geometry and composition changes upon resection. Also, investigations of human samples are not amenable to genetic or intravital dye labeling. Therefore, we relied on endogenous contrast mechanisms such as red blood cells which allowed for delineation of the tumor vasculature. We also tested the recently published iDISCO protocol and proposed antibodies (Renier et al., 2014) for immunohistochemistry to label whole tissue blocks. This would expand possible labels and would be highly desirable. This resulted however in unspecific labeling of the secondary antibody and was difficult to separate from endogenous red blood cell signal (data not shown).

In summary, MR-UM shows the capability to depict hallmarks of brain tumors and brain metastasis in the preclinical and clinical setting. We envision MR-UM as a monitoring platform for the development of drugs targeting tumor invasion and neoangiogenesis. MR-UM can be used for both basic mechanistic and therapeutical studies, thus serving as a tool for the neuro-oncological and neuroscience community.

AUTHOR CONTRIBUTIONS

MOB, JB, TK, PW, FW, and BT conceived the experiments. JB, TK, AB, and GS performed tumor injections. MOB, SH, and MH performed MR imaging experiments. MOB, JB, FS, and VV performed histology. FS, AvD, and CH-M processed human material. AH and FK provided analytical tools. MOB, AH, and FK performed data post processing. JB and TK performed UM. MOB and JB analyzed the data. MOB, JB, WW, MP, MB, FW, and BT interpreted the experiments and wrote the paper with input from all co-authors.

ACKNOWLEDGMENTS

We thank Manuel Fischer for excellent support of MRI measurements and Alexander Sommerkamp for experimental help. We acknowledge support from the DKFZ Light Microscopy Core Facility. We acknowledge financial support by Deutsche Forschungsgemeinschaft within the funding programme Open Access Publishing, by the Baden-Württemberg Ministry of Science, Research and the Arts and by Ruprecht-Karls-Universität Heidelberg. AB received a Schrödinger scholarship of the Austrian science fund. FK was supported by the German Research Foundation (DFG KU 3555/1-1). MOB and FK were supported by a physician-scientist fellowship of the Medical Faculty, University of Heidelberg and by the Hoffmann-Klose Foundation (University of Heidelberg). MOB acknowledges funding by the Novartis Foundation and the Else Kröner-Fresenius Stiftung (2017-A25). This study was further funded by the Chica and Heinz Schaller Stiftung (CHS, to BT) and the BMBF (e:Med Juniorverbuende in der Systemmedizin: SUPR-G, file number 01ZX1401A (to BT).

SUPPLEMENTARY MATERIAL

The Supplementary Material for this article can be found online at: https://www.frontiersin.org/articles/10.3389/fnins.2018.01004/full#supplementary-material

Supplementary Figure 1 | MRI of a metastasis at the skull base in the A2058 melanoma model ($n = 5$ mice; **A**). Quantification of the tumor volume **(B)** and permeability **(C)**. MRI of a subcortical metastasis over time (early and late stage) **(D)**. T2* after contrast administration and correlated ultramicroscopy image illustrate neovessel formation **(E)**. Scale bars are 1 mm in **(A,B)**, 100 μm in **(C,D)** and 20 μm in insets.

Supplementary Figure 2 | *Ex vivo* MRI of a cerebellar metastasis **(A)** and ultramicroscopy **(B)**. H&E staining of paraffin section **(C)** and immunohistochemistry for the cytokeratin marker A1/A3 **(D)**. Scale bars are 2 mm in **(A)** and 200 μm in **(B)**.

Supplementary Figure 3 | *In vivo* MRI of human oligodendroglioma (*IDH1* mutant) patient and after specimen resection **(A,B)**. Ultramicroscopy the brain/tumor architecture without apparent tissue distortion or neovascularization. (Auto-) fluorescent signals are caused by red blood cells **(C)**. H&E staining of paraffin section, IDH1R132H and CD31 immunohistochemistry **(D)**. ceT1: Gd-contrast enhanced T1-weighted image. SWI: susceptibility weighted imaging. Scale bars are 1 mm in **(B,D)** and 100 μm in **(C)** and magnified images in **(D)**.

Supplementary Movie 1 | Ultramicroscopy of S24-tdTomato tumors shows the extent of tumor infiltration.

Supplementary Movie 2 | Segmentation of the corpus callosum showing S24 glioma infiltration.

Supplementary Movie 3 | Segmentation of the posterior commissure showing S24 glioma infiltration along the white matter.

Supplementary Movie 4 | Segmentation of tumor vessels in a human IDH1 wildtype glioblastoma specimen.

REFERENCES

Alves, S., Bode, J., Bemelmans, A.-P., von Kalle, C., Cartier, N., and Tews, B. (2016). Ultramicroscopy as a novel tool to unravel the tropism of AAV gene therapy vectors in the brain. *Sci. Rep.* 6:28272. doi: 10.1038/srep28272

Birner, P., Piribauer, M., Fischer, I., Gatterbauer, B., Marosi, C., Ambros, P. F., et al. (2003). Vascular patterns in glioblastoma influence clinical outcome and associate with variable expression of angiogenic proteins: evidence for distinct angiogenic subtypes. *Brain Pathol.* 13, 133–143. doi: 10.1111/j.1750-3639.2003.tb00013.x

Breckwoldt, M. O., Bode, J., Kurz, F. T., Hoffmann, A., Ochs, K., Ott, M., et al. (2016). Correlated magnetic resonance imaging and ultramicroscopy (MR-UM) is a tool kit to assess the dynamics of glioma angiogenesis. *Elife* 5:e11712. doi: 10.7554/eLife.11712

Carmeliet, P., and Jain, R. K. (2011). Molecular mechanisms and clinical applications of angiogenesis. *Nature* 473, 298–307. doi: 10.1038/nature10144

Chen, J., McKay, R. M., and Parada, L. F. (2012). Malignant glioma: lessons from genomics, mouse models, and stem cells. *Cell* 149, 36–47. doi: 10.1016/j.cell.2012.03.009

de Oliveira, E. A., Lazovic, J., Guo, L., Soto, H., Faintuch, B. L., Akhtari, M., et al. (2017). Evaluation of magnetonanoparticles conjugated with new angiogenesis peptides in intracranial glioma tumors by MRI. *Appl. Biochem. Biotech*. 183, 265–279. doi: 10.1007/s12010-017-2443-2

Di Ieva, A., Grizzi, F., Sherif, C., Matula, C., and Tschabitscher, M. (2011). Angioarchitectural heterogeneity in human glioblastoma multiforme: a fractal-based histopathological assessment. *Microvasc. Res.* 81, 222–230. doi: 10.1016/j.mvr.2010.12.006

Farrar, C. T., Kamoun, W. S., Ley, C. D., Kim, Y. R., Kwon, S. J., Dai, G., et al. (2010). *In vivo* validation of MRI vessel caliber index measurement methods with intravital optical microscopy in a U87 mouse brain tumor model. *Neuro Oncol.* 12, 341–350. doi: 10.1093/neuonc/nop032

Fukumura, D., Duda, D. G., Munn, L. L., and Jain, R. K. (2010). Tumor microvasculature and microenvironment: novel insights through intravital imaging in pre-clinical models. *Microcirculation* 17, 206–225. doi: 10.1111/j.1549-8719.2010.00029.x

Furnari, F. B., Fenton, T., Bachoo, R. M., Mukasa, A., Stommel, J. M., Stegh, A., et al. (2007). Malignant astrocytic glioma: genetics, biology, and paths to treatment. *Genes Dev.* 21, 2683–2710. doi: 10.1101/gad.1596707

Hambardzumyan, D., Amankulor, N. M., Helmy, K. Y., Becher, O. J., and Holland, E. C. (2009). Modeling adult gliomas using RCAS/t-va technology. *Transl. Oncol.* 2, 89–95. doi: 10.1593/tlo.09100

Haubold, C., Schiegg, M., Kreshuk, A., Berg, S., Koethe, U., and Hamprecht, F. A. (2016). Segmenting and tracking multiple dividing targets using ilastik. *Adv. Anat. Embryol. Cell Biol.* 219, 199–229. doi: 10.1007/978-3-319-28549-8_8

Holland, E. C. (2001). Gliomagenesis: genetic alterations and mouse models. *Nat. Rev. Genet.* 2, 120–129. doi: 10.1038/35052535

Hyare, H., Thust, S., and Rees, J. (2017). Advanced MRI techniques in the monitoring of treatment of gliomas. *Curr. Treat. Opt. Neurol.* 19: 11. doi: 10.1007/s11940-017-0445-6

Ishii, N., Maier, D., Merlo, A., Tada, M., Sawamura, Y., Diserens, A. C., et al. (1999). Frequent co-alterations of TP53, p16/CDKN2A, p14ARF, PTEN tumor suppressor genes in human glioma cell lines. *Brain Pathol.* 9, 469–479. doi: 10.1111/j.1750-3639.1999.tb00536.x

Jain, R. K., di Tomaso, E., Duda, D. G., Loeffler, J. S., Sorensen, A. G., and Batchelor, T. T. (2007). Angiogenesis in brain tumours. *Nat. Rev. Neurosci.* 8, 610–622. doi: 10.1038/nrn2175

Jones, D. T. W., Jäger, N., Kool, M., Zichner, T., Hutter, B., Sultan, M., et al. (2012). Dissecting the genomic complexity underlying medulloblastoma. *Nature* 488, 100–105. doi: 10.1038/nature11284

Jung, E., Osswald, M., Blaes, J., Wiestler, B., Sahm, F., Schmenger, T., et al. (2017). Tweety-homolog 1 drives brain colonization of gliomas. *J. Neurosci.* 37, 6837–6850. doi: 10.1523/JNEUROSCI.3532-16.2017

Koul, D., Shen, R., Bergh, S., Sheng, X., Shishodia, S., Lafortune, T. A., et al. (2006). Inhibition of Akt survival pathway by a small-molecule inhibitor in human glioblastoma. *Mol. Cancer Ther.* 5, 637–644. doi: 10.1158/1535-7163.MCT-05-0453

Lagerweij, T., Dusoswa, S. A., Negrean, A., Hendrikx, E. M. L., de Vries, H. E., Kole, J., et al. (2017). Optical clearing and fluorescence deep-tissue imaging for 3D quantitative analysis of the brain tumor microenvironment. *Angiogenesis* 20, 533–546. doi: 10.1007/s10456-017-9565-6

Lemke, D., Pfenning, P.-N., Sahm, F., Klein, A.-C., Kempf, T., Warnken, U., et al. (2012). Costimulatory protein 4IgB7H3 drives the malignant phenotype of glioblastoma by mediating immune escape and invasiveness. *Clin. Cancer Res.* 18, 105–117. doi: 10.1158/1078-0432.CCR-11-0880

Northcott, P. A., Buchhalter, I., Morrissy, A. S., Hovestadt, V., Weischenfeldt, J., Ehrenberger, T., et al. (2017). The whole-genome landscape of medulloblastoma subtypes. *Nature* 547, 311–317. doi: 10.1038/nature22973

Osswald, M., Blaes, J., Liao, Y., Solecki, G., Gömmel, M., Berghoff, A. S., et al. (2016). Impact of blood-brain barrier integrity on tumor growth and therapy response in brain metastases. *Clin. Cancer Res.* 22, 6078–6087. doi: 10.1158/1078-0432.CCR-16-1327

Osswald, M., Jung, E., Sahm, F., Solecki, G., Venkataramani, V., Blaes, J., et al. (2015). Brain tumour cells interconnect to a functional and resistant network. *Nature* 528, 93–98. doi: 10.1038/nature16071

Park, S.-H., Masamoto, K., Hendrich, K., Kanno, I., and Kim, S.-G. (2008). Imaging brain vasculature with BOLD microscopy: MR detection limits determined by *in vivo* two-photon microscopy. *Magn. Reson. Med.* 59, 855–865. doi: 10.1002/mrm.21573

Plaisier, C. L., O'Brien, S., Bernard, B., Reynolds, S., Simon, Z., Toledo, C. M., et al. (2016). Causal mechanistic regulatory network for glioblastoma deciphered using systems genetics network analysis. *Cell Syst.* 3, 172–186. doi: 10.1016/j.cels.2016.06.006

Plate, K. H., Scholz, A., and Dumont, D. J. (2012). Tumor angiogenesis and anti-angiogenic therapy in malignant gliomas revisited. *Acta Neuropathol.* 124, 763–775. doi: 10.1007/s00401-012-1066-5

Qutaish, M. Q., Sullivant, K. E., Burden-Gulley, S. M., Lu, H., Roy, D., Wang, J., et al. (2012). Cryo-image analysis of tumor cell migration, invasion, and dispersal in a mouse xenograft model of human glioblastoma multiforme. *Mol. Imaging Biol.* 14, 572–583. doi: 10.1007/s11307-011-0525-z

Radaelli, E., Ceruti, R., Patton, V., Russo, M., Degrassi, A., Croci, V., et al. (2009). Immunohistopathological and neuroimaging characterization of murine orthotopic xenograft models of glioblastoma multiforme recapitulating the most salient features of human disease. *Histol. Histopathol.* 24, 879–891. doi: 10.14670/HH-24.879

Renier, N., Wu, Z., Simon, D. J., Yang, J., Ariel, P., and Tessier-Lavigne, M. (2014). iDISCO: a simple, rapid methodto immunolabel large tissue samples for volume imaging. *Cell* 159, 896–910. doi: 10.1016/j.cell.2014.10.010

Sahm, F., Capper, D., Jeibmann, A., Habel, A., Paulus, W., Troost, D., et al. (2012). Addressing diffuse glioma as a systemic brain disease with single-cell analysis. *Arch. Neurol.* 69, 523–526. doi: 10.1001/archneurol.2011.2910

Schmitt, M., and Pawlita, M. (2009). High-throughput detection and multiplex identification of cell contaminations. *Nucleic Acids Res.* 37, e119. doi: 10.1093/nar/gkp581

Schwarz, M. K., Scherbarth, A., Sprengel, R., Engelhardt, J., Theer, P., and Giese, G. (2015). Fluorescent-protein stabilization and high-resolution imaging of cleared, intact mouse brains. *PLoS ONE* 10:e0124650.. doi: 10.1371/journal.pone.0124650

Sherwin, S. A., Sliski, A. H., and Todaro, G. J. (1979). Human melanoma cells have both nerve growth factor and nerve growth factor-specific receptors on their cell surfaces. *Proc. Natl. Acad. Sci. U.S.A.* 76, 1288–1292. doi: 10.1073/pnas.76.3.1288

Smits, M., and van den Bent, M. J. (2017). Imaging correlates of adult glioma genotypes. *Radiology* 284, 316–331. doi: 10.1148/radiol.2017151930

Vakoc, B. J., Lanning, R. M., Tyrrell, J. A., Padera, T. P., Bartlett, L. A., Stylianopoulos, T., et al. (2009). Three-dimensional microscopy of the tumor microenvironment *in vivo* using optical frequency domain imaging. *Nat. Med.* 15, 1219–1223. doi: 10.1038/nm.1971

Wälchli, T., Mateos, J. M., Weinman, O., Babic, D., Regli, L., Hoerstrup, S. P., et al. (2015). Quantitative assessment of angiogenesis, perfused blood vessels and endothelial tip cells in the postnatal mouse brain. *Nat. Protoc.* 10, 53–74. doi: 10.1038/nprot.2015.002

Weil, S., Osswald, M., Solecki, G., Grosch, J., Jung, E., Lemke, D., et al. (2017). Tumor microtubes convey resistance to surgical lesions and chemotherapy in gliomas. *Neuro Oncol.* 19, 1316–1326. doi: 10.1093/neuonc/nox070

Wen, P. Y., and Kesari, S. (2008). Malignant gliomas in adults. *NEJM* 359, 492–507. doi: 10.1056/NEJMra0708126

Wilson, D., Roy, D., Steyer, G., Gargesha, M., Stone, M., and McKinley, E. (2008). Whole mouse cryo-imaging. *Proc. SPIE Int. Soc. Opt. Eng.* 6916, 69161I–69161I9. doi: 10.1117/12.772840

Zhu, Z., Khan, M. A., Weiler, M., Blaes, J., Jestaedt, L., Geibert, M., et al. (2014). Targeting self-renewal in high-grade brain tumors leads to loss of brain tumor stem cells and prolonged survival. *Cell Stem Cell* 15, 185–198. doi: 10.1016/j.stem.2014.04.007

Conflict of Interest Statement: The authors declare that the research was conducted in the absence of any commercial or financial relationships that could be construed as a potential conflict of interest.

Copyright © 2019 Breckwoldt, Bode, Sahm, Krüwel, Solecki, Hahn, Wirthschaft, Berghoff, Haas, Venkataramani, von Deimling, Wick, Herold-Mende, Heiland, Platten, Bendszus, Kurz, Winkler and Tews. This is an open-access article distributed under the terms of the Creative Commons Attribution License (CC BY). The use, distribution or reproduction in other forums is permitted, provided the original author(s) and the copyright owner(s) are credited and that the original publication in this journal is cited, in accordance with accepted academic practice. No use, distribution or reproduction is permitted which does not comply with these terms.

frontiers in Neuroscience

ORIGINAL RESEARCH
published: 11 January 2019
doi: 10.3389/fnins.2018.01008

Clinical Value of Machine Learning in the Automated Detection of Focal Cortical Dysplasia Using Quantitative Multimodal Surface-Based Features

*Jia-Jie Mo[1], Jian-Guo Zhang[1], Wen-Ling Li[2], Chao Chen[3], Na-Jing Zhou[4], Wen-Han Hu[1], Chao Zhang[1], Yao Wang[1], Xiu Wang[1], Chang Liu[1], Bao-Tian Zhao[1], Jun-Jian Zhou[1] and Kai Zhang[1]**

[1] Department of Functional Neurosurgery, Beijing Tiantan Hospital, Capital Medical University, Beijing, China, [2] Department of Functional Neurosurgery, The Second Hospital of Hebei Medical University, Shijiazhuang, China, [3] Key Laboratory of Complex System Control Theory and Application, Tianjin University of Technology, Tianjin, China, [4] Department of Pharmacology, Hebei Medical University, Shijiazhuang, China

Objective: To automatically detect focal cortical dysplasia (FCD) lesion by combining quantitative multimodal surface-based features with machine learning and to assess its clinical value.

Methods: Neuroimaging data and clinical information for 74 participants (40 with histologically proven FCD type II) was retrospectively included. The morphology, intensity and function-based features characterizing FCD lesions were calculated vertex-wise on each cortical surface and fed to an artificial neural network. The classifier performance was quantitatively and qualitatively assessed by performing statistical analysis and conventional visual analysis.

Results: The accuracy, sensitivity, specificity of the neural network classifier based on multimodal surface-based features were 70.5%, 70.0%, and 69.9%, respectively, which outperformed the unimodal classifier. There was no significant difference in the detection rate of FCD subtypes (*Pearson's Chi-Square* = 0.001, $p = 0.970$). *Cohen's kappa score* between automated detection outcomes and post-surgical resection region was 0.385 (considered as fair).

Conclusion: Automated machine learning with multimodal surface features can provide objective and intelligent detection of FCD lesion in pre-surgical evaluation and can assist the surgical strategy. Furthermore, the optimal parameters, appropriate surface features and efficient algorithm are worth exploring.

Keywords: focal cortical dysplasia, machine learning, metabolic, morphological, quantitative

OPEN ACCESS

Edited by:
John Ashburner,
University College London,
United Kingdom

Reviewed by:
Irene Wang,
Cleveland Clinic, United States
Seok Jun Hong,
Child Mind Institute, United States

****Correspondence:***
Kai Zhang
zhangkai62035@sina.com

Specialty section:
This article was submitted to Brain Imaging Methods, a section of the journal Frontiers in Neuroscience

Received: *24 September 2018*
Accepted: *14 December 2018*
Published: *11 January 2019*

Citation:
Mo J-J, Zhang J-G, Li W-L, Chen C, Zhou N-J, Hu W-H, Zhang C, Wang Y, Wang X, Liu C, Zhao B-T, Zhou J-J and Zhang K (2019) Clinical Value of Machine Learning in the Automated Detection of Focal Cortical Dysplasia Using Quantitative Multimodal Surface-Based Features. Front. Neurosci. 12:1008. doi: 10.3389/fnins.2018.01008

INTRODUCTION

Focal cortical dysplasia (FCD) was intrinsically epileptogenic and was a significant cause of medically refractory epilepsy (Fauser, 2015). FCD had been reported as being increasingly frequent in a series of patients who had undergone epilepsy surgery and was the most common histopathological diagnosis among children (Blumcke et al., 2017). For patients in whom FCD

lesions were focal, epilepsy surgery may be an option. Complete resection of the FCD lesions, including surrounding epileptogenic areas, correlated with a satisfied prognosis and fewer complications (Timoney and Rutka, 2017). Therefore, accurate detection of the localization and extent of epileptogenic lesions during pre-surgical evaluation was crucial because it affected not only surgical decisions, but also the intracranial electroencephalogram (iEEG) implantation strategy when the lesions were located in highly functional areas (e.g., speech, motor skills) (Chassoux et al., 2017).

Focal cortical dysplasia constituted a broad spectrum of histopathological and clinical features ranging from FCD type I (small or subtle in conventional magnetic resonance imaging [MRI]) to FCD type III (severe pathology with other associated epileptogenic lesions) (Blümcke et al., 2011). Radiologically, the features of FCD included the following: (1) local cortical thinning or thickening; (2) blurring of the gray-white matter (GM/WM) boundary; (3) gyration anomalies; (4) abnormal signal intensity on fluid-attenuated inversion recovery (FLAIR)/T2-weighted MRI (including the *Transmantle* sign in FCD IIb); (5) abnormal interhemispheric asymmetry in structural patterns; (6) lobar hypoplasia/atrophy; and (7) diffuse or multifocal occurrence in any of the above features (Lee et al., 1998; Bernasconi, 2003; Colombo et al., 2012). Additionally, ^{18}fluoro-2-deoxy-d-glucose (^{18}FDG) positron emission tomography–computed tomography (PET-CT) was performed to help with the localization of epileptogenic disturbances in metabolism, which may aid the identification of occult FCD that were missed on MRI. PET-CT often revealed focal hypometabolism in the FCD region and has been shown to have a diagnostic sensitivity of 78–83% in FCD detection (Chassoux et al., 2010; Yh et al., 2011). The accuracy increased further with the use of PET/MRI co-registration (Salamon et al., 2008). Despite enormous progress in neuroimaging techniques and computational methods, many lesions remain subtle to identify, as the sensitivity is approximately 70% of patients with FCD (Wang et al., 2013; Kini et al., 2016). Approximately 30% of patients with visually negative MRI cause inherent difficulty in identifying the epileptogenic zone (EZ). Furthermore, in some cases, re-examination of MRI images indicates that lesions were missed during initial interpretation, and the pre-operative evaluation process was time-consuming and depends upon the experience of the interpreters, which may hinder the localization of the EZ and advancements of surgical treatments.

To overcome the limitations of radiological assessment of FCD, quantitative computational analysis and machine learning methods have built a series of feature measures into an identification algorithm to improve the detection rate (Adler et al., 2017; Hong et al., 2017; Jin et al., 2018; Tan et al., 2018). For example, morphometric analysis on T1-weighted MRI was designed to generate *z*-score maps to identify the abnormal extension of the GM/WM boundary and GM/WM junction (Wong-Kisiel et al., 2018); voxel-based 3-dimensional (3-D) MRI analysis evaluated FCD by voxel-wise subtraction of the mean GM density map of the normal database, and the resulting dataset is searched for local and global maxima (Kassubek et al., 2010); an automated algorithm was trained on MRI-negative patients with histologically confirmed FCD to improve the diagnostic accuracy (Hong et al., 2014); and quantification of the ^{18}F-FDG PET could help identify subtle lesions as a complement to the visual analysis (Mendes et al., 2017). To date, developing an accurate diagnostic tool that combines machine learning and quantitative imaging features, to identify potential epileptogenic foci was expected.

Our overall approach was to combine machine learning methods with quantitative multimodal surface-based features for the automated detection of FCD lesions. First, we included eligible structural and functional images [T1-magnetization prepared rapid gradient echo (T1-MPRAGE) sequence, T2-FLAIR sequence and PET], performed image pre-processing [space standardization, cortical construction, co-registration and drawing the region of interest (ROI)] and extracted surface features (morphological and metabolic characteristics). Then, we configured a machine learning model by choosing an appropriate algorithm and defining related parameters, training the model with labeled feature inputs and making predictions on the new dataset. Finally, we evaluated the clinical value of this method both quantitatively and qualitatively by performing statistical analysis and conventional visual analysis.

MATERIALS AND METHODS

The flow diagram outlining the study design and results is shown in **Figure 1**.

Participants

Forty participants with medically refractory epilepsy who had undergone pre-surgical assessment in the Epilepsy Centre of Beijing Tiantan Hospital between 2015 and 2018 were retrospectively included in the present study. The pathologic diagnosis was confirmed and subtyped according to the International League Against Epilepsy 2010 classification (Kwan et al., 2010). To accurately label the lesion, only the patients with histopathological proven FCD type II and positive imaging were included. To assess specificity and perform inter-subject normalization, we additionally included 33 patients with short duration (less than 3 years) and histopathological confirmation of hippocampal sclerosis (HS) or epidermoid cyst (EC) as control group because it was difficult to find healthy subjects with PET images who were free of central nervous system disease in the clinical setting. In addition, other clinical centers also adapted patients with HS and EC as reference group (Adler et al., 2017; Tan et al., 2018). All patients in control group underwent epilepsy surgery and had histopathological verification of the absence of FCD. Simultaneously, an iEEG was applied to confirm the EZ was located at mesio-temporal regions, in some cases.

All the included participants fulfilled the following inclusion criteria: (1) complete clinical data (including demographic information, origin T1-MPRAGE, T2-FLAIR and PET imaging, and histological diagnosis); and (2) performance of lesionectomy. The following patients were excluded: (1) patients who were less than 3 years old, as the myelination of the neonatal brain does not reach maturity (Soun et al., 2016), which may influence imaging data normalization; (2) patients with low-quality images resulting

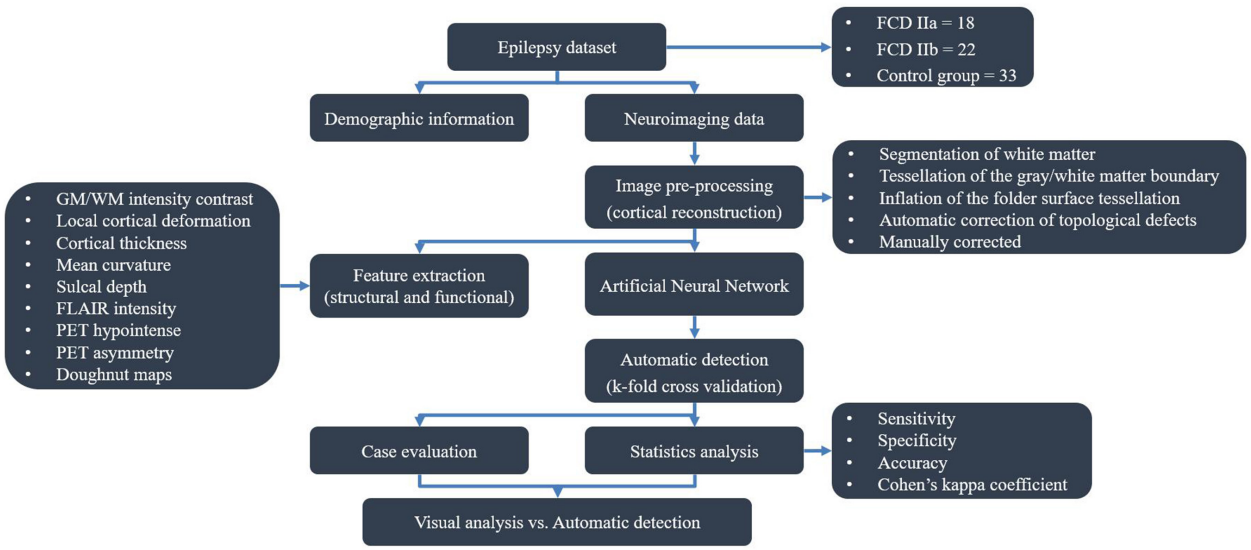

FIGURE 1 | Flow diagram of study design.

from head motion, noise or other image artifacts; and (3) patients with FCD III on histopathology, as other principle lesions may affect the performance of the artificial neural network (ANN).

Brain imaging data were visually analyzed by expert neuroradiologists according to established MRI and PET characteristic features (Lee et al., 1998; Bernasconi, 2003; Chassoux et al., 2010; Colombo et al., 2012). The determination of location and border of suspected lesions was validated by an epilepsy multidisciplinary team that consisted of neurosurgeons, neurologists, neurophysiologists and neuropsychologists. The surgery strategy was decided based on pre-surgical evaluation (semiology, structural and functional imaging and EEG data) during an epilepsy surgery meeting. We postulated that the EZ was located inside the resection region, based on seizure improvement following surgery. Surgical outcome data were obtained via direct clinical assessment or telephone interview and were determined based on the International League Against Epilepsy (ILAE) classification system (Wieser et al., 2010).

The overall procedure of the automated detection approach is shown in **Figure 2**.

MRI and PET Imaging Data

In our centre, all neuroimages were acquired at 3.0 T field strength using dedicated MRI epilepsy protocols, including 3-dimensional (3D) T1-MPRAGE sequence [repetition time (TR) = 2,300 ms, echo time (TE) = 2.53 ms, flip angle = 12°, slice thickness = 1 mm, no gap, voxel size = 1 mm × 1 mm × 1 mm], and axial T2-FLAIR (TR = 7,000 ms, TE = 80 ms, flip angle = 12°, slice thickness = 1 mm, no gap, voxel size = 1 mm × 1 mm × 1 mm). T1-MPRAGE and T2-FLAIR sequences offered advantages in identifying subtle differences in cortical tissue (Viviani et al., 2017). FDG-PET scans were acquired in the interictal state under standard resting conditions (eyes closed, dimmed ambient light). Approximately 45 min following the intravenous administration of ^{18}F-labeled FDG, PET images of the brain were obtained from the vertex to the skull base (voxel size was 1 mm, slice thickness was 3.27 mm). Images were attenuation-corrected using non-contrast CT transmission information.

Pre-processing and Normalization

Pre-processing involved T1-MPRAGE and T2-FLAIR images undergoing automated intensity non-uniformity correction and intensity normalization, which could upgrade the accuracy of registration performance (Bagci et al., 2010). Then, T1-MPRAGE images were linearly registered to the *Montreal Neurological Institute (MNI) 152* symmetric template (Evans et al., 1993). Following that step, T2-FLAIR and PET images were linearly mapped to the T1-MPARAGE images in *MNI* space, and subsequently, analysis was performed using the *SPM12* software package (available for free download[1]) (**Figure 2**).

Surface Reconstruction

FreeSurfer software v5.3[2] (NeuroImage. Cortical surface-based analysis, 1999; Fischl and Dale, 2000) was used to perform the cortical reconstruction and to register the T2-FLAIR sequence and PET scans to the T1-MPRAGE with the *recon-all* pipeline (NeuroImage. Cortical surface-based analysis, 1999). The pipeline provided a full processing stream for structural images, including the following: (1) motion correction and averaging volumetric T1 weighted images; (2) removal of non-brain tissue; (3) automated *Talairach* transformation; (4) segmentation of the subcortical white matter and deep gray matter volumetric structures; (5) tessellation of the gray matter white matter boundary; (6) automated topology correction; and

[1]http://www.fil.ion.ucl.ac.uk/spm/software/

[2]http://surfer.nmr.mgh.harvard.edu/

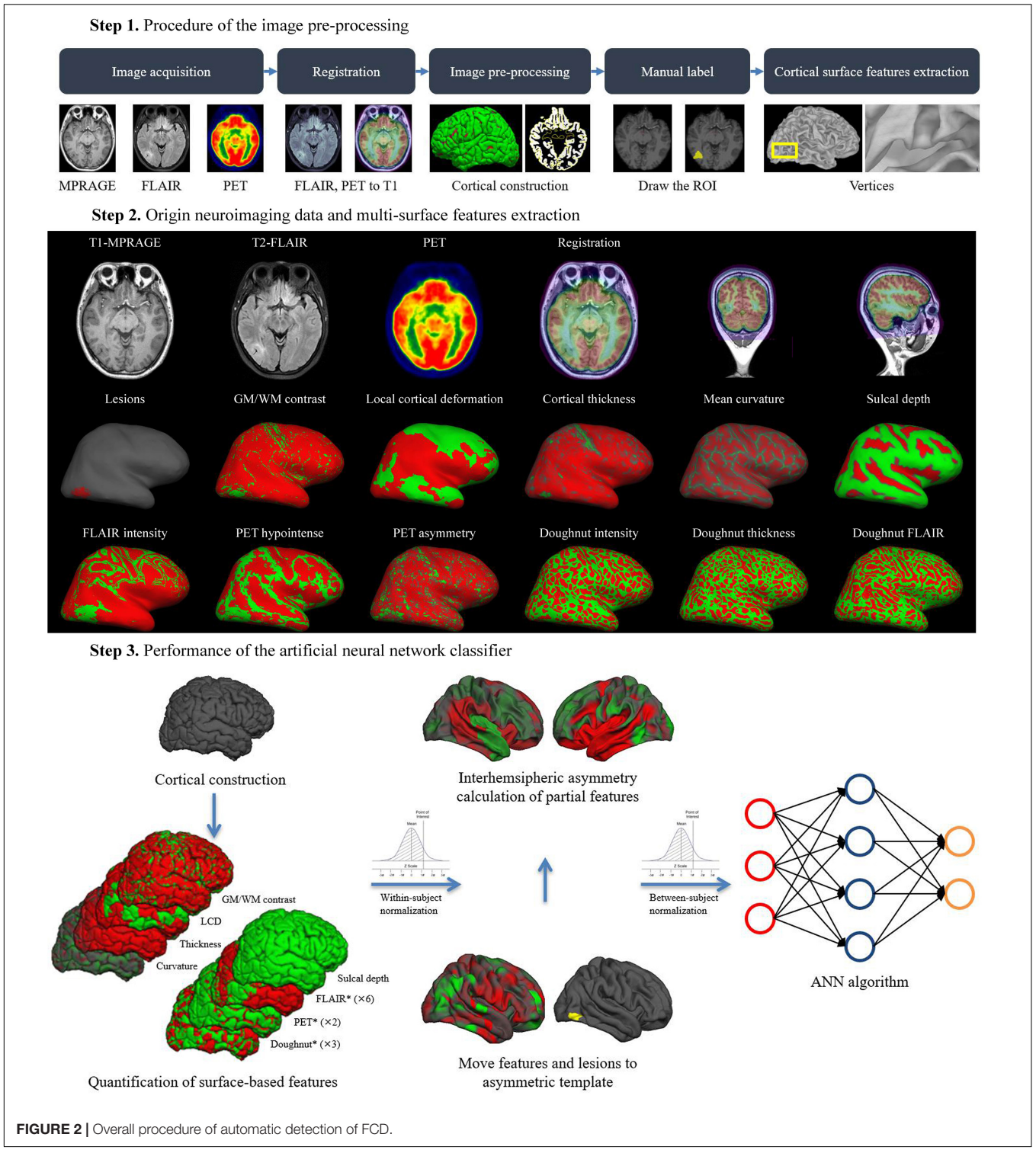

FIGURE 2 | Overall procedure of automatic detection of FCD.

(7) surface deformation to optimally place the GM/WM and GM/cerebrospinal fluid (CSF) borders at the location. Once the cortical models were complete, a number of deformable procedures could be performed for further data processing and analysis, including surface inflation (NeuroImage. Cortical surface-based analysis, 1999). Additionally, cortical surface data and brain volumes could be displayed in *tksurfer* and *freeview*, respectively. These steps were illustrated in detail in the tutorials and a prior study (Reuter et al., 2012). The results of reconstruction and surface extraction were validated by visual inspection, and any inaccuracies were manually corrected.

Manual Lesion Masks

Manual lesion labels of FCD were created for 40 patients in *freeview* on an axial T1-MPRAGE volumetric scan. The location of the lesions were confirmed by the outcomes of pre-surgical evaluation (the neuroimaging features in combination with seizure semiology, clinical examination and video EEG). After that, the labels were converted to surface for compatibility with the surface reconstructions and normalized to zero-mean, *MNI* standard space. Non-lesional tissues were sampled from the contralateral, healthy, homotopic cortex.

FCD Feature Extraction From MRI and PET

Labels of vertex morphologic [GM/WM intensity contrast, local cortical deformation (LGD), cortical thickness, mean curvature, sulcal depth, doughnut intensity, doughnut thickness], intensity (FLAIR intensity at a different level of the cortical depth, doughnut FLAIR) and metabolic (PET hypointense, PET asymmetry) features were calculated. The MRI and PET features were computed after first warping surfaces back into each subject's MRI native space and subsequently into PET native space by inversely transforming the previously performed PET-to-MRI registration. These features were then resampled on the *MNI* surface template using the related transformation. The technical details of these features were described in a prior study (Adler et al., 2017), and all codes are freely available at https://github.com/kwagstyl/FCDdetection. The measurements of features were represented below.

Measures of Morphological Features

GM/WM intensity contrast was measured as the ratio of the GM signal intensity to the WM signal intensity (Fauser, 2015; Adler et al., 2017). The GM and WM signal intensities were measured 30% through the thickness of the cortical ribbon and 1 mm below the GM/WM interface, respectively (Salat et al., 2009). FCD lesions with blurring of the GM/WM boundary were expected to have low GM/WM intensity contrast values compared to those of the non-FCD cortex; (Blumcke et al., 2017) LGD was measured as the degree of cortical intrinsic curvature of a 25 mm radius ring that was centered on a vertex (Ronan et al., 2011; Adler et al., 2017; Timoney and Rutka, 2017). The cortical thickness was measured as the shortest distance between corresponding vertices on the GM/WM surfaces (Fischl and Dale, 2000; Chassoux et al., 2017). The mean curvature was measured as the area-minimizing flow that defines the deviation from the cortical surface to a sphere at the GM/WM boundary (Blümcke et al., 2011; Jin et al., 2018) The sulcal depth was measured as the geodesic distance between the given vertices within sulci and the gyral crown vertices (Boucher et al., 2009). As reported in prior studies, small FCD lesions were located at the bottom of a deep sulcus (Hofman et al., 2011).

Measures of Intensity Features

FLAIR intensities at the GM/WM boundary as well as at 25%, 50%, and 75% of cortical thickness, and at 0.5 mm and 1 mm below the boundary, were sampled. Decreased vertical gradient indicated the blurring of the GM/WM boundary (Hong et al., 2017).

Measures of Metabolic Features

Details about extraction of PET features can be found elsewhere (Tan et al., 2018). (1) PET hypointensity was measured as normalized intensity at each vertex of the FCD lesion; (2) PET asymmetry was calculated to compare the relatively lower PET intensity in the FCD lesion to that of the homotopic location in the contralateral brain hemisphere.

Doughnut Map

Comparison of the GM/WM intensity contrast, cortical thickness and FLAIR intensities between a 6 mm radius circle on the inflated surface and the surrounding region around the circle was conducive to identifying the local change and reducing the spurious motion effect (Adler et al., 2017).

Features Smoothing and Normalization

Prior to classification, all the features were smoothed with a 10 mm full-width-at-half-maximum (FWHM) *Gaussian* surface kernel (Merkx et al., 2012). Then, for each type of feature across all the vertices within a given individual, we would perform the within-subject *z*-score normalization, followed by the between-subject *z*-score normalization, so that feature values at a given vertex were normalized to the control group.

Interhemispheric Asymmetry

The morphological, intensity, metabolic features and doughnut maps performed the interhemispheric registration on the average space (*fsaverage_sym*). Interhemispheric registration of feature maps allowed quantification of the interhemispheric asymmetry of surface-based metrics at each vertex. An initial template was created from only the left hemisphere value, and bilateral hemisphere values were aligned with this initial left template. A new template was then created from these bilateral surfaces, and the surfaces were reregistered to it. This new template was a mixture of left and right hemisphere and thus was less biased (Greve et al., 2013).

Performance of Machine Learning

Automated detection of FCD lesion was performed using an ANN classifier implemented in MATLAB R2017b (MathWorks, Natick, MA, United States). The neural network classifier was trained on the aforementioned neuroimaging features sampled from the vertices of the labeled lesion and selected non-lesional vertices. Each vertex in the training data was given two values: "1" for the lesion in the mask; "0" for the non-lesional hemisphere. The feedforward network was widely used and provides a proven method of building a non-parametric classifier. It contained input, hidden and output layers. The non-linear behavior of the hidden and output layers generated classifier behavior (Haykin, 1994). Principal component analysis (PCA) was applied to reduce the input dimension and speed up the learning algorithm. Every node in the proceeding layer took a weighted average of the

outputs of the previous layer, until an output was reached. The value of output layers from the weighted sum of inputs determines the property of each vertex. And 70% of the available data was allocated for training. The remaining 30% of data were equally partitioned as validation and test datasets. Feature selection, training, and performance evaluation were carried out using *k*-fold cross validations ($k = 5$) with 100 iterations. At each iteration, the dataset was randomly partitioned into k equal sized subsets. Then, a single subset was retained as the validation data for testing the model, and the remaining k – 1 subsets were used as training data (Rodriguez et al., 2010). The threshold of probability maps at the highest detection and lowest false-positive rates were set in all the classification schemes. The evaluation of classification accuracy was assessed with regards to post-surgical resection regions and the standard-of-care clinical evaluation.

Statistical Analysis

All numeric data had a non-parametric statistical distribution according to the *Shapiro–Wilk* test. For descriptive data compared between the patient group and control group, *Pearson's Chi-square test* or *Fisher's exact test* and *Student t-test* or *Mann–Whitney test* were used. Statistical significance was set at the 5% level. All results were considered as concordant if there was a major positive cluster located at the surgically resected areas. The findings of each diagnostic output were separated into true positive (TP), true negative (TN), false positive (FP), and false negative (FN). A comparison of automated detection outcomes to surgical resection regions were visually determined. TP (also called the detection rate) was defined as the proportion of patients in whom a detected cluster correctly overlapped with the post-surgical resection region. TN was calculated as the proportion of controls in whom no FCD lesion cluster was falsely identified. The sensitivity was calculated as TP/(TP + FN), specificity as TN/(TN + FP) and accuracy as (TP + TN)/(TP + FP + FN + TN). Agreement in correctly identifying the resection area was determined between automated detection outcomes using *Cohen's kappa scores*. According to a prior study, *kappa* values were classified as slight (0.00–0.20), fair (0.21–0.40), moderate (0.41–0.60), substantial (0.61–0.80), and almost perfect (0.81–1.00) (Landis and Koch, 1977). Statistical analysis was performed with SPSS software, version 20.0.0 (IBM corp., United States).

RESULTS

Patient Demographics and Clinical Information

Demographics information and lesion characteristics were summarized in **Table 1**. In total, seventy-three cases (36 female, 37 male) were eligibly included in the present study. In the patient group, 18 patients (24.3%) had histologically confirmed FCD IIa, 22 (29.7%) had FCD IIb; and in the control group, 32 (43.2%) had HS and 1 (1.4%) had EC. The sex proportion of the control group was not significantly different from that of the patient group (*Pearson's Chi-Square* = 0.117, $p = 0.733$), nor was the hemisphere lateralization (*Pearson's Chi-Square* = 0.030, $p = 0.862$). At the same time, there was no significant difference in duration between the each group (*Mann–Whitney U*: $p = 0.942$, as the variables of the patient group did not correspond to a normal distribution). The epilepsy duration ranged from 0.1 to 33 years [mean 11.2 years, standard deviation (SD) 8.3 years] in the patient group and from 0.5 to 32 years (mean 11.3 years, SD 8.3 years) in the control group. Seizure freedom was achieved in 82.5% (33/40) of participants 1 year after surgery.

Performance of the Neural Network Classifier (Quantitative Analysis)

The statistical analysis of automated detection outcomes is available in **Figure 3**. According to the final output, the detected clusters colocalized with the post-surgical resection region in 31 patients, yielding a TP of 77.5% (31/40), and 13 lesional clusters were identified in the control group, resulting in 60.6% (20/33) TN. Therefore, according to the aforementioned formulas, the sensitivity was calculated as 70.5%, specificity as 70.0% and

TABLE 1 | Overview of the clinical features of the 73 patients with MRI lesion and pathologic diagnosis.

	Patient group	Control group	*P*-value
Participants	40	33	–
Sex (%)	Female: 19 (47.5%) Male: 21 (52.5%)	Female: 17 (51.5%) Male: 16 (48.5%)	0.733[a]
Duration (mean ± SD, years)	11.2 ± 8.3, range 0.1–33	11.3 ± 8.3, range 0.5–32	0.942[b]
Pathology (%)	FCD IIa 18 (45.0%) FCD IIb 22 (55.0%)	HS 32 (97.0%) EC 1 (3.0%)	–
Hemisphere (%)	Left 21 (52.5%) Right 19 (47.5%)	Left 18 (54.5%) Right 15 (45.5%)	0.862[a]
Lesion location (%)	Frontal lobe 26 (65.0%) Temporal lobe 4 (10.0%) Parietal lobe 5 (12.5%) Occipital lobe 2 (5.0%) Insular lobe 3 (7.5%)	–	–

FCD, focal cortical dysplasia; HS, hippocampal sclerosis; EC, epidermoid cyst; SD, standard deviation. [a]Pearson's Chi-Square test; [b]Mann–Whitney U test.

A Patient-level analysis

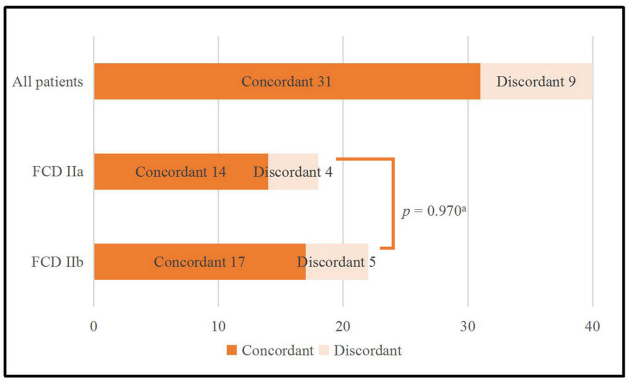

B Overall prediction analysis

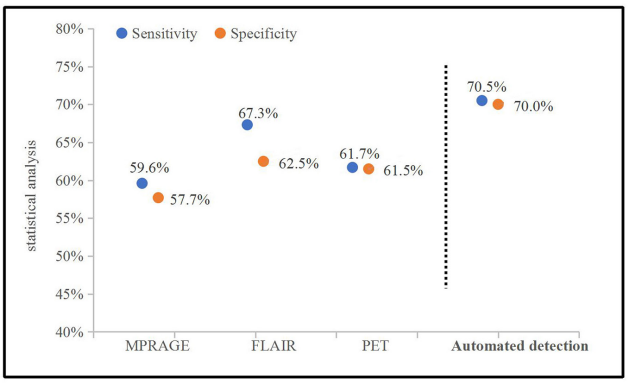

C Confusion matrix for artificial neural network performance

		Prediction			Statistical analysis
		Positive	Negative	Total	Sensitivity = 70.5%
Actual	Positive	31	9	40	Specificity = 70.0%
	Negative	13	20	33	Accuracy = 69.9%
	Total	44	29	73	*Kappa* score = 0.385

D. Comparison of FCD lesion detection accuracy across different evaluations

Patients	Visual MPRAGE	Visual FLAIR	Visual PET	Visual MRI/PET	Automated detection	Good surgical outcome (ILAE I)
Overall (n = 40)	24 (60.0%)	29 (72.5%)	25 (62.5%)	33 (82.5%)	31 (77.5%)	33 (82.5%)
FCD IIa (n = 18)	7 (38.9%)	11 (61.1%)	10 (55.6%)	13 (72.2%)	13 (72.2%)	14 (77.8%)
FCD IIb (n = 22)	17 (77.3%)	18 (81.8%)	15 (68.2%)	20 (90.9%)	18 (81.8%)	19 (86.4%)

FIGURE 3 | Automated detection outcomes. **(A)** Patient-level analysis. Numbers in histograms represented number of patients. The percentage of patients in whom automated outcomes were concordant with the surgical resection is 77.5% (31/40) in all patients, 72.2% (13/18) in FCD IIa subgroup, and 81.8% (18/22) in FCD IIb subgroup. There was no significant difference between subgroups (*Pearson's Chi-Square* = 0.001, $p = 0.970$). **(B)** The plot showed the sensitivity and specificity of separate neural networks operating on unimodal and multimodal features. **(C)** Confusion matrix for neural networks showed the outcomes of statistical analysis. **(D)** The detection rates of different images and the automated detection outcomes**. ILAE I:** completely seizure-free without auras in ILAE classification. [a]*Pearson's Chi-Square* test.

accuracy as 69.9%. There was no significant difference in the detection rate of FCD subtypes (*Pearson's Chi-Square* = 0.001, $p = 0.970$). The outcomes of separate neural networks operating on unimodal (lesional features derived from only one modality, such as T1-MPRAGE, T2-FLAIR or PET) were lower than the performance on multimodal classifiers, and the statistical analysis is shown in **Figures 3B,D**. *Cohen's kappa score* between the automated detection outcomes and post-surgical resection region was 0.385 (considered as fair).

Case Evaluation (Qualitative Analysis)

Pre-surgical imaging data, automated detection outcomes, surgical resection and a follow-up survey are available in **Figure 4**. Here, we take patient 3 as an example to display the qualitative analysis.

Patient 3, a 4-year-old, right-handed male pediatric patient, started having seizures 3 years ago. His familial and personal history was irrelevant. Seizure symptomatology was characterized by impaired awareness, facial flushing, and upper limb flexion. Seizures occurred more than 10 times per day and lasted about half a minute. Neurologic examination was normal, and neuropsychological evaluation revealed no memory dysfunctions. During video-EEG monitoring, interictal spikes were recorded over the left frontal lobe and central area (C3, F3), and ictal activity appeared in the same areas. The initial MRI report revealed abnormal signs in the left frontal lobe. A careful visual analysis of FDG-PET and registered PET-MRI

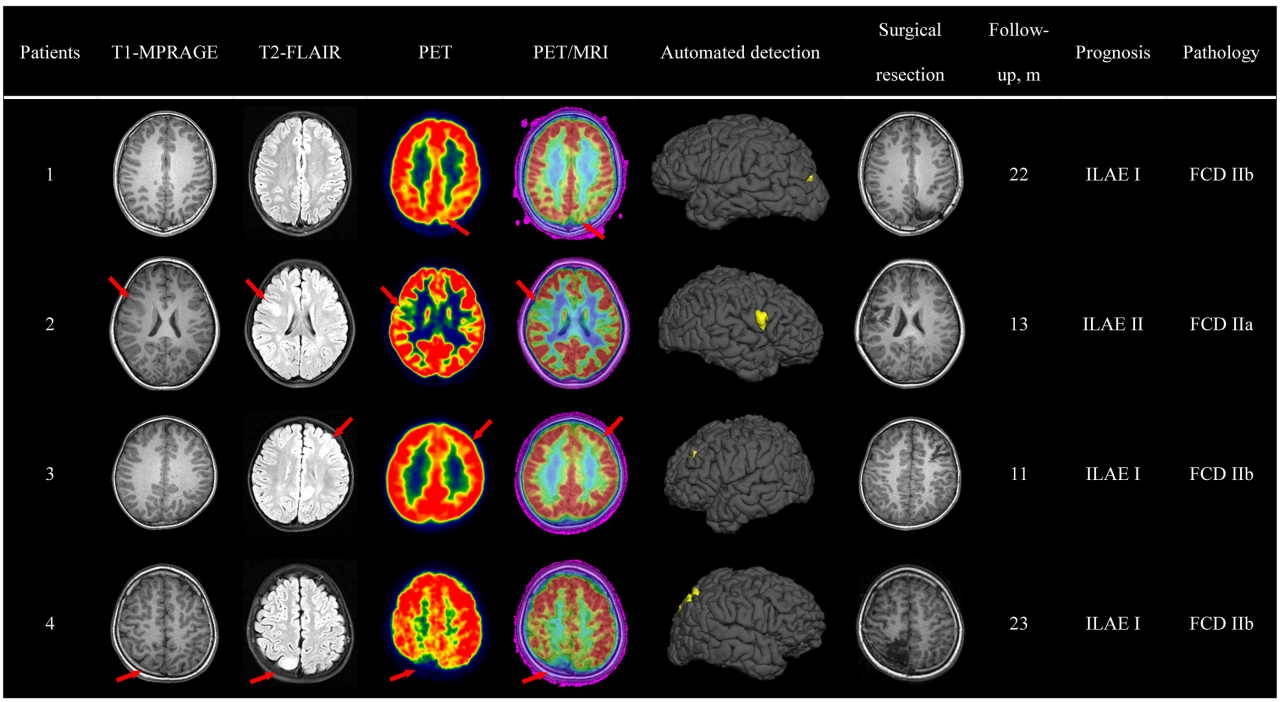

FIGURE 4 | Case evaluation. Examples of automated detection outcomes in four patients with the diagnosis of FCD. Red arrows pointed to the lesion. The absence of red arrows indicated negative diagnosis in the initial report. Evaluation of surgical outcome based on the International League Against Epilepsy (ILAE) classification system.

revealed hypometabolism of the left occipital lobe (bottom of middle frontal gyrus). The outcomes of semiology, EEG and neuroimaging data pointed to the same suspected epileptogenic area; thus, SEEG was unnecessary. A lesionectomy (from the anterior boundary of lesion to the precentral sulcus) was performed, and the patient has remained seizure-free for 11 months, with no neurological deficit. Pathologic examination showed FCD IIb. In addition, the automated detection outcome was concordant with the surgical resection region.

DISCUSSION

Achievement

Focal cortical dysplasia caused medically refractory epilepsy and was amenable to surgical treatment (Blümcke et al., 2011). Completeness of resection of the dysplastic tissue and additional epileptogenic tissue was considered to be one critical factor in determining outcome after surgery (Blount, 2017). Even with the most advanced imaging techniques, the subtle radiographic appearance of FCD still rendered visual identification challenging. Meanwhile, the interpretation of neuroimaging was time-consuming, subjective and based on the interpreters' experience, which may result in erroneous or miss-diagnosis. Clearly, to accurately localize the lesions, achieve better prognosis and minimize the resection of uninvolved regions, an objective and machine-aided diagnostic tool was necessary. Therefore, the aim of the present study was to combine machine learning methods with quantitative neuroimaging features for automated identification of the site and extent of the FCD type II lesion. The neural network classifier performance was evaluated quantitatively and qualitatively by performing statistical analysis and conventional visual analysis. Overall, in the present study, the neuroimaging data and demographic information of seventy-three participants were included to train the neural network classifier. The accuracy, sensitivity, and specificity of the classifier were 70.5%, 70.0%, and 69.9%, respectively. *Cohen's kappa score* between the automated detection outcomes and post-surgical resection region was 0.385 (considered as fair). There was no significant difference in the detection rate of FCD subtypes. In summary, the proposed method had great potential to become an auxiliary tool for diagnosis of epilepsy in pre-surgical evaluation. We considered that future strategies for exploring optimal parameters, appropriate surface features and an efficient algorithm were worthwhile.

Correlated Literatures

Currently, an improvement in magnetic field strength (De Ciantis et al., 2016) and sequences of MRI had improved the detection of FCD. Texture analysis (Antel et al., 2003; Besson et al., 2008; Wong-Kisiel et al., 2018) and voxel-based analysis (Huppertz et al., 2001; Kassubek et al., 2010) had been used to identify FCD characteristics in a quantitative fashion. But these methods were criticized for their subjective inspection. In addition, voxel-based methods neglect anatomical relationships

across the folded cortex and amplify unwanted partial volume effects, which also led to less remarkable outcomes (Hong et al., 2014). To overcome these drawbacks, Tan et al. (2018) introduced an algorithm reliant on surface-based features that statistically combine morphology, intensity and metabolism and has better performance (Hong et al., 2014). At the same time, as the increasing number and complexity of medical images threatens to overwhelm radiologists' capacity to interpret them, machine learning provided an effective way to automate the analysis and diagnosis of medical images (Wang and Summers, 2012). Machine learning methods were increasingly popular in imaging diagnosis prognostic estimation. The approaches were able to process enormous amounts of clinical data and perform quantitative analysis to make the conclusion more objective. However, many scientific and practical challenges still needed to be addressed: variation in imaging protocols, weak labels, interpretation of results and so on (Bruijne, 2016). In the present study, we took advantage of the availability of PET scans and expected to achieve superior sensitivity in FCD detection using feature modeling of combined MRI and PET, compared to that using quantitative MRI alone (Hong et al., 2014; Adler et al., 2017; Mendes et al., 2017; Jin et al., 2018). However, our neural network classifier underperformed in identifying the FCD lesion [the detection rate was lower than that in previous work (Adler et al., 2017; Jin et al., 2018; Tan et al., 2018)]. Several reasons may explain this phenomenon. First, multimodal surface features (morphology, intensity, and metabolism) of FCD were extracted to train the classifier. However, only several features were confirmed as valuable, such as cortical thickness and GM/WM matter intensity (Hong et al., 2014; Jin et al., 2018). Therefore, the unsatisfied performance may result from other irrelevant and noisy features (the so-called "overfitting problem") when we fed all the features to ANN (Hawkins, 2004). Though the cross validation had been used for evaluation, the problem could not be avoided completely. Second, different protocols of available neuroimaging data may have an influence on data consistency. On the other hand, relatively low TN rates (60.6%, 20/33) in the control group suggested that the classifier failed to ignore healthy tissue and disregard FCD-unrelated pathology in the control group. This outcome may also be attributable to the redundant multimodal surface features. Moreover, extra-primary clusters were found in several patients. However, no post-surgical pathology was available, as these regions were not resected. Prior studies revealed that these clusters presented similar features to those of FCD but were extensive and somewhat different (Hong et al., 2014). In addition, these findings suggested that extra-primary clusters may potentially be epileptogenic, as they were too subtle to discover in the visual analysis and were ignored easily, which could explain why not all patients with complete resection of the primary FCD lesion became seizure-free, especially the patients with FCD I or FCD IIa (Kwon et al., 2016).

Undoubtedly, technological advances have revolutionized the field of epilepsy in recent years. However, individual treatment according to the presurgical data was still important. For example, integration of clinical symptoms with analysis of pre-ictal EEG was conducive to establish an anatomical-electro-clinical correlation, which helped clinicians obtain the hypothesis of epileptic network. Also, substantial progress of imaging technology and computer-assistant methods was beneficial for the localization of lesions and establishment of a surgical plan. For some complex cases, in particular in surgical candidates with invisible lesions and discordant presurgical evaluation, invasive EEG technique based on a reasonable hypothesis should be preferred as it carries the advantage of allowing a three-dimensional definition of the EZ, which contributed to complete resection of the EZ and better surgical outcomes. In summary, optimization of personalized treatment was deeply connected to and dependent on the novel technology as well as the clinical information.

Limitation

Our study had several limitations. First, as PET-CT is an expensive, radioactive medical technique, it was unethical to perform on the healthy population, so we could only include patients with HS and HC as the reference group. Herein, the neuroimaging of controls will influence the accuracy of the neural network classifier because some cases of epilepsy were dual pathology, which means that HS and FCD were combined (Chacón et al., 2008). Second, the overfitting problem discussed above may influence the final outcome. It is possible that a reduction in unnecessary components could be a solution in future research. Regularization is a way to reduce overfitting by artificially penalizing higher degree polynomials (in brief, the technique discourages learning a more complex model) (Cuingnet et al., 2013). Meanwhile, other potentially useful surface features to detect FCD may have not yet been discovered in the current literature. Third, the absence of a ground truth for each lesion label made it impossible to assess the extent to which discrepancies between manual and automated detection are errors. Additionally, we noticed the alarmingly high FP rate in the present study, which may be related to the HS controls and the low specificity of PET modality. Though the FP rate could not be completely avoided in medical testing, inclusion ideal controls and prudent consideration of PET features were helpful to alleviate it.

CONCLUSION

In conclusion, automated machine learning with multimodal surface features could provide objective and intelligent detection of FCD lesion in pre-surgical evaluation and assist surgical strategy. Furthermore, the optimal parameters, appropriate surface features and efficient algorithm were worth exploring.

ETHICS STATEMENT

All patients gave their informed consent to have their clinical and particularly neuroimaging data evaluated with regard to epilepsy research. Evaluation of clinical value was approved by the Ethics Committee of the Beijing Tiantan Hospital.

AUTHOR CONTRIBUTIONS

JM: acquisition of data, statistical analysis, and drafting the manuscript. WL, CC, and NZ: acquisition and interpretation of data, revising the manuscript for intellectual content. WH, CC, and YW: acquisition of data and revising the manuscript for intellectual content. XW, CL, BZ, and J-jZ: acquisition and interpretation of data. J-gZ and KZ: study design, study supervision, and final revising the manuscript for intellectual content.

FUNDING

The research reported in this publication was supported by the Grant of Clinic and Basic Research from Capital Medical University (17JL05), Capital (China) Health Research and Development Special Fund (2016-1-1071), Beijing Municipal Science and Technology Commission (Z161100000216130 and Z131107002213065), Application Technology Research and Development and the Beijing Municipal Administration of Hospitals' Ascent Plan (DFL20150503) (to KZ and JZ).

REFERENCES

Adler, S., Wagstyl, K., Gunny, R., Ronan, L., Carmichael, D., Cross, J. H., et al. (2017). Novel surface features for automated detection of focal cortical dysplasias in paediatric epilepsy. *Neuroimage Clin.* 14, 18–27. doi: 10.1016/j.nicl.2016.12.030

Antel, S. B., Collins, D. L., Bernasconi, N., Andermann, F., Shinghal, R., Kearney, R. E., et al. (2003). Automated detection of focal cortical dysplasia lesions using computational models of their MRI characteristics and texture analysis. *Neuroimage* 19, 1748–1759. doi: 10.1016/S1053-8119(03)00226-X

Bagci, U., Udupa, J. K., and Bai, L. (2010). "The influence of intensity standardization on medical image registration," in *Proceedings of SPIE – The International Society for Optical Engineering* (Bellingham: SPIE). doi: 10.1117/12.843969

Bernasconi, A. (2003). Advanced MRI analysis methods for detection of focal cortical dysplasia. *Epileptic Disord.* 5, S81–S84.

Besson, P., Bernasconi, N., Colliot, O., Evans, A., and Bernasconi, A. (2008). Surface-based texture and morphological analysis detects subtle cortical dysplasia. *Med. Image Comput. Comput. Assist. Interv.* 11(Pt 1), 645–652. doi: 10.1007/978-3-540-85988-8_77

Blount, J. P. (2017). Extratemporal resections in pediatric epilepsy surgery an overview. *Epilepsia* 58(Suppl. 1), 19–27. doi: 10.1111/epi.13680

Blumcke, I., Spreafico, R., Haaker, G., Coras, R., Kobow, K., Bien, C. G., et al. (2017). Histopathological findings in brain tissue obtained during epilepsy surgery. *New Engl. J. Med.* 377, 1648–1656. doi: 10.1056/NEJMoa1703784

Blümcke, I., Thom, M., Aronica, E., Armstrong, D. D., Vinters, H. V., Palmini, A., et al. (2011). The clinico-pathological spectrum of focal cortical dysplasias: a consensus classification proposed by an ad hoc Task Force of the ILAE diagnostic methods commission. *Epilepsia* 52, 158–174. doi: 10.1111/j.1528-1167.2010.02777.x

Boucher, M., Whitesides, S., and Evans, A. (2009). Depth potential function for folding pattern representation, registration and analysis. *Med. Image Anal.* 13, 203–214. doi: 10.1016/j.media.2008.09.001

Bruijne, M. D. (2016). Machine learning approaches in medical image analysis: from detection to diagnosis. *Med. Image Anal.* 33, 94–97. doi: 10.1016/j.media.2016.06.032

Chacón, L. M., Estupiñán, B. O., Lorigados, L., Trápaga, O., Garcia, I., Sanchez, A., et al. (2008). Intraoperative electrocorticography patterns in medial temporal lobe epilepsy with dual pathology. *Clin. Neurophysiol.* 119:e108. doi: 10.1016/j.clinph.2008.04.051

Chassoux, F., Navarro, V., Catenoix, H., Valton, L., and Vignal, J. (2017). Planning and management of SEEG. *Clin. Neurophysiol.* 48, 25–37. doi: 10.1016/j.neucli.2017.11.007

Chassoux, F., Rodrigo, S., Semah, F., Beuvon, F., Landre, E., Devaux, B., et al. (2010). FDG-PET improves surgical outcome in negative MRI taylor-type focal cortical dysplasias. *Neurology* 75, 2168–2175. doi: 10.1212/WNL.0b013e31820203a9

Colombo, N., Tassi, L., Deleo, F., Citterio, A., Bramerio, M., Mai, R., et al. (2012). Focal cortical dysplasia type IIa and IIb: MRI aspects in 118 cases proven by histopathology. *Neuroradiology* 54, 1065–1077. doi: 10.1007/s00234-012-1049-1

Cuingnet, R., Glaunes, J. A., Chupin, M., Benali, H., and Colliot, O. (2013). Spatial and anatomical regularization of SVM: a general framework for neuroimaging data. *IEEE Trans. Pattern Anal. Mach. Intell.* 35, 682–696. doi: 10.1109/TPAMI.2012.142

De Ciantis, A., Barba, C., Tassi, L., Cosottini, M., Tosetti, M., Costagli, M., et al. (2016). 7T MRI in focal epilepsy with unrevealing conventional field strength imaging. *Epilepsia* 57, 445–454. doi: 10.1111/epi.13313

Evans, A. C., Collins, D. L., Mills, S. R., Brown, E. D., Kelly, R. L., and Peters, T. M. (1993). "3D statistical neuroanatomical models from 305 MRI volumes," in *Proceedings of the Nuclear Science Symposium and Medical Imaging Conference* (Piscataway, NJ: IEEE). doi: 10.1109/NSSMIC.1993.373602

Fauser, S. (2015). A S. In response: long-term seizure outcome in 211 patients with focal cortical dysplasia. *Epilepsia* 56, 66–76. doi: 10.1111/epi.12876

Fischl, B., and Dale, A. M. (2000). Measuring the thickness of the human cerebral cortex from magnetic resonance images. *Proc. Natl. Acad. Sci. U.S.A.* 97, 11050–11055. doi: 10.1073/pnas.200033797

Greve, D. N., Van der Haegen, L., Cai, Q., Stufflebeam, S., Sabuncu, M. R., Fischl, B., et al. (2013). A surface-based analysis of language lateralization and cortical asymmetry. *J. Cogn. Neurosci.* 25, 1477–1492. doi: 10.1162/jocn_a_00405

Hawkins, D. M. (2004). The problem of overfitting. *J. Chem. inf. Comput. Sci.* 44, 1–12. doi: 10.1021/ci0342472

Haykin, S. (1994). *Neural Networks: a Comprehensive Foundation*. Upper Saddle River, NJ: Prentice Hall.

Hofman, P. A., Fitt, G. J., Harvey, A. S., Kuzniecky, R. I., and Jackson, G. (2011). Bottom-of-sulcus dysplasia: imaging features. *Am. J. Roentgenol.* 196, 881–885. doi: 10.2214/AJR.10.4423

Hong, S. J., Bernhardt, B. C., Caldairou, B., Hall, J. A., Guiot, M. C., Schrader, D., et al. (2017). Multimodal MRI profiling of focal cortical dysplasia type II. *Neurology* 88, 734–742. doi: 10.1212/WNL.0000000000003632

Hong, S. J., Kim, H., Schrader, D., Bernasconi, N., Bernhardt, B. C., and Bernasconi, A. (2014). Automated detection of cortical dysplasia type II in MRI-negative epilepsy. *Neurology* 83, 48–55. doi: 10.1212/WNL.0000000000000543

Huppertz, H. J., Kassubek, J., Juengling, F. D., and Schulze-Bonhage, A. (2001). Detection of focal cortical dysplasia by voxel-based morphometry. *Neuroimage* 13:S156. doi: 10.1016/S1053-8119(01)91499-5

Jin, B., Krishnan, B., Adler, S., Wagstyl, K., Hu, W., Jones, S., et al. (2018). Automated detection of focal cortical dysplasia type II with surface-based magnetic resonance imaging postprocessing and machine learning. *Epilepsia* 59, 982–992. doi: 10.1111/epi.14064

Kassubek, J., Huppertz, H. J., Spreer, J., and Schulzebonhage, A. (2010). Detection and localization of focal cortical dysplasia by voxel-based 3-D MRI analysis. *Epilepsia* 43, 596–602. doi: 10.1046/j.1528-1157.2002.41401.x

Kini, L. G., Gee, J. C., and Litt, B. (2016). Computational analysis in epilepsy neuroimaging: a survey of features and methods. *Neuroimage Clin.* 11, 515–529. doi: 10.1016/j.nicl.2016.02.013

Kwan, P., Arzimanoglou, A., Berg, A. T., Brodie, M. J., Allen, H. W., Mathern, G., et al. (2010). Definition of drug resistant epilepsy: consensus proposal by the ad hoc task force of the ILAE Commission on therapeutic strategies. *Epilepsia* 51, 1069–1077. doi: 10.1111/j.1528-1167.2009.02397.x

Kwon, H. E., Eom, S., Kang, H. C., Lee, J. S., Kim, S. H., Kim, D. S., et al. (2016). Surgical treatment of pediatric focal cortical dysplasia: clinical spectrum and surgical outcome. *Neurology* 87, 945–951. doi: 10.1212/WNL.0000000000003042

Landis, J. R., and Koch, G. G. (1977). The measurement of observer agreement for categorical data. *Biometrics* 33, 159–174. doi: 10.2307/2529310

Lee, B. C., Schmidt, R. E., Hatfield, G. A., Bourgeois, B., and Park, T. S. (1998). MRI of focal cortical dysplasia. *Neuroradiology* 40, 675–683. doi: 10.1007/s002340050664

Mendes, V. C., Morita, M. E., Amorim, B. J., Ramos, C. D., Yasuda, C. L., Tedeschi, H., et al. (2017). automated online quantification method for 18F-FDG positron emission Tomography/CT improves detection of the epileptogenic zone in patients with pharmacoresistant epilepsy. *Front. Neurol.* 8:453. doi: 10.3389/fneur.2017.00453

Merkx, M. A. G., Bescós, J. O., Geerts, L., Bosboom, E. M. H., Vosse, F. N. V. D., and Breeuwer, M. (2012). Accuracy and precision of vessel area assessment: manual versus automatic lumen delineation based on full-width at half-maximum. *J. Magn. Reson. Imaging* 36, 1186–1193. doi: 10.1002/jmri.23752

NeuroImage. Cortical surface-based analysis. Ii. (1999). Inflation, flattening, and a surface-based coordinate system. *Neuroimage* 9, 195–207.

Reuter, M., Schmansky, N. J., Rosas, H. D., and Fischl, B. (2012). Within-subject template estimation for unbiased longitudinal image analysis. *Neuroimage* 61, 1402–1418. doi: 10.1016/j.neuroimage.2012.02.084

Rodriguez, J. D., Perez, A., and Lozano, J. A. (2010). Sensitivity analysis of k-Fold cross validation in prediction error estimation. *IEEE Trans. Pattern Anal. Mach. Intell.* 32, 569–575. doi: 10.1109/TPAMI.2009.187

Ronan, L., Pienaar, R., Williams, G., Bullmore, E., Crow, T. J., Roberts, N., et al. (2011). Intrinsic curvature: a marker of millimeter-scale tangential cortico-cortical connectivity? *Int. J. Neural Syst.* 21, 351–366. doi: 10.1142/S0129065711002948

Salamon, N., Kung, J., Shaw, S. J., Koo, J., Koh, S., Wu, J. Y., et al. (2008). FDG-PET/MRI coregistration improves detection of cortical dysplasia in patients with epilepsy. *Neurology* 71, 1594–1601. doi: 10.1212/01.wnl.0000334752.41807.2f

Salat, D. H., Lee, S. Y., Aj, V. D. K., Greve, D. N., Fischl, B., and Rosas, H. D. (2009). Age-associated alterations in cortical gray and white matter signal intensity and gray to white matter contrast. *Neuroimage* 48, 21–28. doi: 10.1016/j.neuroimage.2009.06.074

Soun, J. E., Liu, M. Z., Cauley, K. A., and Grinband, J. (2016). Evaluation of neonatal brain myelination using the T1- and T2-weighted MRI ratio. *J. Magn. Reson. Imaging* 46, 690–696. doi: 10.1002/jmri.25570

Tan, Y. L., Kim, H., Lee, S., Tihan, T., Ver, H. L., Mueller, S. G., et al. (2018). Quantitative surface analysis of combined MRI and PET enhances detection of focal cortical dysplasias. *Neuroimage* 166, 10–18. doi: 10.1016/j.neuroimage.2017.10.065

Timoney, N., and Rutka, J. T. (2017). Recent advances in epilepsy surgery and achieving best outcomes using high-frequency oscillations, diffusion tensor imaging, magnetoencephalography, intraoperative neuromonitoring, focal cortical dysplasia, and bottom of sulcus dysplasia. *Neurosurgery* 64, 1–10. doi: 10.1093/neuros/nyx239

Viviani, R., Stöcker, T., and Stingl, J. C. (2017). Multimodal FLAIR/MPRAGE segmentation of cerebral cortex and cortical myelin. *Neuroimage* 152, 130–141. doi: 10.1016/j.neuroimage.2017.02.054

Wang, S., and Summers, R. M. (2012). Machine learning and radiology. *Med. Image Anal.* 16, 933–951. doi: 10.1016/j.media.2012.02.005

Wang, Z. I., Alexopoulos, A. V., Jones, S. E., Jaisani, Z., Najm, I. M., and Prayson, R. A. (2013). The pathology of magnetic-resonance-imaging-negative epilepsy. *Mod. Pathol.* 26, 1051–1058. doi: 10.1038/modpathol.2013.52

Wieser, H. G., Blume, W. T., Fish, D., Goldensohn, E., Hufnagel, A., King, D., et al. (2010). ILAE commission report. Proposal for a new classification of outcome with respect to epileptic seizures following epilepsy surgery. *Epilepsia* 42, 282–286. doi: 10.1046/j.1528-1157.2001.4220282.x

Wong-Kisiel, L. C., Quiroga, D. F. T., Kenney-Jung, D. L., Witte, R. J., Santana-Almansa, A., Worrell, G. A., et al. (2018). Morphometric analysis on T1-weighted MRI complements visual MRI review in focal cortical dysplasia. *Epilepsy Res.* 140, 184–191. doi: 10.1016/j.eplepsyres.2018.01.018

Yh, K., Hc, K., Ds, K., Sh, K., Kw, S., Hd, K., et al. (2011). Neuroimaging in identifying focal cortical dysplasia and prognostic factors in pediatric and adolescent epilepsy surgery. *Epilepsia* 52, 722–727. doi: 10.1111/j.1528-1167.2010.02950.x

Conflict of Interest Statement: The authors declare that the research was conducted in the absence of any commercial or financial relationships that could be construed as a potential conflict of interest.

Copyright © 2019 Mo, Zhang, Li, Chen, Zhou, Hu, Zhang, Wang, Wang, Liu, Zhao, Zhou and Zhang. This is an open-access article distributed under the terms of the Creative Commons Attribution License (CC BY). The use, distribution or reproduction in other forums is permitted, provided the original author(s) and the copyright owner(s) are credited and that the original publication in this journal is cited, in accordance with accepted academic practice. No use, distribution or reproduction is permitted which does not comply with these terms.

frontiers in Neuroscience

REVIEW
published: 11 January 2019
doi: 10.3389/fnins.2018.00995

Tracking Neural Progenitor Cell Migration in the Rodent Brain Using Magnetic Resonance Imaging

Christiane L. Mallett[1,2†], Dorela D. Shuboni-Mulligan[1,2†] and Erik M. Shapiro[1,2]*

[1] *Molecular and Cellular Imaging Laboratory, Department of Radiology, Michigan State University, East Lansing, MI, United States,* [2] *Institute for Quantitative Health Science and Engineering, Michigan State University, East Lansing, MI, United States*

The study of neurogenesis and neural progenitor cells (NPCs) is important across the biomedical spectrum, from learning about normal brain development and studying disease to engineering new strategies in regenerative medicine. In adult mammals, NPCs proliferate in two main areas of the brain, the subventricular zone (SVZ) and the subgranular zone, and continue to migrate even after neurogenesis has ceased within the rest of the brain. In healthy animals, NPCs migrate along the rostral migratory stream (RMS) from the SVZ to the olfactory bulb, and in diseased animals, NPCs migrate toward lesions such as stroke and tumors. Here we review how MRI-based cell tracking using iron oxide particles can be used to monitor and quantify NPC migration in the intact rodent brain, in a serial and relatively non-invasive fashion. NPCs can either be labeled directly *in situ* by injecting particles into the lateral ventricle or RMS, where NPCs can take up particles, or cells can be harvested and labeled *in vitro*, then injected into the brain. For *in situ* labeling experiments, the particle type, injection site, and image analysis methods have been optimized and cell migration toward stroke and multiple sclerosis lesions has been investigated. Delivery of labeled exogenous NPCs has allowed imaging of cell migration toward more sites of neuropathology, which may enable new diagnostic and therapeutic opportunities for as-of-yet untreatable neurological diseases.

Keywords: MRI – magnetic resonance imaging, neural progenitor and stem cells, cell transplantation, neurogenesis, rodents (rats, mice, guinea pigs, voles)

OPEN ACCESS

Edited by:
Oscar Arias-Carrión, Hospital General Dr. Manuel Gea González, Mexico

Reviewed by:
Benito de Celis Alonso, Benemérita Universidad Autónoma de Puebla, Mexico
Kevin C. Chan, New York University, United States

***Correspondence:**
Erik M. Shapiro
shapir86@msu.edu

† These authors have contributed equally to this work

Specialty section:
This article was submitted to Brain Imaging Methods, a section of the journal Frontiers in Neuroscience

Received: *11 October 2018*
Accepted: *11 December 2018*
Published: *11 January 2019*

Citation:
Mallett CL, Shuboni-Mulligan DD and Shapiro EM (2019) Tracking Neural Progenitor Cell Migration in the Rodent Brain Using Magnetic Resonance Imaging. Front. Neurosci. 12:995. doi: 10.3389/fnins.2018.00995

INTRODUCTION

The potential of using stem cells to repair the brain after traumatic injury (Lepore et al., 2006; Lin et al., 2018; Mundim et al., 2019), stroke (Hoehn et al., 2002; Zhang et al., 2003; Huang et al., 2014), cancer (Zhang et al., 2004; Muldoon et al., 2006; Barish et al., 2017), Parkinson's disease (Lamm et al., 2014; Ramos-Gomez and Martinez-Serrano, 2016), neonatal hypoxia-ischemia (Obenaus et al., 2011) and multiple sclerosis (Ben-Hur et al., 2007; Reekmans et al., 2011; Harris et al., 2018), as well as other diseases, is significant. For example, when NPCs are injected directly into the brain in rodent models of ischemic stroke, there are marked improvements in both behavioral and physiological markers (Obenaus et al., 2011; Daadi et al., 2013; Huang et al., 2014). NPC independently migrate through tissue to the site of disease using a chemotaxis sense, moving toward

Abbreviations: BrdU, bromodeoxyuridine; GBM, glioblastoma multiforme; heNSC, human embryonic neural stem cell; MCAO, middle cerebral artery occlusion; ML, magnetoliposomes; MPI, magnetic particle imaging; MPIO, micron-sized iron oxide particles; NPC, neural progenitor cell; NSC, neural stem cell; OB, olfactory bulb; PLGA, poly(lactic co-glycolic acid); RMS, rostral migratory stream; SPIO, superparamagnetic iron oxide nanoparticles; SVZ, subventricular zone; USPIO, ultrasmall superparamagnetic iron oxide particles.

the presence of cytokines caused by disease, a process called homing (Peng et al., 2004; Kokovay et al., 2010; Reaux-Le Goazigo et al., 2013). In glioma, NPCs actively migrate to tumors (Aboody et al., 2000; Diaz-Coranguez et al., 2013; Bago et al., 2017) and the mere presence of NPCs could impede the growth and proliferation of tumors (Glass et al., 2005). The effectiveness of NPCs as therapeutics may be due to integration of cells into existing circuitry, or through their effect on the damaged brain tissue through the secretion of factors or extracellular vesicles (e.g., exosomes) that influence inflammation, neovascularization, and plasticity (Boese et al., 2018).

The SVZ is one of two well-characterized regions of the brain where neurogenesis persists after development is complete, the other being the subgranular zone of the dentate gyrus (Gage, 2002; Gonzalez-Perez, 2012). NPCs originating in the SVZ migrate to the OB in a well-organized chain of cells called the RMS.

The SVZ is located proximal to the lateral ventricles (**Figure 1**). The region is populated by several cell types. The ependymal cells and type B cells (astrocytes) line the ventricle wall. Astrocytes are divided into two subtypes: type B1 cells have apical projections into the cerebral spinal fluid (CSF) while type B2 cells do not contact the ventricle. Type B cells can differentiate into type C cells (transit amplifying cells or intermediate precursor cells), which then differentiate into type A cells (neuroblasts). Neuroblasts migrate through a sheath formed by type B cells toward the OB, forming the RMS. In the developing rodent brain, a constant stream of regenerating NPCs travel from the SVZ through the RMS to the OB, where they differentiate and replace dead neurons or create/reinforce neural pathways (reviewed in Ihrie and Álvarez-Buylla, 2011; Butti et al., 2014). NPC proliferation and migration can be upregulated and redirected by signals along inflammatory signaling pathways or by growth and neurotrophic factors (reviewed in Christie and Turnley, 2013). Of note, the SVZ has a mix of NSCs (multipotent, self-renewing) and NPCs (pluripotent, limited self-renewal), but the exact proportion of each cell type in the SVZ and their relevant markers remain in dispute (Seaberg and van der Kooy, 2003; Abrous et al., 2005). Although these characteristics are important, for simplicity we will use the general term, NPC, to refer to all cells in brain with self-renewing potential.

Cell migration in the RMS has been studied on excised tissues using a variety of methods to label cells. One *in situ* method is to inject viral vectors into the SVZ or the lateral ventricle leading to transfection of nearby cells; this has been used to transfer genes encoding for fluorescent (Suzuki and Goldman, 2003; Rogelius et al., 2005; Ventura and Goldman, 2007) or bioluminescent proteins (Guglielmetti et al., 2014). Such injections can also be used to label cells with BrdU, which incorporates into the DNA of dividing cells and can then be detected using histologic techniques (Betarbet et al., 1996; Arvidsson et al., 2002; Mundim et al., 2019). Each of these methods shares the drawback that analysis can only be performed after excision of the tissue after the animal has been euthanized, such that only a single time point per animal can be assessed, and this is usually done on histological sections that further limit the study by reducing the sample size. Migration of fluorescent cells can be detected using two-photon microscopy through a cranial window (e.g., Lin et al., 2018). Using this method, only a limited area of the brain can be imaged. Bioluminescence imaging can also be used to track transplanted cells, but has limited resolution (e.g., Rogall et al., 2018).

Studying NPCs *in vivo* using magnetic resonance imaging (MRI) avoids some of these drawbacks but can introduce new challenges. In this technique, cells are labeled with superparamagnetic iron oxide particles (SPIO), either *in vitro* or *in situ*, and the animal can be serially imaged, allowing for tracking of NPCs and monitoring of treatment response. The SPIO cause local in homogeneities in the magnetic field that appear as hypointensities or dark contrast in gradient echo-based MR images. The artifact is much larger than the particle itself, to the extent that single labeled cells are detectable by MRI (Heyn et al., 2006a; Shapiro et al., 2006b), offering excellent sensitivity for tracking NPCs in the rodent brain. This technique has been used to track NPCs, immune cells, and cancer cells in the brain (Kleinschnitz et al., 2003; Heyn et al., 2006b; Shapiro et al., 2006a) and elsewhere in the body (Beckmann et al., 2003; Shapiro et al., 2006a; Tai et al., 2006). Compared to histological techniques, MRI allows for serial tracking within subjects, reducing the error variance associated with differences between subjects and allowing for a more complete understanding of a dynamic process through the power of repeated measures, without using ionizing radiation. MRI has the flexibility to provide both anatomical and functional data. For example, with MRI we can assess changes in lesion size for stroke (structure), then measure changes in perfusion and/or permeability (function) following NPC treatment (Jiang et al., 2005; Daadi et al., 2009, 2013). Unlike histology, MRI enables dynamic and repeated measures of these parameters over time and can sample the whole brain.

Our objectives in this review are to demonstrate the use of MRI to track NPCs in the rodent brain, describe the tools and methods of labeling cells, and discuss what we have learned about regeneration using imaging. Two main strategies are used for labeling NPCs: (1) injecting the iron oxide particles directly into the brain or ventricles to label proliferating NPCs *in situ*, or (2) labeling cells *in vitro* with iron oxide particles and then transplanting them into the animal either within the brain or vascular system. In both approaches, migration toward the OB or to the site of an injury can be monitored over time. As these techniques have matured, challenges related to the optimal way to label the cells, where the cells or particles should be injected, and how best to visualize and quantify the labeled cells have been defined by the many groups working on tracking NPCs *in vivo*. We will discuss the methods, current applications and future directions of both techniques.

IRON OXIDE CONTRAST AGENTS AND MAGNETIC CELL LABELING

A variety of SPIO contrast agents are available for labeling cells *in vitro* and *in situ*. Micron-sized particles of iron oxide (MPIOs) are 0.86–1.63 μm diameter particles that can also be fluorescent. They have a high iron content (∼1 pg/particle), so that a single particle is detectable by MRI, but their polystyrene coating

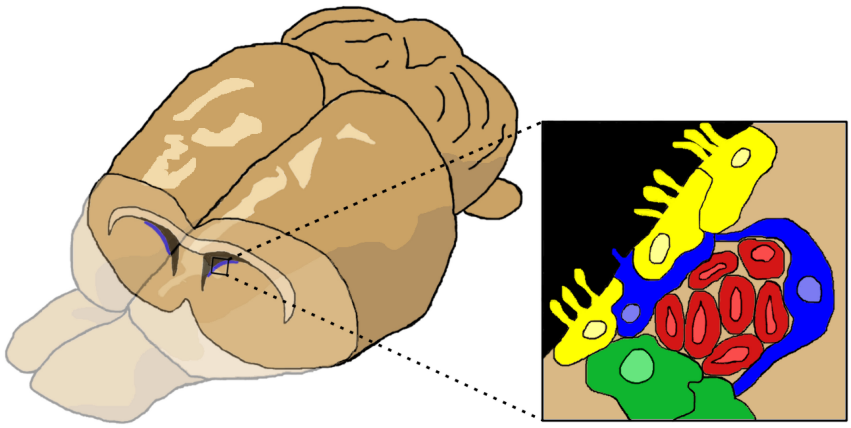

FIGURE 1 | The cells of the subventricular zone (SVZ). The SVZ is located just below the lateral ventricles. Cells (inset) consist of ependymal cells (yellow), type B or astrocytes (blue), type C or transit amplifying cells (green), and type A cells or neuroblasts (red). Figure inspired by García-Verdugo et al. (1998), Ihrie and Álvarez-Buylla (2011).

is non-biodegradable and is therefore not a clinically viable agent (Shapiro et al., 2004). Smaller dextran coated particles (SPIO) such as Feridex/Endorem (ferumoxides) and Resovist (ferucarbotran) have been shown to label NPC *in vitro* (Song et al., 2007; Lu et al., 2017) and are clinically approved, though as of this writing they are no longer available for purchase in North America. Feraheme (ferumoxytol), an ultrasmall iron oxide particle (USPIO) is clinically approved as a treatment for anemia and has been used in cell tracking studies, although not in NPCs transplantation in humans as of yet. Pre-clinically, these agents have been shown to effectively label human NSC *in vitro* and that labeled cells continue to home to disease in mice (Gutova et al., 2013). However, the FDA has recently issued a black-box warning because fatal allergic reactions were seen in some patients with anemia following intravenous administration of ferumoxytol. There are other dextran coated particles in development that are commercially (FeraTrack Direct; Aswendt et al., 2015; Kim et al., 2016) or laboratory (Song et al., 2007; Barrow et al., 2015) derived and have been applied to NSC tracking.

Iron oxide particles with unique features have been fabricated in individual laboratories and used for cellular imaging experiments. PLGA encapsulated iron oxide particles have been described as a clinically viable source of contrast for MRI-based cell tracking (Nkansah et al., 2011; Granot et al., 2014; Shapiro, 2015). These particles vary in size from 100 nm to 2 μm and efficiently package iron within their polymer shell comprised of a FDA-approved material. *In vitro* labeling of NPCs with these particles does not impair the ability of these cells to differentiate down neuronal, astrocyte or oligodendrocyte lineages (Granot et al., 2014). Magnetoliposomes consisting of SPIO enclosed in a phospholipid bilayer have been used to label NPCs *in situ* (Vreys et al., 2011), as well as custom-made targeted glyconanoparticles as described by Elvira et al. (2012).

Chemical tools that were originally developed for transfecting genes into cells have been adapted for cell labeling and can increase the efficiency of particle uptake into cells *in situ* or *in vitro*. These include the use of poly-L-lysine (PLL) (Frank et al., 2002; Daadi et al., 2009, 2013) or protamine sulfate (Guzman et al., 2008; Panizzo et al., 2009) which are co-incubated with particles and cells for *in vitro* labeling and co-injected with particles for *in situ* labeling. More complex methods for *in vitro* labeling include electroporation (Obenaus et al., 2011) or sonoporation (Xie et al., 2010) or a gene gun (Zhang et al., 2003; Jiang et al., 2005); all of these methods have been used with some success.

MRI PROTOCOLS AND SEQUENCES

There are several methods for using MRI to detect magnetically labeled cells, with most manipulating some aspect of the local magnetic inhomogeneity caused by close proximity of the superparamagnetic nanoparticles. The most commonly reported methods make use of gradient recalled echo (GRE) based pulse sequences. The local magnetic inhomogeneity induced by the superparamagnetic nanoparticles accelerates the dephasing of water protons near the particles following radiofrequency excitation, essentially quenching the NMR signal. This results in a dark spot in the MRI image (Shapiro et al., 2006b). The sensitivity of this method to iron oxide nanoparticles can be increased by lengthening the echo time (TE), making the dark spot larger, but this can also result in image deformation with longer TE. Spin echo sequences can also be used to probe this phenomenon, but due to the ability to rapidly acquire 3D volumes using short flip angle and fast repetition time (TR), GRE techniques have advantages over spin echo techniques.

Another approach to exploit the magnetic field inhomogeneity near the superparamagnetic nanoparticles to detect magnetically labeled cells is to form images based on quantitative measurement of the magnetic susceptibility, or quantitative susceptibility mapping (QSM; Wang and Liu, 2015). As normal tissue has much lower magnetic susceptibility than iron oxide nanoparticles, nanoparticle-laden cells can be readily distinguished using this approach. An added advantage is the ability to discriminate the

iron oxide MRI signal from other structures that cause dark contrast such as air and blood vessels (Haacke et al., 2015). Other techniques negate the magnetic susceptibility effect and generate images principally characterized by T1 effects of the iron oxide nanoparticles. These pulse sequences, such as ultrashort echo time (UTE; Hong et al., 2017) and SWeep Imaging with Fourier Transformation (SWIFT; Magnitsky et al., 2017, 2018), use very short echo times to prevent dephasing of the excited protons, capturing the signal from the water near the nanoparticles, and instead use T1 weighting to create hypointensity at the spot of the labeled cells. The exciting nature of the pulse sequences described in this paragraph is the quantitative nature of these sequences, enabling the *in vivo* measurement of iron concentrations (Ring et al., 2018). These types of pulse sequences and data analyses might be most useful for determining the relative number of cells in a large cell transplant, for example.

The above-mentioned pulse sequences enable measurement of iron concentrations, but the conversion of iron concentration to cell number is not straightforward as individual cells can have different amounts of iron. The use of very high resolution *in vivo* MRI is one approach to solving the challenge of cell enumeration. MRI detection of single cells has been demonstrated by employing GRE based techniques (Shapiro et al., 2006b). Mills et al. (2008, 2011) used phase map cross correlation to discriminate individual magnetically labeled immune cells in rat heart and brain. Mori et al. (2014) used high resolution GRE images to detect and enumerate magnetically labeled microglia in the brain, making use of signal thresholding to identify cells. Afridi et al. (2017), acquired GRE images of rat brain following injection of magnetically labeled mesenchymal stem cells, where individual cells were visible as dark spots. Machine learning was used to non-invasively quantify the number of cells that were delivered to the brain. Whereas not all cell transplant or stem cell migration paradigms are amenable to this type of analysis, measurement of cell number is clearly an open area of research in the field of MRI-based cell tracking of neural cells.

MRI OF ENDOGENOUS NPCs

Magnetic resonance imaging of endogenous NPCs is accomplished by magnetically labeling proliferating NPCs *in situ* and using MRI to serially monitor migration away from the SVZ; in healthy animals, cells travel along the RMS to the OB, however, disease stimulates these cells to migrate away from the RMS and toward lesions in the brain. In this section, we will describe how the work on this elegant technique for tracking migrating cells has focused on developing and improving the labeling methods and determining which particles offer the best labeling and imaging, with the large MPIO particles offering the best detection of migrating NPC. We will discuss the application of labeling of endogenous NPC to the study of disease models such as multiple sclerosis and neonatal hypoxia-ischemia. Another option for tracking endogenous NPCs is to transfect them with one of the recently described MRI reporter genes; the genes used in this emerging technique and the opportunities they enable will be discussed below.

In situ Labeling Methods

In situ labeling of NPCs with iron oxides first involved injecting very small ∼20 nm particles into the carotid artery, then disrupting the blood-brain barrier (BBB) with mannitol to allow the particles to enter the brain and label NPC (Neuwelt et al., 1994). Shapiro et al. (2006a) developed the technique of injecting MPIOs in a volume of 10–50 μL of stock particles (1.63 μm diameter particles, ∼3 μg Fe/μL) into the anterior horn of the lateral ventricle to label NPCs and track them over time in their migration through the RMS to the OB. This foundational work has been the basis for endogenous NPC labeling tracking studies. **Figure 2** shows an example of migrating cells in the RMS and OB after injection of MPIO particles into the SVZ. The literature since has used several different doses and coordinates (**Table 1**). Granot et al. (2011) attempted to further optimize *in situ* labeling and found that a more rostral injection site and a smaller dose of 20 μL of MPIOs produced the best labeling of NPCs in the RMS, however, in a later publication the same authors used different, more rostral coordinates (Granot and Shapiro, 2014).

Smaller particles were less effective for monitoring migration in the RMS and OB. The clinically approved SPIO called Endorem has a particle size of 120–180 nm, and these particles were evaluated for NPC labeling after injection into the ventricles of healthy rats either with, or without, co-injection of protamine sulfate at a dose of ∼7 μg Fe/μL in a volume of 2.5 μL (Panizzo et al., 2009). The protamine sulfate-Endorem complexes labeled the NPC *in situ* while the uncomplexed Endorem did not, and in fact, was shown to spread throughout the ventricles after injection. Migrating cells labeled with these smaller Endorem

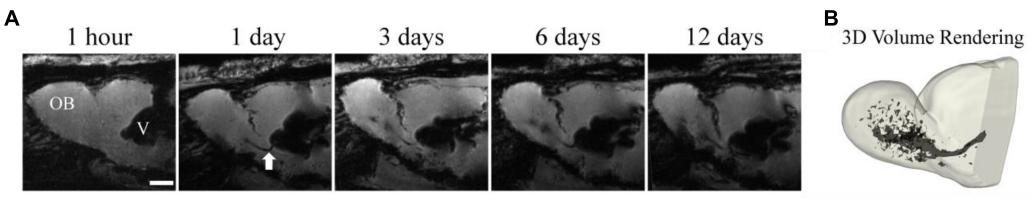

FIGURE 2 | Temporal resolution during early migratory events. MPIOs (50 μL) were injected into the anterior horn of the lateral ventricle proximal to the SVZ in healthy adult rats. 3D gradient echo images of a rat brain were serially acquired at 1 h, 1 days, 3 days, 6 days, and 12 days **(A)** post injection. The RMS is visible on the day 1 images as a dark line extending from the ventricle (white arrow). Migration across the entire OB is visible by day 12, the 3D volume rendering of the OB **(B)** shows the extent of cells within the structure (Adapted from Shuboni-Mulligan et al., 2018).

TABLE 1 | *In situ* NPC labeling technique.

Citation	Species/strain	Age	Injection Volume	Coordinates		
				AP	LM	DV
Shapiro et al., 2006a	Sprague-Dawley	6 weeks	5–50 μL	−2.0 mm	2.0 mm	−3.0 mm
Sumner et al., 2007	Sprague-Dawley	6 weeks	50 μL	−2.0 mm	2.0 mm	−3.0mm
Sumner et al., 2009	Rat/Sprague-Dawley	6 weeks	50 μL	−2.0 mm	2.0 mm	−3.0 mm
Panizzo et al., 2009	Rat/Sprague-Dawley	Not given	20 μL	−0.08 mm	0.14 mm	−0.38 mm
Vreys et al., 2010	Mouse/C57BL/6J	Not given	10 or 1.5 μL	0.3 or 1.7 mm	1 or 0.7 mm	−2.3 or 4.1 mm
Nieman et al., 2010	Mouse/ICR	6–10 weeks	50 nl	−1.2 mm	0.8 mm	−2.5 mm
Granot et al., 2011	Rat/Sprague-Dawley	6 weeks	20–30 μL	−1.5 or −2 mm	1.5 or 2 mm	−3.0 mm
Granot et al., 2014	Rat/Sprague-Dawley	Not given	20 μL	−1.5 mm	1.5 mm	−3.0 mm
Granot and Shapiro, 2014	Rat/Sprague-Dawley	Not given	20 μL	−0.8 mm	1.2 mm	−4.0 mm
Pothayee et al., 2017	Rat/Sprague-Dawley	6 weeks	20 μL	1.9–2.0 mm	1.9–2.0 mm	−4.0 mm
Shuboni-Mulligan et al., 2018	Rat/Fischer 344	6 weeks–2 years	50 μL	0.3 mm	1 mm	−3.5 mm

particles after co-injection with protamine sulfate were visible in the RMS, but not strongly, when imaged *in situ* at 2.35T, and were not visible in the OB. *Ex vivo* imaging at 9.4T was needed to visualize NPC in the OB after labeling with Endorem particles (Panizzo et al., 2009).

Transfection agents have also been used to assist *in situ* cell labeling with MPIOs. In healthy mice, co-injection of 1.5 μL of a mixture of MPIOs and PLL (∼0.67 μg Fe/μL) provided better labeling than an injection of MPIOs and saline in the same volume. Use of the transfection reagent led to good labeling that enabled visualization of cells in the RMS and there seemed to be minimal effects of the labeling on NPC proliferation and no significant inflammation. A higher dose (10 μL, ∼3 μg Fe/μL) of MPIOs did reduce NPC proliferation (Vreys et al., 2010; Guglielmetti et al., 2014).

Specificity of *in situ* Cell Labeling

When MPIOs or SPIOs are injected into the lateral ventricle, uptake of the label is not restricted only to NPCs – scavenger cells and other non-migrating cells can also internalize the particles along the ventricles and choroid plexus. Migrating cells in the RMS can also be 'pruned' (Brunjes and Armstrong, 1996; Winner et al., 2002) and the label may be taken up by microglia during this process. This could lead to signals in the MRI image that are not associated with NPCs. The extent and significance of these nonspecific signals has been addressed in a number of studies. Sumner et al. (2009) used flow cytometry to determine the relative proportion of labeled cell types in excised and digested RMS and OB. At 2 weeks post-injection (50 μL, 3 μg Fe/μL) they observed that ∼40% of the labeled cells were astrocytes, ∼30% oligodendrocytes, ∼30% neurons, with ∼5% microglia in these excised samples of the RMS and SVZ. In the OB, the fraction of astrocytes remained the same, but the proportion of oligodendrocytes increased slightly and neurons decreased to 10% of labeled cells, with a greater percent of microglia (over 10%; Sumner et al., 2009). In contrast, another study in mice using histological staining found that 2 days after labeling with 1.63 μm particles (50 nL, 3 μg Fe/μL), the label was predominantly confined to migrating NPCs (∼60%) and astrocytes (∼25%), but after 21 days, up to 35% of labeled cells were microglia instead of migrating cells, with NPCs remaining at ∼50% and astrocytes ∼25%; there was no difference between the labeled populations in the RMS and the OB (Nieman et al., 2010). This suggests that as the experiment progresses, the label is less likely to be inside migrating cells derived from NPCs. One suggestion is that labeled microglia can be discriminated from labeled NPCs because the microglia will be stationary, while the NPCs will be moving (Shapiro et al., 2006a), though this experiment would be time consuming, requiring multiple scans.

Migration of free particles could also be a problem and is not easily differentiated from labeled cells by MRI. Sumner et al. (2009) found that MPIOs did not migrate spontaneously along the RMS but needed to be carried by a migrating cell. In another experiment, cortical stroke was induced in rats by the injection of ET1, followed by injection of 20 μL of MPIO (0.86 μm, 2 μg Fe/μL). Signal voids were seen at the site of the stroke; however, they were not caused by labeled NPCs, but were due to migration of free particles that were carried by the CSF through the corpus callosum toward the lesion. In this model, the ET1 also acts to disrupt the blood–brain barrier and allow the influx of particles into the brain, which is not a concern in healthy animals, but this does indicate that the location of the lesion must be chosen carefully to avoid the migration of free particles (Granot and Shapiro, 2014). In another study, when magnetoliposomes were injected into the RMS of mice (1.5 μL at 0.67 μg Fe/μL), free magnetoliposomes were seen in white matter tracts and in the RMS but were rarely seen encapsulated in migrating cells (Vreys et al., 2011). They also observed that there was less free motion of cationic magnetoliposomes than anionic ones, so the authors concluded that it may be possible to use larger cationic magnetoliposomes to label NPCs without the risk of migration of free particles (Vreys et al., 2011).

Elvira et al. (2012) made targeted magnetic glyconanoparticles (4 nm diameter) conjugated to Nilo2, an antibody directed against NPCs. These particles were injected into the contralateral ventricle of mice with astrocytoma (1 μL of particles at 0.1 μg Fe/μL). One day after injection, contrast was seen in the tumors as the NPCs at the site of the particle injection migrated to

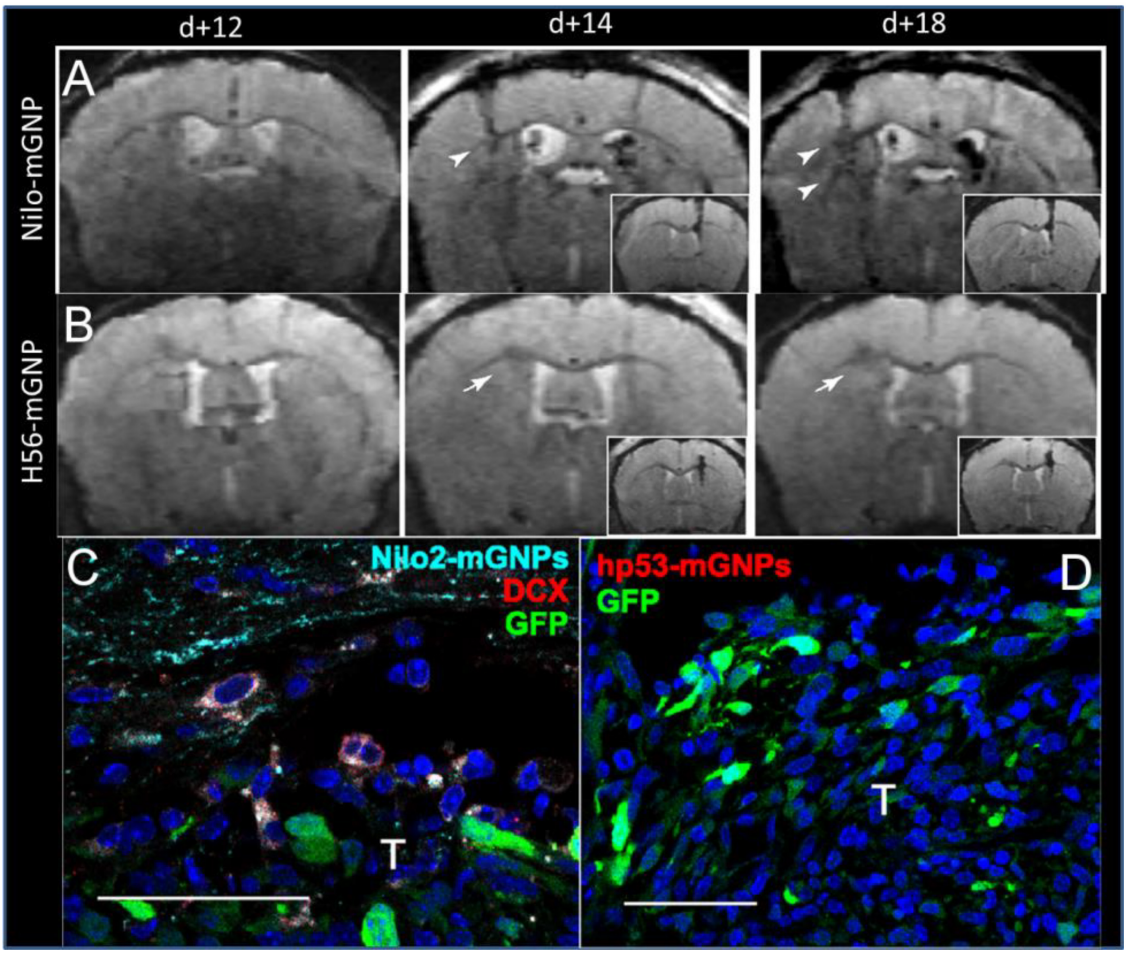

FIGURE 3 | Targeted magnetic glyconanoparticles (mGNP) specifically labeled NPC and the NPC migrated to astrocytomas. mGNP were fabricated with **(A)** antibodies that target NPC (Nilo) or **(B)** control antibodies (H56) and injected contralaterally to CT-2A astrocytoma on day 13 of tumor growth. Arrowheads indicate hypointense signal at the tumors as early as 1 day after NPC injection, while arrows indicate absence of hypointense signals. No control particles were detected at the tumor. **(C)** NPC (red) were labeled with the mGNP (light blue) and migrated to the tumor (green). **(D)** No control nanoparticle labeled cells were detected near the tumor. T, tumor, scale bar is 50 μm (Elvira et al., 2012). Reproduced via Plos One Creative Commons Attribution (CC BY) license.

the tumor; indeed, most of the neuroblasts at the tumor were labeled. When a non-targeted particle was injected, there was no accumulation of contrast at the tumor, although NPCs were present (**Figure 3**). Another study used SPIOs conjugated to CD15 to label *in situ* NPCs (Zhong et al., 2015), increasing the labeling efficiency while decreasing distortions caused by direct MPIO injection. The authors go on to demonstrate the effectiveness of the technique using a stroke model (Zhang et al., 2016). These studies show the potential of using small particles for MR tracking of NPCs in the situation where large numbers of labeled cells are expected to be localized in the brain. It is anticipated that the use of smaller magnetic particles would not have allowed for single-cell detection if the labeled cells were sparsely distributed.

Image Analysis Methods

The contrast due to iron labeled cells is visually apparent for qualitative analysis, although there can be some ambiguity with respect to other hypointense structures in the brain; these depend on the acquisition parameters. Some more complex image analysis methods have also been used to quantify the signal or to discern more subtle or time-dependent effects. Sumner et al. (2009) plotted signal over a line segment to show that the signal in the RMS dropped 60% from the background when there were migrating labeled cells present, while similar studies in phantoms from the same group found that a single cell labeled with MPIOs would cause a 30% signal drop (Shapiro et al., 2005). Subsequently, Granot et al. (2011) registered images of rat brains pre- and post-MPIO injection and looked for regions with a signal decrease of >30% to quantify the migration of cells in the OB. Using this method, they were able to quantify the volume of the OB that was occupied by signal from migrating cells. This signal appeared 2–3 days after MPIO injection, increased linearly until day 7, and then plateaued (Granot et al., 2011). Nieman et al. (2010) used image registration and intensity-based analysis to identify labeled

cells and determine their speed of migration. They estimated that labeled NPCs move at 100–120 μm/h in the RMS and 50 μm/h in the OB (Nieman et al., 2010; Pothayee et al., 2017; Shuboni-Mulligan et al., 2018), slightly slower than the speeds of 150–700 μm/h that were measured in mice with tumors (Elvira et al., 2012). These migration rates are not far from those determined in studies of neurogenesis that employ immunohistochemical methods of detection, which determined a migration rate of 70–80 μm/h in naïve rodents (Nam et al., 2007). Recently, the technique demonstrated that both environmental stimuli, olfactory activity (Pothayee et al., 2017) and aging (Shuboni-Mulligan et al., 2018) impacted migration rates *in vivo*. Understanding the dramatic decrease in NPC migration as animals aged is critical, as many diseases that recruit NPC are more prevalent in older individuals (Wang et al., 2013).

Applications of Endogenous NPCs MRI

Magnetic resonance imaging of endogenous NPCs has also been applied in brain diseases and disorders where there is a need for regeneration of neurons. In neonatal rats with hypoxia-ischemia caused by a ligation for 5 min of the left common carotid artery and then placement into hypoxic chamber (8% O_2 and 92% N_2) for 2 h, MPIOs (10 μL of 0.86 μm particles, 2 μg Fe/μL) were injected into the ventricles to label NPCs. As expected, labeled NPCs migrated through the RMS in healthy rats, but a small portion also migrated toward ischemic regions in the hypoxic-ischemic rats (Yang et al., 2009). The therapeutic effect of the migrating cells was examined using endogenous NPC from the SVZ in a study labeling cells with intraventricular injection of anti-CD15 SPIOs. Proliferation of NPCs in the SVZ was blocked using Ara-A infusion, which ceased migration of cells and prevented the decrease in infarct size over time (Zhang et al., 2016). In another experiment, NPC were labeled with MPIOs (1.63 μm particles, 1.5 μL, 0.67 μg Fe/μL) plus PLL to see if NPC from the SVZ were the source of remyelination following cuprizone treatment in a mouse model of MS. There was no migration of cells from the SVZ to the splenium, so the origin of the new cells was not determined (Guglielmetti et al., 2014).

Reporter Genes in NPCs

Magnetic resonance imaging reporter genes can be used to induce cells to produce proteins that create MRI contrast; one example of such a protein is the iron storage protein, ferritin. Cell tracking with ferritin-overexpressing cells would allow for specific imaging of NPCs without confounding images from label uptake by microglia or free particles, and the label would not be lost through cell division. These are two properties that comprise the strengths of reporter genes, however, the limitation is the requirement of genetically engineering the cells. Ferritin consists of a light chain (L) and a heavy chain (H) that form a shell that can be filled with excess intracellular iron. A ferritin transgene (H and L chains) in an adenoviral vector was injected into the striatum of mice and a clear signal loss was seen at the injection site as soon as 5 days post-transplant from transfected glia and neurons (Genove et al., 2005). The specificity and sensitivity of detecting the ferritin gene following transfection via lentiviral and adenoviral vectors has been assessed (Vande Velde et al., 2011). In this study, the control lentivirus, with the gene encoding green fluorescent protein (GFP), caused a hypointense signal in the brain that was equivalent to the contrast induced when the lentivirus containing the gene for ferritin was used; this was due to an inflammatory response (Vande Velde et al., 2011). This inflammatory response was not seen when an adenovirus construct was used in the same study. A further study injected the lentiviral vector with the ferritin gene into the SVZ or striatum of mice. Despite extensive correction of the RF field bias, there was only minimal signal from migrating NPCs, and it required T_2* mapping (Vande Velde et al., 2012). Lentiviral transfection with ferritin of exogenous NPCs could be visualized with MRI and fluorescence imaging when reintroduced intracranially into rats with acute ischemic stroke but also not of the migration of single cells (Zhang et al., 2017).

A different adenovirus encoding the L*H chains of ferritin has also been injected into mice and in this study, some astrocytes and neurons were transfected (Iordanova et al., 2010; Iordanova and Ahrens, 2012). Some of the transfected cells in the SVZ were proliferative as indicated by Ki67 staining, but transfection was not specific to proliferative cells. In the OB, transfected cells were visible by histology, but not by MRI (Iordanova and Ahrens, 2012). Sensitivity was quantified as 10^4 cells per voxel. A follow-up study used the neurotrophic HSV virus, which was thought to target neurons selectively over glia. In this study, the amount of signal correlated with the amount of virus injected, and this study supports the use of the ferritin as a means to quantify gene delivery in nucleic acid based therapies, rather than a method for tracking the migration of individual transfected neurons (Iordanova et al., 2013). Further modifications to the genetic construct may offer more functionality, and toward this end, inducible ferritin constructs have been used in culture to monitor the differentiation of mesenchymal stem cells into neural cells (Song et al., 2015).

MRI OF EXOGENOUSLY ADMINISTERED NPCs

An alternative method to visualize iron labeled NPCs is to label the cells exogenously and reintroduce them back into an animal. For several disease models, exogenously introduced NPCs have been shown to have a capability to home to areas of disease or injury. There are two distinct applications for monitoring the exogenous administration of NPCs: (1) the monitoring of integrated cells in regenerative medicine and (2) the identification of cell migration to disease area for treatment with modified cells. These applications will be examined here in the context of stroke and glioma.

In vitro NPC Labeling Methods

There are various sources of NPC that can be used for this purpose (**Table 2**): they can be isolated from the SVZ of adult rodents (e.g., Zhang et al., 2003; Jiang et al., 2005), immortalized cell lines isolated from embryonic rodent brain (e.g., Hoehn et al., 2002; Guzman et al., 2008; Obenaus et al., 2011), and finally human NPC can be isolated from human fetal tissue (e.g.,

TABLE 2 | Exogenous neural progenitor cells in stroke.

Citation	Rat breed	Cell type	SPIO	Cell origin	Injection type
(a) Mouse neural stem cells (mNSC)					
Hoehn et al., 2002	Wistar	HT22 mNSC	Ferumoxtran-10, Sinerem®	Immortalized primary mouse hippocampal neural cells derived from parent HT4 cells	Intracranial – Corpus Callosum/Cortex border
Modo et al., 2004	Sprague-Dawley	MHP36 mNSC	Gadolinium-Rhodamine Dextran (GRID)	Cell line isolated from hippocampal proliferative zone of fetal mice (H-2K^b-tsA58)	Intracranial -Striatum
Modo et al., 2009	Sprague-Dawley	MHP36 mNSC	Gadolinium-Rhodamine Dextran (GRID)	Cell line isolated from hippocampal proliferative zone of fetal mice (H-2K^b-tsA58)	Intracranial -Striatum
Guzman et al., 2008	Sprague-Dawley	C17.2 mNSC	Ferumoxides, Feridex® IV	Immortalized cell line established from neonatal mouse (CD1 × C57BL/6) cerebellum	Intracranial – Cortex
Obenaus et al., 2011	Sprague -Dawley	C17.2 mNSC	Ferumoxides, Feridex® IV	Immortalized cell line established from neonatal mouse (CD1 × C57BL/6) cerebellum	Intracranial – Striatum or Intraventricular – Lateral Ventricle
(b) Rat neural stem cells (rNSC)					
Zhang et al., 2003	Wistar	rNSC	MPIO, Bangs	Isolated rNSC from young adult rat brain (SVZ)	Intracistern -Cisterna Magna
Jiang et al., 2005	Wistar	rNSC	MPIO, Bangs	Isolated rNSC from the lateral wall of the lateral ventricle of adult Wistar rat	Intracistern -Cisterna Magna
Li et al., 2006	Wistar	rNSC	MPIO, Bangs	Isolated rNSC from the adult rat brain near the lateral ventricle	Intracistern -Cisterna Magna
Li et al., 2010	Wistar	rNSC	Ferumoxides, Feridex® IV	Isolated rNSC from young adult rat brain (SVZ)	
Wen et al., 2014	Sprague-Dawley	rNSC	Polymersomes PEI-PDDLA	Isolated rNSC from the new born rat brain near the lateral ventricle	Intracranial -Striatum
(c) Human neural stem Cells (hNSC)					
Daadi et al., 2009	Sprague-Dawley	hNSC	Ferumoxides, Feridex® IV	H7 Human embryonic stem cell (WiCell) derived with supplemented media	Intracranial -Striatum
Daadi et al., 2013	Sprague-Dawley	hNSC	Ferumoxides, Feridex® IV	H7 Human embryonic stem cell (WiCell) derived with supplemented media	Intracranial -Striatum
Song et al., 2009	Sprague-Dawley	HB1.F3 hNSC	Ferumoxides, Feridex® IV	Immortalized hNSC established from human fetal brain (ventricular zone)	Intracranial – Striatum or Intravascular – IV
Ashwal et al., 2014	Sprague-Dawley	HFB 2050 hNSC	Ferumoxides, Feridex® IV	Cell line isolated from the ventricular zone of a human fetal cadaver	Intraventricular – Lateral Ventricle

Daadi et al., 2013; Ashwal et al., 2014; Song et al., 2015; Barish et al., 2017). Feridex has been the most common particle used for labeling NPCs in culture (Nucci et al., 2015). Typical iron concentrations for magnetic cell labeling range from 11.2 μg Fe/mL (Ashwal et al., 2014) to 112.3 μg Fe/mL (Song et al., 2009). The simplest method of labeling is incubating cells with particles for 3 days (Song et al., 2009) or for 1 day following trypsinization (Ashwal et al., 2014). Labeling cells with iron oxide particles using these methods had no significant effect on cell viability or on ability to differentiate and migrate (Ben-Hur et al., 2007), especially at low (but still MR-visible) doses. However, some studies with mesenchymal stem cells (Bulte et al., 2004) have found differentiation along some lineages can be impaired; other studies have seen no effect (Arbab et al., 2005b; Kassis et al., 2010). Each cell type that is labeled in this way should be evaluated for effects on cell function prior to conducting studies *in vivo*.

Applications of Exogenous NPCs in Regenerative Medicine

The aim of regenerative medicine is to repair damaged tissues or organs within an organism through replacement or restoration (Mason and Dunnill, 2008). Stem cells, such as NPCs in the brain, play an important role in regeneration and have been evaluated in several disease and injury models. These cell replacement techniques have been paired with MRI in the investigation of recovery from spinal cord injury (Lepore et al., 2006), reducing autoimmune damage in multiple sclerosis (Ben-Hur et al., 2007; Reekmans et al., 2011), and to restore function in stroke models (Hoehn et al., 2002; Zhang et al., 2003).

The disease that has been the most extensively researched using exogenously labeled NPCs and MRI is stroke. In the United States, stroke is the fourth leading cause of death and occurs in one out of every 19 fatalities (Kochanek et al., 2011). Over the past 10 years, stroke-attributed deaths have decreased (Go et al., 2014) thus increasing the demand for regenerative medicine treatment of survivors, who suffer from the adverse effects of stroke. Promising data has been collected in both animal models and clinical trials using exogenous NPCs to reverse or repair damage induced by stroke. Incorporation of MR imaging into the evaluation of NPCs as cell-based therapies is a way for researchers to gain an understanding of the relevant cellular processes, and to guide the development of this approach into a viable strategy for effective regenerative medicine.

In rodent models of ischemic stroke, where the middle cerebral artery (MCAO) is occluded, administration of NPCs has led to marked improvements in both behavioral and physiological markers of animals. The use of iron oxide particles to label cells has allowed researchers to use MRI to visualize the movement and incorporation of cells into the site of stroke (Hoehn et al., 2002; Zhang et al., 2003) and has demonstrated that the migration is directly triggered by the onset of disease (**Figure 4**; Guzman et al., 2008). Additionally, many studies have established that of exogenous NPCs labeled with magnetic particles retain normal function with the same positive effect on restoration of function as control cells without particles. In these studies, magnetically labeled NPCs have been shown to reduce the size of the lesion (Obenaus et al., 2011; Daadi et al., 2013), increase angiogenesis (Jiang et al., 2005; Li et al., 2006) and improve glucose utilization (Daadi et al., 2013) in damaged areas of the brain, and recover sensorimotor functions (Zhang

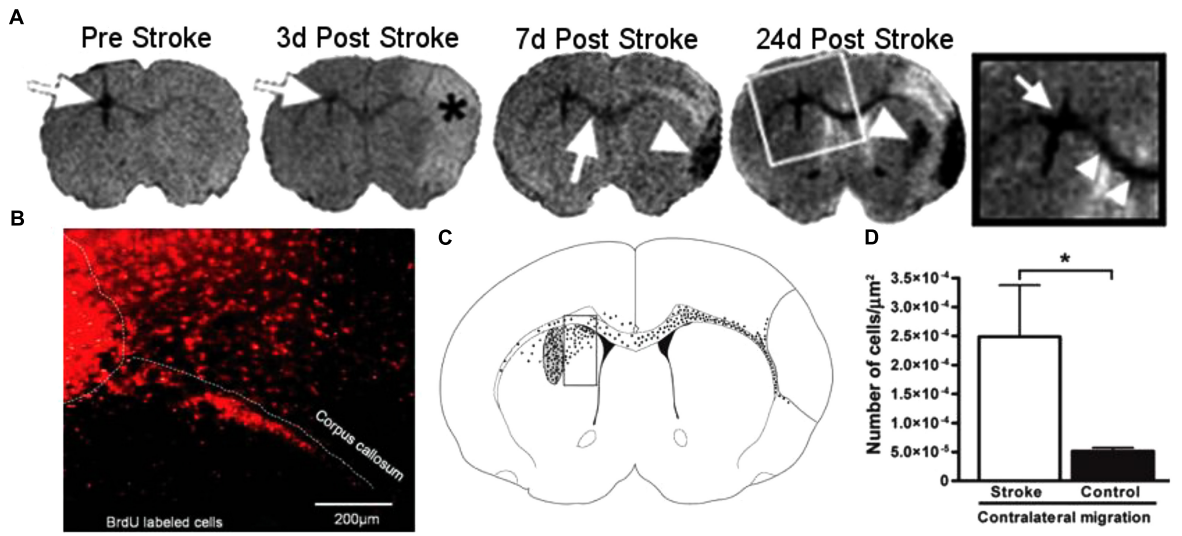

FIGURE 4 | Magnetic resonance imaging (MRI) of NPCs migrating to stroke (Guzman et al., 2008, reproduced with permission). The top panel **(A)** shows a representative MRI of animals injected with NPCs before and over 24 days after the induction of stroke. White arrows show the location of labeled cells, moving from the site of injection to the area of stroke, denoted with an asterisk (*). The bottom panel **(B–D)** shows the histology of animals 24 days after stroke. Cells labeled with BrdU (red, **B**) were observed migrating away from the site of injection and into the corpus callosum. To quantify the migration, the area adjacent to the injection site was analyzed by counting cells in a counting box **(C)**. The graph shows significantly greater migration away from the injection site in animals that received a stroke than the sham controls. Reproduced with permission.

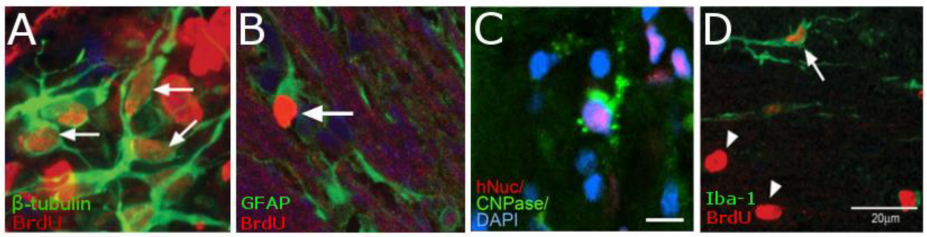

FIGURE 5 | Histology demonstrating the cell types of NPCs after differentiation *in vivo*. NPCs are double-labeled with BrdU (red) and either β-tubulin (green, **A**) showing that cells are differentiation into neurons. Cells that have differentiated into astrocytes are double-labeled with BrdU (red) and GFAP (Green, **B**). While those cells that have differentiated into oligodendrocytes are triple-labeled for hNSC (red), CNPase (green), and the nucleus with DAPI (blue **C**). However, there is very little macrophages-positive staining (OX6, Green) that is co-localized for BrdU (red, **D**). [Data from Guzman et al., 2008, reproduced with permission); Daadi et al., 2008, Reproduced via Plos One Creative Commons Attribution (CC BY) license].

et al., 2003; Daadi et al., 2009). In a large animal, porcine, model of ischemia, NPCs injected into the region of stroke decrease the immune response and reduced changes in cerebral blood perfusion and brain metabolism (Baker et al., 2017). Additionally, rodent studies have demonstrated that labeled cells that migrated into the site of the infarct have functionally incorporated into the tissue (**Figure 5**) and differentiated into neurons (β-tubulin and NeuN), astrocytes (GFAP), and oligodendrocytes (CNPase) (Song et al., 2009; Daadi et al., 2013). These cells did not, however, counterstain with antibodies that were specific for microglia and macrophages (OX6; Song et al., 2009). The cellular and molecular mechanisms that lead to functional improvement have not yet been established, although several hypotheses have been proposed (reviewed in Boese et al., 2018). The effects could be mediated by replacement of lost circuitry, neuroprotective function, improved vascular recovery, paracrine stimulation of surviving neurons and other cells, recruitment of endogenous progenitors, or reduced inflammation.

Factors Affecting MRI of Exogenous NPCs

Implementation of MR imaging of cellular fates in stroke research has the potential for making NPC transplantation a realistic therapy for patients suffering from this disease. Through imaging we can refine our understanding of the optimal route and timing of injection, the effective dose of cells for a given lesion, rapid determination of lesion size, and the relevant cell types for reversing the damage and restoring function. In stroke, four routes of administration of cells have been used: intracerebral, intraventricular, intracisternal, and intravascular. The most common route used in animal studies is intra-cerebral injections into the striatum (**Table 2**) and this is also being evaluated in clinical trials. Investigation in the field of regenerative medicine originally focused on this approach because researchers wanted to limit the distance cells would have to migrate and eliminate the complications of requiring cells to penetrate the blood brain barrier (Willing and Shahaduzzaman, 2013). However, intra-cerebral injection is an invasive procedure that involves complex stereotactic surgery in patients already weakened by stroke; therefore, other routes of administration would be preferable. Intra-ventricular and intracisternal injections are less invasive and may minimize tissue damage by targeting the brain ventricles or subarachnoid spaces, respectively. Both methods have been demonstrated to allow cell migration to the site of stroke (Li et al., 2006; Obenaus et al., 2011; Ashwal et al., 2014); however, only one study compared these methods directly to intracerebral injection. In this study (Obenaus et al., 2011), more cellular migration was observed with intra-ventricular injections compared to intracerebral injections into the striatum, however, no statistics or compelling images were provided to bolster these claims.

The least invasive routes of NPCs administration are peripheral injections, either venous (IV; Song et al., 2009) or arterial (IA; Li et al., 2010). When comparing these two vascular routes of administration to intracisternal injections, Li et al. (2010) found that IA injections had the fastest and greatest dispersion of cells within the stroke area while IV injection had the slowest and least number of cells, however, animals that received IA injections also had a higher mortality. This study, while providing interesting insights into the migration of NPCs after these injection routes, did not address the full range of physiological effects, the overall localization of cells, or the cause of mortality. More in depth investigation will be required prior to drawing any conclusions and developing an effective treatment plan for patients is identified to minimize complications while providing optimal care.

The relationship between cell dose and recovery is more straight-forward. When heNSCs labeled with Feridex were injected into the striatum of rats with stroke, the number of cells administered was inversely proportional to the size of the stroke after treatment (Daadi et al., 2009, 2013). Thus, studies comparing injection routes should control for number of cells to avoid confounding results. Additionally, the relationship between the number of transplanted cells and stroke recovery is even more complicated. The more severe and larger the initial stroke volume, the less of an impact treatment with NPCs has on the outcome of adult (Daadi et al., 2013) and infant (Ashwal et al., 2014) animals with stroke. Others have determined that, paradoxically, a lower dose of NPC is more effective at achieving homing toward a tumor (Barish et al., 2017).

There are still many questions that have yet to be addressed with these models; including the best cell type and the best

methodology for labeling cells, since a wide variety of each have been used, as well as, the interaction of the transplanted cells with those of the tissue. Rodent studies have used cells isolated from the SVZ of adult rats, immortalized NPC lines from rodent embryos, or those isolated from human fetuses. In humans, there are two abstracts that have used NPCs derived from human fetal tissue and demonstrate improved symptoms in patients (Kalladka et al., 2013; Qiao et al., 2014). The authors of one abstract are currently running two clinical trials (NCT01151124 and NCT02117635, ClinicalTrial.gov) using the cell line CTX0E03 DP, an immortalized human stem cell line derived from third trimester human fetal cortex (Pollock et al., 2006). These different types of cells have never been compared in terms of efficiency; therefore, generalizations between studies should be analyzed in this light. The phase I escalation trial showed no adverse effects of the cell injection and modest neurological improvements in some patients (Kalladka et al., 2016), the phase II trial has completed recruitment, but no results have been published.

Applications of Exogenous NPCs in Glioma Therapies

Another application of magnetically labeled exogenous NPCs is their use in the detection or targeted treatment of glioma. Gliomas arise within the nervous system and are classified by histopathology and immunohistochemistry (Tsankova and Canoll, 2014). GBM is a particularly aggressive primary brain tumor with a grim prognosis for patients; the average lifespan is less than 12 months (Towner et al., 2011). Because the brain is an immune-privileged area within the body and is protected by the blood–brain barrier, detection and treatment of these tumors presents a particular challenge. Research into the use of NPCs in the treatment of glioma has made progress in harnessing the unique characteristics of NPCs in migrating toward glioma cells and the power of cell tracking via MRI.

Early studies used histological methods to demonstrate that (1) NPCs actively migrate into the tumor itself (Aboody et al., 2000) and (2) the mere presence of NPCs could act to impede the growth and proliferation of tumors (Glass et al., 2005). Both results were later replicated using MRI-based cell tracking. Brekke et al. (2007) used gadolinium-based particles to determine that NPCs injected contralateral to the tumor site migrated across the corpus callosum to the site of the tumor (**Figure 6**) and that tumor doubling time was significantly decreased, probably due to reduced edema formation (Brekke et al., 2007). Others have explored different routes of administration and found migration to the tumor following IV (Gutova et al., 2013), intracisternal (Zhang et al., 2004) and intracerebral (Thu et al., 2009; Chaumeil et al., 2012) injections of NPCs, demonstrating that cells also penetrate the tumor with these routes. The effects of NPC presence on tumor growth, however, were trivial and did not greatly alter the course of the disease.

The next step in the progression of the NPCs/glioma research focused on modifying NPCs to deliver agents to the site of the tumor and have a greater impact on tumor growth. Cells can be altered to (1) deliver specific cytokines, (2) impact angiogenesis, or (3) to function as "suicide cells" that deliver prodrugs to the effective area (Kwiatkowska et al., 2013). MRI labeling of NPCs with MPIOs has been used in prodrug delivery studies to optimize the timing of the activation of the suicide cell. Researchers have established cell lines that can produce an enzyme that can convert a prodrug into a chemotherapeutic agent for the purpose of directed delivery (Aboody et al., 2013). The effectiveness of this method has been verified in combination with iron labeling to demonstrate the advantages of using the combination, and patients were recruited into a phase I clinical trial (NCT01172964, ClinicalTrial.gov). This trial has completed their recruitment, and while no results have been published, two additional trials have been launched (NCT02015819 and NCT02192359) to test the addition of the combination of Leucovorin or to modify cells to sensitize them to the drug Irinotecan (Mutukula and Elkabetz, 2017).

Another novel approach in the use of MRI and magnetically labeled NPCs in the treatment of GBM is their possible use in the detection of tumor recurrence. Recurrence of tumors in GBM patients is a universal trait of the disease and is believed to be a major contributor to the poor survival of patients (Park et al., 2010). New treatments designed to reduce tumor size have been shown to increase the migration of tumor cells and the formation of recurrent masses further from the

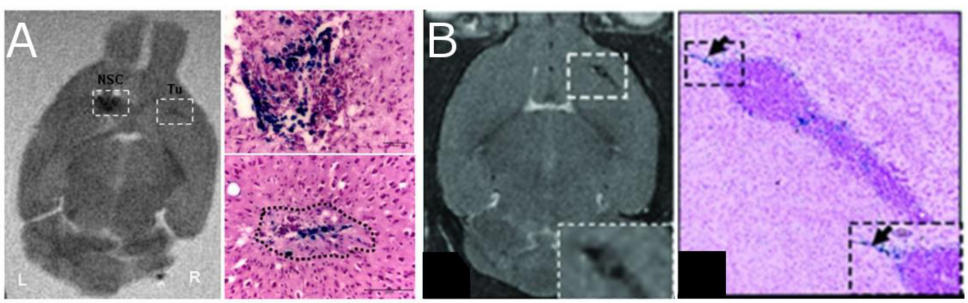

FIGURE 6 | Neural progenitor cells (NPCs) migrating to glioma after injection of SPIO labeled cells. The left two panels **(A)** show coronal *ex vivo* MRI images (T_2-weighted) and Prussian Blue staining of tumor in animals with tumors 4 days after contralateral intracranial NPCs injection [Thu et al., 2009, reproduced via Plos One Creative Commons Attribution (CC BY) license]. Cells migrate away from the injection site and into the tumor. The right two panels **(B)** show *in vivo* MRI images (T_2-weighted) and the Prussian blue histology of animals with IV injections of NPC (Gutova et al., 2013, reproduced with permission).

original site (Ogura et al., 2013). One suggestion is to use MPIO-labeled stem cells as a diagnostic tool for identifying small masses of tumor (<1 mm^2) that are not detectible with current MRI methods (Bennewitz et al., 2012). While the authors suggested the use of mesenchymal stem cells, NPCs might provide a more attractive alternative. Indeed, there is already some anecdotal data showing the ability of NPCs to detect individual glioma cells (Zhang et al., 2004), however, this is based on immunohistochemistry demonstrating a single NPC near a glioma cell within the corpus callosum. This hypothesis merits further investigation but it is imperative to examine the signals that recruit cells to the tumor and the ability of NPCs to home to early tumors and micro-metastases in a more prospectively designed experiment.

Additionally, others suggested the use of NPCs as a method to infect remaining tumor cells with a conditionally replicative adenovirus after surgical resection of the mass. In a preliminary study, Morshed et al. (2015) imaged NPCs carrying a cytotoxic adenovirus infiltrating the margins of the tumor. This study is an initial step but shows a promising new avenue for the combination of MRI and NPCs in the treatment of GBM.

Obstacles for Tracking Exogenously Labeled NPCs

Beyond the lack of consistency with regards to techniques for cell administration in the preclinical and clinical studies mentioned above, the tracking of exogenously labeled NPCs is limited by factors related to health of the injected cells and the persistence of the loaded particles in cells after transfer. Selection of cells and particles within an experiment is, therefore, an important component of the quality control in tracking studies.

The health of cells being injected into patients is important for the transfer of therapeutic effect as well as for both the short and long-term ability to monitoring cells *in vivo* over time. Immediately following injection of cells, there is a possibility of the grafted cells being rejected, and this has been examined in a handful of models. Mesenchymal stem cells (MSC) can be obtained from patient and the use of such autologous grafts should reduce the likelihood of rejection (Akgun et al., 2015). MSC can be harvested in the operating room, cultured and labeled, then reintroduced into the targeted area of the patient (Callera and de Melo, 2007; Kassis et al., 2010). The importance of using autologous MSCs has not been definitively established (Kode et al., 2009). For ischemic cardiomyopathy, allogeneic, and autologous MSC produced similar positive therapeutic results, and neither triggered an immune response (Hare et al., 2012). In contrast, NPCs cannot easily be harvested from patients; therefore, these cells are collected from donors, i.e., fetal cadavers. The sex of the NPC donor was found not to be relevant to the success of the graft in a rat study (Ashwal et al., 2014), however, other parameters have not been fully examined. Taken together these studies suggest that the risk of rejection is low. However, a recent article, Bago et al. (2017) demonstrated the possibility of using donor fibroblasts to *trans*-differentiate into NSCs and allowing for autologous cells to be cultured into cytotoxic agents against glioblastoma.

A major criticism of using iron oxide nanoparticles for cell tracking is that the signal is retained even after the labeled cells are no longer viable. MRI does, however, have the potential to differentiate between live and dead cells. In immunosuppressed rats, there was a clear difference in the MRI appearance and image intensity and graft size over time between live and dead NPCs (Guzman et al., 2007). When live cells were injected, the size of the hypointensity was constant with time, while transfer of dead cells led to a decrease (Guzman et al., 2007). In a different study of immunocompetent rats, live cells were observed to migrate leading to an increase in the size of the hypointense region, and since dead cells don't migrate the size of the hypointense region remained constant (Flexman et al., 2011). In a model where animals rejected grafted cells, hypointensity persisted in rejected grafts since the label from dead cells is likely taken up by microglia (Berman et al., 2011). In grafts that survived, the signal is lost over time presumably due to the label being diluted during cell division, (Berman et al., 2011). In another study, when SPIO-labeled NPC were injected into the rat brain and subsequently rejected, the hypointensity persisted at the site of injection in both cases, but again no migration was seen (Bernau et al., 2015). This demonstrates that with proper image processing, the appearance of the MR scan could be used to determine the success of a graft. This would comprise an important diagnostic and prognostic tool that could potentially indicate if a NPC transplant had been successful, or if another graft is required. However, to generate that data to inform these algorithms will require more research using disease models in which cell migration away from the site of injection is expected.

The introduction of stem cells into patients raises the possibility of long term complications due to development of tumors from the transplanted cells. A major safety concern with the use of embryonic stem cells is the formation of benign teratomas (Blum et al., 2009). The formation can be reduced by differentiating the cells beyond the pluripotent state in culture prior to transfer; however, differentiation is usually not 100% leaving stem cells and the potential risk. In addition, other factors can influence the formation of tumors from stem cells (Erdo et al., 2003). When NPCs selected from human embryonic stem cells were injected into mouse eyes, teratomas formed in 50% of animals at 8 weeks post-transplant (Arnhold et al., 2004). Tissue devoid of pluripotent stem cells, derived from either fetal or adult cells, may provide a safer mode of cell generation while still maintaining the cells' potency to differentiate (Pollard et al., 2006; Kosztowski et al., 2009). A majority of the studies in stroke models use fetal or adult cell lines and none report any incidence of tumor formation. In one study, cells implanted into animals were successfully monitored for more than a year (58 weeks) with no report of tumors (Obenaus et al., 2011).

Another obstacle in monitoring exogenously labeled cells is the loss of signal over time due to changes in the cells, particles or both. Reduction in signal has been attributed to several different mechanisms: (1) degradation of the particles over time, (2) dilution of the contrast agent, per cell, during cell proliferation, or (3) release of the particles to endogenous cells upon death of the transplanted NPC. Any of these alone, or in combination, can significantly disrupt plans for prolonged *in vivo* imaging of NPC

migration and distribution. By understanding these mechanisms and the vulnerable points in a cell tracking study, they can in part be circumvented.

The degradation of particles is dependent on the chemical and physical properties of the agent used. Particles enter the cells through endocytosis and are then exposed to the acidic environment of the lysosome, leading to degradation of the agent over time. By mimicking the conditions inside of lysosomes (lysosomal conditions: pH 4.5, sodium citrate buffer) it was shown that ferumoxides (Feridex) release free iron after 7 days, and when evaluated in cultured MSCs, the particles aggregated within the lysosomes and began degradation after 5 days (Arbab et al., 2005a). Poly (lactic co-glycolic acid) (PLGA) encapsulated iron oxide nanoparticles persist for a longer period of time under these conditions but undergo a distinct burst and plateau phase; particles degrade by approximately 80% over a 12-week period (Nkansah et al., 2011). There have been no comprehensive studies published that directly examine and compare the dissolution of different particle types in NPC, either *in vitro* or *in vivo*.

Cells can also be transfected with DNA encoding modified forms of the iron storage protein, ferritin, and then transplanted into the brain. The goal would be to increase specificity of the markers and ensure iron persistence over time, while still having the signal inextricably linked to cell viability. When ferritin- or luciferase-transfected (negative control) cells were transplanted into the striatum of healthy rats, similar hypointensities were observed in the brains of these animals (Bernau et al., 2015). This unexpected result is likely due to the fact that injection of either transfected cell type caused hemorrhage at the site of injection. Moreover, the signal loss persisted even when the cells were rejected (observed after withdrawal of an anti-rejection agent), and no migration of the cells was observed this study (Bernau et al., 2015). At the present time, there are no genetically encoded MR reporters that can be transfected into exogenous cells, or endogenous cells, and used for spatiotemporal MR imaging of cell migration *in vivo*.

When NPCs proliferate and differentiate *in vitro* or *in vivo*, particle concentration per cell is diluted with each division. Differentiation can involve asymmetric cell division with different amounts of contrast agent being retained within each daughter cell (Walczak et al., 2007). Labeling cells with Feridex does not seem to influence the ability of NPCs to differentiate (Cohen et al., 2010). However, the rate of differentiation *in vivo* will vary with the tissue environment, i.e., disease model, and the cell type used. In shiverer mouse models of hereditary demyelination, iron oxide loaded cells were not detectable by MR after 6 days presumably due to dilution of the agent with cell division (Walczak et al., 2007). In contrast, similarly labeled cells transferred into models of glioma and stroke could be monitored for weeks without the loss of signal. It is important to note that these anecdotal studies have not been supported, to date, with studies directly examining either cell division rates or the differentiation of transplanted cells in glioma or stroke models. Cell division is typically assessed *ex vivo* using a dye, CFSE, which is diluted with cell division and flow cytometry to assess dye concentrations—such experiments are labor intensive and expensive.

Death of transplanted cells can also confound imaging studies. When implanted NPCs die, particles are released and made available to endogenous cells that can pick up the contrast and shuttled it away from the site of injection, reducing the MRI signal. The mononuclear phagocytic system is the major route of clearance for circulating particles and those found within many organs including the brain, it internalizes and metabolize the free-floating particles (Arami et al., 2015). Excess particles from intraventricular injections are taken up by macrophages and leads to the buildup of iron in macrophage-rich organs including the choroid plexus, liver and spleen (Gorman et al., 2018). Alternatively, the contrast can be taken up by resident microglia to create a false positive signal that persists within the brain. In a variety of different disease models, exogenous NPCs have been shown to primarily differentiate into neurons, astrocytes, and oligodendrocytes and not microglia or macrophages. In a study looking at the injection of dead NPCs, it was demonstrated that particles are found in astrocytes that accumulate at the site of injection and not within cells that migrate (Flexman et al., 2011). This suggests that moving particles may be indicative of live NPC, and stationary particles may have been released by the death of their original host. Nonetheless, there are a number of patterns of iron oxide distribution in the brain following transfer of labeled cells, and these patterns are indicative of the fates and function of both transplanted and endogenous cells. Working out the significance of the hypointensity patterns in MR images may be possible and become useful in guiding the development of cell-based therapies for brain injury and disease.

THE FUTURE OF NPCs AND MRI

Magnetic resonance imaging has successfully been used to image the migration of endogenous and transplanted NPC in rodents, providing the opportunity to monitor neural stem/progenitor cell fates, function and migration in the brain with applications to the study of brain development and treatment of focal and diffuse disease. However, some questions remain that must be solved before cellular MRI can be used in patients. These largely relate to the impact of the uncertain availability of particles for cell tracking in humans, the basic questions of the mechanism of uptake of particles, the need to transition from small animal models to large animals and humans, and the effect of ever increasing availability of high field clinical MRI scanners.

Current work has shown that the most sensitive labels for imaging are the MPIOs, but these particles have a non-biodegradable polystyrene coating and are unlikely to be approved for use in humans. Other particles such as Feridex have been taken off the market, while ferumoxytol has a black box warning from the FDA. There is a clinical need for biodegradable particles containing large amounts of iron to be developed so that this technique can be applied in human patients. One solution could be iron crystals encapsulated in the clinically approved polymer PLGA; these particles are non-toxic and the size can easily be manipulated during fabrication (Nkansah et al., 2011; Granot et al., 2014).

Magnetic particle imaging (MPI) is an emerging technique for imaging magnetically labeled cells that has recently been applied to stem cell imaging in the brain. MPI directly detects the non-linear magnetization of magnetic particles by measuring the effect of an oscillating magnetic field that is rastered through the sample (Gleich and Weizenecker, 2005). MPI shows promise for direct quantification of the amount of iron (and therefore the number of cells). MSC and hESC-derived neural cells have been injected into the rodent brain and imaged *in vivo* (Bulte et al., 2015; Zheng et al., 2015). Current sensitivity is about 200 cells *in vitro* and 50,000 cells *in vivo* (Bulte et al., 2015; Zheng et al., 2015) and new particles specifically designed for MPI may increase sensitivity. MPI has the advantage that there is no background signal from normal brain tissue. One drawback to this technique is that the MPI image does not contain any anatomical information, so it must be acquired in a scanner that combines MPI and another imaging modality such as MRI or CT to accurately locate the source of the MPI signal. The resolution of the MPI is also quite coarse as it is applied in these papers, on the order of 1 mm (Bulte et al., 2015; Zheng et al., 2015).

One largely unknown factor is the mechanism of particle uptake when cells are labeled *in situ*. An understanding of this process could allow us to design particles that are specific to NPCs (Elvira et al., 2012; Zhong et al., 2015; Zhang et al., 2016). Additionally, there is a trend to develop 'smart' contrast agents that specifically cause a signal when they are within a particular, pre-determined, cell type (e.g., Granot and Shapiro, 2011; Gallo et al., 2014); application of this approach to NPC transplantation in the brain would greatly improve these tracking experiments.

In preclinical work, tracking of labeled NPCs has so far been limited to rodent models of disease. Larger animal models, such as cats, dogs, and pigs, should also be used as a precursor to transition to the clinic. The existence of a RMS in humans is currently debated and even proliferation of cells in the adult SVZ is controversial (reviewed in Butti et al., 2014). It is well established, however, that neurogenesis decreased with age (Enwere et al., 2004; Apostolopoulou et al., 2017) and demonstrated via *in situ* labeling to impact migration rates, as well as, NPC total number in the RMS and OB (Shuboni-Mulligan et al., 2018). Further studies are needed to determine if there are treatments that can restart directed proliferation and migration of NPCs in the damaged and diseased brain.

In these imaging studies, the field strength of the MRI system is critical to sensitive detection. Most of the studies described in this review were performed at field strengths above the clinical standard of 3T (at 4.7T, 7T, 9.4T and above). Sensitivity to labeled cells increases with field strength, even in rodent models (Panizzo et al., 2009), and high fields accelerate acquisition of the high-resolution images that are needed for single-cell tracking. However, there may not be a significant gain in sensitivity with increasing field strength (e.g., 7.0T and 11.7T; Shapiro et al., 2005). For translation of NPC tracking to human studies, the importance of high field needs to be determined. Zhu et al. (2006) injected autologous NPCs labeled with SPIOs into patients with traumatic brain injury, and migration of the cells toward the lesion was visible, even with a 3.0T system. In a study of the spine transplanted CD34+ cells labeled with large particles were visible with a 1.0T magnet (Callera and de Melo, 2007). High-field human MRI systems (7.0T) are becoming more common but still present technical challenges related to coil design and energy deposition; however, their use might increase the feasibility and significance of NPC tracking in humans (van der Kolk et al., 2013).

CONCLUSION

Enabling MR imaging of NPCs through labeling with iron oxide particles creates an opportunity for examining the migration and homing of NPCs in the healthy and diseased brain. *In situ* labeling with iron oxide particles is achieved by direct injection of particles into the lateral ventricle, these particles are phagocytosed by NPC in the SVZ and carried within the cells as they migrate to the OB. MRI allows for the serial monitoring of single cell migration along the RMS within an individual subject over time. Basic science studies using the technique have revealed the true rate of migration across the RMS *in vivo* and the importance of these migratory cells in olfaction and aging. Pre-clinically, the technique has demonstrated the homing of endogenous NPC to stroke and highlighted the importance of endogenous cells in minimizing the longitudinal negative effects of ischemia, as blocking endogenous migration with Ara-A leads to larger infarcts over time. Labeling methods in rats are well defined and easily replicated between laboratories; particles can be large non-biodegradable particles that are sensitive at the single-cell level or smaller particles that have already received clinical approval. There have been some strides to create particles that are targeted to NPC and would allow for lower dose injections in animal studies. Synthesis of biocompatible PLGA SPIOs are also providing a promising avenue for a clinically viable source of contrast for MRI-based cell tracking. Although there are some remaining challenges to the technique, *in situ* labeling has and will continue to lead to a greater understanding of how these cells function in therapy and the role of NPCs in normalizing the brain.

In vitro labeling followed by cellular transplantation into the brain has been used to determine the homing and treatment mechanisms of NPCs in many disease, including stroke, traumatic brain injury, cancer, Parkinson's disease and multiple sclerosis. The literature of MRI and *in vitro* SPIO labeling is most rich in the fields of stroke and glioma and has lead from basic science experiments into multiple phase I clinical trials. In glioma, exogenous NPC can be derived from patient fibroblast and are genetically altered to synthesize an enzyme that can convert a prodrug into a chemotherapeutic. MRI tracking then allows researchers to watch the migration of the cells into the tumor and give the prodrug at the optimal time to kill as many neighboring tumor cells. This method provides a unique treatment for an aggressive disease, whose standard of care has not altered since the advent of the Stupp protocol in 2009. Methodologically, *in vitro* NPC labeling in rodents has determined the best type of isolated cells for minimal immune response, optimal route of administration, rate of particle degradation, and causes of signal loss. Clearly, the field of

regenerative medicine has made great strides in the application of NPC in therapeutics and MRI cell tracking has provided an excellent tool for elevating the research.

The future of NPC tracking using MRI holds many promising avenues to transform both *in situ* and *in vitro* labeling and imaging. Transfection of NPCs with MRI reporter genes is in its infancy and is not yet at a point where it can be adapted for cell tracking studies due to the very low signals compared to signals from cells labeled *in situ* or *in vitro* with iron oxide particles but promises imaging of cellular fates and function. PLGA coated iron oxide nanocrystals provide a possible solution to the current ban on clinically approved cell tracking particles, as they are non-toxic and comprised of a FDA-approved material. Surface manipulation of particles is also being explored to improve NPC uptake *in vitro* and targeting endogenous cells *in situ*. Finally, imaging methods are improving with the growth of human 7.0T MRI and the advent of MPI technology, allowing for higher sensitivity and increased detection of labeled cells. We are at the very early stages of this burgeoning field of research, and the tools being developed hold tremendous promise for improving human health and treating disease.

AUTHOR CONTRIBUTIONS

All authors listed have made a substantial, direct and intellectual contribution to the work, and approved it for publication.

FUNDING

Funds for open access publication fees originated from the Department of Radiology, Michigan State University. ES was supported by "National Institutes of Health" with the grant numbers NIDDK R01 DK107697, NINDS R01 NS104306, NIBIB R21 EB017881, NCI R21 CA185163, and NIA R21 AG041266.

REFERENCES

Aboody, K. S., Najbauer, J., Metz, M. Z., D'Apuzzo, M., Gutova, M., Annala, A. J., et al. (2013). Neural stem cell-mediated enzyme/prodrug therapy for glioma: preclinical studies. *Sci. Transl. Med.* 5:184ra59. doi: 10.1126/scitranslmed.3005365

Aboody, K. S., Brown, A., Rainov, K. G., Bower, K. A., Liu, S., Yang, W., et al. (2000). Neural stem cells display extensive tropism for pathology in adult brain: evidence from intracranial gliomas. *Proc. Natl. Acad. Sci. U.S.A.* 97, 12846–12851. doi: 10.1073/pnas.97.23.12846

Abrous, D. N., Koehl, M., and Moal, M. L. (2005). Adult neurogenesis: from precursors to network and physiology. *Physiol. Rev.* 85, 523–569. doi: 10.1152/physrev.00055.2003

Afridi, M. J., Ross, A., Liu, X., Bennewitz, M. F., Shuboni, D. D., and Shapiro, E. M. (2017). Intelligent and automatic *in vivo* detection and quantification of transplanted cells in MRI. *Magn. Reson. Med.* 78, 1991–2002. doi: 10.1002/mrm.26571

Akgun, I., Unlu, M. C., Erdal, O. A., Ogut, T., Erturk, M., Ovali, E., et al. (2015). Matrix-induced autologous mesenchymal stem cell implantation versus matrix-induced autologous chondrocyte implantation in the treatment of chondral defects of the knee: a 2-year randomized study. *Arch. Orthop. Trauma Surg.* 135, 251–263. doi: 10.1007/s00402-014-2136-z

Apostolopoulou, M., Kiehl, T. R., Winter, M., de la Hoz, E. C., Boles, N. C., Bjorsson, C. S., et al. (2017). Non-montonic changes in progenitor cell behavior and gene expression during aging of the adult V-SVZ neural stem cell niche. *Stem Cell Rep.* 9, 1931–1947. doi: 10.1016/j.stemcr.2017.10.005

Arami, H., Khandhar, A., Liggitt, D., and Krishnan, K. M. (2015). *In vivo* delivery, pharmacokinetics, biodistribution and toxicity of iron oxide nanoparticles. *Chem. Soc. Rev.* 44, 8576–8607. doi: 10.1039/c5cs00541h

Arbab, A. S., Wilson, L. B., Ashari, P., Jordan, E. K., Lewis, B. K., and Frank, J. A. (2005a). A model of lysosomal metabolism of dextran coated superparamagnetic iron oxide (SPIO) nanoparticles: implications for cellular magnetic resonance imaging. *NMR Biomed.* 18, 383–389.

Arbab, A. S., Yocum, G. T., Rad, A. M., Khakoo, A. Y., Fellowes, V., Read, E. J., et al. (2005b). Labeling of cells with ferumoxides–protamine sulfate complexes does not inhibit function or differentiation capacity of hematopoietic or mesenchymal stem cells. *NMR Biomed.* 18, 553–559. doi: 10.1002/nbm.991

Arnhold, S., Klein, H., Semkova, I., Addicks, K., and Schraermeyer, U. (2004). Neurally selected embryonic stem cells induce tumor formation after long-term survival following engraftment into the subretinal space. *Invest. Opthalmol. Vis. Sci.* 45, 4251–4255. doi: 10.1167/iovs.03-1108

Arvidsson, A., Collin, T., Kirik, D., Kokaia, Z., and Lindvall, O. (2002). Neuronal replacement from endogenous precursors in the adult brain after stroke. *Nat. Med.* 8, 963–970. doi: 10.1038/nm747

Ashwal, S., Ghosh, N., Turenius, C. I., Dulcich, M., Denham, C. M., Tone, B., et al. (2014). Reparative effects of neural stem cells in neonatal rats with hypoxic–ischemic injury are not influenced by host sex. *Pediatr. Res.* 75, 603–611. doi: 10.1038/pr.2014.7

Aswendt, M., Henn, N., Michalk, S., Schneider, G., Steiner, M. S., Bissa, U., et al. (2015). Novel bimodal iron oxide particles for efficient tracking of human neural stem cells *in vivo*. *Nanomedicine* 10, 2499–2512. doi: 10.2217/NNM.15.94

Bago, J. R., Okolie, O., Dumitru, R., Ewend, M. G., Parker, J. S., Werff, R. V., et al. (2017). Tumor-homing cytotoxic human unduced neural stem cells for cancer therapy. *Sci. Transl. Med.* 9:eaah6510. doi: 10.1126/scitranslmed.aah6510

Baker, E. W., Platt, S. R., Lau, V. W., Grace, H. E., Holmes, S. P., Wang, L., et al. (2017). Induced pluripotent stem cell-derived neural stem cell theraphy enhances recovery in an ischemic stroke pig model. *Sci. Rep.* 7:10075. doi: 10.1038/s41598-017-10406-x

Barish, M. E., Herrmann, K., Tang, Y., Herculian, S. A., Metz, M., Aramburo, S., et al. (2017). Human neural stem cell biodistribution and predicted tumor coverage by a diffusible therapeutic in a mouse glioma model. *Stem Cells Transl. Med.* 6, 1522–1532. doi: 10.1002/sctm.16-0397

Barrow, M., Taylor, A., Nieves, D. J., Bogart, L. K., Mandal, P., Collins, C. M., et al. (2015). Tailoring the surface charge of dextran-based polymer coated SPIONs for modulated stem cell uptake and MRI contrast. *Biomater. Sci.* 3, 608–616. doi: 10.1039/c5bm00011d

Beckmann, N., Falk, R., Zurbrügg, S., Dawson, J., and Engelhardt, P. (2003). Macrophage infiltration into the rat knee detected by MRI in a model of antigen-induced arthritis. *Magn. Reson. Med.* 49, 1047–1055. doi: 10.1002/mrm.10480

Ben-Hur, T., van Heeswijk, R. B., Einstein, O., Aharonowiz, M., Xue, R., Frost, E. E., et al. (2007). Serial in vivo MR tracking of magnetically labeled neural spheres transplanted in chronic EAE mice. *Magn. Reson. Med.* 57, 164–171. doi: 10.1002/mrm.21116

Bennewitz, M. F., Tang, K. S., Markakis, E. A., and Shapiro, E. M. (2012). Specific chemotaxis of magnetically labeled mesenchymal stem cells: implications for mri of glioma. *Mol. Imaging Biol.* 14, 676–687. doi: 10.1007/s11307-012-0553-3

Berman, S. C., Galpoththawela, C., Gilad, A. A., Bulte, J. W. M., and Walczak, P. (2011). Long-term MR cell tracking of neural stem cells grafted in immunocompetent versus immunodeficient mice reveals distinct differences in contrast between live and dead cells. *Magn. Reson. Med.* 65, 564–574. doi: 10.1002/mrm.22613

Bernau, K., Lewis, C. M., Petelinsek, A. M., Reagan, M. S., Niles, D. J., Mattis, V. B., et al. (2015). *In Vivo* tracking of human neural progenitor cells in the rat brain using magnetic resonance imaging is not enhanced by

ferritin expression. *Cell Transplant.* 25, 575–592. doi: 10.3727/096368915X688614

Betarbet, R., Zigovz, T., Barkay, R., and Luskin, M. (1996). Migration patterns of neonatal subventricular zone progenitor cells transplanted into the neonatal striatum. *Cell Transplant.* 5, 165–178. doi: 10.1177/096368979600500207

Blum, B., Bar-Nur, O., Golan-Lev, T., and Benvenisty, N. (2009). The anti-apoptotic gene survivin contributes to teratoma formation by human embryonic stem cells. *Nat. Biotechnol.* 27, 281–287. doi: 10.1038/nbt.1527

Boese, A. C., Le, Q.-S. E., Pham, D., Hamblin, M. H., and Lee, J.-P. (2018). Neural stem cell therapy for subacute and chronic ischemic stroke. *Stem Cell Res. Ther.* 9:154. doi: 10.1186/s13287-018-0913-2

Brekke, C., Williams, S. C., Price, J., Thorsen, F., and Modo, M. (2007). Cellular multiparametric MRI of neural stem cell therapy in a rat glioma model. *Neuroimage* 37, 769–782. doi: 10.1016/j.neuroimage.2007.06.006

Brunjes, P. C., and Armstrong, A. M. (1996). Apoptosis in the rostral migratory stream of the developing rat. *Dev. Brain Res.* 92, 219–222. doi: 10.1016/0165-3806(96)00006-5

Bulte, J. W. M., Kraitchman, D. L., Mackay, A. M., and Pittenger, M. F. (2004). Chondrogenic differentiation of mesenchymal stem cells is inhibited after magnetic labeling with ferumoxides. *Blood* 104, 3410–3413. doi: 10.1182/blood-2004-06-2117

Bulte, J. W. M., Walczak, P., Janowski, M., Krishnan, K. M., Arami, H., Halkola, A., et al. (2015). Quantitative "hot spot" imaging of transplanted stem cells using superparamagnetic tracers and magnetic particle imaging (MPI). *Tomography* 1, 91–97. doi: 10.18383/j.tom.2015.00172

Butti, E., Cusimano, M., Bacigaluppi, M., and Martino, G. (2014). Neurogenic and non-neurogenic functions of endogenous neural stem cells. *Front. Neurosci.* 8:92. doi: 10.3389/fnins.2014.00092

Callera, F., and de Melo, C. M. (2007). Magnetic resonance tracking of magnetically labeled autologous bone marrow cd34 + cells transplanted into the spinal cord via lumbar puncture technique in patients with chronic spinal cord injury: cd34 + cells' migration into the injured site. *Stem Cells Dev.* 16, 461–466. doi: 10.1089/scd.2007.0083

Chaumeil, M. M., Gini, B., Yang, H., Iwanami, A., Sukumar, S., Ozawa, T., et al. (2012). Longitudinal evaluation of MPIO-labeled stem cell biodistribution in glioblastoma using high resolution and contrast-enhanced MR imaging at 14.1Tesla. *Neuro –Oncol.* 14, 1050–1061. doi: 10.1093/neuonc/nos126

Christie, K. J., and Turnley, A. M. (2013). Regulation of endogenous neural stem/progenitor cells for neural repair—factors that promote neurogenesis and gliogenesis in the normal and damaged brain. *Front. Cell. Neurosci.* 6:70. doi: 10.3389/fncel.2012.00070

Cohen, M. E., Muja, N., Fainstein, N., Bulte, J. W. M., and Ben-Hur, T. (2010). Conserved fate and function of ferumoxides-labeled neural precursor cells *in vitro* and *in vivo*. *J. Neurosci. Res.* 88, 936–944. doi: 10.1002/jnr.22277

Daadi, M. M., Hu, S., Klausner, J., Li, Z., Sofilos, M., Sun, G., et al. (2013). Imaging neural stem cell graft-induced structural repair in stroke. *Cell Transplant.* 22, 881–892. doi: 10.3727/096368912X656144

Daadi, M. M., Li, Z., Arac, A., Grueter, B. A., Sofilos, M., Malenka, R. C., et al. (2009). Molecular and magnetic resonance imaging of human embryonic stem cell–derived neural stem cell grafts in ischemic rat brain. *Mol. Ther.* 17, 1282–1291. doi: 10.1038/mt.2009.104

Daadi, M. M., Maag, A.-L., and Steinberg, G. K. (2008). Adherent self-renewable human embryonic stem cell-derived neural stem cell line: functional engraftment in experimental stroke model. *PLoS One* 3:e1644. doi: 10.1371/journal.pone.0001644

Diaz-Coranguez, M., Segovia, J., Lopez-Ornelas, A., Puerta-Guardo, H., Ludert, J., Chavez, B., et al. (2013). Transmigration of neural stem cells across the blood brain barrier induced by glioma cells. *PLoS One* 8:e60655. doi: 10.1371/journal.pone.0060655

Elvira, G., Garcia, I., Benito, M., Gallo, J., Desco, M., Penades, S., et al. (2012). Live imaging of mouse endogenous neural progenitors migrating in response to an induced tumor. *PLoS One* 7:e44466. doi: 10.1371/journal.pone.0044466

Enwere, E., Shingo, T., Gregg, C., Fujikawa, H., Ohta, S., and Weiss, S. (2004). Aging results in reduced epidermal growth factor receptor signaling, diminished olfactory neurogenesis, deficits in fine olfactory discrimination. *J. Neurosci.* 24, 8354–8365. doi: 10.1523/JNEUROSCI.2751-04.2004

Erdo, F., Behrle, C., Blunk, J., Hoehn, M., Xia, Y., Fleischmann, B., et al. (2003). Host-dependent tumorigenesis of embryonic stem cell transplantation in experimental stroke. *J. Cereb. Blood Flow Metab.* 23, 780–785. doi: 10.1097/01.WCB.0000071886.63724.FB

Flexman, J. A., Cross, D. J., Tran, L. N., Sasaki, T., Kim, Y., and Minoshima, S. (2011). Quantitative analysis of neural stem cell migration and tracer clearance in the rat brain by MRI. *Mol. Imaging Biol.* 13, 104–111. doi: 10.1007/s11307-010-0311-3

Frank, J. A., Zywicke, H., Jordan, E. K., Mitchell, J., Lewis, B. K., Miller, B., et al. (2002). Magnetic intracellular labeling of mammalian cells by combining (FDA-approved) superparamagnetic iron oxide MR contrast agents and commonly used transfection agents. *Acad. Radiol.* 9, S484–S487. doi: 10.1016/S1076-6332(03)80271-4

Gage, F. H. (2002). Neurogenesis in the adult brain. *J. Neurosci.* 22, 612–613. doi: 10.1523/JNEUROSCI.22-03-00612.2002

Gallo, J., Kamaly, N., Lavdas, I., Stevens, E., Nguyen, Q.-D., Wylezinska-Arridge, M., et al. (2014). CXCR4-Targeted and MMP-responsive iron oxide nanoparticles for enhanced magnetic resonance imaging. *Angew. Chem. Int. Ed.* 53, 9550–9554. doi: 10.1002/anie.201405442

García-Verdugo, J. M., Doetsch, F., Wichterle, H., Lim, D. A., and Alvarez-Buylla, A. (1998). Architecture and cell types of the adult subventricular zone: in search of the stem cells. *J. Neurobiol.* 36, 234–248. doi: 10.1002/(SICI)1097-4695(199808)36:2<234::AID-NEU10>3.0.CO;2-E

Genove, G., DeMarco, U., Xu, H., Goins, W. F., and Ahrens, E. T. (2005). A new transgene reporter for *in vivo* magnetic resonance imaging. *Nat. Med.* 11, 450–454. doi: 10.1038/nm1208

Glass, R., Synowitz, M., Kronenberg, G., Walzlein, J. H., Markovic, D. S., and Wang, L. P. (2005). Glioblastoma-induced attraction of endogenous neural precursor cells is associated with improved survival. *J. Neurosci.* 25, 2637–2646. doi: 10.1523/JNEUROSCI.5118-04.2005

Gleich, B., and Weizenecker, J. (2005). Tomographic imaging using the nonlinear response of magnetic particles. *Nature* 435, 1214–1217.

Go, A. S., Mozaffarian, D., Roger, V. L., Benjamin, E. J., Berry, J. D., Blaha, M. J., et al. (2014). Heart disease and stroke statistics–2014 update: a report from the american heart association. *Circulation* 129, e28–e292. doi: 10.1038/nature03808

Gonzalez-Perez, O. (2012). Neural stem cells in the adult human brain. *Biol. Biomed. Rep.* 2, 59–69. doi: 10.1161/01.cir.0000441139.02102.80

Gorman, A. W., Deh, K. M., Schwiedrzik, C. M., White, J. R., Groman, E. V., Fisher, C. A., et al. (2018). Brain iron distribution after multiple doses of ultra-small supraparamagnetic iron oxide particles in rats. *Comp. Med.* 68, 139–147.

Granot, D., Nkansah, M. K., Bennewitz, M. F., Tang, K. S., Markakis, E. A., and Shapiro, E. M. (2014). Clinically viable magnetic poly(lactide-co-glycolide) particles for MRI-based cell tracking. *Magn. Reson. Med.* 71, 1238–1250. doi: 10.1002/mrm.24741

Granot, D., Scheinost, D., Markakis, E. A., Papademetris, X., and Shapiro, E. M. (2011). Serial monitoring of endogenous neuroblast migration by cellular MRI. *Neuroimage* 57, 817–824. doi: 10.1016/j.neuroimage.2011.04.063

Granot, D., and Shapiro, E. M. (2011). Release activation of iron oxide nanoparticles: (reaction) A novel environmentally sensitive MRI paradigm. *Magn. Reson. Med.* 65, 1253–1259. doi: 10.1002/mrm.22839

Granot, D., and Shapiro, E. M. (2014). Accumulation of micron sized iron oxide particles in endothelin-1 induced focal cortical ischemia in rats is independent of cell migration. *Magn. Reson. Med.* 71, 1568–1574. doi: 10.1002/mrm.24788

Guglielmetti, C., Praet, J., Rangarajan, J. R., Vreys, R., De Vocht, N., Maes, F., et al. (2014). Multimodal imaging of subventricular zone neural stem/progenitor cells in the cuprizone mouse model reveals increased neurogenic potential for the olfactory bulb pathway, but no contribution to remyelination of the corpus callosum. *Neuroimage* 86, 99–110. doi: 10.1016/j.neuroimage.2013.07.080

Gutova, M., Frank, J. A., D'Apuzzo, M., Khankaldyyan, V., Gilchrist, M. M., Annala, A. J., et al. (2013). Magnetic resonance imaging tracking of ferumoxytol-labeled human neural stem cells: studies leading to clinical use. *Stem Cells Transl. Med.* 2, 766–775. doi: 10.5966/sctm.2013-0049

Guzman, R., Bliss, T., De Los Angeles, A., Moseley, M., Palmer, T., and Steinberg, G. (2008). Neural progenitor cells transplanted into the uninjured brain undergo targeted migration after stroke onset. *J. Neurosci. Res.* 86, 873–882. doi: 10.1002/jnr.21542

Guzman, R., Uchida, N., Bliss, T. M., He, D., Christopherson, K. K., Stellwagen, D., et al. (2007). Long-term monitoring of transplanted human neural stem cells in developmental and pathological contexts with MRI. *Proc. Natl. Acad. Sci. U.S.A.* 104, 10211–10216. doi: 10.1073/pnas.0608519104

Haacke, E. M., Liu, S., Buch, S., Zheng, W., Wu, D., and Ye, Y. (2015). Quantitative susceptibility mapping: current status and future directions. *Magn. Reson. Imaging* 33, 1–25. doi: 10.1016/j.mri.2014.09.004

Hare, J. M., Fishman, J. E., Gerstenblith, G., DiFede Velazquez, D. L., Zambrano, J. P., Suncion, V. Y., et al. (2012). Comparison of allogeneic vs autologous bone marrow–derived mesenchymal stem cells delivered by transendocardial injection in patients with ischemic cardiomyopathy: the poseidon randomized trial. *JAMA* 308, 2369–2379. doi: 10.1001/jama.2012.25321

Harris, V. K., Stark, J., Vyshkina, T., Blackshear, L., Joo, G., Stefanova, V., et al. (2018). Phase I trial of intrathecal mesenchymal stem cell-derived neural progenitors in progressive multiple sclerosis. *eBioMed.* 29, 23–30. doi: 10.1016/j.ebiom.2018.02.002

Heyn, C., Ronald, J. A., Mackenzie, L. T., MacDonald, I. C., Chambers, A. F., Rutt, B. K., et al. (2006a). In vivo magnetic resonance imaging of single cells in mouse brain with optical validation. *Magn. Reson. Med.* 55, 23–29. doi: 10.1002/mrm.20747

Heyn, C., Ronald, J. A., Ramadan, S. S., Snir, J. A., Barry, A. M., MacKenzie, L. T., et al. (2006b). *In vivo* MRI of cancer cell fate at the single-cell level in a mouse model of breast cancer metastasis to the brain. *Magn. Reson. Med.* 56, 1001–1010.

Hoehn, M., Küstermann, E., Blunk, J., Wiedermann, D., Trapp, T., Wecker, S., et al. (2002). Monitoring of implanted stem cell migration *in vivo*: a highly resolved *in vivo* magnetic resonance imaging investigation of experimental stroke in rat. *Proc. Natl. Acad. Sci. U.S.A.* 99, 16267–16272. doi: 10.1073/pnas.242435499

Hong, W., He, Q., Fan, S., Carl, M., Shao, H., Chen, J., et al. (2017). Imaging and quantification of iron-oxide nanoparticles (IONP) using MP-RAGE and UTE based sequences. *Magn. Reson. Med.* 78, 226–232. doi: 10.1002/mrm.26371

Huang, L., Wong, S., Snyder, E. Y., Hamblin, M. H., and Lee, J.-P. (2014). Human neural stem cells rapidly ameliorate symptomatic inflammation in early-stage ischemic-reperfusion cerebral injury. *Stem Cell Res. Ther.* 5:129. doi: 10.1186/scrt519

Ihrie, R. A., and Álvarez-Buylla, A. (2011). Lake-front property: a unique germinal niche by the lateral ventricles of the adult brain. *Neuron* 70, 674–686. doi: 10.1016/j.neuron.2011.05.004

Iordanova, B., and Ahrens, E. T. (2012). *In vivo* magnetic resonance imaging of ferritin-based reporter visualizes native neuroblast migration. *Neuroimage* 59, 1004–1012. doi: 10.1016/j.neuroimage.2011.08.068

Iordanova, B., Goins, W. F., Clawson, D. S., Hitchens, T. K., and Ahrens, E. T. (2013). Quantification of HSV-1-mediated expression of the ferritin MRI reporter in the mouse brain. *Gene Ther.* 20, 589–596. doi: 10.1038/gt.2012.70

Iordanova, B., Robison, C. S., and Ahrens, E. T. (2010). Design and characterization of a chimeric ferritin with enhanced iron loading and transverse NMR relaxation rate. *J. Biol. Inorg. Chem.* 15, 957–965. doi: 10.1007/s00775-010-0657-7

Jiang, Q., Zhang, Z. G., Ding, G. L., Zhang, L., Ewing, J. R., Wang, L., et al. (2005). Investigation of neural progenitor cell induced angiogenesis after embolic stroke in rat using MRI. *Neuroimage* 28, 698–707. doi: 10.1016/j.neuroimage.2005.06.063

Kalladka, D., Sinden, J., Pollock, K., Haig, C., McLean, J., Smith, W., et al. (2016). Human neural stem cells in patients with chronic ischaemic stroke (PISCES): a phase 1, first-in-man study. *Lancet* 388, 787–796. doi: 10.1016/S0140-6736(16)30513-X

Kalladka, D., Sinden, J., Pollock, K., McLean, J., Dunn, L., Santosh, C., et al. (2013). Pilot investigation of stem cells in stroke [pisces]. *Cerebrovasc. Dis.* 35(Suppl. 3):551.

Kassis, I., Vaknin-Dembinsky, A., Bulte, J., and Karussis, D. (2010). Effects of supermagnetic iron oxide labeling on the major functional properties of human mesenchymal stem cells from multiple sclerosis patients. *Int. J. Stem Cells* 3, 144–153. doi: 10.15283/ijsc.2010.3.2.144

Kleinschnitz, C., Bendszus, M., Frank, M., Solymosi, L., Toyka, K. V., and Stoll, G. (2003). *In Vivo* monitoring of macrophage infiltration in experimental ischemic brain lesions by magnetic resonance imaging. *J. Cereb. Blood Flow Metab.* 23, 1356–1361. doi: 10.1097/01.WCB.0000090505.76664.DB

Kim, S. J., Lewis, B., Steiner, M-S., Bissa, U. V., Dose, C., and Frank, J. A. (2016). Superparamagnetic iron oxide nanoparticles for direct labeling of stem cells and *in vivo* MRI tracking. *Contrast Media Mol. Imaging* 11, 55–64. doi: 10.1002/cmmi.1658

Kochanek, K. D., Xu, J., Murphy, S. L., Mini-o, A. M., and Kung, H.-C. (2011). National Vital Statistics Reports. Hyattsville, MD: National Center for Health Statistics.

Kode, J. A., Mukherjee, S., Joglekar, M. V., and Hardikar, A. A. (2009). Mesenchymal stem cells: immunobiology and role in immunomodulation and tissue regeneration. *Cytotherapy* 11, 377–391. doi: 10.1080/14653240903080367

Kokovay, E., Goderie, S., Wang, Y., Lotz, S., Lin, G., Sun, Y., et al. (2010). Adult SVZ Lineage cells home to and leave the vascular niche via differential responses to SDF1/CXCR4 signaling. *Cell Stem Cell* 7, 163–173. doi: 10.1016/j.stem.2010.05.019

Kosztowski, T., Zaidi, H. A., and Quiñones-Hinojosa, A. (2009). Applications of neural and mesenchymal stem cells in the treatment of gliomas. *Expert Rev. Anticancer Ther.* 9, 597–612. doi: 10.1586/era.09.22

Kwiatkowska, A., Nandhu, M., Behera, P., Chiocca, E., and Viapiano, M. (2013). Strategies in gene therapy for glioblastoma. *Cancers* 5, 1271–1305. doi: 10.3390/cancers5041271

Lamm, O., Ganz, J., Melamed, E., and Offen, D. (2014). Harnessing neurogenesis for the possible treatment of Parkinson's disease. *J. Comp. Neurol.* 522, 2817–2830. doi: 10.1002/cne.23607

Lepore, A. C., Walczak, P., Rao, M. S., Fischer, I., and Bulte, J. W. M. (2006). MR imaging of lineage-restricted neural precursors following transplantation into the adult spinal cord. *Exp. Neurol.* 201, 49–59. doi: 10.1016/j.expneurol.2006.03.032

Li, L., Jiang, Q., Ding, G., Zhang, L., Zhang, Z. G., Li, Q., et al. (2010). Effects of administration route on migration and distribution of neural progenitor cells transplanted into rats with focal cerebral ischemia, an MRI study. *J. Cereb. Blood Flow Metab.* 30, 653–662. doi: 10.1038/jcbfm.2009.238

Li, L., Jiang, Q., Zhang, L., Ding, G., Wang, L., Zhang, R., et al. (2006). Ischemic cerebral tissue response to subventricular zone cell transplantation measured by iterative self-organizing data analysis technique algorithm. *J. Cereb. Blood Flow Metab.* 26, 1366–1377. doi: 10.1038/sj.jcbfm.9600288

Lin, G., He, X., Liang, F., Guo, Y., Sunnassee, G., Cao, X., et al. (2018). Transplanted human neural precursor cells integrate into the host neural circuit and ameliorate neurological deficits in a mouse model of traumatic brain injury. *Neurosci. Lett.* 674, 11–17. doi: 10.1016/j.neulet.2018.02.064

Lu, C., Hsiao, J., Liu, H., and Wu, C. (2017). Characterization of an iron oxide nanoparticle labelling and MRI-based protocol for inducing human mesenchymal stem cells into neural-like cells. *Sci. Rep.* 7:3587. doi: 10.1038/s41598-017-03863-x

Magnitsky, S., Pickup, S., Garwood, M., and Idiyatullin, D. (2018). Imaging of a high concentration of iron labeled cells with positive contrast in a rat knee. *Magn. Reson. Med.* doi: 10.1002/mrm.27520 [Epub ahead of print].

Magnitsky, S., Zhang, J., Idiyatullin, D., Mohan, G., Garwood, M., Lane, N. E., et al. (2017). Positive contrast from cells labeled with iron oxide nanoparticles: quantitation of imaging data. *Magn. Reson. Med.* 78, 1900–1910. doi: 10.1002/mrm.26585

Mason, C., and Dunnill, P. (2008). A brief definition of regenerative medicine. *Regen. Med.* 3, 1–5. doi: 10.2217/17460751.3.1.1

Mills, P. H., Hitchens, T. K., Foley, L. M., Link, T., Ye, Q., Weiss, C. R., et al. (2011). Automated detection and characterization of SPIO-labeled cells and capsules using magnetic field perturbations. *Magn. Reson. Med.* 67, 278–289. doi: 10.1002/mrm.22998

Mills, P. H., Wu, Y., Ho, C., and Ahrens, E. T. (2008). Sensitive and automated detection of iron-oxide-labeled cells using phase image cross-correlation analysis. *Magn. Reson. Imaging* 26, 618–628. doi: 10.1016/j.mri.2008.01.007

Modo, M., Beech, J. S., Meade, T. J., Williams, S. C. R., and Price, J. (2009). A chronic 1 year assessment of MRI contrast agent-labelled neural stem cell transplants in stroke. *Neuroimage* 47, T133–T142. doi: 10.1016/j.neuroimage.2008.06.017

Modo, M., Mellodew, K., Cash, D., Fraser, S. E., Meade, T. J., Price, J., et al. (2004). Mapping transplanted stem cell mgration after a stroke: a serial, *in vivo* magnetic resonance imaging study. *Neuroimage* 21, 311–317. doi: 10.1016/j.neuroimage.2003.08.030

Mori, Y., Chen, T., Fujisawa, T., Kobashi, S., Ohno, K., Yoshida, S., et al. (2014). From cartoon to real time MRI: *in vivo* monitoring of phagocytes migration in mouse brain. *Sci. Rep*. 4:6997. doi: 10.1038/srep06997

Morshed, R. A., Gutova, M., Juliano, J., Barish, M. E., Hawkins-Daarud, A., Oganesyan, D., et al. (2015). Analysis of glioblastoma tumor coverage by oncolytic virus-loaded neural stem cells using MRI-based tracking and histological reconstruction. *Cancer Gene Ther.* 22, 55–61. doi: 10.1038/cgt.2014.72

Muldoon, L. L., Tratnyek, P. G., Jacobs, P. M., Doolittle, N. D., Christoforidis, G. A., Frank, J. A., et al. (2006). Imaging and nanomedicine for diagnosis and therapy in the central nervous system: report of the eleventh annual blood-brain barrier disruption consortium meeting. *Am. J. Neuroradiol.* 27, 715–721.

Mundim, M. V., Zamproni, L. N., Pinto, A. A. S., Galindo, L. T., Xavier, A. M., Glezer, I., et al. (2019). A new function for prokineticin 2: recruitment of SVZ-derived neuroblasts to the injured cortex in a mouse model of traumatic brain injury. *Mol. Cell. Neurosci.* 94, 1–10. doi: 10.1016/j.mcn.2018.10.004

Mutukula, N., and Elkabetz, Y. (2017). "Neural killer" cells: autologous cytotoxic neural stem cells for fighting glioma. *Cell Stem Cell* 20, 426–428. doi: 10.1016/j.stem.2017.03.019

Nam, S. C., Kim, Y., Dryanovski, D., Walker, A., Goings, G., Woolfrey, K., et al. (2007). Dynamic features of postnatal subventricular zone cell motility: a two-photon time-lapse study. *J. Comp. Neurol.* 505, 190–208. doi: 10.1002/cne.21473

Neuwelt, E. A., Weissleder, R., Nilaver, G., Kroll, R. A., Roman-Goldstein, S., Szumowski, J., et al. (1994). Delivery of virus-sized iron oxide particles to rodent CNS neurons. *Neurosurgery* 34, 777–784.

Nieman, B. J., Shyu, J. Y., Rodriguez, J. J., Garcia, A. D., Joyner, A. L., and Turnbull, D. H. (2010). *In vivo* MRI of neural cell migration dynamics in the mouse brain. *Neuroimage* 50, 456–464. doi: 10.1016/j.neuroimage.2009.12.107

Nkansah, M. K., Thakral, D., and Shapiro, E. M. (2011). Magnetic poly(lactide-co-glycolide) and cellulose particles for MRI-based cell tracking. *Magn. Reson. Med.* 65, 1776–1785. doi: 10.1002/mrm.22765

Nucci, L. P., Silva, H. R., Giampaoli, V., Mamani, J. B., Nucci, M. P., and Gamarra, L. F. (2015). Stem cells labeled with supraparamagnetic iron oxide nanoparticles in a preclinical model of cerebral ischemia: a systematic review with meta-analysis. *Stem Cell Res. Ther.* 6:27. doi: 10.1186/s13287-015-0015-3

Obenaus, A., Dilmac, N., Tone, B., Tian, H. R., Hartman, R., Digicaylioglu, M., et al. (2011). Long-term magnetic resonance imaging of stem cells in neonatal ischemic injury. *Ann. Neurol.* 69, 282–291. doi: 10.1002/ana.22168

Ogura, K., Mizowaki, T., Arakawa, Y., Ogura, M., Sakanaka, K., Miyamoto, S., et al. (2013). Initial and cumulative recurrence patterns of glioblastoma after temozolomide-based chemoradiotherapy and salvage treatment: a retrospective cohort study in a single institution. *Radiat. Oncol.* 8:97. doi: 10.1186/1748-717X-8-97

Panizzo, R. A., Kyrtatos, P. G., Price, A. N., Gadian, D. G., Ferretti, P., and Lythgoe, M. F. (2009). *In vivo* magnetic resonance imaging of endogenous neuroblasts labelled with a ferumoxide–polycation complex. *Neuroimage* 44, 1239–1246. doi: 10.1016/j.neuroimage.2008.10.062

Park, J. K., Hodges, T., Arko, L., Shen, M., Dello Iacono, D., McNabb, A., et al. (2010). Scale to predict survival after surgery for recurrent glioblastoma multiforme. *J. Clin. Oncol.* 28, 3838–3843. doi: 10.1200/JCO.2010.30.0582

Peng, H., Huang, Y., Rose, J., Erichsen, D., Herek, S., Fujii, N., et al. (2004). Stromal cell-derived factor 1-mediated CXCR4 signaling in rat and human cortical neural progenitor cells. *J. Neurosci. Res.* 76, 35–50. doi: 10.1002/jnr.20045

Pollard, S. M., Conti, L., Sun, Y., Goffredo, D., and Smith, A. (2006). Adherent Neural Stem (NS) cells from fetal and adult forebrain. *Cereb. Cortex* 16, i112–i120. doi: 10.1093/cercor/bhj167

Pollock, K., Stroemer, P., Patel, S., Stevanato, L., Hope, A., Miljan, E., et al. (2006). A conditionally immortal clonal stem cell line from human cortical neuroepithelium for the treatment of ischemic stroke. *Exp. Neurol.* 199, 143–155. doi: 10.1016/j.expneurol.2005.12.011

Pothayee, N., Cummings, D. M., Schoenfeld, T. J., Dodd, S., Cameron, H. A., Belluscio, L., et al. (2017). Magnetic resonance imaging of odorant activity-dependent migration of neural precursor cells and olfactory bulb growth. *Neuroimage* 158, 232–241. doi: 10.1016/j.neuroimage.2017.06.060

Qiao, L., Huang, F., Zhao, M., Xie, J., Shi, J., Wang, J., et al. (2014). A two-year follow-up study of cotransplantation with neural stem/progenitor cells and mesenchymal stromal cells in ischemic stroke patients. *Cell Transplant.* 23, 65–72. doi: 10.3727/096368914X684961

Ramos-Gomez, M., and Martinez-Serrano, A. (2016). Tracking of iron-labeled human neural stem cells by magnetic resonance imaging in cell replacement therapy for Parkinson's Disease. *Neural Regen. Res.* 11, 49–52. doi: 10.4103/1673-5374.169628

Reaux-Le Goazigo, A., Van Steenwinckel, J., Rostene, W., and Parsadaniantz, S. M. (2013). Current status of chemokines in the adult CNS. *Prog. Neurobiol.* 104, 67–92. doi: 10.1016/j.pneurobio.2013.02.001

Reekmans, K. P., Praet, J., De Vocht, N., Tambuyzer, B. R., Bergwerf, I., Daans, J., et al. (2011). Clinical potential of intravenous neural stem cell delivery for treatment of neuroinflammatory disease in mice? *Cell Transplant.* 20, 851–869. doi: 10.3727/096368910X543411

Ring, H. L., Zhang, J., Klein, N. D., Eberly, L. E., Haynes, C. L., and Garwood, M. (2018). Establishing the overlap of IONP quantification with echo and echoless MR relaxation mapping. *Magn. Reson. Med.* 79, 1420–1428. doi: 10.1002/mrm.26800

Rogall, R., Rabenstein, M., Vay, S., Bach, A., Pikhovych, A., Baermann, J., et al. (2018). Bioluminescence imaging visualizes osteopontin-induced neurogenesis and neuroblast migration in the mouse brain after stroke. *Stem Cell Res. Ther.* 9:182. doi: 10.1186/s13287-018-0927-9

Rogelius, N., Ericson, C., and Lundberg, C. (2005). *In vivo* labeling of neuroblasts in the subventricular zone of rats. *J. Neurosci. Methods* 142, 285–293. doi: 10.1016/j.jneumeth.2004.09.008

Seaberg, R. M., and van der Kooy, D. (2003). Stem and progenitor cells: the premature desertion of rigorous definitions. *Trends Neurosci.* 26, 125–131. doi: 10.1016/S0166-2236(03)00031-6

Shapiro, E. M. (2015). Biodegradable, polymer encapsulated, metal oxide particles for MRI-based cell tracking. *Magn. Reson. Med.* 73, 376–389. doi: 10.1002/mrm.25263

Shapiro, E. M., Gonzalez-Perez, O., Manuel García-Verdugo, J., Alvarez-Buylla, A., and Koretsky, A. P. (2006a). Magnetic resonance imaging of the migration of neuronal precursors generated in the adult rodent brain. *Neuroimage* 32, 1150–1157.

Shapiro, E. M., Sharer, K., Skrtic, S., and Koretsky, A. P. (2006b). In vivo detection of single cells by MRI. *Magn. Reson. Med.* 55, 242–249.

Shapiro, E. M., Skrtic, S., and Koretsky, A. P. (2005). Sizing it up: cellular MRI using micron-sized iron oxide particles. *Magn. Reson. Med.* 53, 329–338. doi: 10.1002/mrm.20342

Shapiro, E. M., Skrtic, S., Sharer, K., Hill, J. M., Dunbar, C. E., and Koretsky, A. P. (2004). MRI detection of single particles for cellular imaging. *PNAS* 101, 10901–10906. doi: 10.1073/pnas.0403918101

Shuboni-Mulligan, D. D., Chakravarty, S., Mallett, C. L., Wolf, A. M., Forton, S., and Shapiro, E. M. (2018). Age-dependent visualization of neural progenitor cells within the rostral migratory stream via MRI and endogenously labeled micron-sized iron oxide particles. *bioRxiv*. doi: 10.1101/429787

Song, C., Wang, J., Mo, C., Mu, S., Jiang, X., Li, X., et al. (2015). Use of ferritin expression, regulated by neural cell-specific promoters in human adipose tissue-derived mesenchymal stem cells, to monitor differentiation with magnetic resonance imaging *in vitro*. *PLoS One* 10:e0132480. doi: 10.1371/journal.pone.0132480

Song, M., Kim, Y., Kim, Y., Ryu, S., Song, I., Kim, S. U., et al. (2009). MRI tracking of intravenously transplanted human neural stem cells in rat focal ischemia model. *Neurosci. Res.* 64, 235–239. doi: 10.1016/j.neures.2009.03.006

Song, M., Moon, W. K., Kim, Y., Lim, D., Song, I., and Yoon, B. (2007). Labeling efficiency of supraparamagnetic iron oxide nanoparticles to human neural stem cells: comparison of ferumoxides, monocrystalline iron oxide, cross-linked iron oxide (clio)-nh2 and tat-Clio. *Korean J. Radiol.* 8, 365–371. doi: 10.3348/kjr.2007.8.5.365

Sumner, J. P., Conroy, R., Shapiro, E., Moreland, J., and Koretsky, A. P. (2007). Delivery of fluorescent probes using iron oxide particels as carriers enables in vivo labeling of migrating neural progenitors for MRI and optical imaging. *J. Biomed. Opt.* 12:0515504.

Sumner, J. P., Shapiro, E. M., Maric, D., Conroy, R., and Koretsky, A. P. (2009). *In vivo* labeling of adult neural progenitors for MRI with micron sized particles of iron oxide: quantification of labeled cell

phenotype. *Neuroimage* 44, 671–678. doi: 10.1016/j.neuroimage.2008.07.050

Suzuki, S. O., and Goldman, J. E. (2003). Multiple cell populations in the early postnatal subventricular zone take distinct migratory pathways: a dynamic study of glial and neuronal progenitor migration. *J. Neurosci.* 23, 4240–4250. doi: 10.1523/JNEUROSCI.23-10-04240.2003

Tai, J. H., Foster, P., Rosales, A., Feng, B., Hasilo, C., Martinez, V., et al. (2006). Imaging islets labeled with magnetic nanoparticles at 1.5 tesla. *Diabetes* 55, 2931–2938. doi: 10.2337/db06-0393

Thu, M. S., Najbauer, J., Kendall, S. E., Harutyunyan, I., Sangalang, N., Gutova, M., et al. (2009). Iron labeling and pre-clinical MRI visualization of therapeutic human neural stem cells in a murine glioma model. *PLoS One* 4:e7218. doi: 10.1371/journal.pone.0007218

Towner, R. A., Smith, N., Doblas, S., and He, T. (2011). "Assessment of rodent glioma models using magnetic resonance imaging techniques," in *Advances in the Biology, Imaging and Therapies for Glioblastoma*, ed. C. C. Chen (Rijeka: InTech), 251–272.

Tsankova, N. M., and Canoll, P. (2014). Advances in genetic and epigenetic analyses of gliomas: a neuropathological perspective. *J. Neurooncol.* 119, 481–490. doi: 10.1007/s11060-014-1499-x

van der Kolk, A. G., Hendrikse, J., Zwanenburg, J. J. M., Visser, F., and Luijten, P. R. (2013). Clinical applications of 7 T MRI in the brain. *Eur. J. Radiol.* 82, 708–718. doi: 10.1016/j.ejrad.2011.07.007

Vande Velde, G., Raman Rangarajan, J., Vreys, R., Guglielmetti, C., Dresselaers, T., Verhoye, M., et al. (2012). Quantitative evaluation of MRI-based tracking of ferritin-labeled endogenous neural stem cell progeny in rodent brain. *Neuroimage* 62, 367–380. doi: 10.1016/j.neuroimage.2012.04.040

Vande Velde, G., Rangarajan, J. R., Toelen, J., Dresselaers, T., Ibrahimi, A., Krylychkina, O., et al. (2011). Evaluation of the specificity and sensitivity of ferritin as an MRI reporter gene in the mouse brain using lentiviral and adeno-associated viral vectors. *Gene Ther.* 18, 594–605. doi: 10.1038/gt.2011.2

Ventura, R. E., and Goldman, J. E. (2007). Dorsal radial glia generate olfactory bulb interneurons in the postnatal murine brain. *J. Neurosci.* 27, 4297–4302. doi: 10.1523/JNEUROSCI.0399-07.2007

Vreys, R., Soenen, S. J. H., De Cuyper, M., and Van der Linden, A. (2011). Background migration of USPIO/MLs is a major drawback for in situ labeling of endogenous neural progenitor cells. *Contrast Media Mol. Imaging* 6, 1–6. doi: 10.1002/cmmi.390

Vreys, R., Velde, G. V., Krylychkina, O., Vellema, M., Verhoye, M., Timmermans, J.-P., et al. (2010). MRI visualization of endogenous neural progenitor cell migration along the RMS in the adult mouse brain: validation of various MPIO labeling strategies. *Neuroimage* 49, 2094–2103. doi: 10.1016/j.neuroimage.2009.10.034

Walczak, P., Kedziorek, D. A., Gilad, A. A., Barnett, B. P., and Bulte, J. W. M. (2007). Applicability and limitations of MR tracking of neural stem cells with asymmetric cell division and rapid turnover: the case of the Shiverer dysmyelinated mouse brain. *Magn. Reson. Med.* 58, 261–269. doi: 10.1002/mrm.21280

Wang, Y., and Liu, T. (2015). Quantitative susceptibility mapping (QSM): decoding MRI data for a tissue magnetic biomarker. *Magn. Reson. Med.* 73, 82–101. doi: 10.1002/mrm.25358

Wang, Y., Rudd, A. G., and Wolfe, C. D. A. (2013). Age and ethnic disparities in incidence of stroke over time: the South London stroke register. *Stroke* 44, 3298–3304. doi: 10.1161/STROKEAHA.113.002604

Wen, X., Wang, Y., Zhang, F., Zhang, X., Lu, L., Shuai, X., et al. (2014). *In vivo* monitoring neural stem cells after transplantation in acute cerebral infarction with dual-modal MR imaging and optical imaging. *Biomaterial* 35, 4627–4635. doi: 10.1016/j.biomaterials.2014.02.042

Willing, A. E., and Shahaduzzaman, M. (2013). "Delivery routes for cell therapy in stroke," in *Cell-Based Therapies in Stroke*, eds J. Jolkkonen and P. Walczak (Vienna: Springer), 15–28. doi: 10.1007/978-3-7091-1175-8_2

Winner, B., Cooper-Kuhn, C. M., Aigner, R., Winkler, J., and Kuhn, H. G. (2002). Long-term survival and cell death of newly generated neurons in the adult rat olfactory bulb. *Eur. J. Neurosci.* 16, 1681–1689. doi: 10.1046/j.1460-9568.2002.02238.x

Xie, D., Qiu, B., Walczak, P., Li, X., Ruiz-Cabello, J., Minoshima, S., et al. (2010). Optimization of magnetosonoporation for stem cell labeling. *NMR Biomed.* 23, 480–484. doi: 10.1002/nbm.1485

Yang, J., Liu, J., Niu, G., Chan, K. C., Wang, R., Liu, Y., et al. (2009). *In vivo* MRI of endogenous stem/progenitor cell migration from subventricular zone in normal and injured developing brains. *Neuroimage* 48, 319–328. doi: 10.1016/j.neuroimage.2009.06.075

Zhang, F., Duan, X., Lu, L., Zhang, X., Chen, M., Mao, J., et al. (2017). *In vivo* long-term tracking of neural stem cells transplanted into an acute ischemic stroke model with reporter gene-based bimodal MR and optical imaging. *Cell Transplant.* 26, 1648–1662. doi: 10.1177/0963689717722560

Zhang, F., Duan, X., Lu, L., Zhang, X., Zhong, X., Mao, J., et al. (2016). *In vivo* targeting MR Imaging of endogenous neural stem cells in Ischemic Stroke. *Molecules* 21:E1143. doi: 10.3390/molecules21091143

Zhang, Z., Jiang, Q., Jiang, F., Ding, G., Zhang, R., Wang, L., et al. (2004). *In vivo* magnetic resonance imaging tracks adult neural progenitor cell targeting of brain tumor. *Neuroimage* 23, 281–287. doi: 10.1016/j.neuroimage.2004.05.019

Zhang, Z. G., Jiang, Q., Zhang, R., Zhang, L., Wang, L., Zhang, L., et al. (2003). Magnetic resonance imaging and neurosphere therapy of stroke in rat. *Ann. Neurol.* 53, 259–263. doi: 10.1002/ana.10467

Zheng, B., Vazin, T., Goodwill, P. W., Conway, A., Verma, A., Ulku Saritas, E., et al. (2015). Magnetic particle imaging tracks the long-term fate of *in vivo* neural cell implants with high image contrast. *Sci. Rep.* 5:14055. doi: 10.1038/srep14055

Zhong, X., Zhang, F., Yang, M., Wen, X., Zhang, X., Duan, X., et al. (2015). In vivo targeted magnetic resonance imaging of endogenous neural stem cells in the adult rodent brain. *Biomed. Res. Int.* 2015:131054. doi: 10.1155/2015/131054

Zhu, J., Zhou, L., and XingWu, F. (2006). Tracking neural stem cells in patients with brain trauma. *N. Engl. J. Med.* 355, 2376–2378. doi: 10.1056/NEJMc055304

Conflict of Interest Statement: The authors declare that the research was conducted in the absence of any commercial or financial relationships that could be construed as a potential conflict of interest.

Copyright © 2019 Mallett, Shuboni-Mulligan and Shapiro. This is an open-access article distributed under the terms of the Creative Commons Attribution License (CC BY). The use, distribution or reproduction in other forums is permitted, provided the original author(s) and the copyright owner(s) are credited and that the original publication in this journal is cited, in accordance with accepted academic practice. No use, distribution or reproduction is permitted which does not comply with these terms.

frontiers in Neuroscience

ORIGINAL RESEARCH
published: 18 January 2019
doi: 10.3389/fnins.2018.00968

Brain Vital Signs: Expanding From the Auditory to Visual Modality

Gabriela M. Pawlowski[1,2]*, *Sujoy Ghosh-Hajra*[1,3], *Shaun D. Fickling*[1,3], *Careesa C. Liu*[1,3], *Xiaowei Song*[1,3], *Stephen Robinovitch*[2], *Sam M. Doesburg*[2] *and Ryan C. N. D'Arcy*[1,2,3]*

[1] NeuroTech Laboratory, Faculty of Applied Sciences, Simon Fraser University, Burnaby, BC, Canada, [2] Biomedical Physiology and Kinesiology, Faculty of Science, Simon Fraser University, Burnaby, BC, Canada, [3] Health Sciences and Innovation, Surrey Memorial Hospital, Fraser Health, Surrey, BC, Canada

The critical need for rapid objective, physiological evaluation of brain function at point-of-care has led to the emergence of brain vital signs—a framework encompassing a portable electroencephalography (EEG) and an automated, quick test protocol. This framework enables access to well-established event-related potential (ERP) markers, which are specific to sensory, attention, and cognitive functions in both healthy and patient populations. However, all our applications to-date have used auditory stimulation, which have highlighted application challenges in persons with hearing impairments (e.g., aging, seniors, dementia). Consequently, it has become important to translate brain vital signs into a visual sensory modality. Therefore, the objectives of this study were to: 1) demonstrate the feasibility of visual brain vital signs; and 2) compare and normalize results from visual and auditory brain vital signs. Data were collected from 34 healthy adults (33 ± 13 years) using a 64-channel EEG system. Visual and auditory sequences were kept as comparable as possible to elicit the N100, P300, and N400 responses. Visual brain vital signs were elicited successfully for all three responses across the group (N100: $F = 29.8380$, $p < 0.001$; P300: $F = 138.8442$, $p < 0.0001$; N400: $F = 6.8476$, $p = 0.01$). Initial auditory-visual comparisons across the three components showed attention processing (P300) was found to be the most transferrable across modalities, with no group-level differences and correlated peak amplitudes (rho = 0.7, $p = 0.0001$) across individuals. Auditory P300 latencies were shorter than visual ($p < 0.0001$) but normalization and correlation ($r = 0.5$, $p = 0.0033$) implied a potential systematic difference across modalities. Reduced auditory N400 amplitudes compared to visual ($p = 0.0061$) paired with normalization and correlation across individuals ($r = 0.6$, $p = 0.0012$), also revealed potential systematic modality differences between reading and listening language comprehension. This study provides an initial understanding of the relationship between the visual and auditory sequences, while importantly establishing a visual sequence within the brain vital signs framework. With both auditory and visual stimulation capabilities available, it is possible to broaden applications across the lifespan.

Keywords: electroencephalogram (EEG), event-related potentials (ERPs), clinical assessment, neurology, point-of-care, vital signs

OPEN ACCESS

Edited by:
Feng Liu,
Tianjin Medical University General Hospital, China

Reviewed by:
Xiaochen Tang,
Shanghai Key Laboratory of Psychotic Disorders, Shanghai Mental Health Center, China
Li Dong,
University of Electronic Science and Technology of China, China

***Correspondence:**
Gabriela M. Pawlowski
gabriela_pawlowski@sfu.ca
Ryan C. N. D'Arcy
ryan_darcy@sfu.ca

Specialty section:
This article was submitted to Brain Imaging Methods, a section of the journal Frontiers in Neuroscience

Received: *24 August 2018*
Accepted: *04 December 2018*
Published: *18 January 2019*

Citation:
Pawlowski GM, Ghosh-Hajra S, Fickling SD, Liu CC, Song X, Robinovitch S, Doesburg SM and D'Arcy RCN (2019) Brain Vital Signs: Expanding From the Auditory to Visual Modality. Front. Neurosci. 12:968. doi: 10.3389/fnins.2018.00968

INTRODUCTION

There is an increasing need for objective, neurophysiological measures, such as EEG, to provide unbiased measures of brain function across a range of different points-of-care. In terms of deployable technologies, EEG benefits from being low-cost, non-invasive, and is particularly well-suited for clinical applications (Connolly et al., 1995; D'Arcy et al., 2003; Gawryluk et al., 2010; Giacino et al., 2014; Sculthorpe-Petley et al., 2015; Ghosh-Hajra et al., 2016a; Fickling et al., 2018). From EEG, a range of markers indexing information processing from low-level sensory to higher-level cognitive processing can be extracted as event-related potentials (ERPs) reflecting underlying sensory, attentional, cognitive processing (D'Arcy et al., 2000; Gawryluk et al., 2010). The translation of EEG/ERP research into neurophysiological assessment applications compatible with the clinical environment has been demonstrated with rapid non-invasive implementations, such as the Halifax Consciousness Scanner (HCS; D'Arcy et al., 2011) and more recently in the brain vital signs framework (Ghosh-Hajra et al., 2016a). Typically ERPs are studied individually using lengthy testing times. However, the brain vital signs framework combines well-established methods utilizing a rapid, integrated, and fully automated ERP stimulation sequence to elicit three targeted ERP responses. A results report is generated based on normalized ERP characteristics. This has been validated in large samples of healthy individuals by reliably eliciting the targeted ERPs across individuals (Ghosh-Hajra et al., 2016a). Changes in these targeted ERPs have been observed in patients with acquired brain injuries (Fleck-Prediger et al., 2014) and athletes with concussions (Fickling et al., 2018).

The brain vital signs framework focuses on three well-established ERPs: (1) the N100 reflecting sensory processing (Davis, 1939); (2) the P300 reflecting attention processing (Sutton et al., 1967); and N400 reflecting semantic/language processing (Kutas and Hillyard, 1980). Individual-level results evaluate response amplitudes and latencies compared to a normative dataset, to form Elemental Brain Scores (EBS) (Ghosh-Hajra et al., 2016a). EBS comparisons are a linear transformation into standardized and normalized scores ranging from 0 to 1, ranked based on the range in the normative group (Ghosh-Hajra et al., 2016a). Therefore larger response amplitudes and shorter response latencies result in higher scores for each of the three ERP responses (3 responses * 2 metrics = 6 EBS). Importantly, EBS results enable standardization across different modalities and acquisition systems. EBS results can then be presented graphically on a radar plot to provide a simple output with a typically normative hexagonal shape (**Figure 4**).

The auditory brain vital signs stimulus sequence utilizes an interlaced design to elicit the three ERPs in parallel and optimize the number of trials per unit time, therefore avoiding the traditionally lengthy serial testing procedures (see Ghosh-Hajra et al., 2016a). The auditory stimulus sequence consists of a passive auditory oddball paradigm and spoken word pairs. The oddball paradigm includes tones divided into standard and deviant conditions, where the N100 and P300 components are derived from the deviant condition. Prime-target word pairs are divided into congruent (e.g., bread-butter), and incongruent (e.g., bread-window) pairs. The N400 is derived from the incongruent word pairs and shows comparable features to the conventional semantic N400 (Ghosh-Hajra et al., 2016a, 2018).

To date, brain vital sign applications have been developed using the auditory sensory modality (Ghosh-Hajra et al., 2016a; Fickling et al., 2018). However, as the aging population grows (Grenier, 2017) there will be an increasing demand for accessibility to objective testing of cognitive function, such as with brain vital signs. The adaptation to a visual modality will address critical limitations around hearing loss and impairments in aging populations and enable wider application across the lifespan. Accordingly, the aim of this study was to expand the brain vital signs application by translating the established brain vital signs auditory test into a visual test to elicit similar targeted ERP responses.

Translation From the Auditory to Visual Modality

The established auditory brain vital signs sequence structure can easily be adapted into the visual modality by utilizing previous research on the well-established visual ERPs: N100, P300, and N400. Previous studies have successfully utilized a simple visual oddball paradigm using brightness of stimuli to elicit the visual N100 (Johannes et al., 1995; Polich et al., 1996; Carrillo-de-la-Peña et al., 1999). A more recent comparison study used changing black and white full-view flashes in both an active (counting) and passive (no counting) task to evoke and record a frontal-central N100 (Huang et al., 2011). The anterior N100 subcomponent typically occurs around 80-150ms and is best recorded at frontal and central electrode sites (Fz and Cz), similar to the auditory N100 (Vogel and Luck, 2000; Knott et al., 2003; Huang et al., 2011).

Similarly, the P300 response has typically been elicited within the visual modality by randomly changing physical visual characteristics, such as colors, shapes, letters, words, or pictures (Comerchero and Polich, 1998; Bennington and Polich, 1999; Bernat et al., 2001; Bledowski, 2004; Cano et al., 2009; Duncan et al., 2009; Kappenman and Luck, 2012, pp.159-180; Mertens and Polich, 1997; Stevens et al., 2000; Knott et al., 2003). A robust P300 response has also been observed to a particularly relevant and salient stimulus, such as a subject's own name (SON) when presented with low probability (see review of SON paradigms: Berlad and Pratt, 1995; Perrin et al., 1999, 2006). When presented visually, the SON response has shown an enhanced P300 response at central electrodes compared to other similar or differing stimuli within a 350–850 ms interval (Zhao et al., 2009, 2011; Tacikowski and Nowicka, 2010; Cygan et al., 2014). Besides being particularly salient, SON paradigms also have benefits for a rapid, visual sequence, because it has been found to be particularly resistant to repetition blindness during rapid serial visual presentations (Arnell, 2006; Tacikowski and Nowicka, 2010).

Lastly, the N400 can be readily elicited by visual word pair paradigms involving violations of semantic expectancies (Kutas

and Hillyard, 1982; Bentin et al., 1985; Rugg, 1985; Brown and Hagoort, 1993; Kutas and Van Petten, 1994; Chwilla et al., 1998; D'Arcy and Connolly, 1999; Brown et al., 2000; D'Arcy et al., 2005; Lau et al., 2008). The N400 is typically found between 200 and 600 ms post-stimulus (Kutas and Federmeier, 2011; Ghosh-Hajra et al., 2018), irrespective of the modality, with maximal amplitudes at midline central or parietal sites and noticeably smaller amplitudes at prefrontal and lateral frontal sites (Duncan et al., 2009). We recently reported a functional neuroimaging study using magnetoencephalography (MEG) that confirmed similar neuroanatomical correlates for the N400, which is the latest and highest-level ERP component within the brain vital signs framework (Ghosh-Hajra et al., 2018).

Objectives

This study aimed to develop and validate a visual brain vital signs sequence on healthy adults to increase accessibility for individuals with hearing impairments. This challenge has been identified frequently as a central issue for developing brain vital sign monitoring in age-related cognitive impairment and dementia, in which hearing loss can be a major barrier. There were two main objectives:

1. Translate the brain vital signs framework into a visual version and validate the new sequence by assessing if the targeted ERPs (N100, P300, and N400) were evoked successfully; and
2. Compare the ERP responses (amplitudes and latencies) between visual and auditory modalities, and evaluate the relationship between modalities within individuals.

METHODS

Participants

Thirty-four (34) healthy, adult participants were enrolled in the study (mean age: 33 ± 13 years, 16 females). Informed consent was given from each participant. Participants had no history of neurological problems or psychoactive medications. All individuals were fluent in English and had normal or corrected-to-normal vision and hearing. The Research Ethics Boards at Simon Fraser University and Fraser Health Authority approved the study.

Stimulus Sequence

The stimulus sequence was adapted from previous brain vital signs studies which utilizes an interlaced structure with an oddball paradigm and word pair paradigm (Ghosh-Hajra et al., 2016a). An oddball paradigm consists of frequent, standard stimuli and deviant, rare stimuli conditions. The oddball paradigm was split into 67% standard and 33% deviant, with the N100 and the P300 derived from the deviant condition. The 72-paired words were divided into congruent prime pairs (e.g., romeo-juliet, 50%) and incongruent prime pairs (romeo-coffee, 50%). The N400 was derived from the incongruent words condition. Both sequences were passive tasks (no response required). The auditory sequence consisted of tones (250 ms duration, standard 75 dB tones, deviant 100 db tones), and spoken word pairs (∼1000 ms duration).

The interlaced structure of the visual stimulus was designed to be similar to that of the auditory sequence; a 4.6 min interlaced oddball and word pair sequence (see **Figure 1**). The level of intensity and difficulty of the auditory and visual needed to be matched because such factors can affect the amplitude and

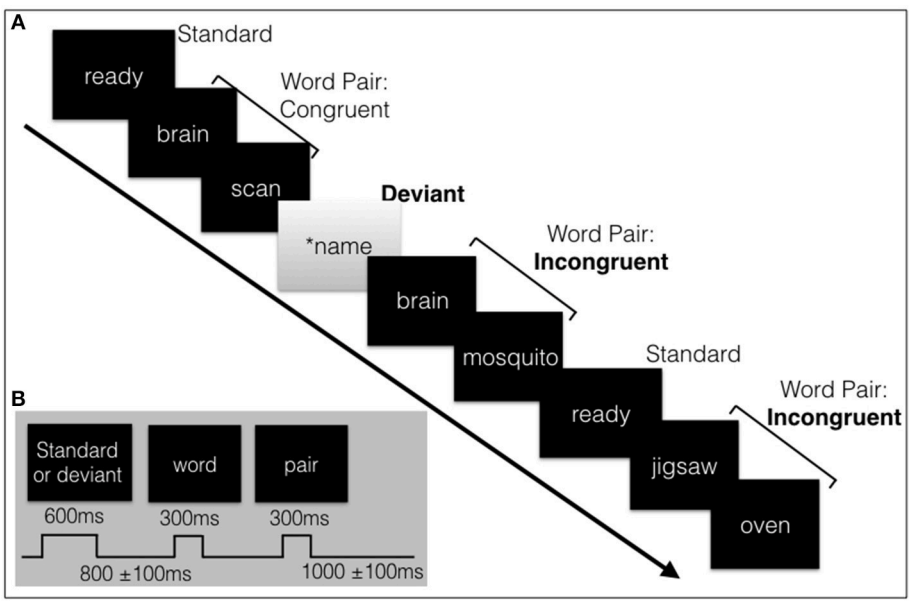

FIGURE 1 | (A) Schematic illustration of a sample of the visual stimulus sequence, containing the subjects' name, and word pairs. **(B)** The length of the stimuli and inter-stimulus intervals with jitter. Total sequence is around 4.6 minutes in length.

latency of components, particularly the P300 in a passive task. A response does not add much value for the N100 (sensory processing) and N400 (sematic processing) (Kappenman and Luck, 2012, pp. 397–440) but does affect the P300 (attention processing). When compared to active tasks, the passive oddball paradigm in both modalities has shown reduced amplitudes (Bennington and Polich, 1999). Nonetheless, passive paradigms have still shown highly comparable and reliable P300 responses (Polich and McIsaac, 1994). A passive task is preferred for patient populations that may struggle with responses or demanding tasks, such as young children or dementia patients (Perrin et al., 1999; Marchand et al., 2002; Huang et al., 2011; Sculthorpe-Petley et al., 2015; Ghosh-Hajra et al., 2016b, 2018; Hajra et al., 2018). Based on past research, a salient passive visual task, a contrast flip and SON, was chosen to ensure a N100 response and a robust visual P300 response. Another advantage of a passive task is that it requires much less time than an active task which requires time for a response, and also greatly reduces the potential for unnecessary muscle movement artifact to the EEG data collection.

All visual stimuli were presented serially in the center of the screen. The words were presented in white font (Sans serif, size 56) on a black background. The standard ("ready") or deviant (SON in inverse contrast) had a duration of 600 ms followed by the prime and target words pairs, duration of 300 ms each. A random jitter was incorporated into the inter-stimulus-interval (ISI) (800 ms ± 100 ms) and in the inter-block interval (IBI) (1000 ms ± 100 ms) to avoid repetition blindness, habituation, and potential entrainment of alpha rhythm with the stimulus timing which can affect the amplitude and/or latency of components and quality of the data (Luck, 2014, pp. 203–204; Ravden and Polich, 1998).

EEG Data Acquisition

Each participant was assessed with both visual and auditory brain vital sign versions, using a counterbalanced order across participants. Data were collected in a dedicated EEG room with consistent conditions (i.e., brightness) across participants. Visual stimuli were presented on a computer monitor centered 75 cm in front of the participant. Acoustic stimuli were delivered binaurally through insert headphones, with participants maintaining visual fixation on a cross displayed in the center of the screen. Both the auditory and visual sequences were delivered using Presentation® software (Version 18.0, Neurobehavioral Systems, Inc., Berkeley, CA, www.neurobs.com). All EEG data were recorded using a 64-channel EEG system using active Ag/AgCl electrodes (BrainAmp 64-channel system actiCAP). Raw EEG data were recorded by BrainVision Recorder (Version 1.20.0801 Brain Products GmbH). The impedance for each electrode within the 64-channel cap was maintained below 20 kΩ; it was checked at the start of data collection and in the breaks between runs.

EEG Pre-processing and ERP Analysis

EEG analysis was done using Brain Vision Analyzer® software, version 2.03 (Brain Products, Gilching, Germany). EEG data were down-sampled from 1000 to 500 Hz. All 64- channels were inspected for noise and re-referenced offline from the BrainVision Recorder's own initial reference channel, FCz, to the average of the two mastoids (electrodes TP9 and TP10), We chose this after careful consideration in literature and for compatibility with other bimodal comparison studies (Holcomb et al., 1992; Huang et al., 2011; Campanella et al., 2012; Dreo et al., 2017). A 0.1–50 Hz zero phase-shift, 4th order Butterworth bandpass filter and 60 Hz notch filter was applied to the data. EEG data were segmented into epochs from −100 to 900 ms time-locked to stimulus onset. Artifact rejection was done using gradients (maximal allowed voltage step: 10 uV/ms and maximal allowed difference of values in intervals: 100 uV), and visually reviewed for each subject. In line with prior work (Liu et al., 2017, 2018), independent component analysis (ICA) was performed for artifact correction (e.g., blinks, saccades, cardiac activity, muscle contractions, breathing) using the Infomax algorithm (Lee et al., 1999). Segments were baseline corrected (−100 to 0 ms), low-passed filtered at 20 Hz, and averaged based on experimental condition (Luck, 2014). Data from four participants were excluded due to EEG noise and task compliance issues.

Targeted ERP Responses: Mean Amplitude Analysis

Mean amplitude analysis was chosen to address Objective 1. Mean amplitude measures were used in order to avoid selection bias when first establishing the sequence (Objective 1) (Luck, 2014, pp. 285–290). This method is also advantageous because conditions with differing number of trials (i.e., standard and deviant) or noise levels (i.e., artifacts) do not affect the results, allowing for all trials to be kept, providing greater statistical power (reducing Type I error rate). Mean amplitude analysis was done using MATLAB (Mathworks, USA) and ERPLAB, an open-source Matlab package (Lopez-Calderon and Luck, 2014). Mean amplitudes were calculated for each stimulus type for each individual at 3 midline electrode sites (Fz, Cz, and Pz). Each latency window was guided by past literature recommendations and visual inspection of the grand average (GA) waveforms (Chronaki et al., 2012; Pfabigan et al., 2014). The N100 was indexed by differential activity within a 50 ms window, as recommended for early components (Vogel and Luck, 2000; Luck, 2014, pp. 286–287). The P300 was measured over a 200 ms window (Wood et al., 2006; Cano et al., 2009). The N400 was measured over a shorter latency for visual (400 ms) than auditory (500 ms), because the visual N400 is typically shorter in duration compared to the auditory N400 (Kutas and Van Petten, 1994; Kutas and Federmeier, 2011). Mean amplitudes were calculated over the following latency windows for the auditory data: 114–164 ms (N100), 250–450 ms (P300), and 200–700 ms (N400). The indexed windows chosen for measuring mean amplitudes in the visual data were: 87–137 ms (N100), 300–500 ms (P300), and 200–600 ms (N400).

Statistical analysis was performed using JMP (JMP®, Version 12.2.0 SAS Institute Inc., Cary, NC). Normality was assessed using the Shapiro-Wilk W test. To assess the difference between stimulus types, a repeated-measures ANOVA was used with the mean amplitude values for each component within each modality, with two factors: stimulus (standard vs. deviant or congruent vs. incongruent) and electrode site (Fz, Cz, and/or Pz).

The number of levels for site was specific to each component based on previously reported maximal sites; frontal-central channels (Fz and Cz) were chosen for N100 (Vogel and Luck, 2000; Knott et al., 2003; Huang et al., 2011), central sites (Fz, Cz, and Pz) were chosen for P300 (Zhao et al., 2009, 2011; Tacikowski and Nowicka, 2010; Cygan et al., 2014) and central-parietal (Cz and Pz) for the N400 (Duncan et al., 2009). Greenhouse-Geisser adjusted values were used to correct for any violations of sphericity assumptions. Student *t*-tests with Tukey-Kramer correction for multiple comparisons were applied for all *post-hoc* comparisons to adjust alpha levels. For data that did not pass the Shapiro-Wilk W test of normality, the Wilcoxon signed-rank test was used.

Comparison and Normalization of Auditory and Visual Sequences: Adjusted Baseline Amplitude and Peak Latency Measures

Once the targeted components were confirmed using mean amplitude analysis, adjusted baseline amplitude and peak latency were measured for all 3 components in both modalities. Adjusted baseline amplitude measures were calculated at Cz from peak amplitudes relative to the two adjacent peaks of opposite polarity (D'Arcy et al., 2011; Ghosh-Hajra et al., 2016a). All peaks were obtained with a semi-automatic process using Brain Vision Analyzer, within expected latency windows, identifying local peak amplitudes (as defined by Luck, 2014, p. 285) of expected polarity (Marchand et al., 2002). Latency windows vary across studies, depending on stimulus types, task conditions, subject age, etc. (Polich and Kok, 1995; Polich, 1997; Cano et al., 2009). Hence it is recommended to choose latency windows based on both literature and visual inspection of the GA waveforms (Cassidy et al., 2012; Chronaki et al., 2012; Pfabigan et al., 2014; López Zunini et al., 2016). Due to the wide range of age (19-66yrs) and two modalities within this study, latency windows for each component were chosen according to several previous studies. For both modalities, the N100 peak, was measured between 75 and 200 ms (Johannes et al., 1995; Covington and Polich, 1996; Niznikiewicz et al., 1997; Hillyard and Lourdes, 1998; Knott et al., 2003; Huang et al., 2011). Shorter latencies were used for P300 in auditory (250-500ms) compared to visual (250–600 ms) (Comerchero and Polich, 1998; Bernat et al., 2001; Knott et al., 2003; Cano et al., 2009; Tacikowski and Nowicka, 2010; Campanella et al., 2012). The latency window for N400 peaks was 300–650 ms for auditory and visual (Marchand et al., 2002; D'Arcy et al., 2003; Kutas and Federmeier, 2011).

EBS results comprised of six total ERP measures (3 components × 2 measures), generated through a linear transformation. Each measure, amplitude or latency values, were normalized and ranked from 0 to 1 based on the normative group mean and the best possible outcome following the methods as shown before in Fickling et al. (2018) and (Ghosh-Hajra et al., 2016a). The normative group used was the subjects recruited in this study, separate for each modality. Mathematically, EBS measures can be expressed as shown in Equations (1, 2) below:

$$\text{Score} = 1 - \text{abs}\left[(M - \text{best})/(\max - \min)\right]$$

$$\text{Score} = 1 - \text{abs}\left[(\text{best} - M)/(\max - \min)\right]$$

The M represents the mean value of either the amplitude or latency. The max and min are the maximum value and the minimum value, respectively. The best variable is the "ideal" value that should be achieved, which can either be the max or the min value depending on whether the lowest or the highest value represents the ideal situation. For instance, an "ideal" value for latency is generally shorter because it represents faster (better) processing, whereas for amplitude values, depending on the targeted ERP component, the highest positive value or lowest negative value is thought to represent "ideal" processing (Ghosh-Hajra et al., 2016a). Both larger amplitudes and shorter latencies translate to higher EBS scores. Equation (1) is utilized for N100 and N400 amplitude and latency as well as P300 latency, whereas Equation (2) is used for P300 amplitude. This translation allows for complex ERP data to become accessible metrics, while preserving the underlying ERP results. This technique also will enable normalization within modalities to account for the known differences while preserving the relationship across modalities.

Adjusted baseline amplitude and peak latency values, as well as EBS values were compared at the group-level across modalities using JMP (JMP®, Version 12.2.0 SAS Institute Inc., Cary, NC). Normality was assessed using the Shapiro-Wilk W test. Normality was assessed using the Shapiro-Wilk W test. Only the measures for visual P300 amplitude did not pass the normality test, therefore the Wilcoxon test was used for comparison. All others were compared using matched pairs *t*-test. Results are presented as mean ± SD.

Pearson correlation coefficient (Pearson r) was used to evaluate the relationship between individual values across modalities. This statistic assumes a linear relationship and is confirmed by inspection of the r-value, associated p-value and scatter plot. Pearson R correlation analysis was used for all except P300 amplitude values. The visual P300 amplitude values failed the Shapiro-Wilk test of normality (i.e., non-parametric distribution) so Spearman rho was used for correlation analysis.

RESULTS

Targeted ERP Responses

Mean Amplitude Analysis

The targeted N100 and P300 components were successfully evoked using oddball paradigms within the auditory and visual sequences (**Figure 2**). Similarly, the targeted N400 component was evoked by the word pair paradigm within the auditory and visual sequences (**Figure 3**).

ANOVAs for the mean amplitudes within each modality revealed main effects for stimulus type across all three components, with no interaction effect found. **Tables 1**,**2** provide quantitative mean amplitude measures for group-level N100, P300, and N400. **Table 3** provides a summary of ANOVA effects tests. For box plots illustrating the difference in mean amplitudes for each condition and ERP for both modalities, see **Supplementary Figures 1–3**.

Comparison and Normalization of Auditory and Visual Sequences

Adjusted Baseline Amplitude and Peak Latency Measures

Table 4 provides group averaged adjusted baseline amplitude and peak latency measures for the 3 components across

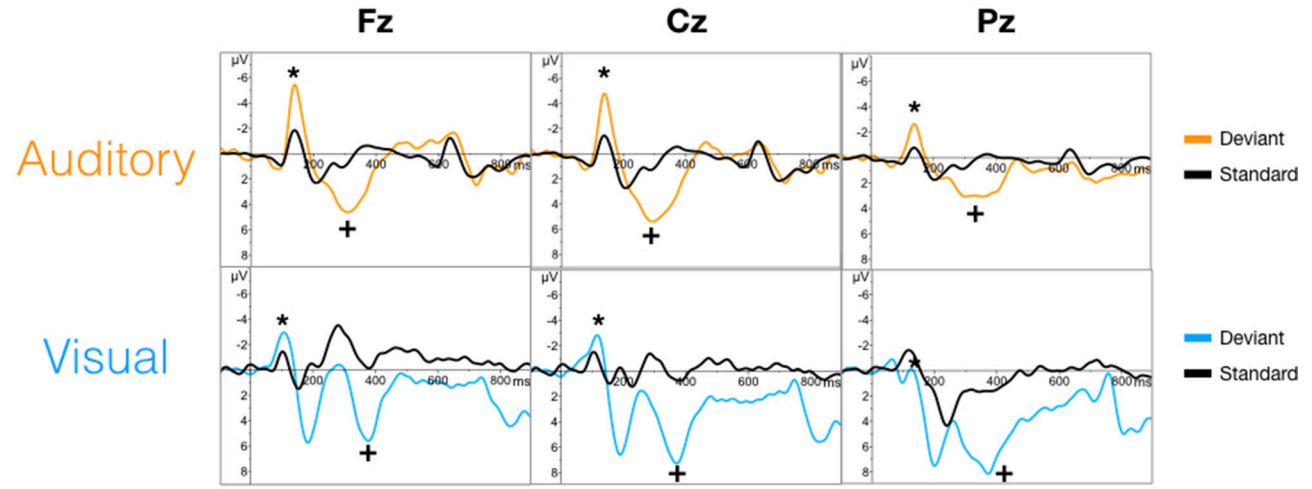

FIGURE 2 | Grand averaged waveforms for the N100 (*) and P300 (+) component in auditory **(top)** and visual **(bottom)** modalities.

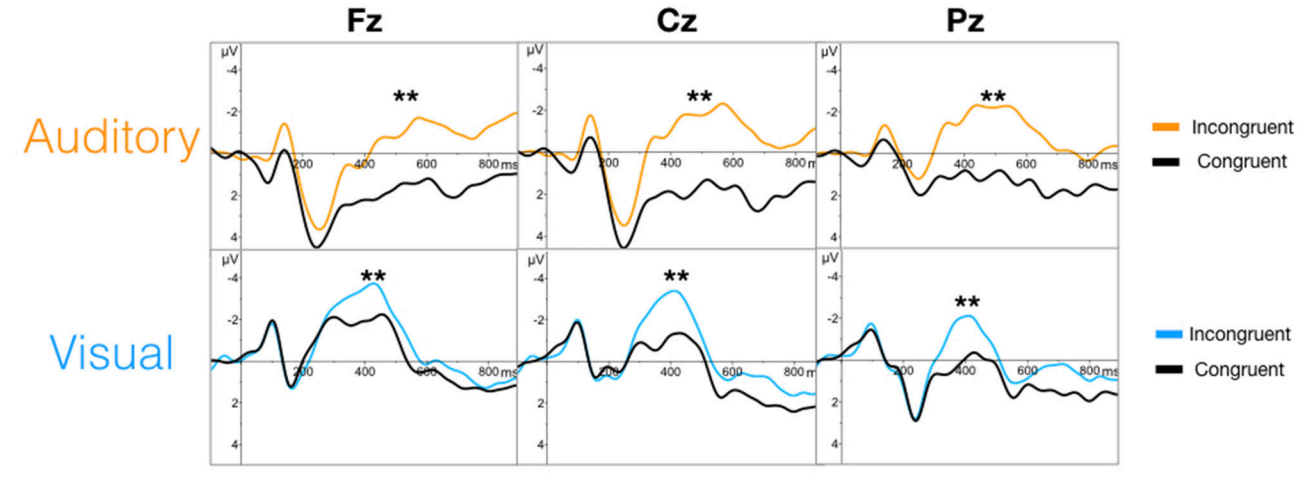

FIGURE 3 | Grand averaged waveforms for the N400 (**) in the auditory **(top)** and visual **(bottom)** modalities.

modalities. There was no significant difference for amplitude in either the N100 and P300. However, the N400 amplitudes showed a significant difference between auditory (-5.82 ± 2.11 μV) and visual (-6.82 ± 1.80 μV) modalities ($p = 0.0061$). As expected, all three ERP components showed significant latency differences. For a bar-graph illustrating the adjusted baseline amplitude and latency measures pairwise comparisons (matched pairs *t*-tests) across modalities, please see **Supplementary Figures 4** and **5**.

Elemental Brain Scores (EBS)

No significant differences were found for any comparisons using the mean EBS in matched pairs *t*-tests (see **Table 5**). Auditory and visual group EBS in all 6 measures results are also depicted visually (see **Figure 4**).

Correlation Analysis

See **Table 6** for all correlations and **Figure 5**, **6** for amplitude and latency scatter plots. Moderate to high correlations were found across modalities in amplitude for P300 (rho = 0.7, p =0.0001) and N400 ($r = 0.6$, $p = 0.0012$) and P300 latency ($r = 0.5$, $p = 0.0033$). The N100 amplitude and latency, and N400 latency showed no significant correlations.

DISCUSSION

The current study had two objectives: (1) Translate the interlaced, rapid auditory sequence into a visual sequence and validate it by assessing if the targeted EPRs (N100, P300, and N400) are successfully evoked in a healthy population; and (2) Compare the ERP responses (amplitudes and latencies) between visual

TABLE 1 | Summary Statistics: Mean amplitude measures for group-level N100 and P300 (μV).

ERP	Channel	Auditory oddball stimulus (μV)		Visual oddball stimulus (μV)	
		Standard	Deviant	Standard	Deviant
N100	Fz	−1.46 ± 1.84	−4.09 ± 2.69	−0.90 ± 2.12	−2.60 ± 2.63
	Cz	−0.97 ± 1.45	−3.42 ± 2.29	−1.05 ± 2.20	−2.27 ± 2.44
P300	Fz	0.01 ± 1.06	2.81 ± 2.50	−1.22 ± 3.03	2.57 ± 4.62
	Cz	0.22 ± 0.94	3.40 ± 2.34	−0.12 ± 3.02	4.74 ± 4.28
	Pz	0.21 ± 0.64	2.42 ± 2.15	1.01 ± 2.10	5.81 ± 3.61

Mean ± SD.

TABLE 2 | Summary Statistics: Mean amplitude measures for group-level N400 (μV).

ERP	Channel	Auditory word pair stimulus (μV)		Visual word pair stimulus (μV)	
		Congruent	Incongruent	Congruent	Incongruent
N400	Cz	4.26 ± 4.47	−1.15 ± 4.62	−1.28 ± 6.92	−2.88 ± 7.04
	Pz	2.31 ± 3.18	−2.27 ± 3.45	1.58 ± 5.67	−0.25 ± 6.13

Mean ± SD.

TABLE 3 | Summary of the Effects Tests: *F*-ratio and *p*-values of all the main effects and interaction effects of mean amplitude ANOVAs.

ERP	Source	Auditory		Visual	
		F Ratio	Prob > F	F Ratio	Prob > F
N100	Stimulus	**78.4661**	**<0.0001**	**29.8380**	**<0.0001**
	Channel	3.8962	0.0516	1.0253	0.3142
	Stimulus* Channel	0.0907	0.7640	1.3884	0.2420
P300	Stimulus	**137.0415**	**<0.0001**	**138.8442**	**<0.0001**
	Channel	1.7835	0.1717	**17.2778**	**<0.0001**
	Stimulus* Channel	1.4747	0.2323	0.8177	0.4435
N400	Stimulus	**86.3009**	**<0.0001**	**6.8476**	**0.0105**
	Channel	**8.1326**	**0.0054**	**17.6354**	**<0.0001**
	Stimulus* Channel	0.5831	0.4471	0.0327	0.8570

Significance of <0.05 is denoted with bold text.

TABLE 4 | Summary Statistics: adjusted baseline amplitude and peak latency measures for group-level ERP characteristics at Cz.

ERP	Measure	Auditory	Visual	*P*-value
N100	Amplitude (μV)	−9.17 ± 3.12	−8.80 ± 3.26	0. 8089
	Latency (ms)	**139.33 ± 10.60**	**123.13 ± 21.43**	**0.0009**
P300	Amplitude (μV)	8.06 ± 3.79	8.87 ± 2.63	0.5040
	Latency (ms)	**309.00 ± 42.82**	**369.07 ± 58.56**	***p* < 0.0001**
N400	Amplitude (μV)	**−5.82 ± 2.11**	**−6.82 ± 1.80**	**0.0061**
	Latency (ms)	**488.73 ± 58.97**	**414.40 ± 30.47**	***p* < 0.0001**

Mean ± SD. Significance of <0.05 is denoted with bold text.

TABLE 5 | Elemental Brain Scores (EBS) measures for group-level ERP characteristics.

ERP	Measure	Auditory scores	Visual scores	*P*-value
N100	Amplitude (μV)	0.52 ± 0.17	0.49 ± 0.17	0.4491
	Latency (ms)	0.49 ± 0.17	0.49 ± 0.17	0.9343
P300	Amplitude (μV)	0.53 ± 0.17	0.56 ± 0.17	0.1818
	Latency (ms)	0.46 ± 0.16	0.50 ± 0.17	0.2629
N400	Amplitude (μV)	0.52 ± 0.17	0.47 ± 0.17	0.0995
	Latency (ms)	0.53 ± 0.17	0.50 ± 0.17	0.4279

Mean ± SD within-subject elemental brain scores across modalities.

and auditory modalities, and evaluate the relationship between modalities within individuals.

Objective 1: Targeted ERP Responses

As an initial validity check, the results demonstrated that the targeted ERPs (N100, P300, and N400) were evoked and detectable by comparing mean amplitudes for each stimulus conditions within each modality at a group-level. As expected, significant conditional differences were found for the N100, P300, and N400 responses for both auditory and visual modalities (**Tables 1–3**). Within the visual modality, the increased N100 amplitude to the contrast change is consistent with past studies using similar stimuli (Dustman et al., 1982; Johannes et al., 1995; Covington and Polich, 1996; Carrillo-de-la-Peña et al., 1999). The increased P300 amplitude to viewing one's own name further was consistent with the allocation of information processing resources associated with self-relevant information (Müller and Kutas, 1996; Herzmann et al., 2004; Perrin et al., 2005; Herzmann and Sommer, 2007; Polich, 2007; Zhao et al., 2009, 2011; Tacikowski and Nowicka, 2010; Cygan et al., 2014; Sculthorpe-Petley et al., 2015). Similarly, larger visual N400 amplitudes to incongruent word stimuli was due to increased processing in response to violations of semantic expectancies

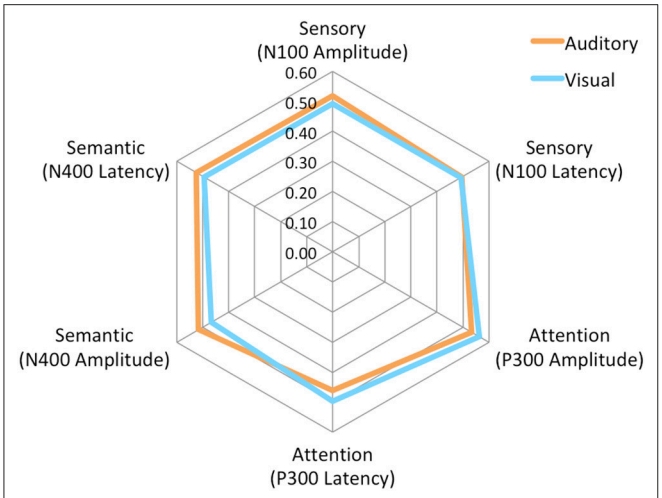

FIGURE 4 | Radar Plot of amplitude and latency EBS values for both modalities across all 3 ERP components.

TABLE 6 | Correlations of amplitude and latency measures at Cz.

ERP	Measure	Correlation (r)	*p*-value
N100	Amplitude (μV)	0.3	0.1737
	Latency (ms)	0.04	0.8470
P300	Amplitude (μV)	**0.7***	**0.0001**
	Latency (ms)	**0.5**	**0.0033**
N400	Amplitude (μV)	**0.6**	**0.0012**
	Latency (ms)	0.2	0.3135

*Pearson r correlation coefficient used for all normally distributed data and Spearman rho used for non-parametric data, P300 amplitude. *Significance of <0.05 is denoted with bold text.*

(Rugg, 1985; Brown and Hagoort, 1993; Osterhout and Holcomb, 1996; Chwilla et al., 1998; Brown et al., 2000; Lau et al., 2008; Kutas and Federmeier, 2011; Ghosh-Hajra et al., 2016a).

Effects of channel location differed across the two modalities for the N400 response. On average larger mean amplitudes were found at Cz compared to Pz for the auditory presented words [$p = 0.0054$, estimated mean difference= 1.54 μV ($SE = 0.54$)]. Whereas for the visually presented words, slightly larger estimated means were found at Pz compared to Cz [$p < 0.0001$, estimated mean difference= 2.75 μV ($SE = 0.65$)]. Despite the on average larger mean amplitudes measured at Pz for visual words across stimulus conditions, the difference between congruent and incongruent conditions is of interest when establishing the N400 effect. Further *post-hoc* analysis showed the estimated mean difference between stimulus conditions at the two electrodes was only slightly larger at Pz (1.83 μV, $SE = 0.26$) compared to Cz (1.59 μV, $SE = 0.26$). Despite the small difference between Cz and Pz, the N400 effect was still measurable at Cz, which is the site used in past brain vital signs research and the site chosen for modality comparison in this study (Ghosh-Hajra et al., 2016a; Fickling et al., 2018). The results are in line with previous literature, with the N400 effect typically being measured at midline centro-parietal scalp sites (Kutas and Hillyard, 1982; Kutas et al., 1987; van Petten and Rheinfelder, 1995; Kutas and Federmeier, 2011).

Objective 2: Comparison and Normalization of Auditory and Visual Sequences

As expected, there were significant modality-related latency differences for all three components (see **Table 4**). The only difference in ERP activation (at Cz) was a significant increase in amplitude of the visual N400. However, the standardized conversion of all three ERP components into EBS allowed for normalization of both response latencies and amplitudes, with no significant difference (see **Figure 4** and **Table 5**). The translation into EBS, however, did not affect the correlation across modalities within individuals because the linear translation from ERP measures to EBS are calculated only relative to the normative database ($N = 30$) within each modality separately, therefore not affecting the relationship across modalities. Correlations done with EBS and ERP measures were identical. Correlation analysis showed significant, moderate to strong (0.5–0.7) correlations for amplitude measures for P300 amplitude and latency as well as N400 amplitude across modalities (see **Table 6** and **Figures 5**, **6**). The combination of all these results and comparison between modalities across the targeted ERP components has given us initial insight into the relationship between modalities.

The N100 is typically reported with earlier peak latencies for the auditory modality (Niznikiewicz et al., 1997; Knott et al., 2003), however this trend was reversed in the current results, which was likely due to increasing the intensity contrast between black and white stimuli (Dustman et al., 1982; Carrillo-de-la-Peña et al., 1999). Significant group-level differences and non-significant correlations for sensory (N100) latencies between modalities suggest that speed in sensory processing differs and is not predictive within individuals across modalities. The lack of correlation between the auditory and visual N100 amplitudes at Cz possibly reflects that inconsistent levels of sensory processing were being evoked by the auditory and visual stimuli within individuals. Further analysis of the location of the max N100 amplitude for each modality is needed.

It is notable that the P300 results arose from two very different manipulations; no significant difference was found at the group-level and a strong correlation of adjusted baseline amplitude between modalities was found (rho = 0.7, $p = 0.0001$; **Table 6**). These results imply that similar levels of attention allocation (marked by P300 activation) were being evoked within individuals from either sequence despite the different oddball approaches. Given that the P300 is produced by a distributed network of brain processes associated with attention and memory operations (Polich, 2007), the visual P300 latency delay found was likely related to more complex information processing required for visual identification of SON versus a simple auditory deviant tone (Kramer et al., 1986; Verleger, 1997; Halgren et al., 1998; Bennington and Polich, 1999; Patel and Azzam, 2005; Polich, 2007; Duncan et al., 2009). Based on past literature and the correlated ($r = 0.5$; $p = 0.0033$) but differing group-level peak latencies ($p < 0.0001$) found, it can be concluded that similar functional processes of attention

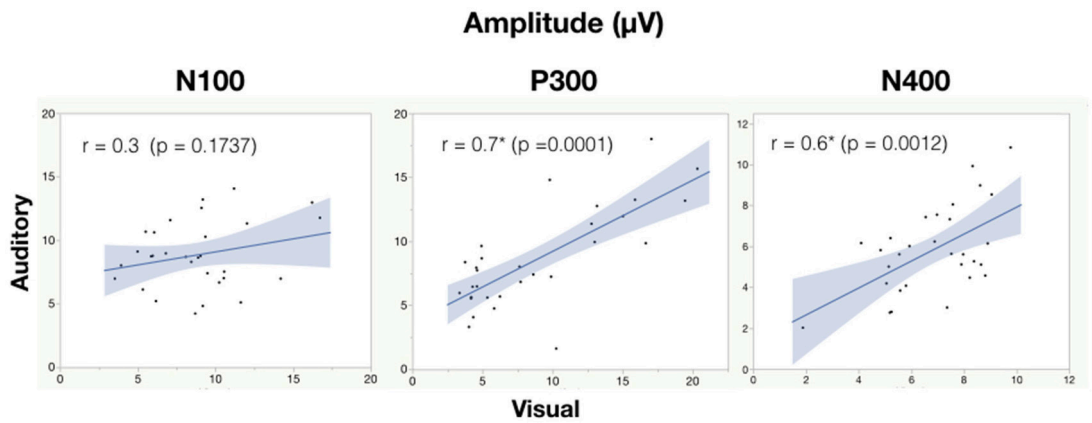

FIGURE 5 | Correlation analysis between auditory and visual adjusted baseline amplitude values for each subject. Significance of < 0.05 is denoted with *.

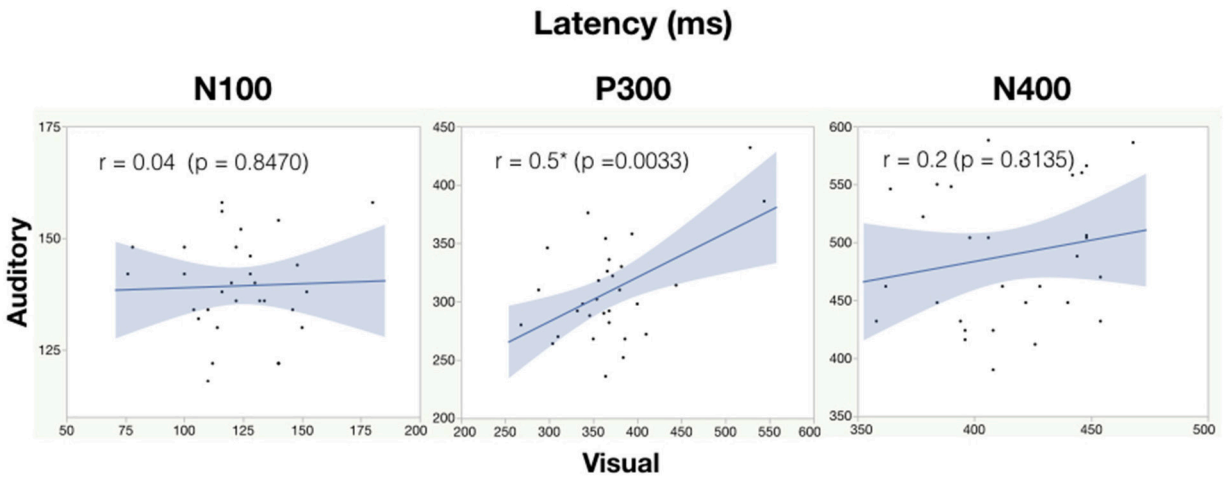

FIGURE 6 | Correlation analysis between auditory and visual peak latency values for each subject. Significance of < 0.05 is denoted with *.

were evoked with a possible systematic difference of modalities, where the visual deviant stimulus requires slightly longer time for detection and processing compared to the auditory deviant stimulus. The correlation also implies that the individual relative speed of detection and classification of the deviant stimuli was similar across modalities; reflecting that attention processing speed within an individual is similar regardless of the stimulus modality.

The visual deviant condition was primarily used to evoke a sensory response (N100), however, it was presented in combination with the SON. It was chosen in order to reach our first objective of developing a passive visual sequence that successfully evokes the targeted ERP responses. This salient stimulus may have affected the P300, however, such a change in brightness has been documented to elicit an early N100 response and a P200 prior to the P300 (Dustman et al., 1982; Carrillo-de-la-Peña et al., 1999; Hruby and Marsalek, 2003). These early visual sensory (N100-P200) responses often occur with P300 components in visual oddball paradigms and should not have interfered with the P300 evoked from participants recognizing their own names. The stimulus was presented for 600 ms, allowing plenty of time for participants to react and adjust to the contrast change and recognize their names. The change in contrast may have caused participants to increase their engagement in the task and level of attention to when their names were presented, in turn potentially affecting the magnitude (amplitude) of the P300 response to the SON. However, the visual oddball paradigm used appeared to be evoking similar levels of attentional responses as the auditory paradigm within individuals; no significant difference at the group-level and a strong correlation of adjusted baseline amplitude between modalities was found (rho $= 0.7$, $p = 0.0001$). These results imply that similar levels of attention allocation (marked by P300 activation) were being evoked in subjects from either sequence

despite the different oddball approaches. Future work could be done to compare SON without a contrast flip to see the impact on the P300 response and if there is a confounding effect.

In spite of being modality independent, aspects of the N400 have been found to differ across visual and auditory processing of words (Kutas and Hillyard, 1980; McCallum et al., 1984; Bentin et al., 1985; Kutas et al., 1987; Holcomb and Neville, 1990; Kutas and Federmeier, 2011). In general, the auditory N400 tends to be characterized by a lower amplitude, later peak, and longer duration response (Kutas and Federmeier, 2011). This pattern was reflected in our results and, despite the significant amplitude differences, was notably equated by the EBS transformation and showed a significant moderate correlation of amplitude ($r = 0.6$, $p = 0.0012$). These results imply that the modality amplitude difference is possibly systematic; a similar level of semantic processing relative to each modality is being evoked within individuals across modality paradigms.

Emerging neuroimaging technologies have allowed for further investigation into theories of early word processing and recognition (Carreiras et al., 2014). Competing theories still debate on the precise initial recognition process of printed and spoken words, however, data shows that both reading and listening are incremental and largely a serial processes (Rayner et al., 2009; review by Carreiras et al., 2014). Nevertheless, reading (visual linguistic processing) is faster than listening (auditory linguistic processing) (Breznitz and Berman, 2003), with reading able to reach relatively high speeds (250–350 wpm for most skilled readers) not thought achievable for listening comprehension (Rayner et al., 2009). This difference in speed between reading and listening processing is reflected in ERP studies, with shorter latencies and durations typical of a visual N400 relative to an auditory N400 (Holcomb et al., 1992; Luck, 2005; Kutas and Federmeier, 2011). This may account for the differing latencies we found across modalities. Furthermore, the lack of correlation in latency also implies that fast reading ability is not predictive of fast speech comprehension and vice versa. Individual differences may have been a factor; for instance, some participants may have stronger reading skills than auditory comprehension skills.

Overall, our analyses demonstrated a clear pattern of results that supported the concept of visual brain vital signs. Specifically, the results confirmed the following observations: (1) All three visual components were measurable at central electrode locations, showing potential for portable EEG application in the future, as done with previous brain vital signs studies (Ghosh-Hajra et al., 2016a; Fickling et al., 2018); (2) Overall modality comparison analysis at the central electrode site (Cz) revealed that primarily attention (P300), as well as semantic (N400) processing, are potentially transferrable and comparable across modalities, however sensory (N100) processing is not; and (3) it was possible to show that the brain vital sign framework can be implemented in visual modality format in order to facilitate clinical applications where this is necessary, such as cognitive impairment in aging populations with hearing loss (Lin et al., 2013).

Limitations

Within the modality comparison analysis, the current study focused largely on temporal component differences in terms of response amplitudes and latencies (at Cz). It did not evaluate spatial distribution differences and/or source localization differences—for which there would be full expectation of underlying neuroanatomical differences that cannot/should not be standardized. Future studies will better characterize boundary limits for spatial overlap. (For initial exploratory analysis see **Supplementary Figures 10–15**, which illustrate topographical maps using CSD for each ERP component in each modality.) Aspects of the EEG analysis, such as the reference chosen may affect further analysis. The linked mastoid reference was chosen after careful consideration for this study; however, referencing methods have limitations because a truly neutral point on the body is impossible. Other referencing methods such as the reference electrode standardization technique (REST) provide a reference of scalp EEG recordings to a point at infinity (Yao, 2001; Dong et al., 2017). Initial exploratory analysis of REST was undertaken (see **Supplementary Figures 6–9**). Further comparison analysis of references will be done in the future. Another important limitation relates to the need for separate patient/clinical validation studies for visual brain vital signs to replicate the auditory modality results in concussion, aging, and dementia. That is, the assumption cannot be made that a common pattern of results exists for a specific condition (e.g., dementia). Instead, it will be important to conduct similar comparison based studies for particular neurological conditions and characterize the relationship of results across modalities. However, comparisons across modalities will likely be an important feature of brain vital sign monitoring in terms complex issues related to diagnostic sensitivity and specificity. For instance, in the case of dementia, it can help discriminate age-related hearing loss vs. the detection of cognitive impairment.

CONCLUSION

The current study reinforced the viability of the brain vital sign framework through successful expansion from the auditory to the visual modality. Despite some modality differences found, comparison analysis showed that modality differences can be standardized within EBS results, and that attentional and language processing are potentially transferrable between modalities. Visual modality brain vital signs provide an important alternative, particularly for populations in which monitoring cognitive function changes may be complicated by hearing loss (e.g., elderly and dementia). Further investigation into modality differences should examine spatial distribution differences together with comparison validation studies for specific neurological conditions like dementia. Nonetheless, with visual brain vital signs added to the overall framework it is possible to expand clinical applications and provide further insight into point-of-care monitoring of brain function.

ETHICS STATEMENT

This study was carried out in accordance with the recommendations of Ethical Conduct for Research Involving Humans (the TCPS-2), Research Ethics Boards at Simon Fraser University and Fraser Health Authority with written informed consent from all subjects. All subjects gave written informed consent in accordance with the Declaration of Helsinki. The protocol was approved by the Research Ethics Boards at Simon Fraser University and Fraser Health Authority.

AUTHOR CONTRIBUTIONS

All authors contributed to conceptualization and study design. GP, SG-H, CL, SF, and RD: literature search. GP, SG-H, CL, and SF: data collection. SG-H, CL, SF, SR, and RD: analysis planning. GP: data analysis. GP, SG-H, CL, SF, XS, and RD: result presentation. GP, SG-H, CL, SF, XS, and RD: analysis outcome verification. All authors contributed to result interpretation, manuscript preparation and editing and approved the final draft.

This publication is the original work of the authors and RD will serve as guarantor of its contents.

FUNDING

This work was supported in part by Mathematics of Information Technology and Complex Systems (MITACS, IT07832 / R652354).

ACKNOWLEDGMENTS

We would like to thank the volunteers for participating in the research. We acknowledge everyone at the NeuroTech Lab for their helpful input and support throughout this study and preparation of this manuscript.

SUPPLEMENTARY MATERIAL

The Supplementary Material for this article can be found online at: https://www.frontiersin.org/articles/10.3389/fnins.2018.00968/full#supplementary-material

REFERENCES

Arnell, K. M. (2006). Visual, auditory, and cross-modality dual-task costs: electrophysiological evidence for an amodal bottleneck on working memory consolidation. *Percept. Psychophys.* 68, 447–457. doi: 10.3758/BF03193689

Bennington, J. Y., and Polich, J. (1999). Comparison of P300 from passive and active tasks for auditory and visual stimuli. *Int. J. Psychophysiol.* 34, 171–177. doi: 10.1016/S0167-8760(99)00070-7

Bentin, S., McCarthy, G., and Wood, C. C. (1985). Event-related potentials, lexical decision and semantic priming. *Electroencephalogr. Clin. Neurophysiol.* 60, 343–355. doi: 10.1016/0013-4694(85)90008-2

Berlad, I., and Pratt, H. (1995). P300 in response to the subject's own name. *ELSEVIER Electroencephal. Clin. Neurophysiol.* 96, 472–474.

Bernat, E., Shevrin, H., and Snodgrass, M. (2001). Subliminal visual oddball stimuli evoke a P300 component. *Clin. Neurophysiol.* 112, 159–171. doi: 10.1016/S1388-2457(00)00445-4

Bledowski, C. (2004). Localizing P300 generators in visual target and distractor processing: a combined event-related potential and functional magnetic resonance imaging study. *J. Neurosci.* 24, 9353–9360. doi: 10.1523/JNEUROSCI.1897-04.2004

Breznitz, Z., and Berman, L. (2003). The underlying factors of word reading rate. *Educ. Psychol. Rev.* 15, 247–265. doi: 10.1023/A:1024696101081

Brown, C., and Hagoort, P. (1993). The processing nature of the n400: evidence from masked priming. *J. Cogn. Neurosci.* 5, 34–44. doi: 10.1162/jocn.1993.5.1.34

Brown, C. M., Hagoort, P., and Chwilla, D. J. (2000). An event-related brain potential analysis of visual word priming effects. *Brain Lang.* 72, 158–190. doi: 10.1006/brln.1999.2284

Campanella, S., Delle-Vigne, D., Kornreich, C., and Verbanck, P. (2012). Greater sensitivity of the P300 component to bimodal stimulation in an event-related potentials oddball task. *Clin. Neurophysiol.* 123, 937–946. doi: 10.1016/j.clinph.2011.10.041

Cano, M. E., Class, Q. A., and Polich, J. (2009). Affective valence, stimulus attributes, and P300: color vs. black/white and normal vs. scrambled images. *Int. J. Psychophysiol.* 71, 17–24. doi: 10.1016/j.ijpsycho.2008.07.016

Carreiras, M., Armstrong, B. C., Perea, M., and Frost, R. (2014). The what, when, where and how of visual word recognition. *Trends Cogn. Sci.* 18, 90–98. doi: 10.1016/j.tics.2013.11.005

Carrillo-de-la-Peña, M., Rodríguez Holguín, S., Corral, M., and Cadaveira, F. (1999). The effects of stimulus intensity and age on visual-evoked potentials (VEPs) in normal children. *Psychophysiology* 36, 693–698. doi: 10.1111/1469-8986.3660693

Cassidy, S. M., Robertson, I. H., and O'Connell, R. G. (2012). Retest reliability of event-related potentials: evidence from a variety of paradigms. *Psychophysiology* 49, 659–664. doi: 10.1111/j.1469-8986.2011.01349.x

Chronaki, G., Broyd, S., Garner, M., Hadwin, J. A., Thompson, M. J. J., and Sonuga-Barke, E. J. S. (2012). Isolating N400 as neural marker of vocal anger processing in 6-11-year old children. *Dev. Cogn. Neurosci.* 2, 268–276. doi: 10.1016/j.dcn.2011.11.007

Chwilla, D. J., Hagoort, P., and Brown, C. M. (1998). The mechanism underlying backward priming in a lexical decision task: spreading activation versus semantic matching. *Q. J. Exp. Psychol.* 51A, 531–560. doi: 10.1080/713755773

Comerchero, M. D., and Polich, J. (1998). P3a, perceptual distinctiveness, and stimulus modality. *Cogn. Brain Res.* 7, 41–48. doi: 10.1016/S0926-6410(98)00009-3

Connolly, J. F., Phillips, N. A., and Forbes, K. A. K. (1995). The effects of phonological and semantic features of sentence ending workds on visual event related potentials. *Electroencephalogr. Clin. Neurophysiol.* 94, 276–287. doi: 10.1016/0013-4694(95)98479-R

Covington, J. W., and Polich, J. (1996). P300, stimulus intensity, and modality *Electroencephalogr. Clin. Neurophysiol.* 100, 579–584. doi: 10.1016/S0168-5597(96)96013-X

Cygan, H. B., Tacikowski, P., Ostaszewski, P., Chojnicka, I., and Nowicka, A. (2014). Neural correlates of own name and own face detection in autism spectrum disorder. *PLoS ONE* 9:e86020. doi: 10.1371/journal.pone.0086020

D'Arcy, R. C. N., and Connolly, J. F. (1999). An event-related brain potential study of receptive speech comprehension using a modified Token Test. *Neuropsychologia* 37, 1477–1489.

D'Arcy, R. C. N., Connolly, J. F., and Eskes, G. A. (2000). Evaluation of reading comprehension with neuropsychological and event-related brain potential (ERP) methods. *J. Int. Neuropsychol. Soc.* 6, 556–567.

D'Arcy, R. C. N., Hajra, S. G., Liu, C., Sculthorpe, L. D., and Weaver, D. F. (2011). Towards brain first-aid: a diagnostic device for conscious awareness. *IEEE Trans. Biomed. Eng.* 58, 750–754. doi: 10.1109/TBME.2010.2090880

D'Arcy, R. C. N., Marchand, Y., Eskes, G. A., Harrison, E. R., Phillips, S. J., Major, A., et al. (2003). Electrophysiological assessment of language function following stroke. *Clin. Neurophysiol.* 114, 662–672. doi: 10.1016/S1388-2457(03)00007-5

D'Arcy, R. C. N., Service, E., Connolly, J. F., and Hawco, C. S. (2005). The influence of increased working memory load on semantic neural systems: a high-resolution event-related brain potential study. *Cogn. Brain Res.* 22, 177–191. doi: 10.1016/j.cogbrainres.2004.08.007

Davis, P. A. (1939). Effects of acoustic stimuli on the waking human brain. *Am. Physiol. Soc.* 494–499. doi: 10.1152/jn.1939.2.6.494

Dong, L., Li, F., Liu, Q., Wen, X., Lai, Y., Xu, P., et al. (2017). "MATLAB toolboxes for reference electrode standardization technique (REST) of scalp EEG." *Front. Neurosci.* 11:601. doi: 10.3389/fnins.2017.00601

Dreo, J., Attia, D., Pirtošek, Z., and Repovš, G. (2017). The P3 cognitive ERP has at least some sensory modality-specific generators: evidence from high-resolution EEG. *Psychophysiology* 54, 416–428. doi: 10.1111/psyp.12800

Duncan, C. C., Barry, R. J., Connolly, J. F., Fischer, C., Michie, P. T., Näätänen, R., et al. (2009). Event-related potentials in clinical research: guidelines for eliciting, recording, and quantifying mismatch negativity, P300, and N400. *Clin. Neurophysiol.* 120, 1883–1908. doi: 10.1016/j.clinph.2009.07.045

Dustman, R., Shearer, D., and Snyder, E. (1982). Age differences in augmenting/reducing of occipital visually evoked potentials. *Electroencephalogr. Clin. Neurophysiol.* 54, 99–110. doi: 10.1016/0013-4694(82)90152-3

Fickling, S. D., Smith, A. M., Pawlowski, G., Ghosh-Hajra, S., Liu, C. C., Farrell, K., et al. (2018). Brain vital signs detect concussion-related neurophysiological impairments in ice-hockey. *Brain* 142:2.

Fleck-Prediger, C., Hajra, S., Dick, B., and Gray, D. (2014). Clinical applicatios of the halifax consciousness scanner: tracking recovery in a severely brain injured patient. *Int. Brain Org.* 1–12. Available online at: http://www.internationalbrain.org/clinical-applications-of-the-halifax-consciousness-scanner/

Gawryluk, J. R., D'Arcy, R. C., Connolly, J. F., and Weaver, D. F. (2010). Improving the clinical assessment of consciousness with advances in electrophysiological and neuroimaging techniques. *BMC Neurol.* 10:11. doi: 10.1186/1471-2377-10-11

Ghosh-Hajra, S., Liu, C. C., Song, X., Fickling, S., Cheung, T., and D'Arcy, R. C. N. (2016b). Developing an electrophysiological indicator of contextual orientation. *Alzheimers Dement.* 12:P920. doi: 10.1016/j.jalz.2016.06.1905

Ghosh-Hajra, S., Liu, C. C., Song, X., Fickling, S., Liu, L. E., Pawlowski, G., et al. (2016a). Developing brain vital signs: initial framework for monitoring brain function changes over time. *Front. Neurosci.* 10:211. doi: 10.3389/fnins.2016.00211

Ghosh-Hajra, S., Liu, C. C., Song, X., Fickling, S. D., Cheung, T. P. L., and D'Arcy, R. C. N. (2018). Multimodal characterization of the semantic N400 response within a rapid evaluation brain vital sign framework. *J. Transl. Med.* 16:151. doi: 10.1186/s12967-018-1527-2

Giacino, J. T., Fins, J. J., Laureys, S., and Schiff, N. D. (2014). Disorders of consciousness after acquired brain injury: the state of the science. *Nat. Rev. Neurol.* 10, 99–114. doi: 10.1038/nrneurol.2013.279

Grenier, É. (2017). Canadian seniors now outnumber children for 1st time, 2016 census shows. *CBC*. Available online at: http://www.cbc.ca/news/politics/2016-census-age-gender-1.4095360

Hajra, S. G., Liu, C. C., Song, X., Fickling, S. D., Cheung, T. P., and D'Arcy, R. C. (2018). Accessing knowledge of the'here and now': a new technique for capturing electromagnetic markers of orientation processing. *J. Neural Eng.* 16:016008. doi: 10.1088/1741-2552/aae91e

Halgren, E., Marinkovic, K., and Chauvel, P. (1998). Generators of the late cognitive potentials in auditory and visual oddball tasks. *Electroencephalogr. Clin. Neurophysiol.* 106, 156–164. doi: 10.1016/S0013-4694(97)00119-3

Herzmann, G., Schweinberger, S. R., Sommer, W., and Jentzsch, I. (2004). What's special about personally familiar faces? A multimodal approach. *Psychophysiology* 41, 688–701. doi: 10.1111/j.1469-8986.2004.00196.x

Herzmann, G., and Sommer, W. (2007). Memory-related ERP components for experimentally learned faces and names: characteristics and parallel-test reliabilities. *Psychophysiology* 44, 262–276. doi: 10.1111/j.1469-8986.2007.00505.x

Hillyard, S., and Lourdes, A.-V. (1998). Event-related brain potentials in the study of visual selective attention. *Proc. Natl. Acad. Sci. U.S.A.* 95, 781–787. doi: 10.1073/pnas.95.3.781

Holcomb, P. J., Coffey, S., and Neville, H. (1992). Visual and auditory sentence processing: a developmental analysis using event-related brain potentials. *Dev. Neuropsychol.* 8, 203–241. doi: 10.1080/87565649209540525

Holcomb, P. J., and Neville, H. J. (1990). Auditory and visual semantic priming in lexical decision: a comparison using event-related brain potentials. *Lang. Cogn. Process* 5, 281–312. doi: 10.1080/01690969008407065

Hruby, T., and Marsalek, P. (2003). Event-related potentials–the P3 wave. *Acta Neurobiol. Exp.* 63, 55–63.

Huang, M.-W., Chou, F. H.-C., Lo, P.-Y., and Cheng, K.-S. (2011). A comparative study on long-term evoked auditory and visual potential responses between Schizophrenic patients and normal subjects. *BMC Psychiatry* 11:74. doi: 10.1186/1471-244X-11-74

Johannes, S., Munte, T. F., Heinze, H. J., and Mangun, G. R. (1995). Luminance and spatial attention effects on early visual processing. *Cogn. Brain Res.* 2, 189–205. doi: 10.1016/0926-6410(95)90008-X

Kappenman, E. S., and Luck, S. J. (eds). (2012). *The Oxford Handbook of Event-Related Potential Components*, New York, NY: Oxford University Press. doi: 10.1093/oxfordhb/9780195374148.001.0001

Knott, V., Bradford, L., Dulude, L., Millar, A., Alwahabi, F., Lau, T., et al. (2003). Effects of stimulus modality and response mode on the P300 event-related potential differentiation of young and elderly adults. *Clin. EEG Neurosci.* 34, 182–190. doi: 10.1177/155005940303400404

Kramer, A., Schneirder, W., Fisk, A., and Donchin, E. (1986). The effects of practice and task structure on components of the event-related potential. *Soc. Psychophysiol. Res.* 23, 33–47. doi: 10.1111/j.1469-8986.1986.tb00590.x

Kutas, M., and Federmeier, K. D. (2011). Thirty years and counting: finding meaning in the N400 component of the event-related brain potential (ERP). *Annu. Rev. Psychol.* 62, 621–647. doi: 10.1146/annurev.psych.093008.131123

Kutas, M., and Hillyard, S. A. (1980). Reading senseless sentences: brain potentials reflect semantic incongruity. *Am. Assoc. Adv. Sci.* 207, 203–205. doi: 10.1126/science.7350657

Kutas, M., and Hillyard, S. A. (1982). The lateral distribution of event-related potentials during sentence processing. *Neuropsychologia* 20, 579–590. doi: 10.1016/0028-3932(82)90031-8

Kutas, M., Neville, H. J., and Holcomb, P. J. (1987). *A* preliminary comparison of the N400 response to semantic anomalies during reading, listening and signing. *Electroencephalogr. Clin. Neurophysiol. Suppl.* 39:325–330.

Kutas, M., and Van Petten, C. (1994). "ERP Psycholinguistics electrified: Event-related brain potential investigations." in *Handbook of Psycholinguistics*, *1st Edn*, ed M. A. Gernsbacher (New York, NY: Academic Press), 83–143.

Lau, E. F., Phillips, C., and Poeppel, D. (2008). A cortical network for semantics: (de)constructing the N400. *Nat. Rev. Neurosci.* 9, 920–933. doi: 10.1038/nrn2532

Lee, T. W., Girolami, M., and Sejnowski, T. J. (1999). Independent component analysis using an extended infomax algorithm for mixed subgaussian and supergaussian sources. *Neural Comput.* 11, 417–441. doi: 10.1162/089976699300016719

Lin, F. R., Yaffe, K., Xia, J., Xue, Q.-L., Harris, T. B., Purchase-Helzner, E., et al. (2013). Hearing loss and cognitive decline in older adults. *JAMA Intern. Med.* 173, 293–299. doi: 10.1001/jamainternmed.2013.1868

Liu, C. C., Ghosh Hajra, S., Cheung, T. P. L., Song, X., and D'Arcy, R. C. N. (2017). Spontaneous blinks activate the precuneus: characterizing blink-related oscillations using magnetoencephalography. *Front. Hum. Neurosci.* 11:489. doi: 10.3389/fnhum.2017.00489

Liu, C. C., Hajra, S. G., Song, X., Doesburg, S. M., Cheung, T. P. L., and D'Arcy, R. C. N., (2018) Cognitive loading via mental arithmetic modulates effects of blink-related oscillations on precuneus and ventral attention network regions. *Hum. Brain Mapp.* 1–17. doi: 10.1002/hbm.24378

López Zunini, R. A., Knoefel, F., Lord, C., Breau, M., Sweet, L., Goubran, R., et al. (2016). P300 amplitude alterations during inhibitory control in persons with Mild Cognitive Impairment. *Brain Res.* 1646, 241–248. doi: 10.1016/j.brainres.2016.06.005

Lopez-Calderon, J., and Luck, S. J. (2014). ERPLAB: an open-source toolbox for the analysis of event-related potentials. *Front. Hum. Neurosci.* 8:213. doi: 10.3389/fnhum.2014.00213

Luck, S. J. (2005). "An introduction to event-related potentials and their neural origins," in *An Introduction to the Event-Related Potential Technique* (MIT Press), 2–50. doi: 10.1007/s10409-008-0217-3

Luck, S. J. (2014). *An Introduction to the Event-Related Potential Technique (Second Edi)*. Cambridge: MIT Press.

Marchand, Y., D'Arcy, R., and Connolly, J. (2002). Linking neurophysiological and neuropsychological measures for aphasia assessment. *Clin. Neurophysiol.* 113, 1715–1722. doi: 10.1016/S1388-2457(02)00224-9

McCallum, W. C., Farmer, S. F., and Pocock, P. V. (1984). The effects of physical and semantic incongruites on auditory event-related potentials. *Electroencephalogr. Clin. Neurophysiol. Evoked Potentials* 59, 477–488. doi: 10.1016/0168-5597(84)90006-6

Mertens, R., and Polich, J. (1997). P300 from a single-stimulus paradigm: Passive versus active tasks and stimulus modality. *Electroencephalogr. Clin. Neurophysiol. Evoked Potentials* 104, 488–497. doi: 10.1016/S0168-5597(97)00041-5

Müller, H. M., and Kutas, M. (1996). What's in a name? Electrophysiological differences between spoken nouns, proper names and one's own name. *Neuroreport* 8, 221–225.

Niznikiewicz, M. A., O'Donnell, B. F., Nestor, P. G., Smith, L., Law, S., Karapelou, M., et al. (1997). ERP assessment of visual and auditory language processing in schizophrenia. *J. Abnorm. Psychol.* 106, 85–94.

Osterhout, L., and Holcomb, P. J. (1996). Event-related potentials and language comprehension. *Electrophysiol. Mind* 6, 171–216. doi: 10.1093/acprof:oso/9780198524168.003.0006

Patel, S. H., and Azzam, P. N. (2005). Characterization of N200 and P300: Selected studies of the event-related potential. *Int. J. Med. Sci.* 2, 147–154. doi: 10.7150/ijms.2.147

Perrin, F., García-Larrea, L., Mauguière, F., and Bastuji, H. (1999). A differential brain response to the subject's own name persists during sleep. *Clin. Neurophysiol.* 110, 2153–2164.

Perrin, F., Maquet, P., Peigneux, P., Ruby, P., Degueldre, C., Balteau, E., et al. (2005). Neural mechanisms involved in the detection of our first name: a combined ERPs and PET study. *Neuropsychologia* 43, 12–19. doi: 10.1016/j.neuropsychologia.2004.07.002

Perrin, F., Schnakers, C., Schabus, M., Degueldre, C., Goldman, S., Bredart, S., et al. (2006). Brain response to one's own name in vegetative state, minimally conscious state, and locked-in syndrome. *Arch. Neurol.* 63, 562–569. doi: 10.1001/archneur.63.4.562

Pfabigan, D. M., Seidel, E. M., Sladky, R., Hahn, A., Paul, K., Grahl, A., et al. (2014). P300 amplitude variation is related to ventral striatum BOLD response during gain and loss anticipation: An EEG and fMRI experiment. *Neuroimage* 96, 12–21. doi: 10.1016/j.neuroimage.2014.03.077

Polich, J. (1997). On the relationship between EEG and P300: Individual differences, aging, and ultradian rhythms. *Int. J. Psychophysiol.* 26, 299–317. doi: 10.1016/S0167-8760(97)00772-1

Polich, J. (2007). Updating P300: an integrative theory of P3a and P3b. *Clin. Neurophysiol.* 118, 2128–2148. doi: 10.1016/j.clinph.2007.04.019

Polich, J., Ellerson, P. C., and Cohen, J. (1996). P300, stimulus intensity, modality, and probability. *Int. J. Psychophysiol.* 23, 55–62. doi: 10.1016/0167-8760(96)00028-1

Polich, J., and Kok, A. (1995). Cognitive and biological determinants of P300: an integrative review. *Biol. Psychol.* 41, 103–146. doi: 10.1016/0301-0511(95)05130-9

Polich, J., and McIsaac, H. K. (1994). Comparison of auditory P300 habituation from active and passive conditions. *Int. J. Psychophysiol.* 17, 25–34. doi: 10.1016/0167-8760(94)90052-3

Ravden, D., and Polich, J. (1998). Habituation of P300 from visual stimuli. *Int. J. Psychophysiol.* 30, 359–365. doi: 10.1016/S0167-8760(98)00039-7

Rayner, K., Clifton, C., and Clifton, C. Jr. (2009). Language processing in reading and speech perception: implications for event related potential research. *Biol. Psychol.* 80, 4–9. doi: 10.1016/j.biopsycho.2008.05.002

Rugg, M. D. (1985). The effects of semantic priming and work repetition on event-related potentials. *Psychophysiology*. 22, 642–647. doi: 10.1111/j.1469-8986.1985.tb01661.x

Sculthorpe-Petley, L., Liu, C., Hajra, S. G., Parvar, H., Satel, J., Trappenberg, T. P., et al. (2015). A rapid event-related potential (ERP) method for point-of-care evaluation of brain function: development of the Halifax Consciousness Scanner. *J. Neurosci. Methods*, 245, 64–72. doi: 10.1016/j.jneumeth.2015.02.008

Stevens, A. A., Skudlarski, P., Gatenby, J. C., and Gore, J. C. (2000). Event-related fMRI of auditory and visual oddball tasks. *Magn. Reson. Imaging*, 18, 495–502. doi: 10.1016/S0730-725X(00)00128-4

Sutton, S., Tueting, P., Zubin, J., and John, E. R. (1967). Information Delivery and the sensory evoked potential. *Science* 155, 1436–1439. doi: 10.1126/science.155.3768.1436

Tacikowski, P., and Nowicka, A. (2010). Allocation of attention to self-name and self-face: an ERP study. *Biol. Psychol.* 84, 318–324. doi: 10.1016/j.biopsycho.2010.03.009

van Petten, C. K., and Rheinfelder, H. (1995). Conceptual relationships between words and environmental sounds: event-related brain potentials measures. *Neuropsychologia* 33, 485–508. doi: 10.1016/0028-3932(94)00133-A

Verleger, R. (1997). On the utility of P3 latency as an index of mental chronometry. *Psychophysiology*. 34, 131–135.doi: 10.1111/j.1469-8986.1997.tb02125.x

Vogel, E. K., and Luck, S. J. (2000). The visual N1 component as an index of a discrimination process. *Psychophysiology* 37, 190–203. doi: 10.1111/1469-8986.3720190

Wood, S. M., Potts, G. F., Hall, J. F., Ulanday, J. B., and Netsiri, C. (2006). Event-related potentials to auditory and visual selective attention in schizophrenia. *Int. J. Psychophysiol.* 60, 67–75. doi: 10.1016/j.ijpsycho.2005.05.005

Yao, D. (2001). A method to standardize a reference of scalp EEG recordings to a point at infinity. *Physiol. Meas.* 22, 693–711. doi: 10.1088/0967-3334/22/4/305

Zhao, K., Wu, Q., Zimmer, H. D., and Fu, X. (2011). Electrophysiological correlates of visually processing subject's own name. *Neurosci. Lett.* 491, 143–147. doi: 10.1016/j.neulet.2011.01.025

Zhao, K., Yuan, J., Zhong, Y., Peng, Y., Chen, J., Zhou, L., et al. (2009). Event-related potential correlates of the collective self-relevant effect. *Neurosci. Lett.* 464, 57–61. doi: 10.1016/j.neulet.2009.07.017

Conflict of Interest Statement: One of the authors (RD) is associated with HealthTech Connex Inc. which may qualify them to financially benefit from the commercialization of a NeuroCatch^{TM}platform capable of measuring brain vital signs. The remaining authors declare that the research was conducted in the absence of any commercial or financial relationships that could be construed as a potential conflict of interest.

Copyright © 2019 Pawlowski, Ghosh-Hajra, Fickling, Liu, Song, Robinovitch, Doesburg and D'Arcy. This is an open-access article distributed under the terms of the Creative Commons Attribution License (CC BY). The use, distribution or reproduction in other forums is permitted, provided the original author(s) and the copyright owner(s) are credited and that the original publication in this journal is cited, in accordance with accepted academic practice. No use, distribution or reproduction is permitted which does not comply with these terms.

frontiers in Neuroscience

ORIGINAL RESEARCH
published: 31 January 2019
doi: 10.3389/fnins.2019.00024

The Local Brain Abnormalities in Patients With Transient Ischemic Attack: A Resting-State fMRI Study

Yating Lv[1,2,3†], Lingyu Li[1,2,3†], Yulin Song[3], Yu Han[4], Chengshu Zhou[3], Dan Zhou[3], Fuding Zhang[3], Qiming Xue[5], Jinling Liu[6], Lijuan Zhao[3], Cairong Zhang[3] and Xiujie Han[3*]*

[1] Institutes of Psychological Sciences, Hangzhou Normal University, Hangzhou, China, [2] Zhejiang Key Laboratory for Research in Assessment of Cognitive Impairments, Hangzhou, China, [3] Department of Neurology, Anshan Changda Hospital, Anshan, China, [4] Department of Neurology, The First Affiliated Hospital, Dalian Medical University, Dalian, China, [5] Department of Image, Anshan Changda Hospital, Anshan, China, [6] Department of Ultrasonics, Anshan Changda Hospital, Anshan, China

OPEN ACCESS

Edited by:
Bradley J. MacIntosh,
Sunnybrook Research Institute,
Canada

Reviewed by:
Hui-Jie Li,
Institute of Psychology (CAS), China
Xiaoyun Liang,
The Florey Institute of Neuroscience and Mental Health, Australia
Qihong Zou,
Peking University, China

***Correspondence:**
Yating Lv
lvyating198247@gmail.com
Xiujie Han
ashanxj@163.com

[†] These authors have contributed equally to this work and share first-authorship

Specialty section:
This article was submitted to Brain Imaging Methods, a section of the journal Frontiers in Neuroscience

Received: 04 October 2018
Accepted: 11 January 2019
Published: 31 January 2019

Citation:
Lv Y, Li L, Song Y, Han Y, Zhou C, Zhou D, Zhang F, Xue Q, Liu J, Zhao L, Zhang C and Han X (2019) The Local Brain Abnormalities in Patients With Transient Ischemic Attack: A Resting-State fMRI Study. Front. Neurosci. 13:24. doi: 10.3389/fnins.2019.00024

Background: Transient ischemic attack (TIA) is an important risk factor for stroke. Despite the transient episodes of clinical symptoms, brain alterations are still observed in patients with TIA. However, the functional mechanism of transient ischemia is still unclear. Here, we employed resting-state functional magnetic resonance imaging (rs-fMRI) to explore the functional abnormalities in patients with TIA.

Methods: 48 TIA patients and 41 age- and sex-matched healthy controls (HCs) were enrolled in the study. For each participant, we collected rs-fMRI data and clinical/physiological/biochemical data. Amplitude of low frequency fluctuation (ALFF), regional homogeneity (ReHo), and degree centrality (DC) were then calculated. Two sample *t*-tests were performed to compare the ALFF, ReHo, and DC maps between the two groups. Furthermore, a correlation analysis was performed to explore the relationship between local brain abnormalities and clinical/physiological/biochemical characteristics tests in TIA patients.

Results: Compared with the HCs, the TIA patients exhibited decreased ALFF in the left middle temporal gyrus, decreased DC in the triangular part of right inferior frontal gyrus, and no significant statistical difference in ReHo. No correlation was found between local abnormalities and clinical/physiological/biochemical scores in the patients with TIA.

Conclusion: Collectively, we found decreased ALFF and DC in patients with TIA which provide evidence for local brain dysfunctions and may help to understand the pathological mechanism for the disease.

Keywords: resting-state fMRI, transient ischemic attack, amplitude of low frequency fluctuation, regional homogeneity, degree centrality

INTRODUCTION

Transient ischemic attack (TIA) is an episode of reversible temporary neurologic dysfunction caused by focal cerebral ischemia of the brain (Albers et al., 2002; Easton et al., 2009). Despite the transient episodes of clinical symptoms, structural and functional brain alterations are still observed in patients with TIA. For example, using structural MRI, one previous study reported that patients

with TIA exhibited gray matter (GM) atrophy in specific regions of the default mode network (Li et al., 2015). Functionally, based on arterial spin labeling (ASL) MRI, several studies identified TIA-related perfusion deficits as characterized by decreased cerebral blood flow (CBF) in widespread brain regions (MacIntosh et al., 2010; Kleinman et al., 2012; Zaharchuk et al., 2012; Qiao et al., 2013). Moreover, TIA is an important risk factor for eventual stroke or a silent stroke (Giles and Rothwell, 2007; Easton et al., 2009), and thus represents a key time window for early diagnosis and intervention of stroke. However, the local brain functional mechanism of transient ischemia still unclear.

Resting-state functional magnetic resonance imaging (rs-fMRI) is a promising tool to investigate functional alterations of the human brain, which has unique advantages in clinical conditions because it does not require participants to engage in cognitive activities (Biswal et al., 1995; Fox and Raichle, 2007). Although the majority of analytic techniques [functional connectivity (FC), graph theory, independent component analysis (ICA), etc] for rs-fMRI data characterize the function of brain network, the local dynamics cannot be fully addressed with these approaches. Recently, several methods have been proposed to characterize the local properties of the rs-fMRI signal: amplitude of low frequency fluctuation (ALFF) (Zang et al., 2007), regional homogeneity (ReHo) (Zang et al., 2004), and degree centrality (DC) (Buckner et al., 2009).

ALFF is defined as the mean amplitude of fluctuations within low frequency range. It provides direct characterization to spontaneous brain activity at each voxel (Zang et al., 2007; Zuo et al., 2010). ReHo is proposed as a voxel-wise measure of the synchronization of the time courses of neighboring voxels based on the hypothesis that voxels within a functional brain area synchronize their metabolic activity depending on specific conditions (Zang et al., 2004). While DC is proposed to map the degree of intrinsic FC across the brain in order to reflect a stable property of cortical network architecture at the voxel level (Buckner et al., 2009). The three local metrics have been widely utilized to investigate functional modulations in many neuropsychiatric disorders (Liu et al., 2006; Zang et al., 2007; Wu et al., 2009; Hoptman et al., 2010; Paakki et al., 2010; Liang et al., 2011; Premi et al., 2014; Zhao et al., 2014; Dai et al., 2015). Specifically, in patients with brain ischemia, several research groups have reported local functional alterations (Guo et al., 2014; Tsai et al., 2014; Shi et al., 2017). For example, Tsai and colleagues reported decreased ALFF in precuneus and posterior cingulate cortex regions in acute stroke patients as compared with healthy controls (HCs) (Tsai et al., 2014).

The three voxel-wised metrics define brain functional characteristics from different perspectives and present the progressive relationship. For a single voxel, ALFF characterizes neural activity intensity of this voxel, ReHo reveals the importance of this voxel among the nearest voxels, while DC portrays the importance of this voxel in the whole brain. Regional abnormalities could be identified with greater sensitivity by applying these three metrics. For example, An and colleagues showed the group differences of ADHD patients and HCs using both ALFF and ReHo, they observed that regions exhibiting group differences in ReHo and ALFF metrics were not completely the same (An et al., 2013), which suggest that these metrics complement each other and characterize local brain abnormalities from different perspectives.

In the current study, we employed rs-fMRI to explore the local abnormalities in patients with TIA from different perspectives. Specifically, we sought to determine whether and how TIA disrupts the local function using three local metrics (ALFF, ReHo, and DC) and whether those local abnormalities (if observed) are associated with clinical/physiological/biochemical characteristics scores of the patients.

MATERIALS AND METHODS

Participants

From April 2015 to June 2016, 51 suspected TIA patients who had transient neurologic symptoms which had been evaluated to have a possible vascular etiology judged by clinical neurologists were recruited from Department of Neurology, Anshan Changda Hospital. Patients with hemorrhage, leukoaraiosis, migraine, epilepsy or psychiatric diseases history were excluded. All patients underwent electrocardiogram (ECG), carotid duplex ultrasound examination (CDU) and MRI scan. The study was approved by the Ethics Committee of the Center for Cognition and Brain Disorders, Hangzhou Normal University. Written informed consent was obtained from all participants.

For each patient, we recorded information as follows: (1) history of TIA and stroke; (2) previous risk factors: hypertension, diabetes mellitus, coronary artery disease, current smoking and drinking; (3) medications used before the MRI scanning; (4) in-hospital evaluation of arterial stenosis (carotid duplex ultrasound and MR angiography), atrial fibrillation (ECG) and brain infarcts (diffusion-weighted imaging and T2-FLAIR); (5) one-year telephone follow-up of stroke and/or TIA attack. Notably, four patients dropped out in one-year follow-up. Based on the methods described by Johnston et al. (2007), an ABCD2 score was generated for each patient to evaluate the risk for subsequent stroke.

41 age- and sex-matched HCs with no physical diseases or history of psychiatric or neurologic disorders from local community were also recruited in this study.

Three patients were excluded from the final analysis due to image quality of multimodal MRI (see below for details), leaving 48 TIA patients and 41 HCs in the final analysis. Out of the 48 patients, 4 (8.3%) experienced stroke, 25 (52.1%) experienced TIA, and 23 (47.9%) were first episode. Detailed demographic and clinical information for all participants are summarized in **Table 1**.

Physiological and Biochemical Tests

All participants completed a series of physiological/biochemical tests within 24 h before the MRI data acquisition, including blood systolic pressure, blood diastolic pressure, blood sugar level, total cholesterol, triglycerides, high-density lipoprotein cholesterol (HDL-C), and low-density lipoprotein cholesterol (LDL-C). Additionally, all participants underwent the mini-mental state

TABLE 1 | Demographics and clinical characteristics of all participants.

	TIA (n = 48)	HCs (n = 41)	*p*-value
Age (years)	57.604 ± 9.778	55.024 ± 8.033	0.182[a]
Sex (M/F)	37/11	30/11	0.670[b]
MMSE	29.208 ± 2.609	28.615 ± 1.664	0.222[a]
Blood systolic pressure (mmHg)	145.542 ± 20.753	126.940 ± 19.758[c]	< 0.001[a]
Blood diastolic pressure (mmHg)	86.667 ± 10.383	80.030 ± 10.896[c]	0.007[a]
Blood sugar level (mmol/L)	6.299 ± 2.113	5.200 ± 0.740[c]	< 0.001[a]
Total cholesterol (mmol/L)	5.275 ± 1.173	4.753 ± 1.011[c]	0.037[a]
Triglycerides (mmol/L)	1.603 ± 0.940	1.917 ± 1.345[c]	0.234[a]
HDL-C (mmol/L)	1.111 ± 0.238	1.051 ± 0.290[c]	0.311[a]
LDL-C (mmol/L)	3.314 ± 0.974	2.691 ± 0.904[c]	0.004[a]
ABCD2 scores, median	4 (2–6)	–	–
Smoking, No. (%)	31 (64.6%)	19 (46.3%)	0.084[b]
Drinking, No. (%)	20 (41.7%)	21 (51.2%)	0.367[b]
Hypertension, No. (%)	22 (45.8%)	6 (14.6%)	0.002[b]
Diabetes, No. (%)	8 (16.7%)	0 (0%)	0.006[b]
Coronary artery disease, No. (%)	2 (4.2%)	0 (0%)	0.186[b]
Atrial fibrillation, No. (%)	1 (2.1%)	–	–
Medication	–	–	–
Antiplatelets, No. (%)	48 (100%)	–	–
Statins, No. (%)	2 (4.2%)	–	–
DWI hyperintensity, No. (%)	6 (12.5%)	–	–
Vessel stenosis, No. (%)	9 (18.8%)	–	–
TIA/stroke attack in one-year follow-up, No. (%)	12 (27.3%)[d]	–	–

TIA, transient ischemic attack; HCs, healthy controls; M, male; F, female; HDL-C, high-density lipoprotein cholesterol; LDL-C, low-density lipoprotein cholesterol; MMSE, mini-mental state examination; DWI, diffusion weighted imaging. [a]Data were obtained using two-sample two-side t-tests. [b]Data were obtained using Pearson Chi-square tests. [c]Data were missing for six controls. [d]Four patients dropped out in the one-year follow-up.

examination (MMSE) to evaluate global cognition (Schultz-Larsen et al., 2007).

MR Data Acquisition

MR data was acquired using a GE MR-750 3.0 T scanner (GE Medical Systems, Inc., Waukesha, WI, United States) at Anshan Changda Hospital, China. The time interval between the last TIA attack and subsequent MRI scanning was 0.25–6 days for the patients. During the data acquisition, participants were instructed to keep awake, relax with their eyes closed and remain motionless as much as possible.

Resting-state fMRI (rs-fMRI) data was obtained using an echo-planar imaging sequence with following protocols: 43 axial slices, TR = 2000 ms, TE = 30 ms, flip angle = 60°, matrix = 64 × 64, in-plane resolution of 3.44 mm × 3.44 mm, thickness/gap = 3.2/0 mm, 240 contiguous EPI functional volumes, 8 min.

3D high resolution T1-weighted anatomical images were acquired using a 3D-MPRAGE sequence: 176 sagittal slice, TR = 8100 ms, TE = 3.1 ms, matrix = 256 × 256, voxel size: 1 mm × 1 mm × 1 mm, thickness/gap = 1/0 mm. This session lasted for about 5 min.

Three patients were excluded from further analysis due to incomplete coverage of the whole brain for rs-fMRI scan (2) or the lost of 3D T1 image (1).

Data Preprocessing

Resting-state fMRI data was processed using Data Processing & Analysis for Brain Imaging (DPABI) (Yan et al., 2016) including: (1) removing first 10 time points to make the longitudinal magnetization reach steady state and to let the participant get used to the scanning environment; (2) slice-timing to correct the differences in image acquisition time between slices; (3) head motion correction; (4) spatial normalization to the Montreal Neurological Institute (MNI) space via the deformation fields derived from tissue segmentation of structural images (resampling voxel size = 3 mm × 3 mm × 3 mm); (5) spatial smoothing with an isotropic Gaussian kernel with a full width at half maximum (FWHM) of 6 mm; (6) removing linear trend of the time course; (7) regressing out the head motion effect (using Friston 24 parameter) from the fMRI data (Friston et al., 1996); (8) band-pass filtering (0.01–0.08 Hz). No participants were excluded from further analysis due to large head motion (more than 3.0 mm of maximal translation in any direction of x, y or z or 3.0° of maximal rotation throughout the course of scanning). Then, 3 voxel-wise whole-brain analytic methods, i.e., ALFF, ReHo, and DC, were further applied to the preprocessed fMRI data.

ALFF Calculation

After data preprocessing, the time course for each voxel was transformed to the frequency domain with a fast Fourier transform and the power spectrum was then obtained. The square root was calculated at each frequency of the power spectrum and the averaged square root was obtained across 0.01–0.08 Hz at each voxel as the ALFF value, which was further divided by the global mean ALFF of each individual for group comparison (Zang et al., 2007).

ReHo Calculation

The Kendall's coefficient of concordance (KCC) was used to measure the local synchronization of the time series of neighboring voxels as follows (Zang et al., 2004):

$$W = \frac{\sum(R_i)^2 - n(\bar{R})^2}{\frac{1}{12}K^2(n^3 - n)} \quad (1)$$

where W is the KCC among given voxels, ranged from 0 to 1; R_i is the sum rank of the ith time point; $\bar{R} = (n+1)K/2$ is the mean of the R_i's; K is the number of time series within a measured cluster (K = 7, 19, and 27, respectively. 27 in the current study); n is the number of ranks. The ReHo value of each voxel was then divided by the global mean ReHo of each individual for standardization purposes. Note that the spatial smoothing (FWHM = 6 mm) was performed after ReHo calculation.

DC Calculation

Several nuisance signals (white matter, cerebrospinal fluid, and global mean signal) were further regressed out from each voxel's time series. For a weighted graph, DC is defined as the sum of weights from edges connecting to a node (also sometimes referred to as the node strength) (Zuo et al., 2012). Pearson's correlation of time series was performed between each voxel and every other voxel in the entire brain to calculate a correlation matrix R = (r_{ij}), j = 1...N (N is the number of voxels), $i \neq 1$ (Buckner et al., 2009; Zuo et al., 2012). The correlation coefficients with $r_{ij} \geq 0.32$ ($p < 0.05$, Bonferroni-corrected over whole-brain voxels) were summed up for each voxel and then a weighted DC was obtained for each voxel. The threshold was used to eliminate counting voxels that had low temporal correlation (Buckner et al., 2009).

The weighted DC of each voxel was further divided by the global mean weighted DC of each individual for group comparison.

Statistical Analysis

The age, clinical/physiological/biochemical variables were analyzed with the Statistical Package for the Social Sciences (SPSS) (SPSS Inc., Chicago, IL, United States). The differences between the patients and the HCs in age, clinical/physiological/biochemical tests were tested with Student's t-tests. Sex difference was tested with the Pearson Chi-Square test.

Two sample t-tests were performed to compare the ALFF, ReHo, and DC maps between patients with TIA and HCs respectively. Individual age and sex were treated as covariates during the group comparisons to minimize their potential effects on our results. The resultant T-maps were thresholded with voxel $p < 0.001$, cluster $p < 0.05$ (Gaussian Random Field theory (GRF) correction for multiple comparisons). The analyses were performed using DPABI (Yan et al., 2016).

For any measure (ALFF, ReHo, or DC) showing TIA-related alterations, a Pearson correlation analysis was used to assess its associations with clinical/physiological/biochemical characteristics of the patients (including blood systolic pressure, blood diastolic pressure, blood sugar level, total cholesterol, triglycerides, HDL-C, LDL-C). The correlations were considered significant at a threshold of $p < 0.05$.

RESULTS

Participants' Characteristics

As shown in **Table 1**, there were no significant differences in sex (p = 0.670), age (p = 0.182), MMSE scores (p = 0.222), smoking (p = 0.084), drinking (p = 0.367), or coronary artery disease (p = 0.186) between TIA patients and HCs. Hypertension (p = 0.002) and diabetes (p = 0.006) showed significant between-group differences. Significantly higher blood systolic pressure ($p < 0.001$), diastolic pressure (p = 0.007), blood sugar level ($p < 0.001$), total cholesterol (p = 0.037) and LDL-C (p = 0.004) were observed in the patients compared with the HCs. The median ABCD2 score for the patients with TIA was four (**Table 1**).

TABLE 2 | Regions showing abnormal ALFF and DC in patients with TIA as compared with HCs.

Regions	Cluster size	Peak T value	MNI coordinate (mm)		
			X	Y	Z
ALFF					
Left middle temporal gyrus	40	−4.869	−51	−66	9
DC					
Triangular part of right inferior frontal gyrus	56	−4.557	48	33	27

Disrupted Local Function in TIA

Compared with HCs, the TIA patients exhibited decreased ALFF in the left middle temporal gyrus (voxel $p < 0.001$, cluster $p < 0.05$, GRF correction, cluster size >31 voxels) (**Table 2** and **Figure 1**).

The triangular part of right inferior frontal gyrus showed decreased DC in TIA patients as compared with HCs (voxel $p < 0.001$, cluster $p < 0.05$, GRF correction, cluster size >28 voxels) (**Table 2** and **Figure 1**).

No regions showed significant between-group differences in ReHo (voxel $p < 0.001$, cluster $p < 0.05$, GRF correction, cluster size >78 voxels).

Relationship Between Local Metrics and Clinical/Physiological/Biochemical Characteristics

No significant correlation was found between local brain abnormalities and clinical/physiological/biochemical characteristics in TIA patients ($p > 0.05$) (**Table 3**).

DISCUSSION

The ALFF, ReHo, and DC define brain local function from different perspectives and present the progressive relationship. Regional abnormalities could be identified with greater sensitivity by applying three metrics. In this study, we used these three rs-fMRI analysis metrics to investigate local brain functional alterations in patients with TIA and further examined the relevance of these alterations induced by brain ischemia with respect to clinical/physiological/biochemical characteristics scores. Our results showed that compared with the HCs, the TIA patients exhibited decreased ALFF in the left middle temporal gyrus, decreased DC in the triangular part of right inferior frontal gyrus. These findings have implications for understanding the functional mechanisms in the early stage of brain ischemia.

ALFF was supposed to reflect the extent of spontaneous neuronal activity (Zang et al., 2007). In the present study, the left middle temporal gyrus of TIA patients showed decreased ALFF, which indicated decreased spontaneous neuronal activity within the local brain region. The middle

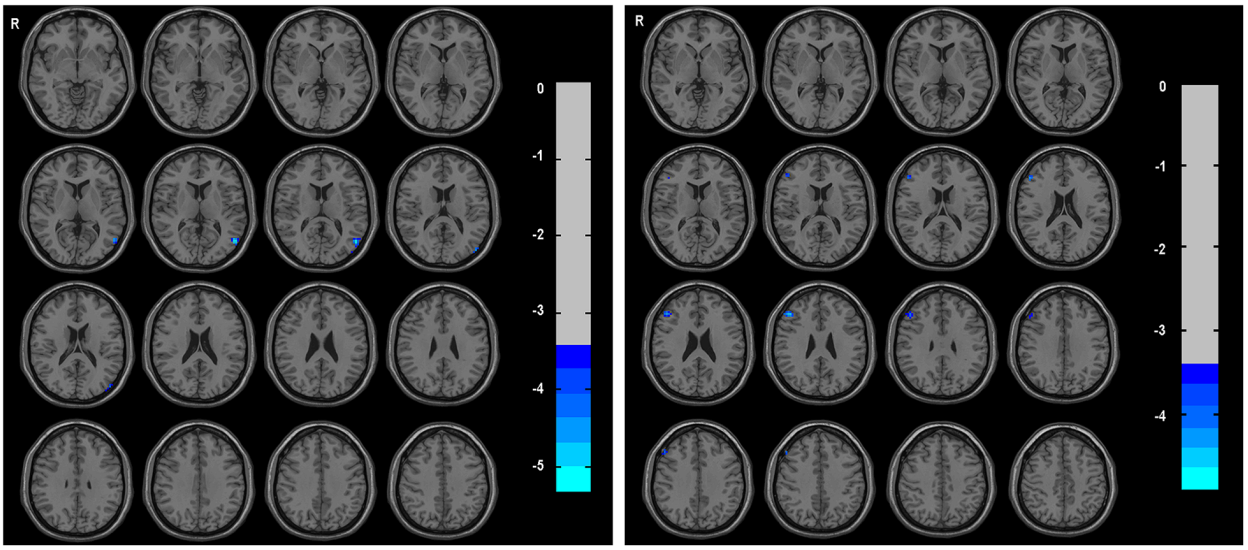

FIGURE 1 | The group differences of ALFF (left) and DC (right) between TIA patients and healthy controls, respectively. Cold colors indicate decreased ALFF in left middle temporal gyrus and decreased DC in triangular part of right inferior frontal gyrus in patients with TIA as compared to that in healthy controls (voxel $p < 0.001$, cluster $p < 0.05$, GRF correction, set cluster size >31 voxels for ALFF metric and cluster size >28 voxels for DC metric).

TABLE 3 | Correlation between local metrics and clinical/physiological/biochemical characteristics.

	ALFF	DC
Clinical/physiological/biochemical characteristics	**Left middle temporal gyrus**	**Triangular part of right inferior frontal gyrus**
Blood systolic pressure	$r = -0.050$ $p = 0.736$	$r = 0.256$ $p = 0.069$
Blood diastolic pressure	$r = -0.167$ $p = 0.256$	$r = 0.043$ $p = 0.771$
Blood sugar level	$r = 0.218$ $p = 0.136$	$r = -0.011$ $p = 0.941$
Total cholesterol	$r = -0.046$ $p = 0.756$	$r = 0.075$ $p = 0.614$
Triglycerides	$r = -0.125$ $p = 0.397$	$r = -0.062$ $p = 0.673$
HDL-C	$r = 0.030$ $p = 0.841$	$r = -0.170$ $p = 0.248$
LDL-C	$r = -0.042$ $p = 0.778$	$r = 0.164$ $p = 0.266$
MMSE	$r = -0.213$ $p = 0.147$	$r = -0.280$ $p = 0.054$

HDL-C, high-density lipoprotein cholesterol; LDL-C, low-density lipoprotein cholesterol; MMSE, mini-mental state examination.

temporal gyrus was involved in several cognitive processes, including language and semantic memory processing, as well as visual perception (Söderfeldt et al., 1997; Cabeza and Nyberg, 2000; Li et al., 2013; Bonilha et al., 2017). Previous study showed that decreased FC in left middle temporal gyrus within the default mode network in patients with TIA as compared with HCs (Li et al., 2013). Thus, we speculate that the decreased local neuronal activity (ALFF) in the left middle temporal gyrus could be the reason for the aberrant FC in TIA. Moreover, despite the transient episodes of the clinical symptoms, TIA was also accompanied by cognitive impairments in multiple domains including executive function, information processing speed and abstraction (Bakker et al., 2003; Sachdev et al., 2004). The difficulties in language processing in patients with TIA may be attributable to the decreased ALFF in left temporal gyrus.

ReHo reflects the local synchronization of spontaneous BOLD signal. The decreased ReHo indicates decreased local synchronization of low frequency fluctuations of the BOLD signal (Lv et al., 2013). When applying threshold of $p < 0.001$ (GRF correction for multiple comparisons), there was no significant difference in ReHo between TIA and HCs. While using voxel $p < 0.05$ and cluster size larger than 25 contiguous voxels, Guo and colleagues found decreased ReHo in the right dorsolateral prefrontal cortex, inferior prefrontal cortex, ventral anterior cingulate cortex, and dorsal posterior cingulate cortex in patients with TIA (Guo et al., 2014). We also found decreased ReHo in right inferior prefrontal gyrus and cingulate cortex using the same threshold (voxel $p < 0.05$, cluster size >25 voxels) as Guo et al. (additional data are given in Online Resource, **Supplementary Figure S1**). These findings may indicate that some true positive brain regions may not survive the multiple comparison correction when using strict threshold to decrease false positive (Eklund et al., 2016).

DC reflects the role and status of voxels in brain network and represents the most local and directly quantifiable centrality measure (Buckner et al., 2009). Here, the triangular part of right inferior frontal gyrus exhibited decreased DC, which indicated decreased importance of this region in the brain of TIA. The triangular part of right inferior frontal gyrus was involved in several cognitive processes, including attention and motor inhibition processes, as well as language performance (Hampshire et al., 2010; Tanaka et al., 2013; Hassa et al., 2016). Liu and colleagues showed decreased FC between the inferior frontal cortex and dorsal attention network in patients with post-stroke memory dysfunction (Liu et al., 2017). Moreover, the activation of the right inferior frontal gyrus may be essential

for language performance in patients experiencing aphasia after left hemispheric stroke (Winhuisen et al., 2005, 2007). Thus, we speculate that the decreased DC in the triangular part of right inferior frontal gyrus may indicate the decreased FC with attention and language network, and may induce attention, inhibitory control, and language impairments in TIA.

The present study has some limitations. First, this study lacked cognitive data for the patients. It would be interesting to investigate the relationships between functional alterations and cognitive dysfunction associated with TIA. Second, we did not collect MRI data during the follow up period, and thus cannot examine how functional brain networks reorganize as TIA continues to advance. Future longitudinal studies are warranted to examine whether the current approach could be used to monitor disease progression of TIA.

ETHICS STATEMENT

The study has been approved by the local ethics committee and has been performed in accordance with the ethical standards laid down in the 1964 Declaration of Helsinki and its later amendments. Written informed consent has been obtained from all study participants.

AUTHOR CONTRIBUTIONS

YL and XH designed the study. YS, YH, chZ, DZ, FZ, QX, JL, LZ, and caZ performed the experiments and collected the data. YL and LL analyzed and interpreted the data, wrote the manuscript.

FUNDING

This work was supported by grants from National Key R&D Program of China (No. 2017YFC1310000), National Natural Science Foundation of China (Nos. 81771911 and 81301210).

SUPPLEMENTARY MATERIAL

The Supplementary Material for this article can be found online at: https://www.frontiersin.org/articles/10.3389/fnins.2019.00024/full#supplementary-material

REFERENCES

Albers, G. W., Caplan, L. R., Easton, J. D., Fayad, P. B., Mohr, J. P., Saver, J. L., et al. (2002). Transient ischemic attack–proposal for a new definition. *N. Engl. J. Med.* 347, 1713–1716. doi: 10.1056/NEJMsb020987

An, L., Cao, Q. J., Sui, M. Q., Sun, L., Zou, Q. H., Zang, Y. F., et al. (2013). Local synchronization and amplitude of the fluctuation of spontaneous brain activity in attention-deficit/hyperactivity disorder: a resting-state fMRI study. *Neurosci. Bull.* 29, 603–613. doi: 10.1007/s12264-013-1353-8

Bakker, F. C., Klijn, C. J., Jennekens-Schinkel, A., van der Tweel, I., Tulleken, C. A., and Kappelle, L. J. (2003). Cognitive impairment in patients with carotid artery occlusion and ipsilateral transient ischemic attacks. *J. Neurol.* 250, 1340–1347. doi: 10.1007/s00415-003-0222-1

Biswal, B., Yetkin, F. Z., Haughton, V. M., and Hyde, J. S. (1995). Functional connectivity in the motor cortex of resting human brain using echo-planar MRI. *Magn. Reson. Med.* 34, 537–541. doi: 10.1002/mrm.1910340409

Bonilha, L., Hillis, A. E., Hickok, G., den Ouden, D. B., Rorden, C., and Fridriksson, J. (2017). Temporal lobe networks supporting the comprehension of spoken words. *Brain* 140, 2370–2380. doi: 10.1093/brain/awx169

Buckner, R. L., Sepulcre, J., Talukdar, T., Krienen, F. M., Liu, H., Hedden, T., et al. (2009). Cortical hubs revealed by intrinsic functional connectivity: mapping, assessment of stability, and relation to Alzheimer's disease. *J. Neurosci.* 29, 1860–1873. doi: 10.1523/JNEUROSCI.5062-08.2009

Cabeza, R., and Nyberg, L. (2000). Imaging cognition II: an empirical review of 275 PET and fMRI studies. *J. Cogn. Neurosci.* 12, 1–47. doi: 10.1162/08989290051137585

Dai, Z., Yan, C., Li, K., Wang, Z., Wang, J., Cao, M., et al. (2015). Identifying and mapping connectivity patterns of brain network hubs in Alzheimer's disease. *Cereb. Cortex* 25, 3723–3742. doi: 10.1093/cercor/bhu246

Easton, J. D., Saver, J. L., Albers, G. W., Alberts, M. J., Chaturvedi, S., Feldmann, E., et al. (2009). Definition and evaluation of transient ischemic attack: a scientific statement for healthcare professionals from the American Heart Association/American Stroke Association Stroke Council; Council on Cardiovascular Surgery and Anesthesia; Council on Cardiovascular Radiology and Intervention; Council on Cardiovascular Nursing; and the Interdisciplinary Council on Peripheral Vascular Disease. The American Academy of Neurology affirms the value of this statement as an educational tool for neurologists. *Stroke* 40, 2276–2293. doi: 10.1161/STROKEAHA.108.192218

Eklund, A., Nichols, T. E., and Knutsson, H. (2016). Cluster failure: why fMRI inferences for spatial extent have inflated false-positive rates. *Proc. Natl. Acad. Sci. U.S.A.* 113, 7900–7905. doi: 10.1073/pnas.1602413113

Fox, M. D., and Raichle, M. E. (2007). Spontaneous fluctuations in brain activity observed with functional magnetic resonance imaging. *Nat. Rev. Neurosci.* 8, 700–711. doi: 10.1038/nrn2201

Friston, K. J., Williams, S., Howard, R., Frackowiak, R. S., and Turner, R. (1996). Movement-related effects in fMRI time-series. *Magn. Reson. Med.* 35, 346–355. doi: 10.1002/mrm.1910350312

Giles, M. F., and Rothwell, P. M. (2007). Risk of stroke early after transient ischaemic attack: a systematic review and meta-analysis. *Lancet Neurol.* 6, 1063–1072. doi: 10.1016/S1474-4422(07)70274-0

Guo, J., Chen, N., Li, R., Wu, Q., Chen, H., Gong, Q., et al. (2014). Regional homogeneity abnormalities in patients with transient ischaemic attack: a resting-state fMRI study. *Clin. Neurophysiol.* 125, 520–525. doi: 10.1016/j.clinph.2013.08.010

Hampshire, A., Chamberlain, S. R., Monti, M. M., Duncan, J., and Owen, A. M. (2010). The role of the right inferior frontal gyrus: inhibition and attentional control. *Neuroimage* 50, 1313–1319. doi: 10.1016/j.neuroimage.2009.12.109

Hassa, T., de Jel, E., Tuescher, O., Schmidt, R., and Schoenfeld, M. A. (2016). Functional networks of motor inhibition in conversion disorder patients and feigning subjects. *Neuroimage Clin.* 11, 719–727. doi: 10.1016/j.nicl.2016.05.009

Hoptman, M. J., Zuo, X. N., Butler, P. D., Javitt, D. C., D'Angelo, D., Mauro, C. J., et al. (2010). Amplitude of low-frequency oscillations in schizophrenia: a resting state fMRI study. *Schizophr. Res.* 117, 13–20. doi: 10.1016/j.schres.2009.09.030

Johnston, S. C., Rothwell, P. M., Nguyen-Huynh, M. N., Giles, M. F., Elkins, J. S., Bernstein, A. L., et al. (2007). Validation and refinement of scores to predict very early stroke risk after transient ischaemic attack. *Lancet* 369, 283–292. doi: 10.1016/S0140-6736(07)60150-0

Kleinman, J. T., Zaharchuk, G., Mlynash, M., Ogdie, A. A., Straka, M., Lansberg, M. G., et al. (2012). Automated perfusion imaging for the evaluation of transient ischemic attack. *Stroke* 43, 1556–1560. doi: 10.1161/STROKEAHA.111.644971

Li, R., Guo, J., Ma, X., Wang, S., Zhang, J., He, L., et al. (2015). Alterations in the gray matter volume in transient ischemic attack: a voxel-based morphometry study. *Neurol. Res.* 37, 43–49. doi: 10.1179/1743132814Y.0000000406

Li, R., Wang, S., Zhu, L., Guo, J., Zeng, L., Gong, Q., et al. (2013). Aberrant functional connectivity of resting state networks in transient ischemic attack. *PLoS One* 8:e71009. doi: 10.1371/journal.pone.0071009

Liang, P., Liu, Y., Jia, X., Duan, Y., Yu, C., Qin, W., et al. (2011). Regional homogeneity changes in patients with neuromyelitis optica revealed by resting-state functional MRI. *Clin. Neurophysiol.* 122, 121–127. doi: 10.1016/j.clinph.2010.05.026

Liu, H., Liu, Z., Liang, M., Hao, Y., Tan, L., Kuang, F., et al. (2006). Decreased regional homogeneity in schizophrenia: a resting state functional magnetic resonance imageing study. *Neuroreport* 17, 19–22. doi: 10.1097/01.wnr.0000195666.22714.35

Liu, J., Wang, Q., Liu, F., Song, H., Liang, X., Lin, Z., et al. (2017). Altered functional connectivity in patients with post-stroke memory impairment: a resting fMRI study. *Exp. Ther. Med.* 14, 1919–1928. doi: 10.3892/etm.2017.4751

Lv, Y., Margulies, D. S., Villringer, A., and Zang, Y. F. (2013). Effects of finger tapping frequency on regional homogeneity of sensorimotor cortex. *PLoS One* 8:e64115. doi: 10.1371/journal.pone.0064115

MacIntosh, B. J., Lindsay, A. C., Kylintireas, I., Kuker, W., Günther, M., Robson, M. D., et al. (2010). Multiple inflow pulsed arterial spin-labeling reveals delays in the arterial arrival time in minor stroke and transient ischemic attack. *AJNR Am. J. Neuroradiol.* 31, 1892–1894. doi: 10.3174/ajnr.A2008

Paakki, J. J., Rahko, J., Long, X., Moilanen, I., Tervonen, O., Nikkinen, J., et al. (2010). Alterations in regional homogeneity of resting-state brain activity in autism spectrum disorders. *Brain Res.* 1321, 169–179. doi: 10.1016/j.brainres.2009.12.081

Premi, E., Cauda, F., Gasparotti, R., Diano, M., Archetti, S., Padovani, A., et al. (2014). Multimodal fMRI resting-state functional connectivity in granulin mutations: the case of fronto-parietal dementia. *PLoS One* 9:e106500. doi: 10.1371/journal.pone.0106500

Qiao, X. J., Salamon, N., Wang, D. J., He, R., Linetsky, M., Ellingson, B. M., et al. (2013). Perfusion deficits detected by arterial spin-labeling in patients with TIA with negative diffusion and vascular imaging. *AJNR Am. J. Neuroradiol.* 34, 2125–2130. doi: 10.3174/ajnr.A3551

Sachdev, P. S., Brodaty, H., Valenzuela, M. J., Lorentz, L., Looi, J. C., Wen, W., et al. (2004). The neuropsychological profile of vascular cognitive impairment in stroke and TIA patients. *Neurology* 62, 912–919. doi: 10.1212/01.WNL.0000115108.65264.4B

Schultz-Larsen, K., Lomholt, R. K., and Kreiner, S. (2007). Mini-Mental Status Examination: a short form of MMSE was as accurate as the original MMSE in predicting dementia. *J. Clin. Epidemiol.* 60, 260–267. doi: 10.1016/j.jclinepi.2006.06.008

Shi, Y., Zeng, Y., Wu, L., Liu, Z., Zhang, S., Yang, J., et al. (2017). A study of the brain functional network of post-stroke depression in three different lesion locations. *Sci. Rep.* 7:14795. doi: 10.1038/s41598-017-14675-4

Söderfeldt, B., Ingvar, M., Rönnberg, J., Eriksson, L., Serrander, M., and Stone-Elander, S. (1997). Signed and spoken language perception studied by positron emission tomography. *Neurology* 49, 82–87. doi: 10.1212/WNL.49.1.82

Tanaka, N., Liu, H., Reinsberger, C., Madsen, J. R., Bourgeois, B. F., Dworetzky, B. A., et al. (2013). Language lateralization represented by spatiotemporal mapping of magnetoencephalography. *AJNR Am. J. Neuroradiol.* 34, 558–563. doi: 10.3174/ajnr.A3233

Tsai, Y. H., Yuan, R., Huang, Y. C., Yeh, M. Y., Lin, C. P., and Biswal, B. B. (2014). Disruption of brain connectivity in acute stroke patients with early impairment in consciousness. *Front. Psychol.* 4:956. doi: 10.3389/fpsyg.2013.00956

Winhuisen, L., Thiel, A., Schumacher, B., Kessler, J., Rudolf, J., Haupt, W. F., et al. (2005). Role of the contralateral inferior frontal gyrus in recovery of language function in poststroke aphasia: a combined repetitive transcranial magnetic stimulation and positron emission tomography study. *Stroke* 36, 1759–1763. doi: 10.1161/01.STR.0000174487.81126.ef

Winhuisen, L., Thiel, A., Schumacher, B., Kessler, J., Rudolf, J., Haupt, W. F., et al. (2007). The right inferior frontal gyrus and poststroke aphasia: a follow-up investigation. *Stroke* 38, 1286–1292. doi: 10.1161/01.STR.0000259632.04324.6c

Wu, T., Long, X., Zang, Y., Wang, L., Hallett, M., Li, K., et al. (2009). Regional homogeneity changes in patients with Parkinson's disease. *Hum. Brain Mapp.* 30, 1502–1510. doi: 10.1002/hbm.20622

Yan, C. G., Wang, X. D., Zuo, X. N., and Zang, Y. F. (2016). DPABI: data processing & analysis for (resting-state) brain imaging. *Neuroinformatics* 14, 339–351. doi: 10.1007/s12021-016-9299-4

Zaharchuk, G., Olivot, J. M., Fischbein, N. J., Bammer, R., Straka, M., Kleinman, J. T., et al. (2012). Arterial spin labeling imaging findings in transient ischemic attack patients: comparison with diffusion- and bolus perfusion-weighted imaging. *Cerebrovasc. Dis.* 34, 221–228. doi: 10.1159/000339682

Zang, Y., Jiang, T., Lu, Y., He, Y., and Tian, L. (2004). Regional homogeneity approach to fMRI data analysis. *Neuroimage* 22, 394–400. doi: 10.1016/j.neuroimage.2003.12.030

Zang, Y. F., He, Y., Zhu, C. Z., Cao, Q. J., Sui, M. Q., Liang, M., et al. (2007). Altered baseline brain activity in children with ADHD revealed by resting-state functional MRI. *Brain Dev.* 29, 83–91. doi: 10.1016/j.braindev.2006.07.002

Zhao, Z., Lu, J., Jia, X., Chao, W., Han, Y., Jia, J., et al. (2014). Selective changes of resting-state brain oscillations in aMCI: an fMRI study using ALFF. *Biomed Res. Int.* 2014:920902. doi: 10.1155/2014/920902

Zuo, X. N., Di Martino, A., Kelly, C., Shehzad, Z. E., Gee, D. G., Klein, D. F., et al. (2010). The oscillating brain: complex and reliable. *Neuroimage* 49, 1432–1445. doi: 10.1016/j.neuroimage.2009.09.037

Zuo, X. N., Ehmke, R., Mennes, M., Imperati, D., Castellanos, F. X., Sporns, O., et al. (2012). Network centrality in the human functional connectome. *Cereb. Cortex* 22, 1862–1875. doi: 10.1093/cercor/bhr269

Conflict of Interest Statement: The authors declare that the research was conducted in the absence of any commercial or financial relationships that could be construed as a potential conflict of interest.

Copyright © 2019 Lv, Li, Song, Han, Zhou, Zhou, Zhang, Xue, Liu, Zhao, Zhang and Han. This is an open-access article distributed under the terms of the Creative Commons Attribution License (CC BY). The use, distribution or reproduction in other forums is permitted, provided the original author(s) and the copyright owner(s) are credited and that the original publication in this journal is cited, in accordance with accepted academic practice. No use, distribution or reproduction is permitted which does not comply with these terms.

frontiers in Neuroscience

SYSTEMATIC REVIEW
published: 07 February 2019
doi: 10.3389/fnins.2019.00023

Clinical Applications for Diffusion MRI and Tractography of Cranial Nerves Within the Posterior Fossa: A Systematic Review

Jonathan Shapey[1,2,3]*, *Sjoerd B. Vos*[1,4,5], *Tom Vercauteren*[3], *Robert Bradford*[2], *Shakeel R. Saeed*[2,6,7], *Sotirios Bisdas*[8] *and Sebastien Ourselin*[3]

[1] *Wellcome/EPSRC Centre for Interventional and Surgical Sciences, University College London, London, United Kingdom,* [2] *Department of Neurosurgery, National Hospital for Neurology and Neurosurgery, London, United Kingdom,* [3] *School of Biomedical Engineering and Imaging Sciences, King's College London, London, United Kingdom,* [4] *Translational Imaging Group—Centre for Medical Image Computing, University College London, London, United Kingdom,* [5] *Epilepsy Society MRI Unit, Chalfont St Peter, United Kingdom,* [6] *The Ear Institute, University College London, London, United Kingdom,* [7] *The Royal National Throat, Nose and Ear Hospital, London, United Kingdom,* [8] *Neuroimaging Analysis Centre, London, United Kingdom*

OPEN ACCESS

Edited by:
Itamar Ronen,
Leiden University, Netherlands

Reviewed by:
Lauren Jean O'Donnell,
Harvard Medical School,
United States
Matthew D. Budde,
Medical College of Wisconsin,
United States

***Correspondence:**
Jonathan Shapey
j.shapey@ucl.ac.uk

Specialty section:
This article was submitted to Brain Imaging Methods, a section of the journal Frontiers in Neuroscience

Received: *30 August 2018*
Accepted: *11 January 2019*
Published: *07 February 2019*

Citation:
Shapey J, Vos SB, Vercauteren T, Bradford R, Saeed SR, Bisdas S and Ourselin S (2019) Clinical Applications for Diffusion MRI and Tractography of Cranial Nerves Within the Posterior Fossa: A Systematic Review. Front. Neurosci. 13:23. doi: 10.3389/fnins.2019.00023

Objective: This paper presents a systematic review of diffusion MRI (dMRI) and tractography of cranial nerves within the posterior fossa. We assess the effectiveness of the diffusion imaging methods used and examine their clinical applications.

Methods: The Pubmed, Web of Science and EMBASE databases were searched from January 1st 1997 to December 11th 2017 to identify relevant publications. Any study reporting the use of diffusion imaging and/or tractography in patients with confirmed cranial nerve pathology was eligible for selection. Study quality was assessed using the Methodological Index for Non-Randomized Studies (MINORS) tool.

Results: We included 41 studies comprising 16 studies of patients with trigeminal neuralgia (TN), 22 studies of patients with a posterior fossa tumor and three studies of patients with other pathologies. Most acquisition protocols used single-shot echo planar imaging (88%) with a single b-value of 1,000 s/mm^2 (78%) but there was significant variation in the number of gradient directions, in-plane resolution, and slice thickness between studies. dMRI of the trigeminal nerve generated interpretable data in all cases. Analysis of diffusivity measurements found significantly lower fractional anisotropy (FA) values within the root entry zone of nerves affected by TN and FA values were significantly lower in patients with multiple sclerosis. Diffusivity values within the trigeminal nerve correlate with the effectiveness of surgical treatment and there is some evidence that pre-operative measurements may be predictive of treatment outcome. Fiber tractography was performed in 30 studies (73%). Most studies evaluating fiber tractography involved patients with a vestibular schwannoma (82%) and focused on generating tractography of the facial nerve to assist with surgical planning. Deterministic tractography using diffusion tensor imaging was performed in 93% of cases but the reported success rate and accuracy of generating fiber tracts from the acquired diffusion data varied considerably.

Conclusions: dMRI has the potential to inform our understanding of the microstructural changes that occur within the cranial nerves in various pathologies. Cranial nerve tractography is a promising technique but new avenues of using dMRI should be explored to optimize and improve its reliability.

Keywords: MRI—magnetic resonance imaging, diffusion MRI (dMRI), tractography, cranial nerves, brain tumors, trigeminal neuralgia (TN)

INTRODUCTION

Diffusion magnetic resonance imaging (dMRI) is a non-invasive magnetic resonance imaging (MRI) technique that is able to provide a quantitative assessment of a tissue's microstructure. dMRI is sensitive to the displacement of water subject to thermally driven Brownian motion and can reveal a tissue's orientational organization (Le Bihan et al., 2001; Basser and Jones, 2002; Jellison et al., 2004). Fiber tractography is a three-dimensional reconstruction of the dMRI data enabling visualization of neural tracts and the brain's connectivity (Mori and van Zijl, 2002; Parker and Alexander, 2005; Gong et al., 2009). Diffusion tensor imaging (DTI) was the initial model to describe the orientational information in dMRI data; it has become a well-established method for imaging the brain's white matter tracts and is now an essential tool in neuroimaging analysis and diagnosis (Assaf and Pasternak, 2008; Ciccarelli et al., 2008). White matter fiber tractography is routinely used in preoperative surgical planning (Nimsky et al., 2005; Yogarajah et al., 2009; Duncan et al., 2016) and may also be incorporated into the neuronavigation system to guide surgery intraoperatively (Coenen et al., 2001; Nimsky et al., 2005; Nowell et al., 2015).

More recently, there has been growing clinical interest in utilizing tractography of the cranial nerves in order to assist clinical diagnosis of various neurological pathologies and to inform the surgical planning of neurosurgical procedures such as brain tumor surgery. There are twelve sets of paired cranial nerves (CN I-XII) that typically relay information between the brain and regions of the head and neck and are numbered according to their rostral-caudal position when viewing the brain. The first two cranial nerves—the olfactory [CN I] and optic nerves [CN II] are both sensory nerves, composed of afferent fibers relaying smell and vision, respectively, entering the brain within the anterior and middle cranial fossae. The remaining ten cranial nerves (the oculomotor [CN III], trochlear [CN IV], trigeminal [CN V], abducens [CN VI], facial [CN VII], vestibulocochlear [CN VIII], glossopharyngeal [CN IX], vagus [CN X], spinal accessory [CN XI], and hypoglossal [CN XII]) emerge from the brainstem and course through the posterior fossa and fluid cisterns before exiting the skull (Matsuno et al., 1988). Diffusion MRI and tractography of the cranial nerves in this region is technically challenging due to the nerves' small size (typically 1–5 mm in maximal diameter) and their anatomical location within cerebrospinal fluid (CSF) and close to tissue-air and tissue-bone interfaces (**Figure 1**).

This paper provides a systematic review of the clinical applications of dMRI and tractography of the cranial nerves within the posterior fossa (CN III-XII). Its aim is to inform clinical readers who are unfamiliar with this imaging modality of the technique's clinical potential, but technical readers with an interest in diffusion imaging form a secondary readership. To aid the reader's understanding, we begin with a brief summary of the biological and physical basis of diffusion MRI and tractography. This is followed by a critical summary and appraisal of different imaging techniques employed that will be of interest to both clinical and technical readers. Finally, we review the effectiveness of these advanced imaging techniques in the context of cranial nerve imaging, examining the various clinical applications for this emerging technology.

BASIC PRINCIPLES OF DIFFUSION IMAGING AND TRACTOGRAPHY

Diffusion MRI

Diffusion-weighted MRI creates image contrast based on the relative diffusion of water molecules in tissue. In water, water molecules are able to diffuse freely, and diffusion is equal in all directions (termed *isotropic* diffusion). However, the diffusion of water molecules inside organic tissues is often *anisotropic* (Tanner, 1979) as a result of a tissue's cellular microstructure. In white matter tracts and cranial nerves, diffusion is primarily restricted by axonal membranes, and myelin sheaths causing restricted diffusion perpendicular to the length of the axon with the direction of maximum diffusivity being parallel to the axonal orientation (Moseley et al., 1990).

To sensitize the MRI signal to diffusion, a diffusion-weighting magnetic gradient is applied along a certain axis. Acquiring multiple dMRI images with different diffusion-weighting magnetic gradient orientations can then provide information on the orientation of maximum diffusion. Information concerning the tissue's anisotropy was first described within the *diffusion tensor* framework, which is an abstract mathematical model of diffusion in three-dimensional space (Basser et al., 1994). The tensor model consists of a 3×3 matrix derived from diffusivity measurements in at least six non-collinear directions. The diagonal elements (D_{xx}, D_{yy}, D_{zz}) of the tensor represent the diffusion coefficients measured in a frame of reference along each of the principal (x-, y-, and z-) directions. The off-diagonal terms reflect correlation between each pair of principal directions. Conceptually, a diffusion tensor may be visualized as an ellipsoid where the principal major axis is orientated in the direction of maximum diffusivity (Basser et al., 1994). The ellipsoid is characterized by three orthogonal *eigenvectors* (ε_1, ε_2, and ε_3) and its shape determined by three *eigenvalues* (λ_1, λ_2, and

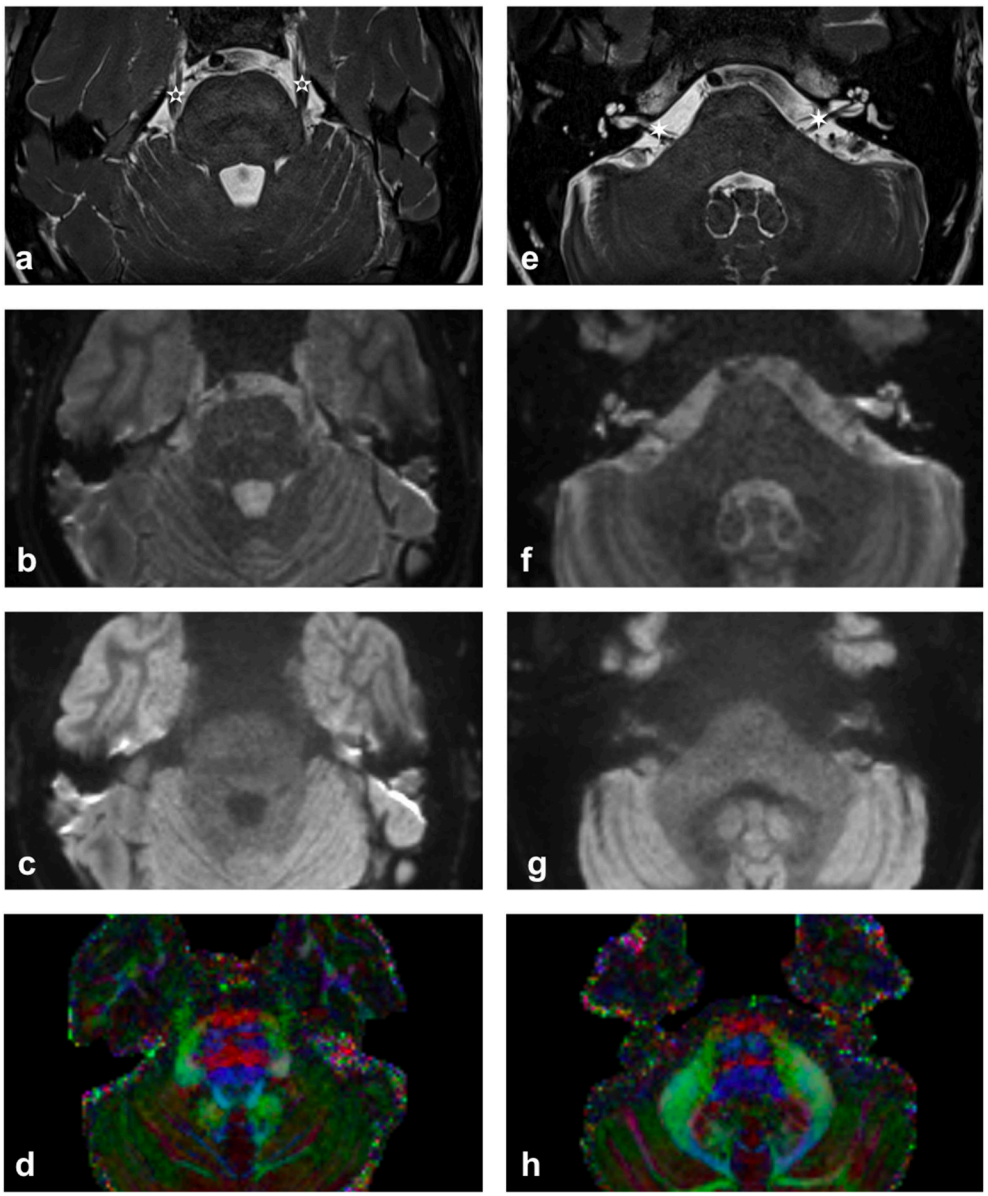

FIGURE 1 | Imaging of upper **(a–d)** and lower **(e–h)** pons. **(a,e)** High contrast T2-weighted images illustrating the trigeminal nerve (white 5-pointed star) and the facial and vestibulocochlear nerves (white 6-pointed star). [acquired with a ZOOMit sequence and a 0.5 × 0.5 × 0.5 mm voxel size]. **(b,f)** mean b0 diffusion weighted image. **(c,g)** mean b1000 diffusion weighted image. **(d,h)** Diffusion-encoded-color map. Note the green anterior trigeminal projections from the brainstem in **(d)** and the red right-left projections of the CN VII/VIII complex in **(h)** [more pronounced on the subject's right-hand side].

λ_3). The eigenvectors represent the major, medium, and minor principal axes of the ellipsoid and the eigenvalues represent the diffusivities in these three directions, respectively (Mori et al., 1999; Basser et al., 2000).

Specific quantitative diffusivity metrics may be calculated from the tensor including axial (AD), radial (RD), and mean diffusivities (MD), as well as a composite metric, fractional anisotropy (FA). The local fiber orientation may also be visualized in a directionally-encoded color (DEC) map of the diffusion tensor that is based on the orientation of the diffusion tensor's first eigenvector (ε_1). These maps are generated by mapping the major eigenvector's directional components in the x-, y-, and z-planes into RGB color channels and weighting the color brightness by FA.

Fractional anisotropy (FA) is a measure of the coherence of the underlying microstructure and has been shown to correlate both with axonal counts (Schmierer et al., 2007; Gouw et al., 2008) and myelin content (Schmierer et al., 2007). Mean diffusivity (MD) detects the overall diffusion coefficient and is an index proportional to free water and a sensitive marker of inflammation

(Werring et al., 1999; Beaulieu, 2002). Another measure of average diffusion is the Apparent Diffusion Coefficient (ADC); the difference being that the ADC is usually derived from the DWI data directly while MD is derived from the tensor fitting on the DWI data. However, as evidenced by the studies included in this review, this terminology is not always strictly followed. Axial diffusivity (AD) indicates diffusion along the main axis of the ellipsoid and radial diffusivity (RD) is a measure of diffusion along the other two orthogonal directions. Animal studies have shown that the AD and RD are good predictors of axonal loss and demyelination, respectively (Song et al., 2002, 2003; Budde et al., 2007) and these have been used as surrogate *in vivo* markers to illustrate axonal integrity (AD) and myelin damage (RD) (Concha et al., 2006; Kraus et al., 2007; Naismith et al., 2009). Despite a high sensitivity to microstructural changes, these quantitative metrics are also affected by factors not incorporated in the diffusion tensor model; such as crossing fibers and other complex fiber architecture, or partial voluming—reducing their specificity (Alexander et al., 2001; Vos et al., 2011, 2012). For a more detailed introduction to DTI and other advanced diffusion methods, readers are referred to a review by Tournier et al. (2011).

Tractography

The brain's white matter tracts are composed of bundles of axons that share a similar destination and may be delineated using tractography or fiber-tracking algorithms (Parker and Alexander, 2005; Assaf and Pasternak, 2008; Ciccarelli et al., 2008; Gong et al., 2009). Similarly, peripheral nerves are comprised of axons that connect the central nervous system to an end organ. As diffusion imaging and tractography methods have advanced, this technique has been applied to reconstruct ever smaller white matter structures including the cranial nerves.

Tractography uses the voxel-wise information provided by diffusion MRI to infer connections between adjacent voxels that may belong to the same tract to reconstruct the white matter architecture in 3D (Mori and van Zijl, 2002; Lazar et al., 2003). The commonest type of tractography algorithm, *deterministic* tractography, delineates white matter pathways by using an in-line propagation technique whereby data within each voxel directs the tracts subsequent extension. Deterministic tractography is reliant upon three elements: the identification of a suitable starting position to initiate the algorithm (the seed point); continued propagation of the track along the estimated fiber orientation; and the termination of the track when appropriate criteria are met (Mori and van Zijl, 2002; Tournier et al., 2011). Selecting an appropriate seed point is typically performed by the operator but other methods such as selecting the seed point based on functional MR data exist (Tournier et al., 2011). Deterministic DTI tracking uses the first eigenvector of the diffusion tensor to provide a suitable estimate of the fiber orientation within each voxel and then propagates the track according to a fixed user-specified step-size. The most common way of terminating a track is to set a threshold based on a measure of diffusion anisotropy (typically FA) such that if the anisotropy falls below a certain value (e.g., FA < 0.2), the track is not allowed to propagate any further.

Probabilistic tractography aims to address the problem of uncertainty of directional information by creating multiple streamlines from a selected distribution of possible fiber orientations with the results presented in the form of a probability distribution, rather than a single "best fit" (Behrens et al., 2007; Tournier et al., 2011). Most probabilistic methods are based on the same underlying model as their deterministic counterparts and so are affected by the same limitations; however, they are able to provide an estimate of the "precision" with which a tract has been reconstructed (Tournier et al., 2011). Several studies examining large matter tracts have demonstrated advantages of using probabilistic tracking over standard deterministic tracking (Farquharson et al., 2013; Li et al., 2013; Lilja et al., 2014; Mandelli et al., 2014) and Rueckriegel et al. recently described the benefits of probabilistic tracking to depict the auditory pathway in cases of vestibular schwannoma (Rueckriegel et al., 2016).

METHODS

The Preferred Reporting Items for Systematic Reviews and Meta-Analyses (PRISMA) Statement was used in the preparation of this manuscript (Moher et al., 2009) and the study was registered with PROSPERO: an international prospective register of systematic reviews (CRD117068).

A structured search of the Pubmed, Web of Science and EMBASE databases was undertaken over a 20-year period. The last date of the search was December 11th, 2017. Two independent researchers applied the search criteria using the Boolean search terms:

1 (diffusion tensor imaging OR diffusion MRI OR diffusion tensor tracking OR tractography OR fiber tracking OR fiber tracking)

AND

2 (oculomotor nerve OR trochlear nerve OR trigeminal nerve OR abducens nerve OR facial nerve OR vestibular nerve OR vestibulocochlear nerve OR cochlear nerve OR vestibulocochlear complex OR facial-vestibulocochlear complex OR glossopharyngeal nerve OR vagus nerve OR accessory nerve OR hypoglossal nerve OR cranial nerve)

Reference lists of included articles were also reviewed, and expert opinion sought, to identify further eligible publications.

Eligibility for inclusion in the systematic review included peer-reviewed publications in which English-language manuscripts were available through electronic indexing comprising:

1. Clinical studies of patients with associated cranial nerve pathology.
2. Diffusion MRI and/or fiber tractography of lower cranial nerve(s) has been performed.
3. The diffusion imaging technique used has been described.
4. The imaging success rate is reported.

Full articles were obtained and further assessed for eligibility and any discrepancy was resolved through mutual review and involvement of the senior author.

In total, 805 articles were identified through the database searches and an additional record was identified through other sources. Following removal of duplicate and non-English language studies, 534 manuscript titles and abstracts were screened. After applying the eligibility criteria 48 full text articles were reviewed and a further 7 articles were excluded. In all, 41 studies satisfied the inclusion criteria and were included in further qualitative analysis (**Figure 2**).

Data extraction was performed using a table with a predefined set of criteria including:

1. Study design.
2. Study group characteristics, including the number of patients, duration of symptoms (in cases of trigeminal neuralgia), tumor characteristics (where applicable), and treatment modality.
3. Imaging acquisition details, including hardware, data specifics (including sequence(s), number of directions (number of signal averages), acquired voxel size, b-value(s), scan time), and software.
4. Diffusion processing methods, including region of interest, fiber tractography method (type [deterministic or probabilistic], number of ROI(s), Fractional anisotropy threshold.
5. Effectiveness of dMRI analysis, including success rate in generating tractography results and diffusivity measurements of the target cranial nerve(s). In surgical cases, the method and results of any intraoperative validation was also noted.
6. Key findings.

The methodological quality of the included studies was assessed by using the Methodological Index for Non-Randomized Studies (MINORS) scoring system for observational studies (Slim et al., 2003). Observational studies include comparative studies such as case-control and cohort designs, and patient series which may or may not involve comparisons between groups. All studies are scored on the following criteria: (1) A stated aim of the study; (2) Inclusion of consecutive patients; (3) Prospective collection of data; (4) Endpoint appropriate to the study aim; (5) Unbiased evaluation of endpoints; (6) Follow-up period appropriate to the major endpoint; (7) Loss to follow-up not exceeding 5%; (8) Prospective calculation of the study sample size. Comparative studies are also scored with respect to; (9) An adequate control group; (10) Contemporary groups; (11) Baseline equivalence of groups; (12) Adequate statistical analyses. Rating scores out of 16 and 24 for non-comparative and comparative studies, respectively, were generated by the lead author. Studies of greater quality, i.e., those with a higher MINORS score, were given greater weighting in the subsequent qualitative synthesis.

RESULTS

Forty-one studies satisfied the inclusion criteria and underwent qualitative analysis, including 20 case series, 15 non-randomized case-control studies, 4 cohort studies and 2 case reports. A maximum of 959 participants were included across all studies (ranging from 1 to 150 subjects per study), if multiple studies form a single institution did not include overlapping patient groups. Twenty-two studies focused on imaging the cranial nerves in relation to a posterior fossa tumor (Taoka et al., 2006; Chen et al., 2011; Gerganov et al., 2011; Roundy et al., 2012; Zhang et al., 2013, 2017; Choi et al., 2014; Ulrich et al., 2014; Wei et al., 2015, 2016; Yoshino et al., 2015a,b, 2016; Borkar et al., 2016; Hilly et al., 2016; Ma et al., 2016; Song et al., 2016; Behan et al., 2017; d'Almeida et al., 2017; Li et al., 2017; Zolal et al., 2017a,b), 16 studies imaged the trigeminal nerve in patients with trigeminal neuralgia (Herweh et al., 2007; Fujiwara et al., 2011; Leal et al., 2011; Lutz et al., 2011, 2016; Hodaie et al., 2012; Liu et al., 2013; Wilcox et al., 2013; DeSouza et al., 2014, 2015; Lummel et al., 2015; Chen, D. Q. et al., 2016; Chen, S. T. et al., 2016; Lin et al., 2016; Neetu et al., 2016; Hung et al., 2017) and the remaining 3 studies evaluated DTI and tractography of the cranial nerves in various other pathologies including the cochlear nerve in cases of unilateral deafness (Vos et al., 2015), and the trigeminal nerve in patients with herpetic keratouveitis (Rousseau et al., 2015) and short lasting unilateral neuralgiform headache attacks with conjunctival injection and tearing (SUNCT) (Coskun et al., 2017) (**Tables 1–3**).

Study Quality

The quality of the included studies was variable (**Tables 1–4**). In general, the prospective comparative studies evaluating DTI and tractography in patients with trigeminal neuralgia were of high methodological quality. The most common type of comparative study encountered here were case-control studies in which the non-affected side provided the control group to which the affected side was compared. Very few studies involving patients with posterior fossa tumors included consecutive patients or unbiased assessments of study endpoints but there were notable high-quality papers involving patients with posterior fossa tumors and these have been given higher weighting in our discussion (Taoka et al., 2006; Gerganov et al., 2011; Zhang et al., 2013, 2017; Yoshino et al., 2015b; Li et al., 2017; Zolal et al., 2017a). All four cohort studies compared different methods of acquiring tractography data in patients with posterior fossa tumors. One of the listed case reports illustrating the use of tractography in a patient with a petroclival meningioma was contained within a larger technical paper comparing DTI with a more advanced multi-fiber model (HDFT: high definition fiber tractography; Yoshino et al., 2016). However, this advanced method was only used in one illustrative case that satisfied this study's inclusion criteria so the article was listed as a case report and assessed using the MINORS scoring for non-comparative studies. None of the studies included in this review documented a prospective calculation of study size.

Image Acquisition and Processing

A variety of different MR scanners manufactured by Siemens, GE and Philips were used in the acquisition of the diffusion data. Thirty-seven studies (90%) were performed using 3T machines with the remaining 4 studies using 1.5T scanners. Most acquisition protocols used single-shot echo planar imaging (88%) with a single b-value of 1,000 s/mm^2 (78%) but the number of gradient directions, in-plane resolution, and slice

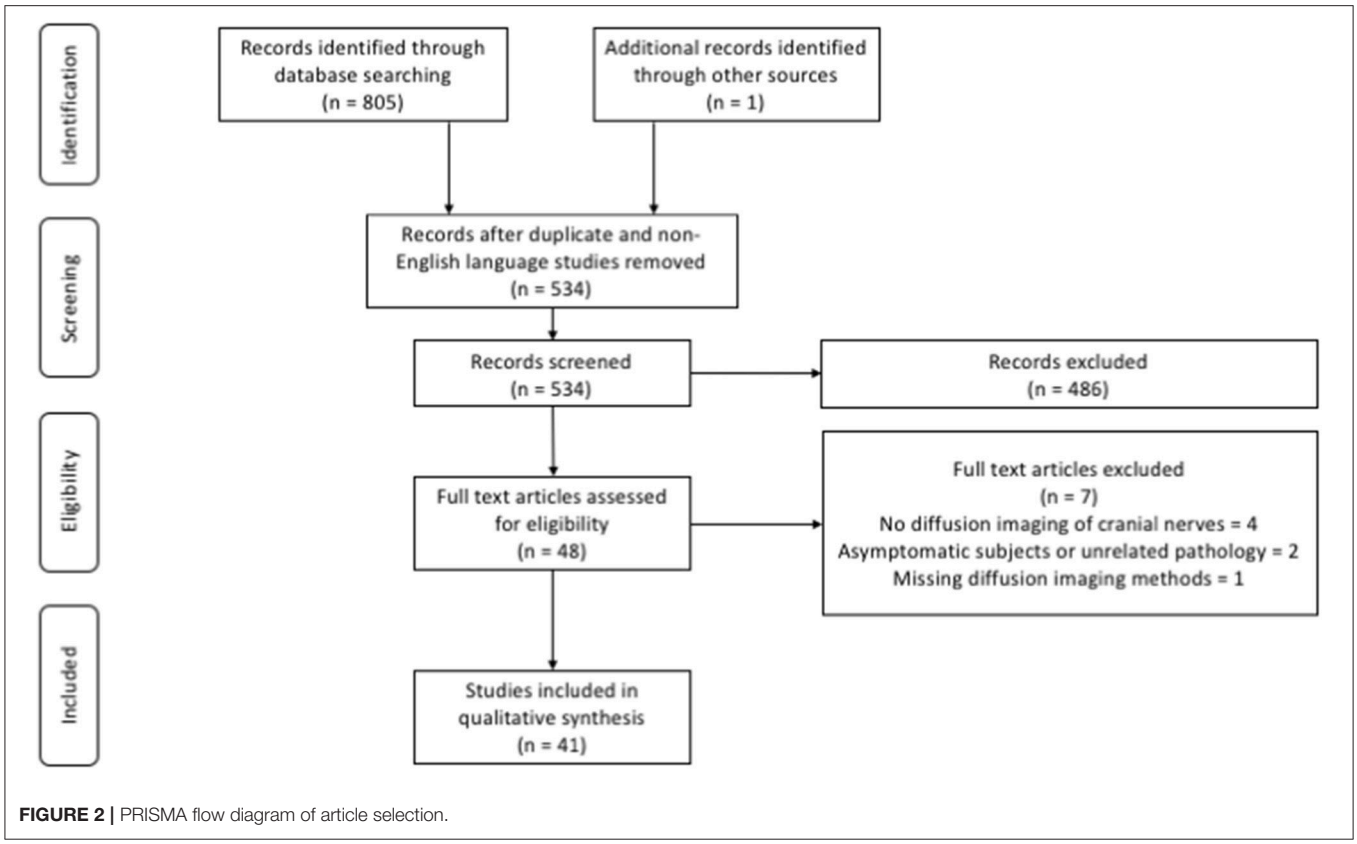

FIGURE 2 | PRISMA flow diagram of article selection.

thickness varied considerably (**Tables 1**–**3**). The acquisition time was documented in a minority of studies (39%); scan time varied greatly but was typically longer in studies that used multi-shot imaging acquisition (Chen, S. T. et al., 2016; Lutz et al., 2016). Various software packages were employed for the post-processing and tractography, including MatLab (The MathWorks, Inc., Natick, MA), dTV (http://www.medimg.info.hiroshima-cu.ac.jp/dTV.II.15g/about.htm) (Masutani et al., 2003), 3D Slicer (https://www.slicer.org) (Norton et al., 2017), DTI- and DSI-Studio (http://dsi-studio.labsolver.org) (Yeh et al., 2013), MedINRIA (https://med.inria.fr) (Toussaint et al., 2007), SPM8 (https://www.fil.ion.ucl.ac.uk/spm) (Friston, 2007), iPLAN (Brainlab iPlan, Heimstetten, Germany), trackvis (http://www.trackvis.org) (Wang et al., 2007), StealthViz (Medtronic Planning Station S7, Louisville, US), DynaSuite Neuro (*in vivo* Corp.; Gainesville, USA), FSL (http://www.fmrib.ox.ac.uk/fsl) (Jenkinson et al., 2012), TEEM toolkit (https://github.com/sinkpoint/hodaie-teem) (Qazi et al., 2009), ExploreDTI (www.exploredti.com) (Leemans et al., 2009) and MRtrix3 (http://www.mrtrix.org) (Tournier et al., 2012), in addition to the hardware manufacturer's own software suites including Leonardo syngo (Siemens), FuncTool (GE), and FiberTrak (Philips) software. All studies selected regions of interest manually and most did so by using fused anatomical and diffusion images (ROIs selected using fused anatomical/diffusion imaging: 51%, diffusion imaging alone: 17%, method not specified: 32%).

Analysis of Diffusivity Measurements

Analysis of diffusivity measurements focused on regions of the trigeminal nerve in all but one study. In the remaining study, diffusion metrics of the cochlea nerve were studied in patients with unilateral deafness, and compared to the patient's unaffected side and values in the nerves of healthy control subjects (Vos et al., 2015).

Analysis of the Trigeminal Nerve in Patients With Trigeminal Neuralgia (TN)

Sixteen non-randomized comparative studies evaluated the diffusion metrics of the trigeminal nerve in patients with trigeminal neuralgia (TN) (**Table 1**). Twelve studies included healthy volunteers as a control group (Herweh et al., 2007; Fujiwara et al., 2011; Leal et al., 2011; Liu et al., 2013; Wilcox et al., 2013; DeSouza et al., 2014, 2015; Lummel et al., 2015; Chen, D. Q. et al., 2016; Lin et al., 2016; Neetu et al., 2016; Hung et al., 2017) and 4 studies compared the patient's own affected and unaffected sides (Lutz et al., 2011, 2016; Hodaie et al., 2012; Chen, S. T. et al., 2016). Two studies also included analysis of trigeminal neuralgia in patients with Multiple Sclerosis (MS) (Lummel et al., 2015; Chen, D. Q. et al., 2016), two studies evaluated patients with non-neurovascular compression TN (n-NVC-TN) (Lin et al., 2016; Neetu et al., 2016) and one study included patients with painful trigeminal neuropathy and painful temporomandibular disorders (TMD) (Wilcox et al., 2013). Analysis of diffusivity measurements was possible in all cases. Ten studies compared

values in the root entry zone (REZ) (Herweh et al., 2007; Leal et al., 2011; Lutz et al., 2011, 2016; Liu et al., 2013; Wilcox et al., 2013; DeSouza et al., 2014; Lummel et al., 2015; Lin et al., 2016; Neetu et al., 2016), two studies focused on changes within the cisternal segment (Fujiwara et al., 2011; Chen, S. T. et al., 2016) and one study evaluated changes at both locations (Chen, D. Q. et al., 2016).

Fractional Anisotropy in TN

In the 10 studies that measured the FA in the REZ of patients with TN caused by neurovascular compression, 8 (80%) found significantly lower FA values on the affected side compared to the unaffected side (Leal et al., 2011; Lutz et al., 2011, 2016; Liu et al., 2013; DeSouza et al., 2014; Lummel et al., 2015; Chen, D. Q. et al., 2016; Neetu et al., 2016). The other two studies failed to demonstrate a statistical difference between sides (Herweh et al., 2007; Wilcox et al., 2013) but there was a trend toward lower FA values in TN-affected nerves (Herweh et al., 2007) in one of the studies. Only two studies examined diffusivity values in the cisternal segment of affected and unaffected nerves; one found no difference in FA values (Fujiwara et al., 2011) whereas the other found significantly higher FA values in the cisternal segment of affected nerves (Chen, D. Q. et al., 2016). Chen et al were also the only group to compare diffusivity values in the REZ and cisternal segment and found that TN-affected nerves appeared to have higher FA in the cisternal segment and lower FA in the REZ when compared to the patient's unaffected side (Chen, D. Q. et al., 2016).

Apparent Diffusion Coefficient and Mean Diffusivity in TN

Seven studies (44%) examined changes in ADC values within TN-affected nerves; four (57%) found ADC to be significantly higher in the REZ of affected nerves (Leal et al., 2011; Lummel et al., 2015; Chen, S. T. et al., 2016; Neetu et al., 2016) whereas the remaining three studies found no difference (Fujiwara et al., 2011; Lutz et al., 2011, 2016). Five studies (31%) examined changes in MD; four found significantly higher MD values in the REZ of idiopathic TN-affected nerves (Liu et al., 2013; DeSouza et al., 2014, 2015; Chen, D. Q. et al., 2016) and one found no statistical difference (Wilcox et al., 2013); however, two of the studies only demonstrated a statistically higher MD value when the REZ of affected nerves was compared to healthy controls with no statistical difference noted when compared to the unaffected side of patients with TN (DeSouza et al., 2014, 2015).

Radial and Axial Diffusivity in TN

Six studies (75%) reported RD and AD values in the affected and unaffected nerves of patients with idiopathic TN (Liu et al., 2013; DeSouza et al., 2014, 2015; Chen, D. Q. et al., 2016; Chen, S. T. et al., 2016; Lin et al., 2016) and a further two studies studied changes in these diffusivity metrics in patients following treatment (Hodaie et al., 2012; Hung et al., 2017). All five studies that examined changes in the REZ of TN-affected nerves reported significantly higher RD values in the REZ compared to the nerves of healthy controls (Liu et al., 2013; DeSouza et al., 2014, 2015; Chen, D. Q. et al., 2016; Lin et al., 2016) but significantly lower RD values were observed in the cisternal segments of affected nerves (Chen, D. Q. et al., 2016; Chen, S. T. et al., 2016). No significant differences were observed in the RD values of TN-affected nerves when compared to the unaffected side in two studies (DeSouza et al., 2014, 2015). Within the REZ it is likely that a change in RD is the main driver of a reduced FA which most likely represents a decrease in axonal integrity rather than a reduced alignment or coherence however further work is required to establish the nature of changes seen within the cisternal segment.

Fewer studies observed a statistically significant difference in AD values: three studies observed higher AD values in the REZ of TN-affected nerves when compared to the nerves of healthy controls and two studies observed no difference in AD values (Liu et al., 2013; Lin et al., 2016). There were no significant changes reported in AD when the REZ of affected nerves were compared to the unaffected side in patients with idiopathic TN but two studies demonstrated significantly higher AD values when TN-affected nerves were compared with the REZ of the nerves of healthy controls (DeSouza et al., 2014, 2015). One of these studies also analyzed changes in the cisternal segment of the nerve and demonstrated significantly lower AD values in the TN-affected nerves when compared to the unaffected side (Chen, D. Q. et al., 2016).

Diffusivity Changes in Patients With Multiple Sclerosis and TN

In patients with MS-associated TN, Lummel et al. found that FA was significantly lower and ADC higher in the REZ of both the TN-affected and unaffected sides when compared to unaffected side of patients with idiopathic TN or healthy controls (Lummel et al., 2015). Chen et al examined different diffusivity values in various nerve segments of patients with idiopathic and MS-associated TN (Chen, D. Q. et al., 2016). They demonstrated FA values were significantly lower in the peri-lesional segments of TN-affected nerves compared to the unaffected side of MS-associated TN patients and significantly lower than the nerves of patients with idiopathic TN and healthy controls. No significant differences were noted in other diffusivity values (MD, RD, or AD) within the peri-lesional segments of MS-associated TN nerves compared to the nerves of patients with idiopathic TN or healthy controls but AD and RD were shown to be significantly higher in the REZ of patients with both idiopathic and MS-associated TN (Chen, D. Q. et al., 2016).

Diffusivity Changes in Patients With TN Following Treatment

Five studies examined differences in the diffusion characteristics of patients' affected trigeminal nerves before and after treatment including microvascular decompression (MVD) (Fujiwara et al., 2011; DeSouza et al., 2015; Hung et al., 2017), Gamma Knife stereotactic radiosurgery (GK SRS) (Hodaie et al., 2012; DeSouza et al., 2015; Hung et al., 2017) and radiofrequency ablation (RFA) (Chen, S. T. et al., 2016). All four studies with diffusivity data from the REZ demonstrated lower FA values in the nerves of those patients who responded to treatment (Fujiwara et al., 2011; Hodaie et al., 2012; DeSouza et al., 2015; Hung

TABLE 1 | Diffusion imaging and tractography of the trigeminal nerve in trigeminal neuralgia.

References	Study design	MINORS	Participants				Hardware	Diffusion MRI data					Software	ROI	Fiber tractography method			Effectiveness & results		
			n	Cohorts	Median symptom duration (patients)	Treatment modality	Scanner	Seq.	Dir. (NSA)	Acq'd voxel size (mm)	b-value (s/mm^2)	Scan time	Software (Model)		Type	ROI	FA-t	Tract-ography success rate	dMRI success rate	Key findings
Herweh et al., 2007	Case-control	14/24	13 HC (*n* = 7)	NVC-TN (*n* = 6)	8y (2–15y) N/A	MVD N/A	1.5T Symphony, Siemens	Flair-EPI	6 (1)	2.5 × 2.5 × 3.0	1,000	2′41″	MatLab (DTI)	REZ M NS	N/A	N/A	N/A	N/A	13/13 (100%)	FA lower in TN-affected nerves vs. unaffected side in 3/6 (50%) of patients
Fujiwara et al., 2011	Case-control	22/24	27	NVC-TN (*n* = 13) HC (*n* = 14)	2y (3m–7y) N/A	MVD & GKRS (*n* = NS) N/A	3T Signa, GE	Single-shot EPI	6 (8)	1.6 × 1.6 × 1.2	1,000	8′30″	dTV (DTI)	CIS M Diff	D	1	0.1	27/27 (100%)	27/27 (100%)	No significant difference in FA or ADC values when TN-affected nerves compared with patients' unaffected side or vs. HC. Positive correlation & reduction in FA following MVD ($p < 0.01$) [$n = 3$]
Leal et al., 2011	Case-control	22/24	16	NVC-TN (*n* = 10) HC (*n* = 6)	5y (3.5–13y) N/A	MVD N/A	3T Achieva, Philips	Single-shot EPI	32 (1)	2.0 × 2.0 × 2.0	1,000	6′02″	MedINRIA (DTI)	REZ M Diff	N/A	N/A	N/A	N/A	16/16 (100%)	FA significantly lower in TN-affected nerves vs. unaffected side & vs. HC ($p < 0.05$). ADC significantly higher in TN-affected nerves vs. affected side & vs. control group ($p < 0.05$)
Lutz et al., 2011	Case-control	22/24	20	NVC-TN (*n* = 20)	4y (1–10y)	MVD	3T Signa, GE	Single-shot EPI	15 (10)	1.6 × 1.6 × 2.0	1,000	11′33	FuncTool (DTI)	REZ M An	N/A	N/A	N/A	N/A	20/20 (100%)	FA significantly lower in TN-affected nerves vs. unaffected side ($p = 0.004$). ADC values nearly identical in both groups
Hodaie et al., 2012	Case series	16/24	5	NVC-TN (*n* = 5)	NS	GKRS	3T Signa, GE	Single-shot EPI	25(1)	NS (ST: 3.0)	1,000	NS	3D Slicer (DTI)	CIS* M NS	D	2	0.2	5/5 (100%)	5/5 (100%)	Treatment with GKRS resulted in significant changes in FA & RD at the "target" ROI [A 47% decrease in FA values ($p = 0.027$) & a 55.8% increase in RD values ($p = 0.002$). No change in AD]
Liu et al., 2013	Case-control	18/24	22	NVC-TN (*n* = 16) HC (*n* = 6)	5y (2–12y) N/A	NS N/A	3T Trio, Siemens	Single-shot Flair-EPI	12 (1)	1.9 × 1.9 × 3.0	1,000	11′46″	Leonardo syngo 2003A (DTI)	REZ M Diff	N/A	N/A	N/A	N/A	22/22 (100%)	FA significantly lower in TN-affected nerves vs. unaffected side & vs. HC. No significant changes in AD. Trend toward significantly higher MD in TN-affected nerves vs. unaffected side
Wilcox et al., 2013	Case-control	16/24	73	NVC-TN (*n* = 9) Neur-opathy (*n* = 18) TMD (*n* = 20) HC (*n* = 26)	7y (2–35y) 3.5y (1.3–11y) 5.25y (1.5–30y) N/A	Meds only N/A	3T Achieva, Philips	Single-shot EPI	32 (4)	2.0 × 2.0 × 2.5	1,000	NS	SPM8 (DTI)	REZ M An	N/A	N/A	N/A	N/A	73/73 (100%)	No significant difference in FA or MD values. in TN-affected nerves vs. unaffected side. No change in DTI values observed in other pathologies.
DeSouza et al., 2014	Case-control	17/24	36	NVC-TN (*n* = 18) HC (*n* = 18)	NS N/A	NS N/A	3T Philips (Model NS)	Single-shot EPI	60 (1)	1.9 × 1.9 × 3.0	1,000	NS	FSL (DTI)	REZ M An	D	1	0.2	36/36 (100%)	36/36 (100%)	FA significantly lower in TN-affected nerves vs. unaffected side & vs. HC ($p < 0.05$). No significant difference in MD, RD or AD in TN-affected nerves vs. unaffected side. Higher MD, RD & AD found bilaterally in TN-patients vs. HC ($p < 0.05$)
DeSouza et al., 2015	Case-control	17/24	28	NVC-TN (*n* = 14) HC (*n* = 14)	5.5y (1–30y) N/A	MVD (*n* = 7) GKRS (*n* = 7) N/A	3T Signa, GE	Single-shot EPI	60 (1)	0.94 × 0.94 × 3.0	1,000	NS	FSL (DTI)	REZ M An	N/A	N/A	N/A	N/A	14/14 (100%)	FA significantly lower & MD, RD & AD significantly higher in TN-affected nerves vs. HC ($p < 0.05$). Effective treatment reversed FA, MD, RD & AD abnormalities & correlated with pain relief after treatment

(Continued)

TABLE 1 | Continued

References	Study design	MINORS	Participants				Hardware	Diffusion MRI data					Software	ROI	Fiber tractography method			Effectiveness & results		
			n	Cohorts	Median symptom duration (patients)	Treatment modality	Scanner	Seq.	Dir. (NSA)	Acq'd voxel size (mm)	b-value (s/mm^2)	Scan time	Software (Model)		Type	ROI	FA-t	Tract-ography success rate	dMRI success rate	Key findings
Lummel et al., 2015	Case-control	22/24	36	MS-TN (*n* = 12) NVC-TN (*n* = 12) HC (*n* = 12)	7 (0.5–11y) 5y (8m–11y) N/A	NS NS N/A	3T Signa, GE	Single-shot EPI	15 (10)	1.7 × 1.7 × 2.0	1,000	11′55″	FuncTool (DTI)	REZ M An	N/A	N/A	N/A	N/A	36/36 (100%)	In NVC-TN, FA significantly lower in TN-affected nerves vs. unaffected side ($p = 0.002$) & vs. HC ($p < 0.001$). ADC significantly higher on TN-affected side vs. unaffected side ($p = 0.007$) & vs. HC ($p = 0.005$). In MS-TN, DTI reveals microstructural changes on both the TN-affected and unaffected sides.
Chen, D. Q. et al., 2016	Case-control	16/24	30	MS-TN (*n* = 10) NVC-TN (*n* = 10) HC (*n* = 10)	NS	NS NS N/A	3T Signa, GE	Single-shot EPI	60 (1)	1.9 × 1.9 × 3.0	1,000	NS	3D Slicer (DTI)	CIS REZ Pons M An	D	1	0.2	SDT: "unsuccessful" MTT: "successful"	30/30 (100%)	Underlying TN-pathology alters the diffusivity pattern of different nerve segments. In NVC-TN, TN-affected nerves showed higher FA in the cisternal segment of & lower FA in the REZ segment vs. unaffected side & vs. controls ($p < 0.05$). In MS-TN, FA was lower in the peri-lesional segments of TN-affected nerves. No significant differences in MD, RD & AD noted.
Chen, S. T. et al., 2016	Case series	19/24	43	NVC-TN (*n* = 43)	5y	RFA	3T Verio, Siemens	Multi-shot EPI (5)	30 (1)	2.0 × 2.0 × 2.0	1,000	20′58″	DSI Studio (DTI)	CIS M An	N/A	N/A	N/A	N/A	43/43 (100%)	FA significantly lower ($p < 0.001$), ADC higher ($p = 0.006$) & RD lower ($p < 0.001$) in TN-affected nerves vs. unaffected side. No difference in AD. Trend toward FA reduction in effective treatment responders ($p = 0.072$)
Lin et al., 2016	Case-control	15/24	150	NVC-TN (*n* = 50) N-NVC-TN (n=50) HC (n=50)	NS	N/A	3T Signa, GE	Single-shot EPI	20 (1)	1.9 × 1.9 × 2.4	1000	5′12″	FuncTool (DTI)	REZ M NS	N/A	N/A	N/A	N/A	150/150 (100%)	RD significantly higher in TN-affected nerves vs. unaffected side ($p = 0.00$) & HC ($p = 0.00$). No difference in AD.
Lutz et al., 2016	Case series	20/24	81	NVC-TN (*n* = 81)	13y (5m–21y)	MVD	3T signa, GE	Single-shot EPI	NS (4)	1.7 × 1.7 × 2.0	NS	11′55″	FuncTool (DTI)	REZ M An	N/A	N/A	N/A	N/A	81/81 (100%)	FA significantly lower in TN-affected nerves vs. unaffected side ($p = 0.005$). No significant difference in ADC values ($p = 0.092$)
Neetu et al., 2016	Case-control	17/24	8	N-NVC-TN (*n* = 4) HC (*n* = 4)	5w N/A	None N/A	3T Signa, GE	Single-shot EPI	15 (1)	1.09 × 1.09 × 1.6	1000	NS	FuncTool (DTI)	REZ M An	N/A	N/A	N/A	N/A	8/8 (100%)	FA significantly lower ($p = 0.001$) & ADC higher ($p = 0.001$) in TN-affected nerves vs. unaffected side. & vs. HC.
Hung et al., 2017	Case-control	19/24	47	NVC-TN-R (*n* = 17) NVC-TN-NR (*n* = 14) HC (*n* = 16)	NS NS N/A	MVD (*n* = 10) GKRS (*n* = 21) N/A	3T Signa, GE	Single-shot EPI	60 (1)	1.9 × 1.9 × 3.0	1000	NS	3D Slicer (DTI)	CIS REZ Pons M NS	D	1	0.2	47/47 (100%)	47/47 (100%)	Treatment outcomes may be predicted by pre-surgical diffusivity alterations: Long-term responders have lower cisternal segment AD & MD values; Non-responders have abnormalities located more centrally with lower FA values in the REZ & higher AD values in the pontine segment

Seq., Sequence; Dir., Directions; NSA, Number of signal average; ROI, Region of Interest; NVC-TN, Neurovascular compression associated trigeminal neuralgia; MS-TN, Multiple Sclerosis associated trigeminal neuralgia; HC, Healthy control; N-NVC-TN, Non-neurovascular compression associated trigeminal neuralgia; N/A, Not applicable; NS, Not specified; MVD, Microvascular Decompression; GKRS, Gamma Knife Radiosurgery; EPI, Echo planar imaging; DTI, Diffusion Tensor Imaging; REZ, Root Entry Zone; CIS; Cisternal segment; M, manual placement of ROI; A, automated placement of ROI; An, ROI placed using anatomical image fused with diffusion data; Diff, ROI placed using diffusion data only; D, Deterministic; SDT, Single-tensor diffusion tractography; MTT, Multi-tensor tractography; FA-t: Fractional anisotropy threshold; FA, Fractional anisotropy; ADC, Apparent Diffusion Coefficient; MD, Mean diffusivity; RD, Radial diffusivity; AD, Axial diffusivity.

**Two distinct ROIs within the cisternal segment were analyzed including the radiosurgical target region and an ROI proximal to the root entry zone (but still within the cisternal segment of the nerve).*

TABLE 2 | Diffusion imaging and tractography of cranial nerves in other pathologies.

References	Study design	MINORS	Patients		Hardware	Diffusion MRI data				Software	Fiber tractography method				Effectiveness & results		
			n	Cohorts	Scanner	Seq.	Dir. (NSA)	Acq'd voxel size (mm)	b-value (s/mm^2)	Scan time	Software (model)	Type	ROI	FA-t	CNs	Tractography success rate	dMIR success rate	Key findings
Rousseau et al., 2015	Case-control	22/24	36	Herpetic Keratouveitis (*n* = 12) HC (*n* = 24)	1.5T Sonata, Siemens	Single-shot EPI	25 (3)	1.9 × 1.9 × 2.0	500	7′30″	MedINRIA (DTI)	D	CIS M Diff	0.2	V	36/36 (100%)	36/36 (100%)	FA significantly lower in REZ of trigeminal nerves on the ipsilateral side to the affected eye vs. unaffected side ($p = 0.03$)
Vos et al., 2015	Case-control	20/24	10	Unilateral deafness (*n* = 5) HC (*n* = 5)	3T Achieva, Philips	Single-shot EPI	22 (2)	1.8 × 1.8 × 1.8	1,000	7′49″	ExploreDTI (DTI)	D	Coch P-sag plane M An	NS	VIII	10/10 (100%)	10/10 (100%)	Significantly lower FA in Cochlea n. of both deaf side ($p = 0.030$) & healthy side ($p = 0.013$) in patients vs. HC. No statistical difference in FA or MD between deaf and healthy sides in patient group
Coskun et al., 2017	Case series	5/16	2	SUNCT Headache (*n* = 2)	3T Verio, Siemens	SIngle-shot EPI	30 (1)	1.8 × 1.8 × 4.0	1,000	NS	NEURO 3D (DTI)	D	CIS M Diff	NS	V	2/2 (100%)	2/2 (100%)	FA lower on affected side. ADC value higher on affected side 1 patient but no difference was observed in the other

Seq., Sequence; Dir., Directions; NSA, Number of signal average; Diff., Diffusion; ROI, Region of Interest; HC, Healthy control; SUNCT, Short-lasting unilateral neuralgiform headache with conjunctival injection and tearing (SUNCT syndrome) ; EPI, Echo planar imaging; D, Deterministic; DTI, Diffusion Tensor Imaging; REZ, Root Entry Zone; M, manual placement of ROI; A, automated placement of ROI; An, ROI placed using anatomical image fused with diffusion data; Diff, ROI placed using diffusion data only; FA-t, Fractional anisotropy threshold; CIS, Cisternal segment; Coch, Cochlea; P-sag plane, 10 voxels (18 mm) to left and right of mid-saggital plane; FA, Fractional anisotropy; ADC, Apparent Diffusion Coefficient; MD, Mean diffusivity.

TABLE 3 | Diffusion imaging and tractography of cranial nerves in patients with posterior fossa tumors.

References	Study design	MINORS	Patients				Hardware	Diffusion MRI data					Software	Fiber tractography method			CNs	Effectiveness & results			
			n	Path	Median tumor size	Median volume (mm^3)	Scanner	Seq.	Dir. (NSA)	Acq'd voxel size (mm)	b-value (s/mm^2)	Scan time	Software (model)	Type	ROI	FA-t	CNs	Tractography success rate	Intra-operative correlation method	Intra-operative accuracy rate	Prevention of facial nerve injury
Taoka et al., 2006	Case series	11/16	8	VS	25.5 mm (18–47 mm)	NS	1.5T Sonata, Siemens	Single-shot EPI	6 (6)	1.8 × 1.8 × 3.0	1,000	NS	dTV-II (DTI)	D	IAM M Diff	0.10	VII	7/8 (88%)	Inspection by surgeon & qualitative EP monitoring	5/7 (71%)	Not assessed
Chen et al., 2011	Case series	4/16	3	VS	NS (10–30 mm)	8,036.72	3T SIGNA HDx, GE	Single-shot EPI	25 (1)	NS (ST: 3.0)	1,000	NS	3D Slicer (DTI)	D	REZ/IC M NS	0.2	V, VII-VIII	3/3 (100%)	Not assessed	Not assessed	Not assessed
Gerganov et al., 2011	Case series	14/16	22	VS	26.0 mm (16–50 mm)	NS	3T Allegra, Siemens	Single-shot EPI	12 (1)	NS ST: 1.6	1,000	NS	iPLAN (DTI)	D	IAM REZ M An	0.10	VII	22/22 (100%)	Inspection by surgeon & qualitative EP monitoring	20/22 (91%)	Not assessed. Facial nerve function 2 weeks after surgery: HB I-II: 14/22 (64%), HB III+: 8/22 (36%)
Roundy et al., 2012	Cohort	17/24	5	VS (*n = 2*) NS (*n = 3*)	35.0 mm (25–52 mm)	NS	3T Philips	Single-shot EPI	S-DTI: 6 (1)	1.8 × 1.8 × 4	1,000	42″	Track Vis (DTI) Philips Software (DTI)	D	Tum M An	0.15	VII	S-DTI: 0/5 (0%)	Inspection by surgeon & qualitative EP monitoring	S-DTI: N/A	Not assessed
									HD-DTI: 32 (2)	1.6 × 1.6 × 1.2	1,000	9′39″						HD DTI 5/5 (100%)		HD DTI: 5/5 (100%)	
Zhang et al., 2013	Case series	12/16	8	VS	38.1 mm (30-55mm)	NS	3T Verio, Siemens	Single-shot EPI	NS (1)	1.8 × 1.8 × 3.0	1,000	NS	NS	D	IAM BS M NS	0.10	VII	7/8 (87.5%)	Inspection by surgeon & qualitative EP monitoring	7/7 (100%)	Not assessed. Facial nerve function 9-12 months after surgery: HB I-II: 8/8 (100%)
Choi et al., 2014	Case series	10/16	11	VS	22.0 mm (18–38 mm)	NS	1.5T Gyroscan Intera, Philips	Single-shot EPI	32 (1)	2.5 × 2.5 × 2.5	1,000	NS	DTI-studio (DTI)	D	IAM REZ M NS	V	VII	11/11 (100%)	Inspection by surgeon & qualitative EP monitoring	11/11 (100%)	Not assessed. Facial nerve function 12 months after surgery: HB I-II: 9/11 (82%), HB III+: 2/11 (18%)
Ulrich et al., 2014	Case series	6/16	7	BC	NS		3T Achieva, Philips	Single-shot EPI	15 (2)	2.1 × 2.1 × 2.1	1,000	5′00″	Philips Software (DTI)	D	NS	NS	V,-VII	7/7 (100%)	Not assessed	Not assessed	Not assessed
Wei et al., 2015	Case series	12/16	23	VS	34.0 mm (16–50 mm)	NS	3T Trio, Siemems	Single-shot EPI	30 (1)	NS (ST: 2.0)	NS	NS	iPlan (DTI)	D	IAM MC M An	V	V-VII	23/23(100%)	Inspection by surgeon & qualitative EP monitoring	21/23 (91%)	Not assessed. Facial nerve function 6 months after surgery: HB I-II: 16/23 (70%), HB III+: 7/23 (30%)
Yoshino et al., 2015a	Case series	7/16	11	VS	28.8 mm (20–40 mm)	NS	3T Signa, GE	Single-shot EPI	30 (1)	2.0 × 2.0 × 2.5	1,000	NS	dTV-II SR (DTI)	D	IAM M Diff	V	VII, VIII	10/11 (82%)	Inspection by surgeon & qualitative EP monitoring	3/10 (30%)	Not assessed. Facial nerve function after surgery (no date specified): HB I-II: 11/11 (100%)
Yoshino et al., 2015b	Cohort	16/24	22	VS	28.7 mm (9–52 mm)	NS	3T Signa, GE	Single-shot EPI	30 (1)	2.0 × 2.0 × 2.5	1,000	NS	dTV-II SR (DTI)	D	IAM M NS	V	VII, VIII	Standard DTI: 18/22 (82%) DTT-CE-FIESTA: 21/22 (95%)	Inspection by surgeon & qualitative EP monitoring	Standard DTI: 3/18 (17%) DTT-CE-FIESTA: 14/21 (67%)	Not assessed. Facial nerve function after surgery (no date specified): HB I-II: 21/22 (95%), HB III+: 1/22 (5%)

(Continued)

TABLE 3 | Continued

References	Study design	MINORS	Patients				Hardware	Diffusion MRI data					Software	Fiber tractography method			CNs	Effectiveness & results			
			n	Path	Median tumor size	Median volume (mm^3)	Scanner	Seq.	Dir. (NSA)	Acq'd voxel size (mm)	b-value (s/mm^2)	Scan time	Software (model)	Type	ROI	FA-t	CNs	Tractography success rate	Intra-operative correlation method	Intra-operative accuracy rate	Prevention of facial nerve injury
Borkar et al., 2016	Case series	8/16	20	VS	44.0 mm (30–61 mm)*	NS	3T Achieva, Philips	Single-shot EPI	15 (3)	0.78 × 0.78 × 1.5	800	NS	Dyna-Suite Neuro 3.0 (DTI)	D	IAM REZ M An	0.12	VII	19/20 (95%)	Inspection by surgeon	16/18 (89%) [the facial nerve was not identified intraoperatively in 1 patient]	Not assessed
Hilly et al., 2016	Case series	7/16	21	VS	44.0 mm (30–61 mm)	NS	3T Achieva, Philips	Single-shot EPI	32 (1)	2.0 × 2.0 × 2.0	NS	NS	FiberTrak (DTI)	D	NS	0.10	VII	20/21 (95%)	Inspection by surgeon	Initial results: 15/20 (75%) Discordant results "re-evaluated" and revised agreement reported: 19/20 (95%)	Not assessed
Wei et al., 2016	Case series	7/16	3	TS	43.0 mm (18–61 mm)	NS	3T Trio, Siemens	Single-shot EPI	30 (1)	NS (ST: 2.0)	NS	NS	iPLAN (DTI)	D	IAM/MC BS M An	NS	V-VIII	12/12 CNs (100%)	Inspection by surgeon & qualitative EP monitoring (CN VII & VIII)	11/12 CNs (92%)	Not assessed. Normal facial function & improved hearing documented in 1 patient at 12 months FU.
Yoshino et al., 2016	Case report	10/16	1	PM	30.0 mm		3T Trio, Siemens	Single-shot EPI	101 (1)	2.4 × 2.4 × 2.4	x12 b-values (max 5,000)	15′00″	DSI-studio (DSI)	D	NS	V	III-VI	CN III-VI (100%)	Inspection by surgeon	1/1 (100%)	Not assessed
Ma et al., 2016	Case series	11/16	12	VS ($n = 9$) M ($n = 3$)	40.0 mm (31–46 mm)	NS	3T GE	Single-shot EPI	32 (1)	1.6 × 1.6 × 2.0	1,000	NS	3D Slicer (DTI)	D	NS M An	0.18	IV-VIII	11/12 (92%)	Inspection by surgeon & qualitative EP monitoring	11/11 (100%)	Not assessed
Song et al., 2016	Case series	10/16	15	VS	35.0 mm (15–45 mm)	NS	3T Discovery 750, GE	Single-shot EPI	30 (2)	1.6 × 1.6 × 1.2	1,000	9′00″	3D Slicer (DTI)	D	IAM REZ M An	0.10	VII	14/15 (93%)	Inspection by surgeon & qualitative EP monitoring	13/14 (93%)	Not assessed
d'Almeida et al., 2017	Case report	4/16	1	PM	NS		1.5T Avanto, Siemens	Single-shot EPI	6 (4)	1.8 × 1.8 × 5.0	1,000	NS	dTV-II (DTI)	D	NS	NS	VII	1/1 (100%)	Inspection by surgeon & qualitative EP monitoring	1/1 (100%)	Not assessed
Zhang et al., 2017	Case series	14/16	30	VS	33.3 mm (20–54 mm)	NS	3T Discovery 750, GE	Single-shot EPI	64 (1)	NS (ST: 2.0)	1,000	NS	iPlan (DTI)	D	IAM REZ M An	V	VII	30/30 (100%)	Inspection by surgeon & qualitative EP monitoring	29/30 (97%)	Not assessed. Facial nerve function 2 weeks after surgery: HB I-II: 21/30 (70%), HB III+: 9/30 (30%)
Zolal et al., 2017a	Cohort	16/24	3	VS ($n = 2$) M ($n = 1$)	NS	NS	3T Verio, Siemens	Multi-shot EPI (NS)	20 (1)	2.0 × 2.0 × 2.0	800	12′00″	D: DSI-Studio (DSI) P:FSL (DTI)	D P	RG/ IAMBS M An	V V	V, VII, VIII	3/3 (100%) 3/3 (100%)	Inspection by surgeon	1/3 (30%) 3/3 (100%)	Not assessed

(Continued)

TABLE 3 | Continued

References	Study design	MINORS	Patients				Hardware	Diffusion MRI data					Software	Fiber tractography method			CNs	Effectiveness & results			
			n	Path	Median tumor size	Median volume (mm^3)	Scanner	Seq.	Dir. (NSA)	Acq'd voxel size (mm)	b-value (s/mm^2)	Scan time	Software (model)	Type	ROI	FA-t	CNs	Tractography success rate		Intra-operative correlation method	Intra-operative accuracy rate	Prevention of facial nerve injury
Zolal et al., 2017b	Case series	11/16	21	VS	NS	3,326.8	3T Verio, Siemens	Multi-shot EPI (NS)	20 (1)	NS (ST: 2.0)	800	NS	FSL (DTI)	P	IAM BS-C M An	V	VII, VIII	21/21 (100%) One pathway: 7/21 Two pathways: 14/21		Inspection by surgeon & qualitative EP monitoring	17/21 (81%)	Not assessed. Facial nerve function 8 days after surgery: HB I-II: 16/21 (76%%), HB III+: 5/21 (24%)
Li et al., 2017	Case series	14/16	19	VS	39.8 mm (25–53 mm)	NS	3T Trio, Siemens	Single-shot EPI	32 (1)	1.8 × 1.8 × 1.0	1,000	NS	StealthViz (DTI)	D	IAM REZ M NS	V	VII	18/19 (95%)		Inspection by surgeon & quantitative EP stimulation recorded with integrated neuro-navigation	17/18 (94%)	Not assessed. Facial nerve function 12 months after surgery: HB I-II: 18/19 (95%), HB III+: 1/19 (5%)
Behan et al., 2017	Cohort	14/24	10	VS ($n = 6$) M ($n = 3$) TS ($n = 1$)	19.5 mm (11.5–29.0 mm)	1,285.8	3T Signa HDx, GE	Single-shot EPI	60 (1)	1.9 × 1.9 × 3.0	1,000	17′30″	3D Slicer (DTI) XST: TEEM (DTI) MRtrix3 (CSD)	D	RG IC M An	0.15	V, VII, VIII	CN V 4/4 (100%) 4/4 (100%) 4/4 (100%)	CN VII/VIII 5/6 (83%) 6/6 (100%) 6/6 (100%)	Not assessed	Not assessed	Not assessed

Path., Pathology; Seq., Sequence; Dir., Directions; NSA, Number of signal average; Diff., Diffusion; ROI, Region of Interest VS, Vestibular schwannoma; NS, Not specified; ST, Slice thickness; EPI, Echo planar imaging; NSA, Number of signal average; DTI, Diffusion Tensor Imaging; DSI, Diffusion spectrum imaging; D, Deterministic; P, Probabilistic CSD, Constrained spherical deconvolution; ROI, Region of Interest; M, manual placement of ROI; A, automated placement of ROI; An, ROI placed using anatomical image fused with diffusion data; Diff, ROI placed using diffusion data only; IAM, Internal Auditory Meatus; Tum, ROI drawn through mid-saggital plane through tumor in a midcisternal location; MC, Meckel's cave; REZ, Root entry zone; RG, retrogasserian ganglion; IC, intracanalicular ROI; BS, Brainstem surface; BS-C, Brainstem surface corresponding to position of facial/cochlear nerve of the other side; FA-t, Fractional anisotropy threshold; V, Variable; HD, High definition; EP, Electrophysiolgogy; HB, House-Brackmann facial nerve grading scale (I-VI); FU, Follow-up.

TABLE 4 | Quality of studies using MINORS criteria.

References	Clear aim	Consecutive patients	Prospective data	Appropriate end points	Unbiased assessment of study endpoints	Appropriate follow up period	Loss to follow up <5%	Prospective calculation of study size	Adequate control group	Contemporary groups	Baseline equivalence of groups	Adequate statistical analysis	TOTAL
TRIGEMINAL NEURALGIA													
Herweh et al., 2007	2	0	0	2	0	2	1	0	2	2	2	1	14/24
Fujiwara et al., 2011	2	2	2	2	2	2	2	0	2	2	2	2	22/24
Leal et al., 2011	2	2	2	2	2	2	2	0	2	2	2	2	22/24
Lutz et al., 2011	2	2	2	2	2	2	2	0	2	2	2	2	22/24
Hodaie et al., 2012	2	1	1	2	0	1	2	0	2	2	2	1	16/24
Liu et al., 2013	2	0	0	2	2	2	2	0	2	2	2	2	18/24
Wilcox et al., 2013	2	0	0	2	0	2	2	0	2	2	2	2	16/24
DeSouza et al., 2014	2	0	1	2	0	2	2	0	2	2	2	2	17/24
DeSouza et al., 2015	2	0	1	2	0	2	2	0	2	2	2	2	17/24
Lummel et al., 2015	2	2	2	2	2	2	2	0	2	2	2	2	22/24
Chen, D. Q. et al., 2016	2	0	0	2	0	2	2	0	2	2	2	2	16/24
Chen, S. T. et al., 2016	2	0	2	2	2	1	2	0	2	2	2	2	19/24
Lin et al., 2016	2	0	0	2	0	1	2	0	2	2	2	2	15/24
Lutz et al., 2016	2	0	2	2	2	2	2	0	2	2	2	2	20/24
Neetu et al., 2016	2	0	1	2	0	2	2	0	2	2	2	2	17/24
Hung et al., 2017	2	0	1	2	2	2	2	0	2	2	2	2	19/24
OTHER													
Rousseau et al., 2015	2	2	2	2	2	2	2	0	2	2	2	2	22/24
Vos et al., 2015	2	0	0	2	2	2	2	0	2	2	2	2	20/24
Coskun et al., 2017	2	0	0	0	0	1	2	0	N/A	N/A	N/A	N/A	5/16
POSTERIOR FOSSA TUMORS													
Taoka et al., 2006	2	0	2	2	1	2	2	0	N/A	N/A	N/A	N/A	11/16
Chen et al., 2011	2	0	2	0	0	0	0	0	N/A	N/A	N/A	N/A	4/16
Gerganov et al., 2011	2	2	2	2	2	2	2	0	N/A	N/A	N/A	N/A	14/16
Roundy et al., 2012	2	0	2	2	1	2	2	0	2	2	2	0	17/24
Zhang et al., 2013	2	2	1	2	1	2	2	0	N/A	N/A	N/A	N/A	12/16
Choi et al., 2014	2	0	2	2	0	2	2	0	N/A	N/A	N/A	N/A	10/16
Wei et al., 2015	2	2	2	2	0	2	2	0	N/A	N/A	N/A	N/A	12/16
Yoshino et al., 2015a	2	0	0	2	1	0	2	0	N/A	N/A	N/A	N/A	7/16
Yoshino et al., 2015b	2	0	0	2	2	0	2	0	2	2	2	2	16/24

(Continued)

TABLE 4 | Continued

References	Clear aim	Consecutive patients	Prospective data	Appropriate end points	Unbiased assessment of study endpoints	Appropriate follow up period	Loss to follow up <5%	Prospective calculation of study size	Adequate control group	Contemporary groups	Baseline equivalence of groups	Adequate statistical analysis	TOTAL
Borkar et al., 2016	2	0	0	2	2	0	2	0	N/A	N/A	N/A	N/A	8/16
Hilly et al., 2016	2	0	0	2	1	0	2	0	N/A	N/A	N/A	N/A	7/16
Wei et al., 2016	2	0	0	2	0	1	2	0	N/A	N/A	N/A	N/A	7/16
Yoshino et al., 2016	2	0	2	2	0	2	2	0	N/A	N/A	N/A	N/A	10/16
Ma et al., 2016	2	0	2	2	1	2	2	0	N/A	N/A	N/A	N/A	11/16
Song et al., 2016	2	0	0	2	2	2	2	0	N/A	N/A	N/A	N/A	10/16
d'Almeida et al., 2017	2	0	0	0	0	0	2	0	N/A	N/A	N/A	N/A	4/16
Ulrich et al., 2014	2	0	1	0	0	1	2	0	N/A	N/A	N/A	N/A	6/16
Zhang et al., 2017	2	2	2	2	2	2	2	0	N/A	N/A	N/A	N/A	14/16
Zolal et al., 2017a	2	0	0	2	0	2	2	0	2	2	2	2	16/24
Zolal et al., 2017b	2	0	2	2	1	2	2	0	N/A	N/A	N/A	N/A	11/16
Li et al., 2017	2	2	2	2	2	2	2	0	N/A	N/A	N/A	N/A	14/16
Behan et al., 2017	2	0	0	2	0	2	2	0	2	2	2	0	14/24

et al., 2017) with a trend toward FA reduction demonstrated in the cisternal segment following effective treatment (Chen, S. T. et al., 2016). Effective treatment also appears to reduce other diffusivity changes seen in TN-affected nerves (Hodaie et al., 2012; DeSouza et al., 2015). Most recently, Hung et al demonstrated that treatment outcomes may be predicted by alterations in pre-surgical diffusivity measurements with long-term treatment responders having lower cisternal AD and MD values and non-responders having lower FA values in the REZ and higher AD values in the pontine segment (Hung et al., 2017).

Analysis of the Trigeminal Nerve in Other Pathologies

Rousseau et al. examined the potential impact of recurrent HSV and VSV keratitis on the axonal architecture of trigeminal nerves by assessing changes in the diffusivity metrics of patients' trigeminal nerves (Rousseau et al., 2015). They discovered FA to be significantly lower in the REZ of trigeminal nerves on the ipsilateral side to the affected event and demonstrated that the asymmetry was more than the intra-individual variability in controls (Rousseau et al., 2015). No such significant differences were observed in ADC values.

Coskun et al. reported diffusivity analysis in 2 patients with SUNCT, again demonstrating FA to be lower on the affected side (Coskun et al., 2017). ADC values were higher in the affected side in one patient with no difference observed in the other (Coskun et al., 2017).

Analysis of the Cochlear Nerve

Vos et al. assessed diffusivity changes in the cochlear nerves of patients with profound unilateral sensorineural hearing loss (Vos et al., 2015). Here, the authors assumed any changes in DTI metrics of the vestibulocochlear nerve would reflect changes in the cochlear nerve as it is the largest nerve and no changes are expected in the facial or vestibular nerves in unilateral deafness. They reported no significant difference in diffusivity values between patients' deaf-sided and healthy-sided cochlear nerves but there was a small but significant reduction in FA values in both cochlear nerves in patients compared with normal-hearing controls (Vos et al., 2015).

Fiber Tractography

Fiber tractography of one or more cranial nerves was performed in 30 studies (73%). All 22 studies involving patients with brain tumors focused on generating tractography of the surrounding cranial nerves. Eighteen of those (82%) involved patients with a vestibular schwannoma (**Figure 3**) but cranial nerve tractography was also assessed in patients with trigeminal schwannomas (Wei et al., 2016), meningiomas (Ma et al., 2016; Yoshino et al., 2016; Behan et al., 2017; d'Almeida et al., 2017; Zolal et al., 2017a), brainstem cavernomas (Ulrich et al., 2014) and other unspecified cerebellopontine angle tumors (Roundy et al., 2012). Given the functional importance of preserving the facial nerve during surgery, almost all tumor studies (21/22, 95%) included tractography of CN VII or the VII/VIII complex, but tractography of other cranial nerves within the posterior fossa has also been demonstrated including CN IV (Ma et al.,

2016; Yoshino et al., 2016), CN V (Chen et al., 2011; Ulrich et al., 2014; Wei et al., 2016; Yoshino et al., 2016; Behan et al., 2017; Zolal et al., 2017a) and CN VI (Ulrich et al., 2014; Yoshino et al., 2016). Eight non-tumor studies reported tractography results; seven studies detailed tractography of the trigeminal nerve (Fujiwara et al., 2011; Hodaie et al., 2012; DeSouza et al., 2014; Rousseau et al., 2015; Chen, D. Q. et al., 2016; Coskun et al., 2017; Hung et al., 2017) [five of which were in patients with TN (Fujiwara et al., 2011; DeSouza et al., 2014; Chen, D. Q. et al., 2016; Hung et al., 2017)] with the other study focusing on the cochlea nerve (Vos et al., 2015).

A deterministic method of generating fiber tractography was used in the majority of studies (93%). The reported success rate in generating fiber tracts of the cranial nerves within the posterior fossa varied considerably (0–100% success) but was not lower in those studies imaging smaller nerves [100% success rate was reported in all studies imaging trochlear (Ma et al., 2016; Yoshino et al., 2016) or abducens nerve (Ulrich et al., 2014; Yoshino et al., 2016)]; however, further studies are needed to confirm this observation. Zolal et al. recently published their experience using probabilistic methods (Zolal et al., 2017a,b). One of their studies provided a comparison of both techniques and appeared to suggest that probabilistic tracking was more effective at depicting the cranial nerves (Zolal et al., 2017a). In 15 studies (50%), a single region of interest (ROI) was used to seed the tractography, whereas 12 studies (40%) used a two ROIs, one to seed and one to select [methods not specified in 3 studies]. Details of thresholding was available in 25 of the 30 studies that performed tractography. A variety of fixed FA thresholds (range 0.02–0.20) were chosen in 16/25 studies (64%) (Taoka et al., 2006; Chen et al., 2011; Fujiwara et al., 2011; Gerganov et al., 2011; Hodaie et al., 2012; Roundy et al., 2012; Zhang et al., 2013; DeSouza et al., 2014; Rousseau et al., 2015; Borkar et al., 2016; Chen, D. Q. et al., 2016; Hilly et al., 2016; Ma et al., 2016; Song et al., 2016; Behan et al., 2017; Hung et al., 2017) with a variable approach to selecting the FA threshold used in the other 9 studies (36%) (Choi et al., 2014; Wei et al., 2015; Yoshino et al., 2015a,b, 2016; Li et al., 2017; Zhang et al., 2017; Zolal et al., 2017a,b), including the two studies that employed diffusion spectrum imaging (DSI).

In studies that involved patients undergoing surgery, fiber tractography of the facial nerve was correlated with the surgeon's intraoperative finding in 19 studies (86%) but the reported accuracy of facial nerve tractography was extremely variable (17–100%) (**Table 3**). The accuracy of the tractography was assessed by the operating surgeon inspecting and documenting the location of the nerve in relation to the tumor and was usually assisted by the use of qualitative electrophysiological monitoring (79% of studies). Recently, Li et al also managed to quantitatively correlate electrophysiological results by registering the points of stimulation with the patient's tractography results using an intraoperative neuronavigation system (Li et al., 2017). Several studies reported patients' post-operative facial nerve status but none of them evaluated the effectiveness of using fiber tractography to prevent facial nerve injury.

DISCUSSION

There is a clinical need to improve the visualization of cranial nerves within the posterior fossa, particularly in the context of pathology, and to enable detailed analysis of the affected nerves' microstructure. In normal anatomy, the visualization of cranial nerves from the brainstem to the skull base is currently optimized on high contrast T2 sequences (**Figure 1**) but it is still extremely difficult to image the cranial nerves as they traverse the skull, and in patients with associated compressive tumor pathology our experience is that anatomical T2 imaging cannot depict the course of adjacent nerves. The prospect of obtaining 7T MR imaging in the routine clinical setting should improve the ability to reliably visualize the larger cranial nerves such as the oculomotor (CN III), trigeminal (CN V) and vestibulocochlear (CN VIII) through the brain's cisterns but anatomical constraints are still likely to impede the visualization of smaller nerves beyond the skull base and in the context of associated pathology such as compressive brain tumors. Consequently, the current focus of this review is to examine the effectiveness of utilizing diffusion MRI to image the cisternal segments of the cranial nerves within the posterior fossa.

Forty-one studies met the study's inclusion criteria and were qualitatively analyzed. The methodological quality of the included studies varied considerably but the available evidence demonstrates that it is possible to acquire diffusion MRI data using a variety of clinical scanners and process this data with various software packages, none of which were shown to be more, or less, effective in this respect. Most clinical studies examining the use of diffusion MRI in patients with cranial nerve pathologies have either focused on performing DTI analyses of the trigeminal nerve in patients with trigeminal neuralgia or generating DTI-based tractography of the cranial nerves in patients with posterior fossa tumors.

Trigeminal Neuralgia

Sixteen studies evaluated diffusivity changes in the trigeminal nerve of patients suffering from trigeminal neuralgia. The trigeminal nerve is the largest cranial nerve within the posterior fossa and all studies successfully managed to acquire diffusion MRI data of adequate quality for tractography and/or quantitative DTI analysis. Ten studies examined changes in FA within the REZ of the trigeminal nerve compared to the patient's unaffected side; lower FA values demonstrated within the REZ of TN-affected nerves in all ten studies and a statistically significant decrease observed in 80% (**Table 1**). However, due to the heterogeneous way data was presented in the various studies, it was not possible to quantitatively calculate the expected difference in FA values between TN-affected and unaffected nerves. A variety of other diffusivity metrics were also analyzed by different studies but no conclusive statements may be drawn from the current evidence given the small number of studies involved and the varying formats in which results were presented. It appears that RD values within the REZ of TN-affected are significantly higher than the unaffected nerves of healthy control subjects (Liu et al., 2013; DeSouza et al., 2014, 2015; Chen, D. Q. et al., 2016; Chen, S. T. et al., 2016; Lin et al., 2016) but

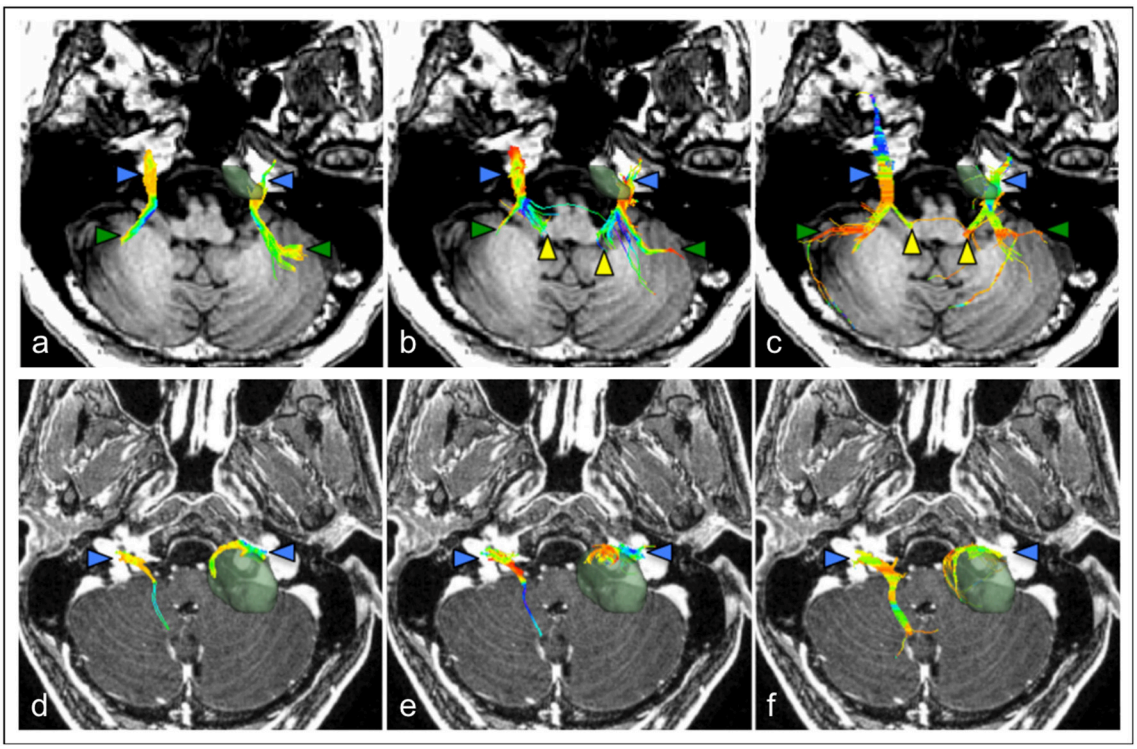

FIGURE 3 | Comparison of cranial nerve fiber tractography methods in patients with posterior fossa tumors. Streamlines are displayed overlaid on a T1 anatomical image. Color triangles indicate particular anatomical landmarks: blue: cranial nerves, green: superior cerebellar fibers, yellow: brainstem nuclei. **(a–c)** Tractography of the trigeminal nerve (CN V) in a patient with a left-sided petroclival meningioma; **(d–f)** Tractography of the facial-vestibulocochlear bundle (CN VII/VIII) in a patient with a left sided vestibular schwannoma. **(a,d)** single diffusion tractography, **(b,e)** extended streamline tractography, **(c,f)** constrained spherical deconvolution. *Images courtesy of* (Behan et al., 2017) *(CC-BY license)*.

De Souza et al. found no significant difference when comparing values with the patient's unaffected side (DeSouza et al., 2014, 2015). Likewise, mixed results were reported in the small number of studies that examined differences in AD values in patients with trigeminal neuralgia.

Interesting observations were noted in the studies that compared diffusivity values in different segments of the nerve (Fujiwara et al., 2011; Chen, D. Q. et al., 2016; Hung et al., 2017) and in the two studies that compared the diffusion metrics of affected trigeminal nerves in patients with MS-associated TN and idiopathic trigeminal neuralgia (Lummel et al., 2015; Chen, D. Q. et al., 2016). In particular, further work is needed to establish whether TN-affected nerves do indeed have a higher FA in the cisternal segment and lower FA in the REZ compared to unaffected nerves (Chen, D. Q. et al., 2016) and whether alterations in pre-surgical diffusivity measurements may be used as a predictive tool to prognosticate surgical response (Hung et al., 2017). In light of Hung et al.'s recent findings that treatment outcomes may be predicted by alterations in pre-surgical diffusivity measurements it would also be worthwhile evaluating if patients with different diffusion signatures respond differently to different treatment modalities. If so, diffusion metrics may also be used to guide treatment choice as well as prognosticating an individual patient's response.

Cranial Nerve Tractography in Patients With Posterior Fossa Tumors

Taoka et al. (2006) were the first to demonstrate the feasibility of using preoperatively-acquired DTI fiber tractography to delineate the course of the VII-VIII cranial nerve complex around a vestibular schwannoma. Since their initial work a further 21 studies have assessed the effectiveness of generating cranial nerve tractography in patients with posterior fossa tumors, the majority of whom had a vestibular schwannoma (82%). Nearly all studies used a deterministic tractography approach. Varying numbers of ROIs were used to select the fiber tracts and different methods of selecting an FA threshold were employed (**Table 3**). Overall, the success rate in generating tractography was extremely variable (0–100% success rate) and correlation with the surgeon's finding was also inconsistent (17–100% accuracy across all studies). However, it is important to note that failure to generate any fiber tracts was only demonstrated in one study using standard DTI acquisition and when Roundy et al. performed higher resolution diffusion imaging, tractography was successfully generated in all patients (Roundy et al., 2012). Similarly, a 17% accuracy rate was reported by Yoshino et al. when standard DTI was used but this increased to 67% when DTI was combined with multifused CE-FIESTA images (Yoshino et al., 2015a). Excluding these results, the

success rate of generating cranial nerve tractography in patients with a posterior fossa tumor rises to 82–100%, similar to that reported by Ung et al. in their brief review of the literature (Ung et al., 2016); however, intraoperative accuracy remains inconsistent (30–100%).

In recent years, several groups have attempted to improve the accuracy of cranial nerve tractography by various means. Wei et al. described a method of "superselective" tracking whereby optimal maps only containing bundles of axons with the lowest density, originating from the brainstem were selected in order to better delineate the anatomical relationship between the bundle and surrounding tissues (Wei et al., 2015). Various FA values were also used to identify the maximal FA value of each fiber. A similar method was replicated in two recent studies with good results (Li et al., 2017; Zhang et al., 2017) although this technique is very time consuming and still does not allow one to specifically distinguish the facial nerve from within the facial-vestibular (CN VII-VIII) complex. Furthermore, manual fiber selection and *ad-hoc* threshold manipulations are mainly based on investigator expectation of the anatomical position of the nerve, and as Zolal et al. highlighted in their recent article (Zolal et al., 2017a), such a method weakens the claims about reliable cranial nerve detection.

Two studies used diffusion spectrum imaging to generate fiber tractography of the cranial nerves (Yoshino et al., 2016; Zolal et al., 2017a), which is one of a number of more complex diffusion techniques that has been developed to address some of the limitations of the diffusion tensor model. DSI requires many more gradient directions along multiple *b*-values and a higher maximum *b*-value to generate the desired orientation information and as such is challenging to do in a clinical setting. Yoshino et al suggested that DSI may have the potential to distinguish the facial nerve from the vestibulocochlear nerve and accurately detect cranial nerve position (Yoshino et al., 2016) although this was not demonstrated in the current study. Zolal et al. subsequently compared the depiction of cranial nerves II, III, V, and the VII+VIII complex using both deterministic and probabilistic methods in a cohort of 30 healthy subjects obtained from the Kirby Repository (KR) and HCP databases (Zolal et al., 2017a). In both instances, for tracking the VII-VIII complex, ROIs were set at the brainstem and in the internal auditory meatus. This study confirmed that using diffusion MRI data with higher angular resolution and overall better quality led to better depictions of the nerves, confirming the finding previously reported by Roundy et al. (2012). Yoshino et al first described this method of gradually increasing the FA threshold in 2015 in deterministic fiber tracking (Yoshino et al., 2015a) and similar results were obtained in the studies utilizing DSI. Probabilistic index of connectivity (PICo maps) were created for each of the nerves, and to find the optimal probability threshold, the PICo maps were filtered at threshold values of 0.05–0.95 in steps of 0.05. Zolal et al. concluded that probabilistic tracking with a gradual PICo threshold increase is more effective at depicting the cranial nerves than the previously described deterministic tracking because it eliminates the erroneous fibers without manual intervention. A small limitation of this method is the increased computational time required in using the probabilistic method (30 min per nerve vs. 15 min per nerve for deterministic tracking) but in our opinion, such a difference is unlikely to impact clinical use given that image processing and fiber tractography is rarely required in real-time.

Recently, Behan et al compared three distinct reconstruction methods to generate tractography of the cranial nerves in patients with associated posterior fossa tumors, including conventional diffusion tensor tractography, a two-tensor reconstruction method (eXtended streamline tractography, XST), and a fiber orientation distribution-based method (constrained spherical deconvolution, CSD) (**Figure 3**) (Behan et al., 2017). They found that XST and CSD-based reconstruction methods produced more detailed projections of CN V and CN VII/VII compared to DTI tractography but CSD-based methods appeared to generate more invalid streamlines. Consequently, the authors favored using XST to visualize the cranial nerves in patients with posterior fossa tumors however a reliable and accurate method to separately depict the facial nerve in these patients is still required.

In a separate article, Zolal et al. used probabilistic tracking to generate preoperative tractography of the facial-cochlear complex in 21 patients undergoing vestibular schwannomas surgery with the accuracy determined intraoperatively by surgical inspection and the use of qualitative electrophysiological monitoring (Zolal et al., 2017a). Preoperative tractography was accurate in 81% of cases but many of the results also contained false-positive pathways, typically dorsal to the tumor. Probabilistic tractography is highly reliant on proper thresholding to achieve high-quality reconstruction of biological pathways and, consequently, tend to generate more invalid fiber bundles compared to deterministic tractography methods (Maier-Hein et al., 2017). In their study, Zolal et al speculated that this was because probabilistic tracking preferentially tracks large axonal bundles which in the case of patients with a vestibular schwannoma includes the larger vestibulocochlear nerve.

LIMITATIONS

The present systematic review was limited by various factors. Firstly, given the variety of ways diffusion data was presented and the small numbers of available studies, it was not possible to perform a meta-analysis and quantitatively analyse the data to draw any firm conclusions concerning diffusivity changes observed in the trigeminal nerve of patients with TN. Secondly, studies evaluating cranial nerve tractography were of mixed methodological quality and used a variety of acquisitions, limiting our discussion to a qualitative report of a small number of higher quality studies.

CONCLUSION

Current work suggests that fiber tractography has the ability to delineate the course of individual nerves within the posterior fossa. Further work is required to incorporate cranial nerve tractography into the intraoperative workflow and new avenues of using diffusion MRI should be explored to optimize and improve its reliability. In particular, new techniques of delineating the facial nerve from the VII-VIII complex should be examined and validated with the use of

quantitative intraoperative electrophysiological measurements. Diffusion MRI has the potential to inform our understanding of the microstructural changes that occur within the cranial nerves in various pathologies and may eventually be able to assist clinicians to deliver individualized treatment plans.

AUTHOR CONTRIBUTIONS

JS conceived the manuscript. JS and SV performed the systematic literature search. JS drafted the initial manuscript. SV, TV, RB, SS, SB, and SO reviewed the final manuscript.

ACKNOWLEDGMENTS

This work was supported by the Wellcome/EPSRC [203145Z/16/Z], EPSRC (EP/H046410/1, EP/J020990/1, EP/K005278), the MRC (MR/J01107X/1), the EU-FP7 project VPH-DARE@IT (FP7-ICT-2011-9-601055), the NIHR Biomedical Research Unit (Dementia) at UCL and the National Institute for Health Research University College London Hospitals Biomedical Research Center (NIHR BRC UCLH/UCL High Impact Initiative-BW.mn.BRC10269).

REFERENCES

Alexander, A. L., Hasan, K. M., Lazar, M., Tsuruda, J. S., and Parker, D. L. (2001). Analysis of partial volume effects in diffusion-tensor MRI. *Mag. Res. Med.* 45, 770–780. doi: 10.1002/mrm.1105

Assaf, Y., and Pasternak, O. (2008). Diffusion Tensor Imaging (DTI)-based white matter mapping in brain research: a review. *J. Mol. Neurosci.* 34, 51–61. doi: 10.1007/s12031-007-0029-0

Basser, P. J., and Jones, D. K. (2002). Diffusion-tensor MRI: theory, experimental design and data analysis–a technical review. *NMR Biomed.* 15, 456–467. doi: 10.1002/nbm.783

Basser, P. J., Mattiello, J., and LeBihan, D. (1994). MR diffusion tensor spectroscopy and imaging. *Biophys. J.* 66, 259–267. doi: 10.1016/S0006-3495(94)80775-1

Basser, P. J., Pajevic, S., Pierpaoli, C., Duda, J., and Aldroubi, A. (2000). *In vivo* fiber tractography using DT-MRI data. *Magn Reson Med.* 44, 625–32. doi: 10.1002/1522-2594(200010)44:4<625::AID-MRM17>3.0.CO;2-O

Beaulieu, C. (2002). The basis of anisotropic water diffusion in the nervous system–a technical review. *NMR Biomed.* 15, 435–455. doi: 10.1002/nbm.782

Behan, B., Chen, D. Q., Sammartino, F., DeSouza, D. D., Wharton-Shukster, E., and Hodaie, M. (2017). Comparison of diffusion-weighted MRI reconstruction methods for visualization of cranial nerves in posterior fossa surgery. *Front. Neurosci.*11:554. doi: 10.3389/fnins.2017.00554

Behrens, T. E., Berg, H. J., Jbabdi, S., Rushworth, M. F., and Woolrich, M. W. (2007). Probabilistic diffusion tractography with multiple fibre orientations: what can we gain? *Neuroimage* 34, 144–155. doi: 10.1016/j.neuroimage.2006.09.018

Borkar, S. A., Garg, A., Mankotia, D. S., Joseph, S. L., Suri, A., Kumar, R., et al. (2016). Prediction of facial nerve position in large vestibular schwannomas using diffusion tensor imaging tractography and its intraoperative correlation. *Neurol. India* 64, 965–970. doi: 10.4103/0028-3886.190270

Budde, M. D., Kim, J. H., Liang, H. F., Schmidt, R. E., Russell, J. H., Cross, A. H., et al. (2007). Toward accurate diagnosis of white matter pathology using diffusion tensor imaging. *Magn. Reson. Med.* 57, 688–695. doi: 10.1002/mrm.21200

Chen, D. Q., DeSouza, D. D., Hayes, D. J., Davis, K. D., O'Connor, P., and Hodaie, M. (2016). Diffusivity signatures characterize trigeminal neuralgia associated with multiple sclerosis. *Mult. Scler.* 22, 51–63. doi: 10.1177/1352458515579440

Chen, D. Q., Quan, J., Guha, A., Tymianski, M., Mikulis, D., and Hodaie, M. (2011). Three-dimensional *in vivo* modeling of vestibular schwannomas and surrounding cranial nerves with diffusion imaging tractography. *Neurosurgery* 68, 1077–1083. doi: 10.1227/NEU.0b013e31820c6cbe

Chen, S. T., Yang, J. T., Yeh, M. Y., Weng, H. H., Chen, C. F., and Tsai, Y. H. (2016). Using diffusion tensor imaging to evaluate microstructural changes and outcomes after radiofrequency rhizotomy of trigeminal nerves in patients with trigeminal neuralgia. *PLoS ONE* 11:e0167584. doi: 10.1371/journal.pone.0167584

Choi, K. S., Kim, M. S., Kwon, H. G., Jang, S. H., and Kim, O. L. (2014). Preoperative identification of facial nerve in vestibular schwannomas surgery using diffusion tensor tractography. *J. Korean Neurosurg. Soc.* 56, 11–15. doi: 10.3340/jkns.2014.56.1.11

Ciccarelli, O., Catani, M., Johansen-Berg, H., Clark, C., and Thompson, A. (2008). Diffusion-based tractography in neurological disorders: concepts, applications, and future developments. *Lancet Neurol.* 7, 715–727. doi: 10.1016/S1474-4422(08)70163-7

Coenen, V. A., Krings, T., Mayfrank, L., Polin, R. S., Reinges, M. H., Thron, A., et al. (2001). Three-dimensional visualization of the pyramidal tract in a neuronavigation system during brain tumor surgery: first experiences and technical note. *Neurosurgery* 49, 86–92; discussion 92–3. doi: 10.1097/00006123-200107000-00013

Concha, L., Gross, D. W., Wheatley, B. M., and Beaulieu, C. (2006). Diffusion tensor imaging of time-dependent axonal and myelin degradation after corpus callosotomy in epilepsy patients. *Neuroimage.* 32, 1090–1099. doi: 10.1016/j.neuroimage.2006.04.187

Coskun, O., Ucar, M., Vuralli, D., Yildirim, F., Cetinkaya, R., Akin Takmaz, S., et al. (2017). MR tractography in short lasting unilateral neuralgiform headache attacks with conjunctival injection and tearing (SUNCT) patients: case reports. *Pain Med.* 18, 1377–1381. doi: 10.1093/pm/pnw334

d'Almeida, G. N., Marques, L., Escada, P., Taoka, T., and Gonçalves-Pereira, P. (2017). Diffusion tensor tractography in the preoperative precise identification of the course of facial nerve in a meningioma of the cerebellopontine angle - technical implications. *Int. Neurosurg. Adv. Tech. Case Manage.* 9, 58–60. doi: 10.1016/j.inat.2017.03.010

DeSouza, D. D., Davis, K. D., and Hodaie, M. (2015). Reversal of insular and microstructural nerve abnormalities following effective surgical treatment for trigeminal neuralgia. *Pain* 156, 1112–1123. doi: 10.1097/j.pain.0000000000000156

DeSouza, D. D., Hodaie, M., and Davis, K. D. (2014). Abnormal trigeminal nerve microstructure and brain white matter in idiopathic trigeminal neuralgia. *Pain* 155, 37–44. doi: 10.1016/j.pain.2013.08.029

Duncan, J. S., Winston, G. P., Koepp, M. J., and Ourselin, S. (2016). Brain imaging in the assessment for epilepsy surgery. *Lancet Neurol.* 15, 420–433. doi: 10.1016/S1474-4422(15)00383-X

Farquharson, S., Tournier, J. D., Calamante, F., Fabinyi, G., Schneider-Kolsky, M., Jackson, G. D., et al. (2013). White matter fiber tractography: why we need to move beyond DTI. *J. Neurosurg.* 118, 1367–1377. doi: 10.3171/2013.2.JNS121294

Friston, K. (2007). "Chapter 2: Statistical parametric mapping," in *Statistical Parametric Mapping*, eds K. J. Friston, J. T. Ashburner, S. J. Kiebel, T. E. Nichols, and W. D. Penny (London: Academic Press), 10–31. doi: 10.1016/B978-012372560-8/50002-4

Fujiwara, S., Sasaki, M., Wada, T., Kudo, K., Hirooka, R., Ishigaki, D., et al. (2011). High-resolution diffusion tensor imaging for the detection of diffusion abnormalities in the trigeminal nerves of patients with trigeminal neuralgia caused by neurovascular compression. *J. Neuroimaging.* 21, e102–e108. doi: 10.1111/j.1552-6569.2010.00508.x

Gerganov, V. M., Giordano, M., Samii, M., and Samii, A. (2011). Diffusion tensor imaging-based fiber tracking for prediction of the position of the facial nerve in relation to large vestibular schwannomas. *J. Neurosurg.* 115, 1087–1093. doi: 10.3171/2011.7.JNS11495

Gong, G., He, Y., Concha, L., Lebel, C., Gross, D. W., Evans, A. C., et al. (2009). Mapping anatomical connectivity patterns of human cerebral cortex using *in vivo* diffusion tensor imaging tractography. *Cerebral Cortex.* 19, 524–536. doi: 10.1093/cercor/bhn102

Gouw, A. A., Seewann, A., Vrenken, H., van der Flier, W. M., Rozemuller, J. M., Barkhof, F., et al. (2008). Heterogeneity of white matter hyperintensities in Alzheimer's disease: post-mortem quantitative MRI and neuropathology. *Brain* 131(Pt 12), 3286–3298. doi: 10.1093/brain/awn265

Herweh, C., Kress, B., Rasche, D., Tronnier, V., Tröger, J., Sartor, K., et al. (2007). Loss of anisotropy in trigeminal neuralgia revealed by diffusion tensor imaging. *Neurology* 68, 776–778. doi: 10.1212/01.wnl.0000256340.16766.1d

Hilly, O., Chen, J. M., Birch, J., Hwang, E., Lin, V. Y., Aviv, R. I., et al. (2016). Diffusion tensor imaging tractography of the facial nerve in patients with cerebellopontine angle tumors. *Otol. Neurotol.* 37, 388–393. doi: 10.1097/MAO.0000000000000984

Hodaie, M., Chen, D. Q., Quan, J., and Laperriere, N. (2012). Tractography delineates microstructural changes in the trigeminal nerve after focal radiosurgery for trigeminal neuralgia. *PLoS ONE* 7:e32745. doi: 10.1371/journal.pone.0032745

Hung, P. S., Chen, D. Q., Davis, K. D., Zhong, J., and Hodaie, M. (2017). Predicting pain relief: use of pre-surgical trigeminal nerve diffusion metrics in trigeminal neuralgia. *Neuroimage Clin.* 15, 710–718. doi: 10.1016/j.nicl.2017.06.017

Jellison, B. J., Field, A. S., Medow, J., Lazar, M., Salamat, M. S., and Alexander, A. L. (2004). Diffusion tensor imaging of cerebral white matter: a pictorial review of physics, fiber tract anatomy, and tumor imaging patterns. *AJNR Am. J. Neuroradiol.* 25, 356–369. Available online at: http://www.ajnr.org/content/25/3/356

Jenkinson, M., Beckmann, C. F., Behrens, T. E., Woolrich, M. W., and Smith, S. M. (2012). FSL. *Neuroimage* 62, 782–790. doi: 10.1016/j.neuroimage.2011.09.015

Kraus, M. F., Susmaras, T., Caughlin, B. P., Walker, C. J., Sweeney, J. A., and Little, D. M. (2007). White matter integrity and cognition in chronic traumatic brain injury: a diffusion tensor imaging study. *Brain* 130(Pt 10), 2508–2519. doi: 10.1093/brain/awm216

Lazar, M., Weinstein, D. M., Tsuruda, J. S., Hasan, K. M., Arfanakis, K., Meyerand, M. E., et al. (2003). White matter tractography using diffusion tensor deflection. *Hum. Brain Mapp.* 18, 306–321. doi: 10.1002/hbm.10102

Le Bihan, D., Mangin, J. F., Poupon, C., Clark, C. A., Pappata, S., Molko, N., et al. (2001). Diffusion tensor imaging: concepts and applications. *J. Magn. Reson. Imaging.* 13, 534–546. doi: 10.1002/jmri.1076

Leal, P. R., Roch, J. A., Hermier, M., Souza, M. A., Cristino-Filho, G., and Sindou, M. (2011). Structural abnormalities of the trigeminal root revealed by diffusion tensor imaging in patients with trigeminal neuralgia caused by neurovascular compression: a prospective, double-blind, controlled study. *Pain* 152, 2357–2364. doi: 10.1016/j.pain.2011.06.029

Leemans, A., Jeurissen, B., Sijbers, J., and Jones, D. K. (2009). "ExploreDTI: a graphical toolbox for processing, analyzing, and visualizing diffusion MR data," in *ISMRM 17th Scientific Meeting & Exhibition*. (Honolulu, HI).

Li, H., Wang, L., Hao, S., Li, D., Wu, Z., Zhang, L., et al. (2017). Identification of the facial nerve in relation to vestibular schwannoma using preoperative diffusion tensor tractography and intraoperative tractography-integrated neuronavigation system. *World Neurosurg.* 107, 669–677. doi: 10.1016/j.wneu.2017.08.048

Li, Z., Peck, K. K., Brennan, N. P., Jenabi, M., Hsu, M., Zhang, Z., et al. (2013). Diffusion tensor tractography of the arcuate fasciculus in patients with brain tumors: Comparison between deterministic and probabilistic models. *J. Biomed. Sci. Eng.* 6, 192–200. doi: 10.4236/jbise.2013.62023

Lilja, Y., Ljungberg, M., Starck, G., Malmgren, K., Rydenhag, B., and Nilsson, D. T. (2014). Visualizing Meyer's loop: a comparison of deterministic and probabilistic tractography. *Epilepsy Res.* 108, 481–490. doi: 10.1016/j.eplepsyres.2014.01.017

Lin, W., Zhu, W. P., Chen, Y. L., Han, G. C., Rong, Y., Zhou, Y. R., et al. (2016). Large-diameter compression arteries as a possible facilitating factor for trigeminal neuralgia: analysis of axial and radial diffusivity. *Acta Neurochir.* 158, 521–526. doi: 10.1007/s00701-015-2673-4

Liu, Y., Li, J., Butzkueven, H., Duan, Y., Zhang, M., Shu, N., et al. (2013). Microstructural abnormalities in the trigeminal nerves of patients with trigeminal neuralgia revealed by multiple diffusion metrics. *Eur. J. Radiol.* 82, 783–786. doi: 10.1016/j.ejrad.2012.11.027

Lummel, N., Mehrkens, J. H., Linn, J., Buchholz, G., Stahl, R., Bochmann, K., et al. (2015). Diffusion tensor imaging of the trigeminal nerve in patients with trigeminal neuralgia due to multiple sclerosis. *Neuroradiology* 57, 259–267. doi: 10.1007/s00234-014-1463-7

Lutz, J., Linn, J., Mehrkens, J. H., Thon, N., Stahl, R., Seelos, K., et al. (2011). Trigeminal neuralgia due to neurovascular compression: high-spatial-resolution diffusion-tensor imaging reveals microstructural neural changes. *Radiology*. 258, 524–530. doi: 10.1148/radiol.10100477

Lutz, J., Thon, N., Stahl, R., Lummel, N., Tonn, J. C., Linn, J., et al. (2016). Microstructural alterations in trigeminal neuralgia determined by diffusion tensor imaging are independent of symptom duration, severity, and type of neurovascular conflict. *J. Neurosurg.* 124, 823–830. doi: 10.3171/2015.2.JNS142587

Ma, J., Su, S., Yue, S., Zhao, Y., Li, Y., Chen, X., et al. (2016). Preoperative visualization of cranial nerves in skull base tumor surgery using diffusion tensor imaging technology. *Turk. Neurosurg.* 26, 805–812. doi: 10.5137/1019-5149.JTN.13655-14.1

Maier-Hein, K. H., Neher, P. F., Houde, J. C., Côt,é, M. A., Garyfallidis, E., Zhong, J., et al. (2017). The challenge of mapping the human connectome based on diffusion tractography. *Nat. Commun.* 8:1349. doi: 10.1038/s41467-017-01285-x

Mandelli, M. L., Berger, M. S., Bucci, M., Berman, J. I., Amirbekian, B., and Henry, R. G. (2014). Quantifying accuracy and precision of diffusion MR tractography of the corticospinal tract in brain tumors. *J. Neurosurg.* 121, 349–358. doi: 10.3171/2014.4.JNS131160

Masutani, Y., Aoki, S., Abe, O., Hayashi, N., and Otomo, K. (2003). MR diffusion tensor imaging: recent advance and new techniques for diffusion tensor visualization. *Eur. J. Radiol.* 46, 53–66. doi: 10.1016/S0720-048X(02)00328-5

Matsuno, H., Rhoton, A. L. Jr., and Peace, D. (1988). Microsurgical anatomy of the posterior fossa cisterns. *Neurosurgery* 23, 58–80. doi: 10.1227/00006123-198807000-00012

Moher, D., Liberati, A., Tetzlaff, J., Altman, D. G., PRISMA Group. (2009). Preferred reporting items for systematic reviews and meta-analyses: the PRISMA statement. *BMJ* 339:b2535. doi: 10.1136/bmj.b2535

Mori, S., Crain, B. J., Chacko, V. P., and van Zijl, P. C. (1999). Three-dimensional tracking of axonal projections in the brain by magnetic resonance imaging. *Ann Neurol.* 45, 265–269. doi: 10.1002/1531-8249(199902)45:2<265::AID-ANA21>3.0.CO;2-3

Mori, S., and van Zijl, P. C. (2002). Fiber tracking: principles and strategies–a technical review. *NMR Biomed.* 15, 468–480. doi: 10.1002/nbm.781

Moseley, M. E., Cohen, Y., Kucharczyk, J., Mintorovitch, J., Asgari, H. S., Wendland, M. F., et al. (1990). Diffusion-weighted MR imaging of anisotropic water diffusion in cat central nervous system. *Radiology* 176, 439–445. doi: 10.1148/radiology.176.2.2367658

Naismith, R. T., Xu, J., Tutlam, N. T., Snyder, A., Benzinger, T., Shimony, J., et al. (2009). Disability in optic neuritis correlates with diffusion tensor-derived directional diffusivities. *Neurology* 72, 589–594. doi: 10.1212/01.wnl.0000335766.22758.cd

Neetu, S., Sunil, K., Ashish, A., Jayantee, K., and Usha Kant, M. (2016). Microstructural abnormalities of the trigeminal nerve by diffusion-tensor imaging in trigeminal neuralgia without neurovascular compression. *Neuroradiol. J.* 29, 13–18. doi: 10.1177/1971400915620439

Nimsky, C., Ganslandt, O., Hastreiter, P., Wang, R., Benner, T., Sorensen, A. G., et al. (2005). Preoperative and intraoperative diffusion tensor imaging-based fiber tracking in glioma surgery. *Neurosurgery* 56, 130–138. doi: 10.1227/01.NEU.0000144842.18771.30

Norton, I., Essayed, W., Zhang, F., Pujol, S., Yarmarkovich, A., Golby, A. J., et al. (2017). SlicerDMRI: open source diffusion MRI software for brain cancer research. *Cancer Res.* 77:e101. doi: 10.1158/0008-5472.CAN-17-0332

Nowell, M., Rodionov, R., Zombori, G., Sparks, R., Winston, G., Kinghorn, J., et al. (2015). Utility of 3D multimodality imaging in the implantation of intracranial electrodes in epilepsy. *Epilepsia* 56, 403–413. doi: 10.1111/epi.12924

Parker, G. J., and Alexander, D. C. (2005). Probabilistic anatomical connectivity derived from the microscopic persistent angular structure of cerebral tissue. *Philos. Trans. R. Soc. Lond. B. Biol. Sci.* 360, 893–902. doi: 10.1098/rstb.2005.1639

Qazi, A. A., , Radmanesh, A., O'Donnell, L., Kindlmann, G., Peled, S., Whalen, S., et al. (2009). Resolving crossings in the corticospinal tract by two-tensor streamline tractography: method and clinical assessment using fMRI. *Neuroimage* 47 (Suppl. 2), T98–T106. doi: 10.1016/j.neuroimage.2008.06.034

Roundy, N., Delashaw, J. B., and Cetas, J. S. (2012). Preoperative identification of the facial nerve in patients with large cerebellopontine angle tumors using high-density diffusion tensor imaging. *J. Neurosurg.* 116, 697–702. doi: 10.3171/2011.12.JNS111404

Rousseau, A., Nasser, G., Chiquet, C., Barreau, E., Gendron, G., Kaswin, G., et al. (2015). Diffusion tensor magnetic resonance imaging of trigeminal nerves in relapsing herpetic keratouveitis. *PLoS ONE* 10:e0122186. doi: 10.1371/journal.pone.0122186

Rueckriegel, S. M., Homola, G. A., Hummel, M., Willner, N., Ernestus, R. I., and Matthies, C. (2016). Probabilistic fiber-tracking reveals degeneration of the contralateral auditory pathway in patients with vestibular schwannoma. *AJNR Am. J. Neuroradiol.* 37, 1610–1616. doi: 10.3174/ajnr.A4833

Schmierer, K., Wheeler-Kingshott, C. A., Boulby, P. A., Scaravilli, F., Altmann, D. R., Barker, G. J., et al. (2007). Diffusion tensor imaging of post mortem multiple sclerosis brain. *Neuroimage* 35, 467–477. doi: 10.1016/j.neuroimage.2006.12.010

Slim, K., Nini, E., Forestier, D., Kwiatkowski, F., Panis, Y., and Chipponi, J. (2003). Methodological index for non-randomized studies (minors): development and validation of a new instrument. *ANZ J. Surg.* 73, 712–716. doi: 10.1046/j.1445-2197.2003.02748.x

Song, F., Hou, Y., Sun, G., Chen, X., Xu, B., Huang, J. H., et al. (2016). *In vivo* visualization of the facial nerve in patients with acoustic neuroma using diffusion tensor imaging-based fiber tracking. *J. Neurosurg.* 125, 787–794. doi: 10.3171/2015.7.JNS142922

Song, S. K., Sun, S. W., Ju, W. K., Lin, S. J., Cross, A. H., and Neufeld, A. H. (2003). Diffusion tensor imaging detects and differentiates axon and myelin degeneration in mouse optic nerve after retinal ischemia. *Neuroimage* 20, 1714–1722. doi: 10.1016/j.neuroimage.2003.07.005

Song, S. K., Sun, S. W., Ramsbottom, M. J., Chang, C., Russell, J., and Cross, A. H. (2002). Dysmyelination revealed through MRI as increased radial (but unchanged axial) diffusion of water. *Neuroimage* 17, 1429–1436. doi: 10.1006/nimg.2002.1267

Tanner, J. E. (1979). Self diffusion of water in frog muscle. *Biophys. J.* 28, 107–116. doi: 10.1016/S0006-3495(79)85162-0

Taoka, T., Hirabayashi, H., Nakagawa, H., Sakamoto, M., Myochin, K., Hirohashi, S., et al. (2006). Displacement of the facial nerve course by vestibular schwannoma: preoperative visualization using diffusion tensor tractography. *J. Magn. Reson. Imaging.* 24, 1005–1010. doi: 10.1002/jmri.20725

Tournier, J.-D., Calamante, F., and Connelly, A. (2012). MRtrix: Diffusion tractography in crossing fiber regions. *Int. J. Imaging Syst. Technol.* 22, 53–66. doi: 10.1002/ima.22005

Tournier, J. D., Mori, S., and Leemans, A. (2011). Diffusion tensor imaging and beyond. *Magn. Reson. Med.* 65, 1532–1556. doi: 10.1002/mrm.22924

Toussaint, N., Souplet, J. C., and Fillard, P. (2007). "MedINRIA: medical image navigation and research tool by INRIA," in *Proceedings of MICCAI'07 Workshop on Interaction in Medical Image Analysis and Visualization* (Brisbane, QLD).

Ulrich, N. H., Ahmadli, U., Woernle, C. M., Alzarhani, Y. A., Bertalanffy, H., and Kollias, S. S. (2014). Diffusion tensor imaging for anatomical localization of cranial nerves and cranial nerve nuclei in pontine lesions: initial experiences with 3T-MRI. *J. Clin. Neurosci.* 21, 1924–1927. doi: 10.1016/j.jocn.2014.03.027

Ung, N., Mathur, M., Chung, L. K., Cremer, N., Pelargos, P., Frew, A., et al. (2016). A systematic analysis of the reliability of diffusion tensor imaging tractography for facial nerve imaging in patients with vestibular schwannoma. *J. Neurol. Surg. B Skull Base.* 77, 314–318. doi: 10.1055/s-0035-1566303

Vos, S. B., Haakma, W., Versnel, H., Froeling, M., Speleman, L., Dik, P., et al. (2015). Diffusion tensor imaging of the auditory nerve in patients with long-term single-sided deafness. *Hear. Res.* 323, 1–8. doi: 10.1016/j.heares.2015.01.010

Vos, S. B., Jones, D. K., Jeurissen, B., Viergever, M. A., and Leemans, A. (2012). The influence of complex white matter architecture on the mean diffusivity in diffusion tensor MRI of the human brain. *Neuroimage* 59, 2208–2216. doi: 10.1016/j.neuroimage.2011.09.086

Vos, S. B., Jones, D. K., Viergever, M. A., and Leemans, A. (2011). Partial volume effect as a hidden covariate in DTI analyses. *Neuroimage* 55, 1566–1576. doi: 10.1016/j.neuroimage.2011.01.048

Wang, R., Benner, T., Sorensen, A., and Wedeen, V. (2007). "Diffusion toolkit: a software package for diffusion imaging data processing and tractography," in *Proceedings of the International Society for Magnetic Resonance in Medicine* (Berlin).

Wei, P. H., Qi, Z. G., Chen, G., Hu, P., Li, M. C., Liang, J. T., et al. (2015). Identification of cranial nerves near large vestibular schwannomas using superselective diffusion tensor tractography: experience with 23 cases. *Acta Neurochir.* 157, 1239–1249. doi: 10.1007/s00701-015-2431-7

Wei, P. H., Qi, Z. G., Chen, G., Li, M. C., Liang, J. T., Guo, H. C., et al. (2016). Identification of cranial nerves around trigeminal schwannomas using diffusion tensor tractography: a technical note and report of 3 cases. *Acta Neurochir.* 158, 429–435. doi: 10.1007/s00701-015-2680-5

Werring, D. J., Clark, C. A., Barker, G. J., Thompson, A. J., and Miller, D. H. (1999). Diffusion tensor imaging of lesions and normal-appearing white matter in multiple sclerosis. *Neurology* 52, 1626–1632. doi: 10.1212/WNL.52.8.1626

Wilcox, S. L., Gustin, S. M., Eykman, E. N., Fowler, G., Peck, C. C., Murray, G. M., et al. (2013). Trigeminal nerve anatomy in neuropathic and non-neuropathic orofacial pain patients. *J. Pain.* 14, 865–872. doi: 10.1016/j.jpain.2013.02.014

Yeh, F. C., Verstynen, T. D., Wang, Y., Fernández-Miranda, J. C., and Tseng, W. Y. (2013). Deterministic diffusion fiber tracking improved by quantitative anisotropy. *PLoS ONE* 8:e80713. doi: 10.1371/journal.pone.0080713

Yogarajah, M., Focke, N. K., Bonelli, S., Cercignani, M., Acheson, J., Parker, G. J., et al. (2009). Defining Meyer's loop-temporal lobe resections, visual field deficits and diffusion tensor tractography. *Brain* 132(Pt 6), 1656–1668. doi: 10.1093/brain/awp114

Yoshino, M., Abhinav, K., Yeh, F. C., Panesar, S., Fernandes, D., Pathak, S., et al. (2016). Visualization of cranial nerves using high-definition fiber tractography. *Neurosurgery* 79, 146–165. doi: 10.1227/NEU.0000000000001241

Yoshino, M., Kin, T., Ito, A., Saito, T., Nakagawa, D., Ino, K., et al. (2015a). Feasibility of diffusion tensor tractography for preoperative prediction of the location of the facial and vestibulocochlear nerves in relation to vestibular schwannoma. *Acta Neurochir.* 157, 939–946; discussion 946. doi: 10.1007/s00701-015-2411-y

Yoshino, M., Kin, T., Ito, A., Saito, T., Nakagawa, D., Ino, K., et al. (2015b). Combined use of diffusion tensor tractography and multifused contrast-enhanced FIESTA for predicting facial and cochlear nerve positions in relation to vestibular schwannoma. *J. Neurosurg.* 123, 1480–1488. doi: 10.3171/2014.11.JNS14988

Zhang, Y., Chen, Y., Zou, Y., Zhang, W., Zhang, R., Liu, X., et al. (2013). Facial nerve preservation with preoperative identification and intraoperative monitoring in large vestibular schwannoma surgery. *Acta Neurochir.* 155, 1857–1862. doi: 10.1007/s00701-013-1815-9

Zhang, Y., Mao, Z., Wei, P., Jin, Y., Ma, L., Zhang, J., et al. (2017). Preoperative prediction of location and shape of facial nerve in patients with large vestibular schwannomas using diffusion tensor imaging-based fiber tracking. *World Neurosurg.* 99, 70–78. doi: 10.1016/j.wneu.2016.11.110

Zolal, A., Juratli, T. A., Podlesek, D., Rieger, B., Kitzler, H. H., Linn, J., et al. (2017a). Probabilistic tractography of the cranial nerves in vestibular schwannoma. *World Neurosurg.* 107, 47–53. doi: 10.1016/j.wneu.2017.07.102

Zolal, A., Sobottka, S. B., Podlesek, D., Linn, J., Rieger, B., Juratli, T. A., et al. (2017b). Comparison of probabilistic and deterministic fiber tracking of cranial nerves. *J. Neurosurg.* 127, 613–621. doi: 10.3171/2016.8.JNS16363

Conflict of Interest Statement: The authors declare that the research was conducted in the absence of any commercial or financial relationships that could be construed as a potential conflict of interest.

Copyright © 2019 Shapey, Vos, Vercauteren, Bradford, Saeed, Bisdas and Ourselin. This is an open-access article distributed under the terms of the Creative Commons Attribution License (CC BY). The use, distribution or reproduction in other forums is permitted, provided the original author(s) and the copyright owner(s) are credited and that the original publication in this journal is cited, in accordance with accepted academic practice. No use, distribution or reproduction is permitted which does not comply with these terms.

frontiers in Neuroscience

ORIGINAL RESEARCH
published: 15 February 2019
doi: 10.3389/fnins.2019.00079

An Information-Theoretic Approach to Quantitative Analysis of the Correspondence Between Skin Blood Flow and Functional Near-Infrared Spectroscopy Measurement in Prefrontal Cortex Activity

Soheil Keshmiri[1]*, *Hidenobu Sumioka*[1], *Masataka Okubo*[1] and *Hiroshi Ishiguro*[1,2]

[1] Hiroshi Ishiguro Laboratories, Advanced Telecommunications Research Institute International, Kyoto, Japan, [2] Graduate School of Engineering Science, Osaka University, Osaka, Japan

OPEN ACCESS

Edited by:
Laura Marzetti,
Università degli Studi G. d'Annunzio Chieti e Pescara, Italy

Reviewed by:
Robin A. A. Ince,
University of Manchester, United Kingdom
Hasan Ayaz,
Drexel University, United States

***Correspondence:**
Soheil Keshmiri
soheil@atr.jp

Specialty section:
This article was submitted to Brain Imaging Methods, a section of the journal Frontiers in Neuroscience

Received: 18 May 2018
Accepted: 25 January 2019
Published: 15 February 2019

Citation:
Keshmiri S, Sumioka H, Okubo M and Ishiguro H (2019) An Information-Theoretic Approach to Quantitative Analysis of the Correspondence Between Skin Blood Flow and Functional Near-Infrared Spectroscopy Measurement in Prefrontal Cortex Activity. Front. Neurosci. 13:79. doi: 10.3389/fnins.2019.00079

Effect of Skin blood flow (SBF) on functional near-infrared spectroscopy (fNIRS) measurement of cortical activity proves to be an illusive subject matter with divided stances in the neuroscientific literature on its extent. Whereas, some reports on its non-significant influence on fNIRS time series of cortical activity, others consider its impact misleading, even detrimental, in analysis of the brain activity as measured by fNIRS. This situation is further escalated by the fact that almost all analytical studies are based on comparison with functional Magnetic Resonance Imaging (fMRI). In this article, we pinpoint the lack of perspective in previous studies on preservation of information content of resulting fNIRS time series once the SBF is attenuated. In doing so, we propose information-theoretic criteria to quantify the necessary and sufficient conditions for SBF attenuation such that the information content of frontal brain activity in resulting fNIRS times series is preserved. We verify these criteria through evaluation of their utility in comparative analysis of principal component (PCA) and independent component (ICA) SBF attenuation algorithms. Our contributions are 2-fold. First, we show that mere reduction of SBF influence on fNIRS time series of frontal activity is insufficient to warrant preservation of cortical activity information. Second, we empirically justify a higher fidelity of PCA-based algorithm in preservation of the fontal activity's information content in comparison with ICA-based approach. Our results suggest that combination of the first two principal components of PCA-based algorithm results in most efficient SBF attenuation while preserving maximum frontal activity's information. These results contribute to the field by presenting a systematic approach to quantification of the SBF as an interfering process during fNIRS measurement, thereby drawing an informed conclusion on this debate. Furthermore, they provide evidence for a reliable choice among existing SBF attenuation algorithms and their inconclusive number of components, thereby ensuring minimum loss of cortical information during SBF attenuation process.

Keywords: functional near-infrared spectroscopy, skin blow flow, transfer entropy, conditional entropy, frontal cortex activity

1. INTRODUCTION

Functional near-infrared spectroscopy (fNIRS) time series of brain cortical activity is subject to various systemic physiological interferences, ranging from cardiac activity and respiration (Orbig et al., 2000; Tonorov et al., 2000; Payne et al., 2003) to motion artifacts (Cooper et al., 2012; Tak and Ye, 2014; Naseer and Hong, 2015) and scalp-hemodynamic (Scholkmann et al., 2014). While detection and correction strategies for most of these physiological and systemic interferences are widely practiced, effect of scalp-hemodynamic and skin blood flow (SBF) has been subject to much divided perspective. Whereas, Takahashi et al. (2011) argued that a major part of task-evoked changes in blood oxygenation hemoglobins (ΔOxy-Hb) in the forehead is due to SBF, Sato et al. (2013) claimed that such changes are highly correlated with blood oxygen level dependent (BOLD) of functional magnetic resonance imaging (fMRI) and gray matter, as opposed to SBF or other soft tissues. This, in part, helps explain the lack of incorporation of analytical steps for SBF attenuation in most recent studies (Liand et al., 2010; Cuiand et al., 2011; Gagnonand et al., 2012; Fishbum et al., 2014; Ozawa et al., 2014; Bakerand et al., 2016; Guand et al., 2017; Liu et al., 2017) as well as NIRS-related analytical toolkits (Koh et al., 2007; Huppertand et al., 2009; Strangmann, 2009; Ye et al., 2009; Feketeand et al., 2011).

However, research suggests that systemic changes due to SBF are unpreventable since they are the result of the activation of the autonomic nervous system and/or varying blood pressure in response to action (Lee et al., 2002; Scremin and Kenney, 2004). In fact, Sato et al. (2016) argued that scalp- and cerebral-hemodynamic (in particular ΔOxy-Hb) increase in a task-related manner, implying their similar temporal profiles. In light of these observations, the field has witnessed a growing number of research on SBF attenuation approaches. One class of SBF filters has considered the direct measurements from short source-detector distances (e.g., $\leq$ 2.0 cm) to attenuate the effect of scalp-hemodynamic on channels with longer distance (e.g., $3.0\ cm \leq d \leq 4.5\ cm$) (Zhang et al., 2009; Gagnon et al., 2011, 2012, 2014; Saager et al., 2011; Haeussinger et al., 2014), where d stands for source-detector distance. Another family of such filters has been built upon the assumption that scalp-hemodynamic changes are more global than cerebral-hemodynamic, thereby introducing mathematically founded techniques for SBF removal. For instance, Zhang et al. (2005) assumed the orthogonality between the spatial interference and the spatial evoked activation subspaces to derive principal components from resting periods, thereby eliminating such components from task period as representatives of SBF. This approach was further extended by Zhang et al. (2016) through application of Gaussian filtering. On the other hand, Kohno et al. (2007) employed independent component analysis (ICA) to extract the most spatially uniform component of ΔOxy-Hb. Furthermore, they showed their extracted component was highly correlated with SBF through its comparison with simultaneous laser Doppler measurement (Johnson et al., 1984; Oberg, 1990). Kiguchi and Funane (2014) further extended this ICA-based approach for its online use. Sato et al. (2016) argued that although these filters offer reliable and accurate tool for SBF attenuation, their reliance on considerably large number of probes for data acquisition makes their application infeasible. In turn, they addressed this limitation through identification of the scalp-hemodynamic component from a small number of short source-detector channels, thereby removing this effect based on general linear model (GLM) (Mardia et al., 1979; Friston et al., 1995, 2011). Their approach showed a significant improvement in contrast with Zhang et al. (2005) and Kohno et al. (2007), as suggested by their fMRI-based comparative analysis.

Although our overview of research on scalp-hemodynamic and SBF demonstrates fascinating approaches with impressive results, it reveals an immediate shortcoming that is lack of quantitative realization of the utility of these methodologies for their verification toward a common consensus on their use. For instance, whereas Zhang et al. (2005) claimed the first three principal components for adequate SBF attenuation, Sato et al. (2016) suggested a non-significant difference in adaptation of first or combination of first two or three components. More importantly, these approaches fall short in assessing the state of fNIRS time series once the SBF attenuation process is complete. For example, Kohno et al. (2007) showed a high correlation between their selected most spatially uniform component with SBF signal while discarding a report on fNIRS content once this component was removed. Although a few have included measures such as correlation coefficient, signal-to-noise ratio, or Pearson R^2 (Zhang et al., 2005; Gagnon et al., 2011), these linear measures fail to detect the nonlinearity in interacting processes (Kinney and Atwal, 2014). Moreover, they cannot provide any causal insight on the observed effect: they are unable to quantify whether they attenuated the confounding effect of the interfering process or information pertinent to cortical activity. In addition, many of these results have derived the quality of their SBF attenuation through comparison of fNIRS data with fMRI recordings (Haeussinger et al., 2014; Sato et al., 2016). Although high spatial resolution of fMRI along with significant correlation between its BOLD and corresponding Blood de-/Oxygenation of fNIRS (Okamoto et al., 2004; Steinbrink et al., 2006; Strangman et al., 2006; Toronov et al., 2007; Cuiand et al., 2011) provide a basis for such comparative analyses, they are highly time-consuming and require extra care to ensure the least environmental and experimental discrepancies, making their adaptation impractical in a broader domain.

In this article, we address these shortcomings through proposal of information-theoretic criteria for preservation of information content of frontal brain activity. We utilize the concept of transfer entropy (TE) (Schreiber, 2000) to quantify the effect of SBF on fNIRS time series of frontal brain activity via transferring undesired information onto fNIRS measurement. TE provides a powerful tool for measuring the strength and direction (i.e., causation) of the coupling between simultaneously observed processes (Kaiser and Schreiber, 2002). Utilization of TE as a measure for information flow becomes more attractive, considering its minimal assumptions on dynamics of the time series under investigation, its numerical stability even for reasonably small sample sizes, and its ability in capturing both, linear as well as nonlinear effects (Lungarella

and Sporns, 2006). In fact, recent years have witnessed a growing interest in application of TE in neuroscientific research (Lungarella and Sporns, 2006; Honey et al., 2007; Vakorin et al., 2010; Liao et al., 2011). Additionally, we exploit the concept of mutual information (MI) and its correspondence with conditional entropy between interacting continuous random variables (Cover and Thomas, 2006; Stone, 2015) to formalize criteria for preservation of the frontal activity's information in resulting fNIRS time series once the SBF attenuation is complete.

Our results suggest that mere reduction of SBF influence on fNIRS time series of frontal activity is insufficient to warrant frontal activity's information is retained. Moreover, they imply a higher fidelity of PCA-based algorithm in frontal activity's information preservation in comparison with ICA-based approach. Furthermore, they indicate that a combination of first two principal components of PCA-based algorithm results in most efficient SBF attenuation while ensuring maximum frontal activity's information preservation. Our results contribute to the field by presenting a systematic approach to quantification of the SBF and its effect as an interfering process during fNIRS measurement, thereby drawing an informed conclusion on this debate. Furthermore, they provide evidence for a reliable choice among existing SBF attenuation algorithms and their inconclusive number of components, thereby ensuring minimum loss of frontal activity's information during SBF attenuation process.

2. MATERIALS AND METHODS

2.1. Formal Statements

2.1.1. Preliminaries

Prior to formalizing our information-theoretic criteria, we restate the definitions of conditional entropy, MI, and TE, along with two Theorems and a Corollary (without proofs) from information theory to help better elaborate on rationale behind our criteria.

Definition 2.1. *If* $(\mathcal{X}, \mathcal{Y}) \sim f(x,y)$, $\forall x \in \mathcal{X}$, $y \in \mathcal{Y}$, *the conditional entropy* $H(\mathcal{X}|\mathcal{Y})$ *is defined as Cover and Thomas (2006)[p. 249]*

$$H(\mathcal{X}|\mathcal{Y}) = -\int f(x,y) log(f(x|y)) dxdy \tag{1}$$

where $f(x,y)$, $\forall x \in \mathcal{X}$, $y \in \mathcal{Y}$ indicates the joint density and $f(x|y)$ is the probability of occurrence of x, given that y occurred. In other words, conditional entropy quantifies the average uncertainty regarding the value of $\mathcal{X}$ when the value of $\mathcal{Y}$ is known (Stone, 2015).

Definition 2.2. *The mutual information* $I(\mathcal{X};\mathcal{Y})$ *between two random variables with joint density* $f(x,y)$, $\forall x \in \mathcal{X}$, $y \in \mathcal{Y}$ *is defined as Cover and Thomas (2006)[p. 251]*

$$I(\mathcal{X};\mathcal{Y}) = \int f(x,y) \log \frac{f(x,y)}{f(x)f(y)} dxdy \tag{2}$$

Mutual information can be expressed in terms of conditional entropy as (ibid.):

$$\begin{aligned} I(\mathcal{X};\mathcal{Y}) &= H(\mathcal{X}) - H(\mathcal{X}|\mathcal{Y}) \\ &= H(\mathcal{Y}) - H(\mathcal{Y}|\mathcal{X}) \\ &= H(\mathcal{X}) + H(\mathcal{Y}) - H(\mathcal{X},\mathcal{Y}) \end{aligned} \tag{3}$$

with $H(.)$ representing the entropy of its argument and $H(\mathcal{X}|\mathcal{Y})$ and $H(\mathcal{X},\mathcal{Y})$ are the conditional entropy and the joint entropy between $\mathcal{X}$ and $\mathcal{Y}$, respectively.

On the other hand, transfer entropy (Schreiber, 2000) aims at extracting directed flow or transfer of information (Lungarella and Sporns, 2006) between interacting processes. In essence, TE quantifies the deviation from generalized Markov property $p(x_{t+1}|x_t, y_t) = p(x_{t+1}|x_t)$, $\forall x_t$, $x_{t+1} \in \mathcal{X}$, $y_t \in \mathcal{Y}$, with $p(x|y)$ being the probability of occurrence of x, given y occurred. TE is expressed as a specific version of Kullback-Leibler divergence (Cover and Thomas, 2006; Stone, 2015) i.e., the relative entropy (Lungarella and Sporns, 2006):

$$T(\mathcal{Y} \to \mathcal{X}) = \sum_{x_{t+1}} \sum_{x_t} \sum_{y_t} p(x_{t+1}, x_t, y_t) \log \frac{p(x_{t+1}|x_t, y_t)}{p(x_{t+1}|x_t)} \tag{4}$$

One can also identify TE as a conditional MI (i.e., a causal inference on shared information) between two interacting processes:

$$T(\mathcal{Y} \to \mathcal{X}) = I(y_t; x_{t+1}|x_t),\ \forall x_{t+1}, x_t \in \mathcal{X},\ y_t \in \mathcal{Y} \tag{5}$$

If this deviation is small, then the state of $\mathcal{Y}$ is assumed to have minimal or no relevance on the transition probabilities of $\mathcal{X}$ (Lungarella and Sporns, 2006), thereby implying an absence and/or a non-significant effect of $\mathcal{Y}$ on $\mathcal{X}$. It is worthy of note that unlike MI, TE is explicitly and strictly non-symmetric under exchange of the role of the interacting processes (Kaiser and Schreiber, 2002). In other words, $TE(\mathcal{Y} \to \mathcal{X}) \neq TE(\mathcal{X} \to \mathcal{Y}), \forall \mathcal{X}, \mathcal{Y}$.

Theorem 2.1. *(Conditioning reduces entropy): For any two random variables* $\mathcal{X}$ *and* $\mathcal{Y}$*, we have (Cover and Thomas, 2006, p. 41 and p. 253)*

$$H(\mathcal{X}|\mathcal{Y}) \leq H(\mathcal{X}) \tag{6}$$

with equality if and only if $\mathcal{X}$ *and* $\mathcal{Y}$ *are independent.*

Theorem 2.2. *(Data Processing Inequality): if* $\mathcal{X} \to \mathcal{Y} \to \mathcal{Z}$[1]*, then (Cover and Thomas, 2006, p. 34)*

$$I(\mathcal{X};\mathcal{Y}) \geq I(\mathcal{X};\mathcal{Z}) \tag{7}$$

Corollary 2.1. *In particular, if* $\mathcal{Z} = g(\mathcal{Y})$*, we have (Cover and Thomas, 2006, p. 35)*

$$I(\mathcal{X};\mathcal{Y}) \geq I(\mathcal{X}; g(\mathcal{Y})) \tag{8}$$

[1] $\mathcal{X} \to \mathcal{Y} \to \mathcal{Z}$ if and only if $\mathcal{X}$ and $\mathcal{Z}$ are conditionally independent, given $\mathcal{Y}$ i.e., they form a Markov chain Cover and Thomas (2006, p. 34).

Concretely, Data Processing Inequality (DPI), as formulated in Equations (7, 8), states that the result of any manipulation of data cannot improve the inferences that are made from the data (Cover and Thomas, 2006; Kinney and Atwal, 2014). In other words, no matter how sophisticated a processing approach is, it inevitably results in loss of information. Implication of DPI in SBF attenuation is 2-fold: (1) it implies that no matter how well-defined an SBF attenuation process is, loss of information is inherent in its steps. (2) Therefore, it is of utmost cruciality to ensure such a loss maximally reflects the undesirable information induced by SBF than actual frontal brain activity.

In what follows, we utilize the aforementioned observations from information theory to formalize our criteria. In essence, Criterion 2.1 through Criterion 2.3 provide necessary and sufficient conditions for quantification of the ability of SBF attenuation algorithms in reducing effect of SBF on fNIRS time series of frontal brain activity. On the other hand, Criterion 2.4 signifies utility of such algorithms in preservation of the frontal brain activity's information in resulting fNIRS times series. Finally, Criterion 2.5 examines whether preservation of the cortical activity in resulting fNIRS time series is maximized by adapted SBF algorithms.

2.1.2. The Criteria

Let X and X' represent the fNIRS time series of cortical activity before and after application of an SBF attenuation algorithm. Furthermore, let Y be the time series, representing SBF. The main premise of any SBF attenuation algorithm is its effectiveness for reducing the impact of SBF on fNIRS time series of cortical activity of human subjects.

Criterion 2.1. *Transferred information from SBF to fNIRS times series is significantly reduced if adapted attenuation process is effective i.e.,* $TE(Y \rightarrow X') \leq TE(Y \rightarrow X)$.

Criterion 2.1, in turn, implies that given different SBF attenuation algorithms, the one with significantly smaller $TE(Y \rightarrow X')$ is more effective in attenuation of SBF influence on fNIRS time series of frontal brain activity in comparison with other SBF attenuation algorithms.

Furthermore, if X primarily represents the frontal activity that is partially contaminated by SBF, then attenuation of SBF must, in principle, have no effect on ability of X to explain X' in absence of Y. This, in turn, implies that $Y \rightarrow X \rightarrow X'$ holds true (as per Theorem 2.2) and $X' = g(X)$ i.e., X' is expressible as a function of X. We utilize this observation in conjunction with Corollary 2.1 to formalize our second criterion.

Criterion 2.2. *fNIRS time series prior to SBF attenuation must, in principle, have more in common with Y than after SBF attenuation is complete i.e.,* $I(Y; X) \geq I(Y; g(X))$. *Using Theorem 2.2 and applying Equation (3), we get*

$$\begin{aligned} & I(Y; X) \geq I(Y; X') \\ \Rightarrow\ & H(Y) - H(Y|X) \geq H(Y) - H(Y|X') \\ \Rightarrow\ & H(Y|X) \leq H(Y|X') \end{aligned} \tag{9}$$

As a direct consequence of Criterion 2.2, an SBF attenuation algorithm with significantly larger $H(Y|X')$ is more effective, in comparison with any other such algorithms.

Criterion 2.1 and Criterion 2.2 provide necessary conditions to validate that outcome of an adapted SBF attenuation algorithm is successful in reducing the correspondence between SBF and fNIRS time series of frontal brain activity. However, they are not sufficient conditions for quantification of significance of such a reduction since $H(Y|X') \neq H(X'|Y)$, $\forall X', Y$. Therefore, it is necessary to validate the sufficient condition of such an algorithm in reducing the SBF effect.

Criterion 2.3. *Y must, in principle, be more informative about fNIRS before than after attenuation is complete i.e.,* $H(X|Y) \leq H(X'|Y)$

As a result of Criterion 2.3, if an SBF attenuation algorithm is more effective, its application must result in significantly larger $H(X'|Y)$ in comparison with other such algorithms.

Moreover, an effective SBF attenuation algorithm ensures the preservation of cortical activity while reducing the undesirable effect of SBF, thereby resulting in higher mutual information between X and X' than X and Y. We formulate this expectation through the fourth criterion.

Criterion 2.4. X' *realizes the information content of X more than Y does i.e.,* $I(X; X') \geq I(X; Y)$. *Applying Equation (3), this is equivalent to*

$$\begin{aligned} H(X) - H(X|X') \geq H(X) - H(X|Y) \\ \Rightarrow H(X|X') \leq H(X|Y) \end{aligned} \tag{10}$$

Considering Criterion 2.4, an effective SBF attenuation algorithm results in significantly smaller $H(X|X')$ in comparison with other SBF attenuation algorithms. Criterion 2.4 forms a necessary condition to ensure that the acquired time series is primarily due to cortical activity that is affected by SBF than vice-versa, as demonstrated through the following Theorem.

Theorem 2.3. *Let X, C, and Y represent recorded fNIRS, actual cortical activity, and SBF such that* $X = C + Y$. *Then, Criterion 2.4 is a necessary condition if C is reflective of cortical activity.*

Proof: Taking derivative of X = C + Y with respect to C (i.e., variable of interest), we have:

$$\frac{dX}{dC} = \frac{d(C+Y)}{dC} = 1 \tag{11}$$

In addition, the entropy of a transformed random variable X is Stone (2015, p. 119):

$$H(X) = H(C) + E[log|\frac{dX}{dC}|] \tag{12}$$

Substituting Equation (11) in Equation (12), we have:

$$H(X) = H(C) + E[log(1)] = H(C) \tag{13}$$

which, in turn, implies that

$$H(X|C) = 0 \tag{14}$$

and therefore,

$$I(X; C) = H(X) - H(X|C) = H(X) \tag{15}$$

Considering the fact that $I(X; C) \geq 0,\ \forall X, C$, we get

$$H(X) \geq 0 \tag{16}$$

which implies that the interval within which X lies i.e., $X \in [a, b]$ must satisfy $b - a \geq 1$ since $b - a < 1 \Rightarrow H(X) < 0$[2]. This observation along with Theorem 2.1 indicate that

$$0 \leq H(X|Y) \leq H(X) \tag{17}$$

with $H(X|Y) = H(X)$ if and only if X and Y are independent and $H(X|Y) = 0$ when $X = Y$. Now, if Criterion 2.4 is not valid, it must only be the case that

$$H(X|Y) < H(X|C) \Rightarrow H(X|Y) < 0 \tag{18}$$

due to Equation (14)[3]. However, this violates the Equation (17). □

In addition, SBF attenuation must ensure that attenuated effect is maximally reflective of Y than X, thereby inducing minimum loss of information content of X once SBF attenuation is complete.

Criterion 2.5. *Preserved information content of X in X' is maximized if attenuation primarily reduces the effect of SBF. Using Theorem 2.1, we have:*

$$H(X|Y) \leq H(X) \tag{19}$$

and

$$H(X'|Y) \leq H(X') \tag{20}$$

Considering Equations (19, 20) and applying Criterion 2.3 and Criterion 2.4, we get:

$$\begin{aligned} H(X|X') \leq H(X|Y) \leq H(X'|Y) \leq H(X') \\ \Rightarrow H(X|X') \leq H(X') \end{aligned} \tag{21}$$

Criterion 2.5, in turn, indicates that an SBF algorithm that significantly (i.e., in comparison with other such algorithms) maximizes the inequality $H(X') - H(X|X') \geq 0$ also attains the maximum frontal activity's information preservation in the resulting fNIRS time series.

[2]Continuous random variables can have negative entropy. For instance, $H(X) < 0$ if $\sigma_X^2 < \frac{1}{2\pi e}$ or $\mu_X < \frac{1}{e}$ in case of normal and Poisson distributions.
[3]If $H(X|Y) \leq 0$ in Equation (18), indicating the possibility for $H(X|Y) = 0$, then $H(X|Y) = 0 \Rightarrow H(X|Y) = H(X|C) \Rightarrow Y = C$ which contradicts X = C + Y.

2.2. Simulation-Based Verification

We simulated (**Figure 2**) four random time series of length 3,000 out of which 600 and 2,500 data points were used as resting and task periods, respectively. We considered four time series to adhere with the number of channels in adapted fNIRS device in this study. In addition, ICA- and PCA-based algorithm require more than a single sequence for their components' calculation. The reason behind 600 and 2,500 data points split was due to the requirement of resting data by PCA-based SBF attenuation algorithm (Zhang et al., 2005) to calculate the global trend in given time series (e.g., global hemodynamic responses such as SBF) in the form of principal components. We chose 600 data points to mimic the 1-min-long resting period in our realtime experimental settings (i.e., 60 s × 10.0 Hz sampling rate of our fNIRS device). This, in turn, resulted in the use of 2,500 data points during the PCA- and ICA-based algorithms analyses. We repeated this random time series simulation for fifty rounds ($M = 5.76$, $SD = 18.61$). Furthermore, we simulated SBF as a Gaussian noise with the same length i.e., 3,000 data points (50 different series one for each round of simulated time series above) with their mean and standard deviation equals 3 times the corresponding simulated channels time series mean and standard deviation ($M = 15.56$, $SD = 43.25$). This noise was also added to the first 600 data points of each of the simulated sequences (i.e., simulated resting portion for PCA-based SBF attenuation) to mimic the global effect of SBF. We report the averaged analysis results of these fifty simulation rounds for simulation-based verification of Criterion 2.1 through Criterion 2.5.

2.3. Participants

We conducted three experiments, namely, verbal fluency task (referred to as VFT hereafter), conversation task experiment (referred to as CTE hereafter), and logical memory test (LMT hereafter). Two different groups of 20 (10 females and 10 males, $M = 70.20$, $SD = 3.78$) and 18 (6 females and 12 males, $M = 72.31$, $SD = 4.16$) older adults participated in VFT and CTE. On the other hand, LMT included thirty two (sixteen females and sixteen males, $M = 20.50$, $SD = 1.80$) younger adults. We were unable to record fNIRS data from two participants during VFT and six participants in LMT. Therefore, these individuals were excluded from our analyses.

Choice of VFT was to ensure the correctness as well as effectiveness of our criteria in quantification of the SBF attenuation and frontal activity's information preservation in a fine-grained working memory task. On the other hand, CTE allowed us to evaluate our analysis results in a naturalistic setting. Last, we included LMT to verify our results are unaffected by age of the participants.

All participants were right-handed (confirmed using FLANDERS (Nicholls et al., 2013) handedness questionnaire), were free of neurological and psychiatric disorders, and had no history of hearing impairment. Prior to the data collection, we received approval (approval code: 16-601-1) from the ethical committee at the Advanced Telecommunications Research Institute International (ATR), Kyoto, Japan. All subjects gave written informed consent. Subjects were seated on an easy

armchair in the sound-attenuated experimental room, with instructions to fully relax and their eyes closed while resting.

2.3.1. VFT

We adapted the protocol by Takahashi et al. (2011) in their study of SBF effect on fNIRS time series. It consisted of two blocks. Each block consisted of a 6-s-long word generation. The word generation period was preceded with 30 s of silence period and followed by 70 s of control periods. During the word generation period, participants had to generate as many words as possible that started with the syllable that was auditorily presented every 20 s. In the control period, participants were instructed to repeat five syllables: /a/, /i/. /u/, /e/, and /o/. This task was also used by Sato et al. (2016) in their comparative fMRI-fNIRS analysis of reduction of SBF interference on fNIRS time series of frontal brain activity using their proposed GLM-based approach.

We started each experiment by acquiring a 1-min-long resting data, followed by its corresponding VFT session. We provided our participants with a 1-min-long resting break (while staying at their seat with their eyes closed) prior to the commencement of the experiment. We kept the content of the two blocks intact. However, we randomized the order of their occurrence among the participants. We used a speaker as a medium and generated the sequences of VFT using PsychoPy.

2.3.2. CTE

It included a 20-min-long conversation with participants about a site-seeing visit to Yakushima Island in southern Japan (in Japanese). We started by acquiring a 1-min-long resting data, followed by its corresponding 20-min-long experimental session. We provided our participants with a 1-min-long resting break (while staying at their seat with their eyes closed) prior to the commencement of the experiment. We kept the content of conversation intact. A female assistant, who was not aware of the purpose of this study, conversed with our participants. We controlled the conversational session in such a way that the operator was in charge of leading the topic, thereby requiring all the participants to respond to same series of statements and questions [e.g., their most interesting visited site(s), preferred cousin, etc.].

2.3.3. LMT

We adapted the protocol by Basso Moro et al. (2013). It started with participants listening to a 20-s-long story of the LMT (D. Wechsler, 1997) which was immediately followed by participants repeating the narrated story aloud, trying to recall as much of a detail as possible. The recall period lasted for 30 s. We started each experiment by acquiring a 1-min-long resting data, followed by its corresponding LMT session. We provided our participants with a 1-min-long resting break (while staying at their seat with their eyes closed) prior to the commencement of the experiment. We kept the content of the LMT story intact. A female assistant, who was not aware of the purpose of this study, read the stories to the participants through a speaker medium.

2.4. Data Acquisition

We used functional near infrared spectroscopy (fNIRS) (Ferrari and Quaresima, 2012; Dix et al., 2013) to collect frontal brain activity of the participants. We acquired fNIRS time series data of the participants using a wearable optical topography system "HOT-1000," developed by Hitachi High-Technologies Corporation (please refer to **Figure 1**). Participants wore this device on their forehead. It records the frontal brain activity through detection of total blood flow via emitting a wavelength laser light (810 nm) at 10.0 Hz sampling rate. Data acquisition is carried out through four channels (i.e., $Left_1$, $Left_3$, $Right_1$, and $Right_3$, as shown in **Figure 1**). Subscripted numerical values that are assigned to these channels specify their respective source-detector distances. In other words, $Left_1$ and $Right_1$ have a 1.0 cm and $Left_3$ and $Right_3$ have 3.0 cm source-detector distances, respectively. Research findings indicate that short source-detector channels [e.g., 0.5 cm (Takahashi et al., 2011), 1.0 cm (Gagnon et al., 2011), 1.5 cm (Sato et al., 2013, 2016; Kiguchi and Funane, 2014), and 2.0 cm (Yamada et al., 2009)] are mostly representatives of scalp hemodynamics than cortical blood flow (CBF). Moreover, choice of 3.0 cm source-detector distance is customary in NIRS-based studies of brain activity (Yamada et al., 2009; Gagnon et al., 2011; Takahashi et al., 2011; Sato et al., 2013, 2016; Kiguchi and Funane, 2014). It is also worth noting that Zhang et al. (2005) and Kohno et al. (2007) adapted this source-detector distance in their original articles on PCA- and ICA-based SBF attenuation algorithms. Therefore, we primarily report our analysis results on long source-detector channels [$Left_3$ in the main body of this article and $Right_3$ in **Supplementary Material** (SM)].

We placed a laser Doppler tissue blood flow meter probe (FLO-C1, Omegawave Incorporated, Tokyo, Japan) on participants' forehead close to the $Left_1$ for SBF recording. It collected data from the scalp layer within 1.0 mm from the probe and its analog output was recorded simultaneously alongside the fNIRS recording. This device uses a laser beam with a wavelength of 780.0 nm and has a sampling rate of 10.0 Hz that matches our fNIRS device sampling rate. This device has also been adapted by Takahashi et al. (2011) during their SBF effect study.

To ensure synchronized data acquisition across sensors, we collected data streams for NIRS and SBF through "*labstreaminglayer*" system.

2.5. Data Preprocessing

First, we baseline-normalized the data via subtracting the mean of 1-min-long resting period. This step that is customary in fMRI/fNIRS research is based on the assumption that it removes the brain activity that was present prior to the start of the task (as reflected in the time series data recorded during the resting period) and hence does not reflect the effect of the brain activation during the task period. Next and in oder to attenuate the effect of systemic physiological artifacts (Tak and Ye, 2014) (e.g., cardiac pulsations, respiration, etc.) we applied a one-degree polynomial butter worth filter with 0.01 Hz and 0.6 Hz for low and high bandpass. This was followed by linear detrending. Detrending of the signal that is adapted from signal processing and time series analysis and forecasting is a necessary step to

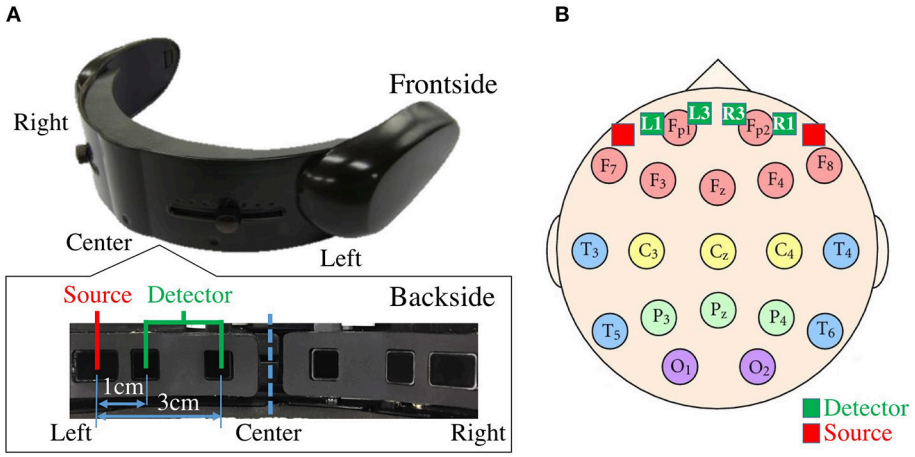

FIGURE 1 | (A) fNIRS device in present study. Bottom subplot on left shows arrangement of source-detector of four channels of this device. Distances between short (i.e., 1.0 cm) and long (i.e., 3.0 cm) source and detector of left and right channels are shown. **(B)** Arrangement of 10–20 International Standard System: In this figure, relative locations of channels of fNIRS device in our study (i.e., L1, L3, R1, and R3) are depicted in red (i.e., sources) and green (i.e., detectors) squares. L1, R1, L3, and R3 are channels with short (i.e., 1.0 cm) and long (i.e., 3.0 cm) source-detector distances.

ensure that assumptions of stationarity and homoscedasticity (as reflected in wide spread application of linear models in analysis of fNIRS/fMRI time series) are not strongly violated (e.g., due to seasonality and/or repetitive increasing/decreasing patterns) by acquired fNIRS signal.

We adapted the SBF attenuation algorithms by Zhang et al. (2005) (referred to as PCA-based hereafter) and Kohno et al. (2007) (referred to as ICA-based hereafter) in present study. The first approach utilizes an eigenvector-based spatial filtering method that is applied to the rest (baseline) period, thereby removing the first r spatial eigenvectors calculated from the baseline data by PCA from the fNIRS time series that are recorded during the task period. We used the resting period time series of the four channels of our device (**Figure 1**), per participant, for this purpose. Given the combination of short (i.e., $Left_1$ and $Right_1$) and long (i.e., $Left_3$, , and $Right_3$) source-detector channels of our device, the PCA-based algorithm is able to capture the components that best represent global hemodynamics, as noted by Zhang et al. (2005). This is due to the results that indicate the short source-detector channels [e.g., 0.5 cm (Takahashi et al., 2011), 1.0 cm (Gagnon et al., 2011), 1.5 cm (Sato et al., 2013, 2016; Kiguchi and Funane, 2014), and 2.0 cm (Yamada et al., 2009)] are mostly representatives of scalp hemodynamics and the long source-detector channels are suitable for recording of the CBF (Yamada et al., 2009; Gagnon et al., 2011; Takahashi et al., 2011; Sato et al., 2013, 2016; Kiguchi and Funane, 2014). It is worth noting that Zhang et al. (2005) also adapted the 3.0 cm source-detector distance (i.e., similar to $Left_3$, , and $Right_3$ in our case) for capturing the CBF in their original article on PCA-based SBF attenuation algorithm. On the other hand, ICA-based SBF attenuation algorithm (Kohno et al., 2007) removes the component that has the highest coefficient of spatial uniformity (i.e., the absolute value of the coefficient of variation; Everitt, 1998) among the independent components as a representative of the global scalp-hemodynamic component. Similar to PCA-based algorithm, we used the four channels of our device to determine the component with coefficient of spatial uniformity. It is worth noting that Kohno et al. (2007) also adapted the 3.0 cm source-detector distance (i.e., similar to $Left_3$, , and $Right_3$ in our case) for capturing the CBF in their original article on ICA-based SBF attenuation algorithm.

Sato et al. (2016) used the PCA-based algorithm after preprocessing steps for SBF attenuation. On the other hand, they utilized the ICA-based algorithm prior to preprocessing steps. These orders for application of SBF attenuation [i.e., preprocessing the fNIRS time series after (in case of ICA-based) and before (in case of PCA-base) SBF attenuation] were reported by Kohno et al. (2007) and Zhang et al. (2005) as well. Therefore, we followed the same orderings while applying these algorithms for attenuation of the effect of SBF on fNIRS time series data of cortical activity of our participants.

Although Zhang et al. (2005) did not provide any specific reason for selection of the number of components, they considered the combination of the first three components (referred to as PC123 hereafter) to be an adequate choice for attenuation of the SBF effect. On the other hand, Sato et al. (2016) argued that the difference between the first three components in contrast with only the first component (referred to as PC1 hereafter) is non-significant. Subsequently, they adapted the first component in their analysis. In present study, we used these two settings. However, considering the explanatory power of the first three components in PCA-based approach (Zhang et al., 2005; Sato et al., 2016), we also included the combination of first two components (referred to as PC12 hereafter) in our analyses. On the other hand, we followed Kohno et al. (2007) and removed the component with highest coefficient of spatial uniformity

(referred to as IC1 hereafter) in case of ICA-based SBF attenuation algorithm.

2.6. Statistical Analysis

First, we applied Wilcoxon rank sum (i.e., one-sample) test to determine the effect of SBF on fNIRS (i.e., $TE(Y \rightarrow X)$) time series of frontal brain activity of participants (in both, VFT and CTE). This was followed by testing Criterion 2.1 through Criterion 2.5 to determine the utility of PCA- and ICA-based algorithms and their respective adapted components (i.e., PC1, PC12, PC123 in case of PCA-based and IC1 in case of ICA-based SBF attenuations) in reduction of the effect of SBF on fNIRS while preserving information content of frontal brain activity.

In case of Criterion 2.1, we performed Kruskal-Wallis test on combination of TE before [i.e., $TE(Y \rightarrow X)$] along side after [i.e., $TE(Y \rightarrow X')$] SBF attenuation by each of PC1, PC12, PC123, and IC1 to determine any significance induced by the choice of these components in reduction of TE. This was followed by *post-hoc* paired Wilcoxon rank sum test.

We followed the same steps in case of Criterion 2.2 and Criterion 2.3, replacing TE before [i.e., $TE(Y \rightarrow X)$] and after [i.e., $TE(Y \rightarrow X')$] with the "reduction of SBF-related information in frontal brain activity before [i.e., $H(Y|X)$] and after [i.e., $H(Y|X')$] SBF attenuation," in case of Criterion 2.2, and "reduction of correspondence between SBF and fNIRS time series of frontal brain activity before [i.e., $H(X|Y)$] and after [i.e., $H(X'|Y)$] SBF attenuation," in case of Criterion 2.3, respectively.

In case of Criterion 2.4, we performed Kruskal-Wallis test on combination of $H(X|Y)$ alongside the measured $H(X|X')$ by each of PC1, PC12, PC123, and IC1 to determine any significance induced by the choice of these components in retaining the correspondence between time series of frontal activity before and after application of SBF attenuation. This was followed by *post-hoc* paired Wilcoxon rank sum test.

In case of Criterion 2.5, we first applied a paired Wilcoxon rank sum (i.e., two-sample) between $H(X|X')$ and $H(X')$ for each of the components (i.e., PC1, PC12, PC123, and IC1) separately, thereby signifying their respective effect in preservation of information content of frontal brain activity. Next, we performed Kruskal-Wallis test on combination of preserved frontal brain activity [i.e., $H(X') - H(X|X')$] by each of PC1, PC12, PC123, and IC1 to quantitatively determine any significance induced by the choice of these components in such an information preservation. This was followed by *post-hoc* paired Wilcoxon rank sum between every pair of these components, thereby determining the component(s) that significantly maximize such a preservation of information content of frontal brain activity in comparison with other components.

For Kruskal-Wallis, we reported the effect size $r = \sqrt{\frac{\chi^2}{N}}$, with N denoting the sample size, as suggested by Rosenthal and DiMatteo (2001). In case of Wilcoxon test, we used $r = \frac{W}{\sqrt{N}}$ (Tomczak and Tomczak, 2014) as effect size with W denoting the Wilcoxon statistics and N is the sample size. All results reported are Bonferroni corrected (i.e., multiplying the p-values with the sample size, given the use of non-parametric tests). We used JIDT (Lizier, 2014) for calculation of TE, MI, and conditional entropies. All statistical analyses were carried out in Matlab R2016a environment. We used Gramm (Morel, 2018) for data visualization. We used Python 2.7 for simulated data generation, realtime data acquisition and processing, and information-theoretic measures computation. All statistical analyses were carried out in Matlab R2016a.

3. RESULTS

3.1. Simulation-Based Verification

Figure 2A corresponds to the grand-average of the computed TE values for lags 1 through 100 (i.e., up to 10 s of lag, considering the sampling rate of 10.0 Hz of our device during the real-time data acquisition). This subplot indicates that maximum transferred information from simulated noise to simulated channels was, on average, at lag = 36 (i.e., 3.6 s in adapted fNIRS device in present study). This was the lag we used during our analyses. **Figure 2B** visualizes a sample spatial map of eigenvectors by PCA-based SBF attenuation algorithm along with the sample original simulated time series (in matrix forms for better visualization purpose) before and after application of PC1, PC12, and PC123 components. Distinctive effect of these components on the simulated data is evident in this subplot. We observed significant differences between data before and after application of PC1 [$p < 0.001$, $W_{(7,\,998)} = 24.21$, $r = 0.27$, $M_{Before} = 8.46$, $SD_{Before} = 12.91$, $M_{PC1} = 1.77$, $SD_{PC1} = 10.10$], PC12 [$p < 0.001$, $W_{(7,\,998)} = 29.74$, $r = 0.33$, $M_{PC12} = 0.52$, $SD_{PC12} = 10.06$], and PC123 [$p < 0.001$, $W_{(7,\,998)} = 35.55$, $r = 0.40$, $M_{PC123} = 0.14$, $SD_{PC123} = 6.22$].

Figure 2C shows a sample Gaussian noise (blue) along with the computed IC1 by ICA-based SBF attenuation algorithm (green) (pertinent to the case in which simulated channel 1 was selected as component with highest coefficient of spatial uniformity). Although this algorithm resulted in selection of different simulated channels as the component with highest coefficient of spatial uniformity (i.e., the absolute value of the coefficient of variation; Everitt, 1998) (**Figure 2D**, Ch1 = 20.00%, Ch2 = 16.00%, Ch3 = 40.00%, Ch4 = 24.00%), these components were significantly correlated with simulated noise (Ch1: $r = 0.73$, $p < 0.001$, Ch2: $r = 0.78$, $p < 0.001$, Ch3: $r = 0.78$, $p < 0.001$, and Ch4: $r = 0.89$, $p < 0.001$). On the other hand, PCA-based algorithm (**Figure 2E**) exhibited a higher specificity in selecting the principal components (PC1 = 89.00%, PC12 = 8.10%, PC123 = 2.90%).

3.1.1. Criterion 2.1: $TE(Y \rightarrow X') \leq TE(Y \rightarrow X)$

Kruskal-Wallis test implied significant effect of choice of components [$p < 0.001$, $H_{(4,\,249)} = 152.35$, $r = 0.61$, $M = 0.22$, $SD = 0.01$]. Moreover, *post-hoc* comparison implied that all components significantly reduced SBF effect in comparison with $TE(Y \rightarrow X)$ [PC1: $p < 0.001$, $W_{(98)} = 8.61$, $r = 0.86$, $M = 0.02$, $SD = 0.01$, PC12: $p < 0.001$, $W_{(98)} = 8.61$, $r = 0.86$, $M = 0.01$, $SD = 0.01$, PC123: $p < 0.001$, $W_{(98)} = 8.61$, $r = 0.86$, , $M = 0.02$, $SD = 0.01$, IC1: $p < 0.001$, $W_{(98)} = 8.61$, $r = 0.86$, $M = 0.02$, $SD = 0.01$]. *Post-hoc* comparison indicated that PC12 significantly performed better in attenuation of the effect of SBF than PC1 [$p < 0.001$, $W_{(98)} = 4.11$, $r = 0.41$], PC123 [$p < 0.001$, $W_{(98)} =$

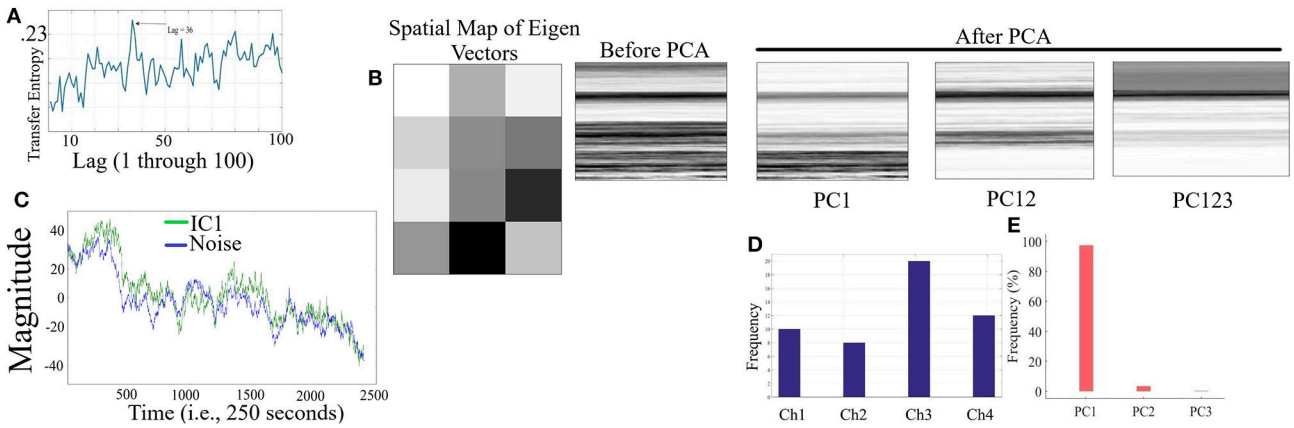

FIGURE 2 | Simulated Time Series **(A)** Grand-average (i.e., fifty rounds of simulation) of computed TE values for Lag = 1, . . . , 100 (i.e., up to 10 s of lag, considering the sampling rate of 10.0 Hz in our device during real-time data acquisition). Maximum TE was, on average, at Lag = 36 (equivalent to time = 3.6 s of adapted fNIRS device in present study (i.e., sampling rate = 10.0 Hz) **(B)** Sample spatial map of eigenvectors by PCA-based SBF attenuation algorithm along with the sample original simulated time series (in matrix forms for better visualization purpose) before and after application of PC1, PC12, and PC123 components. Distinctive effect of these components on the simulated data is evident in this subplot. All matrices are scaled within [0, 1] interval for ease of comparison. **(C)** Sample Gaussian noise (blue) and sample IC1 component (green) computed by ICA-based SBF attenuation algorithm. In this subplot, the plotted IC1 component pertains to the case in which simulated channel 1 was selected as component with highest coefficient of spatial uniformity. **(D)** Frequency of selected simulated channels with highest coefficient of spatial uniformity by ICA-based SBF attenuation algorithm **(E)** Percentages of the variance-explained by each of the principal components (i.e., PC1, PC12, PC123) of PCA-based SBF attenuation algorithm. Subplots **(D,E)** correspond to all fifty rounds of simulations.

6.34, $r = 0.63$], and IC1 [$p < 0.001$, $W_{(98)} = 4.90$, $r = 0.49$]. On the other hand, we observed non-significant differences between PC1 and PC123 [$p = 0.14$, $W_{(98)} = 1.52$, $r = 0.15$], PC1 and IC1 [$p = 0.12$, $W_{(98)} = 1.52$, $r = 0.15$], as well as PC123 and IC1 [$p = 0.13$, $W_{(98)} = 1.52$, $r = 0.15$]. **Figure 3**, subplot C1, illustrates these results.

3.1.2. Criterion 2.2: $H(Y|X) \leq H(Y|X')$

Kruskal-Wallis implied a significant effect of choice of components [$p < 0.001$, $H_{(4, 249)} = 234.13$, $r = 0.94$]. *Post-hoc* comparison indicated a significant reduction of SBF-related information in frontal brain activity of participants by PC1 [$p < 0.001$, $W_{(98)} = 8.61$, $r = 0.86$, $M_{H(Y|X)} = 4.03$, $SD_{H(Y|X)} = 0.01$, $M_{PC1} = 4.06$, $SD_{PC1} = 0.03$], PC12 [$p < 0.001$, $W_{(98)} = 8.61$, $r = 0.86$, $M_{PC12} = 4.13$, $SD_{PC12} = 0.01$]. Interestingly, application of PC123 resulted in a significantly reduced information [$p < 0.001$, $W_{(98)} = 8.6$, $r = 0.86$, $M_{PC12} = 3.96$, $SD_{PC12} = 0.02$], and IC1 [$p < 0.001$, $W_{(98)} = 8.61$, $r = 0.86$, $M_{IC1} = 4.05$, $SD_{IC1} = 0.02$]. Additionally, this comparison indicated that adaptation of PC1 resulted in a significantly more reduced SBF-related information than PC123 [$p < 0.001$, $W_{(98)} = 8.61$, $r = 0.86$] as well as IC1 [$p < 0.001$, $W_{(98)} = 6.61$, $r = 0.86$]. In addition, we found PC12 significantly more effective than PC1 [$p < 0.001$, $W_{(98)} = 8.61$, $r = 0.86$], PC123 [$p < 0.001$, $W_{(98)} = 8.61$, $r = 0.86$] and IC1 [$p < 0.001$, $W_{(98)} = 8.61$, $r = 0.86$]. Last, we observed a significant differences between IC1 and PC123 was significant [$W_{(98)} = 8.61$, $r = 0.86$]. **Figure 3**, subplot C2, shows these results.

3.1.3. Criterion 2.3: $H(X|Y) \leq H(X'|Y)$

Kruskal-Wallis indicated a significant effect of choice of components in resulting fNIRS data [$p < 0.001$, $H_{(4, 249)} = 238.00$, $r = 0.96$]. Whereas *post-hoc* comparison suggested that PC123 was ineffective in satisfying this Criterion 2.3 [PC123: $p < 0.001$, $W_{(98)} = 8.61$, $r = 0.86$, $M_{H(X|Y)} = 3.49$, $SD_{H(X|Y)} = 0.04$, $M_{PC123} = 3.421$, $SD_{PC123} = 0.04$] all other components were significantly effective in reducing the degree of correspondence between SBF and fNIRS time series of frontal brain activity [PC1: $p < 0.001$, $W_{(98)} = 8.61$, $r = 0.86$, $M_{PC1} = 4.17$, $SD_{PC1} = 0.01$, PC12: $p < 0.001$, $W_{(98)} = 8.61$, $r = 0.86$, $M_{PC12} = 4.22$, $SD_{PC12} = 0.01$, IC1: $p < 0.001$, $W_{(98)} = 8.61$, $r = 0.86$, $M_{IC1} = 3.74$, $SD_{IC1} = 0.03$]. In addition, this comparison indicated that adaptation of PC12 yielded a significantly better performance than PC1 [$p < 0.001$, $W_{(98)} = 8.23$, $r = 0.82$], PC123 [$p < 0.001$, $W_{(98)} = 8.61$, $r = 0.86$], as well as IC1 [$p < 0.001$, $W_{(98)} = 8.61$, $r = 0.86$]. Moreover, PC1 was significantly more effective than PC123 [$p < 0.001$, $W_{(98)} = 8.61$, $r = 0.86$] and IC1 [$p < 0.001$, $W_{(98)} = 8.61$, $r = 0.86$]. Additionally, IC1 was significantly different from PC123 [$W_{(98)} = 8.61$, $r = 0.86$]. **Figure 3**, subplot C3, plots these results.

3.1.4. Criterion 2.4: $H(X|X') \leq H(X|Y)$

Kruskal-Wallis indicated a significant effect of choice of components [$p < 0.001$, $H_{(4, 249)} = 239.04$, $r = 0.96$]. *Post-hoc* comparison suggested that all components were significantly effective in retaining the correspondence between time series of frontal activity before and after application of SBF attenuation [PC1: $p < 0.001$, $W_{(98)} = 8.61$, $r = 0.86$, $M_{H(X|Y)} = 3.49$, $SD_{H(X|Y)} = 0.04$ $M_{PC1} = 3.32$, $SD_{PC1} = 0.01$, PC12: $p < 0.001$, $W_{(98)} = 8.61$, $r = 0.86$, $M_{PC1} = 3.28$, $SD_{PC12} = 0.03$, PC123: $p < 0.001$, $W_{(98)} = 8.61$, $r = 0.86$, $M_{PC123} = 3.41$, $SD_{PC123} = 0.05$, IC1: $p < 0.001$, $W_{(98)} = 8.61$, $r = 0.86$, $M_{IC1} = 3.38$, $SD_{IC1} = 0.01$]. Additionally, this comparison implied that PC12 resulted in significantly higher correspondence between time

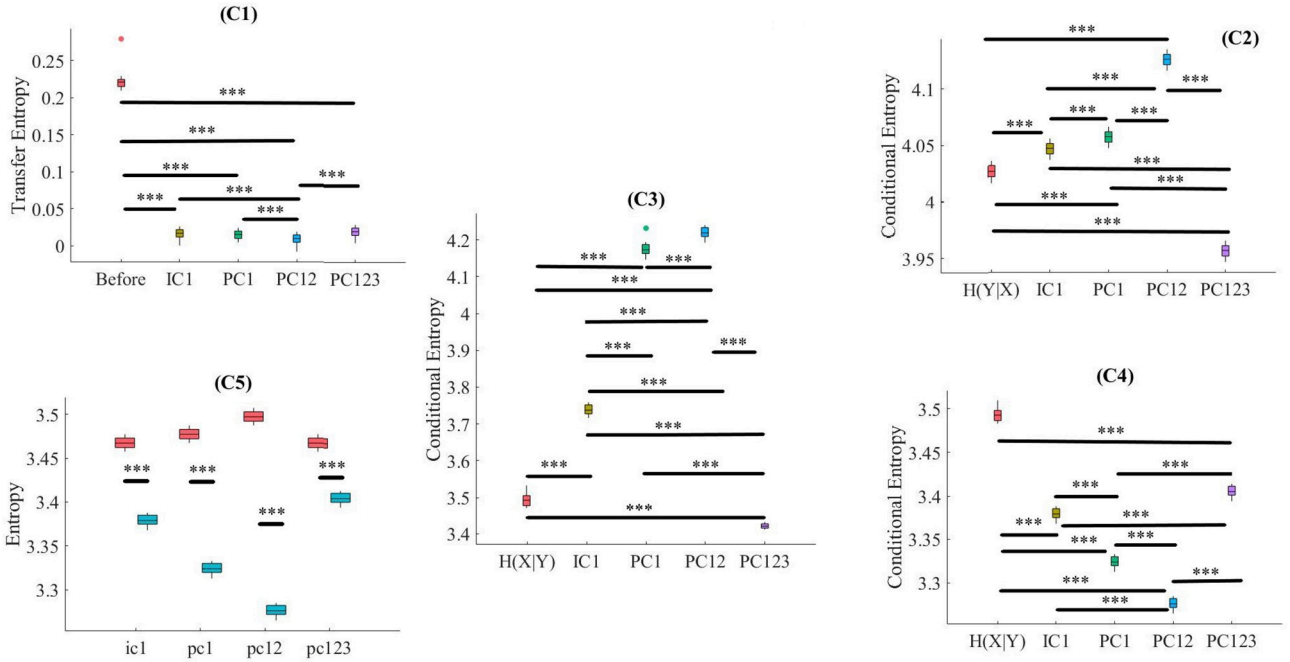

FIGURE 3 | Simulated Data. C1: Criterion 2.1: $TE(Y \rightarrow X') \leq TE(Y \rightarrow X)$, C2: Criterion 2.2: $H(Y|X) \leq H(Y|X')$, C3: Criterion 2.3: $H(X|Y) \leq H(X'|Y)$, C4: Criterion 2.4: $H(X|X') \leq H(X|Y)$, C5: Criterion 2.5: $H(X|X') \leq H(X')$. In these subplots, IC1, PC1, PC12, and PC123 refer to the measured quantity by these components after their respective SBF attenuation algorithms. Asterisks mark the components with significant difference (*$p < 0.05$, **$p < 0.01$, ***$p < 0.001$).

series of frontal brain activity before and after SBF attenuation than PC1 [$p < 0.001$, $W_{(98)} = 8.61$, $r = 0.86$], PC123 [$p < 0.001$, $W_{(98)} = 8.61$, $r = 0.86$], as well as IC1 [$p < 0.001$, $W_{(98)} = 8.613828$ $r = 0.861383$]. Similarly, PC1 performed significantly better than PC123 [$p < 0.001$, $W_{(98)} = 8.61$, $r = 0.86$] and IC1 [$p < 0.001$, $W_{(98)} = 8.61$, $r = 0.86$]. Lastly, IC1 was significantly more effective than PC123 [$p < 0.001$, $W_{(98)} = 8.61$, $r = 0.86$]. **Figure 3**, subplot C4, shows these results.

3.1.5. Criterion 2.5: $H(X|X') \leq H(X')$

Pairwise Wilcoxon rank sum suggested that all components preserved information content of frontal activity [PC1:$p < 0.001$, $W_{(98)} = 8.61$, $r = 0.86$, $M_{H(X|X')} = 3.32$, $SD_{H(X|X')} = 0.05$, $M_{H(X')} = 3.48$, $SD_{H(X')} = 0.06$, PC12:$p < 0.001$, $W_{(98)} = 8.61$, $r = 0.86$, $M_{H(X')} = 3.50$, $SD_{H(X')} = 0.07$, PC123: $p < 0.001$, $W_{(98)} = 8.61$, $r = 0.86$, $M_{H(X')} = 3.46$, $SD_{H(X')} = 0.07$, IC1: $p < 0.001$, $W_{(98)} = 8.61$, $r = 0.86$, $M_{H(X')} = 3.48$, $SD_{H(X')} = 0.06$]. **Figure 3**, subplot C5, depicts these results.

Kruskal-Wallis test indicated a significant effect of choice of component on preservation of information content of fNIRS time series [i.e., $H(X') - H(X|X') \geq 0$] [$p < 0.001$, $H_{(3, 199)} = 186.57$, $r = 0.94$]. *Post-hoc* paired comparison implied a significantly higher preservation of information content of frontal brain activity with respect to PC12 in comparison with PC1 [$p < 0.001$, $W_{(98)} = 8.61$, $r = 0.86$, $M_{PC1} = 0.15$, $SD_{PC1} = 0.01$, $M_{PC12} = 0.22$, $SD_{PC1} = 0.01$], PC123 [$p < 0.001$, $W_{(98)} = 8.61$, $r = 0.86$, $M_{PC123} = 0.06$, $SD_{PC1} = 0.03$], as well as IC1 [$p < 0.001$, $W_{(98)} = 8.61$, $r = 0.86$, $M_{IC1} = 0.09$, $SD_{IC1} = 0.01$].

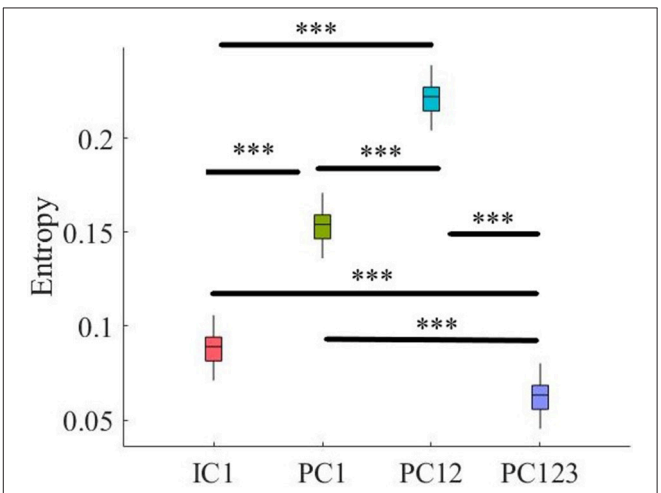

FIGURE 4 | Comparison of maximal preservation of information content of frontal brain activity (i.e., $H(X') - H(X|X') \geq 0$, Criterion 2.5) after application of PCA- and ICA-based SBF attenuation algorithms on simulated data. Asterisks mark the components with significant difference (*$p < 0.05$, **$p < 0.01$, ***$p < 0.001$).

PC1 was significantly more effective than and PC123 [$p < 0.001$, $W_{(98)} = 8.61$, $r = 0.86$] and IC1 [$p < 0.001$, $W_{(98)} = 8.61$, $r = 0.86$]. Last, we found that IC1 was significantly more effective than PC123 [$p < 0.001$, $W_{(98)} = 8.61$, $r = 0.86$]. **Figure 4** shows these results.

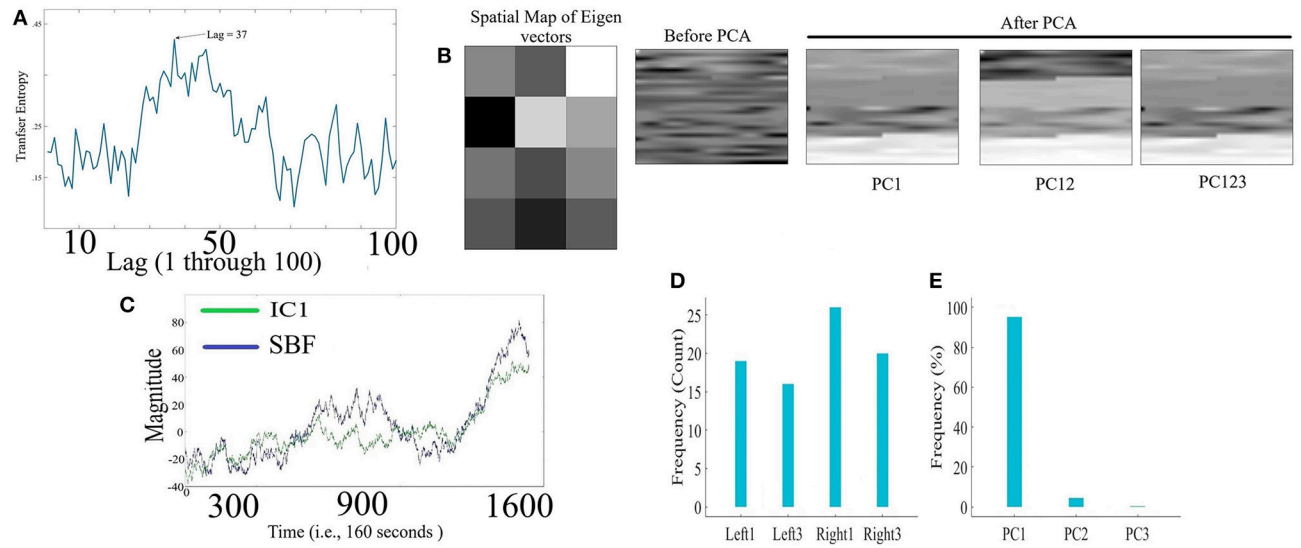

FIGURE 5 | VFT - **(A)** Grand-average of TE values for Lag = 1, . . . , 100 (i.e., up to 10 s of lag, sampling rate of 10.0 Hz in our device). Maximum TE was at Lag = 37 (equivalent to time = 3.7 s) **(B)** Sample spatial map of eigenvectors pertinent to first three principal components along with a sample PFC time series of a participant (in matrix forms for better visualization purpose) before and after application of PC1, PC12, and PC123 components. Distinctive effect of these components on the simulated data is evident in this subplot. All matrices are scaled within [0, 1] interval for ease of comparison. **(C)** Sample SBF (blue) and the corresponding IC1 component (green) computed by ICA-based SBF attenuation algorithm. The depicted IC1 component pertains to the case in which $Right_1$ was selected as component with highest coefficient of spatial uniformity. **(D)** Frequency of selected channels as a component with highest coefficient of spatial uniformity by ICA-based SBF attenuation algorithm for VFT dataset. **(E)** Percentages of the variance-explained by each of the principal components (i.e., PC1, PC12, PC123) of PCA-based SBF attenuation algorithm for VFT dataset.

3.2. VFT

Figure 5A corresponds to the grand-average of the computed TE values for lags 1 through 100 (i.e., up to 10 s of lag, considering the sampling rate of 10.0 Hz of our device) in VFT. This subplot indicates that maximum SBF transferred information was, on average, at lag = 37 (i.e., 3.7 s). This was the lag we used during our analyses. Wilcoxon rank sum test implied significant effect of SBF on fNIRS time series of frontal brain activity of participants while performing VFT working memory task [$p < 0.001$, $W_{(125)} = 7.82$, $M = 0.44$, $SD = 0.15$, $r = 0.87$].

Figure 5B visualizes a sample spatial map of eigenvectors by PCA-based SBF attenuation algorithm along with a sample participant's PFC time series (in matrix forms for better visualization purpose) before and after application of PC1, PC12, and PC123 components. Distinctive effect of these components on participant's PFC time series is evident in this subplot. We observed significant differences between PFC time series before and after application of PC1 [$p < 0.001$, $W_{(2,\ 398)} = 6.67$, $r = 0.14$, $M_{Before} = 149.50$, $SD_{Before} = 19.13$, $M_{PC1} = 144.50$, $SD_{PC1} = 18.76$], PC12 [$p < 0.001$, $W_{(2,\ 398)} = 12.98$, $r = 0.27$, $M_{PC12} = 139.27$, $SD_{PC12} = 8.76$], and PC123 [$p < 0.001$, $W_{(2,\ 398)} = 6.66$, $r = 0.14$, $M_{PC123} = 145.00$, $SD_{PC123} = 16.23$].

Figure 5C shows a sample SBF (blue) along with the computed IC1 by ICA-based SBF attenuation algorithm (green) (pertinent to the case in which $Right_1$ was selected as the component with highest coefficient of spatial uniformity). Although this algorithm resulted in selection of different channels as the component with highest coefficient of spatial uniformity (**Figure 5D**, $Left_1 = 23.46\%$, $Left_3 = 19.75\%$, $Right_1 = 32.10\%$, $Right_3 = 24.69\%$), these components were significantly correlated with SBF ($Left_1$: 0.74, $p < 0.001$, $Left_3$: $r = 0.76$, $p < 0.001$, $Right_1$: $r = 0.80$, $p < 0.001$, and $Right_3$: $r = 0.86$, $p < 0.001$). On the other hand, PCA-based algorithm (**Figure 5E**) exhibited a higher specificity in selecting the principal components (PC1 = 95.15%, PC12 = 4.50%, PC123 = 0.35%).

In what follows, we examine the effectiveness of PCA- and ICA-based SBF attenuation algorithms on reduction of observed impact of SBF on fNIRS frontal brain activity as well as their utility in preservation of information content of this activity in resulting fNIRS time series through investigation of Criterion 2.1 through Criterion 2.5.

3.2.1. Criterion 2.1: $TE(Y \rightarrow X') \leq TE(Y \rightarrow X)$

Kruskal-Wallis test implied significant effect of choice of components [$p < 0.001$, $H_{(4,\ 629)} = 237.33$, $r = 0.61$]. Moreover, *post-hoc* comparison implied that all components significantly reduced SBF effect in comparison with $TE(Y \rightarrow X)$ [PC1: $p < 0.001$, $W_{(250)} = 7.82$, $M = 0.009$, $SD = 0.03$, $r = 0.49$, PC12: $p < 0.001$, $W_{(250)} = 7.82$, $M = 0.009$, $SD = 0.03$, $r = 0.49$, PC123: $p < 0.001$, $W_{(250)} = 7.82$, $M = 0.04$, $SD = 0.03$, $r = 0.49$, IC1: $p < 0.001$, $W_{(250)} = 7.82$, $M = 0.04$, $SD = 0.03$, $r = 0.49$]. On the other hand, whereas this comparison indicated non-significant difference between PC1 and PC12 [$p = 1.00$, $W_{(250)} = 0.002$, $r = 0.0$] as well as PC123 and IC1 [$p = 0.41$, $W_{(250)} = 0.83$, $r = 0.05$), we found significant differences in reduction of TE between PC1 and PC123 [$p < 0.001$, $W_{(250)} = 6.38$, $r = 0.40$], PC1 and IC1[$p < 0.001$, $W_{(250)} = 6.90$, $r = 0.43$], PC12 and PC123 [$p = < 0.001$, $W_{(250)} = 6.62$, $r = 0.42$], as well as PC12 and IC1 [$p <$

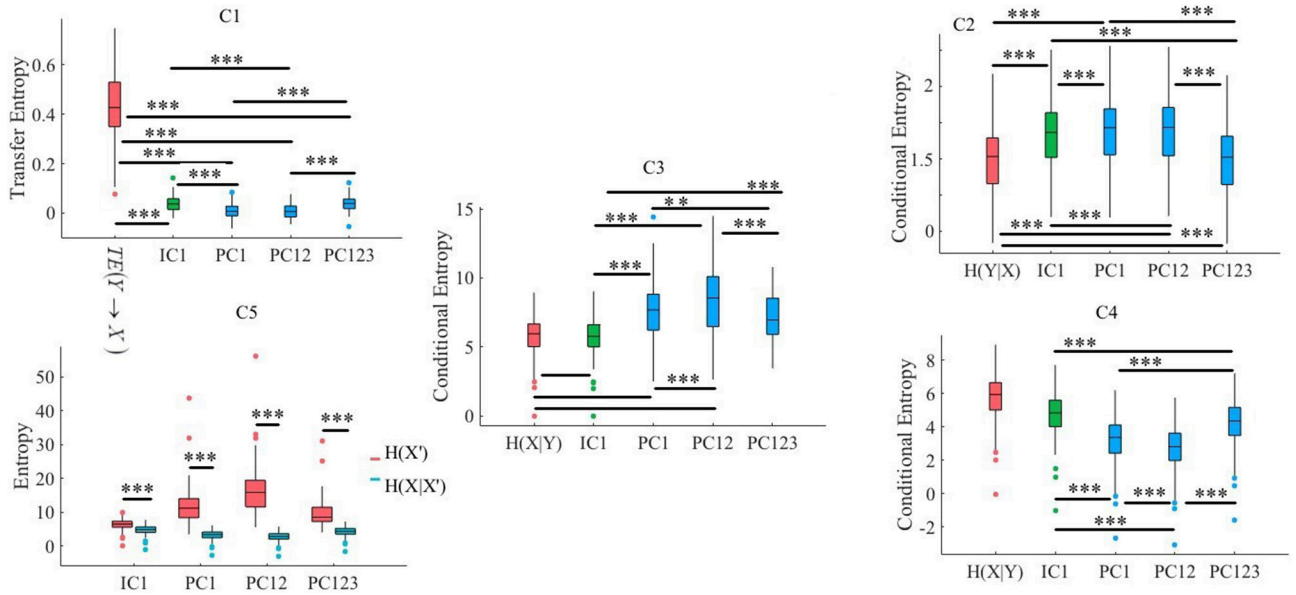

FIGURE 6 | VFT. C1: Criterion 2.1: $TE(Y \rightarrow X') \leq TE(Y \rightarrow X)$, C2: Criterion 2.2: $H(Y|X) \leq H(Y|X')$, C3: Criterion 2.3: $H(X|Y) \leq H(X'|Y)$, C4: Criterion 2.4: $H(X|X') \leq H(X|Y)$, C5: Criterion 2.5: $H(X|X') \leq H(X')$. In these subplots, IC1, PC1, PC12, and PC123 refer to the measured quantity by these components after their respective SBF attenuation algorithms. Asterisks mark the components with significant difference (*$p < 0.05$, **$p < 0.01$, ***$p < 0.001$).

0.001, $W_{(250)} = 6.51$, $r = 0.41$]. **Figure 6**, subplot C1, illustrates these results.

3.2.2. Criterion 2.2: $H(Y|X) \leq H(Y|X')$

Kruskal-Wallis implied a significant effect of choice of components [$p < 0.001$, $H_{(4, 629)} = 47.37$, $r = 0.27$]. *Post-hoc* comparison indicated a significant reduction of SBF-related information in frontal brain activity of participants by PC1 [$p < 0.001$, $W_{(250)} = 7.82$, $M_{H(Y|X)} = 1.52$, $SD_{H(Y|X)} = 0.50$, $M_{PC1} = 1.62$, $SD_{PC1} = 0.50$, $r = 0.49$], PC12 [$p < 0.001$, $W_{(250)} = 7.81$, $M_{PC12} = 1.63$, $SD_{PC12} = 0.50$, $r = 0.49$], and IC1 [$p < 0.001$, $W_{(250)} = 7.81$, $M_{IC1} = 1.57$, $SD_{IC1} = 0.50$, $r = 0.49$]. However, it was non-significant with respect to PC123 [$p = 0.20$, $W_{(250)} = 1.28$, $M_{PC123} = 1.53$, $SD_{PC1} = 0.50$, $r = 0.08$]. Additionally, this comparison indicated that adaptation of PC1 resulted in a significantly more reduced SBF-related information than PC123 [$p < 0.001$, $W_{(250)} = 7.81$, $r = 0.49$] as well as IC1 [$p < 0.001$, $W_{(250)} = 7.79$, $r = 0.49$]. Similarly, we found PC12 significantly more effective than PC123 [$p < 0.001$, $W_{(250)} = 7.82$, $r = 0.49$] and IC1 [$p < 0.001$, $W_{(250)} = 7.55$, $r = 0.49$]. Additionally, difference between IC1 and PC123 was significant [$p < 0.001$, $W_{(250)} = 7.82$, $r = 0.49$]. However, we found non-significant difference between PC1 and PC12 [$p = 0.15$, $W_{(250)} = 1.46$, $r = 0.09$]. **Figure 6**, subplot C2, shows these results.

3.2.3. Criterion 2.3: $H(X|Y) \leq H(X'|Y)$

Kruskal-Wallis indicated a significant effect of choice of components in resulting fNIRS data [$p < 0.001$, $H_{(4, 629)} = 83.87$, $r = 0.36$]. *Post-hoc* comparison suggested that all components were significantly effective in reducing the degree of correspondence between SBF and fNIRS time series of frontal brain activity [PC1:$p < 0.001$, $W_{(250)} = 7.62$, $M_{H(X|Y)} = 5.94$, $SD_{H(X|Y)} = 1.67$, $M_{PC1} = 7.66$, $SD_{PC1} = 2.04$, $r = 0.48$, PC12: $p < 0.001$, $W_{(250)} = 7.82$, $M_{PC12} = 8.37$, $SD_{PC12} = 2.26$, $r = 0.49$, PC123: $p < 0.001$, $W_{(250)} = 7.82$, $M_{PC123} = 7.16$, $SD_{PC123} = 1.71$, $r = 0.49$, IC1: $p < 0.001$, $W_{(250)} = 3.90$, $M_{IC1} = 5.81$, $SD_{IC1} = 1.64$, $r = 0.25$]. In addition, this comparison indicated that adaptation of PC12 yielded a significantly better performance than PC1 [$p < 0.001$, $W_{(250)} = 5.10$, $r = 0.32$], PC123 [$p < 0.001$, $W_{(250)} = 5.21$, $r = 0.33$], as well as IC1 [$p < 0.001$, $W_{(250)} = 7.79$, $r = 0.49$]. Moreover, PC1 was significantly more effective than PC123 [$p < 0.01$, $W_{(250)} = 2.92$, $r = 0.18$] and IC1 [$p < 0.001$, $W_{(250)} = 7.53$, $r = 0.47$]. Additionally, PC123 was significantly different from IC1 [$p < 0.001$, $W_{(250)} = 7.65$, $r = 0.48$]. **Figure 6**, subplot C3, plots these results.

3.2.4. Criterion 2.4: $H(X|X') \leq H(X|Y)$

Kruskal-Wallis indicated a significant effect of choice of components [$p < 0.001$, $H_{(4, 629)} = 136.25$, $r = 0.46$]. *Post-hoc* comparison suggested that all components were significantly effective in retaining the correspondence between time series of frontal activity before and after application of SBF attenuation [PC1: $p < 0.001$, $W_{(250)} = 7.25$, $M_{H(X|Y)} = 5.94$, $SD_{H(X|Y)} = 1.67$, $M_{PC1} = 3.32$, $SD_{PC1} = 1.64$, $r = 0.46$, PC12: $p < 0.001$, $W_{(250)} = 7.54$, $M_{PC12} = 2.88$, $SD_{PC12} = 1.63$, $r = 0.48$, PC123:$p < 0.001$, $W_{(250)} = 5.49$, $M_{PC123} = 4.38$, $SD_{PC123} = 1.65$, $r = 0.35$, IC1: $p < 0.001$, $W_{(250)} = 4.40$, $M_{IC1} = 4.84$, $SD_{IC1} = 1.63$, $r = 0.28$]. Additionally, this comparison implied that PC12 resulted in significantly higher correspondence between time series of frontal brain activity before and after SBF attenuation than PC1 [$p < 0.001$, $W_{(250)} = 7.82$, $r = 0.49$], PC123 [$p < 0.001$, $W_{(250)} =$

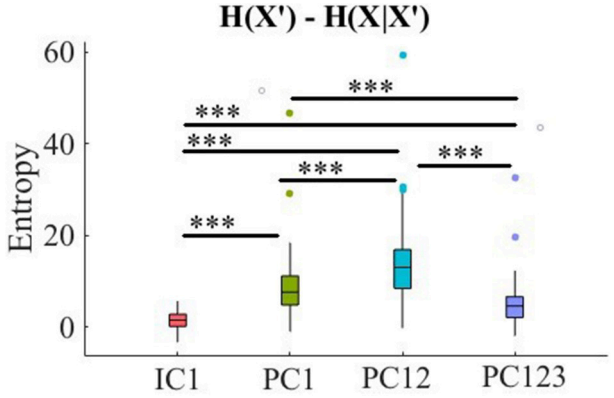

FIGURE 7 | Comparison of maximal preservation of information content of frontal brain activity (i.e., $H(X') - H(X|X') \geq 0$, Criterion 2.5) after application of PCA- and ICA-based SBF attenuation algorithms on VFT. Asterisks mark the components with significant difference (*$p < 0.05$, **$p < 0.01$, ***$p < 0.001$).

7.82, $r = 0.49$], as well as IC1 [$p < 0.001$, $W_{(250)} = 7.82$, $r = 0.49$]. This was followed by significantly better performance by PC1 in contrast with PC123 [$p < 0.001$, $W_{(250)} = 7.82$, $r = 0.49$] and IC1 [$p < 0.001$, $W_{(250)} = 7.82$, $r = 0.49$]. Lastly, PC123 was significantly more effective than IC1 [$p = 0.001$, $W_{(250)} = 7.82$, $r = 0.49$]. **Figure 6**, subplot C4, shows these results.

3.2.5. Criterion 2.5: $H(X|X') \leq H(X')$

Pairwise Wilcoxon rank sum suggested that all components preserved information content of frontal activity [PC1: $p < 0.001$ $W_{(250)} = 7.76$, $M_{H(X|X')} = 3.32$, $SD_{H(X|X')} = 1.64$, $M_{H(X')} = 11.89$, $SD_{H(X')} = 5.73$, $r = 0.49$, PC12: $p < 0.001$ $W_{(250)} = 7.81$, $M_{H(X|X')} = 2.88$, $SD_{H(X|X')} = 1.63$, $M_{H(X')} = 16.75$, $SD_{H(X')} = 7.61$, $r = 0.49$, PC123: $p < 0.001$ $W_{(250)} = 7.62$, $M_{H(X|X')} = 4.38$, $SD_{H(X|X')} = 1.65$, $M_{H(X')} = 9.66$, $SD_{H(X')} = 4.23$, $r = 0.48$, IC1: $p < 0.001$, $W_{(250)} = 5.37$, $M_{H(X|X')} = 4.84$, $SD_{H(X|X')} = 1.63$, $M_{H(X')} = 6.38$, $SD_{H(X')} = 1.82$, $r = 0.34$]. **Figure 6**, subplot C5, depicts these results.

Kruskal-Wallis test indicated a significant effect of choice of component on preservation of information content of fNIRS time series [i.e., $H(X') - H(X|X') \geq 0$] [$p < 0.001$, $H_{(3, 503)} = 68.52$, $r = 0.37$]. *Post-hoc* paired comparison implied a significantly higher preservation of information content of frontal brain activity with respect to PC12 in comparison with PC1 [$p < 0.001$, $W_{(250)} = 7.82$, $M_{PC12} = 13.86$, $SD_{PC12} = 8.42$, $M_{PC1} = 8.57$, $SD_{PC1} = 6.47$], PC123 [$p < 0.001$, $r = 0.49$, $W_{(250)} = 7.52$, $M_{PC123} = 5.27$, $SD_{PC123} = 4.86$, $r = 0.47$], as well as IC1 [$p < 0.001$, $W_{(250)} = 7.82$, $M_{IC1} = 1.54$, $SD_{IC1} = 2.15$, $r = 0.49$]. Furthermore, PC1 was significantly more effective than PC123 [$p < 0.001$, $W_{(250)} = 6.32$, $r = 0.40$] and IC1 [$p < 0.001$, $W_{(250)} = 7.82$, $r = 0.49$]. Lastly, we found PC123 significantly better than IC1 [$p < 0.001$, $W_{(250)} = 7.72$, $r = 0.49$]. **Figure 7** shows these results.

3.3. CTE

Figure 8A corresponds to the grand-average of the computed TE values for lags 1 through 100 (i.e., up to 10 s of lag, considering the sampling rate of 10.0 Hz) in CTE. This subplot indicates that maximum SBF transferred information was, on average, at lag = 30 (i.e., 3.0 s). This was the lag we used during our analyses. Wilcoxon rank sum test implied significant effect of SBF on fNIRS time series of frontal brain activity of participants during conversation [$p < 0.001$, $W_{(17)} = 3.72$, $M = 0.13$, $SD = 0.13$].

Figure 8B visualizes a sample spatial map of eigenvectors by PCA-based SBF attenuation algorithm along with a sample participant's PFC time series (in matrix forms for better visualization purpose) before and after application of PC1, PC12, and PC123 components. Distinctive effect of these components on participant's PFC time series is evident in this subplot. All matrices are scaled within [0, 1] interval for ease of comparison. We observed significant differences between PFC time series before and after application of PC1 [$p < 0.001$, $W_{(87, 998)} = 78.24$, $r = 0.26$, $M_{Before} = 0.71$, $SD_{Before} = 2.02$, $M_{PC1} = 0.03$, $SD_{PC1} = 0.28$], PC12 [$p < 0.001$, $W_{(87, 998)} = 102.05$, $r = 0.34$, $M_{PC12} = 0.004$, $SD_{PC12} = 0.13$], and PC123 [$p < 0.001$, $W_{(87, 998)} = 76.69$, $r = 0.26$, $M_{PC123} = 0.02$, $SD_{PC123} = 0.37$].

Figure 8C shows a sample SBF (blue) along with the computed IC1 by ICA-based SBF attenuation algorithm (green) (pertinent to the grand-average of the cases in which $Right_1$ was selected as the component with highest coefficient of spatial uniformity). Although this algorithm resulted in selection of different channels as the component with highest coefficient of spatial uniformity (**Figure 8D**, $Left_1 = 57.89\%$, $Left_3 = 10.53\%$, $Right_1 = 10.53\%$, $Right_3 = 21.05\%$), these components were significantly correlated with simulated noise ($Left_1$: 0.79, $p < 0.001$, $Left_3$: $r = 0.67$, $p < 0.001$, $Right_1$: $r = 0.81$, $p < 0.001$, and $Right_3$: $r = 0.76$, $p < 0.001$). On the other hand, PCA-based algorithm (**Figure 8E**) exhibited a higher specificity in selecting the principal components (PC1 = 97.42%, PC12 = 2.43%, PC123 = 0.15%).

In what follows, we examine the effectiveness of PCA- and ICA-based SBF attenuation algorithms on reduction of observed impact of SBF on fNIRS frontal brain activity as well as their utility in preservation of information content of this activity in resulting fNIRS time series through investigation of Criterion 2.1 through Criterion 2.5.

3.3.1. Criterion 2.1: $TE(Y \rightarrow X') \leq TE(Y \rightarrow X)$

Kruskal-Wallis implied a significant effect of choice of components [$p < 0.001$, $H_{(4, 89)} = 29.66$, $r = 0.57$]. In addition, *post-hoc* comparison suggested that all components significantly reduced SBF effect in comparison with $TE(Y \rightarrow X)$ [PC1: $p < 0.001$, $W_{(34)} = 3.72$, $M = 0.010$, $SD = 0.03$, $r = 0.62$, PC12: $p < 0.001$, $W_{(34)} = 3.72$, $M = 0.008$, $SD = 0.03$, $r = 0.62$, PC123: $p < 0.001$, $W_{(34)} = 3.72$, $M = 0.016$, $SD = 0.03$, $r = 0.62$, IC1: < 0.001, $W_{(34)} = 3.72$, $M = 0.017$, $SD = 0.03$, $r = 0.62$]. On the other hand, whereas this comparison indicated non-significant difference between PC1 and PC12 [$p = 0.95$, $W_{(34)} = 0.07$, $r = 0.01$] as well as PC123 and IC1 [$p = 0.65$, $W_{(34)} = 0.46$, $r = 0.08$], we found significant differences in reduction of TE between PC1 and PC123 [$p < 0.001$, $W_{(34)} = 3.42$, $r = 0.57$], PC1 and IC1[$p < 0.001$, $W_{(34)} = 3.68$, $r = 0.61$], PC12 and PC123 [$p < 0.05$, $W_{(34)} = 2.11$, $r = 0.35$], as well as PC12 and IC1 [$p < 0.03$, $W_{(34)} = 2.55$, $r = 0.43$]. **Figure 9**, subplot C1, shows these results.

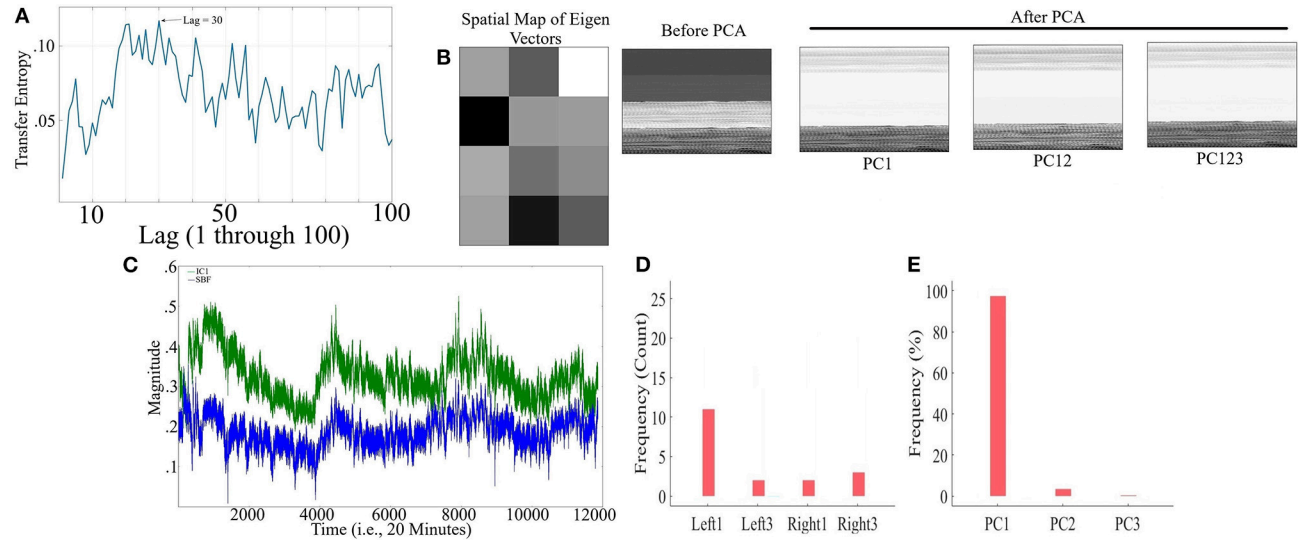

FIGURE 8 | CTE - **(A)** Grand-average of TE values for Lag = 1, . . . , 100 (i.e., up to 10 s of lag, considering the sampling rate of 10.0 Hz in our device). Maximum TE was at Lag = 30 (equivalent to time = 3.0 s) **(B)** Sample spatial map of eigenvectors by PCA-based SBF attenuation algorithm along with a sample participant's PFC time series (in matrix forms for better visualization purpose) before and after application of PC1, PC12, and PC123 components. Distinctive effect of these components on participant's PFC time series is evident in this subplot. All matrices are scaled within [0, 1] interval for ease of comparison. **(C)** Sample SBF (blue) and the corresponding IC1 component computed by ICA-based SBF attenuation algorithm (blue). The depicted IC1 component pertains to the case in which $Right_1$ was selected as component with highest coefficient of spatial uniformity. **(D)** Frequency of selected channels as a component with highest coefficient of spatial uniformity by ICA-based SBF attenuation algorithm for CTE dataset. **(E)** Percentages of the variance-explained by each of the principal components (i.e., PC1, PC12, PC123) of PCA-based SBF attenuation algorithm for CTE dataset.

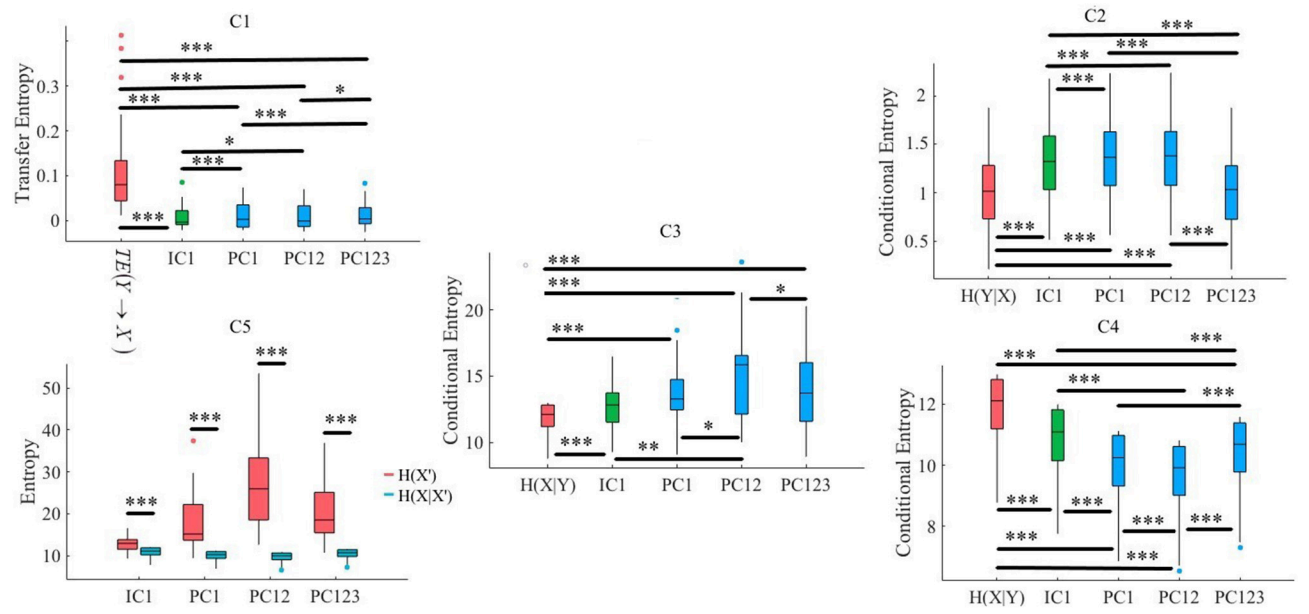

FIGURE 9 | CTE. C1: Criterion 2.1: $TE(Y \rightarrow X') \leq TE(Y \rightarrow X)$, C2: Criterion 2.2: $H(Y|X) \leq H(Y|X')$, C3: Criterion 2.3: $H(X|Y) \leq H(X'|Y)$, C4: Criterion 2.4: $H(X|X') \leq H(X|Y)$, C5: Criterion 2.5: $H(X|X') \leq H(X')$. In these subplots, IC1, PC1, PC12, and PC123 refer to the measured quantity by these components after their respective SBF attenuation algorithms. Asterisks mark the components with significant difference (*$p < 0.05$, **$p < 0.01$, ***$p < 0.001$).

3.3.2. Criterion 2.2: $H(Y|X) \leq H(Y|X')$

Kruskal-Wallis implied a significant effect of choice of components [$p < 0.05$, $H_{(4,\ 89)} = 10.55$, $r = 0.34$]. *Post-hoc* comparison implied a significant reduction of SBF-related information in frontal brain activity of participants by PC1 [$p < 0.001$, $W_{(34)} = 3.72$, $M_{H(Y|X)} = 1.04$, $SD_{H(Y|X)} = 0.47$,

$M_{PC1} = 1.31$ $SD_{PC1} = 0.47$, $r = 0.62$], PC12 [$p < 0.001$, $W_{(34)} = 3.72$, $M_{PC12} = 1.31$, $SD_{PC12} = 0.47$, $r = 0.69$], and IC1 [$p < 0.001$, $W_{(34)} = 3.72$, $M_{IC1} = 1.27$, $SD_{IC1} = 0.47$, $r = 0.69$]. However, it indicated non-significant with respect to PC123 [$p = 0.29$, $W_{(34)} = 1.07$, $M_{PC123} = 1.04$, $SD_{PC123} = 0.47$, $r = 0.18$]. Moreover, this comparison indicated that adaptation of PC1 resulted in a significantly more reduced SBF-related information than PC123 [$p < 0.001$, $W_{(34)} = 3.72$, $r = 0.69$] as well as IC1 [$p < 0.001$, $W_{(34)} = 3.72$, $r = 0.69$]. Similarly, we found PC12 significantly more effective than PC123 [$p < 0.001$, $W_{(34)} = 3.72$, $r = 0.69$] and IC1 [$p < 0.001$, $W_{(34)} = 3.72$, $r = 0.69$]. Additionally, difference between IC1 and PC123 was significant [$p < 0.001$, $W_{(34)} = 3.72$, $r = 0.69$]. However, we found non-significant difference between PC1 and PC12 [$p = 0.45$, $W_{(34)} = 0.76$, $r = 0.13$]. **Figure 9**, subplot C2, shows these results.

3.3.3. Criterion 2.3: $H(X|Y) \leq H(X'|Y)$

We observed a significant effect of choice of components in resulting fNIRS data [$p < 0.01$, $H_{(4, 89)} = 16.47$, $r = 0.51$]. *Post-hoc* comparison suggested that all components were significantly effective in reducing the degree of correspondence between SBF and fNIRS time series of frontal brain activity [PC1: $p < 0.001$, $W_{(34)} = 3.72$, $M_{(X|Y)} = 11.58$, $SD_{(X|Y)} = 1.53$, $M_{PC1} = 13.77$, $SD_{PC1} = 3.02$, $r = 0.69$, PC12: $p < 0.001$, $W_{(34)} = 3.72$, $M_{PC12} = 15.42$, $SD_{PC12} = 3.88$, $r = 0.69$, PC123: $p < 0.001$, $W_{(34)} = 3.72$, $M_{PC123} = 14.07$, $SD_{PC123} = 3.11$, $r = 0.69$, IC1: $p < 0.001$, $W_{(34)} = 3.72$, $M_{IC1} = 12.80$, $SD_{IC1} = 1.98$, $r = 0.69$]. Additionally, this comparison implied that adaptation of PC12 yielded a significantly better performance than PC1 [$p < 0.03$, $W_{(34)} = 2.20$, $r = 0.37$], PC123 [$p < 0.03$, $W_{(34)} = 2.46$, $r = 0.41$], as well as IC1 [$p < 0.01$, $W_{(34)} = 2.90$, $r = 0.48$]. However, we found non-significant difference between PC1 and PC123 [$p = 0.74$, $W_{(34)} = 0.33$, $r = 0.06$], PC1 and IC1 [$p = 0.20$, $W_{(34)} = 1.28$, $r = 0.21$], as well as PC123 and IC1 [$p = 0.17$, $W_{(34)} = 1.42$, $r = 0.24$]. **Figure 9**, subplot C3, shows these results.

3.3.4. Criterion 2.4: $H(X|X') \leq H(X|Y)$

Kruskal-Wallis indicated significant effect of choice of components [$p < 0.001$, $H_{(4, 89)} = 23.52$, $r = 0.51$]. *Post-hoc* comparison suggested that all components were significantly effective in retaining the correspondence between time series of frontal activity before and after application of SBF attenuation algorithms in comparison with SBF [PC1: $p < 0.001$, $W_{(34)} = 3.72$, $M_H(X|Y) = 11.58$, $SD_H(X|Y) = 1.53$, $M_{PC1} = 9.72$, $SD_{PC1} = 1.56$, $r = 0.69$, PC12: $p < 0.001$, $W_{(34)} = 3.72$, $M_{PC12} = 9.40$, $SD_{PC12} = 1.55$, $r = 0.69$, PC123: $p < 0.001$, $W_{(34)} = 3.72$, $M_{PC123} = 10.17$, $SD_{PC123} = 1.55$, $r = 0.69$, IC1: $p < 0.001$, $W_{(34)} = 3.72$, $M_{IC1} = 10.57$, $SD_{IC1} = 1.55$, $r = 0.69$]. Moreover, this comparison implied that PC12 resulted in significantly higher correspondence between time series of frontal brain activity before and after SBF attenuation than PC1 [$p < 0.001$, $W_{(34)} = 3.72$, $r = 0.69$], PC123 [$p < 0.001$, $W_{(34)} = 4.24$, $r = 0.71$], as well as IC1 [$p < 0.001$, $W_{(34)} = 3.72$, $r = 0.69$]. This was followed by significantly better performance by PC1 in contrast with PC123 [$p < 0.001$, $W_{(34)} = 3.72$, $r = 0.69$] and IC1 [$p < 0.001$, $W_{(34)} = 3.72$, $r = 0.69$]. Lastly, PC123 was significantly more effective than IC1 [$p = p < 0.001$, $W_{(34)} = 3.72$, $r = 0.69$]. **Figure 9**, subplot C4, shows these results.

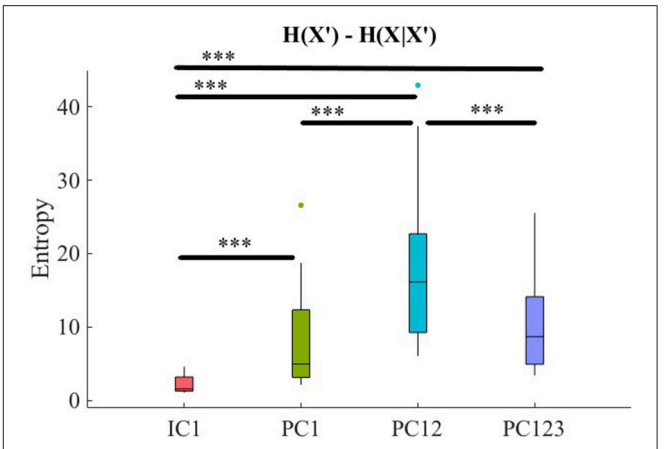

FIGURE 10 | Comparison of maximal preservation of information content of frontal brain activity (i.e., $H(X') - H(X|X') \geq 0$, Criterion 2.5) after application of PCA- and ICA-based SBF attenuation algorithms on CTE. Asterisks mark the components with significant difference (*$p < 0.05$, **$p < 0.01$, ***$p < 0.001$).

3.3.5. Criterion 2.5: $H(X|X') \leq H(X')$

Pairwise Wilcoxon rank sum suggested that all components preserved information content of frontal activity [PC1: $p < 0.001$, $W_{(34)} = 3.72$, $M_{H(X|X')} = 9.72$, $SD_{H(X|X')} = 1.56$, $M_{H(X')} = 18.17$, $SD_{H(X')} = 7.48$, $r = 0.69$, PC12: $p < 0.001$, $W_{(34)} = 3.72$, $M_{H(X|X')} = 9.40$, $SD_{H(X|X')} = 1.55$, $M_{H(X')} = 27.66$, $SD_{H(X')} = 11.71$, $r = 0.69$ PC123: $p < 0.001$, $W_{(34)} = -3.72$, $M_{H(X|X')} = 10.17$, $SD_{H(X|X')} = 1.55$, $M_{H(X')} = 20.58$, $SD_{H(X')} = 7.24$, $r = 0.88$, IC1: $p < 0.001$, $W_{(34)} = 3.72$, $M_{H(X|X')} = 10.57$, $SD_{H(X|X')} = 1.55$ $M_{H(X')} = 12.84$, $SD_{H(X')} = 2.00$, $r = 0.69$]. **Figure 9**, subplot C5, depicts these results.

Kruskal-Wallis test indicated a significant effect of choice of component on preservation of information content of fNIRS time series [i.e., $H(X') - H(X|X') \geq 0$] [$p < 0.01$, $H_{(3, 71)} = 11.15$, $r = 0.39$]. *Post-hoc* comparison implied significantly higher preservation of information content of frontal brain activity with respect to PC12 in comparison with PC1 [$p < 0.001$, $W_{(34)} = 3.51$, $M_{PC12} = 18.27$, $SD_{PC12} = 10.81$, $M_{PC1} = 8.45$, $SD_{PC1} = 7.04$], $r = 0.59$, PC123 [$p < 0.001$, $W_{(34)} = 3.72$, $M_{PC123} = 10.41$, $SD_{PC123} = 6.45$, $r = 0.62$], as well as IC1 [$p < 0.001$, $W_{(34)} = 3.72$, $M_{IC1} = 2.27$, $SD_{IC1} = 1.20$, , $r = 0.62$]. Furthermore, PC1 was significantly more effective than IC1 [$p < 0.001$, $W_{(34)} = 3.33$, $r = 0.56$]. Lastly, we found PC123 significantly better than IC1 [< 0.001, $W_{(34)} = 3.68$, $r = 0.61$]. However, this test implied that difference between PC1 and PC123 was non-significant [$p = 0.29$, $W_{(34)} = 1.07$, $r = 0.18$]. **Figure 10** shows these results.

3.4. LMT

Figure 11A corresponds to the grand-average of the computed TE values for lags 1 through 100 (i.e., up to 10 s of lag, considering the sampling rate of 10.0 Hz of our device) in LMT. This subplot indicates that maximum SBF transferred information was, on average, at lag = 32 (i.e., 3.2 s). This was the lag we used during

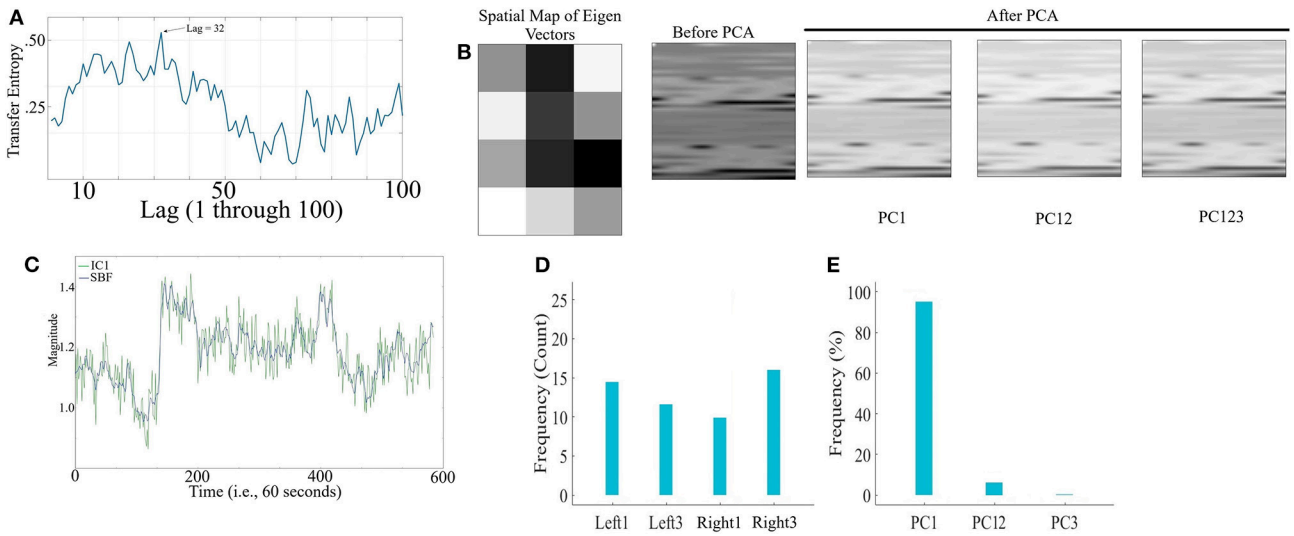

FIGURE 11 | LMT - **(A)** Grand-average of TE values for Lag = 1, . . . , 100 (i.e., up to 10 s of lag, considering the sampling rate of 10.0 Hz in our device). Maximum TE was at Lag = 32 (equivalent to time = 3.2 s) **(B)** Sample spatial map of eigenvectors by PCA-based SBF attenuation algorithm along with a sample participant's PFC time series (in matrix forms for better visualization purpose) before and after application of PC1, PC12, and PC123 components. Distinctive effect of these components on participant's PFC time series is evident in this subplot. All matrices are scaled within [0, 1] interval for ease of comparison. **(C)** Sample SBF (blue) and the corresponding IC1 component computed by ICA-based SBF attenuation algorithm (green). The depicted IC1 component pertains to the case in which $Right_1$ was selected as component with highest coefficient of spatial uniformity. **(D)** Frequency of selected channels as a component with highest coefficient of spatial uniformity by ICA-based SBF attenuation algorithm for LMT dataset. **(E)** Percentages of the variance-explained by each of the principal components (i.e., PC1, PC12, PC123) of PCA-based SBF attenuation algorithm for LMT dataset.

our analyses. Wilcoxon rank sum test implied significant effect of SBF on fNIRS time series of frontal brain activity of participants while performing VFT working memory task [$p < 0.001$, $W_{(25)} = 4.46$, $M = 0.58$, $SD = 0.19$, $r = 0.70$].

Figure 11B visualizes a sample spatial map of eigenvectors by PCA-based SBF attenuation algorithm along with a sample participant's PFC time series (in matrix forms for better visualization purpose) before and after application of PC1, PC12, and PC123 components. Distinctive effect of these components on participant's PFC time series is evident in this subplot. All matrices are scaled within [0, 1] interval for ease of comparison. We observed significant differences in PFC time series between before and after application of PC1 [$p < 0.001$, $W_{(3,\ 358)} = 7.70$, $r = 0.13$, $M_{Before} = 216.53$, $SD_{Before} = 32.81$, $M_{PC1} = 211.56$, $SD_{PC1} = 19.21$], PC12 [$p < 0.001$, $W_{(3,\ 358)} = 9.03$, $r = 0.16$, $M_{PC12} = 210.53$, $SD_{PC12} = 13.97$], and PC123 [$p < 0.001$, $W_{(3,\ 358)} = 6.34$, $r = 0.11$, $M_{PC123} = 212.60$, $SD_{PC123} = 12.86$].

Figure 11C shows a sample SBF (blue) along with the computed IC1 by ICA-based SBF attenuation algorithm (green) (pertinent to the case in which $Right_1$ was selected as the component with highest coefficient of spatial uniformity). Although this algorithm resulted in selection of different channels as the component with highest coefficient of spatial uniformity (**Figure 11D**, $Left_1 = 26.92\%$, $Left_3 = 23.08\%$, $Right_1 = 30.77\%$, $Right_3 = 19.23\%$), these components were significantly correlated with simulated noise ($Left_1$: 0.77, $p < 0.001$, $Left_3$: $r = 0.73$, $p < 0.001$, $Right_1$: $r = 0.70$,$p < 0.001$, and $Right_3$: $r = 0.76$, $p < 0.001$). On the other hand, PCA-based algorithm (**Figure 11E**) exhibited a higher specificity in selecting the principal components (PC1 = 94.53%, PC12 = 5.11%, PC123 = 0.36%).

In what follows, we examine the effectiveness of PCA- and ICA-based SBF attenuation algorithms on reduction of observed impact of SBF on fNIRS frontal brain activity as well as their utility in preservation of information content of this activity in resulting fNIRS time series through investigation of Criterion 2.1 through Criterion 2.5.

3.4.1. Criterion 2.1: $TE(Y \rightarrow X') \leq TE(Y \rightarrow X)$

Kruskal-Wallis test implied significant effect of choice of components [$p < 0.001$, $H_{(4,\ 129)} = 56.39$, $r = 0.66$]. Moreover, *post-hoc* comparison implied that all components significantly reduced SBF effect in comparison with $TE(Y \rightarrow X)$ [PC1: $p < 0.001$, $W_{(50)} = 4.46$, $M = 0.16$, $SD = 0.15$, $r = 0.62$, PC12: $p < 0.001$, $W_{(50)} = 4.43$, $M = 0.08$, $SD = 0.13$, $r = 0.61$, PC123:$p < 0.001$, $W_{(50)} = 4.46$, $M = 0.18$, $SD = 0.16$, $r = 0.62$, IC1: $p < 0.001$, $W_{(50)} = 4.43$, $M = 0.18$, $SD = 0.17$, $r = 0.61$]. *Post-hoc* comparison indicated that PC12 significantly performed better in attenuation of the effect of SBF than PC1 [$p < 0.01$, $W_{(50)} = 2.73$, $r = 0.38$], PC123 [$p < 0.01$, $W_{(50)} = 3.04$, $r = 0.42$], and IC1 [$p < 0.001$, $W_{(50)} = 3.34$, $r = 0.46$]. On the other hand, we observed non-significant differences between PC1 and PC123 [$p = 0.36$, $W_{(50)} = 0.93$, $r = 0.13$], PC1 and IC1 [$p = 0.47$, $W_{(50)} = 0.72$, $r = 0.10$], as well as PC123 and IC1 [$p = 0.75$, $W_{(50)} = 0.32$, $r = 0.04$]. **Figure 12**, subplot C1, illustrates these results.

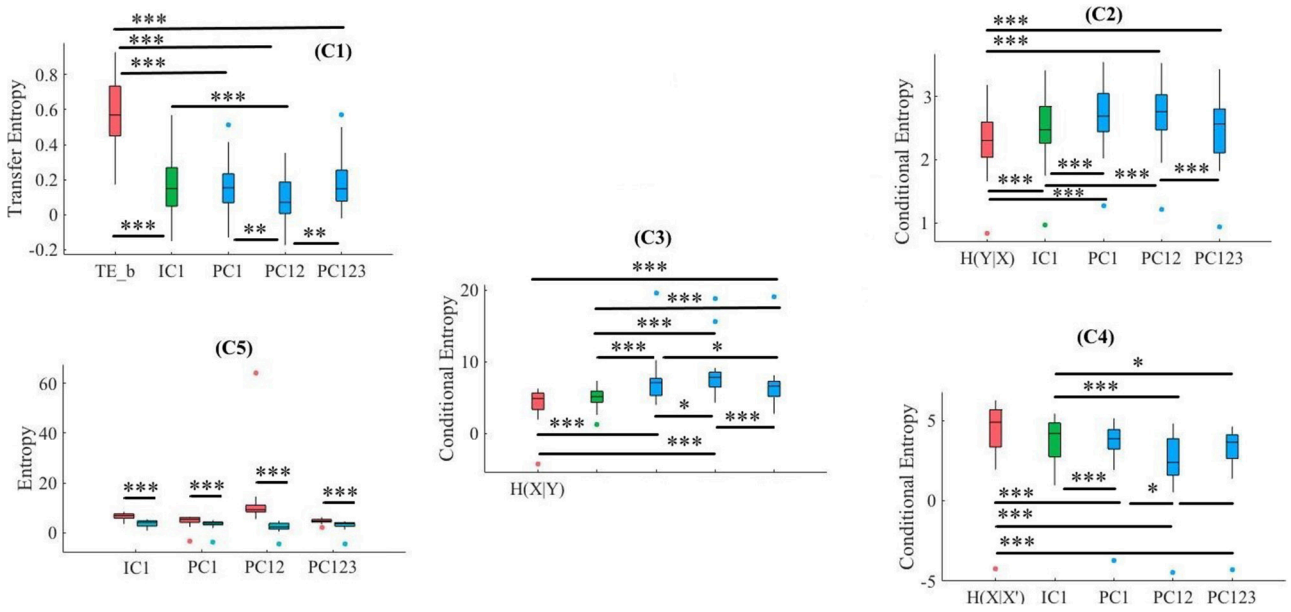

FIGURE 12 | LMT. C1: Criterion 2.1: $TE(Y \rightarrow X') \leq TE(Y \rightarrow X)$, C2: Criterion 2.2: $H(Y|X) \leq H(Y|X')$, C3: Criterion 2.3: $H(X|Y) \leq H(X'|Y)$, C4: Criterion 2.4: $H(X|X') \leq H(X|Y)$, C5: Criterion 2.5: $H(X|X') \leq H(X')$. In these subplots, IC1, PC1, PC12, and PC123 refer to the measured quantity by these components after their respective SBF attenuation algorithms. Asterisks mark the components with significant difference (*$p < 0.05$, **$p < 0.01$, ***$p < 0.001$).

3.4.2. Criterion 2.2: $H(Y|X) \leq H(Y|X')$

Kruskal-Wallis implied a significant effect of choice of components [$p < 0.01$, $H_{(4,\ 129)} = 13.32$, $r = 0.32$]. *Post-hoc* comparison indicated a significant reduction of SBF-related information in frontal brain activity of participants by PC1 [$p < 0.001$, $W_{(50)} = 4.46$, $M_{H(Y|X)} = 2.31$, $SD_{H(Y|X)} = 0.50$, $M_{PC1} = 2.69$, $SD_{PC1} = 0.48$, $r = 0.62$], PC12 [$p < 0.001$, $W_{(50)} = 4.46$, $M_{PC12} = 2.71$, $SD_{PC12} = 0.50$, $r = 0.62$], PC123 [$p < 0.001$, $W_{(50)} = 3.95$, $M_{PC123} = 2.49$, $SD_{PC123} = 0.53$, $r = 0.55$], and IC1 [$p < 0.001$, $W_{(50)} = 4.46$, $M_{IC1} = 2.47$, $SD_{IC1} = 0.53$, $r = 0.62$]. Additionally, this comparison indicated that adaptation of PC1 resulted in a significantly more reduced SBF-related information than PC123 [$p < 0.001$, $W_{(50)} = 4.23$, $r = 0.49$] as well as IC1 [$p < 0.001$, $W_{(50)} = 4.33$, $r = 0.49$]. Similarly, we found PC12 significantly more effective than PC123 [$p < 0.001$, $W_{(50)} = 4.10$, $r = 0.49$] and IC1 [$p < 0.001$, $W_{(50)} = 4.36$, $r = 0.49$]. However, we found non-significant differences between PC1 and PC12 [$p = 0.49$, $W_{(50)} = 0.70$, $r = 0.10$] as well as IC1 and PC123 was significant [$p = 0.14$, $W_{(50)} = 1.49$, $r = 0.21$]. **Figure 12**, subplot C2, shows these results.

3.4.3. Criterion 2.3: $H(X|Y) \leq H(X'|Y)$

Kruskal-Wallis indicated a significant effect of choice of components in resulting fNIRS data [$p < 0.001$, $H_{(4,\ 129)} = 47.41$, $r = 0.61$]. *Post-hoc* comparison suggested that all components were significantly effective in reducing the degree of correspondence between SBF and fNIRS time series of frontal brain activity [PC1: $p < 0.001$, $W_{(50)} = 4.46$, $M_{H(X|Y)} = 4.22$, $SD_{H(X|Y)} = 2.21$, $M_{PC1} = 7.11$, $SD_{PC1} = 3.03$, $r = 0.62$, PC12: $p < 0.001$, $W_{(50)} = 4.46$, $M_{PC12} = 8.17$, $SD_{PC12} = 3.01$, $r = 0.62$, PC123: $p < 0.001$, $W_{(50)} = 4.46$, $M_{PC123} = 6.57$, $SD_{PC123} = 2.96$, $r = 0.62$]. However, we observed that the effect of IC1 was non-significant [IC1: $p = 0.10$, $W_{(50)} = 1.66$, $M_{IC1} = 5.09$, $SD_{IC1} = 1.36$, $r = 0.23$]. In addition, this comparison indicated that adaptation of PC12 yielded a significantly better performance than PC1 [$p < 0.03$, $W_{(50)} = 2.30$, $r = 0.32$], PC123 [$p < 0.001$, $W_{(50)} = 3.42$, $r = 0.47$], as well as IC1 [$p < 0.001$, $W_{(50)} = 4.46$, $r = 0.62$]. Moreover, PC1 was significantly more effective than PC123 [$p < 0.05$, $W_{(50)} = 1.97$, $r = 0.27$] and IC1 [$p < 0.001$, $W_{(50)} = 3.95$, $r = 0.55$]. Additionally, PC123 was significantly different from IC1 [$p < 0.001$, $W_{(50)} = 2.58$, $r = 0.36$]. **Figure 12**, subplot C3, plots these results.

3.4.4. Criterion 2.4: $H(X|X') \leq H(X|Y)$

Kruskal-Wallis indicated a significant effect of choice of components [$p < 0.001$, $H_{(4,\ 129)} = 30.93$, $r = 0.49$]. *Post-hoc* comparison suggested that all components were significantly effective in retaining the correspondence between time series of frontal activity before and after application of SBF attenuation [PC1: $p < 0.001$, $W_{(50)} = 3.24$, $M_{H(X|Y)} = 4.22$, $SD_{H(X|Y)} = 2.22$, $M_{PC1} = 2.71$, $SD_{PC1} = 1.72$, $r = 0.45$, PC12: $p < 0.001$, $W_{(50)} = 4.46$, $M_{PC12} = 1.97$, $SD_{PC12} = 1.88$, $r = 0.62$, PC123: $p < 0.001$, $W_{(50)} = 3.39$, $M_{PC123} = 2.71$, $SD_{PC123} = 1.74$, $r = 0.47$] However, we observed that the effect of IC1 was non-significant [$p = 0.13$, $W_{(50)} = 1.51$, $M_{IC1} = 3.67$, $SD_{IC1} = 1.47$, $r = 0.21$]. Additionally, this comparison implied that PC12 resulted in significantly higher correspondence between time series of frontal brain activity before and after SBF attenuation than PC1 [$p < 0.03$, $W_{(50)} = 2.07$, $r = 0.29$], PC123 [$p < 0.001$, $W_{(50)} = 2.20$, $r = 0.31$], as well as IC1 [$p < 0.001$, $W_{(50)} = 3.85$, $r = 0.53$]. Although PC1 performed significantly better than IC1 [$p <$

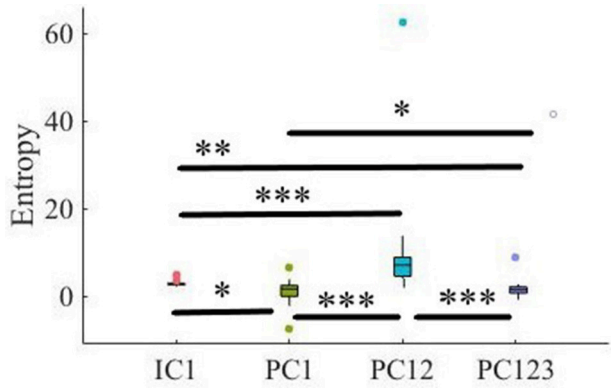

FIGURE 13 | Comparison of maximal preservation of information content of frontal brain activity (i.e., $H(X') - H(X|X') \geq 0$, Criterion 2.5) after application of PCA- and ICA-based SBF attenuation algorithms on LMT. Asterisks mark the components with significant difference ($^{*}p < 0.05$, $^{**}p < 0.01$, $^{***}p < 0.001$).

0.001, $W_{(50)} = 2.22$, $r = 0.31$], its difference with PC123 was non-significant [$p = 0.27$, $W_{(50)} = 1.10$, $r = 0.15$]. Lastly, PC123 was significantly more effective than IC1 [$p = p < 0.03$, $W_{(50)} = 2.30$, $r = 0.32$]. **Figure 12**, subplot C4, shows these results.

3.4.5. Criterion 2.5: $H(X|X') \leq H(X')$

Pairwise Wilcoxon rank sum suggested that all components preserved information content of frontal activity [PC1: $p < 0.001$ $W_{(50)} = 3.67$, $M_{H(X|X')} = 2.71$, $SD_{H(X|X')} = 1.72$, $M_{H(X')} = 4.80$, $SD_{H(X')} = 2.11$, $r = 0.51$, PC12:$p < 0.001$, $W_{(50)} = 4.46$, $M_{H(X|X')} = 1.97$, $SD_{H(X|X')} = 1.88$, $M_{H(X')} = 11.55$, $SD_{H(X')} = 10.94$, $r = 0.62$, PC123: $p < 0.001$, $W_{(50)} = 4.38$, $M_{H(X|X')} = 2.713$, $SD_{H(X|X')} = 1.74$, $M_{H(X')} = 4.83$, $SD_{H(X')} = 0.91$, $r = 0.61$, IC1: $p < 0.001$, $W_{(50)} = 4.46$, $M_{H(X|X')} = 3.67$, $SD_{H(X|X')} = 1.47$, $M_{H(X')} = 6.67$, $SD_{H(X')} = 1.40$, $r = 0.62$]. **Figure 12**, subplot C5, depicts these results.

Kruskal-Wallis test indicated a significant effect of choice of component on preservation of information content of fNIRS time series [i.e., $H(X') - H(X|X') \geq 0$] [$p < 0.01$, $H_{(3,\ 103)} = 16.01$, $r = 0.16$]. *Post-hoc* paired comparison implied a significantly higher preservation of information content of frontal brain activity with respect to PC12 in comparison with PC1 [$p < 0.001$, $W_{(50)} = 4.30$, $M_{PC1} = 2.10$, $SD_{PC1} = 2.46$, $M_{PC12} = 9.58$, $SD_{PC12} = 11.29$, $r = 0.60$], PC123 [$p < 0.001$, $W_{(50)} = 4.43$, $M_{PC123} = 2.12$, $SD_{PC123} = 1.77$, $r = 0.61$], as well as IC1 [$p < 0.001$, $W_{(50)} = 4.43$, $M_{IC1} = 2.10$, $SD_{IC1} = 0.51$, $r = 0.61$]. IC1 was significantly more effective than and PC1 [$p < 0.03$, $W_{(50)} = 2.25$, $r = 0.31$] and PC123 [$p < 0.01$, $W_{(50)} = 3.19$, $r = 0.44$]. Last, we found that PC1 was significantly more effective than PC123 [$p < 0.03$, $W_{(50)} = 2.41$, $r = 0.33$]. **Figure 13** shows these results.

4. DISCUSSION

In this article, we pinpointed the lack of perspective in previous studies on frontal activity's information preservation while attenuating the effect of SBF on fNIRS time series. Subsequently, we proposed five information-theoretic criteria for quantification of the frontal activity's information preservation during SBF attenuation process. We utilized the concept of TE (Schreiber, 2000) to quantify the effect of SBF on fNIRS time series of frontal brain activity via transferring undesired information onto fNIRS measurement. Advantages of TE for this purpose are twofold: First, TE, similar to MI and unlike other correlation measures, is always ≥ 0 that makes it a good quantitative metric for amount of information transferred/shared. Second, TE, unlike MI and other correlation measures, has a direction [i.e., TE(X $\Rightarrow$ Y) $\neq$ TE(Y $\Rightarrow$ X)] which allows for causal reasoning about which process induces the observed effect on transferred/shared information. Additionally, we exploited the concept of MI and its correspondence with conditional entropy between interacting continuous random variables (Cover and Thomas, 2006; Stone, 2015) to formalize criteria for frontal brain activity's information preservation in resulting fNIRS time series once the process of SBF attenuation is complete.

We verified the validity our criteria on PCA- (Zhang et al., 2005) and ICA-based (Kohno et al., 2007) SBF attenuation algorithms using simulated time series with additive Gaussian noise. We chose these SBF attenuation algorithms due to their widespread adaptation in recent literature (Katura et al., 2008; Kiguchi and Funane, 2014; Tak and Ye, 2014; Naseer and Hong, 2015; Sato et al., 2016; Zhang et al., 2016). Although these algorithms make assumption on orthogonality and statistical independence of their components, their well-defined mathematical formulation help eliminate further empirical assumptions on causal and/or explanatory effects (e.g., channels with short source-detector distances as representatives of SBF, etc.). Subsequently, we examined our criteria on two different Working Memory (WM) tasks and a naturalistic conversational settings. Our results implied a significant effect of SBF on fNIRS time series of frontal brain activity through transfer of undesired information. This finding that was founded on analysis of the information flow from SBF onto fNIRS time series of frontal brain activity presented a systematic approach to quantification of the SBF as an interfering process during fNIRS measurement, thereby drawing an informed conclusion on this issue (Takahashi et al., 2011; Sato et al., 2013).

In addition, our results implied that mere reduction of SBF influence on fNIRS time series of frontal activity was insufficient to warrant frontal activity's information preservation. More importantly, we found this observation to hold true, irrespective of the nature of the adapted task or age of the participants. This, in turn, provided further support for inefficiency of such measures as correlation coefficient, signal-to-noise ratio, or Pearson R^2 (Zhang et al., 2005; Kohno et al., 2007; Gagnon et al., 2011) in determination of the significance of the reduced effect of SBF due to their inability in detecting the direction of the information flow (i.e., causality) between interacting processes (Kinney and Atwal, 2014).

Moreover, our results implied a higher fidelity of PCA-based algorithm in preservation of information content of frontal brain activity in comparison with ICA-based approach. This observation was in accord with the findings by Sato et al. (2016). Furthermore, our results revealed a substantial effect of selected number of components on performance of PCA-based

algorithm. Concretely, they indicated that combination of first two principal components of PCA-based algorithm resulted in most efficient SBF attenuation while ensuring a significantly higher (i.e., in comparison with other adapted components) frontal activity's information preservation. This provided an evidence for a reliable choice among existing SBF attenuation algorithms and their inconclusive number of components (Zhang et al., 2005; Sato et al., 2016) to ensure minimum loss of frontal activity's information content during SBF attenuation process.

Further evidence on substantial difference in performance of these algorithms was due to the high variability of ICA-based SBF attenuation in determination of the component with highest coefficient of spatial uniformity. This variability that was originally reported by Kohno et al. (2007) reduces the reliability of this algorithm, given its contingency in selecting the channel of interest (e.g., long source-detector distance channels). On the other hand, PCA-based SBF attenuation algorithm exhibited a stable distribution of the percentages of the variance-explained among its selected components. It is worth noting that observed distribution of these components in our results is in close correspondence with Sato et al. (2016), although their subtle differences is appreciated in light of comparably larger number of channels in their study. Considering these observations, it is apparent that such differences in stability of these algorithms in determination of their respective SBF-related component(s) impose substantial variation in analyses results. Given the observed variability in choice of components, as indicated by our results on simulated as well as real time data and irrespective of the age of participants, it is apparent that an SBF algorithm with the stable choice of component(s) to reduce the effect of SBF to retain the information content pertinent to brain activity of human subjects is highly desirable. Our results suggested that ICA algorithm falls short in achieving this objective.

Taken together, we provided evidence that lack of perspective on preservation of information content of frontal brain activity during SBF attenuation underlies the contrasting findings with inconclusive results in previous studies. We showed that a mere reduction of SBF influence on fNIRS time series of frontal activity is insufficient in warranting frontal activity's information preservation in resulting fNIRS time series data. Subsequently, we showed a higher fidelity of PCA-based algorithm in achieving this information preservation in comparison with ICA-based approach. Lastly, we showed that combination of first two components of PCA-based algorithm resulted in most information preservation while ensuring significant attenuation of SBF effect. Our findings contribute to the field by presenting a systematic approach to quantification of the SBF as an interfering process during fNIRS measurement, thereby drawing an informed conclusion on this debate (Takahashi et al., 2011; Sato et al., 2013). Furthermore, they provide evidence for a reliable choice among existing SBF attenuation algorithms and their inconclusive number of components (Zhang et al., 2005; Sato et al., 2016), thereby ensuring minimum loss of information content of fNIRS cortical activity through SBF attenuation process.

ETHICS STATEMENT

This study was carried out in accordance with the recommendations of the ethical committee of Advanced Telecommunications Research Institute International (ATR) with written informed consent from all subjects. All subjects gave written informed consent in accordance with the Declaration of Helsinki. The protocol was approved by the ATR ethical committee (approval code:16-601-1).

AUTHOR CONTRIBUTIONS

SK proposed the information-theoretic criteria and carried out the analyses. HS acted as research lead, designing the experiments, supervising their progress, and taking part in experimental setups during data collections. MO conducted the experiments and performed data collection. As the head of Hiroshi Ishiguro Laboratories (HIL), HI oversaw the entire activity of all research teams and themes, ensuring the soundness of all proposals, quality of results, and their validity. SK and HS contributed equally in preparation of the manuscript.

ACKNOWLEDGMENTS

The authors would like to extend their gratitude to Mr. Kenta Kawashima for his assistance during data collection.

This research is supported by Impulsing Paradigm Change through Disruptive Technologies Program (ImPACT): Actualize Energetic Life by Creating Brain Information Industries, Brain Robotics for communication, funded by the Japanese Cabinet Office.

SUPPLEMENTARY MATERIAL

The Supplementary Material for this article can be found online at: https://www.frontiersin.org/articles/10.3389/fnins.2019.00079/full#supplementary-material

REFERENCES

Bakerand, J., Liuand, N., Cuiand, X., Vrtickaand, P., Saggarand, M., Hosseiniand, S. H., et al. (2016). Sex differences in neural and behavioral signatures of cooperation revealed by fnirs hyperscanning. *Sci. Rep.* 6:26492. doi: 10.1038/srep26492

Basso Moro, S., Cutini, S., Ursini, M. L., Ferrari, M., and Quaresima, V. (2013). Prefrontal cortex activation during story encoding/retrieval: a multi-channel functional near-infrared spectroscopy study. *Front. Hum. Neurosci.* 7:925. doi: 10.3389/fnhum.2013.00925

Cooper, R. J., Selb, J., Gagnon, L., Phillip, D., Schytz, H., Iversen, H., et al. (2012). A systematic comparison of motion artifact correction techniques for functional near-infrared spectroscopy. *Front. Neurosci.* 6:147. doi: 10.3389/fnins.2012.00147

Cover, T. and Thomas, J. (2006). *Elements of Information Theory, 2nd Edn.* Hoboken, NJ: John Wiley & Sons, Inc.

Cuiand, X., Brayand, S., Bryantand, D., Gloverand, G., and Reiss, A. (2011). A quantitative comparison of NIRS and fMRI across multiple cognitive tasks. *NeuroImage* 14, 2808–2821. doi: 10.1016/j.neuroimage.2010.10.069

Dix, L. M., van Bel, F., Barets, W., and Lemmers, P. (2013). Comparing near-infrared spectroscopy devices and their sensors for monitoring regional cerebral oxygen saturation in the neonate. *Pediat. Res.* 74, 557–563. doi: 10.1038/pr.2013.133

D. Wechsler, D. (1997). *Wechsler Memory Scale*. San Antonio, TX: The Psychological Corporation, 3rd Edn.

Everitt, B. (1998). *The Cambridge Dictionary of Statistics*. London: Cambridge University Press.

Feketeand, T., Rubinand, D., Carlsonand, J., and Mujica-Parodi, L. (2011). The nirs analysis package: noise reduction and statistical inference. *PLoS ONE* 6:e24322. doi: 10.1371/journal.pone.0024322

Ferrari, M. and Quaresima, V. (2012). A brief review on the history of human functional near-infrared spectroscopy (fNIRS) development and fields of application. *Neuroimage (change globally in reference journal title)* 63, 921–93. doi: 10.1016/j.neuroimage.2012.03.049

Fishbum, F. A., Norr, M. E., Medvedev, A. V., and Vaidya, C. J. (2014). Sensitivity of fnirs to cognitive state and load. *Front. Hum. Neurosci.* 8:76. doi: 10.3389/fnhum.2014.00076

Friston, K., Ashburner, J., Kiebel, S., Nichols, T., and Penny, W. (2011). *Statistical Parametric Mapping: The Analysis of Functional Brain Images*. London: Academic Press.

Friston, K., Holmes, A., Worsley, K., Poline, J.-B., Frith, C., and Frackowiak, R. (1995). Statistical parametric maps in functional imaging: a general linear approach. *Hum. Brain Mapp.* 2, 189–210. doi: 10.1002/hbm.460020402

Gagnon, L., Cooper, R. J., Yücel, M., Perdue, K., Greve, D., and Boas, D. (2012). Short separation channel location impacts the performance of short channel regression in NIRS. *NeuroImage* 59, 2518–2528. doi: 10.1016/j.neuroimage.2011.08.095

Gagnon, L., Perdue, K., Greve, D., Goldenholz, D., Kaskhedikar, G., and Boas, D. (2011). Improved recovery of the hemodynamic response in diffuse optical imaging using short optode separations and state-space modeling. *NeuroImage* 56, 1362–1371. doi: 10.1016/j.neuroimage.2011.03.001

Gagnon, L., Yücel, M., Boas, D., and Cooper, R. (2014). Further improvement in reducing superficial contamination in NIRS using double short separation measurements. *NeuroImage* 85, 127–135. doi: 10.1016/j.neuroimage.2013.01.073

Gagnonand, L., Yuceland, M., Dehaesand, M., Cooperand, R., Perdueand, K., Selband, J., et al. (2012). Quantification of the cortical contribution to the NIRS signal over the motor cortex using concurrent NIRS-fMRI measurements. *NeuroImage* 15, 3933–3940. doi: 10.1016/j.neuroimage.2011.10.054

Gu, Y., Miao, S., Han, J., Zeng, K., Ouyang, G., Yang, J., et al. (2017). Complexity analysis of fNIRS signals in ADHD children during working memory task. *Sci. Rep.* 7:829. doi: 10.1038/s41598-017-00965-4

Haeussinger, F. B., Dresler, T., Heinzel, S., Schecklmann, M., Fallgatter, A. J., and Ehlis, A. C. (2014). Reconstructing functional near-infrared spectroscopy (fNIRS) signals impaired by extra-cranial confounds: an easy-to-use filter method. *NeuroImage* 95, 69–79. doi: 10.1016/j.neuroimage.2014.02.035

Honey, C. J., Otter, R., Breakspear, M., and Sporns, O. (2007). Network structure of cerebral cortex shapes functional connectivity on multiple time scales. *Proc. Natl. Acad. Sci. U.S.A.* 104, 10240–10245. doi: 10.1073/pnas.0701519104

Huppertand, T. J., Diamondand, S. G., Franceschiniand, M. A., and Boas, D. A. (2009). Homer: a review of time-series analysis methods for near-infrared spectroscopy of the brain. *Appl. Opt.* 48, D280–D298. doi: 10.1364/AO.48.00D280

Johnson, J. M., Tylor, W. F., Shepherd, A. P., and Park, M. K. (1984). Laser-doppler measurement of skin blood flow: comparison with plethysmography. *J. Appl. Physiol.* 56, 798–803. doi: 10.1152/jappl.1984.56.3.798

Kaiser, A. and Schreiber, T. (2002). Information transfer in continuous processes. *Physica* 166, 43–62. doi: 10.1016/S0167-2789(02)00432-3

Katura, T., Fuchino, Y., Yoshida, T., Atsumori, H., Kiguchi, M., Maki, A., et al. (2008). Extracting task-related activation components from optical topography measurement using independent components analysis. *J. Biomed. Opt.* 13:054008. doi: 10.1117/1.2981829

Kiguchi, M. and Funane, T. (2014). Algorithm for removing scalp signals from functional near-infrared spectroscopy signals in real time using multidistnace optodes. *J. Biomed.* 19:110505. doi: 10.1117/1.JBO.19.11.110505

Kinney, J. B. and Atwal, G. S. (2014). Equitability, mutual information, and the maximal information coefficient. *Proc. Natl. Acad. Sci. U.S.A.* 111, 3354–3359. doi: 10.1073/pnas.1309933111

Koh, P. H., Glaser, D. E., Flandin, G., Kiebel, S., Butterworth, B., Maki, A., et al. (2007). Functional optical signal analysis: a software tool for near-infrared spectroscopy data processing incorporating statistical parametric mapping. *J. Biomed. Opt.* 12:064010. doi: 10.1117/1.2804092

Kohno, S., Miyai, I., Seiyama, A., Oda, I., Ishikawa, A., Tsuneishi, S., et al. (2007). Removal of the skin blood flow artifact in functional near-infrared spectroscopic imaging data through independent component analysis. *J. Biomed. Opt.* 12:062111. doi: 10.1117/1.2814249

Lee, S., Williams, W., and Schneider, S. (2002). Role of skin blood flow and sweating rate in exercise thermoregulation after bed rest. *J. Appl. Physiol.* 92, 2026–2034. doi: 10.1152/japplphysiol.00105.2001

Liand, T., Luoand, Q., and Gong, H. (2010). Gender-specific hemodynamic in prefrontal cortex during a verbal working memory task by near-infrared spectroscopy. *Behav. Brain Res.* 209, 148–153. doi: 10.1016/j.bbr.2010.01.033

Liao, W., Ding, J., Marinazzo, D., Xu, Q., Wang, Z., Yuan, C., et al. (2011). Small-world directed networks in the human brain: Multivariate granger causality analysis of resting-state fMRI. *NeuroImage* 54, 2683–2694. doi: 10.1016/j.neuroimage.2010.11.007

Liu, Y., Piazza, E., Simony, E., Shewokis, P., Onaral, B., Hasson, U., et al. (2017). Measuring speaker-listener neural coupling with functional near infrared spectroscopy. *Sci. Rep.* 7:43293. doi: 10.1038/srep43293

Lizier, J. (2014). JIDT: an information-theoretic toolkit for studying dynamics of complex systems. *Front. Robot. AI* 1:11. doi: 10.3389/frobt.2014.00011

Lungarella, M. and Sporns, O. (2006). Mapping information flow in sensorimotor networks. *PLoS Comput. Biol.* 2:e144. doi: 10.1371/journal.pcbi.0020144

Mardia, K., Kent, J., and Bibby, J. (1979). *Multivariate Analysis*. London: Academic Press.

Morel, P. (2018). Gramm: grammar of graphics plotting in Matlab. *JOSS*, 3, 568.

Naseer, N. and Hong, K. (2015). fNIRS-based brain-computer interfaces: a review. *Front. Hum. Neurosci.* 9:3. doi: 10.3389/fnhum.2015.00003

Nicholls, M. E., Thomas, N. A., Loetscher, T., and Grimshaw, G. M. (2013). The flinders handedness survey (flanders): a brief measure of skilled hand preference. *Cortex* 49, 2914–2926. doi: 10.1016/j.cortex.2013.02.002

Oberg, P. (1990). Laser-doppler flowmetry. *Crit. Rev. Biomed. Eng.* 18, 125–163.

Okamoto, M., Dan, H., Shimizu, K., Takeo, K., Amita, T., and Oda, I. (2004). Multimodal assessment of cortical activation during apple peeling by NIRS and fMRI. *NeuroImage* 21, 1275–1288. doi: 10.1016/j.neuroimage.2003.12.003

Orbig, H., Neufang, M., Wenzel, R., Kohl, M., Steinbrink, J., Einhaupl, K., et al. (2000). Spontaneous low frequency oscillations of cerebral hemodynamic and metabolism in human adults. *NeuroImage* 12, 623–639. doi: 10.1006/nimg.2000.0657

Ozawa, S., Matsuda, G., and Hiraki, K. (2014). Negative emotion modulates prefrontal cortex activity during a working memory task: a NIRS study. *Front. Hum. Neurosci.* 8:46. doi: 10.3389/fnhum.2014.00046

Payne, S. J., Selb, J., and Boas, D. A. (2003). Effects of autoregulation and co2 reactivity on cerebral oxygen transport. *Ann. Biomed. Eng.* 37,2288–2298. doi: 10.1007/s10439-009-9763-5

Rosenthal, R. and DiMatteo, M. R. (2001). Meta-analysis: recent developments n quantitative methods for literature reviews. *Ann. Rev. Psychol* 52, 59–82. doi: 10.1146/annurev.psych.52.1.59

Saager, R. B., Telleri, N. L., and Berger, A. J. (2011). Two-detector corrected near infrared spectroscopy (C-NIRS) detects hemodynamic activation responses more robustly than single-detector NIRS. *NeuroImage* 55, 1679–1685. doi: 10.1016/j.neuroimage.2011.01.043

Sato, H., Yahata, N., Funane, T., Takizawa, R., Katura, T., Atsumori, H., et al. (2013). A NIRS-fMRI investigation of prefrontal cortex activity during a working memory task. *NeuroImage* 83, 158–173. doi: 10.1016/j.neuroimage.2013.06.043

Sato, T., Nambu, I., Takeda, K., Aihara, T., Yamashita, O., Isogaya, Y., et al. (2016). Reduction of global interference of scalp-hemodynamic in functional near-infrared spectroscopy using short distance probes. *NeuroImage* 141, 120–132. doi: 10.1016/j.neuroimage.2016.06.054

Scholkmann, F., Kieiser, S., Metz, A. J., Zimmermann, R., Pavia, J., Wolf, U., et al. (2014). A review on continuous wave functional near-infrared spectroscopy and imaging instrumentation and methodology. *NeuroImage* 85, 6–27. doi: 10.1016/j.neuroimage.2013.05.004

Schreiber, T. (2000). Measuring information transfer. *Phys. Rev. Lett.* 85, 461–464. doi: 10.1103/PhysRevLett.85.461

Scremin, G. and Kenney, W. L. (2004). Aging and the skin blood flow response to the unloading of barorecptors during heat and cold stress. *J. Appl. Physiol.* 96, 1019–1025. doi: 10.1152/japplphysiol.00928.2003

Steinbrink, J., Villringer, A., Kempf, F., Haux, D., Boden, S., and Obrig, H. (2006). Illuminating the bold signal: combined fMRI-fNIRS studies. *Magn. Res. Imag.* 24, 495–505. doi: 10.1016/j.mri.2005.12.034

Stone, J. (2015). *Information Theory: A Tutorial Introduction*. Exeter: Sebtel Press.

Strangman, G., Culver, J. P., Thompson, J., and Boas, D. (2006). A quantitative comparison of simultaneous bold fMRI and nIRS recordings during functional brain activation. *NeuroImage* 17, 719–731. doi: 10.1006/nimg.2002.1227

Strangmann, G. (2009). Near-infrared neuroimaging with ninpy. *Front. Neuroinform.* 3:12. doi: 10.3389/neuro.11.012.2009

Tak, S. and Ye, J. C. (2014). Statistical analysis of fNIRS data: a comprehensive review. *NeuroImage* 85, 72–91. doi: 10.1016/j.neuroimage.2013.06.016

Takahashi, T., Takikawa, Y., Kawagoe, R., and Shibuya, S. (2011). Influence of skin blood flow on near-infrared spectroscopy signals measured on the forehead during a verbal fluency task. *NeuroImage* 57, 991–1002. doi: 10.1016/j.neuroimage.2011.05.012

Tomczak, M. and Tomczak, E. (2014). The need to report effect size estimates revisited. an overview of some recommended measures of effect size. *Trends Sport Sci.* 1, 19–25.

Tonorov, V., Franceschini, M., Filiaci, M., Fantini, S., Wolf, M., Michalos, A., et al. (2000). Near-infrared study of fluctuations in cerebral hemodynamic during rest and motor stimulation: temporal analysis and spatial mapping. *Med. Phys.* 27, 801–815. doi: 10.1118/1.598943

Toronov, V. Y., Zhang, X., and Webb, A. G. (2007). A spatial and temporal comparison of hemodynamic signals measured using optical and functional magnetic resonance imaging during activation in the human primary visual cortex. *NeuroImage* 34, 1136–1148. doi: 10.1016/j.neuroimage.2006.08.048

Vakorin, V. A., Kovacevic, N., and McIntosh, A. R. (2010). Exploring transient transfer entropy based on a group-wise ICA decomposition of EEG data. *NeuroImage* 49, 1593–1600. doi: 10.1016/j.neuroimage.2009.08.027

Yamada, T., Umeyama, S., and Matsuda, K. (2009). Multidistance probe arrangement to eliminate artifacts in functional near-infrared spectroscopy. *J. Biomed. Opt.* 14:064034. doi: 10.1117/1.3275469

Ye, J., Tak, S., Jang, K., Jung, J., and Jang, J. (2009). NIRS-SPM: statistical parametric mapping for near-infrared spectroscopy. *NeuroImage* 44, 428–447. doi: 10.1016/j.neuroimage.2008.08.036

Zhang, Q., Strangman, G., and Ganis, G. (2009). Adaptive filtering to reduce global interference in non-invasive NIRS measures of brain activation: how well and when does it work? *NeuroImage* 45, 788–794. doi: 10.1016/j.neuroimage.2008.12.048

Zhang, X., Noah, J. A., and Hirsch, J. (2016). Separation of the global and local components in functional near-infrared spectroscopy signals using principal component spatial filtering. *Neurophotonics* 3:015004. doi: 10.1117/1.NPh.3.1.015004

Zhang, Y., Brooks, D. H., Franceschini, M., and Boas, D. (2005). Eigenvector-based spatial filtering for reduction of physiological interference in diffuse optical imaging. *J. Biomed. Opt.* 10:11014. doi: 10.1117/1.1852552

Conflict of Interest Statement: The authors declare that the research was conducted in the absence of any commercial or financial relationships that could be construed as a potential conflict of interest.

Copyright © 2019 Keshmiri, Sumioka, Okubo and Ishiguro. This is an open-access article distributed under the terms of the Creative Commons Attribution License (CC BY). The use, distribution or reproduction in other forums is permitted, provided the original author(s) and the copyright owner(s) are credited and that the original publication in this journal is cited, in accordance with accepted academic practice. No use, distribution or reproduction is permitted which does not comply with these terms.

frontiers in Neuroscience

ORIGINAL RESEARCH
published: 19 February 2019
doi: 10.3389/fnins.2019.00081

Detecting Microglial Density With Quantitative Multi-Compartment Diffusion MRI

Sue Y. Yi[1], *Brian R. Barnett*[1], *Maribel Torres-Velázquez*[2], *Yuxin Zhang*[3,4], *Samuel A. Hurley*[3], *Paul A. Rowley*[3], *Diego Hernando*[3,4] *and John-Paul J. Yu*[1,2,3,5]*

[1] Neuroscience Training Program, Wisconsin Institutes for Medical Research, University of Wisconsin–Madison, Madison, WI, United States, [2] Department of Biomedical Engineering, College of Engineering, University of Wisconsin–Madison, Madison, WI, United States, [3] Department of Radiology, University of Wisconsin School of Medicine and Public Health, Madison, WI, United States, [4] Department of Medical Physics, University of Wisconsin School of Medicine and Public Health, Madison, WI, United States, [5] Department of Psychiatry, University of Wisconsin School of Medicine and Public Health, Madison, WI, United States

Neuroinflammation plays a central role in the neuropathogenesis of a wide-spectrum of neurologic and psychiatric disease, but current neuroimaging methods to detect and characterize neuroinflammation are limited. We explored the sensitivity of quantitative multi-compartment diffusion MRI, and specifically neurite orientation dispersion and density imaging (NODDI), to detect changes in microglial density in the brain. Monte Carlo simulations of water diffusion using a NODDI acquisition scheme were performed to measure changes in a virtual MRI signal following modeled cellular changes within the extra-neurite space. 12-week-old C57BL/6J male mice ($n = 48$; 24 control, 24 treated with colony stimulating factor 1 receptor (CSF1R) inhibitor, PLX5622) were sacrificed at 0, 1, 3, and 7 days following withdrawal of CSF1R inhibition and were imaged *ex-vivo* to obtain measures of the orientation dispersion index (ODI). Following imaging, all brains were immunostained with Iba-1, NeuN, and GFAP for quantitative fluorescence microscopy. Cell populations were calculated with the ImageJ particle analyzer tool; correlation between microglial density and mean ODI values were calculated with Kendall's tau. Monte Carlo simulations demonstrate the sensitivity and positive correlation of ODI to increased occupancy in the extra-neurite space. Commensurate with our simulation data, *ex-vivo* NODDI imaging demonstrates an increase in ODI as microglia repopulate the brain following the withdrawal of CSF1R inhibition. Quantitative immunofluorescence of microglial density reveals that microglial density is positively correlated with ODI and greater hindered diffusion in the extra-neurite space ($\tau = 0.386$, $p < 0.05$). Our results demonstrate that clinically feasible multi-compartment diffusion weighted imaging techniques such as NODDI are sensitive to microglial density and the cellular changes associated with microglial activation and highlights its potential to improve clinical diagnostic accuracy, patient risk stratification, and therapeutic monitoring of neuroinflammation in neurologic and psychiatric disease.

Keywords: diffusion weighted imaging, NODDI, neuroinflammation, microglia, MRI, DWI, multi-compartment models

OPEN ACCESS

Edited by:
John Ashburner,
University College London,
United Kingdom

Reviewed by:
Hui Zhang,
University College London,
United Kingdom
Mara Cercignani,
University of Sussex, United Kingdom

***Correspondence:**
John-Paul J. Yu
jpyu@uwhealth.org

Specialty section:
This article was submitted to Brain Imaging Methods, a section of the journal Frontiers in Neuroscience

Received: *11 October 2018*
Accepted: *25 January 2019*
Published: *19 February 2019*

Citation:
Yi SY, Barnett BR, Torres-Velázquez M, Zhang Y, Hurley SA, Rowley PA, Hernando D and Yu J-P (2019) Detecting Microglial Density With Quantitative Multi-Compartment Diffusion MRI. Front. Neurosci. 13:81. doi: 10.3389/fnins.2019.00081

INTRODUCTION

Neuroinflammation plays a critical role in the neuropathogenesis of disorders of the central nervous system (CNS) from ischemic stroke and traumatic brain injury (Iadecola and Anrather, 2011; Woodcock and Morganti-Kossmann, 2013) to Alzheimer's disease, schizophrenia, and major depression (Lull and Block, 2010; Mondelli et al., 2017). Neuroimaging techniques have been developed to characterize neuroinflammatory processes, which generally fall into two methodological categories: positron emission tomography (PET) and MRI (Albrecht et al., 2016). However, despite active research efforts toward PET and MR imaging of neuroinflammation, there remains no routine, widespread, and easily accessible neuroimaging tool available for the study of neuroinflammation.

Advanced MRI diffusion weighted imaging (DWI) methods represent a conceptually innovative and technically sensitive approach for measuring cellular changes associated with neuroinflammation and microglial activation. Multi-compartment DWI methods such as neurite orientation dispersion and density imaging (NODDI) are designed to measure water diffusion arising from distinct tissue compartments including the extra-neurite compartment (Zhang H. et al., 2012). In the NODDI model, diffusivity in the extra-neurite compartment is measured by ODI (orientation dispersion index). ODI was originally conceptualized to measure how changes in neurite dispersion influence water diffusivity in the extra-neurite space without accounting for the potential contribution that glial cells (such as microglia) can have on quantitative measures of ODI. However, within the extra-neurite compartment reside glial cells, which account for a large percentage of non-neuronal cells in the mouse and human brain (35 and 50%, respectively) (Herculano-Houzel et al., 2006; Azevedo et al., 2009; Herculano-Houzel, 2014; Mota and Herculano-Houzel, 2014; von Bartheld et al., 2016). As microglia comprise 5–15% of all glial cells (Alliot et al., 1999; Ginhoux et al., 2010) and in response to inflammatory stimuli, undergo substantial changes in both morphology and density (Hinwood et al., 2012; Yang et al., 2013), these changes would be expected to significantly alter the degree of hindered diffusion in the extra-neurite compartment. These changes thus offer a potential opportunity to assess microglial activation and microglial-mediated neuroinflammation by probing water diffusion using DWI (**Figure 1**).

We aimed to characterize the relationship between microglial density and water diffusivity specific to the extra-neurite compartment with multi-compartment diffusion MRI, with a specific focus on NODDI given its clinical feasibility (Rae et al., 2016). While previous work has examined quantitative histological measures of NODDI in the spinal cord (Grussu et al., 2017), the work presented herein is the first to corroborate histological measurements with quantitative measures of diffusion MRI from the extra-neurite space in the brain. We hypothesize that changes in microglial density will alter water diffusivity in the extra-neurite space thus serving as a potential measure of microglial density across a broad spectrum of acute and chronic neuroinflammatory states. To evaluate this hypothesis, we performed Monte Carlo simulations of pulsed gradient measurements of water diffusion, *ex-vivo* NODDI imaging of mice following CSF1R (colony stimulating factor 1 receptor) antagonism, and quantitative histological measurements of microglial density. Together, these data represent a reconceptualization and potential application of multi-compartment diffusion imaging for the sensitive detection of microglial-mediated neuroinflammation.

MATERIALS AND METHODS

Theory and *in silico* Simulation

Multi-compartment diffusion models biophysically model the total DWI signal as a sum of the diffusion weighted signal arising from a combination of biophysical compartments with different underlying cellular microstructures:

$$S = S_0 \sum_{i=0}^{n} w_i S_i \tag{1}$$

where S_0 is the signal for the non-diffusion weighted (or $b0$) acquisitions, w_i the volume fraction and S_i the signal function for the *ith* of n total compartments (Harms et al., 2017). In the NODDI model, the diffusion MRI signal is described as a sum of three non-exchanging biophysical compartments:

$$S = (1 - v_{iso})\,(v_{ic} S_{ic} + (1 - v_{ic})\,S_{ec}) + v_{iso} S_{iso} \tag{2}$$

where S is the entire normalized signal; S_{ic}, S_{ec}, and S_{iso} are the normalized signals of the intracellular, extracellular, and CSF compartments, respectively, and v_{ic} and v_{iso} are the normalized volume fractions of the intracellular and CSF compartments (Zhang H. et al., 2012).

To test how cellular changes in the extra-neurite space (microglial density) impacts the measured diffusion signal from the extra-neurite space (ODI, orientation dispersion index), an *in silico* diffusion experiment using multiple Monte Carlo random walk simulations as implemented in Camino[1] (Hall and Alexander, 2009) was performed by varying the number of modeled cells in the extra-neurite space. To generate the components of the multi-compartment diffusion model, basic geometrical components representing white matter axons and microglia were constructed in Blender (Blender Foundation, Amsterdam, Netherlands). We constructed a series of 6 undulating cylinders (with no dispersion) modeling axons in a similar manner as previously described (Kamiya et al., 2017) with radius $= 1\,\mu m$, length $= 40\,\mu m$, undulation amplitude $A = 2$, to yield a final $\lambda = 1.024$ to simulate a voxel in a white matter tract. Icospheres were next modeled as simplified microglia in the extra-neurite space and were generated with a radius $= 5\,\mu m$ (Kozlowski and Weimer, 2012). The cylinders were then hexagonally packed without touching within the simulated volume ($40 \times 40 \times 40\,\mu m$) with all components placed within the model in MatLab (version 2015a, MathWorks, Natick, MA, USA). 10 simulations of 0, 5, 15, and 25 spheres were performed

[1] http://camino.cs.ucl.ac.uk/

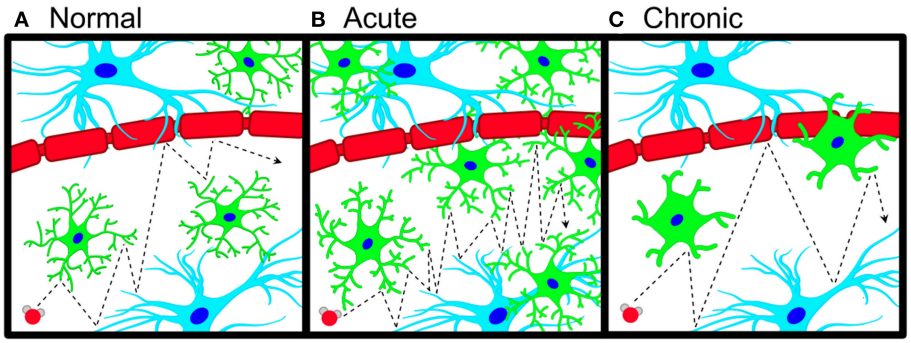

FIGURE 1 | Schematic of microglial neuroinflammation and accompanying changes in water diffusion. **(A)** Pictorial representation of anisotropic water diffusion (red sphere) in the extra-neurite environment in the presence of astrocytes (blue), neuronal/axonal projections (red), and microglia (green). **(B)** During acute neuroinflammation, microglia become hyper-ramified and increase their density in the extra-neurite space, leading to an increase in hindered water diffusion (increased ODI). **(C)** Chronic inflammatory insults cause microglial process to thicken and shorten with a commensurate decrease in microglial density, which leads to decreased occupancy of the extra-neurite space with a decrease in hindered water diffusion (decreased ODI).

with spheres randomly distributed throughout the extra-neurite space of the modeled volume. The volume fraction of the bundled axons is 2.7%; the volume fraction of the spheres is 6.3%, 18.9%, and 31.5% for 5, 15, and 25 spheres, respectively. Each simulation comprised of 100,000 spins and 5,000 time steps. The free diffusivity was set at 0.6×10^{-9} m^2/s per recommendations in Camino (Cook et al., 2006). From the simulated random walks of particles, a virtual MRI signal was obtained using the NODDI acquisition scheme used in our *ex-vivo* samples with the addition of Gaussian noise to the simulated signal with SNR = 50 of the b = 0 signal for each run. The mean ODI was calculated for each simulation. Diffusion tensor indices of fractional anisotropy (FA) and mean diffusivity (MD) were also calculated.

Animals and Reagents

All experiments were performed in accordance with animal protocols approved by the Institutional Animal Care and Use Committee at our institution (Protocol #: M005899). 12-week-old C57BL/6J male mice (Charles River Laboratories, MA, USA) were used for all experiments and were randomly assigned to control or experimental CSF1R inhibition cohorts. Control animals were maintained on AIN-76A standard chow (Research Diets, NJ, USA); animals receiving CSF1R inhibition received AIN-76A admixed with the CSF1R inhibitor PLX5622 (Plexxikon, CA, USA; 1,200 mg/kg) as previously described (Elmore et al., 2014). Animals receiving CSF1R inhibition were maintained on their admixed diet for 8-days; on day 8, CSF1R inhibition was withdrawn by replacing their chow with standard chow (AIN-76A). For each time point, mice from the control and the experimental groups were sacrificed on days 0, 9, 11, and 15 ($n = 48$; $n = 6$, each time point; control and experimental).

MRI Acquisition

Data Acquisition

On days 0, 9, 11, and 15, mice were brought to a surgical plane of anesthesia with isoflurane then transcardially perfused with phosphate-buffered solution (PBS) followed by 4% paraformaldehyde (PFA) in 0.1 M PBS. Brains were extracted from the cranial vault and post-fixed in PFA. Imaged brains were placed in a custom-built holder immersed in Fluorinert (FC-3283, 3M, St. Paul, MN, USA) and imaged with a 4.7-T Agilent MRI system with a 3.5-cm diameter quadrature volume RF coil. Multi-slice, diffusion-weighted, spin echo images were used to acquire 10 non-diffusion weighted images (b = 0 $s \bullet mm^{-2}$) and 75 diffusion-weighted images (25: b = 800 $s \bullet mm^{-2}$, 50: b = 2,000 $s \bullet mm^{-2}$), using non-colinear diffusion-weighting directions. Other imaging parameters: TE/TR = 24.17/2000-ms, FOV = 30×30 mm^2, matrix = 192×192 reconstructed to 256×256 for an isotropic voxel size of 0.25-mm over two signal averages. All animals were used in subsequent analyses.

Data Preprocessing and Region of Interest (ROI) Analysis

Raw data files were converted to NIfTI format and FSL was used to correct for eddy current artifacts with Eddy-correct. FSL output volumes were converted to NIfTI tensor format for use with the DTI-TK software package. DTI-TK (Zhang et al., 2006) was used to estimate a study-specific tensor template, to which subject tensor volumes were spatially normalized. The NODDI model was then voxel-wise fitted to the diffusion data in Matlab (The MathWorks, Inc., Natick, MA) with the NODDI toolbox[2]. An additional compartment of isotropic restriction was employed for *ex-vivo* studies as recommended (Alexander et al., 2010). A manual ROI was drawn over the left dentate gyrus from anatomically defined areas on a normalized mean diffusion map. The ROI was overlaid over subjects from each of the two groups (± CSF1R treatment) and ODI, FA, and MD were calculated.

Immunofluorescent Staining and Quantification

Following imaging, brains were removed from their custom holders and were returned to ice-cold 4% PFA for 24 h, then in a 30% sucrose solution (Alfa Aesar, Ward Hill, MA; Cat# 36508) in 0.1 M PBS (Growcells, Irvine, CA; Cat# MRGF-6235).

[2]http://nitrc.org/projects/noddi_toolbox

Frozen coronal sections were taken at 40 μm using a cryostat (Leica CM 1850, Wetzlar, Germany) and stored short-term in PBS at 4°C until staining. Floating sections were incubated in blocking solution formulated with 0.1 M PBS, 2% bovine serum albumin (Fisher Scientific, Hampton, NH; Cat# BP9706-100) and 0.1% sodium azide (Sigma, St. Louis, MO; Cat# S2002) for 1 h at room temperature (RT), then incubated overnight at 4C with primary antibodies for Iba-1 (rabbit Anti-Iba-1, dilution 1:2000, Abcam, Cambridge, MA, Cat # AB178847), NeuN (chicken Anti-NeuN, dilution 1:1500; EMD Millipore, Billerica, MA Cat# ABN91MI), and GFAP (mouse Anti-GFAP, dilution 1:1000; Thermo Fisher Scientific, Waltham, MA Cat# PIMA512023). Sections were incubated for 1 h at RT with the corresponding Alexa 488-, 555-, 647-labeled species specific secondary antibodies (goat anti-rabbit, Abcam, Cambridge, MA, Cat# AB150077; goat anti-chicken, Thermo Fisher Scientific, Waltham, MA former Invitrogen Cat# A-21437; goat anti-mouse, Abcam, Cambridge, MA, Cat# AB150115; all diluted at 1:2000). Sections were counterstained with 0.1 μm/mL 4',6-diamidino-2-phenylindole (DAPI) (Novus Biologicals, Littleton, CO; Cat# NBP2-31156) for 5 min at RT, then mounted with Fluoromount-G (Southern Biotech, Birmingham, AL, Cat# 0100-01). Images of the left hippocampus were acquired with a Leica DMi8 Inverted Fluorescent microscope (Wetzlar, Germany) with a 10x dry objective lens. All microscopy images were analyzed using ImageJ. The Region of Interest (ROI) manager tool was used to isolate the hippocampus. Images were made binary via manual thresholding, then the Particle Analyzer tool was used to automatically count cells.

Statistical Analysis

Imaging sample sizes and power analyses are based on standard deviations from previous studies with a significance level of 5% and power of 90% (Ong et al., 2018). Statistical tests were performed in GraphPad Prism or R. Analysis of cell counts between control and CSF1R-inhibitor diet were performed using a two-tailed unpaired Student's *t*-test; $p < 0.05$ was established as the significance level. Kendall's tau coefficient was calculated to measure the non-parametric, ordinal association between microglial cell counts and mean ODI from three time-points in CSF1R administered animals.

RESULTS

Computational Modeling of the Extra-Neurite Space in Multi-Compartment MRI

As the NODDI model includes parameters to measure water diffusion in the extra-neurite space, we hypothesized that changes in microglial density would change the water diffusivity measured within the extra-neurite compartment. To test this hypothesis and to first ascertain the sensitivity of the extra-neurite compartment to the cellular changes of neuroinflammation, we performed an *in silico* diffusion experiment utilizing a Monte Carlo random walk simulation with NODDI acquisition parameters (**Figure 2**, **Supplementary Figures 1, 2**). Within a simulated voxel with a modeled undulating axon bundle (to replicate a white matter tract) (Kamiya et al., 2017), we varied the number of modeled microglia within the simulated voxel over multiple iterative simulations to assess the sensitivity of NODDI to these microglial changes in the extra-neurite space expected during neuroinflammation. FA and MD were also calculated (**Supplementary Figure 3**). As shown in **Figure 2**, an increase in the number of microglia accompanies a concomitant increase in ODI, demonstrating that increased occupancy within the extra-neurite space is coupled with increased hindered water diffusion. Our simulation of a voxel in a white matter tract also importantly finds that measures of ODI are independent of neurite dispersion, for which ODI was originally modeled to measure. In Monte Carlo simulations with only the axon bundle present (no microglia), our simulations return a non-zero value of ODI, supporting the hypothesis that any structure localizing to the extra-neurite space (such as the modeled axon bundle) is able to contribute to alterations in water diffusivity within the extra-neurite compartment and thus to calculated values of ODI.

Quantitative Diffusion MRI of the Extra-Neurite Space Is Sensitive to Microglial Density

The extra-neurite compartment includes microglia and other cell populations including astrocytes, oligodendrocytes, ependymal cells, and vascular structures, all of which could be expected to impact the degree of hindered diffusion in the extra-neurite space. To examine the contribution of microglia to the measured diffusion tensor arising from the extra-neurite compartment in the NODDI model, we selectively eliminated microglia from the brain via CSF1R inhibition to specifically characterize the relationship between quantitative measures of ODI and microglial density (Elmore et al., 2014). Following the complete elimination of microglia from the brain following CSF1R inhibition, CSF1R inhibition was withdrawn and NODDI imaging of the dentate gyrus of the hippocampus was performed 1, 3, and 7 days after inhibitor withdrawal (Elmore et al., 2014). At day 1 post-withdrawal during which few microglia are present, we find a statistically significant decrease in ODI when compared to control animals (no CSF1R inhibition) consistent with results derived from our *in silico* model (**Figure 3**, **Supplementary Figure 4**). As microglia begin to repopulate the brain following the cessation of CSF1R inhibition, there is an increase in ODI on days 3 and 7, consistent with our *in silico* model's prediction, and further supports both the role of microglia and their contribution to water diffusivity in the extra-neurite space as well as the overall sensitivity of NODDI to capture the cellular changes in microglial density throughout the extra-neurite space (**Figure 3**). No statistically significant changes in FA or MD were found.

Microglial Density Is Strongly Correlated With ODI

To further establish whether the measured increase in mean ODI correlates with changes in microglial density, sections of the imaged brains at 1, 3, and 7 days following CSF1R inhibition

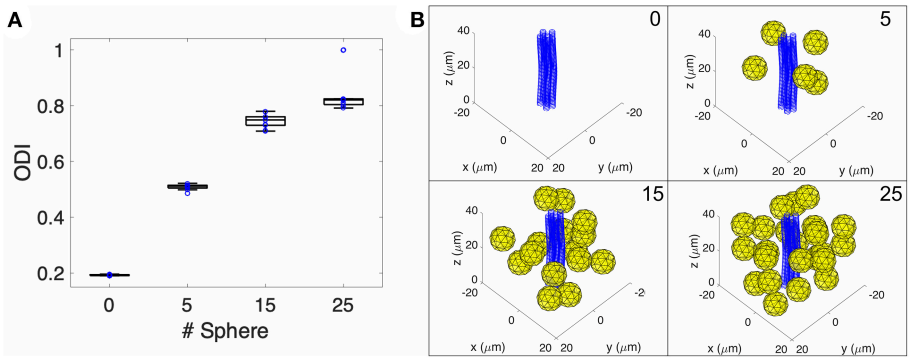

FIGURE 2 | Monte-Carlo NODDI diffusion MRI simulation. **(A)** Box plot of pulsed gradient water diffusion simulations within a representative voxel were performed with 0, 5, 15, and 25 spheres present (representing extra-neurite cellular elements) demonstrating increased ODI as a function of increased occupancy of the extra-neurite space. **(B)** Pictorial representation of the geometry within a single voxel in the Monte-Carlo simulation with blue tubes representing an axon bundle and yellow spheres representing microglia.

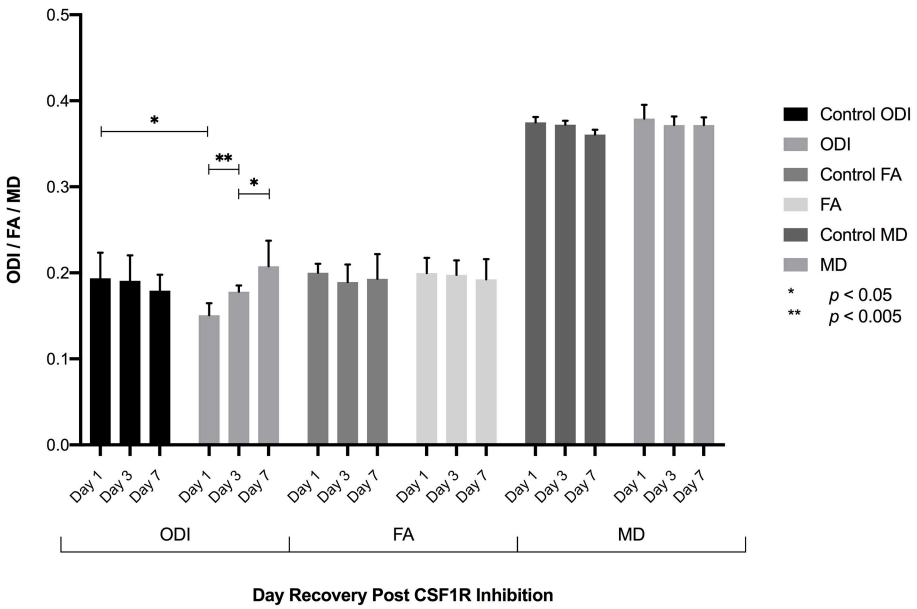

FIGURE 3 | Following the elimination of microglia, CSF1R inhibition was withdrawn allowing microglia to repopulate the brain. ROI analysis of the dentate gyrus 1, 3, and 7 days following inhibitor withdrawal demonstrate an increase in ODI as microglia repopulate the brain with statistically significant differences in ODI between control and day 1 animals, day 1-day 3, and day 3-day 7 animals . No significant difference in ODI is observed between control and D7 animals, consistent with fully repopulated microglial populations in the brain. No significant differences in FA or MD were found.

were stained with Iba1, NeuN, and GFAP to identify microglia, neurons, and astrocytes, respectively. Stained and quantified sections were taken at the level of the hippocampal head that were to co-registered to mean FA maps. Immunofluorescent (IF) staining showed successful microglial depletion following 8 days of CSF1R inhibition with further IF quantification demonstrating no significant difference in neurons or astrocytes (data not shown), recapitulating data previously shown by Elmore et al. (2014). At 1, 3, and 7 days following withdrawal of CSF1R inhibition, there is a steady repopulation of microglia throughout the dentate gyrus (**Figure 4**), again with no significant change in other major cells populations present in the extra-neurite space (**Figure 5**, **Supplementary Figure 5**).

With ODI values and quantitative IF data for the number of microglia present, a Kendall's tau coefficient was calculated to measure the non-parametric, ordinal association between microglial cell counts and mean ODI from these three time-points in CS1R administered animals. With a Kendall's tau of 0.386 ($p = 0.028$), we demonstrate that there is a significant association between measured values of ODI and microglial density (**Figure 6**). These results also align with our *in silico* analysis and show that microglial density is positively correlated

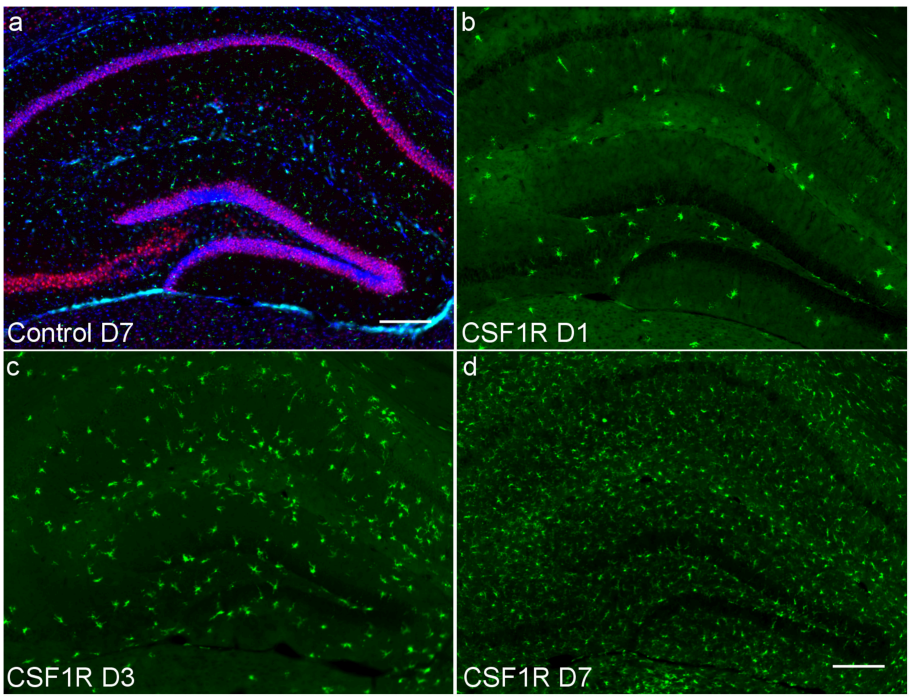

FIGURE 4 | Hippocampal photomicrographs (10X) representative of C57BL/6J mice during microglial repopulation. **(a)** Representative control animal immunostained with antibodies for neurons (anti-NeuN, red), microglia (anti-Iba1, green), and astrocytes (anti-GFAP, cyan), counterstained for nuclei with DAPI (blue). **(b)** Day 1 post CSF1R inhibition display scant microglia present as microglia begin to start repopulating the brain. **(c)** 3 days post-withdrawal and **(d)** 7 days post-withdrawal show microglial recovery over the span of a week. Only microglial counts show a significant increase during the time course. Scale bar = 200 μm.

with quantitative measures of greater hindered diffusion arising from the extra-neurite space.

DISCUSSION

The development of DWI and subsequent introduction of diffusion tensor imaging (DTI) have demonstrated water molecules diffuse differently in tissues depending on their type, integrity, and architecture (Soares et al., 2013) making diffusion imaging a promising tool for studying the microstructure of the brain. As an extension of DTI, more sophisticated diffusion imaging techniques as CHARMED (Assaf and Basser, 2005), AxCaliber (Assaf et al., 2008), and NODDI (Zhang H. et al., 2012) model water diffusion in distinct compartments in the brain (intra-neurite, extra-neurite) and provide greater tissue specificity than DWI/DTI. Of these, NODDI represents the first clinically feasible multi-compartment DWI method owing to the prohibitive scan times and the complexity of analyzing data in other multi-compartment methods (Van Hecke et al., 2016). As with the other multi-compartment DWI models, the NODDI model includes terms to measure water diffusion arising from the extra-neurite compartment. With microglia in the extra-neurite compartment undergoing dynamic changes in density and morphology throughout all stages of neuroinflammation (Yang et al., 2013), we hypothesized that these changes were likely to disrupt and alter water diffusivity in the extra-neurite compartment thus raising the possibility of employing multi-compartment DWI for the sensitive detection of the density changes associated with microglial-mediated neuroinflammation.

In this work, we first demonstrate the sensitivity of the NODDI model to capture changes in microglial density, whereby increased occupancy of the extra-neurite space is correlated with greater hindered diffusion. We also show that NODDI is sensitive to microglial density following microglial depletion with CSF1R inhibition and subsequent repopulation after drug removal, revealing that microglial density is a key contributor to quantitative measures of hindered diffusion in the extra-neurite space. Finally, we demonstrate the significant statistical correlation between microglial density with quantitative measures of ODI, showing that microglial density is positively correlated with hindered diffusion in the extra-neurite space. Together these data provide the first example of MRI to track the cellular changes associated with microglial activation during neuroinflammation.

The ability to track microglial activation via changes in microglial density throughout stages of neuroinflammation (Dheen et al., 2007) suggests an exciting potential for NODDI to be a major advance in clinical care and research across a large spectrum of neurologic and psychiatric disease, particularly in clinical diagnostic accuracy, patient risk stratification, and therapeutic monitoring of neuroinflammation. Previous work has examined the impact of peripheral inflammation on NODDI metrics of NDI and ODI (Dowell et al., 2018) and interestingly

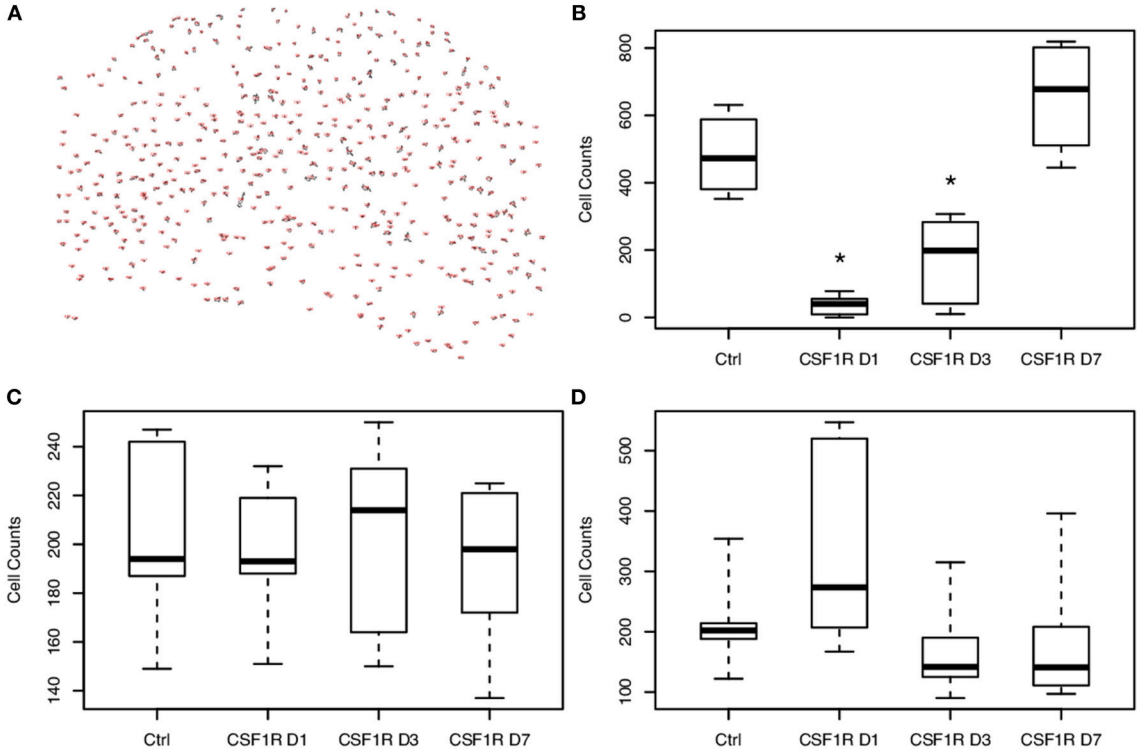

FIGURE 5 | Analysis of cellular density show temporally-dependent increase in microglial density following CSF1R inhibitor withdrawal. **(A)** Representative image of microglial counts from the hippocampus of a control animal produced by ImageJ. Cells were counted following thresholding with the particle analyzer tool. **(B)** Microglia are depleted with CSF1R inhibition and begin to repopulate the brain following CSF1R inhibitor withdrawal. On days 1 and 3 post-withdrawal, microglial counts are still significantly reduced compared to control (*$p < 0.05$). Neurons **(C)** and astrocytes **(D)** demonstrate no significant change in density throughout CSF1R inhibitor treatment or withdrawal.

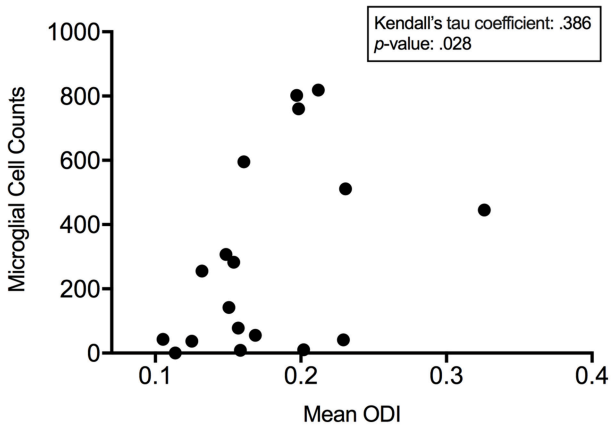

FIGURE 6 | ODI is positively correlated to microglial density. Kendall's tau demonstrates a significant association between measured microglial cell counts and mean orientation dispersion index 1, 3, and 7 days post CSF1R inhibition demonstrating that microglial density is positively correlated with quantitative measures of anisotropic diffusion arising from the extra-neurite space.

demonstrate that while no changes in NDI or ODI were found following the administration of interferon-α (IFN-α) the changes in NDI observed, however, could predict the development of long-term fatigue in a subset of patients. These findings highlight the potential of sensitive quantitative multi-compartment diffusion methods in diagnosis and monitoring of neuropsychiatric disease. As a parallel to tracking disease progression, NODDI may also provide a useful neuroimaging biomarker for evaluating the efficacy of new therapeutics. In diseases like Alzheimer's disease (AD), where neuroinflammation is recognized as a key driving force of disease progression (Readhead et al., 2018), therapeutic research is shifting toward targets that may help control the inflammatory response (Ferretti et al., 2012). Clinical evaluation of AD is difficult and relies heavily on observation of symptoms. Although PET has been proposed as a potential method of monitoring AD progression as well as responsivity to anti-inflammatory therapies (Jack et al., 2013), PET methods such as TSPO (translocator protein) imaging harbor a number of limitations including genotypic variation, complex tracer kinetics, and variability of plasma free fractions across human clinical cohorts (Turkheimer et al., 2015). Further studies evaluating use of NODDI vis-à-vis to TSPO imaging in models of neuroinflammation will clarify which imaging modality may have greater sensitivity and clinical viability.

Importantly, we acknowledge that the original formulation of NODDI does not fully account for the biological observations seen in the data presented herein and cautiously temper the

translation of this approach in *in vivo* applications (both preclinical and clinical). ODI, as derived from a Watson distribution of stick functions with terms for extracellular diffusion (Zhang H. et al., 2012), was not designed to capture changes in microglial density. Despite this limitation, it is readily apparent that the model is responsive to biophysical changes associated with microglial density to yield new insights into the organization of brain tissue in both health and disease. Results from our simulation experiment should also be interpreted with caution as the simulated voxel size is small and large voxels are known to generate somewhat more realistic dMRI signals (Romascano et al., 2018). Further to this point and potentially also limiting the simulation data are that our *in-silica* model of white matter is not a realistic model of white matter with a low volume of intra-axonal space (2.7%). Additionally, we acknowledge that PFA fixation can subtly alter tissue microstructure and diffusion MR measurements (Zhang J. et al., 2012). Nevertheless, *ex-vivo* imaging is pursued herein as higher SNR and spatial resolution are made possible by longer scan times thereby leading to increased imaging sensitivity and to additionally allow for direct radiologic-pathologic comparisons between our histological and imaging measurements, obviating potential discrepancies that could potentially arise if we were to compare quantitative *in vivo* diffusion measurements and *ex vivo* histopathology. Another potential limitation of our work is that while we have demonstrated the robust sensitivity of measures of ODI to changes in microglial density, other cellular changes taking place in the extra-neurite compartment could have a similar effect on ODI and limit the broad application of our approach. In particular, changes such as the regional breakdown of the blood-brain barrier permitting the infiltration of peripherally circulating lymphocytes and monocytes into the brain parenchyma (as could be seen in the setting of tumors or ischemia), could lead to non-specific findings and would limit the clinical translation of our approach. Although NODDI may not specifically track changes in microglia, this work demonstrates the ability of diffusion weighted imaging to track cellular changes in the brain. Furthermore, these potential shortcomings can be averted with appropriate patient selection (e.g., exclusion of patients with brain tumors or large territory stroke) coupled with future technical development to address issues of specificity. Comparing the performance of other multi-compartment models (e.g., CHARMED, AxCaliber) to NODDI would also contribute to validating the application of multi-compartment diffusion models for the sensitive detection of microglial activation in neuroinflammation, but might be of limited clinical benefit due to acquisition scan times that are outside of potential clinical translation.

In summary, our results demonstrate that NODDI parameters corresponding to the extra-neurite compartment can sensitively detect a broad range of microglial densities in the extra-neurite compartment. With microglial density serving as an important biomarker of disease activity and chronicity across a broad-spectrum of neurologic and psychiatric disease, our results highlight the potential for NODDI and other multi-compartment diffusion MRI techniques to detect the cellular changes of microglial-mediated neuroinflammation toward improving clinical diagnostic accuracy, patient risk stratification, and therapeutic monitoring.

AUTHOR CONTRIBUTIONS

SY and JY wrote the manuscript. SY, BB, MT, YZ, SH, and PR performed all experimental work. DH and JY interpreted the experimental data. JY is the guarantor of this work, and as such, had full access to all the data in the study and assumes responsibility for the integrity of the data and the accuracy of the data analyses.

FUNDING

This work was supported by the Department of Radiology at the University of Wisconsin School of Medicine and Public Health (JY), the Brain and Behavior Research Foundation (NARSAD) Young Investigator Grant (JY), and a RSNA R&E Foundation Research Fellow Grant (RF #1417) (JY). Additional support was provided by the Clinical and Translational Science Award (CTSA) program, through the NIH National Center for Advancing Translational Sciences (NCATS), grant UL1TR002373 (JY). This work was also supported under NIH Grant T32 GM 007507 (BB). Additional support under NIH awards UL1TR000427 and TL1TR000429 was also provided (MT). Additional imaging support was provided by the University of Wisconsin Carbone Cancer Center Support Grant P30CA014520. The content is solely the responsibility of the authors and does not necessarily represent the official views of the NIH.

SUPPLEMENTARY MATERIAL

The Supplementary Material for this article can be found online at: https://www.frontiersin.org/articles/10.3389/fnins.2019.00081/full#supplementary-material

REFERENCES

Albrecht, D. S., Granziera, C., Hooker, J. M., and Loggia, M. L. (2016). *In vivo* imaging of human neuroinflammation. *ACS Chem. Neurosci.* 7, 470–483. doi: 10.1021/acschemneuro.6b00056

Alexander, D. C., Hubbard, P. L., Hall, M. G., Moore, E. A., Ptito, M., Parker, G. J., et al. (2010). Orientationally invariant indices of axon diameter and density from diffusion MRI. *NeuroImage* 52, 1374–1389. doi: 10.1016/j.neuroimage.2010.05.043

Alliot, F., Godin, I., and Pessac, B. (1999). Microglia derive from progenitors, originating from the yolk sac, and which proliferate in the brain. *Brain Res. Dev Brain Res.* 117, 145–152.

Assaf, Y., and Basser, P. J. (2005). Composite hindered and restricted model of diffusion (CHARMED) MR imaging of the human brain. *NeuroImage* 27, 48–58. doi: 10.1016/j.neuroimage.2005.03.042

Assaf, Y., Blumenfeld-Katzir, T., Yossi, Y., and Basser, P. J. (2008). AxCaliber: a method for measuring axon diameter distribution from diffusion MRI. *Magn. Reson. Med*. 59, 1347–1354. doi: 10.1002/mrm.21577

Azevedo, F. A., Carvalho, L. R., Grinberg, L. T., Farfel, J. M., Ferretti, R. E., Leite, R. E., et al. (2009). Equal numbers of neuronal and nonneuronal cells make the human brain an isometrically scaled-up primate brain. *J. Comp. Neurol*. 513, 532–541. doi: 10.1002/cne.21974

Cook, P. A., Bai, Y., Nedjati-Gilani, S., Seunarine, K. K., Hall, M. G., Parker, G. J., et al. (2006). "Camino: open-source diffusion-mri reconstruction and processing," in *14th Scientific Meeting of the International Society for Magnetic Resonance in Medicine*, 2759.

Dheen, S. T., Kaur, C., and Ling, E. A. (2007). Microglial activation and its implications in the brain diseases. *Curr Med Chem*. 14, 1189–1197. doi: 10.2174/092986707780597961

Dowell, N. G., Bouyagoub, S., Tibble, J., Voon, V., Cercignani, M., and Harrison, N. A. (2018). Interferon-alpha-induced changes in NODDI predispose to the development of fatigue. *Neuroscience*. doi: 10.1016/j.neuroscience.2017.12.040. [Epub ahead of print].

Elmore, M. R., Najafi, A. R., Koike, M. A., Dagher, N. N., Spangenberg, E. E., Rice, R. A., et al. (2014). Colony-stimulating factor 1 receptor signaling is necessary for microglia viability, unmasking a microglia progenitor cell in the adult brain. *Neuron* 82, 380–397. doi: 10.1016/j.neuron.2014.02.040

Ferretti, M. T., Allard, S., Partridge, V., Ducatenzeiler, A., and Claudio Cuello, A. (2012). Minocycline corrects early, pre-plaque neuroinflammation and inhibits BACE-1 in a transgenic model of Alzheimer's disease-like amyloid pathology. *J. Neuroinflammation* 9:62. doi: 10.1186/1742-2094-9-62

Ginhoux, F., Greter, M., Leboeuf, M., Nandi, S., See, P., and Gokhan, S. (2010). Fate mapping analysis reveals that adult microglia derive from primitive macrophages. *Science* 330:841–845. doi: 10.1126/science.1194637

Grussu, F., Schneider, T., Tur, C., Yates, R. L., Tachrount, M., and Ianuş, A. (2017). Neurite dispersion: a new marker of multiple sclerosis spinal cord pathology? *Ann. Clin. Transl. Neurol*. 663–79. doi: 10.1002/acn3.445

Hall, M. G., and Alexander, D. C. (2009). Convergence and parameter choice for monte-carlo simulations of diffusion MRI. *IEEE Trans. Med. Imaging*. 28, 1354–1364.

Harms, R. L., Fritz, F. J., Tobisch, A., Goebel, R., and Roebroeck, A. (2017). NeuroImage robust and fast nonlinear optimization of Di Ff Usion MRI microstructure models. *NeuroImage* 155:82–96. doi: 10.1016/j.neuroimage.2017.04.064

Herculano-Houzel, S. (2014). The glia/neuron ratio: how it varies uniformly across brain structures and species and what that means for brain physiology and evolution. *Glia* 62, 1377–1391. doi: 10.1002/glia.22683

Herculano-Houzel, S., Mota, B., and Lent, R. (2006). Cellular scaling rules for rodent brains. *Proc. Nat. Acad. Sci. U. S. A*. 103, 12138–12143. doi: 10.1073/pnas.0604911103

Hinwood, M., Morandini, J., Day, T. A., and Walker, F. R. (2012). Evidence that microglia mediate the neurobiological effects of chronic psychological stress on the medial prefrontal cortex. *Cerebral Cortex* 22, 1442–1454. doi: 10.1093/cercor/bhr229

Iadecola, C., and Anrather, J. (2011). The immunology of stroke: from mechanisms to translation. *Nat. Med*. 17:796–808. doi: 10.1038/nm.2399.

Jack, C. R., Knopman, D., Jagust, W., Petersen, R. C., Weiner, W. W., and Aisen, P. (2013). Update on hypothetical model of Alzheimer's disease biomarkers. *Lancet Neurol*. 12, 207–216. doi: 10.1016/S1474-4422(12)70291-0.Update

Kamiya, K., Hori, M., Irie, R., Miyajima, M., Nakajima, M., and Kamagata, K. (2017). Diffusion imaging of reversible and irreversible microstructural changes within the corticospinal tract in idiopathic normal pressure hydrocephalus. *NeuroImage Clin*. 14, 663–671. doi:10.1016/j.nicl.2017.03.003

Kozlowski, C., and Weimer, R. M. (2012). An automated method to quantify microglia morphology and application to monitor activation state longitudinally *in vivo*. *PLoS ONE* 7:e31814. doi: 10.1371/journal.pone.0031814

Lull, M. E., and Block, M. L. (2010). Microglial activation and chronic neurodegeneration. *Neurotherapeutics* 7, 354–365. doi: 10.1016/j.nurt.2010.05.014

Mondelli, V., Vernon, A. C., Turkheimer, F., Dazzan, P., and Pariante, C. M. (2017). Brain microglia in psychiatric disorders. *Lancet Psychiatry* 4, 563–572. doi: 10.1016/S2215-0366(17)30101-3

Mota, B., and Herculano-Houzel, S. (2014). All brains are made of this: a fundamental building block of brain matter with matching neuronal and glial masses. *Front. Neuroanat*. 8:127. doi: 10.3389/fnana.2014.00127

Ong, I. M., Gonzalez, J. G., McIlwain, S. J., Sawin, E. A., Schoen, A. J., Adluru, N., et al. (2018). Gut microbiome populations are associated with structure-specific changes in white matter architecture. *Transl. Psychiatry* 8:6. doi: 10.1038/s41398-017-0022-5

Rae, C. L., Davies, G., Garfinkel, S. N., Gabel, M. C., Dowell, N. G., Cercignani, M., et al. (2016). Deficits in neurite density underlie white matter structure abnormalities in first-episode psychosis. *Biol. Psychiatry* 82, 716–25. doi: 10.1016/j.biopsych.2017.02.008

Readhead, B., Haure-Mirande, J. V., Funk, C. C., Richards, M. A., Shannon, P., Haroutunian, V., et al. (2018). Multiscale analysis of independent alzheimer's cohorts finds disruption of molecular, genetic, and clinical networks by human herpesvirus. *Neuron* 99, 64–82.e7. doi: 10.1016/j.neuron.2018.05.023

Romascano, D., Rafael-Patino, J., Jelescu, I., Barakovic, M., Tim, B., Jean-Philippe, D., et al. (2018). "Voxel size matters: big voxels are required to generate realistic extra-axonal DMRI signals from monte carlo simulations," in *ISMRM*, 1–2.

Soares, J. M., Marques, P., Alves, V., and Sousa, N. (2013). A hitchhiker's guide to diffusion tensor imaging. *Front. Neurosci*. 7:31. doi: 10.3389/fnins.2013.00031

Turkheimer, F. E., Rizzo, G., Bloomfield, P. S., Howes, O., Zanotti-Fregonara, P., Bertoldo, A., et al. (2015). The methodology of TSPO imaging with positron emission tomography. *Biochem. Soc. Trans*. 43, 586–592. doi: 10.1042/BST20150058

Van Hecke, W., Emsell, W., and Stefan, S. (2016). *Diffusion Tensor Imaging: A Practical Handbook*. New York, NY: Springer.

von Bartheld, C. S., Bahney, J., and Herculano-Houzel, S. (2016). The search for true numbers of neurons and glial cells in the human brain: a review of 150 years of cell counting. *J. Comp. Neurol*. 524, 3865–3895. doi: 10.1002/cne.24040

Woodcock, T., and Morganti-Kossmann, M. C. (2013). The role of markers of inflammation in traumatic brain injury. *Front. Neurol*. 4:4. doi: 10.3389/fneur.2013.00018

Yang, T. T., Lin, C., Hsu, C. T., Wang, T. F., Ke, F. Y., and Kuo, Y. M. (2013). Differential Distribution and Activation of Microglia in the Brain of Male C57BL/6J Mice. *Brain Struct. Funct*. 218, 1051–1060. doi: 10.1007/s00429-012-0446-x

Zhang, H., Schneider, T., Wheeler-Kingshott, C. A., and Alexander, D. C. (2012). NODDI: practical *in vivo* neurite orientation dispersion and density imaging of the human brain. *NeuroImage* 61, 1000–1016. doi: 10.1016/j.neuroimage.2012.03.072

Zhang, H., Yushkevich, P. A., Alexander, D. C., and Gee, J. C. (2006). deformable registration of diffusion tensor MR images with explicit orientation optimization. *Med. Image Anal*. 10, 764–785. doi: 10.1016/j.media.2006.06.004

Zhang, J., Jones, M. V., McMahon, M. T., Mori, S., and Calabresi, P. A. (2012). *In vivo* and *ex vivo* diffusion tensor imaging of cuprizone-induced demyelination in the mouse Corpus Callosum. *Magnet. Reson. Med*. 67, 750–759. doi: 10.1002/mrm.23032

Conflict of Interest Statement: The authors declare that the research was conducted in the absence of any commercial or financial relationships that could be construed as a potential conflict of interest.

Copyright © 2019 Yi, Barnett, Torres-Velázquez, Zhang, Hurley, Rowley, Hernando and Yu. This is an open-access article distributed under the terms of the Creative Commons Attribution License (CC BY). The use, distribution or reproduction in other forums is permitted, provided the original author(s) and the copyright owner(s) are credited and that the original publication in this journal is cited, in accordance with accepted academic practice. No use, distribution or reproduction is permitted which does not comply with these terms.

frontiers in Neuroscience

ORIGINAL RESEARCH
published: 14 March 2019
doi: 10.3389/fnins.2019.00211

Brain Connectivity and Information-Flow Breakdown Revealed by a Minimum Spanning Tree-Based Analysis of MRI Data in Behavioral Variant Frontotemporal Dementia

Valentina Saba[1], Enrico Premi[2], Viviana Cristillo[2], Stefano Gazzina[2], Fernando Palluzzi[1], Orazio Zanetti[3], Roberto Gasparotti[4], Alessandro Padovani[2], Barbara Borroni[2] and Mario Grassi[1]*

[1] Medical and Genomic Statistics Unit, Department of Brain and Behavioral Sciences, University of Pavia, Pavia, Italy, [2] Neurology Unit, Department of Clinical and Experimental Sciences, Centre for Neurodegenerative Disorders, University of Brescia, Brescia, Italy, [3] Alzheimer's Research Unit, IRCCS Fatebenefratelli, Brescia, Italy, [4] Neuroradiology Unit, University of Brescia, Brescia, Italy

OPEN ACCESS

Edited by:
Zhi Yang,
Shanghai Mental Health Center, China

Reviewed by:
Hyunjin Park,
Sungkyunkwan University, South Korea
Sunghyon Kyeong,
Yonsei University College of Medicine, South Korea

***Correspondence:**
Valentina Saba
valentina.saba01@universitadipavia.it

Specialty section:
This article was submitted to Brain Imaging Methods, a section of the journal Frontiers in Neuroscience

Received: *17 September 2018*
Accepted: *25 February 2019*
Published: *14 March 2019*

Citation:
Saba V, Premi E, Cristillo V, Gazzina S, Palluzzi F, Zanetti O, Gasparotti R, Padovani A, Borroni B and Grassi M (2019) Brain Connectivity and Information-Flow Breakdown Revealed by a Minimum Spanning Tree-Based Analysis of MRI Data in Behavioral Variant Frontotemporal Dementia. Front. Neurosci. 13:211. doi: 10.3389/fnins.2019.00211

Brain functional disruption and cognitive shortfalls as consequences of neurodegeneration are among the most investigated aspects in current clinical research. Traditionally, specific anatomical and behavioral traits have been associated with neurodegeneration, thus directly translatable in clinical terms. However, these qualitative traits, do not account for the extensive information flow breakdown within the functional brain network that deeply affect cognitive skills. Behavioural variant Frontotemporal Dementia (bvFTD) is a neurodegenerative disorder characterized by behavioral and executive functions disturbances. Deviations from the physiological cognitive functioning can be accurately inferred and modeled from functional connectivity alterations. Although the need for unbiased metrics is still an open issue in imaging studies, the graph-theory approach applied to neuroimaging techniques is becoming popular in the study of brain dysfunction. In this work, we assessed the global connectivity and topological alterations among brain regions in bvFTD patients using a minimum spanning tree (MST) based analysis of resting state functional MRI (rs-fMRI) data. Whilst several graph theoretical methods require arbitrary criteria (including the choice of network construction thresholds and weight normalization methods), MST is an unambiguous modeling solution, ensuring accuracy, robustness, and reproducibility. MST networks of 116 regions of interest (ROIs) were built on wavelet correlation matrices, extracted from 41 bvFTD patients and 39 healthy controls (HC). We observed a global fragmentation of the functional network backbone with severe disruption of information-flow highways. Frontotemporal areas were less compact, more isolated, and concentrated in less integrated structures, respect to healthy subjects. Our results reflected such complex breakdown of the frontal and temporal areas at

both intra-regional and long-range connections. Our findings highlighted that MST, in conjunction with rs-fMRI data, was an effective method for quantifying and detecting functional brain network impairments, leading to characteristic bvFTD cognitive, social, and executive functions disorders.

Keywords: functional connectivity, functional magnetic resonance imaging, resting state, minimum spanning tree, graph theory, behavioral variant frontotemporal dementia, neurodegeneration

INTRODUCTION

The bvFTD is clinically defined by personality changes and behavioral disturbances, impairment of executive functions and emotional blunting (Gorno-Tempini et al., 2011; Rascovsky et al., 2011). Abnormal intracellular accumulation of either tau or TDP-43 protein is found in most cases (Mann and Snowden, 2017).

Recently, the increasing interest in unraveling functional and structural features of the brain, has benefitted from complex network analyses, such as graph theory, a multidisciplinary approach that allows to analyse complex systems in a straightforward computable way and to describe cerebral areas as nodes, and their connections as edges (Rubinov and Sporns, 2010). Both structural (anatomical) and functional (statistical relationship between two nodes) connectivity can be assessed (Zhang et al., 2016).

Applying graph theoretical methods to neuroimaging techniques is becoming popular in the study of brain dysfunction (Bullmore and Sporns, 2009; Drakesmith et al., 2015; Chiang et al., 2016). Recently, a few studies have considered graph theory analysis applied to rs-fMRI data in patients with bvFTD and have better described FTD-related brain changes (Agosta et al., 2013; Filippi et al., 2017). However, although conventional graph theoretical analyses are helpful in dissecting disease mechanisms (Bullmore and Sporns, 2012), the methodology is significantly hampered by a number of arbitrary choices. Descriptive metrics and their normalization, network type (weighted or unweighted networks), threshold value (fixed cut-off, fixed average degree, fixed edge density, or variable threshold over a range of values) are some of the critical points making network results difficult to reproduce (van Wijk et al., 2010; Telesford et al., 2011; Stam et al., 2014; Drakesmith et al., 2015; Yu et al., 2016). In addition, several network metrics and node centrality indices may assume different importance at either local or global scale (Telesford et al., 2011; Antonenko et al., 2018), whether the graph model accounts for time variant (i.e., dynamic) or invariant (i.e., static) connectivity (Rashid et al., 2014; Park et al., 2018), and the parcellation type, according to Independent Component Analysis (ICA; McKeown et al., 2003; Griffanti et al., 2014) and specific atlases (see Materials and Methods, for data pre-processing in this work).

Minimum Spanning Tree, a unique acyclic subgraph that connects N nodes with (N-1) edges, and maximizing synchronization between brain areas (i.e., minimizes edge connections), is a promising unambiguous solution to describe complex brain networks (Stam et al., 2014). The use of MST avoids methodological confounding thanks to an efficient integration of topological properties and functional connectivity information (Tewarie et al., 2014; van Diessen et al., 2016; van Lutterveld et al., 2017), ensuring network robustness and reproducibility respect to classical graph analytical approaches (Otte et al., 2015; Tewarie et al., 2015). MST is a tree which has the minimum total edge weight of all possible spanning trees of the original graph. If the brain network can be interpreted as a kind of transport network, an MST might represent the critical backbone of information flow in weighted networks (i.e., contains with high probability all the shortest paths in the network). Given MSTs efficiency and high sensitivity to small fluctuations of connection weights (Van Mieghem and Magdalena, 2005), they can intrinsically provide an accurate representation of subtle and critical topological perturbations, at local scale. On the other hand, MST sparseness could raise issues at global scale. However, it has been demonstrated that if the MST weight distribution is consistent with a power law with sufficiently small exponent value, the global information flow of the underlying network follows entirely MST paths (Van Mieghem and Magdalena, 2005; Van Mieghem and van Langen, 2005; Meier et al., 2015). Moreover, TOMs can be applied to the original adjacency matrix to modulate neighborhood characteristics in MST nodes (Ravasz et al., 2002). In addition, we used wavelet decomposition and correlation to obtain noise-free and robust functional relationships between brain areas (Achard et al., 2006; Zhang et al., 2016).

Collectively, these aspects enable data-driven network comparison of healthy and diseased groups, without normalization or standardization steps, as recently illustrated in EEG and MEG data (Stam et al., 2014; van Dellen et al., 2014; Numan et al., 2017). Furthermore, network robustness and reproducibility should ensure univocal results, minimizing room for ambiguous interpretations. Besides graph theoretical aspects, data acquisition and pre-processing issues may affect results, including brain parcellation and data acquisition technologies. These aspects should follow the principles of common usage, availability, cost effectiveness, and non-invasivity, that can secondarily affect methodological choices and issues (Hohenfeld et al., 2018). Despite objective difficulties in generating a consensus functional brain map, especially for rare disorders, a set of reference resting state functional networks have been replicated in many different studies (Hohenfeld et al., 2018). According to well-established rs-fMRI literature, three reference networks are mainly involved in bvFTD functional breakdown: the default-mode network (DMN), the salience

Abbreviations: AAL, automated anatomical labeling; bvFTD, behavioral variant Frontotemporal Dementia; HC, healthy controls; MST, minimum spanning tree; ROI, regions of interest; rs-fMRI, resting state functional MRI; SPT, shortest path tree; TOM, topological overlap measures.

network (SN), and the executive network (EN), accounting for the cognitive, emotional, and social impairments characterizing this pathology (Raichle, 2015; Trojsi et al., 2015; Sedeño et al., 2016; Hohenfeld et al., 2018).

In this study, we leverage MST-based analysis of rs-fMRI data to investigate large-scale functional network alterations, inspecting global and local network properties in bvFTD patients, compared to a group of HC, and providing a novel MST procedure, combining individual tree-based global evidences and two-group topological aspects.

MATERIALS AND METHODS

The analysis workflow of the rs-fMRI data is illustrated in **Figure 1** and described in detail below.

Subjects

Forty-one patients with a probable bvFTD diagnosis, according to current criteria (Gorno-Tempini et al., 2011), were recruited at the Center for Neurodegenerative Disorders, University of Brescia, Italy All patients underwent an extensive neuropsychological assessment, as previously published (Gazzina et al., 2016), genetic screening for the most frequent monogenic causes of FTD (i.e., *Granulin*, *C9orf72*, and *Microtubule Associated Protein* Tau; Cosseddu et al., 2018) and brain MRI structural imaging study. In the present study, none of the bvFTD cases carried pathogenic mutations of monogenic bvFTD.

Thirty-nine HC, recruited from voluntary individuals, were used as control group. HC underwent a brief standardized neuropsychological assessment (Mini-Mental State Examination; MMSE >=27). **Table 1** shows the demographic information of the participants. The study, in conformity with the Helsinki Declaration, was approved by the Brescia Hospital Ethics Committee. Informed consent was obtained from all participants.

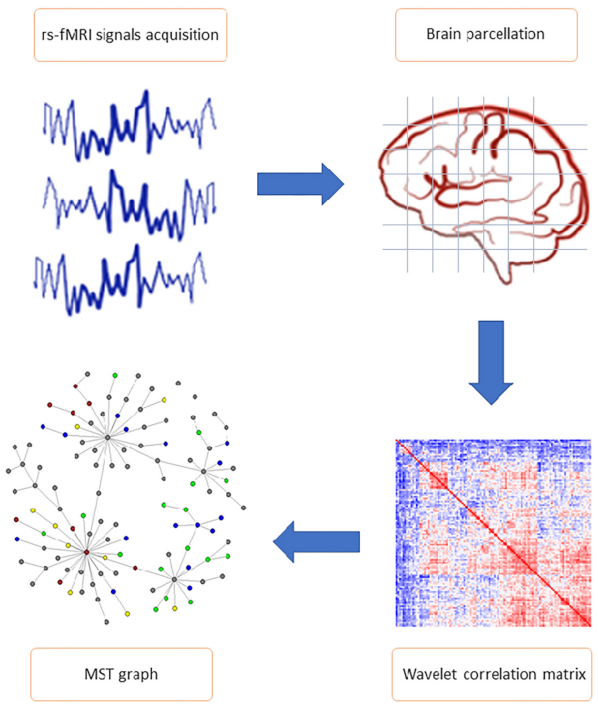

FIGURE 1 | General study workflow. The most important steps of connectome extraction. MRI signals acquisition and brain parcellation represent the first phases of resting state functional magnetic resonance imaging data pre-processing. Wavelet correlation matrix and minimum spanning tree (MST) network calculation are included in the analysis phase. Wavelet transformation was applied to the average voxel time series mapped to AAL 116 brain regions of interest (ROI), allowing to obtain the statistical relationships between nodes (i.e., wavelet correlation matrices). Each matrix is the input of the MST algorithm, from which parameters and topological features (including edges partition and nodes cluster) have been calculated.

MRI Acquisition

All imaging was obtained using a 1.5T Siemens Avanto MRI scanner (Siemens, Erlangen, Germany), equipped with a circularly polarized transmit-receive coil. In a single session, the following scans were collected from each subject:

(i) dual-echo TSE [repetition time = 2500 ms, echo time (TE) = 50 ms], to exclude presence of macroscopic brain abnormalities, according to exclusion criteria;
(ii) 3D MPRAGE T1-weighted scan (TR = 2050 ms, TE = 2.56 ms, matrix = 1 × 1 × 1, in-plane field of view [FOV] = 256 × 256 mm^2, slice thickness = 1 mm, flip angle = 15°);
(iii) T2*-weighted EPI sensitized to BOLD contrast [TR = 2500 ms, TE = 50 ms, 29 axial slices parallel to anterior commissure-posterior commissure line (AC-PC) line, matrix = 64 × 64, field of view = 224 mm, slice thickness = 3.5 mm], gap between slices 1.75 mm for rs-fMRI.

Echo planar images were collected during rest for an 8-min period, resulting in a total of 195 volumes.

Neuroimaging Pre-processing

Functional data were pre-processed using FSL 5.0.8 neuroimaging software, as reported in Jenkinson et al. (2012): (i) the first two volumes were removed to allow signal stabilization; each volume was motion-corrected to a reference volume using MCFLIRT; (ii) non-brain structures were removed using Brain Extraction Tool (BET); (iii) the effect of TR during slice acquisition was reduced using slice-timing correction and the data were spatially smoothed applying the Gaussian kernel with

TABLE 1 | Demographic and clinical characteristic of the participants.

	bvFTD (*n* = 41)	HC (*n* = 39)	*P*-value
Age (year)	65.6 ± 7.01	61.7 ± 6.5	0.010[a]
Sex (male/female)	26/15	13/26	0.014[b]
Education (year)	9.1 ± 3.82	10.3 ± 3.84	0.161[a]
CDR	6.7 ± 3.84	0.0 ± 0.0	–

Values for bvFTD and HC are reported as mean ± SD; a, independent two-group t-test; b, Pearson chi-squared test; CDR, Clinical Dementia Rating.

a full width and half maximum (FWHM) of about 7 mm; (iv) grand-mean intensity of the entire data was adjusted by a single multiplicative factor; (v) high-pass temporal filtering Gaussian-weighted least-squares straight line fitting (100 s) was applied; (vi) functional data were co-registered into equivalent native-space T1 weighted image using Boundary-Based Registration (BBR); and (vii) each T1 weighted image was co-registered into standard space template MNI152 using linear (affine with 12 degree of freedom) brain image registration (FLIRT).

To control for motion effect, we included in the further steps only subjects with head motion in a range below or equal to 1 mm (translation) and one degree (rotation). Motion parameters were derived from six degree of freedom registration using MCFLIRT (Jenkinson et al., 2012).

After pre-processing, we applied an automatic approach called "FMRIB's ICA-based X-noiseifier" (FIX) to detect non-signal components in resting state images which combines the classifiers approach and the Independent Component Analysis (ICA) in a MATLAB environment (Griffanti et al., 2014, 2015). We applied FIX procedure in three steps. First, for each subject we estimate the amount of Gaussian noise of the true dimensionality of the data, i.e., the number of activation and non-Gaussian noise sources using a probabilistic ICA approach implemented in MELODIC (Beckmann and Smith, 2004). Then, we made a random selection of subjects (10 healthy subjects and 10 bvFTD subjects, covering approximately 25% of the whole sample set) to create a subsample to train the FIX's multi-level classifier. For these subjects, we manually selected the components (white matter, susceptibility artifact, head motion, cardiac pulsation) looking into the thresholded spatial map estimated from single-ICA and the power spectrum of the time series for each component (Griffanti et al., 2014). Lastly, to test if FIX successfully detected the noise components and regressed out the variance (including the six motion parameters derived from MCFLIRT), we looked into a sample of subjects to confirm classification of bad components. The "cleaned" rs-fMRI images (after noise and motion variance regression) of each subject were subsequently used for brain parcellation.

Brain Parcellation

The ALL atlas (AAL; Tzourio-Mazoyer et al., 2002) was used to parcel brain into 116 (90 cortical and subcortical, and 26 cerebellar) regions of interest (ROIs, **Supplementary Table 1**). Mean time series were extracted from each ROI by averaging the signal from all voxels within each region, using Marsbar software ([1]Brett et al., 2002). A subsequent descriptive aggregation was applied to obtain 8 (right and left) macro-ROI (referred to as lobes or "macro-regions"): Frontal, Insular, Limbic, Occipital, Parietal, Subcortical Gray Matter (SCGM; including Thalamus), Temporal, and Cerebellum (including Vermis).

Wavelet Correlation Analysis

For each subject, the final dataset (Saba et al., 2018) was composed by 193 mean time-series extracted from each brain region. Different correlation estimates define statistical relationship between brain region pairs (Zalesky et al., 2012): in the present study, we used wavelet correlation.

Each temporal series was decomposed using wavelet analysis and characterized by weighted coefficients, proportional to the total amount of energy emitted from the system, relative to a specific scale and brain location. Considering total energy as a frequency-time, wavelet decomposition enables data processing at different hierarchical scale resolutions. Indeed, low-frequency components correspond to coefficients of approximative scale, while high-frequency components correspond to finer scale coefficients (Bullmore et al., 2004). The high flexibility for non-stationary characteristics of the data in each decomposition scale favors wavelet multi-modularity application to fMRI data. Therefore, wavelet correlation results in a higher robustness and noise reduction, with a more homogeneous representation of the original time series and their transformations (Bullmore et al., 2004; Zhang et al., 2016).

Consistent with (Zhang et al., 2016) guidelines, the maximal overlap discrete wavelet transform (MODWT; Achard et al., 2006) with a Daubechies wavelet filter (length equal to 8), was used to band-pass filter on mean time series, and extract wavelet coefficients for the wavelet scales. Given our (TR = 2500 ms, Nyquist frequency = 0.2 Hz), four frequency bands (i.e., scales) were used; scale one: 0.2–0.1 Hz; scale two: 0.05–0.1 Hz; scale three: 0.025–0.05 Hz; and scale four: 0.013–0.025 Hz. Then, we defined a correlation matrix whose *ij*th elements were set by the estimated wavelet correlations between brain regions $i\left(\lambda_i^{(s)}\right)$ and region $j\left(\lambda_j^{(s)}\right)$:

$$r_{ij} = \frac{cov\left(\lambda_i^{(s)}; \lambda_j^{(s)}\right)}{\sqrt{var\left(\lambda_i^{(s)}\right) var\left(\lambda_j^{(s)}\right)}}$$

we focused on wavelet decomposition scale two ($s = 2$), as only this scale reached the significance in three distinct bvFTD/HC connectivity-based Wilcoxon rank sum tests (**Supplementary Table 2**). Specifically, we quantified bivariate connectivity of the wavelet correlation matrix for each subject (Lynall et al., 2010), with three global measures: (i) *strength*, defined as the average of columns mean; (ii) *diversity,* defined as the average of the columns variance, and (iii) *zero correlation,* defined as the number of correlations with $P > 0.05$, testing the null hypothesis, $H_0 : \rho ij = 0$.

Minimum Spanning Tree (MST) Structures and Graph Metrics

The MST method overcomes issues concerning arbitrary threshold selection in weighted connected graphs, by joining edges with minimum weight. In other words, it assembles connections minimizing the sum of edge-weights, excluding edges that form a cycle. MST is an extremely efficient binary representation of a full graph G (N, E) characterized by N nodes and E = (N-1) edges. It yields perfectly comparable networks

[1]http://marsbar.sourceforge.net/

among different samples, without dependences from vertices and edges number variability, and a best possible synthesis of the original graph information, achieved through the most important subgraph (Stam et al., 2014). Among existing methods for MST search, we applied the Prim's algorithm (Cormen et al., 2001), to obtain a MST from each subjects' wavelet correlation matrix.

The MST method handles very different network configurations with their extremes represented by linear or star shapes. In the former, each node has a maximum of two edges (i.e., path-like tree) and two extreme leaves (i.e., nodes with only one link). Whereas, in a star, all nodes are leaves, except the central node to which the other ones are connected (Stam et al., 2014).

Every network can be described through a set of graph metrics (e.g., topological indices) characterized according to its configuration (either linear or star) and its specific graph metrics values. We used global MST measures providing information on graph centrality (maximum degree k_{max}, maximum betweenness B_{max}), distance (diameter *d*, eccentricity *Ecc*), association (assortativity *Ass*), and topological aspects (degree divergence *K*, leaf fraction *Lf)*. Their definitions are given in **Table 2**.

Short distances and overload prevention aspects suggest a good tree configuration or network integration. If a tree has a star-like (i.e., highly connected) topology, it will be characterized by a greater information exchange capacity (i.e., spread of information across the tree), yet a greater probability of central node overload. The opposite behavior is true if the graph has a line-like topology. In particular, an increase of maximum betweenness B_{max} and leaf fraction *Lf*, with a decrease of diameter d and eccentricity *Ecc,* tend to have a star-type configuration and a better network integration (van Lutterveld et al., 2017). In addition, maximum betweenness B_{max} and degree divergence *K* correlate positively with the presence of some high-degree tree nodes (hub communication) in networks with a scale-free degree distribution (a scale-free network has a large number of nodes with a lower degree and few highly connected hubs; Albert and Barabási, 2002; Mears and Pollard, 2016).

Finally, positive assortativity ($Ass > 0$) indicates that nodes are likely to be connected to other nodes with the same degree, and therefore that the high degree nodes (hubs) tend to be connected to each other (Bullmore and Sporns, 2009). Negative assortativity ($Ass < 0$) is typical of biological networks with hierarchical structure where hubs are connected to nodes with lower degree nodes (Newman, 2003).

Topological Overlap Measures (TOM) and Shortest Path Tree (SPT)

In the present study, we implemented pre-processing procedures to avoid some of the intrinsic limitations of the MST approach: the absence of triangular connections (i.e., absence of clustering metric) e graph sparseness with a limited number of edges of the resulted network.

First, we applied *topological overlap measures (TOM*; Ravasz et al., 2002; Zhang and Horvath, 2005) to the network adjacency matrix to compensate the absence of triangular connections in the MST. This allowed to analyse MSTs in terms of aggregation or clustering without biases. Specifically:

$$TOM_{ij} = \frac{l_{ij} + a_{ij}}{min\{k_i, k_j\} + 1 - a_{ij}}$$

where $l_{ij} = \sum_u a_{iu} a_{ju}$ is the overlap estimate between two nodes neighborhoods, a_{ij} is the ijth-element of adjacency matrix, k_i and k_j are the degree measures of ith-node and jth-node, expressed as $ki = \sum_{u \neq i} a_{iu}$; $k_j = \sum_{u \neq j} a_{ju}$. A higher overlap is associated with a greater relationship between two nodes, and a greater relationship with their common nodes (Mumford et al., 2010). Therefore, TOM modulates neighborhood characteristics of nodes, by quantifying the topological overlap between two nodes against all other nodes in the network. High TOM values identify nodes that constitute a neighborhood (Ravasz et al., 2002).

Secondly, MST is characterized by (*N*-1) edges, resulting a sparse graph with a limited number of edges. Therefore, we evaluate the network performance of MST through the SPT problem (Van Mieghem and Magdalena, 2005; Meier et al., 2015), quantifying if MST is a good representation of the whole graph (i.e., whether the sparse tree may be considered as a critical backbone of original network; Tewarie et al., 2014).

TABLE 2 | Description of minimum spanning tree global measures.

Measure	Definition
k_{max}	*Degree (k)* of a node is the number of links connecting one node to another in the network, and *maximum degree* k_{max} indicates the highest value of node degree in the network
B_{max}	*Betweenness centrality* (*B)* of a node indicates the number of shortest paths passing through the normalized node such that $B \epsilon [0,1]$, and *maximum betweenness* B_{max} indicates the highest value of betweenness centrality in the network
d	*Diameter (d)* identifies the longest distance, measured in number of edges, between any two nodes; *d* has a range from 2 to *N*-1
Ecc	*Eccentricity (Ecc)* of a node indicates the distance of a node with respect to any other node, in term of longest distance between them. Here, *Ecc* represents the average value (i.e., the arithmetic mean) for all nodes
Ass	*Assortativity (Ass)* describes node tendency to link to other nodes, characterized by the same or similar degree, which can be quantified by computing the Pearson correlation coefficient of the degrees of pairs of nodes connected by an edge
K	*Degree divergence (K)* is a measure of broadness of the degree distribution in the whole network, defined as the ratio between the variability and the average of node connections
Lf	*Leaf fraction (Lf)* is the ratio between the number of nodes with only one edge (i.e., "end-points" in the graph) and the maximum possible number of edges (i.e., the number of nodes minus 1, *N*-1). Stars-type graph is defined by $Lf = (N-1)/(N-1) = 1$, while linear-type graph by $Lf = 2/(N-1)$

N, number of nodes in a minimum spanning tree.

The shortest path is the path with minimum sum of weights from a source to a destination node, and a SPT is the union of the shortest paths from a source node to all other nodes in the graph. An SPT is mainly sensitive to the small, non-negative link weights, around zero. Starting with a full graph G, the probability distribution for the link weights of G around zero can be described by a power distribution: $F(x) = \Pr(X \leq x) \sim x^{\alpha}$, where x ∈ [0, 1] represents weights, and the exponent α > 0, defines the *extreme value index* of the probability distribution (Van Mieghem and Magdalena, 2005).

Three specials α−trees correspond to precise α ranges. The $\alpha \to \infty$ regime matches a unique weight for all links (i.e., $w = 1$). In the $\alpha = 1$ regime, link weights result to be uniformly distributed. Finally, in the $\alpha \to 0$ regime, link weights show strong fluctuations. For $\alpha \to 0$, defined as the *stronger disorder condition*, the SPT of the full graph coincide with a MST (Van Mieghem and Magdalena, 2005; Van Mieghem and van Langen, 2005), and the information flow within the network follows only MST links (Meier et al., 2015).

Therefore, we tested the $\alpha \to 0$ regime (i.e., MST) of the weighted full (i.e., original) graph G for each subject in three steps:

(1) Define a full graph G (N, E) by fixing to zero the not statistically significant ($P > 0.05$) wavelet correlations, r_{ij}. The null hypothesis: $H_0 : \rho ij = 0$ was evaluated with the Mutual Information test, $MI = -N \ln\left(1 - r_{ij}^2\right)/2$ (Edwards et al., 2010).
(2) Apply topological overlap measures (i.e., TOM) to the $r_{ij}^{(0)} = r_{ij}$ if $P < 0.05$ and $r_{ij}^{(0)} = 0$ if $P \geq 0.05$. MST was created by edges weights defined as $w_{ij} = \min\left(1/TOM_{ij}; 100\right)/100$. This transformation ensures that weights are enclosed in the range (0, 1), and the most important edges (with small weights, i.e., large TOM values) represent the strongest neighborhood connections.
(3) Ranking weights w_{ij} in descending order and estimating the α exponent from the power function$F(x) = c \cdot x^{\alpha}$, by plotting Y = log10 [$F(x)$] versus X = log10 [(x)]. A straight line with an R-squared index approaching 1 is indicative of good fit to the power function, and slope indicates SPT coincidence with MST.

Edges Partition and Nodes Clustering in MST

Two-group comparisons of topological MST properties were applied to the individual wavelet correlation matrices, between bvFTD and HC, averaged over subjects. Topological structure of nodes and links in an MST have a key role to capture paths with higher importance in information flow (Meier et al., 2015). It is possible to identify an MST subnetwork showing a higher average node (or link) betweenness centrality compared to the rest of MST (Wu et al., 2006). In other terms, this subset of nodes (or links) is used more often than others, and their paths can be considered as a set of *superhighways* (SHW) in MST, i.e., the most important "roads." Other links in MST constitute "secondary roads." Identifying SHW enabled to subdivide MST edges (links) in two distinct components with significantly different transport properties.

Based on SHW's definition, we applied the method suggested by Wu et al. (2006), on both scale-free and Erdos–Renyi (i.e., random) networks, for edges partition in MST. Briefly, considering the fully connected network with the previous TOM-based link weights, we extracted one MST for each case-control group. Through an iterative process, we removed links in descending order of their weights and calculated the degree divergence value (K), which decreases in each cycle with link removals. As demonstrated by Braunstein et al. (2007), the process ends when $K < 2$, and the largest remaining component is the SHW set. Lastly, we measured node betweenness differences (i.e., bvFTD – HC) to assess the amplitude of information flow connectivity gain or loss, and we defined a threshold b as the non-zero median of the absolute betweenness differences. Areas showing differences above b (or below $-b$), will be taken as markers of functional connectivity gain (or loss).

Clustering nodes in a tree is more complex respect to other graphs. Several types of clustering algorithms have been developed which revealed to be limited and unsuitable to MST characteristics (Yu et al., 2015). Here, we used a novel approach for MST clustering suggested by Yu et al. (2015) based on the geodesic distance matrix D, where the ijth-elements of D represent the number of links of a shortest path between two nodes. As proposed by the authors, we computed vector similarities as the Spearman's distance, $d_S = 1 - r_S$, where r_S is the Spearman's rank correlation between all row pairs of D. Next, we applied the iterative hierarchical clustering algorithm, using d_S as input and *average-linkage* method (Gordon et al., 2016) to define the distance between two clusters. This method merges node pairs into corresponding clusters by decreasing similarity until all nodes are merged into one cluster. The different stages of the algorithm were represented in the form of a dendrogram. We partitioned the case-control MSTs in an equal number of clusters using the same cut-off value (0.2) on each case-control dendrogram.

Statistical Analysis

Global network connectivity (strength, diversity, and zero correlation), and MST global parameters (maximum degree, maximum betweenness, diameter, eccentricity, assortativity, degree divergence, leaf fraction, extreme value index, R-squared), provided a dataset of 80 rows (subjects) and 12 columns (parameters) for further statistical analysis. Since data were generally not Gaussian, non-parametric, Wilcoxon signed rank test was used to compare FTD and HC groups P-values were adjusted using Benjamini–Hochberg correction, and fixing the significance threshold at $P < 0.05$ (two sided). Sex and age showed significant differences between groups, therefore data were corrected for age, sex and age*sex interaction.

Global measures from the two case-control average correlation matrices were also compared by permutation tests as follows: (i) by computing the observed absolute difference between the global measure in FTD and HC groups, (ii) by permuting group assignments of the individuals' values of the global measures for FTD and HC groups (B = 10000 iterations), and (iii) by repeating

step (i) to obtain $B = 10000$ sampled permutations of the absolute differences between FTD and HC groups. Then, P-values were obtained using the sample permutation distribution with the same significant threshold of the individual signed rank tests.

Methodological Comparison

Minimum spanning tree properties were compared with other conventional graph theory approaches, to measure the extent of network metrics reproducibility and wavelet scale specificity. The first method we applied uses the efficiency cost optimization (ECO; De Vico Fallani et al., 2017) criterion, imposing a fixed edge density threshold, based on the trade-off between network efficiency and wiring cost. We further applied two methods defining per subject optimal correlation thresholds, based on the extended Bayesian information criterion (EBIC; Chen and Chen, 2008), and spectral analysis (Perkins and Langston, 2009). Finally, we tested the performances of a scale free model-based method that chooses the correlation threshold optimizing power law fitting for each subject (Mumford et al., 2010). Differently from MST topology, these networks include triangular connections and cycles (i.e., they are not acyclic graphs), where classical clustering-based indices can be calculated. MST-specific indices are leaf fraction and alpha, while non-MST indices include clustering coefficient, average path length, and efficiency. Common metrics include maximum degree, maximum betweenness, degree divergence, diameter, eccentricity, and assortativity. Wilcoxon rank sum tests were calculated for every method at each wavelet scale.

Software

Network analyses, graph visualization, and statistical analyses were performed in R (R Core team, 2018), using packages *igraph* (Csardi and Nepusz, 2006), *WGCNA* (Langfelder and Horvath, 2008), *brainwaver* (Achard, 2015), *brainGraph* (Watson, 2018), and custom R functions.

RESULTS

Global Functional Connectivity of rs-fMRI Data

For each subject, we examined the complexity of rs-fMRI data (Saba et al., 2018) using bivariate measures (i.e., strength, diversity, and zero correlation) computed as summary regional values of the wavelet correlations (**Supplementary Table 2**). Scale 2 was the only reaching significance at these three tests (**Figure 2** and **Supplementary Table 2**). Diversity and zero correlation showed a significant increase in bvFTD respect to HC, while strength showed significant decrease ($P < 0.05$ for every test). The significant increment of wavelet correlation diversity and its percentage of zeros (median HC: 25% vs. median bvFTD: 35%) indicated a decreased heterogeneity and increased null functional connectivity between brain regions in bvFTD compared to HCs. In addition, strength decrease denounces a generalized connectivity weakening in bvFTD respect to HCs.

Stronger Disorder Limit

By analyzing TOM-based weighted fully connected graphs for each subject (see Materials and Methods), we obtained good fitting for the power function (**Figure 2** and **Supplementary Table 2**). High R^2 (R-squared) indices were observed in both groups (0.93–0.97 for HC and 0.90–0.99 for bvFTD). When the extreme value index was estimated ($\hat{\alpha}$), excluding outliers, low values (0.14–0.57 for HC and 0.10–0.42 for bvFTD) were found. Values of $\hat{\alpha}$ less than one indicated a strong disorder limit tendency.

MST Global Graph Metrics

Minimum spanning trees indicated brain connections alterations in bvFTD patients when compared to controls (**Figure 2** and **Supplementary Table 2**). Data suggested a reduction of the degree centrality and leaf fraction, and an increment of distance metrics in the bvFTD group. Their trees were composed by nodes with a lower maximum degree and number of leafs. Moreover, the trees were characterized by a higher inter-distance, translating in a higher diameter and eccentricity in bvFTD compared to HC trees. These measures indicated brain impairments in bvFTD, highlighting less node-connections and loss of efficiency in exchange information capacity, that support a linear-shaped configuration network. Conversely, HC tree metrics showed a better network integration, characterized by parameter values that tend to a star-type configuration (i.e., an increase in the number of hubs and leaf points, and a decrease of diameter and eccentricity). Although assortativity index was not significant, it confirmed the topological hierarchy and biological nature of all MSTs, with assortativity values less than 0, for both groups. Lastly, permutation testing of two-group differences on the average correlation matrices yielded similar results (data not shown).

MST Topological Two-Group Comparison

Cluster, spatial, and anatomical data were integrated through a network representation, showing the topological properties of the two-group average for HC and bvFTD graphs (see Materials and Methods section). The results of edge partitioning and node clustering are shown in **Figures 3A,B**, **4A,B**. Every node in **Figures 3A,B**, colored by cluster membership, correspond to a single brain area belonging to a specific macro-region or lobe (i.e., node name), and traversed by two kinds of functional connections: (i) superhighways (bold gray), and (ii) secondary functional routes (thin gray). Finally, **Figures 5A,B** displays lobe partition (node color), node degree centrality (node size), and superhighways information flow connectivity (edge thickness) for bvFTD and HC groups, respectively.

In **Figures 3A,B**, **5A,B** emerged the HC multiple-star structure, whose central nodes, namely Lingual-L, Occipital-Inf-R, Precuneus-L, and Cerebellum-6-L regions (nodes #47, #54, #67, and #99 in **Figure 5B**), serve as starting points for superhighways and bridge components in the tree backbone. This architecture was impaired in the MST of bvFTD patients, where few conserved stars, namely Precuneus-L, and Cerebellum-6-L (nodes #67 and #99 in **Figure 5A**), maintained a reduced

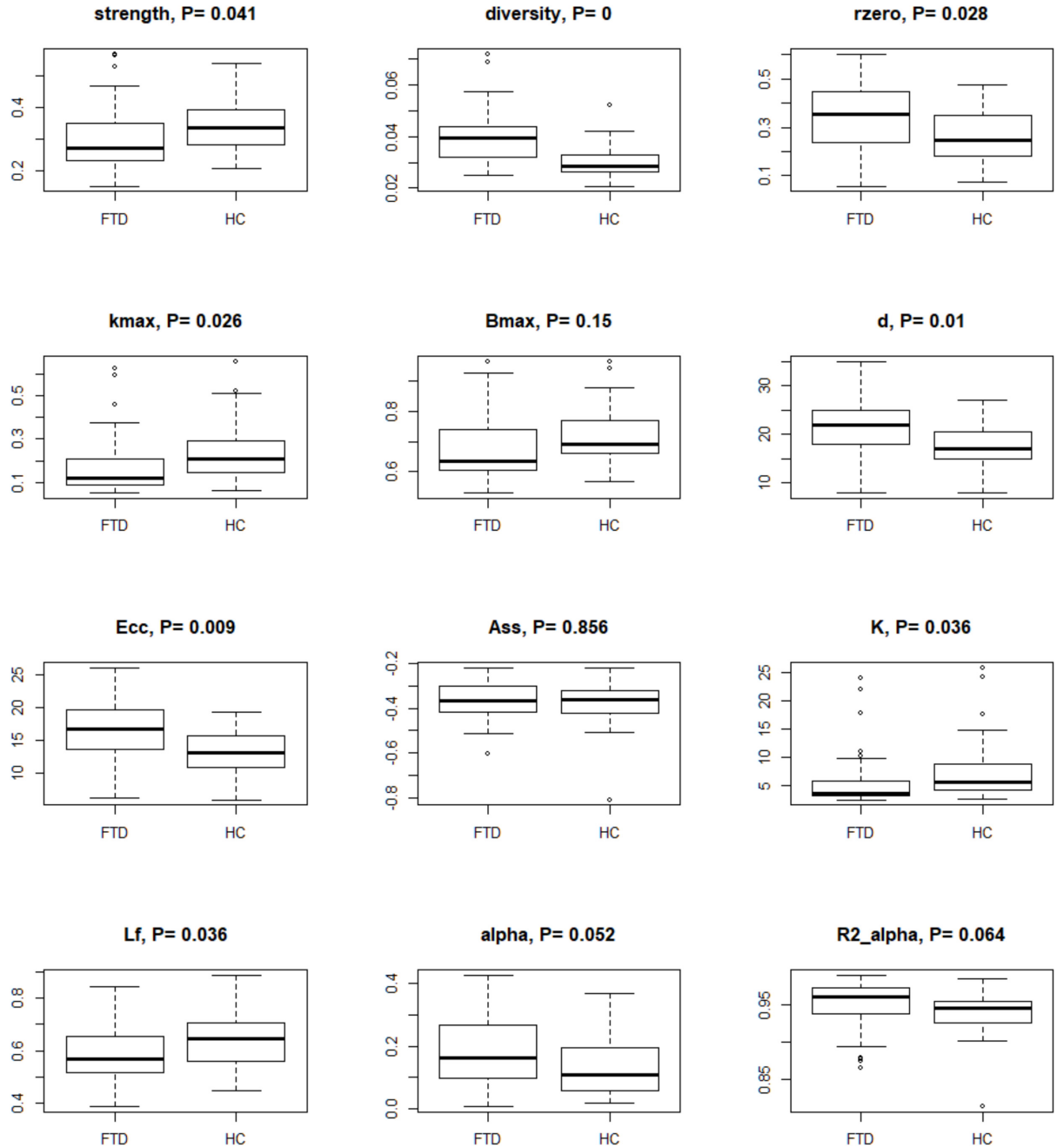

FIGURE 2 | Box-plots and *P*-values of Wilcoxon rank sum test for global connectivity measures and minimum spanning tree global parameters. The null hypothesis of the test is that the distributions of the HC and bvFTD do not differ (i.e., true location shift equal to 0). Data were corrected by age, sex, and age*sex interaction, and *P*-values were adjusted by Benjamini–Hochberg correction. Legend: rzero, zero correlation; kmax, maximum degree; Bmax, maximum betweenness; d, diameter; Ecc, eccentricity; Ass, assortativity; K, degree divergence; Lf, leaf fraction; alpha, extreme value index; R2 alpha, R-square of the extreme value index.

functional connectivity, leading to a general isolation of Frontal and Temporal areas from central nodes. Network complexity reduction from HC to bvFTD is evident from bvFTD hierarchical clustering in **Figure 3A**, where Frontal and Temporal areas (green and red clusters, respectively) are almost completely separated from Parietal (yellow cluster) and Occipital-Cerebellar regions (cyan cluster). On the other hand, HC heatmap in **Figure 3B**, shows two highly connected network communities (green-brown and red-cyan clusters). Specifically, two different groups of Frontal-Parietal regions (brown and red clusters) are highly connected to Frontal (green cluster) and Temporal-Occipital-Cerebellar regions (cyan cluster), respectively. Notably, network star nodes (i.e., Lingual-L, Occipital-Inf-R, Precuneus-L, and Cerebellum-6-L) traverse and integrate these two highly

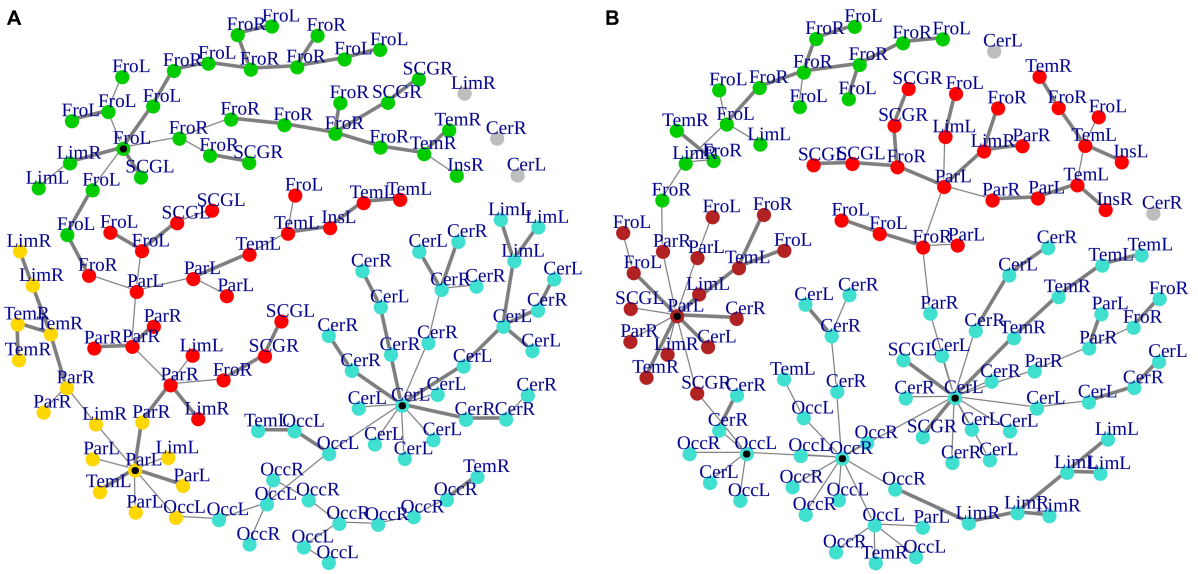

FIGURE 3 | (A,B) Clusters and superhighways differences in brain macro-regions. MSTs for both bvFTD and HCs are shown on the left **(A)** and right **(B)** panel, respectively. Clusters are defined by node colors, while thick edges show superhighway paths. Hubs (i.e., nodes having degree centrality >5) are marked with a black dot. Nodes are labeled according to macro-regions (i.e., lobes) membership (see **Supplementary Table 1** for label encodings).

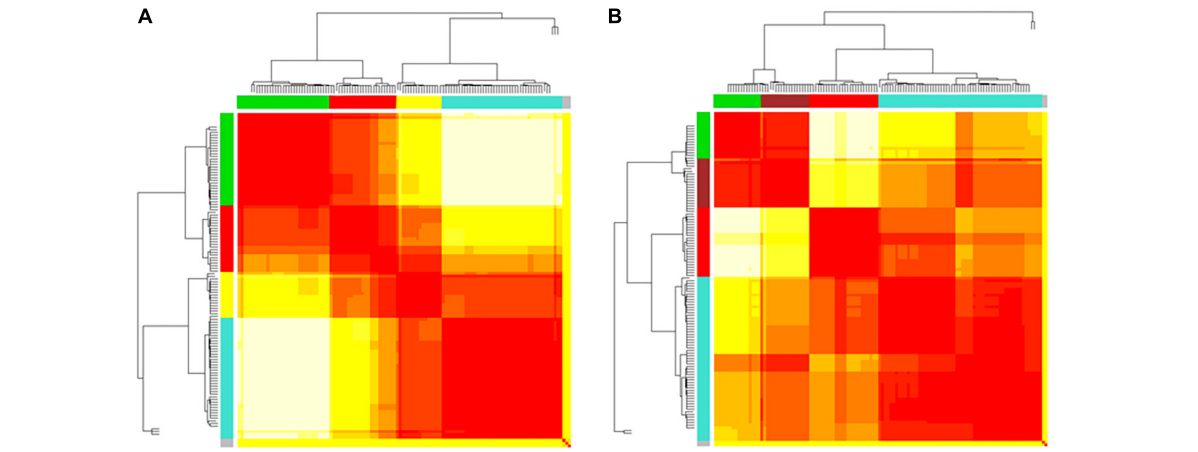

FIGURE 4 | (A,B) Heatmaps and dendrograms of brain areas clustering elaboration. Hierarchical subdivision of brain areas and clustering for both bvFTD and HCs are shown on the left **(A)** and right **(B)** panel, respectively. The same number of clusters for both groups is obtained through the application of a cutting-height on dendrograms. We applied a cut-off equal to 0.2 to obtain four clusters (yellow-to-red squares within clustering areas). The four clusters (showed as colored boxes), reveal a clearer subdivision in the bvFTD group **(A)** respect to HCs **(B)**.

connected communities in HC (**Figure 5B**). Conversely, bvFTD clusters are much more homogeneous (i.e., areas from the same lobe tend to cluster together), involving fewer and isolated stars. This is evident in **Figure 5**, where the bvFTD network panel (A) shows a clear lobe segregation (i.e., node color), especially for Frontal (red), Parietal (yellow), Occipital (light blue), and Cerebellum (blue) lobes, while the HC network panel (B) shows a much higher level of integration.

The survival ratio (i.e., the intersection between graphs calculated as the fraction of links found common in two MSTs) was equal to 42%, defining dissimilar topological structures of MSTs in the two groups. These differences are highlighted in **Figure 6**, where edges present in the bvFTD graph but not in the HC one panel (A), and vice versa panel (B), are shown. More specifically, highly connected star-clusters seen in the HC group were absent in the bvFTD graph. Conversely, leafs and short linear structures seen in the bvFTD group were absent in the HC graph.

Nodes and edges in the axial orientation (x-y)-coordinates of the anatomical automatic labeling (AAL 116) brain atlas are shown in **Figures 7A,B**, providing a complete frontotemporal brain state representation, through the visualization of type,

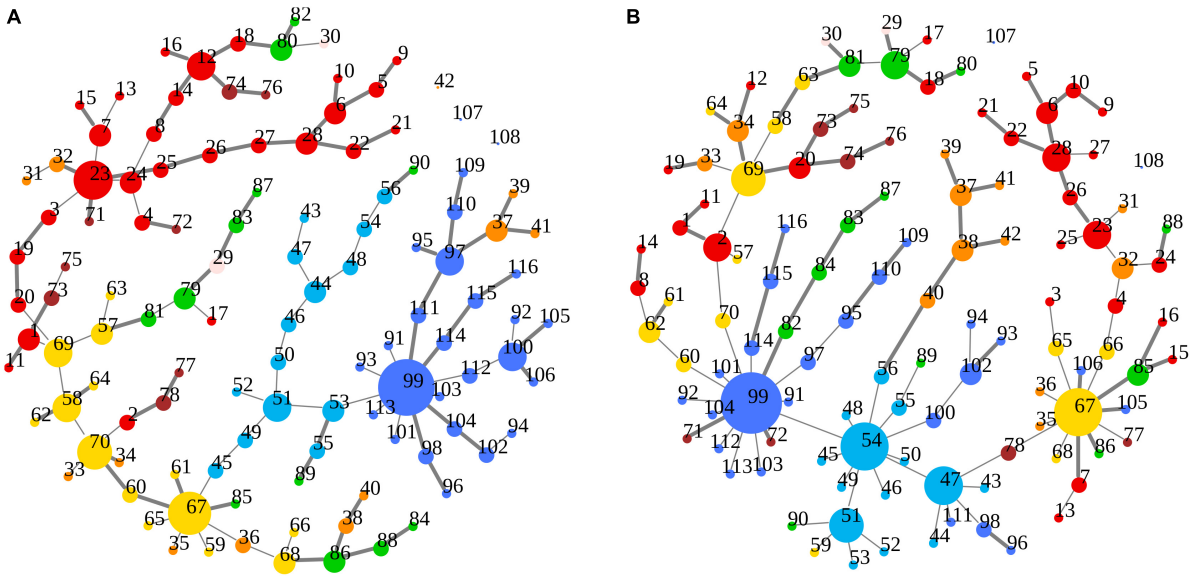

FIGURE 5 | (A,B) Node degree centrality and superhighway routes in brain macro-regions. MSTs for both bvFTD and HCs are shown on the left **(A)** and right **(B)** panel, respectively. Macro-regions (i.e., lobes) are defined by node colors. Thick edges show superhighway paths and node size is proportional to degree centrality. Nodes are labeled by AAL 116 region identifier. Identifiers and corresponding areas and macro-regions can be found in **Supplementary Table 1**. Macro-region color code: Red, Frontal; Green, Temporal; Yellow, Parietal; Orange, Limbic; Cyan, Occipital; Brown, Subcortical Gray Matter; Light pink, Insula; Blue, Cerebellum.

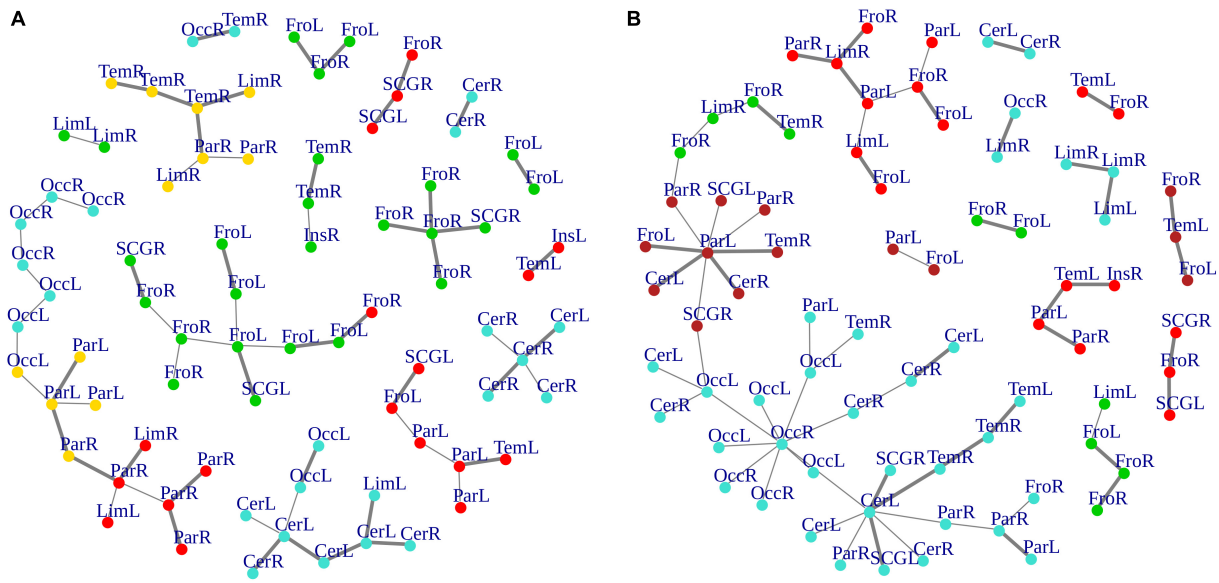

FIGURE 6 | (A,B) Graph-edges difference between the two groups. MSTs differences for both bvFTD and HCs are shown. Left **(A)** panel shows bvFTD-HC residual graph, while right **(B)** panel reports the difference HC-bvFTD. Node colors follow cluster membership, as in **Figure 3**. Nodes are labeled according to macro-regions membership (see **Supplementary Table 1** for label encodings).

number, and origin of connections, confirming the abnormalities found in bvFTD, compared to HC. The most evident feature is a massive grouping of Frontal areas (red nodes in **Figure 7A**), disconnected from both Temporal lobes (green nodes in **Figure 7A**) and other areas (yellow nodes in **Figure 7A**), including the conserved star nodes Precuneus-L and Cerebellum-6-L (nodes #67 and #99 in **Figure 7A**). Strikingly, the massive frontal aggregation in bvFTD belongs entirely to a single cluster (red nodes in **Figures 5A**, **7A**), at the center of which is present a new bvFTD-specific star node (Frontal Sup-Medial-L, node #23 in **Figures 5A**, **7A**), indicative of a new isolated functional macro-region in bvFTD. Notably, comparing superhighways distribution between groups (**Figures 7A,B**), HCs show a deeply intertwined connectivity that integrates star nodes with Frontal

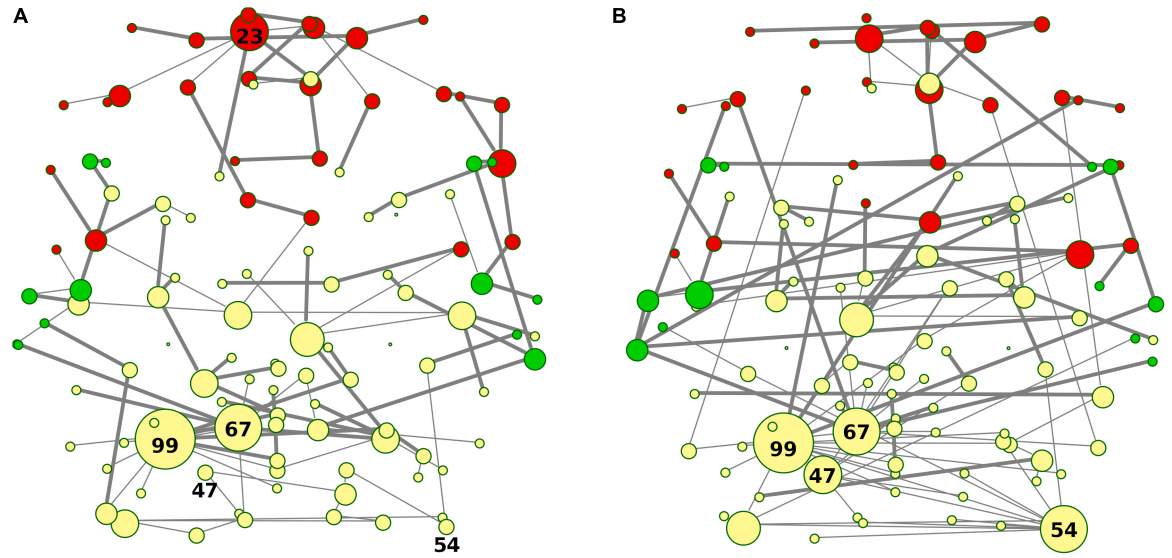

FIGURE 7 | (A,B) Spatial location of areas and superhighway routes according to x-y AAL 116 coordinates. MSTs for both bvFTD and HCs are shown on the left **(A)** and right **(B)** panel, respectively. Thick edges show superhighway paths and node size is proportional to degree centrality. Red nodes correspond to Frontal areas, while Temporal areas are colored in green. Hubs (i.e., nodes having degree centrality >5) are labeled by AAL 116 region identifier. Left MST **(A)** reports conserved hubs (areas #67 and #99), lost hubs (areas #47 and #54), and the gained frontal hub (area #23) in bvFTD, respect to HCs.

and Temporal areas, linking them each other. Conversely, bvFTD superhighway connectivity collapses around conserved hubs and within the Frontal macro-region, causing their isolation.

Methodological Comparison

Minimum spanning tree network metrics were compared to other classical graph theory approaches (see Materials and Methods), to assess network properties reproducibility and wavelet scale specificity. Network metrics and Wilcoxon rank sum test results are reported in **Supplementary Table 2**. Beside the MST, only the efficiency/cost trade-off based method (i.e., ECO) showed significant bvFTD/HC specifically at scale 2, while all the other scales were non-informative (i.e., non-significant bvFTD/HC differences). The EBIC-based method reported few significant indices not directly related to information exchange efficiency (i.e., maximum degree, degree divergence, and assortativity), for both scales 1 and 2, indicating poor discriminant power. Lastly, spectral analysis and scale free model-based methods did not show significant case/control differences at any wavelet scale. Notably, both MST and ECO are based on the optimization of the information flow exchange across the functional network, maximizing graph integration and minimizing wiring costs. Common metrics between MST and ECO showing significant results at scale 2 were the same in both methods. However, differently from MST, ECO yielded several disconnected nodes (up to 74) per subject.

DISCUSSION

In the present study, we evaluated the power of MST representation within the framework of bvFTD, combining rs-fMRI data and graph theory analysis. Different neuroimaging methods have been proposed to highlight brain damage in bvFTD (Whitwell et al., 2011; Rohrer et al., 2015). However, since the description of the BOLD signal (Ogawa et al., 1990), functional neuroimaging allowed to go beyond the mere anatomical description of brain connectivity, identifying functionally connected (i.e., synchronized time-dependent fluctuations of the BOLD signal) networks of cortical and subcortical regions (Seeley et al., 2008). In bvFTD, multiple independent studies identified the frontal brain regions as the affected core networks (Seeley et al., 2009; Zhou et al., 2010; Whitwell et al., 2011; Borroni et al., 2012; Farb et al., 2013; Lee et al., 2014).

Graph theory has already been applied in a few MRI studies on bvFTD, demonstrating disruption of the global topologic organization, increased path length and assortativity, with loss of cortical hubs and network centrality, extending the list of sensible target regions to salience and executive functions (Agosta et al., 2013; Trojsi et al., 2015; Sedeño et al., 2016; Hohenfeld et al., 2018). Despite the wide use of graph theory in the analysis of neurodegenerative disorders, many methodological aspects are left to the experimenter choice, leading to possible confounding results.

When comparing graphs with the same number of nodes (N) and edges (N-1), the MST is an unambiguous method for brain network analysis, allowing to avoid methodological biases (Tewarie et al., 2015). Although it does not completely replace traditional graph theory approaches, MST remains the simplest and most effective representation of a full graph (Stam et al., 2014), where minimum weight (i.e., maximum connectivity) links constitute significant information flow paths. Moreover, it has been recently demonstrated how MST provides robust network estimates, with results in

accordance to classical network analytical data (Otte et al., 2015; Tewarie et al., 2015). As indicated by our methodological comparison (see Results), algorithms based on information flow optimization and wiring cost minimization (including MST and ECO methods) achieved the best bvFTD/HC separation performances (**Supplementary Table 2**). On the other hand, fixed-correlation threshold and scale free model-based graphs showed poor or non-significant results, indicating that enforcing an arbitrary correlation threshold or network nature (i.e., scale free power law distribution) strongly limit network descriptive power. Conversely, MST has the advantage of requiring no correlation thresholds, network density or *a priori* distribution, ensuring full reproducibility and robustness in different conditions. Furthermore, since our results indicated a strong disorder limit tendency in both groups, the MST was able to preserve the connectivity features of the underlying functional networks (Tewarie et al., 2014). Through our TOM-adjusted edge weights, MSTs and relative parameters conserved their neighborhood node characteristics, highlighting nodes aggregation (i.e., star-type configurations), and providing a valid method to identify a set of shortest paths in MSTs that may be considered as the "critical backbone" of original graph (Tewarie et al., 2014).

Our MSTs suggest that the differences between groups may be attributed to functional alterations of such major organization, since they represent the information-flow highways of the fully connected network. Shape-linear configuration tendency in bvFTD graphs highlights different impairments: high distance between nodes, low centrality parameter values, and a low exchange information capacity (i.e., low network integration). Connection efficiency loss is particularly evident in **Figure 7**, where the superhighway system in HCs, linking hubs to Frontal and Temporal brain areas, is replaced by a local (i.e., isolated) network surrounding conserved hubs. Functional isolation is a generalized process in bvFTD, where brain areas tend to interact within lobes (i.e., colors in **Figure 5**), showing a homogeneous brain area distribution, longer distances between hubs, and longer within-lobe superhighways. Therefore, bvFTD functional breakdown is not merely described by connectivity loss, but though disease-specific reorganizations and regularization of the information flow. This contrasts with the marked integration of a healthy functional network, where superhighways serve as shortcuts to connect areas from different brain macro-regions. Network regularization has already been observed as a distinctive FTD trait, respect to other neurodegenerative disorders, including Alzheimer's disease (de Haan et al., 2009; Zhou et al., 2010). We further investigated this aspect by gathering evidences from both global and local network metrics.

Although global functional parameters (i.e., strength, diversity, and zero correlation) showed a significantly weaker and reduced connectivity in bvFTD, edge-level and node-level features (i.e., superhighways, and node degree and betweenness centrality), highlighted a more complex scenario, explaining some of the key dysfunctions observed in large scale resting-state functional networks, including the DMN, SN, and EN networks (Zhou et al., 2010; Trojsi et al., 2015; Sedeño et al., 2016; Hohenfeld et al., 2018). The first evidence from our data is the formation of a new FTD-specific hub (area #23: Frontal_Sup_Medial_L, **Figure 5A**), absent in HCs. This hub is the starting point of a huge superhighway, fully extending within frontal lobe, clearly derived from an elongation of the original route in HCs (**Figure 5B**). Specifically, our data showed the involvement of regions: Frontal_Sup_Medial_L/R, Frontal_Sup_Orb_L/R, Frontal_Mid_Orb_L/R, Frontal_Med_Orb_L/R, Rectus_L/R, and Olfactory_L/R (areas #23, #24, #5, #6, #9, #10, #25, #26, #27, #28, #21, and #22 in **Supplementary Table 1** and **Figure 5A**). Notably, all the elements of this superhighway are part of the DMN (Zhou et al., 2010; Trojsi et al., 2015; Hohenfeld et al., 2018), strongly supporting the evidence of a compensation mechanism and frontal DMN decreased connectivity with areas from other lobes. However, this process is not exclusive of the Frontal lobe. Within-lobe superhighway formation, and consequent isolation, involves also the two conserved nodes in bvFTD: Precuneus_L (area #67, parietal lobe in yellow in **Figure 5A**) and Cerebellum_6_L (area #99, blue in **Figure 5A**), where the former plays a key role in the DMN network. Betweenness difference (b) is a good local indicator of these impairments at node level (threshold set at $b = \pm 435$, (see **Supplementary Table 3**). Notably, while areas #23 and #67 show a strongly increased node betweenness ($b_{23} = 1545$, and $b_{67} = 879$) from bvFTD to HCs, area #99 loses a great portion of its centrality ($b_{99} = -1534$), supporting the evidence of a functional deterioration of the cerebellar lobule VI, that has been associated with cerebellar atrophy in both bvFTD and Alzheimer's disease (Guo et al., 2016; Schmahmann, 2016). Nevertheless, area #99 is the center of an enlarged intra-cerebellar superhighway system, showing that superhighway elongation is due to a generalized network centrality reorganization, rather than a region-specific impairment. It has been recently suggested that long-distance connections have an important role in integrating distinct brain areas, leading to a greater functional diversification, robustness, and specialization (Betzel and Bassett, 2018). However, long-range connections number and length is strictly controlled by their metabolic demand. In contrast, bvFTD long within-lobe superhighways seem not to contribute to the overall functional integration, but rather being the result of a compensatory mechanism, in response to a generalized functional deterioration. To verify this hypothesis, we focused our attention to those areas showing a strong betweenness centrality loss ($b < -435$) in bvFTD respect to HCs. The clearest example in our data is given by three connected areas (**Figure 5B**): Angular_R (area #66, $b_{66} = -1552$), Frontal_Sup_R (area #4, $b_4 = -1359$), and Cingulum_Ant_R (area #32, $b_{32} = -1299$), being involved in DMN, EN, and EN/SN, respectively. As shown in **Figure 5B**, these three areas connect the Precuneus_L (parietal area #67) and its superhighway system to the frontal superhighway starting from area #23 (Frontal_Sup_Medial_L), that in bvFTD is markedly enlarged (**Figure 5A**). In the bvFTD network, area #23 is a new hub, and the #23–67 connection is now a much longer and linear path, suggesting that superhighway elongation

could be a compensatory reaction to a less efficient network integration. Notably, Cingulum_Ant_R (area #32) is part of the limbic system, involved in both DMN and salience/executive functions, suggesting that limbic system failure could be an underlying cause of the global network rearrangement observed in bvFTD subjects.

A further support to this hypothesis is represented by the disruption of two HC network hubs (**Figure 5B**): Occipital_Inf_R (area #54, $b_{54} = -4054$) and Lingual_L (area #47, $b_{47} = -2913$), replaced by a long linear-shaped sequence of occipital areas (**Figure 5A**), denouncing a massive loss of degree and betweenness centrality also in this part of the network. Beside hubs, two adjacent connector areas experienced huge loss of betweenness: Fusiform_R (area #56, $b_{56} = -531$) and ParaHippocampal_R (area #40, $b_{40} = -540$). Strikingly, while the former is a direct bridge to the hub group, the latter is the first node of a limbic superhighway (**Figure 5B**), whose nodes occupy distinct peripheral positions in bvFTD (**Figure 5A**), including: Hippocampus_L/R (area #37–38), ParaHippocampal_L/R (areas #39–40), and Amygdala_L/R (areas #41–42).

Collectively, these evidences show an underlying involvement of the limbic system in the observed bvFTD functional deterioration, associated to the well-studied impairments affecting emotion recognition, social inference, and executive functions typical of this neurodegenerative disorder (Zhou et al., 2010; Trojsi et al., 2015; Sedeño et al., 2016; Hohenfeld et al., 2018).

CONCLUSION

The present work had the primary goal of highlighting alterations in brain connectivity of bvFTD subjects, providing at the same time a detailed description of the observed functional impairments, and insights about their possible causes. According to the most recent fMRI literature (Guo et al., 2017; Cui et al., 2018), we applied an MST model to wavelet correlation matrices from bvFTD and HC subjects, exploiting three strongpoints of MST-based methods: (i) assumption-free network construction and reproducibility, (ii) independence from node and edge number during network comparison, and (iii) simplicity of representation (i.e., three branching is directly interpretable in terms of most efficient shortest paths). On the other hand, MSTs have one main limitation: the resulting network is a sparse representation, implicitly excluding triangular connections, thus causing non-applicability of some common clustering metrics (e.g., transitivity and coreness) and evaluation of the network small-worldness. However, we coped with this issue by using TOM (Zhang and Horvath, 2005) and the extreme value index evaluation (Van Mieghem and Magdalena, 2005).

The combination of this theoretical model with rs-fMRI data allowed us not only to generate a clear picture of the functional divergence of bvFTD from HCs, but also to shed light on the possible causes of topological and functional rearrangements, and compensatory mechanisms, underlying cognitive, social, and executive impairments characterizing bvFTD phenotype.

Further developments to the present work, that now constitute main limitations, are represented by: (i) the lack of clinical and/or metabolic parameters that could confirm or reveal new causal hypotheses, and (ii) a combination with anatomical variables (e.g., gray matter mass), to achieve a better model resolution, and associate degenerative processes to functional deterioration.

Collectively, the application of MST-based analysis to rs-fMRI data looks a promising way to clarify the role of degenerative processes involved in FTD functional breakdown, improving the discovery of new fMRI biomarkers.

DATA AVAILABILITY

Pre-processed and parceled data (ItalianFTD-fMRI_May2018) for this study can be found in the SOURCEFORGE repository at: https://sourceforge.net/projects/bionet-finder/.

AUTHOR CONTRIBUTIONS

VS performed the literature research, drafted the manuscript, performed the data analysis and R coding, and wrote, reviewed, and edited the manuscript. EP conceived and designed the study, acquired the data, analyzed the image, and wrote, reviewed, and edited the manuscript. VC performed the literature research and analyzed the image. FP revised the data analysis, results, and discussion, and wrote, reviewed, and edited the manuscript. SG, OZ, RG, and AP acquired the data. BB conceived and designed the study, recruited the patients, drafted the manuscript, and supervised the study. MG conceived and designed the study, administered the project, performed the data analysis and R coding, and wrote, reviewed, and edited the manuscript. All authors have read and approved the final manuscript.

FUNDING

This research did not receive any specific grant from funding agencies in the public, commercial, or not-for-profit sectors (Materials and Methods section, Subjects).

ACKNOWLEDGMENTS

The authors would like to thank patients, their families and all volunteers for allowing and supporting this research. The authors would also like to acknowledge the support of Raffaele Ferrari (Department of Molecular Neuroscience, University College London, London, United Kingdom) for scientific discussion and revision of the article.

SUPPLEMENTARY MATERIAL

The Supplementary Material for this article can be found online at: https://www.frontiersin.org/articles/10.3389/fnins.2019.00211/full#supplementary-material

REFERENCES

Achard, S. (2015). *Basic Wavelet Analysis of Multivariate Time Series With a Visualisation and Parametrisation Using Graph Theory. CRAN Repository*. Available at: https://cran.r-project.org/web/packages/brainwaver/brainwaver.pdf

Achard, S., Salvador, R., Whitcher, B., Suckling, J., and Bullmore, E. (2006). A resilient, low-frequency, small-world human brain functional network with highly connected association cortical hubs. *J. Neurosci.* 26, 63–72. doi: 10.1523/JNEUROSCI.3874-05.2006

Agosta, F., Sala, S., Valsasina, P., Meani, A., Canu, E., Magnani, G., et al. (2013). Brain network connectivity assessed using graph theory in frontotemporal dementia. *Neurology* 81, 134–143. doi: 10.1212/WNL.0b013e31829a33f8

Albert, R., and Barabási, A. L. (2002). Statistical mechanics of complex networks. *Rev. Mod. Phys.* 74, 47–97. doi: 10.1103/RevModPhys.74.47

Antonenko, D., Külzow, N., Sousa, A., Prehn, K., Grittner, U., and Flöel, A. (2018). Neuronal and behavioral effects of multi-day brain stimulation and memory training. *Neurobiol. Aging* 61, 245–254. doi: 10.1016/j.neurobiolaging.2017.09.017

Beckmann, C. F., and Smith, S. M. (2004). Probabilistic independent component analysis for functional magnetic resonance imaging. *IEEE Trans. Med. Imaging* 23, 137–152. doi: 10.1109/TMI.2003.822821

Betzel, R. F., and Bassett, D. S. (2018). Specificity and robustness of long-distance connections in weighted, interareal connectomes. *PNAS* 115, E4880–E4889. doi: 10.1073/pnas.1720186115

Borroni, B., Alberici, A., Cercignani, M., Premi, E., Serra, L., Cerini, C., et al. (2012). Granulin mutation drives brain damage and reorganization from preclinical to symptomatic FTLD. *Neurobiol. Aging* 33, 2506–2520. doi: 10.1016/j.neurobiolaging.2011.10.031

Braunstein, L. A., Wu, Z., Chen, Y., Buldyrev, S. V., Kalisky, T., Sreenivasan, S., et al. (2007). Optimal path and minimal spanning trees in random weighted networks. *Int. J. Bifurcat. Chaos* 17, 2215–2255. doi: 10.1142/S0218127407018361

Brett, M., Anton, J.-L., Valabregue, R., and Poline, J.-B. (2002). Region of interest analysis using an SPM toolbox. *Neuroimage* 16, 1140–1141. doi: 10.1016/S1053-8119(02)90013-3

Bullmore, E., Fadili, J., Maxim, V., Sendur, L., Whitcher, B., Suckling, J., et al. (2004). Wavelets and functional magnetic resonance imaging of the human brain. *Neuroimage* 23(Suppl. 1), S234–S249. doi: 10.1016/j.neuroimage.2004.07.012

Bullmore, E., and Sporns, O. (2009). Complex brain networks: graph theoretical analysis of structural and functional systems. *Nat. Rev. Neurosci.* 10, 186–198. doi: 10.1038/nrn2575

Bullmore, E., and Sporns, O. (2012). The economy of brain network organization. *Nat. Rev. Neurosci.* 13, 336–349. doi: 10.1038/nrn3214

Chen, J., and Chen, Z. (2008). Extended Bayesian information criteria for model selection with large model spaces. *Biometrika* 95, 759–771. doi: 10.1093/biomet/asn034

Chiang, S., Cassese, A., Guindani, M., Vannucci, M., Yeh, H. J., Haneef, Z., et al. (2016). Time-dependence of graph theory metrics in functional connectivity analysis. *Neuroimage* 125, 601–615. doi: 10.1016/j.neuroimage.2015.10.070

Cormen, T. H., Leiserson, C. E., Rivest, R. L., and Stein, C. (2001). *Introduction to Algorithms*, 2nd Edn. Cambridge, MA: MIT Press.

Cosseddu, M., Benussi, A., Gazzina, S., Turrone, R., Archetti, S., Bonomi, E., et al. (2018). Mendelian forms of disease and age at onset affect survival in frontotemporal dementia. *Amyotroph. Lateral Scler. Frontotemporal Degener.* 19, 87–92. doi: 10.1080/21678421.2017.1384020

Csardi, G., and Nepusz, T. (2006). The igraph software package for complex network research. *InterJournal Complex Syst.* 1695, 1–9.

Cui, X., Xiang, J., Guo, H., Yin, G., Zhang, H., Lan, F., et al. (2018). Classification of Alzheimer's disease, mild cognitive impairment, and normal controls with subnetwork selection and graph kernel principal component analysis based on minimum spanning tree brain functional network. *Front. Comput. Neurosci.* 12:31. doi: 10.3389/fncom.2018.00031

de Haan, W., Pijnenburg, Y. A., Strijers, R. L., van der Made, Y., van der Flier, W. M., Scheltens, P., et al. (2009). Functional neural network analysis in frontotemporal dementia and Alzheimer's disease using EEG and graph theory. *BMC Neurosci.* 10:101. doi: 10.1186/1471-2202-10-101

De Vico Fallani, F., Latora, V., and Chavez, M. (2017). A topological criterion for filtering information in complex brain networks. *PLoS Comput. Biol.* 13:e1005305. doi: 10.1371/journal.pcbi.1005305

Drakesmith, M., Caeyenberghs, K., Dutt, A., Lewis, G., David, A. S., and Jones, D. K. (2015). Overcoming the effects of false positives and threshold bias in graph theoretical analyses of neuroimaging data. *Neuroimage* 118, 313–333. doi: 10.1016/j.neuroimage.2015.05.011

Edwards, D., de Abreu, G. C. G., and Labouriau, R. (2010). Selecting high-dimensional mixed graphical models using minimal AIC or BIC forests. *BMC Bioinformatics* 11:18. doi: 10.1186/1471-2105-11-18

Farb, N. A. S., Grady, C. L., Strother, S., Tang-Wai, D. F., Masellis, M., Black, S., et al. (2013). Abnormal network connectivity in frontotemporal dementia: evidence for prefrontal isolation. *Cortex* 49, 1856–1873. doi: 10.1016/j.cortex.2012.09.008

Filippi, M., Basaia, S., Canu, E., Imperiale, F., Meani, A., Caso, F., et al. (2017). Brain network connectivity differs in early-onset neurodegenerative dementia. *Neurology* 89, 1764–1772. doi: 10.1212/WNL.0000000000004577

Gazzina, S., Premi, E., Zanella, I., Biasiotto, G., Archetti, S., Cosseddu, M., et al. (2016). Iron in frontotemporal lobar degeneration: a new subcortical pathological pathway? *Neurodegener Dis.* 16, 172–178. doi: 10.1159/000440843

Gordon, E., Rohrer, J. D., and Fox, N. C. (2016). Advances in neuroimaging in frontotemporal dementia. *J. Neurochem.* 138(Suppl. 1), 193–210. doi: 10.1111/jnc.13656

Gorno-Tempini, M. L., Hillis, A. E., Weintraub, S., Kertesz, A., Mendez, M., Cappa, S. F., et al. (2011). Classification of primary progressive aphasia and its variants. *Neurology* 76, 1006–1014. doi: 10.1212/WNL.0b013e31821103e6

Griffanti, L., Dipasquale, O., Laganà, M. M., Nemni, R., Clerici, M., Smith, S. M., et al. (2015). Effective artifact removal in resting state fMRI data improves detection of DMN functional connectivity alteration in Alzheimer's disease. *Front. Hum. Neurosci.* 9:449. doi: 10.3389/fnhum.2015.00449

Griffanti, L., Salimi-Khorshidi, G., Beckmann, C. F., Auerbach, E. J., Douaud, G., Sexton, C. E., et al. (2014). ICA-based artefact removal and accelerated fMRI acquisition for improved resting state network imaging. *Neuroimage* 95, 232–247. doi: 10.1016/j.neuroimage.2014.03.034

Guo, C. C., Tan, R., Hodges, J. R., Hu, X., Sami, S., and Hornberger, M. (2016). Network-selective vulnerability of the human cerebellum to Alzheimer's disease and frontotemporal dementia. *Brain* 139, 1527–1538. doi: 10.1093/brain/aww003

Guo, H., Liu, L., Chen, J., Xu, Y., and Jie, X. (2017). Alzheimer classification using a minimum spanning tree of high-order functional network on fMRI dataset. *Front. Neurosci.* 11:639. doi: 10.3389/fnins.2017.00639

Hohenfeld, C., Werner, C. J., and Reetz, K. (2018). Resting-state connectivity in neurodegenerative disorders: is there potential for an imaging biomarker? *Neuroimage Clin.* 18, 849–870. doi: 10.1016/j.nicl.2018.03.013

Jenkinson, M., Beckmann, C. F., Behrens, T. E. J., Woolrich, M. W., and Smith, S. M. (2012). FSL. *Neuroimage* 62, 782–790. doi: 10.1016/j.neuroimage.2011.09.015

Langfelder, P., and Horvath, S. (2008). WGCNA: an R package for weighted correlation network analysis. *BMC Bioinformatics* 9:559. doi: 10.1186/1471-2105-9-559

Lee, S. E., Khazenzon, A. M., Trujillo, A. J., Guo, C. C., Yokoyama, J. S., Sha, S. J., et al. (2014). Altered network connectivity in frontotemporal dementia with C9orf72 hexanucleotide repeat expansion. *Brain* 137, 3047–3060. doi: 10.1093/brain/awu248

Lynall, M.-E., Bassett, D. S., Kerwin, R., McKenna, P. J., Kitzbichler, M., Muller, U., et al. (2010). Functional connectivity and brain networks in schizophrenia. *J. Neurosci.* 30, 9477–9487. doi: 10.1523/JNEUROSCI.0333-10.2010

Mann, D. M. A., and Snowden, J. S. (2017). Frontotemporal lobar degeneration: pathogenesis, pathology and pathways to phenotype. *Brain Pathol.* 27, 723–736. doi: 10.1111/bpa.12486

McKeown, M. J., Hansen, L. K., and Sejnowsk, T. J. (2003). Independent component analysis of functional MRI: what is signal and what is noise? *Curr. Opin. Neurobiol.* 13, 620–629. doi: 10.1016/j.conb.2003.09.012

Mears, D., and Pollard, H. B. (2016). Network science and the human brain: using graph theory to understand the brain and one of its hubs, the amygdala, in health and disease. *J. Neurosci. Res.* 94, 590–605. doi: 10.1002/jnr.23705

Meier, J., Tewarie, P., and Van Mieghem, P. (2015). The union of shortest path trees of functional brain networks. *Brain Connect.* 5, 575–581. doi: 10.1089/brain.2014.0330

Mumford, J. A., Horvath, S., Oldham, M. C., Langfelder, P., Geschwind, D. H., and Poldrack, R. A. (2010). Detecting network modules in fMRI time series: a weighted network analysis approach. *Neuroimage* 52, 1465–1476. doi: 10.1016/j.neuroimage.2010.05.047

Newman, M. E. J. (2003). Mixing patterns in networks. *Phys. Rev. E* 67(2 Pt 2):026126. doi: 10.1103/PhysRevE.67.026126

Numan, T., Slooter, A. J. C., van der Kooi, A. W., Hoekman, A. M. L., Suyker, W. J. L., Stam, C. J., et al. (2017). Functional connectivity and network analysis during hypoactive delirium and recovery from anesthesia. *Clin. Neurophysiol.* 128, 914–924. doi: 10.1016/j.clinph.2017.02.022

Ogawa, S., Lee, T. M., Kay, A. R., and Tank, D. W. (1990). Brain magnetic resonance imaging with contrast dependent on blood oxygenation. *Proc. Natl. Acad. Sci. U.S.A.* 87, 9868–9872. doi: 10.1073/pnas.87.24.9868

Otte, W. M., van Diessen, E., Paul, S., Ramaswamy, R., Subramanyam Rallabandi, V. P., Stam, C. J., et al. (2015). Aging alterations in whole-brain networks during adulthood mapped with the minimum spanning tree indices: the interplay of density, connectivity cost and life-time trajectory. *Neuroimage* 109, 171–189. doi: 10.1016/j.neuroimage.2015.01.011

Park, B.-Y., Moon, T., and Park, H. (2018). Dynamic functional connectivity analysis reveals improved association between brain networks and eating behaviors compared to static analysis. *Behav. Brain Res.* 337, 114–121. doi: 10.1016/j.bbr.2017.10.001

Perkins, A. D., and Langston, M. A. (2009). Threshold selection in gene co-expression networks using spectral graph theory techniques. *BMC Bioinformatics* 10:S4. doi: 10.1186/1471-2105-10-S11-S4

R Core team (2018). *R: A Language and Environment for Statistical Computing*. Vienna: The R Foundation for Statistical Computing.

Raichle, M. E. (2015). The brain's default mode network. *Annu. Rev. Neurosci.* 38, 433–447. doi: 10.1146/annurev-neuro-071013-014030

Rascovsky, K., Hodges, J. R., Knopman, D., Mendez, M. F., Kramer, J. H., Neuhaus, J., et al. (2011). Sensitivity of revised diagnostic criteria for the behavioural variant of frontotemporal dementia. *Brain* 134, 2456–2477. doi: 10.1093/brain/awr179

Rashid, B., Damaraju, E., Pearlson, G. D., and Calhoun, V. D. (2014). Dynamic connectivity states estimated from resting fMRI Identify differences among Schizophrenia, bipolar disorder, and healthy control subjects. *Front. Hum. Neurosci.* 8:897. doi: 10.3389/fnhum.2014.00897

Ravasz, E., Somera, A. L., Mongru, D. A., Oltvai, Z. N., and Barabási, A. L. (2002). Hierarchical organization of modularity in metabolic networks. *Science* 297, 1551–1555. doi: 10.1126/science.1073374

Rohrer, J. D., Nicholas, J. M., Cash, D. M., van Swieten, J., Dopper, E., Jiskoot, L., et al. (2015). Presymptomatic cognitive and neuroanatomical changes in genetic frontotemporal dementia in the genetic frontotemporal dementia initiative (GENFI) study: a cross-sectional analysis. *Lancet Neurol.* 14, 253–262. doi: 10.1016/S1474-4422(14)70324-2

Rubinov, M., and Sporns, O. (2010). Complex network measures of brain connectivity: uses and interpretations. *Neuroimage* 52, 1059–1069. doi: 10.1016/j.neuroimage.2009.10.003

Saba, V., Premi, E., Cristillo, V., Gazzina, S., Palluzzi, F., Zanetti, O., et al. (2018). *ItalianFTD-fMRI_May2018. SourceForge*. Available at: https://sourceforge.net/projects/bionet-finder/

Schmahmann, J. D. (2016). Cerebellum in Alzheimer's disease and frontotemporal dementia: not a silent bystander. *Brain* 139, 1314–1318. doi: 10.1093/brain/aww064

Sedeño, L., Couto, B., García-Cordero, I., Melloni, M., Baez, S., Morales Sepúlveda, J. P., et al. (2016). Brain network organization and social executive performance in frontotemporal dementia. *J. Int. Neuropsychol. Soc.* 22, 250–262. doi: 10.1017/S1355617715000703

Seeley, W. W., Crawford, R., Rascovsky, K., Kramer, J. H., Weiner, M., Miller, B. L., et al. (2008). Frontal paralimbic network atrophy in very mild behavioral variant frontotemporal dementia. *Arch. Neurol.* 65, 249–255. doi: 10.1001/archneurol.2007.38

Seeley, W. W., Crawford, R. K., Zhou, J., Miller, B. L., and Greicius, M. D. (2009). Neurodegenerative diseases target large-scale human brain networks. *Neuron* 62, 42–52. doi: 10.1016/j.neuron.2009.03.024

Stam, C. J., Tewarie, P., Van Dellen, E., van Straaten, E. C. W., Hillebrand, A., and Van Mieghem, P. (2014). The trees and the forest: characterization of complex brain networks with minimum spanning trees. *Int. J. Psychophysiol.* 92, 129–138. doi: 10.1016/j.ijpsycho.2014.04.001

Telesford, Q. K., Joyce, K. E., Hayasaka, S., Burdette, J. H., and Laurienti, P. J. (2011). The ubiquity of small-world networks. *Brain Connect.* 1, 367–375. doi: 10.1089/brain.2011.0038

Tewarie, P., Hillebrand, A., Schoonheim, M. M., van Dijk, B. W., Geurts, J. J. G., Barkhof, F., et al. (2014). Functional brain network analysis using minimum spanning trees in multiple sclerosis: an MEG source-space study. *Neuroimage* 88, 308–318. doi: 10.1016/j.neuroimage.2013.10.022

Tewarie, P., van Dellen, E., Hillebrand, A., and Stam, C. J. (2015). The minimum spanning tree: an unbiased method for brain network analysis. *Neuroimage* 104, 177–188. doi: 10.1016/j.neuroimage.2014.10.015

Trojsi, F., Esposito, F., de Stefano, M., Buonanno, D., Conforti, F. L., Corbo, D., et al. (2015). Functional overlap and divergence between ALS and bvFTD. *Neurobiol. Aging* 36, 413–423. doi: 10.1016/j.neurobiolaging.2014.06.025

Tzourio-Mazoyer, N., Landeau, B., Papathanassiou, D., Crivello, F., Etard, O., Delcroix, N., et al. (2002). Automated anatomical labeling of activations in SPM using a macroscopic anatomical parcellation of the MNI MRI single-subject brain. *Neuroimage* 15, 273–289. doi: 10.1006/nimg.2001.0978

van Dellen, E., Douw, L., Hillebrand, A., de Witt Hamer, P. C., Baayen, J. C., Heimans, J. J., et al. (2014). Epilepsy surgery outcome and functional network alterations in longitudinal MEG: a minimum spanning tree analysis. *Neuroimage* 86, 354–363. doi: 10.1016/j.neuroimage.2013.10.010

van Diessen, E., Otte, W. M., Stam, C. J., Braun, K. P. J., and Jansen, F. E. (2016). Electroencephalography based functional networks in newly diagnosed childhood epilepsies. *Clin. Neurophysiol.* 127, 2325–2332. doi: 10.1016/j.clinph.2016.03.015

van Lutterveld, R., van Dellen, E., Pal, P., Yang, H., Stam, C. J., and Brewer, J. (2017). Meditation is associated with increased brain network integration. *Neuroimage* 158, 18–25. doi: 10.1016/j.neuroimage.2017.06.071

Van Mieghem, P., and Magdalena, S. M. (2005). Phase transition in the link weight structure of networks. *Phys. Rev. E Stat. Nonlin. Soft Matter Phys.* 72:056138. doi: 10.1103/PhysRevE.72.056138

Van Mieghem, P., and van Langen, S. (2005). Influence of the link weight structure on the shortest path. *Phys. Rev. E Stat. Nonlin. Soft Matter Phys.* 71:056113. doi: 10.1103/PhysRevE.71.056113

van Wijk, B. C. M., Stam, C. J., and Daffertshofer, A. (2010). Comparing brain networks of different size and connectivity density using graph theory. *PLoS One* 5:e13701. doi: 10.1371/journal.pone.0013701

Watson, C. G. (2018). *Graph Theory Analysis of Brain MRI Data. CRAN Repository*. Available at: https://github.com/cwatson/brainGraph

Whitwell, J. L., Josephs, K. A., Avula, R., Tosakulwong, N., Weigand, S. D., Senjem, M. L., et al. (2011). Altered functional connectivity in asymptomatic MAPT subjects: a comparison to bvFTD. *Neurology* 77, 866–874. doi: 10.1212/WNL.0b013e31822c61f2

Wu, Z., Braunstein, L., Havlin, S., and Stanley, H. (2006). Transport in weighted networks: partition into superhighways and roads. *Phys. Rev. Lett.* 96:148702. doi: 10.1103/PhysRevLett.96.148702

Yu, M., Gouw, A. A., Hillebrand, A., Tijms, B. M., Stam, C. J., van Straaten, E. C. W., et al. (2016). Different functional connectivity and network topology in behavioral variant of frontotemporal dementia and Alzheimer's disease: an EEG study. *Neurobiol. Aging* 42, 150–162. doi: 10.1016/j.neurobiolaging.2016.03.018

Yu, M., Hillebrand, A., Tewarie, P., Meier, J., van Dijk, B., Van Mieghem, P., et al. (2015). Hierarchical clustering in minimum spanning trees. *Chaos* 25:023107. doi: 10.1063/1.4908014

Zalesky, A., Fornito, A., and Bullmore, E. (2012). On the use of correlation as a measure of network connectivity. *Neuroimage* 60, 2096–2106. doi: 10.1016/j.neuroimage.2012.02.001

Zhang, B., and Horvath, S. (2005). A general framework for weighted gene co-expression network analysis. *Stat. Appl. Genet. Mol. Biol.* 4:Article17. doi: 10.2202/1544-6115.1128

Zhang, Z., Telesford, Q. K., Giusti, C., Lim, K. O., and Bassett, D. S. (2016). Choosing wavelet methods, filters, and lengths for functional brain network construction. *PLoS One* 11:e0157243. doi: 10.1371/journal.pone.0157243

Zhou, J., Greicius, M. D., Gennatas, E. D., Growdon, M. E., Jang, J. Y., Rabinovici, G. D., et al. (2010). Divergent network connectivity changes in behavioural variant frontotemporal dementia and Alzheimer's disease. *Brain* 133, 1352–1367. doi: 10.1093/brain/awq075

Conflict of Interest Statement: The authors declare that the research was conducted in the absence of any commercial or financial relationships that could be construed as a potential conflict of interest.

Copyright © 2019 Saba, Premi, Cristillo, Gazzina, Palluzzi, Zanetti, Gasparotti, Padovani, Borroni and Grassi. This is an open-access article distributed under the terms of the Creative Commons Attribution License (CC BY). The use, distribution or reproduction in other forums is permitted, provided the original author(s) and the copyright owner(s) are credited and that the original publication in this journal is cited, in accordance with accepted academic practice. No use, distribution or reproduction is permitted which does not comply with these terms.

frontiers in Neuroscience

ORIGINAL RESEARCH
published: 05 April 2019
doi: 10.3389/fnins.2019.00332

Multilevel Mapping of Sexual Dimorphism in Intrinsic Functional Brain Networks

Nina de Lacy[1], Elizabeth McCauley[1], J. Nathan Kutz[2] and Vince D. Calhoun[3,4]*

[1] Department of Psychiatry and Behavioral Sciences, University of Washington, Seattle, WA, United States, [2] Department of Applied Mathematics, University of Washington, Seattle, WA, United States, [3] Mind Research Network, Albuquerque, NM, United States, [4] Department of Electrical and Computer Engineering, University of New Mexico, Albuquerque, NM, United States

Differences in cognitive performance between males and females are well-described, most commonly in certain spatial and language tasks. Sex-related differences in cognition are relevant to the study of the neurotypical brain and to neuropsychiatric disorders, which exhibit prominent disparities in the incidence, prevalence and severity of symptoms between men and women. While structural dimorphism in the human brain is well-described, controversy exists regarding the existence and degree of sex-related differences in brain function. We analyzed resting-state functional MRI from 650 neurotypical young adults matched for age and sex to determine the degree of sexual dimorphism present in intrinsic functional networks. Multilevel modeling was pursued to create 8-, 24-, and 51-network models of whole-brain data to quantify sex-related effects in network activity with increasing resolution. We determined that sexual dimorphism is present in the majority of intrinsic brain networks and affects ∼0.5–2% of brain locations surveyed in the three whole-brain network models. It is particularly common in task-positive control networks and is pervasive among default mode networks. The size of sex-related effects varied by network but can be moderate or even large in size. Female > male effects were on average larger, but male > female effects spread across greater network territory. Using a novel methodology, we mapped dimorphic locations to meta-analytic association test maps derived from task fMRI, demonstrating that the neurocognitive footprint of intrinsic neural correlates is much larger in males. All results were replicated in a motion-matched sub-sample. Our findings argue that sex is an important biological variable in human brain function and suggest that observed differences in neurocognitive performance have identifiable intrinsic neural correlates.

Keywords: intrinsic networks, ICA, sex-related differences, functional MRI, male, female

OPEN ACCESS

Edited by:
Laura Marzetti,
Università degli Studi "G. d'Annunzio" Chieti – Pescara, Italy

Reviewed by:
Angela R. Laird,
Florida International University, United States
Antonello Baldassarre,
Mediterranean Neurological Institute (IRCCS), Italy

****Correspondence:***
Nina de Lacy
delacyn@uw.edu

Specialty section:
This article was submitted to Brain Imaging Methods, a section of the journal Frontiers in Neuroscience

Received: *14 July 2018*
Accepted: *21 March 2019*
Published: *05 April 2019*

Citation:
de Lacy N, McCauley E, Kutz JN and Calhoun VD (2019) Multilevel Mapping of Sexual Dimorphism in Intrinsic Functional Brain Networks. Front. Neurosci. 13:332. doi: 10.3389/fnins.2019.00332

INTRODUCTION

Research in human neuroscience and psychology has described many differences in the performance of neurocognitive tasks between males and females. More recently, a newer generation of studies has re-examined these findings in a more nuanced fashion, attempting to take into account the influence of potential co-varying factors such as gender identification and socialization. While this latter work has de-emphasized the wide scope of earlier findings, some types of

cognitive tasks have been confirmed to show significant differences in performance between males and females. Broadly, males tend to exhibit superior performance in selected spatial and visuospatial tasks and are somewhat disproportionately represented among high performers in mathematics, whereas females perform better at reading and certain tasks of verbal fluency, recognition memory, and episodic memory (Miller and Halpern, 2014). However, differences may be quite task specific. For example, men reliably show superior performance on tasks of mental rotation but only inconsistently in mental folding, and the performance gap in mental rotation is wider for 3-dimensional versus (vs.) 2-dimensional objects (Voyer et al., 1995). In some types of tasks differences in performance are striking and appear to straddle cultural and educational environments: in a sample of 1.5 million children across 75 nations, girls consistently outperformed boys on reading (Stoet and Geary, 2013). Considerable variation also exists at the level of the individual.

Sex-related differences in cognition are of interest not only for the study of the neurotypical brain, but also in the context of neuropsychiatric disorders. Sex profoundly influences the prevalence, incidence and severity of various neuropsychiatric disorders. Well-known examples include the increased prevalence of attention deficit hyperactivity disorder (ADHD) and autism in males, vs. higher lifetime rates of depression and anxiety in females. The incidence of anxiety disorders accelerates faster in adolescent females, whereas schizophrenia onsets earlier in males, with a more severe course. Sex-related differences are also present in the diseases of senescence, with Alzheimer's disproportionately affecting females, but Parkinson's disease and Lewy body dementia being 2-4x more common in men (Podcasy and Epperson, 2016). While altered brain function associated with diagnosis has been described in most neuropsychiatric disorders, sex-related differences appear to further mediate disrupted function, suggesting interactions between sex and the requisite developmental or disease process. For example, diagnosis × sex interactions in brain function have been identified in autism (Yang and Lee, 2018) and our own work in ADHD (de Lacy et al., 2018). Similar phenomena occur in aging and dementia. For example, rates of cognitive decline with aging differ between males and females, and sex-related differences have been reported in the cognitive impairment attributable to Alzheimer's disease (Li and Singh, 2014).

The continuous development of non-invasive imaging technologies with good spatial resolution such as magnetic resonance imaging (MRI) has enabled the investigation of sex-related differences in human brain structure and function, building bridges between observed differences in cognitive performance and their potential neural correlates. Perhaps the most robust findings have been of a greater proportion of gray matter in females as compared to white matter and larger absolute brain volume in males, even after correcting for body size (Gur et al., 1999). The former finding is present even in childhood. Other work suggests that dimorphism also exists in cortical thickness and gyrification (Im et al., 2006; Mutlu et al., 2013). A recent large study of older adults from the UK brain biobank confirmed overall thicker cortices in women, but more variation among men in regional volumes, gyrification and cortical thickness (Ritchie et al., 2018). Further, a number of studies indicate that volumetric and white-matter differences between men and women are regionally specific (Sacher et al., 2013; Guadalupe et al., 2017) and include differences in the topology of anatomic (white matter) connectivity (Gong et al., 2011).

Given the close relationship between brain function and cognitive performance, identifying the functional neural correlates of sex-related cognitive differences is of considerable interest. The latter have been explored using functional MRI (fMRI). In fMRI during task performance, sex-related differences have been observed paralleling the psychological literature, such as visuospatial tasks (Gur et al., 2000). In the task-free state, intrinsic or spontaneous brain activity is recorded *in vivo* using resting-state fMRI (rsfMRI). This activity is spatio-temporally organized, and replicable macroscale intrinsic neural networks have been identified with specific neurocognitive associations (Laird et al., 2011). Considerable controversy exists regarding dimorphism in intrinsic networks. For example, several studies have described sex-related differences in fronto-parietal, cingulo-opercular and temporal connections in typically developing adults (Biswal et al., 2010; Zuo et al., 2010) or individual networks such as the salience and default mode network (DMN) in healthy aging (Jamadar et al., 2018). Conversely, others have found no differences between men and women in certain prominent intrinsic networks and suggested sex need not be modeled as a variable in rsfMRI studies (Weissman-Fogel et al., 2010). Given the large and growing number of rsfMRI studies, this is a pressing research question.

The relative ease of acquisition of rsfMRI render it a tractable medium for examining brain function across ages, species and cognitive levels. Further, macroscale intrinsic networks observed in the resting condition are similar to those detected during task performance (Smith et al., 2009), being theorized to represent historical activity patterns and/or task activation 'templates.' It may therefore be hypothesized that intrinsic brain networks may have differences in their spatial characteristics in men and women that map onto those cognitive abilities exhibiting sex-related differential performance in the population. One way to examine these relationships is to analyze differences in intrinsic networks and correlate them to ex-scanner or in-scanner task performance. Experimentally, these approaches are challenged by the difficulties inherent in constructing the requisite required large array of cognitive tasks and administering them to a sufficiently well-powered group of subjects. To address this, we recently developed a novel methodology allowing *in silico* mapping of statistical effects identified in intrinsic networks onto meta-analytic association test maps of neurocognitive functions. This approach allows the construction of a computational 'bridge' from brain networks observed during rsfMRI to neurocognitive maps derived from hundreds of task fMRI experiments.

To advance the debate on sex-related differences in intrinsic brain networks, we asked whether we could isolate male > female (M > F) and female > male (F > M) effects in intrinsic brain networks in a large sample of typically developing young adults matched for age and sex, and how these effects related

to brain maps associated with nine neurocognitive functions with good evidence of sex-related performance differences. As noted above, sex-related performance differences have also historically been detected in many other cognitive tasks, albeit less consistently or less frequently reported. For comparison purposes, we therefore also elected to survey a selection of cognitive control functions, where there is a less robust evidence base for sex-related performance differences. Given the existing controversy in this field, we formulated a design where intrinsic brain networks were obtained using independent component analysis (ICA), a popular and very well-established (Calhoun and Adali, 2012) data-driven method of discovering networks, and pursued multilevel modeling. Here, three separate whole-brain models of 8, 24, and 51 networks were formulated to describe functional brain organization with increasing refinement and to assess whether major findings were stable across different model orders, since there is currently no standard method to determine the optimal number of intrinsic networks when modeling whole-brain rsfMRI. Multivariate modeling of M > F and F > M effects was applied in 8-, 24-, and 51-network models, where the data-driven functional brain parcellation estimated with ICA was the same for all participants within each model. Further, we performed a replication analysis in a subsample of subjects matched for head motion.

MATERIALS AND METHODS

Data

This study uses data from the Brain Genomics Superstruct project, collected from > 3,000 individuals in the Boston community enrolled in studies of normal brain function or as controls in clinical studies[1]. From this larger initiative, the originators formed and released a repository in 2015 comprising demographic, MRI and behavioral data from a subset of 1570 healthy young adults ages 18–35, where age was specified within 2-year bins. For example, the 19-year-old bin includes subjects aged 18 and 19 at the time of scanning. Our study uses data from subjects in this latter sample, where the "dispersion of estimated IQ scores [was] positively shifted relative to the general population" but personality traits "have distributions that would be expected of a clinically screen population-based sample (Holmes et al., 2015). Of note, IQ scores were derived from Shipley-Hartford Age-Corrected T scores. The present study was deemed not human subjects research by the University of Washington Institutional Review Board.

MRI Pre-processing

In this step, unprocessed rsfMRI data was processed with a standard SPM12 pipeline to prepare it for modeling with ICA. MRI scans were collected using matched 3T TIM Trio systems at Harvard University and Massachusetts General Hospital using vendor-supplied 12-channel head coils, on 5 different scanners. 124 volumes (6.12 min) of functional MRI were acquired with 47 slices, interleaved sequence, voxel size 3.0 mm × 3.0 mm × 3.0 mm and TR = 3 s. Resting state scans were acquired with participants instructed to "remain still, stay awake and keep their eyes open while blinking normally" (Holmes et al., 2015). A fixation cross was not employed. Full details of parameters may be obtained from the Brain Genomics Superstruct website[2]. The originators of the data kept scan time relatively short at 6.12 min to reduce the risk of movement. Prior work has also demonstrated that 5–7 min of rsfMRI is sufficient to obtain stable estimates of intrinsic networks (Fox et al., 2005; Van Dijk et al., 2010). In addition, extensive quality control was performed by the originators of the data, including screening for "artifacts, acquisition problems, processing errors and excessive motion with each image viewed on a per-slice basis along each principal axis" and data from 54 participants were excluded from release on this basis (Holmes et al., 2015). Slice-based temporal signal-to-noise ratio (sSNR) was also computed (Holmes et al., 2015) and 88 participants with sSNR < 100 were excluded from release, thus ensuring that all subjects in the present study have sSNR > 100. As recommended by the originators of the data, the first 4 volumes of each scan were removed to account for scanner equilibration effects, with 120 timepoints remaining. Subsequently, volumes were slice-time corrected to the middle volume, realigned to the first volume, resliced, coregistered, and normalized to the functional template and smoothed at 6 mm full width half maximum using standard algorithms in SPM12. After processing, data were submitted to quality control to assess the quality of the normalization and degree of subject motion by computing (1) spatial regression between each normalized functional image and a group mask constructed from all subjects and (2) root mean square difference of volume N to volume N+1, also known as DVARS (Christodoulou et al., 2013; Power et al., 2014). All subjects had > 85% correspondence between their normalized image and the group mask with one exception. Normalization for this subject proved uncorrectable and this participant was eliminated from further consideration.

Subject Sample Construction

In this step, two samples of participants were prepared from the total of 1569 GSP subjects remaining after pre-processing (see MRI Pre-processing). The first was a 670-subject sample matched for age and sex, the second a 535-subject sample additionally matched for motion. The 670-subject sample for this study was constructed by selecting right-handed subjects with estimated IQ scores available, and then sex-matching within age bins. Subject demographics may be viewed in **Table 1** and a list of subjects inspected in **Supplementary Table 1**. In this sample, there was a significant difference in head motion as measured by DVARS between males and females ($p = 6.995 \times 10^{-9}$), with males having higher average scores. Accordingly, we also created a sub-sample of 534 subjects that were similarly all right-handed and matched for age and sex but were also matched for head motion as defined by DVARS score. A list of the 136 subjects removed to create this motion-matched sample is in **Supplementary Table 2**. There was no significant difference in estimated IQ between groups in the

[1]https://www.neuroinfo.org/gsp/

[2]https://static1.squarespace.com/static/5b58b6da7106992fb15f7d50/t/5b68650d8a922db3bb807a90/1533568270847/GSP_README_140630.pdf

TABLE 1 | Subject demographics.

	Male	Female
Number of subjects	335	335
Average estimated IQ	114.9	113.0
Age range	19–35	19–35

two samples. The terms 'sex,' 'male' and 'female' are used in this paper in accordance with the phenotypic nomenclature used by the Brain Genomics Superstruct project.

Construction of Whole Brain Models of Intrinsic Networks

In this step, pre-processed rsfMRI data (see MRI Pre-processing) for the two subject groups (see Subject Sample Construction) was used to generate 8-, 24-, and 51 network models of brain function by submitting the pre-processed data to group spatial ICA (see Group Spatial ICA). Gray matter components were identified in each of the 3 models by taking the entire output (all components) of the group ICA and eliminating noise components (see Sorting Components From the Spatial ICA). The resulting gray matter components were thresholded in order to construct spatial maps of each intrinsic network representing the strongest and most consistent coactivations between brain regions within a network (see Construction of Intrinsic Functional Network Spatial Maps). These spatial maps were used to attribute the neurocognitive labels for each IN (see Functional Intrinsic Network Attribution and Grouping), and served as the inputs for the remainder of the analyses. This process was followed for each brain map in each of the 3 ICA models.

Group Spatial ICA

Using the pre-processed rsfMRI data (see MRI Pre-processing), we performed group spatial ICA using the Group ICA of fMRI Toolbox (GIFT) developed in our group, and widely used in ICA of fMRI (Calhoun et al., 2001; Calhoun and Adali, 2012). ICA is a popular method of providing data-driven functional brain parcellations in rsfMRI data and resultant sets of intrinsic networks for further analysis. Currently, no method exists to determine an optimal number of components/networks for any specific individual model. Rather, the number of components selected for a study is an analytic choice. Generally, higher model orders with more components provide more detailed views of brain function, i.e., more networks. The ultimate number of networks estimated by an ICA model depends therefore on (1) The initial number of components specified for the model minus (2) The number of noise components eliminated after model estimation. In the present study, we performed 3 ICA decompositions to test the sensitivity of results to model parameters and provide an increasingly detailed view of brain networks. Resting-state scans were first pre-whitened followed by a subject-specific data reduction principal components analysis retaining 20, 50, and 110 principle components (PCs) respectively, with the objective of stabilizing back reconstruction and retaining maximum variance at the individual level. Group ICA decompositions were then performed with 15, 40, and 100 components respectively using the Infomax algorithm run 10 times with random initialization using ICASSO (Himberg et al., 2004; Li et al., 2007). Aggregate spatial maps were estimated as the centrotypes of component clusters to reduce sensitivity to initial algorithm parameters. Single-subject images were concatenated in time to perform the single group ICA estimation and subject specific spatial maps estimated using back reconstruction (Erhardt et al., 2011) with the group information guided ICA (GIG-ICA) algorithm (Du et al., 2016), an approach which we have shown well-captures individual subject variability (Allen et al., 2012). GIG-ICA estimates single-subject images and timecourses from the single group ICA estimation, thereby allowing individual variation in spatial maps constructed from each component (see below). The resulting independent components were scaled by converting each subject component image and the time course to *z*-scores.

Sorting Components From the Spatial ICA

Using the output of all components from each of the 3 ICA decompositions (see Group Spatial ICA), we sorted components into gray-matter networks vs. artefactual noise components with a combination of expert visual inspection by NdL and VC, and quantitative metrics in order to isolate gray-matter or neural components. To do this we computed the quantitative spectral metrics of (1) Fractional amplitude of low frequency fluctuations and (2) Dynamic range (Allen et al., 2011) for every component. The former is the ratio of the integral of spectral power below 0.10 Hz to the integral of power between 0.15 and 0.25 Hz. Dynamic range is the difference between the peak power and minimum power at frequencies to the right of the peak. Generally, components representing gray matter have higher values in these metrics, while artefactual components (such as signals accruing from cerebrospinal fluid, vascular pulsations, white matter or head motion) have lower values, though there are currently no absolute cut-off points for inclusion or exclusion. Components were inspected by NdL and VC and those with poor overlap with cerebral gray matter or low spectral metrics were discarded. Where components were deemed to be 'mixed' components containing a probable mixture of gray-matter signal and noise, we discarded these components to promote a more conservative approach with higher-quality networks. In particular, sub-cortical/cerebellar components tend in our empirical experience to appear as 'mixed' components. For example, in the present analysis we accepted only a single cerebellar network in the 24- and 51-network models. We retained 8 components from the 15-component ICA, 24 from the 40-component and 51 from the 100-component ICA, each considered a set of functional intrinsic brain networks (INs). Thus, 40–50% of the components were discarded from each component set, a ratio in line with comparable studies using ICA in other data samples (Allen et al., 2011; Rashid et al., 2014; de Lacy et al., 2017).

Construction of Intrinsic Functional Network Spatial Maps

After the sorting process (see Sorting Components From the Spatial ICA) we constructed a spatial map for each gray-matter

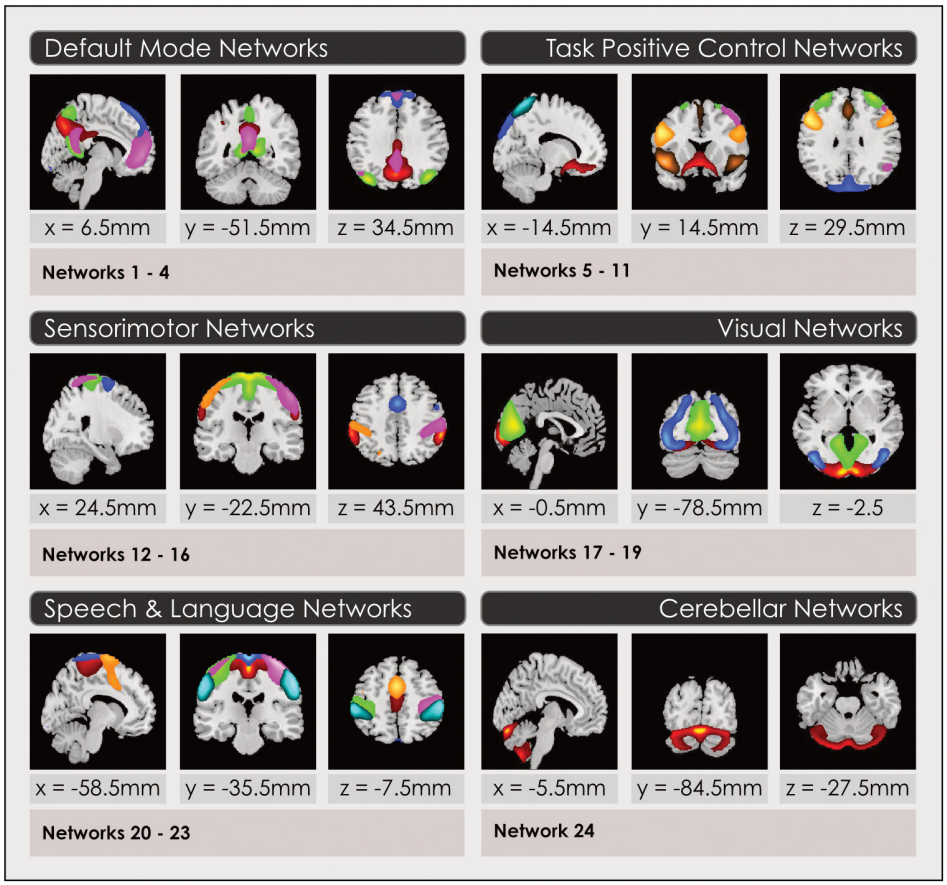

FIGURE 1 | Intrinsic networks grouped by neurocognitive function for 24-network model. Group spatial maps are displayed in 2-dimensional format for a representative slice, for the 24-network model of intrinsic networks grouped by neurocognitive function. Spatial maps are created by thresholding gray-matter components from the group ICA at (mean + 4 standard deviations). Neurocognitive attributions were made using three methods described in the Section "Functional Intrinsic Network Attribution and Grouping." Readers may explore 3-dimensional maps of each network in Neurovault at https://neurovault.org/collections/4030/ (8-network model), https://neurovault.org/collections/4031/ (24-network model) and https://neurovault.org/collections/4032/ (51-network model), where networks are labeled with numbers and their neurocognitive attributions.

IN that had been retained to select voxels that represented the strongest and most consistent coactivations within each IN, by performing a voxelwise one-sample *t*-test on the individual subject timecourses and thresholding individual voxels at (mean + 4 standard deviations), again following an established pipeline (Allen et al., 2011) using GIFT. Thus, these spatial maps represent the brain regions most associated with each component's timecourse, instantiated in thresholded brain maps. This procedure enabled us to construct a group spatial map for each of the INs assembled from the relevant individual subject timecourses, in each of the model orders. These spatial maps were used to attribute the neurocognitive labels for each IN, and served as the inputs for the remainder of the analyses. Three-dimensional renderings of the resulting 3 sets of intrinsic networks may be inspected in Neurovault at https://neurovault.org/collections/4030/ (8-network model), https://neurovault.org/collections/4031/ (24-network model) and https://neurovault.org/collections/4032/ (51-network model). Each intrinsic network is labeled with its attributed neurocognitive function and numbers, that correspond to **Figures 1**, **3**, **4**, **6**, **7**.

Functional Intrinsic Network Attribution and Grouping

The primary neurocognitive function of each IN spatial map constructed in Section "Construction of Intrinsic Functional Network Spatial Maps" was attributed by visual inspection and quantitative comparisons using three methods in order to assign it an associated neurocognitive function and label. The output of this final step of the ICA process was 3 sets of thresholded spatial maps of intrinsic networks with associated neurocognitive labels. The subsequent statistical analysis to identify sex-related effects and map these to neurocognitive functions was performed on these 3 models of whole-brain function. To label each IN, we first determined the coordinates in Montreal Neurologic Space (MNI) associated with peak intensities for each IN in each of the 3 sets of maps. The top 3 co-ordinates were compared with the literature. We found multiple literature-based confirmatory sources that gave specific Talairach or MNI coordinates and

associated these with network labels for all networks in the task-positive network group, the DMN and primary sensorimotor and visual networks (Fox et al., 2005; Dosenbach et al., 2006, 2007; Seeley et al., 2007; Smith et al., 2009; Laird et al., 2011; Spreng et al., 2013; Vernet et al., 2014) but not for INs in the subcortical or speech/language groups. Secondly, the top 5 spatial locations in each IN were examined using the Brodmann Interactive Atlas[3]. Thirdly, network correlations with association test maps of regional activations associated with specific neurocognitive functions were inspected in Neurosynth (Yarkoni et al., 2011). Attributions using the third method may be explored by readers by loading a spatial map in Neurovault and accessing the 'Cognitive Decoding' function.

Statistical Analysis to Identify Sex-Related Effects in IN Spatial Maps

In this step, we used the group ICA output of 3 sets of labeled, thresholded spatial maps of INs (see Construction of Whole Brain Models of Intrinsic Networks) as the substrate for a multivariate statistical analysis aimed at finding sex-related differences in each IN in each of the 3 models of whole brain function. We first performed a multivariate analysis of covariance (MANCOVA) using the MANCOVAN toolbox and an established method (Allen et al., 2011) in GIFT, to compare the effects of sex with other possible predictors of variance in the 3 sets of network maps for (a) The original 670-subject sample and (b) The 534-subject motion-matched sample. To optimize for the large dimensions of the data but enable statistical testing at each voxel, predictors were submitted to the MANCOVA with an F-test at each iteration to produce a final reduced model for each outcome measure and network, before univariate testing of significant predictors was performed on the original model with correction for multiple comparisons (among all networks analyzed within a set) and false discovery rate (FDR) at $\alpha = 0.01$. As detailed above, the GSP project acquired data on 5 different matched Siemens scanners and we controlled for scanner site in our analysis. We used sex, age bin, estimated IQ-level, scanner bin and DVARS measure as predictors for all three analyses. The effects of age, estimated IQ-level, DVARS and scanner bin were regressed from the analysis using the general linear model, to isolate the effects of sex. However, we retained all variables including scanner site to test for any residual effects on the statistical analyses. For example, we tested for residual DVARS × sex effects. Significant effects were computed for both positively correlated voxels in each network ($F > M$ effect) and for negatively correlated voxels ($M > F$ effect).

For each predictor that proved significant in the univariate analysis, the effect size (beta) was determined by computing connected voxel clusters (similarly to the bwlabeln function in MATLAB) and then calculating an average beta over the cluster of voxels. The fraction of the network map accounted for by each effect was determined by calculating the fraction of the total voxels in each network map represented by voxels with significant effects (significant voxels/total voxels). The size and fraction of both $F > M$ and $M > F$ effects were computed for each of the 3 IN sets in both subject groups.

[3]http://www.fmriconsulting.com/brodmann/Interact.html

Mapping Significant Effects to Neurocognitive Functional Maps

In this final step, we used the output of the multivariate analysis (see Statistical Analysis to Identify Sex-Related Effects in IN Spatial Maps) which identified significant sex-related effects in each IN in each model as the input to a mapping process where we mapped effects of sex in each IN to neurocognitive functional maps using a method which we recently developed and published (de Lacy et al., 2018). The aim of this analysis was to identify and compare the cognitive 'footprint' of sex-related differences in IN function across 16 cognitive functions and see how this varied between sexes, cognitive functions and 8-, 24-, and 51-network models of brain function. First, effect maps were created to map voxels with significant ($\alpha < 0.01$, corrected for FDR and multiple comparisons) $F > M$ and $M > F$ effects in the univariate analysis for each network. For example, a map of the effects of $M > F$ in the right fronto-parietal network. Association test maps were created using custom code written in Python to access the Neurosynth (Yarkoni et al., 2011) database and analytic engine for each of the following terms: visuospatial; spatial; verbal; verbal fluency; semantic memory; rotation; recognition memory; reading and arithmetic. We selected these terms based on a qualitative review of the prior literature pertaining to significant performance differences between male and female subjects in psychological and neurocognitive performance (See, for example, the excellent review by Miller and Halpern (2014). In addition, we performed a comparison with a set of major cognitive control function terms: cognitive flexibility; goal selection; reaction time; response selection; selective attention; sustained attention and working memory. We accessed the entire database of task fMRI studies available in Neurosynth at the time of our analysis, which was performed between April and July 2018, prior to the recent Neurosynth update. Of note, Neurosynth recently changed the terminology used to refer to neurocognitive maps, now preferring the terms 'uniformity test map' and 'association test map.' At the time our analysis was performed the terms in use were 'forward inference map' and 'reverse inference map.' In this manuscript we use the updated term 'association test map' though at the time our analysis was performed these neurocognitive maps were referred to as 'reverse inference maps.' Limitations remain, reviewed below (See: Limitations).

Neurosynth association test maps are z-score fMRI activation maps derived from a database at the time of our analysis of > 11,000 studies in the neuroscience literature in task-based fMRI. Neurosynth[4] uses text mining to identify terms of interest (e.g., "spatial") within neuroscience articles occurring at a frequency of > 1/10,000 words, and extracts fMRI activation coordinates from tables in the corresponding article text. These term to activation mappings are used to construct the database. Automated meta-analysis is performed for a psychological term of interest (e.g., "recognition memory") to construct a whole-brain association test map of the posterior probability of a term of interest occurring given activation at each voxel. This contrasts with forward inference maps such that are commonly obtained

[4]http://neurosynth.org/

in task-based fMRI, or conventional meta-analyses, which often display the probability of brain activation given a task, or term. Therefore, association test maps may be conceptualized as meta-analytic maps identifying brain location activations, that are relatively more selective for the neurocognitive function of interest than forward inference maps. This procedure controls for the fact that many brain locations are implicated in multiple functions and are non-specifically activated in experiments. The process by which maps are generated by Neurosynth is wholly automated, and multiple validation techniques were applied by the original authors to compare results with manual techniques (Yarkoni et al., 2011). Overall, their results demonstrated that for broad domains of cognition, such as are considered in the present study, the composite Neurosynth algorithm extracts the majority of coordinates accurately to form the underlying database and produces results comparable in sensitivity and specificity to manual meta-analytic approaches. In the present study, we used custom Python code to access the Neurosynth database and generate association test maps corresponding to terms of interest, but otherwise all computational procedures were similar.

Custom code was written in MATLAB to identify locations (voxels) in the brain where individual effect maps were spatially coincident with activations in association test maps for each neurocognitive function. This code is available in GitHub at ninadelacy/effect-mapping. Every combination of significant F > M and M > F effects and association test maps was computed, to determine voxels that were present in both maps for each combination. To create aggregated maps of effects in each subject across each neurocognitive function, overlapping voxels from F > M and M > F were collected, and redundancies eliminated to determine only unique voxels. We calculated the relative numbers of brain locations implicated in each neurocognitive functional map for F > M and M > F by summing the unique voxels for each neurocognitive functional map and dividing into the relative proportions for each subject group.

RESULTS

Sexual Dimorphism Was Present in the Majority of Intrinsic Functional Networks

We determined the spatial location of significant sex-related effects in each of the 8-, 24-, and 51-network models (**Figure 2**).

Our analyses revealed that significant ($\alpha < 0.01$, corrected for multiple comparisons and false discovery rate) sex-related differences were widely present in intrinsic networks in each of the three models (**Figures 3**, **4**), ranging from ∼60% in the 51-network model to >80% in the 24-network model (**Supplementary Tables 3–5**). In nearly all INs with sex-related differences, both types of effects (M > F and F > M) were present within the same network. Exceptions - where an effect of only one type was present in an individual network (i.e., F > M or M > F only) - were relatively rare. In these asymmetric cases, the unpaired effect typically occupied a relatively small proportion of the network, albeit these instances were more frequent as model order increased. Specifically, INs associated with language comprehension, gesture and the orbitofrontal cortex displayed only F > M effects in the 24-network model. In the 51-network model, the auditory, two motor, and two DMNs, and one of nine visual networks only displayed F > M effects, and a parietal network and frontoparietal network associated with working memory only M > F effects. In the motion-matched sample the number of effects increased overall, with nearly 90% of INs exhibiting significant ($\alpha < 0.01$, corrected for multiple comparisons and false discovery rate) sex-related differences in the 8- and 24-network models, and >70% in the 51-network model (**Supplementary Table 6**).

Of note, occasional differences were observed among networks with similar neurocognitive functions. For example, among the speech and language group, we identified only F > M effects in an IN associated with language comprehension in the 24-network model, but both M > F and F > M effects in a similar IN in the 51-network model. In the motion-matched sample these asymmetries were typically reduced given the increased number of sex-related effects present.

Sex Differences Were Pervasive in Default Mode Networks

Analyzing 3 model orders permitted the examination of sex-related effects in brain networks in increasing detail. For example, while one sensorimotor network was present in the 8-network model, 9 sensorimotor networks were present in the 51-network model, associated with differing functional emphases. A consistent finding was that both M > F and F > M effects were present in all default mode networks, regardless of model order (**Figures 3**, **4**). The only exceptions were 2 default mode networks of the 9 present in the 51-network model, where only F > M effects were detected (**Figure 4**). However, in the motion-matched sample these exceptions were not present (**Supplementary Table 5**), and all default mode networks showed sex-related differences. This striking finding contrasts with other network types, where sex-related effects were less pervasive, particularly in the 51-network model. In particular, visual and sub-cortical networks exhibited a relative paucity of sex-related effects, excepting the cerebellum, and no dimorphism was detected in attentional networks. This latter finding is most clearly seen in the 51-network model, where subnetworks associated with attentional function were isolated such as the dorsal attention network, visual attention networks and the temporo-parietal junction (associated with the ventral attention network).

Sex-Related Effects Were on Average Larger in Females, but Occupied More Brain Territory in Males

The size of sex-related effects varied across individual INs, as did the spatial area of each network that displayed dimorphism. As may be appreciated in **Figure 5**, some smaller-sized effects such as those in the anterior DMN or supplementary motor INs nonetheless occupied relatively larger proportions of the networks in question. This was also observed in the 8- and 51-network models (**Figures 6**, **7**). Within each network grouping there were few discernible patterns. For example, within the

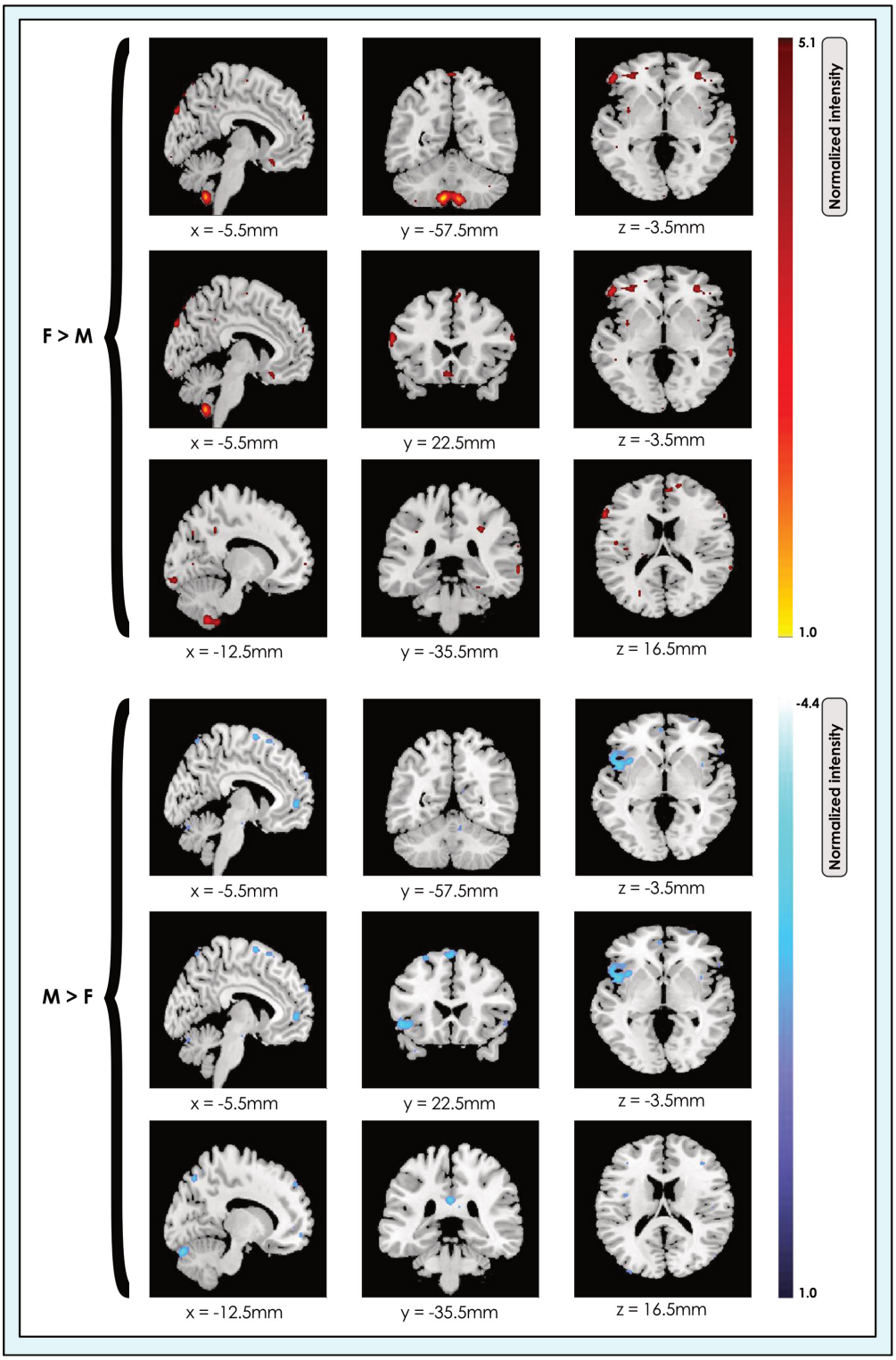

FIGURE 2 | Locations of sex-related effects in a 24-network model of whole brain function in 670 neurotypical young adults. The effect of sex is shown for M > F and F > M in young adult functional brain networks ($\alpha < 0.01$, corrected for multiple comparisons and false discovery rate). We present maps showing all dimorphic locations concatenated across networks in a 24-network whole-brain model in resting-state fMRI data from 670 neurotypical adults ages 19–35 matched for age and sex. We tested for significant sex-related differences at every voxel. Accordingly, both M > F (blue) and F > M effects (red-yellow) are possible within each network. Effects of each type are shown at three different slice locations with pairs of locations shown for each effect type to facilitate comparison. Readers may explore 3-dimensional effect maps available in Neurovault at https://neurovault.org/collections/4034/, where F > M effects are shown in red, and M > F effects in blue.

FIGURE 3 | Sex-related effect sizes among intrinsic networks in 8- and 24-network models of brain function in 670 neurotypical young adults. The effect of sex is shown for M > F and F > M in young adult functional brain networks ($\alpha < 0.01$, corrected for multiple comparisons and false discovery rate). We present both **(a)** 24-network and **(b)** 8-network whole-brain models estimated using 15- and 40-component independent component analyses respectively, performed on resting-state fMRI data from 670 neurotypical adults ages 18–35 matched for age and sex. We tested for significant sex-related differences at every voxel in each network. Accordingly, both M > F and F > M effects are possible within each network. Vis spat/attn, Visuospatial/Attention; L, Left; R, Right; Post, Posterior; Ant, Anterior; Lang Comp, Language Comprehension; Prim, Primary; Motor Cont, Motor Control; SM, Sensorimotor; Supp, Supplementary; OFC, Orbitofrontal; DMN, Default Mode Network. Network labels correspond with numbers and attributions for 3-dimensional maps available in Neurovault.

DMN group, some subnetworks displayed larger F > M effects while others had larger M > F effects. Exceptions were the sensorimotor and language groups where, as model order increased, there was a trend toward most effect sizes being larger in females.

We also observed that M > F effects consistently occupied a larger average proportion of network territory than F > M. This phenomenon was replicated across all models in both the original and motion-matched samples (**Figures 5–7** and **Supplementary Tables 3–5**). The disparity between the network area affected by differences between M > F and F > M increased as model order increased, being largest in the 51-network model. In contrast, average effect size was greater in F > M vs. M > F in all 3 models in the motion-matched sample, and in the 24- and 51-network models in the original sample. The percentage of each network's area displaying dimorphic effects also varied among models. On average, sex-related differences were present in ∼1–2% of total network area in the 8- and 24-network models and ∼0.5% of total network area in the 51-network model (**Figures 6**, **7** and **Supplementary Tables 3–5**).

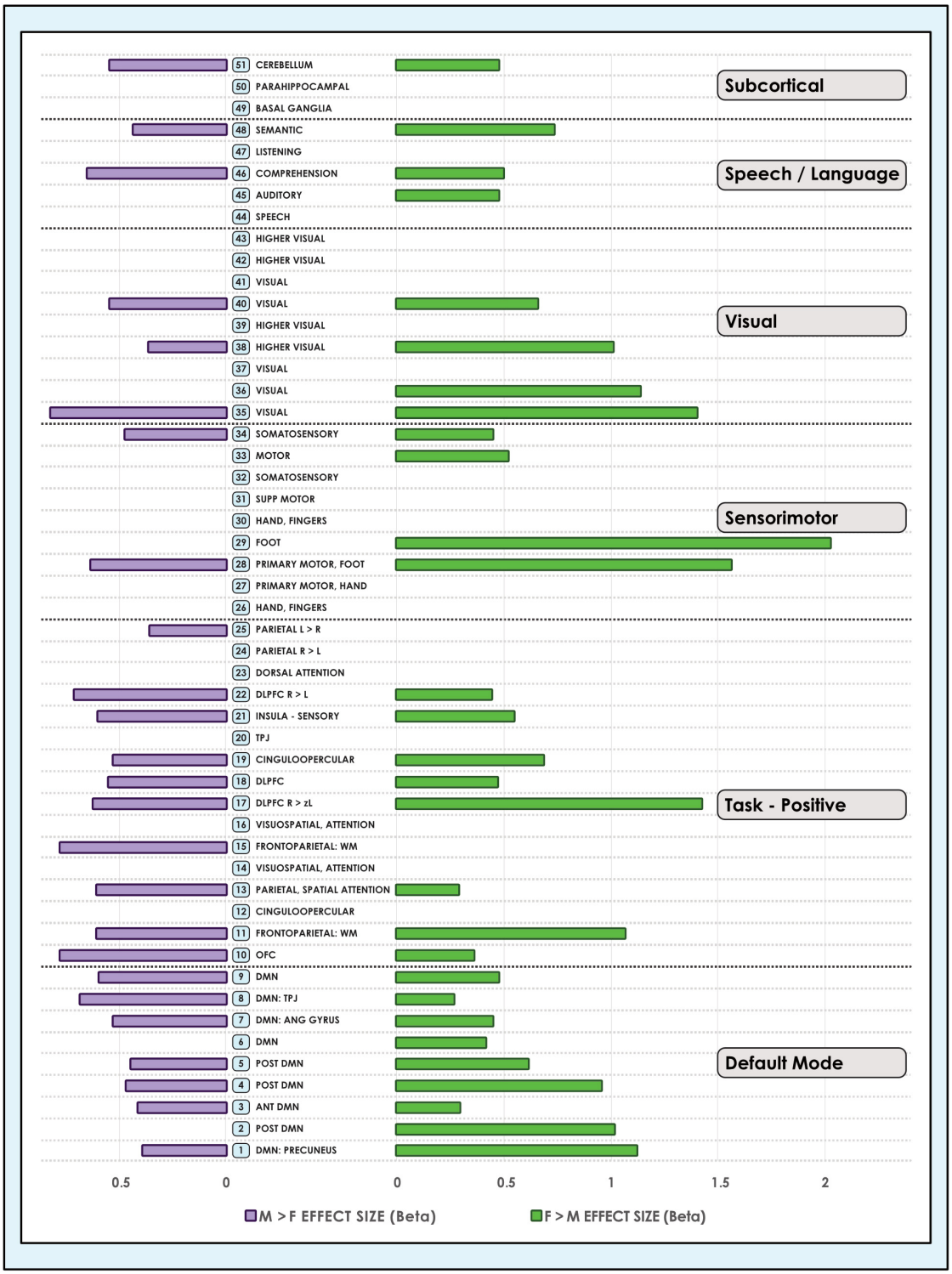

FIGURE 4 | Sex-related effect sizes among intrinsic networks in a 51-network model of brain function in neurotypical young adults. The effect of sex is shown for M > F and F > M in young adult functional brain networks ($\alpha < 0.01$, corrected for multiple comparisons and false discovery rate). Effect sizes are shown for a 51-network whole-brain model estimated using a 100-component independent component analysis performed on resting-state fMRI data from in 670 neurotypical adults ages 18–35 matched for age and sex. We tested for significant sex-related differences at every voxel in each network. Accordingly, both M > F and F > M effects are possible within each network. L, Left; R, Right; Post, Posterior; Ant, Anterior; SM, Sensorimotor; Supp, Supplementary; DLPFC, Dorsolateral Prefrontal Cortex; TPJ, Temporoparietal Junction; WM, Working Memory; OFC, Orbitofrontal; DMN, Default Mode Network; Ang Gyrus, Angular Gyrus. Network labels correspond with numbers and attributions for 3-dimensional maps available in Neurovault.

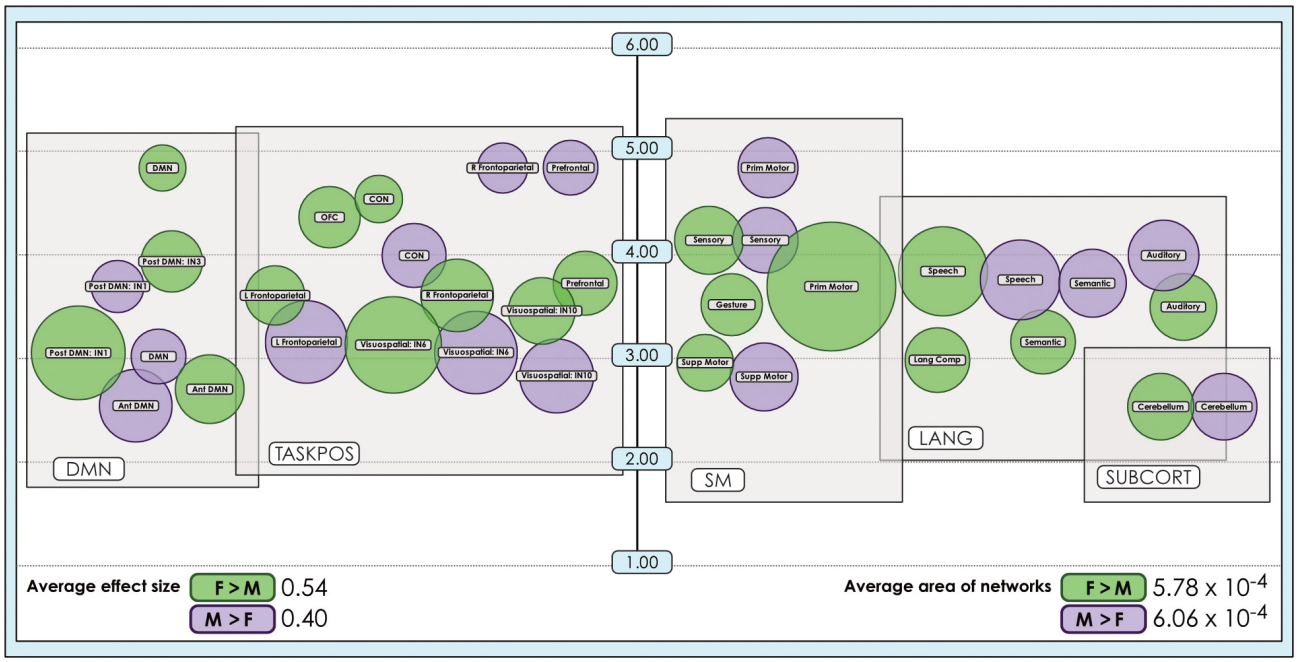

FIGURE 5 | Comparison of size of sex-related effects in intrinsic networks and proportion of network affected by dimorphism in a 24-network model of brain function. The size of significant ($\alpha < 0.01$, corrected for multiple comparisons and false discovery rate) effects of sex is shown for M > F and F > M in a 24-network model of functional brain networks estimated using independent component analysis in 670 neurotypical young adults matched for age and sex. Effect sizes (size of bubble) are compared to the fraction of the network map (position on vertical scale) affected by significant sex-related effects, computed as a percentage of all voxels analyzed from resting-state functional MRI. Vertical scale is a $\log_{10}$ scale. Average area is calculated as the arithmetic mean of fractions pertaining to each individual network. Vis spat/attn, Visuospatial/Attention; L, Left; R, Right; Post, Posterior; Ant, Anterior; Lang Comp, Language Comprehension; Prim, Primary; Motor Cont, Motor Control; SM, Sensorimotor; Supp, Supplementary; OFC, Orbitofrontal; DMN, Default Mode Network; CON, Cinguloopercular network. Network labels correspond with numbers and attributions for 3-dimensional maps available in Neurovault. Of note, the position of the bubbles relative to the *x*-axis has no quantitative meaning and has been set to support visual clarity.

		Effect Size		Area of Network	
Network #	Network Name	F > M	M > F	F > M	M > F
1	Ant DMN	0.29	0.39	3.57×10^{-4}	7.04×10^{-3}
2	Post DMN	0.45	0.25	1.24×10^{-4}	8.79×10^{-4}
3	R Frontoparietal	0.38	0.28	5.33×10^{-4}	2.16×10^{-4}
4	L Frontoparietal	0.42	0.22	3.74×10^{-4}	2.16×10^{-4}
5	Vis Spat/Attn	0.18	0.46	2.88×10^{-4}	1.87×10^{-4}
6	Sensorimotor	1.00	0.36	2.02×10^{-4}	5.47×10^{-4}
7	Visual	-	-	-	-
8	Visual	-	-	-	-

Average effect size F > M 0.34 M > F 0.25

Average area of networks F > M 9.91×10^{-4} M > F 1.51×10^{-3}

FIGURE 6 | Comparison of size of sex-related effects in intrinsic networks and proportion of network affected by dimorphism in a 8-network model of brain function in 670 neurotypical young adults. The size of significant ($\alpha < 0.01$, corrected for multiple comparisons and false discovery rate) effects of sex and proportion of network affected is shown for M > F and F > M in an 8-network model of functional brain networks. The fraction of each network map with sex-related effects was computed as a percentage of all voxels analyzed from resting-state functional MRI. Average area is calculated as the arithmetic mean of fractions pertaining to each individual network. Vis spat/attn, Visuospatial/Attention; L, Left; R, Right; Post, Posterior; Ant, Anterior; DMN, Default Mode Network. Network labels correspond with numbers and attributions for 3-dimensional maps available in Neurovault.

Network #	Network Name	Effect Size F>M	Effect Size M>F	Area of Network F>M	Area of Network M>F
1	DMN: Precuneus	1.12	0.39	3.46×10^{-4}	2.88×10^{-5}
2	Post DMN	1.02	0.67	1.44×10^{-3}	2.45×10^{-4}
3	Ant DMN	0.29	0.41	2.02×10^{-4}	1.87×10^{-3}
4	Post DMN	0.96	0.47	1.44×10^{-4}	8.64×10^{-4}
5	Post DMN	0.61	0.44	1.44×10^{-4}	1.15×10^{-4}
6	DMN	0.41	-	4.32×10^{-5}	-
7	DMN: Ang Gyrus	0.45	0.52	4.32×10^{-5}	4.75×10^{-4}
8	DMN: TPJ	0.27	0.68	4.32×10^{-4}	5.76×10^{-5}
9	DMN	0.47	0.59	3.89×10^{-4}	1.73×10^{-4}
10	OFC	0.36	0.77	6.19×10^{-4}	7.92×10^{-4}
11	Frontoparietal: WM	1.07	0.60	6.48×10^{-4}	6.05×10^{-4}
12	Cinguloopercular	-	-	-	-
13	Parietal, spatial attention	0.29	0.60	2.02×10^{-4}	1.15×10^{-3}
14	Visuospatial, attention	-	-	-	-
15	Frontoparietal: WM	-	0.77	-	2.59×10^{-4}
16	Visuospatial, attention	-	-	-	-
17	DLPFC R>L	1.42	0.62	5.33×10^{-4}	6.62×10^{-4}
18	DLPFC	0.47	0.54	7.35×10^{-4}	4.32×10^{-4}
19	Cinguloopercular	0.69	0.53	5.47×10^{-4}	2.45×10^{-4}
20	TPJ	-	-	-	-
21	Insula - sensory	0.55	0.59	1.83×10^{-3}	3.50×10^{-3}
22	DLPFC R>L	0.44	0.71	2.17×10^{-3}	2.81×10^{-3}
23	Dorsal attention	-	-	-	-
24	Parietal R>L	-	-	-	-
25	Parietal L>R	-	0.35	-	4.32×10^{-5}
26	SM:Hand, fingers	-	-	-	-
27	SM: Primary Motor, hand	-	-	-	-
28	SM: Primary Motor, foot	1.56	0.63	4.90×10^{-4}	1.86×10^{-3}
29	SM: Foot	2.03	-	1.44×10^{-4}	-
30	SM: Hand, fingers	-	-	-	-
31	SM: Supp Motor	-	-	-	-
32	SM: Somatosensory	-	-	-	-
33	SM: Motor	0.52	-	1.01×10^{-4}	-
34	SM: Somatosensory	0.44	0.47	9.36×10^{-4}	2.88×10^{-4}
35	Visual	1.40	0.82	2.02×10^{-4}	5.76×10^{-5}
36	Visual	1.14	-	1.44×10^{-5}	-
37	Visual	-	-	-	-
38	Higher	1.01	0.36	2.88×10^{-5}	2.13×10^{-3}
39	Higher Visual	-	-	-	-
40	Visual	0.66	0.54	3.31×10^{-4}	1.15×10^{-4}
41	Visual	-	-	-	-
42	Higher Visual	-	-	-	-
43	Higher Visual	-	-	-	-
44	Speech	-	-	-	-
45	Auditory	0.48	-	1.44×10^{-4}	-
46	Comprehension	0.50	0.64	2.45×10^{-4}	2.42×10^{-3}
47	Listening	-	-	-	-
48	Semantic	0.73	0.43	7.20×10^{-5}	1.87×10^{-4}
49	Basal Ganglia	-	-	-	-
50	Parahippocampal	-	-	-	-
51	Cerebellum	0.48	0.54	1.38×10^{-3}	6.19×10^{-4}

Average effect size		Average area of networks	
F > M	0.43	F > M	2.83×10^{-4}
M > F	0.29	M > F	4.40×10^{-4}

FIGURE 7 | Comparison of size of sex-related effects in intrinsic networks and proportion of network affected by dimorphism in a 51-network model of brain function in 670 neurotypical young adults. The effect of sex and proportion of network affected is shown for M > F and F > M effects in a 51-network model of functional brain networks ($\alpha < 0.01$, corrected for multiple comparisons and false discovery rate). The fraction of each network map with sex-related effects was computed as a percentage of all voxels analyzed from resting-state functional MRI. Average area is calculated as the arithmetic mean of the fractions pertaining to each individual network. L, Left; R, Right; Post, Posterior; Ant, Anterior; SM, Sensorimotor; Supp, Supplementary; DLPFC, Dorsolateral Prefrontal Cortex; TPJ, Temporoparietal Junction; WM, Working Memory; OFC, Orbitofrontal; DMN, Default Mode Network; Ang Gyrus, Angular Gyrus. Network labels correspond with numbers and attributions for 3-dimensional maps available in Neurovault.

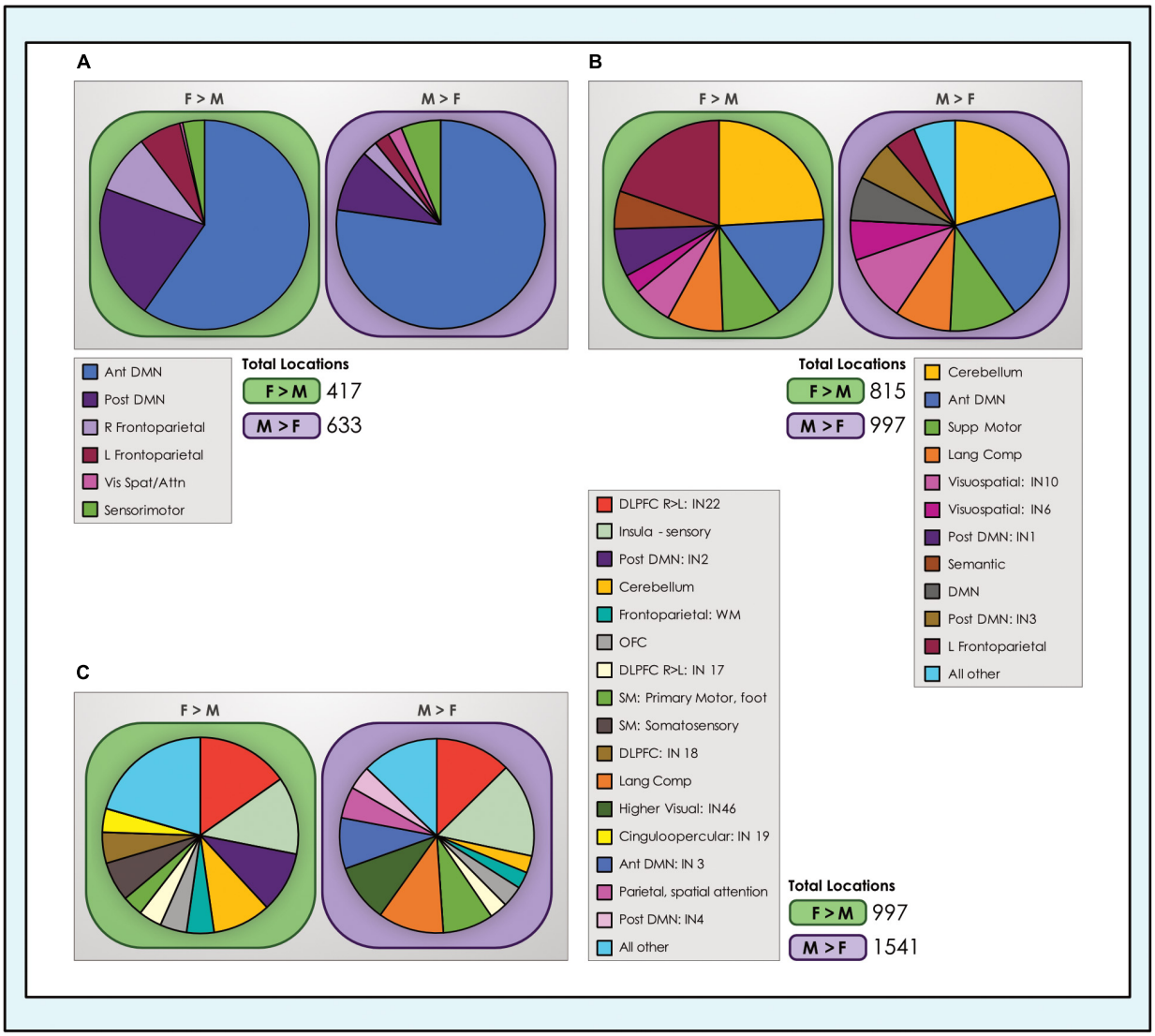

FIGURE 8 | Number of dimorphic locations in intrinsic networks. The number of unique dimorphic locations (voxels) in each intrinsic network is shown for each of the **(A)** 8-network; **(B)** 24-network and **(C)** 51-network whole-brain models of brain function in neurotypical young adults. For clarity, networks with fewer than 25 and 40 dimorphic locations in the 24- and 51-network models respectively have been grouped into 'all other' categories. Vis spat/attn, Visuospatial/Attention; L, Left; R, Right; Post, Posterior; Ant, Anterior; Lang Comp, Language Comprehension; SM, Sensorimotor; Supp, Supplementary; DLPFC, Dorsolateral Prefrontal Cortex; TPJ, Temporoparietal Junction; WM, Working Memory; OFC, Orbitofrontal; DMN, Default Mode Network.

Locations Exhibiting Dimorphic Effects Were Concentrated in Default Mode and Task-Positive Control Systems and the Cerebellum

We computed the proportion of total locations with dimorphic effects accounted for by each network (**Figure 8**). Comparing across network types revealed that the preponderance of locations with sex-related differences were in control systems (default mode and task-positive INs) and the cerebellum, again regardless of model order. In the 8- and 24-network models, the anterior subnetwork of the DMN system and the left fronto-parietal network were particularly prominent. In the 51-network model, with closer delineation of subnetworks, INs anchored in the dorsolateral prefrontal cortex (IN22, a right-lateralized IN) and insula were highlighted. Interestingly, as the single cingulooperecular network observed in the 24-network model split into two INs in the 51-network model - one with more cingulate involvement and the other an insula-dominated network associated with sensory function - it was the latter that continued to exhibit sex-related differences. Other networks related to language (comprehension and semantic) and sensorimotor function also represented a meaningful share of dimorphic locations. These trends were replicated in the motion-matched sample (**Supplementary Table 7**), where the number of dimorphic locations increased. Typically, ∼400–600

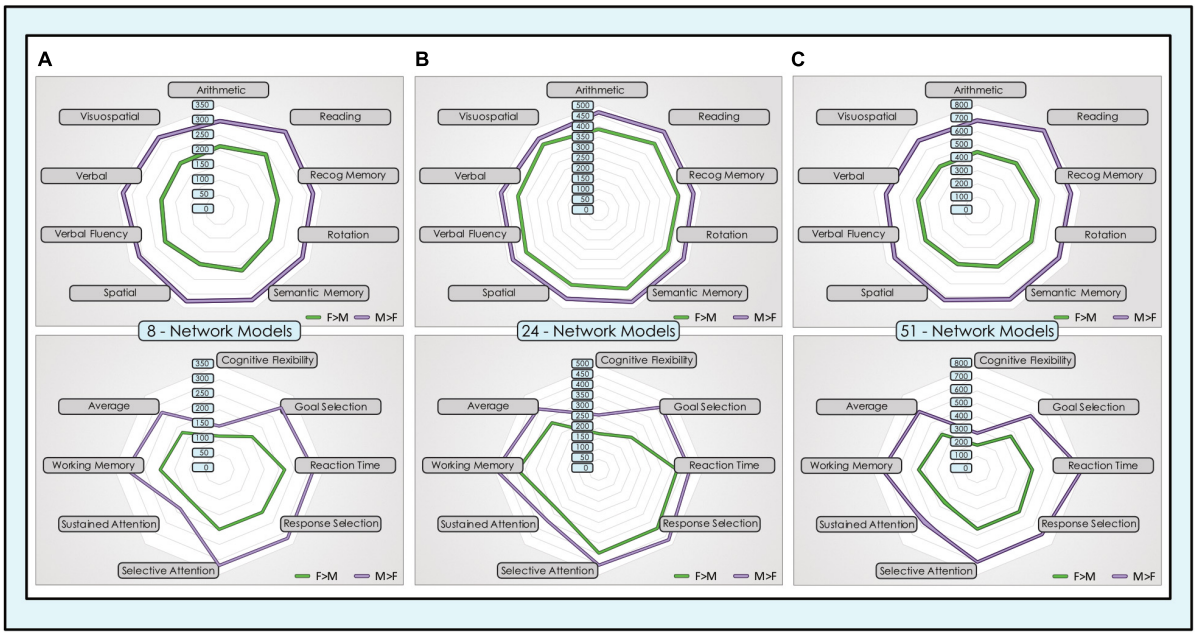

FIGURE 9 | Dimorphic locations in intrinsic networks mapped to neurocognitive functions. Unique locations (voxels) with significant sex-related effects were mapped to 17 neurocognitive association test maps of brain function, derived from meta-analysis of task fMRI experiments. The top group of 9 neurocognitive functions was chosen for their prior evidence of differential performance in males and females in psychological experiments. The lower group of 8 cognitive control functions was chosen for comparison purposes. The absolute number of unique locations with dimorphic effects in all intrinsic networks concatenated across **(A)** 8-network model, **(B)** 24-network model and **(C)** 51-network model is displayed for F > M (green) and M > F (purple) effects.

more locations exhibited significant sex-related effects in each of the motion-matched models than in the original sample.

The Footprint of Sex-Related Effects Across Neurocognitive Functions Was Consistently Larger in Males Than Females

We computed the spatial overlap between unique locations with significant dimorphic effects (concatenated across all networks) and association test maps for individual neurocognitive functions that have been most frequently associated with sex-related differences in task performance and in a set of cognitive control functions. In both sets of functions, the sex-related neurocognitive footprint was consistently and substantially larger in males than females, across all tasks and model orders (**Figure 9**). In the core set of functions most often associated with sex-related differences in neurocognitive performance, males showed 40–70% more locations in the 8-network model, 8–23% more locations in the 24-network model and 50–70% more locations in the 51-network model, averaging 55, 18, and 58% respectively. This spread was largest in the association test map associated with 'rotation' in the 8- and 24-network models, and 'reading' in the 51-network model. In the comparison set of functions less consistently associated in the behavioral literature with sex-related differences in performance, males showed 30–88% more locations in the 8-network model, 15–92% in the 24-network model and 51–90% in the 51-network model, averaging 53, 35, and 62% respectively. Across all models, the largest absolute number of dimorphic locations was consistently in 'reading,' in both sexes, with the exception of the 51-network model in the motion-matched sample where 'reading' was second behind 'recognition memory.'

These findings were replicated in the motion-matched sample, where the number of unique dimorphic locations overlapping neurocognitive association test maps was increased. Typically, ∼200 more overlapping dimorphic locations overlapped neurocognitive maps in the 8- and 24-network models, and ∼400 more in the 51-network model (**Supplementary Table 7**). Of note, in the motion-matched sample there were three exceptions to our otherwise consistent findings, in the 'spatial' and 'sustained attention' maps in the 8-network model and the 'visuospatial' map in the 24-network model. Here, the number of unique M > F locations was slightly smaller than F > M.

Results Summary

- Sexual dimorphism was present in the majority of intrinsic functional networks in a large group of neurotypical young adults, regardless of model order.
- The proportion of intrinsic networks with significant sex-related differences in activity ranged from 60 to 80% of all networks tested over 3 models of whole brain function.
- Significant sex-related effects were present in all sub-networks of the default mode network group in all 3 models. This contrasted with other network groupings (e.g., visual or sensorimotor networks) where sex-related effects were less pervasive

- On average, the effect size of significant sex-related differences in intrinsic network maps was larger in females, but occupied a greater spatial proportion of the network in males. The size of sex-related effects and proportion of network affected did not appear to be related.
- Control networks (default mode and task-positive intrinsic networks) and the cerebellar networks contained the largest numbers of individual brain locations (voxels) with significant sex-related differences in activity
- While our major results were replicated in the motion-matched sample, we observed a greater number of individual brain locations with significant sex-related differences in the smaller motion-matched sample of 535 subjects vs. the sample of 670 subjects matched for age and sex, but not head motion.

DISCUSSION

Multilevel Modeling of Intrinsic Functional Brain Networks Revealed That the Majority Exhibit a Mosaic of Sex-Related Differences in Young Adults

A key finding of our study was that most intrinsic networks exhibit significant sex-related effects, with both F > M and M > F effects usually found within the same IN. This pervasive sexual dimorphism is present regardless of model order, appearing in each of the 8-, 24-, and 51-network models, and before or after motion-matching. This accords with previous work using ICA in rsfMRI in a 28-network model in 603 subjects (80% aged 13–30) by Allen et al. (2011) that were almost balanced for age and sex but not matched for motion. Using a different methodology with a grid-based schema and *a posteriori* assignment of nodes to network identifications in youth (average age 15 years), dimorphism was also detected by another group in a majority of intrinsic networks (Satterthwaite et al., 2015). We provide a significant contribution to previous work by performing functional parcellations with increasing model orders, determining that this phenomenon is present regardless of how refined a functional parcellation is constructed, and validating this in a motion-matched sample. These findings suggest that sex is an important biological variable in analyses of brain function in neurotypical adults, and that most networks do contain a mosaic of sex-related differences, with both M > F and F > M effects present within individual networks. Therefore, our work supports the inclusion of sex as an important biological and analytic variable in studies of intrinsic brain function using rsfMRI.

Control Network Systems Are Most Influenced by Dimorphic Effects

Our analysis enlarges current understanding of the role of sex in functional brain networks by providing a detailed picture of dimorphism in individual network types. While we detected dimorphism in networks of all types, it was most prominent in control network systems, i.e., task-positive control networks associated with neurocognitive functions such as working memory and cognitive control (though not attention *per se*), and in the default mode networks. In the latter, we detected dimorphism across every sub-network, even as the overall default mode system split into increasingly smaller networks in the 51-network model, with some indication that posterior components of the system had larger effect sizes. Control networks – especially the DMN – dominated the spatial extent of sex-related effects, consistently occupying the lion's share (>50%) of dimorphic locations in all models. The cerebellum was also highlighted. Our results suggest that the function of control networks and the cerebellum, especially the default mode system, may be most strongly influenced by sex in comparison to other network types. Our work therefore disagrees with smaller studies that failed to detect sex-related differences in default mode and control network function (Weissman-Fogel et al., 2010) but is congruent with others that have found sex-related differences in these networks (Biswal et al., 2010; Zuo et al., 2010). It is an intriguing finding since default mode intrinsic networks are prominently implicated in a wide variety of human neurological and neuropsychiatric disorders that have sex-related differences in incidence, prevalence and severity and have been associated with differences in cognitive control function (Mohan et al., 2016). Earlier work using task-based fMRI demonstrated that control networks including the default mode system are associated with general-purpose brain state control activities such as task initiation, maintenance and switching (Dosenbach et al., 2006, 2007), though sex-related differences were not examined. More recent studies using task-based fMRI suggest that sex-related differences do exist in task-control and default mode network function that may be specific to the task being performed and mediate clinical presentations (Dumais et al., 2018; McCarthy et al., 2019). We note that our estimates of total dimorphic functional locations across the brain varied from ∼1–2500 in the original sample to ∼2–4000 in the motion-matched sample, representing a range of ∼0.5–2% of total locations (voxels) surveyed from whole brain imaging. This is concordant with previous estimates in younger subjects using a grid-based method by Sattherthwaite et al. (2015), who found significant sex-related differences in ∼2% of nodes and ∼0.5% of edges. Thus, it appears likely that functional differences attributable to sex are present in a relatively small spatial proportion of the brain regardless of the analytic methodology applied. Similarly, a relatively small proportion of each network displays dimorphism, on average ∼0.5–1.5% of the total area of each network. Taken together, our results juxtaposed with prior studies suggest that while sex-related differences affect a relatively small spatial proportion of intrinsic network function, they may nonetheless significantly modulate information processing and behaviors, particularly those influenced by control networks and the cerebellum. Further studies will be required to test this hypothesis.

The Neurocognitive Footprint of Intrinsic Neural Correlates Is Much Larger in Males

A remarkable finding in our work was that the neurocognitive footprint of sex-related effects was consistently larger in

all models and all cognitive functions in males. The sole three exceptions were in the spatial and sustained attention maps in the 8-network model and the visuospatial map in the 24-network model in the motion-matched sample. This phenomenon was present across the range of cognitive functions we surveyed, including tasks previously associated with superior male (e.g., mental rotation) and female (e.g., reading) performance and also in a set of cognitive control functions where there has been much less consistent evidence of sex-related differences in performance. While our analytic strategy does not impute causation, this finding does suggest that cognitive task performance is not simply associated with the spatial extent of dimorphism in intrinsic networks, since the larger footprint of M > F effects was present in cognitive functions where both superior and inferior performance has been observed in males and in a range of cognitive control functions where sex-related performance differences are less robustly found. Rather, it may link to prior work suggesting males and females recruit different brain regions to accomplish similar tasks, which would also be consistent with our finding of a mosaic of M > F and F > M effects within the same networks. For example, Hugdahl et al. (2006) found that men activated the superior parietal lobule during a task of mental rotation, whereas women preferentially employed the inferior frontal. Other tasks with good evidence of sex-related differences associated with specific neural correlates include emotional face processing (Fusar-Poli et al., 2009) and emotional memory (Cahill, 2003). Our work extends these observations by revealing that the spatial extent of sex-sensitive cognitive maps is generally simply greater in males than females and involves more unique individual locations in intrinsic functional networks. In turn, this may link to the increased prevalence of neuropsychiatric disorders that involve cognitive disturbance in males (e.g., autism, schizophrenia, ADHD) vs. those that tend to have fewer cognitive impacts in females (e.g., depression, anxiety). For example, in autism a hypothesis has been advanced that male sex may confer vulnerability, or female sex protective effects, operating at the genetic and/or neural levels. An interesting comparison can be made with our prior work in ADHD, a developmental disorder with a much higher reported incidence in males, where we surveyed a similar set of cognitive control functions and found that the neurocognitive footprint across these functions was much larger in youth with ADHD vs. neurotypical youth (de Lacy et al., 2018). More broadly, our results suggest that sex-related differences in cognitive performance may have intrinsic neural correlates. For example, it is striking that we consistently found the greatest overlap between sex-sensitive locations across intrinsic networks and a neurocognitive map was with the 'reading' map, since reading is the task that has perhaps most robustly been determined to have sex-related performance differentials from early ages. While much work remains to be done regarding the relationship between sex/gender and neural function, and also the observed sex-related differences in both neural structure and function and human behavior (Grabowska, 2017), our results suggest that the link between sex-related differences in neural network function and cognitive task performance is not a simple quantitative relationship.

The Effect Size of Sex, Number of Dimorphic Locations and Footprint Across Neurocognitive Functions Increased in More Refined Functional Parcellations

An important result of our study, which provides the first whole-brain surveys of dimorphism with simultaneous multilevel modeling of brain functional networks, is that sex becomes a more influential variable as increasingly detailed functional parcellations are formulated. Previous work suggests that higher model orders constructed using ICA produce increasingly refined networks and it is also reasonable to suppose that as model order increases, larger networks split into subnetworks with more closely delineated functional associations. For example, work by Andrews-Hanna et al. (2010) demonstrated that the DMN, often considered as a single network in earlier studies, in fact consists of separable sub-networks with somewhat dissociable cognitive functions. More broadly, as research methods become more advanced it is becoming increasingly popular in rsfMRI studies to construct sophisticated models of brain function containing many intrinsic networks. As we constructed more refined parcellations, the average effect size, number of dimorphic locations, and their neurocognitive footprints all increased, highlighting the particular importance of incorporating sex as a variable in more detailed models of brain function, with implications for analytic strategies and modeling. Since there is currently no principled way of determining the number of networks in human brain functional data, model order is a parameterized choice by the investigator. Our analysis suggests that the statistical significance of sex varies according to the model order chosen. While sex is associated with significant differences in the function of most intrinsic networks, its influence appears more profound as model order increases. This may also help explain disparities in prior studies which have given rise to disputes regarding the significance of sex to differences in brain function.

Sex-Related Differences in Head Motion May Also Exist

While in general our effects were replicated in a motion-matched sample, motion may still play an important role and should always be carefully considered in fMRI studies. We found a significant difference in head motion as measured using DVARS between males and females after matching for age and sex in a sample of 670 neurotypical young adults. In the foundational dataset used for the present study, where imaging is available from a larger sample of 1570 young adults (not matched for age or sex), this was also the case ($p = 9.365 \times 10^{-18}$). In both cases higher levels of head motion obtained in males, particularly younger adult subjects. It is also notable that historically, higher levels of head motion have been detected in subjects with conditions such as autism and ADHD, which are more common in males, as well as in younger subjects more generally. Indeed, while efforts are increasingly devoted to identifying sources of disparity in head motion in brain

imaging research, and eliminating and controlling for the effects of motion, the relationship between sex and head motion has not been extensively explored. While further studies will inform the generalizability of our findings, the current study suggests the relationship between sex and motion should be carefully accounted for in functional brain imaging studies.

Limitations

Limitations exist in the present study. Firstly, IQ scores derived from the Shipley-Hartford Age-Corrected T-scores were provided in the original dataset and used in the current analysis, that are estimates of IQ rather than the result of full IQ testing, and as may be seen in **Table 1**, the average estimated IQ of this sample is above the population average. Secondly, we did not attempt to control for potential effects of hemodynamic lag on the BOLD time series. Thirdly, association test maps were utilized that represent the results of meta-analyses. While these provide the benefit of increased power, the search terms we used may be inexact or underspecified. For example, we used the term 'mental rotation' but the Neurosynth database at the time of our analysis did not provide the capability to specify 2- vs. 3-dimensional mental rotation. In our models of brain functional networks, we provide 3 model orders for comparison purposes, but note that the 8-network model is a relatively low model order for ICA, and did not break out certain networks or regions such as subcortical components. Moreover, while recent studies indicate that the cerebellum may be fractionated into multiple sub-networks (Buckner et al., 2011; Riedel et al., 2015) we include only a single cerebellar network in our 24- and 51-network models. Finally, we did not map all possible neurocognitive functions, but rather selected functions based on a review of the existing literature and a set of cognitive control functions selected as a comparator group. Thus, it is possible that we have not included other functions that may display sexual dimorphism.

CONCLUSION

Using a multilevel modeling strategy to survey sex-related differences in intrinsic functional networks in increasing model orders of 8-, 24-, and 51-network models derived from whole-brain imaging, we identified a mosaic of sex-related effects in the majority of networks, affecting in total a small proportion of ∼0.5–2% of all brain locations. Dimorphism proved most prominent in the control networks and cerebellum, being particularly pervasive in the DMN system, with a much larger neurocognitive footprint in males. We conclude that modeling sex as a biological variable and as a covariate in analyses of human brain function using rsfMRI is required, and that high-order models which include a greater number of networks and/or more detailed functional parcellations are likely to be even more sensitive to sex-related differences. Our results extend prior investigations using task fMRI to provide additional support derived from intrinsic brain function measured in the resting state to suggest that males and females may recruit different spatial locations and proportions of brain networks to perform similar neurocognitive tasks. We highlight that our results pertain to brain function in a single, albeit comparatively large, cross-sectional sample of young adults. No conclusions can be drawn as to the causes or dynamic evolution of observed sex-related network differences in this group. The development of neural functional connectivity is a dynamic process with considerable reorganization and resculpting observed during maturation through young adulthood (Power et al., 2010). Many biological, behavioral and environmental factors are known to impact brain function and likely influence differences between groups, including sex-related differences. There is considerable individual variation and sex-related differences may exist on a spectrum. Further studies positioned within this framework will help disambiguate the origins and evolution of observed functional dimorphism in young adult brain networks and the drivers of this important phenomenon (Fine, 2014).

ETHICS STATEMENT

The present study uses secondary data and was deemed not human subjects research by the University of Washington Institutional Review Board.

AUTHOR CONTRIBUTIONS

NdL designed the study, performed the analysis, and wrote the manuscript. VC helped design the study and contributed to writing the manuscript. JK and EM contributed to study design and writing the manuscript.

FUNDING

We gratefully acknowledge the help of B. Ernesto Johnson in preparing figures. This study was supported by the National Center for Advancing Translational Sciences of the National Institutes of Health under Award Number KL2TR000421 to NdL, and NIH 2R01EB005846, P20GM103472, and R01EB020407 and NSF 153906 to VC. The content is solely the responsibility of the authors and does not necessarily represent the official views of the NIH. Data were provided in part by the Brain Genomics Superstruct Project of Harvard University and the Massachusetts General Hospital (Principal Investigators: Randy Buckner, Joshua Roffman, and Jordan Smoller), with support from the Center for Brain Science Neuroinformatics Research Group, the Athinoula A. Martinos Center for Biomedical Imaging, and the Center for Human Genetic Research. Twenty individual investigators at Harvard and MGH generously contributed data to the overall project.

SUPPLEMENTARY MATERIAL

The Supplementary Material for this article can be found online at: https://www.frontiersin.org/articles/10.3389/fnins.2019.00332/full#supplementary-material

REFERENCES

Allen, E. A., Erhardt, E. B., Damaraju, E., Gruner, W., Segall, J. M., Silva, R. F., et al. (2011). A baseline for the multivariate comparison of resting-state networks. *Front. Syst. Neurosci.* 5:2. doi: 10.3389/fnsys.2011.00002

Allen, E. A., Erhardt, E. B., Wei, Y., Eichele, T., and Calhoun, V. D. (2012). Capturing inter-subject variability with group independent component analysis of fMRI data: a simulation study. *Neuroimage* 59, 4141–4159. doi: 10.1016/j.neuroimage.2011.10.010

Andrews-Hanna, J. R., Reidler, J. S., Sepulcre, J., Poulin, R., and Buckner, R. L. (2010). Functional-anatomic fractionation of the brain's default network. *Neuron* 65, 550–562. doi: 10.1016/j.neuron.2010.02.005

Biswal, B. B., Mennes, M., Zuo, X. N., Gohel, S., Kelly, C., Smith, S. M., et al. (2010). Toward discovery science of human brain function. *Proc. Natl. Acad. Sci. U.S.A.* 107, 4734–4739. doi: 10.1073/pnas.0911855107

Buckner, R. L., Krienen, F. M., Castellanos, A., Diaz, J. C., and Yeo, B. T. (2011). The organization of the human cerebellum estimated by intrinsic functional connectivity. *J. Neurophysiol.* 106, 2322–2345. doi: 10.1152/jn.00339.2011

Cahill, L. (2003). Sex-related influences on the neurobiology of emotionally influenced memory. *Ann. N.Y. Acad. Sci.* 985, 163–173. doi: 10.1111/j.1749-6632.2003.tb07080.x

Calhoun, V. D., and Adali, T. (2012). Multisubject independent component analysis of fMRI: a decade of intrinsic networks, default mode, and neurodiagnostic discovery. *IEEE Rev. Biomed. Eng.* 5, 60–73. doi: 10.1109/RBME.2012.2211076

Calhoun, V. D., Adali, T., Pearlson, G. D., and Pekar, J. J. (2001). A method for making group inferences from functional MRI data using independent component analysis. *Hum. Brain Mapp.* 14, 140–151. doi: 10.1002/hbm.1048

Christodoulou, A. G., Bauer, T. E., Kiehl, K. A., Feldstein Ewing, S. W., Bryan, A. D., and Calhoun, V. D. (2013). A quality control method for detecting and suppressing uncorrected residual motion in fMRI studies. *Magn. Reson. Imaging* 31, 707–717. doi: 10.1016/j.mri.2012.11.007

de Lacy, N., Doherty, D., King, B. H., Rachakonda, S., and Calhoun, V. D. (2017). Disruption to control network function correlates with altered dynamic connectivity in the wider autism spectrum. *Neuroimage Clin.* 15, 513–524. doi: 10.1016/j.nicl.2017.05.024

de Lacy, N., Kodish, I., Rachakonda, S., and Calhoun, V. D. (2018). Novel in silico multivariate mapping of intrinsic and anticorrelated connectivity to neurocognitive functional maps supports the maturational hypothesis of ADHD. *Hum Brain Mapp.* 39, 3449–3467. doi: 10.1002/hbm.24187

Dosenbach, N. U., Fair, D. A., Miezin, F. M., Cohen, A. L., Wenger, K. K., Dosenbach, R. A., et al. (2007). Distinct brain networks for adaptive and stable task control in humans. *Proc. Natl. Acad. Sci. U.S.A.* 104, 11073–11078. doi: 10.1073/pnas.0704320104

Dosenbach, N. U., Visscher, K. M., Palmer, E. D., Miezin, F. M., Wenger, K. K., Kang, H. C., et al. (2006). A core system for the implementation of task sets. *Neuron* 50, 799–812. doi: 10.1016/j.neuron.2006.04.031

Du, Y., Allen, E. A., He, H., Sui, J., Wu, L., and Calhoun, V. D. (2016). Artifact removal in the context of group ICA: A comparison of single-subject and group approaches. *Hum. Brain Mapp.* 37, 1005–1025. doi: 10.1002/hbm.23086

Dumais, K. M., Chernyak, S., Nickerson, L. D., and Janes, A. C. (2018). Sex differences in default mode and dorsal attention network engagement. *PLoS One* 13:e0199049. doi: 10.1371/journal.pone.0199049

Erhardt, E. B., Rachakonda, S., Bedrick, E. J., Allen, E. A., Adali, T., and Calhoun, V. D. (2011). Comparison of multi-subject ICA methods for analysis of fMRI data. *Hum. Brain Mapp.* 32, 2075–2095. doi: 10.1002/hbm.21170

Fine, C. (2014). Neuroscience. His brain, her brain? *Science* 346, 915–916. doi: 10.1126/science.1262061

Fox, M. D., Snyder, A. Z., Vincent, J. L., Corbetta, M., Van Essen, D. C., and Raichle, M. E. (2005). The human brain is intrinsically organized into dynamic, anticorrelated functional networks. *Proc. Natl. Acad. Sci. U.S.A.* 102, 9673–9678. doi: 10.1073/pnas.0504136102

Fusar-Poli, P., Placentino, A., Carletti, F., Landi, P., Allen, P., Surguladze, S., et al. (2009). Functional atlas of emotional faces processing: a voxel-based meta-analysis of 105 functional magnetic resonance imaging studies. *J. Psychiatry Neurosci.* 34, 418–432.

Gong, G., He, Y., and Evans, A. C. (2011). Brain connectivity: gender makes a difference. *Neuroscientist* 17, 575–591. doi: 10.1177/1073858410386492

Grabowska, A. (2017). Sex on the brain: are gender-dependent structural and functional differences associated with behavior? *J. Neurosci. Res.* 95, 200–212. doi: 10.1002/jnr.23953

Guadalupe, T., Mathias, S. R., vanErp, T. G. M., Whelan, C. D., Zwiers, M. P., Abe, Y., et al. (2017). Human subcortical brain asymmetries in 15,847 people worldwide reveal effects of age and sex. *Brain Imaging Behav.* 11, 1497–1514. doi: 10.1007/s11682-016-9629-z

Gur, R. C., Alsop, D., Glahn, D., Petty, R., Swanson, C. L., Maldjian, J. A., et al. (2000). An fMRI study of sex differences in regional activation to a verbal and a spatial task. *Brain Lang.* 74, 157–170. doi: 10.1006/brln.2000.2325

Gur, R. C., Turetsky, B. I., Matsui, M., Yan, M., Bilker, W., Hughett, P., et al. (1999). Sex differences in brain gray and white matter in healthy young adults: correlations with cognitive performance. *J. Neurosci.* 19, 4065–4072. doi: 10.1523/JNEUROSCI.19-10-04065.1999

Himberg, J., Hyvarinen, A., and Esposito, F. (2004). Validating the independent components of neuroimaging time series via clustering and visualization. *Neuroimage* 22, 1214–1222. doi: 10.1016/j.neuroimage.2004.03.027

Holmes, A. J., Hollinshead, M. O., O'Keefe, T. M., Petrov, V. I., Fariello, G. R., Wald, L. L., et al. (2015). Brain genomics superstruct project initial data release with structural, functional, and behavioral measures. *Sci. Data* 2:150031. doi: 10.1038/sdata.2015.31

Hugdahl, K., Thomsen, T., and Ersland, L. (2006). Sex differences in visuo-spatial processing: an fMRI study of mental rotation. *Neuropsychologia* 44, 1575–1583. doi: 10.1016/j.neuropsychologia.2006.01.026

Im, K., Lee, J. M., Lee, J., Shin, Y. W., Kim, I. Y., Kwon, J. S., et al. (2006). Gender difference analysis of cortical thickness in healthy young adults with surface-based methods. *Neuroimage* 31, 31–38. doi: 10.1016/j.neuroimage.2005.11.042

Jamadar, S. D., Sforazzini, F., Raniga, P., Ferris, N. J., Paton, B., Bailey, M. J., et al. (2018). Sexual dimorphism of resting-state network connectivity in healthy ageing. *J. Gerontol. B Psychol. Sci. Soc. Sci.* doi: 10.1093/geronb/gby004 [Epub ahead of print].

Laird, A. R., Fox, P. M., Eickhoff, S. B., Turner, J. A., Ray, K. L., McKay, D. R., et al. (2011). Behavioral interpretations of intrinsic connectivity networks. *J. Cogn. Neurosci.* 23, 4022–4037. doi: 10.1162/jocn-a-00077

Li, R., and Singh, M. (2014). Sex differences in cognitive impairment and Alzheimer's disease. *Front. Neuroendocrinol.* 35, 385–403. doi: 10.1016/j.yfrne.2014.01.002

Li, Y. O., Adali, T., and Calhoun, V. D. (2007). Estimating the number of independent components for functional magnetic resonance imaging data. *Hum. Brain Mapp.* 28, 1251–1266. doi: 10.1002/hbm.20359

McCarthy, J. M., Dumais, K. M., Zegel, M., Pizzagalli, D. A., Olson, D. P., Moran, L. V., et al. (2019). Sex differences in tobacco smokers: Executive control network and frontostriatal connectivity. *Drug Alcohol Depend* 195, 59–65. doi: 10.1016/j.drugalcdep.2018.11.023

Miller, D. I., and Halpern, D. F. (2014). The new science of cognitive sex differences. *Trends Cogn. Sci.* 18, 37–45. doi: 10.1016/j.tics.2013.10.011

Mohan, A., Roberto, A. J., Mohan, A., Lorenzo, A., Jones, K., Carney, M. J., et al. (2016). The significance of the default mode network (DMN) in neurological and neuropsychiatric disorders: a review. *Yale J. Biol. Med.* 89, 49–57.

Mutlu, A. K., Schneider, M., Debbane, M., Badoud, D., Eliez, S., and Schaer, M. (2013). Sex differences in thickness, and folding developments throughout the cortex. *Neuroimage* 82, 200–207. doi: 10.1016/j.neuroimage.2013.05.076

Podcasy, J. L., and Epperson, C. N. (2016). Considering sex and gender in Alzheimer disease and other dementias. *Dial. Clin. Neurosci.* 18, 437–446.

Power, J. D., Fair, D. A., Schlaggar, B. L., and Petersen, S. E. (2010). The development of human functional brain networks. *Neuron* 67, 735–748. doi: 10.1016/j.neuron.2010.08.017

Power, J. D., Mitra, A., Laumann, T. O., Snyder, A. Z., Schlaggar, B. L., and Petersen, S. E. (2014). Methods to detect, characterize, and remove motion artifact in resting state fMRI. *Neuroimage* 84, 320–341. doi: 10.1016/j.neuroimage.2013.08.048

Rashid, B., Damaraju, E., Pearlson, G. D., and Calhoun, V. D. (2014). Dynamic connectivity states estimated from resting fMRI Identify differences among Schizophrenia, bipolar disorder, and healthy control subjects. *Front. Hum. Neurosci.* 8:897. doi: 10.3389/fnhum.2014.00897

Riedel, M. C., Ray, K. L., Dick, A. S., Sutherland, M. T., Hernandez, Z., Fox, P. M., et al. (2015). Meta-analytic connectivity and behavioral parcellation of

the human cerebellum. *Neuroimage* 117, 327–342. doi: 10.1016/j.neuroimage.2015.05.008

Ritchie, S. J., Cox, S. R., Shen, X., Lombardo, M. V., Reus, L. M., Alloza, C., et al. (2018). Sex differences in the adult human brain: evidence from 5216 UK biobank participants. *Cereb. Cortex* 28, 2959–2975. doi: 10.1093/cercor/bhy109

Sacher, J., Neumann, J., Okon-Singer, H., Gotowiec, S., and Villringer, A. (2013). Sexual dimorphism in the human brain: evidence from neuroimaging. *Magn. Reson. Imaging* 31, 366–375. doi: 10.1016/j.mri.2012.06.007

Satterthwaite, T. D., Wolf, D. H., Roalf, D. R., Ruparel, K., Erus, G., Vandekar, S., et al. (2015). Linked sex differences in cognition and functional connectivity in youth. *Cereb. Cortex* 25, 2383–2394. doi: 10.1093/cercor/bhu036

Seeley, W. W., Menon, V., Schatzberg, A. F., Keller, J., Glover, G. H., Kenna, H., et al. (2007). Dissociable intrinsic connectivity networks for salience processing and executive control. *J. Neurosci.* 27, 2349–2356. doi: 10.1523/JNEUROSCI.5587-06.2007

Smith, S. M., Fox, P. T., Miller, K. L., Glahn, D. C., Fox, P. M., Mackay, C. E., et al. (2009). Correspondence of the brain's functional architecture during activation and rest. *Proc. Natl. Acad. Sci. U.S.A.* 106, 13040–13045. doi: 10.1073/pnas.0905267106

Spreng, R. N., Sepulcre, J., Turner, G. R., Stevens, W. D., and Schacter, D. L. (2013). Intrinsic architecture underlying the relations among the default, dorsal attention, and frontoparietal control networks of the human brain. *J. Cogn. Neurosci.* 25, 74–86. doi: 10.1162/jocn-a-00281

Stoet, G., and Geary, D. C. (2013). Sex differences in mathematics and reading achievement are inversely related: within- and across-nation assessment of 10 years of PISA data. *PLoS One* 8:e57988. doi: 10.1371/journal.pone.0057988

Van Dijk, K. R., Hedden, T., Venkataraman, A., Evans, K. C., Lazar, S. W., and Buckner, R. L. (2010). Intrinsic functional connectivity as a tool for human connectomics: theory, properties, and optimization. *J. Neurophysiol.* 103, 297–321. doi: 10.1152/jn.00783.2009

Vernet, M., Quentin, R., Chanes, L., Mitsumasu, A., and Valero-Cabre, A. (2014). Frontal eye field, where art thou? Anatomy, function, and non-invasive manipulation of frontal regions involved in eye movements and associated cognitive operations. *Front. Integr. Neurosci.* 8:66. doi: 10.3389/fnint.2014.00066

Voyer, D., Voyer, S., and Bryden, M. P. (1995). Magnitude of sex differences in spatial abilities: a meta-analysis and consideration of critical variables. *Psychol. Bull.* 117, 250–270. doi: 10.1037/0033-2909.117.2.250

Weissman-Fogel, I., Moayedi, M., Taylor, K. S., Pope, G., and Davis, K. D. (2010). Cognitive and default-mode resting state networks: do male and female brains "rest" differently? *Hum. Brain Mapp.* 31, 1713–1726. doi: 10.1002/hbm.20968

Yang, J., and Lee, J. (2018). Different aberrant mentalizing networks in males and females with autism spectrum disorders: evidence from resting-state functional magnetic resonance imaging. *Autism* 22, 134–148. doi: 10.1177/1362361316667056

Yarkoni, T., Poldrack, R. A., Nichols, T. E., Van Essen, D. C., and Wager, T. D. (2011). Large-scale automated synthesis of human functional neuroimaging data. *Nat. Methods* 8, 665–670. doi: 10.1038/nmeth.1635

Zuo, X. N., Kelly, C., Di Martino, A., Mennes, M., Margulies, D. S., Bangaru, S., et al. (2010). Growing together and growing apart: regional and sex differences in the lifespan developmental trajectories of functional homotopy. *J. Neurosci.* 30, 15034–15043. doi: 10.1523/JNEUROSCI.2612-10.2010

Conflict of Interest Statement: The authors declare that the research was conducted in the absence of any commercial or financial relationships that could be construed as a potential conflict of interest.

Copyright © 2019 de Lacy, McCauley, Kutz and Calhoun. This is an open-access article distributed under the terms of the Creative Commons Attribution License (CC BY). The use, distribution or reproduction in other forums is permitted, provided the original author(s) and the copyright owner(s) are credited and that the original publication in this journal is cited, in accordance with accepted academic practice. No use, distribution or reproduction is permitted which does not comply with these terms.

frontiers in Neuroscience

ORIGINAL RESEARCH
published: 30 April 2019
doi: 10.3389/fnins.2019.00400

Effects of Hemodynamic Response Function Selection on Rat fMRI Statistical Analyses

Shin-Lei Peng[1†], Chun-Ming Chen[2†], Chen-You Huang[1], Cheng-Ting Shih[3], Chiun-Wei Huang[4], Shao-Chieh Chiu[4] and Wu-Chung Shen[1,2]*

[1] Department of Biomedical Imaging and Radiological Science, China Medical University, Taichung, Taiwan, [2] Department of Radiology, China Medical University Hospital, Taichung, Taiwan, [3] Department of Medical Imaging and Radiological Sciences, Chung Shan Medical University, Taichung, Taiwan, [4] Center for Advanced Molecular Imaging and Translation, Chang Gung Memorial Hospital, Taoyuan City, Taiwan

The selection of the appropriate hemodynamic response function (HRF) for signal modeling in functional magnetic resonance imaging (fMRI) is important. Although the use of the boxcar-shaped hemodynamic response function (BHRF) and canonical hemodynamic response (CHRF) has gained increasing popularity in rodent fMRI studies, whether the selected HRF affects the results of rodent fMRI has not been fully elucidated. Here we investigated the signal change and *t*-statistic sensitivities of BHRF, CHRF, and impulse response function (IRF). The effect of HRF selection on different tasks was analyzed by using data collected from two groups of rats receiving either 3 mA whisker pad or 3 mA forepaw electrical stimulations (n = 10 for each group). Under whisker pad stimulation with large blood-oxygen-level dependent (BOLD) signal change (4.31 ± 0.42%), BHRF significantly underestimated signal changes ($P < 0.001$) and *t*-statistics ($P < 0.001$) compared with CHRF or IRF. CHRF and IRF did not provide significantly different *t*-statistics ($P > 0.05$). Under forepaw stimulation with small BOLD signal change (1.71 ± 0.34%), different HRFs provided insignificantly different *t*-statistics ($P > 0.05$). Therefore, the selected HRF can influence data analysis in rodent fMRI experiments with large BOLD responses but not in those with small BOLD responses.

Keywords: blood-oxygen-level dependent (BOLD), electric stimulation, barrel, forepaw, boxcar function

OPEN ACCESS

Edited by:
Amir Shmuel,
McGill University, Canada

Reviewed by:
Zhi Yang,
Shanghai Mental Health Center (SMHC), China
Wen-Ju Pan,
Emory University, United States

****Correspondence:***
Shin-Lei Peng
speng@mail.cmu.edu.tw

† These authors have contributed equally to this work

Specialty section:
This article was submitted to Brain Imaging Methods, a section of the journal Frontiers in Neuroscience

Received: *11 July 2018*
Accepted: *08 April 2019*
Published: *30 April 2019*

Citation:
Peng S-L, Chen C-M, Huang C-Y, Shih C-T, Huang C-W, Chiu S-C and Shen W-C (2019) Effects of Hemodynamic Response Function Selection on Rat fMRI Statistical Analyses. Front. Neurosci. 13:400. doi: 10.3389/fnins.2019.00400

INTRODUCTION

Functional magnetic resonance imaging (fMRI) was originally introduced in 1990. Since then, it has been modified to enable investigations on different functional aspects of the brain. The most popular fMRI technique is blood-oxygen-level dependent (BOLD) contrast, which relies on local deoxyhemoglobin changes (Ogawa et al., 1990, 1992). Owing to its advantages of absent radiation burden and non-invasiveness, BOLD fMRI has become a pivotal method for understanding brain function and physiological conditions (Tsurugizawa et al., 2010; Rana et al., 2013; Wu et al., 2014; Nasrallah et al., 2015; Golestani et al., 2016). The applications of BOLD fMRI in animals such as rats, have recently received increased attention. The majority of rodent fMRI studies have been conducted by using electric stimulation to induce somatosensory stimulation and to estimate activations in the primary sensory cortex (Silva et al., 1999; Keilholz et al., 2004; Tenney et al., 2004; Weber et al., 2006; Masamoto et al., 2007; Pelled et al., 2007; Shih et al., 2009, 2011, 2013;

Ramos-Cabrer et al., 2010; Just et al., 2013; Sanganahalli et al., 2013; Nasrallah et al., 2015). Previous works have emphasized the importance of rodent fMRI studies in elucidating crucial topics in neuroscience research. These topics include functional recovery (Pelled et al., 2007; Ramos-Cabrer et al., 2010), pain processing (Shih et al., 2009, 2011), and neurodegenerative diseases (Tenney et al., 2004; Sanganahalli et al., 2013).

The construction of the hemodynamic response function (HRF) of the signal response to an external stimulus is the essential step in the statistical analysis of fMRI data for identifying activation regions. The typical HRF used in rat fMRI studies is the boxcar-shape HRF (BHRF) (Keilholz et al., 2004; Pelled et al., 2007; Shih et al., 2009, 2011; Yang et al., 2013; Nasrallah et al., 2015), which is based on the standard on/off format of the external stimulation. Meanwhile, the use of the so-called canonical HRF (CHRF), a sophisticated HRF based the convolution of a BHRF with the sum of two gamma functions, has also been suggested by other groups (Kim et al., 2007; Yu et al., 2012). The advantage of BHRF is that BHRF can be used for the rapid assessment of brain activation to further refine the CHRF. Although HRF selection in human fMRI studies have been widely discussed (Aguirre et al., 1998; Handwerker et al., 2004; Shan et al., 2014), the body of research that compares the HRF selection in rodent fMRI studies remains insufficient (Chavarrias et al., 2016).

Therefore, the central objective of this study is to systematically investigate whether fMRI activation detection can be affected by the selected HRF. To achieve this objective, three HRFs (Lu et al., 2005; Lindquist et al., 2009; Nasrallah et al., 2015) were employed to model the BOLD signal. The extent of brain activation by electric stimulation is task-dependent, with whisker pad stimulation projecting larger somatosensory regions than forepaw stimulation (Yu et al., 2010). Thus, to map different sensory processing in the brain cortex, we subjected two groups of rats to whisker pad and forepaw electric stimulations. The estimated BOLD signal changes and *t*-statistics among three HRFs were compared. Such a comparison may provide recommendations for future rat fMRI studies.

MATERIALS AND METHODS

Functional Magnetic Resonance Imaging Experiments

A total of 20 male Sprague-Dawley rats (280–345 g) were used in this study. Laboratory animals were housed in plastic cages with soft bedding and were maintained on a 12-h light/dark cycle. Food and water were available *ad libitum*, and the room was temperature controlled. This study was carried out in accordance with the recommendations of National Institutes of Health guide for the care and use of Laboratory animals. The protocol was approved by the China Medical University.

All MRI experiments were conducted on a 7T animal MRI scanner (Bruker ClinScan 70/30, Germany) with a gradient strength of 630 mT/m. A volume coil and a surface coil were used for signal excitation and reception, respectively. All rats were initially anesthetized with 4% isoflurane (ISO), and then was reduced to 1–1.2% ISO during fMRI (Liu et al., 2004). Each rat was secured in a head holder with ear bars and a bite bar to prohibit head motion. The rats were placed on a heated water pad to maintain body temperature at ∼37°C while in the magnet.

Rats were subsequently divided into two groups. In the first group (n = 10), needle electrodes were inserted under the skin of the left whisker pad for mapping the primary somatosensory cortex barrel field (S1BF). In the second group (n = 10), needle electrodes were inserted under the skin of the left forepaw for mapping the primary somatosensory cortex forelimb region (S1FL). Electric stimulation was performed by a stimulator (Isolated Pulse Stimulator Model 2100, Washington, DC, United States) supplying 3 mA, 330 μs pulses repeated at 3 Hz to either the left whisker pad or the forepaw upon demand. The stimulation paradigm of the fMRI experiment consisted of a block design. The stimulation paradigm including an initial 75 s period of resting followed by five cycles alternating 15 s of electric stimulation with 75 s of resting was implemented, with a total duration of 525 s. BOLD MR images were simultaneously acquired during this period. The BOLD imaging parameters were field of view (FOV) = 30 mm × 30 mm, matrix size = 64 × 64, 7 coronal slices, thickness = 1 mm, no gap, repetition time (TR)/echo time (TE) = 1000 ms/25 ms, and single-shot gradient echo echo-planar imaging. Anatomical images were obtained by turbo-spin-echo with scanning parameters of TR = 2560 ms, TE = 38 ms, echo train length = 7, number of excitation = 1, FOV = 30 mm × 30 mm, matrix size = 320 × 320, and slice thickness = 1 mm.

Data Analysis

The data analysis for each animal was performed using first-level analyses in SPM8. The voxel-by-voxel statistical analysis of fMRI data was based on the general linear model (GLM) analysis. The dependent variable was the BOLD signal, and the first regressor was the HRF. Three different types of HRFs were employed in this study to test the influence of HRF selection on fMRI sensitivity. We first employed a block design stimulus function that consisted of alternating blocks of resting and active conditions. This block was designated as the BHRF. The second HRF was designed by convolving a BHRF with the sum of two gamma functions (from SPM8) and was designated as the CHRF (Friston, 2003; Lindquist et al., 2009). The third one was the impulse response function (IRF) that was fitted to a gamma-variate function [$\mathrm{IRF(t)} = \mathrm{kt}^b\mathrm{e}^{-\mathrm{t}/\mathrm{c}}$] appropriate for cerebral blood volume (CBV) weighted fMRI signal under rat whisker stimulation, with k = 0.9, b = 0.64, and c = 4.42 (Lu et al., 2005). The second regressor was the intercept, a vector of ones. A high-pass filter of 1/128 Hz was used to detrend fMRI data (Tanabe et al., 2002).

Three different t-maps and magnitude estimate β maps were generated from the corresponding HRF. For different GLM models, the fractional signal change of each voxel was calculated using the same equation as follows:

$$\frac{\Delta S}{S_{base}} = \frac{S_{act} - S_{base}}{S_{base}} \times 100 = \frac{\beta_1}{\beta_2} \times 100 \quad (1)$$

where S_{base} and S_{act} are the signals at baseline and activation, respectively. β_1 and β_2 are the estimated parameters for the two

regressors from the GLM (Miao et al., 2014). The resulting *t*-value map and signal-change map were used for the following analysis. Voxels with *t*-values higher than the threshold of 4.8 (corresponding to $P = 10^{-6}$) and only groups of at least four activated pixels (Keilholz et al., 2006; Weber et al., 2006) were regarded as significantly activated.

Voxels with *t*-values greater than 4.8 from three HRF analyses were considered as activated voxels and used for regions of interest analysis. Averaged *t*-values and signal changes within S1BF and S1FL were calculated by averaging the *t*-values and signal changes of its constituent activated voxels as defined above, respectively. Differences in *t*-values and estimated BOLD signal changes in the primary somatosensory cortex (S1) among the three HRFs were tested through one-way analysis of variance (ANOVA) tests with repeated measures. If the effect was observed in the ANOVA test results, *post hoc* Tukey's honest significant difference test was employed. Task-based BOLD data were analyzed using in-house Matlab (The MathWorks, Natick, MA, United States) scripts. Data were expressed as mean ± standard error.

RESULTS

Robust fMRI activations in the contralateral side of the brain were detected in all rats under whisker pad or forepaw stimulation. fMRI signal time curves from the S1 of two representative rats under whisker pad stimulation or forepaw stimulation are shown in **Figures 1A,B**, respectively. The fMRI signals gradually increased and then gradually decreased to the baseline.

Figure 2 shows the group-level activation maps of 10 rats under electric stimulation. The maps shown in this figure were obtained through GLM with CHRF. Consistent with previous reports, robust activations were detected in the S1BF, secondary somatosensory cortex (S2), and primary somatosensory cortex upper lip region (S1ULp) of rats under whisker pad stimulation (Yu et al., 2010). Significant activations in the S1BF associated with forepaw stimulation were found. In line with previous studies (Silva et al., 1999; Shih et al., 2013, 2014), activation in the S2 was not easily detectable in animals under forepaw stimulation. Notably, the volume of the active region in rats under forepaw stimulation was smaller than that in rats under whisker pad stimulation as indicated by the decreased cortical somatosensory representation in the rat brain. The presented activations under whisker pad and forepaw stimulation were similar when employing GLM with the BHRF or IRF was employed.

Blood-oxygen-level dependent signal changes and *t*-values quantified through GLM analysis are plotted in **Figures 3A,B**, respectively. The estimated BOLD percentage changes in the S1BF were 4.02 ± 0.38, 4.31 ± 0.42, and 3.22 ± 0.34% when the GLM used CHRF, IRF, and BHRF, respectively. One-way ANOVA with repeated measures showed that HRF had a significant effect on BOLD signal change estimation ($P < 0.001$), where the estimated BOLD signal change in S1BF for GLM with BHRF was significantly lower than those with CHRF ($P < 0.01$) and IRF ($P < 0.01$).

The selection of HRFs also had significant effects on the estimated BOLD signal changes in response to forepaw stimulation ($P < 0.01$). The estimated BOLD signal change in the S1FL for GLM with IRF (1.71 ± 0.34%) was significantly higher than that with BHRF (1.44 ± 0.31%, $P < 0.05$). The comparisons between CHRF and IRF and between CHRF and BHRF were not significantly different (both $P > 0.05$).

The analysis of the influence of HRF selections yielded a similar pattern for the quantification of *t*-values. For whisker pad stimulation, the statistical power of the *t*-values derived from GLM with CHRF or IRF significantly improved relative to those of the *t*-values derived from BHRF (**Figure 3B**, $P < 0.001$), suggesting that the use of CHRF or IRF improved the statistical significance of voxels. The comparison between CHRF and IRF showed insignificant differences ($P > 0.05$). No significant differences in the quantified *t*-values were detected for the data obtained under forepaw stimulation ($P = 0.13$) when the GLM used any HRF.

The voxel-wise comparisons of *t*-values between GLM with CHRF and BHRF are displayed in **Figure 4**. Compared with BHRF, GLM with CHRF significantly improved the activation maps mainly in S1BF under whisker pad stimulation. This result indicated that the CHRF is more appropriate for stimulations with large BOLD signal change. By contrast, BHRF did not increase sensitivity relative to CHRF. No difference was detected under forepaw stimulation in either direction. The comparisons between GLM with IRF and BHRF showed similar patterns.

DISCUSSION

In this study, we found that the choice of the HRF is crucial in the computation of activations in rat fMRI studies, especially in studies involving stimulations with large BOLD signal changes, such as whisker pad stimulation. We tested three types of HRFs: CHRF, IRF, and BHRF. BHRF is simple and popular among rat fMRI studies (Keilholz et al., 2004; Pelled et al., 2007; Nasrallah et al., 2015). However, its statistical estimations tend to vary with the type of responses. Experimental fMRI data have been used to demonstrate that BHRF affects the results of statistical analyses by underestimating BOLD magnitude changes and *t*-values.

Our results demonstrate that BHRF significantly underestimates signal changes and *t*-statistics. Given that the ground truth is unknown, CHRF or IRF may also be overestimating signal changes and *t*-statistics. In addition, the effect of HRF selection may be dependent on the brain area. To address this issue, we simulated the fMRI signal time curves (Shan et al., 2014) with ground truth HRFs (**Supplementary Figure 1**) to test the performance of the different HRF models. Numerical simulations showed that for the fMRI signal time curve simulated from the BHRF with BOLD signal changes of more than 1.7%, GLM with CHRF produced *t*-values that were significantly lower than those produced by GLM with BHRF (**Supplementary Figure 2A**, $P < 0.05$). The same scenario occurred when the fMRI signal time curve was simulated with CHRF but using BHRF in the GLM (**Supplementary Figure 2B**, $P < 0.05$). The potential

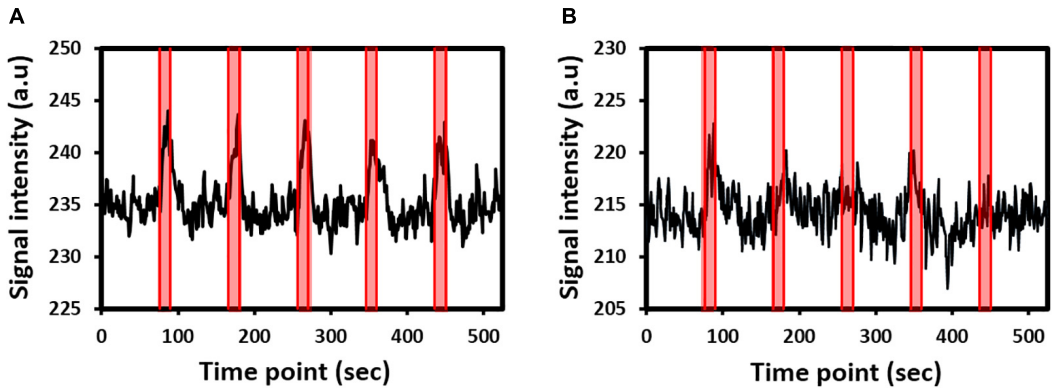

FIGURE 1 | Functional magnetic resonance imaging (fMRI) signal time curves from the primary somatosensory cortex of two representative rats under **(A)** whisker pad stimulation or **(B)** forepaw stimulation. The shaded regions indicate the 15-s stimulation period.

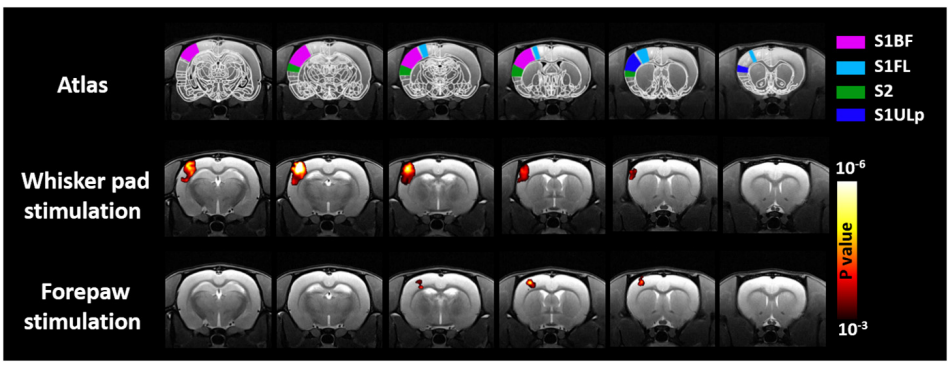

FIGURE 2 | Group-level result of brain regions activated by mysticial pad electrical stimulation and forepaw electrical stimulation. Analyses were performed using a one-sample Student's *t*-test with a cluster size of four voxels.

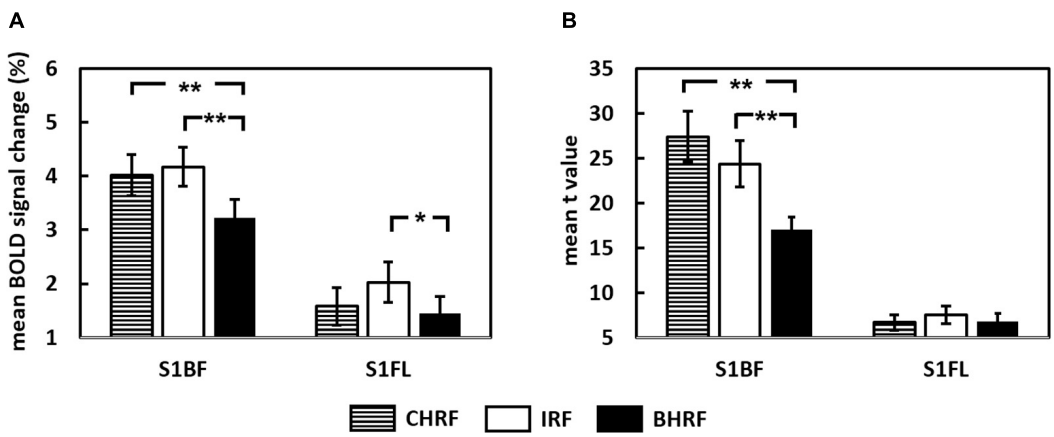

FIGURE 3 | Comparisons of **(A)** estimated BOLD signal changes and **(B)** *t*-statistics between two hemodynamic response functions (HRFs) (**$P < 0.01$, *$P < 0.05$).

explanation to this phenomenon is that when the BOLD signal change is small and the signal-to-noise ratio is low, everything is buried with noise and no difference could be detected among the HRFs, thereby reducing the relative advantage of CHRF. When the BOLD signal change is larger and accompanied with a clear peak instead of a plateau, CHRF is preferred over BHRF due to its existing peak. These simulation results may provide further evidence for the possible underestimation of rodent fMRI results by BHRF, particularly when the BOLD signal change is large and has a clear peak.

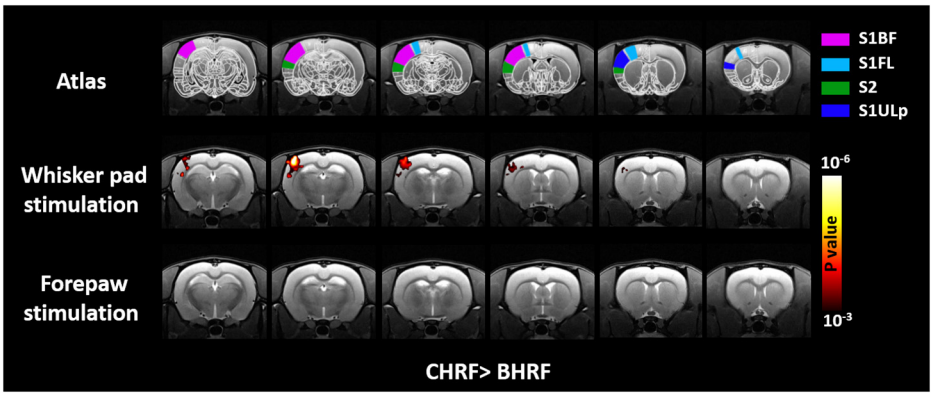

FIGURE 4 | Brain regions showing significant differences in *t*-value quantifications between two HRFs. Relative to that with BHR, GLM with CHRF significantly improved the *t*-statistics for S1BF under whisker pad stimulation. No difference was detected in the opposite direction or under forepaw stimulation in either direction. Analyses were performed using paired Student's *t*-test with a cluster size of four voxels.

Moreover, the effect of HRF selection may be independent of the brain area.

Early work done by Chavarrias et al. (2016) showed that a simple approach using a boxcar response provides better model fitting results than complex approaches. This conclusion is not congruent with our present findings. We found that CHRF and IRF improve the statistical power, especially for stimulations with large BOLD signal changes. This deviation may be attributed to the low temporal resolution of 3 s employed in the aforementioned study compared with the 1 s that we used in functional volume acquisition. When temporal resolution is low, the intrinsic hemodynamic response could be blurred and could also cloud the true response, yielding biased estimations (Kim et al., 1997). Additional comprehensive experiments with different temporal resolution settings may help to further parse out this issue.

Our present results provide some interesting insights into the HRF selection in rat fMRI studies. Our data suggest that when the BOLD signal change is large, such as that under whisker pad stimulation, CHRF and IRF are appropriate candidates for modeling the BOLD response, even though IRF is derived from CBV-fMRI, which may provide a response different from that provided by BOLD. The CHRF is derived from the sum of two gamma functions, whereas the IRF is derived from a single gamma function. The results of these HRFs are similar and comparable. This finding is in agreement with that of a previous human study showing that two gamma functions are neither better nor worse than a single gamma function (Handwerker et al., 2004). In CHRF, the second gamma function is included to model the post-stimulus undershoot. We carefully inspected our data and found that the post-stimulus undershoot is not observed in the data for every rat. Thus, inter-subject variation may restrict the statistical power of the approach and may imply that as long as a peak exists instead of a plateau in HRF, the BOLD response can be correctly modeled. It should also be noted that the parameters of the two gamma functions used in this study were empirically derived from SPM. The application of the default setting from SPM to rodent studies may not be appropriate since the parameters in SPM were originally designed for human studies. However, determining the hemodynamic parameters for animal fMRI studies is non-trivial (Silva et al., 2007) and may not be generally performed across studies. In addition, other factors such as the anesthesia regime and the different targeted brain regions may contribute to the variations in hemodynamic parameters. Therefore, the use of the default setting of the two gamma functions from SPM is simple and convenient, thus gaining increasing popularity in rodent fMRI studies (Just et al., 2013; Niranjan et al., 2016). Although the parameters from CHRF were not optimized in this study, the advantage of CHRF over BHRF in improving the statistical power was demonstrated in this work. Additional research similar to the current one but with different hemodynamic parameters can be an important area for future work.

In the field of rodent fMRI studies, Student's *t*-test (Tenney et al., 2004; Weber et al., 2006; Masamoto et al., 2007; Sanganahalli et al., 2013; Poplawsky and Kim, 2014) and cross-correlation (CC) analysis (Keilholz et al., 2004; Pelled et al., 2007; Shih et al., 2009, 2011; Yang et al., 2013; Nasrallah et al., 2015) are popular statistical strategies for localizing brain regions activated by a task. The principle of Student's *t*-test is to compare the data between "baseline (off)" and "stimulus (on)" phases, thus providing high *t*-scores for large differences with small standard deviations, and low *t*-scores for small differences with large standard deviations. Notably, the comparison between "on" and "off" corresponds to BHRF and may imply that similar to BHRF, the Student's *t*-test may underestimate the *t*-value when the BOLD response is large. CC analysis takes a HRF of expected neural responses and correlates it with the MRI signal variations of each voxel. Correlation coefficients are calculated and converted to *t*-values (Hinkle et al., 2003) to generate the activation map. In this regard, the CHRF or IRF can be considered as complementary HRF when employing CC analysis to assess functional activities.

The results in the present work should be interpreted in the context of several limitations. First, in the present study, each rat was subjected to either whisker pad or forepaw

electrical stimulation. Therefore, we were unable to make within-rat comparisons. The HRF effect on whisker pad or forepaw stimulations may be affected by physiological differences across rats. The duration of ISO anesthesia is known to influence the functional connectivity in rats (Magnuson et al., 2014). Nevertheless, the time-dependent effects of ISO on electric stimulation fMRI studies remain unclear. As a result, we used separate groups to maintain the same duration of anesthesia in our experiments. The different periods of anesthetization should not be a major concern in the experimental design. Second, electrical stimulation parameters are often dependent on the type of anesthetic (Huttunen et al., 2008; Liu et al., 2013) and sensory system used (Melzer et al., 2006; Just et al., 2010). In this study, the stimulation parameters were 3 Hz and 330 μs electrical pulses. These parameters were first identified to induce robust BOLD response to rat forepaw somatosensory stimulus under alpha-chloralose (Brinker et al., 1999; Silva et al., 2007). Thus, optimal stimulus parameters must be employed to clarify the effects of HRF selection on the analysis of fMRI data obtained through whisker pad stimulation under ISO anesthesia.

CONCLUSION

We demonstrated that rat fMRI results could be influenced by HRF selection, especially for stimulations with large BOLD response. BHRF is a simple and straightforward HRF but may underestimate the magnitude of BOLD response and the *t*-values of statistical tests. Sophisticated HRFs, such as CHRF and IRF, provide robust estimation. Our results suggest that CHRF and IRF could serve as complementary HRFs in the analysis of rat fMRI data.

AUTHOR CONTRIBUTIONS

S-LP conceptualized the study. S-LP and C-MC designed the experiments and prepared the manuscript. S-CC, C-YH, and W-CS performed the experiments and conducted data analysis. C-TS, C-WH, and S-CC participated in the data collection.

FUNDING

This work was funded by Ministry of Science and Technology, Taiwan (MOST 107-2314-B-039-056-MY3).

ACKNOWLEDGMENTS

The authors are grateful to Dr. Chih-Feng Chen for kindly supports.

SUPPLEMENTARY MATERIAL

The Supplementary Material for this article can be found online at: https://www.frontiersin.org/articles/10.3389/fnins.2019.00400/full#supplementary-material

REFERENCES

Aguirre, G. K., Zarahn, E., and D'esposito, M. (1998). The variability of human, BOLD hemodynamic responses. *Neuroimage* 8, 360–369. doi: 10.1006/nimg.1998.0369

Brinker, G., Bock, C., Busch, E., Krep, H., Hossmann, K. A., and Hoehn-Berlage, M. (1999). Simultaneous recording of evoked potentials and T2*-weighted MR images during somatosensory stimulation of rat. *Magn. Reson. Med.* 41, 469–473. doi: 10.1002/(sici)1522-2594(199903)41:3<469::aid-mrm7>3.3.co;2-0

Chavarrias, C., Garcia-Vazquez, V., Aleman-Gomez, Y., Montesinos, P., Pascau, J., and Desco, M. (2016). fMRat: an extension of SPM for a fully automatic analysis of rodent brain functional magnetic resonance series. *Med. Biol. Eng. Comput.* 54, 743–752. doi: 10.1007/s11517-015-1365-9

Friston, K. J. (2003). *Statistical Parametric Mapping*. Berlin: Springer.

Golestani, A. M., Wei, L. L., and Chen, J. J. (2016). Quantitative mapping of cerebrovascular reactivity using resting-state BOLD fMRI: validation in healthy adults. *Neuroimage* 138, 147–163. doi: 10.1016/j.neuroimage.2016.05.025

Handwerker, D. A., Ollinger, J. M., and D'esposito, M. (2004). Variation of BOLD hemodynamic responses across subjects and brain regions and their effects on statistical analyses. *Neuroimage* 21, 1639–1651. doi: 10.1016/j.neuroimage.2003.11.029

Hinkle, D. E., Wiersma, W., and Jurs, S. G. (2003). *Applied Statistics for the Behavioral Sciences*, 5th Edn. Boston: Houghton Mifflin Co.

Huttunen, J. K., Grohn, O., and Penttonen, M. (2008). Coupling between simultaneously recorded BOLD response and neuronal activity in the rat somatosensory cortex. *Neuroimage* 39, 775–785. doi: 10.1016/j.neuroimage.2007.06.042

Just, N., Petersen, C., and Gruetter, R. (2010). BOLD responses to trigeminal nerve stimulation. *Magn. Reson. Imaging* 28, 1143–1151. doi: 10.1016/j.mri.2010.02.002

Just, N., Xin, L., Frenkel, H., and Gruetter, R. (2013). Characterization of sustained BOLD activation in the rat barrel cortex and neurochemical consequences. *Neuroimage* 74, 343–351. doi: 10.1016/j.neuroimage.2013.02.042

Keilholz, S. D., Silva, A. C., Raman, M., Merkle, H., and Koretsky, A. P. (2004). Functional MRI of the rodent somatosensory pathway using multislice echo planar imaging. *Magn. Reson. Med.* 52, 89–99. doi: 10.1002/mrm.20114

Keilholz, S. D., Silva, A. C., Raman, M., Merkle, H., and Koretsky, A. P. (2006). BOLD and CBV-weighted functional magnetic resonance imaging of the rat somatosensory system. *Magn. Reson. Med.* 55, 316–324. doi: 10.1002/mrm.20744

Kim, S. G., Richter, W., and Ugurbil, K. (1997). Limitations of temporal resolution in functional MRI. *Magn. Reson. Med.* 37, 631–636. doi: 10.1002/mrm.1910370427

Kim, Y. R., Van Meer, M. P., Mandeville, J. B., Tejima, E., Dai, G., Topalkara, K., et al. (2007). fMRI of delayed albumin treatment during stroke recovery in rats: implication for fast neuronal habituation in recovering brains. *J. Cereb. Blood Flow Metab.* 27, 142–153. doi: 10.1038/sj.jcbfm.9600317

Lindquist, M. A., Meng Loh, J., Atlas, L. Y., and Wager, T. D. (2009). Modeling the hemodynamic response function in fMRI: efficiency, bias and mis-modeling. *Neuroimage* 45, S187–S198. doi: 10.1016/j.neuroimage.2008.10.065

Liu, J. V., Hirano, Y., Nascimento, G. C., Stefanovic, B., Leopold, D. A., and Silva, A. C. (2013). fMRI in the awake marmoset: somatosensory-evoked responses, functional connectivity, and comparison with propofol anesthesia. *Neuroimage* 78, 186–195. doi: 10.1016/j.neuroimage.2013.03.038

Liu, Z. M., Schmidt, K. F., Sicard, K. M., and Duong, T. Q. (2004). Imaging oxygen consumption in forepaw somatosensory stimulation in rats under isoflurane anesthesia. *Magn. Reson. Med.* 52, 277–285. doi: 10.1002/mrm.20148

Lu, H., Soltysik, D. A., Ward, B. D., and Hyde, J. S. (2005). Temporal evolution of the CBV-fMRI signal to rat whisker stimulation of variable duration and intensity: a linearity analysis. *Neuroimage* 26, 432–440. doi: 10.1016/j.neuroimage.2005.02.016

Magnuson, M. E., Thompson, G. J., Pan, W. J., and Keilholz, S. D. (2014). Time-dependent effects of isoflurane and dexmedetomidine on functional connectivity, spectral characteristics, and spatial distribution of spontaneous BOLD fluctuations. *NMR Biomed.* 27, 291–303. doi: 10.1002/nbm.3062

Masamoto, K., Kim, T., Fukuda, M., Wang, P., and Kim, S. G. (2007). Relationship between neural, vascular, and BOLD signals in isoflurane-anesthetized rat somatosensory cortex. *Cereb. Cortex* 17, 942–950. doi: 10.1093/cercor/bhl005

Melzer, P., Champney, G. C., Maguire, M. J., and Ebner, F. F. (2006). Rate code and temporal code for frequency of whisker stimulation in rat primary and secondary somatic sensory cortex. *Exp. Brain Res.* 172, 370–386. doi: 10.1007/s00221-005-0334-1

Miao, X., Gu, H., Yan, L., Lu, H., Wang, D. J., Zhou, X. J., et al. (2014). Detecting resting-state brain activity by spontaneous cerebral blood volume fluctuations using whole brain vascular space occupancy imaging. *Neuroimage* 84, 575–584. doi: 10.1016/j.neuroimage.2013.09.019

Nasrallah, F. A., Yeow, L. Y., Biswal, B., and Chuang, K. H. (2015). Dependence of BOLD signal fluctuation on arterial blood CO2 and O2: Implication for resting-state functional connectivity. *Neuroimage* 117, 29–39. doi: 10.1016/j.neuroimage.2015.05.035

Niranjan, A., Christie, I. N., Solomon, S. G., Wells, J. A., and Lythgoe, M. F. (2016). fMRI mapping of the visual system in the mouse brain with interleaved snapshot GE-EPI. *Neuroimage* 139, 337–345. doi: 10.1016/j.neuroimage.2016.06.015

Ogawa, S., Lee, T. M., Kay, A. R., and Tank, D. W. (1990). Brain magnetic resonance imaging with contrast dependent on blood oxygenation. *Proc. Natl. Acad. Sci. U.S.A.* 87, 9868–9872.

Ogawa, S., Tank, D. W., Menon, R., Ellermann, J. M., Kim, S. G., Merkle, H., et al. (1992). Intrinsic signal changes accompanying sensory stimulation: functional brain mapping with magnetic resonance imaging. *Proc. Natl. Acad. Sci. U.S.A.* 89, 5951–5955. doi: 10.1073/pnas.89.13.5951

Pelled, G., Chuang, K. H., Dodd, S. J., and Koretsky, A. P. (2007). Functional MRI detection of bilateral cortical reorganization in the rodent brain following peripheral nerve deafferentation. *Neuroimage* 37, 262–273. doi: 10.1016/j.neuroimage.2007.03.069

Poplawsky, A. J., and Kim, S. G. (2014). Layer-dependent BOLD and CBV-weighted fMRI responses in the rat olfactory bulb. *Neuroimage* 91, 237–251. doi: 10.1016/j.neuroimage.2013.12.067

Ramos-Cabrer, P., Justicia, C., Wiedermann, D., and Hoehn, M. (2010). Stem cell mediation of functional recovery after stroke in the rat. *PLoS One* 5:e12779. doi: 10.1371/journal.pone.0012779

Rana, M., Gupta, N., Dalboni Da Rocha, J. L., Lee, S., and Sitaram, R. (2013). A toolbox for real-time subject-independent and subject-dependent classification of brain states from fMRI signals. *Front. Neurosci.* 7:170. doi: 10.3389/fnins.2013.00170

Sanganahalli, B. G., Herman, P., Behar, K. L., Blumenfeld, H., Rothman, D. L., and Hyder, F. (2013). Functional MRI and neural responses in a rat model of Alzheimer's disease. *Neuroimage* 79, 404–411. doi: 10.1016/j.neuroimage.2013.04.099

Shan, Z. Y., Wright, M. J., Thompson, P. M., Mcmahon, K. L., Blokland, G. G., De Zubicaray, G. I., et al. (2014). Modeling of the hemodynamic responses in block design fMRI studies. *J. Cereb. Blood Flow Metab.* 34, 316–324. doi: 10.1038/jcbfm.2013.200

Shih, Y. Y., Chen, C. C., Shyu, B. C., Lin, Z. J., Chiang, Y. C., Jaw, F. S., et al. (2009). A new scenario for negative functional magnetic resonance imaging signals: endogenous neurotransmission. *J. Neurosci.* 29, 3036–3044. doi: 10.1523/JNEUROSCI.3447-08.2009

Shih, Y. Y., Chen, Y. Y., Lai, H. Y., Kao, Y. C., Shyu, B. C., and Duong, T. Q. (2013). Ultra high-resolution fMRI and electrophysiology of the rat primary somatosensory cortex. *Neuroimage* 73, 113–120. doi: 10.1016/j.neuroimage.2013.01.062

Shih, Y. Y., Huang, S., Chen, Y. Y., Lai, H. Y., Kao, Y. C., Du, F., et al. (2014). Imaging neurovascular function and functional recovery after stroke in the rat striatum using forepaw stimulation. *J. Cereb. Blood Flow Metab.* 34, 1483–1492. doi: 10.1038/jcbfm.2014.103

Shih, Y. Y., Wey, H. Y., De La Garza, B. H., and Duong, T. Q. (2011). Striatal and cortical BOLD, blood flow, blood volume, oxygen consumption, and glucose consumption changes in noxious forepaw electrical stimulation. *J. Cereb. Blood Flow Metab.* 31, 832–841. doi: 10.1038/jcbfm.2010.173

Silva, A. C., Koretsky, A. P., and Duyn, J. H. (2007). Functional MRI impulse response for BOLD and CBV contrast in rat somatosensory cortex. *Magn. Reson. Med.* 57, 1110–1118. doi: 10.1002/mrm.21246

Silva, A. C., Lee, S. P., Yang, G., Iadecola, C., and Kim, S. G. (1999). Simultaneous blood oxygenation level-dependent and cerebral blood flow functional magnetic resonance imaging during forepaw stimulation in the rat. *J. Cereb. Blood Flow Metab.* 19, 871–879. doi: 10.1097/00004647-199908000-00006

Tanabe, J., Miller, D., Tregellas, J., Freedman, R., and Meyer, F. G. (2002). Comparison of detrending methods for optimal fMRI preprocessing. *Neuroimage* 15, 902–907. doi: 10.1006/nimg.2002.1053

Tenney, J. R., Duong, T. Q., King, J. A., and Ferris, C. F. (2004). FMRI of brain activation in a genetic rat model of absence seizures. *Epilepsia* 45, 576–582. doi: 10.1111/j.0013-9580.2004.39303.x

Tsurugizawa, T., Uematsu, A., Uneyama, H., and Torii, K. (2010). Effects of isoflurane and alpha-chloralose anesthesia on BOLD fMRI responses to ingested L-glutamate in rats. *Neuroscience* 165, 244–251. doi: 10.1016/j.neuroscience.2009.10.006

Weber, R., Ramos-Cabrer, P., Wiedermann, D., Van Camp, N., and Hoehn, M. (2006). A fully noninvasive and robust experimental protocol for longitudinal fMRI studies in the rat. *Neuroimage* 29, 1303–1310. doi: 10.1016/j.neuroimage.2005.08.028

Wu, W. C., Lien, S. H., Chang, J. H., and Yang, S. C. (2014). Caffeine alters resting-state functional connectivity measured by blood oxygenation level-dependent MRI. *NMR Biomed.* 27, 444–452. doi: 10.1002/nbm.3080

Yang, P. F., Chen, Y. Y., Chen, D. Y., Hu, J. W., Chen, J. H., and Yen, C. T. (2013). Comparison of fMRI BOLD response patterns by electrical stimulation of the ventroposterior complex and medial thalamus of the rat. *PLoS One* 8:e66821. doi: 10.1371/journal.pone.0066821

Yu, X., Glen, D., Wang, S., Dodd, S., Hirano, Y., Saad, Z., et al. (2012). Direct imaging of macrovascular and microvascular contributions to BOLD fMRI in layers IV-V of the rat whisker-barrel cortex. *Neuroimage* 59, 1451–1460. doi: 10.1016/j.neuroimage.2011.08.001

Yu, X., Wang, S., Chen, D. Y., Dodd, S., Goloshevsky, A., and Koretsky, A. P. (2010). 3D mapping of somatotopic reorganization with small animal functional MRI. *Neuroimage* 49, 1667–1676. doi: 10.1016/j.neuroimage.2009.09.021

Conflict of Interest Statement: The authors declare that the research was conducted in the absence of any commercial or financial relationships that could be construed as a potential conflict of interest.

Copyright © 2019 Peng, Chen, Huang, Shih, Huang, Chiu and Shen. This is an open-access article distributed under the terms of the Creative Commons Attribution License (CC BY). The use, distribution or reproduction in other forums is permitted, provided the original author(s) and the copyright owner(s) are credited and that the original publication in this journal is cited, in accordance with accepted academic practice. No use, distribution or reproduction is permitted which does not comply with these terms.

frontiers in Neuroscience

ORIGINAL RESEARCH
published: 07 June 2019
doi: 10.3389/fnins.2019.00573

Quantification of Phase-Amplitude Coupling in Neuronal Oscillations: Comparison of Phase-Locking Value, Mean Vector Length, Modulation Index, and Generalized-Linear-Modeling-Cross-Frequency-Coupling

Mareike J. Hülsemann[1], Ewald Naumann[2] and Björn Rasch[1]*

[1] Division of Cognitive Biopsychology and Methods, Department of Psychology, University of Fribourg, Fribourg, Switzerland,
[2] Department of General Psychology and Methodology, Faculty I – Psychology, University of Trier, Trier, Germany

OPEN ACCESS

Edited by:
Amir Shmuel,
McGill University, Canada

Reviewed by:
Jennifer R. Stapleton-Kotloski,
Wake Forest School of Medicine, United States
Roberto C. Sotero,
University of Calgary, Canada

***Correspondence:**
Mareike J. Hülsemann
mareike.huelsemann@unifr.ch

Specialty section:
This article was submitted to Brain Imaging Methods, a section of the journal Frontiers in Neuroscience

Received: *28 August 2018*
Accepted: *20 May 2019*
Published: *07 June 2019*

Citation:
Hülsemann MJ, Naumann E and Rasch B (2019) Quantification of Phase-Amplitude Coupling in Neuronal Oscillations: Comparison of Phase-Locking Value, Mean Vector Length, Modulation Index, and Generalized-Linear-Modeling-Cross-Frequency-Coupling. Front. Neurosci. 13:573. doi: 10.3389/fnins.2019.00573

Phase-amplitude coupling is a promising construct to study cognitive processes in electroencephalography (EEG) and magnetencephalography (MEG). Due to the novelty of the concept, various measures are used in the literature to calculate phase-amplitude coupling. Here, performance of the three most widely used phase-amplitude coupling measures – phase-locking value (PLV), mean vector length (MVL), and modulation index (MI) – and of the generalized linear modeling cross-frequency coupling (GLM-CFC) method is thoroughly compared with the help of simulated data. We combine advantages of previous reviews and use a realistic data simulation, examine moderators and provide inferential statistics for the comparison of all four indices of phase-amplitude coupling. Our analyses show that all four indices successfully differentiate coupling strength and coupling width when monophasic coupling is present. While the MVL was most sensitive to modulations in coupling strengths and width, only the MI and GLM-CFC can detect biphasic coupling. Coupling values of all four indices were influenced by moderators including data length, signal-to-noise-ratio, and sampling rate when approaching Nyquist frequencies. The MI was most robust against confounding influences of these moderators. Based on our analyses, we recommend the MI for noisy and short data epochs with unknown forms of coupling. For high quality and long data epochs with monophasic coupling and a high signal-to-noise ratio, the use of the MVL is recommended. Ideally, both indices are reported simultaneously for one data set.

Keywords: phase-amplitude cross-frequency coupling, phase-locking value, mean vector length, modulation index, GLM-CFC, simulated EEG/MEG data

INTRODUCTION

Phase-amplitude coupling is a promising measure to study cognitive processes (Jensen and Lisman, 1998; Jensen, 2006; Lisman and Jensen, 2013; Vosskuhl et al., 2015). There is no convention yet of how to calculate phase-amplitude coupling, but instead much heterogeneity of phase-amplitude calculation methods used in the literature. Most of these are reasonable measures from a theoretical

point of view. To provide empirical evidence for choosing one of these measures over another, this work thoroughly compares the performance of the three most widely used phase-amplitude coupling measures with the help of simulated EEG data. The measures are the phase-locking value (PLV) as used in Mormann et al. (2005) (first introduced by Vanhatalo et al., 2004), mean vector length (MVL) by Canolty et al. (2006), and modulation index (MI) by Tort et al. (2008). Additionally the GLM-CFC (Kramer and Eden, 2013) is examined.

From a historical viewpoint, the first amplitude modulations that have been detected are amplitude fluctuations of specific frequency bands, becoming apparent in the fast Fourier transform (FFT) of constituents of these signals (Pfurtscheller, 1976; Novak et al., 1992; Burgess and Ali, 2002). Because the FFT approach can solely reveal that the amplitude of a higher frequency oscillates at a lower frequency (characteristic of one signal), these amplitude modulations should not be misinterpreted to account for true temporal coupling between the instantaneous phase of the lower frequency and the amplitude envelope of the higher frequency (association between two signals and definition of phase-amplitude coupling). Neither the lower frequency itself nor its instantaneous phase are extracted in this approach.

Some of the most widely used phase-amplitude coupling measures today are the PLV (Mormann et al., 2005), also called synchronization index (SI) by Cohen (2008), the MVL (Canolty et al., 2006), the MI (Tort et al., 2008), the envelope-to-signal correlation (ESC) (Bruns and Eckhorn, 2004), the generalized linear modeling (GLM) method (Penny et al., 2008; Kramer and Eden, 2013), phase binning combined with analysis of variance (ANOVA) (BA) (Lakatos et al., 2005), and the weighted phase locking factor (wPLF) (Maris et al., 2011). Recent approaches (Sotero, 2016; Martínez-Cancino et al., 2019) use mutual information in order to compute phase-amplitude coupling. The computation of mutual information is sensitive to the amount of data and noise, but advantageous when handling non-linear relationships (Cohen, 2014). All of these measures use the instantaneous phase and amplitude of band-pass filtered signals to calculate a measure that represents coupling strength. However, conceptual ideas and mathematical principles differ substantially between measures.

Several of these phase-amplitude coupling measures were compared with the help of simulated and real data in previous reviews. Tort et al. (2010) executed the most extensive comparison so far, including most of the above listed measures and evaluating their performance pertaining to tolerance to noise, amplitude independence (independence from the amplitude of the amplitude-providing frequency band), sensitivity to multimodality, and sensitivity to modulation width. The MI, introduced by the same group (Tort et al., 2008), is well-rated in all aspects while, amongst others, the PLV has poor ratings in all aspects. The MVL has good ratings in some aspects (e.g., tolerance to noise), but weaknesses in others (e.g., amplitude dependence).

Penny et al. (2008) introduced the GLM method and compared it to the PLV, MVL, and envelope-to-signal correlation in respect to noise level, coupling phase, data length, sample rate, signal non-stationarity, and multimodality. They found that the methods discriminated between data simulated with and without coupling to different extents, ranging from below chance level to perfect discrimination. Performance of the measures differed under poor conditions (high noise, low sampling rate, etc.), however, all measures performed equally well under good conditions (longer epochs, less noise, etc.).

Kramer and Eden (2013) introduced a new GLM method (GLM-CFC). It proves to be valid and performs equally well as the MI. The advantages of this method are that it can be interpreted as percentage change in amplitude strength due to modulation. Additionally confidence intervals are easily computed and the measure can detect biphasic coupling. The disadvantage of this measure is an especially high computation time due to generating the design matrix for the GLM and fitting the GLM.

When Onslow et al. (2011), compared three phase-amplitude coupling measures (MVL, envelope-to-signal correlation, cross-frequency coherence), they found that "no one measure unfailingly out-performed the others" (p. 56) (Onslow et al., 2011). They concluded that each measure seems to be particularly suited for specific data conditions. MVL for example is suitable for noisy data, exploratory analyses (analyzing a broad frequency spectrum) and when the power of the amplitude providing frequency band is low.

Samiee and Baillet (2017) statistically compared the PLV, MVL, and MI especially focusing on data length effects and the accuracy of finding the contributing coupling frequencies within exploratory analyses for broad frequency ranges. Here all three measures performed equally well in accurately finding coupling frequencies. However, their results indicate that MVL estimates coupling strength most correctly and MI is most robust to noise regarding detecting the correct coupling frequencies in the aforementioned exploratory analysis. The authors show that the performance of the direct MVL (Özkurt and Schnitzler, 2011) can be significantly increased when using sophisticated methods for detecting the actual coupling frequencies for phase and amplitude in the data and that this method allows to estimate coupling strength for very short data segments (see Samiee and Baillet, 2017 for details).

The above cited reviews do not point to a single optimal measure for calculating phase-amplitude coupling. They rather show that most – but not all – of the used measures perform well and are equally affected by various confounders. Despite the availability of manifold measures, 79% of studies use the PLV adapted for phase-amplitude coupling, MVL, or MI (Hülsemann, 2016). The three measures are indeed the three most often used. Why is this the case? The PLV is derived from a long-used, phase-phase coupling measure that is easily adapted for the purpose of phase-amplitude measurement. Its familiarity in the scientific community might have promoted its application. Possibly the predominant application of MVL is due to its mathematical directness. The MI is conceptually intuitive.

The majority of reviews used very straightforward data simulation methods. Oftentimes, a sinusoidal oscillation is constructed at a lower phase-providing frequency and at a higher amplitude-providing frequency. Phase-amplitude coupling is introduced by multiplying both signals (cf. Onslow et al., 2011).

Amplitude is then extracted from the so constructed signal and phase is extracted from the pure sinusoidal oscillation of the lower frequency. White noise is added to both signals. There are two disadvantages in this approach. Both sinusoidal signals reflect a plain prototype of phase-amplitude coupling, but in real neuronal data, pure sinusoidal oscillation cannot be filtered; rather, frequency bands containing different amounts of various frequencies are extracted. Second, white noise is added to the simulated data, even though it is known that not white noise but fractional Brownian noise is inherent to brain dynamics (Miller et al., 2009; He et al., 2010).

Because none of the hitherto existing reviews simultaneously meet the requirements of realistic simulation of EEG data, providing inferential statistics for comparison of the measures, investigating moderators of phase-amplitude coupling, and including the three most widely used measures (PLV, MVL, and MI), a new comparison of these methods is presented here. Additionally the GLM-CFC is included in the comparison. We aim to combine the best aspects of all previous reviews. EEG data is simulated rather realistically according to the procedure described by Kramer and Eden (2013). The influence of several moderators (multimodality, data length, sampling rate, noise level, modulation strength, and modulation width) inspired by Tort et al. (2010) is investigated. Sensitivity and specificity of the phase-amplitude coupling measures are checked according to the methods described in Onslow et al. (2011). For all these comparisons, inferential statistics are provided.

MATERIALS AND METHODS

Simulation of EEG Data and Implementation of Phase-Amplitude Coupling

A characteristic of natural EEG data is the proportionality of its frequency spectrum to a power law $P(f) \sim (1/f^{\beta})$. Namely, the higher the frequency f, the weaker the amplitude P(f). The exponent β defines the strength of the amplitude decrease. White noise is defined by $\beta = 0$, pink noise by $\beta = 1$ and Brownian (red) noise by $\beta = 2$. Different investigations have shown that the frequency spectrum of human brain activity relates to fractional Brownian (red) noise, with $2 < \beta < 3$ (Miller et al., 2009; He et al., 2010). Because of this, Brownian noise was generated using MATLAB code provided by Zhivomirov (2013, 2018), in order to simulate EEG data (**Figure 1A**).

Simulated data was then filtered at a low phase-providing frequency, from here on referred to as phase time series, with a narrow bandwidth of 2 Hz. The same data was filtered at a high amplitude-providing frequency, from here on referred to as amplitude time series, with a broad bandwidth. The exact bandwidth of the amplitude time series should depend on the frequency of the phase time series (Berman et al., 2012; Dvorak and Fenton, 2014). Because of this data was filtered such that the sidebands of the modulating frequency were always included (i.e., center frequency of amplitude-providing frequency band ± upper boundary of phase-providing frequency band).

A zero-phase Hamming-windowed sinc finite impulse response (FIR) filter implemented in EEGLAB (function *pop_eegfiltnew* contributed by A. Widmann) was used. This function automatically chooses the optimal filter order and transition band width for a precisely selectable filter bandwidth. Low frequency was set to 5–7 Hz (for *theta*-low gamma coupling) and 8–10 Hz (for *alpha*-high gamma coupling). High frequency was set to 33–47 Hz (for theta-*low gamma* coupling) and 50–70 Hz (for alpha-*high gamma* coupling). Filtering can seriously distort raw data (Widmann et al., 2015), therefore only continuous data was filtered and data segments at the beginning and end, where edge artifacts can occur, were later on discarded.

To introduce coupling, the procedure of Kramer and Eden (2013) was followed. A Hanning window plus one (i.e., each data point of the Hanning window is added with one) was multiplied with the amplitude time series. This multiplication of the Hanning window with the amplitude time series was not done continuously, but centered at either the relative maxima (peaks) or the relative maxima and minima (peaks and troughs) of the phase time series, in order to simulate monophasic and biphasic coupling, respectively. Extremum times are chosen because they are easy to detect. They relate to phase angles of 0 and 180°/−180°. Phase-amplitude coupling measures would not change if the coupling were to be introduced at another phase angle. The Hanning window itself is multiplied with the factor I to graduate the intensity of phase-amplitude coupling. To double the amplitude of the time series at the specified time I = 1.0 is chosen. I = 0.0 reflects no phase-amplitude coupling (i.e., not modulating the amplitude time series). The length of the Hanning window was also modulated to simulate different "widths" of phase-amplitude modulation. Parameters chosen for these moderators are specified below. In a final step, additional noise was added to the phase and amplitude time series. Therefore, Brownian noise of the same length was simulated, band-pass filtered at the same frequencies as the phase and amplitude time series, and added to the original phase and modulated amplitude time series, respectively. Frequency matched noise is disruptive to the modulated phase-amplitude coupling and therefore allows to check for the robustness of the phase-amplitude coupling measures.

Subsequently, phase and amplitude were extracted from the correspondent time series via Hilbert transform, using the Signal Processing Toolbox of MATLAB (The MathWorks, Inc.). Then continuous phase and amplitude time series were segmented. This was done to introduce data discontinuities, which are present in real data as well. Filtering, Hilbert transform, and phase or amplitude extraction were always conducted on continuous data, to prevent filtering or other artifacts in the later analyzed data epochs.

Each simulated data set was then modified. Data sets with a length of 42, 105, and 180 s were subsampled. This amount of data is sufficient to simulate 30 trials with a length of 400, 2500, and 5000 ms plus additional 30 s to introduce data discontinuities when segmenting the data. These parameters were chosen to mirror typical properties of event-related EEG data: (1) at least 30

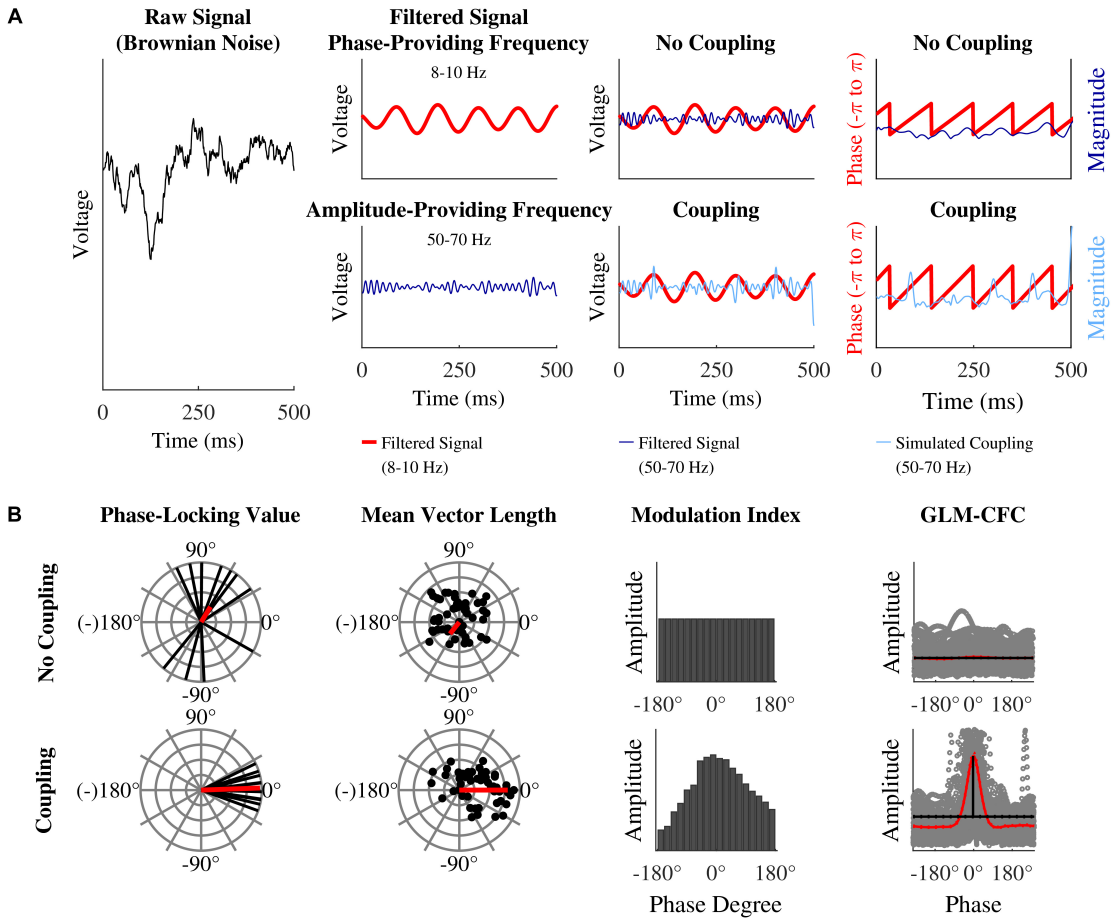

FIGURE 1 | Simulation of the EEG signal and calculation of phase-amplitude coupling: **(A)** (from left to right) Brownian noise is generated. This signal is band pass filtered to extract the slow phase-providing frequency (here 8–10 Hz, red line) and the fast amplitude-providing frequency (here 50–70 Hz, dark blue line). To simulate coupling (light blue line) the amplitude-providing band pass filtered signal is multiplied with a Hanning window plus one (not depicted here), which results in stronger amplitude at the peaks of the phase-providing frequency (lower middle right panel). Before extracting phase and amplitude (most right panels) band pass filtered noise (same frequencies) is added to the filtered data (not depicted here). The simulated coupling (light blue line) amplitude is most pronounced for phases at 0°. This is not the case for the original signal (dark blue line). **(B)** Idealized depiction PLV (outer left panels), MVL (inner left panels), MI (inner right panels), and GLM-CFC (outer right panels) for a uniform distribution (upper panels) and phase-amplitude coupling (lower panels). PLV: each black line represents the phase lag between two signals at one data point. The red vector is the mean of all black vectors. The upper panel shows inconsistent, widespread phase lags. The widespread phase lags lead to a relatively short mean vector (red line). The outer left lower panel shows an example of a relative constant phase lag around 0°. A relative constant phase lag leads to a relatively long mean vector. MVL: each black dot represents one data point of the analytical signal. In case of coupling, a portion of the dots (or vectors) are especially long (reflecting strong amplitudes) at a specific narrow range of phase angles (here 0° in the lower panel). The red vector is the mean of all black vectors. It reflects coupling strength (short for no coupling – long for coupling). In case of phase-amplitude coupling it is indicating the preferred phase. MI: all possible phases are binned into 18 bins of 20° from –180 to 180°. Each bar reflects the mean amplitude of the amplitude-providing signal for the specified phase of the phase-providing frequency. This phase-amplitude plot is quantified with Shannon entropy. Shannon entropy is maximal for uniform distributions (upper panel). The Kullback–Leibler distance measures how much a given distribution (for example the one in the lower panel) deviates from the uniform distribution (depicted in the upper panel). The more phase-amplitude coupling there is in the data, the more the given phase-amplitude plot deviates from the uniform distribution and the higher the MI becomes. GLM-CFC: each circle in the scatter plot represents on data point. If there is no phase-amplitude coupling, amplitude values are rather similar across all possible phase values. In this case, a horizontal line would best model the data and the phase value would have no predictive power. If there is phase-amplitude coupling, amplitude values are specifically high at certain phase values. In this case, a curve that follows the amplitude pattern would best model the data. In case of phase-amplitude coupling, the curve (red line) differs from the horizontal line (black line) that represents no coupling. In case of no phase-amplitude coupling the curve barely differs from the null model horizontal line that represents no coupling.

trials per unique condition for which phase-amplitude coupling will be calculated (Luck, 2014), (2) trial length between 400 and 5000 ms, and (3) data discontinuities between trials. Sampling rate was set to 1000 Hz (Cohen, 2014). In addition, simulated data was resampled to 500 Hz in order to investigate the influence of sampling rate. Noise was scaled by the factor 0.9, 1.0, and 1.1 in order to simulate different signal-to-noise ratios. Scaling factor 0.9, 1.0, and 1.1 correspond to a noise signal strength of 90, 100, and 110% compared to the data signal strength. Four modulation strengths were realized: I = 0.0 for no coupling and I = 0.9, I = 1.0, and I = 1.1 for increasing coupling strength (I = 1.0 doubling the original amplitude strength). These values lie

within the range of former studies (e.g., Kramer and Eden, 2013). The length of the Hanning Window ranged between 22.5 and 27.5% of one low frequency cycle to modulate different "widths" of phase-amplitude modulation. This width is equivalent to about a quarter of one cycle and therefore covers the peak (or trough) phases of that low frequency cycle. At these phases, amplitude of the higher frequency was increased. All parameters were realized for mono- and bi-phasic coupling (factor multimodality).

Measuring Phase-Amplitude Coupling

To calculate phase-amplitude coupling, first, raw data is band-pass filtered in the frequency bands of interest. Second, the real-valued band-pass filtered signal is transformed into a complex-valued analytic signal. Finally, phase or amplitude is extracted from the complex-valued analytic signal. All these steps can essentially be implemented in MATLAB with four lines of code:

```
filtered_data = pop_eegfiltnew(raw_data,lower_frequency_bound,upper_frequency_bound);
analytic_signal = hilbert(filtered_data);
phase = phase(analytic_signal);
amplitude = abs(analytic_signal).
```

Phase-Locking-Value as Used in Mormann et al. (2005)

For the calculation of the PLV, phase is extracted from the low frequency filtered analytic signal and amplitude is extracted from the high frequency filtered analytic signal. The amplitude time series is then again Hilbert transformed and phase is extracted from the "second" analytic signal. By these steps, one obtains phase angles for both time series for each data point. For each data point the phase angle of the Hilbert transformed amplitude time series is subtracted from the phase angle of the phase time series, obtaining phase angle differences.

These phase angle differences can be plotted in a polar plane as vectors of the length one with the angle representing the respective phase angle difference (**Figure 1B**, outer left panels). A constant phase lag between both time series indicates phase-amplitude coupling. A constant phase lag leads to vectors in the polar plane with a similar direction. Then all vectors are averaged: if they have a constant phase lag, they point into the same direction leading to a rather long mean vector. If there is a variable phase lag, the vectors are scattered around the polar plane, leading to a rather short mean vector. The length of the mean vector indicates the amount of phase-amplitude coupling (coupling strength). The direction of the vector represents the mean phase lag present between the two time series and the preferred coupling phase can be inferred from the phase lag. The PLV is calculated by the following formula:

$$PLV = \left| \frac{\sum_{t=1}^{n} e^{i(\theta_{lt} - \theta_{ut})}}{n} \right| \quad (1)$$

where n is the total number of data points, t is a data point, θ_{lt} is the phase angle of the lower frequency band at data point t and θ_{ut} is the phase angle of the Hilbert transformed upper frequency band amplitude time series.

The logic for this measure is as follows: if phase-amplitude coupling exists, the amplitude of the high frequency time series will oscillate at the lower frequency. In this case, extracting instantaneous phase information from this signal will return some constant phase lag to the instantaneous phase information of the low frequency band. Otherwise, inconsistent phase lags to the instantaneous phase of the lower frequency signal will be extracted, indicating no phase-amplitude coupling. A potential disadvantage of this measure is that invalid phase information will be extracted from the Hilbert transformed amplitude time series if it does not oscillate at a specific frequency. This disadvantage can be counteracted by filtering the Hilbert transformed amplitude time series in the low frequency range before extracting phase information (see Vanhatalo et al., 2004).

One should be aware that meaningful phase information can only be extracted from narrow band oscillations (Aru et al., 2015). The Hilbert transformed amplitude time series does not necessarily need to be such a narrow band oscillation.

Mean Vector Length by Canolty et al. (2006)

For the phase-amplitude coupling measure MVL, introduced by Canolty et al. (2006), phase is extracted from the low frequency filtered analytic signal and amplitude is extracted from the high frequency filtered analytic signal. MVL utilizes phase angle and magnitude of each complex number (i.e., each data point) of the corresponding analytic signal in a quite direct way to estimate the degree of coupling. Each complex value of the analytic time series is a vector in the polar plane. Phase-amplitude coupling is present, when the magnitude M of a fraction of all vectors is especially high at a specific phase or at a narrow range of phases (**Figure 1B**, inner left panels). Averaging all vectors creates a mean vector with a specific phase and length (red vector in **Figure 1B**). The length of this vector represents the amount of phase-amplitude coupling. The direction represents the mean phase where amplitude is strongest. When no coupling is present, all vectors cancel each other out and the mean vector will be short. Then its direction does not represent any meaningful phase. The MVL is calculated by the following formula:

$$MVL = \left| \frac{\sum_{t=1}^{n} a_t e^{i\theta_t}}{n} \right| \quad (2)$$

where n is the total number of data points, t is a data point, a_t is the amplitude at data point t and θ_t is the phase angle at data point t. This value cannot become negative because it represents the length of the mean vector. The length of a vector cannot be negative.

Three caveats come along with this measure: (1) the value is dependent on the general absolute amplitude of the amplitude providing frequency (independent of outliers), (2) amplitude outliers can strongly influence the MVL, and (3) phase angles are often not uniformly distributed (Cohen, 2014). All caveats are simultaneously counteracted by non-parametric permutation testing (see section "Permutation Testing"). One of the reviews cited in the introduction (Tort et al., 2010) finds faults with the MVL being amplitude

dependent. However, this is only true for the raw, but not for the permuted MVL.

In the interest of completeness, it should be mentioned that Özkurt and Schnitzler (2011) proposed a direct MVL which is amplitude-normalized and ranges between 0 and 1. When applying permutation testing to both MVL and direct MVL return essentially the same values. That is, when applied along with permutation testing, both measures are exchangeable. Without permutation testing, the usage of the direct MVL is recommended because it takes care of the possible amplitude differences in raw data.

Modulation Index by Tort et al. (2008)

Tort et al. (2008) suggest a very different way of computing phase-amplitude coupling, which anyways is based on the same parameters of the analytic signal, amplitude magnitude and phase angle. For calculating the MI according to Tort et al. (2008), all possible phases from −180 to 180° are first binned into a freely chosen amount of bins. Tort et al. (2008) established to use 18 bins of 20° each, which many authors follow. The amount of bins can influence the results, as will be explained below. The average amplitude of the amplitude-providing frequency in each phase bin of the phase-providing frequency is computed and normalized by the following formula:

$$p(j) = \frac{\bar{a}}{\sum_{k=1}^{N} \bar{a}_k} \tag{3}$$

where ā is the average amplitude of one bin, k is the running index for the bins, and N is the total amount of bins; p is a vector of N values. With the help of these calculations, one obtains the data for the phase-amplitude plot, which depicts the actual phase-amplitude coupling graphically (**Figure 1B**, inner right panels).

Subsequently Shannon entropy is computed; a measure that represents the inherent amount of information of a variable. If Shannon entropy is not maximal, there is redundancy and predictability in the variable. Shannon entropy is maximal, if the amplitude in each phase bin is equal (uniform distribution, **Figure 1B**, inner right upper panel). Shannon entropy is computed by the following formula:

$$H(p) = -\sum_{j=1}^{N} p(j)\log p(j) \tag{4}$$

where p is the vector of normalized averaged amplitudes per phase bin and N is the total amount of bins. It does not matter which logarithm base is used if permutation testing is applied later on (Cohen, 2014). Like in Tort et al. (2008) the natural logarithm is used here. Shannon entropy is dependent on the amount of bins used and this is why the MI is likewise dependent on the number of bins. The higher the amount of bins, the larger Shannon entropy can become. Complying with the original study and most other studies, 18 bins have been employed here.

Phase-amplitude coupling is defined by a distribution that significantly deviates from the uniform distribution. Kullback–Leibler distance, a measure for the disparity of two distributions is calculated by the following formula:

$$KL(U, X) = \log N - H(p) \tag{5}$$

where U is the uniform distribution, X is the distribution of the data, N is the total amount of bins, and H(p) is the Shannon entropy according to Eq. 4. The uniform distribution is represented by log(N). The final raw MI is calculated by the following formula:

$$MI = \frac{KL(U, X)}{\log N} \tag{6}$$

where KL(U, X) is the Kullback–Leibler distance according to Eq. 5 and N is the total amount of bins.

GLM-CFC by Kramer and Eden (2013)

For this measure, the idea of predicting a set of observed variables (response variables; here the amplitude values of the relatively higher frequency band) by another set of variables (predictor variables; here the phase values of the relatively lower frequency band) using a mathematic function (link function; here a log link function) is applied. Extending the linear regression model, GLMs allow non-normal distributions for response variables (e.g., gamma distribution) and non-linear link functions (e.g., log link). They are thereby optimal for phase-amplitude coupling: phase and amplitude do exhibit a non-linear relationship and instantaneous amplitude values (extracted from the amplitude envelope) are always real and positive, which is best reflected in the gamma distribution (but not the normal distribution).

For calculating the GLM-CFC, phase is extracted from the low frequency filtered analytic signal and amplitude is extracted from the high frequency filtered analytic signal. Phase and amplitude values can then be depicted in a scatter plot (compare **Figure 1B**, outer right panels). If there is phase-amplitude coupling in the data, then amplitude values are specifically high at certain phase values. If there is no phase-amplitude coupling, amplitude values are rather similar across all possible phase values. In this case, a horizontal line would best model the data and the phase value would have no predictive power. If there is phase-amplitude coupling in the data, a curve (3rd order polynomial) that follows the amplitude pattern would best model the data.

In case of phase-amplitude coupling, the curve – which is called spline model – (red lines in **Figure 1B**, outer right panels) differs from the horizontal line that represents no coupling – and is called null model – (black lines in **Figure 1B**, outer right panels). In case of no phase-amplitude coupling the spline model barely differs from the null model. That is, the more the spline model differs from the null model, the more phase-amplitude coupling is present in the data. In fact, the GLM-CFC finds the maximum absolute difference between both models, and calculates this difference as percentage change.

The modeled curve closely resembles a 3rd order polynomial. However, not a polynomial, but a set of splines placed between control points, which are evenly spaced between –pi and pi, are used. The set of splines are easier to compute and, moreover, its characteristics can be better controlled than those of a

polynomial. On the other hand, a degree of freedom is introduced (the amount of control points), that can influence the results. Kramer and Eden (2013) therefore included an evaluation of the Akaike information criterion (AIC) to define the optimal number of control points.

For an exact mathematical description of the GLM-CFC see the original article by Kramer and Eden (2013), who also provide the MATLAB code that was used in this analysis.

Permutation Testing

All methods are subjected to permutation testing in order to quantify the meaningfulness of the derived value (Cohen, 2014). For permutation testing, the observed coupling value is compared to a distribution of shuffled coupling values. Shuffled coupling values are constructed by calculating the coupling value between the original phase time series and a permuted amplitude time series (or vice versa). The permuted amplitude time series is constructed by cutting the amplitude time series at a random data point and reversing the order of both parts. Generating surrogate data this way is most conservative, because it leaves all characteristics of the EEG data intact, except the studied one, namely the temporal relationship between phase angle and amplitude magnitude. Shuffling is usually repeated 200 to 1000 times (here we used 1000). The observed coupling value is standardized to the distribution of the shuffled coupling values according to the following formula:

$$CV_z = \frac{CV_{observed} - \mu_{CV_{shuffled}}}{\sigma_{CV_{shuffled}}} \quad (7)$$

where CV denotes coupling value, μ denotes the mean and σ denotes the standard deviation (SD). Only when the observed CV is larger than 95% of shuffled values (which are expected to be uncorrelated), it is defined as significant.

Statistical Analyses

All statistical analyses were conducted with IBM Statistics for Windows Version 23 (SPSS, Inc., IBM company), except otherwise specified. Significance level were set to $p < 0.05$. Violations of sphericity were, whenever appropriate corrected by Greenhouse–Geisser ε (Geisser and Greenhouse, 1958). Further analyses of significant results were conducted *post hoc* with Dunn's multiple comparison procedure (Dunn, 1961) or *post hoc* *t*-tests. Effect size measure ω^2 is reported for significant results (Hays, 1973). It is an estimator for the population effect Ω^2, which specifies the systematic portion of variance in relation to the overall variance (Rasch et al., 2006).

Specificity of Phase-Amplitude Coupling Measures

In a first step 5,000 data sets without coupling were simulated by setting the modulation strength to I = 0. Simulations were carried out for the frequency pairs 5–7 Hz/33–47 Hz (for phase and amplitude time series respectively) and 8–10 Hz/50–70 Hz (for phase and amplitude time series respectively). Each data set was modified in data length (400, 2500, 5000 ms), sampling rate (500, 1000 Hz), and noise level (90, 100, 110%), resulting in a total of 90,000 data sets for which coupling was calculated. Phase-amplitude coupling values were generally compared in a 4 × 3 × 2 × 3 analysis of variance (ANOVA) with the repeated measurement factors method (PLV, MVL, MI, GLM-CFC), data length (400, 2500, 5000 ms), sampling rate (500, 1000 Hz), and noise level (90, 100, 110%).

As described above, non-parametric permutation testing was performed. Raw phase-amplitude coupling measures were z-standardized to the shuffled phase-amplitude coupling distribution. Normal z-values directly imply *p*-values; a value of 1.64 corresponds to a *p*-value of 5%. The phase-amplitude coupling value distribution which is expected under the null-hypothesis does not have to match the standardized normal distribution. Therefore, significance was not inferred from the standardized normal distribution, but instead by that phase-amplitude coupling value, at which 5% of simulated data (with no coupling) was classified as false positive. Shuffling for permutation testing was done within trials. Coupling measures were then calculated on concatenated trials.

Specificity of measures was analyzed by counting false positives (significant coupling according to critical z-value found in the prior analysis, even though it was not engineered into the simulated data) depending on (1) method, (2) data length, (3) sampling rate, and (4) noise level. To be able to conduct an ANOVA, the 5,000 simulations were divided into 100 subsamples of 50 simulations each. For each subsample false positives were counted. Each subsample was treated as a case in the subsequent 4 × 2 × 3 × 3 ANOVA with the repeated measurement factors method (PLV, MVL, MI, GLM-CFC), data length (400, 2500, 5000 ms), sampling rate (500, 1000 Hz), and noise level (90, 100, 110%) and the dependent variable false positives.

Sensitivity of Phase-Amplitude Coupling Measures as a Function of Moderating Variables

Performance of phase-amplitude coupling measures were quantified by simulating 100 independent data sets and modifying the parameters (1) modulation strength, and (2) modulation width, (3) multimodality, (4) data length, (5) sampling rate, and (6) noise level within each dataset. Six two-way ANOVAs were calculated. Each ANOVA included the repeated measurement factor method and was individually combined with the repeated measurement factors modulation strength (90, 100, 110%), modulation width (22.5, 25.0, 27.5% of one low frequency cycle), multimodality (monophasic, biphasic), data length (400, 2500, 5000 ms), sampling rate (500, 1000 Hz), and noise level (90, 100, 110% compared to signal strength).

RESULTS

Specificity of Phase-Amplitude Coupling Measures

Theta-Low Gamma Coupling (5–7 to 33–47 Hz)

Phase-amplitude coupling values did not differ depending on data length, sampling rate, or noise level. Because of the high number of simulations (n = 5,000), some other main effects and interactions became significant. However, all effect sizes were below $\omega^2 < 0.01$, therefore these differences

are negligible. Phase-amplitude coupling values did differ depending on method [$F(3,14997) = 4471.38$, $p < 0.01$, $\omega^2 = 0.40$]. *Post hoc* t-tests showed that the GLM-CFC (mean ± SE: 0.29 ± 0.00) was significantly larger than all other methods [PLV:.02 ± 0.00, $t(4999) = 74.75$, $p < 0.01$, $\omega^2 = 0.36$; MVL: 0.02 ± 0.00, $t(4999) = 78.09$, $p < 0.01$, $\omega^2 = 0.38$; MI: 0.00 ± 0.00, $t(4999) = 187.48$, $p < 0.01$, $\omega^2 = 0.78$], which did not differ significantly from each other (all $\omega^2 < 0.01$).

Five percent of the simulated data were falsely classified as containing coupling when setting the critical z-value for the PLV at 1.91, for the MVL at 1.91, for the MI at 1.94, and for the GLM-CFC at 2.08. Thus, these values were defined as critical z-values. This implies that the PLV and the MVL are most specific, followed by the MI. The GLM-CFC is least specific compared to the three other methods.

The amount of false positives according to the previous established critical z-value did differ depending on data length [$F(2,198) = 35.57$, $p < 0.01$, $\omega^2 = 0.19$, $\text{Dunn}_{\text{crit}} = 0.14$]. There were significantly more false positives during short epochs (400 ms; 2.77 ± 0.04) compared to medium (2500 ms: 2.36 ± 0.04) and long epochs (5000 ms: 2.32 ± 0.05). Medium and long epochs did not differ in their false positive rates. The main effect was qualified by a method by data length interaction [$F(6,594) = 51.66$, $p < 0.01$, $\omega^2 = 0.20$, $\text{Dunn}_{\text{crit}} = 0.20$]. This revealed that the above-described pattern was driven by the PLV and MVL. There were no differences in false positive rate within the MI and the GLM-CFC.

Alpha-High Gamma Coupling (8–10 to 50–70 Hz)

Phase-amplitude coupling values did not differ depending on data length, sampling rate, or noise level. Because of the high number of simulations (n = 5,000), some other main effects and interactions became significant. However, all effect sizes were below $\omega^2 < 0.01$, therefore these differences are negligible. Phase-amplitude coupling values did differ depending on method [$F(3,14997) = 3959.41$, $p < 0.01$, $\omega^2 = 0.37$]. *Post hoc* t-tests showed that the GLM-CFC (0.24 ± 0.00) was significantly larger than all other methods [PLV: 0.01 ± 0.00, $t(4999) = 70.29$, $p < 0.01$, $\omega^2 = 0.33$; MVL: 0.01 ± 0.00, $t(4999) = 75.56$, $p < 0.01$, $\omega^2 = 0.36$; MI: 0.00 ± 0.00, $t(4999) = 161.05$, $p < 0.01$, $\omega^2 = 0.72$], which did not differ significantly from each other (all $\omega^2 < 0.01$).

Figure 2 shows the phase-amplitude coupling value distribution for the PLV, the MVL, the MI, and the GLM-CFC for alpha-high gamma coupling. Five percent of the simulated data were falsely classified as containing coupling when setting the critical z-value for the PLV at 1.86, for the MVL at 1.87, for the MI at 1.97, and for the GLM-CFC at 2.05. Thus, these values were defined as critical z-values. This implies that the PLV and the MVL are most specific, followed by the MI. The GLM-CFC is least specific compared to the three other methods.

The amount of false positives according to the previous established critical z-value did differ depending on data length [$F(2,198) = 4.72$, $p < 0.01$, $\omega^2 = 0.02$, $\text{Dunn}_{\text{crit}} = 0.17$]. There were significantly more false positives during short epochs (400 ms: 2.62 ± 0.05) compared to medium (2500 ms: 2.42 ± 0.05) and long epochs (5000 ms: 2.43 ± 0.05). Medium and long epochs did not differ in their false positive rates. The main effect was qualified by a method by data length interaction [$F(6,594) = 13.28$, $p < 0.01$, $\omega^2 = 0.06$, $\text{Dunn}_{\text{crit}} = 0.18$]. This revealed that the above-described pattern was driven by the PLV and MVL. There were no differences in false positive rate within the MI and the GLM-CFC.

Sensitivity of Phase-Amplitude Coupling Measures as a Function of Moderating Variables

Effect of Method on Phase-Amplitude Coupling Measures

Theta-low gamma coupling (5–7 to 33–47 Hz)

PLV (1.22 ± 0.05) and MVL (1.53 ± 0.06) differed from the MI (7.83 ± 0.49) in their absolute magnitude independently of any other factor [main effect method: $F(3,297) = 220.33$, $p < 0.01$, $\omega^2 = 0.62$, $\text{Dunn}_{\text{crit}} = 0.78$]. PLV and MVL did not differ from each other. The GLM-CFC (3.91 ± 0.18) differed from all other methods.

Alpha-high gamma coupling (8–10 to 50–70 Hz)

PLV (1.77 ± 0.06) and MVL (2.22 ± 0.08) differed from the MI (13.35 ± 0.78) in their absolute magnitude independently of any other factor [main effect method: $F(3,297) = 250.07$,

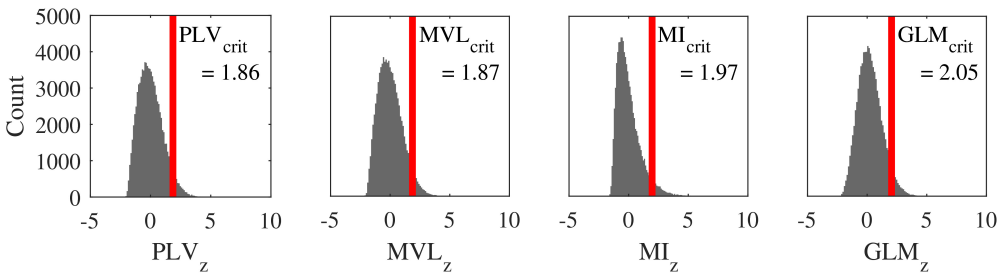

FIGURE 2 | Probability distribution of coupling values under the null hypothesis: phase-amplitude coupling value distribution under the null hypothesis (i.e., no coupling present in the data) of phase-locking value (outer left panel), MVL (inner left panel), MI (inner right panel), and GLM-CFC (outer right panel). These distributions allow defining the significance threshold. The red line marks the critical phase-amplitude coupling z-value (relative cut off of 5%). Choosing an absolute cut off instead would lead to smallest amount of false positives for MVL, followed by the PLV. The GLM-CFC would detect the most false positives followed by the MI.

$p < 0.01$, $\omega^2 = 0.65$, $\text{Dunn}_{\text{crit}} = 1.28$]. PLV and MVL did not differ from each other. The GLM-CFC (5.52 ± 0.23) differed from all other methods.

Effect of Modulation Strength on Phase-Amplitude Coupling Measures

Theta-low gamma coupling (5–7 to 33–47 Hz)

Coupling values of all methods increased with increasing modulation strength [$F(2,198) = 204.74$, $p < 0.01$, $\omega^2 = 0.58$]. The interaction method by modulation strength became significant [$F(6,594) = 154.84$, $p < 0.01$, $\omega^2 = 0.43$]. *Post hoc t*-tests showed that all factor levels within a method differed significantly from each other (all p's < 0.01). The effect of modulation strength was most pronounced for the GLM-CFC ($0.31 < \omega^2 < 0.61$), followed by the MVL ($0.21 < \omega^2 < 0.55$) and the MI ($0.33 < \omega^2 < 0.54$). The PLV was least sensitive to modulation strength ($0.15 < \omega^2 < 0.50$).

Alpha-high gamma coupling (8–10 to 50–70 Hz)

Coupling values of all methods increased with increasing modulation strength [$F(2,198) = 215.60$, $p < 0.01$, $\omega^2 = 0.59$]. The interaction method by modulation strength became significant [$F(6,594) = 167.31$, $p < 0.01$, $\omega^2 = 0.45$; **Figure 3A**]. *Post hoc t*-tests showed that all factor levels within a method differed significantly from each other (all p's < 0.01). The effect of modulation strength was most pronounced for the GLM-CFC ($0.36 < \omega^2 < 0.66$) and the MVL ($0.32 < \omega^2 < 0.66$), followed by the MI ($0.33 < \omega^2 < 0.57$). The PLV was least sensitive to modulation strength ($0.20 < \omega^2 < 0.60$).

The stronger the coupling, the larger PLV, MVL, MI, and GLM-CFC are. As Tort et al. (2010) has shown, this behavior is not inherent to all phase-amplitude coupling measures. Since researchers do not only want to prove the existence of phase-amplitude coupling, but also differentiate its strength, a measure that can do this is indispensable. Of all four methods, the GLM-CFC differentiates best between the different factor levels of modulation strength, closely followed by the MVL and MI.

Effect of Modulation Width on Phase-Amplitude Coupling Measures

Theta-low gamma coupling (5–7 to 33–47 Hz)

Coupling values of all methods increased with increasing modulation width [$F(2,198) = 118.61$, $p < 0.01$, $\omega^2 = 0.44$]. The interaction method by modulation width became significant

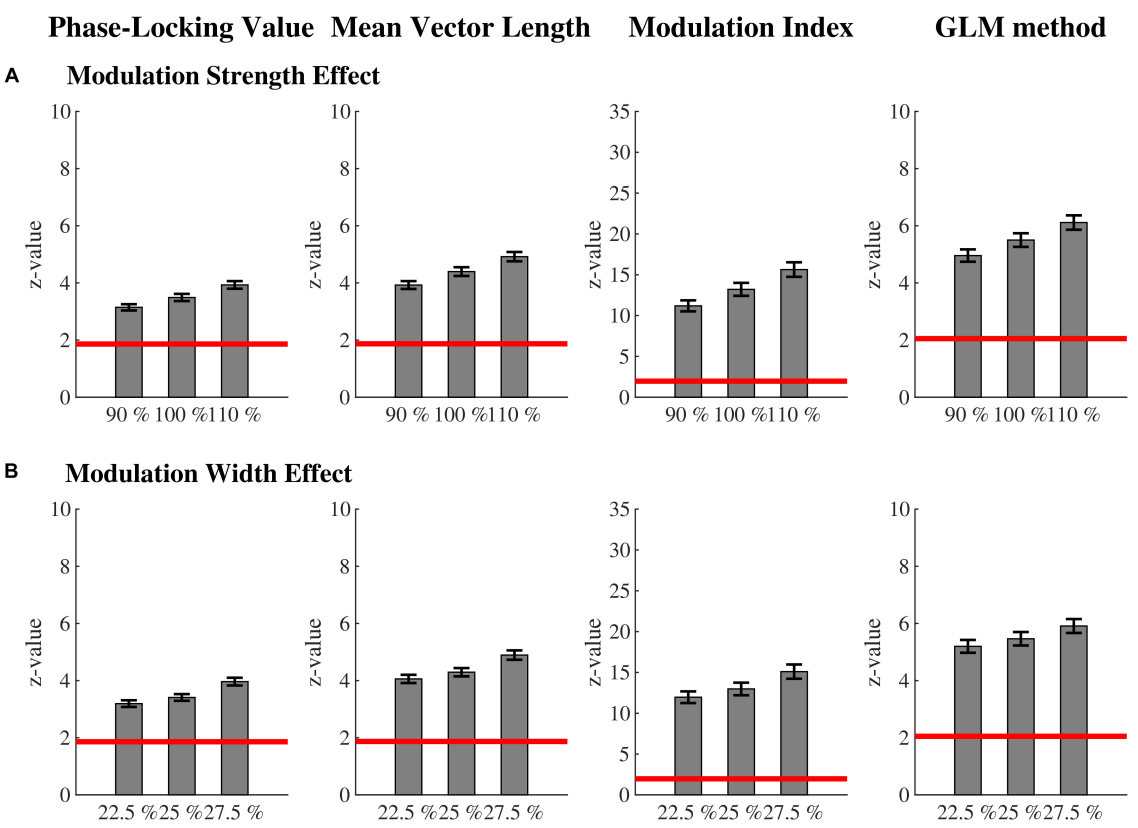

FIGURE 3 | Sensitivity for modulation strength and width: mean (± SEM) phase-amplitude coupling values for each method for the **(A)** modulation strength effect and **(B)** modulation width effect. Coupling values of all methods increased with increasing modulation strength. However, in addition to the GLM-CFC, MVL differentiates best between the different factor levels of modulation strength. Also, coupling values of all methods increased with increasing modulation width. Here, PLV and MVL differentiate best between the different factor levels of modulation width. The red line marks the critical z-value (significance level). All values above this line represent significant phase-amplitude coupling. For each effect, all factor levels within a method are significantly different from each other according to *post hoc t*-tests. Only monophasic coupling values are depicted for the PLV and the MVL.

[$F(6,594) = 79.45$, $p < 0.01$, $\omega^2 = 0.28$]. *Post hoc t*-tests showed that all factor levels within a method differed significantly from each other (all p's < 0.01). The effect of modulation width was most pronounced for the MVL ($0.19 < \omega^2 < 0.51$), followed by the PLV ($0.22 < \omega^2 < 0.48$). MI ($0.15 < \omega^2 < 0.44$) and GLM-CFC ($0.11 < \omega^2 < 0.45$) were least sensitive to modulation width.

Alpha-high gamma coupling (8–10 to 50–70 Hz)

Coupling values of all methods increased with increasing modulation width [$F(2,198) = 145.07$, $p < 0.01$, $\omega^2 = 0.49$]. The interaction method by modulation width became significant [$F(6,594) = 103.84$, $p < 0.01$, $\omega^2 = 0.34$; **Figure 3B**]. *Post hoc t*-tests showed that all factor levels within a method differed significantly from each other (all p's < 0.01). The effect of modulation width was most pronounced for the MVL ($0.11 < \omega^2 < 0.57$), followed by the PLV ($0.10 < \omega^2 < 0.54$) and the GLM-CFC ($0.11 < \omega^2 < 0.53$). The MI was least sensitive to modulation width ($0.12 < \omega^2 < 0.47$).

The broader the coupling width, the larger PLV, MVL, MI, and GLM-CFC are. Of all four methods, MVL differentiates best between the different factor levels of modulation width.

Effect of Multimodality on Phase-Amplitude Coupling Measures

Theta-low gamma coupling (5–7 to 33–47 Hz)

Monophasic coupling (4.89 ± 0.24) led to overall stronger coupling measures than biphasic coupling [2.36 ± 0.15; $F(1,99) = 586.81$, $p < 0.01$, $\omega^2 = 0.75$]. This interaction was further qualified by method [$F(3,297) = 73.81$, $p < 0.01$, $\omega^2 = 0.21$]. Biphasic coupling could not be detected by the PLV [2.42 ± 0.10 vs. 0.02 ± 0.01; $t(99) = 25.20$, $p < 0.01$, $\omega^2 = 0.76$] and MVL [3.04 ± 0.12 vs. 0.02 ± 0.01; $t(99) = 25.54$, $p < 0.01$, $\omega^2 = 0.77$]. The MI was larger in monophasic than in biphasic coupling [9.24 ± 0.53 vs. 6.41 ± 0.45; $t(99) = 18.54$, $p < 0.01$, $\omega^2 = 0.63$]. The GLM-CFC was as well larger in monophasic than in biphasic coupling [4.86 ± 0.22 vs. 2.96 ± 0.14; $t(99) = 21.90$, $p < 0.01$, $\omega^2 = 0.71$].

Alpha-high gamma coupling (8–10 to 50–70 Hz)

Monophasic coupling (7.54 ± 0.34) led to overall stronger coupling measures than biphasic coupling [3.89 ± 0.23; $F(1,99) = 782.07$, $p < 0.01$, $\omega^2 = 0.80$]. This interaction was further qualified by method [$F(3,297) = 74.41$, $p < 0.01$, $\omega^2 = 0.22$]. Biphasic coupling could not be detected by the PLV [3.52 ± 0.12 vs. 0.02 ± 0.01; $t(99) = 29.27$, $p < 0.01$, $\omega^2 = 0.81$] and MVL [4.41 ± 0.15 vs. 0.02 ± 0.01; $t(99) = 29.57$, $p < 0.01$, $\omega^2 = 0.81$]. The MI was larger in monophasic than in biphasic coupling [15.40 ± 0.83 vs. 11.29 ± 0.74; $t(99) = 19.22$, $p < 0.01$, $\omega^2 = 0.65$]. The GLM-CFC was as well larger in monophasic than in biphasic coupling [6.83 ± 0.28 vs. 4.22 ± 0.19; $t(99) = 24.78$, $p < 0.01$, $\omega^2 = 0.75$; **Figure 4A**].

That is, multimodality influences the four methods very differently. PLV and MVL cannot find biphasic coupling as it was implemented here (amplitude of the higher frequency was increased at peak and trough of the lower frequency). Because of the mathematic construct of the MVL (Eq. 2, **Figure 1B**) this is not surprising. Peak and trough appear on opposite sides in the polar plane: their mean will cancel each other out. If other forms of biphasic coupling would be present, the MVL could be able to find it, but would probably underestimate its strength and would furthermore return distorted phase information. Therefore, it is important to have a look at the polar plot before interpreting one's results. Similarly, the PLV cannot detect biphasic coupling, as it was implemented here. For biphasic coupling the amplitude envelope oscillates twice as fast as the lower frequency band. Because of this, the phase lag between lower and upper frequency band spans the entire polar plane. The MI and GLM-CFC are able to find biphasic coupling, but biphasic coupling leads to a reduction in the phase-amplitude coupling value; this undesirable reduction is stronger for the GLM-CFC than for the MI. Literature indicates that biphasic coupling plays a minor role in empirical data. To our knowledge only a very small fraction of studies report biphasic coupling (e.g., van der Meij et al., 2012; Leszczynski et al., 2015; Lega et al., 2016). Most studies report monophasic coupling (e.g., Tort et al., 2008).

Effect of Data Length on Phase-Amplitude Coupling Measures

Theta-low gamma coupling (5–7 to 33–47 Hz)

Coupling values of all methods increased with increasing data length [main effect data length: $F(2,198) = 390.95$, $p < 0.01$, $\omega^2 = 0.72$]. For the shortest epoch of 400 ms, none of the methods could detect significant coupling, even though it was engineered into the data. The interaction method by data length [$F(6,594) = 251.91$, $p < 0.01$, $\omega^2 = 0.56$] became significant. *Post hoc t*-tests showed that all factor levels within a method differed significantly from each other (all p's < 0.01). The data length effect was most pronounced for MVL ($0.60 < \omega^2 < 0.85$), and PLV ($0.57 < \omega^2 < 0.83$), followed by the GLM-CFC ($0.56 < \omega^2 < 0.77$). The MI was least affected by data length ($0.46 < \omega^2 < 0.62$).

Alpha-high gamma coupling (8–10 to 50–70 Hz)

Coupling values of all methods increased with increasing data length [main effect data length: $F(2,198) = 422.16$, $p < 0.01$, $\omega^2 = 0.74$]. For the shortest epoch of 400 ms, none of the methods could detect significant coupling, even though it was engineered into the data. The interaction method by data length [$F(6,594) = 270.73$, $p < 0.01$, $\omega^2 = 0.57$; **Figure 4B**] became significant. *Post hoc t*-tests showed that all factor levels within a method differed significantly from each other (all p's < 0.01). The data length effect was most pronounced for MVL ($0.75 < \omega^2 < 0.87$), and PLV ($0.73 < \omega^2 < 0.86$), followed by the GLM-CFC ($0.66 < \omega^2 < 0.79$). The MI was least affected by data length ($0.54 < \omega^2 < 0.62$).

Overall, the longer the data, the larger PLV, MVL, MI, and GLM-CFC are. This association was found in the data presented here, but must not generally apply. Here coupling was simulated continuously into the data. If coupling is transient and does not proportionally vary with data length, this relationship does not need to apply. Penny et al. (2008) showed, that coupling strength decreases for phase-amplitude coupling, which was simulated transiently. Potentially, the general rule is that the longer the data epochs where coupling occurs, the stronger the phase-amplitude coupling values. This should be tested in a

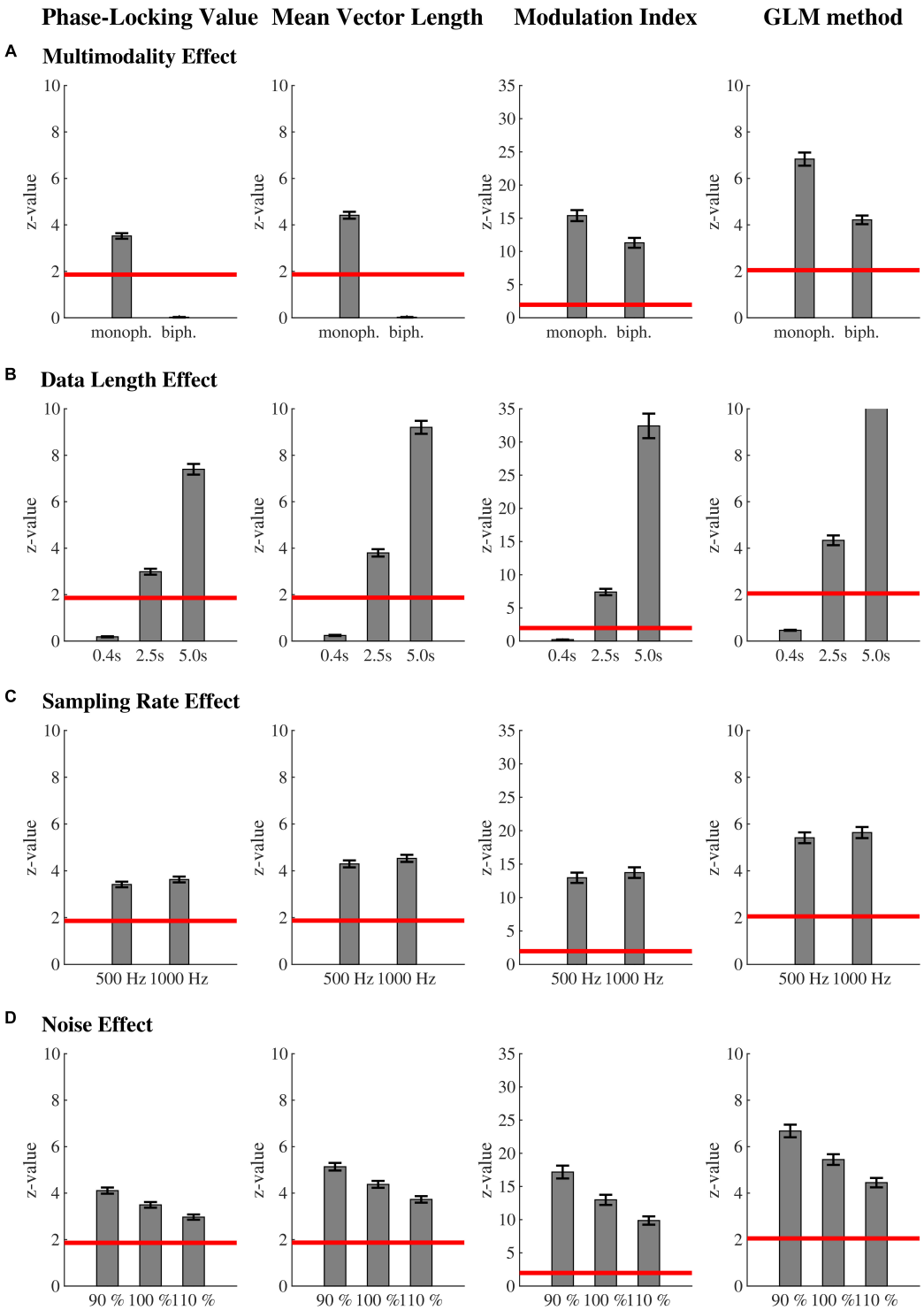

FIGURE 4 | Moderators of the phase-amplitude coupling measures: mean (± SEM) phase-amplitude coupling values for each method for the **(A)** multimodality effect, **(B)** data length effect, **(C)** sampling rate effect, and **(D)** noise effect. In contrast to the MI and GLM-CFC, biphasic coupling could not be detected by the PLV and MVL. This factor might turn out to be not as important, as most studies report monophasic coupling. Coupling values of all methods increased with increasing data length and slightly increase with sampling rate. Sampling rate only becomes relevant when analyzing frequencies close to the Nyquist frequency. Of all four methods, MI is least affected from the confounding factor data length. Coupling values of all methods decreased with increasing noise, while the PLV is least affected from this confounding factor. The red line marks the critical z-value (significance level). All values above this line represent significant phase-amplitude coupling. For each effect, all factor levels within a method are significantly different from each other according to *post hoc t*-tests. For **(B–D)** only monophasic coupling values are depicted for the PLV and the MVL.

follow-up analysis. This analysis further showed that a minimal data length is required for finding coupling, which should exceed at least 400 ms per trial when including 30 trials (also see Cheng et al., 2018). None of the methods were able to detect coupling in the shortest simulated epoch of 400 ms. It might be useful to develop a correction factor (e.g., similar to the pairwise phase consistency that is insensitive to data length variation; Vinck et al., 2010) for data length, to make phase-amplitude coupling values more comparable across studies. Of all four methods, MI is least affected from the confounding factor data length.

Effect of Sampling Rate on Phase-Amplitude Coupling Measures

Theta-low gamma coupling (5–7 to 33–47 Hz)

Sampling rate had no effect on any of the phase-amplitude coupling values [$F(1,99) = 0.10$, $p = 0.75$] and did not interact with method [$F(3,297) = 2.05$, $p = 0.15$].

Alpha-high gamma coupling (8–10 to 50–70 Hz)

Overall coupling values slightly increased with increasing sampling rate [$F(1,99) = 38.65$, $p < 0.01$, $\omega^2 = 0.16$]. The sampling rate effect differed according to the method [$F(3,297) = 27.80$, $p < 0.01$, $\omega^2 = 0.09$; **Figure 4C**]. It was most pronounced in GLM-CFC [$t(99) = 6.26$, $p < 0.01$, $\omega^2 = 0.16$], followed by the MI [$t(99) = 5.71$, $p < 0.01$, $\omega^2 = 0.14$]. PLV [$t(99) = 5.31$, $p < 0.01$, $\omega^2 = 0.12$] and mean vector [$t(99) = 5.28$, $p < 0.01$, $\omega^2 = 0.12$] length were least affected by sampling rate.

The factor sampling rate stands out because of its lacking effect for theta-low gamma coupling and comparatively small effect size for alpha-high gamma coupling. A third set of data was simulated testing PLV, MVL, and MI at 16–18 Hz for the modulating frequency and 202–238 Hz for the modulated frequency (for detailed results see Hülsemann, 2016). This analysis showed that sampling rate is indeed important, but only if the investigated upper frequency band approaches the Nyquist frequency (here 250 Hz). Of all four methods, MVL and PLV are least affected from the confounding factor sampling rate.

Effect of Noise on Phase-Amplitude Coupling Measures

Theta-low gamma coupling (5–7 to 33–47 Hz)

Coupling values of all methods decreased with increasing noise [$F(2,198) = 372.07$, $p < 0.01$, $\omega^2 = 0.71$]. The interaction method by noise became significant [$F(6,594) = 247.63$, $p < 0.01$, $\omega^2 = 0.55$]. *Post hoc t*-tests showed that all factor levels within a method differed significantly from each other (all p's < 0.01). The effect of noise was most pronounced for the GLM-CFC ($0.65 < \omega^2 < 0.75$). MVL ($0.42 < \omega^2 < 0.70$) and MI ($0.53 < \omega^2 < 0.62$) were intermediately affected. The PLV ($0.30 < \omega^2 < 0.65$) was least affected by noise.

Alpha-high gamma coupling (8–10 to 50–70 Hz)

Coupling values of all methods decreased with increasing noise [$F(2,198) = 417.74$, $p < 0.01$, $\omega^2 = 0.74$]. The interaction method by noise became significant [$F(6,594) = 290.04$, $p < 0.01$, $\omega^2 = 0.59$; **Figure 4D**]. *Post hoc t*-tests showed that all factor levels within a method differed significantly from each other (all p's < 0.01). The effect of noise was most pronounced for the GLM-CFC ($0.67 < \omega^2 < 0.79$). MVL ($0.50 < \omega^2 < 0.80$) and MI ($0.55 < \omega^2 < 0.66$) were intermediately affected. The PLV ($0.44 < \omega^2 < 0.76$) was least affected by noise.

Overall, the noisier the data, the lower PLV, MVL, MI, and GLM-CFC are. This aspect is not desired but plausible. Noise obscures the relation between the phase of the lower frequency and amplitude of the higher frequency. The data as a whole contains phase-amplitude coupling to a lesser extent, as the relative amount of noise compared to the relative amount of signal increases. Of all four methods, the GLM-CFC is most and the PLV is least affected from the confounding factor noise. The MVL is stronger affected than the MI.

Interaction Effects

Conducting six-way ANOVAs for each method separately (see Hülsemann, 2016 for detailed results), revealed ordinal interaction for all factors (multimodality, data length, sampling rate, noise, modulation strength, and modulation width). Especially multimodality and data length interacted with the remaining factors, as well as interacted with each other and the remaining factors. Sampling rate only showed significant interactions when analyzing frequencies close to the Nyquist frequency. All interactions had a monotone pattern, following the pattern of each main effect. For example, MVL increased the longer the data, but it increased less when also noise increases (**Figure 5**). This pattern was true for each added factor. Phase-locking value and MVL did not find biphasic coupling at all. Because of this, for these two methods, the described main effect and interaction patterns are only valid for monophasic, but not for biphasic coupling. For the MI and the GLM-CFC the pattern was true for mono- and for biphasic coupling.

We showed empirically that the methods were indifferent to the chosen frequency band combinations. To our knowledge, there is no mathematical reason for a frequency dependency of the methods [compare **Figure 1** showing calculation of all methods graphically and see sections "Phase-Locking-Value as Used in Mormann et al. (2005)," Mean Vector Length by Canolty et al. (2006)," Modulation Index by Tort et al. (2008)," and "GLM-CFC by Kramer and Eden (2013)"]. In order to facilitate the testing of methods, we provide our MATLAB script in **Appendix A**, in which the chosen frequency band combination and parameters can easily be adjusted.

The GLM-CFC behaves best regarding modulation strength and worst regarding noise compared with the three other methods. Regarding the other factors, its performance is in the intermediate range. The most important disadvantage of the GLM-CFC is its extremely high computation time, which exceeds those of the other methods by two (without calculating confidence intervals) or up to four orders of magnitude (with calculating confidence intervals). On a Windows 10 computer (64-bit operating system, CPU: Intel® Core ™i7-8700K, CPU 2 3.70 GHz 3.70 GHz, RAM: 16.0 GB) the calculation took on average 0.61 ms for the PLV, 0.67 ms for the MVL, 2.70 ms for the MI, 269.51 ms for the GLM-CFC (excluding the built-in confidence interval calculation), and 9159.08 ms for the GLM-CFC (including the built-in confidence interval calculation). Increasing

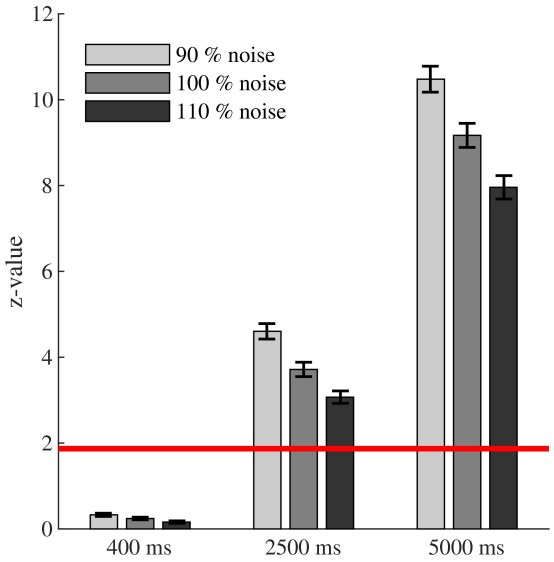

FIGURE 5 | Interaction effects between the moderators of the phase-amplitude coupling measures: mean (± SEM) phase-amplitude coupling values for the MVL for the data length by noise interaction (only monophasic coupling values). Interactions had a monotone pattern, following the pattern of each main effect. Depicted here, MVL increased the longer the data, but it increased less when also noise increased. This pattern was true for each added factor. The red line marks the critical z-value (significance level). All values above this line represent significant phase-amplitude coupling. For each method, all factor levels are significantly different from each other according to Dunn's *post hoc* test. Only values within the 400 ms condition do not differ between the noise levels.

data points increases computation time for all methods in a similar manner (e.g., doubling the data points doubles the computation time). Assuming, that this time-factor will lead to the exclusion of this method for most researchers, it is not further considered in the conclusion of this manuscript. For a more detailed review of this method, see Kramer and Eden (2013).

Comparing the remaining three methods it becomes evident that the MI is least affected by the confounding factors multimodality and data length. However, it is also – like the PLV – less sensitive to variation in modulations strength compared with the MVL. The MI is especially less sensitive to modulation width compared to the MVL and PLV. MVL and MI are similarly – and stronger than the PLV – affected by the confounding factor noise.

CONCLUSION

For long data epochs, recorded at high sampling rates, with a high signal-to-noise ratio, the use of the MVL is recommended, because it is more sensitive to modulation strength and width than both other methods. For noisier data, shorter data epochs, recorded at a lower sampling rate, the use of the MI is recommended, as it is least influenced by the confounding factors compared with both other methods. If it is not clear whether cross-frequency coupling will be mono- or bi-phasic, the MI should be used, even though literature suggests that biphasic coupling can be neglected.

The PLV does not stand out in comparison to the two other measures. So far, no review evaluated this measure explicitly as positive. Its usage is potentially problematic because phase information is extracted from the amplitude envelope of a signal. Phase information can only be correctly extracted from truly oscillating signals; this must not be necessarily the case for an amplitude envelope. However this disadvantage can be counteracted by filtering the amplitude envelope first before extracting phase information from it as is described (Vanhatalo et al., 2004).

Because MVL and MI have complementing strengths and weaknesses, it would be advisably to calculate both. The time-consuming aspect of measuring the two methods is permutation testing. Calculation of both measures on the other hand will not substantially increase the analysis time.

The MI is quantitatively larger than the PLV and MVL. However, even despite substantial quantitative differences in values, the qualitative decision for significance of phase-amplitude coupling is the same for all four methods in our simulation. Nevertheless, comparison of coupling strengths between the methods is problematic and this lack of comparability provides another reason for reporting both, MVL and MI.

In contrast to MVL, the false positive rate of the MI is not affected by any confounding factor. However, this advantage against MVL is counteracted by one disadvantage against the MVL: calculation of the MI includes Shannon's Entropy. The entropy value depends on the amount of bins as well as amount of data squeezed into the same amount of bins. This is an undesirable degree of freedom, which is not present when calculating the MVL.

Due to the dependency on confounding variables (e.g., data length), comparing absolute coupling strengths across studies might be difficult even if using the same method. Comparisons within one study, on the other hand, can be done with confidence. Nevertheless, one should make sure that signal-to-noise ratio is comparable within all experimental conditions and over the course of the experiment.

Generally, it is advisable to work with standardized phase-amplitude coupling measures via permutation testing. It facilitates the interpretation of the measures, first and foremost, by giving the researcher knowledge about the probability that the observed MI would have been also found under the assumption of the null-hypothesis. This aspect is often ignored in the literature.

Kramer and Eden (2013) stated that "an optimal analysis method to assess this cross-frequency coupling (CFC) does not yet exist" (p. 64). Even if it would be ideal, to have a measure that is less susceptible to confounding variables summarizing this analysis, it should be rather concluded that at least two reasonable analysis methods exist.

AUTHOR CONTRIBUTIONS

MH conducted the data simulation and performed the statistical analysis. MH, EN, and BR wrote the manuscript. All authors contributed to manuscript revision, read and approved the submitted version.

FUNDING

This project has received funding from the Research Focus "Psychobiology of Stress" within the research initiative of the state Rhineland-Palatinate by the Ministry of Science and from the European Research Council (ERC) under the European Union's Horizon 2020 Research and Innovation Programme (Grant Agreement No. 677875). Both funding Institutions had no further role in the study design, the collection, analysis, and interpretation of data, the writing of the manuscript, and the decision to submit the paper for publication. The work was performed at Trier University, Faculty I – Psychology, Department of General Psychology and Methodology.

ACKNOWLEDGMENTS

Parts of this study are published in the doctoral dissertation of MH (Hülsemann, 2016).

SUPPLEMENTARY MATERIAL

The Supplementary Material for this article can be found online at: https://www.frontiersin.org/articles/10.3389/fnins.2019.00573/full#supplementary-material

REFERENCES

Aru, J., Aru, J., Priesemann, V., Wibral, M., Lana, L., Pipa, G., et al. (2015). Untangling cross-frequency coupling in neuroscience. *Cur. Opin. Neurobiol.* 31, 51–61. doi: 10.1016/j.conb.2014.08.002

Berman, J. I., McDaniel, J., Liu, S., Cornew, L., Gaetz, W., Roberts, T. P., et al. (2012). Variable bandwidth filtering for improved sensitivity of cross-frequency coupling metrics. *Brain Connect.* 2, 155–163. doi: 10.1089/brain.2012.0085

Bruns, A., and Eckhorn, R. (2004). Task-related coupling from high- to low-frequency signals among visual cortical areas in human subdural recordings. *Int. J. Psychophysiol.* 51, 97–116. doi: 10.1016/j.ijpsycho.2003.07.001

Burgess, A. P., and Ali, L. (2002). Functional connectivity of gamma EEG activity is modulated at low frequency during conscious recollection. *Int. J. Psychophysiol.* 46, 91–100. doi: 10.1016/S0167-8760(02)00108-3

Canolty, R. T., Edwards, E., Dalal, S. S., Soltani, M., Nagarajan, S. S., Kirsch, H. E., et al. (2006). High gamma power is phase-locked to theta oscillations in human neocortex. *Science* 313, 1626–1628. doi: 10.1126/science.1128115

Cheng, N., Li, Q., Wang, S., Wang, R., and Zhang, T. (2018). permutation mutual information: a novel approach for measuring neuronal phase-amplitude coupling. *Brain Topogr.* 31, 186–201. doi: 10.1007/s10548-017-0599-2

Cohen, M. X. (2008). Assessing transient cross-frequency coupling in EEG data. *J. Neurosci. Methods* 168, 494–499. doi: 10.1016/j.jneumeth.2007.10.012

Cohen, M. X. (2014). *Analyzing Neural Time Series Data: Theory and Practice*. Massachusetts, MA: The MIT Press.

Dunn, O. J. (1961). Multiple comparisons among means. *J. Am. Statist. Assoc.* 56, 52–64. doi: 10.1080/01621459.1961.10482090

Dvorak, D., and Fenton, A. A. (2014). Toward a proper estimation of phase-amplitude coupling in neural oscillations. *J. Neurosci. Methods* 225, 42–56. doi: 10.1016/j.jneumeth.2014.01.002

Geisser, S., and Greenhouse, S. W. (1958). An extension of box's results on the use of the f distribution in multivariate analysis. *Ann. Math. Statist.* 29, 885–891. doi: 10.1214/aoms/1177706545

Hays, W. L. (1973). *Statistics for the Social Sciences*. New York, NY: Holt, Rinehart and Winston.

He, B. J., Zempel, J. M., Snyder, A. Z., and Raichle, M. E. (2010). The temporal structures and functional significance of scale-free brain activity. *Neuron* 66, 353–369. doi: 10.1016/j.neuron.2010.04.020

Hülsemann, M. J. (2016). *The Role of Phase-Amplitude Coupling in the Relationship between Acute Stress and Executive Functions*. [dissertation]. Trier: Universität Trier.

Jensen, O. (2006). Maintenance of multiple working memory items by temporal segmentation. *Neuroscience* 139, 237–249. doi: 10.1016/j.neuroscience.2005.06.004

Jensen, O., and Lisman, J. E. (1998). An oscillatory short-term memory buffer model can account for data on the Sternberg task. *J. Neurosci.* 18, 10688–10699. doi: 10.1523/jneurosci.18-24-10688.1998

Kramer, M. A., and Eden, U. T. (2013). Assessment of cross-frequency coupling with confidence using generalized linear models. *J. Neurosci. Methods* 220, 64–74. doi: 10.1016/j.jneumeth.2013.08.006

Lakatos, P., Shah, A. S., Knuth, K. H., Ulbert, I., Karmos, G., and Schroeder, C. E. (2005). An oscillatory hierarchy controlling neuronal excitability and stimulus processing in the auditory cortex. *J. Neurophysiol.* 94, 1904–1911. doi: 10.1152/jn.00263.2005

Lega, B., Burke, J., Jacobs, J., and Kahana, M. J. (2016). Slow-theta-to-gamma phase-amplitude coupling in human hippocampus supports the formation of new episodic memories. *Cereb. Cortex* 26, 268–278. doi: 10.1093/cercor/bhu232

Leszczynski, M., Fell, J., and Axmacher, N. (2015). Rhythmic working memory activation in the human hippocampus. *Cell Rep.* 13, 1272–1282. doi: 10.1016/j.celrep.2015.09.081

Lisman, J. E., and Jensen, O. (2013). The theta-gamma neural code. *Neuron* 77, 1002–1016. doi: 10.1016/j.neuron.2013.03.007

Luck, S. J. (2014). *An Introduction to the Event-Related Potential Technique*. Cambridge: The MIT Press.

Maris, E., van Vugt, M., and Kahana, M. (2011). Spatially distributed patterns of oscillatory coupling between high-frequency amplitudes and low-frequency phases in human iEEG. *NeuroImage* 54, 836–850. doi: 10.1016/j.neuroimage.2010.09.029

Martínez-Cancino, R., Heng, J., Delorme, A., Kreutz-Delgado, K., Sotero, R. C., and Makeig, S. (2019). Measuring transient phase-amplitude coupling using local mutual information. *NeuroImage* 185, 361–378. doi: 10.1016/j.neuroimage.2018.10.034

Miller, K. J., Sorensen, L. B., Ojemann, J. G., and den Nijs, M. (2009). Power-law scaling in the brain surface electric potential. *PLoS Computat. Biol.* 5:e1000609. doi: 10.1371/journal.pcbi.1000609

Mormann, F., Fell, J., Axmacher, N., Weber, B., Lehnertz, K., Elger, C. E., et al. (2005). Phase/amplitude reset and theta-gamma interaction in the human medial temporal lobe during a continuous word recognition memory task. *Hippocampus* 15, 890–900. doi: 10.1002/hipo.20117

Novak, P., Lepicovska, V., and Dostalek, C. (1992). Periodic amplitude modulation of EEG. *Neurosci. Lett.* 136, 213–215. doi: 10.1016/0304-3940(92)90051-8

Onslow, A. C. E., Bogacz, R., and Jones, M. W. (2011). Quantifying phase-amplitude coupling in neuronal network oscillations. *Progr. Biophy. Mol. Biol.* 105, 49–57. doi: 10.1016/j.pbiomolbio.2010.09.007

Özkurt, T. E., and Schnitzler, A. (2011). A critical note on the definition of phase-amplitude cross-frequency coupling. *J. Neurosci. Methods* 201, 438–443. doi: 10.1016/j.jneumeth.2011.08.014

Penny, W. D., Duzel, E., Miller, K. J., and Ojemann, J. G. (2008). Testing for nested oscillation. *J. Neurosci. Methods* 174, 50–61. doi: 10.1016/j.jneumeth.2008.06.035

Pfurtscheller, G. (1976). Ultralangsame schwankungen innerhalb der rhythmischen aktivität im alpha-band und deren mögliche ursachen. *Pflugers Arch.* 367, 55–66. doi: 10.1007/BF00583657

Rasch, B., Friese, M., Hofmann, W., and Naumann, E. (2006). *Quantitative Methoden 2: Einführung in die Statistik*. Berlin: Springer.

Samiee, S., and Baillet, S. (2017). Time-resolved phase-amplitude coupling in neural oscillations. *NeuroImage* 159, 270–279. doi: 10.1016/j.neuroimage.2017.07.051

Sotero, R. C. (2016). Topology, cross-frequency, and same-frequency band interactions shape the generation of phase-amplitude coupling in a neural mass model of a cortical column. *PLoS Computat. Biol.* 12:e1005180. doi: 10.1371/journal.pcbi.1005180

Tort, A. B. L., Komorowski, R., Eichenbaum, H., and Kopell, N. (2010). Measuring phase-amplitude coupling between neuronal oscillations of different frequencies. *J. Neurophysiol.* 104, 1195–1210. doi: 10.1152/jn.00106.2010

Tort, A. B. L., Kramer, M. A., Thorn, C., Gibson, D. J., Kubota, Y., Graybiel, A. M., et al. (2008). Dynamic cross-frequency couplings of local field potential oscillations in rat striatum and hippocampus during performance of a T-maze task. *Proc. Natl. Acad. Sci. U.S.A.* 105, 20517–20522. doi: 10.1073/pnas.0810524105

van der Meij, R., Kahana, M., and Maris, E. (2012). Phase-amplitude coupling in human electrocorticography is spatially distributed and phase diverse. *J. Neurosci.* 32, 111–123. doi: 10.1523/JNEUROSCI.4816-11.2012

Vanhatalo, S., Palva, J. M., Holmes, M. D., Miller, J. W., Voipio, J., and Kaila, K. (2004). Infraslow oscillations modulate excitability and interictal epileptic activity in the human cortex during sleep. *Proc. Natl. Acad. Sci. U.S.A.* 101, 5053–5057. doi: 10.1073/pnas.0305375101

Vinck, M., van Wingerden, M., Womelsdorf, T., Fries, P., and Pennartz, C. M. A. (2010). The pairwise phase consistency: A bias-free measure of rhythmic neuronal synchronization. *NeuroImage* 51, 112–122. doi: 10.1016/j.neuroimage.2010.01.073

Vosskuhl, J., Huster, R. J., and Herrmann, C. S. (2015). Increase in short-term memory capacity induced by down-regulating individual theta frequency via transcranial alternating current stimulation. *Front. Hum. Neurosci.* 9:257. doi: 10.3389/fnhum.2015.00257

Widmann, A., Schröger, E., and Maess, B. (2015). Digital filter design for electrophysiological data – a practical approach. *J. Neurosci. Methods* 250, 34–46. doi: 10.1016/j.jneumeth.2014.08.002

Zhivomirov, H. (2013). Pink, red, blue and violet noise generation with matlab implementation. Available at: http://www.mathworks.com/matlabcentral/fileexchange/42919-pink--red--blue-and-violet-noise-generation-with-matlab-implementation/content/rednoise.m, (accessed April 17),

Zhivomirov, H. (2018). A method for colored noise generation. *Roman. J. Acous. Vibration* 1, 14–19.

Conflict of Interest Statement: The authors declare that the research was conducted in the absence of any commercial or financial relationships that could be construed as a potential conflict of interest.

Copyright © 2019 Hülsemann, Naumann and Rasch. This is an open-access article distributed under the terms of the Creative Commons Attribution License (CC BY). The use, distribution or reproduction in other forums is permitted, provided the original author(s) and the copyright owner(s) are credited and that the original publication in this journal is cited, in accordance with accepted academic practice. No use, distribution or reproduction is permitted which does not comply with these terms.

frontiers in Neuroscience

ORIGINAL RESEARCH
published: 07 June 2019
doi: 10.3389/fnins.2019.00536

Diffusion MRI: Assessment of the Impact of Acquisition and Preprocessing Methods Using the BrainVISA-Diffuse Toolbox

*Lucile Brun, Alexandre Pron, Julien Sein, Christine Deruelle and Olivier Coulon**

Institut de Neurosciences de La Timone, Aix-Marseille University, CNRS, UMR 7289, Marseille, France

Diffusion MR images are prone to severe geometric distortions induced by head movement, eddy-current and inhomogeneity of magnetic susceptibility. Various correction methods have been proposed that depend on the choice of the acquisition settings and potentially provide highly different data quality. However, the impact of this choice has not been evaluated in terms of the ratio between scan time and preprocessed data quality. This study aims at investigating the impact of six well-known preprocessing methods, each associated to specific acquisition settings, on the outcome of diffusion analyses. For this purpose, we developed a comprehensive toolbox called *Diffuse* which automatically guides the user to the best preprocessing pipeline according to the input data. Using MR images of 20 subjects from the HCP dataset, we compared the six pre-processing pipelines regarding the following criteria: the ability to recover brain's true geometry, the tensor model estimation and derived indices in the white matter, and finally the spatial dispersion of six well known connectivity pathways. As expected the pipeline associated to the longer acquisition fully repeated with reversed phase-encoding (RPE) yielded the higher data quality and was used as a reference to evaluate the other pipelines. In this way, we highlighted several significant aspects of other pre-processing pipelines. Our results first established that eddy-current correction improves the tensor-fitting performance with a localized impact especially in the corpus callosum. Concerning susceptibility distortions, we showed that the use of a field map is not sufficient and involves additional smoothing, yielding to an artificial decrease of tensor-fitting error. Of most importance, our findings demonstrate that, for an equivalent scan time, the acquisition of a b0 volume with RPE ensures a better brain's geometry reconstruction and local improvement of tensor quality, without any smoothing of the image. This was found to be the best scan time/data quality compromise. To conclude, this study highlights and attempts to quantify the strong dependence of diffusion metrics on acquisition settings and preprocessing methods.

Keywords: brain, DWI, distortions, preprocessing, toolboxc

OPEN ACCESS

Edited by:
John Ashburner,
University College London,
United Kingdom

Reviewed by:
Bennett Allan Landman,
Vanderbilt University, United States
Stamatios Sotiropoulos,
University of Nottingham,
United Kingdom

***Correspondence:**
Olivier Coulon
olivier.coulon@univ-amu.fr

Specialty section:
This article was submitted to Brain Imaging Methods, a section of the journal Frontiers in Neuroscience

Received: *18 December 2018*
Accepted: *08 May 2019*
Published: *07 June 2019*

Citation:
Brun L, Pron A, Sein J, Deruelle C and Coulon O (2019) Diffusion MRI: Assessment of the Impact of Acquisition and Preprocessing Methods Using the BrainVISA-Diffuse Toolbox. Front. Neurosci. 13:536. doi: 10.3389/fnins.2019.00536

Abbreviations: FS, full-sphere; HCP, Human Connectome Project; HS, half-sphere; MMI, Mattes Mutual Information; RPE, Reverse Phase Encoding; TFE, Tensor Fitting Error.

INTRODUCTION

Diffusion-weighted imaging (DWI) has established itself as a reference technique for the *in vivo* inference of structural brain connectivity and for the investigation of white matter microstructure (Hagmann et al., 2010; Ghosh and Deriche, 2016). If echo-planar imaging (EPI) sequences, commonly used in DWI, provide a high signal to noise ratio (SNR) and rapid scan time, they are nonetheless prone to severe artifacts such as non-zero off-resonance fields (Le Bihan et al., 2006) stemming from the discontinuity of magnetic susceptibility of the tissues and from eddy-currents induced in the nearby conductors. The low bandwidth in the phase-encode direction makes EPI sequences particularly sensitive to these two artifacts which disrupt the spatial encoding gradients (Schmitt et al., 1998). These artifacts can thus induce important geometric distortions due to a voxel-shift in the signal reconstruction, which may lead to wrong interpretations if not corrected properly (Embleton et al., 2010; Yendiki et al., 2014). Despite important technical advances to achieve high quality diffusion signal modeling and fibers reconstruction (e.g., Auría et al., 2015; Ning et al., 2015; Girard et al., 2017; Bastiani et al., 2019), the quality of the preprocessing is should not be neglected (Jones and Cercignani, 2010). Yet, last advances in this area have mostly concerned research-type acquisition protocols (Sotiropoulos et al., 2013; Glasser et al., 2016; Bastiani et al., 2017). Transfer from research to clinical context is still limited because of the complexity of correction methods.

Magnetic susceptibility differences between tissue, air and bone alter the B0 magnetic field and result in local MR frequency variations at tissue interfaces such as the sphenoid sinus, temporal lobe and brain stem. Such susceptibility-induced gradients interfere with the spatial encoding gradients and may cause signal dropout and geometric distortions. Susceptibility-induced distortions do not depend on diffusion gradients and remain constant across volumes, assuming that head movements are not excessive. The susceptibility-induced distortions can be corrected either by measuring the magnetic field at the acquisition using an additional sequence or by estimating it *a posteriori*. The former approach – field map-based – consists in an additional double-echo acquisition (Jezzard and Balaban, 1995; Reber et al., 1998) where the phase difference between the two echoes is used to estimate a B0 field map. This field map is used to estimate the non-linear voxel-wise shift and the signal loss. This method, however, suffers from the non-linearity of susceptibility-induced distortions that causes neighboring voxels to collapse into a single one resulting in an ill-posed problem of intensity retrieval and a potential loss of information (Jones and Cercignani, 2010). In the latter approach – image-based – the distorted magnetic field can be estimated in two ways. One way consists in computing the non-linear deformation field between diffusion-weighted and anatomical (T1 or T2) images, which suffers the same issues as the field map-based approach. The other way consists in acquiring additional non-diffusion weighted volumes with reversed phase-encode direction (FSb0RPE) (Andersson et al., 2003). In this way, the complementary information contained by opposed FSb0RPE images allow recovering the full intensity information.

Diffusion-weighted imaging is also affected by eddy current artifacts due to the rapid switch of strong diffusion encoding gradients which generates electric currents in the nearby conductors, inducing local magnetic fields that interfere with the spatial encoding gradient (Jezzard et al., 1998). Eddy-current artifacts typically induce shearing, stretching and/or compression along the phase-encode direction which add up to the motion-induced translations and rotations and lead to a misalignment between successive volumes. Unlike magnetic susceptibility induced distortions, these effects vary across diffusion gradient orientations and are enhanced by the fact that higher b-values require the application of stronger diffusion gradients for longer periods. To a first approximation, eddy-currents can be considered as originating from a linear combination of the linear gradient coil fields. Hence, a simple affine transformation can be applied to correct for eddy-current induced distortions as well as head movements (Haselgrove and Moore, 1996). This method does not require any specific acquisition but is less appropriate for high *b*-value associated to signal attenuation and increased contrast variation between images (Ben-Amitay et al., 2012) where the affine registration fails to correct the eddy-currents completely. Furthermore, the linear assumption is no longer verified for modern scanners where stronger gradients have a high degree of non-linearity (Haselgrove and Moore, 1996). Indeed, authors in Rohde et al. (2004) and Andersson and Sotiropoulos (2016) have shown that higher order models provided a better fit of the off-resonance field caused by eddy-currents. To correct properly reconstruct the signal intensity, such techniques exploit the fact that two images acquired with reversed diffusion gradient directions or reversed phase-encoding (RPE) directions would have similar diffusion contrast but reversed eddy-current distortions (e.g., Bodammer et al., 2004; Shen et al., 2004; Embleton et al., 2010). These reversed gradient methods require at least that gradients are sampled over the full sphere or that each diffusion gradient is repeated twice with reversed polarity.

This interdependence between a variety of acquisition settings and a variety of correction methods can result in very different diffusion metric assessments and connectivity inferences. Therefore, the choice of acquisition settings has obviously a crucial role in the interpretation of results. This choice – usually driven by the time constraint typically different between clinical and research contexts – should also be done in the light of analyses comparing its influence on final diffusion measurements. For instance, for an equivalent time cost, it is yet debatable whether the acquisition of a B0 field map image would conduct to a better data quality than the acquisition of a single b0 volume with reversed phase encoding direction. Conversely, in a context of uncontrolled external acquisition such as for public or multicentric datasets, the limitations inherent to the quality of the associated pre-treatments are still poorly documented. To date, quantitative comparisons of preprocessing techniques have only been performed in a clinical (e.g., Cusack et al., 2003;

Wang et al., 2017) or a research context (e.g., Rohde et al., 2004). A comprehensive evaluation of the existing and widely used preprocessing methods and their dependence on acquisition settings is still needed.

In the current study, we adopt a holistic approach, to quantify the influence of various acquisition settings and the entire associated preprocessing pipeline on typical DWI measurements, including diffusion and tractography quantification. A holistic approach is crucial for two reasons. First, for a given configuration of acquisition settings, it should help orienting the interpretation of results as well as any inter-study comparison according to the limitations imposed by the corresponding preprocessing methods. Second, for a given scope of analysis, it should guide the choice of acquisition settings in the light of the best data quality for acquisition time constrain. For this purpose, we developed a dedicated and comprehensive toolbox called *Diffuse* which, out of six different preprocessing pipelines, automatically selects the one most adapted to the acquisition settings. *Diffuse* also includes registration methods as well as post-processing methods to perform local signal modeling and tractography. Six different types of acquisition settings were chosen because they are widely used in the literature ranging from clinical to research contexts, and each of them matches to a known dedicated preprocessing pipeline. We selected MRI data of 20 subjects from the HCP database (Van Essen et al., 2013) which is, to our knowledge, the only database that includes all the data necessary to conduct this work. To relate the same experiments in a clinical context, we also acquired a similar acquisition set for one healthy subject in a standard 3T scanner and with lower spatial resolution. In the next section, we describe the six subsets extracted from these data as well as the preprocessing pipelines involved. Then, an overall comparison of the distortion correction pipelines is performed through four different experiments. First, we quantified their ability to recover brain geometry, which is an important step in the normalization process for group measurements, using a similarity measure between the corrected DWI and T1w images. Second, both qualitative and quantitative metrics were used to assess the influence of preprocessing pipelines on the quality of diffusion tensor estimation in white-matter tissues. The same experiment was then performed at a local scale to evaluate the impact on central white-matter regions that are of major interest for pathology studies and used as seeds for tractography. Finally, we used a quantitative metric of tract spatial dispersion to evaluated the distal impact of preprocessing pipelines on the reconstruction of six well-known bundles.

PREPROCESSING PIPELINES

Data

HCP Dataset

The HCP dataset (Van Essen et al., 2013) was found as the only publicly available database including every MRI sequences and acquisition settings necessary to pre-process images through the six pipelines. MRI data of 20 participants were used in this study (subject IDs are listed in the Section "Annexe"). All individuals were right-handed males (age range 25–30). Images were acquired using a modified version of Siemens Skyra 3T scanner (Siemens, Erlangen, Germany) with a maximum gradient strength of 100 mT/m, slew rate of 200 T/m/s and a 32-channel head coil. T1-weighted images were acquired using 3D MPRAGE sequence (TR/TE = 2400/2.14 ms, flip angle = 8°, FOV = 224 × 224 mm^2, resolution = 0.7 mm isotropic). Diffusion-weighted images were acquired with a spin-echo EPI sequence consisting of 3 shells of 90 diffusion-weighted volumes each (b = 1000, 2000, and 3000 s/mm^2) and 6 interleaved b0 volumes each (TR/TE = 5520/89.5 ms, resolution: 1.25 mm isotropic, FOV = 210 × 180 mm^2, 111 axial slices, multiband factor = 3, partial Fourier = 6/8, echo spacing = 0.78 ms). Gradients directions were sampled over the entire sphere, using the electrostatic repulsion method (Caruyer et al., 2013). The entire diffusion sequence was repeated twice with RPE (L- > R, R- > L). A B0 field map image was also acquired using a dual-echo gradient-echo sequence (with delta TE = 2.46 ms, resolution: 2 mm isotropic). Note that the DW images were acquired during a different session from the T1 and field map images. Different subsets of these data were extracted in order to be compatible with the requirements of the six preprocessing pipelines, as detailed in **Table 1**. In particular, to be comparable, the 6 subsets share the same basis consisting in 3 shells of 90 gradient directions and 6 b0 volumes.

Clinical Dataset

The MRI images of a healthy volunteer were acquired using the same sequences with clinical settings. Results from this clinical dataset have no statistical value and are shown to illustrate the consistency of the results even with data other than high quality HCP scans. In particular, we used this data to illustrate the impact of b-value and spatial resolution on the same analyses. A thorough description of the acquisition settings and results can be found in **Supplementary Material S1**.

Data Processing: The *Diffuse* Toolbox

Diffuse is a BrainVISA toolbox, written in the Python language dedicated to diffusion MRI processing and publicly available on Github[1]. *Diffuse* relies on algorithms from FSL[2] (Jenkinson et al., 2012), Dipy[3]. (Garyfallidis et al., 2014), Niftyreg[4]. (Modat et al., 2010) and on functionalities provided by the BrainVISA software platform[5] for neuroimaging (Geffroy et al., 2011). This platform already offers several processing pipelines for other modalities such as structural and functional MRI. In particular, an anatomical pipeline gives access to segmented T1w images, cortical surface meshes and a number of tools providing morphometric and functional measurements on the surface. BrainVISA includes the Anatomist software (Rivière et al., 2011) for visualization and interaction with all associated data formats.

[1]https://github.com/MecaLab/Brainvisa-Diffuse

[2]http://fsl.fmrib.ox.ac.uk/

[3]http://nipy.org/dipy/

[4]http://cmictig.cs.ucl.ac.uk/wiki/index.php/NiftyReg

[5]http://brainvisa.info

TABLE 1 | Acquisition data subsets extracted for each of the six preprocessing pipelines.

Pipeline name	HS	HSfmap	FS	FSfmap	FSb0RPE	FSfullRPE
3 × 90 DW images (L -> R)	•	•	•	•	•	•
3 × 6 b = 0 images (L -> R)	•	•	•	•	•	•
3 × 90 DW images (R -> L)						•
3 × 6 b = 0 images (R -> L)					•	•
B0 field map image		•		•		
Total number of volumes	288	288+1	288	288+1	306	576
Scan duration	∼26 mn	∼26 mn + 2 mn15	∼26 mn	∼26 mn + 2 mn15	∼28 mn	∼53 mn

Example for the HCP dataset. Note that HS and FS pipelines use the same data subset with 3 shells of 90 diffusion gradients directions and 6 b0 volumes each.

All processes can be operated under a unified graphical user interface or as batch and using parallel distribution for processing groups of subjects.

T1w MR images were processed using BrainVISA's Morphologist pipeline, dedicated to the processing of anatomical images (Fischer et al., 2012), to obtain bias corrected T1w images as well as brain extraction, gray and white matter masks and cortical surface meshes. Diffusion-weighted images were processed through the Diffuse workflow described in **Figure 1**. It consists in four steps that are detailed below: (1) importation and reorientation of data, (2) distortion corrections, (3) structural to diffusion space registration and (4) diffusion model estimation and tractography.

Importation and Reorientation of Data

Data files are stored into a database to facilitate filesystem organization and indexation. This is an important practical aspect in the management of diffusion data with various complex data types and, in our case, for testing multiple processing using varying parameters. While input files are imported into the BrainVISA database, the storage orientation of DWI data and gradients vectors are changed to the neurological convention (RAS+)[6] which is supported by both FSL and Dipy tools.

Distortion Corrections

Motion and eddy-currents induced distortions

Motion and eddy-current-induced distortions were corrected using three different methods.

The first method consists in using an affine registration, considering the distortions as a linear combination of translation, rotation, scaling and shearing. In *Diffuse*, we implemented a method called ECCAR (Eddy-Currents Correction by Affine Registration), derived from the previous '*eddy_correct*' tool of FSL (version 5.0.9 and anterior), to align all diffusion-weighted images to the first non-diffusion weighted volume using a two-step approach. To ensure minimal error due to intensity differences between b0 and T1w images (Rohde et al., 2004; Ben-Amitay et al., 2012), volumes are first aligned to the closest interspersed b0 volumes, which are in turn aligned to the first one. For the same reason, we used the mutual information cost function which is adapted to multimodal registration. The two transformations are combined to apply a single resampling to each volume, with a spline interpolation. This single correction step does not require any additional acquisition and constitutes the first preprocessing pipeline called hereafter "**HS pipeline**" (Half-Sphere), in contrast to the full-sphere sampling condition required for the following methods. Note, however, that in this article, for comparison purpose, we applied this pipeline to the first subset of DWI data containing 90 multi-shell diffusion gradient directions sampled over the full sphere and 6 b0 volumes with LR phase-encoding direction.

The second method uses the fact that gradients directions have been sampled over the full sphere. With a sufficient number of samples, images with quasi-opposed gradients directions can be considered with opposed distortions. This method implemented in *Diffuse* calls the '*eddy*' tool from the FSL software (Andersson and Sotiropoulos, 2016). Using pairs of volumes with close orientation but quasi-opposed polarity of diffusion gradients, the algorithm applies a non-parametric Gaussian Process to estimate a higher order distortion field caused by both eddy-currents and motion and recover the midway geometry in the image. During the final resampling, a spline interpolation is combined with a Jacobian modulation to account for signal dilution in areas with stretching. This single correction step constitutes the preprocessing pipeline called hereafter "**FS pipeline**" (Full-Sphere) and could be applied to the same first subset. The method is also embedded in two other pipelines, depending on the magnetic susceptibility-induced distortion method that is used in conjunction, as described in the next sub-section.

The third method also calls the *'eddy'* tool from FSL, but with a different resampling technique. The repetition of all diffusion gradient directions using the RPE direction RL provides a mean to resolve signal intensity recovery in compressed areas where signal has piled-up, with a least-squares reconstruction (Andersson and Sotiropoulos, 2016). This method leads to the pipeline called hereafter "**FSfullRPE.**" It should be emphasized, however, that this method requires twice as much acquisition time as compared to the two methods described above.

Note that in the three methods, to preserve the directional information of DWI data, the diffusion gradient vectors are reoriented using the same rotation parameters used to transform each volume during motion and eddy-current correction. This step is critical to correctly estimate the diffusion parameters and fiber orientation (Leemans and Jones, 2009; Jones and Cercignani, 2010).

[6]RAS+ stands for positive RAS orientation of axes such that X axis goes from left to right, Y axis goes from posterior to anterior and Z axis goes from inferior to superior.

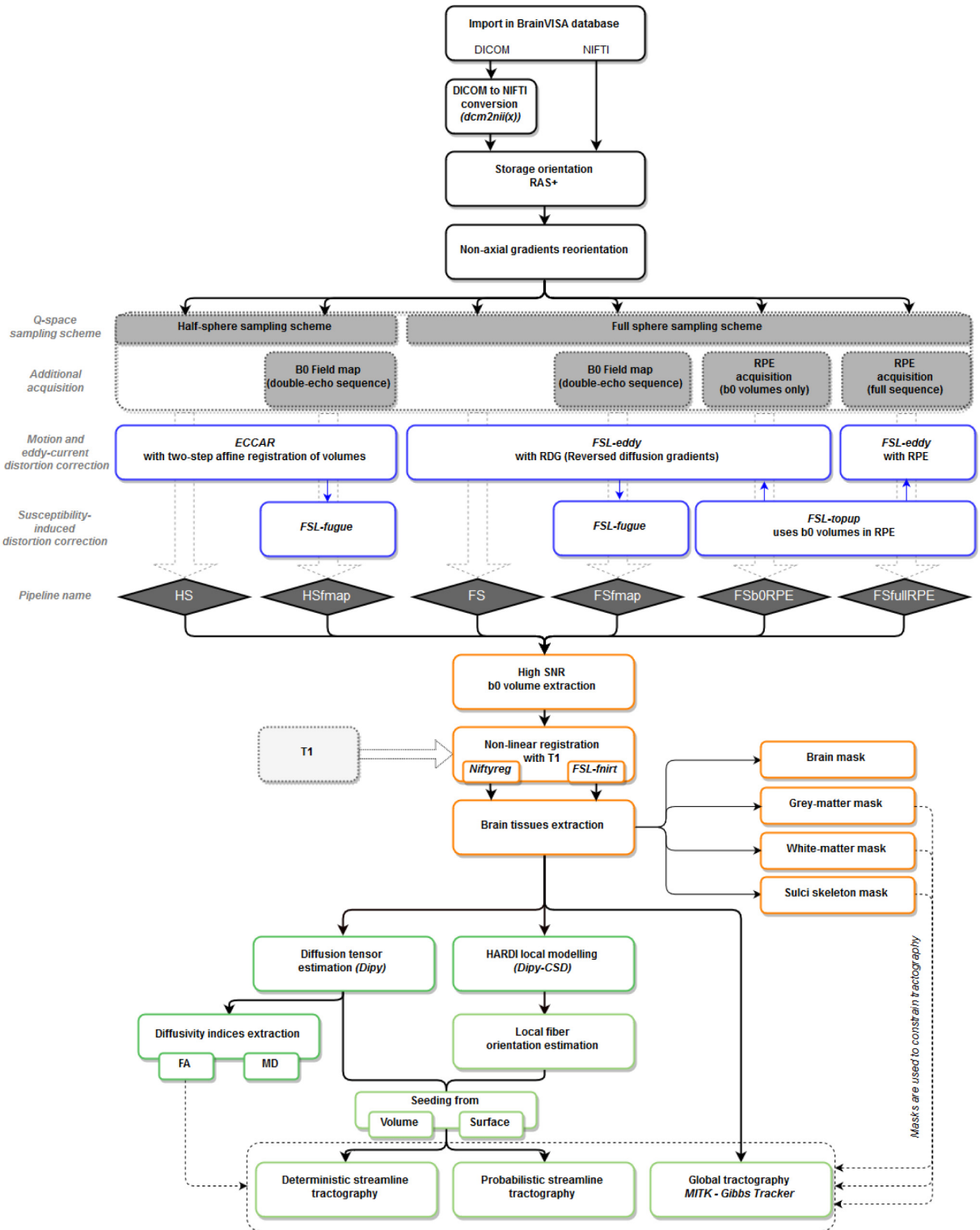

FIGURE 1 | Workflow of the *Diffuse* toolbox for DWI data processing implemented in the *BrainVISA* software platform. It includes the four parts detailed in the Section "Data Processing: The *Diffuse* Toolbox" of the manuscript. (In black) Importation, conversion and reorientation of data into the *BrainVISA* database. (In blue) Distortion correction through the six pre-processing pipelines derived from different acquisition settings. Most of the correction methods use *FSL* tools. The pipelines' names are indicated in blue diamonds. (In orange) The registration with the structural space is performed with either *Niftyreg* or *FSL*. Anatomical masks are extracted from the registered T1 data and can be used to constrain tractography. (In green) The data post-processing includes diffusion model estimation (tensor or CSD) and tractography (deterministic, probabilistic or global). All processes use *Dipy* tools except the global Gibbs tracking package implemented in Matlab.

B0 susceptibility-induced distortions

In *Diffuse,* two approaches were implemented to correct for magnetic susceptibility-induced distortions.

The first procedure uses the acquired B0 field map magnitude and phase images to correct the data through the workflow described in Cusack et al. (2003) involving the *'fugue'* command from FSL (Jenkinson et al., 2012). This correction step is applied after eddy-current and motion correction to ensure that volumes, and thus head-dependent distortion fields, are aligned. This yield two other preprocessing pipelines called **"HSfmap pipeline"** and **"FSfmap pipeline."**

The second method uses non-diffusion weighted volumes acquired with reversed phase-encode direction (FSb0RPE) (Andersson et al., 2003). In the *Diffuse* toolbox, this approach is implemented via the use of the *'topup'* tool from FSL (Smith et al., 2004). '*Topup*' combines pairs of b0 images with opposed distortions to estimate the susceptibility-induced off-resonance field. This distortion field is used as input in the *'eddy'* tool which correct simultaneously for susceptibility, eddy-current distortions and movements. A subset of DWI data containing 90 multi-shell diffusion gradient directions and 6 b0 volumes with LR phase-encoding direction plus 6 b0 volumes with RL phase-encoding direction was processed through the "**FSb0RPE pipeline."** The full subset with 90 multi-shell diffusion gradient directions repeated in both LR and RL phase-encoding directions was processed through the **"FSfullRPE pipeline."**

Structural to Diffusion Space Registration

After distortion correction, all non-diffusion weighted volumes are averaged to create a high SNR b0 image registered into the T1w image referential using non-linear registration. Two methods have been integrated in the toolbox, using either *'fnirt'* from FSL (Andersson et al., 2009) or *'reg f3d'* from Niftyreg[7] (Modat et al., 2010) (**Figure 1**). For both methods, an initialization step is done using the rigid body transformation of *'flirt'* from FSL. Note that the transformation is first estimated between the fractional anisotropy map and the T1w image which show similar gray-white contrasts and then applied to the b0 image. For our experiments, we use *'reg f3d'* which outperformed *'fnirt'*. In particular, '*fnirt*' failed to align regions with high intensities in the FA map such as the brain stem and the corpus callosum (data not presented in this article).

Diffusion Model Estimation and Tractography

Two diffusion models and three tractography algorithms constitute the post-processing steps implemented in the toolbox (**Figure 1**). For our experiments, the diffusion tensor was estimated using Dipy (Garyfallidis et al., 2014) from which were extracted tensor-derived indices such as eigenvalues, eigenvectors, FA and MD [equations (4) and (5) in Section Experiment 2], as well as the signal prediction and the tensor fitting error [TFE, equation (2)]. To perform tracts reconstruction, we used the global Gibbs tracker proposed by Reisert et al. (2011) which consists in estimating fibers trajectory simultaneously in all voxels of the brain in a reasonable computational time. Global tractography does not require any seeding strategy and is more robust to local errors in the fiber orientation estimation than deterministic and probabilistic tractography algorithms (Reisert et al., 2011; Mangin et al., 2013).

[7]http://cmictig.cs.ucl.ac.uk/wiki/index.php/NiftyReg

EXPERIMENTS AND RESULTS

In this section, we investigated the performance of the six preprocessing pipelines on the HCP data in four different experiments, regarding: (1) their capacity to recover brain geometry, (2) their influence on whole-brain diffusivity measurements; (3) their influence on diffusivity in central white-matter regions; (4) their influence on tractography measurements. Experiments 1 and 2 were reproduced on the clinical data, for the multi-shell subset as well as for the 3 separated *b*-values. Note that this dataset was not included in the statistical analyses. For each experiment, complementary analysis was also performed to compare the data corrected through the six preprocessing pipelines with the raw uncorrected data. Results can be found in **Supplementary Materials** and interpretations will be drawn in the "Discussion" Section.

Experiment 1: Performance of Distortion Correction Methods to Recover Brain Geometry

The performance of each distortion correction pipeline was assessed by measuring the similarity between the DWI and the T1w images as done in Cusack et al. (2003). Indeed, after correction for EPI distortions the brain should recover its initial geometry and the similarity with the T1w (considered as non-distorted) image should increase. To preserve local geometry, we only used the initialization step described in Section "Structural to Diffusion Space Registration" to rigidly align the average b0 image onto the T1w. Then, we computed the MMI as a similarity metric between the two images (Mattes et al., 2001). The main effect of distortion correction was evaluated using a one-way repeated measure ANOVA (RM-ANOVA). Reported effect sizes correspond to partial eta-squared (η_p^2) of the within-subject design, defined as follows:

$$\eta_p^2 = \frac{SS_{\text{effect}}}{SS_{\text{effect}} + SS_{\text{error}}} \quad (1)$$

with SS_{effect} the sum of squares of the effect and SS_{error} the sum of squares of the error associated with the effect.

Then, the differences between pipelines of distortion correction were assessed using Student's paired samples *t*-tests. The significance threshold was set to 0.003 (0.05/15pairs) to account for multiple comparisons.

Figure 2A illustrates the results of linear registration of the average b0 image onto the T1w image, for one subject (see **Supplementary Material S2** for the results on clinical dataset). Our results show that the brain geometry in the frontal and temporal lobes (red arrows) are recovered only after explicit correction for susceptibility-induced distortions

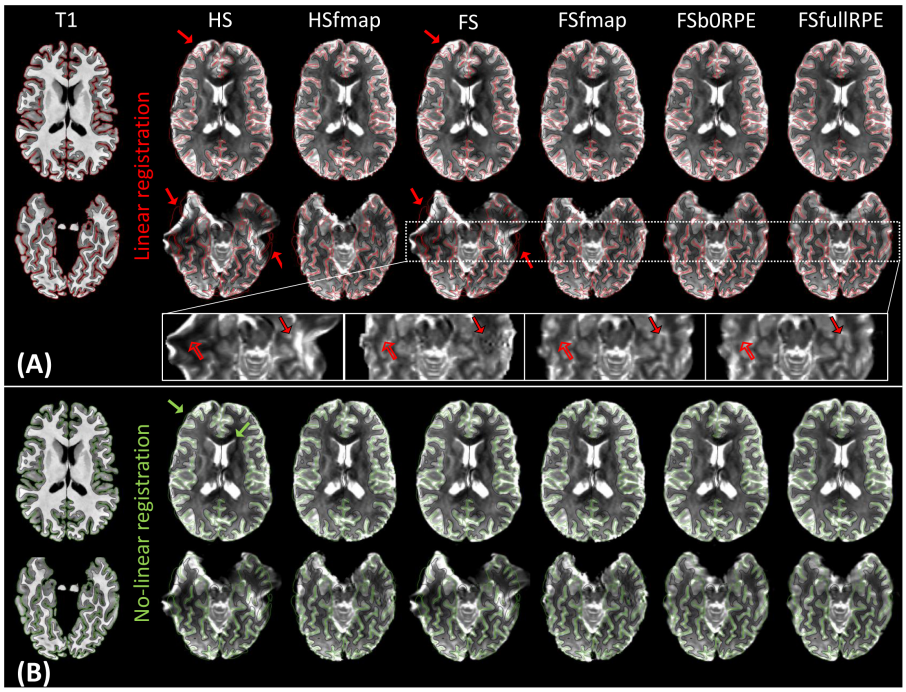

FIGURE 2 | Average b0 image of one subject linearly **(A)** and non-linearly **(B)** registered into the structural space, after distortion correction through the six pipelines. Gray-white interface (black line) and cortical surface (red/green line) of the non-distorted T1w image are overlaid on the b0 image. **(A)** Susceptibility-induced distortions correction enables to recover the true geometry of the brain (red arrows). The signal intensity in stretched areas can be corrected using a B0 field map image (see empty arrows in the zoomed images). But only the use of a reversed phase-encoding acquisition (FSb0RPE and FSfullRPE) can properly reconstruct the signal in compressed areas (see full arrows). Particularly one can observe that the ringing artifact coming from the correction with fmap is not visible after the correction with topup (FSb0RPE and FSfullRPE). **(B)** Non-linear transformation is able to partially correct for residual geometric distortions in particular with a proper geometry of the frontal, temporal lobes and ventricles (green arrows).

(HSfmap, FSfmap, FSb0RPE, and FSfullRPE pipelines). For data processed through the HS and FS pipelines, where susceptibility-induced distortions are not corrected explicitly, images contain high-intensity regions resulting from signal pile-up from surrounding voxels (full arrows) and low-intensity regions due to stretched-out signal diluted into surrounding voxels (empty arrows). The use of a B0 field map enables a sound signal reconstruction in stretched areas. However, we observe the same ringing artifacts in previously compressed areas as in Andersson et al. (2003). These artifacts, that originate from the ill-posed problem of recovering true intensity of two voxels that has been pilled-up into a single one, can only be solved by the acquisition of b0 volumes with RPE scheme (FSb0RPE and FSfullRPE pipelines).

The MMI (**Figure 3A**) quantitatively reflects these observations with a significant effect of preprocessing strategy on the similarity between b0 images and T1w images [$F(5,19) = 244.7$, $\eta_p^2 = 0.93$, $p < 0.0001$]. In particular, we found that the information obtained from either a field map or RPE images significantly improves the similarity score indicating that such corrected images get closer to the subject's true anatomy. *Post hoc* tests revealed that the use of FSb0RPE yielded better results than the use of a field map ($t_{\text{HSfmap} < \text{FSb0RPE}} = 7.9$ and $t_{\text{FSfmap} < \text{FSb0RPE}} = 6.6$, $p < 0.0001$). In general, the best similarity score was obtained using the FSfullRPE pipeline ($t_{\text{FSb0RPE} < \text{FSfullRPE}} = 5.5$, $p < 0.0001$), where susceptibility and eddy-current distortions are estimated and corrected simultaneously with a single deformation field. We notice that the correction of movements and eddy-currents using FS did not improve the registration compared to the ECCAR method with HS pipeline. This is expected since the non-weighted diffusion volumes, used in the similarity measurement, are not impacted by eddy-currents distortions. Yet, while both methods seem to equally perform in motion correction, we observed a high decrease in the similarity measurement when substantive subject motion is not corrected (see **Supplementary Material S3**).

In a second analysis, we computed the similarity metric between images non-linearly registered to evaluate the performance of the non-linear transformation in handling residual geometric distortions. The non-linear registration has been used in several studies to correct for susceptibility-induced distortions (Kybic et al., 2000; Merhof et al., 2007; Tao et al., 2009; Bhushan et al., 2016). However, the generalization of registration parameters setting across subjects is challenging and is highly sensitive to the type of anatomical sequence used or the presence of lesion (Albi et al., 2018). Here, we only evaluated its interest as a complement to the initial pipeline to improve alignment between anatomical and diffusion spaces. After the initial linear registration, the high SNR b0 image was non-linearly registered into the T1w image referential using *'reg f3d'* as described in

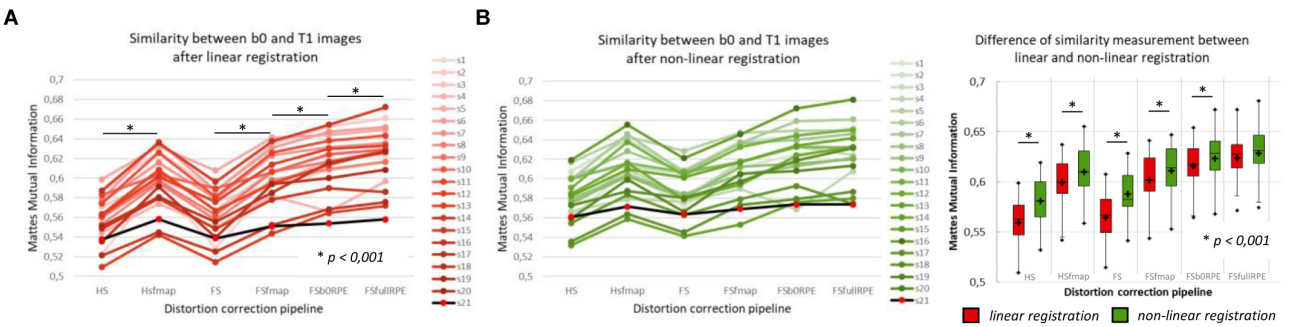

FIGURE 3 | Quantitative assessment of distortion correction methods using the similarity between diffusion and structural images. The Mattes Mutual Information was computed as a similarity measure between the T1w image and the average b0 image registered into structural space, using affine transformation **(A)** or non-linear transformation **(B left)**. The black line with red dots corresponds to the clinical dataset. Student's paired *t*-tests were performed to compare the registration accuracy between linear and non-linear transformation for each pipeline separately **(B right)**. The significant differences attest to the residual distortions corrected with the non-linear registration. Significance threshold was set to 0.001 to account for multiple comparisons.

Section "Structural to Diffusion Space Registration." A first visual assessment in **Figure 2B** shows that the alignment of the b0 images with the gray-white interface boundary is improved for HS and FS pipelines (green arrows). Using Student's paired *t*-test, we quantified the improvement of this method with respect to the linear registration (see **Figure 3B**). We show that the non-linear transformation significantly improves the similarity score between the b0 and the T1w images except for the FSfullRPE pipeline, where results were not different. This effect is particularly visible for pipelines which correct only for eddy-currents distortions (HS and FS: $t_{HS} = -12.77$ and $t_{FS} = -15.13$ respectively, $p < 0.0001$). These results corroborate the fact that the non-linear transformation, based on local deformations of voxels, can partly corrects for residual geometric distortions. This is in line with the observation of Calhoun et al. (2017) who used the T1 MNI template as reference image rather than the individual T1 image. Interestingly, the difference is not significant after Bonferroni correction when using the FSfullRPE pipeline ($t_{FSfullRPE} = -2.638$, $p = 0.016$), suggesting that this method yielded optimal correction with least residual distortions left.

Supplemental analyses were performed (results not presented in this article) to ensure that the effect of non-linear registration was not driven by potential residual deformations between diffusion and T1 images caused by differences of gradient non-linearities due to the change in position between the two sessions.

With the clinical data, we observed similar variations of the MMI between pipelines but with lower amplitude. The non-linear transformation also improved the similarity score. Moreover, we found that the *b*-value had no impact on the similarity metric (see **Supplementary Material S5**).

Experiment 2: Impact on Diffusivity Measurements: Global Differences

In this section, we investigated the impact of each of the 6 preprocessing pipelines on the diffusion signal modeling. For this purpose, the tensor model was estimated using the weighted least square method from Dipy (Garyfallidis et al., 2014) as described in Section "Diffusion Model Estimation and Tractography," on the diffusion data corrected through the six preprocessing pipelines. From the tensor model, we extracted two quantitative (TFE, mean dispersion index) and two qualitative (mean diffusivity, fractional anisotropy) metrics (Kim et al., 2006) to compare the quality of tensor estimation with respect to the distortion correction method.

The tensor-fitting error (TFE) used as a measure of the goodness-of-fit of the model (Papadakis et al., 2003) was defined in each voxel with

$$TFE = \sum_{i=1}^{N} (S_{mi} - S_{fi})^2 \quad (2)$$

where S_{mi} is the measured signal, S_{fi} is the fitted signal and N the number of diffusion-weighted volumes. A low TFE, i.e., more signal information fitted in the tensor calculation, is expected with better pre-processing.

The mean dispersion index (MDI) (Basser and Pajevic, 2000) indicates the directional variations of the principal eigenvector in the neighborhood (S) of each voxel:

$$MDI = \frac{1}{n(S)} \sum_{x \in S} \sqrt{\frac{\lambda_2 + \lambda_3}{2\lambda_1}} \quad (3)$$

where $\lambda_{i=1,2,3}$ are eigenvalues of the mean dyadic tensor derived from principal eigenvectors of the tensor in every voxels x of the neighborhood. This value was extracted for each voxel in the white-matter by considering a neighborhood of two voxels along each axis. Pre-processing should lower the dispersion of the tensor and thus reduce the MDI.

We also evaluated the impact of preprocessing pipelines on the usual diffusion indices of mean diffusivity (MD):

$$MD = \frac{\lambda_1 + \lambda_2 + \lambda_3}{3} \quad (4)$$

and fractional anisotropy (FA):

$$FA = \sqrt{\frac{1}{2}} \frac{\sqrt{(\lambda_1 - \lambda_2)^2 + (\lambda_2 - \lambda_3)^2 + (\lambda_3 - \lambda_1)^2}}{\sqrt{\lambda_1^2 + \lambda_2^2 + \lambda_3^2}} \quad (5)$$

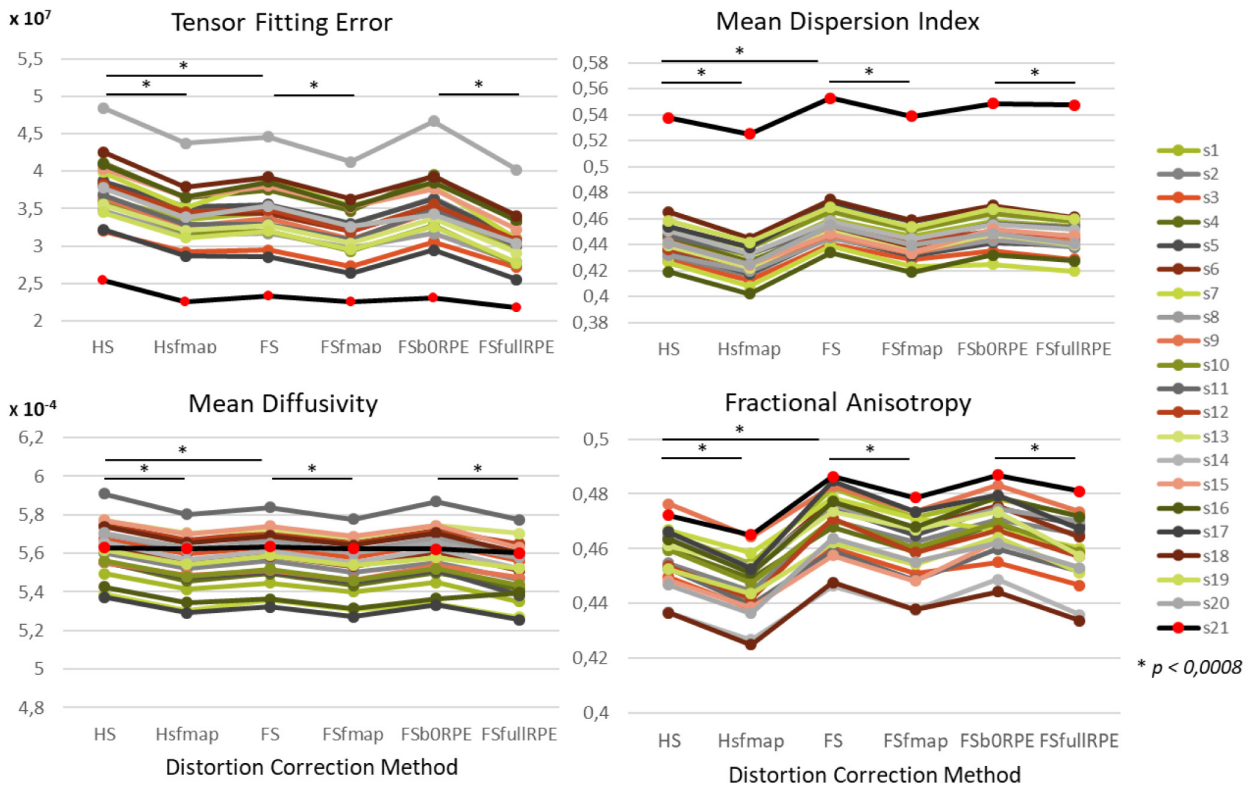

FIGURE 4 | Effect of preprocessing pipelines on the values of four tensor-derived indices TFE, MDI, MD and FA in the white matter. The values of each index were averaged across all white-matter voxels. For every subject represented with different colors for the HCP dataset and in black (red dots) for the clinical dataset, the mean values are plotted as a function of the preprocessing pipeline used to correct distortions.

Values were averaged across all white-matter voxels. The effect of preprocessing on these four indices was assessed using the same statistical analysis as for the MMI. The significance threshold was set to 0.0008 [0.05/(15pairs × 4indices)].

We found an important reduction of the inter-individual variability in all the tensor-derived indices between uncorrected and corrected data (**Supplementary Figure S3**). Yet, as illustrated in **Figure 4**, we observed that the choice of preprocessing pipeline result in significant variations in the values of all tensor-derived indices [$F_{TFE}(5,19) = 390.62$, $\eta_p^2 = 0.95$, $p < 0.0001$; $F_{MDI}(5,19) = 348.88$, $\eta_p^2 = 0.95$, $p < 0.0001$; $F_{FA}(5,19) = 200.3$, $\eta_p^2 = 0.91, p < 0.0001$; $F_{MD}(5,19) = 178.7$, $\eta_p^2 = 0.90, p < 0.0001$], with a particularly high consistency across individuals. *Post hoc* analyses (see statistics in **Table 2**) revealed significant differences between eddy-current correction methods, showing decreased TFE and MD and increased MDI and FA for data corrected by *eddy* (FS, FSfmap, FSb0RPE, and FSfullRPE) compared to ECCAR (HS and HSfmap). Second, we found that, for all subjects, the four metrics were jointly decreased by the additional correction of susceptibility-induced distortions using a field map image. On the contrary, the additional correction of susceptibility-induced distortions using FSb0RPE (compared to FS pipeline) did not yield significant differences in any indices. Thus, the effect of field map-based correction could be attributed to a smoothing effect induced by the second resampling involved in this method, rather than an actual distortion correction. Finally, all the tensor-derived indices were significantly reduced when using FSfullRPE compared to FSb0RPE. These results suggest that susceptibility-induced distortion correction has no impact on the global tensor metrics, but only the method used to correct for motion and eddy-currents do.

The clinical data presented similar variations for all tensor-derived indices, but with a lower TFE and higher MDI. In addition, we found that the *b*-value had an impact on each index: TFE and MDI increased with *b*-values, and MD and FA were largely decreased with higher b-values (see **Supplementary Material S6**).

Experiment 3: Impact on Diffusivity Measurements: Local Differences

The results of previous section could be difficult to interpret for several reasons. First, the comparison between pairs of pipelines can be hampered by a number of confounding factors inherent to the correction methods. Indeed, apart from the distortion correction performances, the methods differ in the number of resampling steps applied to the data (two for HSfmap and FSfmap pipelines, one for the others), in the use of intensity correction, and in the level of SNR in corrected images. Second, the tensor-derived indices should constitute reliable metrics in regions where the tensor is an appropriate model of the diffusion signal,

TABLE 2 | Statistical results of the *post hoc* analyses to compare the impact of distortion correction pipelines on tensor-derived indices, using Student's paired samples *t*-tests.

	***Eddy* vs. ECCAR**	**Use of *fugue* (fieldmap)**		**Use of *topup* (B0)**	**B0 vs. Full sequence Repetition**
	HS < FS	**HS < HSfmap**	**FS < FSfmap**	**FS < FSb0RPE**	**FSb0RPE < FSfullRPE**
TFE	$t = -17.22$	$t = -29.85$	$t = -27.33$	$t = 0.5054$	$t = -23.85$
	$p < 0.00001$*	$p < 0.00001$*	$p < 0.00001$*	$p = 0.616$	$p < 0.00001$*
MDI	$t = 15.48$	$t = -35.38$	$t = -42.29$	$t = -3.506$	$t = -12.42$
	$p < 0.00001$*	$p < 0.00001$*	$p < 0.00001$*	$p = 0.002$	$p < 0.00001$*
MD	$t = -17.32$	$t = -36.35$	$t = -45.85$	$t = 2.504$	$t = -10.74$
	$p < 0.00001$*	$p < 0.00001$*	$p < 0.00001$*	$p = 0.022$	$p < 0.00001$*
FA	$t = 15.10$	$t = -33.21$	$t = -30.18$	$t = -1.588$	$t = -14.50$
	$p < 0.00001$*	$p < 0.00001$*	$p < 0.00001$*	$p = 0.129$	$p < 0.00001$*

*The significance threshold was set to 0.0008 [0.05/(15pairs × 4indices)]. This table contains only the relevant comparisons. *Significant results.*

which excludes regions with crossing fibers and superficial white-matter. Thus, in this section we investigated spatial heterogeneity in the differences observed on the tensor-derived indices in deep white-matter regions with single fiber direction. Indeed, differences caused by interpolation and resampling should have spatially homogeneous effects in the brain whereas differences caused by the performance of the distortion correction should affect preferentially regions closer to susceptibility gradients or adjacent to areas with distinct tissue architecture. For this purpose, we non-linearly aligned the Johns Hopkins University DTI-based white-matter atlas (JHU-ICBM-DTI-48) (Mori et al., 2005) first into the structural space of each individual using '*fnirt*' (which provides preconfigured parameters for MNI standard to T1 image registration), and then into the diffusion space using the non-linear registration of Niftyreg, as described in Section "Structural to Diffusion Space Registration." After registration, all ROIs were binarized using a threshold at 0.5 to prevent overlapping while keeping large enough ROIs to capture tracts (see next section). From the 48 original labels, 10 (mostly included in the brain stem) fell out of the field of view and were excluded from the analysis. Results for one subject are illustrated on **Figure 5**. In the remaining 38 regions, we computed the average TFE, MDI, FA, and MD and compared the distortion pipelines in the same way as in the previous section (see RM-ANOVA results in **Figure 6**). Results of the comparison between four pairs of pipelines are illustrated in **Figure 7**, where only regions showing a statistically significant difference are shown ($p < 8.10^{-5}$ corrected for multiple comparisons).

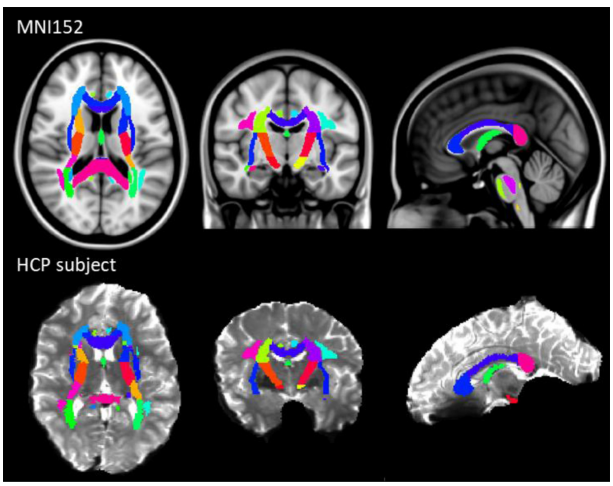

FIGURE 5 | JHU-ICBM-DTI-48 white-matter atlas displayed in the MNI standard coordinate space **(top)** and registered into the diffusion space of an individual after *ECCAR* correction (HS pipeline) **(bottom)**. 38 out of the 48 ROIs were included in the image. Note that even in the case of the simplest correction pipeline, the central brain regions are properly aligned with the subject's anatomy.

Figure 6 shows that, although far from the air/bones interfaces, most of these central regions are significantly impacted by the choice of distortion correction pipelines. The effect size of RM-ANOVA is particularly high for the local TFE index (above 0.5 in 50% of the regions). *Post hoc* paired *t*-tests revealed that the eddy-currents correction methods (HS versus FS pipelines) has a significant influence on the tensor fitting quality in the corpus callosum (genu, body, and splenium), the best fit obtained using FS, with a significant impact on FA and MD indices (see **Figure 7A**). Second, we found that the influence of field map-based correction was highly homogeneous for all indices with significant reduction between FS and FSfmap pipelines in respectively 71, 73, 89, and 87% of ROIs for TFE, MDI, MD and FA (see **Figure 7B**). This result supports the hypothesis of a smoothing effect due to the double resampling of the image. Conversely, we found that the additional correction of susceptibility-induced distortions using FSb0RPE (compared to FS pipeline) yielded spatially heterogeneous differences on local TFE, MDI, and FA, with 47, 29, 8% of ROIs respectively affected (see **Figure 7C**). Interestingly, we can observe a reverse symmetry in the effect size, which reminds the symmetrical signal compression and dilution in both hemispheres due to susceptibility artifacts. Lastly, the use of FSfullRPE compared to FSb0RPE resulted in a homogeneous increase of tensor fitting quality (92% of ROIs for TFE) but a spatially heterogeneous effect for all other tensor-derived metrics with significant differences in 37, 50, and 34% of ROIs in MDI, MD and FA respectively

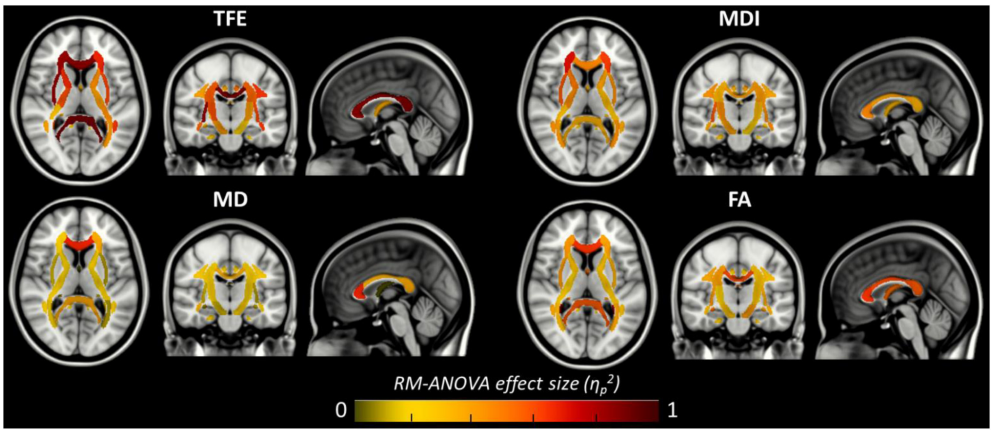

FIGURE 6 | Amplitude of the local main effect of preprocessing pipelines on the four tensor-derived indices TFE, MDI, MD, and FA. For each index, the mean values were computed across the 38 regions of the JHU-ICBM-DTI-48 atlas and compared between the six preprocessing pipelines using a repeated measures ANOVA. Effect sizes (partial eta-squared) are overlaid on the MNI-152 standard brain. A significant effect of preprocessing pipelines was found in regions with partial eta-squared above 0.19 ($p < 0.001$ to account for multiple comparisons across the 38 ROIs).

(see **Figure 7D**). The latter suggests that this is not an effect of resampling as with the fieldmap method. Instead, the significant decrease of Mean Dispersion Index supports a local improvement of the tensor fitting quality. Then, the homogeneous decrease of TFE could be attributed to the higher SNR in images corrected with FSfullRPE.

Experiment 4: Impact of Preprocessing Methods on Tract Reconstruction

In this section, we evaluated the influence of preprocessing pipelines on the trajectory of six well-known fascicles of different sizes. Tracts reconstruction was performed using the global Gibbs tracking algorithm (Reisert et al., 2011), as described in Section "Diffusion Model Estimation and Tractography." The interest of this method in our experiment is many-fold. First, Global tractography principle is based on optimization processes that reconstruct all fibers at the same time, avoiding the need of seeding strategies as opposed to step-by-step approaches which has been found to modulate the shape and density of fibers within fascicles (Girard et al., 2014). In our case, the use of a seeding strategy would prevent any comparison of fiber bundle trajectories between differently pre-processed – thus non-aligned – brains. Second, Global tractography has been found more robust to local errors in the fiber orientation estimation (Reisert et al., 2011; Mangin et al., 2013). In particular, the global Gibbs tractography (Reisert et al., 2011) was found to outperform deterministic and probabilistic methods in various connectivity metrics (Fillard et al., 2011; Neher et al., 2015), in particular showing higher ability to detect valid bundles, higher bundle coverage, and less prematurely ending fibers (Christiaens et al., 2015). Finally, this method was chosen for the valuable compromise between computational time, tractogram quality, and file sizes for a whole-brain tractography (20 subjects with 6 preprocessing pipelines led to 120 tractograms). Global tractography was performed using the default parameters for a dense reconstruction (3.108 iterations, 50 steps, starting/stopping $T° = 0.1/0.001$, $\sigma = 1$ mm, $l = 3$ mm, $w = 0.07$). The whole-brain tractogram was computed using the white-matter mask as constraint, after being registered into the diffusion space. From each individual whole-brain tractogram we extracted the following fascicles: the cortico-spinal tract, the corpus callosum, the superior longitudinal fascicle, the cingulum, the uncinate and the fornix fascicles. These tracts were chosen because they pass through the most distorted areas, cover the three spatial directions, and can be identified for every subject. They were extracted using ROIs of the JHU-ICBM-DTI-48 atlas either as way-points or as exclusion-points following the recommendations described in (Catani and Thiebaut de Schotten, 2008). The labels used are detailed in **Table 3**. To compare the impact of the different preprocessing pipelines on tractography we analyzed the spatial variance of each fascicle as in (Irfanoglu et al., 2012). This measurement first described in Lazar and Alexander (2005) quantifies the spatial dispersion of the fibers trajectory with the distance from the seed. It is obtained by considering all voxels in the fascicle that are at a certain distance (in voxels) from the seed (here the way-point mask), and computing the covariance matrix of these voxels' coordinates, weighted by the density of fibers crossing them. For a full description of the spatial signature of the tracts we extracted the spatial variance along the X, Y, Z axes, given by the diagonal elements of the covariance matrix, as well as the spatial variance along the principal mode, given by the primary eigenvalue. The former corresponds to a description of the 3D shape of the fascicles and can be used to measure their similarity across subjects or across preprocessing pipelines. The latter can be interpreted as a measure of the spatial dispersion of the tract to assess the impact of distortion correction methods. We plotted the spatial variances as functions of the absolute distance to the seed, for each subject. The curves were smoothed by convolution, over a sliding window of size 5, and we computed the average curve across subjects. These tract signatures were compared

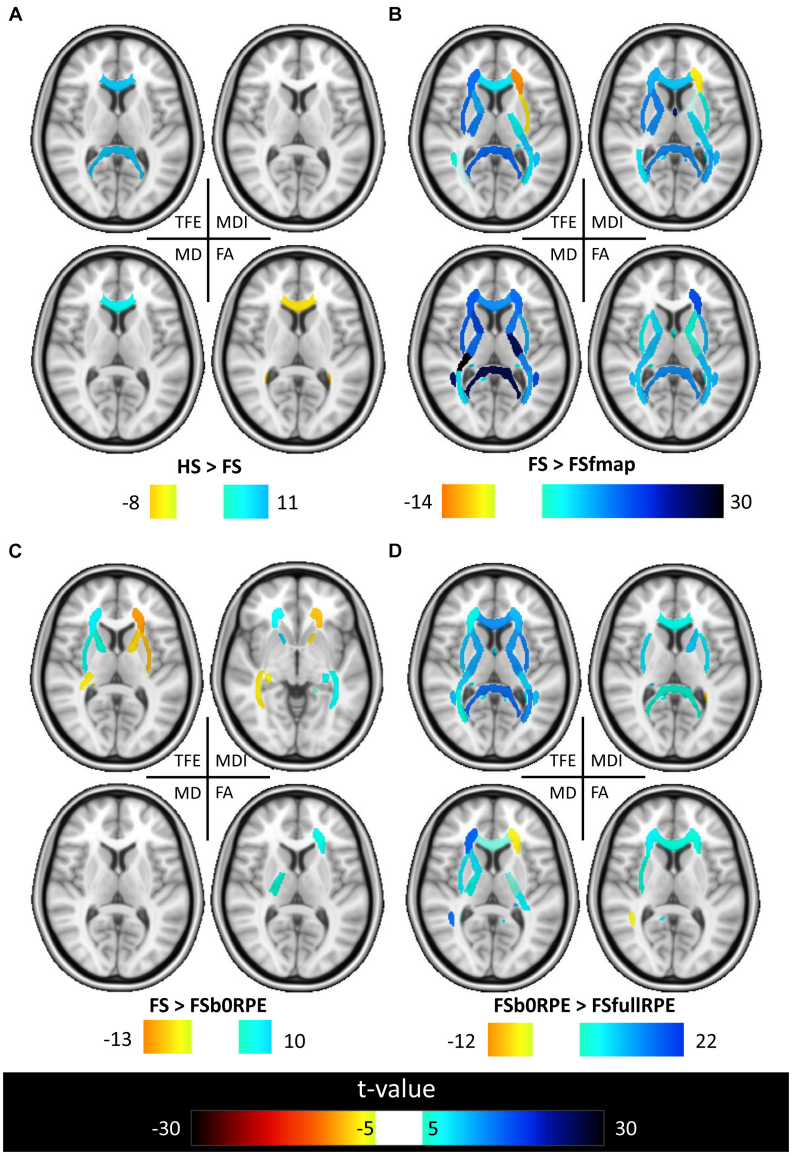

FIGURE 7 | Results of the *post hoc* analyses on the local effect of preprocessing methods on tensor-derived indices. *Post hoc* paired *t*-tests were conducted in all ROIs. Results are shown for the comparison between **(A)** HS and FS pipelines to assess the influence of eddy-current correction method, **(B)** FSfmap and FS pipelines to assess the influence of geometric distortion correction using a B0 field map, **(C)** FSb0RPE and FS pipelines to assess the influence of geometric distortion correction using a b0 with RPE, **(D)** FSfullRPE and FSb0RPE pipelines to compare the influence of using b0 versus the full sequence with RPE. Only regions showing significant differences are shown ($|t| > 5$, $p < 8.10^{-5}$ corrected for multiple comparisons).

TABLE 3 | Labels of the JHU-ICBM-DTI-48 atlas used either as way-points or exclusion-points to extract the fascicles from the "whole brain" tractograms.

Tracts	*Way-points*	*Exclusion-points*
Cortico-spinal	"Posterior limb of internal capsule" (19, 20)	All other ROIs except 15, 16, 17, 18, 21, 22, 23, 24, 25, 26, 27, 28, 43, 44
Corpus callosum	"Genu," "body" and "splenium" of corpus callosum (3, 4, 5)	All other ROIs except 23, 24, 25, 26, 27, 28, 29, 30
Superior longitudinal	"Superior longitudinal fasciculus" (41, 42)	All other ROIs
Cingulum	"Cingulum" (cingulate gyrus and hippocampus) (35, 36, 37, 38)	All other ROIs
Uncinate	"Uncinate fasciculus" (45, 46)	All other ROIs
Fornix	"Fornix" (column, body, cres) and "stria terminalis" 6, 39, 40	All other ROIs

The cortico-spinal and corpus callosum fascicles span through other ROIs of the atlas so that these regions could not be considered as exclusion points. For each tract, we thus extracted only the fibers going through the way-points and which never cross exclusion-points.

between preprocessing pipelines by performing a RM-ANOVA on the area under the curve (AUC).

Figure 8 shows that each tract has a specific spatial signature along the *X, Y, Z* axes. For instance, the cortico-spinal tract showed a distal higher variance along the *Y* axis while the superior longitudinal tract showed a proximal higher variance along the *X* axis. These signatures looked highly similar across subjects and across preprocessing pipelines (as seen on the variance plot of the second column of **Figure 8**) although we observed more variability for smaller fascicles such as the cingulum, the uncinate and the fornix. We found a significant influence of the preprocessing strategy on the tract spatial variance along the principal mode (third column) for the corpus callosum, the superior longitudinal and the cingulum fascicles [respectively $F(5,19) = 3.59$, $\eta_p^2 = 0.16$, $p = 0.005$; $F(5,19) = 7.49$, $\eta_p^2 = 0.28$, $p < 0.00001$; and $F(5,19) = 8.69$, $\eta_p^2 = 0.31$, $p < 0.00001$] with better scores obtained for the FSfullRPE pipeline, and a tendency for the cortico-spinal fascicle [$F(5,19) = 2.62$, $\eta_p^2 = 0.12$, $p = 0.029$] with higher spatial variance observed for the HS pipeline compared to others. The AUC curves (fourth column) indicate the distance from the seed at which the signatures start to differ. The last curves (fifth column) show that the number of fibers does not differ between pipelines, indicating that reductions of variance are not due to a loss of fibers.

DISCUSSION

In this article, we studied the influence of preprocessing distortion correction pipelines on diffusivity metrics and tractography measurements. For this purpose, we developed the *Diffuse* toolbox for DWI data processing which provides, in a guided user interface, the adapted preprocessing pipeline according to the data acquisition settings. Six different distortion correction pipelines are available, compatible with most acquisition type from clinical to research context. Two diffusion models and three tractography algorithms constitute the post-processing steps. Embedded in the BrainVISA open-source platform, the toolbox comes with an automatic indexation of data into a database organization as well as a visualization tool, and an access to processed anatomical data. This software configuration was well suited to investigate the impact of preprocessing methods on diffusivity measurements and tractography.

To our knowledge, the previous work that is most similar to our study is Yamada et al. (2014) where authors compared the following 4 pipelines: 'eddy_correct' using trilinear interpolation; 'eddy_correct' using spline interpolation; 'eddy' combined with 'topup' on 60 diffusion gradients and 2 non-diffusion volumes with RPE, equivalent to our FSb0RPE pipeline; and 'eddy' combined with 'topup' on 30 diffusion gradients repeated with RPE, equivalent to our FSfullRPE pipeline. To assess the differences between these 4 pipelines, authors compared the FA values within the white-matter skeleton, assuming that higher FA should be associated to better distortion correction. Indeed, increased FA could result from restricted perpendicular diffusivity, facilitated parallel diffusivity, or some combination of the two, reflecting a reorganization in tissue structure. However, in our work, we also observed that diffusivity metrics can be affected by other cofounding factors such as interpolation and smoothing effects. The major contributions of our study are:

- We compared quantitatively the impact of the distortion correction using a field map in place of 'topup'.
- We quantified the correction quality with a similarity metric between DWI and T1
- We quantified the quality of tensor fitting with TFE and MDI indices.
- We quantified the impact on tract spatial dispersion.

The Most Performant Acquisition/Preprocessing Choice

From the quantitative analyses of this study, we were able to sort the six pre-processing pipelines regarding the following performance criteria: ability to recover brain's true geometry (through the MMI index); tensor fitting quality (through the TFE index) and tract spatial variance. As expected, for all these quantitative indices, the best score was obtained with the FSfullRPE pipeline, that is when all diffusion gradients are repeated twice with RPE. Importantly, we showed that the FSfullRPE pipeline yielded the best similarity results, i.e., the geometry of the brain was quasi completely recovered, as shown by the equal performance of linear registration compared to non-linear registration. In previous studies, this pipeline has also been shown to outperform the '*eddy_correct*' tool, in terms of eddy-current distortion correction, for *b*-values between 1500 to 7000 s/mm^2 (Andersson and Sotiropoulos, 2016). In terms of susceptibility-induced distortion correction, the 'topup' tool has been shown to outperform the use of a field map acquisition (Andersson et al., 2003). Compared to uncorrected data, this distortion correction pipeline yielded higher FA values in the white matter as found in Yamada et al. (2014) and lower MD values.

In the following, we will discuss the valuable interest of other acquisition/pipeline choices, from the minimum requirements (smaller set of acquired images and HS pipeline) to this optimal preprocessing pipeline that requires a large number of acquisitions, though at the cost of twice longer scan time.

Motion Correction Reduces Inter-Individual Variability in Tensor Metrics

Our results on uncorrected data showed that the similarity between b0 and T1 images (**Supplementary Material S3**) as well as the tensor-derived metrics (**Supplementary Material S4**) were highly impacted by the subject movements. Interestingly, we found that every preprocessing pipeline was able to reduce the inter-individual variability due to a difference in head movements during the scan. This finding emphasizes the importance of motion correction to improve the tensor model estimation.

This should be particularly relevant when comparing healthy subjects and patients who are more likely to move in the scanner (Yendiki et al., 2014; Taylor et al., 2016). Note, however, that we

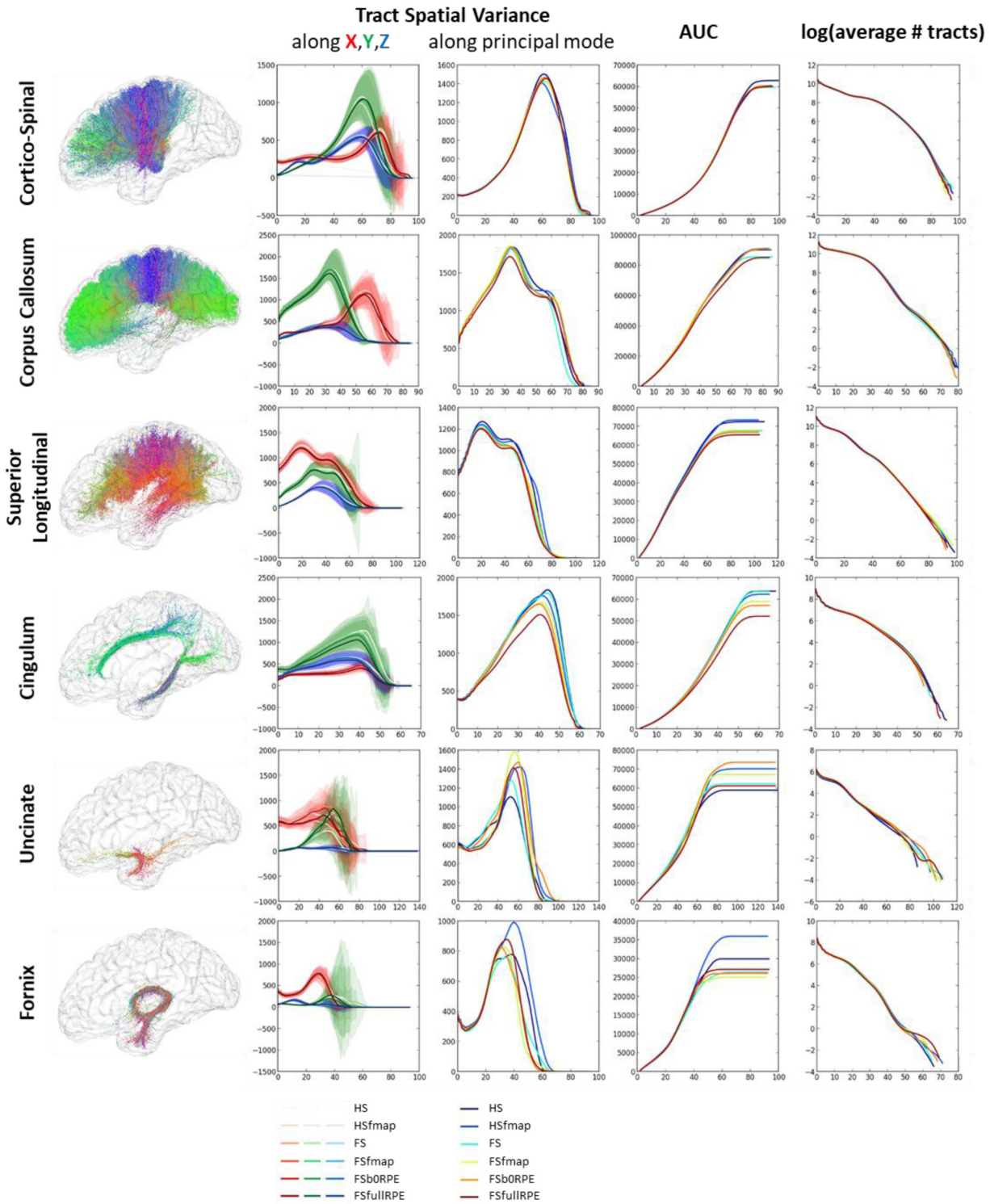

FIGURE 8 | Results of the global tractography reconstruction and spatial dispersion analysis. Six fascicles were extracted from the whole brain tractograms using ROIs of the JHU white-matter atlas as way-points and exclusion-points. **(First column)** On the left are illustrated these fascicles for one subject after data preprocessing using the FSfullRPE pipeline. **(Second column)** On the graphs are plotted the tract signatures for the six pipelines, that is the mean spatial variance of tracts (and standard deviation across subjects) along the *X, Y,* and *Z* axes as a function of the absolute distance to the seed. **(Third column)** The graphs show the spatial dispersion of the tracts, that is the mean spatial variance of tracts along the principal mode. **(Fourth column)** The graphs show the cumulative area under the curve of the spatial variance along the principal mode. It represents the amount of spatial dispersion from the seed. A RM-ANOVA was conducted on the total AUC values to compare the spatial variance between pipelines. **(Fifth column)** The log of the number of fibers is plotted at each distance to the seed.

did not address the issue of signal dropout due to fast "bulk" motion of the subject during the acquisition of a volume. This artifact is likely to occur in a clinical context where patients and children are usually less compliant and more subject to discomfort in the scanner. It can induce important signal loss in several slices that can have dramatic consequences on post-processing and diffusivity measurements (Roalf et al., 2016; Baum et al., 2018). Several methods have been developed to detect and remove (Oguz et al., 2014) or correct (Chang et al., 2005; Farzinfar et al., 2013; Andersson et al., 2016, 2017) this erroneous slices. Once motion correction is performed, we observe a high inter-subject consistency in the variation of MMI as well as tensor derived metrics between the six preprocessing pipelines. This observation reinforces the strength of variations between pre-processing pipelines that we will discuss hereafter.

On the Interest of Eddy-Current Distortion Correction

When considering all the subjects, with and without important head movements, we observed a general (not only for subjects who presented substantial movement) and substantial reduction of TFE and MD, and an increase of MDI and FA in the white matter (see **Supplementary Material S4**). A similar increase of FA was observed in Yamada et al. (2014) with the use of *'eddy_correct'* with spline interpolation. This result, found for both ECCAR (HS) and '*eddy*' (FS) methods in our study highlights the importance of this step in the preprocessing pipeline. Yet, we found significant differences depending on the method used.

On the Benefit of Using a Full-Sphere Sampling Scheme

Our results showed an even better tensor fitting quality when using *'eddy'* (FS, FSfmap, FSb0RPE, FSfullRPE pipelines; full sphere sampling scheme) compared to the ECCAR method (HS and HSfmap pipelines; HS sampling scheme). Note that the HCP data were acquired with strong gradients (up to 100 mT/m), high *b*-values (up to 3000 s/mm^2) and high spatial resolution. In this "research-type" context, images were strongly affected by susceptibility and eddy currents deformations and it is not surprising that the use of a first order affine transform (ECCAR) rather than a high order model (*eddy*) results in a poor alignment between successive volumes, which in turn can affect the quality of the diffusion tensor estimation. Similar conclusions were drawn from the study of Jezzard et al. (1998), where authors performed an in-depth comparison between *'eddy'* and *'eddy_correct'* tools, from which is derived the ECCAR method. In Graham et al. (2016), authors confirmed the higher performance of '*eddy*' over *'eddy_correct'* on realistic numerical simulations of DWI with distortions. Indeed, the performance of eddy-current correction using the *'eddy_correct'* method was found to depend on the *b*-value and/or SNR of DWI data (Nilsson et al., 2015; Graham et al., 2016), with lower registration quality for higher *b*-values. In our case, ECCAR uses a two-step approach to register the DWI volumes, first to the closest b0 volume and second to the first acquired one, in combination to the use of mutual information as cost function. Although this might greatly improve the registration quality compared to *'eddy_correct'*, this is not sufficient to properly correct for eddy-current and motion in high *b*-value data. It would be interesting to further investigate our metrics on data with lower *b*-values and fewer gradient directions, in addressed in Graham et al. (2016) where authors evaluated the robustness of '*eddy*' with *in silico* simulations.

Note that we purposely chose to use the same resampling scheme with spline interpolation in both pipelines to avoid confounding effects. Indeed, interpolation techniques used to resample data are known to play a critical role in the final quality of the image and particularly in the robustness of the registration algorithm (Mahmoudzadeh and Kashou, 2013). Notably, the trilinear interpolation, often used as default parameter, usually results in less intensity errors but more blurring in the image than other methods. Here, we cautiously employed the same interpolation method (spline) in all pipelines. However, further investigations showed that the use of trilinear interpolation for ECCAR had the effect to increase TFE and reduce MDI, FA, and MD. This results corroborates the alternative decreases or increases of FA observed in Yamada et al. (2014) when using respectively trilinear or spline interpolation in *'eddy_correct.'*

Eddy-Current Distortions Also Affect Central White-Matter Regions

ROI-based analysis revealed that the improvement of the tensor fitting is localized in the corpus callosum and is accompanied by a decrease of MD and an increase of FA mostly in the genu of the corpus callosum. Two reasons could explain this finding. First, the corpus callosum is defined by a high anisotropy and a high directionality of the diffusivity. Thus, this area is likely to be sensitive to a small difference in the tensor estimation. Second, a poor alignment of successive volumes could impact differently the tensor model in regions surrounded by different white-matter architectures. Indeed, a **residual shift in voxels position** often leads to a characteristic rim of high anisotropic voxels at the edge of the brain (Alexander et al., 1997; Jones and Cercignani, 2010). However, while this outside effect is visually easy to detect, a similar effect can happen at the intersection between distinct tissue types or micro-structural architectures such as white-matter and CSF (Jezzard et al., 1998). For instance, as observed in local analyses for FA and MD, the genu of the corpus callosum is in a brain region that is highly prone to geometric distortions and is adjacent to the lateral ventricles. Likewise, in the literature, the influence of eddy-current distortion correction on the diffusivity indices has often been reported differently depending on the regions studied. For instance, previous visual observations of fractional anisotropy maps showed sharper contours and reduced blurring after eddy-current corrections using gradients with reversed polarity (Alexander et al., 1997; Bodammer et al., 2004), compared to no correction. Other quantitative studies found increased FA in corrected data using affine registration (Rohde et al., 2004), as well as using FS-equivalent method (Shen et al., 2004), in several regions which were not visible in the anisotropy maps of uncorrected data. However, in Kim et al. (2006), authors found a decrease of FA for several correction methods in the uncinate and corpus callosum tracts. Finally, in Rohde et al. (2004), an artificial

increase of anisotropy in the left-right orientation, in isotropic regions such as gray-matter, was reduced after correction, while MD was not affected.

On the Interest of Susceptibility-Induced Distortion Correction

The first experiment clearly demonstrates the ability of susceptibility-induced distortion corrections to recover the brain's true geometry. In line with Cusack et al. (2003) and Tao et al. (2009) we found that the use of a field map brings significant improvement in the registration accuracy between DWI and T1w data. In Cusack et al. (2003), authors ascertained that this difference did not originate from the slight smoothing produced by the resampling procedure. Here, the significant improvement also measured with the FSb0RPE compared to the FS pipeline, which both use the same resampling procedure, further supports the benefit of susceptibility-induced distortion correction. However, we observed major differences between the use of a field-map and the use of a b0 volume to correct for these distortions.

Reversed b0 Volume Outperforms Field-Map

First it should be noted that the field map images were not acquired during the same session as the diffusion images. Thus, a change in head position in the scanner probably led to slight variations in the field map induced by the interaction between shimming and gradient non-linearities. As a consequence, our field map-based correction shows probably lower performance than it should if the field map was acquired during the dMRI session. Second, compared to the use of a field map, the advantage of FSb0RPE is two-fold. In addition to the improved registration accuracy (results Experiment 1), with a more realistic signal reconstruction in stretched and compressed areas as seen in **Figure 2A**, the FSb0RPE pipeline (as well as the FSfullRPE) combines both motion, eddy-current and susceptibility distortions in a single distortion field to correct simultaneously for all these artifacts (Andersson and Sotiropoulos, 2016). Conversely, the field map-based correction is performed as a second step, involving a second resampling and interpolation of signal intensity which is likely to induce smoothing in the corrected images (Wang et al., 2017).

Indeed, ROI-based analyses showed that, compared to HS and FS pipeline, the additional use of a field map resulted in a highly homogeneous reduction of all tensor-derived metrics, while we expected the effect to be higher in regions prone to severe geometric artifacts, as reported in Wu et al. (2008). To understand this artificial decrease of tensor-derived metrics, one has to understand the effects that a 3D smoothing has on the 4th dimension of DWI data (i.e., across gradient directions). In fact, we can imagine that the smoothing would flatten the ellipsoid of the tensor model by removing high frequency fluctuations in the signal. As a consequence, one can expect that the tensor model would give better fitting performance and the TFE as defined by the equation (2) should be reduced. Besides, when considering only white-matter voxels where the signal is highly anisotropic, i.e., low intensity signal in a given gradient direction and high intensity in the others, the smoothing should flatten the signal of the voxel across volumes which explains the reduced FA and MD. Finally, the differences between neighboring voxels which diffuse in different directions are also flattened, thus decreasing the local variation of the tensor orientation represented by the MDI.

Conversely, ROI-based analyses revealed a local influence of the distortion correction using b0 volumes with RPE compared to the FS pipeline. Interestingly these results concern regions closest to the frontal and temporal lobes, with symmetric effects for TFE and MDI, which echoes the left-right orientation of geometric distortions. Note that this symmetry induces a compensation which might account for the null global effect. Importantly, the methodological difference between FS and FSb0RPE pipelines is that, in the latter, the distortion field used in *eddy* to correct data also includes the susceptibility-induced distortions estimated with *topup*. Besides that, both methods use the same interpolation procedure and the same intensity reconstruction (by Jacobian modulation).

In Cusack et al. (2003), authors highlight another disadvantage of B0 field map acquisition which does not capture the interaction between distortion field and subject movements during the scan which could introduce additional variations across subjects. In particular, this should be kept in mind when comparing different types of population such as healthy volunteers and patients or children who are more prone to motion. These findings emphasizes the benefits of acquiring a single b0 volume with RPE instead of a double-echo field map sequence, for an acquisition time of respectively a few seconds and around 2 min, a substantial difference in the context of clinical acquisitions (Treiber et al., 2016). Note also that equivalent co-registration quality with T1 was found for FSb0RPE and FSfullRPE pipelines after non-linear registration.

Differences Between FSb0RPE and FSfullRPE

The methodological difference between FSb0RPE and FSfullRPE lies in the repetition of all diffusion weighted volumes twice in the latter pipeline. The interest is twofold. First, every pair of volumes with opposed phase-encoding directions are averaged, yielding the same final number of volumes as for the other pipelines. This doubles the amount of information in each voxel, increasing the SNR, which explains the homogeneous decrease of TFE in the white-matter. Indeed, the more information contained in the signal, the easier the tensor model could fit the data. Second, compared to the Jacobian modulation which only account for signal dilution, the least-square restoration provides a better signal reconstruction in compressed areas (Andersson et al., 2003) which could be at the origin of the heterogeneous decrease of MDI, FA and MD. This concords with Yamada et al. (2014), where authors also observed an heterogeneous decrease of FA lateralized in the left hemisphere.

Overall, our results suggest that the correction of susceptibility-induced distortions using RPE scheme provides better tensor fitting performance, in particular with a local influence on tensor-derived metrics. To confirm our hypotheses, it would be interesting to conduct voxel-wise analyses, to test, for instance, the spatial correlation of the four diffusion indices with multiple variables such as signal intensity or local deformation needed to correct for geometric distortions.

Handling Residual Geometric Distortions

A major outcome of this work is that the quality of the registration between diffusion and structural space mostly depend on the susceptibility-induced distortion correction method. As shown in our results, the remaining geometric distortions are hardly handled by an affine transformation. As a consequence, a misalignment between structural and diffusion space may be present when registering an atlas, a template or a group of subjects together. In order to take into account residual distortions, we highly recommend using a non-linear transformation for inter-subject as well as for intra-subject registration of mask, ROIs or atlases for connectivity purpose (Cusack et al., 2003).

Impact on Bundle Trajectories

Our results on tract spatial variance revealed very different signatures for each fascicle, supporting the suitability of this metric to quantify the variability in the shape of fiber bundles. However, the tract signatures obtained in this article look highly different from those obtained in Irfanoglu et al. (2012). Several factors could participate in these different results. First, authors in Irfanoglu et al. (2012) used deterministic and probabilistic tractography algorithm, both requiring potentially different parameters such as the number of iterations, stopping criteria and curvature threshold. They also filtered out isolated fibers while we did not, which can explain the higher distal dispersion of tracts in our results. For these reasons, the tractograms of the two articles are hardly comparable. In our study, the consistency of tract signatures across subjects and preprocessing pipelines (**Figure 8**) illustrates the robustness of the global tractography to reconstruct fascicles regarding inter-individual variability and residual distortions in the image. This observation is particularly true for the largest fascicles of the cortico-spinal, corpus callosum, superior longitudinal, and cingulum pathways.

Despite this robustness, the trajectory of some fascicles is sensitive to the distortion correction strategy. It is the case for the commissural pathway of the corpus callosum and two association pathways, namely the superior longitudinal tract and the cingulum tract which project from the frontal lobe to the temporal lobe. Although this quantitative analysis could not allow a clear distinction between an effect of eddy-current distortions or susceptibility-induced distortions, these two main regions are known to be prone to severe geometrical artifacts due to their proximity to air/bone tissues interfaces. Indeed, as shown in Embleton et al. (2010), the misalignment of voxel-wise fiber orientations in these regions could lead to a premature ending of reconstructed pathways. In the same line, linear and non-linear correction of eddy-current have been found to visually reduce the dispersion of uncinate and corpus callosum tracts, especially in the temporal and frontal parts (Kim et al., 2006). However, the short pathways of uncinate and fornix tracts did not show significant sensitivity to distortion corrections. A possible reason is that the small seeds used to extract these tracts are likely to be subject to higher inter-individual variability and higher registration errors. This could explain why we were not able to distinguish the effect of preprocessing pipelines out of the intrinsic tract variability.

Finally, it should be noted that the global tractography algorithm includes optimization process that takes into account the uncertainty in the DWI data and has been reported to prevent from overfitting (Daducci et al., 2015). Yet, other tractography algorithms such as probabilistic or deterministic tractography might be prone to more important changes due to a higher sensitivity to inter-scan variability.

Relevance Toward Clinical Data

To relate our observations with the clinical context we reproduced the same experiments on a similar dataset but acquired on a Siemens Prisma 3T MR-system with similar maximum gradient strength and slew rate as for the HCP scanner but using different acquisition settings. In particular, the T1w image had a lower resolution which, as we found, did not alter neither the capacity nor the interest of using non-linear registration to improve the alignment between T1 and diffusion weighted images.

Importantly, the performance differences that we observed between pipelines is still valid for the dataset acquired in a context closer to the clinical environment. Although we found differences between the two datasets, common to all pipelines, as a global shift. For instance, the tensor-fitting quality was highly different from the HCP data which could be attributed to a higher SNR in the images, relative to the lower spatial resolution of DW images and the lower acceleration factor.

With this clinical dataset, we also highlighted the impact of *b*-value on the tensor fitting performance. Indeed, we found a better tensor fitting for lower *b*-values. Also, the FA and MD values measured in the white matter showed an important sensitivity to the *b*-value. This finding is probably related to the amount of SNR as well as the quality of distortion correction. Indeed, lower b-values involve lower gradient amplitudes and thus less eddy-currents. Apart from the amount of distortions, a higher SNR in the images could imply that conventional image registration algorithms perform better (Andersson and Sotiropoulos, 2016). It has been reported in the literature that the amount of noise in the raw image can have an influence on the tensor-derived metrics (Manjón et al., 2013; Hutchinson et al., 2017).

Limitations and Future Work

One important limitation in our study lies in the choice of regions restrained to the central white-matter for the ROI-based analysis. These brain areas are not the most impacted by geometric distortions. This work should be extended to the rest of the brain, for instance by including regions of interest with superficial white-matter. In particular, it would be interesting to correlate the variation in diffusivity indices to the amplitude of distortions, or the amount of displacement necessary to align each voxel to the structural image. However, this investigation would require using other metrics that are not based on the tensor model, which reliability is limited to regions with single fiber's direction. More suited models intended to fit the complex white-matter architecture such as NODDI would be more appropriate

(Graham et al., 2016) but require specific acquisition settings with multi-shell sampling of gradients, in particular with a "mini-shell" that can model the high-diffusion compartments.

A second limitation is the difficulty to quantify the differences between pipeline's performance regarding the reconstruction of tracts. Especially, we could not easily reproduce results of previous studies, due to the inability to reproduce the seeds position and the complexity of algorithm parameters settings. One way to overcome these limitations would be to perform similar analyses on numerical phantoms with a known ground truth. Also, further work is necessary to investigate the impact of preprocessing methods on the connectivity measurements between cortical regions. Such analysis would probably be less influenced by outlier fibers that show higher spatial dispersion.

CONCLUSION

The aim of this study was to evaluate the impact of different preprocessing pipelines on the quality of corrected data. While most studies try to isolate the cofounding factors coming from acquisition settings, data or processing quality, we instead found interesting to consider the combination of eddy-current and susceptibility-induced distortion corrections into single pipelines dedicated to distinct acquisition contexts. Hence, we could highlight the resulting differences between outcome data and their consecutive diffusivity and tractography measurements. As these pipelines are optimal for different acquisition contexts, our observations will help for both a careful choice of acquisition settings and a precautious interpretation of DWI analysis. In the light of our results, the acquisition of several interspersed b0 volumes plus an additional b0 volume with RPE is highly recommended as default settings, rather than the acquisition of a field-map. Moreover, we highly recommend to use non-linear registration with anatomical images to handle residual distortions. Ideally, acquisition settings should be chosen depending on the study purpose and on the acquisition and processing times that can be afforded depending on the context (e.g., clinical or research). For instance, to compare two different populations, investigators should focus on an efficient motion correction method. However, if effects are expected in regions exposed to magnetic susceptibility differences, such as temporal and frontal lobes, a particular attention should be paid to geometric distortion correction and signal intensity recovery. Besides, investigators should limit the number of resampling steps applied on images to avoid artificial tensor over-fitting. Finally, optimal correction performance can be obtained with FSfullRPE acquisition but at the expense of long acquisition and processing times. A crucial outcome here is that analysis should never be conducted on datasets which underwent distinct preprocessing pipelines. Finally, further investigations should be performed to evaluate the influence of the same pipelines regarding other acquisition settings such as *b*-value, q-space sampling size, and noise reduction, where the correction of eddy-currents should be of major importance.

The Diffuse software toolbox implemented to conduct the present study is available at this link: https://github.com/MecaLab/Brainvisa-Diffuse. It offers an automatic selection of the optimal preprocessing pipeline given the acquired DWI data. It also provides registration with anatomy, local model reconstruction and tractography algorithms. The Diffuse toolbox is embedded in the BrainVISA platform which gives access to volume-based and surface-based anatomical data processing, as well as to an efficient database management.

ANNEXE

List of subject IDs as provided by the Human Connectome Project: S1:106319, S2:150625, S3:188751, S4:193441, S5:220721, S6:424939, S7:627852, S8:773257, S9:932554, S10:983773, S11:102513, S12:110613, S13:114621, S14:147030, S15:158843, S16:159946, S17:176441, S18:346137, S19:677766, and S20:942658.

ETHICS STATEMENT

Data were provided by the Human Connectome Project, WU-Minn Consortium (Principal Investigators: David Van Essen and Kamil Ugurbil; 1U54MH091657) funded by the 16 NIH Institutes and Centers that support the NIH Blueprint for Neuroscience Research; and by the McDonnell Center for Systems Neuroscience at Washington University. Clinical data were provided by the MRI Center of the Neuroscience Institute of La Timone, in Marseille. The study received the approval of the Ethics Committee (N_ RCB 2012-A00268-35).

AUTHOR CONTRIBUTIONS

LB and AP implemented the data processing toolbox *Diffuse,* processed the HCP dataset through the 6 pipelines and performed the statistical analyses. JS participated to the choice of the optimal database, as well as the tools integrated in the toolbox. JS, CD, and OC brought valuable input to the discussion of the results. LB, AP, and OC released the toolbox publicly on Github. All authors contributed to the preparation and correction of the article, figures, and tables.

FUNDING

This work was supported by Fondation pour la Recherche Medicale (Grants No. ING20150532268).

ACKNOWLEDGMENTS

We warmly thank Denis Riviere for his technical support on the integration of *Diffuse* into the BrainVISA software.

SUPPLEMENTARY MATERIAL

The Supplementary Material for this article can be found online at: https://www.frontiersin.org/articles/10.3389/fnins.2019.00536/full#supplementary-material

REFERENCES

Albi, A., Meola, A., Zhang, F., Kahali, P., Rigolo, L., Tax, C. M. W., et al. (2018). Image registration to compensate for EPI distortion in patients with brain tumors: an evaluation of tract-specific effects. *J. Neuroimaging* 28, 173–182. doi: 10.1111/jon.12485

Alexander, A. L., Tsuruda, J. S., and Parker, D. L. (1997). Elimination of eddy current artifacts in diffusion-weighted echo-planar images: the use of bipolar gradients. *Magn. Reson. Med.* 38, 1016–1021. doi: 10.1002/mrm.1910380623

Andersson, J. L. R., Graham, M. S., Drobnjak, I., Zhang, H., Filippini, N., and Bastiani, M. (2017). Towards a comprehensive framework for movement and distortion correction of diffusion MR images: within volume movement. *Neuroimage* 152, 450–466. doi: 10.1016/j.neuroimage.2017.02.085

Andersson, J. L. R., Graham, M. S., Zsoldos, E., and Sotiropoulos, S. N. (2016). Incorporating outlier detection and replacement into a non-parametric framework for movement and distortion correction of diffusion MR images. *Neuroimage* 141, 556–572. doi: 10.1016/j.neuroimage.2016.06.058

Andersson, J. L. R., Jenkinson, M., and Smith, S. (2009). Non-linear registration aka Spatial normalisation FMRIB. *Neuroimage* 45, S173–S186. doi: 10.1016/j.neuroimage.2008.10.055

Andersson, J. L. R., Skare, S., and Ashburner, J. (2003). How to correct susceptibility distortions in spin-echo echo-planar images: application to diffusion tensor imaging. *Neuroimage* 20, 870–888. doi: 10.1016/S1053-8119(03)00336-7

Andersson, J. L. R., and Sotiropoulos, S. N. (2016). An integrated approach to correction for off-resonance effects and subject movement in diffusion MR imaging. *Neuroimage* 125, 1063–1078. doi: 10.1016/j.neuroimage.2015.10.019

Auría, A., Daducci, A., Thiran, J., and Wiaux, Y. (2015). NeuroImage Structured sparsity for spatially coherent fi bre orientation estimation in diffusion MRI. *Neuroimage* 115, 245–255. doi: 10.1016/j.neuroimage.2015.04.049

Basser, P. J., and Pajevic, S. (2000). Statistical artifacts in diffusion tensor MRI (DT-MRI) caused by background noise. *Magn. Reson. Med.* 44, 41–50. doi: 10.1002/1522-2594

Bastiani, M., Andersson, J., Cordero-Grande, L., Murgasova, M., Hutter, J., Price, A., et al. (2019). Automated processing pipeline for neonatal diffusion MRI in the developing Human Connectome Project. *Neuroimage* 185, 750–763. doi: 10.1016/j.neuroimage.2018.05.064

Bastiani, M., Cottaar, M., Dikranian, K., Ghosh, A., Zhang, H., Alexander, D. C., et al. (2017). Improved tractography using asymmetric fibre orientation distributions. *Neuroimage* 158, 205–218. doi: 10.1016/j.neuroimage.2017.06.050

Baum, G. L., Roalf, D. R., Cook, P. A., Ciric, R., Rosen, A. F. G., Xia, C., et al. (2018). The impact of in-scanner head motion on structural connectivity derived from diffusion MRI. *Neuroimage* 173, 275–286. doi: 10.1016/j.neuroimage.2018.02.041

Ben-Amitay, S., Jones, D. K., and Assaf, Y. (2012). Motion correction and registration of high b-value diffusion weighted images. *Magn. Reson. Med.* 67, 1694–1702. doi: 10.1002/mrm.23186

Bhushan, C., Haldar, J. P., Choi, S., Joshia, A., Shattuckc, D. W., and Leahy, R. M. (2016). Co-registration and distortion correction of diffusion and anatomical images based on inverse contrast normalization. *Neuroimage* 269–280. doi: 10.1016/j.neuroimage.2015.03.050

Bodammer, N., Kaufmann, J., Kanowski, M., and Tempelmann, C. (2004). Eddy current correction in diffusion-weighted imaging using pairs of images acquired with opposite diffusion gradient polarity. *Magn. Reson. Med.* 51, 188–193. doi: 10.1002/mrm.10690

Calhoun, V. D., Wager, T. D., Krishnan, A., Rosch, K. S., Seymour, K. E., Beth Nebel, M., et al. (2017). The impact of T1 versus EPI spatial normalization templates for fMRI data analyses. *Hum. Brain Mapp.* 38, 5331–5342. doi: 10.1002/hbm.23737

Caruyer, E., Lenglet, C., Sapiro, G., and Deriche, R. (2013). Design of multishell sampling schemes with uniform coverage in diffusion MRI. *Magn. Reson. Med.* 69, 1534–1540. doi: 10.1002/mrm.24736

Catani, M., and Thiebaut de Schotten, M. (2008). A diffusion tensor imaging tractography atlas for virtual in vivo dissections. *Cortex* 44, 1105–1132. doi: 10.1016/j.cortex.2008.05.004

Chang, L. C., Jones, D. K., and Pierpaoli, C. (2005). RESTORE: Robust estimation of tensors by outlier rejection. *Magn. Reson. Med.* 53, 1088–1095. doi: 10.1002/mrm.20426

Christiaens, D., Reisert, M., Dhollander, T., Sunaert, S., Suetens, P., and Maes, F. (2015). Global tractography of multi-shell diffusion-weighted imaging data using a multi-tissue model. *Neuroimage* 123, 89–101. doi: 10.1016/j.neuroimage.2015.08.008

Cusack, R., Brett, M., and Osswald, K. (2003). An evaluation of the use of magnetic field maps to undistort echo-planar images. *Neuroimage* 18, 127–142. doi: 10.1006/nimg.2002.1281

Daducci, A., Palù, A. D., Lemkaddem, A., Thiran, J., and Member, S. (2015). COMMIT: convex optimization modeling for microstructure informed tractography. *IEEE Trans. Med. Imaging* 34, 246–257. doi: 10.1109/TMI.2014.2352414

Embleton, K. V., Haroon, H. A., Morris, D. M., Ralph, M. A. L., and Parker, G. J. M. (2010). Distortion correction for diffusion-weighted MRI tractography and fMRI in the temporal lobes. *Hum. Brain Mapp.* 31, 1570–1587. doi: 10.1002/hbm.20959

Farzinfar, M., Oguz, I., Smith, R. G., Verde, A. R., Dietrich, G., Gupta, A., et al. (2013). Diffusion imaging quality control via entropy of principal direction distribution. *Neuroimage* 82, 1–12. doi: 10.1016/j.neuroimage.2013.05.022

Fillard, P., Descoteaux, M., Goh, A., Gouttard, S., Jeurissen, B., and Malcolm, J. (2011). Quantitative evaluation of 10 tractography algorithms on a realistic diffusion MR phantom. *Neuroimage* 56, 220–234. doi: 10.1016/j.neuroimage.2011.01.032

Fischer, C., Operto, G., Laguitton, S., Perrot, M., Denghien, I., Riviere, D., et al. (2012). "Morphologist 2012: the new morphological pipeline of BrainVISA," in *Proceedings of the HBM*, Beijing.

Garyfallidis, E., Brett, M., Amirbekian, B., Rokem, A., van der Walt, S., Descoteaux, M., et al. (2014). Dipy, a library for the analysis of diffusion MRI data. *Front. Neuroinformatics* 8:8. doi: 10.3389/fninf.2014.00008

Geffroy, D., Rivière, D., Denghien, I., Souedet, N., Laguitton, S., and Cointepas, Y. (2011). "BrainVISA?: a complete software platform for neuroimaging," in *Proceedings of the Python in Neuroscience Workshop*, Paris.

Ghosh, A., and Deriche, R. (2016). A survey of current trends in diffusion MRI for structural brain connectivity. *J. Neural Eng.* 13:011001. doi: 10.1088/1741-2560/13/1/011001

Girard, G., Daducci, A., Petit, L., Thiran, J., Whittingstall, K., Deriche, R., et al. (2017). AxTract?: towards microstructure informed tractography. *Hum. Brain Mapp.* 38, 5485–5500. doi: 10.1002/hbm.23741

Girard, G., Whittingstall, K., Deriche, R., and Descoteaux, M. (2014). Towards quantitative connectivity analysis: reducing tractography biases. *Neuroimage* 98, 266–278. doi: 10.1016/j.neuroimage.2014.04.074

Glasser, M. F., Smith, S. M., Marcus, D. S., Andersson, J., Auerbach, E., Behrens, T., et al. (2016). The Human Connectome Project's neuroimaging approach. *Nat. Neurosci.* 19, 1175–1187. doi: 10.1038/nn.4361

Graham, M. S., Drobnjak, I., and Zhang, H. (2016). Realistic simulation of artefacts in diffusion MRI for validating post-processing correction techniques. *Neuroimage* 125, 1079–1094. doi: 10.1016/j.neuroimage.2015.11.006

Hagmann, P., Cammoun, L., Gigandet, X., Gerhardb, S., Grant, P., Wedeend, V., et al. (2010). MR connectomics: principles and challenges. *J. Neurosci. Methods* 194, 34–45. doi: 10.1016/j.jneumeth.2010.01.014

Haselgrove, J. C., and Moore, J. R. (1996). Correction for distortion of echo-planar images used to calculate the apparent diffusion coefficient. *Magn. Reson. Med.* 36, 960–964. doi: 10.1002/mrm.1910360620

Hutchinson, E. B., Avram, A. V., Irfanoglu, M. O., Koay, C. G., Barnett, A. S., Komlosh, M. E., et al. (2017). Analysis of the effects of noise, DWI sampling, and value of assumed parameters in diffusion MRI models. *Magn. Reson. Med.* 78, 1767–1780. doi: 10.1002/mrm.26575

Irfanoglu, M. O., Walker, L., Sarlls, J., Marenco, S., and Pierpaoli, C. (2012). Effects of image distortions originating from susceptibility variations and concomitant fields on diffusion MRI tractography results. *Neuroimage* 61, 275–288. doi: 10.1016/j.neuroimage.2012.02.054

Jenkinson, M., Beckmann, C. F., Behrens, T. E. J., Woolrich, M. W., and Smith, S. M. (2012). FSL. *Neuroimage* 62, 782–790. doi: 10.1016/j.neuroimage.2011.09.015

Jezzard, P., and Balaban, R. S. (1995). Correction for geometric distortion in echo-planar images from B*0* Field Variations. *Magn. Reson. Med.* 34, 65–73. doi: 10.1002/mrm.1910340111

Jezzard, P., Barnett, A. S., and Pierpaoli, C. (1998). Characterization of and correction for eddy current artifacts in echo planar diffusion imaging. *Magn. Reson. Med.* 39, 801–812. doi: 10.1002/mrm.1910390518

Jones, D. K., and Cercignani, M. (2010). Twenty-five pitfalls in the analysis of diffusion MRI data. *NMR Biomed.* 23, 803–820. doi: 10.1002/nbm.1543

Kim, D.-J., Park, H., Kang, K., Shin, Y., Kim, J., and Moon, W. (2006). How does distortion correction correlate with anisotropic indices? A diffusion tensor imaging study. *Magn. Reson. Imaging* 24, 1369–1376. doi: 10.1016/j.mri.2006.07.014

Kybic, J., Thévenaz, P., Nirkko, A., and Unser, M. (2000). Unwarping of unidirectionally distorted EPI images. *IEEE Trans. Med. Imaging* 19, 80–93. doi: 10.1109/42.836368

Lazar, M., and Alexander, A. L. (2005). Bootstrap white matter tractography (BOOT-TRAC). *Neuroimage* 24, 524–532. doi: 10.1016/j.neuroimage.2004.08.050

Le Bihan, D., Poupon, C., Amadon, A., and Lethimonnier, F. (2006). Artifacts and pitfalls in diffusion MRI. *J. Magn. Reson. Imaging* 24, 478–488. doi: 10.1002/jmri.20683

Leemans, A., and Jones, D. K. (2009). The B -matrix must be rotated when correcting for subject motion in DTI data. *Magn. Reson. Med.* 61, 1336–1349. doi: 10.1002/mrm.21890

Mahmoudzadeh, A. P., and Kashou, N. H. (2013). Evaluation of interpolation effects on upsampling and accuracy of cost functions-based optimized automatic image registration. *Int. J. Biomed. Imaging* 2013:395915. doi: 10.1155/2013/395915

Mangin, J.-F., Fillard, P., Cointepas, Y., Le Bihan, D., Frouin, V., and Poupon, C. (2013). Toward global tractography. *Neuroimage* 80, 290–296. doi: 10.1016/j.neuroimage.2013.04.009

Manjón, J. V., Coupé, P., Concha, L., Buades, A., Collins, D. L., and Robles, M. (2013). Diffusion weighted image denoising using overcomplete local PCA. *PLoS One* 8:e73021. doi: 10.1371/journal.pone.0073021

Mattes, D., Haynor, D. R., Vesselle, H., Lewellen, T. K., and Eubank, W. (2001). "Nonrigid multimodality image registration," in *Proceedings of the SPIE International Society for Optical Engineering*, Vol. 4322, (San Diego, CA), 1609–1620.

Merhof, D., Soza, G., Stadlbauer, A., Greiner, G., and Nimsky, C. (2007). Correction of susceptibility artifacts in diffusion tensor data using non-linear registration. *Med. Image Anal.* 11, 588–603. doi: 10.1016/j.media.2007.05.004

Modat, M., Ridgway, G. R., Taylor, Z. A., Lehmann, M., Barnes, J., Hawkes, D., et al. (2010). Fast free-form deformation using graphics processing units. *Comput. Methods Programs Biomed.* 98, 278–284. doi: 10.1016/j.cmpb.2009.09.002

Mori, S., Wakana, S., van Zijl, C. M., and Nagae-Poetscher, L. M. (2005). *MRI Atlas of Human White Matter*. Amsterdam: Elsevier.

Neher, P. F., Descoteaux, M., Houde, J., Stieltjes, B., and Maier-hein, K. H. (2015). Strengths and weaknesses of state of the art fiber tractography pipelines – A comprehensive in-vivo and phantom evaluation study using Tractometer. *Med. Image Anal.* 26, 287–305. doi: 10.1016/j.media.2015.10.011

Nilsson, M., Szczepankiewicz, F., Van Westen, D., and Hansson, O. (2015). Extrapolation-based references improve motion and eddy-current correction of high B-value DWI data: application in Parkinson's disease dementia. *PLoS One* 10:e0141825. doi: 10.1371/journal.pone.0141825

Ning, L., Laun, F., Gur, Y., DiBella, E., Deslauriers-Gauthier, S., Megherbi, T., et al. (2015). Sparse Reconstruction Challenge for diffusion MRI: Validation on a physical phantom to determine which acquisition scheme and analysis method to use? *Med. Image Anal.* 26, 316–331. doi: 10.1016/j.media.2015.10.012

Oguz, I., Farzinfar, M., Matsui, J., Budi, F., Liu, Z., Gerig, G., et al. (2014). DTIPrep: quality control of diffusion-weighted images. *Front. Neuroinformatics* 8:4. doi: 10.3389/fninf.2014.00004

Papadakis, N. G., Martin, K. M., Wilkinson, I. D., and Huang, C. L.-H. (2003). A measure of curve fitting error for noise filtering diffusion tensor MRI data. *J. Magn. Reson.* 164, 1–9. doi: 10.1016/S1090-7807(03)00202-7

Reber, P. J., Wong, E. C., Buxton, R. B., and Frank, L. R. (1998). Correction of off resonance-related distortion in echo-planar imaging using EPI-based field maps. *Magn. Reson. Med.* 39, 328–330. doi: 10.1002/mrm.1910390223

Reisert, M., Mader, I., Anastasopoulos, C., Weigel, M., Schnell, S., and Kiselev, V. (2011). Global fiber reconstruction becomes practical. *Neuroimage* 54, 955–962. doi: 10.1016/j.neuroimage.2010.09.016 PMID:20854913 doi: 10.1016/j.neuroimage.2010.09.016

Rivière, D., Geffroy, D., Denghien, I., Souedet, N., and Cointepas, Y. (2011). "Anatomist: a python framework for interactive 3D visualization of neuroimaging data," in *Proceedings of the Python in Neuroscience Workshop*, Paris.

Roalf, D. R., Quarmley, M., Elliott, M. A., Satterthwaite, T. D., Vandekar, S. N., Ruparel, K., et al. (2016). The impact of quality assurance assessment on diffusion tensor imaging outcomes in a large-scale population-based cohort. *Neuroimage* 125, 903–919. doi: 10.1016/j.neuroimage.2015.10.068

Rohde, G. K., Barnett, A. S., Basser, P. J., Marenco, S., and Pierpaoli, C. (2004). Comprehensive approach for correction of motion and distortion in diffusion-weighted MRI. *Magn. Reson. Med.* 51, 103–114. doi: 10.1002/mrm.10677

Schmitt, F., Stehling, M. K., and Turner, R. (1998). *Echo-Planar Imaging*. Berlin: Springer.

Shen, Y., Larkman, D. J., Counsell, S., Pu, I. M., Edwards, D., and Hajnal, J. V. (2004). Correction of high-order eddy current induced geometric distortion in diffusion-weighted echo-planar images. *Magn. Reson. Med.* 52, 1184–1189. doi: 10.1002/mrm.20267

Smith, S. M., Jenkinson, M., Woolrich, M. W., Beckmann, C. F., Behrens, T. E. J., and Johansen-Berg, H. (2004). Advances in functional and structural MR image analysis and implementation as FSL. *Neuroimage* 23, S208–S219. doi: 10.1016/j.neuroimage.2004.07.051

Sotiropoulos, S. N., Jbabdi, S., Xu, J., Andersson, J., Moeller, S., Auerbach, E., et al. (2013). Advances in diffusion MRI acquisition and processing in the Human Connectome Project. *Neuroimage* 80, 125–143. doi: 10.1016/j.neuroimage.2013.05.057

Tao, R., Fletcher, P. T., Gerber, S., and Whitaker, R. T. (2009). "A Variational image-based approach to the correction of susceptibility artifacts in the alignment of diffusion weighted and structural MRI," in *Information Processing in Medical Imaging. IPMI 2009. Lecture Notes in Computer Science*, Vol. 5636, eds J. L. Prince, D. L. Pham, and K. J. Myers (Berlin: Springer), 664–675. doi: 10.1007/978-3-642-02498-6_55

Taylor, P. A., Alhamud, A., van der Kouwe, A., Saleh, M. G., Laughton, B., and Meintjes, E. (2016). Assessing the performance of different DTI motion correction strategies in the presence of EPI distortion correction. *Hum. Brain Mapp.* 37, 4405–4424. doi: 10.1002/hbm.23318

Treiber, J. M., White, N. S., Steed, T. C., Bartsch, H., Holland, D., Farid, N., et al. (2016). Characterization and correction of geometric distortions in 814 Diffusion Weighted Images. *PLoS One* 11: e0152472. doi: 10.1371/journal.pone.0152472

Van Essen, D. C., Smith, S. M., Barch, D. M., Behrens, T. E. J., Yacoub, E., and Ugurbil, K. (2013). The WU-Minn human connectome project: an overview. *Neuroimage* 80, 62–79. doi: 10.1016/j.neuroimage.2013.05.041

Wang, S., Peterson, D. J., Gatenby, J. C., Li, W., Grabowski, T. J., and Madhyastha, T. M. (2017). Evaluation of Field Map and Nonlinear Registration Methods for Correction of Susceptibility Artifacts in Diffusion MRI. *Front. Neuroinformatics* 11:17. doi: 10.3389/fninf.2017.00017

Wu, M., Chang, L. C., and Walker, L. (2008). Comparison of EPI distortion correction methods in diffusion tensor MRI using a novel framework. *Med. Image Comput. Comput. Assist. Interv.* 11, 321–329. doi: 10.1007/978-3-540-85990-1-39

Yamada, H., Abe, O., Shizukuishi, T., Kikuta, J., and Shinozaki, T. (2014). Efficacy of distortion correction on diffusion imaging?: comparison of FSL Eddy and Eddy_Correct Using 30 and 60 directions diffusion encoding. *PLoS One* 9:e112411. doi: 10.1371/journal.pone.0112411

Yendiki, A., Koldewyn, K., Kakunoori, S., Kanwisher, N., and Fischl, B. (2014). Spurious group differences due to head motion in a diffusion MRI study. *Neuroimage* 88, 79–90. doi: 10.1016/j.neuroimage.2013.11.027

Conflict of Interest Statement: The authors declare that the research was conducted in the absence of any commercial or financial relationships that could be construed as a potential conflict of interest.

Copyright © 2019 Brun, Pron, Sein, Deruelle and Coulon. This is an open-access article distributed under the terms of the Creative Commons Attribution License (CC BY). The use, distribution or reproduction in other forums is permitted, provided the original author(s) and the copyright owner(s) are credited and that the original publication in this journal is cited, in accordance with accepted academic practice. No use, distribution or reproduction is permitted which does not comply with these terms.

frontiers in Neuroscience

ORIGINAL RESEARCH
published: 18 June 2019
doi: 10.3389/fnins.2019.00610

Objective and Automated Detection of Diffuse White Matter Abnormality in Preterm Infants Using Deep Convolutional Neural Networks

*Hailong Li[1], Nehal A. Parikh[1,2,3], Jinghua Wang[4], Stephanie Merhar[1,2], Ming Chen[1,5], Milan Parikh[1], Scott Holland[6,7] and Lili He[1,2]**

[1] The Perinatal Institute, Cincinnati Children's Hospital Medical Center, Cincinnati, OH, United States, [2] Department of Pediatrics, University of Cincinnati College of Medicine, Cincinnati, OH, United States, [3] Department of Pediatrics, Nationwide Children's Hospital, Columbus, OH, United States, [4] Department of Radiology, University of Cincinnati College of Medicine, Cincinnati, OH, United States, [5] Department of Electronic Engineering and Computing Systems, University of Cincinnati, Cincinnati, OH, United States, [6] Medpace Inc., Cincinnati, OH, United States, [7] Department of Physics, University of Cincinnati, Cincinnati, OH, United States

Diffuse white matter abnormality (DWMA), or diffuse excessive high signal intensity is observed in 50–80% of very preterm infants at term-equivalent age. It is subjectively defined as higher than normal signal intensity in periventricular and subcortical white matter in comparison to normal unmyelinated white matter on T_2-weighted MRI images. Despite the well-documented presence of DWMA, it remains debatable whether DWMA represents pathological tissue injury or a transient developmental phenomenon. Manual tracing of DWMA exhibits poor reliability and reproducibility and unduly increases image processing time. Thus, objective and ideally automatic assessment is critical to accurately elucidate the biologic nature of DWMA. We propose a deep learning approach to automatically identify DWMA regions on T_2-weighted MRI images. Specifically, we formulated DWMA detection as an image voxel classification task; that is, the voxels on T_2-weighted images are treated as samples and exclusively assigned as DWMA or normal white matter voxel classes. To utilize the spatial information of individual voxels, small image patches centered on the given voxels are retrieved. A deep convolutional neural networks (CNN) model was developed to differentiate DWMA and normal voxels. We tested our deep CNN in multiple validation experiments. First, we examined DWMA detection accuracy of our CNN model using computer simulations. This was followed by *in vivo* assessments in a cohort of very preterm infants (N = 95) using cross-validation and holdout validation. Finally, we tested our approach on an *independent* preterm cohort (N = 28) to externally validate our model. Our deep CNN model achieved Dice similarity index values ranging from 0.85 to 0.99 for DWMA detection in the aforementioned validation experiments. Our proposed deep CNN model exhibited significantly better performance than other popular machine learning models. We present an objective and automated approach for accurately identifying DWMA that may facilitate the clinical diagnosis of DWMA in very preterm infants.

Keywords: diffuse white matter abnormality, very preterm infants, MRI, deep learning, convolutional neural networks

OPEN ACCESS

Edited by:
Xi-Nian Zuo,
Institute of Psychology (CAS), China

Reviewed by:
Ives R. Levesque,
McGill University, Canada
Tolga Cukur,
Bilkent University, Turkey

****Correspondence:***
Lili He
lili.he@cchmc.org

Specialty section:
This article was submitted to Brain Imaging Methods, a section of the journal Frontiers in Neuroscience

Received: *15 February 2019*
Accepted: *28 May 2019*
Published: *18 June 2019*

Citation:
Li H, Parikh NA, Wang J, Merhar S, Chen M, Parikh M, Holland S and He L (2019) Objective and Automated Detection of Diffuse White Matter Abnormality in Preterm Infants Using Deep Convolutional Neural Networks. Front. Neurosci. 13:610. doi: 10.3389/fnins.2019.00610

INTRODUCTION

Diffuse white matter abnormality (DWMA) is observed in 50–80% of very preterm infants at term-equivalent age (Maalouf et al., 1999; Skiöld et al., 2010; Parikh et al., 2013). It is characterized by either (1) diffusely higher signal intensity in periventricular and subcortical white matter than in normal unmyelinated white matter on T_2-weighted MRI images [also known as diffuse excessive high signal intensity (Skiöld et al., 2012; He and Parikh, 2013b)]; or (2) lower signal intensity than unmyelinated white matter on T_1-weighted and fluid-attenuated inversion recovery (FLAIR) sequences. A number of prior studies (Maalouf et al., 1999; Counsell et al., 2003; Inder et al., 2003; Dyet et al., 2006; Krishnan et al., 2007; Cheong et al., 2009; Hagmann et al., 2009; Hart et al., 2010b; Skiöld et al., 2010; de Bruïne et al., 2011; Iwata et al., 2012; Jeon et al., 2012; He and Parikh, 2013a,b; Parikh et al., 2013) in the past two decades have reported the presence of DWMA in very preterm infants. Despite the well-documented presence of DWMA and emerging evidence of its pathological nature, the significance of DWMA for long-term neurodevelopment remains debatable (Dyet et al., 2006; Krishnan et al., 2007; Hart et al., 2010b; de Bruïne et al., 2011; Iwata et al., 2012; Jeon et al., 2012; He and Parikh, 2013a; Parikh et al., 2016; Volpe, 2017). Much of this debate has been fueled by the nearly universal use of qualitative reporting of DWMA that is subjective and unreliable, likely resulting in measurement error and lack of association with neurodevelopmental impairments in some studies (Hagmann et al., 2009; Hart et al., 2010a; de Bruïne et al., 2011). Volpe has speculated this finding to be a milder form of white matter injury that represents either periventricular leukomalacia with microscopic necrosis or isolated diffuse white matter gliosis (Volpe, 2017). The only DWMA imaging-pathologic correlation study reported some histopathologic overlap with periventricular leukomalacia, but also reported distinctive features, suggesting DWMA may be a form of diffuse white matter gliosis without microscopic necrosis (Parikh et al., 2016).

Only a few studies have attempted to develop reproducible quantitative methods for evaluating DWMA in preterm infants. Manually tracing DWMA regions on T_2-weighted images, slice by slice, produces poor reliability and reproducibility (Hagmann et al., 2009; Hart et al., 2010a; de Bruïne et al., 2011). For example, the inter- and intra-observer agreement for visual diagnosis has ranged from a Kappa statistic of 0.14 to 0.44 (Hart et al., 2010a; Calloni et al., 2015), which is generally considered poor (Landis and Koch, 1977). The use of manual DWMA segmentation also significantly prolongs image processing time, limiting the utility of this approach for large studies (Yoshita et al., 2005). Accurate and automatic detection of DWMA is of crucial importance for resolving the debate about DWMA's biologic nature and potentially risk stratifying high-risk preterm infants that may benefit from early intervention therapies (Hagmann et al., 2009; Mathur et al., 2010; Parikh, 2016). Limited studies have been published for automated detection of DWMA in infants (He and Parikh, 2013a,b; Parikh et al., 2013). These approaches were developed by utilizing only individual voxels for DWMA detection without considering the neighboring spatial information, which contributed to a higher false positive DWMA detection rate.

In adults, DWMA detection has been well investigated by using traditional machine learning techniques, including k-nearest neighbors (Griffanti et al., 2016), Bayesian models (Maillard et al., 2008), random forests (Geremia et al., 2011), logistic regression (Schmidt, 2017), and support vector machine (Lao et al., 2008). These machine learning approaches have been demonstrated to perform consistently well on T_1-weighted or FLAIR MR images by taking advantage of spatial information of a given set of voxels (i.e., small image patches that are comprised of the given voxel and its neighboring voxels). These have enabled automated and objective detection of DWMA to facilitate epidemiological studies investigating the associations between DWMA and clinical outcomes (Guerrero et al., 2018). In recent years, studies using deep convolutional neural networks (CNN) and associated U-net architectures have outperformed traditional machine learning models in identifying DWMA in adults, due to CNN's superior capacity in decoding complex image patterns (Brosch et al., 2013, 2016; Ghafoorian et al., 2016; Kamnitsas et al., 2017; Guerrero et al., 2018; Moeskops et al., 2018).

Deep CNN, inspired by the neuronal organization pattern of the visual cortex, is a class of deep learning models that have been widely applied in a range of machine learning tasks, such as image classification, natural language processing, and pattern recognition (LeCun and Bengio, 1995; LeCun et al., 1998, 2015). Compared to traditional approaches, CNN automatically extracts a hierarchy of increasingly complex image features from raw images without hand-engineered (i.e., unsupervised) feature extraction. This advantage is achieved by assembling a series of alternative operations as network layers into a consecutive multi-layer architecture. Although the individual layers only perform relatively simple operations such as convolution and pooling operations, the assembled CNN models are capable of mapping highly complex non-linearity between inputs and outputs. Various CNN architectures can be designed and modified for diverse machine learning tasks (Bengio and LeCun, 2007; Hinton et al., 2012; Krizhevsky et al., 2012; LeCun et al., 2015; Szegedy et al., 2015; Xu et al., 2015). Segmentation of DWMA on brain images could be implemented in two ways. A popular way is U-net based approaches, which take relatively large patches of original images. These have been applied on the adult applications with T_1-weighted or FLAIR MR images. But, the performance of U-net approaches are still not desirable. Guerrero et al. (2018) reported a 69.5 of Dice score in their recent work. Another way is to apply CNN approaches on small images patches so as to classify individual voxels (Zhang et al., 2015). Considering the small number of sample size and low contrast on T_2-weighted MR images in neonatal studies, we set to purse the second way in this work.

To fill the gap in accurate neonatal DWMA detection, we developed a deep learning approach to automatically identify DWMA regions on T_2-weighted MRI images. Specifically, the detection of DWMA was formulated as an image voxel classification task. Small image patches that are centered on

the given voxels were utilized to represent regional spatial information of individual voxels. A CNN model with the batch normalization technique was developed to differentiate normal white matter from DWMA voxels. The deep CNN architecture consists of feature extraction layers that aim to capture discriminative image patterns and high-level reasoning layers that are designed for decision making. We evaluated the proposed model using computer simulation, as well as internal and external validation using data from two independent very preterm infant cohorts.

TABLE 1 | Baseline demographic information for both very preterm cohorts.

	Cohort 1	Cohort 2
Number of subjects	95	28
Sex	51M (53.7%)	14M (50%)
Birth weight (g)	1136.9 ± 397.5	979 ± 302.1
GA at birth (weeks)	28.5 ± 2.5	26.8 ± 2.1
PMA at scan (weeks)	40.4 ± 0.6	39.4 ± 1.3
Scanner	Siemens	GE

GA, gestational age; PMA, post menstrual age; M, male; F, female. All ± data is mean ± SD.

MATERIALS AND METHODS

Subjects

The data for this study was derived from two independent cohorts of very preterm infants. The Institutional Review Board of Nationwide Children's Hospital (NCH) approved both studies and written parental informed consent was obtained for every subject. Infants with known structural congenital central nervous system anomalies, congenital chromosomal anomalies, congenital cyanotic cardiac defects, or overt brain injury were excluded. In addition, parents were not approached for consent if their infant remained on persistently high mechanical ventilator support (e.g., peak inspiratory pressure >30 and/or fraction of inspired oxygen >50%). All subjects were scanned with a brain MRI at term-equivalent age during natural sleep without the use of any sedation, after being fed and swaddled. MRI noise was minimized using Insta-Puffy Silicone Earplugs (E.A.R. Inc., Boulder, CO.) and Natus Mini Muffs (Natus Medical Inc., San Carlos, CA, United States).

Cohort 1

This cohort included 95 very preterm infants, ≤32 weeks gestational age that were recruited from four Columbus, Ohio area neonatal intensive care units, including NCH, Ohio State University Medical Center, Riverside Methodist Hospital, and St. Ann's Hospital. We collected anatomical axial T_2-weighted MRI images from each subject using the following sequence parameters: Repetition time (TR)/ echo time (TE) = 9,500/147 ms, flip angle (FA) = 90°, imaging matrix = 156 × 192, resolution 0.9 mm^3 × 0.9 mm^3 × 1.1 mm^3 – on a 3T Siemens MAGNETOM Skyra scanner at NCH. Subjects from non-NCH sites had to be discharged from the NICU by term-equivalent age so they could be imaged at NCH. We used data from this cohort for deep CNN model development, internal cross-validation and holdout validation.

Cohort 2

This cohort included 28 very preterm infants, ≤32 weeks gestational age, all cared for in the neonatal intensive care unit at NCH (He et al., 2018). Anatomical scans were obtained with a proton density/T_2-weighted sequence (TR/TE1/TE2 = 11,000/14/185 ms, FA = 90°, resolution 0.35 mm^3 × 0.35 mm^3 × 2 mm^3) on a 3T GE HDX scanner. We used data from this cohort for external validation.

Our inclusion criteria of very preterm infants born at 32 weeks gestational age or younger was selected based on the highest risk group for DWMA. The age range for our two cohorts was 23–32 weeks. Infants more mature than 32 weeks gestational age have a much lower incidence of DWMA and were therefore not included in the study/analyses. We selected a window of 39–44 weeks postmenstrual age for MRI scanning because this is the peak postmenstrual age when DWMA is observed on T_2-weighted MRI (observed in 89% of very preterm infants between 40 and 44 weeks postmenstrual age in the cohort by de Bruïne et al. (2011). In this cohort, it was also found to be absent in infants imaged after 50 weeks postmenstrual age, thus confirming our choice of MRI timing. Demographics information for both cohorts is listed in **Table 1**.

Overview of DWMA Detection Using Deep CNN

We formulated the detection of DWMA into an image voxel classification task. Each T_2-weighted white matter voxel is exclusively assigned into either DWMA or normal group. To utilize the image spatial information around voxels (Zhang et al., 2015), a small neighborhood/image patch centered on a given voxel is sampled. This typically results in a set of $\sim 10^5$ image patches for each subject. The deep CNN model takes each image patch as input and assigns a label to its center voxel (**Figure 1**).

Deep CNN Architectures

We designed a 12-layer deep CNN architecture, based on a prior study (Zhang et al., 2015), for image patches of 13 × 13 (**Figure 2**). The first hidden layer is a convolutional layer that contains 8 convolutional neurons. Each convolutional neuron consists of a trainable 2D filter of size 3 × 3 and a rectified linear unit activation function. Given an input $\mathbf{X}$ (i.e. a 2D n × n image patch), the activation output a_{conv} of the convolutional neuron can be represented by:

$$a_{\text{conv}} = \max(0, \mathbf{X} * \mathbf{W}_{\text{conv}})$$

where $*$ denotes the convolution operator and $\mathbf{W}_{\text{conv}}$ is the trainable weight map of the 2D filter. By using a stride size of one, the first hidden layer outputs eight 11 × 11 feature maps. The second hidden layer is a batch normalization layer, which performs a *batch normalizing transform* $\text{BN}_{\gamma,\beta}$. Since a mini-batch stochastic gradient descent algorithm is applied to optimize the proposed CNN, this normalization step transforming on

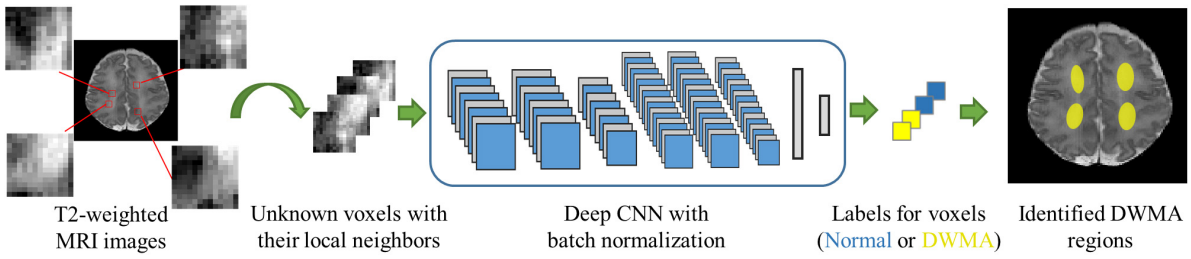

FIGURE 1 | Overview of DWMA detection using deep CNN model.

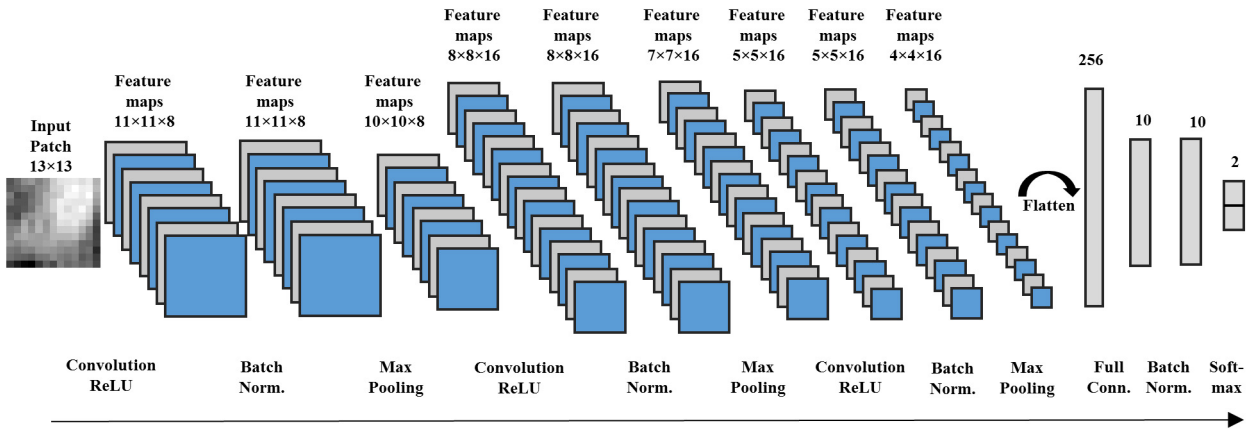

FIGURE 2 | A deep CNN with 12 layers designed for image patches with size 13 × 13 voxels.

a mini-batch $B = [x_{1,\ldots,m}]$ with m activation values can be described as:

$$\mathrm{BN}_{\gamma,\beta}(x_i) = \gamma \frac{x_i - \mu_B}{\sqrt{\sigma_B^2 + \epsilon}} + \beta$$

where μ_B and σ_B are mini-batch mean and variance of mini-batch B. x_i is a particular activation of 2D feature maps. Parameters γ and β control the scale and shift of the normalized values, which are to be optimized during model training. ϵ is a small fuzz f number to avoid dividing by zero. Those 8 feature maps from the first hidden layer are normalized individually. The output of the second hidden layer are the normalized feature maps, which have the same size (e.g., 11 × 11) as the output of the previous layer. The third hidden layer is a max pooling layer, which combines the activation values of neuron clusters at prior layer into a single neuron by using the maximum value of the given cluster. We also applied a stride size of one for max pooling operation. This layer generates 8 feature maps with a size of 10 × 10. In the following, we applied convolutional, batch normalization and max pooling layers consecutively in this CNN architecture from the fourth to ninth hidden layers for feature extraction.

After obtaining sixteen 4 × 4 high-level feature maps, we flattened the feature maps into a single feature vector with 256 dimensions. Then, this feature vector is linked to the tenth hidden layer, a fully connected layer with 10 neurons. We also utilized a rectified linear unit activation function in the neurons of the fully connected layer. Assume that each neuron of the fully connected layer has a weight vector $\mathbf{W}_{\text{full}}$. Because the batch normalization layer is connected in the next layer, the bias $\mathbf{b}$ of neurons are removed. Given a flattened feature vector $\mathbf{v}$, the activation of each neuron can be presented by:

$$a_{\text{full}} = \max(0, \mathbf{v} \cdot \mathbf{W}_{\text{full}})$$

where · indicates the dot product between vectors. The 10th hidden layer transforms the flattened feature vector with 256 dimensions into a new feature vector with 10 dimensions, functioning as a dimension reduction for the features. Again, a batch normalization layer, as the eleventh hidden layer, is applied to normalize the low-dimension feature vector. At the end, the normalized 10-dimension feature vector is input into a 2-way softmax layer (Bengio and LeCun, 2007) (i.e., the output layer) that produces the probability for the normal and DWMA groups. The proposed deep CNN for input patch 13 × 13 has 12 network layers, including a total of 6,264 trainable parameters.

Similarly, we designed different deep CNN architectures for other n × n image patches [n= 7,9,13,17] based on prior work (Zhang et al., 2015). Intuitively, larger input patches contain more neighboring spatial information, requiring a deeper network and more kernels for feature extraction. In contrast, smaller input patches need a shallower CNN and fewer convolutional kernels. The details of different architectures are listed in **Table 2**.

TABLE 2 | Details of four deep CNNs for varying sizes of image patches.

Patch	Hyperparameters	Layer 1	Layer 2	Layer 3	Layer 4	Layer 5	Layer 6	Layer 7	Layer 8	Layer 9	Layer 10	Layer 11	Layer 12
7 × 7	Layer type	Conv.	Norm.	Pooling	Conv.	Norm.	Pooling	Full conn.	Norm.	Softmax	–	–	–
	Filter size	3	–	2 × 2	3	–	2 × 2	10	–	2	–	–	–
	Num of filter	8	–	–	8	–	–	1 × 1	–	–	–	–	–
9 × 9	Layer type	Conv.	Norm.	Pooling	Conv.	Norm.	Pooling	Full conn.	Norm.	Softmax	–	–	–
	Filter size	3	–	2 × 2	3	–	2 × 2	10	–	2	–	–	–
	Num of filter	8	–	–	16	–	–	1 × 1	–		–	–	–
13 × 13	Layer type	Conv.	Norm.	Pooling	Conv.	Norm.	Pooling	Conv.	Norm.	Pooling	Full conn.	Norm.	Softmax
	Filter size	3	–	2 × 2	3	–	2 × 2	3	–	2 × 2	10	–	2
	Num of filter	8	–	–	8	–	–	16	–	–	1 × 1	–	–
17 × 17	Layer type	Conv.	Norm.	Pooling	Conv.	Norm.	Pooling	Conv.	Norm.	Pooling	Full conn.	Norm.	Softmax
	Filter size	3	–	2 × 2	3	–	2 × 2	3	–	2 × 2	10	–	2
	Num of filter	8	–	–	16	–	–	16	–	–	1 × 1	–	–

Conv, convolutional layer; Norm, batch normalization layer; Full conn, fully connected layer.

Deep CNN Training

We adopted cross-entropy as a loss function to train our deep CNN model. Assuming that $p\left(y_i|\mathbf{X}_i;\mathbf{W}\right)$ and y_i are the predicted and true probability values for i^{th} image patch $\mathbf{X}_i$, the loss function for N training samples is calculated by:

$$H(\mathbf{W}) = -\frac{1}{N}\sum_{i=1}^{N} y_i \log(p(y_i|\mathbf{X}_i;\mathbf{W})) + (1-y_i)\log(1-p(y_i|\mathbf{X}_i;\mathbf{W}))$$

A mini-batch stochastic gradient descent algorithm (Johnson and Zhang, 2013) was chosen to minimize the above loss function so as to optimize the weights $\mathbf{W}$ of deep CNN. This algorithm divides the training data into small batches and updates the network weights using only data from every batch. It enables a faster, but more stable convergence for model training. We configured batch size as 256. To further accelerate the training, we applied a Nesterov momentum technique (Nesterov, 2007) for parameter searching. The weights of convolutional and fully connected layers were randomly initialized using Glorot uniform distribution (Glorot and Bengio, 2010). The learning rate was set as 0.1 based on classification performance after testing several empirical values [0.001, 0.01, 0.1, 0.5]. The number of epochs was set as 20 with an early stop mechanism, which would cease the optimization process if three consecutive epochs return the same loss errors.

Model Evaluation

DWMA gold standard information was annotated by two experts guided by an atlas-based method (He and Parikh, 2013a). All T2-weighted MRI data were obtained in Digital Imaging and Communications in Medicine (DICOM) format from two IRB-approved prospective studies (**Table 1**). We transferred MRI data into the Neuroimaging informatics technology Initiative (NIfTI) format. Typical procedure of Anterior Commissure (AC)-Posterior Commissure (PC) correction for each subject was performed using Statistical Parametric Mapping (SPM) package (Friston, 1994). We further conducted skull-stripping and tissue segmentation by using a neonatal structural MRI processing pipeline (He et al., 2018). Tissue probability maps for white matter, gray matter and cerebrospinal fluid voxels of T_2-weighted images were obtained. We normalized T_2-weighted images by using the z-score transformation. After preprocessing, DWMA regions of T_2-weighted images were outlined by identifying the white matter voxels with greater than or equal to $\alpha = 1.4$ standard deviation (SD) above the mean for cerebral tissues. All DWMA false positive voxels in the detected regions and isolated false positive voxels were manually corrected. Two DWMA expert raters evaluated the images individually, then collaborated to conclude a gold-standard DWMA dataset. Compared to normal voxels, the number of DWMA voxels are relatively small, therefore this results in an imbalanced classification problem (a disproportionate ratio of observations in each class). We therefore applied Dice index (Dice, 1945) and balanced accuracy (Brodersen et al., 2010) for the model evaluation on individual testing subjects. Given two sets, A and B, the Dice index is defined as:

$$Dice(A,\ B) = \frac{2|A \cap B|}{|A| + |B|}$$

where $|*|$ denotes the number of elements in a set. The Dice index is a real number in [0, 1], where a larger value indicates a higher similarity between automatically detected DWMA regions and gold standard regions. We denote true positive as TP, representing the number of correctly classified samples among positive samples P; and true negative as TN, representing the number of correctly classified samples among N negative samples. Then, balanced accuracy is defined by:

$$Balanced\ Accuracy = \frac{1}{2}\left(\frac{TP}{P} + \frac{TN}{N}\right)$$

Balanced accuracy measures the average accuracy obtained from both the minority and majority classes. It is equivalent to the traditional accuracy if a model performs equally well on either classes. Conversely, it avoids "falsely" high value due to the model taking advantage of the distribution of the majority class.

To compare the proposed deep CNN model with other popular machine learning models, we developed deep

neural network (DNN) and support vector machine (SVM) models. The DNN architecture design is displayed in the **Supplementary Table**. An SVM classifier was implemented, as suggested in Zhang et al. (2015), using a linear kernel for neonatal brain image segmentation. To optimize the SVM model, the soft margin C was selected via a linear search from a set of empirical values [i.e., $C = (2^{-10}, 2^{-8}, ..., 1, ...2^{8}, 2^{10})$]. The soft margin was determined optimal when the DWMA detection performance of the model on the testing data was maximal. The DNN and SVM models were configured and optimized with flattened vectors of image patch sizes, individually. T-test was applied to test whether there is a significant difference ($p < 0.05$) between the mean performances of two models.

RESULTS

Computer Simulation

We simulated 10 neonatal T_2-weighted brain images with manually drawn synthetic DWMA regions using a method presented in our previous study (He and Parikh, 2013b). Rician noise (SD = 10) was imposed on the simulated images. The signal-to-noise ratio (SNR), defined as the mean cerebral tissue intensity divided by noise SD, of the synthesized brain images was 22.5. Four deep CNN models (**Table 2**) were implemented to detect these synthetic DWMA regions. We applied a leave-one-subject-out cross-validation strategy to evaluate the models. The detection performance of four CNN architectures are displayed in the **Figure 3** box plots. We observed that deeper architectures for the larger patch sizes were generally better than ones for smaller sizes and the CNN architecture for patch size 13 × 13 was slightly more accurate than for patch size 17 × 17.

Next, we examined the Dice index and balanced accuracy of the 12-layer deep CNN model for patch size 13 × 13 across 10 subjects with varying noise levels (**Figure 4**). Different Rician noise [SD = (10, 15, 20, 25, and 30)] was added into the synthetic images, whose corresponding SNR were [22.5, 15, 11.3, 9.0, and 7.6], respectively. Deep CNN was able to achieve the Dice index (mean ± SD, 0.993 ± 0.006) and balanced accuracy (0.996 ± 0.004) when SNR = 22.5. As noise levels were increased, the detection performance of deep CNN decreased, but only marginally. When SNR = 7.6, the deep CNN model achieved 0.931 ± 0.019 for Dice index and 0.976 ± 0.014 for balanced accuracy **Figure 5** shows that the deep CNN-identified brain regions strongly overlap with ground truth.

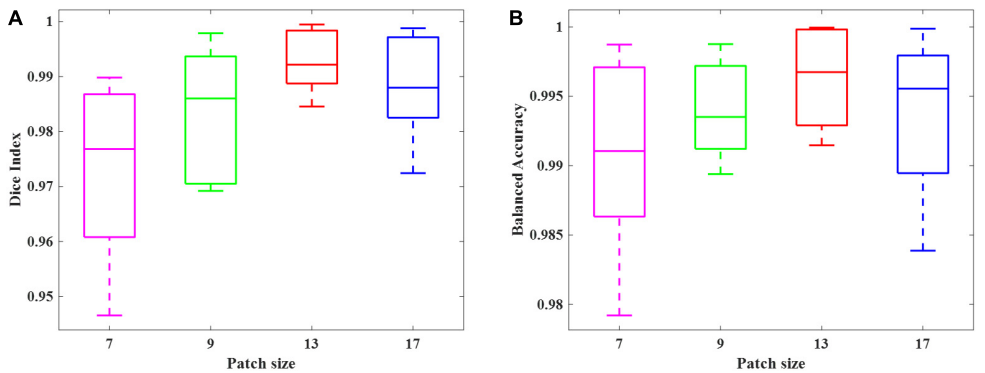

FIGURE 3 | Box plots of the DWMA detection performance, including **(A)** Dice index and **(B)** balanced accuracy using four different deep CNN architectures tested on 10 simulated preterm neonatal brain images. The central line indicates the median, and edges of the box indicate the 25 and 75th percentiles. The whiskers extend to the maximum and minimum values.

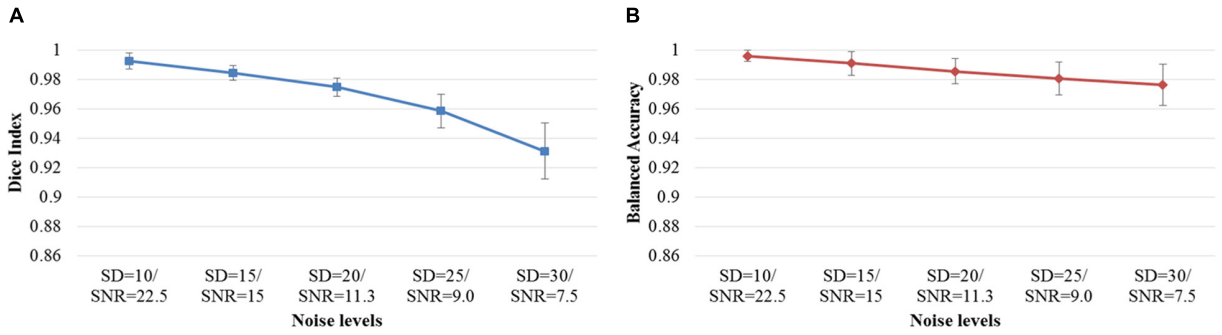

FIGURE 4 | DWMA detection performance, including **(A)** Dice index and **(B)** balanced accuracy of the 12-layer deep CNN model with input patch size of 13 × 13 on 10 simulated preterm neonatal brain images with varying noise levels. The error bars indicate the SD of performance. Increasing noise levels only marginally affect DWMA detection performance. Noise levels were displayed with simulated Rician noise standard deviation (SD) and image signal-to-noise ratio (SNR).

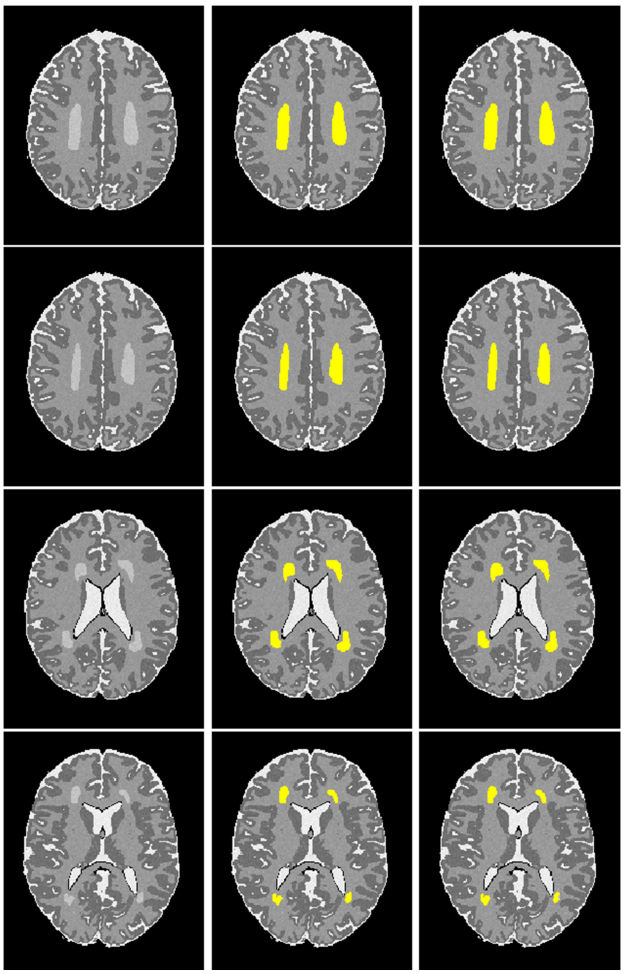

FIGURE 5 | Visualization of automated DWMA detection on simulated preterm neonatal MRI images using a 12-layer deep CNN. Left column, simulated images in axial orientation at the level of the centrum semiovale and lateral ventricles; Middle column, images with outlined ground truth (synthetic DWMA); Right column, images with CNN-detected DWMA.

TABLE 3 | Cross-validation.

	Dice	Balanced accuracy
CNN	**0.864 (0.052)**	**0.942 (0.028)**
DNN	0.831 (0.122)	0.922 (0.018)
SVM	0.818 (0.115)	0.895 (0.071)

Mean (SD) Dice index and balanced accuracy of the three machine learning models for DWMA detection. The proposed CNN model outperformed compared DNN and SVM in the 10-fold cross-validation with 50 subjects. CNN, convolutional neural networks; DNN, deep neural networks; SVM, support vector machine. The boldface denotes the best performance for individual metrics in the validation experiment.

In vivo Data

Internal Cross-Validation

We randomly selected 50 subjects from cohort 1 and conducted a 10-fold cross-validation scheme to validate the deep CNN model using preterm infants' MRI data. The 50 subjects were randomly divided into 10 equal sized portions. For each iteration, 5 subjects ($\sim 5 \times 10^5$ image patches) were held out for the model testing, and the remaining 45 subjects ($\sim 45 \times 10^5$ image patches) were used for model training. This process was repeated for 10 iterations until each of the 10 portions was evaluated once as the testing data. We first compared the DWMA detection performance of four deep CNN architectures (**Table 2**) and reported the Dice index and balanced accuracy for each subject using box plots (**Figure 6**). As we found for the computer simulation (**Figure 3**), the 12-layer CNN designed for patch size 13×13 achieved more accurate detection performance than other architectures.

Next, we compared the proposed 12-layer deep CNN with DNN and SVM models. **Table 3** shows the DWMA detection performance using these different models. The CNN model exhibited a significantly higher Dice index than DNN ($p = 0.019$) and SVM ($p < 0.001$). The balanced accuracy for CNN was also significantly higher than that of DNN ($p = 0.043$) and SVM ($p < 0.001$). **Figure 7** displayed a representative DWMA detection using deep CNN. The automatically detected

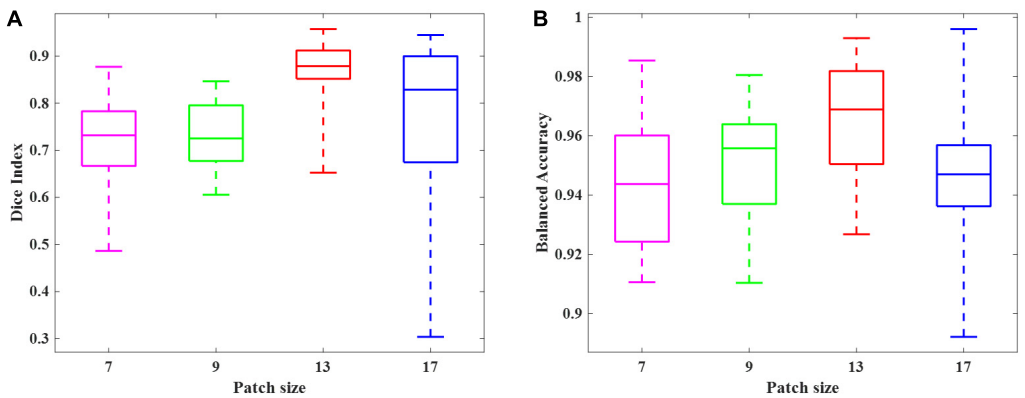

FIGURE 6 | Box plots of DWMA detection performance, including **(A)** Dice index and **(B)** balanced accuracy, using four different deep CNN architectures on 50 very preterm neonatal brain images. The central line indicates the median, and edges of the box indicate the 25 and 75th percentiles. The whiskers extend to the maximum and minimum values.

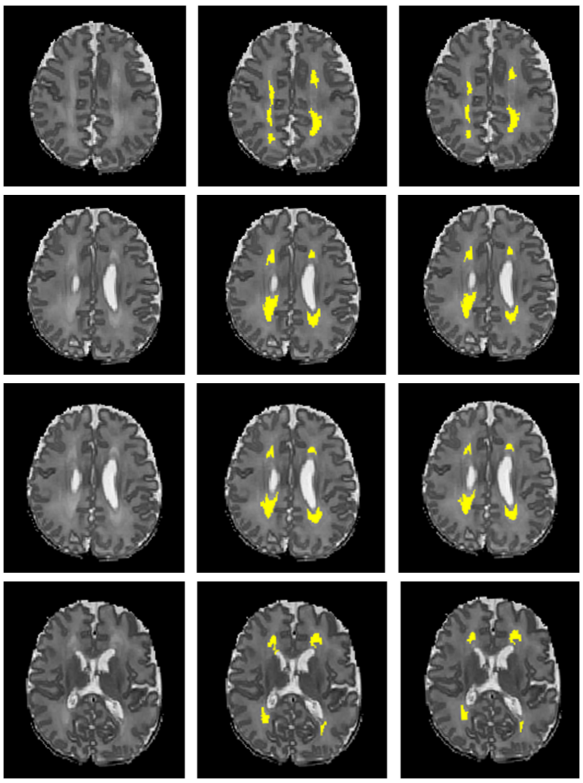

FIGURE 7 | A male subject born at age 28.3 weeks and imaged at term-equivalent age exhibiting DWMA (highlighted in yellow) in periventricular white matter regions on T_2-weighted brain images. Left column, 4 axial levels of T_2-weighted images; Middle column, segmented images with gold standard DWMA; Right column, images with deep CNN-detected DWMA.

DWMA closely approximated the DWMA gold standard regions confirmed by human experts (both highlighted in yellow).

Then, we calculated DWMA volumes – a prognostic biomarker that has been shown to be a significant predictor of later cognitive scores (Dyet et al., 2006; Krishnan et al., 2007; Iwata et al., 2012; He and Parikh, 2013a) – based on detection using the deep CNN, DNN, and SVM. DWMA volumes were normalized by head size, denoted as DWMA-to-brain-ratio [DBR = DWMA volume divided by total brain volume (He and Parikh, 2013a)]. Bland-Altman plots were utilized to assess the degree of agreement between the automatic and gold standard DBRs (**Figure 8**). The mean difference between CNN and gold standard DBRs was near zero (1.007E-04). Compared to this, mean difference between gold standard and the other two automatic DBRs were more than one order of magnitude larger (DNN: +0.003 and SVM: −0.003).

TABLE 4 | Holdout validation.

	Dice	Balanced accuracy
CNN	**0.859 (0.098)**	**0.924 (0.06)**
DNN	0.817 (0.109)	0.905 (0.033)
SVM	0.806 (0.093)	0.885 (0.037)

Mean (SD) Dice index and balanced accuracy of the three machine learning models for DWMA detection. The proposed CNN model achieved better performance than DNN and SVM in the internal holdout validation with 50 subjects as training set and 45 subjects as holdout testing set. CNN, convolutional neural networks; DNN, deep neural networks; SVM, support vector machine. The boldface denotes the best performance for individual metrics in the validation experiment.

Internal Holdout Validation

We further compared our CNN with DNN and SVM models using internal holdout validation. We trained models using 50 randomly selected subjects ($\sim 50 \times 10^5$ image patches) in cohort 1 (N = 95) and tested the models on the remaining 45 subjects ($\sim 45 \times 10^5$ image patches) from the same cohort. **Table 4** highlights the higher performance of the CNN model over the DNN and SVM models with a mean Dice index of 0.859 and a mean balanced accuracy of 0.924. CNN exhibited a significantly higher Dice ratio than DNN (p = 0.027) and SVM (p = 0.036). In addition, balanced accuracy of CNN was also higher than for DNN ($p < 0.001$) and SVM ($p < 0.001$) models.

Similar to cross-validation, we calculated DBR of each subject based on detection using the deep CNN, DNN, and SVM. Bland-Altman plots were utilized to assess the degree of agreement (**Figure 9**). The mean difference between CNN and gold standard DBRs was near zero (1.217E-04). The DBR of our

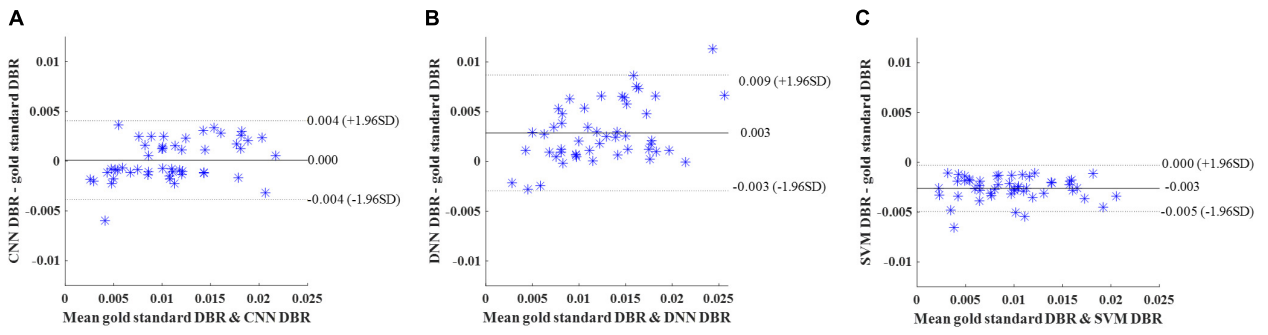

FIGURE 8 | Cross validation. Bland-Altman plots of gold standard DWMA-to-brain-ratio (DBR) and automatic DBRs: **(A)** convolutional neural networks (CNN), **(B)** deep neural networks (DNN), and **(C)** support vector machine (SVM) in the 10-fold cross-validation with 50 subjects. Each blue asterisk represents one subject. Solid horizontal lines represent the mean difference and dashed lines represent the limits of agreement (±1.96 SD).

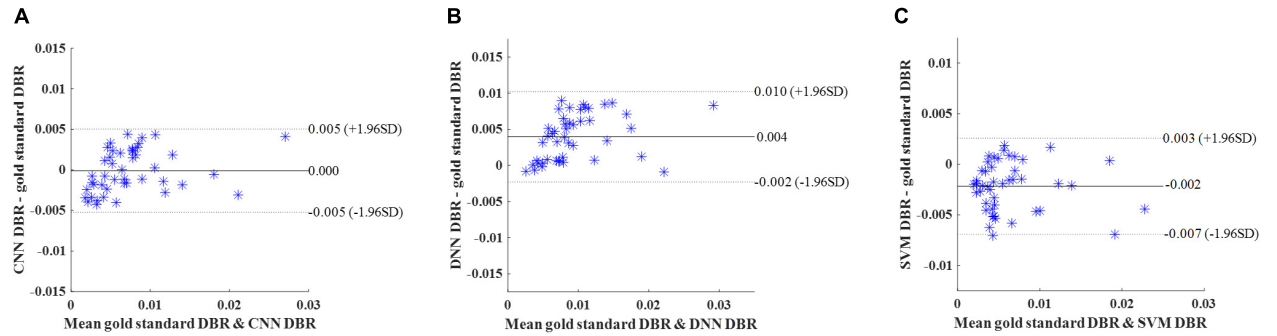

FIGURE 9 | Internal holdout validation. Bland-Altman plots of gold standard DWMA-to-brain-ratio (DBR) and automatic DBRs: using **(A)** convolutional neural networks (CNN), **(B)** deep neural networks (DNN), and **(C)** support vector machine (SVM) in the internal holdout validation with 50 subjects as training set and 45 unseen subjects as holdout testing set. Each blue asterisk represents one subject. Solid horizontal lines represent the mean difference and dashed lines represent the limits of agreement (±1.96 SD).

CNN outperformed other two automatic DBRs (DNN: +0.004 and SVM: −0.002).

External Independent Validation

Last, in order to evaluate the robustness and generalizability of our methods, we tested our models on an independent dataset that was obtained using a different MRI scanner. The models trained using 50 subjects ($\sim 50 \times 10^5$ image patches) from cohort 1 were tested on this independent cohort 2 with 28 subjects ($\sim 28 \times 10^5$ image patches). The CNN performance remained robust and once again significantly outperformed DNN ($p = 0.018$ for Dice ratio; $p = 0.009$ for balanced accuracy) and SVM ($p = 0.021$ for Dice ratio; $p = 0.006$ for balanced accuracy) (**Table 5**).

Again, DBR based on detection using the deep CNN, DNN, and SVM were calculated for individual subjects. Bland-Altman plots were used (**Figure 10**). The mean difference between CNN and gold standard DBRs (0.001) was smaller than the ones between two compared automatic DBRs and god standard DBRs (DNN: +0.005 and SVM: −0.003).

DISCUSSION

We present a deep CNN approach to objectively and automatically quantify DWMA regions on T_2-weighted MRI images. This is the first study to detect DWMA regions and quantify associated volumes in preterm infants by using a state-of-the-art deep learning algorithm. The excellent image pattern recognition capability of deep CNN enabled our proposed approach in automated detection of DWMA with a detection level similar to human experts. The desirable generalizability of our approach, tested on two preterm cohorts and scanner platforms, suggests that we can achieve consistent and reliable diagnosis of DWMA.

TABLE 5 | External validation.

	Dice	Balanced Accuracy
CNN	**0.845 (0.079)**	**0.874 (0.065)**
DNN	0.788 (0.075)	0.836 (0.067)
SVM	0.786 (0.077)	0.832 (0.056)

Mean (SD) Dice index and balanced accuracy of the three machine learning models for DWMA detection. The proposed CNN model outperformed compared DNN and SVM in the external validation with 50 subjects from Siemens scanner as training set and 28 subjects from GE scanner as independent testing set. CNN, convolutional neural networks; DNN, deep neural networks; SVM, support vector machine. The boldface denotes the best performance for individual metrics in the validation experiment.

To date, the diagnosis of DWMA in preterm neonates has lacked sufficient reliability, even by trained neuroradiologists. Reported inter- and intra-observer agreement for qualitative diagnosis of DWMA is poor (Hart et al., 2010a). Technical variations such as imaging protocols and platforms may contribute to the difficulty of consistent DWMA detection. Moreover, DWMA diagnosis can also be confounded by the developmental crossroad regions in frontal and occipital periventricular white matter that contain multiple crossing fibers and rich extracellular matrix (Judaš et al., 2005; Kidokoro et al., 2011). These confounding factors could partly explain the conflicting reports of significant association (Dyet et al., 2006; Krishnan et al., 2007; Iwata et al., 2012; He and Parikh, 2013a) vs. no association with cognitive outcomes (Jeon et al., 2012), and hypotheses about whether DWMA represents a developmental delay or pathologic lesions (Counsell et al., 2003; Inder et al., 2003; Krishnan et al., 2007; Cheong et al., 2009; Hagmann et al., 2009; Hart et al., 2010b; He and Parikh, 2013a). Our experiments on computer simulated and *in vivo* data suggest that the proposed deep CNN approach can yield reproducible DWMA diagnosis across different cohorts.

The computer simulation experiments provided theoretical support to the validity of the proposed approach. Unlike gold standard data that is derived by human experts, the ground truth of DWMA regions in computer-simulated brain images is well grounded. Additionally, confounding factors such as imaging protocol, scanner configuration, and subject motion are not a concern when using computer simulated images. Our proposed CNN approach detected DWMA regions with high accuracy and its tolerance to varying signal noise levels was high. Although noise level for a clinical neonatal MRI scan is dependent on

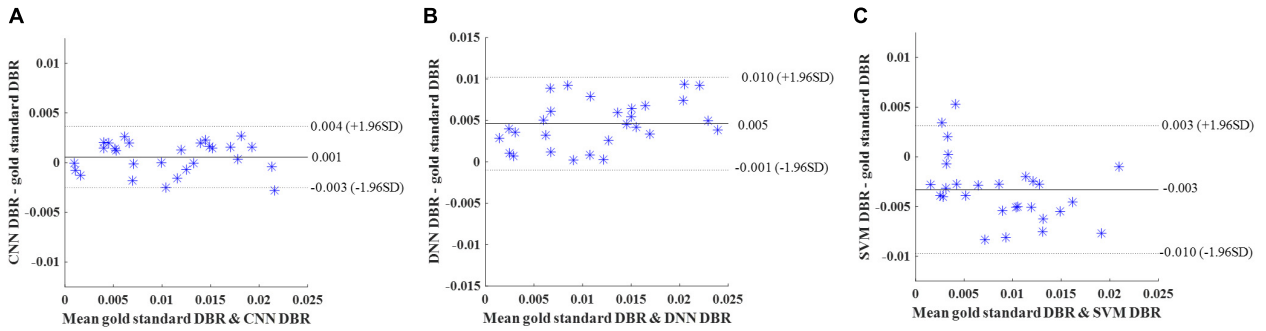

FIGURE 10 | External validation. Bland-Altman plots of gold standard DWMA-to-brain-ratio (DBR) and automatic DBRs: **(A)** convolutional neural networks (CNN), **(B)** deep neural networks (DNN), and **(C)** support vector machine (SVM) in the external validation with 50 subjects as training set and 28 independent subjects as testing set. Each blue asterisk represents one subject. Solid horizontal lines represent the mean difference and dashed lines represent the limits of agreement (±1.96 SD).

scanner and environment, a generally acceptable noise SD is less than 25 (He and Parikh, 2013b). At such a noise level ($\alpha = 25$), the CNN model still achieved a very high Dice index (0.96) and balanced accuracy (0.98).

The comparison of deep CNN architectures, utilizing the computer simulation and cross-validation experiments, demonstrated that deeper architectures perform better for DWMA detection. This is consistent with previous works (Bengio, 2009; Zhang et al., 2015; Goodfellow et al., 2016) on the general trend that a deeper architecture tends to perform better for complex image pattern recognition. Meanwhile, the CNN architecture for patch size 13×13 performed slightly better than the one for patch size 17×17, suggesting that simply increasing the size of patches may not further improve detection. Peak performance for detection of DWMA in infant brain images was achieved by the deep CNN with the patch size 13×13, which may be related to the spatial scale of the regional anatomy. Prior research (Kamnitsas et al., 2017) suggests that increasing the spatial scale may negatively impact the detection of the regional spatial patterns.

With respect to comparing machine learning models, the strong performance of deep CNN for image pattern recognition shown here is consistent with numerous prior image classification studies (Krizhevsky et al., 2012; de Brebisson and Montana, 2015; LeCun et al., 2015). Given sufficiently large training data, deep learning methods have outperformed traditional classifiers (e.g., SVM) in decoding complex image patterns (LeCun et al., 2015). As a specialized neural network, CNN further leverages the performance of DNN by using a convolution function, which improves the utilization of spatial information within images (Goodfellow et al., 2016).

Our experiments of internal holdout validation and external independent validation support the strong generalizability of our CNN approach. In the holdout validation, the performance of CNN on 45 holdout subjects from cohort 1 was comparable to the one achieved for cross-validation experiments. Compared to internal holdout validation, the external validation results for cohort 2 provided additional evidence that this method is generalizable to very preterm infants imaged on different scanners and using different imaging parameters.

Our current work has certain limitations. First, the performance of machine learning methods for automated detection and classification is highly dependent on the training data. Although we had a substantial data set available from very preterm infants, training the CNN with more data that has been classified by experts can be expected to improve performance. Second, although computer simulation and two independent cohorts from separate studies were utilized to evaluate our method, the i*n vivo* data were collected by the same research group (despite enrollment at different centers) and all images were acquired at a field strength of 3 Tesla, limiting the variability of tested MRI images. The sizes of our *in vivo* cohorts are relatively small. Additional data from other institutions or research groups, and possibly at other field strengths would provide further validation of the generalizability of our approach. Third, to ensure deep learning models had adequate training data, we utilized image patches, typically $\sim 10^5$ for each subject, as the training samples. However, this strategy introduced redundancy among overlapping patches, causing expensive computing cost. Fourth, although we strived to obtain a robust gold-standard dataset, it is worth mentioning that the inter-rater variability may be a source of bias in the evaluation of the proposed and peer models. Finally, our current CNN approach was developed based on T_2-weighted images only. Additional imaging modalities (e.g., T_1-weighted images) may further improve the accuracy of DWMA detection.

In summary, we developed a deep CNN approach for automated and objective DWMA detection. The experiments were conducted by applying the proposed method to T_2-weighted anatomical images at term-equivalent age from very preterm infants. The computer simulations and internal and external validation demonstrated very accurate and reproducible DWMA detection performance that may facilitate the clinical diagnosis of DWMA in very preterm infants. Future studies to investigate the association between CNN-detected DWMA volumes and long-term neurodevelopmental outcomes, as we are currently doing, will be important to further validate the clinical significance of this work.

DATA AVAILABILITY

The datasets for this manuscript are not publicly available because the IRB of national children's hospital does not allow publication of preterm infant brain images. Requests to access the data sets should be directed to LH, lili.he@cchmc.org.

ETHICS STATEMENT

This study was carried out in accordance with the recommendations of the Institutional Review Board of Nationwide Children's Hospital (NCH) with written informed consent from all subjects. All subjects gave written informed consent in accordance with the Declaration of Helsinki. The protocol was approved by the Institutional Review Board of Nationwide Children's Hospital.

AUTHOR CONTRIBUTIONS

HL, NP, and LH designed the study. HL, JW, MC, MP, and LH conducted the data processing and analysis. All authors wrote the manuscript.

FUNDING

This study was supported by the National Institutes of Health grant numbers R21-HD094085, R01-NS094200, and R01-NS096037 and a Trustee Grant from Cincinnati Children's Hospital Medical Center.

ACKNOWLEDGMENTS

We sincerely thank Jennifer Notestine, RN, Valerie Marburger, NNP, Julie Gutentag, RN, and Patty Luzader, RN for serving as the study coordinators and Mark Smith, MS, for serving as the study MR tech at Nationwide Children's Hospital. We are grateful to the families and neonatal intensive care unit and clinic staff, also at Nationwide Children's Hospital, that made this study possible.

SUPPLEMENTARY MATERIAL

The Supplementary Material for this article can be found online at: https://www.frontiersin.org/articles/10.3389/fnins.2019.00610/full#supplementary-material

REFERENCES

Bengio, Y. (2009). Learning deep architectures for AI. *Found. Trends Mach. Learn.* 2, 111–127. doi: 10.1561/2200000006

Bengio, Y., and LeCun, Y. (2007). Scaling learning algorithms towards AI. *Large-Scale Kernel Mach.* 34, 1–41.

Brodersen, K. H., Ong, C. S., Stephan, K. E., and Buhmann, J. M. (2010). "The balanced accuracy and its posterior distribution," in *Proceedings of the 20th International Conference Pattern Recognition (ICPR)*, (Istanbul: IEEE), 3121–3124.

Brosch, T., Tam, R., and Alzheimer's Disease Neuroimaging Initiative. (2013). "Manifold learning of brain MRIs by deep learning," in *Medical Image Computing and Computer-Assisted Intervention–MICCAI 2013*, eds K. Mori, I. Sakuma, Y. Sato, C. Barillot, and N. Navab (Berlin: Springer).

Brosch, T., Tang, L. Y., Yoo, Y., Li, D. K., Traboulsee, A., and Tam, R. (2016). Deep 3D convolutional encoder networks with shortcuts for multiscale feature integration applied to multiple sclerosis lesion segmentation. *IEEE Trans. Med. Imag.* 35, 1229–1239. doi: 10.1109/TMI.2016.2528821

Calloni, S. F., Cinnante, C. M., Bassi, L., Avignone, S., Fumagalli, M., Bonello, L., et al. (2015). Neurodevelopmental outcome at 36 months in very low birth weight premature infants with MR diffuse excessive high signal intensity (DEHSI) of cerebral white matter. *Radiol. Med.* 120, 1056–1063. doi: 10.1007/s11547-015-0540-2

Cheong, J., Thompson, D., Wang, H., Hunt, R., Anderson, P., Inder, T., et al. (2009). Abnormal white matter signal on MR imaging is related to abnormal tissue microstructure. *Am. J. Neuroradiol.* 30, 623–628. doi: 10.3174/ajnr.A1399

Counsell, S. J., Allsop, J. M., Harrison, M. C., Larkman, D. J., Kennea, N. L., Kapellou, O., et al. (2003). Diffusion-weighted imaging of the brain in preterm infants with focal and diffuse white matter abnormality. *Pediatrics* 112, 1–7.

de Brebisson, A., and Montana, G. (2015). Deep neural networks for anatomical brain segmentation. *arXiv*

de Bruïne, F. T., van den Berg-Huysmans, A. A., Leijser, L. M., Rijken, M., Steggerda, S. J., van der Grond, J., et al. (2011). Clinical implications of MR imaging findings in the white matter in very preterm infants: a 2-year follow-up study. *Radiology* 261, 899–906. doi: 10.1148/radiol.11110797

Dice, L. R. (1945). Measures of the amount of ecologic association between species. *Ecology* 26, 297–302.

Dyet, L. E., Kennea, N., Counsell, S. J., Maalouf, E. F., Ajayi-Obe, M., Duggan, P. J., et al. (2006). Natural history of brain lesions in extremely preterm infants studied with serial magnetic resonance imaging from birth and neurodevelopmental assessment. *Pediatrics* 118, 536–548.

Friston, K. J. (1994). "Statistical parametric mapping," in *Neuroscience Databases*, ed. R. Kötter (Berlin: Springer).

Geremia, E., Clatz, O., Menze, B. H., Konukoglu, E., Criminisi, A., and Ayache, N. (2011). Spatial decision forests for MS lesion segmentation in multi-channel magnetic resonance images. *NeuroImage* 57, 378–390. doi: 10.1016/j.neuroimage.2011.03.080

Ghafoorian, M., Karssemeijer, N., Heskes, T., van Uder, I., de Leeuw, F.-E., Marchiori, E., et al. (2016). "Non-uniform patch sampling with deep convolutional neural networks for white matter hyperintensity segmentation," in *Proceedings of the Biomedical Imaging (ISBI), 2016 IEEE 13th International Symposium*, (Piscataway, NY: IEEE), 1414–1417.

Glorot, X., and Bengio, Y. (2010). "Understanding the difficulty of training deep feedforward neural networks," in *Proceedings of the Thirteenth International Conference on Artificial Intelligence and Statistics*, Sardinia, 249–256.

Goodfellow, I., Bengio, Y., Courville, A., and Bengio, Y. (2016). *Deep Learning*. Cambridge: MIT press.

Griffanti, L., Zamboni, G., Khan, A., Li, L., Bonifacio, G., Sundaresan, V., et al. (2016). BIANCA (brain intensity AbNormality Classification Algorithm): a new tool for automated segmentation of white matter hyperintensities. *NeuroImage* 141, 191–205. doi: 10.1016/j.neuroimage.2016.07.018

Guerrero, R., Qin, C., Oktay, O., Bowles, C., Chen, L., Joules, R., et al. (2018). White matter hyperintensity and stroke lesion segmentation and differentiation using convolutional neural networks. *NeuroImage Clin.* 17, 918–934. doi: 10.1016/j.nicl.2017.12.022

Hagmann, C. F., De Vita, E., Bainbridge, A., Gunny, R., Kapetanakis, A. B., Chong, W. K., et al. (2009). T2 at MR imaging is an objective quantitative measure of cerebral white matter signal intensity abnormality in preterm infants at term-equivalent age. *Radiology* 252, 209–217. doi: 10.1148/radiol.2522080589

Hart, A. R., Smith, M. F., Rigby, A. S., Wallis, L. I., and Whitby, E. H. (2010a). Appearances of diffuse excessive high signal intensity (DEHSI) on MR imaging following preterm birth. *Pediatr. Radiol.* 40, 1390–1396.

Hart, A. R., Whitby, E. H., Clark, S. J., Paley, M. N., and Smith, M. F. (2010b). Diffusion-weighted imaging of cerebral white matter and the cerebellum

following preterm birth. *Dev. Med. Child Neurol.* 52, 652–659. doi: 10.1111/j.1469-8749.2009.03590.x

He, L., Li, H., Holland, S., Yuan, W., Altaye, M., and Parikh, N. (2018). Early prediction of cognitive deficits in very preterm infants using functional connectome data in an artificial neural network framework. *NeuroImage Clin.* 18, 290–297. doi: 10.1016/j.nicl.2018.01.032

He, L., and Parikh, N. A. (2013a). Atlas-guided quantification of white matter signal abnormalities on term-equivalent age MRI in very preterm infants: findings predict language and cognitive development at two years of age. *PLoS One* 8:e85475. doi: 10.1371/journal.pone.0085475

He, L., and Parikh, N. A. (2013b). Automated detection of white matter signal abnormality using T2 relaxometry: application to brain segmentation on term MRI in very preterm infants. *Neuroimage* 64, 328–340. doi: 10.1016/j.neuroimage.2012.08.081

Hinton, G. E., Srivastava, N., Krizhevsky, A., Sutskever, I., and Salakhutdinov, R. R. (2012). Improving neural networks by preventing co-adaptation of feature detectors. *arXiv*

Inder, T. E., Anderson, N. J., Spencer, C., Wells, S., and Volpe, J. J. (2003). White matter injury in the premature infant: a comparison between serial cranial sonographic and MR findings at term. *Am. J. Neuroradiol.* 24, 805–809.

Iwata, S., Nakamura, T., Hizume, E., Kihara, H., Takashima, S., Matsuishi, T., et al. (2012). Qualitative brain MRI at term and cognitive outcomes at 9 years after very preterm birth. *Pediatrics* 129, e1138–e1147. doi: 10.1542/peds.2011-1735

Jeon, T. Y., Kim, J. H., Yoo, S.-Y., Eo, H., Kwon, J.-Y., Lee, J., et al. (2012). Neurodevelopmental outcomes in preterm infants: comparison of infants with and without diffuse excessive high signal intensity on MR images at near–term-equivalent age. *Radiology* 263, 518–526. doi: 10.1148/radiol.12111615

Johnson, R., and Zhang, T. (2013). Accelerating stochastic gradient descent using predictive variance reduction. *News Physiol. Sci.* 1, 315–323.

Judaš, M., Radoš, M., Jovanov-Milošević, N., Hrabac, P., and Kostović, I. (2005). Structural, immunocytochemical, and MR imaging properties of periventricular crossroads of growing cortical pathways in preterm infants. *Am. J. Neuroradiol.* 26, 2671–2684.

Kamnitsas, K., Ledig, C., Newcombe, V. F., Simpson, J. P., Kane, A. D., Menon, D. K., et al. (2017). Efficient multi-scale 3D CNN with fully connected CRF for accurate brain lesion segmentation. *Med. Image Anal.* 36, 61–78. doi: 10.1016/j.media.2016.10.004

Kidokoro, H., Anderson, P., Doyle, L., Neil, J., and Inder, T. (2011). High signal intensity on T2-weighted MR imaging at term-equivalent age in preterm infants does not predict 2-year neurodevelopmental outcomes. *Am. J. Neuroradiol.* 32, 2005–2010.

Krishnan, M. L., Dyet, L. E., Boardman, J. P., Kapellou, O., Allsop, J. M., Cowan, F., et al. (2007). Relationship between white matter apparent diffusion coefficients in preterm infants at term-equivalent age and developmental outcome at 2 years. *Pediatrics* 120, e604–e609.

Krizhevsky, A., Sutskever, I., and Hinton, G. E. (2012). Imagenet classification with deep convolutional neural networks. *Adv. Neural Inform. Process. Syst.* 25, 1097–1105.

Landis, J. R., and Koch, G. G. (1977). The measurement of observer agreement for categorical data. *Biometrics* 33, 159–174.

Lao, Z., Shen, D., Liu, D., Jawad, A. F., Melhem, E. R., Launer, L. J., et al. (2008). Computer-assisted segmentation of white matter lesions in 3D MR images using support vector machine. *Acad. Radiol.* 15, 300–313. doi: 10.1016/j.acra.2007.10.012

LeCun, Y., and Bengio, Y. (1995). "Convolutional networks for images, speech, and time series," in *The Handbook of Brain Theory and Neural Networks*, ed. M. A. Arbib (Cambridge: MIT Press).

LeCun, Y., Bengio, Y., and Hinton, G. (2015). Deep learning. *Nature* 521, 436–444. doi: 10.1038/nature14539

LeCun, Y., Bottou, L., Bengio, Y., and Haffner, P. (1998). Gradient-based learning applied to document recognition. *Proc. IEEE* 86, 2278–2324.

Maalouf, E. F., Duggan, P. J., Rutherford, M. A., Counsell, S. J., Fletcher, A. M., Battin, M., et al. (1999). Magnetic resonance imaging of the brain in a cohort of extremely preterm infants. *J. Pediatr.* 135, 351–357.

Maillard, P., Delcroix, N., Crivello, F., Dufouil, C., Gicquel, S., Joliot, M., et al. (2008). An automated procedure for the assessment of white matter hyperintensities by multispectral (T1, T2, PD) MRI and an evaluation of its between-centre reproducibility based on two large community databases. *Neuroradiology* 50, 31–42.

Mathur, A. M., Neil, J. J., and Inder, T. E. (2010). Understanding brain injury and neurodevelopmental disabilities in the preterm infant: the evolving role of advanced magnetic resonance imaging. *Semin. Perinatol.* 34, 57–66. doi: 10.1053/j.semperi.2009.10.006

Moeskops, P., de Bresser, J., Kuijf, H. J., Mendrik, A. M., Biessels, G. J., Pluim, J. P., et al. (2018). Evaluation of a deep learning approach for the segmentation of brain tissues and white matter hyperintensities of presumed vascular origin in MRI. *NeuroImage Clin.* 17, 251–262. doi: 10.1016/j.nicl.2017.10.007

Nesterov, Y. (2007). *Gradient Methods for Minimizing Composite Objective Function*. Princeton, NJ: Citeseer.

Parikh, N. A. (2016). Advanced neuroimaging and its role in predicting neurodevelopmental outcomes in very preterm infants. *Semin. Perinatol.* 40, 530–541. doi: 10.1053/j.semperi.2016.09.005

Parikh, N. A., He, L., Bonfante-Mejia, E., Hochhauser, L., Wilder, P. E., Burson, K., et al. (2013). Automatically quantified diffuse excessive high signal intensity on MRI predicts cognitive development in preterm infants. *Pediatr. Neurol.* 49, 424–430. doi: 10.1016/j.pediatrneurol.2013.08.026

Parikh, N. A., Pierson, C. R., and Rusin, J. A. (2016). Neuropathology associated with diffuse excessive high signal intensity abnormalities on magnetic resonance imaging in very preterm infants. *Pediatr. Neurol.* 65, 78–85. doi: 10.1016/j.pediatrneurol.2016.07.006

Schmidt, P. (2017). *Bayesian Inference for Structured Additive Regression Models for Large-Scale Problems With Applications to Medical Imaging*. Munich: Ludwig-Maximilians-Universität München.

Skiöld, B., Horsch, S., Hallberg, B., Engström, M., Nagy, Z., Mosskin, M., et al. (2010). White matter changes in extremely preterm infants, a population-based diffusion tensor imaging study. *Acta Paediatr.* 99, 842–849. doi: 10.1111/j.1651-2227.2009.01634.x

Skiöld, B., Vollmer, B., Böhm, B., Hallberg, B., Horsch, S., Mosskin, M., et al. (2012). Neonatal magnetic resonance imaging and outcome at age 30 months in extremely preterm infants. *J. Pediatr.* 160, 559.e1–566.e1. doi: 10.1016/j.jpeds.2011.09.053

Szegedy, C., Liu, W., Jia, Y., Sermanet, P., Reed, S., Anguelov, D., et al. (2015). "Going deeper with convolutions," in *Proceedings of the IEEE Conference on Computer Vision and Pattern Recognition*, Boston, MA, 1–9.

Volpe, J. J. (2017). Confusions in nomenclature:"periventricular leukomalacia" and "white matter injury"—identical, distinct, or overlapping? *Pediatr. Neurol.* 73, 3–6.

Xu, K., Ba, J., Kiros, R., Courville, A., Salakhutdinov, R., Zemel, R., et al. (2015). Show, attend and tell: Neural image caption generation with visual attention. *arXiv*

Yoshita, M., Fletcher, E., and DeCarli, C. (2005). Current concepts of analysis of cerebral white matter hyperintensities on magnetic resonance imaging. *Top. Mag. Reson. Imaging* 16:399.

Zhang, W., Li, R., Deng, H., Wang, L., Lin, W., Ji, S., et al. (2015). Deep convolutional neural networks for multi-modality isointense infant brain image segmentation. *NeuroImage* 108, 214–224. doi: 10.1016/j.neuroimage.2014.12.061

Conflict of Interest Statement: SH was employed by company Medpace.

The remaining authors declare that the research was conducted in the absence of any commercial or financial relationships that could be construed as a potential conflict of interest.

Copyright © 2019 Li, Parikh, Wang, Merhar, Chen, Parikh, Holland and He. This is an open-access article distributed under the terms of the Creative Commons Attribution License (CC BY). The use, distribution or reproduction in other forums is permitted, provided the original author(s) and the copyright owner(s) are credited and that the original publication in this journal is cited, in accordance with accepted academic practice. No use, distribution or reproduction is permitted which does not comply with these terms.

frontiers in Neuroscience

ORIGINAL RESEARCH
published: 19 June 2019
doi: 10.3389/fnins.2019.00602

Impaired Motor Skill Acquisition Using Mirror Visual Feedback Improved by Transcranial Direct Current Stimulation (tDCS) in Patients With Parkinson's Disease

Mitsuya Horiba[1], Yoshino Ueki[1], Ippei Nojima[2], Yoko Shimizu[1], Kento Sahashi[1], Shogo Itamoto[1], Ayuko Suzuki[3], Gohei Yamada[3], Noriyuki Matsukawa[3] and Ikuo Wada[1]*

[1] Department of Rehabilitation Medicine, Nagoya City University Graduate School of Medical Sciences, Nagoya, Japan, [2] Department of Physical Therapy, Shinshu University Graduate School of Medicine, Nagano, Japan, [3] Department of Neurology and Neuroscience, Nagoya City University Graduate School of Medical Sciences, Nagoya, Japan

OPEN ACCESS

Edited by:
Daniel Baumgarten, UMIT – Private Universität für Gesundheitswissenschaften, Medizinische Informatik und Technik, Austria

Reviewed by:
Vesna Sossi, The University of British Columbia, Canada
Michele Dileone, Los Madroños Hospital, Spain
Aguida Soares Foerster, Independent Researcher, Köln, Germany

***Correspondence:**
Yoshino Ueki
yueki@med.nagoya-cu.ac.jp

Specialty section:
This article was submitted to Brain Imaging Methods, a section of the journal Frontiers in Neuroscience

Received: *17 October 2018*
Accepted: *27 May 2019*
Published: *19 June 2019*

Citation:
Horiba M, Ueki Y, Nojima I, Shimizu Y, Sahashi K, Itamoto S, Suzuki A, Yamada G, Matsukawa N and Wada I (2019) Impaired Motor Skill Acquisition Using Mirror Visual Feedback Improved by Transcranial Direct Current Stimulation (tDCS) in Patients With Parkinson's Disease. Front. Neurosci. 13:602. doi: 10.3389/fnins.2019.00602

Recent non-invasive brain stimulation techniques in combination with motor training can enhance neuroplasticity and learning. It is reasonable to assume that such neuroplasticity-based interventions constitute a useful rehabilitative tool for patients with Parkinson's Disease (PD). Regarding motor skill training, many kinds of tasks that do not involve real motor movements have been applied to PD patients. The purpose of this study is to elucidate whether motor skill training using mirror visual feedback (MVF) is useful to patients with PD in order to improve untrained hand performance dependent on the time course of training; and whether MVF combined with anodal transcranial direct current stimulation (tDCS) over primary motor cortex (M1) causes an additional effect based on increased motor cortical excitability. Eighteen right-handed patients with PD in the off-medication state and 10 age-matched healthy subjects (HS) performed four sessions of right-hand ball rotation using MVF (intervention) on two separate days, 1 week apart (day 1 and day 2). HS subjects received only sham stimulation. The intervention included four sessions of motor-skill training using MVF for 20 min comprised of four sets of training for 30 s each. PD patients were randomly divided into two intervention groups without or with anodal tDCS over the right M1 contralateral to the untrained hand. As the behavior evaluation, the number of ball rotations of the left hand was counted before (pre) and immediately after (post) intervention on both days (pre day 1, post day 1, pre day 2, and post day 2). Motor evoked potential (MEP), input-output function, and cortical silent period were recorded to evaluate the motor cortical excitatory and inhibitory system in M1 pre day 1 and post day 2. The number of ball rotations of the left hand and the facilitation of MEP by intervention were significantly impaired in patients with PD compared to HS. In contrast, if anodal tDCS was applied to

right M1 of patients with PD, the number of ball rotations in accordance with I-O function at 150% intensity was significantly increased after day 1 and retained until day 2. This finding may help provide a new strategy for neurorehabilitation improving task-specific motor memory without real motor movements in PD.

Keywords: neuroplasticity, mirror visual feedback, rehabilitation, Parkinson's disease, transcranial direct current stimulation

INTRODUCTION

Parkinson's disease (PD) is a neurodegenerative disorder and some of its pathophysiology are related to the disruption in the dopaminergic system and the altered basal ganglia (BG)-thalamocortical circuitry (DeLong, 1990). Many kinds of rehabilitation which do not involve real motor movements have been applied to PD patients (Abbruzzese et al., 2015). In a motor imagery task, motor cortical excitability, and brain activation areas during hand action imagination were reduced and altered in PD patients (Thobois et al., 2000; Tremblay et al., 2008; Castiello et al., 2009). However, action observation training of finger movements improved the spontaneous rate of finger movements in PD patients (Pelosin et al., 2013). Moreover, PD patients showed action observation related facilitation of grasping movement only when the model was a Parkinsonian subject (Castiello et al., 2009). Based on these findings, fine visual input seems to be important for the improvement of motor dysfunction in PD patients without real motor training.

Mirror visual feedback (MVF) was first reported by Ramachandran et al. (1995) to alleviate phantom limb pain in amputees (Ramachandran et al., 1995). Since then, MVF has been successfully applied in patients with motor deficits especially due to stroke; motor training of the unimpaired limb with its MVF superimposed over the paretic limb led to a remarkable recovery (Altschuler et al., 1999; Yavuzer et al., 2008). Several studies have focused on the neural mechanisms that underlie the effects of MVF. Functional imaging studies have shown that the neural network related to MVF was attributed to the M1 and other motor-related areas such as premotor cortex and posterior superior temporal sulcus (Giraux and Sirigu, 2003; Sasaki et al., 2012). Nojima et al. (2012, 2015) found that motor-skill training using MVF rather than action observation induced the facilitation of motor cortical excitability in the M1 contralateral to the untrained hand. Recently, it was reported that self-paced sequential finger tapping related MVF increased hand speed as a factor of bradykinesia and the motor cortical excitability in PD patients (Bonassi et al., 2016). Thus, MVF intervention targeting the most clinically affected (severe) untrained side may have a beneficial effect on the acquisition of new motor skills related to increased motor cortical excitability in PD patients.

Non-invasive brain stimulation techniques have been shown to modulate brain processing and thereby influence behavior (Di Pino et al., 2014). The application of anodal tDCS over cortex can facilitate the excitability and anodal tDCS in combination with various kinds of motor training results in excitability changes in the human sensory and motor cortices (Nitsche and Paulus, 2000, 2011; Nitsche et al., 2003; Grundmann et al., 2011; Nitsche, 2011). It has also been reported that anodal tDCS enhances neuroplasticity and learning in older individuals and patients with stroke (Kang et al., 2016). Recently, in both aged and younger healthy subjects, motor skill training using MVF combined with anodal tDCS improved the dexterity of the untrained hand, compared to sham stimulation (Hoff et al., 2015; von Rein et al., 2015). Transcranial Magnetic Stimulation (TMS) is another technique of non-invasive brain stimulation and provide information on the conductivity of corticospinal neurons and the excitatory and inhibitory systems in the primary motor cortex (Cantello et al., 1991, 1992; Ridding and Rothwell, 1997).

Based on these studies, it is not yet known whether motor skill training using MVF is useful to patients with PD in order to improve untrained hand performance dependent on the time course of training; and whether MVF combined with anodal tDCS over M1 causes an additional effect based on increased motor cortical plasticity in PD. To elucidate this, we firstly applied motor skill training using MVF (intervention) to patients with PD and age matched healthy subjects. Then we secondly applied intervention combined with tDCS over M1 contralateral to the untrained hand in patients with PD.

MATERIALS AND METHODS

Subjects

Eighteen patients with PD (mean age ± SD: 70.6 ± 5.4 years, 8 male and 10 female) and 10 age-matched healthy subjects (HS) (mean age ± SD: 68.1 ± 5.6 years, 7 male and 3 female) participated in the study. All of the patients fulfilled the United Kingdom Brain Bank Criteria (Hughes et al., 1992) and corresponded to categories 2 or 3 of the Modified Hoehn and Yahr Scale in the off-medication state. In order to control hand laterality, we recruited right-handed subjects according to the Edinburgh Inventory (Oldfield, 1971). In addition, in all PD patients the left side was the most affected (**Table 1**); as they performed the motor-skill training using MVF, the better performance of the right hand was used. Therefore, it was needed for them to rotate the ball more than twice especially on the right side. Moreover, even though in their affected left side, since we evaluated the number of the ball rotation, we excluded the patients who were not able to rotate the ball at all. All patients were evaluated after being off-medication (levodopa

Abbreviations: APB, abductor pollicis brevis; tDCS, transcranial direct current stimulation.

TABLE 1 | Clinical profile of patients with Parkinson's disease.

Patient	Age (years)	Gender	Duration (years)	Condition	Affected side	Yahr	UPDRS part 3	UPDRS (item 20–25) Affected/unaffected side	Subtype	LEDD (mg/days)
1	76	F	4	Real	Left	2	19	8/3	Tremor	200
2	64	M	3	Real	Left	3	26	8/4	Akinesic-rigid	200
3	74	F	4	Real	Left	2	12	3/2	Akinesic-rigid	175
4	68	M	5	Real	Left	2	19	5/3	Tremor	300
5	69	F	8	Real	Left	3	9	6/3	Akinesic-rigid	350
6	78	F	11	Real	Left	3	7	4/0	Akinesic-rigid	559
7	69	F	8	Real	left	3	9	6/3	Akinesic-rigid	350
8	68	F	2	Real	left	2	6	4/2	Akinesic-rigid	200
9	76	F	13	Real	left	3	10	3/1	Akinesic-rigid	582
10	78	M	8	Sham	left	3	28	8/4	Tremor	100
11	68	F	10	Sham	left	3	25	7/6	Akinesic-rigid	75
12	69	F	7	Sham	left	3	23	5/4	Akinesic-rigid	125
13	70	F	1	Sham	left	3	9	3/2	Tremor	200
14	74	M	4	sham	left	3	19	8/3	Akinesic-rigid	300
15	69	F	9	Sham	left	3	9	4/2	Akinesic-rigid	674
16	72	M	2	Sham	left	2	6	3/0	Akinesic-rigid	250
17	60	M	4	Sham	left	3	17	7/3	Akinesic-rigid	50
18	76	M	13	Sham	left	3	18	6/5	Akinesic-rigid	490

Yahr: Hoehn and Yahr, UPDRS: Unified Parkinson's Disease Rating Scale.

replacement) for 12 h. The motor function of the patients in the off-medication state was assessed in accordance with the motor section of the Unified Parkinson's Disease Rating Scale (UPDRS). The clinical subtype of akinesic-rigid and tremor dominant were diagnosed based on previous paper by two neurologists (Lewis et al., 2005). The Mini-Mental State Examination (MMSE) and the Frontal Assessment Battery (FAB) (Dubois et al., 2000) were also performed. Attention and fatigue were assessed with the visual analog scale questionnaire (Attention scale, 1–7: 1, no attention; 7, highest level of attention) and the Chalder fatigue scale (Chalder et al., 1993) after the experiment on both days. All of the subjects provided written informed consent according to the dictates of the Nagoya City University Hospital Trust Ethics Committee (protocol number 46-13-0004). The experimental procedure was conformed to the Ethics of the World Medical Association (Declaration of Helsinki) and was approved by the university hospital medical information network in Japan. All methods were carried out in accordance with relevant guidelines and regulations.

Experimental Procedure

All HS were recruited to a sham stimulation group. Although it should be interesting to look for any tDCS-induced change also in HS, the previous paper had already reported the effect of tDCS to the motor skill learning related to the same ball rotation task using mirror visual feedback in HS (Hoff et al., 2015; von Rein et al., 2015). Therefore, we plan the protocol of the real tDCS stimulation only to PD. In PD, eighteen patients were randomly divided to tDCS (mean age ± SD: 70.4 ± 6.0 years, 3 male and 6 female) and sham stimulation groups (mean age ± SD: 70.8 ± 5.0 years, 5 male and 4 female). The experimenter who do not perform the intervention and evaluation randomly assigned patient using a random number by Excel software. Since Nojima et al. (2012) reported that the number of ball rotations of left hand increased significantly after the intervention of mirror condition but non-mirror group in HS, we did not apply the non-mirror condition to the PD in this study. To elucidate the effect of motor skill training using MVF dependent on the time course, the intervention was performed on two separate days (day 1 and day 2), 1 week apart (**Figure 1A**). The intervention included four sessions of motor-skill training using MVF for 20 min which was comprised of four sets of training for 30 s each with 30 s of rest between each trial and 90 s rest in final part (**Figure 1A**). Since the intervention consisted of four sessions of motor-skill training using MVF for 20 min, patients were applied either tDCS or sham stimulation during total time of intervention (**Figures 1B,C**).

The behavior evaluation session was performed before (pre) and immediately after (post) intervention on both days (pre day 1, post day 1, pre day 2, and post day 2). In the evaluation session, the motor performance of the left hand was scored using the number of rotations of the two balls performed over 30 s, recorded throughout the evaluation session using a video camera and analyzed offline by a researcher. The mean maximal pinching force (PF) between the index finger and the thumb at five times the pinch gauge (in kgf) and the UPDRS (motor) score were also assessed. Attention and fatigue were assessed after each day (post day 1 and post day 2). The transcranial magnetic stimulation (TMS) measurements included the mean motor-evoked potential (MEP) amplitudes, input-output (I-O) function, and the mean silent period (SP) of the left APB, recorded twice (pre day 1 and post day 2). It took much time when TMS measurements were performed in four time points in PD, which may affect the behavioral data because of sever fatigue. Moreover, our main purpose is to clarify whether this total intervention can produce

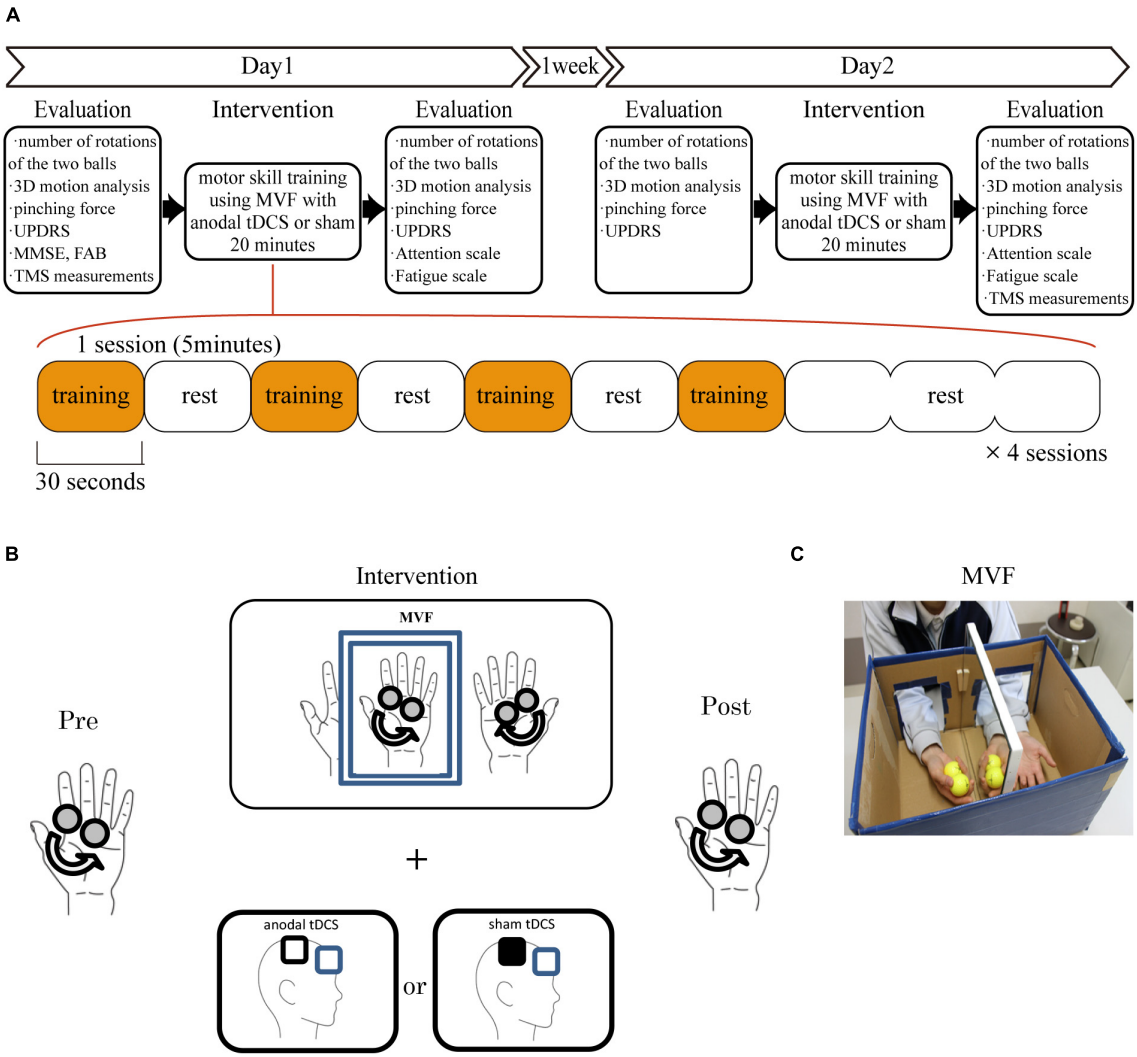

FIGURE 1 | Experimental procedure. **(A)** The motor skill training was performed twice on two separate days (days 1 and 2) 1 week apart. The subjects underwent intervention over the right M1 for 20 min on each day. They performed four sessions of the behavioral task which comprised four sets of motor training for 30 s and rest for 30 s between each trial and 90 s rest in final part. The behavioral evaluation sessions were performed before and after the intervention on each day. The TMS evaluation was performed before day 1 and after intervention on day 2. **(B)** The ball-rotation task involved rotating two cork balls as fast as possible in a counterclockwise direction using the right hand. In PD, subjects were randomly divided the groups with tDCS or sham stimulation over the right M1. **(C)** For motor-skill training using MVF, the subjects placed both hands inside a box made of paper and mirrored glass, and performed the above behavioral task using their right hand.

the change of motor cortical systems in PD. Therefore, we evaluated subject's cortical excitatory and inhibitory systems by means of TMS only two time points. All of the data were stored on a computer, and a researcher blind to subject type analyzed behavioral data.

Behavioral Task and Motor Skill Training Using MVF

The target task was using the right hand to rotate two cork balls (diameter, 30 mm) as fast as possible in a counterclockwise direction (**Figures 1A,B**). For motor skill training using MVF, the subjects were instructed to place both of their hands inside a box made of paper and mirrored glass that prevented the direct view of the right hand but allowed an indirect view via the mirror (**Figure 1B**). The subjects were instructed to observe the movements of the right hand in a mirror that provided MVF of their performance in the ball rotation task. This behavioral task and motor skill training using MVF were originally developed by Nojima et al. (2012).

Transcranial Magnetic Stimulation

Each subject was seated in an armchair with arms placed on the armrest. Surface electromyograms (EMGs) were recorded from the left APB muscle with a pair of silver electrodes. The EMGs were amplified and filtered, and digitized at a sampling rate of

10 kHz using the Labview system. The position of the EMGs was marked on the hand and recorded by video camera. The TMS was produced using a 7-cm figure-of-eight coil connected to a Magstim® 200 Monophasic Transcranial Stimulator (The Magstim Co., Whitland, Dyfed, United Kingdom). At the beginning of each day the optimal motor points for APB were determined following a standard procedure (Rossini et al., 1994). The optimal motor points for eliciting the best motor response from the left APB muscle with the coil held ∼45° to the midsagittal line were established over the right M1, which was determined in 5 mm steps around the presumed motor hand area. The current of TMS was induced by posterior-anterior direction. The determined coil position was marked on the scalp and its coordinates on midsagittal (nasion-inion line) and biauricular (line connecting external auditory meati) axes in relationship to the vertex were recorded according to the previous repetitive TMS study (Filipović et al., 2010). This recorded coil position was also used for the recording in post day 2. The resting motor threshold was defined on pre day 1, in accordance with a previous study, as the lowest stimulus intensity required to elicit MEP with a peak-to-peak amplitude of >50 μV in the left APB muscle in at least five out of 10 trials (Rossini et al., 1994).

In order to assess corticospinal excitability, MEP amplitudes were measured with the fixed stimulus intensity of the TMS machine adjusted to 120% of resting motor threshold at the target APB muscle in pre day 1. The mean peak-to-peak MEP amplitudes for 10 trials were measured. The recruitment of the corticospinal projection (I-O function) from the right M1 was also measured (Ridding and Rothwell, 1997). The intensities of single TMS stimuli were individually adapted according to the resting motor threshold to evaluate the I-O function. Ten MEPs were recorded from the left APB muscle at intensities of 50, 80, 90, 100, 110, 120, and 150% of the resting motor threshold and averaged at each intensity.

The SP was also measured (10 replicates) to assess the motor inhibitory system. We evaluated the SP by applying TMS to the right M1 at 140% of the resting motor threshold during low-force activation of the APB (Fuhr, 1991; Ziemann et al., 1993; Kojima et al., 2013). Subjects maintained a voluntary isometric contraction at approximately 20% of their maximum voluntary contraction by providing feedback from the surface EMG on a computer screen. The duration of ten SP was measured from the end of the MEP until the restart of a constant EMG activity. We employed a method by which the amplitude and onset were measured automatically to minimize observer bias using a custom-made MATLAB program (MathWorks, Natick, MA, United States).

We had also confirmed the hot spot by using TMS just before the intervention of day 2. Moreover, the coil position was measured on the scalp in accordance with midsagittal (nasion-inion line) and biauricular (line connecting external auditory meati) axes relative to the vertex on day 1 and was adjusted before the intervention of day 2.

In PD, during the TMS experiment, EMG background activities were continuously observed online; when rigidity or tremor prominently appeared, the examiner left as long as patients needed to relax throughout the experiment and started recording when the background EMG was silent.

Transcranial Direct Current Stimulation

A weak direct current of 2 mA was delivered via saline-soaked sponge electrodes using a DC Stimulator Plus (neuroConn GmbH, Ilmenau, Germany). TMS was used to identify the functional landmark of the right M1 as the optimal position. The current density at the stimulation electrodes was 0.025 mA/cm^2 in accordance with safety criteria and far below the threshold for tissue damage (Nitsche, 2003). Either anodal tDCS or sham stimulation was applied to the right M1 during the intervention on both day 1 and day 2. The impedance of the stimulation electrodes was kept below 10 kΩ. In all of the conditions, the stimulating electrode was placed above the right M1, while the reference electrode of the cathode was placed above the frontal orbit. During tDCS, the current was increased at the beginning and decreased at the end of the protocol (20 min) over 30 s in a ramp-like manner, on the basis of previous reports (Nitsche et al., 2003). In the sham condition, the current was applied for only 30 s. This protocol has been demonstrated to reliably blind subjects with respect to the stimulation condition (Gandiga et al., 2006).

Behavioral Data Analysis

For evaluation of motor performance, the dexterity of the left hand was examined by counting the number of two-ball rotations during 30 s. Two experimenters separately counted the number of two balls rotation, one of which was marked by color, during 30 s by using Video monitor on off-line and adjusted each number. In addition, for monitoring acceleration of the left thumb, a three-dimensional motion analysis system (Locus 3D MA-3000, Anima Corp., Tokyo, Japan) was used with four infrared cameras to capture and analyze motion with a sampling frequency of 100 Hz (Yamaguchi et al., 2015). Reflective markers of 5-mm diameter were attached on the first joint of the left thumb. The mean peak acceleration of the thumb movements during two-ball rotations during 30 s was calculated and expressed in cm/s^2.

Statistical Analysis

To determine the effect of motor skill training using MVF dependent on time course in patients with PD, we compared the outcome in behavior and TMS parameters between HS and PD-sham. The number of ball rotations, peak acceleration and PF were used as the behavioral variables, while the mean MEP amplitude, I-O function and SP from the TMS were used as the physiological variables. The effect of these variables was evaluated using a two-way repeated measures analysis of variance (RM-ANOVA), with group (PD, HS) as a between-subjects factor and time (pre day 1, post day 1, pre day 2, and post day 2) as behavioral variables or pre day 1 and post day 2 as physiological variables. Attention and fatigue were also evaluated using RM-ANOVA. The Greenhouse-Geisser method was used to correct for non-sphericity. If the effect was significant, a *post hoc t*-test was performed on the data. The Bonferroni correction for multiple comparisons was also used where necessary.

To determine whether the intervention combined with anodal tDCS over the right M1 contributes to motor performance and facilitation in the M1 in patients with PD, the number of ball rotations, peak acceleration, PF and UPDRS motor score were used as the behavioral variables, while the mean MEP amplitude, I-O function and SP from the TMS were used as the physiological variables. The effect of these variables was evaluated using a two-way repeated measures analysis of variance (RM-ANOVA), with condition (sham, tDCS) as a between-subjects factor and time (pre day 1, post day 1, pre day 2, and post day 2) as behavioral variables or pre day 1 and post day 2 as physiological variables. The Greenhouse-Geisser method was used to correct for non-sphericity. If the effect was significant, a *post hoc t*-test was performed on the data. The Bonferroni correction for multiple comparisons was also used where necessary.

Results with *P*-values less than 0.05 were considered significant. All of the statistical analyses were performed with SPSS version 25.0 for Windows (IBM Japan, Tokyo, Japan).

RESULTS

Cognitive scores, measured by mini mental scale examination (MMSE) were 28.6 ± 1.7 in HS, 29.0 ± 1.4 in PD; frontal assessment battery (FAB) was 14.9 ± 2.2 in HS and 15.9 ± 1.5 in PD. The characteristics of PD patients are summarized in **Table 1**.

The Effect of MVF on Behavior: HS vs. PD

Regarding the result of the number of two-ball rotations (**Figure 2**), there was a significant effect of group [$^*P$ = 0.001, $F(1,16)$ = 25.3] and time × group interaction [$^*P$ = 0.002, $F(3,48)$ = 5.88]. Thus, further analysis was performed on each group. In HS, *post hoc* analysis demonstrated the number of ball rotations that could be performed on post day 1, pre day 2, and post day 2 was significantly increased compared to those performed on pre day 1 ($^*P$ = 0.003 on post day 1, $^*P$ = 0.001 on pre day 2, and $^*P$ = 0.01 on post day 2). In contrast, there was no significant additional improvement in the number of ball rotations performed between post day 1 and pre day 2 (P = 0.88), or between pre day 2 and post day 2 (P = 0.76). On the other hand, in PD, *post hoc* analysis demonstrated no significant difference in the number of ball rotations between any time points ($P > 0.05$).

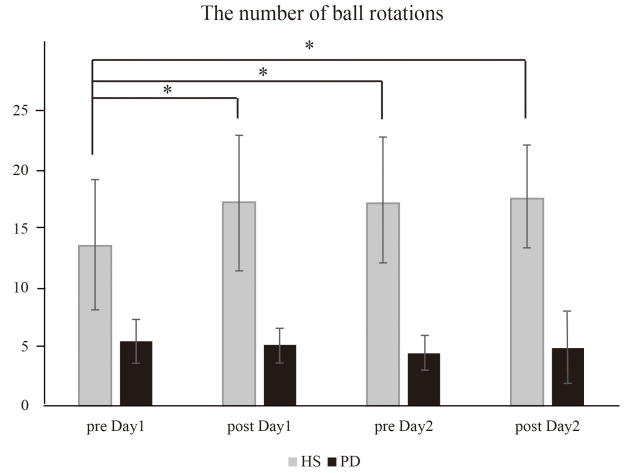

FIGURE 2 | The number of ball rotations (HS vs. PD). In HS, the intervention caused a significant increase in the number of ball rotations on post day 1 ($^*P$ = 0.003), pre day 2 ($^*P$ = 0.001), and post day 2 ($^*P$ = 0.01) compared to that on pre day 1. In contrast, in PD, the intervention caused no significant increase in the number of ball rotations.

The result of the mean peak acceleration in HS and PD are summarized as **Table 2**. There was a significant effect of group [$^*P$ = 0.001, $F(1,16)$ = 28.6] and time × group interaction [$^*P$ = 0.001, $F(1.9,30.4)$ = 9.59]. In HS, *post hoc* analysis demonstrated there were significantly increased peak accelerations between pre day 1 and pre day 2 or post day 2 ($^*P$ = 0.01 on pre day 2 and $^*P$ = 0.008 on post day 2) and between pre day 2 and post day 2 ($^*P$ = 0.02). In contrast, there was no significant additional improvement in the accelerations performed between pre day 1 and post day 1 (P = 0.09) and pre day 2 (P = 0.76). On the other hand, in PD, *post hoc* analysis demonstrated no significant difference in the accelerations between any time points ($P > 0.05$).

The result of the PF in HS and PD are summarized as **Table 3**. There was no significant effect of group (P = 0.16) or time × group interaction (P = 0.27).

The result of the attention and fatigue scores in HS and PD are summarized as **Table 4**. For attention, there was a

TABLE 2 | Mean peak acceleration in HS and PD.

	Mean peak acceleration (cm/s^2)			
	Pre day 1	**Post day 1**	**Pre day 2**	**Post day 2**
HS	60.9 ± 11.6	74.6 ± 29.7	76.3 ± 18.9$^{\#}$	96.5 ± 36.9$^{*,\$}$
PD	38.2 ± 16.5	35.1 ± 15.5	32.8 ± 12.1	31.7 ± 15.9

$^{\#}P$ = 0.01 comparison to pre day 1, $^*P$ = 0.008 comparison to pre day 1, $^{\$}P$ = 0.02 comparison to pre day 2 (post hoc analysis). The values are in means ± standard deviations (SD).

TABLE 3 | Mean maximal pinching force (in kgf) in HS and PD.

	Mean maximal pinching force (in kgf)			
	Pre day 1	**Post day 1**	**Pre day 2**	**Post day 2**
HS	7.4 ± 2.3	8.0 ± 2.4	8.1 ± 2.4	8.1 ± 2.4
PD	6.9 ± 1.4	7.5 ± 1.6	7.4 ± 1.9	7.4 ± 1.8

The values are in means ± standard deviations (SD).

TABLE 4 | Attention and fatigue scores in HS and PD.

	Attention score		Fatigue score	
	Post day 1	**Post day 2**	**Post day 1**	**Post day 2**
HS	6.6 ± 1.0	6.3 ± 0.7	10.3 ± 2.4	11.5 ± 1.0
PD	5.8 ± 0.7	5.8 ± 0.4	14.7 ± 3.6	10.8 ± 5.2*

$^*P$ = 0.01 comparison to post day 1 (post hoc analysis). The values are in means ± standard deviations (SD).

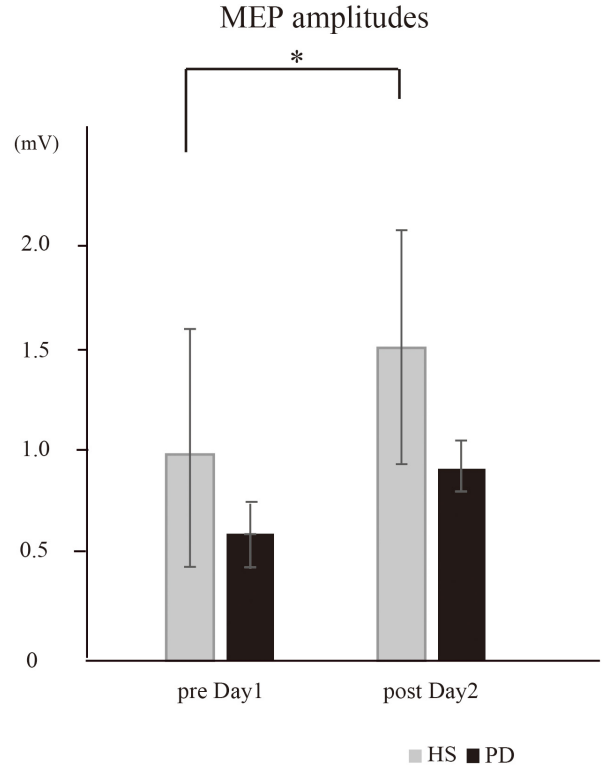

FIGURE 3 | The MEP amplitudes recorded from the right APB (HS vs. PD). In HS, the intervention caused a significant increase in the mean MEP amplitudes on post day 2 compared to those on pre day 1 (*P = 0.03). In PD, the intervention caused no significant increase in the mean MEP amplitudes (P = 0.12).

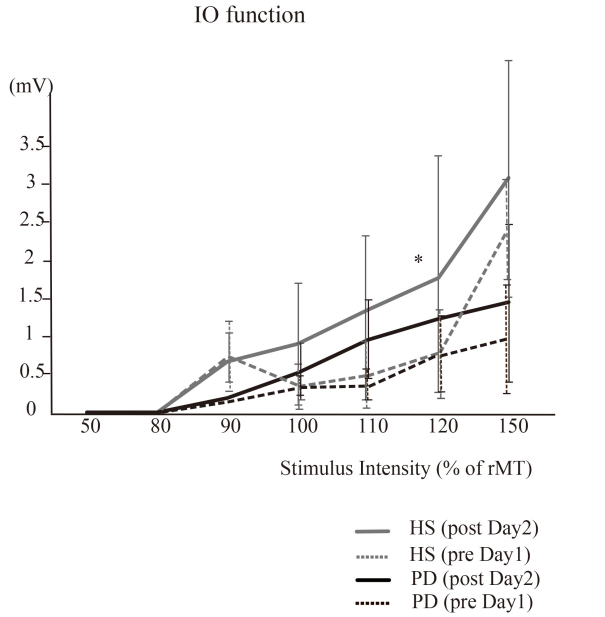

FIGURE 4 | The IO function (HS vs. PD). For the I-O function in HS, MEP amplitudes at the intensity of 120% on post day 2 were significantly increased compared to those performed on pre day 1 (*P = 0.04). In PD, there were no significant differences in the MEPs. At 50, 80, 90, 100, and 150% intensity, there were no significant effects of time or time × group interaction in either HS or PD.

significant main effect of group [*P = 0.03, $F(1,16)$ = 5.49] but no group × time interaction effect [P = 0.41, $F(1,16)$ = 0.71]. For fatigue, there was no significant main effect of group [P = 0.21, $F(1,16)$ = 1.73]; however, there was a group × time interaction effect [*P = 0.002, $F(1,16)$ = 13.6]. In PD, *post hoc* analysis demonstrated there was significantly increased fatigue score on post day 2 compared with post day 1 (*P = 0.01). By contrast, in HS there was no significant change (P = 0.20).

The Effect of MVF on Motor Cortical Excitatory and Inhibitory Systems: HS vs. PD

The resting motor thresholds for the left APB in HS were 54.8 ± 11.2% (pre day 1) and 50.8 ± 12.2% (post day 2) of the maximal stimulator output. The resting motor thresholds in PD patients were 57 ± 10.3% (pre day 1) and 57.1 ± 10.3% (post day 2). There were no significant effects of group (P = 0.19) or group × time interactions (P = 0.07).

The effect of the intervention on the motor cortical excitatory system was evaluated by the changes in MEP amplitude recorded from the left APB between HS and PD. There was a significant effect of group [*P = 0.04, $F(1,16)$ = 4.55] and time × group interaction [*P = 0.05, $F(1,16)$ = 3.8]. Thus, further analysis was performed in each group. In HS, *post hoc* analysis demonstrated the MEP amplitude on post day 2 was significantly increased compared to that in pre day 1 (*P = 0.03); in contrast, MEP amplitude in PD was not affected (P = 0.12) (**Figure 3**).

For the I-O function of MEP amplitudes at an intensity of 120%, there was a significant effect of group [*P = 0.00, $F(1,16)$ = 28.5] and time × group interaction [*P = 0.04, $F(1,16)$ = 4.51]. In HS, *post hoc* analysis demonstrated that the MEPs on post day 2 were significantly increased compared to those on pre day 1 (*P = 0.04) (**Figure 4**). On the other hand, in PD, *post hoc* analysis demonstrated no significant difference in the MEPs ($P > 0.05$). At 50, 80, 90, 100, and 150% intensity, there were no significant effects of time or time × group interaction.

The effect of the intervention on motor cortical inhibitory system was evaluated by the changes in the SP between HS and PD. The SP were 92.5 ± 16 and 85.9 ± 20.3 (pre day 1), and 88.3 ± 16.1 and 87.6 ± 22.4 (post day 2) in the HS and PD groups, respectively. There was no effect of group (P = 0.69) or time × group interaction (P = 0.34).

The Effect of the Intervention (MVF+tDCS) on Behavior and Motor Cortical Excitability: PD-tDCS vs. PD-Sham

Since the number of ball rotations, peak acceleration and motor cortical excitatory system were significantly impaired in PD, we evaluated the effect of tDCS over the right M1 on these factors.

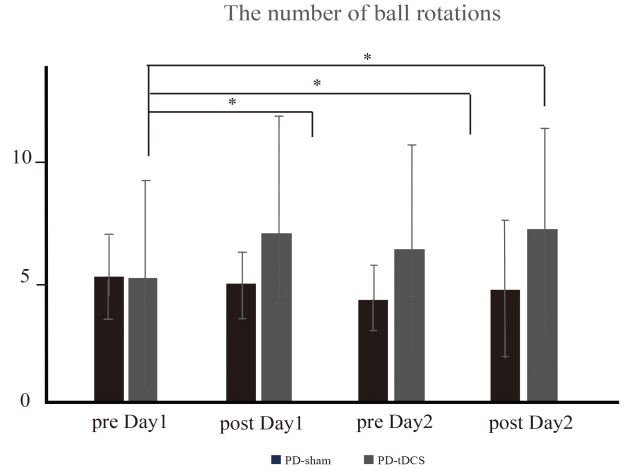

FIGURE 5 | The number of ball rotations (PD-tDCS vs. PD sham). In PD-tDCS, the intervention caused a significant increase in the number of ball rotations on post day 1 (*P = 0.006), pre day 2 (*P = 0.006), and post day 2 (*P = 0.02) compared to that on pre day 1.

For the number of two-ball rotations, there was an effect of condition [*P = 0.05, $F(1,15)$ = 4.12] but no time × condition interaction effect [P = 0.17, $F(3,45)$ = 1.73]. Thus, further analysis was performed in the tDCS condition. The *post hoc* analysis revealed that the intervention + tDCS led to a significant increase in the number of ball rotations on post day 1 and pre day 2 compared to that on pre day 1 (post day 1, *P = 0.006; pre day 2, *P = 0.006; post day 2, *P = 0.02) (**Figure 5**). However, the intervention did not cause a further increase in the number of rotations between post day 1 and pre day 2 (P = 0.05) or between pre day 2 and post day 2 (P = 0.25). There was no significant effect of condition (P = 0.9) or time × condition interaction (P = 0.31) on the mean peak acceleration.

The UPDRS scores were 18.9 ± 7.4 (pre day 1), 18.1 ± 6.3 (post day 1), 18.9 ± 7.4 (pre day 2), and 17.3 ± 7.0 (post day 2) in the PD-sham group, and 15.3 ± 7.2 (pre day 1), 14.5 ± 5.9 (post day 1), 13.8 ± 4.7 (pre day 2), and 13.3 ± 5.9 (post day 2) in the PD-tDCS group. There were no significant main effects of time [P = 0.25, $F(1.29,12.94)$ = 1.49] or condition × time interaction [P = 0.51, $F(1.29,12.94)$ = 0.55] on the UPDRS score.

The resting motor thresholds in PD-tDCS were 55.7 ± 10.8% (pre day 1) and 54.6 ± 9.8% (post day 2). Regarding motor cortical excitability, the mean MEP amplitudes in the PD-tDCS group were 0.79 ± 0.3 mV in pre day 1 and 0.83 ± 0.4 mV in post day 2. There were no significant effects of condition (P = 0.11) or time × condition interaction (P = 0.82).

For the I-O function of MEP amplitudes, at an intensity of 150%, there were significant effects of time [$F(1,15)$ = 4.16, P = 0.05] and condition [$F(1,15)$ = 5.29, P = 0.04], but no time × condition interaction effect [$F(1,15)$ = 2.8, P = 0.1]. The *post hoc* analysis demonstrated that the MEPs on post day 2 were significantly increased compared to those performed on pre day 1 (*P = 0.04). At 50, 80, 90, 100, and 120% intensity, there were no significant effects of time or time × condition interaction.

DISCUSSION

This study revealed that behavioral improvement and motor cortical plasticity caused by motor skill training using MVF were impaired in patients with PD compared to HS; improvements of behavior and motor cortical excitability occurred if anodal tDCS was applied to the right M1 contralateral to the untrained left hand. These findings suggest that the combination of MVF and tDCS could be a promising strategy to improve motor skills in a specific manner dependent on the motor excitatory system.

In HS, the number of ball rotations and the acceleration of the left thumb were significantly increased through repeated motor skill training using MVF both on day 1 and day 2, depending on the facilitated MEP amplitude and I-O function of 120% intensity. These results in HS were compatible with those of previous studies which also demonstrated improved hand dexterity after motor skill training using MVF related to inducing motor cortical plasticity in contralateral M1(Hoff et al., 2015; von Rein et al., 2015). The ball rotation task skill using MVF was acquired on day 1 and was retained until 1 week after the initial training (day 2); however, additional behavioral improvement did not occur on day 2. This behavioral change was likely mediated by an improved dexterity of the left hand as opposed to a change in PF, indicating that the task-specific manner of behavioral improvement depends on the motor excitatory system not inhibitory system. The motor cortical neurons of the M1 are reported to encode specific movement (Muir and Lemon, 1983; Rizzolatti et al., 1996a,b; Kakei et al., 2001). Our results suggest that the encoding of a new motor memory such as ball rotation, although in the form of mirrored movement, can be improved by the enhanced excitability or synaptic efficacy of the appropriate neuronal population in the M1.

On the other hand, in PD, the number of ball rotations and the facilitation of the MEP amplitude did not improve through repeated skill training on day 1 and day 2. Our result suggest that even though combined with the fine visual input the motor skill acquisition did not occur and motor cortical excitability did not changed in PD. Most studies of PD report impaired acquisition in serial reaction time task paradigms, with a relatively preserved early stage of skill acquisition and impaired retention of short and long-term motor memories in adaptation tasks (Agostino et al., 1996; Jessop et al., 2006; Muslimovic et al., 2007; Pendt et al., 2011). Recently, we reported that the repetitive skill training did not result in effective improvement of motor performance in PD, which is related to reduce dopamine release in the contralateral putamen by using ^{11}C-raclopride positron emission tomography (Kawashima et al., 2018). In previous studies of PD using motor imagery tasks, a TMS study reported that motor cortical excitability in the M1 was impaired during action imagination of the hand; a task-based fMRI study reported the activated brain areas including (BG)-thalamocortical circuitry were altered (Thobois et al., 2000; Tremblay et al., 2008). Moreover, the study of an animal model of PD showed that plasticity in the motor cortex is important for the acquisition and that dopamine depletion resulted in structural changes in the motor cortex and atypical synaptic adaptations (Molina-Luna et al., 2009; Guo et al., 2015). Based on these findings, in PD, the impaired

facilitation of the MEP amplitude during the motor skill training using MVF may be caused by dopamine depletion and secondary alteration of modulation in BG-thalamocortical circuitry.

In order to increase the facilitation effect of motor cortical excitability for improving affected hand dexterity in PD, we applied tDCS over the contralateral M1 during motor skill training using MVF. When the tDCS was applied to the right M1 in PD, the number of ball rotations using the untrained left hand were significantly increased on day 1 and the effect was retained after 1 week. Although the MEP amplitude recorded by 120% of resting motor threshold was not increased, I-O function at 150% intensity was significantly increased after day 2. It is well known that application of anodal tDCS in combination with various kinds of motor training results in excitability changes and induction of homeostatic plasticity in the human sensory and motor cortices (Nitsche and Paulus, 2000, 2011, Nitsche et al., 2003, Grundmann et al., 2011; Nitsche, 2011). Moreover, many studies in PD examining the effects of tDCS over the M1, premotor, prefrontal, Cz area, etc., have reported an effect on the change in UPDRS (motor) scores, gait speed, working memory, etc., compared to sham stimulation (Fregni et al., 2006; Benninger et al., 2010; Kaski et al., 2014). Anodal tDCS over the M1 is known to alter the resting membrane potentials of M1 neurons, leading to an increase in cortical excitability that has been proposed to help in the compensation of the reduced BG thalamo-cortical drive (Fregni et al., 2006; Benninger et al., 2010). In this study, the behavioral improvement occurred with facilitated I-O function, which may be caused by the altered excitability of the M1.

Reis et al. (2008) reported beneficial effects of tDCS in combination with motor training, and it is reasonable to assume that such neuroplasticity-based interventions might constitute a useful rehabilitative tool for PD patients. On the other hand, a recent clinical review reported that there was insufficient evidence to determine the effects of tDCS in reducing off time and on time with dyskinesia and for improving the health-related quality of life, disability, and impairment in patients with PD (Elsner et al., 2016). In the present study, the UPDRS (motor) score was not changed by repeated intervention with tDCS over the M1. However, we applied the interventions 1 week apart in this study. Short- and long-term motor skill training typically results in functional brain alterations in a variety of motor-related brain regions, including the M1 (Doyon and Benali, 2005; Doyon, 2008). Moreover, a previous study provides evidence that repeated application of non-invasive brain stimulation over multiple days might even prolong such behavioral effects (Reis et al., 2009). Taken together this evidence could be combined to develop new effective rehabilitation.

In the present study, the motor training time was not so long, since the intervention consisted of 30 s of rest between each trial. However, PD showed significantly increased fatigue score on post day 2 compared with post day 1. A progressive slowing in speed or progressive decrease in the amplitude of repetitive movements are observed in patients with PD, which is known as the sequence effect (Agostino et al., 1992, 1994). This performance decline has also been observed in drug-naïve patients with PD during finger tapping and the repetitive movements involved in a pegboard task (Kang et al., 2010). Although the related pathogenesis is still unclear, it may be caused by freezing rather than fatigue. Considering these findings, the behavioral improvement by tDCS in PD may be explained mostly by the effect on acquired motor skill with MVF not on fatigue.

There are several limitations to our study. Because the sample size was as small as nine cases in each group, a significant difference between tDCS and sham stimulation in PD may not have been detected in TMS parameters other than the I-O curve. In the protocol of this study, we did not apply the intervention of MVF alone without sham stimulation to the PD patients. In PD, it is well known the placebo effect on the improvement of motor behavior and it should be carefully assessed in clinical trials (Frisaldi et al., 2017). In the previous study of sequential finger tapping with MVF, MVF training increased movement speed in untrained hand (Bonassi et al., 2016). Since our result showed no increase of the number of ball rotation in untrained hand by the intervention of MVF with sham stimulation, the involvement of placebo effect seems to be less likely.

Although we applied the interventions 1 week apart in this study, repeated application of tDCS over sequential days might even prolong such behavioral effects and motor cortical plasticity in PD. Further studies are needed to determine how to maximize the beneficial effect of tDCS before this method can be applied to patients with PD.

ETHICS STATEMENT

All of the subjects provided written informed consent according to the dictates of the Nagoya City University Hospital Trust Ethics Committee (protocol number 46-13-0004). The experimental procedure conformed to the Ethics of the World Medical Association (Declaration of Helsinki) and was approved by the university hospital medical information network in Japan. All methods were carried out in accordance with relevant guidelines and regulations.

AUTHOR CONTRIBUTIONS

MH executed the research and statistical analysis and wrote the first draft of the manuscript. YU and IN organized and executed the research and statistical analysis and reviewed and critiqued the manuscript. YS, KS, and SI executed the research. AS, GY, NM, and IW reviewed and critiqued the manuscript.

FUNDING

This work was supported by KAKENHI, Grant-in-Aid for Scientific Research on Innovative Areas, "Willdynamics" (16H06403), the Japan Society for the Promotion of Science (JSPS) KAKENHI Grant Number 15K09355 (YU).

ACKNOWLEDGMENTS

We thank Dr. Mark Hallett and Dr. Tatsuya Mima for useful discussions.

REFERENCES

Abbruzzese, G., Avanzino, L., Marchese, R., and Pelosin, E. (2015). Action observation and motor imagery: innovative cognitive tools in the rehabilitation of Parkinson's disease. *Parkinsons Dis.* 2015:124214. doi: 10.1155/2015/124214

Agostino, R., Berardelli, A., Formica, A., Accornero, N., and Manfredi, M. (1992). Sequential arm movements in patients with Parkinson's disease, huntington's disease and dystonia. *Brain* 115, 1481–1495. doi: 10.1093/brain/115.5.1481

Agostino, R., Berardelli, A., Formica, A., Stocchi, F., Accornero, N., and Manfredi, M. (1994). Analysis of repetitive and nonrepetitive sequential arm movements in patients with Parkinson's disease. *Mov. Disord.* 9, 311–314. doi: 10.1002/mds.870090305

Agostino, R., Sanes, J. N., and Hallett, M. (1996). Motor skill learning in Parkinson's disease. *J. Neurol. Sci.* 139, 218–226. doi: 10.1016/s0022-510x(96)00060-3

Altschuler, E. L., Wisdom, S. B., Stone, L., Foster, C., Galasko, D., Llewellyn, D. M., et al. (1999). Rehabilitation of hemiparesis after stroke with a mirror. *Lancet* 353, 2035–2036. doi: 10.1016/s0140-6736(99)00920-4

Benninger, D. H., Lomarev, M., Lopez, G., Wassermann, E. M., Li, X., Considine, E., et al. (2010). Transcranial direct current stimulation for the treatment of Parkinson's disease. *J. Neurol. Neurosurg. Psychiatry* 81, 1105–1111. doi: 10.1136/jnnp.2009.202556

Bonassi, G., Pelosin, E., Ogliastro, C., Cerulli, C., Abbruzzese, G., and Avanzino, L. (2016). Mirror visual feedback to improve bradykinesia in Parkinson's Disease. *Neural Plast.* 2016:8764238. doi: 10.1155/2016/8764238

Cantello, R., Gianelli, M., Bettucci, D., Civardi, C., De Angelis, M. S., and Mutani, R. (1991). Parkinson's disease rigidity: magnetic motor evoked potentials in a small hand muscle. *Neurology* 41, 1449–1456. doi: 10.1212/wnl.41.9.1449

Cantello, R., Gianelli, M., Civardi, C., and Mutani, R. (1992). Magnetic brain stimulation: the silent period after the motor evoked potential. *Neurology* 42, 1951–1959. doi: 10.1212/wnl.42.10.1951

Castiello, U., Ansuini, C., Bulgheroni, M., Scaravilli, T., and Nicoletti, R. (2009). Visuomotor priming effects in Parkinson's disease patients depend on the match between the observed and the executed action. *Neuropsychologia* 47, 835–842. doi: 10.1016/j.neuropsychologia.2008.12.016

Chalder, T., Berelowitz, G., Pawlikowska, T., Watts, L., Wessely, S., Wright, D., et al. (1993). Development of a fatigue scale. *J. Psychosom. Res.* 37, 147–153.

DeLong, M. R. (1990). Primate models of movement disorders of basal ganglia origin. *Trends Neurosci.* 13, 281–285. doi: 10.1016/0166-2236(90)90110-v

Di Pino, G., Pellegrino, G., Assenza, G., Capone, F., Ferreri, F., Ranieri, F., et al. (2014). Modulation of brain plasticity in stroke: a novel model for neurorehabilitation. *Nat. Rev. Neurol.* 10, 597–608. doi: 10.1038/nrneurol.2014.162

Doyon, J. (2008). Motor sequence learning and movement disorders. *Curr. Opin. Neurol.* 21, 478–483. doi: 10.1097/WCO.0b013e328304b6a3

Doyon, J., and Benali, H. (2005). Reorganization and plasticity in the adult brain during learning of motor skills. *Curr. Opin. Neurobiol.* 15, 161–167. doi: 10.1016/j.conb.2005.03.004

Dubois, B., Slachevsky, A., Litvan, I., and Pillon, B. (2000). The FAB a frontal assessment battery at bedside. *Neurology* 55, 1621–1626. doi: 10.1212/wnl.55.11.1621

Elsner, B., Kugler, J., Pohl, M., and Mehrholz, J. (2016). Transcranial direct current stimulation (tDCS) for idiopathic Parkinson's disease. *Cochrane Database Syst. Rev.* 7:CD010916. doi: 10.1002/14651858.CD010916.pub2

Filipović, S. R., Rothwell, J. C., and Bhatia, K. (2010). Slow (1 Hz) repetitive transcranial magnetic stimulation (rTMS) induces a sustained change in cortical excitability in patients with Parkinson's disease. *Clin. Neurophysiol.* 121, 1129–1137. doi: 10.1016/j.clinph.2010.01.031

Fregni, F., Boggio, P. S., Santos, M. C., Lima, M., Vieira, A. L., Rigonatti, S. P., et al. (2006). Noninvasive cortical stimulation with transcranial direct current stimulation in Parkinson's disease. *Mov. Disord.* 21, 1693–1702. doi: 10.1002/mds.21012

Frisaldi, E., Carlino, E., Zibetti, M., Barbiani, D., Dematteis, F., Lanotte, M., et al. (2017). The placebo effect on bradykinesia in Parkinson's disease with and without prior drug conditioning. *Mov. Disord.* 32, 1474–1478. doi: 10.1002/mds.27142

Fuhr, P. (1991). Spinal motor neuron excitability during the silent period after cortical stimulation. *Electroencephalogr. Clin. Neurophysiol.* 81, 257–262. doi: 10.1016/0168-5597(91)90011-l

Gandiga, P. C., Hummel, F. C., and Cohen, L. G. (2006). Transcranial DC stimulation: a tool for double-blind sham-controlled clinical studies in brain stimulation. *Clin. Neurophysiol.* 117, 845–850. doi: 10.1016/j.clinph.2005.12.003

Giraux, P., and Sirigu, A. (2003). Illusory movements of the paralyzed limb restore motor cortex activity. *Neuroimage* 20(Suppl. 1), S107–S111.

Grundmann, L., Rolke, R., Nitsche, M. A., Pavlakovic, G., Happe, S., Treede, R. D., et al. (2011). Effects of transcranial direct current stimulation of the primary sensory cortex on somatosensory perception. *Brain Stimul.* 4, 253–260. doi: 10.1016/j.brs.2010.12.002

Guo, L., Xiong, H., Kim, J. I., Wu, Y. W., Lalchandani, R. R., Cui, Y., et al. (2015). Dynamic rewiring of neural circuits in the motor cortex in mouse models of Parkinson's disease. *Nat. Neurosci.* 18, 1299–1309. doi: 10.1038/nn.4082

Hoff, M., Kaminski, E., Rjosk, V., Sehm, B., Steele, C. J., Villringer, A., et al. (2015). Augmenting mirror visual feedback-induced performance improvements in older adults. *Eur. J. Neurosci.* 41, 1475–1483. doi: 10.1111/ejn.12899

Hughes, A. J., Daniel, S. E., Kilford, L., and Lees, A. J. (1992). Accuracy of clinical diagnosis of idiopathic Parkinson's disease: a clinico-pathological study of 100 cases. *J. Neurol. Neurosurg. Psychiatry* 55, 181–184. doi: 10.1136/jnnp.55.3.181

Jessop, R. T., Horowicz, C., and Dibble, L. E. (2006). Motor learning and Parkinson disease: refinement of movement velocity and endpoint excursion in a limits of stability balance task. *Neurorehabil. Neural Repair.* 20, 459–467. doi: 10.1177/1545968306287107

Kakei, S., Hoffman, D. S., and Strick, P. L. (2001). Direction of action is represented in the ventral premotor cortex. *Nat. Neurosci.* 4, 1020–1025. doi: 10.1038/nn726

Kang, N., Summers, J. J., and Cauraugh, J. H. (2016). Transcranial direct current stimulation facilitates motor learning post-stroke: a systematic review and meta-analysis. *J. Neurol. Neurosurg. Psychiatry* 87, 345–355. doi: 10.1136/jnnp-2015-311242

Kang, S. Y., Wasaka, T., Shamim, E. A., Auh, S., Ueki, Y., Lopez, G. J., et al. (2010). Characteristics of the sequence effect in Parkinson's disease. *J. Mov. Disord.* 25, 2148–2155.

Kaski, D., Dominguez, R. O., Allum, J. H., Islam, A. F., and Bronstein, A. M. (2014). Combining physical training with transcranial direct current stimulation to improve gait in Parkinson's disease: a pilot randomized controlled study. *Clin. Rehabil.* 28, 1115–1124. doi: 10.1177/0269215514534277

Kawashima, S., Ueki, Y., Kato, T., Ito, K., and Matsukawa, N. (2018). Reduced striatal dopamine release during motor skill acquisition in Parkinson's disease. *PLoS One* 13:e0196661. doi: 10.1371/journal.pone.0196661

Kojima, S., Onishi, H., Sugawara, K., Kirimoto, H., Suzuki, M., and Tamaki, H. (2013). Modulation of the cortical silent period elicited by single- and paired-pulse transcranial magnetic stimulation. *BMC Neurosci.* 14:43. doi: 10.1186/1471-2202-14-43

Lewis, S. J., Foltynie, T., Blackwell, A. D., Robbins, T. W., Owen, A. M., and Barker, R. A. (2005). Heterogeniety of Parkinson's disease in the early clinical stages using a data driven approach. *J. Neurol. Neurosurg. Psychiatry* 76, 343–348. doi: 10.1136/jnnp.2003.033530

Molina-Luna, K., Pekanovic, A., Rohrich, S., Hertler, B., Schubring-Giese, M., Rioult-Pedotti, M. S., et al. (2009). Dopamine in motor cortex is necessary for skill learning and synaptic plasticity. *PLoS One* 4:e7082. doi: 10.1371/journal.pone.0007082

Muir, R. B., and Lemon, R. N. (1983). Corticospinal neurons with a special role in precision grip. *Brain Res.* 261, 312–316. doi: 10.1016/0006-8993(83)90635-2

Muslimovic, D., Post, B., Speelman, J. D., and Schmand, B. (2007). Motor procedural learning in Parkinson's disease. *Brain* 130(Pt 11), 2887–2897. doi: 10.1093/brain/awm211

Nitsche, M. A. (2003). Level of action of cathodal DC polarization induced inhibition of the human motor cortex. *Clin. Neurophysiol.* 114, 600–604. doi: 10.1016/s1388-2457(02)00412-1

Nitsche, M. A. (2011). Beyond the target area: remote effects of non-invasive brain stimulation in humans. *J. Physiol.* 589(Pt 13), 3053–3054. doi: 10.1113/jphysiol.2011.211599

Nitsche, M. A., and Paulus, W. (2000). Excitability changes induced in the human motor cortex by weak transcranial direct current stimulation. *J. Physiol.* 527(Pt 3), 633–639. doi: 10.1111/j.1469-7793.2000.t01-1-00633.x

Nitsche, M. A., and Paulus, W. (2011). Transcranial direct current stimulation–update 2011. *Restor. Neurol. Neurosci.* 29, 463–492. doi: 10.3233/RNN-2011-0618

Nitsche, M. A., Schauenburg, A., Lang, N., Liebetanz, D., Exner, C., Paulus, W., et al. (2003). Facilitation of implicit motor learning by weak transcranial direct current stimulation of the primary motor cortex in the human. *J. Cogn. Neurosci.* 15, 619–626. doi: 10.1162/089892903321662994

Nojima, I., Koganemaru, S., Kawamata, T., Fukuyama, H., and Mima, T. (2015). Action observation with kinesthetic illusion can produce human motor plasticity. *Eur. J. Neurosci.* 41, 1614–1623. doi: 10.1111/ejn.12921

Nojima, I., Mima, T., Koganemaru, S., Thabit, M. N., Fukuyama, H., and Kawamata, T. (2012). Human motor plasticity induced by mirror visual feedback. *J. Neurosci.* 32, 1293–1300. doi: 10.1523/JNEUROSCI.5364-11.2012

Oldfield, R. C. (1971). The assessment and analysis of handedness: the edinburgh inventory. *Neuropsychologia* 9, 97–113. doi: 10.1016/0028-3932(71)90067-4

Pelosin, E., Bove, M., Ruggeri, P., Avanzino, L., and Abbruzzese, G. (2013). Reduction of bradykinesia of finger movements by a single session of action observation in Parkinson disease. *Neurorehabil. Neural Repair.* 27, 552–560. doi: 10.1177/1545968312471905

Pendt, L. K., Reuter, I., and Muller, H. (2011). Motor skill learning, retention, and control deficits in Parkinson's disease. *PLoS One* 6:e21669. doi: 10.1371/journal.pone.0021669

Ramachandran, V. S., Rogers-Ramachandran, D., and Cobb, S. (1995). Touching the phantom limb. *Nature* 377, 489–490. doi: 10.1038/377489a0

Reis, J., Robertson, E. M., Krakauer, J. W., Rothwell, J., Marshall, L., Gerloff, C., et al. (2008). Consensus: can transcranial direct current stimulation and transcranial magnetic stimulation enhance motor learning and memory formation? *Brain Stimul.* 1, 363–369. doi: 10.1016/j.brs.2008.08.001

Reis, J., Schambra, H. M., Cohen, L. G., Buch, E. R., Fritsch, B., Zarahn, E., et al. (2009). Noninvasive cortical stimulation enhances motor skill acquisition over multiple days through an effect on consolidation. *Proc. Natl. Acad. Sci. U.S.A.* 106, 1590–1595. doi: 10.1073/pnas.0805413106

Ridding, M. C., and Rothwell, J. C. (1997). Stimulus/response curves as a method of measureing motor cortical excitability in man. *Elentroencephalogr. Clin. Neurophysiol.* 105, 340–344. doi: 10.1016/s0924-980x(97)00041-6

Rizzolatti, G., Fadiga, L., Gallese, V., and Fogassi, L. (1996a). Premotor cortex and the recognition of motor actions. *Brain Res. Cogn. Brain Res.* 3, 131–141. doi: 10.1016/0926-6410(95)00038-0

Rizzolatti, G., Fadiga, L., Matelli, M., Bettinardi, V., Paulesu, E., Perani, D., et al. (1996b). Localization of grasp representations in humans by PET: 1. Observation versus execution. *Exp. Brain Res.* 111, 246–252.

Rossini, P. M., Barker, A. T., Berardelli, A., Caramia, M. D., Caruso, G., Cracco, R. Q., et al. (1994). Non-invasive electrical and magnetic stimulation of the brain, spinal cord and roots: basic principles and procedures for routine clinical application. Report of an IFCN committee. *Electroencephalogr. Clin. Neurophysiol.* 91, 79–92. doi: 10.1016/0013-4694(94)90029-9

Sasaki, A. T., Kochiyama, T., Sugiura, M., Tanabe, H. C., and Sadato, N. (2012). Neural networks for action representation: a functional magnetic-resonance imaging and dynamic causal modeling study. *Front. Hum. Neurosci.* 6:236. doi: 10.3389/fnhum.2012.00236

Thobois, S., Dominey, P. F., Decety, J., Pollak, P. P., Gregoire, M. C., Le Bars, P. D., et al. (2000). Motor imagery in normal subjects and in asymmetrical Parkinson's disease: a PET study. *Neurology* 55, 996–1002. doi: 10.1212/wnl.55.7.996

Tremblay, F., Leonard, G., and Tremblay, L. (2008). Corticomotor facilitation associated with observation and imagery of hand actions is impaired in Parkinson's disease. *Exp. Brain Res.* 185, 249–257. doi: 10.1007/s00221-007-1150-6

von Rein, E., Hoff, M., Kaminski, E., Sehm, B., Steele, C. J., Villringer, A., et al. (2015). Improving motor performance without training: the effect of combining mirror visual feedback with transcranial direct current stimulation. *J. Neurophysiol.* 113, 2383–2389. doi: 10.1152/jn.00832.2014

Yamaguchi, S., Kitamura, M., Ushikubo, T., Murata, A., Akagi, R., and Sasho, T. (2015). Effect of laterally wedged insoles on the external knee adduction moment a cross different reference frames. *PLoS One* 10:e0138554. doi: 10.1371/journal.pone.0138554

Yavuzer, G., Selles, R., Sezer, N., Sutbeyaz, S., Bussmann, J. B., Koseoglu, F., et al. (2008). Mirror therapy improves hand function in subacute stroke: a randomized controlled trial. *Arch. Phys. Med. Rehabil.* 89, 393–398. doi: 10.1016/j.apmr.2007.08.162

Ziemann, U., Netz, J., Szelenyi, A., and Homberg, V. (1993). Spinal and supraspinal mechanisms contribute to the silent period in the contracting soleus muscle after transcranial magnetic stimulation of human motor cortex. *Neurosci. Lett.* 156, 167–171. doi: 10.1016/0304-3940(93)90464-v

Conflict of Interest Statement: The authors declare that the research was conducted in the absence of any commercial or financial relationships that could be construed as a potential conflict of interest.

Copyright © 2019 Horiba, Ueki, Nojima, Shimizu, Sahashi, Itamoto, Suzuki, Yamada, Matsukawa and Wada. This is an open-access article distributed under the terms of the Creative Commons Attribution License (CC BY). The use, distribution or reproduction in other forums is permitted, provided the original author(s) and the copyright owner(s) are credited and that the original publication in this journal is cited, in accordance with accepted academic practice. No use, distribution or reproduction is permitted which does not comply with these terms.

frontiers in Neuroscience

REVIEW
published: 19 June 2019
doi: 10.3389/fnins.2019.00628

An Integrative Way for Studying Neural Basis of Basic Emotions With fMRI

Simeng Gu[1,2], Fushun Wang[1,3,4], Caiyun Cao[3], Erxi Wu[4,5,6,7], Yi-Yuan Tang[8] and Jason H. Huang[4,5,6,7]*

[1] Institute of Brain and Psychological Science, Sichuan Normal University, Chengdu, China, [2] Department of Psychology, Jiangsu University, Zhenjiang, China, [3] Department of Pharmacology, Nanjing University of Chinese Medicine, Nanjing, China, [4] Department of Neurosurgery, Baylor Scott & White Health, Temple, TX, United States, [5] Department of Surgery, Texas A&M University College of Medicine, Temple, TX, United States, [6] Department of Pharmaceutical Sciences, Texas A&M University College of Pharmacy, College Station, TX, United States, [7] LIVESTRONG Cancer Institutes, Dell Medical School, The University of Texas at Austin, Austin, TX, United States, [8] Department of Psychological Sciences, Texas Tech University, Lubbock, TX, United States

How emotions are represented in the nervous system is a crucial unsolved problem in the affective neuroscience. Many studies are striving to find the localization of basic emotions in the brain but failed. Thus, many psychologists suspect the specific neural loci for basic emotions, but instead, some proposed that there are specific neural structures for the core affects, such as arousal and hedonic value. The reason for this widespread difference might be that basic emotions used previously can be further divided into more "basic" emotions. Here we review brain imaging data and neuropsychological data, and try to address this question with an integrative model. In this model, we argue that basic emotions are not contrary to the dimensional studies of emotions (core affects). We propose that basic emotion should locate on the axis in the dimensions of emotion, and only represent one typical core affect (arousal or valence). Therefore, we propose four basic emotions: joy-on positive axis of hedonic dimension, sadness-on negative axis of hedonic dimension, fear, and anger-on the top of vertical dimensions. This new model about basic emotions and construction model of emotions is promising to improve and reformulate neurobiological models of basic emotions.

Keywords: basic emotions, core affects, monoamine, dimensional studies, fMRI

OPEN ACCESS

Edited by:
Wenbin Guo,
Central South University, China

Reviewed by:
Fu Wenqing,
Soochow University, China
Chaoxiong Ye,
University of Jyväskylä, Finland

***Correspondence:**
Fushun Wang
13814541138@163.com

Specialty section:
This article was submitted to Brain Imaging Methods, a section of the journal Frontiers in Neuroscience

Received: *04 December 2018*
Accepted: *31 May 2019*
Published: *19 June 2019*

Citation:
Gu S, Wang F, Cao C, Wu E, Tang Y-Y and Huang JH (2019) An Integrative Way for Studying Neural Basis of Basic Emotions With fMRI. Front. Neurosci. 13:628. doi: 10.3389/fnins.2019.00628

INTRODUCTION

Emotion is a kind of mental state that occurs at almost all times across life. Despite the critical importance of emotions in our lives, there is currently no scientific consensus on a definition about what emotion is (Gu et al., 2015). Controversy still abounds over the definition of emotions; the number of emotions that exit. Fehr and Russell (1984) wrote that "everyone knows what an emotions is, until asked to give a definition. Then, it seems no one knows" (Fehr and Russell, 1984). Emotions are internal states that are evoked by comparison between the internal bodily needs and the available external materials, and are characterized by induced physiological changes, behavioral

and cognitive changes (Sroufe, 1996; Wang, 2018). The James-Lange Theory of Emotion suggested that the perception of these bodily changes is what is called an emotion. However, emotions themselves are neither physiological changes nor behavioral changes, because emotions can be separated from behavioral changes, for example, you can hold back fighting behaviors even though you are angry (Damasio and Carvalho, 2013; Wang, 2018). Anyway, emotions can only be consciously known by human beings, and only human beings can consciously regulate their emotions (Etkin et al., 2015, 2016; Hay et al., 2015; Milyavsky et al., 2018); animals cannot hold back the emotion related physiological changes or behaviors. Therefore, it is hard to say emotions are only neuromodulators separately or inseparately with behaviors. However, emotions can only be studied with these external expressions, such as physiological or behavioral changes, especially facial expressions, because we still cannot study animal emotions directly as we have no access to an organism's subjective experience (Papini et al., 2018). Darwin was the first to use facial expressions in emotional studies, such as fear, anger, joy, or sadness. Later, behaviorists tried to study behaviors using emotion induced physiological changes, such as saliva in Palov's dog, and other behavior changes by Skinner's pigeon at a reward or punishment. All these studies did not answer one critical question about emotions: How many kinds of emotions humans have. In contrast, the question is getting more emergent.

During the past decades, basic emotion theory has been very influential in the field of affective studies (Saarimaki et al., 2016; Celeghin et al., 2017; Williams, 2017; Hutto et al., 2018; Song and Hakoda, 2018; Vetter et al., 2018; Wang et al., 2018), which proposed that all human emotions are composed of limited number of basic emotions (e.g., fear, anger, joy, sadness), which are considered to be more elementary than others. These emotions are called basic emotions, for they are biologically and psychologically "basic". These basic emotions are related to our basically biological needs (Lindquist and Barrett, 2012; Colombetti, 2014; An et al., 2017), and each emotion has its own dedicated neural circuitry that is architecturally distinct (Ekman, 1992; Russell, 2006; Barrett and Russell, 2015; Scarantino, 2015). For example, Izard argued that the basic emotions are preserved because their biological and social functions are essential in evolution and adaption, and he suggested that basic emotions have innate neural substrates and universal behavioral phenotypes (Damasio and Carvalho, 2013). Even though many psychologists accepted the theory of basic emotion, there is no consensus as to the exact number of basic emotions. For example, Ekman proposed six basic emotions: happiness, anger, sadness, fear, disgust, and surprise, while Izard proposed seven basic emotions: fear, anger, happiness, sadness, disgust, interest, and contempt. In addition, several recent papers, depending on facial expression studies and neural mechanism studies, suggest four basic emotions: fear, anger, joy, and sadness (Jack et al., 2014; Gu et al., 2016, 2018; Zheng et al., 2016). Many other psychologists also proposed many other basic emotions, as reviewed in a paper by Ortony in *Emotion Review* (Clore and Ortony, 2013), shown in the **Table 1**.

The basic emotion theory proposed that each emotion has its own dedicated neural circuitry that is architecturally distinct.

TABLE 1 | Basic emotions.

Theorist	Basic emotions
Arnold	Fear, anger, desire, despair, hope, love, courage, sadness, aversion, hate, dejection
Plutchik	Fear, anger, joy, sadness, anticipation, disgust, surprise, acceptance
Ekman, Friesen, and Ellsworth	**Fear, anger, joy, sadness, disgust, surprise**
Frijda	Joy, surprise, wonder, sorrow, interest, desire
McDougall	Fear, anger, disgust, wonder, elation, subjection, tender-emotion
Izard	Fear, anger, joy, contempt, disgust, distress, shame, guilt, interest, surprise
Tomkins	Fear, anger, joy, interest, contempt, disgust, distress, shame, surprise
Oatley and Johnson-Laird	Anger, happiness, sadness, anxiety, disgust
Gray	Rage and terror, anxiety, joy
Fushun Wang, and Jack RE	Fear, anger, joy, sadness

For example, fear is a kind of emotion that produce subjective feelings through separate neural pathways of the central nervous system, or peripheral nervous systems (Cowen and Keltner, 2018). Therefore, studying the neural basis might be the best way to differentiate the basic emotions and probe into the number of basic emotions. However, many fMRI studies have met some troubles in differentiating the basic emotions (such as fear, anger, joy, sad, and disgust) with distinct universal signals, physiology, especially the localization of the central nervous system (Lindquist and Barrett, 2012; Lindquist et al., 2012), which has led to even more controversies about the basic emotions (Posner et al., 2005; Scarantino and Griffiths, 2011; Scarantino, 2015; Hutto et al., 2018). For example, even though neuroimaging studies found some evidence for basic emotions [such as amygdala for fear (Ohman, 2005), insula for disgust (Wicker et al., 2003), anterior cingulate cortex for sadness, orbitofrontal cortex for anger (Murphy et al., 2003)], these neuroimaging data are not consistent with specific one-to-one correspondence between fMRI localization of anger, sadness, fear, disgust, etc (Lindquist et al., 2012; Clark-Polner et al., 2017). These neuroimaging data have challenged the basic emotion theory (Hamann, 2012; Scarantino, 2012; Barrett and Satpute, 2013; Cowen and Keltner, 2018), leading many psychologists to suspect (if not give up) the basic emotion theory (Scarantino and Griffiths, 2011; Colombetti, 2014; Scarantino, 2015; Cowen and Keltner, 2018; Hutto et al., 2018). Actually, the reason for the complication might be due to the fact that the basic emotions used in these experiments are not "basic" enough, as they can be further divided into even more "basic" emotions; or the "basic emotions" used in previous reports did not in fact represent the most psychologically primitive levels of emotion (Lindquist and Barrett, 2012). Indeed, Colombetti (2014, p. 38) suggested that the six basic emotions in Ekman's study were not chosen "on the basis of a clear rationale" (Colombetti, 2014). Indeed, they chose the six emotions because they could not obtain enough suitable sample photographs (Colmbetti, 2014; Hutto et al., 2018). Here we probe into the question whether humans have four basic emotions, based on fMRI data.

FMRI DATA ON BASIC EMOTIONS

Recent studies with fMRI offer a good opportunity to study the underlying brain mechanisms for basic emotions, and these neuroimaging studies found some specific loci in the brain work for basic emotions, while other regions are generally involved in emotion perception, valuation, or regulation (Phan et al., 2002; Lindquist et al., 2012, 2013b).

Happiness

Happiness is one of the human resources that an individual can pursuit in his life. The psychological study of happiness defined two different conceptions of happiness: hedonic happiness and eudaimonic happiness (Berridge and Kringelbach, 2011). Hedonic happiness is what we feel during the experience of intense physical or psychological pleasure, while eudaimonic happiness is what we feel when we reach our personal goals or when we have expressed our potential, our abilities, or to be who we really are (Berridge and Kringelbach, 2011). Indeed, imagination of happy events from both kinds, compared to the imagination of neutral events, activates the ventral prefrontal cortex (including orbitofrontal cortex) (Kringelbach, 2005). In a functional magnetic resonance imaging (fMRI) experiment, Rolls et al. (2008) found that activations in the ventral prefrontal cortex, the cingulate cortex, and the ventral striatum were associated with the positive hedonic state, depending on the correlations between the ratings of the participants on pleasantness with the blood-oxygen-level dependent (BOLD) signal. Later on, many studies provide evidence for the primordial role played by these areas in hedonic valuation (Rolls et al., 2008; Grabenhorst and Rolls, 2011). There is almost no controversy regarding the involvement of the ventromedial prefrontal cortex in the subjective happiness and hedonic value (Abler et al., 2005). However, it is still uncertain whether these frontal regions can cause pleasure, and data from lobotomised patients do not indicate a total loss of pleasure; on the contrary, some patients showed euphoria, impulsiveness and general disinhibition. Similarly, Beer et al. (2003) demonstrated the performance of good humor and self-satisfaction in patients with orbitofrontal damage. *These data suggest that the OFC could be more important in transforming pleasure stimuli into their cognitive representations* (Burke et al., 2007, 2008, 2009; Takahashi et al., 2009). In addition, there are some reports about the differences between hedonic and eudaimonic happiness; where hedonic pleasure was positively correlated with functional connectivity of bilateral ventral medial prefrontal cortex, while eudaimonic pleasure was shown to be related to bilateral precuneus (Luo et al., 2017). In addition, it is found that ventral striatum activation during eudaimonic decisions predicted longitudinal declines in depressive symptoms, whereas, ventral striatum activation to hedonic decisions were related to longitudinal increases in depressive symptoms (Telzer et al., 2014).

The mesolimbic dopaminergic system has been considered to be able to cause pleasure (Yokel and Wise, 1975; Wise and Rompre, 1989; Wise, 2004, 2006, 2008, 2013). Even though it is hard to visualize the ventral tegmental area (VTA) with fMRI, due to its lacking clear anatomical borders (Trutti et al., 2019), there are some fMRI studies that report the activities of VTA in the reward and happiness (Krebs et al., 2011). In addition, some reports suggest that VTA responses correlated with romantic love scores and inclusion of other in the self (Acevedo et al., 2012; Xu et al., 2012). VTA is the origin of the mesolimbic dopaminergic system, which projects and releases dopamine to the locus coeruleus, prefrontal cortex and anterior cingulate cortex, and it is responsible for the cognitive effects of positive emotion.

Sadness

Sadness is an emotion that is indicative of loss and helplessness (Motoki and Sugiura, 2018), or it is related to failure to get wanted thing (reward), or punishment to get harmful things (Gu et al., 2016). Anterior cingulate cortex (ACC) is related to sadness (Godlewska et al., 2018; Ramirez-Mahaluf et al., 2018a,b). The reason for ACC to be responsible for sadness might be due to the fact that it is the brain side to induce the vocalization for crying response, which is supported by neuroimaging studies. In addition, it is also linked to sadness because of its role in suffering; many studies have suggested ACC is also implicated in pain or the suffering feeling and depression (Taylor et al., 2018). Therefore, ACC is supposed to be the location for frustration, punishment, regret or failure to cope with the situation (Abler et al., 2005). Lateral orbitofrontal area is also involved in unpleasant stimuli, and it is reported that activations in the lateral parts of the orbitofrontal cortex were related to the negative hedonic value.

Fear

The amygdala is an important limbic structure that has been associated with fear (Anthony et al., 2014; Isosaka et al., 2015; Reynaud et al., 2015; Han et al., 2017). Many fMRI studies support the hypothesis that amygdala is the most important hub in a fear reaction (LeDoux, 1998). Several aspects of fear processing have been attributed to the amygdala, including fear conditioning (Davis, 1992; LeDoux, 2007), initiation of fear-induced behaviors in response to stressors (Weiskrantz, 1956; Blanchard and Blanchard, 1972; Prather et al., 2001; Izquierdo et al., 2005; Machado et al., 2009), and memory creation of fear-related stimuli (Cahill et al., 1995; Hamann, 2001). The importance of the amygdala in initiating the fear emotion and fear-related behaviors has been well described by studying amygdala damage in non-human animals, in which decreased fear-related behaviors have been observed with poor amygdala function (Weiskrantz, 1956; Blanchard and Blanchard, 1972; Prather et al., 2001; Izquierdo et al., 2005; Machado et al., 2009). In addition, clinical observations of a well-characterized human case of bilateral amygdala damage confirmed that amygdala is the location of fear (Feinstein et al., 2011). However, many studies have found that amygdala is involved with many other negative emotions too, such as stress or anger (Siep et al., 2018), which might be due to the emotion flow: fear emotion is transient and can induce several other emotions, such as anger (Zheng et al., 2016). Animals under the influence of fear try to flight away from the threat, however, they will defend themselves, usually aggressively, when flight is impossible or difficult (Papini et al., 2018). This kind of "fight or flight" behavior or "fear and anger" emotion usually happens interchangeably (Zheng et al., 2016).

Anger

Orbitofrontal cortex is the location for anger, because of its relation to prey. Many fMRI studies suggest that the interaction between orbitofrontal cortex and amygdala is involved in the regulation of anger (Coccaro et al., 2007; Fulwiler et al., 2012). It is reported that hyperactivity of the interaction between amygdala and orbitofrontal cortex is involved in the altered fear/anger processing at stressful situations (Reynaud et al., 2015). However, some findings also show a hypoactivation in the orbitofrontal cortex (OFC) and the anterior cingulate cortex (ACC), but strong activity in amygdala (Fulwiler et al., 2012; Siep et al., 2018). A meta-analysis study confirmed enhanced activation in the left amygdala to angry stimuli (Bertsch et al., 2018; Krauch et al., 2018). These controversies might be due to the fact that amygdala activity is related to initiation of fear, while activation of the orbitofrontal cortex is involved in the fear extinction (Milad and Rauch, 2007; Siep et al., 2018). Fear extinction is sure to induce anger, which confirmed a previous report that "fight or flight" behavior or "fear and anger" emotion usually happens interchangeably, or that anger is the vent for fear and fear leads to anger (Gu et al., 2016).

Disgust

The emotion of disgust is typically experienced as a feeling of revulsion elicited by offensive stimulations – e.g., bodily fluids and waste, animal products, rotten food, and certain classes of sexual behavior (such as incest), and is accompanied by a strong desire to throw the eliciting stimulus away (Oaten et al., 2018a,b). Although the **insula** has been proposed as the seat of disgust processing, which is considered to be distinguishable from other emotive responses – e.g., fear (Wicker et al., 2003), and anger (Wicker et al., 2003; Felmingham et al., 2008; Williams and Bargh, 2008; Koritnik et al., 2009), meta-analysis of imaging data found that the anterior insula is not more active during disgust than other emotions, such as anger (Wager et al., 2007; Oaten et al., 2018a,b). Indeed, disgust in moral situations often induces anger, which suggests that any investigation of the neural correlates of disgust also include the anger related neural network. This is also supported by past studies that report the words "disgust" and "disgusted" evoke feelings associated with anger-related concepts (Oaten et al., 2018a,b), and this is consistent with the report that disgust and anger might be the same kind of basic emotion (Jack et al., 2014).

Surprise

The surprise emotion alerts the individual of any deviations from expectations, regardless of the outcome value (Litt et al., 2011; Fouragnan et al., 2018). The surprise system works as an attentional mechanism that enables an organism to focus its limited energy on the most salient stimuli (Matsumoto and Hikosaka, 2009; Kahnt et al., 2010; Park et al., 2010). In addition, surprise system can also monitor unexpected information and help plan appropriate behavioral adjustments (Fouragnan et al., 2018). According to meta-analyses of fMRI studies, surprise induced brain regions are predominantly subcortical, including the amygdala and striatum, as well as some cortical regions, such as the ventromedial prefrontal cortex and the cingulate cortex (Behrens et al., 2009; Bartra et al., 2013). This is consistent with the accumulated imaging evidence, which suggest that the amygdala plays a key role in the processing of novel stimuli (Blackford et al., 2010), and also that surprise and fear might be the same basic emotions (Jack et al., 2014).

In all, many imaging data have reported specific loci for specific emotions, such as amygdala for fear (Ohman, 2005), ventromedial frontal cortex for happiness, anterior cingulate cortex for sadness, orbitofrontal cortex for anger (Murphy et al., 2003), insula for disgust (Wicker et al., 2003). Similarly, to previous reports that anger and disgust induce similar facial expressions, "disgust" and "disgusted" evoke feelings associated with anger-related concepts, and both disgust and anger can activate insula. Similarly, fear and surprise also activate similar brain loci, such as amygdala, and surprise can induce ventromedial prefrontal cortex and the cingulate cortex, because happiness can also be involved with surprise.

TWO DIMENSIONS OF BASIC EMOTIONS

Even though imaging data support the four basic emotions, *basic emotions are transient and usually interchangeable, and it might be easy to get confusing data from fMRI studies* (Lindquist et al., 2013a), for example, fear and anger emotion usually activate amygdala. Therefore, many people suspected distinct brain regions for the perception of different emotion categories, and hypothesized that it might be easier to find unique neural signatures for the core affects, such as valence and arousal (Wilson-Mendenhall et al., 2013; Bestelmeyer et al., 2017). All emotions are constructed by core affects, including hedonic (pleasure–displeasure) and arousal (rest-activated) (Russell, 2003; Gu et al., 2016), which constitute two independent dimensions of a quadrant, where all emotions can find their locations. Different location of each emotion on the quadrant reflects varying amounts of hedonic and arousal properties (Posner et al., 2005; Colibazzi et al., 2010). The horizontal dimension means valence (Watson and Clark, 1988), hedonic dimension (Lang et al., 1993), hedonic tone, liking and other identical items (Gu et al., 2015). The vertical dimension addresses tension and energy (Thayer, 1989), which is due to the unexpected way something happened, and is related to the arousal state of the body, so it is called arousal dimension (Zheng et al., 2016). These two dimensions are typical features of emotions, therefore they can be named as core affects (Sieger et al., 2015). Core affect is a term used to describe the feelings of hedonic pleasure and displeasure with some degree of arousal (Kuppens et al., 2013; Barrett and Russell, 2015); or core affect is the neurophysiological state consciously accessible as the simplest raw feelings, which cannot be reduced to anything simpler (Yik et al., 2011). Izard suggested that "core affect" itself is not a mental state of emotion, merely a feature of emotion (Izard, 2009).

At the dawn of emotional studies, Wilhelm Wundt proposed the three-dimensional theory of emotions from the perspective

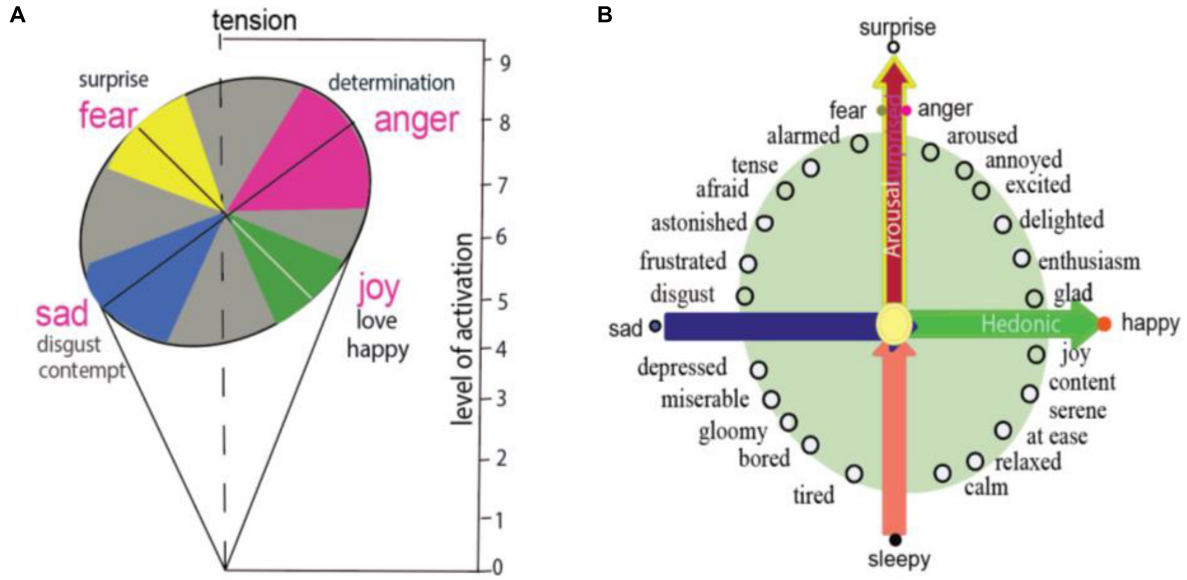

FIGURE 1 | Basic emotion and circumplex. **(A)** Schlosberg proposed two-dimension of facial expression in a roughly circular surface, whose axes are pleasantness–unpleasantness and attention–rejection. The four basic emotions have different levels of activation, for example, fear and anger can reach higher levels of activation. **(B)** Circumplex model of emotion proposed that all emotions locate specially on a circle of the circumplex, means that different emotions have different *arousal or hedonic parameters*. Two core affects of emotions, which are represented on the horizontal dimension and vertical dimension, are induced by two features of a stimulus: the *safety value of the stimulus and the hedonic value of the stimulus.*

of the construction approach, and suggested that emotions are caused by a set of basic common elements (Lindquist and Barrett, 2012). The three-dimensional theory postulated that human emotions result from fusion of a mixture of six basic forms of feelings: pleasure-displeasure, excitement-inhibition, tension-relaxation. Later, Schlosberg (1952) used nine-point rating scales for the tense dimension, trying to obtain independent ratings on a large number of posed facial expressions, and found that it might be better to stabilize the ratings and locate each emotion on a roughly circular surface defined by two dimensions (Schlosberg, 1954). He proposed that the whole range of facial expressions may be described in two-dimension of a roughly circular surface, whose axes are *pleasantness-unpleasantness* and *attention-rejection*. He proposed that the four emotions representing the polar of the four axes are related to activation, for example: fear and anger can reach higher levels of activation (**Figure 1A**), which can be compared to the primary colors as "blue-yellow and red-green axes".

Later on, many names have been given to the two dimensions, for example, the circumplex (**Figure 1B**). The circumplex proposed that every emotion can be spatially represented in a circular arrangement (Posner et al., 2005; Yik et al., 2011), which is anchored on a quadrant with hedonic dimension and arousal dimensions (Kuppens et al., 2013). Barrett proposed that arousal is related to surprise or uncertainty about whether a stimulus will induce threat or reward (Gu et al., 2018). The function of arousal is the rapid detection of potential threats and can initiate appropriate approach/avoidance behaviors (fight or flight), as well as sympathetic nervous induced somatic reactions (Colibazzi et al., 2010; Lindquist et al., 2012).

Arousal

Many psychological constructionists hypothesized that the amygdala is the location for arousal. The amygdala is most likely to be active at surprising situations, which can induce the activity of sympathetic nervous system. In addition, the amygdala has also been found to be activated at many kinds of stimulations, such as novel stimuli (Blackford et al., 2010, 2011; Weierich et al., 2010; Moriguchi et al., 2011), unusual stimuli (Blackford et al., 2011), uncertain stimuli (Herry et al., 2007), or surprise (Holland and Gallagher, 2006; Lee et al., 2006, 2008; Iordanova, 2010; Boll et al., 2013; Vrticka et al., 2014; Kim et al., 2017). Therefore, amygdala activation is not only related to fear, it is related to many highly arousing emotions, such as fear, anger, disgust (Lindquist et al., 2012). Thus, *amygdala might be the location for core affect arousal, which is related to uncertain or surprising stimuli.*

Valence

Neuroimaging data support the idea that arousal and valence are encoded separately in the brain (Morrens, 2014). This proposition was developed on the basis of neurophysiological evidence showing that different types of neurons exhibit differential activity in response to reward or surprise (Schultz et al., 1997; Fiorillo, 2013; Fiorillo et al., 2013a,b). A stimulus that evokes emotions has two qualities: its valence (liked or disliked) and its surprise (unexpected or expected). The valence promotes an individual to reinforce an approach/avoidance behavior, while the arousal component determines the strength of the approach/avoidance behavior (Bartra et al., 2013; Lohani et al., 2017).

INTEGRATIVE MODEL FOR BASIC EMOTIONS APPROACH AND CONSTRUCTION APPROACH

Even though basic emotion theory and dimensional theory have been highly influential in the field of affective studies (Hutto et al., 2018), basic emotion and dimensional theory (or called construction approach) has recently been debated (Lindquist et al., 2013b). The construction approach proposes that all the emotions are constructed from more basic "ingredients" – core affects, characterized as valence and arousal (Wilson-Mendenhall et al., 2013), and emotions are grounded in continuous and fluctuating affective states described as pleasant or unpleasant, with some level of arousal. Actually, basic emotions and dimensional studies are not contrary to each other, instead they can help make each other even clearer. Here we propose that the locations of the basic emotions are also constructed by these basic "ingredients," and can also find their locations on the circumplex. The reason for them to be basic is because they locate specially on the circumplex, which indicates the special relationship between the basic emotions and core affects. *Fear and anger are on the vertical axis, reflecting the surprising way the stimulus happens* (**Figure 2**; Zheng et al., 2016); *while joy and sadness are on the horizontal dimension, depending on the hedonic value of a stimulus*. The special locations of these four basic emotions on the dimensions are the reasons why these basic emotions are "basic" (Gu et al., 2016). The specific location on the axis means that they have the highest values of dimension they locate, and it also means that they are not related to the other axis. In addition, *fear and anger have no hedonic value and happiness and sadness have no safety value* (Gu et al., 2016; Zheng et al., 2016). Of note, the basic emotions can easily interact with each other to make other emotions; for example, surprise and happiness can induce enthusiasm (Hu, 2016); or surprise and sadness might induce frustration (**Figure 2**; Arnott and Elwood, 2009). This is why Hu Hailan gives the equation: Happiness = reward happened – expectation (Hu, 2016). This means the basic emotions used in the experiments might not be so "basic." Thus, we introduce a prerequisite for basic emotions: *Basic emotions should locate on the axis of the two emotional dimensions.*

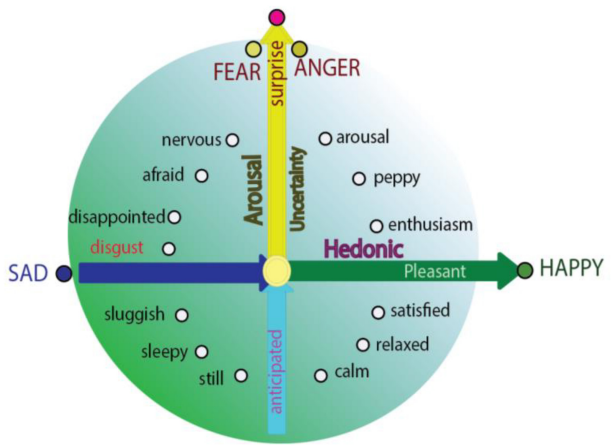

FIGURE 2 | Integrative model for basic emotions and construction approach (dimension theory). Integrative model of emotion proposed that the basic emotions are on the specific locations in the circle of the circumplex; and they are typical emotions which have only one features of core affects: Fear and anger are only related to *the safety value of the stimulus*, while sadness and joy are only related to *the hedonic value of a stimulus; or* the "basic emotion" fear and anger have no hedonic value and happiness and sadness have no safety value (Zheng et al., 2016).

Horizontal Dimension-Direction of Behaviors

Emotion is an innate state, it is a tendency of behavior. Emotions carry behavioral intentions, and the readiness to act in certain ways (Roseman, 1984). The two independent dimensions not only decide two important features of emotions (hedonic value and arousal value), they can also decide the directions of behaviors that they will induce: approach and avoidance direction, and the strength of behavior (LeDoux, 1998; Ledoux and Brown, 2017) (**Figure 3**). Here, basic emotion induced behaviors can also be arranged in a two-dimension coordinate plane (**Figure 3**), with the horizontal dimension representing the direction of the behavior, including the approach/avoidance of the behavior, and the vertical dimension shows the agitation of the behavior. Thus, *the locations of the emotions on the dimensions can also be decided by the behaviors that they will induce.*

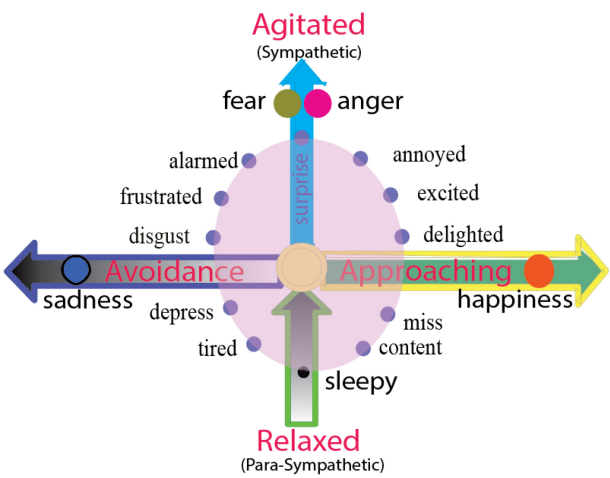

FIGURE 3 | Two dimensions of emotion reflect the directions of behaviors or agitation of autonomous nervous system. The horizontal dimension represents the direction of the behavior, including the approaching/avoidance of the behavior. The emotion happiness and sadness and their behaviors prey or fleeing are on the opposite directions, happiness or joy induce approaching behavior, and sadness and disgust induce avoidance behavior. The vertical dimension represents the energy of the action (agitated or rest). Fear and anger or fight or flight might have same level of agitation, but they are twin emotions, standing back-to-back on the top of vertical axis, facing opposite direction (approaching or avoidance). The zero point of the vertical dimension means normal waking state, and negative axis means sleepy or tired, or the vertical dimensions above zero means sympathetic nervous system, and the dimensions below zero means para-sympathetic nervous system.

"Fear and anger" induced "fight or flight" but these are different in the direction of the actions: Fear is in the negative direction (Certel et al., 2010), while fight is in the positive direction. Therefore, with happiness and sadness induced behaviors that are characteristic of prey or fleeing: Prey is in the positive direction while fleeing in the negative direction.

Vertical Dimension-Agitation of Behaviors

While the horizontal dimension shows the direction of the behavior, the vertical dimension shows the agitation of the behavior, or the activities of autonomous nervous systems. The location above zero point means the activity of sympathetic nervous system, while the location below zero means the activity of the parasympathetic nervous system. "Fear and anger" induced "fight or flight" reflects the highest agitation of the sympathetic nervous system. The zero point means the normal waking state, and the negative axis means lethargy or sleepy. Freezing is in the special location "0" on the two-dimension coordinate plane (**Figure 3**). The fear and anger might have similar agitation, but they are different in the direction of the actions, fear is in the negative valence (Certel et al., 2010), while fight is in the positive direction. The vertical dimension represents the energy of the action (agitated or rest), so the fear and anger have the same volume of arousal.

Fear and Anger Are Twin Emotions

Appraisal theory proposed that emotions are induced by the appraisal of a stimulus. Lazarus suggested that after meeting with a stimulus, the individual would first have an automatic, unconscious, and fast activating evaluation of the stimulus (**Figure 4**). Lazarus proposed that the primary appraisal is an unconscious judgment about the potential threat to an individual from a stressor (Lazarus, 1999). If the stimulus induces a threat, then the secondary appraisal will be induced. The secondary appraisal is conscious and concerned with coping (Lazarus, 1999; Zheng et al., 2016). Ledox also propose that the threat usually first induces fast unconscious fearful emotions, then induces angry emotions through cognitive comparisons (LeDoux, 1996). Thus, fear is related with uncertainty about the situation; and anger is related with trying to control the situation (Moons et al., 2010; Wang et al., 2017, 2018). The coping methods can be angry fight (having sufficient resources) or fearful flight (having insufficient resources). Therefore, we propose that fear can induce anger, while anger is the vent of fear (Gu et al., 2016; Zheng et al., 2016). Both fear and anger can aid survival by influencing an organism to either flight or fight for survival (LeDoux, 1998; Ledoux and Brown, 2017). Fear and anger are activated by norepinephrine systems, and they expressed similar sympathetic nervous activation (LeDoux, 1998; Zheng et al., 2016; Ledoux and Brown, 2017).

After coping with the stressful situation with direct actions, Lazarus suggested a kind of cognitive reappraisal processes: positive emotions will be induced after successfully coping with the situation, which can be named eudaimonic happiness (Berridge and Kringelbach, 2011); or negative emotions will be induced at failure to cope with the situation, which can be named sadness (Aldwin, 1994; Lazarus, 1999). The reappraisal can also be affected by cognition, therefore, positive reappraisal can induce better moods after stressful situations (Gross, 2002; Ochsner et al., 2002; Troy et al., 2010; Wang et al., 2017). The term "eudaimonia" is related to subjective feelings that an individual can feel when he is engaged in activities that are related to his skills or abilities contributing to his personal ambitions and life goals (Ryff, 2014, 2018). So when something unexpected occurs, the individual will first evaluate its threat (fear/anger) and next evaluate its hedonic value (happy/sad) (Gu et al., 2015, 2018). Indeed, basic emotions are transient and interchangeable, which makes it difficult to be differentiated with fMRI studies, which has temporal limitations (Kringelbach, 2005).

FIGURE 4 | Fear and anger are twin emotions. At a surprise or uncertain situation, we humans usually have a safety check with the situation, which is unconscious, similar to Lazarus's primary appraisal. Then the individual will consciously compare the situation with his own ability to see if he can cope with the situation. If the individual feels he has insufficient resources, he would flight away; or he will be angry and fight. Fear and anger occur in a tandem, with fear occurring first, then anger coming immediately afterward. Afterward, the individual will reflect upon the situation, which might be called reappraisal. If he coped successfully with the situation, he will be happy; or he will be sad. Therefore, we humans have four basic emotions. Just like Izard proposed: people need the emotion fear to explain flight for safety; anger to explain tendency to cope with the unexpected situation; joy or happiness to express the pride of achievement, and sadness to express the acceptance of failure (Izard, 2007).

Four Basic Emotions on Two Dimensions

Many psychologists have proposed that disgust and surprise are basic emotions, such as Ekman, Plutchik. However, disgust is kind of strong dislike, or disgust has something to do with the arousal. This means disgust does not locate on the hedonic axis, instead it is biased toward the arousal dimension. Surprise was named as one basic emotion by many psychologists, it actually might be a core affect instead of an emotion. Surprise seems like a

property of a stimulus, instead of an emotion. Therefore, surprise might be a better name for the vertical dimension, or surprise should be a core affect instead of a basic emotion.

All in all, we humans have four basic emotions: Happiness and sadness represent the horizontal dimension, reflecting the hedonic value of the stimulus (**Figure 2**); while fear and anger are on the vertical axis, depending on the surprising way the stimulus happens. Just like what Izard proposed: People need the emotion fear to explain flight for safety; anger to explain tendency to cope with the unexpected situation; joy or happiness to express the pride of achievement, and sadness to express the acceptance of failure (Izard, 2007). With this in mind, it might be easier to understand the fMRI results, which found that some basic emotions induced similar brain activities, for fear, anger and surprise located on the same location of the vertical dimension. This might be the reason that fMRI studies found that activation of limbic and paralimbic brain regions are not specific to special basic emotions (for example, amygdala is not for fear, anger, or surprise), instead they are related to the core affects (Kragel and LaBar, 2016); or the orbitofrontal cortex responds not only to specific instances of positive emotions, instead they respond to hedonic value, and can be named as "salience network". In addition, the analyses found that subjective rating of valence predicted the similar responses in mesolimbic dopaminergic systems (Kamitani and Tong, 2005; Lindquist et al., 2012).

CONCLUSION

The basic emotion theory hypothesizes that basic emotion (and the emotions that are derived from this basic emotion) is produced by the activity of a defined brain locus or an anatomically defined network (Farinelli et al., 2015). Recently, this approach has incorporated efforts to map basic emotions to brain networks that comprise basic emotions (fear, anger, happiness and sadness) (Cowen and Keltner, 2018; Selvaraj et al., 2018). However, fMRI studies cannot achieve consistent imaging data for specific brain areas for a specific emotion. Thus, many researchers suggested an alternative way to explain it: the psychological constructionist model of emotion, hoping that we can get consistent brain activities for core affects in fMRI experiments, or there are specific neural structures that are involved in arousal and hedonic value. Even though hedonic value can achieve consistent activities in the anterior insular, OFC, caudate, thalamus and anterior cingulate, arousal values still demonstrate some trouble in the fMRI studies (Lewis et al., 2007; Kuppens et al., 2013; Lindquist et al., 2013a).

Here we have reviewed brain imaging and neuropsychological data, and addressed this question with an integrative model. In this model, we proposed that basic emotions are not contrary to the dimensional studies of emotions (core affect). Instead, basic emotions can be explained more clearly with the dimensional studies. We also give a criteria for basic emotions: Basic emotion should locate on the axis in the dimensions of emotion, and only represent one typical core affect (arousal or valence). Therefore, we proposed four basic emotions: joy-on positive axis of hedonic dimension, sadness-on negative axis of hedonic dimension, fear and anger which are twin emotions and locate on the top of vertical dimensions. This new model for basic emotions and the construction model of emotions is promised to improve and reformulate neurobiological models of basic emotions.

AUTHOR CONTRIBUTIONS

SG and FW designed the manuscript. SG, FW, EW, YT, and JH wrote the manuscript. CC revised the manuscript.

FUNDING

This work was supported by a grant from Foundation of Humanities and Social Science in Ministry of Education in China (FW, 19YJAZH083). FW is also a member of Jiangsu Six Talent Peak (2015YY006).

REFERENCES

Abler, B., Walter, H., and Erk, S. (2005). Neural correlates of frustration. *Neuroreport* 16, 669–672. doi: 10.1097/00001756-200505120-00003

Acevedo, B. P., Aron, A., Fisher, H. E., and Brown, L. L. (2012). Neural correlates of long-term intense romantic love. *Soc. Cogn. Affect. Neurosci.* 7, 145–159. doi: 10.1093/scan/nsq092

Aldwin, C. M. (1994). *Stress, Coping, and Development*. New York, NY: The Guildford Press.

An, S., Ji, L., Marks, M., and Zhang, Z. (2017). Two sides of emotion: exploring positivity and negativity in six basic emotions across cultures. *Front. Psychol.* 8:610. doi: 10.3389/fpsyg.2017.00610

Anthony, T., Dee, N., Bernard, A., Lerchner, W., Heintz, N., Anderson, D. J., et al. (2014). Control of stress-induced persistent anxiety by an extra-amygdala septohypothalamic circuit. *Cell* 156, 522–536. doi: 10.1016/j.cell.2013.12.040

Arnott, G., and Elwood, R. (2009). Probing aggressive motivation in a cichilid fish. *Biol. Lett.* 5, 762–764. doi: 10.1098/rsbl.2009.0526

Barrett, L., and Russell, J. (2015). *They Psychological Construction of Emotion*. New York, NY: Guildofrd press.

Barrett, L., and Satpute, A. (2013). Large-scale brain networks in affective and social neuroscience: towards an integrative functional architecture of the brain. *Curr. Opin. Neurobiol.* 23, 361–372. doi: 10.1016/j.conb.2012.12.012

Bartra, O., McGuire, J. T., and Kable, J. W. (2013). The valuation system: a coordinate-based meta-analysis of BOLD fMRI experiments examining neural correlates of subjective value. *Neuroimage* 76, 412–427. doi: 10.1016/j.neuroimage.2013.02.063

Beer, J. S., Heerey, E. A., Keltner, D., Scabini, D., and Knight, R. T. (2003). The regulatory function of self-conscious emotion: insights from patients with orbitofrontal damage. *J. Pers. Soc. Psychol.* 85, 594–604. doi: 10.1037/0022-3514.85.4.594

Behrens, T. E., Woolrich, M. W., Walton, M. E., and Rushworth, M. F. (2009). Learning the value of information in an uncertain world. *Nat. Neurosci.* 10, 1214–1221. doi: 10.1038/nn1954

Berridge, K. C., and Kringelbach, M. L. (2011). Building a neuroscience of pleasure and well-being. *Psychol. Well Being* 1, 1–3.

Bertsch, K., Krauch, M., Roelofs, K., Cackowski, S., Herpertz, S. C., Volman, I., et al. (2018). Out of control? Acting out anger is associated with deficient prefrontal emotional action control in male patients with borderline personality disorder. *Neuropharmacology* .

Bestelmeyer, P. E. G., Kotz, S. A., and Belin, P. (2017). Effects of emotional valence and arousal on the voice perception network. *Soc. Cogn. Affect. Neurosci.* 12, 1351–1358. doi: 10.1093/scan/nsx059

Blackford, J. U., Avery, S. N., Cowan, R. L., Shelton, R. C., and Zald, D. H. (2011). Sustained amygdala response to both novel and newly familiar faces characterizes inhibited temperament. *Soc. Cogn. Affect. Neurosci.* 6, 621–629. doi: 10.1093/scan/nsq073

Blackford, J. U., Buckholtz, J. W., Avery, S. N., and Zald, D. H. (2010). A unique role for the human amygdala in novelty detection. *Neuroimage* 50, 1188–1193. doi: 10.1016/j.neuroimage.2009.12.083

Blanchard, D. C., and Blanchard, R. J. (1972). Innate and conditioned reactions to threat in rats with amygdaloid lesions. *J. Comp. Physiol. Psychol.* 81, 281–290. doi: 10.1037/h0033521

Boll, S., Gamer, M., Gluth, S., Finsterbusch, J., and Buchel, C. (2013). Separate amygdala subregions signal surprise and predictiveness during associative fear learning in humans. *Eur. J. Neurosci.* 37, 758–767. doi: 10.1111/ejn.12094

Burke, K. A., Franz, T. M., Miller, D. N., and Schoenbaum, G. (2007). Conditioned reinforcement can be mediated by either outcome-specific or general affective representations. *Front. Integr. Neurosci.* 1:2. doi: 10.3389/neuro.07.002.2007

Burke, K. A., Franz, T. M., Miller, D. N., and Schoenbaum, G. (2008). The role of the orbitofrontal cortex in the pursuit of happiness and more specific rewards. *Nature* 454, 340–344. doi: 10.1038/nature06993

Burke, K. A., Takahashi, Y. K., Correll, J., Brown, P. L., and Schoenbaum, G. (2009). Orbitofrontal inactivation impairs reversal of Pavlovian learning by interfering with 'disinhibition' of responding for previously unrewarded cues. *Eur. J. Neurosci.* 30, 1941–1946. doi: 10.1111/j.1460-9568.2009.06992.x

Cahill, L., Babinsky, R., Markowitsch, H. J., and McGaugh, J. L. (1995). The amygdala and emotional memory. *Nature* 377, 295–296.

Celeghin, A., Diano, M., Bagnis, A., Viola, M., and Tamietto, M. (2017). Basic emotions in human neuroscience: neuroimaging and beyond. *Front. Psychol.* 8:1432. doi: 10.3389/fpsyg.2017.01432

Certel, S. J., Leung, A., Lin, C. Y., Perez, P., Chiang, A. S., Kravitz, E. A., et al. (2010). Octopamine neuromodulatory effects on a social behavior decision-making network in Drosophila males. *PLoS One* 5:e13248. doi: 10.1371/journal.pone.0013248

Clark-Polner, E., Johnson, T. D., and Barrett, L. F. (2017). Multivoxel pattern analysis does not provide evidence to support the existence of basic emotions. *Cereb. Cortex* 27, 1944–1948.

Clore, G. L., and Ortony, A. (2013). Psychological construction in the OCC model of emotion. *Emot. Rev.* 5, 335–343. doi: 10.1177/1754073913489751

Coccaro, E. F., McCloskey, M. S., Fitzgerald, D. A., and Phan, K. L. (2007). Amygdala and orbitofrontal reactivity to social threat in individuals with impulsive aggression. *Biol. Psychiatry* 62, 168–178. doi: 10.1016/j.biopsych.2006.08.024

Colibazzi, T., Posner, J., Wang, Z., Gorman, D., Gerber, A., Yu, S., et al. (2010). Neural systems subserving valence and arousal during the experience of induced emotions. *Emotion* 10, 377–389. doi: 10.1037/a0018484

Colmbetti, G. (2014). *The Feeling Body: Affective Science Meets the Enactive Mind*. Cambridge, MA: MIT press.

Colombetti, G. (2014). *The Feeding Body: Affective Science Meet the Enactive Mind*. Cambfidge, MA: MIT press.

Cowen, A. S., and Keltner, D. (2018). Clarifying the conceptualization, dimensionality, and structure of emotion: response to barrett and colleagues. *Trends Cogn. Sci.* 22, 274–276. doi: 10.1016/j.tics.2018.02.003

Damasio, A., and Carvalho, G. B. (2013). The nature of feelings: evolutionary and neurobiological origins. *Nat. Rev. Neurosci.* 14, 143–152. doi: 10.1038/nrn3403

Davis, M. (1992). The role of the amygdala in fear and anxiety. *Annu. Rev. Neurosci.* 15, 353–375. doi: 10.1146/annurev.neuro.15.1.353

Ekman, P. (1992). An arugment for basic emotions. *Cognit. Emot.* 6, 169–200.

Etkin, A., Buchel, C., and Gross, J. J. (2015). The neural bases of emotion regulation. *Nat. Rev. Neurosci.* 16, 693–700. doi: 10.1038/nrn4044

Etkin, A., Buchel, C., and Gross, J. J. (2016). Emotion regulation involves both model-based and model-free processes. *Nat. Rev. Neurosci.* 17:532. doi: 10.1038/nrn.2016.79

Farinelli, M., Panksepp, J., Gestieri, L., Maffei, M., Agati, R., Cevolani, D., et al. (2015). Do brain lesions in stroke affect basic emotions and attachment? *J. Clin. Exp. Neuropsychol.* 37, 595–613. doi: 10.1080/13803395.2014.991279

Fehr, B., and Russell, J. A. (1984). Concept of emotion viewed from a prototype perspective. *J. Exp. Psychol. Gen.* 113, 464–486. doi: 10.1037//0096-3445.113.3.464

Feinstein, J. S., Adolphs, R., Damasio, A., and Tranel, D. (2011). The human amygdala and the induction and experience of fear. *Curr. Biol.* 21, 34–38. doi: 10.1016/j.cub.2010.11.042

Felmingham, K., Kemp, A. H., Williams, L., Falconer, E., Olivieri, G., Peduto, A., et al. (2008). Dissociative responses to conscious and non-conscious fear impact underlying brain function in post-traumatic stress disorder. *Psychol. Med.* 38, 1771–1780. doi: 10.1017/s0033291708002742

Fiorillo, C. D. (2013). Two dimensions of value: dopamine neurons represent reward but not aversiveness. *Science* 341, 546–549. doi: 10.1126/science.1238699 doi: 10.1126/science.1238699

Fiorillo, C. D., Song, M. R., and Yun, S. R. (2013a). Multiphasic temporal dynamics in responses of midbrain dopamine neurons to appetitive and aversive stimuli. *J. Neurosci.* 33, 4710–4725. doi: 10.1523/jneurosci.3883-12.2013

Fiorillo, C. D., Yun, S. R., and Song, M. R. (2013b). Diversity and homogeneity in responses of midbrain dopamine neurons. *J. Neurosci.* 33, 4693–4709. doi: 10.1523/jneurosci.3886-12.2013

Fouragnan, E., Retzler, C., and Philiastides, M. G. (2018). Separate neural representations of prediction error valence and surprise: evidence from an fMRI meta-analysis. *Hum. Brain Mapp.* 39, 2887–2906. doi: 10.1002/hbm.24047

Fulwiler, C. E., King, J. A., and Zhang, N. (2012). Amygdala-orbitofrontal resting-state functional connectivity is associated with trait anger. *Neuroreport* 23, 606–610. doi: 10.1097/00001756-201207110-00006

Godlewska, B. R., Browning, M., Norbury, R., Igoumenou, A., Cowen, P. J., Harmer, C. J., et al. (2018). Predicting treatment response in depression: the role of anterior cingulate cortex. *Int. J. Neuropsychopharmacol.* 21, 988–996. doi: 10.1093/ijnp/pyy069

Grabenhorst, F., and Rolls, E. T. (2011). Value, pleasure and choice in the ventral prefrontal cortex. *Trends Cogn. Sci.* 15, 56–67. doi: 10.1016/j.tics.2010.12.004

Gross, J. J. (2002). Emotion regulation: affective, cognitive, and social consequences. *Psychophysiology* 39, 281–291. doi: 10.1017/s0048577201393198

Gu, S., Mengdan, G., Yaoyao, Y., Fushun, W., and Huang, J. H. (2018). The neural mechanism underlying cognitive and emotional processes in creativity. *Front. Psychol.* 9:1924. doi: 10.3389/fpsyg.2018.01924

Gu, S., Wang, F., Yuan, T., Guo, B., and Huang, H. (2015). Differentiation of primary emotions through neuromodulators: review of literature. *Int. J. Neurol. Res.* 1, 43–50. doi: 10.17554/j.issn.2313-5611.2015.01.19

Gu, S., Wang, W., Wang, F., and Huang, J. H. (2016). Neuromodulator and emotion biomarker for stress induced mental disorders. *Neural Plast.* 2016:2609128.

Hamann, S. (2001). Cognitive and neural mechanisms of emotional memory. *Trends Cognit. Sci.* 5, 394–400. doi: 10.1016/s1364-6613(00)01707-1

Hamann, S. (2012). Mapping discrete and dimensional emotions onto the brain: controversies and consensus. *Trends Cogn. Sci.* 16, 458–466. doi: 10.1016/j.tics.2012.07.006

Han, W., Tellez, L. A., Rangel, M. J. Jr., Motta, S. C., Zhang, X., Perez, I. O., et al. (2017). Integrated control of predatory hunting by the central nucleus of the amygdala. *Cell* 168, 311–324.

Hay, A. C., Sheppes, G., Gross, J. J., and Gruber, J. (2015). Choosing how to feel: emotion regulation choice in bipolar disorder. *Emotion* 15, 139–145. doi: 10.1037/emo0000024

Herry, C., Bach, D. R., Esposito, F., Di Salle, F., Perrig, W. J., Scheffler, K., et al. (2007). Processing of temporal unpredictability in human and animal amygdala. *J. Neurosci.* 27, 5958–5966. doi: 10.1523/jneurosci.5218-06.2007

Holland, P. C., and Gallagher, M. (2006). Different roles for amygdala central nucleus and substantia innominata in the surprise-induced enhancement of learning. *J. Neurosci.* 26, 3791–3797. doi: 10.1523/jneurosci.0390-06.2006

Hu, H. (2016). Reward and aversion. *Annu. Rev. Neurosci.* 39, 297–324.

Hutto, D. D., Robertson, I., and Kirchhoff, M. D. (2018). A new, better BET: rescuing and revising basic emotion theory. *Front. Psychol.* 9:1217. doi: 10.3389/fpsyg.2018.01217

Iordanova, M. D. (2010). Dopamine transmission in the amygdala modulates surprise in an aversive blocking paradigm. *Behav. Neurosci.* 124, 780–788. doi: 10.1037/a0021111

Isosaka, T., Matsuo, T., Yamaguchi, T., Funabiki, K., Nakanishi, S., Kobayakawa, R., et al. (2015). Htr2a-expressing cells in the central amygdala control the hierarchy between innate and learned fear. *Cell* 163, 1153–1164. doi: 10.1016/j.cell.2015.10.047

Izard, C. E. (2007). Basic emotions, natural kinds, emotion schemas, and a new paradigm. *Perspect. Psychol. Sci.* 2, 260–280. doi: 10.1111/j.1745-6916.2007.00044.x

Izard, C. E. (2009). Emotion theory and research: highlights, unanswered questions, and emerging issues. *Annu. Rev. Psychol.* 60, 1–25. doi: 10.1146/annurev.psych.60.110707.163539

Izquierdo, A., Suda, R. K., and Murray, E. A. (2005). Comparison of the effects of bilateral orbital prefrontal cortex lesions and amygdala lesions on emotional responses in rhesus monkeys. *J. Neurosci.* 25, 8534–8542. doi: 10.1523/jneurosci.1232-05.2005

Jack, R., Garrod, O., and Schyns, P. (2014). Dynamic facial expressions of emotion transmit an evolving hierarchy of signals over time. *Curr. Biol.* 24, 187–192. doi: 10.1016/j.cub.2013.11.064

Kahnt, T., Heinzle, J., Park, S. Q., and Haynes, J. D. (2010). The neural code of reward anticipation in human orbitofrontal cortex. *Proc. Natl. Acad. Sci. U.S.A.* 107, 6010–6015. doi: 10.1073/pnas.0912838107

Kamitani, Y., and Tong, F. (2005). Decoding the visual and subjective contents of the human brain. *Nat. Neurosci.* 8, 679–685. doi: 10.1038/nn1444

Kim, M. J., Mattek, A. M., Bennett, R. H., Solomon, K. M., Shin, J., Whalen, P. J., et al. (2017). Human amygdala tracks a feature-based valence signal embedded within the facial expression of surprise. *J. Neurosci.* 37, 9510–9518. doi: 10.1523/jneurosci.1375-17.2017

Koritnik, B., Azam, S., Andrew, C. M., Leigh, P. N., and Williams, S. C. (2009). Imaging the brain during sniffing: a pilot fMRI study. *Pulm. Pharmacol. Ther.* 22, 97–101. doi: 10.1016/j.pupt.2008.10.009

Kragel, P. A., and LaBar, K. S. (2016). Decoding the nature of emotion in the brain. *Trends Cogn. Sci.* 20, 444–455. doi: 10.1016/j.tics.2016.03.011

Krauch, M., Ueltzhöffer, K., Brunner, R., Kaess, M., Hensel, S., Herpertz, S. C., et al. (2018). Heightened salience of anger and aggression in female adolescents with borderline personality disorder-a script-based fMRI study. *Front. Behav. Neurosci.* 12:57. doi: 10.3389/fnbeh.2018.00057

Krebs, R. M., Heipertz, D., Schuetze, H., and Duzel, E. (2011). Novelty increases the mesolimbic functional connectivity of the substantia nigra/ventral tegmental area (SN/VTA) during reward anticipation: evidence from high-resolution fMRI. *Neuroimage* 58, 647–655. doi: 10.1016/j.neuroimage.2011.06.038

Kringelbach, M. L. (2005). The human orbitofrontal cortex: linking reward to hedonic experience. *Nat. Rev. Neurosci.* 6, 691–702. doi: 10.1038/nrn1747

Kuppens, P., Tuerlinckx, F., Russell, J. A., and Barrett, L. F. (2013). The relation between valence and arousal in subjective experience. *Psychol. Bull.* 139, 917–940. doi: 10.1037/a0030811

Lang, P. J., Greenwald, M. K., Bradley, M. M., and Hamm, A. O. (1993). Looking at pictures: affective, facial, visceral, and behavioral reactions. *Psychophysiology* 30, 261–273. doi: 10.1111/j.1469-8986.1993.tb03352.x

Lazarus, R. S. (1999). *Stress and Emotion: A New Synthesis*. New York: Springer.

Ledoux, and Brown, R. (2017). A higher-order theory of emotional consciousness. *Proc. Natl. Acad. Sci. U.S.A.* 114, E2016–E2025.

LeDoux, J. (1996). *The Emotional Brain: The Mysterous Underpinnings of Emotional Life*. New York, NY: Simon & Schuster.

LeDoux, J. (1998). Fear and the brain: where have we been, and where are we going? *Biol. Psychiatry* 44, 1229–1238. doi: 10.1016/s0006-3223(98)00282-0

LeDoux, J. (2007). The amygdala. *Curr. Biol.* 17, R868–R874.

Lee, H. J., Youn, J. M., Gallagher, M., and Holland, P. C. (2008). Temporally limited role of substantia nigra-central amygdala connections in surprise-induced enhancement of learning. *Eur. J. Neurosci.* 27, 3043–3049. doi: 10.1111/j.1460-9568.2008.06272.x

Lee, H. J., Youn, J. M., O, M. J., Gallagher, M., and Holland, P. C. (2006). Role of substantia nigra-amygdala connections in surprise-induced enhancement of attention. *J. Neurosci.* 26, 6077–6081. doi: 10.1523/jneurosci.1316-06.2006

Lewis, P. A., Critchley, H. D., Rotshtein, P., and Dolan, R. J. (2007). Neural correlates of processing valence and arousal in affective words. *Cereb. Cortex* 17, 742–748. doi: 10.1093/cercor/bhk024

Lindquist, K., and Barrett, L. (2012). A functional architecture of the human brain: emerging insights from the science of emotion. *Trends Cogn. Sci.* 16, 533–540. doi: 10.1016/j.tics.2012.09.005

Lindquist, K., Wager, T., Kober, H., Bliss-Moreau, E., and Barrett, L. (2012). The brain basis of emotion: a meta-analytic review. *Behav. Brain Sci.* 35, 121–143. doi: 10.1017/s0140525x11000446

Lindquist, K. A., Gendron, M., Oosterwijk, S., and Barrett, L. F. (2013a). Do people essentialize emotions? Individual differences in emotion essentialism and emotional experience. *Emotion* 13, 629–644. doi: 10.1037/a0032283

Lindquist, K. A., Siegel, E. H., Quigley, K. S., and Barrett, L. F. (2013b). The hundred-year emotion war: are emotions natural kinds or psychological constructions? Comment on Lench, Flores, and Bench (2011). *Psychol. Bull.* 139, 255–263. doi: 10.1037/a0029038

Litt, A., Plassmann, H., Shiv, B., and Rangel, A. (2011). Dissociating valuation and saliency signals during decision-making. *Cereb. Cortex* 21, 95–102. doi: 10.1093/cercor/bhq065

Lohani, S., Poplawsky, A. J., Kim, S. G., and Moghaddam, B. (2017). Unexpected global impact of VTA dopamine neuron activation as measured by opto-fMRI. *Mol. Psychiatry* 22, 585–594. doi: 10.1038/mp.2016.102

Luo, Y., Qi, S., Chen, X., You, X., Huang, X., Yang, Z., et al. (2017). Pleasure attainment or self-realization: the balance between two forms of well-beings are encoded in default mode network. *Soc. Cogn. Affect Neurosci.* 12, 1678–1686. doi: 10.1093/scan/nsx078

Machado, C. J., Kazama, A. M., and Bachevalier, J. (2009). Impact of amygdala, orbital frontal, or hippocampal lesions on threat avoidance and emotional reactivity in nonhuman primates. *Emotion (Washington, D.C.)* 9, 147–163. doi: 10.1037/a0014539

Matsumoto, M., and Hikosaka, O. (2009). Two types of dopamine neuron distinctly convey positive and negative motivational signals. *Nature* 459, 837–841. doi: 10.1038/nature08028

Milad, M. R., and Rauch, S. L. (2007). The role of the orbitofrontal cortex in anxiety disorders. *Ann. N. Y. Acad. Sci.* 1121, 546–561. doi: 10.1196/annals.1401.006

Milyavsky, M., Webber, D., Fernandez, J. R., Kruglanski, A. W., Goldenberg, A., Suri, G., et al. (2018). To reappraise or not to reappraise? Emotion regulation choice and cognitive energetics. *Emotion* .

Moons, W. G., Eisenberger, N. I., and Taylor, S. E. (2010). Anger and fear responses to stress have different biological profiles. *Brain Behav. Immun.* 24, 215–219. doi: 10.1016/j.bbi.2009.08.009

Moriguchi, Y., Negreira, A., Weierich, M., Dautoff, R., Dickerson, B. C., Wright, C. I., et al. (2011). Differential hemodynamic response in affective circuitry with aging: an FMRI study of novelty, valence, and arousal. *J. Cogn. Neurosci.* 23, 1027–1041. doi: 10.1162/jocn.2010.21527

Morrens, J. (2014). Dopamine neurons coding prediction errors in reward space, but not in aversive space: a matter of location? *J. Neurophysiol.* 112, 1021–1024. doi: 10.1152/jn.00751.2013

Motoki, K., and Sugiura, M. (2018). Disgust, sadness, and appraisal: disgusted consumers dislike food more than sad ones. *Front. Psychol.* 9:76. doi: 10.3389/fpsyg.2018.00076

Murphy, F. C., Nimmo-Smith, I., and Lawrence, A. D. (2003). Functional neuroanatomy of emotions: a meta-analysis. *Cognit. Affect. Behav. Neurosci.* 3, 207–233. doi: 10.3758/cabn.3.3.207

Oaten, M., Stevenson, R. J., Tapp, C., Case, T. I., and Cousins, A. (2018a). The role of disgust in male sexual decision-making. *Front. Psychol.* 9:2602. doi: 10.3389/fpsyg.2018.02602

Oaten, M., Stevenson, R. J., Williams, M. A., Rich, A. N., Butko, M., Case, T. I., et al. (2018b). Moral violations and the experience of disgust and anger. *Front. Behav. Neurosci.* 12:179. doi: 10.3389/fnbeh.2018.00179

Ochsner, K. N., Bunge, S. A., Gross, J. J., and Gabrieli, J. D. E. (2002). Rethinking feelings: an FMRI study of the cognitive regulation of emotion. *J. Cogn. Neurosci.* 14, 1215–1229. doi: 10.1162/089892902760807212

Ohman, A. (2005). The role of the amygdala in human fear: automatic detection of threat. *Psychoneuroendocrinology* 30, 953–958. doi: 10.1016/j.psyneuen.2005.03.019

Papini, M. R., Penagos-Corzo, J. C., and Perez-Acosta, A. M. (2018). Avian emotions: comparative perspectives on fear and frustration. *Front. Psychol.* 9:2707. doi: 10.3389/fpsyg.2018.02707

Park, S. Q., Kahnt, T., Beck, A., Cohen, M. X., Dolan, R. J., Wrase, J., et al. (2010). Prefrontal cortex fails to learn from reward prediction errors in alcohol dependence. *J. Neurosci.* 30, 7749–7753. doi: 10.1523/jneurosci.5587-09.2010

Phan, K. L., Wager, T., Taylor, S. F., and Liberzon, I. (2002). Functional neuroanatomy of emotion: a meta-analysis of emotion activation studies in PET and fMRI. *Neuroimage* 16, 331–348. doi: 10.1006/nimg.2002.1087

Posner, J., Russell, J. A., and Peterson, B. S. (2005). The circumplex model of affect: an integrative approach to affective neuroscience, cognitive development, and psychopathology. *Dev. Psychopathol.* 17, 715–734.

Prather, M. D., Lavenex, P., Mauldin-Jourdain, M. L., Mason, W. A., Capitanio, J. P., Mendoza, S. P., et al. (2001). Increased social fear and decreased fear of objects in monkeys with neonatal amygdala lesions. *Neuroscience* 106, 653–658. doi: 10.1016/s0306-4522(01)00445-6

Ramirez-Mahaluf, J. P., Perramon, J., Otal, B., Villoslada, P., and Compte, A. (2018a). Author correction: subgenual anterior cingulate cortex controls sadness-induced modulations of cognitive and emotional network hubs. *Sci. Rep.* 8:11237.

Ramirez-Mahaluf, J. P., Perramon, J., Otal, B., Villoslada, P., and Compte, A. (2018b). Subgenual anterior cingulate cortex controls sadness-induced modulations of cognitive and emotional network hubs. *Sci. Rep.* 8:8566.

Reynaud, E., Guedj, E., Trousselard, M. E., Khoury-Malhame, M., Zendjidjian, X., Fakra, E., et al. (2015). Acute stress disorder modifies cerebral activity of amygdala and prefrontal cortex. *Cogn. Neurosci.* 6, 39–43. doi: 10.1080/17588928.2014.996212

Rolls, E. T., Grabenhorst, F., and Parris, B. A. (2008). Warm pleasant feelings in the brain. *Neuroimage* 41, 1504–1513. doi: 10.1016/j.neuroimage.2008.03.005

Roseman, I. (1984). *Cognitive Determinants of Emotion: A Structural Theory*. Beverly Hills, CA: Sage.

Russell, J. (2003). Core affect and the psychological construction of emotion. *Psychol. Rev.* 110, 145–172. doi: 10.1037//0033-295x.110.1.145

Russell, J. A. (2006). Emotions are not modules. *Can. J. Philos. Suppl.* 32, 53–71. doi: 10.1353/cjp.2007.0037

Ryff, C. D. (2014). Psychological well-being revisited: advances in the science and practice of eudaimonia. *Psychother. Psychosom.* 83, 10–28. doi: 10.1159/000353263

Ryff, C. D. (2018). Well-being with soul: science in pursuit of human potential. *Perspect. Psychol. Sci.* 13, 242–248. doi: 10.1177/1745691617699836

Saarimaki, H., Gotsopoulos, A., Jääskeläinen, I. P., Lampinen, J., Vuilleumier, P., Hari, R., et al. (2016). Discrete neural signatures of basic emotions. *Cereb. Cortex* 26, 2563–2573. doi: 10.1093/cercor/bhv086

Scarantino, A. (2012). Functional specialization does not require a one-to-one mapping between brain regions and emotions. *Behav. Brain Sci.* 35, 161–162. doi: 10.1017/s0140525x11001749

Scarantino, A. (2015). *Basic Emotions, Psychological Construction and the Problem of Variability*. New York, NY: Guildofrd press.

Scarantino, A., and Griffiths, P. (2011). Dont give up on basic emotions. *Emot. Rev.* 3, 444–454. doi: 10.1177/1754073911410745

Schlosberg, H. (1952). The description of facial expressions in terms of two dimensions. *J. Exp. Psychol.* 44, 229–237. doi: 10.1037/h0055778

Schlosberg, H. (1954). Three dimensions of emotions. *Psychol. Rev.* 61, 81–88.

Schultz, W., Dayan, P., and Montague, P. R. (1997). A neural substrate of prediction and reward. *Science* 275, 1593–1599. doi: 10.1126/science.275.5306.1593

Selvaraj, S., Walker, C., Arnone, D., Cao, B., Faulkner, P., Cowen, P. J., et al. (2018). Effect of citalopram on emotion processing in humans: a combined 5-HT1A [(11)C]CUMI-101 PET and functional MRI study. *Neuropsychopharmacology* 43, 655–664. doi: 10.1038/npp.2017.166

Sieger, T., Serranová, T., Růžièka, F., Vostatek, P., Wild, J., Štastná, D., et al. (2015). Distinct populations of neurons respond to emotional valence and arousal in the human subthalamic nucleus. *Proc. Natl. Acad. Sci. U.S.A.* 112, 3116–3121. doi: 10.1073/pnas.1410709112

Siep, N., Tonnaer, F., van de Ven, V., Arntz, A., Raine, A., Cima, M., et al. (2018). Anger provocation increases limbic and decreases medial prefrontal cortex connectivity with the left amygdala in reactive aggressive violent offenders. *Brain Imaging Behav.* .

Song, Y., and Hakoda, Y. (2018). Selective impairment of basic emotion recognition in people with autism: discrimination thresholds for recognition of facial expressions of varying intensities. *J. Autism Dev. Disord.* 48, 1886–1894. doi: 10.1007/s10803-017-3428-2

Sroufe, L. (1996). *Emotional Development*. New York, NY: Cambridge University Press.

Takahashi, Y. K., Roesch, M. R., Stalnaker, T. A., Haney, R. Z., Calu, D. J., Taylor, A. R., et al. (2009). The orbitofrontal cortex and ventral tegmental area are necessary for learning from unexpected outcomes. *Neuron* 62, 269–280. doi: 10.1016/j.neuron.2009.03.005

Taylor, S. F., Ho, S. S., Abagis, T., Angstadt, M., Maixner, D. F., Welsh, R. C., et al. (2018). Changes in brain connectivity during a sham-controlled, transcranial magnetic stimulation trial for depression. *J. Affect. Disord.* 232, 143–151. doi: 10.1016/j.jad.2018.02.019

Telzer, E. H., Fuligni, A. J., Lieberman, M. D., and Galvan, A. (2014). Neural sensitivity to eudaimonic and hedonic rewards differentially predict adolescent depressive symptoms over time. *Proc. Natl. Acad. Sci. U.S.A.* 111, 6600–6605. doi: 10.1073/pnas.1323014111

Thayer, R. (1989). *The Origion of Everyday Moods: Managing Energy, Tension and Sress*. New York, NY: Oxford University Press.

Troy, A. S., Wilhelm, F. H., Shallcross, A. J., and Mauss, I. B. (2010). Seeing the silver lining: cognitive reappraisal ability moderates the relationship between stress and depressive symptoms. *Emotion* 10, 783–795. doi: 10.1037/a0020262

Trutti, A. C., Mulder, M. J., Hommel, B., and Forstmann, B. U. (2019). Functional neuroanatomical review of the ventral tegmental area. *Neuroimage* 191, 258–268. doi: 10.1016/j.neuroimage.2019.01.062

Vetter, N. C., Drauschke, M., Thieme, J., and Altgassen, M. (2018). Adolescent basic facial emotion recognition is not influenced by puberty or own-age bias. *Front. Psychol.* 9:956. doi: 10.3389/fpsyg.2018.00956

Vrticka, P., Lordier, L., Bediou, B., and Sander, D. (2014). Human amygdala response to dynamic facial expressions of positive and negative surprise. *Emotion* 14, 161–169. doi: 10.1037/a0034619

Wager, T. D., Lindquist, M., and Kaplan, L. (2007). Meta-analysis of functional neuroimaging data: current and future directions. *Soc. Cogn. Affect. Neurosci.* 2, 150–158. doi: 10.1093/scan/nsm015

Wang, F. (2018). *Emotional Psychoogy*. Beijing: Health Press.

Wang, F., Pan, F., Shapiro, L. A., and Huang, J. H. (2017). Stress induced neuroplasticity and mental disorders. *Neural Plast.* 2017:9634501.

Wang, F., Pan, F., Shapiro, L. A., and Huang, J. H. (2018). Stress induced neuroplasticity and mental disorders 2018. *Neural Plast.* 2018:5382537.

Watson, D., and Clark, L. (1988). Developmental and validation of brief measures of positive and negative affect: the PANAS scale. *J. Personal. Soc. Psychol.* 54, 1063–1070. doi: 10.1037//0022-3514.54.6.1063

Weierich, M. R., Wright, C. I., Negreira, A., Dickerson, B. C., and Barrett, L. F. (2010). Novelty as a dimension in the affective brain. *Neuroimage* 49, 2871–2878. doi: 10.1016/j.neuroimage.2009.09.047

Weiskrantz, L. (1956). Behavioral changes associated with ablation of the amygdaloid complex in monkeys. *J. Comp. Physiol. Psychol.* 49, 381–391. doi: 10.1037/h0088009

Wicker, B., Keysers, C., Plailly, J., Royet, J. P., Gallese, V., Rizzolatti, G., et al. (2003). Both of us disgusted in My insula: the common neural basis of seeing and feeling disgust. *Neuron* 40, 655–664. doi: 10.1016/s0896-6273(03)00679-2

Williams, L. E., and Bargh, J. A. (2008). Experiencing physical warmth promotes interpersonal warmth. *Science* 322, 606–607. doi: 10.1126/science.1162548

Williams, R. (2017). Anger as a basic emotion and its role in personality building and pathological growth: the neuroscientific, developmental and clinical perspectives. *Front. Psychol.* 8:1950. doi: 10.3389/fpsyg.2017.01950

Wilson-Mendenhall, C. D., Barrett, L. F., and Barsalou, L. W. (2013). Neural evidence that human emotions share core affective properties. *Psychol. Sci.* 24, 947–956. doi: 10.1177/0956797612464242

Wise, R. A. (2004). Dopamine and food reward: back to the elements. *Am. J. Physiol. Regul. Integr. Comp. Physiol.* 286, R13.

Wise, R. A. (2006). Role of brain dopamine in food reward and reinforcement. *Philos. Trans. R. Soc. Lond. Ser. B Biol. Sci.* 361, 1149–1158. doi: 10.1098/rstb.2006.1854

Wise, R. A. (2008). Dopamine and reward: the anhedonia hypothesis 30 years on. *Neurotox Res.* 14, 169–183. doi: 10.1007/bf03033808

Wise, R. A. (2013). Dual roles of dopamine in food and drug seeking: the drive-reward paradox. *Biol. Psychiatry* 73, 819–826. doi: 10.1016/j.biopsych.2012.09.001

Wise, R. A., and Rompre, P. P. (1989). Brain dopamine and reward. *Annu. Rev. Psychol.* 40, 191–225. doi: 10.1146/annurev.psych.40.1.191

Xu, X., Brown, L., Aron, A., Cao, G., Feng, T., Acevedo, B., et al. (2012). Regional brain activity during early-stage intense romantic love predicted relationship

outcomes after 40 months: an fMRI assessment. *Neurosci. Lett.* 526, 33–38. doi: 10.1016/j.neulet.2012.08.004

Yik, M., Russell, J. A., and Steiger, J. H. (2011). A 12-point circumplex structure of core affect. *Emotion* 11, 705–731. doi: 10.1037/a0023980

Yokel, R. A., and Wise, R. A. (1975). Increased lever pressing for amphetamine after pimozide in rats: implications for a dopamine theory of reward. *Science* 187, 547–549. doi: 10.1126/science.1114313

Zheng, Z., Simeng, G., Lei, Y., Shanshan, L., Wang, W., Yang, L., et al. (2016). Safety needs mediate stressful events induced mental disorders. *Neural Plast.* 2016:8058093.

Conflict of Interest Statement: The authors declare that the research was conducted in the absence of any commercial or financial relationships that could be construed as a potential conflict of interest.

Copyright © 2019 Gu, Wang, Cao, Wu, Tang and Huang. This is an open-access article distributed under the terms of the Creative Commons Attribution License (CC BY). The use, distribution or reproduction in other forums is permitted, provided the original author(s) and the copyright owner(s) are credited and that the original publication in this journal is cited, in accordance with accepted academic practice. No use, distribution or reproduction is permitted which does not comply with these terms.

frontiers in Neuroscience

ORIGINAL RESEARCH
published: 03 July 2019
doi: 10.3389/fnins.2019.00695

Enhanced Regional Homogeneity and Functional Connectivity in Subjects With White Matter Hyperintensities and Cognitive Impairment

Qing Ye[1,2,3†], Xin Chen[1†], Ruomeng Qin[1,2,3], Lili Huang[1], Dan Yang[1], Renyuan Liu[1], Bing Zhang[4], Feng Bai[1,2,3] and Yun Xu[1,2,3]*

[1] Department of Neurology, Affiliated Drum Tower Hospital, Jiangsu Key Laboratory for Molecular Medicine, Nanjing University Medical School, Nanjing, China, [2] Jiangsu Province Stroke Center for Diagnosis and Therapy, Nanjing, China, [3] Nanjing Neuropsychiatry Clinic Medical Center, Nanjing, China, [4] Department of Radiology, Affiliated Drum Tower Hospital, Nanjing University Medical School, Nanjing, China

OPEN ACCESS

Edited by:
Feng Liu,
Tianjin Medical University General Hospital, China

Reviewed by:
Liting Chen,
The First Affiliated Hospital of Nanchang University, China
Xiaonan Guo,
University of Electronic Science and Technology of China, China

***Correspondence:**
Yun Xu
xuyun20042001@aliyun.com

[†]These authors have contributed equally to this work

Specialty section:
This article was submitted to Brain Imaging Methods, a section of the journal Frontiers in Neuroscience

Received: *09 January 2019*
Accepted: *19 June 2019*
Published: *03 July 2019*

Citation:
Ye Q, Chen X, Qin R, Huang L, Yang D, Liu R, Zhang B, Bai F and Xu Y (2019) Enhanced Regional Homogeneity and Functional Connectivity in Subjects With White Matter Hyperintensities and Cognitive Impairment. Front. Neurosci. 13:695. doi: 10.3389/fnins.2019.00695

Objective: White matter hyperintensities (WMH) is an important cause of vascular cognitive impairment (CI). However, a considerable portion of individuals with WMH do not develop CI. The present study aimed to investigate distinctive regional brain activity and connectivity patterns in WMH subjects with and without CI, who displayed comparable WMH burden.

Methods: Fourteen WMH subjects with CI, 16 WMH subjects without CI and 37 healthy subjects underwent multimodal MRI scans and neuropsychological tests. All WMH subjects displayed Fazekas grade 2 of WMH. Regional Homogeneity (ReHo) and functional connectivity (FC) patterns were identified based on resting-state functional MRI data.

Results: No significant differences in WMH volume, the number of WMH lesions and brain volume were shown between the 2 WMH groups. In contrast, the WMH with CI group showed higher ReHo in bilateral superior parietal gyrus (SPG)/superior occipital gyrus (SOG) than the WMH without CI group. Compared with the WMH without CI group, the WMH with CI group also displayed higher FC of the left SPG/SOG with frontal regions, and higher FC of the right SPG/SOG with parietal regions. Furthermore, higher FC of the left SPG/SOG with frontal regions were significantly associated with less worse executive dysfunction in WMH with CI subjects, suggesting a compensatory effect.

Conclusion: Higher local coherence of activities in the SPG/SOG and higher connectivity of the SPG/SOG with parietal and frontal regions are related to CI in WMH subjects. The findings provide novel insights into functional alterations underlying the cognitive variety in WMH subjects.

Keywords: white matter hyperintensities, cognitive impairment, regional homogeneity, functional connectivity, cognitive variety

INTRODUCTION

White matter hyperintensities (WMH), defined in the T_2 weighted magnetic resonance imaging (MRI) representation, is widely common in elderly population. The prevalence of WMH increases remarkably with age and is as high as 72–96% in population over 60 years old (Longstreth et al., 1996; de Leeuw et al., 2001; Zhuang et al., 2018; Lampe et al., 2019). As a MRI marker of cerebral small vessel disease, the pathology of WMH generally reflects loss of axons and myelin, myelin pallor and gliosis (Gouw et al., 2011). These lesions are associated with lacunar infarction occurrence (Xu et al., 2018), and may disrupt white matter tracts or U-fibers that mediate cortical-subcortical or cortical-cortical connections, thus resulting in cognitive impairment (CI).

A large body of evidence shows that WMH causes vascular CI (Prins et al., 2005; Debette and Markus, 2010; Brickman et al., 2015), and WMH is associated with impairments in executive function and processing speed (Prins et al., 2005; Sudo et al., 2013). The baseline WMH burden was related with an increased risk of developing dementia, and the WMH progression was related with declines in global cognitive function and information processing speed (van Dijk et al., 2008). The progression of WMH correlated better with cognitive decline than did the baseline WMH burden (Schmidt R. et al., 2012). However, WMH is widely common in elderly population and not all subjects with WMH will develop CI. A recent study showed that WMH was detected in 77.8% healthy elderly between 60 and 82 years old (Lampe et al., 2019). Investigating the mechanisms underlying the link between CI and WMH may help to understand the cognitive heterogeneity in subjects with WMH.

Resting-state (fMRI) techniques have been increasingly utilized to investigate functional alterations related to the onset of CI in WMH. Recently, a study indicated that Regional Homogeneity (ReHo) in the left cerebellum and the middle cingulate cortex were significantly correlated with CI and executive function deficits respectively in subjects with both CI and WMH (Diciotti et al., 2017). Compared with WMH subjects with normal cognition, WMH subjects with CI displayed lower functional connectivity (FC) of posterior cingulate cortex with anterior cingulate cortex, temporal regions and frontal regions, and higher FC with specific temporal regions and parietal regions (Sun et al., 2011). Several other studies detected altered FC or brain activation patterns across frontal, parietal, temporal and occipital regions in WMH subjects with normal cognition (Lockhart et al., 2015; De Marco et al., 2017; Shi et al., 2017).

Most of the above researches were performed only in WMH subjects with normal cognition or WMH subjects with CI. These findings did not explain why only a portion of the population with WMH would develop CI. The present study recruited WMH subjects with CI, WMH subjects without CI and healthy subjects, and the 2 WMH groups had comparable WMH burden. We hypothesized that different ReHo and FC patterns would be shown between the WMH with and without CI groups and these functional alterations may be related to the mechanism of WMH-mediated CI.

MATERIALS AND METHODS

Participants

The present study was carried out in accordance with the latest version of the Declaration of Helsinki, and approved by the Drum Tower Hospital Research Ethics Committee. Thirty-seven healthy subjects and 30 subjects with WMH (Fazekas grade 2) were recruited at the Drum Tower Hospital, Medical School of Nanjing University. All participants provided written informed consents and underwent multimodal MRI scans and a standardized diagnostic evaluation, including demographic data, medical history and an examination of neuropsychological status.

Neuropsychological Examination

Global cognitive function was measured using a Montreal Cognitive Assessment (MoCA) and a Mini Mental State Examination (MMSE). WMH subjects with MoCA scores lower than education-adjusted norms (the cutoff was $\leq$ 19 for 1∼6 years of education, $\leq$24 for 7∼12 years of education and $<$26 for $>$12 years of education) were defined as the WMH with CI group (n = 14), and other WMH subjects were defined as the WMH without CI group (n = 16). All subjects underwent a neuropsychological battery test including Trail Making Tests (TMT)-A and B and Stroop Color and Word Tests A, B, and C (Stroop-A, B, and C). Three WMH with CI subjects failed to perform some of tests due to subjective unwillingness or hypopsia. The mental statuses were assessed with the *Structured Clinical Interview for Diagnostic and Statistical Manual of Mental Disorders*, Fourth Edition (DSM-IV) Axis I Disorders (SCID-I), the Hamilton Anxiety Scale (HAMA), and the Hamilton Depression Scale (HAMD).

Inclusion and Exclusion Criteria

The inclusion criteria for WMH subjects were as follows: (1) age $>$ 50 years, (2) the presence of Fazekas grade 2 of WMH on MRI images, (3) possible subjective complaints like memory impairment, postural instability, dizziness or depression. WMH were described as hyperintensities on FLAIR images, without cavitation. Fazekas grade 2 of WMH was defined as single lesions between 1 and 2 cm, areas of "grouped" lesions more than 2 cm in any diameter, and no more than "connecting bridges" between individual lesions (Pantoni et al., 2005).

Exclusion criteria were as follows: (1) a history of ischemic stroke with infarcts of more than 1.5 cm in diameter or cardiogenic cerebral infarction, (2) intracranial hemorrhage, (3) carotid artery stenosis ($>$75%) or coronary atherosclerosis heart disease, (4) other neurological disorders, such as Alzheimer disease (AD), Parkinson(ism), epilepsy and multiple sclerosis, (5) systemic disease, such as cancer, shock, anemia and thyroid dysfunction, (6) MRI contraindications, (7) prominent impairments of audition or vision.

MRI Procedures

Magnetic resonance imaging scanning was performed using a 3 Tesla MR scanner (Achieva 3.0 T Ingenia; Philips Medical Systems, Eindhoven, Netherlands) with a 32-channel head coil at

the Drum Tower Hospital, Medical School of Nanjing University. All subjects were told to relax, close their eyes and stay awake during scanning. Their heads were immobilized using belts and foam pads to minimize head motion, and their ears were occluded with earplugs. High-resolution T_1-weighted sagittal images covering the whole brain were obtained by a 3D-magnetization prepared rapid gradient-echo sequence: repetition time (TR) = 9.8 ms; echo time (TE) = 4.6 ms; field of view (FOV) = 256 × 256 mm; acquisition matrix = 256 × 256; flip angle (FA) = 8°; thickness = 1.0 mm, gap = 0 mm; number of slices = 192. Resting-state functional images, including 230 volumes, were obtained by a gradient-recalled echo-planar imaging (GRE-EPI) sequence: TR = 2000 ms; TE = 30 ms; FOV = 192 × 192 mm; acquisition matrix = 64 × 64; FA = 90°; thickness = 4.0 mm; gap = 0 mm; number of slices = 35. Additionally, T_2 FLAIR axial images were obtained with following parameters: TR = 4500 ms; TE = 344 ms; acquisition matrix = 272 × 272; FA = 90°; thickness = 1 mm; gap = 0 mm, number of slices = 200.

WMH Segmentation and Quantification

As shown in **Figure 1**, WMH volume was measured on T_1-weighted and T_2 FLAIR images using the lesion growth algorithm (Schmidt P. et al., 2012) as implemented in the LST toolbox version 2.0.15[1] for Statistical Parametric Mapping software (SPM12[2]). First, the algorithm segments the T_1 images into gray matter, white matter and cerebrospinal fluid. The information is then combined with the coregistered T_2 FLAIR intensities to calculate lesion belief maps. By thresholding these maps with a pre-chosen initial threshold ($\kappa = 0.30$), an initial binary lesion map is obtained and is subsequently grown along voxels that appear hyperintense on the T_2 FLAIR image. The result is a lesion probability map. It should be noted that the κ-value was determined through the visual inspection of the results by 3 experienced raters.

Volume of Brain and Hippocampus

As described in our previous study (Ye et al., 2017), brain volume was assessed using the VBM8 toolbox for SPM12. First, the T_1 images were segmented into gray matter, white matter and cerebrospinal fluid. Second, the segmented images were normalized to the MNI template using a non-linear and affine spatial normalization and re-sampled to a voxel size of 1.5 × 1.5 × 1.5 mm. Third, Jacobian modulation was applied to the segmented images, which could be incorporated to compensate for the effect of spatial normalization. Fourth, the extracted gray matter, white matter and cerebrospinal fluid sets were smoothed with an 8-mm full width at half maximum Gaussian filter to decrease the effects of individual variation in gyral anatomy and to increase the signal-to-noise ratio. Finally, gray matter volume, white matter volume, cerebrospinal fluid volume and whole brain volume were obtained in each subject.

Hippocampal atrophy is a well-established indicator for the early diagnosis of AD (Aisen et al., 2010; Jack et al., 2010), which is the most common type of dementia in the elderly population. To rule out the CI due to AD, the hippocampal volume was assessed. The hippocampus (left and right separately) was isolated using automated anatomical labeling implemented through the Resting State fMRI Data Analysis Toolkit 1.7 software[3]. Then, the hippocampal regions were interpolated to the same sizes, dimension and origins with T_1 images. And a mean volume index of all voxels within the hippocampal region (left and right) was extracted for each subject. Finally, the hippocampal volume was obtained by multiplying the mean volume index by the size of each voxel (1.5 × 1.5 × 1.5 mm) and the number of voxels within the hippocampal region.

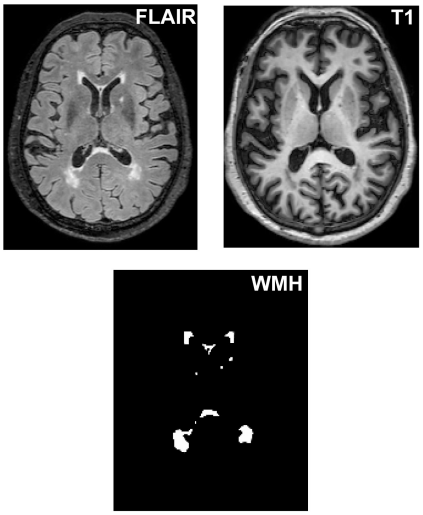

FIGURE 1 | The segmentation of WMH lesions. WMH lesions were segmented and quantified from T_2 FLAIR images and T_1 images.

Resting-State Functional Image Preprocessing

Functional MRI data were preprocessed using a toolbox for Data Processing and Analysis for Brain Imaging (DPABI) V2.3[4]. Owing to T_1 equilibration effects, the first 10 volumes of the scanning session were discarded. The slice timing and realignment procedures were conducted to correct for the time differences in acquisition among slices within one volume, and the motion effects (Friston 24-parameter model) during scanning. A control subject was excluded due to head motion artifacts exceeding 2° in rotation or 2 mm in transition. The resulting images were spatially normalized into a standard stereotaxic space with a 12-parameter affine approach and an EPI template image, and then resampled to 3 × 3 × 3 mm voxels, and smoothed with a Gaussian kernel of 6 × 6 × 6 mm. Then, white matter signal, cerebrospinal fluid signal and 24 head motion parameters were removed as covariates of no interest. The resulting fMRI data were band-pass filtered (0.01–0.08 Hz), and the linear trend of time courses was removed. Finally, scrubbing

[1] www.statistical-modeling.de/lst.html
[2] http://www.fil.ion.ucl.ac.uk/spm
[3] http://restfmri.net/forum/index.php
[4] http://rfmri.org/DPABI

was performed. Volumes with framewise displacement (FD) larger than 0.5 mm with prior 1 and later 2 volumes were deleted, and subjects with fewer than 4 min of remaining data (about 50% volumes) were excluded (Power et al., 2012; Satterthwaite et al., 2013; Chen et al., 2019; Guo et al., 2019). After exclusion, 33 control subjects, 14 WMH without CI subjects and 14 WMH with CI subjects remained.

ReHo Analysis

ReHo analysis was performed without smoothing using a toolbox for DPABI V2.3. According to a previous study (Zang et al., 2004), individual ReHo maps were obtained by calculating the Kendall's coefficient concordance of the time series of a given voxel with those of its nearest neighbors (26 voxels) in a voxel-wise manner. To improve the normality and reliability of ReHo value across subjects (Zuo et al., 2013), all individual ReHo maps were standardized into ReHo z-value by subtracting the average voxel-wise ReHo obtained for the entire brain, and then dividing the resultant value by the standard deviation. Finally, generated ReHo maps were spatially smoothed with a Gaussian kernel of $6 \times 6 \times 6$ mm.

FC Analysis

Regions showing significant difference of ReHo between the WMH with CI group and the WMH without CI group served as seeds for FC analysis. For each subject, a mean time series of each seed region was extracted as a reference time course. Pearson cross-correlation analysis was conducted between the reference time course and time course of each voxel in the brain. Then, a Fisher's z-transformation was used to improve the normality of the correlation coefficients $z = 0.5 \times \ln \frac{1+r}{1-r}$. Finally, the individual FC maps of each region showing significant group difference of ReHo were obtained.

Statistical Analysis

Demographic, Neuropsychological, and Volume Data

A one-way analysis of variance (ANOVA) was performed in the analyses of age, education, volume data and mean FD with significance at $P < 0.05$ among the control group, the WMH without CI group and the WMH with CI group. χ^2 test was applied in the analysis of gender among the three groups. Because neuropsychological data was non-normal distribution, the Kruskal–Wallis test was applied in the analyses of neuropsychological data with significance at $P < 0.05$ among the three groups. The SPSS 19.0 software (SPSS, Inc., Chicago, IL, United States) was employed in these statistical procedures.

ReHo and FC Data

The ReHo or FC differences among the three groups were analyzed by applying a voxel-wise one-way analysis of covariance (ANCOVA), controlling for age, gender, years of education and mean FD (using DPABI V2.3). The thresholds were set at a corrected $P < 0.01$, determined by Monte Carlo simulation for multiple comparisons (voxel-wise $P < 0.01$), and FWHM will be estimated to determine the threshold of cluster size. Then, the mean ReHo or FC strength in each significant cluster was extracted in each subject. A *post hoc* t-test was performed to find the detailed between-group ReHo or FC difference in each cluster employing the SPSS 19.0 software. Multiple comparison correction, i.e., the Bonferroni correction principle, was performed for *post hoc* comparisons. Finally, Pearson correlation analyses were performed between the mean ReHo or FC strength in each cluster and the cognitive test scores in the WMH with CI group using the SPSS 19.0 software with significance at $P < 0.05$.

RESULTS

Demographic and Neuropsychological Data

As shown in **Table 1**, no significant differences in age, education and gender were found among the control group, the WMH without CI group and the WMH with CI group. The WMH with CI group performed significantly worse in MMSE, MoCA, TMT-B, Stroop-B, and Stroop-C tests than both the control group and the WMH without CI group (all $P < 0.05$). No significant differences in cognitive test scores were shown between the WMH without CI group and the control group.

Volume Data

As shown in **Table 1**, both the WMH with CI group and the WMH without CI group displayed significantly larger total WMH volume and more number of WMH lesions than the control group (all $P < 0.05$). Notably, no significant differences in total WMH volume and the number of WMH lesions were found between the WMH with CI group and the WMH without CI group. Furthermore, no significant differences in whole brain volume, gray matter volume, white matter volume, bilateral hippocampal volume and mean FD were shown among the three groups.

ReHo Data

As shown in **Figure 2A**, the three groups displayed significant differences of ReHo in right superior temporal gyrus/Heschl's gyrus, left superior parietal gyrus (SPG)/superior occipital gyrus (SOG) and right SPG/SOG.

Post hoc Analysis

In the right superior temporal gyrus/Heschl's gyrus, both the WMH with CI group and the WMH without CI group displayed lower ReHo than the control group (both $P < 0.001$), and no significant difference of ReHo was shown between the 2 WMH groups ($P = 0.27$) (**Figure 2B**). Interestingly, in the left SPG/SOG and right SPG/SOG, the WMH with CI group showed higher ReHo than both the WMH without CI group ($P = 0.002$ and $P < 0.001$, respectively) and the control group (both $P < 0.001$) (**Figures 2C,D**).

FC Data

Since the 2 WMH groups displayed significant differences of ReHo in the left SPG/SOG and right SPG/SOG, we further investigated the differences of FC pattern of the two regions among the three groups.

TABLE 1 | Demographic, neuropsychological and volume data.

Items	Control (n = 33)	WMH without CI (n = 14)	WMH with CI (n = 14)	F or χ^2	P-value
Age (years)	62.03±7.53	63.75±8.29	66.00±5.13	1.85	0.190
Education (years)	10.88±3.49	10.31±3.89	9.93±2.89	0.76	0.518
Gender (male: female)	16 : 17	8 : 6	7 : 7	0.30	0.861
MMSE	28.47±1.49	28.37±1.32	26.86±2.66[a,b]	–	**0.034**
MoCA	26.41±2.30	25.48±2.38	20.43±2.71[a,b]	–	**<0.001**
TMT-A	49.52±15.87	50.81±22.99	66.69±32.71	–	0.092
TMT-B	82.26±28.86	110.85±64.01	155.90±81.78[a,b]	–	**0.001**
Stroop-A	17.83±6.11	17.19±5.17	22.27±6.56	–	0.079
Stroop-B	19.97±7.12	20.75±6.79	33.55±19.00[a,b]	–	**0.015**
Stroop-C	29.96±7.89	30.73±11.92	52.27±36.68[a,b]	–	**0.007**
Total WMH volume (ml)	1.28±1.12	6.06±2.27[a]	6.60±4.25[a]	37.85	**<0.001**
Number of WMH lesions	8.81±3.53	16.17±6.02[a]	15.43±4.29[a]	20.12	**<0.001**
Whole brain volume (ml)	1239.62±185.18	1230.48±169.59	1246.71±168.05	0.12	0.89
Gray matter volume (ml)	483.74±75.80	483.63±72.96	497.57±62.44	0.21	0.721
White matter volume (ml)	432.87±78.33	424.62±69.04	440.21±63.28	0.29	0.788
Left hippocampal volume (ml)	2.77±0.39	2.53±0.38	2.58±0.28	1.42	0.283
Right hippocampal volume (ml)	2.71±0.55	2.52±0.48	2.68±0.35	0.92	0.408
Mean FD (mm)	0.17±0.05	0.15±0.04	0.18±0.07	1.00	0.376

Values are presented as mean ± stand deviation (SD). One-way ANOVA was applied in the analyses of age, education and volume data. χ^2 test was applied in the analysis of gender. The Kruskal–Wallis test was applied in the analyses of neuropsychological data. P-value < 0.05 appears in bold. [a]P < 0.05, differs from the control group; [b]P < 0.05, differs from the WMH without CI group. CI, cognitive impairment; FD, framewise displacement; MMSE, Mini Mental State Examination; MoCA, Montreal Cognitive Assessment; TMT-A and TMT-B, Trail Making Tests-A and B; WMH, white matter hyperintensities.

As shown in **Figure 3A**, the three groups displayed significant differences of FC of the left SPG/SOG in the right inferior/middle frontal gyrus, left inferior occipital gyrus and left hippocampus. As shown in **Figure 3B**, the three groups displayed significant differences of FC of the right SPG/SOG in the bilateral postcentral gyrus/inferior parietal lobule and bilateral hippocampus and thalamus. The detailed coordinate information of above regions was shown in **Table 2**.

Post hoc analysis: As shown in **Table 3**, first, for the FC of the left SPG/SOG, the WMH with CI group displayed higher FC than the control group in all regions with significances (all $P < 0.001$). In contrast, the WMH without CI group displayed higher FC than the control group only in the left hippocampus ($P = 0.004$). Notably, the WMH with CI group showed higher FC than the WMH without CI group in the right inferior/middle frontal gyrus ($P < 0.001$). Second, for the FC of the right SPG/SOG, the WMH with CI group displayed higher FC than the control group in all regions with significances ($P < 0.001$ for the bilateral postcentral gyrus/inferior parietal lobule, and $P = 0.002$ for the bilateral hippocampus and thalamus). Compared with the control group, the WMH without CI group displayed higher FC in the bilateral hippocampus and thalamus ($P = 0.003$). Notably, the WMH with CI group displayed higher FC than the WMH without CI group in the bilateral postcentral gyrus/inferior parietal lobule ($P < 0.001$).

Behavioral Significance of ReHo and FC Alterations

Correlative analyses between functional brain alterations and cognition were performed in the WMH with CI group. As shown in **Figures 4A,B**, lower ReHo in the right superior temporal gyrus/Heschl's gyrus was significantly associated with longer TMT-B and Stroop-A time ($r = -0.773$, $P = 0.009$ and $r = -0.783$, $P = 0.011$, respectively), i.e., worse executive function and processing speed. As shown in **Figures 4C,D**, higher FC of the left SPG/SOG with the left hippocampus and the right inferior/middle frontal gyrus was significantly associated with shorter Stroop-A and Stroop-C time, respectively ($r = -0.628$, $P = 0.039$ and $r = -0.728$, $P = 0.012$, respectively), suggesting a compensatory effect.

DISCUSSION

The present study was the first to show the differences in ReHo and FC patterns between WMH with and without CI subjects who had comparable WMH burden. Worse global function, executive function and processing speed were shown in the WMH with CI group. The 2 WMH groups showed no significant differences in brain volume data. However, the WMH with CI group displayed higher ReHo in the bilateral SPG/SOG than the WMH without CI group. The WMH with CI group also displayed higher FC of the SPG/SOG with parietal and frontal regions. Furthermore, the ReHo and FC alterations were correlated with cognitive function in WMH with CI subjects.

A previous resting-state fMRI study investigated FC patterns in both WMH subjects with normal cognition and WMH subjects with CI, and found altered FC of posterior cingulate cortex with extensive regions in WMH subjects with CI. However, the WMH burden was not evaluated in the two groups (Sun et al., 2011). WMH is thought to disrupt white matter tracts and result in reorganization of functional brain patterns (Reijmer et al., 2015; De Marco et al., 2017). In the present study, since the 2

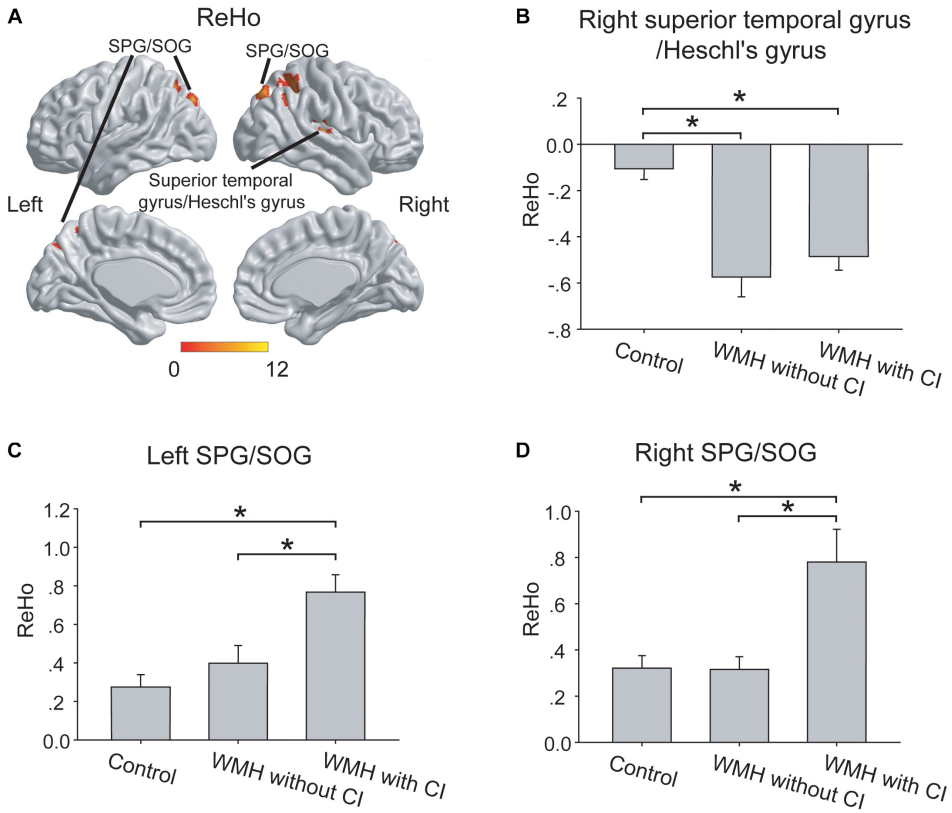

FIGURE 2 | The group differences of ReHo. **(A)** The group differences of ReHo were shown in the right superior temporal gyrus/Heschl's gyrus, left SPG/SOG and right SPG/SOG. **(B)** In the right superior temporal gyrus/Heschl's gyrus, both the WMH with CI group and the WMH without CI group displayed lower ReHo than the control group. **(C,D)** In the left SPG/SOG and right SPG/SOG, the WMH with CI group showed higher ReHo than both the WMH without CI group and the control group. ReHo values have been normalized by subtracting the mean voxel-wise ReHo obtained for the entire brain, and then dividing the resultant value by the standard deviation. The thresholds were set at a corrected $P < 0.01$, determined by Monte Carlo simulation for multiple comparisons (voxel-wise $P < 0.01$, FWHM = 6.9 mm, cluster size > 1782 mm^3). The color bars are presented with F-values. *$P < 0.05$, CI, cognitive impairment; ReHo, Regional Homogeneity; SPG, superior parietal gyrus; SOG, superior occipital gyrus; WMH, white matter hyperintensities.

WMH groups had comparable WMH burden, the differences of functional patterns (i.e., ReHo and FC patterns) between the two groups could not be due to the difference of WMH burden, but could be related to the cognitive differences between the two groups. In the present study, higher ReHo in the SPG/SOG and higher FC of the SPG/SOG with parietal and frontal regions happened in the WMH with CI group, suggesting that the CI could be related to higher local coherence of activities in the SPG/SOG and higher connectivity between the SPG/SOG and parietal and frontal regions. Furthermore, the correlative analyses confirmed the results above.

In the present study, the WMH with CI group displayed poor performances in TMT-B, Stroop-B and Stroop-C tests, and increased ReHo in the SPG/SOG, suggesting that regional activities in parietal and occipital cortex were related to executive function in WMH with CI subjects. Parietal and occipital cortex plays a major role in the maintenance of normal cognition, including decision making, working memory, spatial updating and sensory attention (Medendorp et al., 2007; Tuladhar et al., 2007; Sulpizio et al., 2016), most of which are related to executive function. Furthermore, the maintenance of brain function relies on multiple brain areas that connect and interact with each other to serve different functions (Power et al., 2011). A balance between regional specialization and global integration is of vital importance for brain function (Tononi et al., 1998). A recent study found decreased FC of the default mode network and central executive network in subjects with both WHM and dementia (Kim et al., 2016). Another study investigated posterior cingulate cortex connectivity in WMH subjects with vascular cognitive impairment, no dementia, and showed both decreased FC with extensive regions and increased FC with parietal and temporal regions (Sun et al., 2011). In the present study, higher FC between the SPG/SOG and parietal and frontal regions were shown in the WMH with CI group. Higher FC of the left SPG/SOG with frontal regions were significantly associated with less worse executive dysfunction in WMH with CI subjects, suggesting a compensatory effect.

The mechanisms underlying the link between the functional alterations and CI in WMH subjects could be explained with a prominent cognitive model named "the scaffolding theory of aging and cognition (STAC)" (Reuter-Lorenz and Park, 2014). According to the STAC, cognitive decline is a consequence of

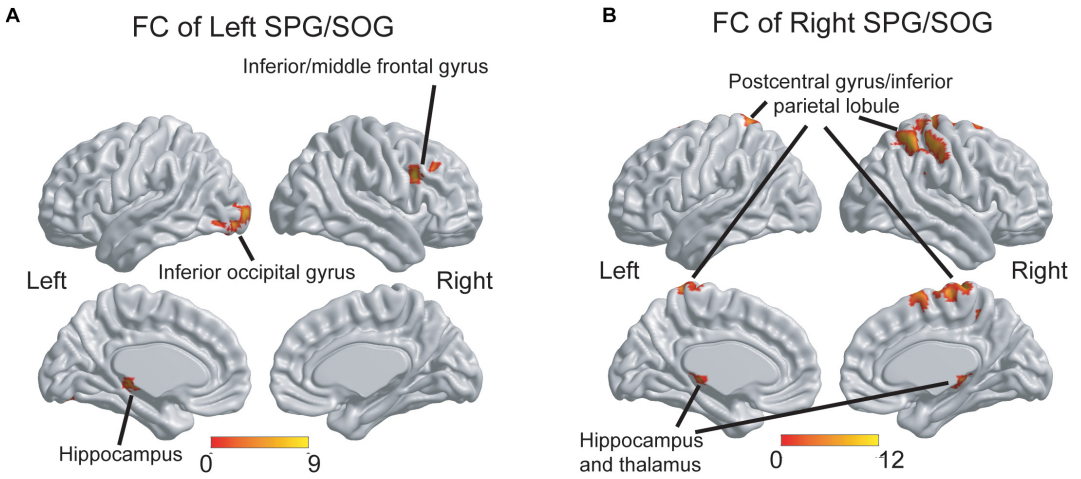

FIGURE 3 | The group differences of FC patterns of the bilateral SPG/SOG. **(A)** Significant group differences of FC of the left SPG/SOG were shown in frontal, temporal and occipital regions. **(B)** Significant group differences of FC of the right SPG/SOG were shown in parietal, temporal, and thalamus regions. The thresholds were set at a corrected $P < 0.01$, determined by Monte Carlo simulation for multiple comparisons (voxel-wise $P < 0.01$, FWHM = 7.4 mm, cluster size > 2160 mm^3). The color bars are presented with *F*-values. FC, functional connectivity; SPG, superior parietal gyrus; SOG, superior occipital gyrus.

"neural degradation," "compensatory scaffolding," and life-course factors. The neural degradation is thought to cause cognitive decline and is categorized as "neural challenges" and "functional deterioration." The former refers to structural changes in the brain, including white matter damages (Reuter-Lorenz and Park, 2014), and the latter is indicators of maladaptive brain activity such as dedifferentiation of activities in visual areas (Park et al., 2004; Voss et al., 2008). In the present study, although the WMH with CI group and the WMH without CI group had comparable WMH burden, only the WMH with CI group displayed higher ReHo, i.e., higher local coherence of activities, in the SPG/SOG. The higher local coherence of activities could be one of indicators of maladaptive brain activity, and suggest functional deterioration in the WMH with CI group. This could be one of inducing factors for CI in WMH subjects. On the other hand, these negative indices might induce the onset of compensatory scaffolding that refers to compensatory reallocation or recruitment of cognitive resources or supplementary neural circuitry (Greenwood, 2007; Cramer et al., 2011; Reuter-Lorenz and Park, 2014). Compensatory scaffolding counteracts or ameliorates the damage effect of neural degradation. The higher FC of the SPG/SOG with parietal and

TABLE 2 | Brain regions with group differences of ReHo or FC.

Items	Brain regions with group differences	BA	Peak MNI coordinates x, y, z (mm)	Peak *F*-value	Cluster size (mm^3)
ReHo					
	Right superior temporal gyrus/Heschl's gyrus	48	42, -51, 39	10.98	2079
	Left SPG/SOG	5, 7	−18, −60, 51	9.52	2268
	Right SPG/SOG	7, 19	24, −68, 36	11.15	1944
FC of Left SPG/SOG					
	Right inferior/middle frontal gyrus	44, 48	43, 14, 30	8.59	2430
	Left inferior occipital gyrus	19	−38, −79, −14	7.95	2862
	Left hippocampus	37	−24, −27, −6	8.10	2241
FC of Right SPG/SOG					
	Bilateral postcentral gyrus/inferior parietal lobule	1–7, 40	9, −33, 75	11.67	14634
	Bilateral hippocampus and thalamus	27	−14, −35, 9	8.23	2295

The thresholds were set at a corrected $P < 0.01$, determined by Monte Carlo simulation for multiple comparisons (voxel-wise $P < 0.01$, for ReHo analysis, FWHM = 6.9 mm, cluster size > 1782 mm^3, and for FC analysis, FWHM = 7.4 mm, cluster size > 2160 mm^3). BA, Brodmann's area; MNI, Montreal Neurological Institute; FC, functional connectivity; SPG, superior parietal gyrus; SOG, superior occipital gyrus.

TABLE 3 | FC data.

Seed	Brain regions	FC strength			*F*	*P*-value
		Control	WMH without CI	WMH with CI		
Left SPG/SOG						
	Right inferior/middle frontal gyrus	0.21±0.16	0.15±0.15	0.46±0.11[a,b]	12.07	< 0.001
	Left inferior occipital gyrus	0.31±0.24	0.39±0.19	0.52±0.25[a]	6.74	0.005
	Left hippocampus	0.12±0.13	0.27±0.15[a]	0.28±0.19[a]	7.05	0.002
Right SPG/SOG						
	Bilateral postcentral gyrus/inferior parietal lobule	0.41±0.11	0.40±0.14	0.69±0.18[a,b]	12.31	< 0.001
	Bilateral hippocampus and thalamus	0.06±0.15	0.21±0.15[a]	0.21±0.18[a]	7.18	< 0.001

The thresholds were set at a corrected P < 0.01, determined by Monte Carlo simulation for multiple comparisons (voxel-wise P < 0.01, for ReHo analysis, FWHM = 6.9 mm, cluster size > 1782 mm^3, and for FC analysis, FWHM = 7.4 mm, cluster size > 2160 mm^3). [a]P < 0.05, differs from the control group; [b]P < 0.05, differs from the WMH without CI group. BA, Brodmann's area; CI, cognitive impairment; MNI, Montreal Neurological Institute; FC, functional connectivity; SPG, superior parietal gyrus; SOG, superior occipital gyrus.

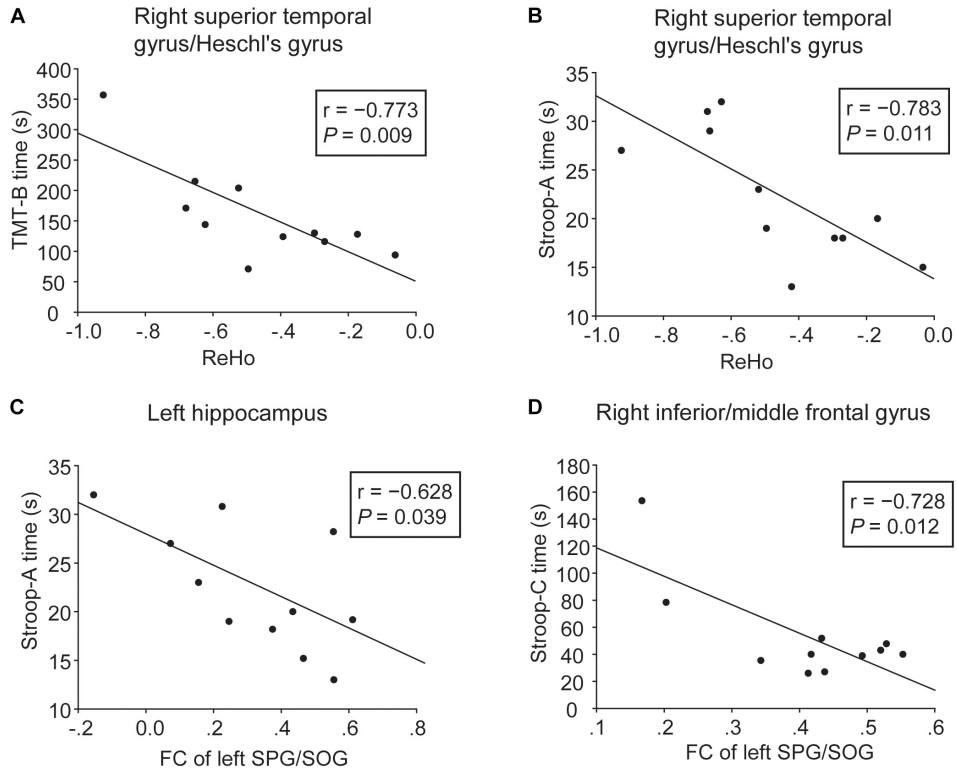

FIGURE 4 | Correlation analyses between cognitive function and ReHo or FC in the WMH with CI group. **(A,B)** Significant negative correlation was shown between cognitive performances (TMT-B and Stroop-A) and ReHo in the right superior temporal gyrus/Heschl's gyrus. **(C,D)** Significant negative correlation was shown between cognitive performances (Stroop-A and Stroop-C) and FC of the left SPG/SOG with the left hippocampus and the right inferior/middle frontal gyrus. Three WMH with CI subjects failed to perform these tests due to subjective unwillingness or hypopsia.

frontal regions in the WMH with CI group indicated enhanced functional communications between the SPG/SOG and other regions. The results of correlative analyses showed that the enhanced communications partly compensated for executive dysfunction in WMH with CI subjects. Thus, the higher ReHo in the SPG/SOG and the higher FC of the SPG/SOG with parietal and frontal regions could represent functional deterioration and compensatory scaffolding, respectively, during the development of CI in WMH subjects.

Most of previous fMRI studies on WMH subjects investigated the effects of WMH burden on brain activities or connectivity. A recent study found that WMH burden modulated brain connectivity in healthy subjects, i.e., high WMH burden was associated with increased FC of default mode network and salience network with temporal cortex and parietal cortex, respectively (De Marco et al., 2017). A study investigated the spatial associations of intrinsic connectivity contrast with WMH volume in elderly subjects, and found that significant associations

were detected between intrinsic connectivity contrast of SOG and WMH volume in subcortical white matter (Shi et al., 2017). A task fMRI study on healthy aging showed that greater WMH volume was associated with increased frontal activation and decreased frontal FC during performing a spatial search task (Lockhart et al., 2015). All these findings supported altered functional brain patterns across frontal, parietal, temporal and occipital regions in WMH subjects and also suggested a compensatory functional enhancement underlying the maintenance of normal cognition in WMH subjects. Consistent with these findings, the present study confirmed altered regional activities in parietal, occipital and temporal regions and increased FC with frontal, parietal and temporal regions in WMH subjects. Notably, the present study was performed on both WMH with and without CI subjects. The WMH without CI group displayed decreased ReHo in temporal regions and increased FC of the SPG/SOG with hippocampus. The increased FC with hippocampus might reflect a compensatory functional enhancement. In addition, compensatory functional enhancements were also shown in WMH with CI subjects. Thus, the present findings extended the compensatory functional enhancements on WMH subjects with mild CI.

Some limitations should be addressed. First, the sample size in the present study is small, especially for WMH subjects, and 3 WMH with CI subjects even failed to perform some of neuropsychological tests. The findings should be validated in a larger sample. We are continuing to recruit new participants with WMH to validate our findings. Second, due to the small sample size and a large number of correlation analyses between functional brain alterations and cognition, the results of correlative analyses would lose significance after correcting for the Bonferroni correction principle. Thus, the present findings should be treated with caution.

CONCLUSION

In conclusion, with comparable WMH burden, WMH subjects with CI have higher local coherence of activities in the SPG/SOG and higher connectivity of the SPG/SOG with parietal and frontal regions than WMH subjects without CI. The findings provide novel insights into the functional alterations underlying the cognitive variety in WMH subjects and shed light on the investigation of surrogate markers for CI in WMH subjects.

ETHICS STATEMENT

This study was carried out in accordance with the recommendations of the Drum Tower Hospital Research Ethics Committee. All subjects gave written informed consent in accordance with the Declaration of Helsinki. The protocol was approved by the Drum Tower Hospital Research Ethics Committee.

AUTHOR CONTRIBUTIONS

YX designed the study and revised the manuscript. QY and XC carried out the data collection and data analysis, and wrote the manuscript. RQ, LH, DY, and RL carried out the data collection. FB and BZ discussed the study. All authors approved the final version of the manuscript.

FUNDING

This work was supported by the National Key Research and Development Program of China (Grant Nos. 2016YFC1300504 and 2016YFC0901004), the National Natural Science Foundation of China (Grant Nos. 81801060 and 81630028), the Fundamental Research Funds for the Central Universities (Grant No. YG1805070+021414380430), the Key Research and Development Program of Jiangsu Province of China (Grant No. BE2016610), the Jiangsu Province Key Medical Discipline (Grant No. ZDXKA2016020), and the Jiangsu Provincial Key Medical Talents (Grant No. ZDRCA2016085).

REFERENCES

Aisen, P. S., Petersen, R. C., Donohue, M. C., Gamst, A., Raman, R., Thomas, R. G., et al. (2010). Clinical core of the Alzheimer's disease neuroimaging initiative: progress and plans. *Alzheimers Dem.* 6, 239–246.

Brickman, A. M., Zahodne, L. B., Guzman, V. A., Narkhede, A., Meier, I. B., Griffith, E. Y., et al. (2015). Reconsidering harbingers of dementia: progression of parietal lobe white matter hyperintensities predicts Alzheimer's disease incidence. *Neurobiol. Aging* 36, 27–32. doi: 10.1016/j.neurobiolaging.2014.07.019

Chen, H., Uddin, L. Q., Guo, X., Wang, J., Wang, R., Wang, X., et al. (2019). Parsing brain structural heterogeneity in males with autism spectrum disorder reveals distinct clinical subtypes. *Hum. Brain Mapp.* 40, 628–637. doi: 10.1002/hbm.24400

Cramer, S. C., Sur, M., Dobkin, B. H., O'Brien, C., Sanger, T. D., Trojanowski, J. Q., et al. (2011). Harnessing neuroplasticity for clinical applications. *Brain* 134(Pt 6), 1591–1609. doi: 10.1093/brain/awr039

de Leeuw, F. E., de Groot, J. C., Achten, E., Oudkerk, M., Ramos, L. M., Heijboer, R., et al. (2001). Prevalence of cerebral white matter lesions in elderly people: a population based magnetic resonance imaging study. the rotterdam scan study. *J. Neurol. Neurosurg. Psychiatry* 70, 9–14. doi: 10.1136/jnnp.70.1.9

De Marco, M., Manca, R., Mitolo, M., and Venneri, A. (2017). White matter hyperintensity load modulates brain morphometry and brain connectivity in healthy adults: a neuroplastic mechanism? *Neural Plast* 2017:4050536. doi: 10.1155/2017/4050536

Debette, S., and Markus, H. S. (2010). The clinical importance of white matter hyperintensities on brain magnetic resonance imaging: systematic review and meta-analysis. *BMJ* 341:c3666. doi: 10.1136/bmj.c3666

Diciotti, S., Orsolini, S., Salvadori, E., Giorgio, A., Toschi, N., Ciulli, S., et al. (2017). Resting state fMRI regional homogeneity correlates with cognition measures in subcortical vascular cognitive impairment. *J. Neurol. Sci.* 373, 1–6. doi: 10.1016/j.jns.2016.12.003

Gouw, A. A., Seewann, A., van der Flier, W. M., Barkhof, F., Rozemuller, A. M., Scheltens, P., et al. (2011). Heterogeneity of small vessel disease: a systematic review of MRI and histopathology correlations. *J. Neurol. Neurosurg. Psychiatry* 82, 126–135. doi: 10.1136/jnnp.2009.204685

Greenwood, P. M. (2007). Functional plasticity in cognitive aging: review and hypothesis. *Neuropsychology* 21, 657–673. doi: 10.1037/0894-4105.21.6.657

Guo, X., Duan, X., Suckling, J., Chen, H., Liao, W., and Cui, Q. (2019). Partially impaired functional connectivity states between right anterior insula and default mode network in autism spectrum disorder. *Hum. Brain Mapp.* 40, 1264–1275. doi: 10.1002/hbm.24447

Jack, C. R. Jr., Wiste, H. J., Vemuri, P., Weigand, S. D., Senjem, M. L., Zeng, G., et al. (2010). Brain beta-amyloid measures and magnetic resonance imaging atrophy both predict time-to-progression from mild cognitive impairment to Alzheimer's disease. *Brain* 133, 3336–3348. doi: 10.1093/brain/awq277

Kim, H. J., Cha, J., Lee, J. M., Shin, J. S., Jung, N. Y., Kim, Y. J., et al. (2016). Distinctive resting state network disruptions among alzheimer's disease, subcortical vascular dementia, and mixed dementia patients. *J. Alzheimers Dis.* 50, 709–718. doi: 10.3233/JAD-150637

Lampe, L., Kharabian-Masouleh, S., Kynast, J., Arelin, K., Steele, C. J., Loffler, M., et al. (2019). Lesion location matters: the relationships between white matter hyperintensities on cognition in the healthy elderly. *J. Cereb. Blood Flow Metab.* 39, 36–43. doi: 10.1177/0271678X17740501

Lockhart, S. N., Luck, S. J., Geng, J., Beckett, L., Disbrow, E. A., Carmichael, O., et al. (2015). White matter hyperintensities among older adults are associated with futile increase in frontal activation and functional connectivity during spatial search. *PLoS One* 10:e0122445. doi: 10.1371/journal.pone.0122445

Longstreth, W. T. Jr., Manolio, T. A., Arnold, A., Burke, G. L., Bryan, N., Jungreis, C. A., et al. (1996). Clinical correlates of white matter findings on cranial magnetic resonance imaging of 3301 elderly people. the cardiovascular health study. *Stroke* 27, 1274–1282. doi: 10.1161/01.str.27.8.1274

Medendorp, W. P., Kramer, G. F., Jensen, O., Oostenveld, R., Schoffelen, J. M., and Fries, P. (2007). Oscillatory activity in human parietal and occipital cortex shows hemispheric lateralization and memory effects in a delayed double-step saccade task. *Cereb. Cortex* 17, 2364–2374. doi: 10.1093/cercor/bhl145

Pantoni, L., Basile, A. M., Pracucci, G., Asplund, K., Bogousslavsky, J., Chabriat, H., et al. (2005). Impact of age-related cerebral white matter changes on the transition to disability – the LADIS study: rationale, design and methodology. *Neuroepidemiology* 24, 51–62. doi: 10.1159/00008 1050

Park, D. C., Polk, T. A., Park, R., Minear, M., Savage, A., and Smith, M. R. (2004). Aging reduces neural specialization in ventral visual cortex. *Proc. Natl. Acad. Sci. U.S.A.* 101, 13091–13095. doi: 10.1073/pnas.0405148101

Power, J. D., Barnes, K. A., Snyder, A. Z., Schlaggar, B. L., and Petersen, S. E. (2012). Spurious but systematic correlations in functional connectivity MRI networks arise from subject motion. *Neuroimage* 59, 2142–2154. doi: 10.1016/j.neuroimage.2011.10.018

Power, J. D., Cohen, A. L., Nelson, S. M., Wig, G. S., Barnes, K. A., Church, J. A., et al. (2011). Functional network organization of the human brain. *Neuron* 72, 665–678.

Prins, N. D., van Dijk, E. J., den Heijer, T., Vermeer, S. E., Jolles, J., Koudstaal, P. J., et al. (2005). Cerebral small-vessel disease and decline in information processing speed, executive function and memory. *Brain* 128(Pt 9), 2034–2041. doi: 10.1093/brain/awh553

Reijmer, Y. D., Schultz, A. P., Leemans, A., O'Sullivan, M. J., Gurol, M. E., Sperling, R., et al. (2015). Decoupling of structural and functional brain connectivity in older adults with white matter hyperintensities. *Neuroimage* 117, 222–229. doi: 10.1016/j.neuroimage.2015.05.054

Reuter-Lorenz, P. A., and Park, D. C. (2014). How does it STAC up? Revisiting the scaffolding theory of aging and cognition. *Neuropsychol. Rev.* 24, 355–370. doi: 10.1007/s11065-014-9270-9

Satterthwaite, T. D., Elliott, M. A., Gerraty, R. T., Ruparel, K., Loughead, J., Calkins, M. E., et al. (2013). An improved framework for confound regression and filtering for control of motion artifact in the preprocessing of resting-state functional connectivity data. *Neuroimage* 64, 240–256. doi: 10.1016/j.neuroimage.2012.08.052

Schmidt, P., Gaser, C., Arsic, M., Buck, D., Forschler, A., Berthele, A., et al. (2012). An automated tool for detection of FLAIR-hyperintense white-matter lesions in multiple sclerosis. *Neuroimage* 59, 3774–3783. doi: 10.1016/j.neuroimage.2011.11.032

Schmidt, R., Berghold, A., Jokinen, H., Gouw, A. A., van der Flier, W. M., Barkhof, F., et al. (2012). White matter lesion progression in LADIS: frequency, clinical effects, and sample size calculations. *Stroke* 43, 2643–2647. doi: 10.1161/strokeaha.112.662593

Shi, L., Miao, X., Lou, W., Liu, K., Abrigo, J., Wong, A., et al. (2017). The spatial associations of cerebral blood flow and spontaneous brain activities with white matter hyperintensities-an exploratory study using multimodal magnetic resonance imaging. *Front. Neurol.* 8:593. doi: 10.3389/fneur.2017.00593

Sudo, F. K., Alves, C. E., Alves, G. S., Ericeira-Valente, L., Tiel, C., Moreira, D. M., et al. (2013). White matter hyperintensities, executive function and global cognitive performance in vascular mild cognitive impairment. *Arq. Neuropsiquiatr.* 71, 431–436. doi: 10.1590/0004-282X20130057

Sulpizio, V., Committeri, G., Lambrey, S., Berthoz, A., and Galati, G. (2016). Role of the human retrosplenial cortex/parieto-occipital sulcus in perspective priming. *Neuroimage* 125, 108–119. doi: 10.1016/j.neuroimage.2015.10.040

Sun, Y. W., Qin, L. D., Zhou, Y., Xu, Q., Qian, L. J., Tao, J., et al. (2011). Abnormal functional connectivity in patients with vascular cognitive impairment, no dementia: a resting-state functional magnetic resonance imaging study. *Behav. Brain Res.* 223, 388–394. doi: 10.1016/j.bbr.2011.05.006

Tononi, G., Edelman, G. M., and Sporns, O. (1998). Complexity and coherency: integrating information in the brain. *Trends Cogn. Sci.* 2, 474–484. doi: 10.1016/s1364-6613(98)01259-5

Tuladhar, A. M., ter Huurne, N., Schoffelen, J. M., Maris, E., Oostenveld, R., and Jensen, O. (2007). Parieto-occipital sources account for the increase in alpha activity with working memory load. *Hum. Brain Mapp.* 28, 785–792. doi: 10.1002/hbm.20306

van Dijk, E. J., Prins, N. D., Vrooman, H. A., Hofman, A., Koudstaal, P. J., and Breteler, M. M. (2008). Progression of cerebral small vessel disease in relation to risk factors and cognitive consequences: rotterdam scan study. *Stroke* 39, 2712–2719. doi: 10.1161/STROKEAHA.107.513176

Voss, M. W., Erickson, K. I., Chaddock, L., Prakash, R. S., Colcombe, S. J., Morris, K. S., et al. (2008). Dedifferentiation in the visual cortex: an fMRI investigation of individual differences in older adults. *Brain Res.* 1244, 121–131. doi: 10.1016/j.brainres.2008.09.051

Xu, X., Gao, Y., Liu, R., Qian, L., Chen, Y., Wang, X., et al. (2018). Progression of white matter hyperintensities contributes to lacunar infarction. *Aging Dis.* 9, 444–452. doi: 10.14336/AD.2017.0808

Ye, Q., Su, F., Gong, L., Shu, H., Liao, W., Xie, C., et al. (2017). Divergent roles of vascular burden and neurodegeneration in the cognitive decline of geriatric depression patients and mild cognitive impairment patients. *Front. Aging Neurosci.* 9:288. doi: 10.3389/fnagi.2017.00288

Zang, Y., Jiang, T., Lu, Y., He, Y., and Tian, L. (2004). Regional homogeneity approach to fMRI data analysis. *Neuroimage* 22, 394–400. doi: 10.1016/j.neuroimage.2003.12.030

Zhuang, F. J., Chen, Y., He, W. B., and Cai, Z. Y. (2018). Prevalence of white matter hyperintensities increases with age. *Neural Regen. Res.* 13, 2141–2146.

Zuo, X. N., Xu, T., Jiang, L., Yang, Z., Cao, X. Y., He, Y., et al. (2013). Toward reliable characterization of functional homogeneity in the human brain: preprocessing, scan duration, imaging resolution and computational space. *Neuroimage* 65, 374–386. doi: 10.1016/j.neuroimage.2012.10.017

Conflict of Interest Statement: The authors declare that the research was conducted in the absence of any commercial or financial relationships that could be construed as a potential conflict of interest.

Copyright © 2019 Ye, Chen, Qin, Huang, Yang, Liu, Zhang, Bai and Xu. This is an open-access article distributed under the terms of the Creative Commons Attribution License (CC BY). The use, distribution or reproduction in other forums is permitted, provided the original author(s) and the copyright owner(s) are credited and that the original publication in this journal is cited, in accordance with accepted academic practice. No use, distribution or reproduction is permitted which does not comply with these terms.

frontiers in Neuroscience

ORIGINAL RESEARCH
published: 03 July 2019
doi: 10.3389/fnins.2019.00642

Performing Sparse Regularization and Dimension Reduction Simultaneously in Multimodal Data Fusion

Zhengshi Yang[1], Xiaowei Zhuang[1], Christopher Bird[1], Karthik Sreenivasan[1], Virendra Mishra[1], Sarah Banks[1], Dietmar Cordes[1,2] and the Alzheimer's Disease Neuroimaging Initiative[†]*

[1] Cleveland Clinic Lou Ruvo Center for Brain Health, Las Vegas, NV, United States, [2] Departments of Psychology and Neuroscience, University of Colorado, Boulder, CO, United States

OPEN ACCESS

Edited by:
Daoqiang Zhang,
Nanjing University of Aeronautics and Astronautics, China

Reviewed by:
Babak A. Ardekani,
Nathan Kline Institute for Psychiatric Research, United States
Mingxia Liu,
University of North Carolina at Chapel Hill, United States

***Correspondence:**
Dietmar Cordes
cordesd@ccf.org

[†] Data used in preparation of this article were obtained from the Alzheimer's Disease Neuroimaging Initiative (ADNI) database (http://adni.loni.usc.edu/). As such, the investigators within the ADNI contributed to the design and implementation of ADNI and/or provided data but did not participate in analysis or writing of this report. A complete listing of ADNI investigators can be found at https://adni.loni.usc.edu/wp-content/uploads/how_to_apply/ADNI_Acknowledgement_List.pdf

Specialty section:
This article was submitted to Brain Imaging Methods, a section of the journal Frontiers in Neuroscience

Received: 14 January 2019
Accepted: 04 June 2019
Published: 03 July 2019

Citation:
Yang Z, Zhuang X, Bird C, Sreenivasan K, Mishra V, Banks S, Cordes D and the Alzheimer's Disease Neuroimaging Initiative (2019) Performing Sparse Regularization and Dimension Reduction Simultaneously in Multimodal Data Fusion. Front. Neurosci. 13:642. doi: 10.3389/fnins.2019.00642

Collecting multiple modalities of neuroimaging data on the same subject is increasingly becoming the norm in clinical practice and research. Fusing multiple modalities to find related patterns is a challenge in neuroimaging analysis. Canonical correlation analysis (CCA) is commonly used as a symmetric data fusion technique to find related patterns among multiple modalities. In CCA-based data fusion, principal component analysis (PCA) is frequently applied as a preprocessing step to reduce data dimension followed by CCA on dimension-reduced data. PCA, however, does not differentiate between informative voxels from non-informative voxels in the dimension reduction step. Sparse PCA (sPCA) extends traditional PCA by adding sparse regularization that assigns zero weights to non-informative voxels. In this study, sPCA is incorporated into CCA-based fusion analysis and applied on neuroimaging data. A cross-validation method is developed and validated to optimize the parameters in sPCA. Different simulations are carried out to evaluate the improvement by introducing sparsity constraint to PCA. Four fusion methods including sPCA+CCA, PCA+CCA, parallel ICA and sparse CCA were applied on structural and functional magnetic resonance imaging data of mild cognitive impairment subjects and normal controls. Our results indicate that sPCA significantly can reduce the impact of non-informative voxels and lead to improved statistical power in uncovering disease-related patterns by a fusion analysis.

Keywords: sparse principal component analysis, PCA, canonical correlation analysis, CCA, data fusion, mild cognitive impairment, MCI

INTRODUCTION

Collecting multiple modalities of neuroimaging data on the same subject is increasingly becoming the norm in clinical practice and research. Neuroimaging multi-modality data were traditionally analyzed and interpreted separately to find disease-related or task-related patterns in the brain. However, analyzing each modality independently does not necessarily find related patterns in both modalities. A single pattern in one modality might be related with a mixture of patterns in another modality. Fusing multiple modalities to find related patterns is a challenge in neuroimaging analysis. In the last decade, several techniques were proposed to utilize multiple imaging modalities,

including data integration (Savopol and Armenakis, 2002; Calhoun and Adal, 2009), asymmetric data fusion (Filippi et al., 2001; Kim et al., 2003; Henson et al., 2010) and symmetric data fusion techniques (Correa et al., 2008; Groves et al., 2011; Sui et al., 2011; Le Floch et al., 2012; Lin et al., 2014; Mohammadi-Nejad et al., 2017). A detailed review about these techniques can be found in Calhoun and Sui (2016). In the data integration technique, each dataset is analyzed independently, and, then, one dataset is overlaid on another without considering the interaction among datasets. Asymmetric data fusion utilizes one dataset to improve the analysis of another dataset. For example, Kim et al. (2003) used the foci of functional magnetic resonance imaging (fMRI) activation as seed points for Diffusion Tensor Imaging fiber reconstruction algorithms. Filippi et al. (2001) integrated conventional magnetic resonance imaging (MRI) and diffusion tensor MRI to better locate white matter lesions in multiple sclerosis subjects. Henson et al. (2010) constrained the electromagnetic sources of Magnetoencephalography and Electroencephalography (MEG, EEG) data with fMRI as empirical priors. Along with advantages of asymmetric data fusion techniques, asymmetric fusion omits the fact that each imaging modality has an essentially unique nature (Calhoun and Sui, 2016). In the symmetric data fusion method, multiple imaging modalities are analyzed conjointly to optimize the information contributed by each modality. Multiple imaging modalities are combined to extract complementary information regarding the integrity of the underlying neural structures and networks (Calhoun and Sui, 2016). In this study, we focus on symmetric data fusion using two modalities. Unless explicitly stated, data fusion refers to symmetric data fusion.

Canonical correlation analysis (CCA) is a multivariate method of finding linear combinations of two multidimensional random variables to maximize their correlation (Hotelling, 1936). CCA and its extensions have been extensively utilized in data fusion to associate related patterns across multiple data. A few CCA-based fusion methods were proposed in the last decade, such as multimodal CCA (Correa et al., 2008), source CCA + joint ICA (Sui et al., 2010) and multimodal CCA + joint ICA (Sui et al., 2011). The variant of CCA with more than two datasets, multiset CCA, was also applied in data fusion (Correa et al., 2010). When CCA is directly applied to the original data in a fusion analysis, some of the canonical variables are perfectly correlated regardless of the association among data, since the feature space is usually high-dimensional and only relatively few observations (subjects) are available (Pezeshki et al., 2004). In the CCA-based fusion methods mentioned above, principal component analysis (PCA) was used to reduce the data dimension. More specifically, a set of principal components with the largest possible variances are found by PCA and then the projections of original data (scores) on the space spanned by principal components are the dimension-reduced input data for the fusion CCA algorithm.

PCA solves the singularity problem in these fusion methods but does not take into account that in many cases only a small proportion of voxels (features), called informative voxels (features), have contribution to the variance, and a large proportion are non-informative. If principal components were obtained with non-informative voxels (features) assigned to zero, the projections of original data on the space spanned by the major principal components are more robust to non-informative voxels and thus helps CCA to better match related patterns across modalities. For example, when fusion analysis is applied to the data acquired from mild cognitive impairment (MCI) subjects and normal controls (NC), brain regions engaged in memory, language, and judgment (e.g., hippocampus, medial temporal lobe, frontal lobe) should be significant in the disease-related patterns (Forsberg et al., 2008; Bai et al., 2009). Specifying non-informative voxels to have zero weight could be beneficial for matching disease-related patterns by a fusion analysis. In general, properly suppressing non-informative voxels will further improve the statistical power of fusion techniques. Even though imaging data can be masked with predetermined regions of interest (ROIs) to address the feature selection process and avoid problems arising from non-informative voxels, ROI selection requires typically unavailable prior knowledge about the disease and patient cohort.

Selection and suppression of non-informative features in principal components can be automated by implementing sparsity in the PCA algorithm, called *sparse* PCA (sPCA) (Zou et al., 2006; Witten et al., 2009). The sPCA method and its extensions have been applied in multiple fields, such as machine learning, pattern recognition, and bioinformatics (Zou et al., 2006; Shen and Huang, 2008; Witten et al., 2009; Jenatton et al., 2010). A brief review of sPCA can be found in Feng et al. (2016). When comparing sPCA+CCA with PCA+CCA, sPCA produces different scores because of the reoriented space spanned by the principal components and, thus, sPCA influences the subsequent CCA step in associating multiple modalities.

Unlike sPCA+CCA having feature selection prior to fusing datasets, sparse CCA (sCCA) (Parkhomenko et al., 2009; Witten and Tibshirani, 2009; Lê Cao et al., 2011; Abdel-Rahman et al., 2014; Avants et al., 2014) has feature selection and data fusion applied at the same time. In this study, the sPCA+CCA method is compared with the sCCA method.

In the following, we first describe the theory behind sPCA and outline how to implement the sPCA algorithm. Then, we develop a cross-validation algorithm to optimally specify the sparsity parameter and the number of major principal components in sPCA. Then, we evaluate the improvement by introducing sparsity constraint to PCA using simulated data. Considering mild cognitive impairment (MCI) impacts both the function and structure in certain regions of the brain (Chetelat et al., 2002; Rombouts et al., 2005), we apply four fusion methods including sPCA+CCA, PCA+CCA [called multimodal CCA in Correa et al. (2008)], sCCA (Witten et al., 2009) and parallel ICA (Liu et al., 2009) on structural and functional MRI data of mild cognitive impairment (MCI) subjects and normal controls (NC), with the hypothesis to find disease-related association between these two modalities. Since disease-related features are visible in all modalities to varying degrees (Groves et al., 2011), fusion methods can match disease-related patterns in a two-group setting. Hence, the group discrimination and the correlation with β-amyloid measurement can be used to evaluate how well fusion methods match disease-related patterns across modalities.

THEORY

Sparse Principal Component Analysis (sPCA)

Derivation of sPCA

Let $\boldsymbol{X}$ denote an $n \times m$ feature matrix with $\text{rank}(\boldsymbol{X}) \leq \min(n, m)$, where n is the number of observations and m is the number of features in each observation. If $\boldsymbol{X}$ is a brain map, as in our case, n is the number of subjects and m is the number of voxels. PCA transforms a set of observations of correlated variables into a set of uncorrelated orthogonal variables called principal components that can be ordered according to the magnitude of their eigenvalues. The first K principal components can be determined by minimizing the least square problem (Eckart and Young, 1936), expressed as

$$f_{obj} = \min_{\widehat{\boldsymbol{X}} \in M(K)} \frac{1}{2} ||\boldsymbol{X} - \widehat{\boldsymbol{X}}||_F^2, \tag{1}$$

where $M(K)$ is a set of matrices with $\text{rank}(M) = K$ and $\|.\|_F^2$ means the squared Frobenius norm (see **Appendix A** in Supplementary Material for more detail). PCA is closely related to singular value decomposition (SVD). Using SVD, $\boldsymbol{X}$ can be decomposed into

$$\boldsymbol{X} = \boldsymbol{U}\boldsymbol{D}\boldsymbol{V}^T,\ \boldsymbol{U}^T\boldsymbol{U} = \boldsymbol{I}_K,\ \boldsymbol{V}^T\boldsymbol{V} = \boldsymbol{I}_K, \tag{2}$$

where $\boldsymbol{U} \in \mathbb{R}^{n \times K}$ *and* $\boldsymbol{V} \in \mathbb{R}^{m \times K}$ are the left and right singular vectors of $\boldsymbol{X}$ satisfying the orthonormality condition, and $\boldsymbol{D} = diag(d_1, \ldots, d_K) \in \mathbb{R}^{K \times K}$ is the diagonal matrix of ordered singular values of $\boldsymbol{X}$ with $d_1 \geq d_2 \geq \ldots \geq d_K > 0$. The optimal $\widehat{\boldsymbol{X}}$ in $M(K)$ can be written as

$$\widehat{\boldsymbol{X}} = \sum\nolimits_{i=1}^{K} d_i \boldsymbol{u}_i \boldsymbol{v}_i^T, \tag{3}$$

where $\boldsymbol{u}_i \in \mathbb{R}^{n \times 1}$ and $\boldsymbol{v}_i \in \mathbb{R}^{m \times 1}$ denote the i-th column vector of $\boldsymbol{U}$ and $\boldsymbol{V}$, respectively. Following the notation in SVD, the objective function f_{obj} for only one component can be written as

$$f_{obj}\left(d, \boldsymbol{u}, \boldsymbol{v}\right) = \frac{1}{2} \left\| \boldsymbol{X} - d\boldsymbol{u}\boldsymbol{v}^T \right\|_F^2,\ s.t.\ \|\boldsymbol{u}\|_2^2 = 1,\ \|\boldsymbol{v}\|_2^2 = 1,\ d > 0 \tag{4}$$

Considering that there are many voxels but few subjects, namely, $m \gg n$, the sparsity in our study is only implemented to set non-informative voxels to be zero. Because $\boldsymbol{V}$ is a set of voxel-wise spatial maps, sparsity was incorporated into the projection vector $\boldsymbol{v}_i$ but not the score vector $\mathbf{u}_i$, which is different than the sPCA method in Witten et al. (2009), who applied sparsity constraint on both singular vectors $\boldsymbol{u}$ and $\boldsymbol{v}$. For this reason, we derived the sPCA formula with an L_1 penalty on variable $\mathbf{v}$ added to the $f_{obj}\left(d, \mathbf{u}, \mathbf{v}\right)$ in Equation (4):

$$f_{obj}\left(d, \boldsymbol{u}, \boldsymbol{v}\right) = \frac{1}{2} \left\| \boldsymbol{X} - d\boldsymbol{u}\boldsymbol{v}^T \right\|_F^2,\ s.t.\ \|\boldsymbol{u}\|_2^2 = 1,\ \|\boldsymbol{v}\|_2^2 = 1,\ \|\boldsymbol{v}\|_1 \leq c,\ d > 0, \tag{5}$$

where the parameter c is the *sparsity tuning parameter*. A smaller c means that more elements in the principal component $\boldsymbol{v}$ are set to zero and the principal component becomes sparser. We would like to emphasize that sPCA has the elastic penalty consisting of the L_1 and L_2 penalty as shown in **Appendix B** in Supplementary Material, and, thus, the principal components from sPCA are well-defined and unique even when $m \gg n$ (Zou et al., 2006). Following the derivation in **Appendix A** in Supplementary Material, Equation (5) can be rewritten as:

$$\underset{\boldsymbol{u},\boldsymbol{v}}{\text{maximize}}\ d = \boldsymbol{u}^T\boldsymbol{X}\boldsymbol{v},\ s.t.\ \|\boldsymbol{u}\|_2^2 = 1,\ \|\boldsymbol{v}\|_2^2 = 1,\ \|\boldsymbol{v}\|_1 \leq c. \tag{6}$$

As shown by Witten et al. (2009), if $\boldsymbol{u}$ or $\boldsymbol{v}$ is fixed, the criterion in Equation (6) is a convex problem in $\boldsymbol{v}$ or $\boldsymbol{u}$.Thus, Equation (6) represents a biconvex problem. Because a convex problem can be solved reliably and efficiently, we solve Equation (6) by converting the equation into two convex sub-problems with **u** and **v** *alternatingly* fixed.

Iterative Algorithm for sPCA

Equation (6) is solved by an iterative algorithm modified based on the sPCA algorithm in Witten et al. (2009). We start with an initial value $\boldsymbol{u} = \frac{\boldsymbol{u}}{\|\boldsymbol{u}\|_2}$ and then update **v** to maximize $\boldsymbol{u}^T\boldsymbol{X}\boldsymbol{v}$ as expressed below

$$\underset{\boldsymbol{v}}{\text{maximize}}\ \boldsymbol{a}^T\boldsymbol{v}\ s.t.\ \|\boldsymbol{v}\|_2^2 = 1,\ \|\boldsymbol{v}\|_1 \leq c,\ \boldsymbol{a} = \boldsymbol{X}^T\boldsymbol{u}. \tag{7}$$

Appendix C in Supplementary Material shows that the optimal solution in Equation (7) is $\boldsymbol{v} = \frac{S(\boldsymbol{a},\mu)}{\|S(\boldsymbol{a},\mu)\|_2}$. The function S is the (vector-valued) soft threshold function given by $S(\boldsymbol{a}, \mu) = sign(\boldsymbol{a}) \max(0, |\boldsymbol{a}| - \mu)$, where the *sign* (.) and |.| operation act on each element of vector $\boldsymbol{a}$. If $\mu = 0$ satisfies $\|\boldsymbol{v}\|_1 \leq c$, then $\boldsymbol{v} = \frac{\boldsymbol{a}}{\|\boldsymbol{a}\|_2}$. Otherwise, μ is determined efficiently by a binary search algorithm to have $\|\boldsymbol{v}\|_1 = c$. At a fixed $\boldsymbol{v}$, Equation (6) becomes

$$\underset{\boldsymbol{u}}{\text{maximize}}\ \boldsymbol{u}^T\boldsymbol{b}\ s.t.\ \|\boldsymbol{u}\|_2^2 = 1,\ \boldsymbol{b} = \boldsymbol{X}^T\boldsymbol{v}. \tag{8}$$

The optimal $\boldsymbol{u}$ is simply the unit vector along direction $\boldsymbol{b}$, namely, $\boldsymbol{u} = \frac{\boldsymbol{b}}{\|\boldsymbol{b}\|_2} = \frac{\boldsymbol{X}\boldsymbol{v}}{\|\boldsymbol{X}\boldsymbol{v}\|_2}$. The alternating iteration stops when a convergence criterion is satisfied. Then $\boldsymbol{X}$ is updated by removing the variance contained in the previous principal component by $\boldsymbol{X} \leftarrow \boldsymbol{X} - d\boldsymbol{u}\boldsymbol{v}^T$, and the next pair of $\boldsymbol{u}$ and $\boldsymbol{v}$ is computed by the same iterative algorithm until K principal components are found.

Parameters Selection in sPCA by Split-Sample Cross Validation

A ten-fold cross validation method is used to estimate the parameters in sPCA, including the optimal sparsity tuning parameter c^* and the best number of principal components K^*. The flow chart for the *split-sample cross validation method* is shown in **Figure 1**. For data matrix $\boldsymbol{X}$, each subject is randomly assigned to one fold. Let $\boldsymbol{X}^{(f)}$ denote the data from the subjects assigned in the f-fold dataset and $\boldsymbol{X}^{(\bar{f})}$ denote the data except the data in the f-fold dataset. Principal components are computed from matrix $\boldsymbol{X}^{(\bar{f})}$, and then these principal components are applied on $\boldsymbol{X}^{(f)}$ to estimate parameters based on a selection criterion, and, finally, the mean value of the

estimated parameters in each fold of the data is used for fusion analysis. Mathematically, K-factor sPCA is applied on matrix $\boldsymbol{X}^{(\bar{f})}$ by $\boldsymbol{X}^{(\bar{f})} \rightarrow \boldsymbol{U}^{(\bar{f})}\boldsymbol{D}^{(\bar{f})}\boldsymbol{V}^{(\bar{f})^T}$ where $\boldsymbol{U}^{(\bar{f})} = [\boldsymbol{u}_1^{(\bar{f})}, \ldots, \boldsymbol{u}_K^{(\bar{f})}]$, $\boldsymbol{V}^{(\bar{f})} = [\boldsymbol{v}_1^{(\bar{f})}, \ldots, \boldsymbol{v}_K^{(\bar{f})}]$ and $\boldsymbol{D}^{(\bar{f})} = diag\left(d_1^{(\bar{f})}, \ldots, d_K^{(\bar{f})}\right)$. Then, the principal components $\boldsymbol{V}^{(\bar{f})}$ are used as regressors in a linear regression model to fit each sample in the untouched data $\boldsymbol{X}^{(f)}$, namely, $\boldsymbol{\beta} = \boldsymbol{V}^{\left(\bar{f}\right)^+}\boldsymbol{X}^{(f)^T}$ and $\widehat{\boldsymbol{X}}^{(f)} = \left(\boldsymbol{V}^{\left(\bar{f}\right)}\boldsymbol{\beta}\right)^T$. The Akaike Information Criterion (*AIC*) (Akaike, 1974; Shumway et al., 2000) is used to evaluate how close the reconstructed matrix $\widehat{\boldsymbol{X}}^{(f)}$ is to $\boldsymbol{X}^{(f)}$. The *AIC* provides a tradeoff between goodness-of-fit (minimum log-likelihood) and complexity of the model (Sui et al., 2010). Witten et al. (2009) used the mean-square-error (MSE) as the criterion in a cross-validation method that is based on an imputation algorithm (Troyanskaya et al., 2001). The optimal sparsity tuning parameter c^* was selected by minimizing MSE with only the first principal component ($K = 1$) considered. This method cannot estimate the number of principal components K^* since MSE always decreases with increasing K. We have revised the cross-validation method in Witten et al. (2009) with *AIC* as the criterion and compared *AIC* with the split-sample cross-validation method. We found that the split-sample method is more reliable and accurate in estimating parameters. **Appendix D** in Supplementary Material describes the calculation of *AIC* and the comparison of these two cross-validation methods in more detail. Let $\{c^{(f)}, K^{(f)}\}$ denote the parameters having minimum *AIC* for the f-fold cross-validation, the optimal sparsity tuning parameter c^* is defined as the average over $c^{(f)}$, and the optimal number of principal components K^* is the rounded integer of the average over $K^{(f)}$. The estimated parameter set $\{c^*, K^*\}$ is used in the sPCA+CCA fusion analysis.

sPCA+CCA

In sPCA+CCA, PCA is replaced by sPCA for dimension-reduction. The sPCA method is applied to reduce the data dimension for each modality separately, i.e., $\boldsymbol{X}_r \rightarrow \widehat{\boldsymbol{X}}_r = \boldsymbol{U}_r\boldsymbol{D}_r\boldsymbol{V}_r^T, \quad r = 1, 2$. In this step, the sparsity tuning parameter c_r^*, r = 1,2, and the number of principal components K_r^*, r = 1,2, are optimized for each modality by using the split-sample cross-validation method described in section Parameters Selection in sPCA by Split-Sample Cross Validation. The dimension-reduced dataset $\boldsymbol{Y}_r \in R^{n \times K_r^*}$ is the principal component score given by

$$\boldsymbol{Y}_r = \widehat{\boldsymbol{X}}_r V_r, \quad r = 1, 2. \tag{9}$$

Then, CCA is applied to link the data $\boldsymbol{Y}_1$ and $\boldsymbol{Y}_2$ by maximizing the canonical correlation between $\boldsymbol{Y}_1\boldsymbol{Z}_1$ and $\boldsymbol{Y}_2\boldsymbol{Z}_2$, where $\boldsymbol{Z}_r, r = 1, 2$, denote the canonical transformation matrices. The resulting canonical variates $\boldsymbol{A}_r = \boldsymbol{Y}_r\boldsymbol{Z}_r$ are called modulation profiles. Only the matched modulation profiles between datasets are correlated, and all other modulation profiles are uncorrelated, i.e.,

$$\begin{aligned} \boldsymbol{A}_{1d}^T\boldsymbol{A}_{2d} &= \rho_d > 0, \; for \; d = 1, \ldots, D; D = \min(K_1^*, K_2^*) \\ \boldsymbol{A}_{r_1 d_1}^T\boldsymbol{A}_{r_2 d_2} &= 0, \; \text{for } d_1 \neq d_2 \text{ and } r_1, r_2 \in \{1, 2\}, \end{aligned} \tag{10}$$

where ρ_d is the canonical correlation between $\boldsymbol{A}_{1d}$ and $\boldsymbol{A}_{2d}$. Finally, the spatial maps $\boldsymbol{C}_1$ and $\boldsymbol{C}_2$ corresponding to $\boldsymbol{A}_1$ and $\boldsymbol{A}_2$, respectively, are calculated by least square estimation according to

$$\boldsymbol{C}_r = \boldsymbol{A}_r^+\widehat{\boldsymbol{X}}_r, \quad r = 1, 2 \tag{11}$$

where the "+" superscript indicates the Moore-Penrose pseudoinverse. In Equations (9) and (11) we could have used the original data matrix $\boldsymbol{X}_r$ instead of $\widehat{\boldsymbol{X}}_r$. A schematic flowchart of sPCA+CCA is shown in **Figure 2**.

MATERIALS AND METHODS

Simulation 1: sPCA vs. PCA

The simulation was carried out to evaluate whether sPCA is sensitive to the noise in the data at different sparsity levels. The simulated data $\boldsymbol{X}$ was generated based on the form $\boldsymbol{X} = \boldsymbol{Y}\boldsymbol{V}^T$, where $\boldsymbol{Y} = [\ldots, \boldsymbol{y_n}, \ldots]$ is the intrinsic principal component scores and $\boldsymbol{V} = [\ldots, \boldsymbol{v_n}, \ldots]$ is a set of orthogonal maps. The simulation consists of 80 samples and 3 intrinsic principal components, hence $\boldsymbol{Y}$ has a dimension of 80 × 3. To analyze whether the improvement made by introducing sparsity to PCA relates to the spatial sparsity level of the signal, we have simulated the data with sparsity levels of 30, 50, and 70%. Here, the sparsity level is defined as the percentage of zero elements in the map. **Figure 3** shows the principal component scores $\boldsymbol{Y}$ in **Figure 3A** and their corresponding spatial maps $\boldsymbol{V}$ at 70% sparsity level in **Figure 3B** without threshold. The images have a dimension of 91×109×3, and only the second slice of the spatial maps is shown.

Gaussian noise $\boldsymbol{N}$ was added to create noisy images and Gaussian smoothing with Full-Width-At-Half-Maximum (FWHM) of 8 mm was applied to introduce spatial correlation. The simulated data were generated with Peak Signal-to-Noise Ratio (PSNR) of 5, 10, and 15 dB, which are similar to the PSNRs used in Sui et al. (2010). PSNR is defined as

$$PSNR = 20 \; log_{10}\frac{maxval}{MSE}. \tag{12}$$

Here, *maxval* is the maximum possible pixel value and MSE is the mean squared error between noisy and noise-free images. A higher PSNR indicates a higher image quality. The simulation was carried out 100 times using the same $\boldsymbol{Y}$ and $\boldsymbol{V}$, but with different noise realizations.

Simulation 2: Comparison of Fusion Methods

The simulation was carried out with sparsity level 70% at moderate signal-to-noise ratio with PSNR=10 dB. The sparsity level used in the simulation is close to the estimated sparsity level in the real data as mentioned below in Parameter Selection section. Two simulated modalities were generated by following the steps described in section Simulation 1: sPCA vs. PCA except we replace the intrinsic principal component scores by modulation profile $\boldsymbol{A}_1$ and $\boldsymbol{A}_2$, respectively, for the first and second modality. The modulation profiles $\{\boldsymbol{A}_1, \boldsymbol{A}_2\}$ satisfy

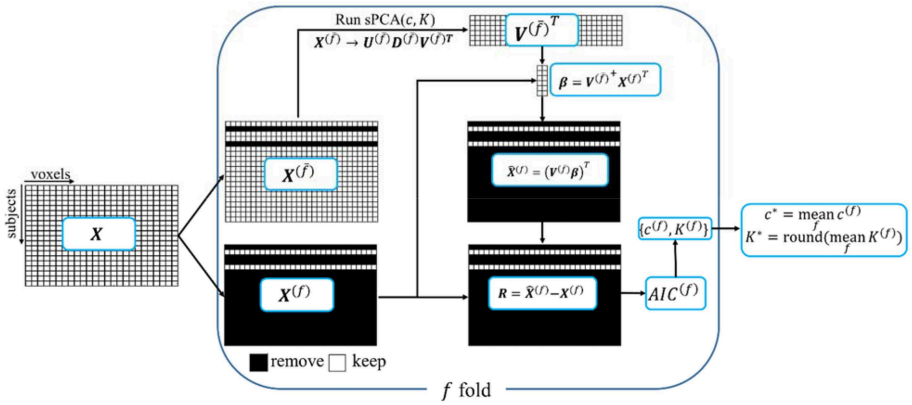

FIGURE 1 | A schematic diagram of the split-sample cross-validation method in sPCA. $\boldsymbol{X}$ is the data matrix. Each subject is randomly assigned to one fold, $\boldsymbol{X}^{(f)}$ denotes the data from the subjects assigned in $\boldsymbol{f}$-fold data and $\boldsymbol{X}^{(f)}$ denotes the data with $\boldsymbol{X}^{(f)}$ excluded. The "+" superscript indicates the Moore-Penrose pseudoinverse.

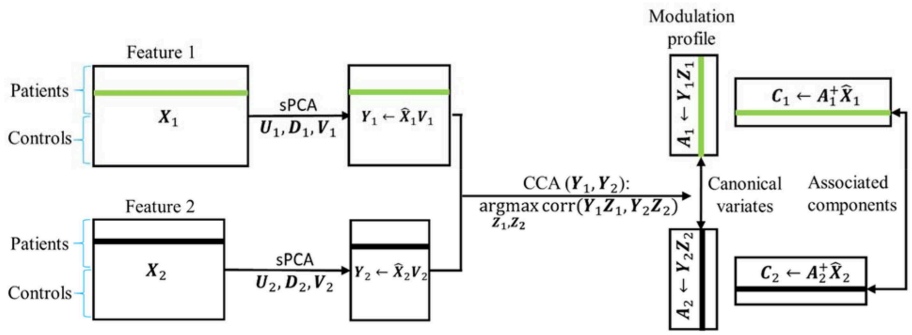

FIGURE 2 | Flow chart of sPCA+CCA. sPCA was carried out reduce data dimensions and to suppress irrelevant features. Then, CCA was carried out for fusion analysis to obtain modulation profiles and associated components. In the flow chart $\widehat{\boldsymbol{X}}_r = \boldsymbol{U}_r\boldsymbol{D}_r\boldsymbol{V}_r^T$ *with* $\boldsymbol{r} = 1, 2$, is the data matrix of the two modalities obtained from sPCA.

the orthogonality condition in Equation (10). The canonical correlations ρ between $\boldsymbol{A}_1$ (red curve) and $\boldsymbol{A}_2$ (black curve) are [0.70, 0.45, 0.22] as shown in **Figure 4A**. The three corresponding pairs of sparse spatial maps are shown in **Figure 4B**. The first pair of canonical variables in $\{\boldsymbol{A}_1, \boldsymbol{A}_2\}$ were simulated to be group-distinct using 40 subjects for each group. The simulation was carried out fifty times using the same modulation profiles and spatial maps, but with different noise realizations. The average performance is reported in the Result section.

MRI/fMRI Data and PET Analysis

Structural MRI and resting-state fMRI data used in this study were downloaded from the publicly available ADNI database. The ADNI was launched in 2003 as a public-private partnership, led by Principal Investigator Michael W. Weiner, MD. The primary goal of ADNI has been to test whether serial MRI, positron emission tomography (PET), other biological markers, and clinical and neuropsychological assessment can be combined to measure the progression of mild cognitive impairment (MCI) and early Alzheimer's disease (AD).

The resting-state fMRI data, T1 structural data, and corresponding clinical data were downloaded from the ADNI 2 database before September 18, 2016. All subjects used in this study had florbetapir (^{18}F) PET scans within 6 months of MRI scans. All MCI subjects had an absence of dementia (clinical dementia rating of 0.5), a memory complaint and objective memory loss measured by education adjusted scores on the Wechsler Logical Memory Scale II, an absence of significant levels of impairment in other cognitive domains and essentially had preserved activities of daily living. All subjects were scanned on a 3.0-Tesla Philips MRI scanner. The magnetization prepared rapid acquisition gradient echo (MP-RAGE) sequence was used to acquire T1-weighted structural images by the investigators of the ADNI consortium. The structural MRI scans were collected with a 24 cm field of view and a resolution of 256 × 256 × 170, to yield a voxel size of 1 × 1 × 1.2 mm. Resting-state fMRI data were acquired from an echo-planar imaging sequence with parameters: 140 time points; TR/TE = 3000/30 ms; flip angle = 80 degrees; 48 slices; spatial resolution = 3.3 mm × 3.3 mm × 3.3 mm and imaging matrix = 64 × 64. Details of

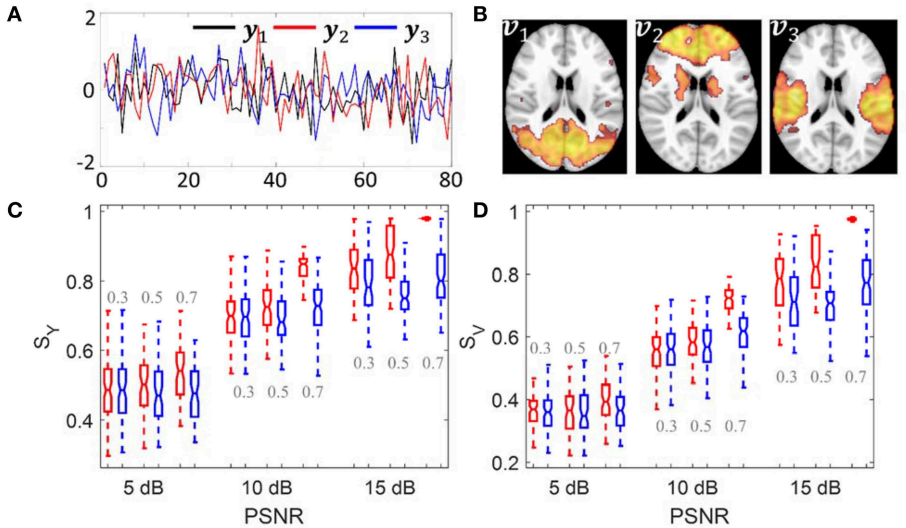

FIGURE 3 | Simulation 1: Comparison of sPCA and PCA. **(A)** Simulated principal component scores $\boldsymbol{Y} = [\boldsymbol{y}_1, \boldsymbol{y}_2, \boldsymbol{y}_3]$. **(B)** The spatial maps $\boldsymbol{V} = [\boldsymbol{v}_1, \boldsymbol{v}_2, \boldsymbol{v}_3]$ corresponding to the scores with 70% voxels having zero values. Simulated data were generated 100 times with PSNR as 5 dB, 10 dB and 15 dB and sparsity level as 0.3, 0.5, and 0.7. **(C)** Boxplot for the similarity value with true principal component scores $\boldsymbol{S}_Y$. **(D)** Boxplot for the similarity value with true spatial maps $\boldsymbol{S}_V$. The boxplot for sPCA is shown in red and for PCA in blue.

the ADNI MRI protocol can be found on ADNI website (http://adni.loni.usc.edu/). If one subject had multiple MRI/fMRI scans satisfying the requirements specified above, the first available MRI/fMRI data set was used for analysis. The Standard Uptake Value Ratio (SUVR) analysis was carried out to measure ß-amyloid on ADNI florbetapir PET scans by site investigators and the SUVR data using a composite reference regions were downloaded from the ADNI website. The correlation between SUVR measurement and the result of fusion methods was used to evaluate the performance of different fusion methods. In total, 37 MCI subjects (age = 73.7 ± 6.7 years; gender = 19 female/18 male) and 42 NC subjects (age = 75.0 ± 7.3 years; gender = 24 female/18 male) were selected.

FMRI Data

Preprocessing

The first 5 volumes were excluded from the analysis. The fMRI time series were slice-timing corrected and realigned to the first volume using SPM12, co-registered to the individual T1 images and then normalized to the MNI152 2 mm template using Advanced Normalization Tools (ANTs) (http://stnava.github.io/ANTs/). Nuisance regression was carried out with six head motion parameters along with signals extracted from white matter and CSF [3-mm radius spheres centered at MNI coordinates (26, −12, 35) and (19, −33, 18)] (Chen et al., 2015). The resulting time series were smoothed further with a 10-mm Gaussian kernel and band-pass filtered to be in the frequency range 0.01–0.1 Hz. These steps were computed with MATLAB (The Mathworks, Inc., version R2015a).

Eigenvector Centrality Mapping (ECM)

Many studies have shown that graph-theoretical analysis methods can help elucidate the disruption of brain network structure in patients compared to normal controls (He and Evans, 2010; Power et al., 2011). In graph theory and network analysis, centrality is a measure of importance of a node in the graph (Bavelas, 1948). We used eigenvector centrality mapping (ECM) to analyze functional networks. ECM is an assumption-free non-parametric method that can efficiently carry out voxel-wise whole brain nodal analysis. A variant of eigenvector centrality that has been applied successfully is Google's PageRank algorithm (Bryan and Leise, 2006), which is used as the Google search engine.

In the ECM algorithm, a $m \times m$ similarity matrix (for example a correlation map between voxel-wise time series) is constructed and the eigenvector centrality map is the eigenvector corresponding to the largest eigenvalue of the similarity matrix. Here, the value at node (voxel) i is defined as the i-th entry in the normalized eigenvector. Because the normalization step in ECM reduces the centrality value in a map with more nodes, a group mask with the same nodes is used for all subjects when applying ECM on fMRI data. Individual masks were first calculated by thresholding the mean fMRI signal intensity at 10% of the maximal mean signal intensity for each individual subject, and then the group mask was chosen to be the intersection of all individual masks and the MNI152 gray matter mask. The ECM maps of resting-state fMRI time series for all subjects were calculated using the Fast ECM algorithm (Wink et al., 2012). Unlike the basic ECM algorithm, the Fast ECM algorithm can estimate voxel-wise eigenvector centralities computationally more efficiently because the Fast ECM computes matrix-vector products directly from the data without explicitly storing the correlation matrix. The 3D ECM map of each subject was masked and reshaped to a one-dimensional vector with 128257 non-zero voxels and the ECM maps of all subjects were represented as a two-dimensional array of dimension 79 × 128257. The ECM maps were corrected by regressing out the effects of age, gender

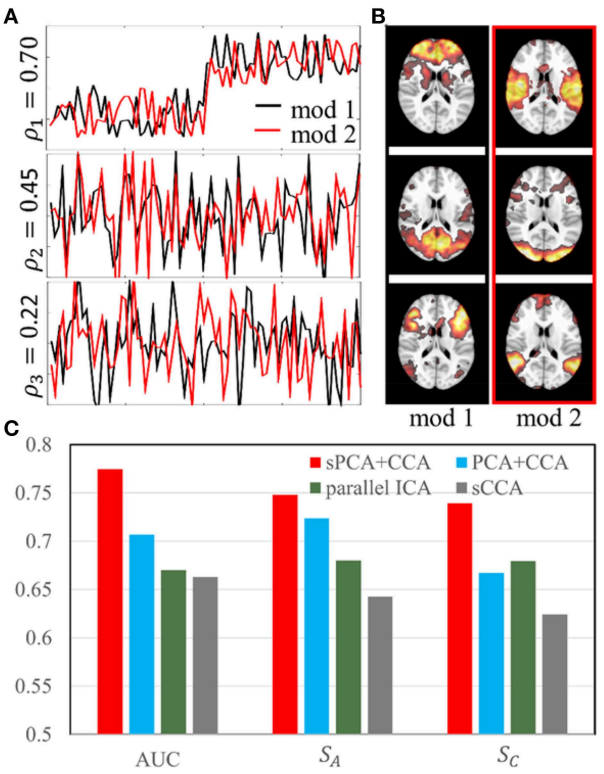

FIGURE 4 | Simulation 2: Comparison of fusion methods. **(A)**. Three pairs of simulated modulation profiles satisfying the orthogonality condition. **(B)**. Simulated spatial maps at sparsity level 70%. **(C)** Bar plot of the **AUC** measurement, similarities ($\mathbf{S}_A$) between estimated and true modulation profiles, and their corresponding spatial maps ($\mathbf{S}_C$).

and handedness. The corrected ECM matrix, denoted as $\mathbf{X}_{ECM}$, was used for fusion analysis.

T1 Images

Voxel-Based Morphometry (VBM)

VBM is a common automated brain segmentation technique that is used to investigate structural brain difference (volume differences) among different populations (Ashburner and Friston, 2000). A standard VBM processing routine was created with the SPM12-DARTEL toolbox (Ashburner, 2007). The following processing steps were carried out for VBM: (a) the raw T1 structural images were bias-corrected for inhomogeneities, brain-extracted and segmented ("Native+DARTEL imported" is selected in "Native Tissue" option) into gray mater, white mater and cerebrospinal fluid probability maps; (b) a customized template was created using the SPM12-DARTEL "create template" module; (c) gray mater volumes for all subjects were normalized and registered to the MNI152 2 mm template using the final DARTEL template in "create template" module and finally smoothed using an 8 mm FWHM Gaussian filter. The 3D VBM map of each subject was masked and reshaped to a one-dimensional vector of 171705 non-zero voxels and the VBM maps of all subjects were represented as a two-dimensional array of dimension 79 x 171705. The VBM maps were corrected by regressing out the effects of age, gender and handedness. The corrected VBM matrix, denoted as $\mathbf{X}_{VBM}$, constitute the other modality used for fusion analysis.

sPCA+CCA, PCA+CCA, sCCA, and Parallel ICA

To see the improvement achieved by replacing PCA with sPCA, both sPCA+CCA and PCA+CCA were performed on simulated and real imaging data. In addition, sPCA+CCA was also compared with parallel ICA using the Fusion ICA Toolbox (FIT, http://mialab.mrn.org/software/fit/). Furthermore, a comparison with *sparse* CCA (sCCA) was carried out.

Parallel ICA

Similar to ICA computing maximally independent components in one dataset, parallel ICA finds the hidden independent components from two datasets simultaneously with the association between modalities considered (Liu et al., 2009). Parallel ICA is realized by jointly maximizing the independence among components in each modality and the correlations between modalities in a *single* algorithm. The maximal number of correlated components n_{cc} are pre-defined and only the correlation above threshold ρ_{thre} is considered. More detailed description can be found in Liu et al. (2009) and the fusion ICA toolbox (Fulop and Fitz, 2006) (http://mialab.mrn.org/software/fit/) documentation. Parallel ICA was carried out with standard PCA and the default "AA" parallel ICA algorithm using the FIT toolbox. Parallel ICA was repeated ten times for consistency. The default ICA options were used in the analysis. The maximally allowed descending trend of entropy was −0.001, the maximum number of steps was 512 and the default learning rates (0.0063, 0.0065) were used. Since the performance of parallel ICA depends on the hyperparameters including the maximal number of correlated components n_{cc} and the correlation threshold ρ_{thre}, we have used five pairs of hyperparameters, $\{n_{cc}, \rho_{thre}\}$=$\{1, 0.2\}$, $\{1, 0.4\}$, $\{3, 0.3\}$, $\{5, 0.2\}$, and $\{5, 0.4\}$ for both simulated and real data. The best performance was used to compare with other fusion methods.

Sparse CCA (sCCA)

Unlike the sPCA+CCA method that enforces sparsity during the dimension reduction step, sCCA associates the original data $\boldsymbol{X}_1$ and $\boldsymbol{X}_2$ directly with a *sparsity constraint applied on the canonical transformation matrices*. The obtained transformation matrices and the canonical variates present the spatial maps $\boldsymbol{C}_r$ and the modulation profiles $\boldsymbol{A}_r$, respectively. The iterative algorithm for sCCA is described in detail in Witten et al. (2009).

Parameter Selection

To avoid overfitting, we carried out parameter selection for all fusion methods. The number of sparse principal components used in sPCA+CCA was determined by the AIC-based *split-sample cross-validation method* described in section Parameters Selection in sPCA by Split-Sample Cross Validation. For the ECM and VBM modalities, the optimal numbers of principal components were 10 and 7, respectively, and the optimal

sparsity levels were 70 and 80%, respectively. The same cross-validation method was also used to determine the number of conventional principal components in PCA+CCA and in parallel ICA by simply replacing sPCA with the standard PCA algorithm. 7 ECM principal components and 6 VBM principal components were found for these two fusion methods. While minimizing MSE based on CCA potentially can be used to select the parameters in sPCA+CCA or PCA+CCA as suggested by Lameiro and Schreier (2016), the high dimensionality of the data and the SVD over a large cross-covariance matrix makes this parameter selection method infeasible for our study because of computational time and memory. The optimal sparsity tuning parameter in sCCA was estimated by the cross-validation method presented in Witten and Tibshirani (2009). With this method, the optimal sparsity level is 73% for the ECM dataset and 79% for the VBM dataset.

To compare how well the sPCA and PCA methods extract the intrinsic principal component scores $\boldsymbol{Y}^{true}$ and the spatial maps $\boldsymbol{V}^{true}$ in simulation 1, the similarity between the estimated and the true scores and maps were computed at different noise levels by following equation

$$S_Y = \frac{\sum_{d=1}^{3} \left| corr\left(\boldsymbol{y_d^{true}}, \boldsymbol{y_d^{est}}\right)\right|}{3} \in [0,1],$$
$$S_V = \frac{\sum_{d=1}^{3} \left| corr\left(\boldsymbol{v_d^{true}}, \boldsymbol{v_d^{est}}\right)\right|}{3} \in [0,1]. \quad (13)$$

The similarity value S_Y close to 1 indicates that the estimated $\boldsymbol{Y}^{est}$ agrees well with the true scores $\boldsymbol{Y}^{true}$. Similarly, the similarity value S_V close to 1 indicates that the estimated $\boldsymbol{V}^{est}$ agrees well with the true spatial maps $\boldsymbol{V}^{true}$.

When comparing the fusion methods in simulation 2, the evaluation is focused on how well these methods distinguish two groups and uncover the modulation profiles and their corresponding spatial maps. The receiver operating characteristic (ROC) was used to evaluate group classification and the area under ROC curves (AUC) were calculated. The similarity between true modulation profiles $\boldsymbol{A}_r^{true}$ and the estimated one, $\boldsymbol{A}_r^{est}$, was computed, namely,

$$S_A = \frac{\sum_{r=1}^{2}\sum_{d=1}^{3} \left| corr\left(\boldsymbol{A}_{rd}^{true}, \boldsymbol{A}_{rd}^{est}\right)\right|}{6} \in [0,1],$$
$$S_C = \frac{\sum_{r=1}^{2}\sum_{d=1}^{3} \left| corr\left(\boldsymbol{C}_{rd}^{true}, \boldsymbol{C}_{rd}^{est}\right)\right|}{6} \in [0,1]. \quad (14)$$

The similarity for spatial maps $\boldsymbol{C}_r^{est}$ as defined in Equation (11) was also computed. Furthermore, we used the correlation error $\rho = \sum_{d=1}^{3}(\rho_d^{true} - \rho_d^{est})$ to measure how close the estimated correlation $\boldsymbol{\rho}^{est}$ and intrinsic (true) correlation $\boldsymbol{\rho}^{true}$ are. A positive sign of $\Delta\rho$ indicates that overall the correlation is underestimated and a negative sign indicates the correlation is overestimated.

For the real imaging data, the ECM array $\boldsymbol{X}_{ECM}$ and VBM array $\boldsymbol{X}_{VBM}$ were used for fusion analysis. Two sample t-tests with unequal variances were applied on modulation profiles $\boldsymbol{A}_{ECM}$ and $\boldsymbol{A}_{VBM}$. ROC analysis was carried out on modulation profiles $\boldsymbol{A}_{ECM}$ and $\boldsymbol{A}_{VBM}$ to determine how well fusion methods extract disease-related modulation profiles and corresponding patterns, and the *AUC* for each modality also was calculated.

RESULTS

Simulations

Conventional PCA and sPCA were carried out 100 times on a series of simulated data with PSNR as 5 dB, 10 and 15 dB and the sparsity level as 30, 50, and 70%. The boxplot for similarity values S_Y and S_V of sPCA (red color) and PCA (blue color) were shown in **Figure 3C** and **Figure 3D**. When the sparsity level and PSNR is low (e.g., sparsity level = 30% and PSNR = 5 dB), the improvement by introducing sparsity constraint is negligible. With increasing PSNR or sparsity level, sPCA outperforms PCA in uncovering the true principal component scores and corresponding spatial maps.

In simulation 2, fusion analysis was carried out fifty times on the simulated data with PSNR 10 dB and sparsity level 70%. **Figure 4C** shows the mean value of AUC, S_A and S_C for these four fusion methods including sPCA+CCA, PCA+CCA, parallel ICA and sCCA. The sPCA+CCA has the best performance among these fusion methods. Compared to PCA+CCA, sPCA+CCA has improved measurements of AUC and S_C by approximately 10%. The correlation error $\Delta\rho$ for sPCA+CCA, PCA+CCA, parallel ICA and sCCA are 0.11, 0.16, 0.17, and −0.35, respectively. Results indicate that sPCA+CCA achieves correlations closest to the simulated correlations, and sCCA significantly overestimates the correlation while all other fusion methods underestimate the correlation.

Real fMRI Data

sPCA vs. PCA

The principal components having largest variance from sPCA and PCA are shown in **Figure 5** without threshold for the ECM maps (**Figure 5A**) and VBM maps (**Figure 5B**). The color bars are different for these spatial maps to better visually represent the principal components. The ECM principal component obtained from sPCA shows a clear default mode network (DMN) pattern and the VBM principal component have non-zero voxels centered at the hippocampus. Compared to the spatial maps of PCA, sPCA has similar principal component maps but with a large proportion of voxels removed. A group comparison of the principal component scores from sPCA and PCA on ECM and VBM modality is applied. The sPCA method has achieved the most significant group difference with uncorrected p-value 0.01 and 0.008 on ECM and VBM modality, respectively. In contrast, PCA has obtained less significant group difference with uncorrected p-value 0.03 and 0.02 on ECM and VBM modality, respectively.

Fusion Analysis

For each fusion method, the modulation profiles $\boldsymbol{A}_{ECM}$ and $\boldsymbol{A}_{VBM}$ were calculated and two-sample t-tests with unequal variance were carried out to assess group difference. The ROC technique was applied on modulation profiles $\boldsymbol{A}_{ECM}$ and $\boldsymbol{A}_{VBM}$, and the AUC was calculated. Group classification accuracy was also

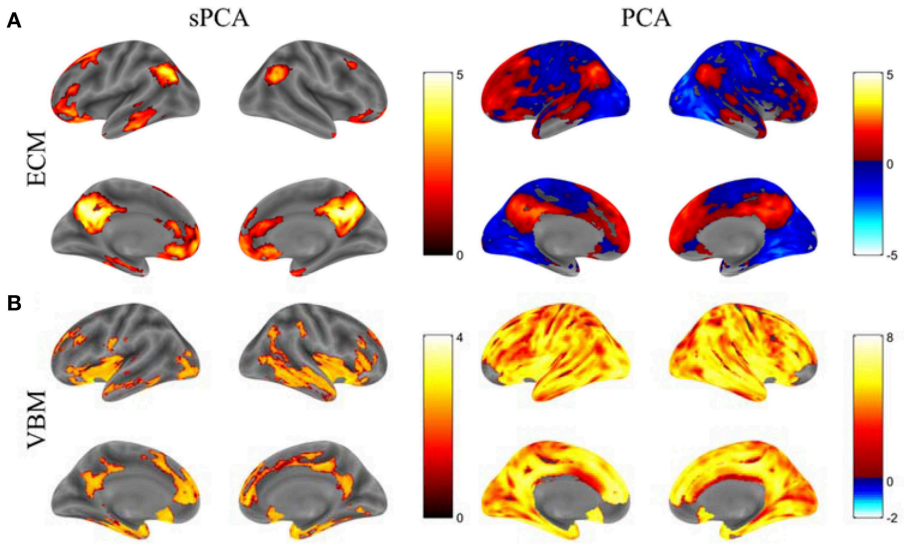

FIGURE 5 | The standardized principal component maps having largest variance from sPCA and PCA. **(A)** ECM principal component, **(B)** VBM principal component.

calculated by running ten-fold quadratic discriminant analysis (QDA) on modulation profiles from both ECM and VBM modalities. The most significant component of $\boldsymbol{A}_{ECM}$ or $\boldsymbol{A}_{VBM}$ from two-sample t-tests always had the largest AUC value. The AUC and Bonferroni-corrected p value for multiple comparisons, denoted as p_{corr}, of the most significant components are shown in **Table 1**. The correlation between the most significant components is also listed in this table. sPCA+CCA found one significant component in both ECM and VBM data (ECM: $p_{corr} = 3.4 \times 10^{-4}$, $AUC = 0.78$; VBM: $p_{corr} = 2.6 \times 10^{-4}$, $AUC = 0.81$). sPCA+CCA associated these two significant components at the 1st pair of canonical variates with canonical correlation $\rho = 0.78$. PCA+CCA found one significant component in both ECM and VBM data ($ECM: p_{corr} = 2.9 \times 10^{-2}$, $AUC = 0.71$; VBM: $p_{corr} = 2.0 \times 10^{-3}$, $AUC = 0.73$). PCA+CCA associated these two significant components at the 1st pair of canonical variates with canonical correlation $\rho = 0.48$. Parallel ICA found one significant component in VBM but not in the ECM data (ECM: $p_{corr} = 0.10$, $AUC = 0.68$; VBM: $p_{corr} = 1.8 \times 10^{-3}$, $AUC = 0.75$). The correlation between the most significant component in ECM and VBM was $\rho = 0.27$. sCCA found two significant ECM components and one VBM component (ECM: $p_{corr} = 1.3 \times 10^{-2}$, $AUC = 0.70$ and $p_{corr} = 4.7 \times 10^{-2}$, $AUC = 0.55$; VBM: $p_{corr} = 1.6 \times 10^{-2}$, $AUC = 0.70$). The correlation between the most significant component in ECM and VBM was $\rho = 0.80$. Among these four fusion methods, sPCA+CCA achieved the highest group classification accuracy 0.68, which was more than 99-percentile of the null distribution. The classification accuracy with concatenated ECM and VBM principal component scores *without fusion* as input features to QDA was 0.57.

The spatial patterns for these four fusion methods were also computed for sPCA+CCA and PCA+CCA by using Equation (11). ECM z-score spatial patterns corresponding to the most significant components in $\boldsymbol{A}_{ECM}$ are shown in **Figure 6**. All spatial maps were thresholded at $z \geq 1.5$ except the one from parallel ICA. The ECM spatial map from parallel ICA only showed an artifact on the brain boundary if thresholded at $z \geq 1.5$, hence the threshold was lowered to $z \geq 1$ for better interpretation. Anterior cingulate cortex (Bianciardi et al., 2009) was shown in the spatial patterns for all fusion methods. Both PCA+CCA and parallel ICA show some artifacts at the boundary of the brain. Bilateral superior temporal gyrus and bilateral amygdala were found in the ECM spatial pattern from sPCA+CCA.

VBM z-score maps corresponding to the most significant components in $\boldsymbol{A}_{VBM}$ are shown in **Figure 7**. The spatial maps were thresholded at $z \geq 2$. The VBM spatial maps are very similar except the one from PCA+CCA. In the VBM spatial maps, all fusion methods show gray matter atrophy in bilateral hippocampus and inferior temporal gyrus.

Since the performance difference among these fusion methods shown in **Figure 6** and **Figure 7** may be affected by the number of remaining principal components, we have run sPCA+CCA, PCA+CCA and parallel ICA with the number of principal components ranging from 4 to 20 for both ECM and VBM datasets. For each fusion method, the most significant p-values for group discrimination with the number of principal components varying from 4 to 20 were recorded and the distribution of p-values is shown in **Figure 8**. The VBM datasets overall has more significant group difference than ECM datasets. Compared to PCA+CCA and parallel ICA, sPCA+CCA tends to have p-value more significant.

Correlation Between Disease-Related Modulation Profiles and β-Amyloid Measurement

The most disease-related modulation profile in $\boldsymbol{A}_{ECM}$ and $\boldsymbol{A}_{VBM}$ were correlated with SUVR, a measure of β-amyloid content

TABLE 1 | Measurements of the modulation profiles in sPCA+CCA, PCA+CCA, parallel ICA and sCCA.

Methods	ECM		VBM		Correlation ρ	Classification accuracy
	p_{corr}	AUC	p_{corr}	AUC		
sPCA+CCA	$\mathbf{3.4 \times 10^{-4}}$	**0.78**	$\mathbf{2.6 \times 10^{-4}}$	**0.81**	0.78	**0.68**
PCA+CCA	2.9×10^{-2}	0.71	2.0×10^{-3}	0.73	0.48	0.61
Parallel ICA	0.10	0.68	1.8×10^{-3}	0.75	0.27	0.58
sCCA	1.3×10^{-2}	0.70	1.6×10^{-2}	0.70	**0.80**	0.60

sCCA obtains the highest correlation due to overfitting, but has very low values in AUC. sPCA+CCA has largest AUC and a large correlation indicating that this method is superior to the other 3 methods. $\mathbf{p_{corr}}$ *denotes the* **p** *value for group discrimination with multiple comparison correction. The group classification accuracy is obtained by running quadratic discriminant analysis on modulation profiles from both modalities. The most significant p-value and the largest value for each measurement are in bold font.*

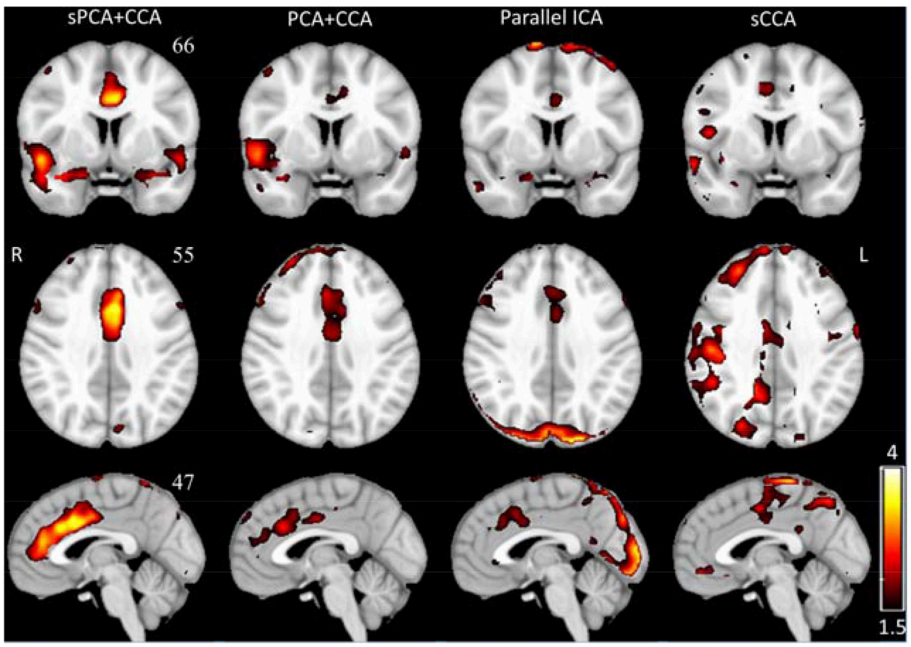

FIGURE 6 | The most significant disease-related ECM z-score maps from sPCA+CCA, PCA+CCA, parallel ICA and sCCA. Maps are displayed in radiological convention (right is left and vice versa). All spatial maps are thresholded at $z \geq 1.5$ except the map from parallel ICA that is thresholded at $z \geq 1$. Parallel ICA would not show the anterior cingulate cortex if the map is thresholded at $z \geq 1.5$.

calculated from the PET scans within 6 months of MRI scans. The correlation plots are shown in **Figure 9**. Each value in the ECM modulation profile measures the strength of functional connectivity for one subject, and a more negative value indicates lower functional connectivity. Similarly, each value in the VBM modulation profile measures the amount of atrophy for one subject, and a more negative value indicates more severe atrophy. Among these plots, only the VBM modulation profile in sPCA had a significant negative correlation with SUVR ($p < 0.05$) and the other correlations were not significant. sPCA+CCA had the strongest correlation with SUVR in both ECM and VBM data.

DISCUSSION

To the best of our knowledge, our study is the first study proposing the sPCA+CCA method *and* comparing it with other methods for fusion analysis of multimodal brain imaging data. A novel split-sample cross-validation algorithm with *AIC* as selection criterion was validated for sPCA to determine the sparsity tuning parameter and the number of principal components. The sPCA+CCA fusion method extracts disease-related modulation profiles with the highest statistical power in real data. While sPCA and its variants were applied for noise elimination and functional segmentation in neuroimaging research (Ulfarsson and Solo, 2007; Ng et al., 2009; Khanna et al., 2015), to the best of our knowledge, this is the first study to implement and validate sPCA in fusion analysis.

Properties of sPCA

Since sPCA is a sparse version of PCA, naturally they have some common properties. Both are linear techniques for dimensionality reduction. High-dimensional data is projected to a subspace spanned by the dominant principal component scores so that most of the variance in the original data is kept in a

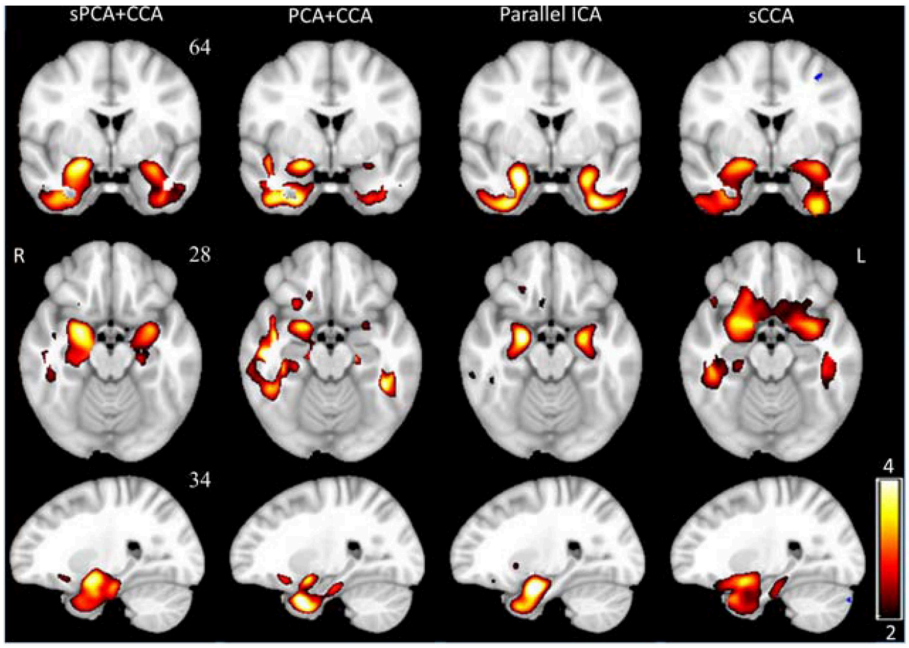

FIGURE 7 | The most significant disease-related VBM z-score maps from sPCA+CCA, PCA+CCA, parallel ICA and sCCA. Maps are displayed in radiological convention (right is left and vice versa). All spatial maps were thresholded at $z > 2$. Note that PCA+CCA does not give a bilateral disease-related pattern.

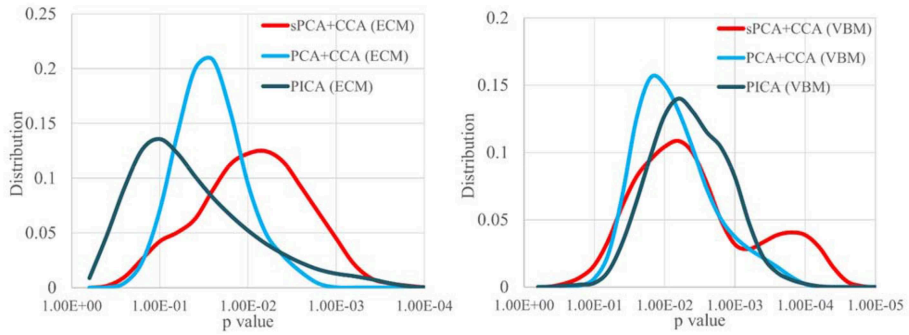

FIGURE 8 | The distribution of *p*-values for group discrimination with the number of principal components ranging from 4 to 20. VBM dataset has more significant *p*-value than ECM dataset. The sPCA+CCA method has more significant group discrimination than PCA+CCA and parallel ICA.

low-dimensional feature space. However, sPCA is different from PCA in terms of robustness, implementation, orthogonality, and computation.

1) *Robustness*: sPCA not only searches for the direction to maximize variance but also discriminates informative voxels from non-informative voxels as a data-driven approach. In other words, sPCA is useful when the number of features is large, while only a small proportion of them are informative. In many cases the salient features such as age- and disease-related features in the modalities are limited to only a few regions but not the entire brain. The sPCA method adjusts principal components by setting non-informative voxels to zero and hence obtains more robust scores (projection of original data on principal components) as the input to the following CCA analysis. In the sPCA+CCA fusion method, sPCA itself does not have discriminatory power. However, it was shown that sPCA is more robust against noise than conventional PCA. The similarity values S_Y and S_V in **Figure 3** indicate that sPCA outperforms PCA in uncovering the true principal component scores and spatial maps, especially when the sparsity level is high. The robust scores from sPCA improve the subsequent CCA analysis to better link related modulation profiles and extract the corresponding spatial patterns in the data.
2) *Implementation*: Unlike PCA, which represents a standard eigenvalue problem, sPCA is a constrained optimization problem and optimized by an iterative algorithm. The objective function in sPCA is a biconvex function and is

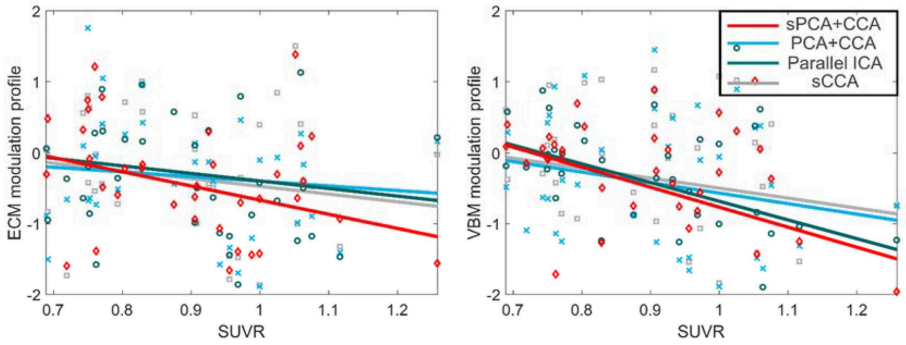

Correlation with SUVR	sPCA+CCA	PCA+CCA	Parallel ICA	sCCA
p_{ECM}	**0.074**	0.58	0.40	0.36
p_{VBM}	**0.025**	0.22	0.06	0.26

FIGURE 9 | Correlation between the most significant modulation profiles in ECM and VBM modalities with SUVR. The significance *p*-values for ECM (p_{ECM}) and VBM data (p_{VBM}) in sPCA+CCA, PCA+CCA, parallel ICA and sCCA are also shown. The SUVR measures the content of ß-amyloid using PET scanning. The ECM modulation profile of the disease-related pattern measures the strength of functional connectivity. A more negative value indicates lower functional connectivity. The VBM modulation profile of the disease-related pattern relates to the amount of atrophy. More atrophy is present for negative values of the VBM modulation profile. Note that sPCA+CCA has the most significant negative correlation with SUVR.

solved by optimizing two convex subproblems, both of which can be solved reliably and efficiently.

3) *Orthogonality*: The orthogonality no longer strictly holds when the L_1 norm penalty term is added in sPCA. However, at the optimal sparsity tuning parameter, the mean absolute correlation with sign ignored between different principal components is 0.054, indicating that the principal components from sPCA are nearly orthogonal.
4) *Computation*: sPCA is more computationally intensive than standard PCA. Along with choosing the number of principal components as in PCA, sPCA also needs to specify the sparsity tuning parameter. Overestimated sparsity would be detrimental since informative voxels are also removed, and underestimated sparsity may not significantly improve the analysis. A grid search in PCA is carried out over the number of principal components, and a grid search in sPCA is carried out over a sparsity tuning parameter and the number of principal components. The grid search process exponentially increases computational time of sPCA because more parameters need to be optimized.

Comparison of Fusion Analysis

Fusion analysis was carried out with simulated and real data. In the simulations, the sPCA+CCA method has improved performance over PCA+CCA by about 10% at sparsity level 70%. We have tested these two fusion methods at different sparsity levels and found that the improvement decreases with lower sparsity level until the performance difference becomes negligible when the sparsity level is about 30%. We would like to point out that parallel ICA does not lead to orthogonal components because orthogonality is not strictly enforced unlike CCA-based fusion methods. Thus, the simulation generated with an orthogonality condition is biased toward CCA-based fusion methods and explains why parallel ICA does not perform well in our simulation. In contrast, generating data without the assumption of orthogonality would make the simulation more biased toward parallel ICA. Among the four fusion methods considered, sCCA overestimates the correlation between modalities and also has low similarity. Unlike sCCA having original voxel-wise input features, sPCA+CCA along with PCA+CCA and parallel ICA reduces the data dimension *before* fusing modalities and thus possibly may discard some correlated features that have low variance. The voxel-wise input features to sCCA, however, are much larger than the number of samples. For example, the number of non-zero features in sCCA is at the order of a thousand, while the number of input features to CCA in sPCA+CCA is of the order of ten. The elastic-net penalty as a sparsity constraint may not be sufficient to alleviate an overestimated canonical correlation relationship and thus sPCA+CCA still outperforms sCCA in both simulated and real data.

In real data, the proposed sPCA+CCA method has the most significant disease-related modulation profiles in both modalities and the highest group classification accuracy. Compared to the accuracy obtained with principal component scores as input, using the modulation profiles as input have improved classification accuracy for all considered fusion methods. ACC is found to be disease-related by all fusion methods in ECM data. A decreased functional connectivity of ACC was consistent with the findings in previous resting-state fMRI studies (Rombouts et al., 2005; Sheline et al., 2009) and ACC was also found to be affected in MCI subjects by other imaging techniques, such as single photon emission computed tomography (SPECT) and structural MRI studies (Huang et al., 2002; Karas et al., 2004). sPCA+CCA found that the amygdala and the superior temporal gyrus *bilaterally*, in addition to ACC, are important disease-related regions in the ECM data. Decreased functional connectivity of the amygdala and superior temporal gyrus in MCI

or Alzheimer's disease subjects were also found in previous fMRI studies (Celone and Calhoun, 2006; Liu and Zhang, 2012; Yao et al., 2013), and are consistent with our results. In the VBM disease-related spatial maps, hippocampus and inferior temporal gyrus are found to have more atrophy in all fusion methods. The hippocampus is a critical region in the limbic system that is involved in motivation, emotion, learning and memory. Atrophy in the hippocampus is closely related to early symptoms in AD patients, such as short-term memory loss and disorientation. Early hippocampal atrophy is an established biomarker of AD (Jack et al., 1999). We also found that the inferior temporal gyrus is affected in MCI. This region is essential in face, pattern, and object recognition, and may already be affected in early-stage MCI subjects (Whitwell et al., 2008).

The disease-related modulation profiles from sPCA+CCA, PCA+CCA, parallel ICA and sCCA were correlated with the measure of β-amyloid, i.e., SUVR (**Figure 9**). Only sPCA+CCA found significant correlation with SUVR in VBM data but not in ECM data. The ECM modulation profile from sPCA+CCA, however, had strongest correlation with SUVR among all of ECM modulation profiles. A more negative value in the ECM modulation profile indicates lower functional connectivity, and a more negative value in the VBM modulation profile indicates more severe atrophy in the disease-related patterns. Since SUVR is used for longitudinal analyses in MCI (Landau et al., 2014), the disease-related spatial pattern and corresponding modulation profile from our fusion method potentially can be used to monitor disease severity.

Similar to other fusion methods, sPCA+CCA has its own assumptions and limitations. From the simulation and the formulation of sPCA+CCA, we illustrate that the CCA step enforces orthogonality on the modulation profile for each modality. In addition, implementing sparsity assumes that the associated effect between modalities is distributed locally instead of globally across the brain. This assumption is realistic because in amnestic MCI or early AD not the entire brain shows atrophy or loss of functional connectivity, but the disease state is limited to sparse brain regions such as the inferior temporal lobes and the posterior cingulate cortex. Enforcing sparsity in fusion analysis is applicable to many neurological diseases in their early stages. On a computational level, enforcing sparsity significantly increases computational time. Computations were run on a Dell workstation with 2 Intel Xeon E5-2643 processors. This is different from parallel ICA and PCA+CCA, where the computation takes only minutes to carry out a fusion analysis. In contrast, sPCA+CCA needs approximately 12 h to complete the analysis, and sCCA needs ∼21 h.

Extension of sPCA+CCA

We would like to emphasize that sPCA also can be applied to other CCA-based fusion methods such as multiset CCA (Correa et al., 2010) and CCA+jICA (Sui et al., 2010, 2011). Unlike CCA that associates only two modalities, multiset CCA is applied when more than two modalities are considered for fusion analysis. In the CCA+jICA method, joint ICA is carried out after CCA to maximize the independence among joint components and to prevent CCA from failing to separate sources. Since PCA is also required in these two methods for dimensionality reduction, sPCA can be incorporated into these methods as well. If the structural information in the brain map is pre-specified, more sophisticated sparse constraints such as structural lasso (Simon et al., 2013; Lin et al., 2014) can potentially be used in sparse fusion methods including sPCA+CCA and sCCA. However, more advanced methods are beyond the scope of the current study.

Limitations and Future Study

The proposed sPCA method has two limitations. First, as in PCA, sPCA preserves the global structure of the data but ignores the Euclidean structure of image space and hence may lead to discrete non-zero voxels in sparse principal components. Second, the property of orthogonality between principal components does not strictly hold because of the lasso penalty used in sPCA. Furthermore, the issue of missing data is not addressed in this study. Some subjects may only have one imaging modality available or have data with partial brain coverage, while some fusion methods have been developed to address this issue (Xiang et al., 2014; Pan et al., 2018), current sPCA+CCA framework cannot use subjects with missing data.

Other dimension reduction methods, such as the locality preserving projection method (He and Niyogi, 2003), were studied extensively in pattern recognition. However, the performance of more sophisticated dimension reduction techniques for neuroimaging studies is unknown. The auto encoder related methods (Bengio, 2009) are currently of high interest in the deep learning research community. This method is appealing for handling non-linear systems and could replace the linear PCA algorithm. One critical reason for requiring dimension reduction in CCA-based fusion analysis is that the number of features in standard CCA algorithm cannot be more than the number of observations. If CCA itself can be revised to select features adaptively and avoid the singularity problem arising from too many features, then the dimension reduction preprocessing step may not be required.

CONCLUSION

We have proposed a sPCA algorithm for data fusion and compared sPCA with three different state-of-the-art fusion methods. We evaluated how well these fusion methods associate related patterns in different modalities and correlated the result from fusion analysis with ß-amyloid measurement (SUVR). We found that sPCA can significantly reduce the impact of non-informative voxels and improve statistical power for uncovering disease-related patterns. The sPCA+CCA method not only achieves the best group discrimination but also has the strongest correlation with the SUVR measurement. In summary, sPCA is a powerful method for sparse regularization and dimensionality reduction, completely data-driven, and self-adaptive without experts' intervention.

AUTHOR CONTRIBUTIONS

ZY and DC: conception and design of the study. ZY, XZ, KS, VM, SB, and DC: analysis and interpretation of data. CB: data

management and quality control. DC and ZY: drafting the article. ZY, XZ, CB, KS, VM, SB, and DC: revising it critically for important intellectual content and final approval of the version to be submitted.

FUNDING

This research project was supported by the NIH (grant 1R01EB014284 and COBRE grant 5P20GM109025), a private grant from Angela and Peter Dal Pezzo, and a private grant from Lynn and William Weidner. Data collection and sharing for this project was funded by the ADNI (National Institutes of Health Grant U01 AG024904) and DOD ADNI (Department of Defense award number W81XWH-12-2-0012).

SUPPLEMENTARY MATERIAL

The Supplementary Material for this article can be found online at: https://www.frontiersin.org/articles/10.3389/fnins.2019.00642/full#supplementary-material

REFERENCES

Abdel-Rahman, E. M., Mutanga, O., Odindi, J., Adam, E., Odindo, A., and Ismail, R. (2014). A comparison of partial least squares (PLS) and sparse PLS regressions for predicting yield of Swiss chard grown under different irrigation water sources using hyperspectral data. *Comput. Electron. Agric.* 106, 11–19. doi: 10.1016/j.compag.2014.05.001

Akaike, H. (1974). A new look at the statistical model identification. *IEEE Trans. Automat. Control* 19, 716–723. doi: 10.1109/TAC.1974.1100705

Ashburner, J. (2007). A fast diffeomorphic image registration algorithm. *Neuroimage* 38, 95–113. doi: 10.1016/j.neuroimage.2007.07.007

Ashburner, J., and Friston, K. J. (2000). Voxel-based morphometry—the methods. *Neuroimage* 11, 805–821. doi: 10.1006/nimg.2000.0582

Avants, B. B., Libon, D. J., Rascovsky, K., Boller, A., McMillan, C. T., Massimo, L., et al. (2014). Sparse canonical correlation analysis relates network-level atrophy to multivariate cognitive measures in a neurodegenerative population. *Neuroimage* 84, 698-711. doi: 10.1016/j.neuroimage.2013.09.048

Bai, F., Watson, D. R., Yu, H., Shi, Y., Yuan, Y., and Zhang, Z. (2009). Abnormal resting-state functional connectivity of posterior cingulate cortex in amnestic type mild cognitive impairment. *Brain Res.* 1302, 167–174. doi: 10.1016/j.brainres.2009.09.028

Bavelas, A. (1948). A mathematical model for group structures. *Hum. Org.* 7, 16–30. doi: 10.17730/humo.7.3.f4033344851gl053

Bengio, Y. (2009). Learning deep architectures for AI. *Found. Trends® Mach. Learn.* 2, 1–127. doi: 10.1561/2200000006

Bianciardi, M., Fukunaga, M., van Gelderen, P., Horovitz, S. G., de Zwart, J. A., Shmueli, K., et al. (2009). Sources of functional magnetic resonance imaging signal fluctuations in the human brain at rest: a 7 T study. *Magnet. Reson. Imag.* 27, 1019–1029. doi: 10.1016/j.mri.2009.02.004

Bryan, K., and Leise, T. (2006). The $25,000,000,000 eigenvector: The linear algebra behind Google. *Siam Rev.* 48, 569–581. doi: 10.1137/050623280

Calhoun, V. D., and Adal, T. (2009). Feature-based fusion of medical imaging data. *IEEE Trans. Info. Technol. Biomed.* 13, 711–720. doi: 10.1109/TITB.2008.923773

Calhoun, V. D., and Sui, J. (2016). Multimodal fusion of brain imaging data: a key to finding the missing link (s) in complex mental illness. *Biol. Psychiatry Cogn. Neurosci. Neuroimaging* 1, 230–244. doi: 10.1016/j.bpsc.2015.12.005

Celone, K. A., Calhoun, V. D., et al. (2006). Alterations in memory networks in mild cognitive impairment and Alzheimer's Disease: an independent component analysis. *J. Neurosci.* 26 10222–10231. doi: 10.1523/JNEUROSCI.2250-06.2006

Chen, J. E., Chang, C., Greicius, M. D., and Glover, G. H. (2015). Introducing co-activation pattern metrics to quantify spontaneous brain network dynamics. *Neuroimage* 111, 476–488. doi: 10.1016/j.neuroimage.2015.01.057

Chetelat, G., Desgranges, B., De La Sayette, V., Viader, F., Eustache, F., and Baron, J.-C. (2002). Mapping gray matter loss with voxel-based morphometry in mild cognitive impairment. *Neuroreport* 13, 1939–1943. doi: 10.1097/00001756-200210280-00022

Correa, N. M., Adali, T., Li, Y. O., and Calhoun, V. D. (2010). Canonical correlation analysis for data fusion and group inferences: examining applications of medical imaging data. *IEEE Sig. Process Mag.* 27, 39–50. doi: 10.1109/MSP.2010.936725

Correa, N. M., Li, Y. O., Adali, T., and Calhoun, V. D. (2008). Canonical correlation analysis for feature-based fusion of biomedical imaging modalities and its application to detection of associative networks in Schizophrenia. *IEEE J Sel Top Signal Proc.* 2, 998–1007. doi: 10.1109/JSTSP.2008.2008265

Eckart, C., and Young, G. (1936). The approximation of one matrix by another of lower rank. *Psychometrika* 1, 211–218. doi: 10.1007/BF02288367

Feng, C. M., Gao, Y. L., Liu, J. X., Zheng, C. H., Li, S. J., and Wang, D. (2016). "A simple review of sparse principal components analysis," in *International Conference on Intelligent Computing* (Springer), 374–383.

Filippi, M., Cercignani, M., Inglese, M., Horsfield, M., and Comi, G. (2001). Diffusion tensor magnetic resonance imaging in multiple sclerosis. *Neurology* 56, 304–311. doi: 10.1212/WNL.56.3.304

Forsberg, A., Engler, H., Almkvist, O., Blomquist, G., Hagman, G., Wall, A., et al. (2008). PET imaging of β-amyloid deposition in patients with mild cognitive impairment. *Neurobiol. Aging* 29, 1456–1465. doi: 10.1016/j.neurobiolaging.2007.03.029

Fulop, S. A., and Fitz, K. (2006). Algorithms for computing the time-corrected instantaneous frequency (reassigned) spectrogram, with applications. *J. Acoust. Soc. Am.* 119, 360–371. doi: 10.1121/1.2133000

Groves, A. R., Beckmann, C. F., Smith, S. M., and Woolrich, M. W. (2011). Linked independent component analysis for multimodal data fusion. *Neuroimage* 54, 2198–2217. doi: 10.1016/j.neuroimage.2010.09.073

He, X., and Niyogi, P. (2003). "Locality preserving projections," in *Advances in Neural Information Processing Systems 16* (Vancouver, BC).

He, Y., and Evans, A. (2010). Graph theoretical modeling of brain connectivity. *Curr. Opin. Neurol.* 23, 341–350. doi: 10.1097/WCO.0b013e32833aa567

Henson, R. N., Flandin, G., Friston, K. J., and Mattout, J. (2010). A Parametric empirical bayesian framework for fMRI-constrained MEG/EEG source reconstruction. *Hum. Brain Mapp.* 31, 1512–1531. doi: 10.1002/hbm.20956

Hotelling, H. (1936). Relations between two sets of variates. *Biometrika* 28, 321–377. doi: 10.1093/biomet/28.3-4.321

Huang, C., Wahlund, L. O., Svensson, L., Winblad, B., and Julin, P. (2002). Cingulate cortex hypoperfusion predicts Alzheimer's disease in mild cognitive impairment. *BMC Neurol.* 2:9. doi: 10.1186/1471-2377-2-9

Jack, C. R., Petersen, R. C., Xu, Y. C., O'Brien, P. C., Smith, G. E., Ivnik, R. J., et al. (1999). Prediction of AD with MRI-based hippocampal volume in mild cognitive impairment. *Neurology* 52, 1397–1397. doi: 10.1212/WNL.52.7.1397

Jenatton, R., Obozinski, G., and Bach, F. (2010). "Structured sparse principal component analysis," in *Proceedings of the Thirteenth International Conference on Artificial Intelligence and Statistics* (Paris), 366–373.

Karas, G. B., Scheltens, P., Rombouts, S. A. R. B., Visser, P. J., van Schijndel, R. A., Fox, N. C., et al. (2004). Global and local gray matter loss in mild cognitive impairment and Alzheimer's disease. *Neuroimage* 23, 708–716. doi: 10.1016/j.neuroimage.2004.07.006

Khanna, R., Ghosh, J., Poldrack, R., and Koyejo, O. (2015). Sparse submodular probabilistic PCA. *Art. Intell. Statist.* 38, 453–461.

Kim, D., Ronen, I., Formisano, E., Kim, K., Kim, M., van Zijl, P., et al. (2003). *Simultaneous Mapping of Functional Maps and Axonal Connectivity in Cat Visual Cortex*. Sendai: HBM.

Lê Cao, K.-A., Boitard, S., and Besse, P. (2011). Sparse PLS discriminant analysis: biologically relevant feature selection and graphical displays for multiclass problems. *BMC Bioinformatics* 12:253. doi: 10.1186/1471-2105-12-253

Lameiro, C., and Schreier, P. J. (2016). *Cross-Validation Techniques for Determing the Number of Correlated Components Between Two Data When the Number of Sampls is Very Small*. Pacific Grove, CA: ICASSP.

Landau, S. M., Baker, S. L., and Jagust, W. J. (2014). "Amyloid change early in disease is related to increased glucose metabolism and episodic memory declinein," in *Human Amyloid Imaging Meeting* (Miami, FL).

Le Floch, E., Guillemot, V., Frouin, V., Pinel, P., Lalanne, C., Trinchera, L., et al. (2012). Significant correlation between a set of genetic polymorphisms and a functional brain network revealed by feature selection and sparse partial least squares. *Neuroimage* 63, 11–24. doi: 10.1016/j.neuroimage.2012.06.061

Lin, D., Calhoun, V. D., and Wang, Y. (2014). Correspondence between fMRI and SNP data by group sparse canonical correlation analysis. *Med. Image Anal.* 18, 891–902. doi: 10.1016/j.media.2013.10.010

Liu, J., Pearlson, G., Windemuth, A., Ruano, G., Perrone-Bizzozero, N. I., and Calhoun, V. (2009). Combining fMRI and SNP data to investigate connections between brain function and genetics using parallel ICA. *Hum. Brain Mapp.* 30, 241–255. doi: 10.1002/hbm.20508

Liu, Z., Zhang, Y., et al. (2012). Altered topological patterns of brain networks in mild cognitive impairment and Alzheimer's disease: a resting-state fMRI study. *Psychiatr. Res. Neuroimaging.* 202, 118–125. doi: 10.1016/j.pscychresns.2012.03.002

Mohammadi-Nejad, A. R., Hossein-Zadeh, G. A., and Soltanian-Zadeh, H. (2017). Structured and sparse canonical correlation analysis as a brain-wide multi-modal data fusion approach. *IEEE. Trans. Med. Imag.* 11, 1–11. doi: 10.1109/TMI.2017.2681966

Ng, B., Abugharbieh, R., and McKeown, M. (2009). Functional segmentation of fMRI data using adaptive non-negative sparse PCA (ANSPCA). *Med. Image Comput. Comp. Assis. Interven.* 2009, 490–497. doi: 10.1007/978-3-642-04271-3_60

Pan, Y., Liu, M., Lian, C., Zhou, T., Xia, Y., and Shen, D. (2018). "Synthesizing missing PET from MRI with cycle-consistent generative adversarial networks for Alzheimer's disease diagnosis," in *International Conference on Medical Image Computing and Computer-Assisted Intervention* (Granada: Springer), 455–463. doi: 10.1007/978-3-030-00931-1_52

Parkhomenko, E., Tritchler, D., and Beyene, J. (2009). Sparse canonical correlation analysis with application to genomic data integration. *Stat. Appl. Genet. Mol. Biol.* 8, 1–34. doi: 10.2202/1544-6115.1406

Pezeshki, A., Scharf, L. L., Azimi-Sadjadi, M. R., and Lundberg, M. (2004). "Empirical canonical correlation analysis in subspaces," in *Signals, Systems and Computers, (2004). Conference Record of the Thirty-Eighth Asilomar Conference on* (Pacific Grove, CA: IEEE), 994–997.

Power, J. D., Cohen, A. L., Nelson, S. M., Wig, G. S., Barnes, K. A., Church, J. A., et al. (2011). Functional network organization of the human brain. *Neuron* 72, 665–678. doi: 10.1016/j.neuron.2011.09.006

Rombouts, S. A. R. B., Barkhof, F., Goekoop, R., Stam, C. J., and Scheltens, P. (2005). Altered resting state networks in mild cognitive impairment and mild Alzheimer's disease: An fMRI study. *Hum. Brain Mapp.* 26, 231–239. doi: 10.1002/hbm.20160

Savopol, F., and Armenakis, C. (2002). Merging of heterogeneous data for emergency mapping: data integration or data fusion? *Int. Arch. Photogramm. Remote Sens. Spatial Info. Sci.* 34, 668–674.

Sheline, Y. I., Raichle, M. E., Snyder, A. Z., Morris, J. C., Head, D., Wang, S., et al. (2009). Amyloid plaques disrupt resting state default mode network connectivity in cognitively normal elderly. *Biol. Psychiatr.* 67:584–587. doi: 10.1016/j.biopsych.2009.08.024

Shen, H., and Huang, J. Z. (2008). Sparse principal component analysis via regularized low rank matrix approximation. *J. Multivar. Anal.* 99, 1015–1034. doi: 10.1016/j.jmva.2007.06.007

Shumway, R. H., Stoffer, D. S., and Stoffer, D. S. (2000). *Time Series Analysis and Its Applications*. New York, NY: Springer.

Simon, N., Friedman, J., Hastie, T., and Tibshirani, R. (2013). A sparse-group lasso. *J. Comput. Graph. Stat.* 22, 231–245. doi: 10.1080/10618600.2012.681250

Sui, J., Adali, T., Pearlson, G., Yang, H., Sponheim, S. R., White, T., et al. (2010). A CCA+ICA based model for multi-task brain imaging data fusion and its application to schizophrenia. *Neuroimage* 51, 123–134. doi: 10.1016/j.neuroimage.2010.01.069

Sui, J., Pearlson, G., Caprihan, A., Adali, T., Kiehl, K. A., Liu, J., et al. (2011). Discriminating schizophrenia and bipolar disorder by fusing fMRI and DTI in a multimodal CCA+ joint ICA model. *Neuroimage* 57, 839–855. doi: 10.1016/j.neuroimage.2011.05.055

Troyanskaya, O., Cantor, M., Sherlock, G., Brown, P., Hastie, T., Tibshirani, R., et al. (2001). Missing value estimation methods for DNA microarrays. *Bioinformatics* 17, 520–525. doi: 10.1093/bioinformatics/17.6.520

Ulfarsson, M. O., and Solo, V. (2007). "Sparse variable principal component analysis with application to fMRI. Biomedical Imaging: From Nano to Macro, 2007," in *4th IEEE International Symposium on IEEE, ISBI 2007* (Arlington, VA), 460–463.

Whitwell, J. L., Shiung, M. M., Przybelski, S., Weigand, S. D., Knopman, D. S., Boeve, B. F., et al. (2008). MRI patterns of atrophy associated with progression to AD in amnestic mild cognitive impairment. *Neurology* 70, 512–520. doi: 10.1212/01.wnl.0000280575.77437.a2

Wink, A. M., de Munck, J. C., van der Werf, Y. D., van den Heuvel, O. A., and Barkhof, F. (2012). Fast eigenvector centrality mapping of voxel-wise connectivity in functional magnetic resonance imaging: implementation, validation, and interpretation. *Brain connectivity* 2, 265–274. doi: 10.1089/brain.2012.0087

Witten, D. M., Tibshirani, R., and Hastie, T. (2009). A penalized matrix decomposition, with applications to sparse principal components and canonical correlation analysis. *Biostatistics* 10, 515–534. doi: 10.1093/biostatistics/kxp008

Witten, D. M., and Tibshirani, R. J. (2009). Extensions of sparse canonical correlation analysis with applications to genomic data. *Stat. Appl. Genet. Mol. Biol.* 8, 1–27. doi: 10.2202/1544-6115.1470

Xiang, S., Yuan, L., Fan, W., Wang, Y., Thompson, P. M., Ye, J., et al. (2014). Bi-level multi-source learning for heterogeneous block-wise missing data. *Neuroimage* 102, 192–206. doi: 10.1016/j.neuroimage.2013.08.015

Yao, H., Liu, Y., Zhou, B., Zhang, Z., An, N., Wang, P., et al. (2013). Decreased functional connectivity of the amygdala in Alzheimer's disease revealed by resting-state fMRI. *Eur J Radiol.* 82, 1531–1538. doi: 10.1016/j.ejrad.2013.03.019

Zou, H., Hastie, T., and Tibshirani, R. (2006). Sparse principal component analysis. *J. Comput. Graph. Stat.* 15, 265–286. doi: 10.1198/106186006X113430

Conflict of Interest Statement: The authors declare that the research was conducted in the absence of any commercial or financial relationships that could be construed as a potential conflict of interest.

Copyright © 2019 Yang, Zhuang, Bird, Sreenivasan, Mishra, Banks, Cordes and the Alzheimer's Disease Neuroimaging Initiative. This is an open-access article distributed under the terms of the Creative Commons Attribution License (CC BY). The use, distribution or reproduction in other forums is permitted, provided the original author(s) and the copyright owner(s) are credited and that the original publication in this journal is cited, in accordance with accepted academic practice. No use, distribution or reproduction is permitted which does not comply with these terms.

frontiers in Neuroscience

ORIGINAL RESEARCH
published: 09 July 2019
doi: 10.3389/fnins.2019.00703

The Effects of Stimulator, Waveform, and Current Direction on Intracortical Inhibition and Facilitation: A TMS Comparison Study

Maximilian J. Wessel[1,2†], Laurijn R. Draaisma[1,2†], Takuya Morishita[1,2] and Friedhelm C. Hummel[1,2,3]*

[1] Defitech Chair of Clinical Neuroengineering, Center for Neuroprosthetics and Brain Mind Institute, Swiss Federal Institute of Technology (EPFL), Geneva, Switzerland, [2] Defitech Chair of Clinical Neuroengineering, Clinique Romande de Réadaptation, Center for Neuroprosthetics and Brain Mind Institute, Swiss Federal Institute of Technology (EPFL Valais), Sion, Switzerland, [3] Department of Clinical Neuroscience, University of Geneva Medical School, Geneva, Switzerland

Background: Cortical function is dependent on the balance between excitatory and inhibitory influences. In the human motor cortex, surrogates of these interactions can be measured *in vivo*, non-invasively with double-pulse transcranial magnetic stimulation (TMS). To compare results from data acquired with different available setups and bring data together, it is inevitable to determine whether different TMS setups lead to comparable or differential results.

Objective: We assessed and compared short intracortical inhibition (SICI) and intracortical facilitation (ICF) testing four different experimental conditions.

Methods: SICI and ICF were studied with different stimulators (Magstim BiStim^2 or MagVenture MagPro X100), waveforms (monophasic or biphasic), current directions (anterior-posterior or posterior-anterior) at interstimulus intervals (ISIs) of 1, 3, 10, 15 ms.

Results: We were not able to detect differences for SICI and ICF, when comparing the tested conditions, except for 3 ms SICI in which the anterior-posterior current direction led to stronger modulation. Correlation analysis suggested comparability for 3 ms SICI for the Magstim monophasic posterior-anterior condition with both tested MagVenture conditions.

Conclusions: 3 ms SICI data sets obtained with two different, commonly used stimulators (Magstim BiStim^2 or MagVenture MagPro X100) with conventionally used stimulation parameters are largely comparable. This may allow the combination of data sets in an open science view.

Keywords: transcranial magnetic stimulation, short intracortical inhibition, intracortical facilitation, Magstim, MagVenture, comparison

OPEN ACCESS

Edited by:
Stephan Bohlhalter, University of Bern, Switzerland

Reviewed by:
Petro Julkunen, Kuopio University Hospital, Finland
Hideyuki Matsumoto, Mitsui Memorial Hospital, Japan

***Correspondence:**
Friedhelm C. Hummel
friedhelm.hummel@epfl.ch

† These authors have contributed equally to this work

Specialty section:
This article was submitted to Brain Imaging Methods, a section of the journal Frontiers in Neuroscience

Received: *19 March 2019*
Accepted: *21 June 2019*
Published: *09 July 2019*

Citation:
Wessel MJ, Draaisma LR, Morishita T and Hummel FC (2019) The Effects of Stimulator, Waveform, and Current Direction on Intracortical Inhibition and Facilitation: A TMS Comparison Study. Front. Neurosci. 13:703. doi: 10.3389/fnins.2019.00703

INTRODUCTION

Inhibitory and excitatory interactions are key components of cortical processing (Kirkwood, 2015). With the use of double-pulse transcranial magnetic stimulation (dpTMS), it is possible to assess correlates of these interactions within the human motor cortex *in vivo* and non-invasively, first described by Kujirai et al. (1993), Chen (2004). It pairs a subthreshold conditioning stimulus (CS)

with a subsequent suprathreshold test stimulus (TS). The test response, mainly measured via the amplitude of motor evoked potentials (MEPs), is inhibited at shorter interstimulus intervals (ISIs) of 1–6 ms, this effect is commonly termed short intracortical inhibition (SICI). At longer ISIs of 8–30 ms the test response is facilitated, here referred to as intracortical facilitation (ICF). SICI and ICF have been widely used to study motor cortex physiology in healthy subjects and neurological disorders, e.g., (Hummel et al., 2009; Heise et al., 2010, 2013). SICI has been associated with $GABA_A$ and ICF with glutamatergic neurotransmission (Ziemann et al., 1998; Di Lazzaro et al., 2000). Importantly, this neurotransmission has been linked to various aspects of human behavior, such as regulation of learning, memory, cognition, or emotions (Ende, 2015).

SICI and ICF are frequently used to study neurological conditions and to validate neurotechnological interventions, such as transcranial direct current stimulation, e.g., (Zimerman et al., 2012). However, as different devices and protocol parameters are used, it is important to determine whether these different devices and protocols lead to comparable data. This would be a crucial prerequisite to judge whether results derived from different experimental setups are comparable. Furthermore, this knowledge will pave the way to comprehensively combine data sets from different sources, e.g., toward open science approaches. Even more importantly, it is a necessary basis for the potential of SICI and ICF as diagnostic tools or biomarkers to predict recovery and treatment response.

Comparative studies of different devices have been conducted to assess motor thresholds, MEP amplitudes, MEP latencies, or TMS-evoked potentials (Kammer et al., 2001; Van Doren et al., 2015). For example, Van Doren et al. (2015) reported a higher magnetic field strength, a shorter magnetic flux duration, lower motor threshold, shorter recovery time from the TMS artifact, a shorter MEP latency, and a reversed first artifact trajectory comparing the MagVenture MagPro with two other devices (the Magstim Rapid and the Deymed DuoMag XT-100 stimulator) operating in biphasic mode.

To the best of our knowledge, however, the effects of the parameter interactions between stimulator, waveform, and current direction have not been studied yet for SICI and ICF. Therefore, our objective was to compliment the available literature by investigating the effects of stimulator, waveform, induced current direction, and ISI on SICI and ICF. We compared two commonly used TMS stimulators, the Magstim BiStim^2 stimulator (Whitland, United Kingdom) and the MagVenture MagPro X100 stimulator (Farum, Denmark). In addition to the commonly used monophasic waveform, we tested a biphasic waveform, which may provide the benefit of lower values for motor thresholds (Sommer et al., 2006). We assessed the effects of the induced current direction, since on the contrary to the most commonly applied posterior to anterior (PA) currents, single-pulse anterior to posterior (AP) currents and SICI rather influence later I-waves (Nakamura et al., 1997; Sakai et al., 1997). Furthermore, we assessed different ISIs to conclude on phase-specific effects.

The aim of the present study was to make inferences about setup related confounds and emphasize between center and study comparability, when assessing SICI or ICF in future.

MATERIALS AND METHODS

Participants

Fifteen young, healthy, right-handed participants were recruited for the study [eight female, mean age 25.20 years, mean laterality quotient Edinburgh handedness inventory 87.63 (Oldfield, 1971)]. The inclusion criteria were as follows: $\geq$18 and $<$35 years, right-handedness, normal values of Mini-mental state examination ($>$26/30), absence of contraindication for transcranial electric stimulation (tES), transcranial magnetic stimulation (TMS) or magnetic resonance imaging. The exclusion criteria were: presence of neuropsychiatric diseases, history of seizures, intake medication that potentially interacts with tES or TMS, musculoskeletal dysfunction that compromise finger movement, pregnancy, professional musician or intense professional usage of a computer keyboard, intake of narcotic drugs, request of not being informed in case of incidental findings. All subjects gave written informed consent in accordance with the Declaration of Helsinki (World Medical Association, 2013). The protocol was approved by the cantonal ethics committee Vaud, Switzerland (project number 2017-00765).

Experimental Design

The objective was to assess the effects of different TMS conditions on SICI and ICF. The following conditions were tested and compared: (A) Magstim BiStim^2 stimulator (Whitland, United Kingdom) with a monophasic waveform and a posterior-anterior current direction (MS PA). (B) Magstim BiStim^2 stimulator (Whitland, United Kingdom) with a monophasic waveform and an anterior-posterior current direction (MS AP). (C) MagVenture MagPro X100 stimulator (Farum, Denmark) with a biphasic waveform and an anterior-posterior to posterior-anterior current direction (MV AP-PA). (D) MagVenture MagPro X100 stimulator (Farum, Denmark) with a monophasic waveform and a posterior-anterior current direction (MV PA), please see also **Figure 1**. The current direction is indicated as induced in the underlying brain tissue throughout the manuscript. The assessments were grouped into one session per stimulator. The order of the respective configurations and sessions followed a pseudorandomized sequence.

Transcranial Magnetic Stimulation

A double-pulse protocol was utilized to assess SICI and ICF at rest (Kujirai et al., 1993). In this protocol, a subthreshold CS was followed by a suprathreshold TS. SICI was tested at ISIs of 1 and 3 ms. ICF at ISIs of 10 and 15 ms, except for MV PA in which technical limitations of the stimulator restrained us from testing a 1 ms interval. The CS was adjusted to 80% of resting motor threshold (RMT) (Kujirai et al., 1993). The RMT was defined as the minimal output of the stimulator that

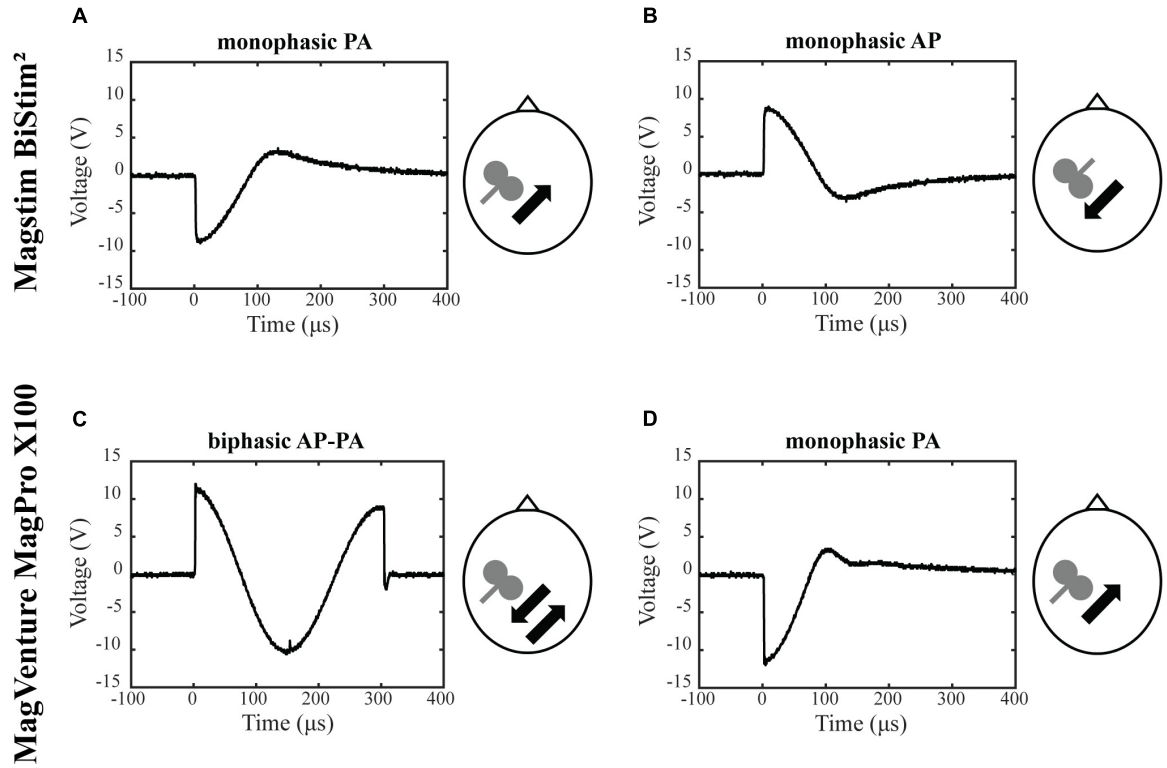

FIGURE 1 | Experimental setup. Depicted are the four experimental conditions. **(A)** Magstim BiStim^2 stimulator, monophasic waveform, posterior-anterior current direction. **(B)** Magstim BiStim^2 stimulator, monophasic waveform, anterior-posterior current direction. **(C)** MagVenture MagPro X100 stimulator, biphasic waveform, anterior-posterior to posterior-anterior current direction. **(D)** MagVenture MagPro X100 stimulator, monophasic waveform, posterior-anterior current direction. The waveforms were measured with a probe fixed above at the coil wire intersection and a single TMS pulse applied at 50% of MSO. Arrows indicate the current directions as induced in the underlying brain tissue.

elicited MEPs with peak-to-peak amplitude of $\geq$50 μV in at least 5 out of 10 consecutive trials (Groppa et al., 2012). The TS was adjusted to evoke MEPs of ∼1 mV (Sanger et al., 2001). The TMS pulses were applied over the left motor hotspot with a figure-of-eight coil. For the MagVenture setup, we used a MC-B70 Butterfly Coil and for the Magstim setup a D70 Alpha Flat Coil, for a comparison of coil specifications please see **Table 1**. The coil was oriented that the handle pointed backward and ∼45° to the midsagittal line. Twenty trials were recorded for the TS and for each double-pulse paradigm with at an inter-trial-interval of 7 s ± 25%. The order followed a pseudorandom sequence, except for the first two participants in which we used a block randomization for MV PA, due to an earlier version of our trigger setup.

EMG Recording

MEPs were recorded from the right first dorsal interosseous (FDI) muscles via surface electrodes positioned in belly tendon montage. The signal was recorded with a Noraxon DTS Receiver (Scottsdale, AZ, United States) (gain 500, sampling rate 3000 Hz, high-pass filter: 10 Hz analog Sallen-Key, low-pass filter: 1000 Hz digital FIR 128th order Butterworth) and for further processing

TABLE 1 | Technical specifications of utilized TMS coils.

Manufacturer	Coil type	Averaged inductance	Focality (half-value spread $S_{1/2}$) (Deng et al., 2013)	Stimulation depth (half-value depth, $d_{1/2}$) (Deng et al., 2013)	Coil wing external diameter	Angle	Wire loops overlap (Thielscher and Kammer, 2004)
Magstim	D70 Alpha Flat Coil (uncoated)	16 μH	14.8 cm^2	1.41 cm	90 mm	180°	No
MagVenture	MC-B70 Butterfly Coil	11.9 μH	13.9 cm^2	1.35 cm	97 mm	150°	Yes

The inductance values were provided by the respective manufacturer. Most prominent difference is the slight bend of the surface of the MC-B70 Butterfly Coil and the overlapping wire loops, which leads to a slight increase in focality.

transferred and saved on a laptop via CED Signal software (version 6.05a, Cambridge, United Kingdom).

TMS Pulse Characterization

The applied TMS waveforms were characterized using a MagVenture MagProbe 3D (Farum, Denmark), with the probe fixed on the intersection of the respective figure-of-eight coil. For the recording of the pulse shapes, the stimulator output was set to 50% of maximum stimulator output (MSO).

Normalization of RMT Between Stimulators

In order to compare the stimulator intensities used for the RMT and to reach a 1 mV TS, the values were normalized by the square root of the maximum energy (W) stored in capacitor (Kammer et al., 2001). For Magstim $W = 578.1$ joules and for MagVenture $W = 300$ joules, as provided by the respective manufacturer.

Data Processing

The data were analyzed offline. The EMG time series were exported to MATLAB (version 2018a, Natick, MA, United States) and analyzed using a custom-designed graphical user interface. All trials were visually inspected. Trials with muscle pre-activation exceeding ± 25 μV from baseline <100 ms and/or ± 100 μV from baseline 500–100 ms before the TMS pulse (Hallett, 2007), trials with technical artifacts, no clear MEPs for the TS and ICF conditions [in analogy to Rossini criterion: peak-to-peak amplitude <50 μV, for review please see (Groppa et al., 2012)], or with documented suboptimal coil placement were rejected from further analysis. The MEP peak-to-peak amplitude was computed in a response window of TMS pulse +20 ms to +50 ms. The resulting peak-to-peak amplitude was averaged per condition. To indicate inhibitory or excitatory modulation, the SICI and ICF conditions were contrasted to the average TS MEPs amplitude and expressed as mean (CS+TS) / mean (TS) * 100.

Statistical Analysis

The statistical analysis was performed with the R software environment (version 3.5.1., 2018) (R Core Team, 2013), correlations and quality control was done with the statistical software JASP (JASP Team, 2018). Statistical significance was assumed at $p < 0.05$. The normality of the distributions was checked with the Shapiro–Wilk test. Normally distributed data were analyzed with a repeated measures analysis of variance (RM-ANOVA), applying pairwise *t*-test *post hoc* comparisons, bonferroni-corrected. Non-normally distributed data were analyzed with a Friedman test, with Wilcoxon–signed rank *post hoc* tests, bonferroni-corrected. To further assess for potential associations between conditions, we calculated Spearman's rank-order correlations, bonferroni-corrected. Conditions that showed significant difference in the main analysis were not taken into account for the correlations. For all the analyses that involved the MS AP condition the data of one participant has been not considered for further statistical processing due to missing values (high motor threshold). Differences between conditions were tested for every ISI separately. Conditions were interpreted as comparable, when following definition was met: (i) absence of detecting differences between the conditions in the applied statistical test (rejection of the alternative hypothesis), and (ii) the presence of a significant positive correlation with an at least moderate effect size between the assessed conditions. Secondly, we tested for differences in effectiveness between SICI and ICF within every condition. Thirdly, the MEP amplitudes of SICI and ICF were compared with the test-pulse amplitude to see, if there was effective modulation in the dpTMS protocols. Lastly, we tested for differences of TS amplitude between conditions. All values in text, figures, and tables are depicted as mean ± SEM.

RESULTS

Condition Comparisons

We tested whether there was a difference in the MEP amplitude between the four different conditions for the different ISIs (SICI and ICF). Analysis of SICI 1 showed a significant condition effect $\chi^2(2) = 7.00$, $p = 0.030$. However, *post hoc* pairwise comparisons did not show any significant differences. There was a significant difference between conditions for SICI 3 $\chi^2(3) = 20.14$, $p < 0.001$. *Post hoc* analysis showed that MS PA (56.78 ± 12.94 %) was significantly larger than MS AP (9.52 ± 1.70 %, $p = 0.005$). MS AP was significantly smaller than MV AP-PA (49.17 ± 11.11 %, $p = 0.002$) and smaller than MV PA (42.05 ± 10.84 %, $p = 0.007$). There were no overall significant differences between conditions for ICF 10 $\chi^2(3) = 6.43$, $p = 0.093$ or between conditions for ICF 15 $\chi^2(3) = 0.94$, $p = 0.815$. To further assess for potential underlying associations between conditions, we calculated Spearman's rank-order correlations. The analysis of the conditions in SICI 1 showed no significant correlations. In the SICI 3, all the conditions were tested except for the MS AP condition. There was a significant correlation between the MS PA and the MV AP-PA condition $r_s = 0.657$, $p = 0.039$. MS PA highly correlated with MV PA $r_s = 0.829$, $p = 0.001$. Finally, there was a trend between MV AP-PA and MV PA $r_s = 0.600$, $p = 0.078$. There were no significant correlations between the ICF 10 conditions as well as the ICF 15 conditions.

In summary, the MS PA condition was classified comparable to the MV AP-PA and the MV PA conditions within the framework of our definition, when assessing SICI at an 3 ms ISI, for details please see **Figure 2** and **Table 2**.

Effectiveness of Stimulation Paradigms

For every condition, we tested whether the four different ISIs resulted in differential MEP modulation. Furthermore, we compared the two inhibition and facilitation paradigms within the conditions to see whether one of the two ISIs was more effective, please see **Figure 3**.

As expected, in all conditions the comparison between the four different paradigms showed significant overall differences in MEP modulation. Results are for MS PA: $\chi^2(3) = 30.44$, $p < 0.001$, MS AP: $\chi^2(3) = 34.71$, $p < 0.001$, MV AP-PA: $\chi^2(3) = 31.24$, $p < 0.001$ and MV PA: $\chi^2(2) = 19.60$,

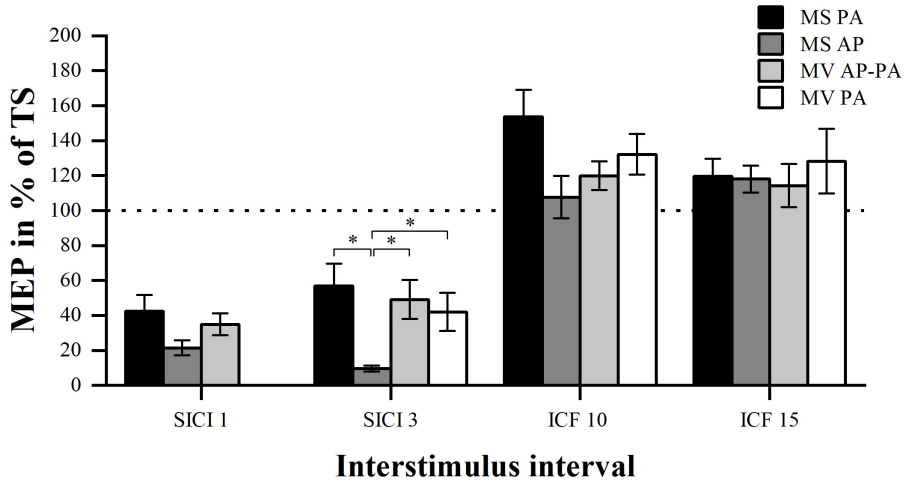

FIGURE 2 | Modulation compared per condition. Comparison of MEP modulation induced by the four different stimulator current direction conditions sorted by ISI (1, 3, 10, and 15 ms). *$p < 0.05$, bonferroni-corrected.

TABLE 2 | Association between conditions.

Condition	SICI 1		SICI 3		ICF 10		ICF 15	
	Rho	*p-value*	Rho	*p-value*	Rho	*p-value*	Rho	*p-value*
MS PA – MS AP	0.165	1.000	n/a	n/a	0.415	0.846	0.297	1.000
MS PA – MV AP-PA	0.407	0.450	0.657	0.039*	0.218	1.000	0.429	0.768
MS PA – MV PA	n/a	n/a	0.829	0.001*	0.178	1.000	0.226	1.000
MS AP – MV AP-PA	−0.095	1.000	n/a	n/a	0.341	1.000	−0.055	1.000
MS AP – MV PA	n/a	n/a	n/a	n/a	0.538	0.300	0.503	0.414
MV AP-PA – MV PA	n/a	n/a	0.600	0.078	0.525	0.342	0.121	1.000

*Spearman's rank-order correlations between the assessed conditions (MS PA, MS AP, MV AP-PA, and MV PA). *p < 0.05, bonferroni-corrected.*

$p < 0.001$, respectively. *Post hoc* comparisons showed that there was no significant difference in MEP magnitude between the two inhibitory paradigms in all the conditions. *Post hoc* comparisons within the facilitation paradigms did also show that there were no significant differences. Overall, different ISIs did not result in significantly different MEP modulation within the inhibitory or facilitatory paradigms.

Modulation Effect

We tested whether the MEP amplitudes assessed at different ISIs were significantly different from the TS, to show whether modulation was present. The results showed that all the inhibitory paradigms resulted in significant modulation for all conditions, please see **Table 3**. However, for the facilitatory paradigms only ICF 10 in MS PA resulted in a significant modulation.

Auxiliary Analysis

To compare the RMT between stimulators, the threshold was normalized to the maximal energy stored in the stimulator (Kammer et al., 2001). There was a significant effect of condition F (3, 39) = 79.01, $p < 0.001$. *Post hoc* comparisons showed that MS PA (1.70 ± 0.07) was significantly smaller than MS AP (2.34 ± 0.11, $p < 0.001$). MS PA was smaller than MV PA (2.28 ± 0.11, $p < 0.001$), MS AP was larger than MV AP-PA (1.67 ± 0.07, $p < 0.001$) and MV AP-PA was smaller than MV PA ($p < 0.001$), see **Figure 4A**.

The achieved TS amplitudes are depicted in **Figure 4B**. Results showed that there were significant differences between the four conditions in terms of TS amplitude F (3, 39) = 3.02, $p = 0.041$. However, *post hoc* pairwise comparisons did not show any significant differences between the conditions.

The stimulator output intensities to achieve a TS MEP of ∼1 mV were normalized to the maximal energy stored in the stimulator. The four conditions turned out to be significantly different from each other F (3, 39) = 77.99, $p < 0.001$. *Post hoc* comparisons showed that MS PA (2.01 ± 0.10) was significantly smaller than MS AP (2.76 ± 0.13, $p = 0.001$), MS PA was smaller than MV PA (2.79 ± 0.14, $p = 0.001$), MS AP was larger than MV AP-PA (2.05 ± 0.15, $p = 0.003$) and MV AP-PA was smaller than MV PA ($p = 0.002$), see **Figure 4C**.

DISCUSSION

In summary, we were not able to detect differences for the assessed conditions (MS PA, MS AP, MV AP-PA, and MV PA) for

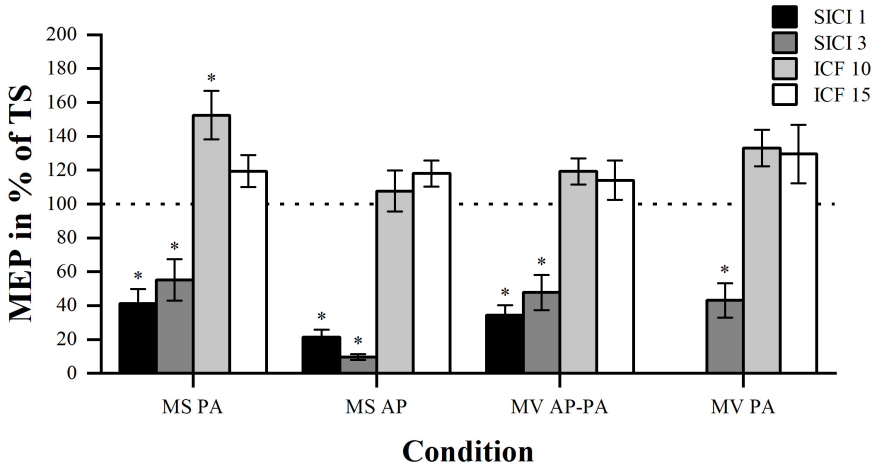

FIGURE 3 | Modulation compared per ISI. Comparison of MEP modulation induced by SICI and ICF at the four different ISIs (1, 3, 10, and 15 ms) sorted by condition. Asterisk indicates significant modulation compared with TS alone. *$p < 0.05$, bonferroni-corrected.

SICI 1, ICF 10, and 15. For SICI 3 the AP current direction led to stronger inhibition. This current direction dependent effect is discussed below.

Subsequently, we evaluated if the conditions are comparable by performing correlation analysis, which suggests that the MS PA condition is comparable with the MV AP-PA, and MV PA conditions, when assessed at an ISI of 3 ms. This finding enables the combination of SICI 3 data sets, which is often an important prerequisite for efficient meta-analysis or open science approaches. Being able to utilize different TMS systems and waveforms further strengthens the potential of SICI 3 to develop into a biomarker suitable for predicting motor recovery (Liuzzi et al., 2014) or treatment response (Zimerman et al., 2012).

Effect of Current Direction

The current direction dependent effect for SICI demonstrated here has been described previously in the literature with the largest difference at an ISI of 3 ms (Hanajima et al., 2008). A proposed mechanism may be that SICI affects mainly later I-waves (Nakamura et al., 1997) and these are mainly targeted by AP currents. In contrast, PA currents mainly evoke I1-waves (Sakai et al., 1997). Depending on the specific research questions, it might be useful to study SICI with different current directions including the unconventional AP direction. This can provide additional information, e.g., when assessing underlying mechanisms of neurological conditions (Hanajima et al., 2008, 2011). A practical technical note to be mentioned is that when utilizing the Magstim BiStim^2 stimulator with a standard D70 alpha flat coil the AP technique is manually more demanding, when the equipment does not provide a switch-option to change the current direction within the coil. Furthermore, the AP condition requires higher stimulation intensities for RMT and 1 mV MEP (Kammer et al., 2001), which could limit its application in specific conditions with increased thresholds, such as in healthy aged populations (Sale et al., 2016) or within neurological disorders such as stroke (McDonnell and Stinear, 2017).

TABLE 3 | Modulation effect.

Condition	SICI 1 *p*-value	SICI 3 *p*-value	ICF 10 *p*-value	ICF 15 *p*-value
MS PA	0.003*	0.034*	0.034*	1.000
MS AP	0.001*	0.001*	1.000	0.245
MV AP-PA	<0.001*	0.012*	0.302	1.000
MV PA	n/a	0.003*	0.288	0.332

*Modulation effect for every ISI compared with the TS. Significant results depict that there was significant inhibition or facilitation compared with the TS. *p < 0.05, bonferroni-corrected.*

Effect of Interstimulus Interval

For SICI two different phases, an early at ∼1 ms and a late at ∼2.5 ms, have been reported (Fisher et al., 2002). These phases seem to have different thresholds and a differential susceptibility toward voluntary muscle activation. Furthermore, they show a low correlation and are most likely mediated by different inhibitory circuits (Roshan et al., 2003). For a comparable CS intensity as used in our study (80% of RMT) a monophasic waveform with a PA current direction has resulted in comparable levels of inhibition for both phases (Roshan et al., 2003). The present study was able to replicate these previous findings. For the AP current direction, we found a trend for stronger inhibition at an ISI of 3 ms compared with 1 ms. Moreover, we found a trend for more facilitation at the 10 ms ISI compared with the 15 ms for the ICF paradigm in the Magstim PA condition. Both may be explained by different threshold levels of the underlying neuronal circuits.

Effect of Waveform

To study the effects of waveform is important since it is assumed that the underlying effect is mediated by different activation sites. Main evidence is based on the recording of TMS-induced

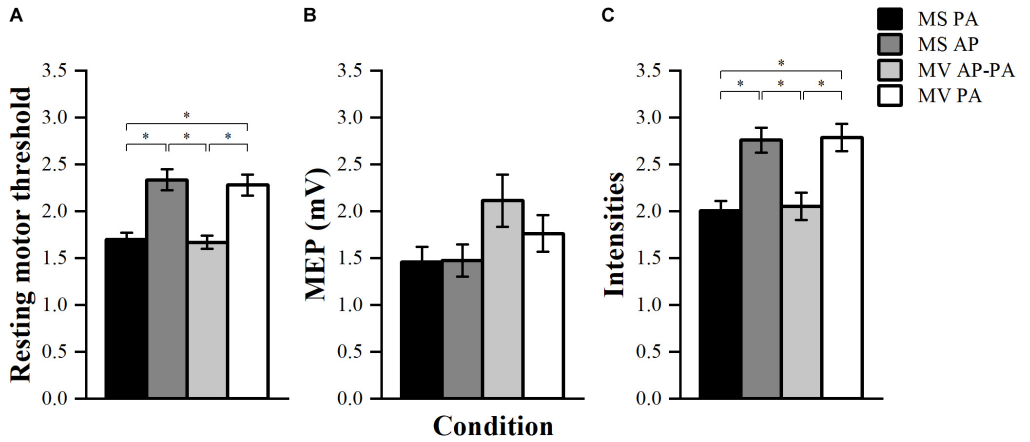

FIGURE 4 | Resting motor threshold, TS amplitude, and stimulator intensities. **(A)** Normalized resting motor threshold (RMT) across conditions. **(B)** Achieved peak-to-peak amplitude for the TS across different conditions. **(C)** Normalized stimulator output intensity at the achieved TS amplitude (∼1 mV) across conditions. *$p < 0.05$, bonferroni-corrected.

descending volleys sampled with epidural recordings (Di Lazzaro et al., 2008). In these, monophasic PA currents mainly affect I-waves at lower intensities, which suggest a main activation site at first and higher-order excitatory interneurons. At higher intensities monophasic PA pulses can also induce a small D-wave, resulting from activation of the proximal part of a pyramidal cell axon. In contrast, monophasic AP currents preferentially induce later I-waves, pointing toward a primary activation site at higher-order excitatory interneurons. Biphasic AP-PA currents result in descending volleys at a slightly different latency and periodicity. The fact that both phases can activate neuronal elements suggests a more widespread activation. In addition, the different waveforms may also affect slightly different neuronal populations as the cortical folding and its impact on the axonal orientation results in different susceptibilities of the targeted cortical neurons (Di Lazzaro et al., 2008).

The effects of waveforms on SICI and ICF was recently investigated by Davila-Pérez et al. (2018). They found less inhibition for a biphasic pulse when compared with a monophasic pulse at a 3 ms ISI in their *post hoc* testing, without a significant main effect. We were not able to replicate these results. Small effects size (no significant main effect) and difference in TS adjustment (120% of RMT versus adjusted to ∼1 mV MEP) may have contributed to the differential findings. Furthermore, Davila-Pérez et al. (2018) reported significant less facilitation for ICF with monophasic waveform and a PA current direction, when compared with the biphasic waveform. These findings were not apparent in our current data, though measured at a different ISI (12 ms versus 10 or 15 ms). A possible explanation for the similarity of the induced effects for the monophasic PA and biphasic AP-PA condition, in our data, could be the similar pattern of supposedly recruited descending volleys (Di Lazzaro et al., 2001).

No Consistent Effect of ICF

It is of note, that we could not find significant facilitation for the ICF paradigm when compared to TS for most conditions, except for the conventional Magstim PA condition at a 10 ms ISI. This complements available literature, which reports low reliability for ICF (Boroojerdi et al., 2000; Maeda et al., 2002; Fleming et al., 2012) and limits its comparability. Discussed underlying biological sources of variability are asynchrony and phase cancelation of descending volleys, inherent changes in cortical excitability (Boroojerdi et al., 2000), and different thresholds for SICI and ICF (Hermsen et al., 2016). Our result for the unconventional AP ICF contradicts the finding of Davila-Pérez, who found only significant facilitation with the AP current direction (Davila-Pérez et al., 2018). A possible reason for the differential findings between these studies might be due to the fact that different ISIs were studied – 10 and 15 ms versus 12 ms.

Limitations

We have identified a few limitations of our study. Our adjustment of the TS amplitude tended to be larger than the aimed 1 mV peak-to-peak amplitude (MS PA: 1.46 ± 0.16 mV, MS AP: 1.48 ± 0.17 mV, MV AP-PA: 2.11 ± 0.28 mV, and MV PA: 1.76 ± 0.19 mV). However, our amplitudes were well in the comparable range for SICI (Sanger et al., 2001; Garry and Thomson, 2009). The impact for ICF paradigms might be larger, since the effect of ICF seems to decrease at higher TS amplitudes (assessed target amplitude 4 mV) (Sanger et al., 2001). However, the range around 4 mV is much higher than in our study. We cannot exclude that suboptimal TS adjustment may have contributed to the inconstant facilitation we found for ICF. Moreover, the Magstim and MagVenture coils differ in design, e.g., inductance, angle of the surface, overlap of the wire loops, please see **Table 1**. Though, they share comparable values for focality and stimulation depth (Deng et al., 2013) and seem to trigger similar physiological effects (Thielscher and Kammer, 2004). It is of note, that in the present study specific intensities and the above mentioned coil designs, which are currently mainly used (Rossi et al., 2009; Deng et al., 2013), have been tested and not the full possible range of parameters for paired pulse paradigms. This should be taken into account, when

prospective assumptions are made toward a larger stimulation parameter space. For statistical analyses, we *a priori* defined to apply Bonferroni correction, a well-established, but rather conservative correction method. In upcoming studies more liberal statistical approaches can be applied to further support the current findings. Furthermore, a rather small sample size may have restrained us from detecting effects with low effect sizes. Lastly, we did not use a coil tracking system, which may improve coil positioning (Washabaugh and Krishnan, 2016). Although, for motor-cortex centered SICI assessments hand-held and navigated approaches have shown to result in comparable reliability (Fleming et al., 2012).

CONCLUSION

In summary, we obtained comparable results for SICI 3, when comparing MS PA to MV AP-PA and MV PA. This opens the opportunity to combine data sets sampled with different experimental setups, supports conduction of multi-center trials, and enables between study comparisons toward open science.

DATA AVAILABILITY

The datasets generated for this study are available on request to the corresponding author.

ETHICS STATEMENT

All subjects gave written informed consent in accordance with the Declaration of Helsinki (World Medical Association, 2013). The protocol was approved by the cantonal ethics committee Vaud, Switzerland (Project Number 2017-00765).

AUTHOR CONTRIBUTIONS

MW and FH developed the study concept and wrote the study protocol. MW and TM implemented the experimental setup. MW and LD collected the data. LD processed and analyzed the data, and performed the statistical analysis. MW, LD, TM, and FH were involved in the data interpretation. MW and LD searched the literature and wrote the first draft of the manuscript. MW, LD, TM, and FH revised and approved the final version of the manuscript.

FUNDING

This work was supported by the Defitech Foundation (Morges, Switzerland), the Wyss Center for Bio and Neuroengineering (WCP024, Geneva, Switzerland), and a grant (#2017−205) of the Strategic Focus Area "Personalized Health and Related Technologies (PHRT)" of the ETH Domain (CH).

REFERENCES

Boroojerdi, B., Kopylev, L., Battaglia, F., Facchini, S., Ziemann, U., Muellbacher, W., et al. (2000). Reproducibility of intracortical inhibition and facilitation using the paired-pulse paradigm. *Muscle Nerve* 23, 1594–1597. doi: 10.1002/1097-4598(200010)23:10<1594::aid-mus19>3.3.co;2-v

Chen, R. (2004). Interactions between inhibitory and excitatory circuits in the human motor cortex. *Exp. Brain Res.* 154, 1–10. doi: 10.1007/s00221-003-1684-1

Davila-Pérez, P., Jannati, A., Fried, P. J., Cudeiro Mazaira, J., and Pascual-Leone, A. (2018). The effects of waveform and current direction on the efficacy and test-retest reliability of transcranial magnetic stimulation. *Neuroscience* 393, 97–109. doi: 10.1016/j.neuroscience.2018.09.044

Deng, Z.-D., Lisanby, S. H., and Peterchev, A. V. (2013). Electric field depth-focality tradeoff in transcranial magnetic stimulation: simulation comparison of 50 coil designs. *Brain Stimul.* 6, 1–13. doi: 10.1016/j.brs.2012.02.005

Di Lazzaro, V., Oliviero, A., Mazzone, P., Insola, A., Pilato, F., Saturno, E., et al. (2001). Comparison of descending volleys evoked by monophasic and biphasic magnetic stimulation of the motor cortex in conscious humans. *Exp. Brain Res.* 141, 121–127. doi: 10.1007/s002210100863

Di Lazzaro, V., Oliviero, A., Meglio, M., Cioni, B., Tamburrini, G., Tonali, P., et al. (2000). Direct demonstration of the effect of lorazepam on the excitability of the human motor cortex. *Clin. Neurophysiol.* 111, 794–799. doi: 10.1016/s1388-2457(99)00314-4

Di Lazzaro, V., Ziemann, U., and Lemon, R. N. (2008). State of the art: physiology of transcranial motor cortex stimulation. *Brain Stimul.* 1, 345–362. doi: 10.1016/j.brs.2008.07.004

Ende, G. (2015). Proton magnetic resonance spectroscopy: relevance of glutamate and gaba to neuropsychology. *Neuropsychol. Rev.* 25, 315–325. doi: 10.1007/s11065-015-9295-8

Fisher, R. J., Nakamura, Y., Bestmann, S., Rothwell, J. C., and Bostock, H. (2002). Two phases of intracortical inhibition revealed by transcranial magnetic threshold tracking. *Exp. Brain Res.* 143, 240–248. doi: 10.1007/s00221-001-0988-2

Fleming, M. K., Sorinola, I. O., Newham, D. J., Roberts-Lewis, S. F., and Bergmann, J. H. M. (2012). The effect of coil type and navigation on the reliability of transcranial magnetic stimulation. *IEEE Trans. Neural Syst. Rehabil. Eng.* 20, 617–625. doi: 10.1109/TNSRE.2012.2202692

Garry, M. I., and Thomson, R. H. S. (2009). The effect of test TMS intensity on short-interval intracortical inhibition in different excitability states. *Exp. Brain Res.* 193, 267–274. doi: 10.1007/s00221-008-1620-5

Groppa, S., Oliviero, A., Eisen, A., Quartarone, A., Cohen, L. G., Mall, V., et al. (2012). A practical guide to diagnostic transcranial magnetic stimulation: report of an IFCN committee. *Clin. Neurophysiol.* 123, 858–882. doi: 10.1016/j.clinph.2012.01.010

Hallett, M. (2007). Transcranial magnetic stimulation: a primer. *Neuron* 55, 187–199. doi: 10.1016/j.neuron.2007.06.026

Hanajima, R., Okabe, S., Terao, Y., Furubayashi, T., Arai, N., Inomata-Terada, S., et al. (2008). Difference in intracortical inhibition of the motor cortex between cortical myoclonus and focal hand dystonia. *Clin. Neurophysiol.* 119, 1400–1407. doi: 10.1016/j.clinph.2008.02.009

Hanajima, R., Terao, Y., Shirota, Y., Ohminami, S., Nakatani-Enomoto, S., Okabe, S., et al. (2011). Short-interval intracortical inhibition in parkinson's disease using anterior-posterior directed currents. *Exp. Brain Res.* 214, 317–321. doi: 10.1007/s00221-011-2829-2

Heise, K. F., Steven, B., Liuzzi, G., Thomalla, G., Jonas, M., Muller-Vahl, K., et al. (2010). Altered modulation of intracortical excitability during movement preparation in Gilles de la Tourette syndrome. *Brain* 133, 580–590. doi: 10.1093/brain/awp299

Heise, K. F., Zimerman, M., Hoppe, J., Gerloff, C., Wegscheider, K., and Hummel, F. C. (2013). The aging motor system as a model for plastic changes of GABA-mediated intracortical inhibition and their behavioral relevance. *J. Neurosci.* 33, 9039–9049. doi: 10.1523/JNEUROSCI.4094-12.2013

Hermsen, A. M., Haag, A., Duddek, C., Balkenhol, K., Bugiel, H., Bauer, S., et al. (2016). Test-retest reliability of single and paired pulse transcranial magnetic stimulation parameters in healthy subjects. *J. Neurol. Sci.* 362, 209–216. doi: 10.1016/j.jns.2016.01.039

Hummel, F. C., Steven, B., Hoppe, J., Heise, K., Thomalla, G., Cohen, L. G., et al. (2009). Deficient intracortical inhibition (SICI) during movement preparation after chronic stroke. *Neurology* 72, 1766–1772. doi: 10.1212/WNL.0b013e3181a609c5

JASP Team (2018). *JASP(Version 0.9.2)*. Available at: https://jasp-stats.org/ .(accessed June 11, 2019).

Kammer, T., Beck, S., Thielscher, A., Laubis-Herrmann, U., and Topka, H. (2001). Motor thresholds in humans: a transcranial magnetic stimulation study comparing different pulse waveforms, current directions and stimulator types. *Clin. Neurophysiol.* 112, 250–258. doi: 10.1016/s1388-2457(00)00513-7

Kirkwood, A. (2015). Balancing excitation and inhibition. *Neuron* 86, 348–350. doi: 10.1016/j.neuron.2015.04.009

Kujirai, T., Caramia, M. D., Rothwell, J. C., Day, B. L., Thompson, P. D., Ferbert, A., et al. (1993). Corticocortical inhibition in human motor cortex. *J. Physiol.* 471, 501–519. doi: 10.1113/jphysiol.1993.sp019912

Liuzzi, G., Horniss, V., Lechner, P., Hoppe, J., Heise, K., Zimerman, M., et al. (2014). Development of movement-related intracortical inhibition in acute to chronic subcortical stroke. *Neurology* 82, 198–205. doi: 10.1212/WNL.0000000000000028

Maeda, F., Gangitano, M., Thall, M., and Pascual-Leone, A. (2002). Inter- and intra-individual variability of paired-pulse curves with transcranial magnetic stimulation (TMS). *Clin. Neurophysiol.* 113, 376–382. doi: 10.1016/s1388-2457(02)00008-1

McDonnell, M. N., and Stinear, C. M. (2017). TMS measures of motor cortex function after stroke: a meta-analysis. *Brain Stimul.* 10, 721–734. doi: 10.1016/j.brs.2017.03.008

Nakamura, H., Kitagawa, H., Kawaguchi, Y., and Tsuji, H. (1997). Intracortical facilitation and inhibition after transcranial magnetic stimulation in conscious humans. *J. Physiol.* 498(Pt 3), 817–823. doi: 10.1113/jphysiol.1997.sp021905

Oldfield, R. C. (1971). The assessment and analysis of handedness: the edinburgh inventory. *Neuropsychologia* 9, 97–113. doi: 10.1016/0028-3932(71)90067-4

R Core Team (2013). *R: A Language and Environment for Statistical Computing*. Vienna: Foundation for Statistical Computing.

Roshan, L., Paradiso, G. O., and Chen, R. (2003). Two phases of short-interval intracortical inhibition. *Exp. Brain Res.* 151, 330–337. doi: 10.1007/s00221-003-1502-9

Rossi, S., Hallett, M., Rossini, P. M., Pascual-Leone, A., and Safety of TMS Consensus Group (2009). Safety, ethical considerations, and application guidelines for the use of transcranial magnetic stimulation in clinical practice and research. *Clin. Neurophysiol.* 120, 2008–2039. doi: 10.1016/j.clinph.2009.08.016

Sakai, K., Ugawa, Y., Terao, Y., Hanajima, R., Furubayashi, T., and Kanazawa, I. (1997). Preferential activation of different I waves by transcranial magnetic stimulation with a figure-of-eight-shaped coil. *Exp. Brain Res.* 113, 24–32. doi: 10.1007/bf02454139

Sale, M. V., Lavender, A. P., Opie, G. M., Nordstrom, M. A., and Semmler, J. G. (2016). Increased intracortical inhibition in elderly adults with anterior-posterior current flow: a TMS study. *Clin. Neurophysiol.* 127, 635–640. doi: 10.1016/j.clinph.2015.04.062

Sanger, T. D., Garg, R. R., and Chen, R. (2001). Interactions between two different inhibitory systems in the human motor cortex. *J. Physiol.* 530, 307–317. doi: 10.1111/j.1469-7793.2001.0307l.x

Sommer, M., Alfaro, A., Rummel, M., Speck, S., Lang, N., Tings, T., et al. (2006). Half sine, monophasic and biphasic transcranial magnetic stimulation of the human motor cortex. *Clin. Neurophysiol.* 117, 838–844. doi: 10.1016/j.clinph.2005.10.029

Thielscher, A., and Kammer, T. (2004). Electric field properties of two commercial figure-8 coils in TMS: calculation of focality and efficiency. *Clin. Neurophysiol.* 115, 1697–1708. doi: 10.1016/j.clinph.2004.02.019

Van Doren, J., Langguth, B., and Schecklmann, M. (2015). TMS-related potentials and artifacts in combined TMS-EEG measurements: comparison of three different TMS devices. *Neurophysiol. Clin.* 45, 159–166. doi: 10.1016/j.neucli.2015.02.002

Washabaugh, E. P., and Krishnan, C. (2016). A low-cost system for coil tracking during transcranial magnetic stimulation. *Restor. Neurol. Neurosci.* 34, 337–346. doi: 10.3233/RNN-150609

World Medical Association (2013). World medical association declaration of helsinki: ethical principles for medical research involving human subjects. *JAMA* 310, 2191–2194. doi: 10.1001/jama.2013.281053

Ziemann, U., Chen, R., Cohen, L. G., and Hallett, M. (1998). Dextromethorphan decreases the excitability of the human motor cortex. *Neurology* 51, 1320–1324. doi: 10.1212/wnl.51.5.1320

Zimerman, M., Heise, K. F., Hoppe, J., Cohen, L. G., Gerloff, C., and Hummel, F. C. (2012). Modulation of training by single-session transcranial direct current stimulation to the intact motor cortex enhances motor skill acquisition of the paretic hand. *Stroke* 43, 2185–2191. doi: 10.1161/STROKEAHA.111.645382

Conflict of Interest Statement: The authors declare that the research was conducted in the absence of any commercial or financial relationships that could be construed as a potential conflict of interest.

Copyright © 2019 Wessel, Draaisma, Morishita and Hummel. This is an open-access article distributed under the terms of the Creative Commons Attribution License (CC BY). The use, distribution or reproduction in other forums is permitted, provided the original author(s) and the copyright owner(s) are credited and that the original publication in this journal is cited, in accordance with accepted academic practice. No use, distribution or reproduction is permitted which does not comply with these terms.

frontiers in Neuroscience

ORIGINAL RESEARCH
published: 09 August 2019
doi: 10.3389/fnins.2019.00579

Transcranial Recording of Electrophysiological Neural Activity in the Rodent Brain *in vivo* Using Functional Photoacoustic Imaging of Near-Infrared Voltage-Sensitive Dye

Jeeun Kang[1,2], *Haichong K. Zhang*[1,2], *Shilpa D. Kadam*[3], *Julie Fedorko*[2], *Heather Valentine*[2], *Adarsha P. Malla*[4], *Ping Yan*[5], *Maged M. Harraz*[4], *Jin U. Kang*[1], *Arman Rahmim*[2], *Albert Gjedde*[2,6], *Leslie M. Loew*[5], *Dean F. Wong*[2,4,6,7,8,9] *and Emad M. Boctor*[1,2]*

[1] Whiting School of Engineering, Johns Hopkins University, Baltimore, MD, United States, [2] Russell H. Morgan Department of Radiology and Radiological Science, Johns Hopkins Medical Institutions, Baltimore, MD, United States, [3] Department of Neurology, Hugo W. Moser Research Institute at Kennedy Krieger, Johns Hopkins Medical Institutions, Baltimore, MD, United States, [4] Solomon H. Snyder Department of Neuroscience, Johns Hopkins University, Baltimore, MD, United States, [5] R. D. Berlin Center for Cell Analysis and Modeling, University of Connecticut Health, Farmington, CT, United States, [6] Department of Neuroscience, University of Copenhagen, Copenhagen, Denmark, [7] Department of Psychiatry and Behavioral Sciences, Johns Hopkins Medical Institutions, Baltimore, MD, United States, [8] Department of Neurology, Johns Hopkins Medical Institutions, Baltimore, MD, United States, [9] Department of Environmental Sciences and Engineering, Johns Hopkins University, Baltimore, MD, United States

OPEN ACCESS

Edited by:
Mohammadreza Nasiriavanaki, Wayne State University, United States

Reviewed by:
Vassiliy Tsytsarev, University of Maryland, College Park, United States
Jun Xia, University at Buffalo, United States

***Correspondence:**
Emad M. Boctor
eboctor1@jhmi.edu

Specialty section:
This article was submitted to Brain Imaging Methods, a section of the journal Frontiers in Neuroscience

Received: *11 January 2019*
Accepted: *22 May 2019*
Published: *09 August 2019*

Citation:
Kang J, Zhang HK, Kadam SD, Fedorko J, Valentine H, Malla AP, Yan P, Harraz MM, Kang JU, Rahmim A, Gjedde A, Loew LM, Wong DF and Boctor EM (2019) Transcranial Recording of Electrophysiological Neural Activity in the Rodent Brain in vivo Using Functional Photoacoustic Imaging of Near-Infrared Voltage-Sensitive Dye. Front. Neurosci. 13:579. doi: 10.3389/fnins.2019.00579

Minimally-invasive monitoring of electrophysiological neural activities in real-time—that enables quantification of neural functions without a need for invasive craniotomy and the longer time constants of fMRI and PET—presents a very challenging yet significant task for neuroimaging. In this paper, we present *in vivo* functional PA (fPA) imaging of chemoconvulsant rat seizure model with intact scalp using a fluorescence quenching-based cyanine voltage-sensitive dye (VSD) characterized by a lipid vesicle model mimicking different levels of membrane potential variation. The framework also involves use of a near-infrared VSD delivered through the blood-brain barrier (BBB), opened by pharmacological modulation of adenosine receptor signaling. Our normalized time-frequency analysis presented *in vivo* VSD response in the seizure group significantly distinguishable from those of the control groups at sub-mm spatial resolution. Electroencephalogram (EEG) recording confirmed the changes of severity and frequency of brain activities, induced by chemoconvulsant seizures of the rat brain. The findings demonstrate that the near-infrared fPA VSD imaging is a promising tool for *in vivo* recording of brain activities through intact scalp, which would pave a way to its future translation in real time human brain imaging.

Keywords: photoacoustic, neuroimaging, near-infrared, voltage-sensitive dye, transcranial, seizure

INTRODUCTION

The quantification and monitoring of brain function is a major goal of neuroscience and clinical researches into the underlying mechanisms of the working brain (Raichle and Mintun, 2006; Friston, 2009). Toward this objective, several modalities have been introduced for the purpose of neuroimaging; however, existing methods have limitations. Positron emission tomography (PET) provides high molecular resolution and pharmacological specificity, but suffers from low spatial and temporal resolution. In particular the low temporal resolution is a methodological challange in obtaining measures o neurotransmitter release in ms rather than several minutes as in brain activation studies of the dopamine system (Wong et al., 2006; Anderson et al., 2016). Functional magnetic resonance imaging (fMRI) provides higher spatial resolution of brain activity; however, the recorded blood-oxygenation level dependent (BOLD) signal has comparatively low temporal resolution and involves uncertain interpretation (Berman et al., 2006; Logothetis, 2008). Optical imaging approaches have been used to monitor the brain function of small animals but have limited dynamic ranges and cover only superficial tissue depths because of light scattering and absorbance during penetration of biological tissue (Hillman, 2007; Devor et al., 2012). These optical approaches require invasive craniotomy for imaging of deeper brain region, with problematic long-term consequences such as dural regrowth, greater likelihood of inflammatory cascade initiation, and lack of translational practicality to non-human primate and ultimately to human studies, including those for neuropsychiatric disorders (Heo et al., 2016). Near-infrared spectroscopy (NIRS) monitors brain function non-invasively in real-time (∼1 ms) at several-mm depth for human brain, but suffers from poor spatial resolution (∼1 cm) at those depths (Strangman et al., 2013; Torricelli et al., 2014). Therefore, minimally-invasive monitoring of electrophysiological brain activities in real-time remains a task at hand in neuroimaging, with the aim to quantify brain functions in the depths of brain tissue at sub-mm spatial resolution, without need for invasive craniotomy or skull thinning techniques.

To overcome the current challenges, photoacoustic (PA) imaging has been investigated as a promising hybrid modality that provides the molecular contrast of brain function with acoustic transcranial penetration and spatial resolution (Wang et al., 2003; Nie et al., 2012; Wang and Hu, 2012; Li et al., 2018). In PA imaging, radio-frequency (RF) acoustic pressure is generated, depending on the thermo-elastic property and light absorbance of a target illuminated by pulsed laser, and it is detected by an ultrasound transducer. Based on this imaging mechanism, a transcranial neurovascular PA imaging have been extensively studied (Tsytsarev et al., 2011; Gottschalk et al., 2017). These approaches are completely non-invasive and provide indirect measure of neural activity without any use of extrinsic dye. However, it lacks temporal information of dynamic neural activities due to the prolonged duration of neurovascular coupling, extending up to tens of seconds from a brief electrophysiologic activity. Alternatively, several PA neuroimaging approaches using extrinsic dye have been recently applied to detect electrophysiological brain activities in both tomographic and microscopic imaging configurations; Deán-Ben et al. presented *in vivo* whole brain monitoring of zebrafish using real-time PA tomography of a genetically encoded calcium indicator, GCaMP5G (Deán-Ben et al., 2016). Ruo et al. reported PA imaging *in vivo* of mouse brain responses to electrical stimulation and 4-aminopyridine-induced epileptic seizures by means of hydrophobic anions such as dipicrylamine (DPA) (Ruo et al., 2017). However, these studies used voltage sensing in the visible spectral range (488 and 530 nm for GCaMP5G; 500 and 570 nm for DPA), which may not be optimal for recording deep brain activity because of the optical attenuation. To address this, we recently presented a novel mechanism of near-infrared cyanine voltage sensitive dye (VSD) based on selective fluorescence quenching upon membrane potential variations (Zhang et al., 2017).

Here, we propose *in vivo* functional PA (fPA) imaging of chemoconvulsant rat seizure model with intact scalp using our near-infrared cyanine VSD validated by a lipid vesicle model mimicking various membrane potential levels. As a step toward minimally-invasive external neuroimaging in primates and human brains, the results demonstrate that the fPA imaging of the fluorescence quenching VSD mechanism is a promising approach to the recording brain activities of chemoconvulsant rat model at sub-mm spatial resolution, without need for any invasive craniotomy or skull thinning techniques.

MATERIALS AND METHODS

fPA VSD Imaging Setup

An ultrasound research system was comprised by a 128-channel ultrasound linear array transducer (L14-5/38, Ultrasonix Corp., Canada; 6.9 MHz center frequency; 78.25% of −6 dB fractional bandwidth; 0.3048 mm element pitch) connected to a real-time data acquisition system (SonixDAQ, Ultrasonix Corp., Canada; 40 MHz sampling frequency; 21 dB gain in low-noise amplification; 30 dB gain in programmable-gain amplification). To induce the PA signals, pulsed laser light was generated by a second-harmonic (532 nm) Nd:YAG laser pumping an optical parametric oscillator (OPO) system (Phocus Inline, Opotek Inc., USA). The tunable range of the laser system was 690–900 nm and the maximum pulse repetition frequency was 20 Hz. The laser pulse was fed into a fiber optic bundle delivering to bifurcated outlets, each 40 mm long and 0.88 mm wide (**Figure 1A**). The customized, 3-D printed shell fixes the ultrasound probe between the outlets of the bifurcated fiber optic bundle outlets for evenly distributed laser energy density in lateral direction. The bifurcated output beams were overlapped at 20 mm depth. The PA probe was located at around 2.2 mm from bregma to obtain the cross-section of motor cortexes (**Figure 1C**). The distance between fPA probe and rat skin surface was 20 mm, and the resultant energy density was at 3.5 mJ/cm^2, which is far below the maximum permissible exposure (MPE) of skin to laser radiation by the ANSI safety standards. A wavelength of 790 nm was used, at which the light energy was sufficiently absorbed by the near-infrared VSD, i.e., IR780 perchlorate. Also, probing at this wavelength prevented the undesired error by

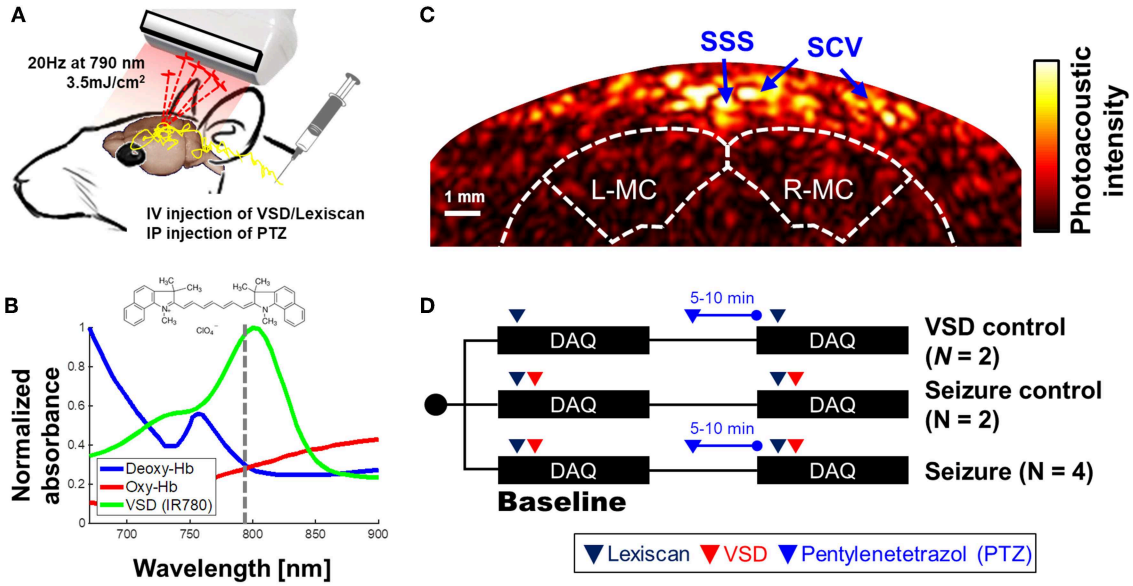

FIGURE 1 | Transcranial VSD sensing setup using fPA imaging system: **(A)** schematic diagram of experimental setup; **(B)** absorbance spectra of VSD, deoxy- and oxy-hemoglobin. Dotted line indicates the wavelength used in *in vivo* experiment, i.e., 790 nm; **(C)** cross-sectional PA image of cerebral cortex; **(D)** *in vivo* experimental protocol. SSS, Superior sagittal sinus; SCV, Superior cortical veins. L-MC/R-MC: left/right motor cortex. Note that the outlines for brain and motor cortex in **Figure 1C** was drawn based on the rat brain atlas (Bregma 2.2 mm) (Paxinos and Watson, 2014). The success of seizure induction on motor cortex was confirmed by tonic-clonic movements in the fore and hind-limbs of the anesthetized rat during the experiments (see **Movie S1**).

time-variant oxygen change, being at the isosbestic point of Hb and HbO_2 absorption spectra (**Figure 1B**). The bias from blood context would be removed by the proposed back-end signal processing (see section Normalized Time-Frequency Analysis). Spatial resolution was 479.5 ± 2.7 and 470.8 ± 24.0 μm in axial and lateral directions by applying an effective signal bandwidth at 1–5 MHz for envelope detection—The spatial resolution is optimized to detect the clusters of contrast chance generated by VSD redistribution in brain circuitries at sub-mm scale, rather than differentiating individual neuronal cells (∼10 of μm) or micro-vasculatures [mostly ∼20 μm in diameter, (Zhang et al., 2014a)] in rat brain. See the section Criteria for Selecting Region-of-Interest, criteria for selecting brain region-of-interest, and the **Supplementary Information** for detailed *in vivo* imaging performance. **Figure 1C** presents a representative cross-sectional PA image of a rat brain. The dotted white outlines for the brain and motor cortex were drawn based on the rat brain atlas (Paxinos and Watson, 2014).

Fluorescence Quenching-Based Near-Infrared Voltage-Sensitive Dye

Several cyanine VSDs have been proposed as markers for real-time electrical signal detection (Treger et al., 2014) and fluorescence tracking of electrical signal propagation on a heart (Martišiene et al., 2016). Recently we presented the mechanism of action of a cyanine VSD for fPA neuroimaging at near-infrared wavelength essential for deep transcranial neuroimaging (Zhang et al., 2017). The discussed VSD redistribution mechanism proposes a suppressive PA contrast as a product of fluorescence quenching when neuronal depolarization occurs. In the present study, we used the near-infrared cyanine VSD, IR780 perchlorate (576409, Sigma-Aldrich Co. LLC, MO, United States) with the analogous chemical structure of PAVSD800-2 in our previous study. Note that the response time of the given VSD redistribution mechanism through cell membrane should be in sub-second scale as presented in our previous study (Zhang et al., 2017).

Lipid Vesicle Phantom Preparation for VSD Validation

The physicochemical and biophysical studies regarding the interaction of exogenous molecules with a biological membrane have been extensively investigated using a single cell patch clamping (Jurkat-Rott and Lehmann-Hom, 2004) or using lipid vesicle models for precise control and measurement of cell membrane potential (Mazur et al., 2017; Paxton et al., 2017; Rosilio, 2018). In this study, we employ the lipid vesicle model considering our VSD redistribution mechanism in a tissue-scale between extracellular space and the cytoplasm of polarized cells as a function of membrane potential variation. The single cell patch clamping is optimized for an individual cell, rather than the cluster of cells. There is also an approach to control a cell membrane potential using valinomycin and varying the external K^+ on a cell suspension, while being monitored in fluorescence or PA microscopy (Ruo et al., 2017). However, this treatment for membrane potential control may affect the biological state of living cells by causing them to swell and bleb

in practice (Ramnath et al., 1992; Takahashi et al., 1995). On the contrary, the lipid vesicle model is free from these concerns, and more consistent measurements could be allowed between lipid vesicle model and translational *in vivo* experiments by using our cross-sectional imaging system described in section fPA VSD Imaging Setup.

The lipid vesicle model was prepared using the same procedure as in Zhang et al. (2017); 25-mg soybean phosphatidylcholine (type II) suspended in 1 mL of K^+ buffer was used as the lipid vesicles. This vesicle contains 100 mM K_2SO_4 and 20 mM HEPES. The suspension was vortexed for 10 min, and followed by 60 min of sonication within bath-type sonicator to yield a translucent vesicle suspension. A Na^+ buffer was also prepared, containing 100 mM Na_2SO_4 and 20 mM HEPES. Afterwards, 25:1, 50:1, and 100:1 K^+ gradients across vesicle membrane were established with 2.5, 5.0, and 10.0 μL of lipid vesicle suspensions, respectively added to 1 mL of Na^+ buffers. In the lipid vesicle model prepared, negative membrane potential (polarized state) was mimicked by adding 2.5 μL of 10 μM valinomycin—a K^+ specific ionophore, thereby K^+ ions were transported from inside to outside of vesicle membranes. On the other hand, 2.5 μL of 1 mM gramicidin, a non-specific monovalent cation ionophore, enabled Na^+ cations to move from outside to inside of vesicle membranes to short circuit the membrane potential (depolarized state). From these controls, our near-infrared VSD positively charged can move in and out through the membrane, leading to the change in fluorescence quenching depending on their aggregation status. From this lipid vesicle model, we expected the logarithmic change in membrane potential levels based on the Nernst equation (Archer, 1989): −83, −102, and −120 mV. This will yield a corresponding suppression in PA intensity. The quantum yields of the VSD in depolarized states (Φ'_F) were estimated based on the equations in our previous literature (Equations 8 and 9 in Zhang et al., 2017).

Animal Preparation

For the proposed *in vivo* experiments. 8–9 weeks-old male Sprague Dawley rats weighing 275–390 g were used (Charles Rivers Laboratory, Inc., MA, United States). The use of animals for the proposed *in vivo* protocol was approved by the Institutional Research Board Committee of Johns Hopkins Medical Institute (RA16M225). All animals were anesthetized by intraperitoneal injection with a ketamine (100 mg/ml)/xylazine (20 mg/ml) cocktail (3:1 ratio based on body weight at 1 ml/kg). The hair was shaved from the scalp of each rat for better optical and acoustic coupling. The head of the anesthetized rat was fixed to a stable position using a standard stereotaxic device. This fixation procedure was required to prevent any unpredictable movement during the fPA recording.

Chemoconvulsant Seizure Induction

Penetylenetetrazole (PTZ), a gamma-aminobutyric acid (GABA) A receptor antagonist was used to induce acute seizures in the animals (Löscher, 2017). PTZ suppresses the inhibitory effects of GABA, thus leading to generation of synchronized depolarizations of neurons in form of epileptiform discharges and seizures (Bradford, 1995). To induce global episodic acute seizures in rat brain, an intraperitoneal (IP) injection of PTZ (45 mg/ml) was utilized based on the animal's body weight in a volume of 1 ml/kg. Subsequent doses were given if no acute motor seizure was observed in 5–10 min after the first PTZ injection. Generally, 1–2 doses were sufficient to induce the motor seizures in our experiments.

Pharmacological Treatment for VSD Delivery Into Blood-Brain-Barrier

The lumen of the brain microvasculature consists of brain endothelial cells, and the blood-brain barrier (BBB) is comprised of their tight junctions to control the chemical exchange between neural cells and cerebral nervous system (CNS). In this study, the penetration through BBB were achieved with a pharmacological method using FDA-approved regadenoson (Lexiscan, Astellas Pharma US, Inc. IL, United States). This modulates the Adenosine receptor signaling at BBB layer (Carman et al., 2011). The dosage and IV administration method indicated by the manufacturer was utilized: A volume of 150 μl of the standard concentration of 0.08 mg/1 ml was given to each animal regardless of the weight, followed by 150 μl flush of 0.9% sodium chloride for injection. The experimental protocol was designed based on the pharmacological assumption that the VSD delivery through BBB would occur during the Lexiscan's biological half-life, i.e., 2–3 min. The efficiency of the pharmacological BBB opening was evaluated by the frozen-section histopathological analysis with near-infrared fluorescence microscopy. Three different groups were compared in this study: (1) Negative control: VSD-/Lexiscan-; (2) Control: VSD+/Lexiscan-; (3) BBB opening: VSD+/Lexiscan+.

In vivo Experimental Protocol

Figure 1D shows the detailed protocol for VSD control, seizure control, and seizure groups. Note that each data acquisition was performed for 10 min to cover the biological half-life of Lexiscan for VSD delivery (2–3 min). Each dosing protocol of Lexiscan and VSD was as follows: Through the jugular vein catheter port located in the neck, 150 μl of Lexiscan 0.4 mg/5 ml concentration was injected, and 300 μl of VSD was subsequently administrated at 0.1 mg/ml concentration, followed by 150 μl of saline solution flush. The seizure control ($n = 2$) and seizure groups ($n = 4$) were designed to distinguish the chemoconvulsant effects on neural activity: both groups received VSD and Lexiscan, but only seizure group had IP injection of PTZ (45 mg/ml/kg). The induction of seizure was confirmed by monitoring motor seizure, and another dose of PTZ was injected when no motor seizure was observed in 5–10 min. In particular, the success of the rat seizure model was determined by the behavioral observation to identify the tonic-clonic movements in whisker, fore and hind-limbs of the anesthetized rat. Once the seizure is developed, the behavioral seizure activity was maintained for entire time domain (0–10 min) in all the data sets presented in this paper. The VSD control group ($n = 2$) was designed to validate the inability of Lexiscan and PTZ to generate any bias on the quantification of fPA VSD responses. In this group, the baseline was obtained with the Lexiscan dosage, and subsequence data set was obtained

during the chemoconvulsant seizure with secondary Lexiscan dosage without VSD.

Criteria for Selecting Region-of-Interest

The coronal sections of interest were selected to include motor cortices at bregma 2.2 mm, at which the synchronized depolarizations of neurons are confirmed by behavioral observation of motor seizure (see **Movie S1**). In the superficial depth, the signals from superior sagittal sinus (SSS) and superior cortical veins (SCV) are dominant as they contain abundant blood context. Skin surface was less obvious as the melanin contents, a major absorber in scalp, has low absorbance at near-infrared range (Jacques and Prahl, 2013). Since the intracerebral vasculatures in rat brain [mostly <20-μm in diameter, (Zhang et al., 2014a)] is narrower than the spatial resolution available, i.e., ∼500 μm, we used the relative position to SSS and brain atlas by Paxinos as a criteria to localize brain tissue region (Paxinos and Watson, 2014). In axial direction, there are four layers between SSS and brain tissue. The SSS is in the middle of dura mater (300 μm) which is above the arachnoid (75 μm), subarachnoid space (750 μm), and pia mater (75 μm) layers covering a rat brain (Nowak et al., 2011). Therefore, the expectable distance between SSS and brain atlas map should be 1,050 μm, and motor cortex is extended at 3–4 mm from the brain surface [bregma 2.2–3.2 mm (Paxinos and Watson, 2014)]. From the anatomical criteria, entire brain region was selected as the region-of-interest (ROI) to reject any subjective bias.

Normalized Time-Frequency Analysis

Figure 2 demonstrates the flow chart of our normalized time-frequency analysis method based on a short-time Fourier transform (STFT) to detect the suppressive VSD contrast in rat brain. The detailed task in each step is as following:

- **Step 1: Reconstruction of PA image sequence** using a delay-and-sum beamforming for the radio-frequency (RF) channel data moving-averaged for 2-s duration (40 frames) with 0.25-s

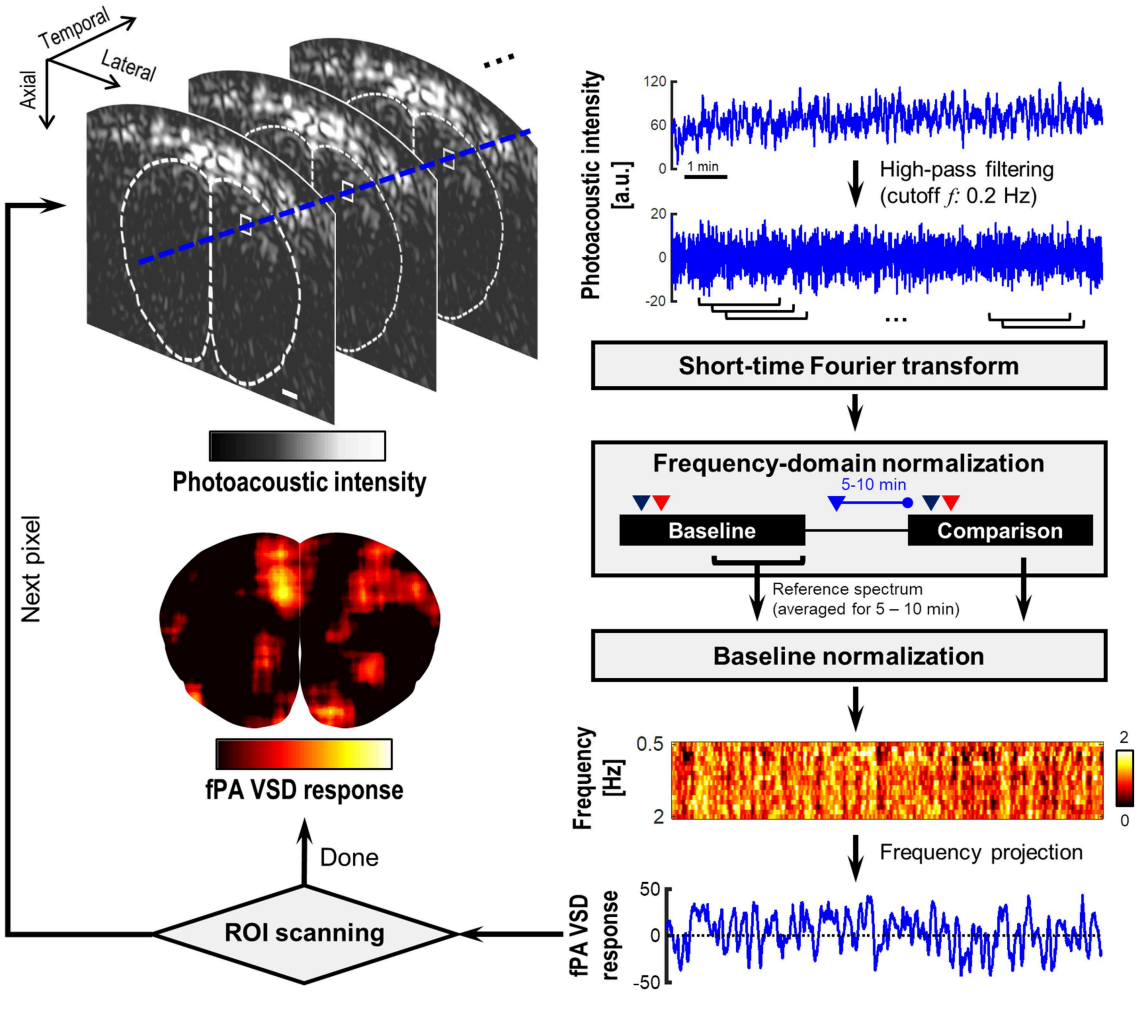

FIGURE 2 | Flow chart of the short-time Fourier transform (STFT)-based normalized time-frequency analysis method. The dotted contour is boundary of brain tissue drawn based on rat brain atlas. White bar indicates 1 mm.

interval (five frames). The signal envelope was detected in the bandwidth 1–5 MHz. This led to 4 Hz refreshing rate, and enables the frequency analysis up to 2 Hz with high sensitivity. The higher imaging speed would be redundant considering slow VSD response in sub-second scale;

- **Step 2: High-pass filtering** at 0.2 Hz cutoff frequency in temporal direction at each pixel of envelope-detected PA cross-section image to exclude the seizure-induced hemodynamic changes extended in few tens of seconds, which would extend up to 0.1 Hz in frequency domain (Sigal et al., 2016);
- **Step 3: Short-time Fourier transform (STFT)** at each image pixel point with an analysis window across 40 temporal samples. $PA(t, f)$ denotes a STFT spectrogram at a time point t;
- **Step 4: Frequency-domain normalization** by the averaged intensity at low-frequency band f_L (i.e., 0.3–0.5 Hz) at each t: $PA(t, \underline{f}) = \log_{10}(PA(t, f)/E\{PA(t, f)\}_{f\underline{L}})$, where $PA(t, f)$ and $PA(t, \underline{f})$ are the PA sequence before and after the normalization. This procedure is to fairly evaluate the amount of suppression at high-frequency range (0.5–2 Hz) relative to the reference intensity at f_L. The logarithm procedure is to present the PA intensity in negative decibel level with an emphasis on suppressive PA contrast;
- **Step 5: Baseline normalization:** $PA(\underline{t}, \underline{f}) = PA(\underline{t}, \underline{f})/PA_0(\underline{f})$, in which the $PA_0(t, \underline{f})$ is the reference spectrum time-averaged for 5–10-min period in the baseline phase. In this step, the suppressive VSD contrast is converted into positive contrast in $PA(\underline{t}, \underline{f})$—More suppressive contrast relative to the baseline would yield higher $PA(\underline{t}, \underline{f})$;
- **Step 6: fPA quantification of VSD response:** A fPA VSD response at each pixel is defined by a $PA(\underline{t}, \underline{f})$ projected over 0.5–2 Hz range: $(E\{PA(\underline{t}, \underline{f})\}_{f=0.5--2\text{Hz}} - 1) \times 100$. This reflects how much fractional suppression have produced compared to the reference STFT spectrum. Repeat steps 1–6 until all the pixels in brain cross-section are processed.
- In our signal processing, high-pass filtering (Step 2) performs an important role to reject seizure-induced change in hemodynamics. All the gradual increasing bias and instantaneous changes in blood context would not be account in the outcome (**Figure 2**). On the other hand, the electrophysiological seizure activity would be broadly extends from few Hz to several tens of Hz (Siemen et al., 2011), at which the suppressive VSD mechanism in fPA imaging will be presented.

EEG Validation of Neural Seizure Activity

To obtain the EEG records of electrical spike discharges that originated from brain tissue, sub-dermal scalp EEG recording electrodes were located at the corresponding locations on motor cortex (see the **Figure 9A**), the schematic of the rat cranium (three electrodes, 1 recording and 1 reference over motor cortex, 1 ground electrode over rostrum). Silver wire sub-dermal electrodes made for use in humans (IVES EEG; Model #SWE-L25–MA, IVES EEG solutions, USA) were implanted sub-dermally, which records with a low, steady impedance, i.e., 5 KΩ. Electrodes were fixed in position with cyanoacrylate adhesive (KrazyGlue, USA). The EEG signal at motor cortex was recorded with the identical preparation procedures in fPA imaging including animal preparation, administration of VSD, Lexiscan, and PTZ, time duration for recording, and interval between sequences in the protocol. Data acquisition was done using Sirenia software (Pinnacle Technologies Inc., Kansas, United States) with synchronous video capture. Briefly, the data acquisition and conditioning system had a 14-bit resolution, sampling rates of 400 Hz, high pass filters of 0.5 Hz and low pass filters of 60 Hz. The files were stored in .EDF format and scored manually for protocol stages using real time annotations added to the recording during the experiments. EEG power for 10 s epoch displays within the scoring software package was done using an automated module in Sirenia. Further details of our proposed EEG data acquisition and analysis used in this study are as presented in previous studies (Adler et al., 2014; Johnston et al., 2014).

RESULTS

Figure 3 presents the experimental results for a lipid vesicle model in various K^+ gradient levels. The membrane potential of soybean lipid vesicle model is manipulated by the valinomycin and gramicidin, by which the quantum yield change of VSD could accordingly triggered (**Figure 3A**). From the spectrophotometric and spectrofluorometric measurements (**Figure 3B**), the fractional change in fluorescence emission of the depolarized state over the polarized state were 19.70, 61.63, and 69.69% at −83, −102, and −120 mV of membrane potential levels, respectively (i.e., 25-, 50-, and 100-fold K^+ gradient levels), while preserving a comparable level of absorbance: i.e., 0.07, 0.70, and 0.21% of fractional changes, respectively. The fPA intensity change presented in **Figure 3C** indicates the corresponding suppressive contrast in depolarized state from a polarized state: -4.91 ± 4.00, -11.49 ± 2.00, and -14.68 ± 1.41% at −83, −102, and −120 mV of membrane potential levels ($p < 0.005$). The expectable fPA contrast derived from the lipid vesicle experiments is -12.24 ± 1.18%/100 mV. The quantum yield changes according to the given K^+ gradient levels were also estimated based on the theoretical model in our previous literature (Zhang et al., 2017). The median value in the estimated quantum yield range for each K^+ gradient level presents a proportionally-increasing trend as depolarized (**Figure 3D**). Note that the non-specific quantum yield at 25-fold K^+ gradient is due to a limited sensitivity to differentiate the subtle membrane potential variation—The specificity of the estimation becomes proportionally improved as more K^+ gradient is given.

With this validated VSD mechanism, we conducted the *in vivo* validation for the transcranial fPA sensing of electrophysiological neural activity in the rat brain. The fPA probe imaged the coronal cross-section at bregma 2.2 mm to cover the motor cortex where the seizure was confirmed by behavioral observation. **Figure 4A** shows the fPA VSD response maps projected for 10 min in each group to compare the activated brain regions among groups. All images have same range in the fPA VSD response, i.e., 0.00–3.00. In

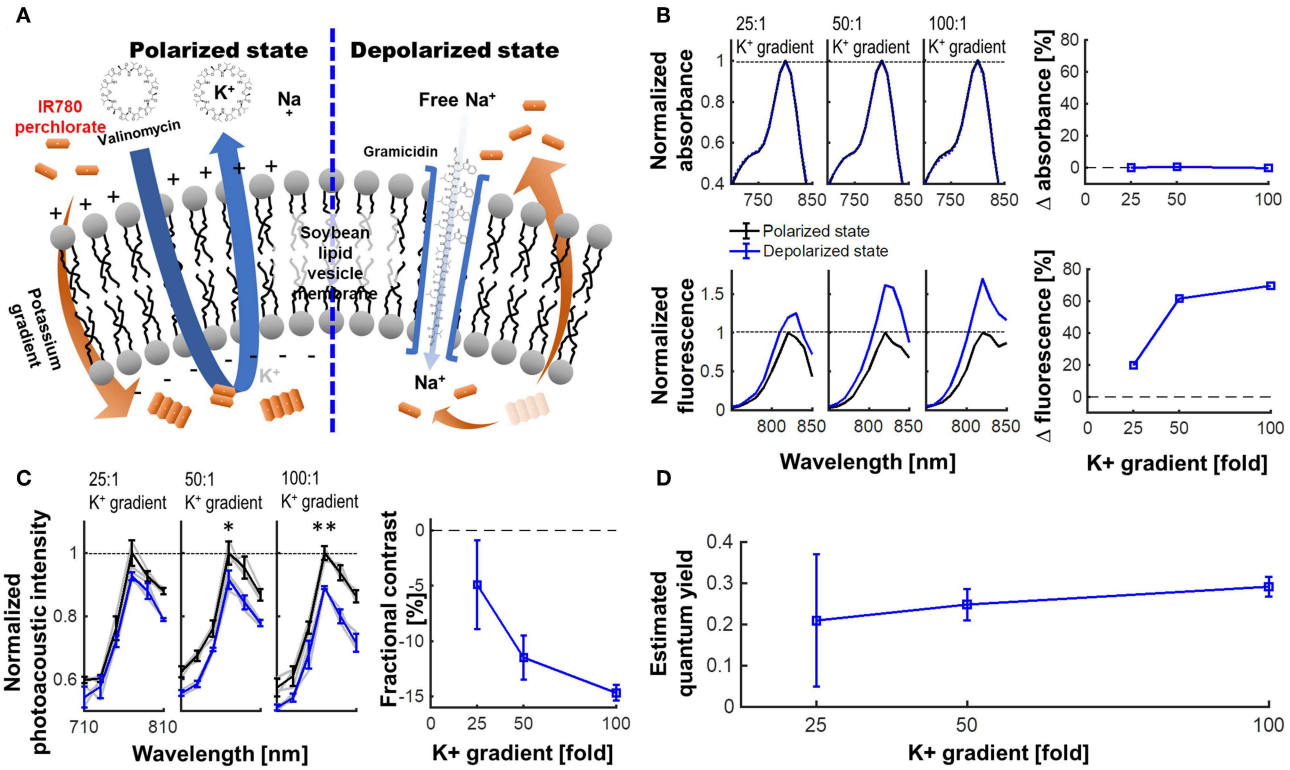

FIGURE 3 | VSD characterization using a lipid vesicle model. **(A)** Schematic diagram of a lipid vesicle model. **(B)** Fractional changes of the spectrophotometric and spectrofluorometric measurements in the polarized (black) and depolarized (blue) states. **(C)** PA intensity spectrum at 25-, 50-, and 100-fold K^+ gradients and fractional changes at 790 nm ($p = 0.055$, 0.010, and 0.002) between polarized and depolarized states for 25-, 50-, and 100-fold K^+ gradients, respectively. **(D)** The estimated quantum yield change for each K^+ gradient level (Zhang et al., 2017). The median values were presented in the estimated quantum yield range for each K^+ gradient level.

the seizure group, the chemoconvulsant seizure induced substantial VSD responses, while the control groups revealed limited activity in cortical region throughout comparison phase. **Figure 4B** compares fPA VSD responses in each group projected within whole brain region. Note that they were normalized by the mean value derived from the seizure group. As a result, the seizure group scored 81.3 and 97.9% more fPA VSD response than those in VSD control and seizure control groups. The seizure group indicated significant difference in comparison to the projection of the control groups: 1.00 ± 0.31 ($n = 4$) vs. 0.53 ± 0.10 ($n = 4$); $p < 0.05$.

The appropriate VSD delivery into brain tissue was confirmed by the histopathological analysis on the harvested rat brains (**Figure 5**). Three different groups were compared: (1) negative control group, VSD–/Lexiscan–; (2) control group, VSD+/Lexiscan–; and (3) BBB opening group, VSD+/Lexiscan+. From the ROIs indicated at cortical regions, the substantially-enhanced VSD uptake have been identified on the BBB opening group compared to that shown in the control group: 121.03 ± 7.14 vs. 79.19 ± 2.16; $p < 0.001$. The negative control group did not present any distinguishable fluorescence contrast as anticipated. The result presents the effectiveness of BBB opening based on pharmacological adenosine receptor signaling modulation by regadenoson, which is consistent with our recent fluorescence validation *in vivo* (Pak et al., 2018).

We validated the chemoconvulsant-induced seizure activity in the identical *in vivo* protocol with EEG recording. Using a well-established model of chemoconvulsant-induced *status epilepticus*, we replicated the classic evolution of chemoconvulsant-induced *status epilepticus* using PTZ (**Figure 6**) (Löscher, 2017). These evolutions as related to bursts of synchronized neural activity *in vivo* were assessed by EEG using the experimental protocols mirrored from that of fPA imaging experiments. We recorded vEEGs of seizure inductions using PTZ (45 mg/kg IP injections) in anesthetized rats. EEG baseline recording continued until a stable seizure induction profile (i.e., continuous burst discharges indicating synchronized neuronal depolarization-related action potentials) was recorded using sub-dermal EEG scalp electrodes. The seizure activity in EEG was associated with tonic-clonic movements in the fore- and hind-limbs of the anesthetized rats, indicating motor cortex involvement (**Movie S1**). The PTZ evolution of status on EEG did not alter with VSD treatment.

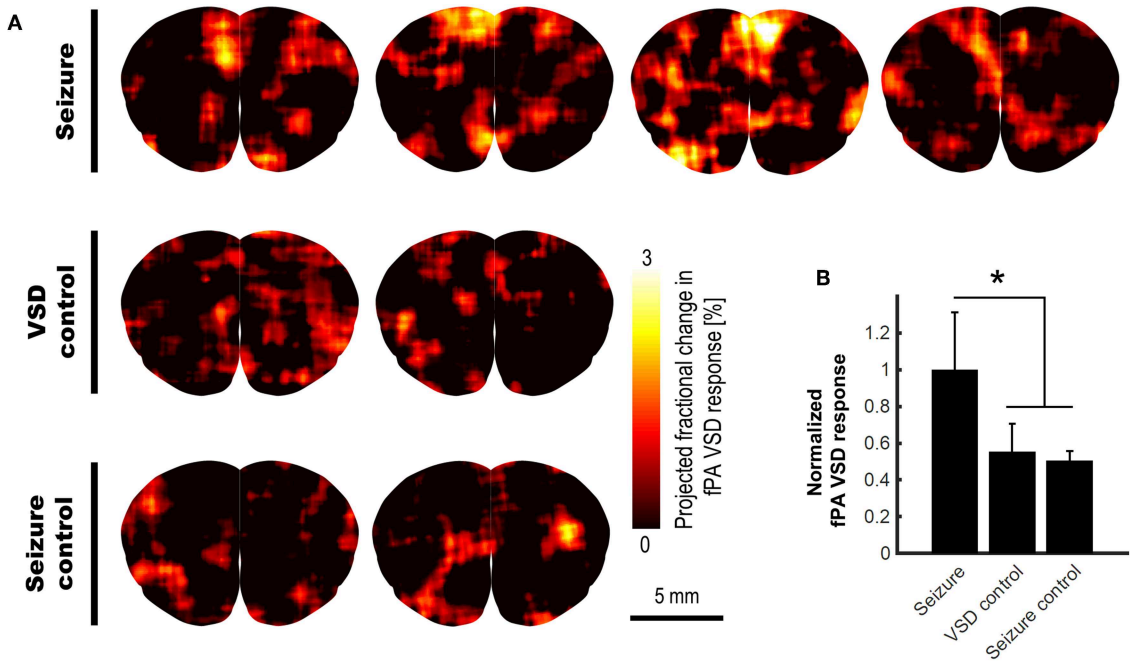

FIGURE 4 | *In vivo* transcranial fPA VSD imaging for seizure, VSD control, and seizure control groups: **(A)** The fPA VSD response maps in each group. Note that each column indicates an individual rat included in each group; **(B)** The mean and standard deviation of the fPA VSD response in each group. The region-of-calculation for each rat was extended to an entire brain region. The representative examples in ROI selections and corresponding fractional PA intensity change map are presented in **Figure S2**.

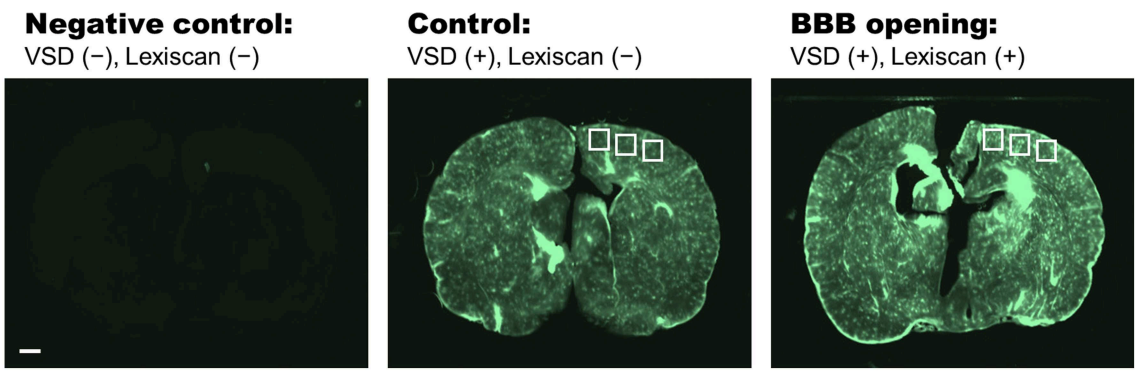

FIGURE 5 | Histopathological analysis on negative control (VSD–, Lexiscan–), control (VSD+, Lexiscan–), and BBB opening (VSD+, Lexiscan+) groups. Scale bar indicate 1 mm.

DISCUSSION

Here, we present comprehensive characterization of our near-infrared cyanine VSD mechanism using the lipid vesicle model, and a transcranial fPA VSD imaging of brain activity *in vivo* at sub-mm spatial resolution using rat seizure model with intact scalp. The near-infrared cyanine VSD, IR780 perchlorate, clearly revealed the VSD mechanism-of-action for different amount of membrane depolarization with the fractional contrast at $-12.24 \pm 1.18\%/100\,\text{mV}$ (**Figure 3**). Also, the proof-of-concept *in vivo* validation study demonstrated that the non-invasive fPA VSD imaging without any invasive craniotomy or skull thinning procedures is capable of differentiating the generalized depolarization events in the seizure group from those in control groups (**Figure 4**), which also well agreed with EEG validation (**Figure 6**). Normalized time-frequency analysis method successfully extracted suppressive VSD contrast in coronal cross-section of rat brain over the increasing hemodynamic change with chemoconvulsant seizure using PA intensity envelope-detected in 1–5 MHz bandwidth. In addition, the pharmacological enhancement of VSD delivery into rat brain by increased permeability of the BBB was

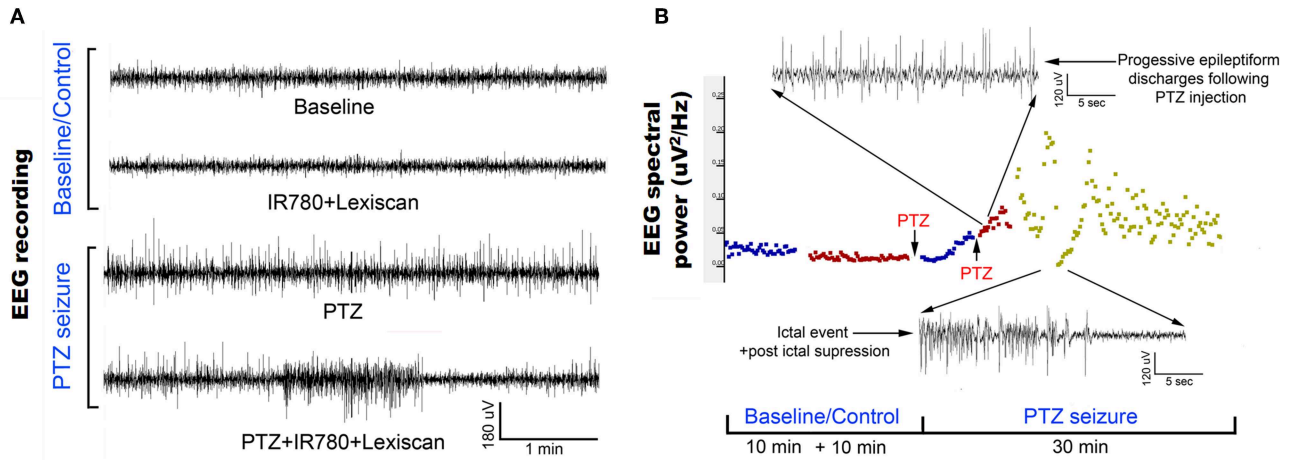

FIGURE 6 | Evolution of EEG signal in the *in vivo* protocol identical to transcranial fPA imaging: **(A)** Representative EEG traces recorded from rat motor cortex before and during induction of status epilepticus using chemoconvulsant PTZ. The baseline and control EEG traces represent EEG activity in an anesthetized rat (see methods) with and without IR780 + lexiscan given at the dosage found to not alter baseline EEG activity in the pilot study. PTS seizure induction proceeded in classical style described previously wherein episodic epileptiform burst activity evolved into status epilepticus with intermittent occurrence of seizures and stable interictal activity. **(B)** EEG spectral quantitation of the EEG recording done every 10 s epoch during the EEG showed the expected progression in EEG power associated with evolution of the PTZ induced status epilepticus. Time line of PTZ injections indicated with arrows. Expanded EEG traces on top show the uniform epileptiform discharges after following second PTZ injection and below a seizure event followed of post-ictal suppression indicating the termination of that event.

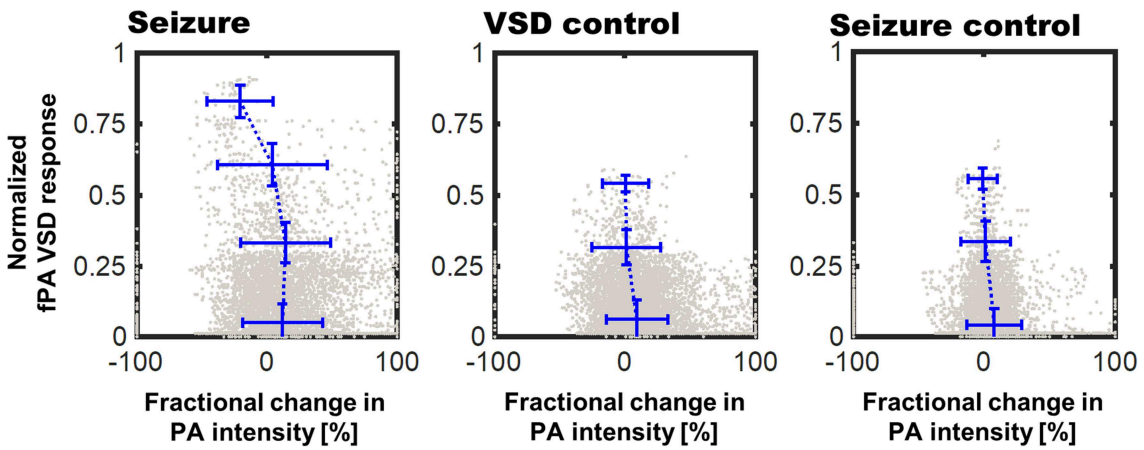

FIGURE 7 | Correlation of fPA VSD response to the fractional change in PA intensity between baseline and comparison phases. Pixels were categorized to four bins of distinct fPA VSD response ranges: 0–0.25, 0.25–0.5, 0.5–0.75, and 0.75–1.

confirmed by histopathological validation (**Figure 5**). These results demonstrate the feasibility of transcranial fPA VSD imaging at sub-mm spatial resolution without any needs for highly-complex tomographic system and/or invasive procedures required in fPA imaging approaches at visible wavelength range.

The pixel-by-pixel correlation between fPA VSD response and the fractional PA intensity provided interesting perspectives (**Figure 7**). In seizure group, the pixels presenting 2.25–3.00 of the fPA VSD response projected over 10 min indicated −20.94% of suppressive PA contrast, which corresponds to the proposed VSD mechanism. Interestingly, not all the suppressive changes in PA intensity was converted into high fPA VSD response, which also validate a role of the normalized time-frequency analysis method to isolate the VSD response from the hemodynamic changes. Otherwise, the control groups did not present high fPA VSD response at the cortical regions, whereas the seizure was also confirmed by behavioral observation in VSD control group. On the other hand, it would be also noteworthy that there was a case in seizure control group with unexpectedly localized yet high fPA VSD response at the primary somatosensory cortex region according to the rat brain atlas (the second rat case in **Figure 4**). We hypothesize that neural activity might be real as the ketamine-xylazine does enable spontaneous and well as evoked cortical activity in anesthetized brains especially in

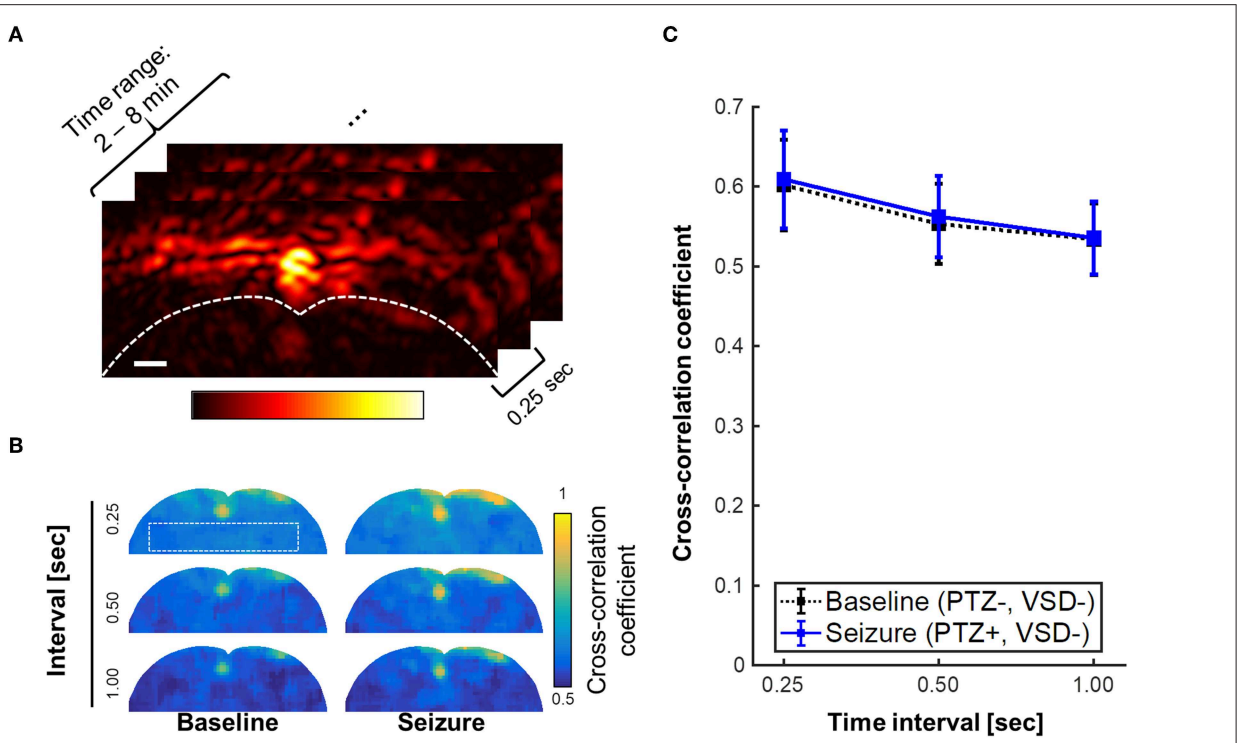

FIGURE 8 | Minimal correlation projection (MCP) image using cross-correlation coefficients with varying time interval, i.e., 0.25, 0.5, and 1 s, which respectively corresponds to 1, 2, and 4 frame intervals with the imaging rate at 4 frames per second. **(A)** region of interest for the inter-frame cross-correlations, **(B)** MCP images of baseline (PTZ–, VSD–) and seizure groups (PTZ+, VSD–) for brain tissue region. **(C)** Cross-correlation coefficient for varying time intervals. Scale bar indicate 1 mm.

periods after >30 min following induction (Goss-Sampson and Kriss, 1991; Ordek et al., 2013). *In vivo* experimental protocol will be further regulated in our future investigation to reject any sensory interferences.

The potentially confounding factors for the *in vivo* experiments need to be carefully considered and eliminated. The change in CBV during chemoconvulsant seizure can generate proportional change of PA intensity that can be misinterpreted as the VSD response (Goldman et al., 1992; Hoshi and Tamura, 1993; Nehlig et al., 1996). Zhang et al. suggested that time frame of the CBV change induced by chemoconvulsant seizure model: The time length of gradual CBV change from PTZ injection to seizure onset was ∼2 min on average (Zhang et al., 2014b). However, it was sufficiently covered by ∼10 min of stabilization phase in our *in vivo* protocol (**Figure 1D**). There is also an instantaneous hemodynamic change, but it extends in tens of seconds, and was rejected using high-pass filtering as described in the Materials and Methods section. Moreover, potential interference due to heart beating would not affect the results, as every individual fPA frame was compounded for 2 s that include 11–16 heart cycles of a rat (typically 5.5–8 beats per second).

The stability of stereotaxic fixation against the induced motor seizure was also investigated. The counter-hypothesis of this concern was an abrupt disorientation of rat brain due to motor seizure that will induce instantaneous decorrelation between adjacent PA frames. Also, based on the behavioral observation during seizure, we anticipated the decorrelation within a sub-second time scale, if it happened. For these hypotheses, we calculated the cross-correlation maps throughout PA frames obtained from 2 to 8 min (1920 frames, 240 frames/min). Three different time intervals for decorrelation calculation were tested: 0.25, 0.5, and 1 s, which, respectively correspond to 1, 2, and 4 frame intervals (**Figure 8**). From the minimal correlation projection (MCP) map projected in entire temporal direction, motor seizure did not yield a significant decorrelation in the adjacent PA images when comparing to normal condition for the given time period. Even with 1 s of interval, baseline and seizure phases present consistent minimal correlation value in the brain tissue region: 0.53 ± 0.04 vs. 0.54 ± 0.04, respectively. Therefore, the interference by motor seizure could be rejected as potential cause of artifacts in the results.

Toxic CNS effects of VSD is another factor that alters brain activity. We tested our protocols with varying VSD concentration in rats as a direct application to the cortex. Rats were anesthetized with IP injection to ketamine/xylazine and a cranial window was made over the right motor cortex. After recording a baseline EEG in the rat for 10-min duration with the craniotomy, the follow-on EEG recording continued to record EEG following application of increasing concentrations of vehicle alone and VSD + vehicle for the same duration of EEG recordings (i.e., 10 min) allowing comparisons of EEG responses to each increasing gradient of VSD on cortical activity as compared to baseline EEG signature

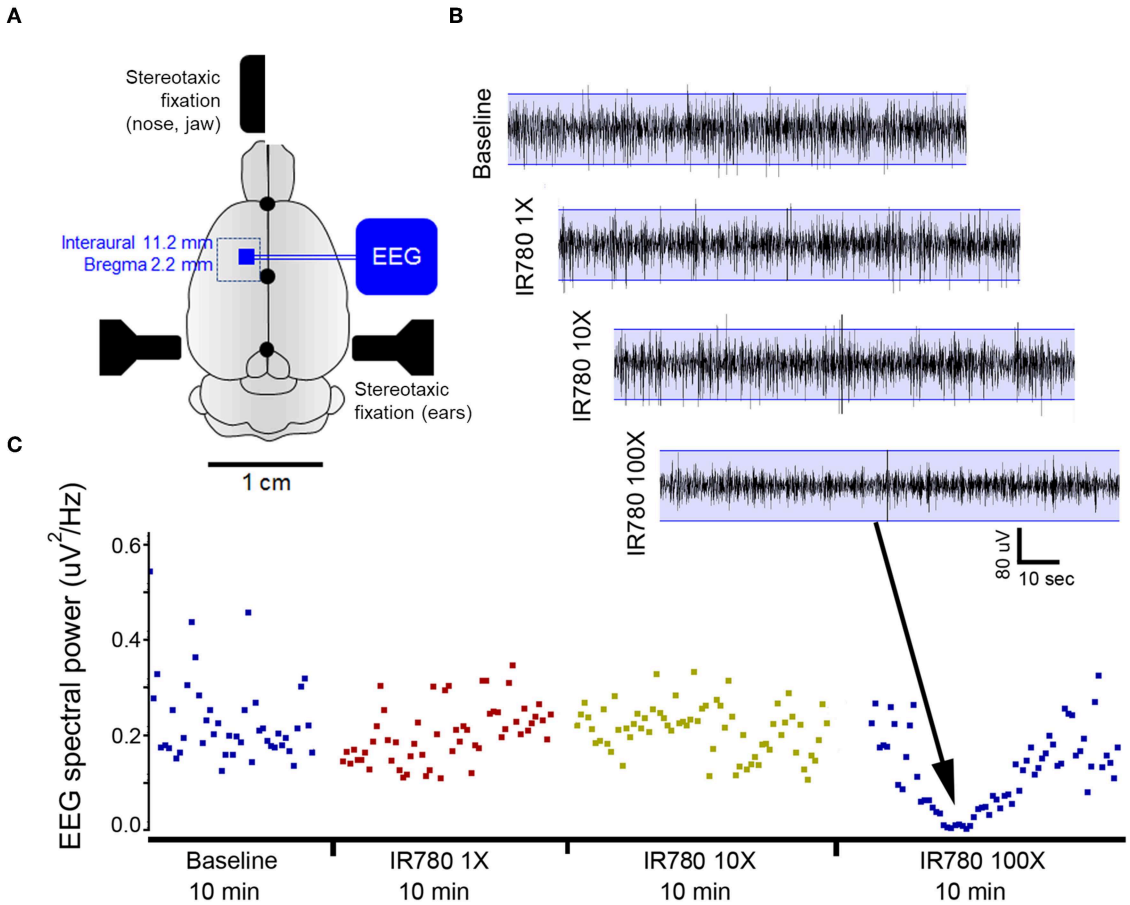

FIGURE 9 | VSD toxicity study using EEG recordings during direct cortical applications using a cranial window in rats. **(A)** Schematic of experimental protocol. A rectangular cranial window drilled under anesthesia overlying unilateral motor cortex. Duramater was kept intact. Following craniotomy, a small window was made in duramater without traversing blood vessels. **(B)** EEG recording of baseline brain activity under anesthesia was followed by using a hamilton micro sssyringe to apply increasing concentrations of IR780 directly to the cortical surface via window made in duramater. Base EEG remained unaltered at lower concentrations but showed significant background suppression after applying a 100X solution. This study allowed us to determine the concentration of IR780 10X for all PA experiments. **(C)** EEG power spectral quantification for every 10-s epoch of EEG over the duration of the recording confirmed EEG suppression with the 100X dose.

in the same rat. Results for VSD with cortical application with cranial windows used in six male rats yielded reliable and reproducible EEG signatures for each concentration (**Figure 9**). This protocol identified that VSD concentrations had no effect in altering the baseline EEG in the same rat, indicating no toxic effect on cortical circuit function. Direct cortical application with 100X VSD resulted in significant EEG background suppression in 4/6 rats, indicating that the certain concentrations of VSD could alter baseline circuit function in the motor cortex. This EEG suppression was recovered to baseline over the 10-min recording period, indicating that the transient effect from the time of application as the 100X VSD either diluted or cleared out of the focal application zone over the 10-min period. We reject the toxic CNS effects of VSD as we used 10X concentration based on this result.

We plan a number of follow-up efforts to further advance the concept. We will further regulate the experimental protocol, including possible visual or audible perceptions for rats during the experiments, and also collect more *in vivo* data sets. In addition, there would be several improvements in imaging system: we plan to use a custom transducer at the optimal bandwidth (1–5 MHz) with appropriate elevation focusing depth (10–20 mm) in our future studies, which will significantly improve the transcranial signal sensitivity. Using 2-D PA probe would also provide the most reliable setup as it enables the absolute positioning of specific brain parts. Also, the sensing speed of our current fPA imaging system would be improved. Current fPA sensing speed is limited to 4 frames per second to obtain sufficient transcranial signal sensitivity in the deep brain cortex region. This speed may limit its applicability in research, as it is well-known that resting electrophysiological neural activity ranges up to several tens of Hz (e.g., delta: 1–4 Hz; theta: 4–8 Hz; alpha: 8–13 Hz; beta: 13–30 Hz; gamma: 30–80 Hz). Having another dimension in spectral dimension would be beneficial to quantify the VSD response and hemodynamic changes at the same time. Successful improvements will substantially increase the capability to understand brain circuit functionality in real-time using the proposed fPA imaging technology.

To pave the way to its translation, we will further evaluate its feasibility in larger-scale brain models, as in primates and eventually living human brain. Localized stimulation and detection of fPA VSD response in deeper brain regions of rodent animal have been our first step; We recently presented a success to monitor the activities in hippocampus at ∼5 mm depth through intact scalp in rat animal (Kang et al., 2018b). In this study, a dentate gyrus (DG) gatekeeping function was selectively stimulated by focal N-methyl-D-aspartate (NMDA) infusion using a reversed microdialysis, while collecting dialysate samples by a forward microdialysis. On the other hand, the fPA VSD neuroimaging in sagittal direction was concurrently performed at the contralateral side of the microdialysis. The configuration enabled the quantification of an extracellular glutamate concentration as a marker of excitatory neurotransmittance focally manipulated at the DG and its correlation to fPA VSD response. As a result, we presented the positive correlation of fPA VSD response to the dose-dependent changes of extracellular glutamate concentration at the hippocampal circuitry. We will also step forward to use the larger brain models of porcine and non-human primate animals, which will provide practical size and anatomy of brain as well as thicker skull and scalp when compared to humans. We also achieved an encouraging progress to obtain the sufficient sensitivity on the physiological hemodynamic changes through thick scalp and skull layers intact with 5 mJ/cm^2 energy density (Kang et al., 2018a).

Having near-infrared VSD with a faster time response is definitely in interest for our further studies, and we are working on to secure better kinetics and absorbance. It would be largely beneficial for more profound level of neuroscientific researches. For example, evaluating instantaneous responses to various controlled stimulations at a specific neural compartment would also requires the faster VSD. However, use of such faster VSD would necessitate much higher standard in fPA imaging sensitivity to overcome background noise caused by various factors such as laser energy fluctuation, heart beating, and other biological variations, etc. Therefore, faster laser system with sufficient energy density will be needed to secure a sufficient transcranial imaging sensitivity. In addition, employing advanced image quality enhancing algorithms such as deep learning-based filtering or adaptive beamforming would be also investigated.

Even though we succeed to detect brain activities at the VSD concentration below the threshold interfering brain activity (**Figure 9**), there have been no long-term and comprehensive toxicity study. The toxicity and biodegradability of our VSD is an important issue that deserves further evaluation. However, we are optimistic about this issue as the metabolic products of IR780 perchlorate should be very similar to ICG, FDA-approved near-infrared cyanine dye, because they are basically comprised by same chromophore. This strongly suggests its biocompatibility of our cyanine VSD. We will further prove our hypothesis in our future works.

Furthermore, the integration of localized neural stimulation methods to our fPA imaging will allow us to substantially elevate our understanding on how brain respond to a controlled stimuli (Lewis et al., 2016). The integration of the proposed fPA VSD imaging with a transcranial neuromodulation method may have a huge impact on the neuroscientific and clinical efforts by enabling the breakthrough beyond the passive brain investigation. In addition, there could be additional benefits on non-pharmacological BBB opening with a specific modality such as focused ultrasound (Tufail et al., 2011; Chu et al., 2015).

ETHICS STATEMENT

This study was carried out in accordance with the recommendations of name of guidelines, name of committee with written informed consent from all subjects. All subjects gave written informed consent in accordance with the Declaration of Helsinki. The protocol was approved by the Institutional Research Board Committee of Johns Hopkins Medical Institute (RA16M225).

AUTHOR CONTRIBUTIONS

JK planned and conducted lipid vesicle and *in vivo* experiments, developed and validated fPA image reconstruction method, analyzed the data, and wrote the first draft. HZ conducted lipid vesicle experiments and analysis. SK conducted *in vivo* EEG measurements and analysis. JF and HV prepared animal model and conducted *in vivo* experiments. PY and LL provided VSD compound with the guidance for its *in vivo* use. AM and MH conducted histopathological validation of VSD delivery to brain. JUK funded and participated in the development of the current fPA imaging system. DW, AR, and AG provided the original funding and substantial contributions to planning and interpretation of the *in vivo* experiments. EB led the development, system specification, and funding of the current fPA VSD imaging system. He also confirmed the final manuscript. All authors edited the manuscript.

FUNDING

Financial support was provided by the NIH Brain Initiative under Grant No. R24MH106083-03, the NIH National Institute of Biomedical Imaging and Bioengineering under Grant No. R01EB01963, the National Institute of Child Health & Human Development under Grant No. R01HD90884, the NIH National Institute of Heart, Lung, and Blood Institute under grant No. R01HL139543, and the Intuitive Surgical Technology research grant in 2018. JK was partially supported by Basic Science Research Program through the National Research Foundation of Korea (NRF) funded by the Ministry of Education (2018R1A6A3A03011551). EB was supported by the National Science Foundation CAREER award 1653322.

ACKNOWLEDGMENTS

Authors thank Dr. Abhinav K. Jha for proof reading the manuscript and providing helpful comments. Also, authors thank Drs. Diane S. Abou and Daniel L. J. Thorek for providing equipment and facilities for lipid vesicle experiments with helpful comments. Special thanks to Anthony Grace, University of Pittburgh.

SUPPLEMENTARY MATERIAL

The Supplementary Material for this article can be found online at: https://www.frontiersin.org/articles/10.3389/fnins.2019.00579/full#supplementary-material

Supplementary Figure S1 | PA imaging characterization. **(a)** spatial full-width-half-maximum (FWHM) beam profile in axial and lateral directions at various depth-of-interest (i.e., 20, 25, and 30 mm). **(b)** Fractional change in energy fluctuation with various number of frame averaging (i.e., 1, 5, 10, 20, 40 frames). **(c)** Long-term comparison in laser energy fluctuation between 0–2 min to 8–10 min time ranges. **(d)** Normalized PA intensity for 8 min. PA intensity averaged for 1–2 min was used as a reference intensity. White dotted rectangular in the PA image of seizure control rat indicates the photo-bleaching ROIs.

Supplementary Figure S2 | Representative examples in ROI selection for fPA VSD response reconstruction and its correlation to the corresponding fractional change in PA intensity from baseline to comparison phases.

Supplementary Movie S1 | Tonic-clonic movements in the fore- and hind-limbs of the anesthetized rats, indicating motor cortex involvement.

REFERENCES

Adler, D. A., Ammanuel, S., Lei, J., Dada, T., Borbiev, T., Johnston, M. V., et al. (2014). Circadian cycle-dependent EEG biomarkers of pathogenicity in adult mice following prenatal exposure to *in utero* inflammation. *Neurosci. Res.* 275, 305–313. doi: 10.1016/j.neuroscience.2014.06.022

Anderson, B. A., Kuwabara, H., Wong, D. F., Gean, E. G., Rahmim, A., Brasic, J. R., et al. (2016). The role of dopamine in value-based attentional orienting. *Current Biol.* 26, 550–555. doi: 10.1016/j.cub.2015.12.062

Archer, M. D. (1989). *Electrochemistry, Past and Present*. eds J. T. Stoke and M. V. Orna. Washington, DC: American Chemical Society.

Berman, M. G., Jonides, J., and Nee, D. E. (2006). Studying mind and brain with fMRI. *Soc. Cogn. Affect. Neurosci.* 1, 158–161. doi: 10.1093/scan/nsl019

Bradford, H. F. (1995). Glutamate, GABA and epilepsy. *Prog. Neurobiol.* 47, 477–511. doi: 10.1016/0301-0082(95)00030-5

Carman, A. J., Mills, J. H., Krenz, A., Kim, D.-G., and Bynoe, M. S. (2011). Adenosine receptor signaling modulates permeability of the blood-brain barrier. *J. Neurosci.* 31, 13272–13280. doi: 10.1523/JNEUROSCI.3337-11.2011

Chu, P.-C., Liu, H.-L., Lai, H.-Y., Lin, C.-Y., Tsai, H.-C., and Pei, Y.-C. (2015). Neuromodulation accompanying focused ultrasound-induced blood-brain barrier opening. *Sci. Rep.* 5:15477. doi: 10.1038/srep15477

Deán-Ben, X. L., Sela, G., Lauri, A., Kneipp, M., Ntziachristos, V., Westmeyer, G. G., et al. (2016). Functional optoacoustic neuro-tomography for scalable whole-brain monitoring of calcium indicators. *Light Sci. Appl.* 5, e16201–e16207. doi: 10.1038/lsa.2016.201

Devor, A., SakadŽić, S., Srinivasan, V. J., Yaseen, M. A., Nizar, K., Saisan, P. A., et al. (2012). Frontiers in optical imaging of cerebral blood flow and metabolism. *J. Cereb. Blood Flow Metab.* 32, 1259–1276. doi: 10.1038/jcbfm.2011.195

Friston, K. J. (2009). Modalities, modes, and models in functional neuroimaging. *Science* 326, 399–403. doi: 10.1126/science.1174521

Goldman, H., Berman, R. F., Hazlett, H., and Murphy, S. (1992). Cerebrovascular responses to pentylenetetrazol: time and dose dependent effects. *Epilepsy Res.* 12, 227–242. doi: 10.1016/0920-1211(92)90077-7

Goss-Sampson, M. A., and Kriss, A. (1991). Effects of pentobarbital and ketamine-xylazine anaesthesia on somatosensory, brainstem auditory and peripheral sensory-motor responses in the rat. *Lab. Anim.* 25, 360–366. doi: 10.1258/002367791780810074

Gottschalk, S., Fehm, T. F., Deán-Ben, X. L., Tsytsarev, V., and Razansky, D. (2017). Correlation between volumetric oxygenation responses and electrophysiology identifies deep thalamocortical activity during epileptic seizures. *Neurophotonics* 4:011007. doi: 10.1117/1.NPh.4.1.011007

Heo, C., Park, H., Kim, Y.-T., Baeg, E., Kim, Y. H., Kim, S.-G., et al. (2016). A soft, transparent, freely accessible cranial window for chronic imaging and electrophysiology. *Sci. Rep.* 6:27818. doi: 10.1038/srep27818

Hillman, E. M. C. (2007). Optical brain imaging *in vivo*: techniques and applications from animal to man. *J. Biomed. Opt.* 12:051402. doi: 10.1117/1.2789693

Hoshi, Y., and Tamura, M. (1993). Dynamic changes in cerebral oxygenation in chemically induced seizures in rats: study by near-infrared spectrophotometry. *Brain Res.* 603, 215–221. doi: 10.1016/0006-8993(93)91240-S

Jacques, S. L., and Prahl, S. (2013). *Extinction Coefficient of Melanin*. OMLC. Available online at: https://omlc.org/spectra/melanin/extcoeff.html.

Johnston, M. V., Ammanuel, S., O'Driscoll, C., Wozniak, A., Naidu, S., and Kadam, S. D. (2014). Twenty-four hour quantitative-EEG and *in-vivo* glutamate biosensor detects activity and circadian rhythm dependent biomarkers of pathogenesis in Mecp2 null mice. *Front. Syst. Neurosci.* 8:118. doi: 10.3389/fnsys.2014.00118

Jurkat-Rott, K., and Lehmann-Hom, F. (2004). The patch clamp technique in ion channel research. *Curr. Pharm. Biotechnol.* 5, 387–395. doi: 10.2174/1389201043376715

Kang, J., Boctor, E. M., Adams, S., Kulikowicz, E., Zhang, H. K., Koehler, R. C., et al. (2018a). Validation of noninvasive photoacoustic measurements of sagittal sinus oxyhemoglobin saturation in hypoxic neonatal piglets. *J. Appl. Physiol.* 125, 983–989. doi: 10.1152/japplphysiol.00184.2018

Kang, J., Kadam, S. D., Elmore, J. S., Sullivan, B. J., Valentine, H., Malla, A. P., et al. (2018b). Transcranial photoacoustic imaging of NMDA-evoked focal circuit dynamics in rat forebrain. *bioRxiv* 308585, 1–26. doi: 10.1101/308585

Lewis, P. M., Thomson, R. H., Rosenfeld, J. V., and Fitzgerald, P. B. (2016). Brain neuromodulation techniques: a review. *Neuroscientist* 22, 406–421. doi: 10.1177/1073858416646707

Li, W., Chen, R., Lv, J., Wang, H., Liu, Y., Peng, Y., et al. (2018). *In vivo* photoacoustic imaging of brain injury and rehabilitation by high-efficient near-infrared dye labeled mesenchymal stem cells with enhanced brain barrier permeability. *Adv. Sci. (Weinh)* 5, 1700277–1700211. doi: 10.1002/advs.201700277

Logothetis, N. K. (2008). What we can do and what we cannot do with fMRI - ProQuest. *Nature* 453, 869–878. doi: 10.1038/nature06976

Löscher, W. (2017). Animal models of seizures and epilepsy: past, present, and future role for the discovery of antiseizure drugs. *Neurochem. Res.* 42, 1873–1888. doi: 10.1007/s11064-017-2222-z

Martišiene, I., Mačianskiene, R., Treinys, R., Navalinskas, A., Almanaityte, M., Karčiauskas, D., et al. (2016). Voltage-sensitive fluorescence of indocyanine green in the heart. *BPJ.* 110, 723–732. doi: 10.1016/j.bpj.2015.12.021

Mazur, F., Bally, M., Städler, B., and Chandrawati, R. (2017). Liposomes and lipid bilayers in biosensors. *Adv. Colloid Interface Sci.* 249, 88–99. doi: 10.1016/j.cis.2017.05.020

Nehlig, A., Vergnes, M., Waydelich, R., Hirsch, E., Charbonne, R., Marescaux, C., et al. (1996). Absence seizures induce a decrease in cerebral blood flow: human and animal data. *J. Cereb. Blood Flow Metab.* 16, 147–155. doi: 10.1097/00004647-199601000-00017

Nie, L., Cai, X., Maslov, K., Garcia-Uribe, A., Anastasio, M. A., and Wang, L. V. (2012). Photoacoustic tomography through a whole adult human skull with a photon recycler. *J. Biomed. Opt.* 17:110506. doi: 10.1117/1.JBO.17.11.110506

Nowak, K., Mix, E., Nowak, K., Strauss, U., Gimsa, J., Benecke, R., et al. (2011). Optimizing a rodent model of parkinson's disease for exploring the effects and mechanisms of deep brain stimulation. *Parkinson's Dis.* 2011, 1–19. doi: 10.4061/2011/414682

Ordek, G., Groth, J. D., and Sahin, M. (2013). Differential effects of ketamine/xylazine anesthesia on the cerebral and cerebellar cortical activities in the rat. *J. Neurophysiol.* 109, 1435–1443. doi: 10.1152/jn.00455.2012

Pak, R. W., Kang, J., Valentine, H., Loew, L. M., Thorek, D. L., Boctor, E. M., et al. (2018). Voltage-sensitive dye delivery through the blood brain barrier using adenosine receptor agonist Regadenoson. *Biomed. Opt. Express* 9, 3915–3922. doi: 10.1364/BOE.9.003915

Paxinos, G., and Watson, C. (2014). *The Rat Brain in Stereotaxic Coordinates, 7th Edn*. Elsevier Academic Press. Available online at: https://books.google.co.in/books?id=FuqGAwAAQBAJ&printsec=frontcover&redir_esc=y#v=onepage&q0&f=true

Paxton, W. F., McAninch, P. T., Achyuthan, K. E., Shin, S. H. R., and Monteith, H. L. (2017). Monitoring and modulating ion traffic in hybrid lipid/polymer vesicles. *Colloids Surf. B Biointerfaces* 159, 268–276. doi: 10.1016/j.colsurfb.2017.07.091

Raichle, M. E., and Mintun, M. A. (2006). Brain work and brain imaging. *Annu. Rev. Neurosci.* 29, 449–476. doi: 10.1146/annurev.neuro.29.051605.112819

Ramnath, R. R., Strange, K., and Rosenberg, P. A. (1992). Neuronal injury evoked by depolarizing agents in rat cortical cultures. *Neurosci. Res.* 51, 931–939. doi: 10.1016/0306-4522(92)90530-F

Rosilio, V. (2018). How can artificial lipid models mimic the complexity of molecule–membrane interactions? *Adv. Biomembr. Lipid Self Assembly* 27, 107–146. doi: 10.1016/bs.abl.2017.12.004

Ruo, B., Zhang, R., Li, L., Shao, J.-Y., and Wang, L. V. (2017). Photoacoustic imaging of voltage responses beyond the optical diffusion limit. *Sci. Rep.* 7:2560. doi: 10.1038/s41598-017-02458-w

Siemen, H., Colas, D., Heller, H. C., Brüstle, O., and Pera, R. A. R. (2011). Pumilio-2 function in the mouse nervous system. *PLoS ONE* 6:e25932. doi: 10.1371/journal.pone.0025932

Sigal, I., Koletar, M. M., Ringuette, D., Gad, R., Jeffrey, M., Carlen, P. L., et al. (2016). Imaging brain activity during seizures in freely behaving rats using a miniature multi-modal imaging system. *Biomed. Opt. Express* 7, 3596–3514. doi: 10.1364/BOE.7.003596

Strangman, G. E., Li, Z., and Zhang, Q. (2013). Depth sensitivity and source-detector separations for near infrared spectroscopy based on the Colin27 brain template. *PLoS ONE* 8:e66319. doi: 10.1371/journal.pone.0066319

Takahashi, M., Liou, S. Y., and Kunihara, M. (1995). Ca(2+)- and Cl(-)-dependent, NMDA receptor-mediated neuronal death induced by depolarization in rat hippocampal organotypic cultures. *Brain Res.* 675, 249–256. doi: 10.1016/0006-8993(95)00078-5

Torricelli, A., Contini, D., Pifferi, A., Caffini, M., Re, R., Zucchelli, L., et al. (2014). Time domain functional NIRS imaging for human brain mapping. *NeuroImage* 85(Pt 1), 28–50. doi: 10.1016/j.neuroimage.2013.05.106

Treger, J. S., Priest, M. F., Iezzi, R., and Bezanilla, F. (2014). Real-time imaging of electrical signals with an infrared FDA-approved dye. *Biophys. J.* 107, L09–L012. doi: 10.1016/j.bpj.2014.07.054

Tsytsarev, V., Hu, S., Yao, J., Maslov, K., Barbour, D. L., and Wang, L. V. (2011). Photoacoustic microscopy of microvascular responses to cortical electrical stimulation. *J. Biomed. Opt.* 16:076002. doi: 10.1117/1.3594785

Tufail, Y., Yoshihiro, A., Pati, S., Li, M. M., and Tyler, W. J. (2011). Ultrasonic neuromodulation by brain stimulation with transcranial ultrasound. *Nat. Protoc.* 6, 1453–1470. doi: 10.1038/nprot.2011.371

Wang, L. V., and Hu, S. (2012). Photoacoustic tomography: *in vivo* imaging from organelles to organs. *Science* 335, 1458–1462. doi: 10.1126/science.1216210

Wang, X., Pang, Y., Ku, G., Xie, X., Stoica, G., and Wang, L. V. (2003). Noninvasive laser-induced photoacoustic tomography for structural and functional *in vivo* imaging of the brain. *Nat. Biotechnol.* 21, 803–806. doi: 10.1038/nbt839

Wong, D. F., Kuwabara, H., Schretlen, D., Bonson, K., Zhou, Y., Nandi, A., et al. (2006). Increased occupancy of dopamine receptors in human striatum during cue-elicited cocaine craving. *Neuropsychopharmacology* 31, 2716–2727. doi: 10.1038/sj.npp.1301194

Zhang, H. K., Yan, P., Kang, J., Abou, D. S., Le, H. N. D., Jha, A. K., et al. (2017). Listening to membrane potential: photoacoustic voltage-sensitive dye recording. *J. Biomed. Opt.* 22:045006. doi: 10.1117/1.JBO.22.4.045006

Zhang, M. Q., Sun, D. N., Xie, Y. Y., Peng, G. Y., Xia, J., Long, H. Y., et al. (2014a). Three-dimensional visualization of rat brain microvasculature following permanent focal ischaemia by synchrotron radiation. *BJR.* 87, 20130670–20130678. doi: 10.1259/bjr.20130670

Zhang, T., Zhou, J., Jiang, R., Yang, H., Carney, P. R., and Jiang, H. (2014b). Pre-seizure state identified by diffuse optical tomography. *Sci. Rep.* 4, 113–110. doi: 10.1038/srep03798

Conflict of Interest Statement: The subject matter described in this article is included in patent applications filed by the University of Connecticut and Johns Hopkins University. LL and PY are founders and owners of Potentiometric Probes LLC, which sells voltage sensitive dyes.

The remaining authors declare that the research was conducted in the absence of any commercial or financial relationships that could be construed as a potential conflict of interest.

Copyright © 2019 Kang, Zhang, Kadam, Fedorko, Valentine, Malla, Yan, Harraz, Kang, Rahmim, Gjedde, Loew, Wong and Boctor. This is an open-access article distributed under the terms of the Creative Commons Attribution License (CC BY). The use, distribution or reproduction in other forums is permitted, provided the original author(s) and the copyright owner(s) are credited and that the original publication in this journal is cited, in accordance with accepted academic practice. No use, distribution or reproduction is permitted which does not comply with these terms.

frontiers in Neuroscience

PROTOCOLS
published: 24 September 2019
doi: 10.3389/fnins.2019.01025

A Novel Approach for Manual Segmentation of the Amygdala and Hippocampus in Neonate MRI

Niloofar Hashempour[1,2], Jetro J. Tuulari[1,2,3], Harri Merisaari[4], Kristian Lidauer[1], Iiris Luukkonen[1], Jani Saunavaara[5], Riitta Parkkola[6], Tuire Lähdesmäki[7], Satu J. Lehtola[1], Maria Keskinen[1], John D. Lewis[8], Noora M. Scheinin[1,2,9], Linnea Karlsson[1,10] and Hasse Karlsson[1,2]*

[1] FinnBrain Birth Cohort Study, Turku Brain and Mind Center, Institute of Clinical Medicine, University of Turku, Turku, Finland, [2] Department of Psychiatry, Turku University Hospital, University of Turku, Turku, Finland, [3] Turku Collegium for Science and Medicine, University of Turku, Turku, Finland, [4] Department of Biomedical Engineering, Case Western Reserve University, Cleveland, OH, United States, [5] Department of Medical Physics, Turku University Hospital, Turku, Finland, [6] Department of Radiology, Turku University Hospital, University of Turku, Turku, Finland, [7] Department of Pediatric Neurology, Turku University Hospital, University of Turku, Turku, Finland, [8] Montreal Neurological Institute, McGill University, Montreal, QC, Canada, [9] Turku PET Centre, University of Turku, Turku, Finland, [10] Department of Child Psychiatry, Turku University Hospital, University of Turku, Turku, Finland

OPEN ACCESS

Edited by:
John Ashburner, University College London, United Kingdom

Reviewed by:
Heath R. Pardoe, New York University School of Medicine, United States
Bonnie Alexander, Murdoch Children's Research Institute (MCRI), Australia

***Correspondence:**
Niloofar Hashempour
niloofar.hashempour@utu.fi

Specialty section:
This article was submitted to Brain Imaging Methods, a section of the journal Frontiers in Neuroscience

Received: *24 September 2018*
Accepted: *09 September 2019*
Published: *24 September 2019*

Citation:
Hashempour N, Tuulari JJ, Merisaari H, Lidauer K, Luukkonen I, Saunavaara J, Parkkola R, Lähdesmäki T, Lehtola SJ, Keskinen M, Lewis JD, Scheinin NM, Karlsson L and Karlsson H (2019) A Novel Approach for Manual Segmentation of the Amygdala and Hippocampus in Neonate MRI. Front. Neurosci. 13:1025. doi: 10.3389/fnins.2019.01025

The gross anatomy of the infant brain at term is fairly similar to that of the adult brain, but structures are immature, and the brain undergoes rapid growth during the first 2 years of life. Neonate magnetic resonance (MR) images have different contrasts compared to adult images, and automated segmentation of brain magnetic resonance imaging (MRI) can thus be considered challenging as less software options are available. Despite this, most anatomical regions are identifiable and thus amenable to manual segmentation. In the current study, we developed a protocol for segmenting the amygdala and hippocampus in T2-weighted neonatal MR images. The participants were 31 healthy infants between 2 and 5 weeks of age. Intra-rater reliability was measured in 12 randomly selected MR images, where 6 MR images were segmented at 1-month intervals between the delineations, and another 6 MR images at 6-month intervals. The protocol was also tested by two independent raters in 20 randomly selected T2-weighted images, and finally with T1 images. Intraclass correlation coefficient (ICC) and Dice similarity coefficient (DSC) for intra-rater, inter-rater, and T1 vs. T2 comparisons were computed. Moreover, manual segmentations were compared to automated segmentations performed by iBEAT toolbox in 10 T2-weighted MR images. The intra-rater reliability was high ICC $\geq$ 0.91, DSC $\geq$ 0.89, the inter-rater reliabilities were satisfactory ICC $\geq$ 0.90, DSC $\geq$ 0.75 for hippocampus and DSC $\geq$ 0.52 for amygdalae. Segmentations for T1 vs. T2-weighted images showed high consistency ICC $\geq$ 0.90, DSC $\geq$ 0.74. The manual and iBEAT segmentations showed no agreement, DSC $\geq$ 0.39. In conclusion, there is a clear need to improve and develop the procedures for automated segmentation of infant brain MR images.

Keywords: magnetic resonance imaging, manual segmentation, automated segmentation, infants, brain, amygdala, hippocampus

INTRODUCTION

The study of infants' brain structures provides us with the means to investigate the timing of the structural and functional development (Jernigan et al., 2011). In infants, magnetic resonance imaging (MRI) is a safe tool that aids the investigation of postnatal maturational changes, such as myelination, and how these changes relate to behavioral development (Jernigan et al., 2011; Devi et al., 2017).

Brain MRI segmentation is one of the most critical tasks in many clinical applications (Balafar et al., 2010). Segmentation of different tissue types from brain magnetic resonance (MR) images is an important step in studying and analyzing brain anatomy and, consequently, the dynamic processes that occur during development (Wang et al., 2012).

Despite the good availability of automated and semi-automated software for adult brain segmentation, fewer tools are available for infant brain segmentation. Similar to adult studies, manual segmentation of the infant's brain is considered the most reliable and accurate method to identify and study brain structures (Devi et al., 2017). Manual segmentation of the brain is the "gold standard" method for segmentation (Morey et al., 2009). During the first 2 years of life, segmentation of brain MRI can be challenging due to the ongoing myelination process and frequently occurring artifacts in infant MR images due to movement (Weisenfeld et al., 2006).

Several studies have provided protocols for manual segmentation of adult MR images (e.g., Pruessner et al., 2000; Morey et al., 2009; Moore et al., 2014; Wenger et al., 2014). However, due to different contrast and the comparatively lower resolution of the infants' brain MR images (Gousias et al., 2012), the adult protocols cannot be used directly in segmenting the infant's brain. The resolution of the infant images, even at the standard 1 mm^3, is comparatively worse than that for typical adult scans as the infant brain size is roughly one-third of the adult brain (Hill et al., 2010; Holland et al., 2014). Additionally, matching the resolution of the infants' images to the resolution of the adults' images would require an increase in total acquisition time that is not feasible. A few manual segmentation protocols have been specifically designed for segmentation of infants' brains (e.g., Gousias et al., 2012; De Macedo Rodrigues et al., 2015; Alexander et al., 2017, 2019). However, the focus of the first study was on 15 preterm infants and only 5 term infants. The second study was done on infants who were between 0 and 2 years old, and only four of the subjects were 1–4 weeks old. The third and fourth studies replicated adult atlas in infants by manually segmenting 10 neonate MR images. Moreover, several automated methods exist for infant brain segmentation (e.g., Prastawa et al., 2005; Weisenfeld et al., 2006; Chiverton et al., 2007; Shi et al., 2010; Wang et al., 2011; Dai et al., 2012; Guo et al., 2015; Beare et al., 2016; Devi et al., 2017; Makropoulos et al., 2018; Zhu et al., 2019). A number of studies have validated manual segmentation methods for adults and compared them to automated segmentation methods; however, few studies have done this for infants. Existing studies have compared brain automated segmentation methods to manual tracing in the infant brain, but for structures other than the hippocampus and amygdala (e.g., Kempton et al., 2013; Išgum et al., 2015). To the best of our knowledge there has been no previous comparison of automated and manual segmentation of the hippocampus and amygdala in infants.

Similar to other parts of the brain, the amygdala and hippocampus start to grow and develop in the prenatal period and continue to mature into early adulthood (Uematsu et al., 2012; Thompson et al., 2013). The hippocampus is a curved structure that is located in the medial temporal lobe of the brain, beneath the cortical surface; it is one of the main structures in the limbic system. It is involved in storing long-term memory and spatial navigation among other functions (Bouix et al., 2001; Bonnici et al., 2012; Zeidman and Maguire, 2016). The amygdala is another structure in the limbic system and is closely related to the hippocampus. It is located in the temporal lobe of the brain, anterior to the hippocampus and is responsible for the perception of emotions and motivation among other functions (Hajek et al., 2009; Solano-Castiella et al., 2010; Hanson et al., 2012).

Therefore, the aim of this work was to develop a simple, easy-to-follow, and practical strategy for manual segmentation of the amygdala and hippocampus in T2-weighted infants' brain MRI. The protocol was tested in both T1- and T2-weighted MR images. Additionally, we compared the results from manually segmented data to automated segmented data performed by iBEAT software, which is specifically designed for automated segmentation of T2-weighted infant brain. iBEAT is a freely available package running on the Linux platform; it uses advanced image processing algorithms and can perform tasks like voxel analysis and infant brain labeling (Dai et al., 2012).

MATERIALS AND METHODS

Participants

For this study, a representative sample of 31 infants between 2 and 5 weeks of age was chosen from a larger dataset that included 175 MRI scans. **Table 1** shows the distribution of the selected background characteristics. The data were obtained from self-report questionnaires filled in by the participants at gestational week 14.

Image Acquisition

The infants underwent MRI scans in the Turku University Hospital at 2–5 weeks after birth (mean 17.8 days, range 12–52), counted from the estimated due date (Tuulari et al., 2017). A Siemens Magnetom Verio 3T scanner (Siemens Medical Solutions, Erlangen, Germany) was used for the imaging. Before the scan, the infants were fed to help them sleep and then swaddled into a vacuum mattress to reduce possible limb movement. The infants were scanned during natural sleep; thus, no anesthetics were used. All children were provided with double hearing protection (ear wax and ear muffs), which provided approximately 42 dB noise reduction. The duration of the whole scanning protocol was a maximum of 60 min. The family was free to discontinue the study at any point during the protocol and the scan was aborted if the baby

TABLE 1 | Information about the participants (N = 31) is reported as mean and *SD*.

Age from conception to MRI (days)	Mean: 305.80, *SD*: 8.26
Age at MRI scan (days)	Mean: 28, *SD*: 6.24
Birth weight (g)	Mean: 3639.48, *SD*: 417.81
Birth height (cm)	Mean: 50.67, *SD*: 1.51
Head circumference (cm)	Mean: 35.03, *SD*: 1.43
Ph of the umbilical artery	Mean: 7.24, *SD*: 0.073
Ph of the umbilical vein	Mean: 7.37, *SD*: 0.055
Sex	22 girls, 9 boys
Gestational age weeks 40 + (date of birth–due date)/7	Mean: 39.87, *SD*: 1.18
Maternal BMI [height/(weight/100) ** 2]	Mean: 25.44, *SD*: 5.005
Maternal age at birth moment (years)	Mean: 29.70, *SD*: 5.093
Medication taken by mothers	Two mothers used selective serotonin reuptake inhibitor (SSRI)/serotonin norepinephrine reuptake inhibitor (SNRI) and one used medicine that affects central nervous system
Nicotine and alcohol used by mothers	None
Father's age at due date (mean and *SD*, years)	31.57, 4.86
Race	Caucasian, Finnish
Education divided into three classes	Low, mid 9/31 High, vocation 7/31 High 11/30 Data not available 2/31

was not soundly asleep and/or still in the scanner, or if the baby woke up in the middle of the scanning and did not fall asleep again.

The scanning protocol included Axial Dual Echo Turbo Spin Echo (TSE) sequence, where repetition time (TR) of 12,070 ms and effective echo time (TE) of 13 and 102 ms were used to produce both PD-weighted and T2-weighted images from the same acquisition. Slice thickness was 1 mm in order to acquire isotropic 1.0 × 1.0 × 1.0 mm voxels. The total number of slices was 128. A T1-weighted 3D Magnetization Prepared Rapid Acquisition Gradient Echo (MPRAGE) sequence with isotropic 1.0 × 1.0 × 1.0 mm voxels was used for anatomical imaging as well. Acquisition parameters relevant to image contrast were TR of 1900 ms, TE of 3.26 ms, inversion time (TI) of 900 ms, and flip angle of 9 degrees. All the successful brain images were evaluated by a radiologist specializing in pediatric neuroradiology. If the neuroradiologist found abnormalities in the images, the families were offered an opportunity for a child neurological examination and consultation by an experienced pediatric neurologist. The sample in the current study is free from participants with incidental findings.

Ethics

The study was conducted in accordance with the Declaration of Helsinki. The Joint Ethics Committee of South-Western Hospital District and the University of Turku, as well as all the relevant research sites have given their approval for all parts of the present study. Parents gave written informed consent on behalf of their baby. The ethical approval number for this study is ETMK 31/180/2011.

Image Processing

Raw MRI DICOM images were converted to Neuroimaging Informatics Technology Initiative (NIfTI) format using dcm2nii software[1]. We then rigidly co-registered individual T1- and T2-weighted volumes to one another with FSL's flirt (6 degrees of freedom) and matched the orientation of the UNC infant template[2] (Shi et al., 2011) in order to similarly align all the images to the same "upright" orientation. Then the NIfTI images were converted to MINC format using the MINC tools' version 1.5.1 developed at McConnell Brain Imaging Centre, Montreal, Canada. The computer used for segmentation was iMAC OS X 10.11.6 (EI Capitan) with 4 GHz Intel Core i7 processor and with an AMD Radeon R9 M395 2048 MB graphics card.

Manual Segmentation

Manual segmentation of the hippocampus and amygdala was performed with the developed protocol using the Display software package version 2.0 which is a part of MINC software package. For an accurate segmentation, a brush size of 0.5 mm was selected (images had a 1-mm^3 resolution). For better visualization, brightness and contrast were adjusted and simultaneous assessment in different axial, coronal, and sagittal planes was used. In all subjects, the manual segmentation of the amygdala and hippocampus was performed in a slice-by-slice manner to carefully trace the relevant anatomical borders. Manual segmentation was performed on one hemisphere at a time. For a three-dimensional consistency of the segmentations, the images were reviewed and revised in axial, coronal, and sagittal planes. Once the segmentations were done, the delineation of the amygdala and hippocampus, in both hemispheres, was double-checked, and the necessary adjustments were made. Finally, extra segmented voxels or empty voxels had to be removed or added in order to have smooth and even segmentation. After delineating the structures, the volumes of the manually segmented amygdala and hippocampus were automatically calculated with the minc tools' "volume_stats" function.

Manual Segmentation of the Hippocampus

The hippocampus is a curved structure that is located in the medial temporal lobes of both hemispheres. With respect to the hippocampal subregions, the dentate gyrus, hippocampus proper, or cornu ammonis (CA) including CA4 region (hilus), dentate gyrus, CA3, CA2, CA1, and subiculum between CA1 and fornix were included in the segmentation as a whole (**Figure 1A**). The hippocampus includes three gross anatomical parts, the hippocampus head which is located in the most anterior part, hippocampus body in the medial part, and hippocampus tail in the most posterior region (**Figure 1B**). In this protocol, the hippocampus was defined as one region including the posterior uncus; the hooked shaped structure of hippocampus that lies at the most anterior part of the parahippocampal gyrus. The

[1]https://www.nitrc.org/projects/dcm2nii

[2]https://www.nitrc.org/projects/pediatricatlas

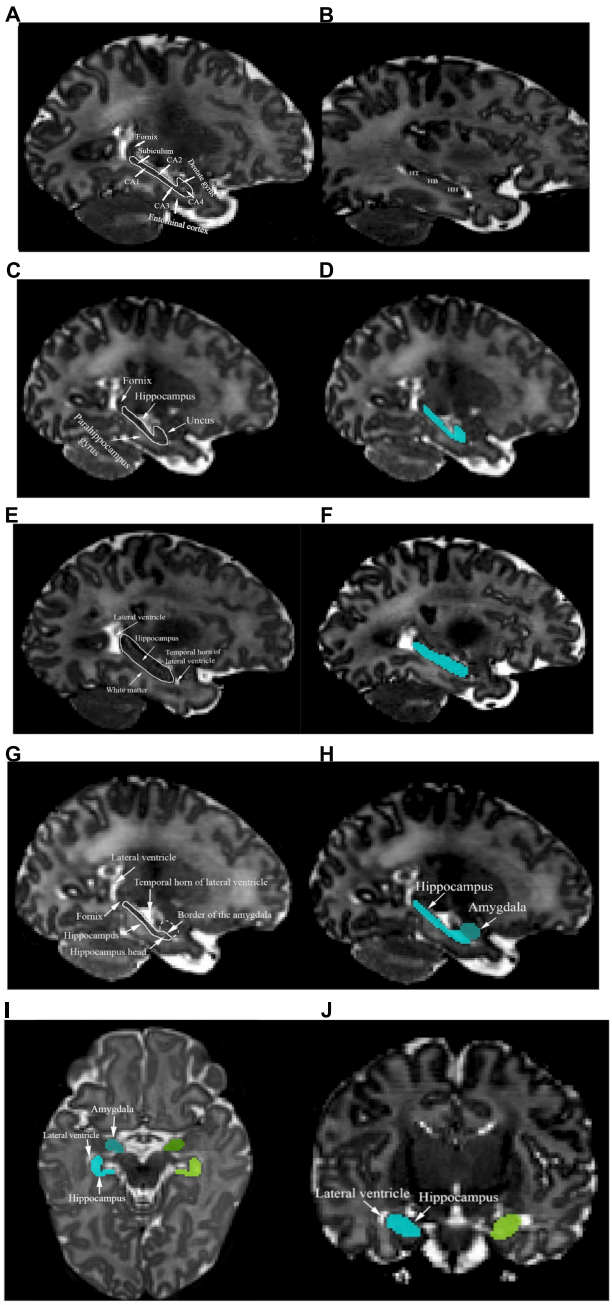

FIGURE 1 | (A) Structures of the left fornix, entorhinal cortex, subiculum, CA1, CA2, CA3, CA4, and dentate gyrus are shown. **(B)** Left hippocampus tail (HT), hippocampus body (HB), and hippocampus head (HH) are presented. **(C)** The left fornix, parahippocampal gyrus, and uncus are presented in the sagittal plane. **(D)** The segmented left hippocampus in the sagittal plane is shown (cyan color). Left hippocampus mass was identified using landmarks such as the lateral ventricle, white matter, and the temporal horn of the lateral ventricle **(E)** and the segmented structure is shown in **(F)**. **(G)** Left hippocampus head and amygdala's border in the sagittal view are shown. **(H)** The sagittal plane of the segmented left hippocampus and amygdala. **(I)** The axial plane of the superomedial portion of the left hippocampus (cyan), left amygdala (blue), right hippocampus (chartreuse), right amygdala (green), and lateral ventricles. **(J)** The coronal plane of the superomedial portion of the left hippocampus (cyan), right hippocampus (chartreuse), and lateral ventricle.

white matter track of the fimbria at the posterior portion of the hippocampus is included in the segmentation up to the point where it separates from the hippocampus and forms the fornix (De Macedo Rodrigues et al., 2015). The white matter fibers of the fornix and parahippocampal gyrus were carefully excluded from the segmentation (**Figure 1C**). **Figure 1D** shows an example of the segmented hippocampus structure.

Segmentation of the hippocampus began with identifying the borders of the most lateral hippocampal slice in the sagittal plane. Segmentation was performed on hippocampus mass, where the lateral ventricle defines the hippocampus tail and the temporal horn of the lateral ventricle appears next to hippocampus head. Moreover, the white matter appears along the hippocampus body. The inferior border of the hippocampus should be delineated, with attention paid to the contrast change between hippocampus and white matter (**Figure 1E**). **Figure 1F** represents the segmented hippocampus.

Moving inferiorly in the sagittal plane, tracing of the hippocampus mass was continued until the borders of the amygdala first became visible and the head of the hippocampus was identified using the horn of the lateral ventricle (**Figure 1G**). An example of the hippocampus and amygdala segmentation is shown in **Figure 1H**. The coronal and axial planes were used to identify the superomedial portion of the hippocampus, as the hippocampus borders are clearly distinguishable from the lateral ventricle in those planes (**Figures 1I,J**). When moving posteriorly in the axial view, special attention was paid to when the hippocampus and amygdala started to touch. All of the three views were referred to in order to precisely determine the borders and slices in which both the amygdala and hippocampus were present.

Manual Segmentation of the Amygdala

The amygdala is an olive-shaped structure that is located in the medial temporal lobes of both hemispheres where it is superior and anterior to the hippocampus. Tracing the amygdala in MR images is more complicated than tracing the hippocampus, due to its location in the superomedial temporal lobe, where basal ganglia and entorhinal cortex merge into the posterior and inferior borders of this structure (Pruessner et al., 2000). As it is often not easy to identify the borders of amygdala it is important to trace the amygdala slice by slice with the help and reference to all three planes. Circa 10 slices of the amygdala were identified in each of our T2-weighted MRI data. The amygdala segmentation was started by moving superiorly in the sagittal plane from where the thalamus starts to form its walnut shape, the superomedial borders of amygdala appear superior to the hippocampus (**Figure 2A**). The superior border of the amygdala is attached to the ambient cistern. Therefore, it is easiest to distinguish it in the axial view. For consistency, one row of voxels at the cerebral cortex lying anterior to the amygdala was systematically excluded from delineation (**Figure 2B**). In the coronal plane, the temporal horn of the lateral ventricle was used to define the inferior and anterior borders of the amygdala and hippocampus, as they both were visible in the same slice (**Figure 2C**). Moving anteriorly in the coronal plane the lateral and inferior parts of the amygdala were identified

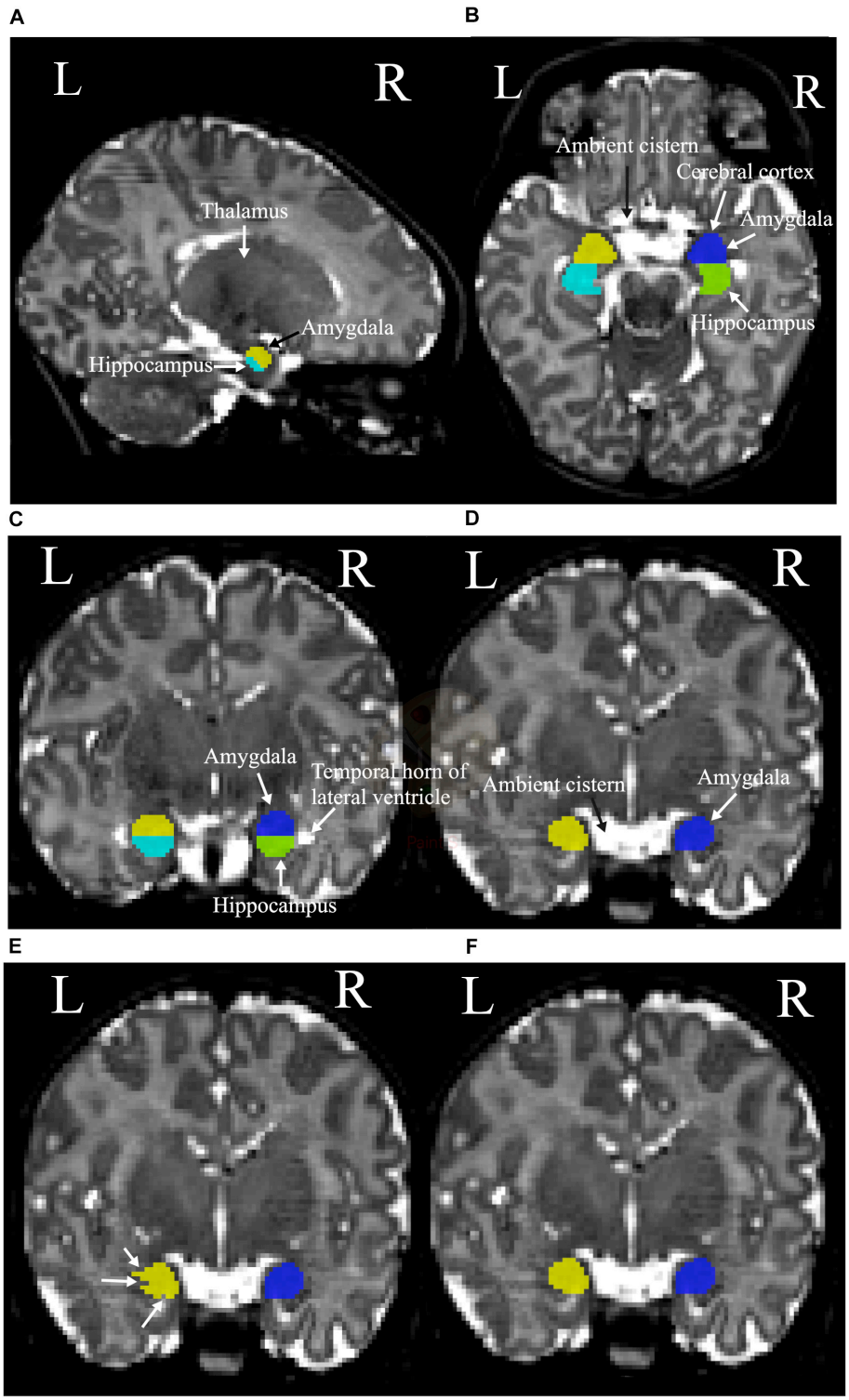

FIGURE 2 | (A) The sagittal plane of the left thalamus, hippocampus (cyan), and amygdala (yellow). **(B)** Left and right hippocampus (cyan and green, respectively), and superior borders of the left amygdala (yellow), right amygdala (blue), ambient cistern, and cerebral cortex. **(C)** The coronal plane of the temporal horn of the lateral ventricles and left and right amygdala and hippocampus. Left amygdala with yellow, left hippocampus with cyan, right amygdala with blue, and right hippocampus with green colors are presented. **(D)** The ambient cistern, left amygdala (yellow), and right amygdala (blue) in coronal view. **(E)** Segmentation before the final adjustments is shown with white arrows. **(F)** The structure after the corrections.

(**Figure 2D**). Finally, extra segmented voxels or empty voxels had to be removed or added in order to have smooth an even segmentation (**Figures 2E,F**).

The coordinates for identifying the landmarks of the hippocampus and the amygdala are presented in **Table 2**. MRIcron[3] and UNC infant template (see text footnote 2) were used to specify the coordinates. It should be noted that as the MRI image of each brain varies among each individual, the coordinates are roughly applicable. A summary schematic of the performed steps for hippocampus and amygdala segmentation in sagittal, coronal, and axial planes is shown in **Figures 3A–F**.

Statistical Analysis

Descriptive analyses of the manual segmentation volumes were reported by mean and standard deviation (*SD*). Hemispheric volume differences between right and left amygdala and hippocampus were assessed using a paired *t*-test and *p*-values <0.05 were considered statistically significant. Data normality was checked by visual confirmation and by the Shapiro–Wilk test. The analyses were carried out using SPSS 24, Armonk, NY, United States. Additionally, Dice similarity coefficient (DSC) (Dice, 1945) was computed using Python version 2.7 in order to estimate the degree of volumetric overlap between the delineations.

We performed four different assessments: (1) intra-rater reliabilities of the main rater (NH) for baseline, 1-month intervals (N = 6) and 6-month (N = 6) intervals in between the segmentations, (2) inter-rater reliabilities between the primary rater and two less experienced raters after ca. 2 months training (N = 20), (3) the segmentation of the primary rater for T1- and T2-weighted images from the same participants (N = 10), and (4) agreement of manual tracings of the primary rater to iBEAT segmentations (N = 10).

[3]https://www.nitrc.org/projects/mricron

TABLE 2 | The MNI coordinates for anatomical landmarks: obtained by opening the UNC-infant-neo-withSkull infant template in MRIcron to help reproducibility.

Structures	*X*	*Y*	*Z*	Hemisphere
Hippocampus tail started to be visible	21	−26	−1	R
	−20	−24	0	L
Hippocampus head started to be visible	21	−12	−14	R
	−20	−11	−13	L
Hippocampus tail ended	13	−22	−2	R
	−13	−22	−2	L
Hippocampus head ended	13	−16	−12	R
	−11	−18	−9	L
Superior border of the amygdala started to be visible	15	−5	−8	R
	−15	−3	−7	L
Inferior border of the amygdala started to be visible	17	−3	−15	R
	−17	−3	−14	L
Superior border of the amygdala ended	20	−6	−9	R
	−20	−6	−8	L
Inferior border of the amygdala ended	21	−5	−15	R
	−20	−5	−14	L
Border of the amygdala and hippocampus	19	−9	−13	R
	−18	−9	−12	L

Intra-Rater Reliability Measurements

Re-segmentation was performed on 12 randomly selected MR images. Six images were segmented with 1-month intervals, and another six images with 6-month intervals. The stability of the protocol and the intra-rater reliability were assessed by comparing the segmentation volumes. Intra-rater reliability tests for the left and right amygdala and hippocampus were computed using a two-way mixed-model and absolute agreement intraclass correlation coefficient (ICC) (Shrout and Fleiss, 1979) and DSC.

Inter-Rater Reliability Measurement

Re-segmentation was performed on 20 randomly selected MR images from the 31 images by two less experience raters using the same protocol. Each rater segmented the amygdala and hippocampus of 10 different brains. The segmentation was performed blind to the subjects' genders and age. The volumes of the segmented structures were used to compute inter-rater reliability using a two-way mixed-model, absolute agreement, and multiple raters ICC (Shrout and Fleiss, 1979; Koo and Li, 2016). Moreover, DSC was used to report the volumetric overlap of the left and right amygdala and hippocampus between rater 1 and the main rater, and rater 2 and the main rater.

Comparison of Manual Tracing in T1- and T2-Weighted MR Images

Manual segmentation was performed using the established protocol on 10 T1- and 10 T2-weighted images of the same subjects. Because of the ongoing myelination process and higher water content in the infant brain, the contrast in T1-weighted images is lower compared to T2-weighted images (Dubois et al., 2014; Dean et al., 2018). In the case of infants between 2 and 5 weeks of age, the intensity pattern of the white and gray matter in T1-weighted images is more similar to the adult T2-weighted images, since the white matter has lower intensity than the gray matter (Paus et al., 2001; Dean et al., 2018). Conversely, the contrast between the white and gray matter in T2-weighted images of the infants in this age group is similar to that in the T1-weighted images of adults.

By adjusting the brightness and contrast of the images, the amygdala and hippocampus are distinguishable in T1-weighted images but not as clearly as in T2-weighted images. The volumetric differences of the left and right hippocampus and amygdala in T1 and T2 images of the same subjects were extracted from the segmentations. To analyze the consistency between T1 and T2 manual segmentation, ICC and DSC were computed. T2-weighted MR images have better tissue contrast compared to T1-weighted MR images at this developmental stage. However, if the T2-weighted images are exposed to, e.g., motion artifacts, T1-weighted images could be valuable for studying different brain structures and were thus included in the protocol to study if they can be used interchangeably.

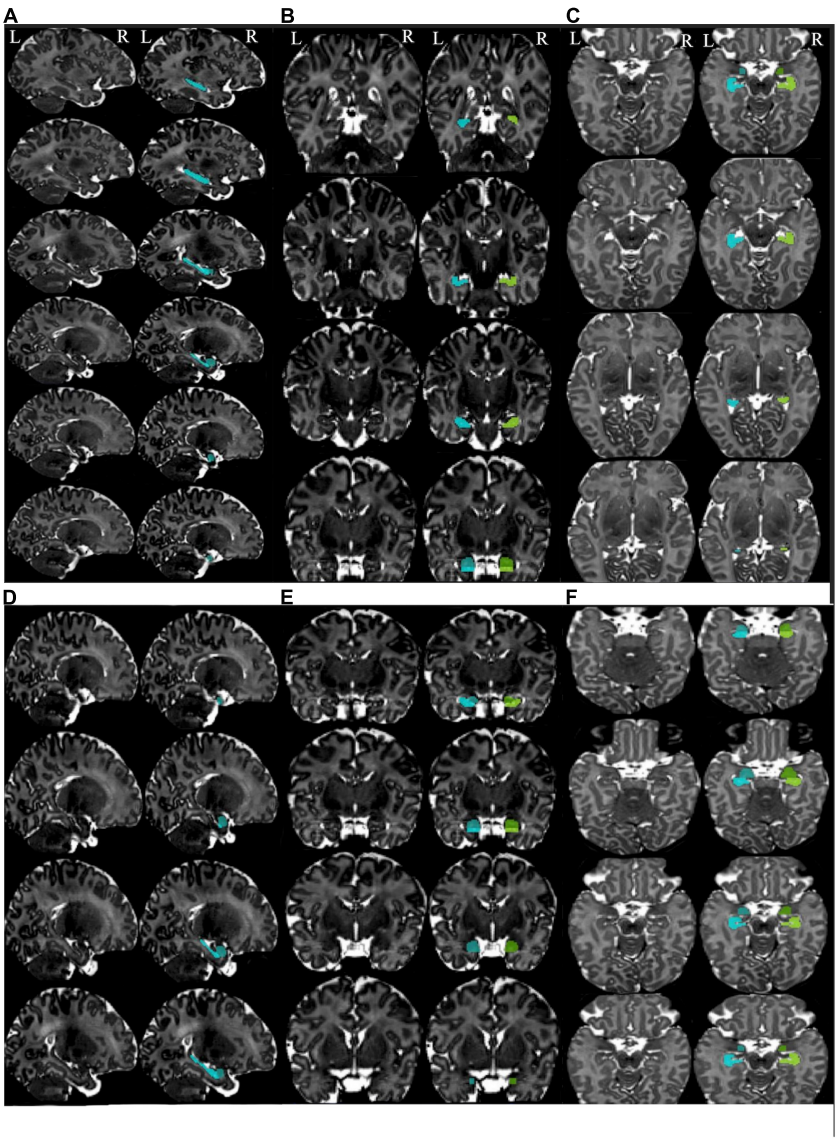

FIGURE 3 | Summary of the steps for segmentation of the hippocampus and amygdala in the different planes. Summary of the steps for segmentation of hippocampus in the sagittal **(A)**, coronal **(B)**, and axial planes **(C)**. Summary of the steps for segmentation of the amygdala in the sagittal **(D)**, coronal **(E)**, and axial planes **(F)**. Left images are the templates (non-segmented) and the images at the right side present segmented structures. Left hippocampus is shown in the cyan color and the left amygdala in blue. Right hippocampus is presented in chartreuse and right amygdala in green.

Comparison of Automated Segmentation to Manual Tracing

Automated (using iBEAT software) and manual segmentations (using Display software) were performed on 10 T2-weighted MR images. As iBEAT software does not take infants' T1-weighted images as input, only T2-weighted images were used for the comparison with manual segmentation. To validate the success of the automated segmentation results of the limbic structures (the hippocampus and amygdala) in iBEAT software we compared the extracted volumetric results from iBEAT to the manually defined volumes. The volumetric results from the iBEAT software and the manual segmentation were compared. Additionally, the difference between the automated segmentation results and the manual segmentation results was calculated as a percentage using Eq. 1 (Schoemaker et al., 2016):

$$\%VD = [(Va - Vm)/Vm] * 100\% \quad (1)$$

TABLE 3 | Mean and *SD* of left and right amygdala and hippocampus across 31 subjects from T2-weighted imaged done by the primary rater of the segmentation.

	Left amygdala	Right amygdala	Left hippocampus	Right hippocampus
Mean volume (mm^3)	382.29	363.96	826.38	793.35
Standard deviation	124.61	110.08	109.19	148.79

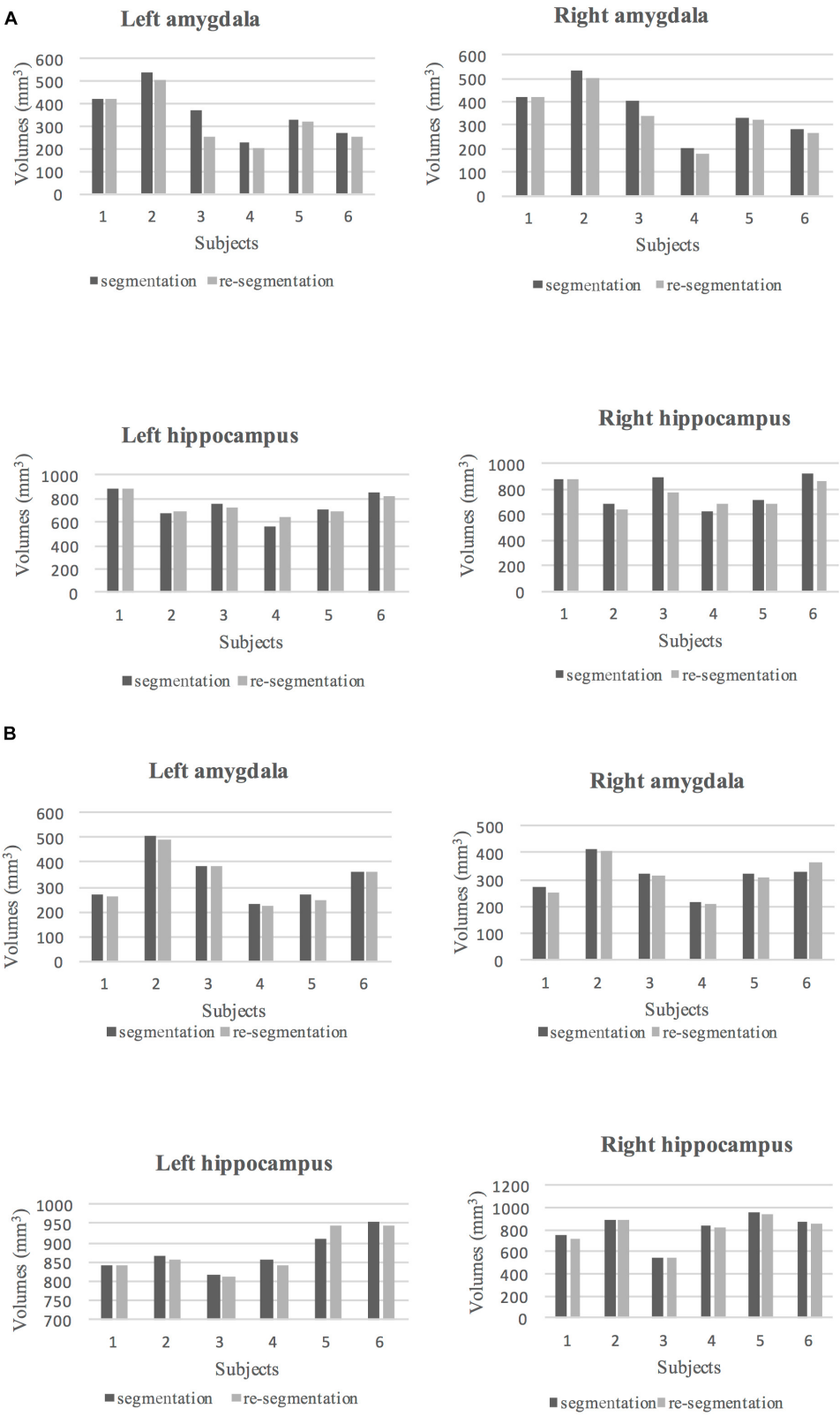

FIGURE 4 | (A) The volumes of segmented (dark gray) and re-segmented (light gray) left and right amygdala and hippocampus for six subjects with 1-month intervals to the segmentation. **(B)** The volumes of segmented (dark gray) and re-segmented (light gray) left and right amygdala and hippocampus for six subjects with 6-month intervals to the segmentation.

Using formula (1), negative percentages indicate an underestimation of the automated segmentation volumes compared to manual segmentation and positive percentages indicate an overestimation of volumes compared to manual segmentations.

Moreover, ICC and DSC were performed on the extracted volumes for the automated and manual segmentations.

RESULTS

Hemispheric Difference

The mean volumes and *SD* of the left and right amygdala and hippocampus across 31 subjects are shown in **Table 3**. The *t*-test did not reveal significant differences between the left and right amygdala ($M_{\text{left amygdala}}$ = 382.29 (mm^3), $SD_{\text{left amygdala}}$ = 124.61 and $M_{\text{right amygdala}}$ = 363.96 (mm^3), and $SD_{\text{right amygdala}}$ = 110.08, t = 1.02, p = 0.31). Similarly, no significant difference was observed between hippocampus at the left and right hemispheres ($M_{\text{left hippocampus}}$ = 826.38 (mm^3), $SD_{\text{left hippocampus}}$ = 109.19 and $M_{\text{right hippocampus}}$ = 793.35 (mm^3), $SD_{\text{right hippocampus}}$ = 148.79, t = 1.64, p = 0.11).

Intra-Rater Reliability Results

To assess intra-rater reliability, ICC and DSC were calculated at two time points (at 1-month and 6-month intervals). The volumes of the segmented left and right amygdala and hippocampus at these two points are shown in **Figures 4A,B**. The ICC and DSC scores for intra-rater reliability with a 1-month and 6-month intervals for the left and right amygdala and hippocampus are presented in **Table 4**. High intra-rater reliability results were observed (ICC $\geq$ 0.91 and DSC ranged between 0.89 and 0.94). Thus, the manual tracings were highly replicable for a single rater.

Inter-Rater Reliability

The ICC and DSC results for inter-rater reliability of raters are presented in **Table 5**. The volumes of the segmented amygdala and hippocampus by two raters are shown in **Figures 5A,B**. Strong ICC and satisfactory DSC results were observed for hippocampus tracings among raters (ICC $\geq$ 0.90, DSC $\geq$ 0.75). The ICC scores for amygdala tracing were high as well (ICC $\geq$ 0.92). However, the DSC scores were not strong for the amygdala segmentation between the raters (DSC $\geq$ 0.52) and importantly, they indicated a systematic difference between the raters with regard to the placement of the regions of interest (ROIs) although the volumes show better agreement.

TABLE 4 | ICC, mean DSC, and *SD* results at two time points.

	Left amygdala	Right amygdala	Left hippocampus	Right hippocampus
1-Month interval ICC	0.94	0.98	0.96	0.91
6-Month interval ICC	0.99	0.98	0.97	0.99
1-Month interval DSC (*SD*)	0.91 (0.10)	0.92 (0.11)	0.94 (0.045)	0.94 (0.051)
6-Month interval DSC (*SD*)	0.89 (0.22)	0.93 (0.11)	0.91 (0.18)	0.94 (0.10)

TABLE 5 | ICC, mean DSC, and *SD* results of rater 1 and 2 compared to the primary rater for the amygdala and hippocampus in both hemispheres.

	Left amygdala	Right amygdala	Left hippocampus	Right hippocampus
Rater 1 ICC	0.93	0.93	0.90	0.93
Rater 2 ICC	0.92	0.93	0.96	0.98
Rater 1 DSC (*SD*)	0.55 (0.16)	0.55 (0.22)	0.78 (0.067)	0.76 (0.086)
Rater 2 DSC (*SD*)	0.52 (0.11)	0.54 (0.14)	0.75 (0.033)	0.76 (0.048)

Comparison of Manual Tracing in T1- and T2-Weighted MR Images

Manual segmentation of hippocampal and amygdala volumes in T1- and T2-weighted MR images of the same subjects showed slightly different volumes compared to each other. Generally, manually segmented volumes in T2 images showed lower values, likely due to better contrast at the borders. Therefore, manual segmentation in T1 images was associated with a slight overestimation of volumes for left and right amygdala and hippocampus.

ICC and DSC values for manual segmentations of the left and right amygdala and hippocampus in T1- and T2-weighted images of 10 subjects are presented in **Table 6**. Strong ICC and DSC scores were seen in both the amygdala and hippocampal segmentations in T1 and T2 images (ICC $\geq$ 0.90 and DSC $\geq$ 0.74).

Comparison of Automated Segmentation to Manual Tracing

The volumes of the manually defined structures were differential compared to iBEAT automated segmentation for both the hippocampal and amygdala segmentations. In general, automated segmentation volumes of the left and right amygdala showed greater values related to manual segmentation of those regions. Likewise, automated segmentation of the left and right hippocampus produced greater values than manual segmentation (**Figure 6**).

The mean percentages and SD of volume difference between the two segmentation methods for the left and right amygdala and left and right hippocampus were calculated in all the subjects (**Table 7**). In all of the subjects, automated segmentation overestimated volumes of the left and right hippocampus and left and right amygdala. The left and right hippocampus and left and right amygdala yielded large percentage of volume differences. The mean and standard deviation of the percentage of volume difference for the left and right amygdala were 111.8%, *SD* = 71.6 and 55.9%, *SD* = 70.5, respectively. The mean percentage of volume difference and standard deviation for the left hippocampus were 130.3%, *SD* = 32.8 and for the right hippocampus 128.4%, *SD* = 39.3. Overall, automated segmentation overestimated the volumes of amygdala and hippocampus compared to manual tracing (**Figures 7A–C**).

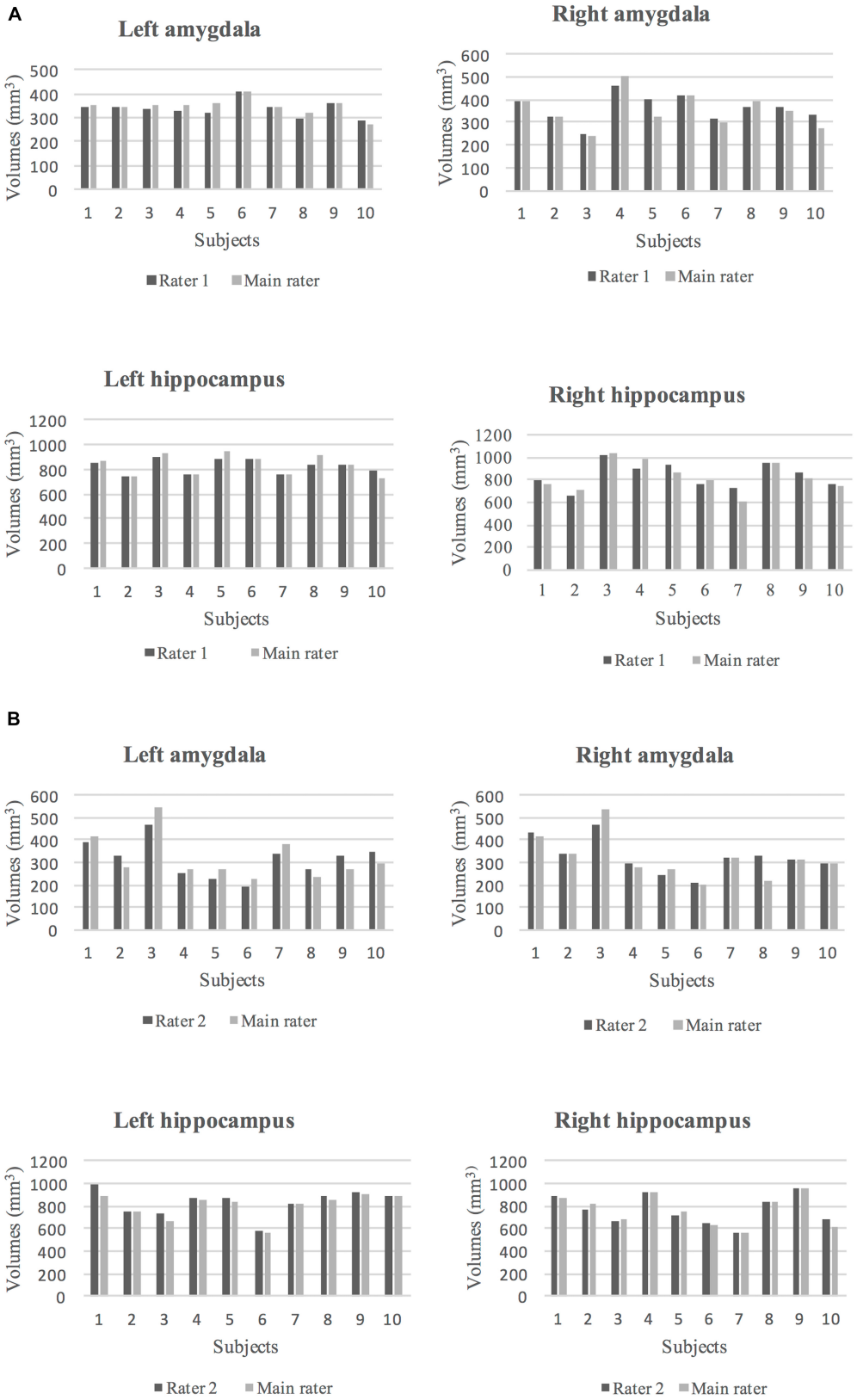

FIGURE 5 | (A) The volumes of segmented left and right amygdala and hippocampus by rater 1 (dark gray) and the main rater (light gray) for 10 subjects are shown. **(B)** The volumes of segmented left and right amygdala and hippocampus by rater 2 (dark gray) and the main rater (light gray) for 10 subjects are shown.

TABLE 6 | ICC, mean DSC, and *SD* between left and right amygdala and hippocampus in T1- and T2-weighted images.

	Left amygdala	Right amygdala	Left hippocampus	Right hippocampus
ICC	0.95	0.97	0.97	0.90
DSC (*SD*)	0.82 (0.23)	0.80 (0.22)	0.79 (0.24)	0.74 (0.28)

ICC and DSC results between manual segmentation and automated segmentation methods for the left and right amygdala and hippocampus are presented in **Table 8**. No strong ICC and DSC were observed between the two methods (ICC ≥ -0.07 and DSC ≥ 0.39).

DISCUSSION

We have developed a protocol for segmenting the amygdala and hippocampus in T2-weighted MR images of infants between 2 and 5 weeks old and confirmed that this protocol provides accurate delineations of these structures for a single rater. On the other hand, while the ICC values were satisfactory for inter-rater assessments the DSC values indicate that the labeling is not overlapping consistently; for studies using multiple raters, this is imperative to assess. We also observed a low agreement of manual tracings to automated segmentation results, but we would like to stress that we think iBEAT is a well working software for the rest of the brain (Lehtola et al., 2018), and would like to point out the importance of assessing carefully, whether a given pipeline produces the wanted and reliable outcome metrics.

Based on our experience, the overall anatomy of infants' amygdala and hippocampus structures is quite similar to the adult brain. Nevertheless, the hippocampal folding is slightly less pronounced, and the central amygdala is frequently easier to see than in adult T1-weighted images. However, the inferior and lateral borders of both structures are more challenging to find. In this protocol, the macro-anatomical structures and boundaries were carefully included in the segmentations. Much attention has been directed to detecting and omitting the fornix and parahippocampal gyrus as parts of the hippocampus, as well as accurately identifying the boundaries of the amygdala and hippocampus adjacent to the temporal horn of the lateral ventricles. The structures and boundaries of ROIs were identified using all the three planes (sagittal, axial, and coronal); in other studies, one plane was considered as the default view and other planes were reviewed whenever needed. This protocol was tested by two raters with very little previous knowledge about manual

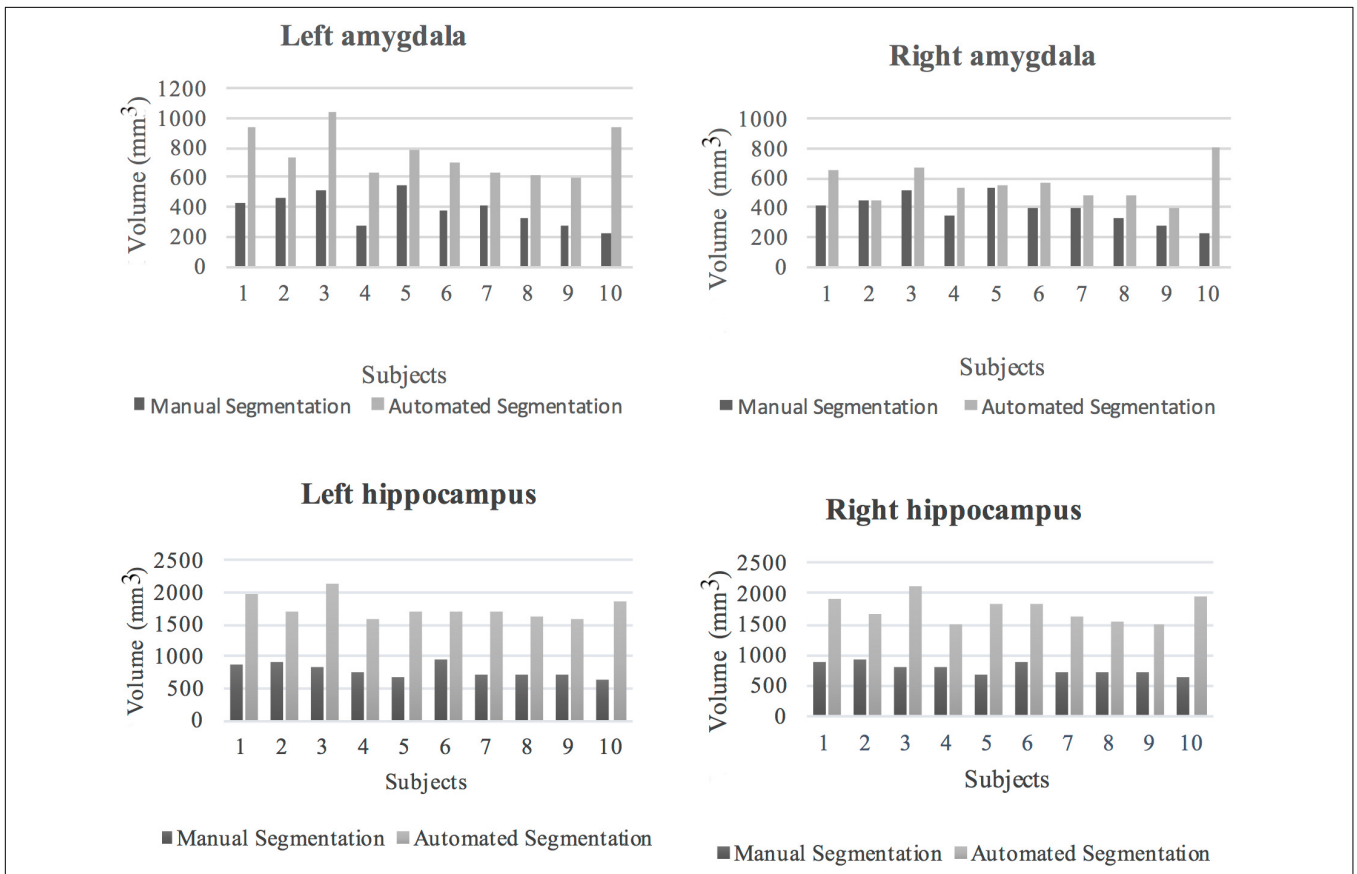

FIGURE 6 | Volumes of the left and right amygdala and hippocampus from manual and automated segmentation for all 10 subjects. Volumes extracted from automated and manual segmentation are shown in light gray and dark gray, respectively.

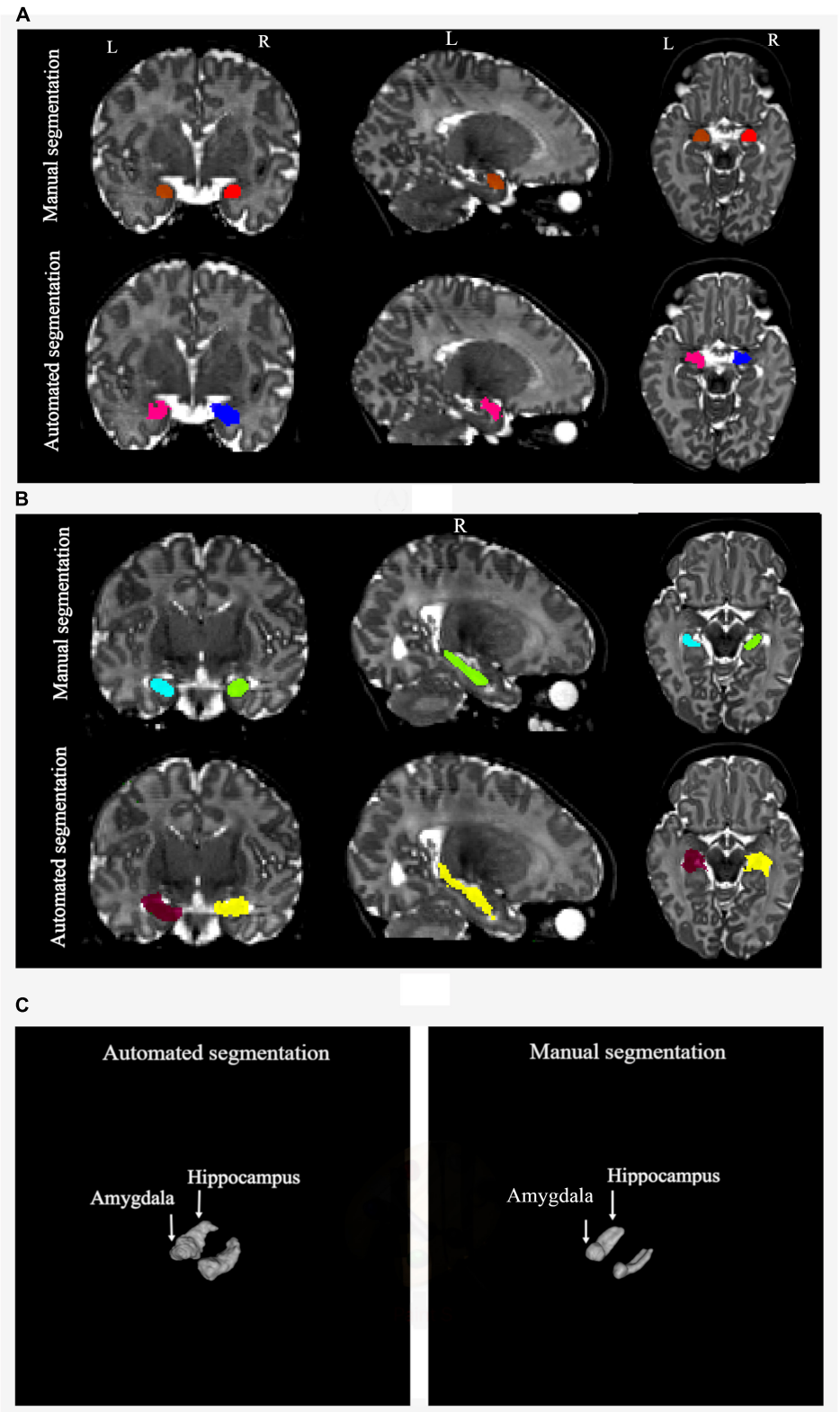

FIGURE 7 | (A) Manual and automated segmentation of amygdala are compared. In automated segmentation performed by iBEAT, amygdala volume is overestimated. It is extended to CSF and lateral ventricles. **(B)** Manual and automated segmentation of hippocampus are compared. In automated segmentation performed by iBEAT, hippocampus volume is overestimated. It is extended to CSF, lateral ventricles, and fornix. **(C)** 3D surface render for comparing of automated and manual segmentation.

TABLE 7 | The mean percentage of volume difference and *SD* between automated and manual tracing of the left and right amygdala and hippocampus.

Mean % of left amygdala	111.8
SD of left amygdala	71.6
Mean % of right amygdala	55.9
SD of right amygdala	70.5
Mean % of left hippocampus	130.3
SD of left hippocampus	32.8
Mean % of right hippocampus	128.4
SD of right hippocampus	39.3

TABLE 8 | ICC, mean DSC, and *SD* between automated and manual segmentation.

	Left amygdala	Right amygdala	Left hippocampus	Right hippocampus
ICC	0.36	−0.07	0.21	0.08
DSC (*SD*)	0.41 (0.09)	0.46 (0.09)	0.39 (0.04)	0.40 (0.04)

segmentation, and they were able to quickly learn and apply the strategy employed in this protocol. High intra-rater and inter-rater reliability evaluated using intraclass correlation coefficient tests confirm that the designed protocol in this study delivers a precise step-by-step guide for the hippocampal and amygdala delineation in infant brain MRIs. Similarly, the Dice coefficient scores for intra-rater test were high. However, the DSC values for inter-rater reliability of the amygdala were not high. This is likely due to the systematic difference between the raters and small size of the amygdala and the difficulty delineating it.

Additionally, the designed protocol was used to study the variations between segmenting T1- and T2-weighted images of the same participants. Compared to T1-weighted images, manual delineations of infant T2-weighted images were easier to perform due to the better contrast at the boundaries of the structures. Segmentation of T1- and T2-weighted images provided similar, but not the same, results. Segmented volumes of the amygdala and hippocampus from T1-weighted images showed a small overestimation compared to those based on T2-weighted images. According to the strong correlation and high DSC scores between T1- and T2-weighted images, it can be concluded that T1- or T2-weighted images can be substituted for one another in the related studies (Dean et al., 2018). However, the scan type should likely be included as a covariate as the small differences may be crucial. Overall, the designed protocol offers reliable and relatively simple guidelines for segmenting the complex amygdala and hippocampal structures in infants and it is potentially useful for infant neuroimaging research projects.

We also reported the accuracy of automated segmentations of the amygdala and hippocampus performed by iBEAT software in contrast to manual segmentations of these structures. According to the calculated volume difference, percentage of volume difference, ICC, and DSC between iBEAT and manually defined structures of the amygdala and hippocampus, automatic segmentation with iBEAT was not be able to be validated against manual segmentation, which was considered the "gold standard." iBEAT overestimated the volumes of the left and right amygdala by 111.8 and 55.9%, respectively. 130.3 and 128.4% volume overestimation were observed for the left and right hippocampus, respectively. Also, results from the correlation between manual and automated segmentation showed a high degree of disagreement between the two methods. iBEAT overestimates the amygdala segmentation by considering parts of the CSF and lateral ventricles as the structure of the amygdala. Overestimation of the hippocampus is mainly due to extending the segmentation of this structure to the CSF, fornix, and lateral ventricles. iBEAT's overestimation of the hippocampal and amygdala volumes is likely due to the limited contrast in the infant brain, and adjacent cortical gray matter is likely being misclassified as being part of the hippocampus and amygdala.

CONCLUSION

In pediatric studies, it is important to evaluate and validate automatically segmented structures. Automated approaches can be validated by using a dataset of manually segmented structures. In this study, we have described a manual segmentation protocol by which such a dataset can be produced. We hope this protocol assists the development and assessment of automated segmentation procedures of neonatal brain.

ETHICS STATEMENT

The study was conducted in accordance with the Declaration of Helsinki. The Joint Ethics Committee of South-Western Hospital District and the University of Turku, as well as all the relevant research sites have given their approval for all parts of the present study. Parents gave a written informed consent on behalf of their baby. The ethical approval number for this study is ETMK 31/180/2011.

AUTHOR CONTRIBUTIONS

NH analyzed the data (preprocessing, manual and automated segmentation, and statistical analyses) and drafted the manuscript. JT supervised NH. HM and JT planned the analyses. KL and IL performed the manual segmentation. JS implemented the scanning protocol. RP planned the studies and screened the images. TL performed the clinical examinations to those with incidental findings. SL collected the data. MK and SL recruited the participants. JL planned the imaging sequences. NS was involved in planning the study and supervising the data collection. HK planned and established the cohort and provided funding for the data collection. LK co-planned and established the cohort with HK. The manuscript was revised and accepted by all co-authors.

FUNDING

This research was supported by the Orion Foundation (NH), the Hospital District of Southwest Finland State Research Grant (JT, LK, and HK), the Alfred Kordelin Foundation (JT), the Turku

University Foundation (JT), the Emil Aaltonen Foundation (JT), the Sigrid Juselius Foundation (HM), the Brain and Behavior Research Foundation YI Grant #1956 (LK), the Jane and Aatos Erkon Foundation (HK), the Academy of Finland (LK and HK), and the Signe and Ane Gyllenberg Foundation (HK).

ACKNOWLEDGMENTS

We thank all of the families and infants who participated in the MRI scans, and Kristiina Kuvaja for performing the scans with the investigators.

REFERENCES

Alexander, B., Loh, W., Matthews, L., Murray, A., Adamson, C., Beare, R., et al. (2019). Desikan-Killiany-Tourville atlas compatible Version of M-CRIB neonatal parcellated whole brain atlas: the M-CRIB 2.0. *Front. Neurosci.* 13:34. doi: 10.3389/fnins.2019.00034

Alexander, B., Murray, A., Loh, W., Matthews, L., Adamson, C., Beare, R., et al. (2017). A new neonatal cortical & subcortical brain atlas: the Melbourne Children's regional infant brain (M-CRIB) atlas. *Neuroimage* 147, 841–851. doi: 10.1016/j.neuroimage.2016.09.068

Balafar, M. A., Ramli, A. R., Saripan, M. I., and Mashohor, S. (2010). Review of brain MRI image segmentation methods. *Artif. Intell. Rev.* 33, 261–274. doi: 10.1007/s10462-010-9155-9150

Beare, R., Chen, J., Kelly, C., Alexopoulos, D., Smyser, C., Rogers, C., et al. (2016). Neonatal brain tissue classification with morphological adaptation and unified segmentation. *Front. Neuroinform.* 10:12. doi: 10.3389/fninf.2016.00012

Bonnici, H. M., Chadwick, M. J., Kumaran, D., Hassabis, D., Weiskopf, N., and Maguire, E. A. (2012). Multi-voxel pattern analysis in human hippocampal subfields. *Front. Hum. Neurosci.* 6:290. doi: 10.3389/fnhum.2012.00290

Bouix, S., Pruessner, J. C., Collins, D. L., and Siddiqi, K. (2001). "Hippocampal shape analysis using medial surfaces," in *Medical Image Computing and Computer-Assisted Intervention – MICCAI 2001. MICCAI 2001. Lecture Notes in Computer Science*, Vol. 2208, eds W. J. Niessen, and M. A. Viergever, (Heidelberg: Springer), 33–40. doi: 10.1007/3-540-45468-3_5

Chiverton, J., Wells, K., Lewis, E., Chen, C., Podda, B., and Johnson, D. (2007). Statistical morphological skull stripping of adult and infant MRI data. *Comput. Biol. Med.* 37, 342–357. doi: 10.1016/j.compbiomed.2006.04.001

Dai, Y., Shi, F., Wang, L., Wu, G., and Shen, D. (2012). IBEAT: a toolbox for infant brain magnetic resonance image processing. *Neuroinformatics* 11, 211–225. doi: 10.1007/s12021-012-9164-z

De Macedo Rodrigues, K., Ben-Avi, E., Sliva, D. D., Choe, M., Drottar, M., Wang, R., et al. (2015). A FreeSurfer-compliant consistent manual segmentation of infant brains spanning the 0-2 year age range. *Front. Hum. Neurosci.* 9:21. doi: 10.3389/fnhum.2015.00021

Dean, D. C., Planalp, E. M., Wooten, W., Schmidt, C. K., Kecskemeti, S. R., Frye, C., et al. (2018). Investigation of brain structure in the 1-month infant. *Brain Struct. Funct.* 223, 1953–1970. doi: 10.1007/s00429-017-1600-2

Devi, C. N., Chandrasekharan, A., Sundararaman, V. K., and Alex, Z. C. (2017). Automatic segmentation of infant brain MR images: with special reference to myelinated white matter. *Integr. Med. Res.* 37, 1–16. doi: 10.1016/j.bbe.2016.11.004

Dice, L. R. (1945). Measures of the amount of ecologic association between species. *Ecology* 26, 297–302. doi: 10.2307/1932409

Dubois, J., Dehaene-Lambertz, G., Kulikova, S., Poupon, C., Hüppi, P., and Hertz-Pannier, L. (2014). The early development of brain white matter: a review of imaging studies in fetuses, newborns and infants. *Neuroscience* 276, 48–71. doi: 10.1016/j.neuroscience.2013.12.044

Gousias, I. S., Edwards, A. D., Rutherford, M. A., Counsell, S. J., Hajnal, J. V., Rueckert, D., et al. (2012). Magnetic resonance imaging of the newborn brain: manual segmentation of labelled atlases in term-born and preterm infants. *Neuroimage* 62, 1499–1509. doi: 10.1016/j.neuroimage.2012.05.083

Guo, Y., Wu, G., Yap, P., Jewells, V., Lin, W., and Shen, D. (2015). Segmentation of infant hippocampus using common feature representations learned for multimodal longitudinal data. *Lecture Notes Comput. Sci.* 9351, 63–71. doi: 10.1007/978-3-319-24574-4_8

Hajek, T., Kopecek, M., Kozeny, J., Gunde, E., Alda, M., and Höschl, C. (2009). Amygdala volumes in mood disorders - Meta-analysis of magnetic resonance volumetry studies. *J. Affect. Disord.* 115, 395–410. doi: 10.1016/j.jad.2008.10.007

Hanson, J. L., Suh, J. W., Nacewicz, B. M., Sutterer, M. J., Cayo, A. A., Stodola, D. E., et al. (2012). Robust automated amygdala segmentation via multi-atlas diffeomorphic registration. *Front. Neurosci.* 6:166. doi: 10.3389/fnins.2012.00166

Hill, J., Dierker, D., Neil, J., Inder, T., Knutsen, A., Harwell, J., et al. (2010). A surface-based analysis of hemispheric asymmetries and folding of cerebral cortex in term-born human infants. *J. Neurosci.* 30, 2268–2276. doi: 10.1523/JNEUROSCI.4682-09.2010

Holland, D., Chang, L., Ernst, T. M., Curran, M., Buchthal, S. D., Alicata, D., et al. (2014). Structural growth trajectories and rates of change in the first 3 months of infant brain development. *JAMA Neurol.* 71, 1266–1274. doi: 10.1001/jamaneurol.2014.1638

Išgum, I., Benders, M. J. N. L., Avants, B., Cardoso, M. J., Counsell, S. J., Gomez, E. F., et al. (2015). Evaluation of automatic neonatal brain segmentation algorithms: the NeoBrainS12 challenge. *Med. Image Anal.* 20, 135–151. doi: 10.1016/j.media.2014.11.001

Jernigan, T. L., Baaré, W. F., Stiles, J., and Madsen, K. S. (2011). Postnatal brain development: structural imaging of dynamic neurodevelopmental processes. *Prog. Brain Res.* 189, 77–92. doi: 10.1016/B978-0-444-53884-0.00019-1

Kempton, M. J., Underwood, T. S. A., Brunton, S., Stylios, F., Ettinger, U., Smith, M. S., et al. (2013). A comprehensive testing protocol for MRI neuroanatomical segmentation techniques: evaluation of a novel lateral ventricle segmentation method. *Neuroimage* 58, 1051–1059. doi: 10.1016/j.neuroimage.2011.06.080

Koo, T. K., and Li, M. Y. (2016). A guideline of selecting and reporting intraclass correlation coefficients for reliability research. *J. Chiropr. Med.* 15, 155–163. doi: 10.1016/j.jcm.2016.02.012

Lehtola, S., Tuulari, J., Karlsson, L., Parkkola, R., Merisaari, H., Saunavaara, J., et al. (2018). Associations of age and sex with brain volumes and asymmetry in 2–5-week-old infants. *Brain Struct. Funct.* 224, 501–513. doi: 10.1007/s00429-018-1787-x

Makropoulos, A., Robinson, E., Schuh, A., Wright, R., Fitzgibbon, S., Bozek, J., et al. (2018). The developing human connectome project: a minimal processing pipeline for neonatal cortical surface reconstruction. *Neuroimage* 173, 88–112. doi: 10.1016/j.neuroimage.2018.01.054

Moore, M., Hu, Y., Woo, S., O'Hearn, D., Iordan, A. D., Dolcos, S., et al. (2014). A comprehensive protocol for manual segmentation of the medial temporal lobe structures. *J. Vis. Exp.* 89, 1–8. doi: 10.3791/50991

Morey, R. A., Petty, C. M., Xu, Y., Hayes, J. P., Wagner, H. R. II, Lewis, D. V., et al. (2009). 'A comparison of automated segmentation and manual tracing for quantifying hippocampal and amygdala volumes'. *Neuroimage* 49, 1841–1850. doi: 10.1016/j.jacc.2007.01.076

Paus, T., Collins, D., Evans, A., Leonard, G., Pike, B., and Zijdenbos, A. (2001). Maturation of white matter in the human brain: a review of magnetic resonance studies. *Brain Res. Bull.* 54, 255–266. doi: 10.1016/s0361-9230(00)00434-2

Prastawa, M., Gilmore, J. H., Lin, W., and Gerig, G. (2005). Automatic segmentation of MR images of the developing newborn brain. *Med. Image Anal.* 9, 457–466. doi: 10.1016/j.media.2005.05.007

Pruessner, J. C., Li, L. M., Serles, W., Pruessner, M., Collins, D. L., Kabani, N., et al. (2000). Volumetry of hippocampus and amygdala with high-resolution MRI and three-dimensional analysis software: minimizing the discrepancies between laboratories. *Cereb. Cortex* 10, 433–442. doi: 10.1093/cercor/10.4.433

Schoemaker, D., Buss, C., Head, K., Sandman, C. A., Davis, E. P., Chakravarty, M. M., et al. (2016). Hippocampus and amygdala volumes from magnetic resonance images in children: assessing accuracy of FreeSurfer and FSL against manual segmentation. *Neuroimage* 129, 1–14. doi: 10.1016/j.neuroimage.2016.01.038

Shi, F., Fan, Y., Tang, S., Gilmore, J., Lin, W., and Shen, D. (2010). Neonatal brain image segmentation in longitudinal MRI studies. *Neuroimage* 49, 391–400. doi: 10.1016/j.neuroimage.2009.07.066

Shi, F., Yap, P., Wu, G., Jia, H., Gilmore, J., Lin, W., et al. (2011). Infant brain atlases from Neonates to 1- and 2-Year-Olds. *PLoS One* 6:e18746. doi: 10.1371/journal.pone.0018746

Shrout, P., and Fleiss, J. (1979). Intraclass correlations: uses in assessing rater reliability. *Psychol. Bull.* 86, 420–428. doi: 10.1037//0033-2909.86.2.420

Solano-Castiella, E., Anwander, A., Lohmann, G., Weiss, M., Docherty, C., Geyer, S., et al. (2010). Diffusion tensor imaging segments the human amygdala in vivo. *Neuroimage* 49, 2958–2965. doi: 10.1016/j.neuroimage.2009.11.027

Thompson, D. K., Adamson, C., Roberts, G., Faggian, N., Wood, S. J., Warfield, S. K., et al. (2013). Hippocampal shape variations at term equivalent age in very preterm infants compared with term controls: perinatal predictors and functional significance at age 7. *Neuroimage* 70, 278–287. doi: 10.1016/j.neuroimage.2012.12.053

Tuulari, J. J., Scheinin, N. M., Lehtola, S., Merisaari, H., Saunavaara, J., Parkkola, R., et al. (2017). Neural correlates of gentle skin stroking in early infancy. *Dev. Cogn. Neurosci.* 35, 36–41. doi: 10.1016/j.dcn.2017.10.004

Uematsu, A., Matsui, M., Tanaka, C., Takahashi, T., Noguchi, K., Suzuki, M., et al. (2012). Developmental trajectories of amygdala and hippocampus from infancy to early adulthood in healthy individuals. *PLoS One* 7:e46970. doi: 10.1371/journal.pone.0046970

Wang, L., Shi, F., Lin, W., Gilmore, J., and Shen, D. (2011). Automatic segmentation of neonatal images using convex optimization and coupled level sets. *Neuroimage* 58, 805–817. doi: 10.1016/j.neuroimage.2011.06.064

Wang, L., Shi, F., Yap, P. T., Gilmore, J. H., Lin, W., and Shen, D. (2012). 4D multi-modality tissue segmentation of serial infant images. *PLoS One* 7:e44596. doi: 10.1371/journal.pone.0044596

Weisenfeld, N. I., Mewes, A. U. J., and Warfield, S. K. (2006). "Highly accurate segmentation of brain tissue and subcortical gray matter from newborn MRI," in *Medical Image Computing and Computer-Assisted Intervention – MICCAI 2006. MICCAI 2006. Lecture Notes in Computer Science*, Vol. 9, eds R. Larsen, M. Nielsen, and J. Sporring, (Heidelberg: Springer), 199–206. doi: 10.1007/11866565_25

Wenger, E., Mårtensson, J., Noack, H., Bodammer, N. C., Kühn, S., Schaefer, S., et al. (2014). Comparing manual and automatic segmentation of hippocampal volumes: reliability and validity issues in younger and older brains. *Hum. Brain Mapp.* 35, 4236–4248. doi: 10.1002/hbm.22473

Zeidman, P., and Maguire, E. A. (2016). Anterior hippocampus: the anatomy of perception, imagination and episodic memory. *Nat. Rev. Neurosci.* 17, 173–182. doi: 10.1038/nrn.2015.24

Zhu, H., Shi, F., Wang, L., Hung, S., Chen, M., Wang, S., et al. (2019). Dilated dense U-Net for infant hippocampus subfield segmentation. *Front. Neuroinform.* 13:30. doi: 10.3389/fninf.2019.00030

Conflict of Interest: The authors declare that the research was conducted in the absence of any commercial or financial relationships that could be construed as a potential conflict of interest.

Copyright © 2019 Hashempour, Tuulari, Merisaari, Lidauer, Luukkonen, Saunavaara, Parkkola, Lähdesmäki, Lehtola, Keskinen, Lewis, Scheinin, Karlsson and Karlsson. This is an open-access article distributed under the terms of the Creative Commons Attribution License (CC BY). The use, distribution or reproduction in other forums is permitted, provided the original author(s) and the copyright owner(s) are credited and that the original publication in this journal is cited, in accordance with accepted academic practice. No use, distribution or reproduction is permitted which does not comply with these terms.

frontiers in Neuroscience

PERSPECTIVE
published: 04 October 2019
doi: 10.3389/fnins.2019.01024

White Matter fMRI Activation Cannot Be Treated as a Nuisance Regressor: Overcoming a Historical Blind Spot

Lukas A. Grajauskas[1,2,3], *Tory Frizzell*[3,4], *Xiaowei Song*[1,3] *and Ryan C. N. D'Arcy*[1,3,4,5]*

[1] Department of Biomedical Physiology and Kinesiology, Simon Fraser University, Burnaby, BC, Canada, [2] Cumming School of Medicine, University of Calgary, Calgary, AB, Canada, [3] ImageTech Lab, Surrey Memorial Hospital, Fraser Health, Surrey, BC, Canada, [4] Faculty of Applied Sciences, Simon Fraser University, Burnaby, BC, Canada, [5] Djavad Mowafaghian Centre for Brain Health, University of British Columbia, Vancouver, BC, Canada

Despite past controversies, increasing evidence has led to acceptance that white matter activity is detectable using functional magnetic resonance imaging (fMRI). In spite of this, advanced analytic methods continue to be published that reinforce a historic bias against white matter activation by using it as a nuisance regressor. It is important that contemporary analyses overcome this blind spot in whole brain functional imaging, both to ensure that newly developed noise regression techniques are accurate, and to ensure that white matter, a vital and understudied part of the brain, is not ignored in functional neuroimaging studies.

Keywords: white matter, BOLD, fMRI, motion regression, fMRI analysis

OPEN ACCESS

Edited by:
Hanzhang Lu,
Johns Hopkins University,
United States

Reviewed by:
Domenico Zaca,
Siemens, Italy
Baxter P. Rogers,
Vanderbilt University, United States

***Correspondence:**
Ryan C. N. D'Arcy
rdarcy@sfu.ca;
ryan_darcy@sfu.ca

Specialty section:
This article was submitted to Brain Imaging Methods, a section of the journal Frontiers in Neuroscience

Received: *12 June 2019*
Accepted: *09 September 2019*
Published: *04 October 2019*

Citation:
Grajauskas LA, Frizzell T, Song X and D'Arcy RCN (2019) White Matter fMRI Activation Cannot Be Treated as a Nuisance Regressor: Overcoming a Historical Blind Spot. Front. Neurosci. 13:1024. doi: 10.3389/fnins.2019.01024

INTRODUCTION

White matter is a vital part of the human brain, but in functional magnetic resonance imaging (fMRI), it remains largely overlooked and misunderstood. More than 15 years of evidence has shown that neural activation occurring in white matter can be detected using blood-oxygenation level dependent (BOLD) fMRI, and the existing literature has been well reviewed by Gawryluk et al. (2014b) and Gore et al. (2019). Despite this, white matter activation in fMRI is largely underrepresented and a great deal of research even ignores this evidence entirely and treats white matter in an inappropriate manner. Operating on the outdated assumption that white matter BOLD signal has no physiological component, many researchers have used the signal from white matter as a "nuisance regressor" to remove noise from fMRI signals. The evidence showing that physiological signals are present means the use of this technique is incorrect, however, these approaches continue to be employed (e.g., Jo et al., 2013; Power et al., 2014; Ciric et al., 2017). Several recent papers that used white matter as a nuisance regressor even cited literature supporting the existence of physiological signals in white matter, but then proceeded regardless of this evidence, offering little in the form of counterargument. For example, Bartoň et al. (2019) acknowledged the existence of fMRI detectable white matter activation, but then continued to use white matter signals as a nuisance regressor, with no justification or rationale. Similarly, Yang et al. (2019) acknowledged some of the white matter activation literature, but then also disregarded it, citing the "lack of neurons in white matter," a statement that is clearly anatomically incorrect (Kukley et al., 2007; García-Marín et al., 2010). These examples and others like them underscore the blind spot that has been carried into even the most contemporary fMRI research. The field needs to update its understanding and give appropriate credence to the evidence for detectable white matter BOLD signals in fMRI.

PHYSIOLOGICAL PRECEDENT

The belief that white matter activation cannot be detected has become engrained in field of fMRI research, but this idea is not based on fundamental physiological principles. Instead, researchers have come to this belief simply because of a lack of reports in the literature. However, this absence may have simply stemmed from the difficulty of detecting the lower magnitude white matter BOLD signals on early 1.5T scanners, as field strength has been shown to play a large role in the detection of white matter activity (Mazerolle et al., 2013; Gawryluk et al., 2014b). Despite this, there is physiological evidence that suggests a BOLD response can be detected in white matter, albeit one that is smaller and harder to detect. While our traditional understanding is that the BOLD response is primarily driven by the high energy demands of synaptic transmission, there is evidence that action potentials alone could drive a BOLD response. Histology indicates there is vasculature in white matter (Lierse and Horstmann, 1965; Duvernoy et al., 1981), and that this vasculature stems largely from the medullary artery which has no vascular interaction with cortical tissue (Nonaka et al., 2003; Akashi et al., 2017), meaning the energy demands of gray matter will not influence its oxygenation. The axons in white matter have been shown to be metabolically active (Takii et al., 2003), containing mitochondria all along their length (Misgeld et al., 2007), which require oxygen to produce ATP for cellular processes such as the re-establishment of ionic gradients after the transmission of action potentials. Oxygen uptake in isolated axons has been shown to be modified by changes in Na-/K+ pump activity (Hargittai et al., 1987), and oxygen demand increases in axons undergoing repeated action potentials (Ritchie, 1967). Furthermore, a linkage between active axons and glia has been shown (Hargittai and Lieberman, 1991), where glia will activate potassium pumps to help restore ionic balance during an action potential (Petzold and Murthy, 2011) and therefore require oxygen in a task dependent manner. Overall, the evidence to support task dependent hemodynamic changes in white matter coupled with accumulating evidence from imaging should cause researchers to rethink their assumptions about white matter fMRI.

REPORTS OF fMRI ACTIVATION IN WHITE MATTER

Alongside this physiological precedent, more than 15 years of fMRI evidence has been published to support the existence of a detectable white matter BOLD signal, across a range of different tasks. One of the most robust methods for detection of white matter BOLD is using an "interhemispheric transfer task" to drive communication between hemispheres. This has consistently elicited detectible activation in the corpus callosum (Tettamanti et al., 2002; Omura et al., 2004; Weber et al., 2005; D'Arcy et al., 2006; Mazerolle et al., 2008; Gawryluk et al., 2009, 2011a). Mazerolle et al. (2010) further combined DTI with white matter BOLD to show that activated areas in the corpus callosum were structurally connected to the cortical areas activated by the interhemispheric transfer task. Fabri et al. (2011) also showed distinct patterns of activation in the corpus callosum for tactile, gustatory, visual, and motor tasks. Activation has also been shown in the corticospinal tract during swallowing (Mosier et al., 1999) and during a finger tapping task (Gawryluk et al., 2011b; Mazerolle et al., 2013), in the optic radiations during a visual task (Brandt et al., 2000), and in the internal capsule during a symbol digit modalities test (Gawryluk et al., 2014a). Weis et al. (2011) also found white matter activation during a memory task in both healthy controls and Alzheimer's patients. White matter activation has also been studied in resting state MRI, for example Ding et al. (2013) showed that functional connectivity within white matter tracts in the corpus callosum and optic radiations was greater within the tract than when compared with other voxels matched in distance from the seed. Ding et al. (2018) also used resting state MRI to show that there was connectivity between cortical regions and specific white matter tracts. This group was also able to create "functional connectivity tensors" similar to diffusion tensors by assessing the degree of signal correlation between a voxel and its adjacent neighbors, and representing the directionality of this correlation as a tensor (Ding et al., 2016). These functional correlation tensors present an interesting new methodology for investigating white matter activity and connectivity within the brain. Overall, these studies have taken great care to rule out partial volume effects (Gawryluk et al., 2014b), and the correspondence between the nature of the task and the white matter tract activated gives credence to the idea that this represents real activation, not simply artifact.

To add to this, recently published work has also made it clear that white matter has a different hemodynamic profile than the models that have been traditionally used in gray matter. A recent paper focused on characterizing the hemodynamic response function (HRF) at different depths of white matter was published in Nature Communications (Li et al., 2019), showing that the HRFs differed significantly from gray matter, and even varied within the white matter based on the depth of the tract. Importantly, the authors confirmed prior work by Courtemanche et al. (2018) which evaluated the differences between gray matter and white matter HRFs. The differences in HRFs between gray matter and white matter also may have contributed to the lack of reports of white matter BOLD activation, as analysis techniques using the traditional gray matter HRF would not effectively capture the hemodynamic profile of white matter, further perpetuating the blind spot surrounding white matter BOLD. A number of new MRI techniques are promising for the detection of white matter BOLD, but at the very least, researchers should make use of a white matter specific HFR.

NEW TOOLS FOR BETTER DETECTION OF WHITE MATTER BOLD fMRI

The increasing evidence and acceptance surrounding white matter BOLD fMRI is well timed, as a number of technological advances allow for the better detection of white matter activation. Increases in spatial resolution will allow for the isolation of signals coming from small white matter tracts,

and increases in temporal resolution will allow for better modeling of white matter hemodynamic responses and better characterization of resting state correlations. The increasing accessibility of ultra-high field scanners (7T and above) will allow for investigations with high spatial resolution, as well as improved signal- and contrast- to-noise ratios, allowing for enhanced detection and characterization of white matter signals. Multiband excitation, a technique which optimizes tradeoffs related to spatial resolution in shorter time limits, is more available (Poser and Setsompop, 2018), and high-density channel coils have also become more common, further increasing spatial and temporal resolution through parallel imaging (Hardy et al., 2008). Additionally, new developments in other neuroimaging modalities such as magnetoencephalography will allow for multi-modal investigations of white matter function (Papadelis et al., 2012; Yoshida et al., 2017). All of these techniques are already challenging previously established limits in functional neuroimaging (Feinberg and Setsompop, 2013; Petridou et al., 2013), and will have a particularly large impact on the characterization of white matter signals.

DISCUSSION

White matter represents a major component of functional neural tissue and plays a critical role in neural networks. Despite this, white matter activation has become a blind spot in fMRI research. Because it could not be easily detected in the early development stages of fMRI, an assumption developed that white matter activation did not exist or was not detectable. This assumption led to a self-fulfilling prophecy as analysis methods were designed to prioritize the detection of gray matter activation. Given the state of the field and the clear evidence of white matter activation, these assumptions need to be revisited otherwise the researchers will continue to proceed with a blind spot that encompasses approximately 50% of the functional neural tissue in the brain. At a minimum, fMRI analysis methodology is best to restrict the choice of nuisance regressors to non-neural tissue, such as CSF. While this paper offers a caution, it also has a more exciting perspective. Accepting the existence of detectable white matter activation opens up a host of new research questions, such as altered white matter function in injury or disease states, direct measures of functional connectivity in neural networks, and neuroplasticity changes at the network level. With increasing temporal and spatial resolution in modern MRIs, expanding our research field to include white matter activation has become readily accessible. All it will take to open up an exciting new chapter in fMRI research is for scientists to move past this outdated blind spot, and begin answering new questions using white matter BOLD fMRI.

AUTHOR CONTRIBUTIONS

LG contributed as primary author. TF assisted in writing the manuscript. XS and RD'A assisted in editing the manuscript and acted as lab PI.

FUNDING

This study received support from the Natural Sciences and Engineering Research Council Discovery Grant #206875.

REFERENCES

Akashi, T., Takahashi, S., Mugikura, S., Sato, S., Murata, T., Umetsu, A., et al. (2017). Ischemic white matter lesions associated with medullary arteries: classification of MRI findings based on the anatomic arterial distributions. *Am. J. Roentgenol.* 209, W160–W168. doi: 10.2214/AJR.16.17231

Bartoň, M., Mareček, R., Krajčovičová, L., Slavíček, T., Kašpárek, T., Zemánková, P., et al. (2019). Evaluation of different cerebrospinal fluid and white matter fMRI filtering strategies-quantifying noise removal and neural signal preservation. *Hum. Brain Mapp.* 40, 1114–1138. doi: 10.1002/hbm.24433

Brandt, T., Stephan, T., Bense, S., Yousry, T. A., and Dieterich, M. (2000). Hemifield visual motion stimulation: an example of intrehemispheric crosstalk. *NeuroReport* 11, 2803–2809. doi: 10.1097/00001756-200008210-00039

Ciric, R., Wolf, D. H., Power, J. D., Roalf, D. R., Baum, G. L., Ruparel, K., et al. (2017). Benchmarking of participant-level confound regression strategies for the control of motion artifact in studies of functional connectivity. *Neuroimage* 154, 174–187. doi: 10.1016/j.neuroimage.2017.03.020

Courtemanche, M. J., Sparrey, C. J., Song, X., MacKay, A., and D'Arcy, R. C. N. (2018). Detecting white matter activity using conventional 3 Tesla fMRI: an evaluation of standard field strength and hemodynamic response function. *NeuroImage* 169, 145–150. doi: 10.1016/j.neuroimage.2017.12.008

D'Arcy, R. C. N., Hamilton, A., Jarmasz, M., Sullivan, S., and Stroink, G. (2006). Exploratory data analysis reveals visuovisual interhemispheric transfer in functional magnetic resonance imaging. *Magn. Reson. Med.* 55, 952–958. doi: 10.1002/mrm.20839

Ding, Z., Huang, Y., Bailey, S. K., Gao, Y., Cutting, L. E., Rogers, B. P., et al. (2018). Detection of synchronous brain activity in white matter tracts at rest and under functional loading. *Proc. Nat. Acad. Sci. U.S.A.* 115, 595–600. doi: 10.1073/pnas.1711567115

Ding, Z., Newton, A. T., Xu, R., Anderson, A. W., Morgan, V. L., and Gore, J. C. (2013). Spatio-Temporal correlation tensors reveal functional structure in human brain. *PLoS One* 8:e82107. doi: 10.1371/journal.pone.0082107

Ding, Z., Xu, R., Bailey, S. K., Wu, T., Morgan, V. L., Cutting, L. E., et al. (2016). Visualizing functional pathways in the human brain using correlation tensors and magnetic resonance imaging. *Magn. Reson. Imag.* 34, 8–17. doi: 10.1016/j.mri.2015.10.003

Duvernoy, H. M., Delon, S., and Vannson, J. L. (1981). Cortical blood vessels of the human brain. *Brain Res. Bull.* 7, 519–579. doi: 10.1016/0361-9230(81)90007-1

Fabri, M., Polonara, G., Mascioli, G., Salvolini, U., and Manzoni, T. (2011). Topographical organization of human corpus callosum: an fMRI mapping study. *Brain Res.* 1370, 99–111. doi: 10.1016/j.brainres.2010.11.039

Feinberg, D. A., and Setsompop, K. (2013). Ultra-fast MRI of the human brain with simultaneous multi-slice imaging. *J. Magn. Reson.* 229, 90–100. doi: 10.1016/j.jmr.2013.02.002

García-Marín, V., Blazquez-Llorca, L., Rodriguez, J. R., Gonzalez-Soriano, J., and DeFelipe, J. (2010). Differential distribution of neurons in the gyral white matter of the human cerebral cortex. *J. Comp. Neurol.* 518, 4740–4759. doi: 10.1002/cne.22485

Gawryluk, J. R., Brewer, K. D., Beyea, S. D., and D'Arcy, R. C. N. (2009). Optimizing the detection of white matter fMRI using asymmetric spin echo spiral. *NeuroImage* 45, 83–88. doi: 10.1016/j.neuroimage.2008.11.005

Gawryluk, J. R., D'Arcy, R. C. N., Mazerolle, E. L., Brewer, K. D., and Beyea, S. D. (2011a). Functional mapping in the corpus callosum: a 4T fMRI study of white matter. *NeuroImage* 54, 10–15. doi: 10.1016/j.neuroimage.2010.07.028

Gawryluk, J. R., Mazerolle, E. L., Brewer, K. D., Beyea, S. D., and D'Arcy, R. C. N. (2011b). Investigation of fMRI activation in the internal capsule. *BMC Neurosci.* 12:56. doi: 10.1186/1471-2202-12-56

Gawryluk, J. R., Mazerolle, E. L., Beyea, S. D., and D 'Arcy, R. C. N. (2014a). Functional MRI activation in white matter during the symbol digit modalities test. *Fron. Hum. Neurosci.* 8:589. doi: 10.3389/fnhum.2014.00589

Gawryluk, J. R., Mazerolle, E. L., and D'Arcy, R. C. N. (2014b). Does functional MRI detect activation in white matter? a review of emerging evidence, issues, and future directions. *Front. Neurosci.* 8:239. doi: 10.3389/fnins.2014.00239

Gore, J. C., Li, M., Gao, Y., Wu, T., Schilling, K. G., Huang, Y., et al. (2019). Functional MRI and resting state connectivity in white matter - a mini- review. *Magn. Reson. Imag.* 63, 1–11. doi: 10.1016/j.mri.2019.07.017

Hardy, C. J., Giaquinto, R. O., Piel, J. E., Rohling, K. W., Marinelli, L., Blezek, D. J., et al. (2008). 128-channel body MRI with a flexible high-density receiver-coil array. *J. Magn. Reson. Imag.* 28, 1219–1225. doi: 10.1002/jmri.21463

Hargittai, , P. T., and Lieberman, E. M. (1991). Axon-glia interactions in the crayfish: glial cell oxygen consumption is tightly coupled to axon metabolism. *Glia* 4, 417–423. doi: 10.1002/glia.440040410

Hargittai, P. T., Ginty, D. D., and Lieberman, E. M. (1987). A pyrene fluorescence technique and microchamber for measurement of oxygen consumption of single isolated axons. *Anal. Biochem.* 163, 418–426. doi: 10.1016/0003-2697(87)90243-0

Jo, H. J., Gotts, S. J., Reynolds, R. C., Bandettini, P. A., Martin, A., Cox, R. W., et al. (2013). Effective preprocessing procedures virtually eliminate distance-dependent motion artifacts in resting state FMRI. *J. Appl. Math.* 2013:9. doi: 10.1155/2013/935154

Kukley, M., Capetillo-Zarate, E., and Dietrich, D. (2007). Vesicular glutamate release from axons in white matter. *Nat. Neurosci.* 10:311. doi: 10.1038/nn1850

Li, M., Newton, A. T., Anderson, A. W., Ding, Z., and Gore, J. C. (2019). Characterization of the hemodynamic response function in white matter tracts for event-related fMRI. *Nat. Commun.* 10, 1–11. doi: 10.1038/s41467-019-09076-2

Lierse, W., and Horstmann, E. (1965). Quantitative anatomy of the cerebral vascular bed with especial emphasis on homogeneity and inhomogeneity in small parts of the gray and white matter. *Acta Neurol. Scand.* 41, 15–19. doi: 10.1111/j.1600-0404.1965.tb01946.x

Mazerolle, E. L., Beyea, S. D., Gawryluk, J. R., Brewer, K. D., Bowen, C. V., and D'Arcy, R. C. N. (2010). Confirming white matter fMRI activation in the corpus callosum: co-localization with DTI tractography. *NeuroImage* 50, 616–621. doi: 10.1016/j.neuroimage.2009.12.102

Mazerolle, E. L., D'Arcy, R. C., and Beyea, S. D. (2008). Detecting functional magnetic resonance imaging activation in white matter: interhemispheric transfer across the corpus callosum. *BMC Neurosci.* 9:84. doi: 10.1186/1471-2202-9-84

Mazerolle, E. L., Gawryluk, J. R., Dillen, K. N. H., Patterson, S. A., Feindel, K. W., Beyea, S. D., et al. (2013). Sensitivity to white matter fMRI activation increases with field strength. *PLoS One* 8:e58130. doi: 10.1371/journal.pone.0058130

Misgeld, T., Kerschensteiner, M., Bareyre, F. M., Burgess, R. W., and Lichtman, J. W. (2007). Imaging axonal transport of mitochondria *in vivo*. *Nat. Methods* 4, 559–561. doi: 10.1038/nmeth1055

Mosier, K. M., Liu, W. C., Maldjian, J. A., Shah, R., and Modi, B. (1999). Lateralization of cortical function in swallowing: a functional MR imaging study. *Am. J. Neuroradiol.* 20, 1520–1526.

Nonaka, H., Akima, M., Hatori, T., Nagayama, T., Zhang, Z., and Ihara, F. (2003). Microvasculature of the human cerebral white matter: arteries of the deep white matter. *Neuropathology* 23, 111–118. doi: 10.1046/j.1440-1789.2003.00486.x

Omura, K., Tsukamoto, T., Kotani, Y., Ohgami, Y., Minami, M., and Inoue, Y. (2004). Different mechanisms involved in interhemispheric transfer of visuomotor information. *Neuroreport* 15, 2707–2711.

Papadelis, C., Leonardelli, E., Staudt, M., and Braun, C. (2012). Can magnetoencephalography track the afferent information flow along white matter thalamo-cortical fibers? *Neuroimage* 60, 1092–1105. doi: 10.1016/j.neuroimage.2012.01.054

Petridou, N., Italiaander, M., van de Bank, B. L., Siero, J. C. W., Luijten, P. R., and Klomp, D. W. J. (2013). Pushing the limits of high-resolution functional MRI using a simple high-density multi-element coil design. *NMR Biomed.* 26, 65–73. doi: 10.1002/nbm.2820

Petzold, G. C., and Murthy, V. N. (2011). Role of astrocytes in neurovascular coupling. *Neuron* 71, 782–797. doi: 10.1016/j.neuron.2011.08.009

Poser, B. A., and Setsompop, K. (2018). Pulse sequences and parallel imaging for high spatiotemporal resolution MRI at ultra-high field. *NeuroImage* 168, 101–118. doi: 10.1016/j.neuroimage.2017.04.006

Power, J. D., Mitra, A., Laumann, T. O., Snyder, A. Z., Schlaggar, B. L., and Petersen, S. E. (2014). Methods to detect, characterize, and remove motion artifact in resting state fMRI. *Neuroimage* 84, 320–341. doi: 10.1016/j.neuroimage.2013.08.048

Ritchie, J. M. (1967). The oxygen consumption of mammalian non-myelinated nerve fibres at rest and during activity. *J. Physiol.* 188, 309–329. doi: 10.1113/jphysiol.1967.sp008141

Takii, Y., Takoh, K., Nishizawa, M., and Matsue, T. (2003). Characterization of local respiratory activity of PC12 neuronal cell by scanning electrochemical microscopy. *Electrochim. Acta* 48, 3381–3385. doi: 10.1016/S0013-4686(03)00408-0

Tettamanti, M., Paulesu, E., Scifo, P., Maravita, A., Fazio, F., Perani, D., et al. (2002). Interhemispheric transmission of visuomotor information in humans: fMRI evidence. *J. Neurophysiol.* 88, 1051–1058. doi: 10.1152/jn.2002.88.2.1051

Weber, B., Treyer, V., Oberholzer, N., Jaermann, T., Boesiger, P., Brugger, P., et al. (2005). Attention and interhemispheric transfer: a behavioral and fMRI study. *J. Cogn. Neurosci.* 17, 113–123. doi: 10.1162/0898929052880002

Weis, S., Leube, D., Erb, M., Heun, R., Grodd, W., and Kircher, T. (2011). Functional neuroanatomy of sustained memory encoding performance in healthy aging and in Alzheimer's disease. *Int. J. Neurosci.* 121, 384–392. doi: 10.3109/00207454.2011.565892

Yang, Z., Zhuang, X., Sreenivasan, K., and Mishra, V. (2019). Robust motion regression of resting-state data using a convolutional neural network model. *Front. Neurosci.* 13:169. doi: 10.3389/fnins.2019.00169

Yoshida, F., Hirata, M., Onodera, A., Goto, T., Sugata, H., and Yorifuji, S. (2017). Noninvasive spatiotemporal imaging of neural transmission in the subcortical visual pathway. *Sci. Reports* 7:4424. doi: 10.1038/s41598-017-04700-x

Conflict of Interest: The authors declare that the research was conducted in the absence of any commercial or financial relationships that could be construed as a potential conflict of interest.

Copyright © 2019 Grajauskas, Frizzell, Song and D'Arcy. This is an open-access article distributed under the terms of the Creative Commons Attribution License (CC BY). The use, distribution or reproduction in other forums is permitted, provided the original author(s) and the copyright owner(s) are credited and that the original publication in this journal is cited, in accordance with accepted academic practice. No use, distribution or reproduction is permitted which does not comply with these terms.

frontiers in Neuroscience

ORIGINAL RESEARCH
published: 24 October 2019
doi: 10.3389/fnins.2019.01128

Deep Learning-Based Deep Brain Stimulation Targeting and Clinical Applications

Seong-Cheol Park[1,2†], Joon Hyuk Cha[1,3†], Seonhwa Lee[1,4], Wooyoung Jang[5], Chong Sik Lee[6] and Jung Kyo Lee[7]*

[1] Department of Neurosurgery, Seoul Metropolitan Government – Seoul National University Boramae Medical Center, Seoul, South Korea, [2] Department of Neurosurgery, Gangneung Asan Hospital, University of Ulsan, Gangneung, South Korea, [3] School of Medicine, Inha University, Incheon, South Korea, [4] Department of Bio-Convergence Engineering, College of Health Science, Korea University, Seoul, South Korea, [5] Department of Neurology, Gangneung Asan Hospital, University of Ulsan, Gangneung, South Korea, [6] Department of Neurology, Asan Medical Center, University of Ulsan, Seoul, South Korea, [7] Department of Neurosurgery, Asan Medical Center, University of Ulsan, Seoul, South Korea

OPEN ACCESS

Edited by:
John Ashburner, University College London, United Kingdom

Reviewed by:
Dong-Hoon Lee, The University of Sydney, Australia
Francisca Ferreira, University College London, United Kingdom

****Correspondence:***
Seong-Cheol Park
pscpscp@gmail.com

† These authors have contributed equally to this work as co-first authors

Specialty section:
This article was submitted to Brain Imaging Methods, a section of the journal Frontiers in Neuroscience

Received: *27 April 2019*
Accepted: *04 October 2019*
Published: *24 October 2019*

Citation:
Park S-C, Cha JH, Lee S, Jang W, Lee CS and Lee JK (2019) Deep Learning-Based Deep Brain Stimulation Targeting and Clinical Applications. Front. Neurosci. 13:1128. doi: 10.3389/fnins.2019.01128

Background: The purpose of the present study was to evaluate deep learning-based image-guided surgical planning for deep brain stimulation (DBS). We developed deep learning semantic segmentation-based DBS targeting and prospectively applied the method clinically.

Methods: T2* fast gradient-echo images from 102 patients were used for training and validation. Manually drawn ground truth information was prepared for the subthalamic and red nuclei with an axial cut ∼4 mm below the anterior–posterior commissure line. A fully convolutional neural network (FCN-VGG-16) was used to ensure margin identification by semantic segmentation. Image contrast augmentation was performed nine times. Up to 102 original images and 918 augmented images were used for training and validation. The accuracy of semantic segmentation was measured in terms of mean accuracy and mean intersection over the union. Targets were calculated based on their relative distance from these segmented anatomical structures considering the Bejjani target.

Results: Mean accuracies and mean intersection over the union values were high: 0.904 and 0.813, respectively, for the 62 training images, and 0.911 and 0.821, respectively, for the 558 augmented training images when 360 augmented validation images were used. The Dice coefficient converted from the intersection over the union was 0.902 when 720 training and 198 validation images were used. Semantic segmentation was adaptive to high anatomical variations in size, shape, and asymmetry. For clinical application, two patients were assessed: one with essential tremor and another with bradykinesia and gait disturbance due to Parkinson's disease. Both improved without complications after surgery, and microelectrode recordings showed subthalamic nuclei signals in the latter patient.

Conclusion: The accuracy of deep learning-based semantic segmentation may surpass that of previous methods. DBS targeting and its clinical application were made possible using accurate deep learning-based semantic segmentation, which is adaptive to anatomical variations.

Keywords: deep learning, deep brain stimulation, convolutional neural network, semantic segmentation, clinical application

INTRODUCTION

Deep learning is a machine learning technique using neural networks with multiple layers that are partly similar to a biological brain (Marcus, 2018). The majority of medical deep learning analyses are performed for diagnostic purposes rather than for surgical planning (Choi and Jin, 2016; De Fauw et al., 2018; Naylor, 2018). In a recent review and study, image-guided surgery was considered as a potential application of deep learning (Mehrtash et al., 2017; Naylor, 2018). However, the clinical application of deep learning in surgical planning remains almost unexplored. In the present study, we demonstrate deep learning-based surgical planning for deep brain stimulation (DBS) and its clinical application.

Current clinical approaches to surgical planning for DBS rely on imaging interpretation and processing, including magnetic resonance imaging (MRI)-based direct targeting (Holl et al., 2010; Foltynie et al., 2011; Aviles-Olmos et al., 2014) and image fusion techniques using co-registration with computed tomography (CT) and 1.5T and 3T MRI (Neumann et al., 2015). Atlas-based coordinates can be used when visualization of targets is insufficient, or to improve accuracy (Kochunov et al., 2002). Direct targeting using deep learning-based image analysis may be possible when target visualization is achieved with sufficient resolution. Later, electrophysiologic information, including microelectrode recording and intraoperative stimulation effects, can be considered for final decisions regarding electrode positions (Hariz, 2002; Amirnovin et al., 2006; Park et al., 2017). Here, we demonstrate deep learning-based surgical planning for DB for the first time to our knowledge. We investigated DBS in the subthalamic nucleus (STN) and in the posterior subthalamic area, a closely related target (Plaha et al., 2008; Blomstedt et al., 2009, 2010). The STN is an important target for Parkinson's disease (Bejjani et al., 2000; Foltynie et al., 2011; Aviles-Olmos et al., 2014) and the posterior subthalamic area is an effective target for essential tremor (Plaha et al., 2008; Blomstedt et al., 2009, 2010).

Semantic segmentation results in pixel-wise image classification into predetermined classes, for example, anatomical structures (Mehta and Sivaswamy, 2017; Shelhamer et al., 2017). Semantic segmentation combines classification information ("what") and location information ("where") from image data (Shelhamer et al., 2017). Semantic segmentation can classify and identify the margins of multiple types of objects (Shelhamer et al., 2017). Recent convolutional neural network segmentation studies have not been optimized for the STN or red nucleus but instead for basal ganglia structures (Mehta and Sivaswamy, 2017; Milletari et al., 2017) or the striatum (Choi and Jin, 2016) only. Therefore, deep learning-based semantic segmentation of the STN and red nucleus is not well investigated. Thus, the current state-of-the-art methods for STN and red nucleus semantic segmentation are non-deep learning methods (Kim et al., 2019; Shamir et al., 2019).

Automatic targeting methods for DBS have potential clinical utility and may be non-inferior to manual methods (Pallavaram et al., 2015). However, the clinical application of automatic targeting methods is still under investigation (Pallavaram et al., 2015). In previous automatic methods, wide and robust applicability may have been limited due to the high variability of the STN anatomy (Naylor, 2018). We found that deep learning-based semantic segmentation shows highly accurate adaptability to considerable variations in STN shape, which enables real-world clinical application.

In the present study, we show the earliest cases of deep learning-based surgical planning. The results support the concept that accurate, deep learning-based semantic segmentation and surgical planning can be applied safely and successfully for DBS in clinical practice.

MATERIALS AND METHODS

Institutional Approval

This study was pre-approved by the institutional review boards of Gangneung Asan Hospital (2018-07-22) and Asan Medical Center (S2016-1230-0005). Before clinical application, all patients and families signed informed consent forms that had been approved by the institutional review boards.

Deep Learning and Imaging Methods

Training datasets were collected from patients who had undergone the DBS procedure and evaluation at Asan Medical Center between April 2014 and September 2017 (Park et al., 2017, 2018). Training and validation data were generated by using 3-Tesla (3T) T2* fast gradient-echo MRI sequences with a repetition time (TR) of 1026.3 ms, an echo time (TE) of 25 ms, and a flip angle of 30°. The field of view was anterior to posterior (AP) (mm) = 192, right to left (RL) (mm) = 192, and foot to head (FH) (mm) = 70. The voxel size was 0.375 mm, and the matrix size was 512.

Axial images from about 4 mm below the anterior–posterior commissure line and showing the mammillothalamic tract were obtained for semantic segmentation training and targeting using Leksell SurgiPlan version 9.0 (Elekta, Stockholm, Sweden) (**Figure 1A**; Bejjani et al., 2000; Starr et al., 2002; Aviles-Olmos et al., 2014; Park et al., 2017, 2018). MRI images from around

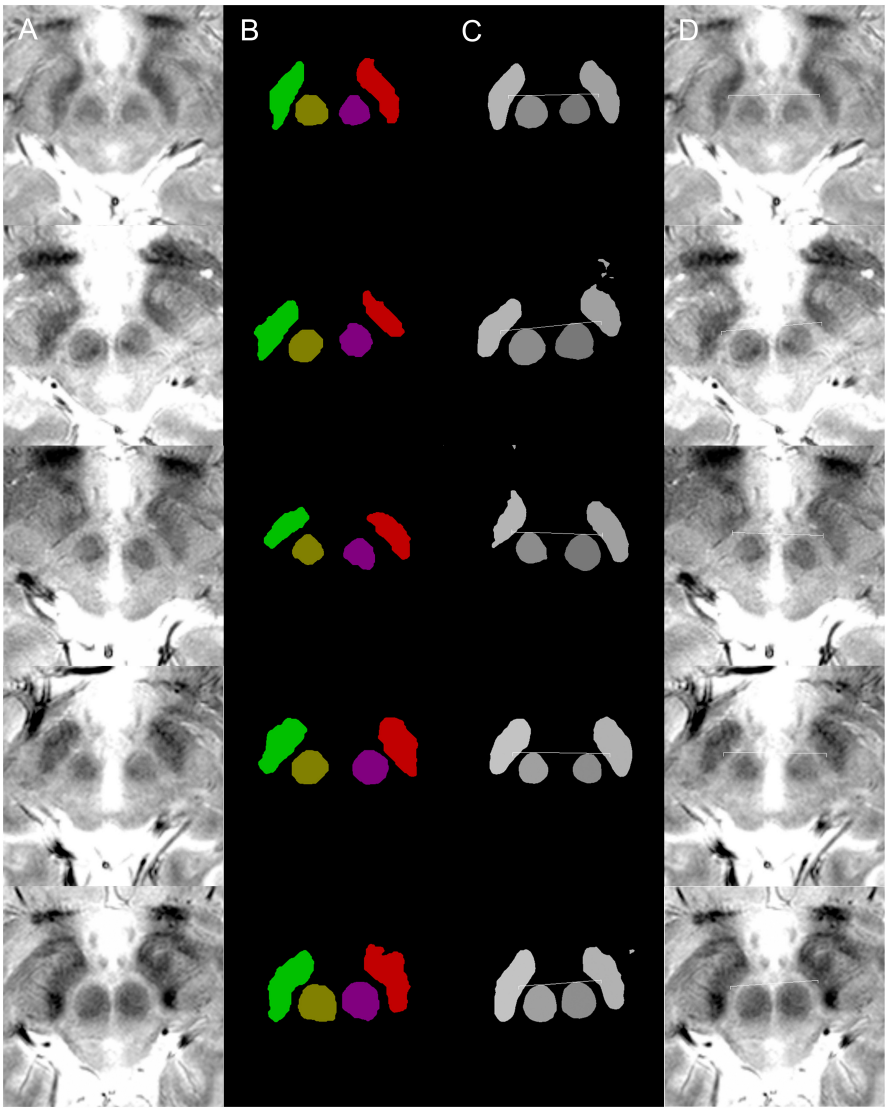

FIGURE 1 | Examples of targeting. Each row of images is from a single patient. **(A)** MRI T2* fast-acquisition gradient-echo input images. **(B)** Ground truth images of supervised semantic segmentation training or validation. **(C)** Semantic segmentation results and automatic targeting results from a deep learning network trained by 62 non-augmented images. **(D)** Automatic targeting results superimposed on the original image. The automatic targets shown in these figures are for subthalamic nucleus deep brain stimulation. Deep learning-based semantic segmentation and targeting adaptability is shown for various anatomical variations, including right and left asymmetries in the second and third rows, the large inter-red nuclei distance in the fourth row, and large red nuclei in the fifth row.

the midbrain and basal ganglia were magnified and stored in 500 × 500-pixel RGB jpg format to be processed by the Caffe deep learning tool (Shelhamer et al., 2017).

For the deep learning algorithm used, the necessity of augmentation was known to be low or non-existent when the large and variable VOC-2011-2 dataset was used (Shelhamer et al., 2017). Thus, no positional or rotational augmentation was performed. Instead, we noted that the segmentation results were susceptible to contrasts. Thus, we only performed contrast adjustments and augmentation. For optimal images, the contrast was adjusted in the surgical planning software, Leksell SurgiPlan version 9.0 (Elekta, Stockholm, Sweden), to ensure good visualization of the STN and red nucleus. Next, image brightness preprocessing and data augmentation were performed using Matlab® (Natick, MA, United States). The Matlab image processing toolbox "Imadjust" function was used, with no additional options, to produce images of improved contrast automatically by saturating the upper and lower 1% of pixels. Various image contrast adjustments were then used to augment the original data nine times. Specifically, the low-in and high-in options of the "imadjust" function were set to 0–0.2 and 0.8–1.0, respectively, without low-out or high-out options. Examples of contrast augmentation are shown in **Figure 2**. Thus, when 102 images were augmented nine times, a total of 918 images were obtained.

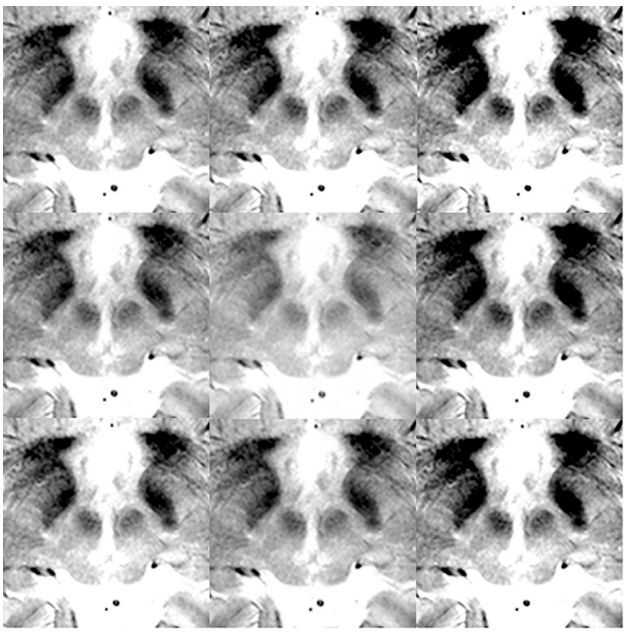

FIGURE 2 | Data augmentation examples for training and validation images.

In total, 102 matched T2* MRI images (**Figure 1A**), along with ground truth information (**Figure 1B**), were collected. The ground truth boundaries of the STN and red nucleus were drawn manually. These images were all of equal size (500 × 500 pixels) and were stored in 8-bit indexed color png file formats. Each ground truth image was matched to corresponding MRI images of the same filename and size. Four image classes were used: right STN, right red nucleus, left red nucleus, and left STN. These were filled with different colors to designate the semantic segmentation classes (**Figures 1, 3, 4**). This ground truth information was used for training, as well as for calculating the accuracy of the validation dataset.

The network used was the VGG-16-derived, semantic segmentation, fully convolutional network (FCN-VGG-16) (Shelhamer et al., 2017). This network was trained using the above-mentioned manually drawn ground truth information for the STN and red nucleus. First, we performed training using FCN-32s, a coarse semantic segmentation network that uses higher layer information, with 100,000 iterations. The FCN-32s-trained Caffe deep learning model was then retrained using 50,000 iterations of the FCN-8s, a fine semantic segmentation network (Shelhamer et al., 2017).

In the section "Results," two measures of semantic segmentation accuracy are shown: mean accuracy and mean intersection over the union (mean IoU) (Rezatofighi et al., 2019), otherwise known as the Jaccard score (Shelhamer et al., 2017). That is, the mean accuracy is the semantic segmentation accuracy as calculated by averaging the accuracy of all classes (Shelhamer et al., 2017). The mean IoU is the similarity between sample sets, defined as the size of the intersection divided by the size of the union of the sample sets (Rezatofighi et al., 2019).

When ground truth pixels are A and semantic segmentation result pixels are B, IoU was defined as follows:

$$\text{Intersection over the union (IoU)} = \frac{A \cap B}{A + B - A \cap B}$$

Thus, mean IoU is lower than mean accuracy, and it is considered more important in semantic segmentation studies (Shelhamer et al., 2017; Rezatofighi et al., 2019). For this reason, only mean IoU is shown in the graph (**Figure 4C**) and is converted to the Dice coefficient (Dice, 1945) for the purposes of comparison with the literature (Choi and Jin, 2016; Visser et al., 2016; Mehta and Sivaswamy, 2017; Milletari et al., 2017; Kim et al., 2019; **Figure 4C**). The following method was used for the conversion:

$$\text{Dice coefficient} = \frac{2A \cap B}{\text{A} + \text{B}} = \frac{\frac{2A \cap B}{A+B-A \cap B}}{\frac{A+B}{A+B-A \cap B}} = \frac{2\frac{A \cap B}{A+B-A \cap B}}{1 + \frac{A \cap B}{A+B-A \cap B}} = \frac{2IoU}{1 + IoU}$$

This conversion is exact for single-class IoU, and we performed approximate conversion for the mean IoU of four classes.

We also performed qualitative evaluations of the semantic segmentation results manually. When there was a blob or island of wrong segmentation outside of the ground truth or the segmentation territory was substantially smaller, approximately 80% less than the ground truth, we defined the semantic segmentation as being inadequate. Examples of qualitatively inadequate segmentations are shown in row B of **Figure 5** and rows B and C of **Figure 6**.

Deep Brain Stimulation Imaging Protocols for Clinical Applications

A Leksell Frame G (Elekta, Stockholm, Sweden) was fixed in parallel with the anterior-commissure and posterior commissure considering external landmarks, and imaging followed the DBS protocol (Park et al., 2017, 2018). Bilateral lines crossing the lower margin of the orbit rim and external auditory canal were used as external landmarks during frame applications to verify pitch and lateral tilt angle of frames (Starr et al., 1999). Roll and yaw of frames were maintained parallel with a midline drawn from the nasion to the apex and a horizontal line drawn 3 cm above the eyebrows. Ear bars were also used to facilitate orthogonal frame alignment.

For surgical planning and pre- and post-operative coregistrations and accuracy measurements, Medtronic Stealth Cranial version 3.0.1 was used alongside StealthMerge™ from the Stealth DBS software suite (Medtronic, Dublin, Ireland).

Three-dimensional, magnetization-prepared gradient-echo (3D-MPRAGE) sequences were obtained and used to define the anterior commissure, posterior commissure, and midline.

In both patients, we obtained 3.0-T MRI T2 images 2 mm in thickness using an Achieva 3.0-Tesla MRI Machine and software release 2.1.3.2 (Phillips Healthcare, Amsterdam, Netherlands), with a TR of 3000 ms, a TE of 80 ms, and a flip angle of 90° to determine the margins of the STN and red nucleus before surgery. The field of view was AP (mm) = 300, RL (mm) = 239, and FH (mm) = 100. The voxel size was 0.57 × 0.57 × 2 mm,

and the matrix size was 528. In Patient 1, the MRI for targeting was obtained with the stereotactic frame applied, while for Patient 2, the MRI was obtained before stereotactic frame fixation. Preoperative CT images were obtained using a LightSpeed 16-channel CT System (GE Healthcare, Little Chalfont, Buckinghamshire, United Kingdom) with a section thickness of 1.25 mm.

Magnetic resonance imaging without a metal stereotactic frame were coregistered with preoperative, frame-applied stereotactic CT images to calculate the Leksell stereotactic coordinate. Using this process, deep learning-based 3T MRI analysis targeting results could be applied to the Leksell coordinate system for DBS using the stereotactic frame.

After surgery, stereotactic CT images were obtained using the same protocol with the stereotactic frame in both patients. The post-operative stereotactic CT images were coregistered with the preoperative CT images, and the stereotactic error in comparison to preoperative deep learning-based planning was checked in the probe's eye view (Ellenbogen et al., 2018).

Deep Learning-Based Targeting

Because deep learning-based semantic segmentation of the STN could be performed at a level that was qualitatively similar to that of humans and at least quantitatively similar to inter-rater variations (Ewert et al., 2019), no further complex machine learning algorithm was required for automatic targeting. Unlike previous automatic targeting algorithms, which have tended to operate based on coregistration or an atlas (Pallavaram et al., 2015), we used the semantic segmented anterior margins of the red nuclei and the borders of the STN, as a human surgeon does (**Figure 3**; Bejjani et al., 2000).

The automatic targeting method closely mimics the Bejjani method (Bejjani et al., 2000), which is performed by human surgeons after the anatomical structure margins have been determined manually. At first, a horizontal line (C and D) crossing the anterior margins of both red nuclei is drawn (**Figure 3**). Next, the points where the horizontal line crosses the medial margins of the STN are identified (A and B). In the present study, the distance between A and B was measured and designated as C. Our target was slightly lateral and posterior to points A and B. The targets were calculated as lengths D and E from points A and B. The angle between D and E was 90°. We determined lengths D and E using relative ratios compared with length C. Considering the usual locations of the STN (Daniluk et al., 2010), length C was approximately 20 mm. For the posterior subthalamic area target in Patient 1, the ratio between C and D was 20:2, while the ratio between C and E was 20:4. For the STN target in Patient 2, the ratio between C and D was 20:2 and the ratio between C and E was 20:1. Thus, the posterior STN target (Blomstedt et al., 2009, 2010) is more posteriorly located than the STN target, which is closer to the red nuclei anterior margin line (Foltynie et al., 2011; Aviles-Olmos et al., 2014).

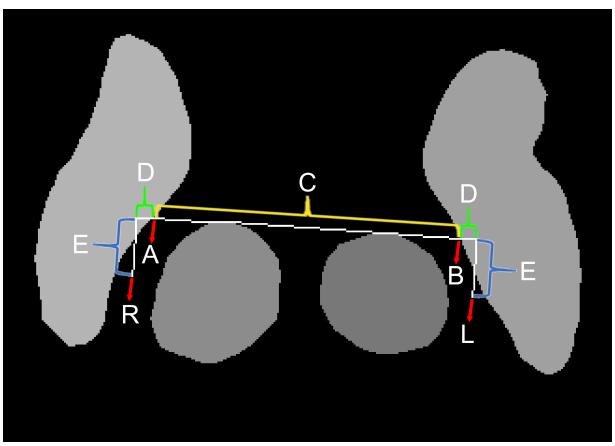

FIGURE 3 | Method for automatic targeting using the semantic segmentation margins.

Automatic targeting based on the margins of anatomical structures was performed using a custom-made Python-based program. We defined targeting success in terms of the identification of cross points (A and B in **Figure 3**) along a line crossing the anterior margins of two red nuclei (**Figure 3**) and both medial margins of the STN. In contrast, targeting failure was defined as a failure to identify these points. If semantic segmentation is performed incorrectly or if image quality is poor, the red nucleus or STN may contain anomalous shapes (**Figure 5B**). In this case, targeting failure may occur.

Indirect targets, i.e., targets determined within Talairach coordinates from anatomical markers, the anterior commissure, posterior commissure, and midline, were not used preoperatively for targeting, and only deep learning-based targeting was used (Kochunov et al., 2002). However, indirect targets have been shown for comparison (**Figures 7E, 8E**). For Patient 1, the indirect target was lateral: −12.5 mm, anterior–posterior: −6.5 mm, and vertical: −4 mm from the midcommissural point based on Talairach coordinates (**Figure 7E**). The indirect target for Patient 2 was lateral: ±12 mm, anterior–posterior: −2.5 mm, and vertical: −4.0 mm.

For clinical applications, Medtronic Stealth Cranial version 3.0.1 included in the Stealth DBS software suite (Medtronic, Dublin, Ireland) was used to capture images for targeting. Deep learning-based targeting was performed using these images. After the targets had been determined, they were overlaid onto the same pixels of the input image under maximum magnification using the surgical planning software. The Leksell coordinates of the targets were identified and calibrated, taking into account systematic stereotactic errors (Holl et al., 2010; Park et al., 2018), and numerically rounded up to the nearest 0 or 0.5.

Operation Procedures, Intraoperative Microelectrode Recordings, and Macrostimulations

Both patients were operated on under local anesthesia. C-arms were used intraoperatively to check electrode positions. For Patient 1, microelectrode recording was not performed because the posterior subthalamic area was not a target with a conspicuous microelectrode recording signal (Plaha et al., 2008;

Blomstedt et al., 2009, 2010). Thus, for Patient 1, a microdrive and Ben's gun, a microdrive component with five electrode passage holes to select the electrode track (Pollak et al., 2002), were not used. Instead, the macrostimulation effect was checked using a portable stimulator.

For Patient 2, bilateral microelectrode recordings were performed using a microTargeting^{TM} microdrive (FHC Inc., Bowdoin, ME, United States) and Ben's gun (Hariz, 2002; Amirnovin et al., 2006; Shamir et al., 2019). Two tracks of microelecrodes were used for each side. Intraoperative macrostimulation using microtargeting^{TM} microelectrodes was also performed. Stimulations were performed using 1–4 volts.

Using electrical stimulation, the effects of stimulation, including tremor, rigidity, or bradykinesia reduction were assessed by physical examination. Side effects, including eyeball deviations, dystonia, paresthesia, and speech disturbances, were checked.

Medtronic 3389 DBS electrodes (Medtronic, Dublin, Ireland) were used. For both patients, Activa SCs (Medtronic, Dublin, Ireland) were implanted posterior to the pectoralis major muscles. After implantation, the functions and resistances of the DBS systems were checked before wound closure.

RESULTS

Semantic Segmentation and Targeting Results

Semantic segmentation was able to adapt to anatomical asymmetry and individual variation (**Figure 1**). In addition, the algorithm has good regularization characteristics, and the margins of the anatomical structure were smoother (**Figure 1C**) than in the more irregular training ground truth dataset (**Figure 1B**). Non-augmented data from 62 patient images were used to produce **Figure 1**. Later, after increment and augmentation of this data, the semantic segmentation results further improved, and the minor speckles shown in **Figure 1C** disappeared.

As the iteration progressed, qualitatively ambiguous and intermixed segmentations were progressively more accurately classified, and semantic segmentation accuracy increased (**Figures 4–6**). Semantic segmentation using FCN-8s produced qualitatively smoother segmentation borders than FCN-32s (**Figures 4A,B**), as expected based on the network characteristics (Shelhamer et al., 2017). As we increased the number of training images, the semantic segmentation accuracy metrics and quality increased progressively (**Figures 4C, 5, 6**).

The mean accuracy of semantic segmentation after FCN-32s training increased, as shown in **Table 1**. The mean IoU is also shown in **Figure 4C**. In total, 918 augmented training and validation images were used.

When we converted the best 0.821 mean IoU into a Dice coefficient (Dice, 1945), the speculated approximate mean Dice coefficient was 0.902 (**Table 1**), supposing that all class accuracies were identical.

Qualitatively, when 40, 50, or 62 training images were used, 17, 28, or 3 of the 360 augmented validation images (4.7, 7.8, or 0.8%) were inadequately segmented, respectively. When 558 or 720 augmented images were used, none of the images were inadequately segmented.

Targeting failure only occurred in 1 of 17 cases when data from 50 patients were used. When training images from 62 or more patients were used, targets could be identified in all 40 of the patient validation images that were available before data augmentation (**Figure 5**). Thus, when the network was trained using the data from 62 patients, we began clinical application after manual confirmation of the deep learning-based target. The total number of patients from which the training and validation data were obtained was 102; these images were then augmented nine times to yield a dataset of 918 images (**Figures 4C, 6**).

Prospective Clinical Applications

The deep learning-based targeting and clinical applications were pre-planned before surgical application. They were then prospectively applied to surgery after manual confirmation of target applicability. Before DBS surgeries, we manually confirmed that the safety of deep learning-planned targets was acceptable for clinical applications following institutional review board-approved protocols.

Patient 1

The deep learning-based automatic targeting method for the posterior subthalamic area was first applied to a 74-year-old woman with essential tremor on May 24, 2018 (**Figure 7**).

The patient's tremor grade was III in both hands before surgery, and her score on the essential tremor rating assessment scale was 35. The deep learning Caffe model network trained using 62 patient images was used, and targeting was performed immediately before surgery after frame-fixed MRI images had been acquired.

Table 2 shows the Talairach coordinates of the deep learning-based targeting, as well as the Leksell coordinates after they were rounded up to the nearest 0.5 or whole number.

The lead implantation was performed under local anesthesia by S-CP. In particular, left unilateral posterior subthalamic DBS was performed to the deep learning-planned target position. During surgery, the patient's right hand tremor was checked; it decreased from grade II to grade I after bipolar electrical stimulation using the zero electrode as the anode and the 3rd electrode as the cathode. No hemorrhage or infection occurred.

After surgery, the patient's tremor had decreased from grade III to grade I, and her essential tremor rating assessment scale score had decreased to 20. Electrical stimulation on the 2nd electrode caused the tremor to be reduced further, and patient follow-up over 8 months was uneventful. The final optimal stimulation setting was as follows: bipolar electrode, 2–1+ with 1.5 V, 60 μs, and 130 Hz stimulation frequency.

Patient 2

This patient was a 71-year-old woman with Parkinson's disease who underwent surgery on December 4, 2018. She had been prescribed levodopa and other medications since 2004 to treat

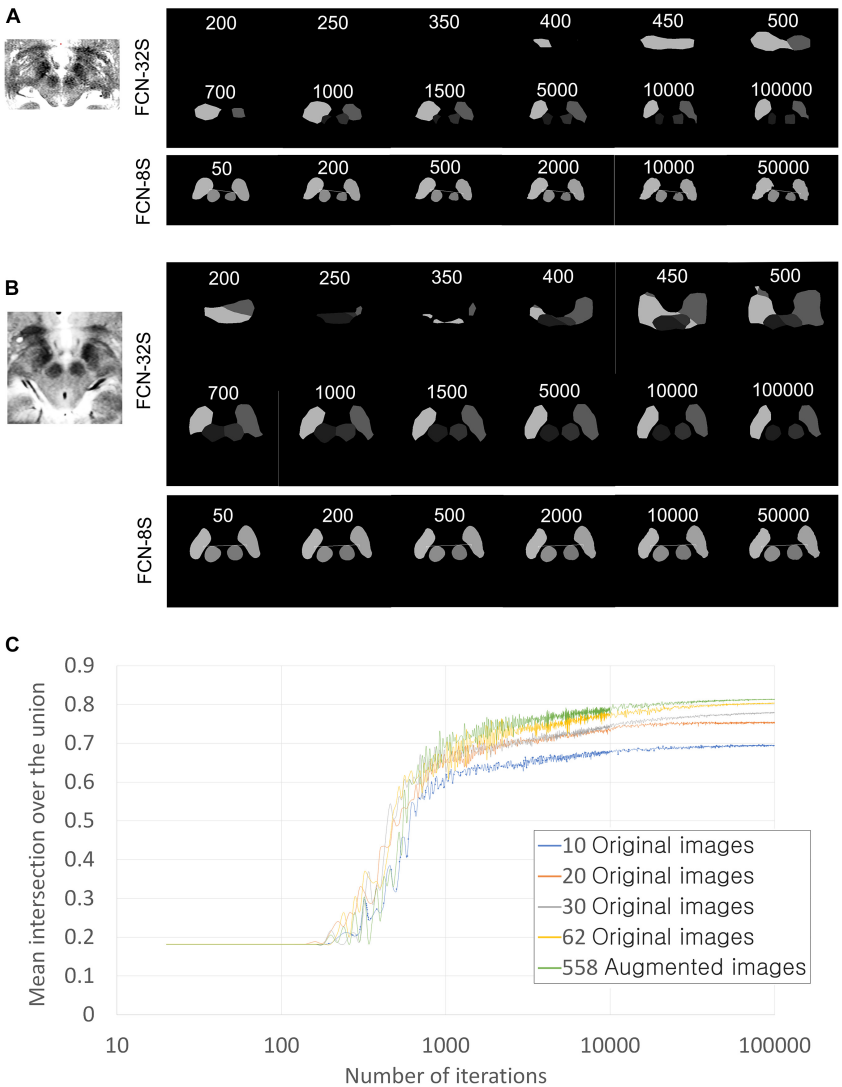

FIGURE 4 | Training progression according to training iterations and training networks. **(A)** Qualitative training progression for the MRI of Patient 1. Upper two rows: training progression images using the FCN-32s coarse segmentation network. Lowest row: training continuation using FCN-8s, which showed the fine segmentation network. Segmentation using FCN-8s has smoother and clearer margins than that using FCN-32s only. **(B)** Training progression for MRI of Patient 2. **(C)** Quantitative improvements in semantic segmentation accuracy in terms of mean intersection over the union (IoU) values according to the number of training iterations and the amount of data used. Validations were performed in 360 augmented images for all graphs. The numbers of iterations are displayed on a log scale for better visualization of improvement curves.

her motor disorder, and she underwent MRI in 2013 that showed no abnormality or severe brain atrophy. She underwent FP-CIT-PET in January 2018, which showed bilateral decreased dopamine transporter binding in the putamina and caudate nuclei, with rostrocaudal and ventrodorsal gradients. The probable clinical and FP-CIT-PET diagnosis was Parkinson's disease.

Before surgery, the patient's most severe Unified Parkinson's Disease Rating Scale (UPDRS) motor score in the "medication off" state was 37, while her score in the "medication on" state was 21. Her bilateral rigidity and tremor were minimal, but bradykinesia and gait disturbances were major symptoms.

Because our targets were selected using deep learning algorithm-based automatic targeting, manual indirect or direct targeting methods were not used. Instead, indirect targets are shown for comparison (**Figure 8E**).

The deep learning network model trained by 558 augmented images and validated using 360 augmented images was used for targeting. **Table 2** shows the deep learning-planned target coordinates and actual post-operative electrode locations.

The MRI image for targeting was obtained before stereotactic frame fixation using a 3T T2 MRI sequence 2 mm in thickness. Deep learning-based targeting was performed 1 day before the surgery.

The lead implantation was performed under local anesthesia by S-CP. The left side was operated on first. On the left side, center and medial tracks were used. Our target was

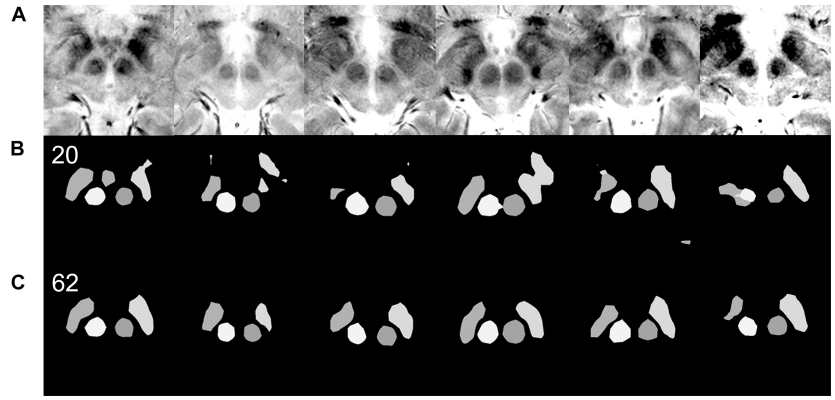

FIGURE 5 | Qualitative differences in semantic segmentation results depending on the amount of training data. Each column of images is from a single patient. Images that are inadequately segmented by the network trained with 20 original images are qualitatively well segmented by the network trained with 62 original images. **(A)** Input MRI T2* sequence images with various contrast settings. **(B)** Results of semantic segmentation by the coarse segmentation network, FCN-32s, trained with 20 images. Twenty images were not enough for qualitatively and quantitatively accurate semantic segmentation (**Figure 4C**). **(C)** Results of semantic segmentation by the coarse segmentation network, FCN-32s, trained with 62 images.

close to the medial margin of the STN, and the STN signal was only recorded in the center electrode. The length of the microelectrode passage that showed the STN signals is depicted in **Figure 8H**. The microelectrode recording showed that the STN extended from −4.5 to −1.0 mm in the left center track. The electrode was positioned in the center track, with the target at a depth of +0 mm.

On the right side, the center and lateral tracks were used, and the STN signal was recorded from −6.0 to −1.0 mm on the right center track and on the lateral track. The electrode was positioned in the center track −1 mm from the target depth. Because deep learning-based targets are located close to the center target, center-track microelectrode recordings with STN signals directly support that the deep learning-based targets were correctly located within the STN. During surgery, electrical stimulation improved the patient's bradykinesia.

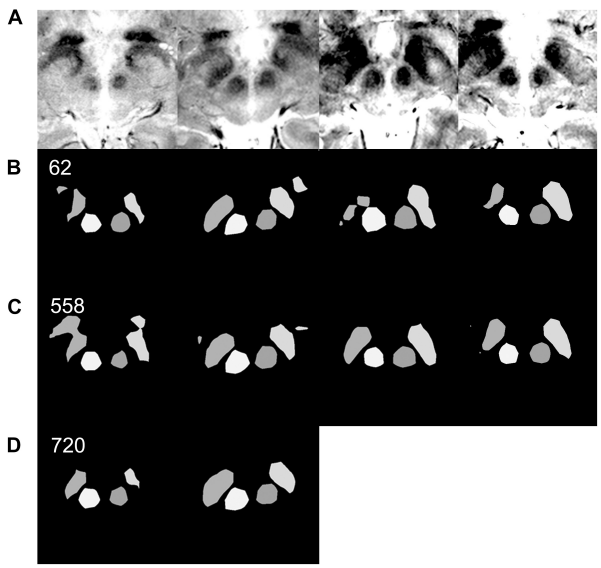

FIGURE 6 | Effect of data augmentation on semantic segmentation quality. **(A)** Input MRI T2* sequence images with various contrast settings. **(B)** Results of semantic segmentation by the coarse segmentation network, FCN-32s, trained with 62 images. Sixty-two images are sufficient to achieve qualitatively accurate semantic segmentation for most patients (**Figure 5**). However, examples of inadequate segmentation by the network trained with 62 images are shown in this row. **(C)** Results of semantic segmentation by the coarse segmentation network, FCN-32s, trained with 558 augmented images. In the right two columns, semantic segmentations are qualitatively accurate. **(D)** Results of semantic segmentation by the coarse segmentation network, FCN-32s, trained with 720 augmented images. Semantic segmentation is qualitatively improved in the left two image columns, without segmentation blobs outside of the ground truth.

TABLE 1 | Semantic segmentation accuracy improvements according to the number of training images in the validation dataset with 360 augmented images.

Number of training images	Mean accuracy	Mean intersection over the union	Approximate Dice coefficient converted from mean intersection over the union*
10 original images	0.770	0.673	0.804
20 original images	0.837	0.757	0.861
30 original images	0.876	0.778	0.875
62 original images	0.904	0.804	0.891
558 augmented images from 62 original images	0.911	0.813	0.897
720 augmented images from 80 original images†	0.912	0.821	0.902

**Dice coefficient = $\frac{2IoU}{1+IoU}$ when supposing that all class accuracies were identical. IoU mean intersection over the union. †Among a total of 918 augmented training and validation images, the remaining 198 augmented images were used for validation.*

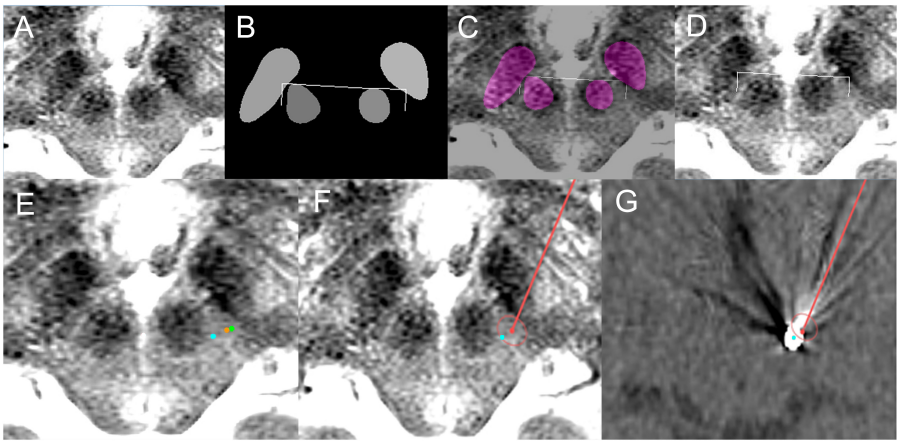

FIGURE 7 | Deep learning-based automatic targeting application for Patient 1. **(A)** Input image for targeting. **(B)** Semantic segmentation results and automatic targeting results. Bilateral ends of the bent edges of the white line are automatic targets calculated using the method shown in **Figure 3**. **(C)** Semantic segmentation imaging and automatic targets superimposed on the input MRI. **(D)** Automatic targets superimposed on the input MRI. **(E)** Orange dot indicates the deep learning-based automatic target in the left posterior subthalamic area, while the green dot is the indirect target. The cyan dot is the post-operative location of the electrode. **(F)** Planned trajectory and target (red dot and line) and location of the post-operative electrode (cyan dot) superimposed on the preoperative MRI. **(G)** Planned trajectory and target (red dot and line) and location of the post-operative electrode (cyan dot) superimposed on the post-operative CT image.

The stereotactic errors are shown in **Table 2** and **Figure 8**. No hemorrhagic or infectious complications occurred.

The patient's post-operative UPDRS motor score, without stimulation and under minimal levodopa medication (300 mg a day), was 15. Later, her levodopa dose was increased to 450 mg a day, and pramipexole was added. Her UPDRS motor score was 13 without stimulation under medication. Electrical stimulation was turned on after 1 month. After surgery, the most effective electrodes were right 3 (2.5 V, 80 Hz, 60 μs pulse width) and left 3 (1.5 V, 80 Hz, 60 μs). At the best stimulation setting and with the correct medication, the patient's UPDRS motor score was 7. Under right stimulation, her left bradykinesia improved from grade 2 to grade 1. Under left stimulation, her right bradykinesia improved from grade 2 to grade 1. Her gait disturbances improved from grade 1 to grade 0, and she showed no complications over 3 months of outpatient follow-up visits.

DISCUSSION

Deep Learning-Based Semantic Segmentation and Targeting Characteristics

Recent state-of-the-art adaptive atlas-based studies using 3T or 7T MRI reported a Dice coefficient of 0.64–0.67 in the STN (Ewert et al., 2019; Kim et al., 2019), and another study indicated that the red nucleus is easier to segment, with an approximate 0.85 Dice coefficient (Visser et al., 2016). Thus, we speculate that the mean Dice coefficient, including both the STN and the red nucleus, may have been about 0.75–0.77 in previous studies (Visser et al., 2016; Ewert et al., 2019; Kim et al., 2019). A recent two-dimensional deep learning study had a mean Dice coefficient of 0.85 for basal ganglia structures on MRI (Mehta and Sivaswamy, 2017). However, this study did not segment the STN and red nucleus (Mehta and Sivaswamy, 2017). The Dice coefficient-converted accuracy in the present study (∼90.2%) (**Table 1**) was numerically higher than those of previous non-deep learning studies (Visser et al., 2016; Mehta and Sivaswamy, 2017; Milletari et al., 2017; Ewert et al., 2019; Kim et al., 2019). The present study involved a two-dimensional image analysis similar to a recent fast and memory-efficient deep learning study (Mehta and Sivaswamy, 2017). However, a few non-deep learning studies were three-dimensional (Ewert et al., 2019; Kim et al., 2019). Thus, these results should be compared with caution.

Various analytical factors differed between previous studies and the present study (Visser et al., 2016; Mehta and Sivaswamy, 2017; Milletari et al., 2017; Ewert et al., 2019; Kim et al., 2019). Thus, we cannot ascertain which algorithms are superior. Considering the moderately different results from the other deep learning studies, we speculate that not only the algorithm but also MRI image quality control, sequence types, focused magnification, and high image contrasts influenced accuracy.

Because our deep learning-based surgical targeting achieved high accuracy, we could apply it in real clinical patients and conduct manual verification. Individual anatomical variability has been a major obstacle to atlas- and coregistration-based automatic targeting methods (Ashkan et al., 2007; Patel et al., 2008; Daniluk et al., 2010; Xiao et al., 2014; Pallavaram et al., 2015). The center positions of the STN are highly variable, fluctuating over 3–6 mm depending on the axis direction (Daniluk et al., 2010). In addition, the shape, size, and position of the STN may be asymmetric, variable, or irregular, as shown in **Figure 1**. Thus, atlas-based or coregistration-based methods may inevitably be inaccurate due to individual differences in the atlas or other structures (Ewert et al., 2019; Kim et al., 2019;

TABLE 2 | Stereotactic coordinates of deep learning targets and post-operative electrode locations.

		Directions	Patient 1 left posterior subthalamic area	Patient 2 right subthalamic nucleus	Patient 2 left subthalamic nucleus
Talairach coordinate from midcommissural point	Deep learning-based target	Lateral	−11.3	9.2	−10.79
		A–P	−6.7	−4.3	−3.38
		Vertical	−3.7	−4.5	−4.12
	Post-operative electrode	Lateral	−9.5	10.3	−8.86
		A–P	−7.6	−4.2	−3.52
		Vertical	−3.7	−3.1	−4.15
Leksell coordinate	Deep learning-based target	X	113.5	92.0	112.0
		Y	84.5	91.0	92.5
		Z	110.5	110.0	109.5
	Trajectory	Ring	67	77.0	71
		Arc	107.5	67.0	108
	Post-operative electrode	X	111.6	90.9	110.1
		Y	83.2	90.7	92.3
		Z	110.7	108.6	109.5
Stereotactic errors			1.6	0.8	1.7

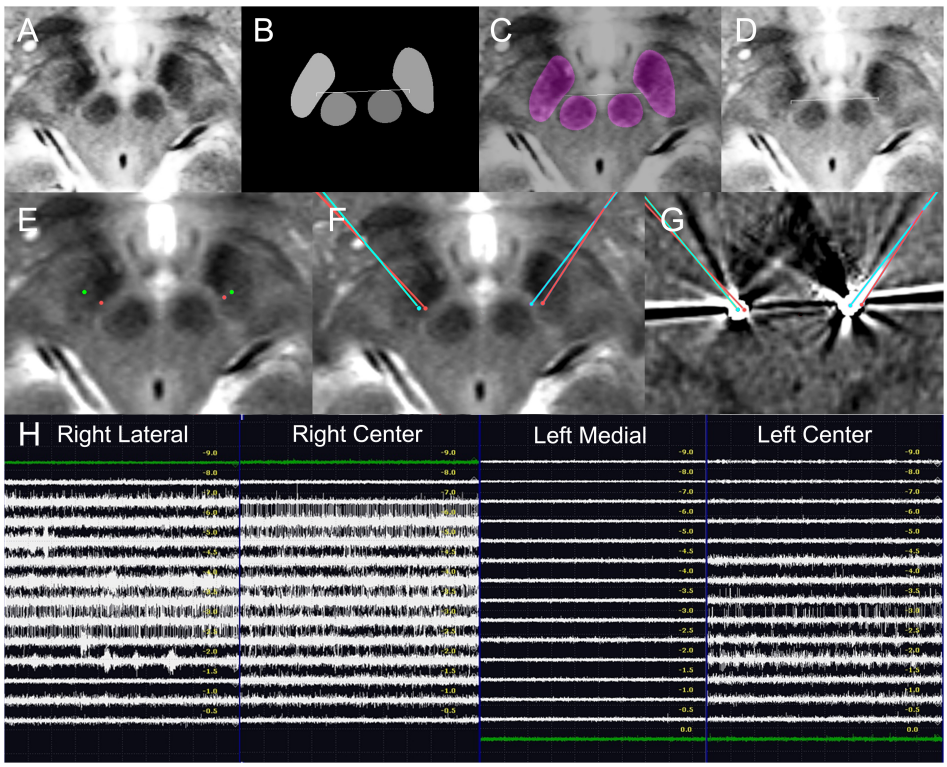

FIGURE 8 | Deep learning-based automatic targeting and application in Patient 2. **(A–D)** Figure parts are arranged similarly to **Figure 4**. **(E)** Bilateral indirect targets (green dots) and bilateral deep learning-based targets (red dots). Talairach coordinates of bilateral indirect targets are shown for comparison. **(F)** Planned bilateral trajectories and targets (red points and lines) and the bilateral post-operative electrode (cyan dot) superimposed on the preoperative magnetic resonance image. **(G)** Planned bilateral trajectories and targets (red dots and lines) and the bilateral locations of post-operative electrodes (cyan dots) superimposed on post-operative CT images. **(H)** Intraoperative microelectrode recordings.

Shamir et al., 2019). Non-deep learning adaptive algorithms, as well as semantic segmentation studies of the basal ganglia and brainstem structure, have used simpler image features than deep learning (Visser et al., 2016; Shamir et al., 2019). It follows that deep learning may be more adaptive to anatomical variation and better at generalization using more abstractive features

(**Figure 1**). Thus, the final segmentation accuracy may be higher when deep learning is used.

Training and Validation MRI Image Protocol Selection

Image quality was crucially important to ensure the best performance for the algorithm in the present study. Various MRI sequences, including T2- (Bot et al., 2016), 3T T2*- (O'Gorman et al., 2011; Kerl et al., 2012a,b), and T2*- (Lefranc et al., 2014; Nagahama et al., 2015) weighted angiography, susceptibility-weighted imaging (O'Gorman et al., 2011; Polanski et al., 2015), and fluid-attenuated inversion recovery imaging (Heo et al., 2015) have been used for STN segmentation or posterior subthalamic area targeting. All of these are probably practical for clinical use. Because the STN has a high iron content, susceptibility-weighted sequences are beneficial for STN visualization (Polanski et al., 2015). However, excessive susceptibility artifacts can distort and exaggerate the STN size and margins, so the accuracy of susceptibility-weighted image margins has been questioned (Bot et al., 2016). Thus, to balance visibility, measurement accuracy, familiarity for many users, and broad applicability, we selected the T2* sequence, which is similar to the frequently used T2 sequence and has moderate susceptibility weighting capabilities. In addition, the 3T MRI used in the present study with or without frames may be better for visualization and direct targeting of DBS than is stereotactic 1.5T MRI (Cheng et al., 2014; Southwell et al., 2016).

Distortion of 3T MRI with a frame is still being investigated, and it is not yet fully confirmed for stereotactic use (Neumann et al., 2015). Thus, coregistration between 3T MRI and CT was required (Neumann et al., 2015).

Recently, the cross-center reproducibility of deep learning algorithms has been an important issue (Zech et al., 2018). Algorithms require matched or similar preoperative MRI sequences of the best possible quality to ensure accurate performance. In the present study, the T2* MRI sequence used in training and validation was unavailable in the hospital in which the clinical application was carried out. Thus, a T2 MRI sequence was used for targeting in the hospital. T2 and T2* mostly share similar image contrasts, and we could perform cross-MRI sequence application of the algorithm (**Figures 7**, **8**). We partly showed that cross-center and cross-MRI-sequence application of T2-related MRI sequences with similar image contrast values and acceptable quality was possible.

However, MRI sequences with worse quality cannot be used. Worse MRI image contrast due to lower magnetic field (Cheng et al., 2014; Southwell et al., 2016), 1-mm thickness T2 slicing, and higher noise from metal artifacts or any cause (O'Gorman et al., 2011) can result in a lower contrast-to-noise ratio, which is not suitable for machine learning algorithm application.

In this regard, the inclusion of lower quality images during training may improve algorithm robustness toward lower quality images. However, image quality can be controlled preoperatively to ensure the best outcomes for DBS. Thus, we suggest that algorithms will perform better if poor quality images are not used.

Deep Learning Network and Training Characteristics

The semantic segmentation accuracy of fully convolutional neural networks has been reported based on the VOC-2011-2 dataset, which has 20 classes and 11,530 images containing 27,450 annotated objects (Shelhamer et al., 2017). The present study had fewer classes, and the shapes of each class may have been less variable than in the VOC-2011-2 dataset. However, the mean IoU in the present study was approximately 15% higher than in VOC-2011-2 (82.1% vs. about 67%), even though the same network architecture was used (FCN-VGG-16) (Shelhamer et al., 2017). We speculate that our study showed high accuracy because we used fewer classes with more constant shapes and positions and with less structural variability and used grayscale images. High contrast anatomical structures in T2* MRI sequences are also probably related to high validation accuracy.

Similar to a previous report, only a short amount of time was required in the present study for a single iteration and semantic segmentation – about 250 ms (four images processed per second). This time is related to the size of the deep network and the number of VGG16-based network parameters. The speed in the present study was fast enough to allow clinical application without delay during the procedure.

When we expanded the data to include over 50 images, the accuracy only improved slightly and then plateaued (**Figure 4C**). Thus, increasing the number of images is not likely to further improve the segmentation accuracy. Considering that the mean IoU was over 80% in the present study – a very high semantic segmentation accuracy (**Figure 4C**) – we concluded that qualitatively and quantitatively sufficient training data were used to allow four-class semantic segmentation. Thus, deep learning-based semantic segmentation of basal ganglia is possible with a smaller number of samples than the VOC-2011-2 dataset – 62 images for four-class classification.

In a previous semantic segmentation study that used the VOC-2011-2 dataset, data augmentation yielded no improvements in semantic segmentation results (Shelhamer et al., 2017). However, in the present study, a small increase in accuracy was noted (**Figure 4C**). It follows that data augmentation using variable contrast data improves semantic segmentation adaptiveness when using various contrast settings. The differences may be that the VOC-2011-2 dataset was already highly variable and that data comprising a higher number of images no longer required augmentation.

Deep Learning-Based Targeting, Direct and Indirect Targets, and Targeting Standardization

There are two kinds of deep learning-based targeting methods: direct and indirect. Direct targets are based on MRI anatomical structure margins (Holl et al., 2010; Foltynie et al., 2011; Aviles-Olmos et al., 2014). Because our deep learning-based targeting was also performed based on MRI anatomical structure margins, our deep learning-based targeting method can be considered a type of MRI-based direct targeting method (Bejjani et al., 2000). Indirect targeting is based on Talairach coordinates

calculated from the anterior commissure, posterior commissure, and midline (Kochunov et al., 2002; Tu et al., 2018). The present study did not identify these anatomical points, and as such, our deep learning-based method is not a substitution for indirect targets. Nonetheless, indirect targets were manually determined and are shown for comparison purposes (**Figures 7, 8**).

The exact locations of DBS targets can vary among surgeons, and DBS centers and best locations are controversial. Some surgeons target the center of the STN (Bejjani et al., 2000), while others target more medial sites (Toda et al., 2009), medial–posterior sites, or other locations (Aviles-Olmos et al., 2014). We used targets that were close to the medial margin of the STN and slightly posterior to the anterior margins of the red nucleus (Foltynie et al., 2011; Aviles-Olmos et al., 2014). This target is similar to that used in a previous image-guided DBS study (Aviles-Olmos et al., 2014).

Indeed, individual surgeons may not be consistent in this regard. Thus, the location of a quantified point or line (e.g., 1 mm lateral from the medial border of the STN) may vary among individual surgeons when targeting is manually applied. However, when identical deep learning algorithm models and input images are used, targeting is completely identical and can be standardized without subjective differences.

The results of different DBS-related clinical trials may be influenced by target variations among surgeons. Deep learning-based automatic segmentation and targeting would be more consistent and regular than manual methods. Thus, deep learning DBS may allow standardization of targeting locations in multi-center clinical trials involving multiple surgeons. Therefore, deep learning-based targets may be used to aid manual targeting, similar to indirect targets, for better standardization of targets.

In the near future, the exact targeting location may also be automatically optimized based on post-operative outcomes using the deep learning-based targeting observed in the present study as well as the outcome-guided machine learning recently reported from our group (Park and Chung, 2018).

Once trained, deep learning-based targeting does not need to be retrained or re-experience an early learning curve during clinical applications in the same way that trained human surgeons do. Deep learning-based targeting can be applied in the fully trained state from large-scale anatomy-electrode location-outcome data. Thus, consistently high targeting quality can probably be achieved with potentially low cost.

Related Studies

Deep learning-based morphometry of basal ganglia structures is related to the present study (Mehta and Sivaswamy, 2017; Milletari et al., 2017). A recent study reported microelectrode recording verification of a machine learning, active shape modeling-based segmentation of the STN (Shamir et al., 2019). Another recent report did not involve segmentation-classified deep learning networks to select image patches and reported good DBS post-operative outcomes (Bermudez et al., 2018). A recent conference proceeding reported microelectrode recording signal analysis using a deep neural network (Guillén-Rondon and Robinson, 2016). Recently, biopsy needle or catheter position was analyzed with deep learning in relation to image-guided surgery or interventions (Mehrtash et al., 2019; Paolo et al., 2019). However, none of these studies are directly related or applicable to deep learning-based automatic targeting.

Limitations

Because the present study is the first application of deep learning-based targeting for DBS, the algorithm and clinical applications were made as simple as possible. Thus, there are many avenues for further investigations and development. First, the algorithm uses a two-dimensional axial slice image only. Selecting the main Bejjani target point by deep learning is possible only by using a single axial image (Bejjani et al., 2000). The subsequent trajectory planning processes considering upper and lower T2 MRI axial images or three-dimensional anatomies were performed manually. The selection of the axial image for targeting was manual, and this step determined the targeting depth.

Second, we only used 3T MRI data, and we found that the applicability of 1.5T or poor-quality MRI images was qualitatively inadequate (not shown). The algorithm may be further improved by including lower quality MRI training data for increased robustness in various clinical settings. However, DBS preoperative MRI quality can be electively controlled to be optimal in most centers, and the use of only high-quality MRI is also a good option. In the present study, relative distances from semantically segmented anatomical structures and the deep learning-based targets were manually adjusted to mimic targets used by neurosurgeons. However, the exact target location can be improved using information about targets via an outcome-guided machine learning method (Park and Chung, 2018). The number of clinical applications in the present study is few. Further investigations into more clinical applications of this technique are warranted.

CONCLUSION

Using a deep learning algorithm and 3T MRI data magnified for midbrain structures, we achieved high semantic segmentation accuracy that was adaptive for anatomical variability of the STN and red nucleus. We could automatically determine the DBS target from the segmented anatomical structures. The deep learning-based target could be applied in real patients successfully without target modification and electrode track change. This study is the first to show that deep learning-based DBS surgical planning is clinically applicable in image-guided surgeries. A deep learning-based targeting technique is potentially more objective, consistent, and analyzable than manual methods. Deep learning-based DBS targeting can potentially be improved for better outcomes in the near future.

DATA AVAILABILITY STATEMENT

The datasets generated for this study are available on request to the corresponding author.

ETHICS STATEMENT

This study was pre-approved by the institutional review boards of Gangneung Asan Hospital (2018-07-22) and Asan Medical Center (S2016-1230-0005). Before the clinical application, all patients and families signed informed consent forms that had been approved by the institutional review boards.

AUTHOR CONTRIBUTIONS

S-CP designed the study and mediated correspondence regarding the manuscript, applied for and acquired a national research foundation grant, wrote the manuscript and made all the figures, participated in training DBS dataset patient surgeries, guided training through ground truth dataset drawing, designed and verified the training and validation dataset, modified the open-source Caffe deep learning semantic segmentation program and performed validation dataset analysis with various amount of data up to 918 images, performed data augmentation and tested performance, designed the targeting method, recruited Patient 1, performed clinical application of DBS, and verified the DBS target before clinical application. JC adapted the open-source Caffe deep learning semantic segmentation program for the present study, performed the initial training with data on 62 patients, and designed the Python-based targeting program. SL constructed the ground truth training dataset and collected and arranged the data. WJ performed the clinical application, patient evaluation, and management, and recruited Patient 2. CL and JL established the training dataset. CL performed the patient recruitment and perioperative management for the training dataset patients. JL performed the operations, and set up MRI and DBS protocols for the training dataset patients.

FUNDING

This research was supported by the Basic Science Research Program of the National Research Foundation of Korea, which is funded by the Ministry of Education (2016R1C1B1012374) (70%) and (2019R1F1A1063692) (30%).

REFERENCES

Amirnovin, R., Williams, Z. M., Cosgrove, G. R., and Eskandar, E. N. (2006). Experience with microelectrode guided subthalamic nucleus deep brain stimulation. *Oper. Neurosurg.* 58, ONS96–ONS102.

Ashkan, K., Blomstedt, P., Zrinzo, L., Tisch, S., Yousry, T., Limousin-Dowsey, P., et al. (2007). Variability of the subthalamic nucleus: the case for direct MRI guided targeting. *Br. J. Neurosurg.* 21, 197–200. doi: 10.1080/02688690701272240

Aviles-Olmos, I., Kefalopoulou, Z., Tripoliti, E., Candelario, J., Akram, H., Martinez-Torres, I., et al. (2014). Long-term outcome of subthalamic nucleus deep brain stimulation for Parkinson's disease using an MRI-guided and MRI-verified approach. *J. Neurol. Neurosurg. Psychiatry* 85, 1419–1425. doi: 10.1136/jnnp-2013-306907

Bejjani, B. P., Dormont, D., Pidoux, B., Yelnik, J., Damier, P., Arnulf, I., et al. (2000). Bilateral subthalamic stimulation for Parkinson's disease by using three-dimensional stereotactic magnetic resonance imaging and electrophysiological guidance. *J. Neurosurg.* 92, 615–625. doi: 10.3171/jns.2000.92.4.0615

Bermudez, C., Rodriguez, W., Huo, Y., Hainline, A. E., Li, R., Shults, R., et al. (2018). Towards machine learning prediction of deep brain stimulation (DBS) intra-operative efficacy maps. *arXiv [Preprint arXiv:1811.10415]*.

Blomstedt, P., Sandvik, U., Fytagoridis, A., and Tisch, S. (2009). The posterior subthalamic area in the treatment of movement disorders: past, present, and future. *Neurosurgery* 64, 1029–1038, discussion 1038–1042. doi: 10.1227/01.NEU.0000345643.69486.BC

Blomstedt, P., Sandvik, U., and Tisch, S. (2010). Deep brain stimulation in the posterior subthalamic area in the treatment of essential tremor. *Mov. Disord.* 25, 1350–1356. doi: 10.1002/mds.22758

Bot, M., Bour, L., De Bie, R. M., Contarino, M. F., Schuurman, P. R., and Van Den Munckhof, P. (2016). Can we rely on susceptibility-weighted imaging for subthalamic nucleus identification in deep brain stimulation surgery? *Neurosurgery* 78, 353–360. doi: 10.1227/NEU.0000000000001130

Cheng, C. H., Huang, H. M., Lin, H. L., and Chiou, S. M. (2014). 1.5*T versus* 3T MRI for targeting subthalamic nucleus for deep brain stimulation. *Br. J. Neurosurg.* 28, 467–470. doi: 10.3109/02688697.2013.854312

Choi, H., and Jin, K. H. (2016). Fast and robust segmentation of the striatum using deep convolutional neural networks. *J. Neurosci. Methods* 274, 146–153. doi: 10.1016/j.jneumeth.2016.10.007

Daniluk, S., Davies, K. G., Ellias, S. A., Novak, P., and Nazzaro, J. M. (2010). Assessment of the variability in the anatomical position and size of the subthalamic nucleus among patients with advanced Parkinson's disease using magnetic resonance imaging. *Acta Neurochir.* 152, 201–210, discussion 210. doi: 10.1007/s00701-009-0514-z

De Fauw, J., Ledsam, J. R., Romera-Paredes, B., Nikolov, S., Tomasev, N., Blackwell, S., et al. (2018). Clinically applicable deep learning for diagnosis and referral in retinal disease. *Nat. Med.* 24, 1342–1350. doi: 10.1038/s41591-018-0107-6

Dice, L. R. (1945). Measures of the amount of ecologic association between species. *Ecology* 26, 297–302. doi: 10.2307/1932409

Ellenbogen, J. R., Tuura, R., and Ashkan, K. (2018). Localisation of DBS electrodes post-implantation, to CT or MRI? Which is the best option? *Stereotact. Funct. Neurosurg.* 96, 347–348. doi: 10.1159/000493576

Ewert, S., Horn, A., Finkel, F., Li, N., Kühn, A. A., and Herrington, T. M. (2019). Optimization and comparative evaluation of nonlinear deformation algorithms for atlas-based segmentation of DBS target nuclei. *Neuroimage* 184, 586–598. doi: 10.1016/j.neuroimage.2018.09.061

Foltynie, T., Zrinzo, L., Martinez-Torres, I., Tripoliti, E., Petersen, E., Holl, E., et al. (2011). MRI-guided STN DBS in Parkinson's disease without microelectrode recording: efficacy and safety. *J. Neurol. Neurosurg. Psychiatry* 82, 358–363. doi: 10.1136/jnnp.2010.205542

Guillén-Rondon, P., and Robinson, M. D. (2016). "Deep brain stimulation signal classification using deep belief networks," in *Proceedings of the International Conference on Computational Science and Computational Intelligence (CSCI) 2016*, Las Vegas, NV, 155–158.

Hariz, M. I. (2002). Safety and risk of microelectrode recording in surgery for movement disorders. *Stereotact. Funct. Neurosurg.* 78, 146–157. doi: 10.1159/000068960

Heo, Y. J., Kim, S. J., Kim, H. S., Choi, C. G., Jung, S. C., Lee, J. K., et al. (2015). Three-dimensional fluid-attenuated inversion recovery sequence for visualisation of subthalamic nucleus for deep brain stimulation in Parkinson's disease. *Neuroradiology* 57, 929–935. doi: 10.1007/s00234-015-1555-z

Holl, E. M., Petersen, E. A., Foltynie, T., Martinez-Torres, I., Limousin, P., Hariz, M. I., et al. (2010). Improving targeting in image-guided frame-based deep brain stimulation. *Neurosurgery* 67, 437–447. doi: 10.1227/NEU.0b013e3181f7422a

Kerl, H. U., Gerigk, L., Huck, S., Al-Zghloul, M., Groden, C., and Nolte, I. S. (2012a). Visualisation of the zona incerta for deep brain stimulation at 3.0 *Tesla*. *Clin. Neuroradiol.* 22, 55–68. doi: 10.1007/s00062-012-0136-3

Kerl, H. U., Gerigk, L., Pechlivanis, I., Al-Zghloul, M., Groden, C., and Nolte, I. (2012b). The subthalamic nucleus at 3.0 Tesla: choice of optimal sequence and orientation for deep brain stimulation using a standard installation protocol: clinical article. *J. Neurosurg.* 117, 1155–1165. doi: 10.3171/2012.8.JNS111930

Kim, J., Duchin, Y., Shamir, R. R., Patriat, R., Vitek, J., Harel, N., et al. (2019). Automatic localization of the subthalamic nucleus on patient-specific clinical

MRI by incorporating 7 T MRI and machine learning: application in deep brain stimulation. *Hum. Brain Mapp.* 40, 679–698. doi: 10.1002/hbm.24404

Kochunov, P., Lancaster, J., Thompson, P., Toga, A. W., Brewer, P., Hardies, J., et al. (2002). An optimized individual target brain in the Talairach coordinate system. *Neuroimage* 17, 922–927. doi: 10.1016/s1053-8119(02)91084-0

Lefranc, M., Derrey, S., Merle, P., Tir, M., Constans, J. M., Montpellier, D., et al. (2014). High-resolution 3-dimensional T2*-weighted angiography (HR 3-D SWAN): an optimized 3-T magnetic resonance imaging sequence for targeting the subthalamic nucleus. *Neurosurgery* 74, 615–626, discussion 627. doi: 10.1227/NEU.0000000000000319

Marcus, G. (2018). Deep learning: a critical appraisal. *arXiv [preprint arXiv:1801.00631]*.

Mehrtash, A., Ghafoorian, M., Pernelle, G., Ziaei, A., Heslinga, F. G., Tuncali, K., et al. (2019). Automatic needle segmentation and localization in MRI with 3-D convolutional neural networks: application to MRI-targeted prostate biopsy. *IEEE Trans. Med. Imaging* 38, 1026–1036. doi: 10.1109/TMI.2018.2876796

Mehrtash, A., Pesteie, M., Hetherington, J., Behringer, P. A., Kapur, T., Wells, W. M., et al. (2017). DeepInfer: open-source deep learning deployment toolkit for image-guided therapy. *Proc. SPIE Int. Soc. Opt. Eng.* 10135:101351K. doi: 10.1117/12.2256011

Mehta, R., and Sivaswamy, J. (2017). "M-net: a convolutional neural network for deep brain structure segmentation," in *Proceedings of the 2017 IEEE 14th International Symposium on Biomedical Imaging (ISBI 2017)*, Melbourne, VIC, 437–440.

Milletari, F., Ahmadi, S.-A., Kroll, C., Plate, A., Rozanski, V., Maiostre, J., et al. (2017). Hough-CNN: deep learning for segmentation of deep brain regions in MRI and ultrasound. *Comput. Vis. Image Underst.* 164, 92–102. doi: 10.1016/j.cviu.2017.04.002

Nagahama, H., Suzuki, K., Shonai, T., Aratani, K., Sakurai, Y., Nakamura, M., et al. (2015). Comparison of magnetic resonance imaging sequences for depicting the subthalamic nucleus for deep brain stimulation. *Radiol. Phys. Technol.* 8, 30–35. doi: 10.1007/s12194-014-0283-0

Naylor, C. D. (2018). On the prospects for a (deep) learning health care system. *JAMA* 320, 1099–1100.

Neumann, J. O., Giese, H., Biller, A., Nagel, A. M., and Kiening, K. (2015). Spatial distortion in MRI-guided stereotactic procedures: evaluation in 1. 5-, 3- and 7-Tesla MRI scanners. *Stereotact. Funct. Neurosurg.* 93, 380–386. doi: 10.1159/000441233

O'Gorman, R. L., Shmueli, K., Ashkan, K., Samuel, M., Lythgoe, D. J., Shahidiani, A., et al. (2011). Optimal MRI methods for direct stereotactic targeting of the subthalamic nucleus and globus pallidus. *Eur. Radiol.* 21, 130–136. doi: 10.1007/s00330-010-1885-5

Pallavaram, S., D'haese, P. F., Lake, W., Konrad, P. E., Dawant, B. M., and Neimat, J. S. (2015). Fully automated targeting using nonrigid image registration matches accuracy and exceeds precision of best manual approaches to subthalamic deep brain stimulation targeting in Parkinson disease. *Neurosurgery* 76, 756–765. doi: 10.1227/NEU.0000000000000714

Paolo, Z., Guillaume, P., Andre, M., Alireza, M., Hongtao, Z., Ron, K., et al. (2019). Fully automatic catheter segmentation in MRI with 3D convolutional neural networks: application to MRI-guided gynecologic brachytherapy. *Phys. Med. Biol.* 64:165008. doi: 10.1088/1361-6560/ab2f47

Park, S. C., and Chung, C. K. (2018). Postoperative seizure outcome-guided machine learning for interictal electrocorticography in neocortical epilepsy. *J. Neurophysiol.* 119, 2265–2275. doi: 10.1152/jn.00225.2017

Park, S. C., Lee, C. S., Kim, S. M., Choi, E. J., and Lee, J. K. (2017). Comparison of the stereotactic accuracies of function-guided deep brain stimulation, calculated using multitrack target locations geometrically inferred from three-dimensional trajectory rotations, and of magnetic resonance imaging-guided deep brain stimulation and outcomes. *World Neurosurg.* 98, 734.e7–749.e7. doi: 10.1016/j.wneu.2016.11.046

Park, S. C., Lee, J. K., Kim, S. M., Choi, E. J., and Lee, C. S. (2018). Systematic stereotactic error reduction using a calibration technique in single-brain-pass and multitrack deep brain stimulations. *Oper. Neurosurg.* 15, 72–80. doi: 10.1093/ons/opx183

Patel, N. K., Khan, S., and Gill, S. S. (2008). Comparison of atlas- and magnetic-resonance-imaging-based stereotactic targeting of the subthalamic nucleus in the surgical treatment of Parkinson's disease. *Stereotact. Funct. Neurosurg.* 86, 153–161. doi: 10.1159/000120427

Plaha, P., Khan, S., and Gill, S. S. (2008). Bilateral stimulation of the caudal zona incerta nucleus for tremor control. *J. Neurol. Neurosurg. Psychiatry* 79, 504–513. doi: 10.1136/jnnp.2006.112334

Polanski, W. H., Martin, K. D., Engellandt, K., Von Kummer, R., Klingelhoefer, L., Fauser, M., et al. (2015). Accuracy of subthalamic nucleus targeting by T2, FLAIR and SWI-3-Tesla MRI confirmed by microelectrode recordings. *Acta Neurochir.* 157, 479–486. doi: 10.1007/s00701-014-2328-x

Pollak, P., Krack, P., Fraix, V., Mendes, A., Moro, E., Chabardes, S., et al. (2002). Intraoperative micro- and macrostimulation of the subthalamic nucleus in Parkinson's disease. *Mov. Disord.* 17(Suppl. 3), S155–S161.

Rezatofighi, H., Tsoi, N., Gwak, J., Sadeghian, A., Reid, I., and Savarese, S. (2019). Generalized intersection over union: a metric and a loss for bounding box regression. *arXiv [Preprints]*. Available: https://ui.adsabs.harvard.edu/abs/2019arXiv190209630R (accessed February 01, 2019).

Shamir, R. R., Duchin, Y., Kim, J., Patriat, R., Marmor, O., Bergman, H., et al. (2019). Microelectrode recordings validate the clinical visualization of subthalamic-nucleus based on 7T magnetic resonance imaging and machine learning for deep brain stimulation surgery. *Neurosurgery* 84, 749–757. doi: 10.1093/neuros/nyy212

Shelhamer, E., Long, J., and Darrell, T. (2017). Fully convolutional networks for semantic segmentation. *IEEE Trans. Pattern Anal. Mach Intell.* 39, 640–651. doi: 10.1109/TPAMI.2016.2572683

Southwell, D. G., Narvid, J. A., Martin, A. J., Qasim, S. E., Starr, P. A., and Larson, P. S. (2016). Comparison of deep brain stimulation lead targeting accuracy and procedure duration between 1.5- and 3-Tesla interventional magnetic resonance imaging systems: an initial 12-month experience. *Stereotact. Funct. Neurosurg.* 94, 102–107. doi: 10.1159/000443407

Starr, P. A., Christine, C. W., Theodosopoulos, P. V., Lindsey, N., Byrd, D., Mosley, A., et al. (2002). Implantation of deep brain stimulators into the subthalamic nucleus: technical approach and magnetic resonance imaging-verified lead locations. *J. Neurosurg.* 97, 370–387. doi: 10.3171/jns.2002.97.2.0370

Starr, P. A., Vitek, J. L., Delong, M., and Bakay, R. A. (1999). Magnetic resonance imaging-based stereotactic localization of the globus pallidus and subthalamic nucleus. *Neurosurgery* 44, 303–313, discussion 313–314. doi: 10.1097/00006123-199902000-00031

Toda, H., Sawamoto, N., Hanakawa, T., Saiki, H., Matsumoto, S., Okumura, R., et al. (2009). A novel composite targeting method using high-field magnetic resonance imaging for subthalamic nucleus deep brain stimulation. *J. Neurosurg.* 111, 737–745. doi: 10.3171/2008.12.JNS0861

Tu, P. H., Liu, Z. H., Chen, C. C., Lin, W. Y., Bowes, A. L., Lu, C. S., et al. (2018). Indirect targeting of subthalamic deep brain stimulation guided by stereotactic computed tomography and microelectrode recordings in patients with Parkinson's disease. *Front. Hum. Neurosci.* 12:470. doi: 10.3389/fnhum.2018.00470

Visser, E., Keuken, M. C., Forstmann, B. U., and Jenkinson, M. (2016). Automated segmentation of the substantia nigra, subthalamic nucleus and red nucleus in 7T data at young and old age. *Neuroimage* 139, 324–336. doi: 10.1016/j.neuroimage.2016.06.039

Xiao, Y., Jannin, P., D'albis, T., Guizard, N., Haegelen, C., Lalys, F., et al. (2014). Investigation of morphometric variability of subthalamic nucleus, red nucleus, and substantia nigra in advanced Parkinson's disease patients using automatic segmentation and PCA-based analysis. *Hum. Brain Mapp.* 35, 4330–4344. doi: 10.1002/hbm.22478

Zech, J. R., Badgeley, M. A., Liu, M., Costa, A. B., Titano, J. J., and Oermann, E. K. (2018). Variable generalization performance of a deep learning model to detect pneumonia in chest radiographs: a cross-sectional study. *PLoS Med.* 15:e1002683. doi: 10.1371/journal.pmed.1002683

Conflict of Interest: The authors declare that the research was conducted in the absence of any commercial or financial relationships that could be construed as a potential conflict of interest.

Copyright © 2019 Park, Cha, Lee, Jang, Lee and Lee. This is an open-access article distributed under the terms of the Creative Commons Attribution License (CC BY). The use, distribution or reproduction in other forums is permitted, provided the original author(s) and the copyright owner(s) are credited and that the original publication in this journal is cited, in accordance with accepted academic practice. No use, distribution or reproduction is permitted which does not comply with these terms.

frontiers in Neuroscience

ORIGINAL RESEARCH
published: 06 November 2019
doi: 10.3389/fnins.2019.01159

More Reliable EEG Electrode Digitizing Methods Can Reduce Source Estimation Uncertainty, but Current Methods Already Accurately Identify Brodmann Areas

Seyed Yahya Shirazi and Helen J. Huang*

Department of Mechanical and Aerospace Engineering, University of Central Florida, Orlando, FL, United States

Electroencephalography (EEG) and source estimation can be used to identify brain areas activated during a task, which could offer greater insight on cortical dynamics. Source estimation requires knowledge of the locations of the EEG electrodes. This could be provided with a template or obtained by digitizing the EEG electrode locations. Operator skill and inherent uncertainties of a digitizing system likely produce a range of digitization reliabilities, which could affect source estimation and the interpretation of the estimated source locations. Here, we compared the reliabilities of five digitizing methods (ultrasound, structured-light 3D scan, infrared 3D scan, motion capture probe, and motion capture) and determined the relationship between digitization reliability and source estimation uncertainty, assuming other contributors to source estimation uncertainty were constant. We digitized a mannequin head using each method five times and quantified the reliability and validity of each method. We created five hundred sets of electrode locations based on our reliability results and applied a dipole fitting algorithm (DIPFIT) to perform source estimation. The motion capture method, which recorded the locations of markers placed directly on the electrodes had the best reliability with an average electrode variability of 0.001 cm. Then, in order of decreasing reliability were the method using a digitizing probe in the motion capture system, an infrared 3D scanner, a structured-light 3D scanner, and an ultrasound digitization system. Unsurprisingly, uncertainty of the estimated source locations increased with greater variability of EEG electrode locations and less reliable digitizing systems. If EEG electrode location variability was ∼1 cm, a single source could shift by as much as 2 cm. To help translate these distances into practical terms, we quantified Brodmann area accuracy for each digitizing method and found that the average Brodmann area accuracy for all digitizing methods was >80%. Using a template of electrode locations reduced the Brodmann area accuracy to ∼50%. Overall, more reliable digitizing methods can reduce source estimation uncertainty, but the significance of the source estimation uncertainty depends on the desired spatial resolution. For accurate Brodmann area identification, any of the digitizing methods tested can be used confidently.

Keywords: electrocortical dynamics, electrode position, 3D scanning, source localization, spatial accuracy, independent component analysis (ICA), mobile brain/body imaging (MoBI)

OPEN ACCESS

Edited by:
Enkelejda Kasneci,
University of Tübingen, Germany

Reviewed by:
Evangelia-Regkina Symeonidou,
University of Florida, United States
Solomon G. Diamond,
Dartmouth College, United States

****Correspondence:***
Seyed Yahya Shirazi
shirazi@ieee.org

Specialty section:
This article was submitted to Brain Imaging Methods, a section of the journal Frontiers in Neuroscience

Received: *01 March 2019*
Accepted: *14 October 2019*
Published: *06 November 2019*

Citation:
Shirazi SY and Huang HJ (2019) More Reliable EEG Electrode Digitizing Methods Can Reduce Source Estimation Uncertainty, but Current Methods Already Accurately Identify Brodmann Areas. Front. Neurosci. 13:1159. doi: 10.3389/fnins.2019.01159

1. INTRODUCTION

Estimating active cortical sources using electroencephalography (EEG) is becoming widely adopted in multiple research areas as a non-invasive and mobile functional brain imaging modality (Nyström, 2008; Landsness et al., 2011; Bradley C. et al., 2016; Tsolaki et al., 2017). EEG is the recording of the electrical activity on the scalp and is appealing for studying cortical dynamics during movements and decision making due to the high temporal (i.e., millisecond) resolution of electrical signals. One of the challenges of using EEG is that the signal recorded in an EEG electrode is a mixture of electrical activity from multiple sources, which include the cortex, muscles, heart, eye, 60 Hz noise from power lines, and motion artifacts from cable sway and head movements (Kline et al., 2015; Symeonidou et al., 2018). To meaningfully correlate EEG analyses with brain function, the unwanted source content such as muscle activity, eye blinks, and motion artifacts need to be attenuated or separated from the cortical signal content. A multitude of tools such as independent component analysis, artifact rejection algorithms, and phantom heads have been developed to address the need to separate the source signals to extract the underlying cortical signal (Delorme et al., 2012; Mullen et al., 2013; Artoni et al., 2014; Oliveira et al., 2016; Nordin et al., 2018). Using high-density EEG and improving EEG post-processing techniques have also improved spatial resolution of source estimation to ∼1 cm in experimental studies (He and Musha, 1989; Lantz et al., 2003; Scarff et al., 2004; Klamer et al., 2015; Hedrich et al., 2017; Seeber et al., 2019).

Source estimation requires knowing the EEG signals and the locations of the EEG electrodes to estimate the locations of the cortical sources that produced the EEG signals measured on the scalp. An intuitive assumption of source estimation is that precise placement of the EEG electrodes on the scalp is essential for accurate estimation of source locations (Keil et al., 2014). Computational studies reported shifts of 0.5–1.2 cm in estimated source locations as a result of 0.5 cm (or 5°) error in the electrode digitization (Kavanagk et al., 1978; Khosla et al., 1999; Wang and Gotman, 2001; Beltrachini et al., 2011; Akalin Acar and Makeig, 2013). For EEG studies conducted inside a magnetic resonance imaging (MRI) device, the electrode locations with respect to the cortex can be captured and processed with <0.3 cm position error, which results in near perfect alignment of identified brain areas (Scarff et al., 2004; Marino et al., 2016). However, for studies that do not involve MRI, the electrode locations should be "digitized," i.e., recorded digitally via a three-dimensional (3D) position recording method (Koessler et al., 2007). These digitized locations can then be coupled with either a subject-specific or an averaged template of the brain structure obtained from MRI or other imaging techniques to perform EEG source estimation.

Just one decade ago in the mid-2000's, the main digitizing technologies available were based on ultrasound and electromagnetism, which were expensive, time consuming, and needed trained operators (Koessler et al., 2007; Rodríguez-Calvache et al., 2018). An ultrasound digitizing system uses differences in ultrasound-wave travel times from emitters on the person's face and a digitizing wand to an array of receivers to estimate the 3D location of the tip of the digitizing wand with respect to the face emitters. An electromagnetic system tracks the locations of receivers placed on the person's head and on a wand in an emitted electromagnetic field to estimate the position of the tip of the wand with respect to the head receivers. The environment must be clear of magnetic objects when using an electromagnetic digitizing system, otherwise the electrode locations will be warped (Engels et al., 2013; Cline et al., 2018).

Recent efforts have focused on developing technologies to make digitization more accessible and convenient, mainly by incorporating image-based technologies (Baysal and Sengül, 2010; Koessler et al., 2010). For example, using photogrammetry and motion capture methods for digitization can provide accurate electrode locations in a short period of time (Reis and Lochmann, 2015; Clausner et al., 2017). Photogrammetry involves using cameras to take a series of color images at different view angles. These images can then be analyzed to identify the locations of specific points in the 3D space (Russell et al., 2005; Clausner et al., 2017). Motion capture typically uses multiple infrared cameras around the capture volume to take simultaneous images to identify the locations of reflective or emitting markers. If markers are placed directly on the EEG electrodes, a motion capture system could conveniently record the position of all of the electrodes at once (Engels et al., 2013; Reis and Lochmann, 2015). Motion capture could also be used to record the position of the tip of a probe, a rigid body with multiple markers, to digitize 3D locations of the electrodes with respect to the reflective face markers. Several recent commercial digitizing systems use simple motion capture approaches to digitize EEG electrode locations with or without a probe (Cline et al., 2018; Song et al., 2018; ANT-Neuro, 2019; Rogue-Resolutions, 2019).

Another option for digitizing EEG electrodes that has also gained much interest recently are 3D scanners. A common approach for 3D scanning is detecting the infrared or visible reflections of projected light patterns with a camera to estimate the shape of an object (Chen and Kak, 1987). The 3D scanned shapes can then be plotted in a software program such as MATLAB, and the locations of specific points on the 3D scanned shape can be determined. Recently, common EEG analysis toolboxes such as EEGLAB (Delorme and Makeig, 2004) and FieldTrip (Oostenveld et al., 2010) support using 3D scanners to digitize the electrode locations. Studies suggest that 3D scanners can improve digitization accuracy and significantly reduce digitization time (Taberna et al., 2019). Using other camera-based systems such as time-of-flight scanners and virtual reality headsets were also reported to provide comparable digitization reliabilities as the ultrasound or electromagnetic digitizing methods, while reducing the time spent for digitizing the EEG electrodes (Vema Krishna Murthy et al., 2014; Zhang et al., 2014; Cline et al., 2018).

The purposes of this study were (1) to compare the reliability and validity of five digitizing methods and (2) to quantify the relationship between digitization reliability and source estimation uncertainty. We determined source estimation uncertainty using spatial metrics and Brodmann areas. We hypothesized that digitizing methods with less reliability would increase uncertainty in the estimates of the electrocortical

source locations. For our analyses, we assumed that all other contributors to source estimation uncertainty such as variability of head-meshes and assumptions of electrical conductivity values were constant.

2. METHODS

We fitted a mannequin head with a 128-channel EEG cap (ActiveTwo EEG system, BioSemi B.V., Amsterdam, the Netherlands, **Figure 1A**) and used this mannequin head setup to record multiple digitizations of the locations of the EEG electrodes and fiducials, i.e., right preauricular, left preauricular, and nasion (Klem et al., 1999). To prevent the cap from moving from digitization to digitization, we taped the cap to the mannequin head (**Figure 1A**). To help ensure that the fiducials were digitized at the same locations for every digitizing method, we marked the fiducials with small 4-mm markers on the mannequin head and with small o-rings on the cap (**Figure 1A**).

2.1. Digitizing Methods

We compared five methods for digitization: ultrasound, structured-light 3D scanning, infrared 3D scanning, motion capture with a digitizing probe, and motion capture with reflective markers. We calibrated each digitizing device only once and completed collecting data for each digitizing in a single session (see **Table S1** in the supplement for the calibration results). We also kept the position of the mannequin head, mannequin head orientation, start and endpoint of digitizing, lighting, and temperature constant to avoid introducing additional sources of error to our data collection and analysis.

For each method, four different members of the laboratory digitized the mannequin head five times (one person performed the digitization twice). All of the operators had prior experience in digitizing and were asked to follow each method's specific guidelines. We imported the digitization data to MATLAB (version 9.4, R2018a, Mathworks, Natick, MA) and performed all analyses in MATLAB.

2.1.1. Ultrasound

We used a Zebris positioning system with ElGuide software version 1.6 (Zebris Medical GmBH, Tübingen, Germany, **Figure 1B**) to digitize the electrodes with an ultrasound method. Following the Zebris manual, we placed 3 ultrasound emitters on the face of the mannequin head, placed the receiver module in front of the mannequin head, and used the digitizing wand to record the electrode locations. We calibrated the system using the ElGuide calibration procedure. We marked the fiducials repeatedly until we obtained fiducials with a digitized 3D location of nasion that was < 2 mm with respect to the midline and with preauriculars that had a difference of $<$ 5 mm in the anterior/posterior and top/bottom directions. Operators followed the interactive ElGuide template to digitize each electrode location. This process involved fully placing the wand tip into the electrode wells and ensuring that the receivers were able to see all emitters at the time of recording electrode locations, so that the estimated position of the wand tip was stable.

2.1.2. Structured-Light 3D Scan

We used an Einscan Pro+ (Shining 3D Tech. Co. Ltd., Hangzhou, China, **Figure 1C**) to digitize the electrodes with a structured-light 3D scanner. This scanner estimates the shape of an object from reflections of the projected visible lights. We calibrated the Einscan Pro+ one time with the Einscan's calibration board and followed the software's step-by-step instructions. We used the scanner's hand-held rapid mode with high details and allowed the scanner to track both texture and markers during the scanning process. Each operator scanned the mannequin head until the scan included the cap, fiducials, and the face. We then applied the watertight model option to the scan and exported the model as a PLY file to continue the digitization process in MATLAB.

After acquiring the 3D scan, the 3D head model needed to be imported into a software program, where the operator manually marked the EEG electrode locations on the 3D scanned head model. We followed the FieldTrip toolbox documentation for digitization using 3D scanners (FieldTrip, 2018) and created a MATLAB script file for importing and digitizing 3D models of the mannequin head. The operator first marked the fiducials on the mannequin head model in MATLAB to build up the head coordinate system. Then, the operator marked the locations of the electrodes on the screen in each section of the cap in alphanumerical order (A, B, C, D, and the fiducials, total: 131 locations, **Figure 1A**). The operators referred to a physical EEG cap for guidance to help mark the locations in the expected order because these scans were not in color and the letter labels of the electrodes were not visible on the 3D model.

2.1.3. Infrared 3D Scan

We used the Structure sensor (model ST01, Occipital Inc., San Francisco, CA) integrated with an Apple® iPad (10-inch Pro) to digitize the electrodes with an infrared dot-projection 3D scanner (**Figure 1D**). This scanner shares similar working principles as a structured-light scanner but uses infrared light projection to estimate the shape of objects. We calibrated the sensor in daylight and office light according to the manual. We scanned the head using the high color and mesh resolutions. When the mannequin head was completely in the sensor's field of view, the operator started scanning. The Structure sensor interface gives the operator visual feedback to help the operator obtain a complete high-quality scan. We visually inspected that the scanned model matched the mannequin and then exported the model to the MATLAB environment. We used the FieldTrip toolbox to import and digitize the 3D mannequin head scans following the same procedure described for the structured-light 3D scan digitization.

2.1.4. Motion Capture Probe

We used a digitizing probe and a 22-camera motion capture system (OptiTrack, Corvallis, OR) to digitize the electrodes. The probe is a solid rigid body with four fixed reflective markers (**Figure 1E**). We placed three reflective makers on the face of the mannequin to account for possible movements of the head during data collection. Each operator digitized the fiducials and each section of the cap (A, B, C, D, **Figure 1A**) in separate takes. We placed double o-rings 7 mm away from the probe tip to

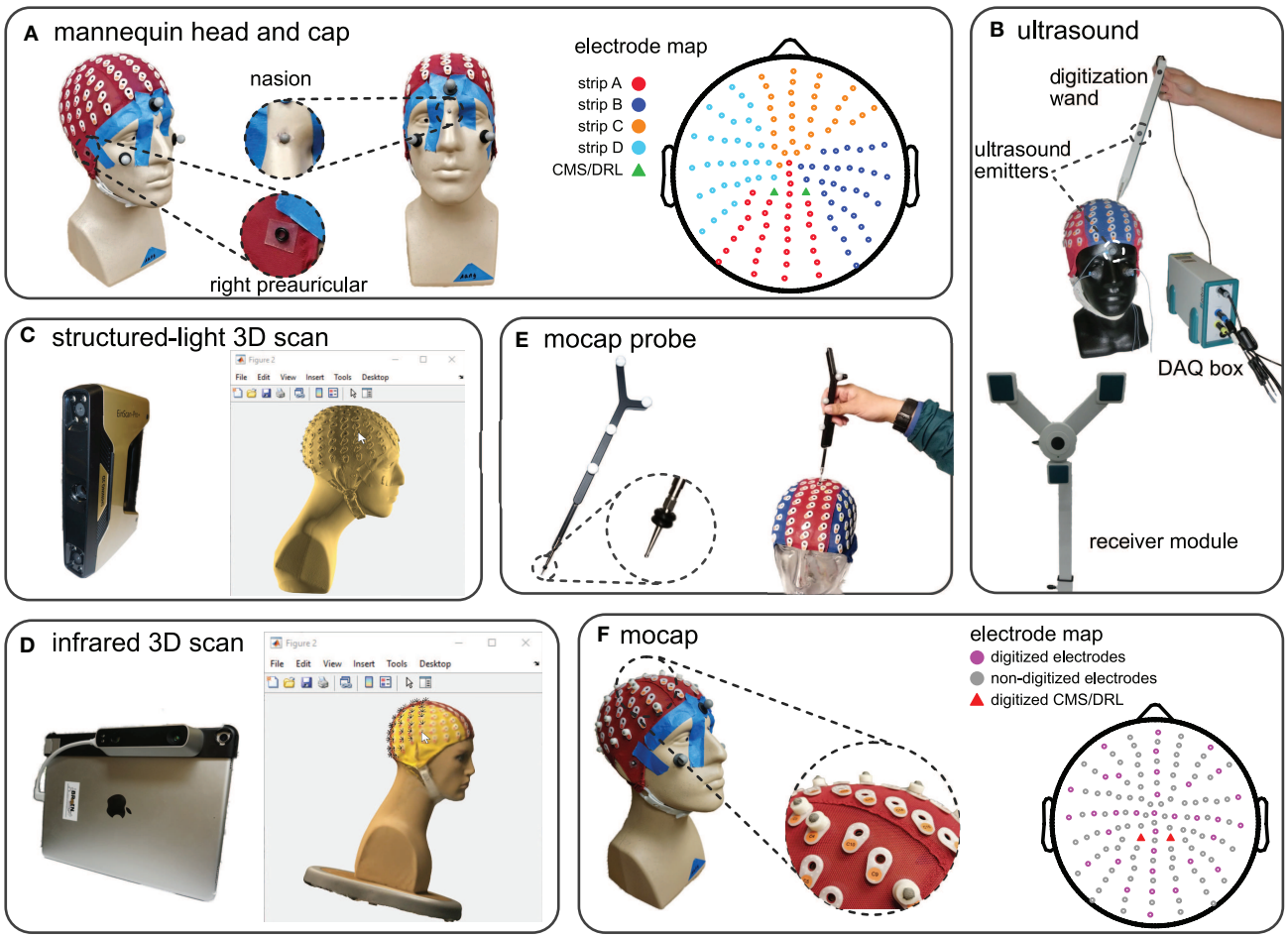

FIGURE 1 | The mannequin head used for digitization and the five digitizing methods tested. **(A)** The mannequin head fit with the 128-electrode EEG cap used for all of the digitizing recordings. The right and left preauriculars were marked by o-rings and nasion was marked with a reflective marker. The color-coded map of the cap shows the different electrode strips and the order of digitization from (A–D). **(B)** The ultrasound digitizing system and an operator placing the tip of the wand in the electrode well on the cap. Two of the total five ultrasound emitters on the face and wand, as well as the data acquisition (DAQ) box and the receiver module are also indicated. **(C)** The structured-light 3D scanner and an operator manually marking the locations of individual electrodes of the scanned model in MATLAB. **(D)** The infrared 3D scanner and an operator manually marking the locations of individual electrodes of the colored 3D scan in MATLAB. **(E)** The motion capture digitizing probe with a close-up view of the o-rings placed 7 mm away from the tip. The probe has a similar role to the wand in the ultrasound system. **(F)** The EEG cap with 35 3D-printed EEG electrode shaped reflective markers, 3 face markers, and 3 fiducial markers used for the motion capture digitization. We placed reflective markers on top of the preauricular o-rings to be able to capture fiducial locations. The electrode map depicts the approximate locations of the digitized electrodes and grounds.

ensure consistent placement of the tip inside the electrode wells (**Figure 1E**). The tracking error of the motion capture system was <0.4 mm.

2.1.5. Motion Capture

We used the motion capture system to record the locations of 35 3D printed reflective markers that resembled a 4-mm reflective marker on top of a BioSemi active pin electrode (**Figure 1F**). We did not use actual BioSemi electrodes, which have wires that could prevent the cameras from seeing the markers. We placed 27 EEG electrode shaped markers to approximate the international 10–20 EEG cap layout and placed an additional eight EEG electrode shaped markers randomly on the cap to add asymmetry to improve tracking of the markers. We recorded 2-s takes of the positions of the 35 markers, three markers on the fiducials, and three face markers. Before transforming the locations to the head coordinate system, we identified and canceled movements of the head during data collection using the three face markers.

2.2. Transformation to Head Coordinates

We developed a dedicated pipeline to convert the digitized electrode locations for each digitizing method to a format that could be imported to the common toolboxes for EEG analyses. Because EEGLAB and FieldTrip can easily read Zebris ElGuide's output file (an SFP file), we created SFP files for all digitizations.

The head coordinate system in ElGuide defines the X-axis as the vector connecting the left preauricular to the right preauricular and the origin as the projection of the naison to the X-axis. Therefore, the Y-axis is the vector from the origin to the

naison, and the Z-axis is the cross product of the X and Y unit vectors, which starts from the origin.

2.3. Digitization Reliability and Validity

Variations in the digitized electrode locations could originate from random errors and systematic bias. The effects of random errors can be quantified as variability. Reliability is inversely related to variability. Systematic bias can be quantified as the difference between measured locations and the ground truth locations. Validity is inversely related to systematic bias.

2.3.1. Digitization Reliability

To assess the effects of random errors, we quantified digitization variability. We averaged the five digitized locations for each electrode to find the centroid. We then calculated the average Euclidean distances of the five digitized points to the centroid for each electrode and averaged those distances for all of the electrodes to quantify within-method variability. We identified and excluded outliers, single measurements that were beyond five standard deviations of the average variability for a digitizing method (1 out of 655 measurements for ultrasound, 4 out of 655 measurements for motion capture probe and 2 out of 190 measurements for motion capture). If there were outliers, we recalculated the average digitization reliability with the updated dataset. Throughout the paper, we use "variability" to refer to "within-method variability." Because reliability is inversely related to the variability, the most reliable method has the least variability.

2.3.2. Digitization Validity

To quantify the systematic bias of a digitizing method, we calculated the average Euclidean distance between the centroid for a digitizing method and the ground-truth centroid for the same electrode. We used the electrode centroids from the most reliable digitizing method as the ground-truth (Dalal et al., 2014). Then, we averaged the Euclidean distances for the 128 electrodes to obtain the magnitude of the systematic bias for each digitizing method. Because validity is inversely related to the systematic bias, the most valid method has the least systematic bias.

2.4. Source Estimation Uncertainty

To generalize the possible effects of digitization reliability, we synthesized 500 sets of electrode locations with a Gaussian distribution using the variability average and standard deviation calculated for each digitizing method in section 2.3.1. We excluded the motion capture method from the source estimation uncertainty analyses because we only recorded the locations of 35 EEG electrode shaped reflective markers instead of all 128 EEG electrode locations. We used a single representative 128-channel EEG dataset from a separate study for the source estimation analyses. We applied the Adaptive Mixture Independent Component Analysis (AMICA) to decompose EEG signals into independent components (ICs) (Palmer et al., 2007), which has been reported to represent dipolar activities of different brain and non-brain sources (Delorme et al., 2012).

We used EEGLAB's DIPFIT toolbox version 2.3 to estimate a dipole equivalent for each IC and applied DIPFIT 500 times for each digitizing method. Each DIPFIT iteration used one of the 500 sets of synthesized electrode locations, the Montreal Neurological Institute (MNI) head model (Evans et al., 1993), and the ICs from the AMICA. The MNI head model is an averaged structural head model from 305 participants and provides 1 $\times$ 1 $\times$ 1 mm resolution. To convert the mannequin head to be compatible with the MNI model, we warped the electrode locations to the MNI model using only the fiducials to preserve individual characteristics of the mannequin head. We used the dipoles produced with the electrode location centroids from the digitizing method with the highest reliability and identified the dipoles that described >85% of the IC signal variance. We also excluded any dipole that was estimated to be outside of the brain volume for any of the DIPFIT results (500/method $\times$ five methods = 2,500 DIPFIT results). In the end, 23 ICs remained.

2.4.1. Spatial Uncertainty

We fitted an enclosing ellipsoid with the minimum volume to each IC's cluster of 500 dipoles (Moshtagh, 2005) and quantified spatial uncertainty in terms of the volume and width of the ellipsoid. A larger ellipsoid volume indicated that a single dipole could reside within a larger volume, and thus, had greater volumetric uncertainty. A larger ellipsoid width indicated that a single dipole could have a larger shift in location. We calculated the ellipsoid's width as the maximum distance that the IC's dipoles could have from one another. We averaged the volumes and widths of all 23 ICs to quantify the spatial uncertainty for each digitizing method.

2.4.2. Brodmann Area Accuracy

To identify Brodmann areas, we used a modified version of the `eeg_tal_lookup` function from EEGLAB's Measure Projection Toolbox (MPT). This function looks for the anatomic structures and Brodmann areas in a 10-mm vicinity of each dipole and assigns the dipole to the Brodmann area with the highest posterior probability (Lancaster et al., 2000; Bigdely-Shamlo et al., 2013). We identified the "ground-truth" Brodmann areas from the dipoles estimated using the centroid electrode locations of the most reliable digitizing method. Then, we calculated Brodmann area accuracy as the percentage of the other 500 Brodmann area assignments that matched the "ground-truth" Brodmann area.

We also analyzed Brodmann area accuracy using a template of electrode locations based on the MNI head model (Oostenveld and Praamstra, 2001). Because the BioSemi 128-electrode cap is not based on the 10-10 electrode map, instead of using the 10-10 electrode locations, we warped the BioSemi electrode locations to reside on the outer surface of the MNI head model. We then compared the Brodmann area identified from the template to the "ground-truth" Brodmann area. Since there is only one template for the Biosemi 128-electrode location on the MNI head model and the locations are fixed, we could not calculate a percentage of assignments; thus, the template's Brodmann area for each IC was either a hit or miss. However, we did calculate and compare the distance between the template's dipole to the "ground truth" dipole. We also compared the distance between each digitizing method's dipoles to the "ground truth" dipole. These distances

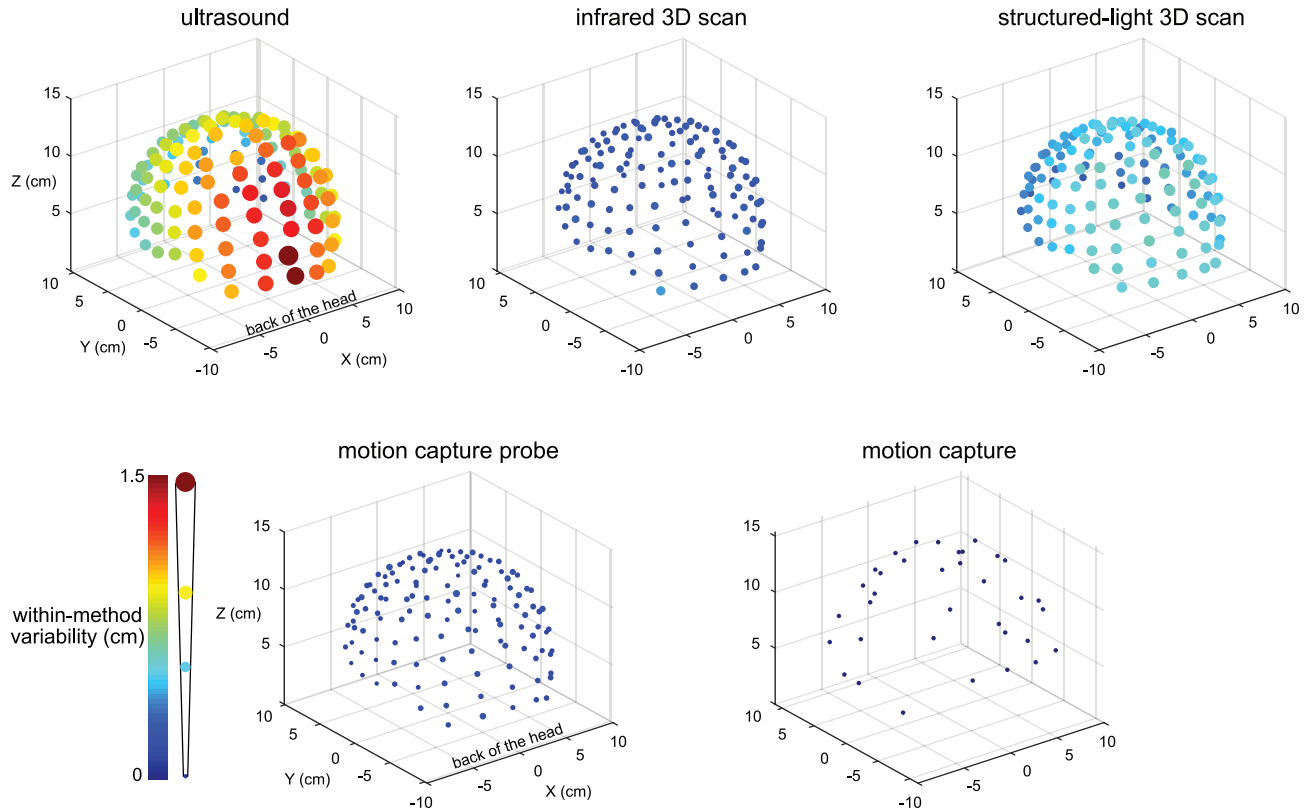

FIGURE 2 | Visualization of the digitization reliability. Colored and scaled dots show the electrode location within-method variability for all 128 electrodes for the five digitizing methods. Ultrasound had the greatest variability and was the least reliable. The electrodes at the back of the head also tended to have the greatest variability. The motion capture method had the least variability and was the most reliable. The color bar and scale for the radii of the dots illustrate the magnitude of variability.

indicated whether the dipoles estimated using each digitization method were near the "ground truth" dipole.

2.5. Statistical Analysis

We used a one-way repeated measures analysis of variance (rANOVA) to compare the reliability and validity of the digitizing methods, the spatial uncertainty of the estimated dipoles, and the Brodmann area accuracy. For significant rANOVA's, we performed Tukey–Kramer's *post-hoc* analysis to determine which comparisons were significant. We also performed a one-sided Student t-test to identify if the Brodmann area accuracy of each digitizing method was different from the template. The level of significance for all statistics was $\alpha = 0.05$. For rANOVA, we reported degrees of freedom (DF), Fisher's F-test result and the probability value (*p*-value). We used *p*-values to report *post-hoc* and Student t-test results.

Additionally, we fit a polynomial, using a step-wise linear model (MATLAB `stepwiselm` function), to describe spatial uncertainty as a function of digitization variability. We forced the y-intercept of the first-order polynomials and the y-intercept and y'-intercept of the higher-order polynomials to be zero. We set the y-intercepts to be zero for two reasons: (1) when we used the exact same electrode locations and performed DIPFIT 100 times, the maximum distance between source locations was on the order of 10^{-4} cm, and (2) the fit should not model the uncertainty values < 0 for positive digitization variability values. The step-wise linear model started with a zero order model and only added a higher-order polynomial term when necessary. The criterion for adding a higher-order polynomial term to the model was a statistically significant decrease of the sum of the squared error between the data points and the predicted values.

3. RESULTS

The variability results for the five digitizing methods were visibly different, and electrodes located at the back of the head tended to have greater variability (**Figure 2**). The variability for the ultrasound method was generally the largest compared to the other methods and could be as large as ∼1.5 cm for electrodes at the back of the head. The variability for all electrodes digitized with the motion capture method was small, being no greater than 0.001 cm.

There was a range of reliabilities among the digitizing methods (**Figure 3A**). The motion capture digitizing method had the smallest variability of 0.001 ± 0.0003 cm (mean ± standard deviation) and hence, the greatest digitization reliability. The motion capture probe was the next most reliable method with an average variability of 0.147 ± 0.03 cm, followed by the infrared

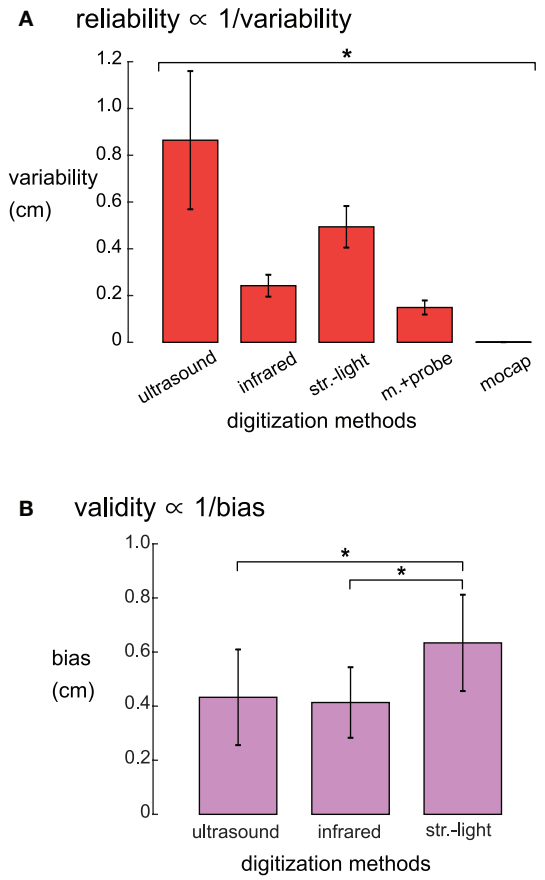

FIGURE 3 | (A) Reliabilities, quantified as the average variability, were significantly different for the five digitizing methods. The reliability of each digitizing method was significantly different from all other methods (*Tukey–Kramer *p*'s < 0.001 for all pair-wise comparisons). **(B)** Validity, quantified as the average systematic bias showed that the structured-light 3D scan had the largest systematic bias compared to ultrasound and the infrared 3D scan. The motion capture probe method was assumed to be the ground truth and thus has no systematic bias and is not shown. *Tukey–Kramer *p*'s < 0.001. Error bars are the standard deviation. Infrared = infrared 3D scan; str.-light = structured-light 3D scan; m.+probe = motion capture probe; mocap = motion capture.

3D scan (0.24 ± 0.05 cm), the structured-light scan (0.50 ± 0.09 cm), and the ultrasound digitization (0.86 ± 0.3 cm). The variability for the digitizing methods were significantly different (rANOVA $DF = 4$, $F = 1{,}121$, $p < 0.001$), and the variability for each digitizing method was significantly different from all other digitizing methods (*post-hoc* Tukey–Kramer, *p*'s < 0.001).

The systematic biases, thus validities, of the digitizing methods were significantly different (rANOVA $DF = 2$, $F = 143.1$, $p < 0.01$, **Figure 3B**). The digitization validity of the structured-light 3D scan was the worst of the digitizing methods with a systematic bias of 0.63 ± 0.18 cm that was significantly larger than the other digitizing methods (*post-hoc* Tukey–Kramer, *p*'s <0.001). The digitization validity of the ultrasound and the infrared 3D scans were similar, with systematic biases of 0.43 ± 0.18 and 0.41 ± 0.13 cm, respectively.

Within a given digitizing method, dipoles generally showed similar spatial uncertainty while different digitizing methods generally showed differences in spatial uncertainty (**Figure 4**). Ellipsoid sizes for the motion capture probe, infrared 3D scan, structured-light 3D scan, and ultrasound digitization increased in order from the smallest to the largest, respectively. The enclosing ellipsoids of adjacent ICs also overlapped when the ellipsoid size was large, on the order of 1 cm^3, such as for the ultrasound method.

Ellipsoid volumes increased significantly with increasing digitization variability among the digitizing methods and had a cubic relationship ($r^2 = 1.00$, **Figure 5A**). The motion capture probe and infrared 3D scan had the smallest uncertainty volumes (mean ± standard error) 0.007 ± 0.0007 and 0.029 ± 0.0027 cm^3, respectively, whereas ultrasound had the largest uncertainty volume (1.37 ± 0.13 cm^3). Structured-light 3D scan had an average uncertainty volume of 0.21 ± 0.014 cm^3. The volumes of the enclosing ellipsoids showed a significant between-group difference (rANOVA, $DF = 3$, $F = 114.4$, $p < 0.001$), and all uncertainty volume combinations of paired digitizing methods were significantly different (Tukey–Kramer *post-hoc*, *p*'s<0.001).

Ellipsoid widths also increased significantly with increasing digitization variability among the digitizing methods but had a linear relationship where the ellipsoid width was twice the size of the digitization variability ($r^2 = 1.00$, **Figure 5B**). The average ellipsoid width was the smallest for the motion capture probe (mean ± standard error), 0.34 ± 0.018 cm. The average ellipsoid widths for the two 3D scans were 0.53 ± 0.028 cm for the infrared 3D scan and 1.09 ± 0.051 cm for the structured-light 3D scan. The largest average ellipsoid width was for the ultrasound digitization, 1.90 ± 0.081 cm. The rANOVA for the widths of the enclosing ellipsoids showed a significant between-group difference ($DF = 3$, $F = 434.8$, $p < 0.001$) and all combinations of paired digitizing methods had significantly different uncertainty widths (Tukey–Kramer *post-hoc* *p*'s<0.001).

The Brodmann area accuracy among the digitizing methods could be extremely consistent within some ICs and could also be drastically different for other ICs (**Figure 6** and in **Figure S1**). In general, the digitizing method with the highest reliability also had the highest Brodmann area accuracy within a given IC. For some ICs, all digitizing methods had >98% Brodmann area accuracy. For other ICs, the Brodmann area accuracy decreased as reliability decreased. The most drastic example for this dataset was BA18 in **Figure 6**, where the Brodmann area accuracy was 86% with the motion capture probe method but dropped to 26% with the ultrasound method.

The Brodmann area accuracy for the digitizing methods and the template were significantly different (**Figure 7**). The motion capture probe had the highest Brodmann area accuracy, 93% ± 16 (mean ± standard deviation). The remaining digitizing methods in order of decreasing Brodmann area accuracy were the infrared 3D scan (91 ± 19%), the structured light 3D scan (87 ± 23%), and the ultrasound digitization (79 ± 25%). The rANOVA for the Brodmann area accuracy showed a significant between-group difference ($DF = 4$, $F = 306.4$, $p < 0.001$). *Post-hoc* Tukey–Kramer analysis showed significant pair-wise differences between all groups except the motion capture probe and infrared 3D scan.

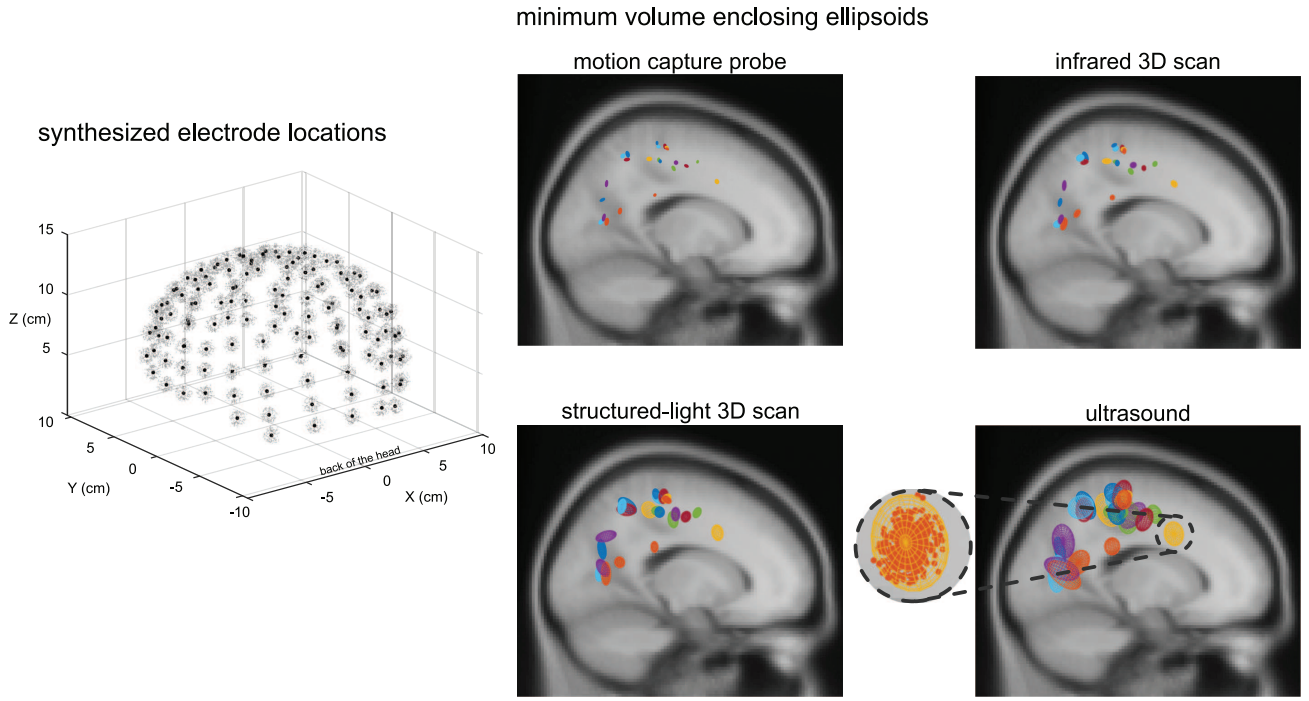

FIGURE 4 | An example depiction of the synthesized electrode locations with a Gaussian distribution using the same averaged variability and standard deviation as the structured-light 3D scans, and the enclosing ellipsoids of the 500 dipoles for each independent component (IC) and digitizing method. Black dots = centroids of the electrode locations. Light gray dots = first 150 out of 500 synthesized electrode locations. Each color represents a different IC (23 ICs total). A close-up view of the ellipsoid fit for an Anterior Cingulate IC based on the reliability of the ultrasound digitizing method.

Using the MNI electrode template decreased the Brodmann area accuracy to 53% and was significantly different compared to any of the digitizing methods (p's$<$0.001). The average distance of the dipoles of each digitizing method to the "ground-truth" dipole was $<$0.4 cm while the average distance of the template dipoles to the "ground-truth" dipole was $\sim$1.4 cm.

4. DISCUSSION

We found that there was a range of reliability and validity values among the digitizing methods. We also observed that less reliable digitizing methods translated to greater uncertainty in source estimation and poorer Brodmann area accuracy, assuming all other contributors to source estimation uncertainty were constant. Of the five digitizing methods (ultrasound, structured-light 3D scan, infrared 3D scan, motion capture probe, and motion capture), the most reliable digitizing method was the motion capture while ultrasound was the least reliable. The structured-light digitizing method had the greatest systematic bias and was thus the least valid method. We had hypothesized that less reliable digitizing methods would lead to greater source estimation uncertainty. In support of our hypothesis, digitizing methods with decreased reliability resulted in increased spatial uncertainty of the dipole locations and decreased Brodmann area accuracy. Surprisingly, any digitizing method led to an average Brodmann area accuracy of $>$80%. Using a template of electrode locations decreased Brodmann area accuracy to 53%. Overall, these results indicate that electrode digitization is crucial for accurate Brodmann area identification using source estimation and that more reliable digitizing methods are beneficial if the functional resolution for interpreting source estimation is more specific than Brodmann areas.

To help summarize the advantages of the different digitization systems, we created a table comparing the digitization reliability, dipole uncertainty, speed, affordability, and ease-of-use score, which are different factors that could influence which digitization a laboratory might choose to use (**Table 1**). We estimated the digitizing speed as how much time each digitization required. The fastest digitizing method that required manual electrode marking was the motion capture probe method, which took 5 min to mark each electrode and 5 min to calibrate the system. The least expensive system was the infrared 3D scanner, which is likely to become even less expensive as cameras on smartphones become more advanced and could soon be used to obtain an accurate 3D scan for digitizing EEG electrodes. We also surveyed the operators to score each digitization on a scale of 1–5, with 1 being easy to use. While performing the actual 3D scan was perceived as being easy, marking the electrodes in MATLAB was not an easy task. The operators indicated that the motion capture was the easiest and that ultrasound was the most difficult method to use. To create a final ranking, we averaged the rankings for each factor (digitization reliability, dipole uncertainty, speed, affordability, and ease-of-use) to obtain a method score. Based on the method score, the best digitizing method was the motion capture. The next best method was tied between the motion capture probe and infrared

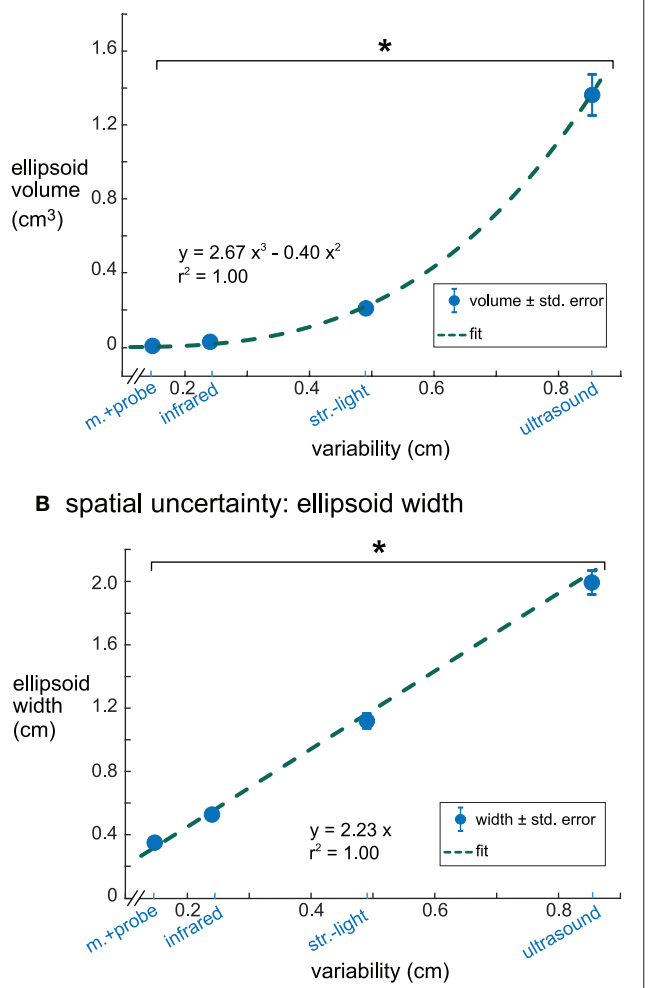

FIGURE 5 | The relationships between digitization variability and dipole spatial uncertainty. **(A)** Digitization variability and ellipsoid volume had a cubic relationship with an r^2 of 1.00. **(B)** Digitization variability and ellipsoid width had a linear relationship with an r^2 of 1.00. Error bars are the standard error. *Tukey–Kramer p's < 0.001 for all pair-wise comparisons. m.+probe = motion capture probe; infrared = infrared 3D scan; str.-light = structured-light 3D scan.

3D scan. The fourth best digitizing method was the structured-light 3D scan, and the worst digitizing method was the ultrasound method, which ranked poorly for all factors.

Our results suggest that the motion capture method currently provides the most reliable electrode digitization. The average variability of the motion capture digitization was less than the mean calibration error reported by the motion capture system (0.001 vs. <0.04 cm, respectively). This difference might be because of the different natures of the two variabilities. The digitization variability is defined for a seated subject (or mannequin) and multiple sub-second snapshots of the static electrodes placed on the cap. However, the mean calibration error is defined for a set of moving markers in a much larger volume across several minutes of a calibration period. Using the same position for mannequin placement and lack of head movement may have also contributed to the small digitization variability using motion capture. In a previous study, Reis and Lochmann developed an active-electrode motion capture approach for an EEG system with 30 electrodes and reported small deviation of the digitized locations from the ground truth locations (Reis and Lochmann, 2015). In addition to having sub-millimeter variability, the motion capture method only required 1–2 s to digitize, assuming that the markers were already placed on the EEG electrodes. However, tracking 64+ markers on an EEG cap may be challenging for most motion capture systems. Determining the maximum number of EEG electrodes that could be digitized using a motion capture approach could be beneficial and pursued in future work. Laboratories that already have a motion capture system and do not need to digitize more than 64 EEG electrodes could conveniently use the motion capture method, which would provide a cost-effective, fast, and easy digitizing process. For laboratories that need to digitize 64+ electrodes and have a motion capture system already, the motion capture probe digitizing method would be the recommended option.

Our results support recent efforts to use 3D scanners as a reliable and cost-effective method to digitize EEG electrodes (Chen et al., 2019; Homölle and Oostenveld, 2019; Taberna et al., 2019). Both the structured-light and infrared 3D scanning methods were more reliable than digitizing with the ultrasound method. Furthermore, our reliability results for the two 3D scanners align well with a recent study that showed that an infrared 3D scan could automatically digitize electrode locations on three different EEG caps and achieve good reliability after additional post-processing (Taberna et al., 2019). Of the two 3D scanners we tested, the less expensive infrared 3D scanner was more reliable, had higher validity, and resulted in less dipole uncertainty, compared to the structured-light 3D scanner. Even though the structured-light 3D scanner provides more details from the mannequin head and cap, those details did not seem to be important for improving digitization reliability or validity. Additionally, the highly detailed structured-light 3D scans created large files and resulted in sluggish refresh rates that made using FieldTrip toolbox to rotate and manipulate the 3D scans difficult. The infrared 3D scan, unlike the structured-light 3D scan, was in color, which was helpful for the operators to identify the EEG electrodes more easily on the computer screen. In the future, artificial intelligence approaches may be able to fully automate the digitizing process and use the additional topographic details from high resolution 3D scans. A continuous image-based digitizing method such as using a regular video recorded using a typical smartphone could also potentially be developed to digitize EEG electrode locations.

Compared to simulation studies, our experimental results demonstrated that source estimation uncertainty increased steeply with increasing EEG electrode variability. We showed that a digitizing method with an average variability of 1 cm could lead to a shift of a single dipole by more than 2 cm, which is >20% of the head radius. There is just one simulation study that we know of that also showed a two-fold increase

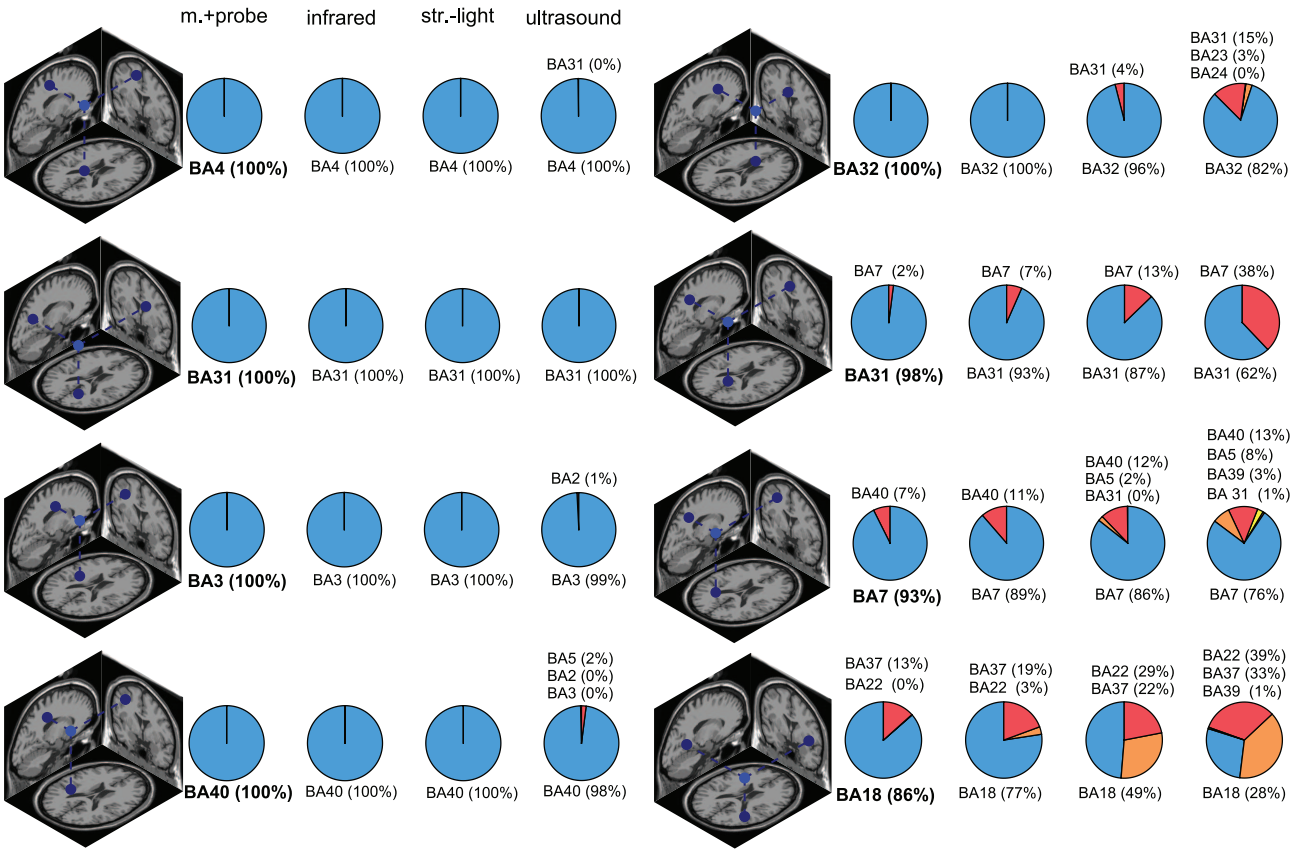

FIGURE 6 | Brodmann area (BA) accuracy for a subset of ICs. The dipole depicts the "ground truth" dipole produced from the most reliable digitizing method, the motion capture probe method. The pie charts show the distribution of the Brodmann area assignments compared to the "ground truth" Brodmann area (shown in bold). ICs in the left column had consistent Brodmann area assignments regardless of digitizing method while the ICs in the right column had more varied Brodmann area assignments for the different digitizing methods. In general, less reliable digitizing methods led to less consistent Brodmann area assignments. Infrared = infrared 3D scan; str.-light = structured-light 3D scan; m.+probe = motion capture probe.

in source uncertainty for every unit of digitization variability (Akalin Acar and Makeig, 2013). In that study, digitization variabilities were created using systematic rotations applied to every electrode location. The majority of the simulation studies however, suggest that source uncertainty could only be as large as the digitization variability (Khosla et al., 1999; Van Hoey et al., 2000; Wang and Gotman, 2001; Beltrachini et al., 2011). In one of the mathematical studies, the theoretical lower bound of source estimation uncertainty was 0.1 cm for 0.5 cm shifts in EEG electrode location (Beltrachini et al., 2011), which is 10x smaller than our experimental results. While simulation studies can be insightful, results should also be cross-validated with a conventional source estimation method (e.g., DIPFIT, LORETA, or minimum norm) to determine whether simulation results are indicative of real-world source estimation uncertainty.

Because researchers often use Brodmann areas to describe the function of a source, we translated our results to be in terms of Brodmann area accuracy, which led to a few surprising revelations. The main revelation was that despite the range of digitization reliabilities, any of the digitizing methods we tested produced an average Brodmann area accuracy >80%. As long as sources are only discussed according to Brodmann areas or larger cortical spatial regions, any current digitizing method can be used. The second revelation was that using the template electrode locations, instead of digitizing the electrodes, significantly decreased Brodmann area accuracy from >80% to ∼50%, which may be due to a ∼1.5 cm shift in dipoles locations (**Figure 7**). This shift may occur because the template removes information related to individual's head shape. The third revelation was that for several sources, the same Brodmann area was almost always identified, regardless of the digitizing method used (left column in **Figure 6**). For other sources, less reliable digitizing methods led to more potential Brodmann area assignments (right column in **Figure 6**), but those different Brodmann areas may be functionally similar. Most likely, the proximity of a source to the boundary of a Brodmann area as well as the size of the Brodmann area contribute to Brodmann area accuracy. Ultimately, the accuracy of source estimation will depend on the target volumes of cortical regions of interest.

This study does not account for all of the possible sources of errors contributing to digitizing EEG electrodes or source estimation. We placed markers on the fiducials to control for the digitization error of the fiducials, but in practice, marking the fiducials while the subject wears the cap can be challenging.

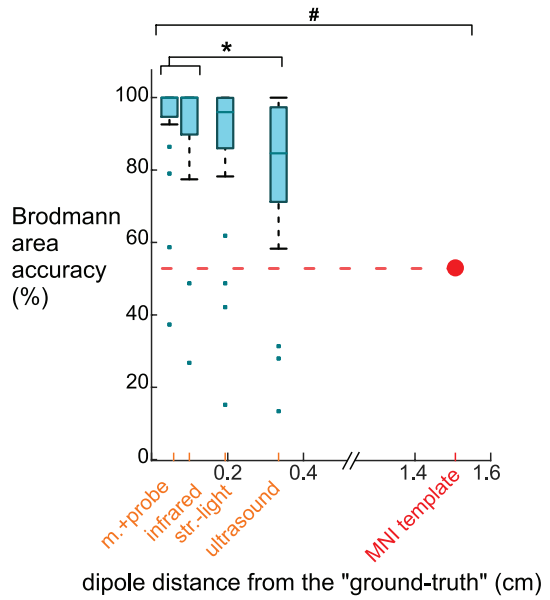

FIGURE 7 | Brodmann area accuracy plotted vs. the average dipole distance from the "ground truth" dipole when using different digitizing methods and the MNI template. Because larger distances between the dipoles and the "ground truth" likely would decrease Brodmann area accuracy, we plotted the methods on the x-axis at the method's averaged dipole distance from the "ground truth" dipole. The box-whisker plot contains the Brodmann area accuracy averages for the 23 ICs. The Brodmann area accuracy average for an IC was the average of the percentage of the 500 iterations when the Brodmann area identified matched the "ground truth" Brodmann area for that IC. For the template, 53% of the Brodmann areas assigned for the 23 ICs using the template matched the "ground truth" Brodmann area. The Brodmann area accuracy was significantly different among the digitizing methods, except between the motion capture probe and infrared 3D scan (*Tukey–Kramer p's < 0.001). The template's Brodmann area accuracy was significantly different than all digitizing methods ($^{\#}$ Student's t-test p's < 0.001). m.+probe = motion capture probe; infrared = infrared 3D scan; str.-light = structured-light 3D scan.

Mismarking a fiducial can significantly shift every dipole location by 2 times the distance of the fiducial mismarking (Shirazi and Huang, 2019a). We also used a mannequin to control for the head movements and relative cap movements to the head. In reality, participants may move their head and the cap may slightly change position during digitization or data collection that would affect the location of the EEG electrodes with respect to the head. Further, we only calibrated our digitizing devices once for multiple data collections. Nevertheless, in a real laboratory setup, device calibration might be required before each instance of data collection. We, however, included digitization by multiple experienced operators to acknowledge that in a research laboratory different members might complete the digitization for different participants. Overall, our results suggest that as long as all sources of digitization error do not create variability >1 cm, Brodmann area accuracy would be >80%. Using the same electrical head model and source localization approach helped us to only quantify the effects of digitization variability on source estimation uncertainty. In reality, the EEG signal noise, number and distribution of EEG electrodes, electrical properties of the head model, head model shape and mesh accuracy, and solving approach are among the other potential contributors to source estimation uncertainty (Akalin Acar and Makeig, 2013; Dalal et al., 2014; Song et al., 2015; Akalin Acar et al., 2016; Mahjoory et al., 2017; Beltrachini, 2019).

Limitations of this study were that we tested a subset of all digitizing methods, used a mannequin head, and not an actual human head for the digitization, and did not perform source estimation using other common algorithms. Even though we did not test many of the marketed digitizing systems, we replicated and tested the fundamental methods used by most of the marketed digitizing systems. One widely used EEG electrode digitizing method we did not test is an electromagnetic digitizing method (e.g., Polhemus Patriot or Fastrack system). Another study using similar digitization reliability analyses reported an average variability of 0.76 cm for an electromagnetic digitization system (Clausner et al., 2017), which is slightly better than the ultrasound digitizing method, with a variability of 0.86 ± 0.3 cm. Collecting digitization data from an actual participant might have helped in having a better distribution of the sources inside the brain volume, but we decided to use a mannequin to better control for head movements, relative cap movements and other environmental factors. Here, we used the EEG data only to provide a platform to understand the relationship between the digitization variability and source uncertainty, and locations of the sources do not have any neurological implications. Last, we did not use other different source estimation algorithms such as LORETA or beam-forming. Studies indicate that commonly used source estimation algorithms generally identify the similar source locations (Song et al., 2015; Bradley A. et al., 2016; Mahjoory et al., 2017), which suggests that the choice of the source estimation algorithm used would probably not significantly alter our results.

Future efforts to improve source estimation, so that sources can be interpreted in terms of cortical spatial regions smaller than Brodmann areas, will involve more than just developing more reliable, convenient, and cost-effective digitizing methods to help reduce source estimation uncertainty. Even if a perfect digitizing method could be developed, there would still be uncertainty in source estimation as result of other factors such as improper head-model meshes and inaccurate electrical conductivity values (Akalin Acar et al., 2016; Beltrachini, 2019), which were assumed to have a constant contribution to the source estimation uncertainty in our analyses. Obtaining and using as much subject specific information, such as subject-specific MRI scans in addition to digitizing EEG electrode locations, should improve source estimation. EEGLAB's Neuroelectromagnetic Forward Head Modeling Toolbox (NFT) could be used to warp the MNI head model to the digitized electrode locations to retain the individual's head shape but is computationally expensive (Acar and Makeig, 2010). Using subject-specific MRIs instead of the MNI head model is also limited to groups with access to an MRI at an affordable cost per scan.

5. CONCLUSION

In summary, there was a range of digitization reliabilities among the five digitizing methods tested (ultrasound,

TABLE 1 | Rankings for each digitizing method based on factors related to performance, cost, and convenience.

Method	Digitization reliability		Dipole uncertainty		Speed		Affordability		Ease-of-use (1 is easiest)	Method score (lower is better)
	Mean ± SD (cm)	#	Mean ± SD (cm)	#	Time (min)	#	Cost (USD)	#		
Ultrasound	0.86 ± 0.30	5	1.90 ± 0.39	4	30	5	15k	5	4.2	4.6
Infrared 3D scan	0.24 ± 0.05	3	0.53 ± 0.136	2	20 (10 for scan + 10 for marking in software)	3	1k	1	2.5	2.3
Str.-light 3D scan	0.50 ± 0.09	4	1.09 ± 0.24	3	25 (10 for scan + 15 for marking in software)	4	5k	2	3.4	3.3
Mocap probe	0.15 ± 0.03	2	0.34 ± 0.08	1	10 (5 for digitizing + 5 for calibration)	2	1k* (probe) 12k**(+mocap)	4	2	2.2
Mocap	0.001 ± 0.0003	1	N/A	-	5.1 (0.1 for digitizing + 5 for calibration)	1	11k**	3	1	1.5

*# is the rank of each method among all five methods and for the specified factor. The digitization reliability values and dipole uncertainty scalar width values were taken from our results. Speed was the approximate time a digitizing method required to obtain the file of electrode locations. The ease-of-use score was the average score operators provided in a survey with a score of 5 being the most difficult and 1 being the easiest method to do. The method score is the average rank of all factors for a given method and was defined as score=$\sum$ #/N. Dipole uncertainty was not available for motion capture digitization. Mocap = motion capture; Str.-Light 3D = structured-light 3D scan. *The probe price is for the OptiTrack digitizing probe. **Motion capture cost was for an eight-camera system (Optitrack Flex13, $8000) and the Optitrack Motive software ($3000).*

structured-light 3D scanning, infrared 3D scanning, motion capture with a digitizing probe, and motion capture with reflective markers), and less reliable digitization resulted in greater spatial uncertainty in source estimation and poorer Brodmann area accuracy. We found that the motion capture digitizing method was the most reliable while the ultrasound method was the least reliable. Interestingly, Brodmann area accuracy for a source only dropped from ∼90 to ∼80%, when using the most and least reliable digitizing methods, respectively. If source locations will be discussed in terms of Brodmann areas, any of the digitizing methods tested could provide accurate Brodmann area identification. Using a template of EEG electrode locations, however, decreased the Brodmann area accuracy to ∼50%, suggesting that digitizing EEG electrode locations for source estimation results in more accurate Brodmann area identifications. Even though digitizing EEG electrodes is just one of the factors that affects source estimation, developing more reliable and accessible digitizing methods can help reduce source estimation uncertainty and may allow sources to be interpreted in terms of cortical regions more specific than Brodmann areas in the future.

DATA AVAILABILITY STATEMENT

The datasets generated for this study are available on request to the corresponding author.

AUTHOR CONTRIBUTIONS

HH proposed the problem. SS and HH designed the experiment, conducted data collections, analyzed the data, and wrote and edited the manuscript.

FUNDING

This work was partially supported by the National Institute on Aging of the National Institutes of Health, under award number R01AG054621. The content is solely the responsibility of the authors and does not necessarily represent the official views of the National Institutes of Health.

ACKNOWLEDGMENTS

This manuscript has been released as a Pre-Print at BioRxiv (Shirazi and Huang, 2019b). MATLAB functions and dependencies for the motion capture and 3D scan digitizing methods are available on GitHub at: github.com/neuromechanist/eLocs.

SUPPLEMENTARY MATERIAL

The Supplementary Material for this article can be found online at: https://www.frontiersin.org/articles/10.3389/fnins.2019.01159/full#supplementary-material

REFERENCES

Acar, Z. A., and Makeig, S. (2010). Neuroelectromagnetic forward head modeling toolbox. *J. Neurosci. Methods* 190, 258–270. doi: 10.1016/j.jneumeth.2010.04.031

Akalin Acar, Z., Acar, C. E., and Makeig, S. (2016). Simultaneous head tissue conductivity and EEG source location estimation. *Neuroimage* 124(Pt A):168–180. doi: 10.1016/j.neuroimage.2015.08.032

Akalin Acar, Z., and Makeig, S. (2013). Effects of forward model errors on EEG source localization. *Brain Topogr.* 26, 378–396. doi: 10.1007/s10548-012-0274-6

ANT-Neuro (2019). *xensor^{TM}*. ANT neuro. Available online at: https://www.ant-neuro.com/products/xensor (accessed February 8, 2019).

Artoni, F., Menicucci, D., Delorme, A., Makeig, S., and Micera, S. (2014). RELICA: a method for estimating the reliability of independent components. *Neuroimage* 103, 391–400. doi: 10.1016/j.neuroimage.2014.09.010

Baysal, U., and Sengül, G. (2010). Single camera photogrammetry system for EEG electrode identification and localization. *Ann. Biomed. Eng.* 38, 1539–1547. doi: 10.1007/s10439-010-9950-4

Beltrachini, L. (2019). Sensitivity of the projected subtraction approach to mesh degeneracies and its impact on the forward problem in EEG. *IEEE Trans. Biomed. Eng.* 66, 273–282. doi: 10.1109/TBME.2018.2828336

Beltrachini, L., von Ellenrieder, N., and Muravchik, C. H. (2011). General bounds for electrode mislocation on the EEG inverse problem. *Comput. Methods Programs Biomed.* 103, 1–9. doi: 10.1016/j.cmpb.2010.05.008

Bigdely-Shamlo, N., Mullen, T., Kreutz-Delgado, K., and Makeig, S. (2013). Measure projection analysis: a probabilistic approach to EEG source comparison and multi-subject inference. *Neuroimage* 72, 287–303. doi: 10.1016/j.neuroimage.2013.01.040

Bradley, A., Yao, J., Dewald, J., and Richter, C. P. (2016). Evaluation of electroencephalography source localization algorithms with multiple cortical sources. *PLoS ONE* 11:e0147266. doi: 10.1371/journal.pone.0147266

Bradley, C., Joyce, N., and Garcia-Larrea, L. (2016). Adaptation in human somatosensory cortex as a model of sensory memory construction: a study using high-density EEG. *Brain Struct. Funct.* 221, 421–431. doi: 10.1007/s00429-014-0915-5

Chen, C., and Kak, A. (1987). "Modeling and calibration of a structured light scanner for 3-D robot vision," in *1987 IEEE International Conference on Robotics and Automation* (Raleigh, NC). doi: 10.1109/ROBOT.1987.1087958

Chen, S., He, Y., Qiu, H., Yan, X., and Zhao, M. (2019). Spatial localization of EEG electrodes in a TOF+CCD camera system. *Front. Neuroinform.* 13:21. doi: 10.3389/fninf.2019.00021

Clausner, T., Dalal, S. S., and Crespo-Garcia, M. (2017). Photogrammetry-Based head digitization for rapid and accurate localization of EEG electrodes and MEG fiducial markers using a single digital SLR camera. *Front. Neurosci.* 11:264. doi: 10.3389/fnins.2017.00264

Cline, C. C., Coogan, C., and He, B. (2018). EEG electrode digitization with commercial virtual reality hardware. *PLoS ONE* 13:e0207516. doi: 10.1371/journal.pone.0207516

Dalal, S. S., Rampp, S., Willomitzer, F., and Ettl, S. (2014). Consequences of EEG electrode position error on ultimate beamformer source reconstruction performance. *Front. Neurosci.* 8:42. doi: 10.3389/fnins.2014.00042

Delorme, A., and Makeig, S. (2004). EEGLAB: an open source toolbox for analysis of single-trial EEG dynamics including independent component analysis. *J. Neurosci. Methods* 134, 9–21. doi: 10.1016/j.jneumeth.2003.10.009

Delorme, A., Palmer, J., Onton, J., Oostenveld, R., and Makeig, S. (2012). Independent EEG sources are dipolar. *PLoS ONE* 7:e30135. doi: 10.1371/journal.pone.0030135

Engels, L., Warzee, N., and De Tiege, X. (2013). *Method of Locating EEG and MEG Sensors on a Head*. U.S. Patent No. EP2561810:A1.

Evans, A. C., Collins, D. L., Mills, S. R., Brown, E. D., Kelly, R. L., and Peters, T. M. (1993). "3D statistical neuroanatomical models from 305 MRI volumes," in *1993 IEEE Conference Record Nuclear Science Symposium and Medical Imaging Conference* (San Francisco, CA), 1813–1817. doi: 10.1109/NSSMIC.1993.373602

FieldTrip (2018). *Tutorial:3dscanner [FieldTrip]*. Available online at: http://www.fieldtriptoolbox.org/tutorial/electrode (accessed January 29, 2019).

He, B., and Musha, T. (1989). Effects of cavities on EEG dipole localization and their relations with surface electrode positions. *Int. J. Biomed. Comput.* 24, 269–282. doi: 10.1016/0020-7101(89)90022-6

Hedrich, T., Pellegrino, G., Kobayashi, E., Lina, J. M., and Grova, C. (2017). Comparison of the spatial resolution of source imaging techniques in high-density EEG and MEG. *Neuroimage* 157, 531–544. doi: 10.1016/j.neuroimage.2017.06.022

Homölle, S., and Oostenveld, R. (2019). Using a structured-light 3D scanner to improve EEG source modeling with more accurate electrode positions. *J. Neurosci. Methods* 326:108378. doi: 10.1016/j.jneumeth.2019.108378

Kavanagk, R. N., Darcey, T. M., Lehmann, D., and Fender, D. H. (1978). Evaluation of methods for three-dimensional localization of electrical sources in the human brain. *IEEE Trans. Biomed. Eng.* 25, 421–429. doi: 10.1109/TBME.1978.326339

Keil, A., Debener, S., Gratton, G., Junghöfer, M., Kappenman, E. S., Luck, S. J., et al. (2014). Committee report: publication guidelines and recommendations for studies using electroencephalography and magnetoencephalography. *Psychophysiology* 51, 1–21. doi: 10.1111/psyp.12147

Khosla, D., Don, M., and Kwong, B. (1999). Spatial mislocalization of EEG electrodes – effects on accuracy of dipole estimation. *Clin. Neurophysiol.* 110, 261–271. doi: 10.1016/S0013-4694(98)00121-7

Klamer, S., Elshahabi, A., Lerche, H., Braun, C., Erb, M., Scheffler, K., et al. (2015). Differences between MEG and high-density EEG source localizations using a distributed source model in comparison to fMRI. *Brain Topogr.* 28, 87–94. doi: 10.1007/s10548-014-0405-3

Klem, G. H., Lüders, H. O., Jasper, H. H., and Elger, C. (1999). The ten-twenty electrode system of the international federation. the international federation of clinical neurophysiology. *Electroencephalogr. Clin. Neurophysiol. Suppl.* 52, 3–6.

Kline, J. E., Huang, H. J., Snyder, K. L., and Ferris, D. P. (2015). Isolating gait-related movement artifacts in electroencephalography during human walking. *J. Neural Eng.* 12:046022. doi: 10.1088/1741-2560/12/4/046022

Koessler, L., Cecchin, T., Ternisien, E., and Maillard, L. (2010). 3D handheld laser scanner based approach for automatic identification and localization of EEG sensors. *Conf. Proc. IEEE Eng. Med. Biol. Soc.* 2010, 3707–3710. doi: 10.1109/IEMBS.2010.5627659

Koessler, L., Maillard, L., Benhadid, A., Vignal, J. P., Braun, M., and Vespignani, H. (2007). Spatial localization of EEG electrodes. *Neurophysiol. Clin.* 37, 97–102. doi: 10.1016/j.neucli.2007.03.002

Lancaster, J. L., Woldorff, M. G., Parsons, L. M., Liotti, M., Freitas, C. S., Rainey, L., et al. (2000). Automated talairach atlas labels for functional brain mapping. *Hum. Brain Mapp.* 10, 120–131. doi: 10.1002/1097-0193(200007)10:3<120::AID-HBM30>3.0.CO;2-8

Landsness, E. C., Goldstein, M. R., Peterson, M. J., Tononi, G., and Benca, R. M. (2011). Antidepressant effects of selective slow wave sleep deprivation in major depression: a high-density EEG investigation. *J. Psychiatr. Res.* 45, 1019–1026. doi: 10.1016/j.jpsychires.2011.02.003

Lantz, G., Grave de Peralta, R., Spinelli, L., Seeck, M., and Michel, C. M. (2003). Epileptic source localization with high density EEG: how many electrodes are needed? *Clin. Neurophysiol.* 114, 63–69. doi: 10.1016/S1388-2457(02)00337-1

Mahjoory, K., Nikulin, V. V., Botrel, L., Linkenkaer-Hansen, K., Fato, M. M., and Haufe, S. (2017). Consistency of EEG source localization and connectivity estimates. *Neuroimage* 152, 590–601. doi: 10.1016/j.neuroimage.2017.02.076

Marino, M., Liu, Q., Brem, S., Wenderoth, N., and Mantini, D. (2016). Automated detection and labeling of high-density EEG electrodes from structural MR images. *J. Neural Eng.* 13:056003. doi: 10.1088/1741-2560/13/5/056003

Moshtagh, N. (2005). *Minimum Volume Enclosing Ellipsoid*. Available online at: semanticscholar.org

Mullen, T., Kothe, C., Chi, Y. M., Ojeda, A., Kerth, T., Makeig, S., et al. (2013). Real-time modeling and 3D visualization of source dynamics and connectivity using wearable EEG. *Conf. Proc. IEEE Eng. Med. Biol. Soc.* 2013, 2184–2187. doi: 10.1109/EMBC.2013.6609968

Nordin, A. D., Hairston, W. D., and Ferris, D. P. (2018). Dual-electrode motion artifact cancellation for mobile electroencephalography. *J. Neural Eng.* 15:056024. doi: 10.1088/1741-2552/aad7d7

Nyström, P. (2008). The infant mirror neuron system studied with high density EEG. *Soc. Neurosci.* 3, 334–347. doi: 10.1080/17470910701563665

Oliveira, A. S., Schlink, B. R., Hairston, W. D., Konig, P., and Ferris, D. P. (2016). Induction and separation of motion artifacts in EEG data using a mobile phantom head device. *J. Neural Eng.* 13:036014. doi: 10.1088/1741-2560/13/3/036014

Oostenveld, R., Fries, P., Maris, E., and Schoffelen, J.-M. (2010). FieldTrip: Open source software for advanced analysis of MEG, EEG, and invasive electrophysiological data. *Comput. Intell. Neurosci.* 2011:156869. doi: 10.1155/2011/156869

Oostenveld, R., and Praamstra, P. (2001). The five percent electrode system for high-resolution EEG and ERP measurements. *Clin. Neurophysiol.* 112, 713–719. doi: 10.1016/S1388-2457(00)00527-7

Palmer, J. A., Kreutz-Delgado, K., Rao, B. D., and Makeig, S. (2007). "Modeling and estimation of dependent subspaces with non-radially symmetric and skewed densities," in *Independent Component Analysis and Signal Separation*, eds M.

E. Davies, C. J. James, S. A. Abdallah, and M. D. Plumbley (Berlin; Heidelberg: Springer), 97–104.

Reis, P. M., and Lochmann, M. (2015). Using a motion capture system for spatial localization of EEG electrodes. *Front. Neurosci.* 9:130. doi: 10.3389/fnins.2015.00130

Rodríguez-Calvache, M., Calle, A., Valderrama, S., López, I. A., and López, J. D. (2018). "Analysis of exact electrode positioning systems for multichannel-EEG," in *Applied Computer Sciences in Engineering*, eds J. Figueroa-Garca, E. Lpez-Santana, and J. Rodriguez-Molano (Cham: Springer International Publishing), 523–534.

Rogue-Resolutions (2019). *Brainsight TMS Navigation - Rogue Resolutions.* Available online at: https://www.rogue-resolutions.com/catalogue/neuro-navigation/brainsight-tms-navigation/ (accessed February 8, 2019).

Russell, G. S., Jeffrey Eriksen, K., Poolman, P., Luu, P., and Tucker, D. M. (2005). Geodesic photogrammetry for localizing sensor positions in dense-array EEG. *Clin. Neurophysiol.* 116, 1130–1140. doi: 10.1016/j.clinph.2004.12.022

Scarff, C. J., Reynolds, A., Goodyear, B. G., Ponton, C. W., Dort, J. C., and Eggermont, J. J. (2004). Simultaneous 3-T fMRI and high-density recording of human auditory evoked potentials. *Neuroimage* 23, 1129–1142. doi: 10.1016/j.neuroimage.2004.07.035

Seeber, M., Cantonas, L.-M., Hoevels, M., Sesia, T., Visser-Vandewalle, V., and Michel, C. M. (2019). Subcortical electrophysiological activity is detectable with high-density EEG source imaging. *Nat. Commun.* 10:753. doi: 10.1038/s41467-019-08725-w

Shirazi, S. Y., and Huang, H. J. (2019a). "Influence of mismarking fiducial locations on EEG source estimation*," in *2019 9th International IEEE/EMBS Conference on Neural Engineering (NER)* (San Francisco, CA), 377–380.

Shirazi, S. Y., and Huang, H. J. (2019b). More reliable EEG electrode digitizing methods can reduce source estimation uncertainty, but current methods already accurately identify brodmann areas. *bioRxiv* 557074. doi: 10.1101/557074

Song, C., Jeon, S., Lee, S., Ha, H. G., Kim, J., and Hong, J. (2018). Augmented reality-based electrode guidance system for reliable electroencephalography. *Biomed. Eng. Online* 17:64. doi: 10.1186/s12938-018-0500-x

Song, J., Davey, C., Poulsen, C., Luu, P., Turovets, S., Anderson, E., et al. (2015). EEG source localization: sensor density and head surface coverage. *J. Neurosci. Methods* 256, 9–21. doi: 10.1016/j.jneumeth.2015.08.015

Symeonidou, E.-R., Nordin, A. D., Hairston, W. D., and Ferris, D. P. (2018). Effects of cable sway, electrode surface area, and electrode mass on electroencephalography signal quality during motion. *Sensors* 18:E1073. doi: 10.3390/s18041073

Taberna, G. A., Marino, M., Ganzetti, M., and Mantini, D. (2019). Spatial localization of EEG electrodes using 3D scanning. *J. Neural Eng.* 16:026020. doi: 10.1088/1741-2552/aafdd1

Tsolaki, A. C., Kosmidou, V., Kompatsiaris, I. Y., Papadaniil, C., Hadjileontiadis, L., Adam, A., et al. (2017). Brain source localization of MMN and P300 ERPs in mild cognitive impairment and Alzheimer's disease: a high-density EEG approach. *Neurobiol. Aging* 55, 190–201. doi: 10.1016/j.neurobiolaging.2017.03.025

Van Hoey, G., Vanrumste, B., D'Havé, M., Van de Walle, R., Lemahieu, I., and Boon, P. (2000). Influence of measurement noise and electrode mislocalisation on EEG dipole-source localisation. *Med. Biol. Eng. Comput.* 38, 287–296. doi: 10.1007/BF02347049

Vema Krishna Murthy, S., MacLellan, M., Beyea, S., and Bardouille, T. (2014). Faster and improved 3-D head digitization in MEG using kinect. *Front. Neurosci.* 8:326. doi: 10.3389/fnins.2014.00326

Wang, Y., and Gotman, J. (2001). The influence of electrode location errors on EEG dipole source localization with a realistic head model. *Clin. Neurophysiol.* 112, 1777–1780. doi: 10.1016/S1388-2457(01)00594-6

Zhang, J., Chen, J., Chen, S., Xiao, G., and Li, X. (2014). Multimodal spatial calibration for accurately registering EEG sensor positions. *Comput. Math. Methods Med.* 2014:826019. doi: 10.1155/2014/826019

Conflict of Interest: The authors declare that the research was conducted in the absence of any commercial or financial relationships that could be construed as a potential conflict of interest.

Copyright © 2019 Shirazi and Huang. This is an open-access article distributed under the terms of the Creative Commons Attribution License (CC BY). The use, distribution or reproduction in other forums is permitted, provided the original author(s) and the copyright owner(s) are credited and that the original publication in this journal is cited, in accordance with accepted academic practice. No use, distribution or reproduction is permitted which does not comply with these terms.

frontiers in Neuroscience

ORIGINAL RESEARCH
published: 26 November 2019
doi: 10.3389/fnins.2019.01275

A Parallel Multiscale Filter Bank Convolutional Neural Networks for Motor Imagery EEG Classification

Hao Wu[1], Yi Niu[1], Fu Li[1]*, Yuchen Li[1], Boxun Fu[1], Guangming Shi[1] and Minghao Dong[2]**

[1] *Key Laboratory of Intelligent Perception and Image Understanding of Ministry of Education, School of Artificial Intelligence, Xidian University, Xi'an, China,* [2] *Engineering Research Center of Molecular and Neuroimaging, Ministry of Education, School of Life Sciences and Technology, Xidian University, Xi'an, China*

Objective: Electroencephalogram (EEG) based brain–computer interfaces (BCI) in motor imagery (MI) have developed rapidly in recent years. A reliable feature extraction method is essential because of a low signal-to-noise ratio (SNR) and time-dependent covariates of EEG signals. Because of efficient application in various fields, deep learning has been adopted in EEG signal processing and has obtained competitive results compared with the traditional methods. However, designing and training an end-to-end network to fully extract potential features from EEG signals remains a challenge in MI.

Approach: In this study, we propose a parallel multiscale filter bank convolutional neural network (MSFBCNN) for MI classification. We introduce a layered end-to-end network structure, in which a feature-extraction network is used to extract temporal and spatial features. To enhance the transfer learning ability, we propose a network initialization and fine-tuning strategy to train an individual model for inter-subject classification on small datasets. We compare our MSFBCNN with the state-of-the-art approaches on open datasets.

Results: The proposed method has a higher accuracy than the baselines in intra-subject classification. In addition, the transfer learning experiments indicate that our network can build an individual model and obtain acceptable results in inter-subject classification. The results suggest that the proposed network has superior performance, robustness, and transfer learning ability.

Keywords: EEG, BCI, motor imagery, deep learning, convolutional neural networks

OPEN ACCESS

Edited by:
Feng Liu,
Tianjin Medical University General Hospital, China

Reviewed by:
Tao Zhang,
University of Electronic Science and Technology of China, China
Li Dong,
University of Electronic Science and Technology of China, China

****Correspondence:***
Yi Niu
niuyi@mail.xidian.edu.cn
Fu Li
fuli@mail.xidian.edu.cn
Minghao Dong
dminghao@xidian.edu.cn

Specialty section:
This article was submitted to Brain Imaging Methods, a section of the journal Frontiers in Neuroscience

Received: *23 August 2019*
Accepted: *11 November 2019*
Published: *26 November 2019*

Citation:
Wu H, Niu Y, Li F, Li Y, Fu B, Shi G and Dong M (2019) A Parallel Multiscale Filter Bank Convolutional Neural Networks for Motor Imagery EEG Classification. Front. Neurosci. 13:1275. doi: 10.3389/fnins.2019.01275

INTRODUCTION

Brain–computer interfaces (BCI) establish a direct pathway between the human brain and a computer via brain signal recording and decoding techniques (Lance et al., 2012). Early BCI systems were mainly used for stroke rehabilitation or to improve quality of life for the disabled patients. BCI have been applied to control the devices such as electric wheelchairs (Galán et al., 2008), text spellers (Guan et al., 2005), and prosthetic artificial limbs (Schwartz et al., 2006). Recently, BCI have been widely applied not only for the disabled, but also for healthy people (Lance et al., 2012; Van Erp et al., 2012; Miranda et al., 2015; Saproo et al., 2016). Such BCI are mainly based on non-invasive systems with electroencephalogram (EEG) features, which may be integrated into wearable devices (Mullen et al., 2013, 2015). Functional magnetic resonance imaging (fMRI) based BCI are mainly used in medical treatment (Dong et al., 2014, 2019; Jin et al., 2018). However, it is difficult for such BCI to achieve real-time interaction. In general, BCI contain five major processing steps (Nicolas-Alonso and Gomez-Gil, 2012; Vernon et al., 2018): data collection, preprocessing (Bashashati et al., 2007),

feature extraction (Mcfarland et al., 2006), classification (Lotte et al., 2007), and feedback. Because EEG signals have a low signal-to-noise ratio (SNR) and time-dependent covariates, traditional research relies on expert-level experience and prior domain knowledge to design the paradigms and train the classifiers (Schlögl et al., 2005; Wang et al., 2005; Mcfarland et al., 2006; Lotte et al., 2007; Herman et al., 2008; Hsu and Sun, 2009; Suk and Lee, 2013) that would only apply to certain datasets (Wang et al., 2004). It is difficult to extend such strategy to other experiments and datasets (Krepki et al., 2007; Meng et al., 2016).

As a classic paradigm, motor imagery (MI) has been researched and developed for decades. Its physiological basis is that the body movement can produce mu (8–12 Hz) and beta (16–26 Hz) rhythms with event-related (de-)synchronization (ERS/ERD) in the motor sensory areas of the brain. Some research on MI-based devices (such as wheelchairs, prosthetics, and robots) has medical applications and provides human augmentation technologies. The dominant feature extraction algorithms for MI-EEG classification are the common spatial pattern (CSP) and its variants (Ramoser et al., 2000). The idea of CSP is to find a set of spatial filters that optimally discriminate multiple classes of EEG recordings. Benefiting from manual feature selection, filter-bank CSP (FBCSP) (Keng et al., 2012) algorithm selects optimal spatial filters to extract the features. This method has the advantages of simplicity and accuracy. Other CSP-based approaches also extract potentially valuable components of EEG signals after a certain analysis. Unfortunately, EEG features vary over time and change significantly in different individuals (Guger et al., 2003; Blankertz et al., 2010). For new applications of MI, a demand for robust and more general feature extraction techniques is gradually increasing.

Deep learning has made great achievements in computer vision, natural language processing, and speech recognition (Lecun et al., 2015; Schmidhuber, 2015). Currently, end-to-end DL frameworks unify multiple processing stages into one model and build a direct projection from input to output, having demonstrated excellent performance in various tasks (Sutskever et al., 2014; Chan et al., 2016; Redmon et al., 2016). This trend suggests that certain neural computing units, such as convolutional layers in convolutional neural networks (CNNs), can extract implicit features from the signals to improve the performance. The development of DL has also gained interest in the BCI community. Related research includes investigating DL-based models in EEG feature extraction (Li et al., 2015), epilepsy prediction and monitoring (Antoniades et al., 2016; Thodoroff et al., 2016), classification (Bashivan et al., 2015; Vernon et al., 2018), and auditory music retrieval (Stober et al., 2014). DL-based MI is reviewed in detail in the following subsection. However, the application of DL in EEG-based BCI has two challenges: (1) a low SNR and the time-dependent covariates of the EEG signal complicates the feature extraction; (2) insufficient datasets and individual differences in EEG signals among subjects lead to poor performance of transfer learning.

In this paper, we propose a new end-to-end architecture for MI EEG classification. In our layered network architecture, a parallel multiscale filter bank is designed to fully extract the temporal features. Additionally, square and log non-linear operations enhance the non-linear expression ability of the feature reduction layer. To enhance the transfer learning ability, the network initialization and fine-tuning strategy are proposed to train an individual model for inter-subject classification on small datasets. The classification accuracy of the proposed method in the intra-subject experiment is superior to the current well-known end-to-end networks. Inter-subject experiments prove that our proposed network not only obtains competitive results in transfer learning but also has acceptable performance on small datasets.

The rest of this paper is organized as follows. Related work is briefly introduced in section "Related Work." Section "Materials and Methods" describes the proposed MSFBCNN network in detail. The experiments and results are presented in section "Experiments and Results." In section "Discussion," we conclude the paper.

RELATED WORK

According to the input styles of the networks, DL-based MI is categorized into two types: the feature input network and the raw signal input network.

In the former input style, the MI is accomplished in two stages. First, EEG signals are transformed into vectors by traditional feature-extraction approaches (such as spectrograms, wavelets, and spatial filtering). Next, these feature vectors are fed into the networks. DL is adopted to train a model and classify the features. Kumar et al. (2017) used multilayer perceptrons (MLPs) to replace the traditional support vector machine classifier. Sakhavi et al. (2015) combined CNN and MLP as a new classifier to deal with multiclass MI-EEG tasks. To improve performance of networks, transfer learning and knowledge distillation were explored in which CNN was used as a specific 2D-input classifier (Sakhavi and Guan, 2017). Huijuan et al. adopted augmented-CSP and CNN to discriminate MI-EEG signals, surpassing FBCSP with a novel feature map selection scheme (Yang et al., 2015). Tabar and Halici (2017) fed time-frequency features generated by short-time Fourier transform into a CNN with stacked autoencoders and obtained a competitive accuracy. Bashivan et al. (2015) transformed the temporal EEG into topology-preserving multispectral images and trained a deep recurrent-convolutional network. Zhu et al. (2019) proposed a separated channel convolutional network to encode the multi-channel data. Then, the encoded features are concatenated and fed into a recognition network to perform the final MI task recognition.

The other input style fed time series EEG signals, i.e., the C (channel) $\times$ T (time point) matrices, into deep neural networks directly. Therefore, it is an end-to-end approach. In this network, the steps of feature extraction and classification are combined in a single end-to-end model, with (or without) only minimum preprocessing. The DL model has to learn both an optimal intermediate representation and a classifier for EEG signals in a supervised manner. Several end-to-end models have been proposed and obtained competitive performance in different tasks. As a light network, EEGNet used a few parameters to

achieve considerable performance on various EEG classification tasks. Inspired by FBCSP, Schirrmeister et al. (2017) proposed a shallow CNN and a deeper CNN respectively. Both of them yielded higher accuracies compared with FBCSP. Hauke et al. used a simplified CNN model to validate that a DL model was effective in transfer learning tasks for recordings from 109 subjects (Goldberger et al., 2000) without any preprocessing (Dose et al., 2018).

Both input styles have their advantages and disadvantages. The two-stage approach is interpretable and robust, which is guaranteed by handcrafted feature-extraction algorithms. Thus, it is suitable for small training sets and outperforms the traditional methods.

However, the feature input network lost some potential information after the handcrafted feature extraction, which affected the performance. On the contrary, end-to-end models may learn useful features automatically from raw EEG data and achieve satisfactory results. However, for small training datasets, it is hard for the end-to-end methods to train a satisfactory model. As follows from the literature, designing a feasible end-to-end deep neural architecture for MI-EEG classification remains a challenge.

In this paper, to overcome the problem of insufficient number of training samples and improve the robustness of the network, we will focus on the end-to-end style and propose a layered end-to-end network structure of CNNs for MI-EEG signal classification. It is well known that the insufficient number of training samples is prone to cause the overfitting problem of large networks. A common solution is to reduce the scale of network by dropout, network pruning, etc. These tricks work well for the signals with significant features like images and videos. For these signals, the network maybe confused to learn the most general distinguishable features from a small training set, thus one can sacrifice the network capacity to increase the generality and robustness. However, extracting the cerebral activity features from low SNR EEG signal is very challenging. A crude reduction of network connections may decrease the feature extraction capability of network. Therefore, we propose a layered network structure to accomplish the feature extraction task and feature reduction task separately. For feature extraction layer, we propose a MSFBCNN structure to extract sufficient potential features. For feature reduction layer, we adopt a set of non-linear operators followed by dropout connection strategy. In this way, the network is expected to be simplified without loss of feature extraction capacity which fits the characteristic of EEG signals.

MATERIALS AND METHODS

In this section, we first introduce the current datasets of MI. Next, a detailed architecture of the proposed network is described. Finally, a training strategy is presented.

Datasets Description

Currently, there are three publicly available MI-EEG datasets. The main differences of the datasets are the number of channels, trials, subjects, tasks, and sampling rates.

The first two datasets are the BCI Competition IV datasets 2a and 2b (Keng et al., 2012). Both of them have been preprocessed with a band-pass filter between 0.5 and 100 Hz. 2a is a 25-channel [22 EEG and 3 electro-oculogram (EOG)], 4-class MI (left/right hand, feet, and tongue) EEG dataset recorded from 9 different subjects with 250 Hz sampling rate. In the dataset, 9 train sets and 9 test sets are explicitly separated. In the subset, there are 72 trials in each class. The feedback is not provided. 2b is a 6-channel (3 EEG and 3 EOG), 2-class MI (left/right hand) dataset also recorded from 9 different subjects. For each subject, the MI task is separated into five sessions. Unlike the 2a dataset, the first two sessions in the 2B dataset run without feedback, except for the rest sessions.

The last dataset is a high gamma dataset (HGD) (Schirrmeister et al., 2017). In this dataset, 44-channel EEG signals are recorded from 14 subjects with 500 Hz sampling rate. Except subjects 1 and 5, the train sets from the remaining 12 subjects contain over 800 trials, thereby providing comparable data for further experiments.

Methods

End-to-end CNN has been widely used in MI classification and acquired satisfactory results. To fully use feature information in end-to-end networks to improve their performance, we proposed a layered network that is a feature-extraction network embedded into an end-to-end network.

For example, for a 3-s EEG signal with 22 electrodes and a 250 Hz sampling rate, the size of an input sample is 22×750. In end-to-end networks, CNN models process these rectangular EEG matrices and output their class labels. We propose a multilayer end-to-end network that consists of three parts: a front feature extraction layer, feature reduction layer, and classification layer. The detailed network architecture is described as follows.

Feature Extraction Layer

The features of EEG data are in two domains: temporal and spatial. Thus, we use separable 2D convolutions with kernel sizes $[k, 1]$ and $[1, c]$ (where k and c are integers) to extract temporal and spatial features, respectively. To fully extract temporal features and spatial features, we design a parallel multiscale filter bank convolutional neural network (MSFBCNN). The length of the filter is set manually, depending on the features and the sampling rate of the signal. The extracted temporal features are combined as an input of the spatial convolution after batch normalization. Next, we use a spatial convolution to extract spatial features and reduce dimensions of the feature map. After the spatial convolution, the dimension of EEG channel is squeezed to 1. Both temporal and spatial convolutions expand a third dimension of the feature maps.

Feature Reduction Layer

To enhance the non-linear expression ability of the network, we use square and log non-linear functions to extract features that are related to the band power. The temporal dimension and the third dimension are further reduced by a max-pooling layer. Because these operations are in the middle of the model, we call it a feature reduction layer.

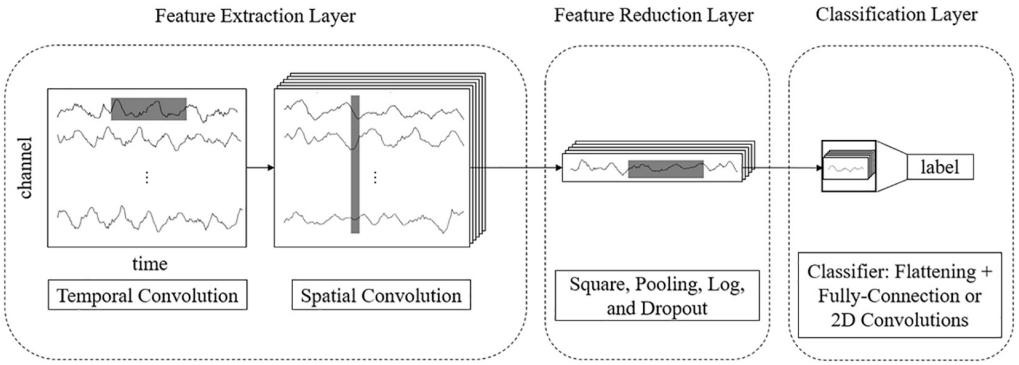

FIGURE 1 | Framework of the proposed MSFBCNN network.

Classification Layer

The classifier predicts the result after the previous step. As other CNN-based detection networks, the classification is performed by a fully connected layer (Simonyan and Zisserman, 2014).

The framework of the proposed MSFBCNN is shown in **Figure 1**. Unlike other EEG networks [such as EEGNet, ShallowFBCSPNet, and DeepNet (Schirrmeister et al., 2017)] or a simpler CNN model, we select the multiscale temporal convolution to extract the features and design the non-linear function, improving the network expression ability. Furthermore, we can set different learning rates in the layers of three subnetworks to avoid overfitting caused by insufficient data.

The detailed network architecture is described in **Figure 2** and **Table 1**. In **Table 1**, T is the number of time points, C is the number of channels, F_T is the temporal filter, F_S is the spatial filter, D is the ratio of F_T to F_S, and N_C is the number of classes. According to the receptive field theory, units in the last module interact with much broader range than that in the temporal convolutional module. Therefore, we simply design multiscale kernels in the temporal convolutional layer inspired by Inception (Szegedy et al., 2016) and Wide-ResNet (Zagoruyko and Komodakis, 2016). This reinforces the capacity of the temporal convolutions of extracting frequency-domain features. We concatenate the output feature maps to feed into the spatial convolutional module. As shown in **Table 1**, the kernel lengths of temporal filter F_T are set to 64, 40, 26, and 16. The length of the spatial filter is equal to the channel of the EEG data. In the feature reduction layer, the activation of the square and the logarithm operation is non-linear. A dropout layer follows the pooling layer to avoid overfitting, where dropout rate $p = 0.5$. A convolutional classifier outputs the predicted label. For the temporal convolution, the kernel length is likely to be selected arbitrarily.

Network Training

In the proposed MSFBCNN, we use a network training algorithm similar to those of CNNs. As for MI classification, the categorical cross-entropy loss function is defined as:

$$C(p, q) = -\sum_{i} p_i \log q_i, \quad i = 1, 2, \cdots, n \tag{1}$$

where p is the target distribution, q is the observed distribution, and n is the number of classes. We use the Adam method (Kingma and Ba, 2014) for optimization.

MI datasets have two drawbacks: (1) the number of samples is insufficient; (2) the features of the EEG data are different for each subject. The current MI networks are designed, trained, and tested for specific datasets. To improve the robustness of our proposed network, we design two strategies to enhance the transfer learning ability.

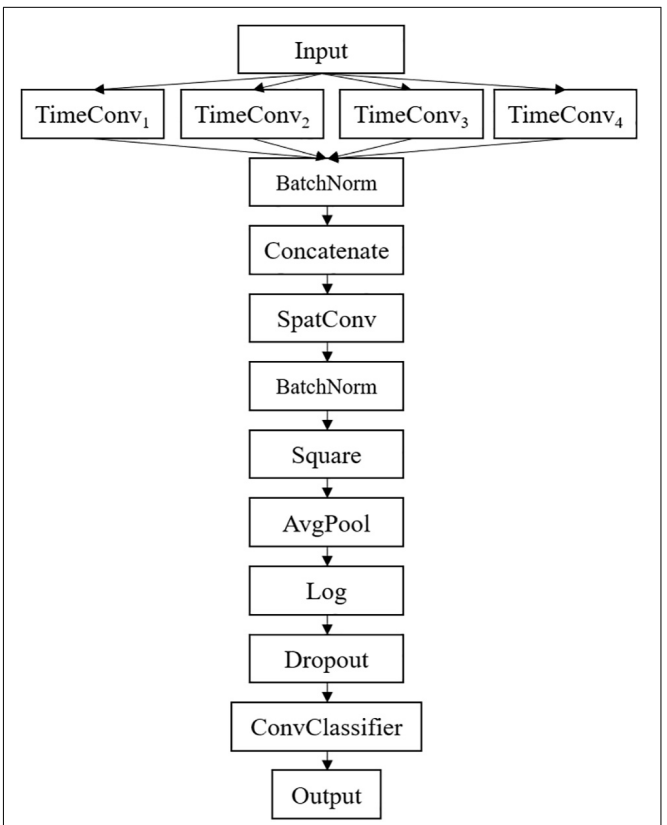

FIGURE 2 | Proposed MSFBCNN architecture.

TABLE 1 | Detailed architecture of the proposed network.

Layer	# Filters	Kernel	Stride	# Params	Output	Activation	Padding
Input					(C, T)		
Reshape					(1, T, C)		
TimeConv$_1$	F_T	(64, 1)	(1, 1)	$64 * F_T$	(F_T, T, C)	Linear	Same
TimeConv$_2$	F_T	(40, 1)	(1, 1)	$40 * F_T$	(F_T, T, C)	Linear	Same
TimeConv$_3$	F_T	(26, 1)	(1, 1)	$26 * F_T$	(F_T, T, C)	Linear	Same
TimeConv$_4$	F_T	(16, 1)	(1, 1)	$16 * F_T$	(F_T, T, C)	Linear	Same
Concat					($4 * F_T$, T, C)		
BatchNorm				$2 * F_T$	($4 * F_T$, T, C)		
SpatialConv	F_S	(1, C)	(1, 1)	$C * 4 * F_T * F_S$	(F_S, T, 1)	Linear	Valid
BatchNorm				$2 * F_S$	(F_S, T, 1)		
Non-Linear					(F_S, T, 1)	Square	
AveragePool		(75, 1)	(15, 1)		(F_S, T//15, 1)		Valid
Non-Linear						Log	
Dropout					(F_S, T//15, 1)		
Classifier	N_C	(T//15, 1)	(1, 1)	$F_S * (T//15) * N_C$	N_C	Linear	Valid

Network Initialization

The convolution layer weights are initialized using the normal distribution with zero mean and unit variance. The batch normalization layer weights use 1 for initialization. The learning rate is 1e−3, and the decay weight is 1e−7. The batch size is 64. These initialization parameters are acquired from the experiment in advance.

Fine-Tuning

First, we use the initial parameters to train the proposed network and acquire a coarse model from the open dataset. Next, for a specific subject dataset, the individual training data are mixed with a randomly selected open dataset and a validation set for further training. To avoid overfitting, we use a layered learning rate in the calibration experiment. The learning rates of the feature extraction layer, feature reduction layer, and classification layer are 1/27, 1/9, and 1/3 of the default learning rate, respectively.

Obviously, the coarse model has learned a general classifier. However, the fine-tuning strategy can further help the network to match the specific pattern of the individual subject. This strategy expands our training data and improves the transfer ability. Subsequently, the classifier is fine-tuned to match the specific pattern that relies on data from a specific subject.

EXPERIMENTS AND RESULTS

To verify the feasibility and performance of our proposed method, we conduct a series of experiments for MI classification. These experiments are run upon the Braindecode framework, which is supported by PyTorch.

The three datasets described in section "Datasets Description" are used for classification. Because the data collecting paradigms of the three datasets are similar, we extract the data of an epoch between 0 and 4.5 s after the corresponding trial starts from all datasets. To keep the same sampling rate for the first two datasets, the EEG recordings in HGD are resampled to 250 Hz. We do basic preprocessing, such as frequency filtering and normalization, to augment the SNR of the EEG data. All datasets are denoised by a low-pass filter of 38 Hz and a high-pass filter of 4 Hz. The amplitude of all EEG recordings is normalized by an exponential weighted moving average.

Intra-Subject Classification

The intra-subject classification experiment is a general benchmark to verify the performance of the proposed network for an individual subject. Each EEG dataset is divided into a train set, validation set, and test set. We use three state-of-the-art networks as baselines: DeepNet, EEGNet, and ShallowFBCSPNet. The same pipeline is used for all methods. The average accuracy of each network is collected after each model is trained and tested 10 times. The results are shown in **Table 2**. **Table 2** shows that our proposed MSFBCNN network acquires the best results on all datasets compared with the baselines. This is because our proposed network can fully extract the temporal features thanks to multiscale filter banks and the outstanding non-linear expression ability.

Inter-Subject Transfer Learning

To verify the transfer ability of the proposed method, we have conducted the inter-subject transfer experiment. In this experiment, EEG recordings from other subjects are used to train a model in advance. Next, the fine-tuning strategy is adopted to

TABLE 2 | Accuracy in intra-subject experiments.

	Dataset		
Network	**2a**	**2b**	**HGD**
DeepNet	66.8	83.6	84.8
EEGNet	66.7	83.1	84.0
ShallowFBCSPNet	72.3	81.5	91.6
MSFBCNN	75.8	84.3	94.4

further train the individual model. To verify the generality of the proposed fine-tuning strategy, we use this strategy for DeepNet, EEGNet, and ShallowFBCSPNet on three datasets. The results are shown in **Table 3**. Our proposed method has a higher accuracy than the baselines in inter-subject transfer learning. In addition, compared with the intra-subject experiment, the performance of all networks is improved after the fine-tuning, which proves that the proposed strategy is effective.

Transfer Learning on Small Datasets

Classification remains a challenge for a small number of training samples, because it is difficult for a model to learn the full distribution from insufficient data. This experiment verifies the performance of the proposed method for transfer learning on small datasets. It is a desideratum to use as few training samples as possible to achieve a satisfactory accuracy of the classification model. In this experiment, we select 10, 20, 50, and 100 samples, which are used in the inter-subject transfer learning experiment for fine-tuning. The classification accuracy results are shown in **Table 4**. The accuracy increases with the increase of the sample size. Moreover, we also find that our method obtains acceptable results with 100 samples compared with the inter-subject experiment in 2a and 2b datasets, which proves that the proposed fine-tuning strategy can enhance the transfer learning ability on small datasets.

Effects of Parallel Multiscale Filter Bank in Different Models

Existing MI networks are designed, trained and tested for specific datasets. As shown in **Table 2**, compared with DeepNet and EEGNet, ShallowFBCSPNet has better performance on 2a and HGD dataset but not on 2b dataset. In the proposed method, we introduce a parallel MSFBCNN for EEG-based BCI. The results on all of the three datasets prove that the performance of our MSFBCNN is better than other MI networks, which verifies that our method is robust on datasets.

TABLE 3 | Accuracy of inter-subject transfer learning.

	Dataset		
Network	**2a**	**2b**	**HGD**
DeepNet	71.9	84.1	90.9
EEGNet	69.9	83.6	88.6
ShallowFBCSPNet	73.8	83.7	92.3
MSFBCNN	75.9	84.7	94.9

TABLE 4 | Results of fine-tuning on a small number of training samples.

	Dataset		
Training samples	**2a**	**2b**	**HGD**
10	60.0	74.8	84.7
20	65.6	78.9	84.9
50	67.6	81.8	86.8
100	75.0	83.1	89.3

In the proposed method, we design a parallel multiscale filter bank convolution in our network. The essential is to fully extract potential features. To verify the validity of the parallel multiscale filter bank convolution structure, we embed the structure in EEGNet and DeepNet, named as T-EEGNet and T-DeepNet, respectively. We also carry out the experiments on the three datasets. The results are shown in **Table 5**. According to **Table 5**, impressive improvements are acquired compared with the original EEGNet and DeepNet after the adoption of the parallel multiscale filter bank convolution.

Although ShallowFBCSPNet has a parallel filter bank convolution, the kernel size is constant. It ignores the effect of multiscale on feature extraction. As shown in **Table 2**, our proposed method performs better than ShallowFBCSPNet.

DISCUSSION

Our work is devoted to designing and training an end-to-end network to fully extract temporal and spatial features from EEG signals. Compared with other three networks, we add a parallel multiscale filter bank convolution to our network and acquire impressive improvements. In addition, we embed the parallel multiscale filter bank convolution structure in EEGNet and DeepNet to verify the validity of the proposed structure.

In order to explore the parameter impact on the results, we did some experiments. There are two hyper-parameters in the proposed technique, F_T and F_s which denote the kernel number of temporal convolution and spatial convolution, respectively. To optimize the network, we have to search all the possible combinations of F_T and F_s. To accelerate the greedy search process, we introduce an intermediate parameter D which is the merchant of F_T and F_s. Like EEGNet, we enumerate a small range of D firstly, and adjust F_s with fixed D. For a comprehensive comparison work, we traverse the super-parameters of EEGNet. Effects of different F_T and D with comparison to the original are shown in **Table 6**. It can be observed that, the proposed MSFBCNN technique outperforms EEGNet's best performances in most of the cases. With the setup $F_T = 40$, $D = 1$ MSFBCNN achieves the best performances (75.8%).

To verify the network extracted features are valid, we do some feature visualizations. We plot the features map after extracting temporal feature on HGD, which is a 4-class MI (left/right hand, feet, and rest) dataset. The results are shown in **Figure 3**.

The visualization results show that the feature distributions are different from each other among different tasks. The extracted

TABLE 5 | Comparison of EEGNet, DeepNet, T-EEGNet, and T-DeepNet.

	Dataset		
Network	**2a**	**2b**	**HGD**
EEGNet	66.7	83.1	84.0
T-EEGNet	70.8	85.3	91.7
DeepNet	68.8	83.6	88.1
T-DeepNet	70.9	84.9	92.8

TABLE 6 | Effects of different F_T and D with comparison to the original.

			2a	2b
MSFBCNN	F_T	10	64.5	81.0
		20	67.9	80.8
		50	67.2	80.0
		80	66.6	79.9
	D	0.5	64.4	80.5
		2	65.3	80.0
		$F_T = 40, D = 1$	75.8	84.3
EEGNet	F_T	4	61.5	79.2
		16	63.6	77.1
		32	58.4	75.0
		40	56.2	72.0
	D	1	63.5	78.1
		4	55.4	76.8
		$F_T = 8, D = 2$	66.7	83.1

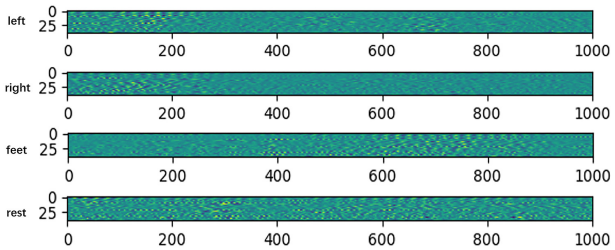

FIGURE 3 | Features map after extracting temporal feature on HGD. The x-axis denotes time, and the y-axis denotes the channel.

features of left-hand and right-hand tasks are mainly distributed in the 200 ms after the imaging, but they are different in channels. The feature of left-hand imagination is distributed from channel 0 to channel 25, while the feature of left-hand is mainly distributed in the channel from 25 to 44. The feature of feet task arises in the rear part of the 1 s dataset. The feature of rest task is distributed in all of the 1 s dataset.

Benefitting from the fine-tuning strategy with multilayer end-to-end structure, we can easily set layered learning rate for each of the three parts to avoid overfitting caused by insufficient data. In section "Inter-Subject Transfer Learning," we conduct the inter-subject transfer learning experiment. Compared with the intra-subject experiment results in **Table 2**, the performances of all networks in **Table 3** are improved after the fine-tuning, which proves that the proposed strategy is effective.

In transfer learning on small dataset experiment, our method obtains acceptable results with 100 samples compared with the inter-subject experiment in 2a and 2b datasets, which proves that the proposed fine-tuning strategy can enhance the transfer learning ability on small datasets.

Training network consumes a rather long time, but the network initialization and transfer learning on small dataset strategy can help us to build an individual model quickly on small training samples. After the training, the proposed method only takes 0.0128 s for prediction. Thus, we can build an online MI system to control the devices such as electric wheelchairs and prosthetic artificial limbs. Furthermore, we can use the proposed method on MI driver assistant system and human-machine collaborative system to improve the abilities of human.

The current work is mainly evaluated on datasets but not online. In our future work, we will further improve the efficiency transfer learning on small dataset experiment and try to build online human-machine collaborative system.

CONCLUSION

In this study, we propose a parallel MSFBCNN for EEG-based BCI, which can fully extract potential features from EEG and obtain an outstanding model in the presence of limited data. We introduce our layered end-to-end network structure in detail. The proposed structure has three parts: the front feature extraction layer, feature reduction layer, and classification layer. To enhance the transfer learning ability, we propose a network initialization and fine-tuning strategy for training the network. Finally, we compare our MSFBCNN with the state-of-the-art approaches for intra-subject classification. The classification accuracy indicates that our method outperforms the baselines. Additionally, inter-subject and small dataset experiments verify that our fine-tuning strategy can meet the transfer learning demands and obtain acceptable results.

DATA AVAILABILITY STATEMENT

The datasets 2a and 2b for this study can be found in the http://www.bbci.de/competition/iv/. The datasets HGD can be found in the https://github.com/robintibor/high-gamma-dataset/.

AUTHOR CONTRIBUTIONS

HW processed and analyzed the data, and wrote the manuscript. HW and YL developed the parallel multiscale filter bank convolutional neural network. BF helped in data analysis. YL helped in manuscript editing. FL, YN, and MD supervised the development of work, helped in manuscript editing and evaluation. FL and GS designed the research content and research direction.

FUNDING

This work was supported in part by the NSFC (Nos. 61672404, 61632019, 61751310, 61875157, and 61572387), National Key Research and Development Project (2018YFB2202400), National Defense Basic Scientific Research Program of China (JCKY2017204B102), Joint Fund of Ministry of Education of China (6141A020223), the Fundamental Research Funds of the Central Universities of China (Nos. JC1904, JBG160228, and JBG160213), and Natural Science Basic Research Plan in Shaanxi Province of China (Program No. 2016ZDJC-08).

REFERENCES

Antoniades, A., Spyrou, L., Took, C. C., and Sanei, S. (2016). "Deep learning for epileptic intracranial EEG data," in *Proceedings of the IEEE International Workshop on Machine Learning for Signal Processing*, Arlington, VA, 1–6.

Bashashati, A., Fatourechi, M., Ward, R. K., and Birch, G. E. (2007). A survey of signal processing algorithms in brain–computer interfaces based on electrical brain signals. *J. Neural Eng.* 4, R32–R57.

Bashivan, P., Rish, I., Yeasin, M., and Codella, N. C. (2015). Learning representations from EEG with deep recurrent-convolutional neural networks. *arXiv* [Preprint].

Blankertz, B., Sannelli, C., Halder, S., Hammer, E. M., Kübler, A., Müller, K.-R., et al. (2010). Neurophysiological predictor of SMR-based BCI performance. *Neuroimage* 51, 1303–1309. doi: 10.1016/j.neuroimage.2010.03.022

Chan, W., Jaitly, N., Le, Q. V., and Vinyals, O. (2016). "Listen, attend and spell: a neural network for large vocabulary conversational speech recognition," in *Proceedings of the International Conference on Acoustics, Speech, and Signal Processing*, Lujiazui, 4960–4964.

Dong, M., Jun, L., Xinfa, S., Shudan, G., Shijun, F., Zongquan, L., et al. (2019). Altered baseline brain activity in experts measured by amplitude of low frequency fluctuations (ALFF): a resting state fMRI study using expertise model of acupuncturists. *Front. Hum. Neurosci.* 9:99. doi: 10.3389/fnhum.2015.00099

Dong, M., Qin, W., Zhao, L., Yang, X., Yuan, K., Zeng, F., et al. (2014). Expertise modulates local regional homogeneity of spontaneous brain activity in the resting brain: an fMRI study using the model of skilled acupuncturists. *Hum. Brain Mapp.* 35, 1074–1084. doi: 10.1002/hbm.22235

Dose, H., Moller, J. S., Iversen, H. K., and Puthusserypady, S. J. E. S. W. A. (2018). An end-to-end deep learning approach to MI-EEG signal classification for BCIs. *Expert Syst. Appl.* 114, 532–542. doi: 10.1088/1741-2552/ab3471

Galán, F., Nuttin, M., Lew, E., Ferrez, P. W., Vanacker, G., Philips, J., et al. (2008). A brain-actuated wheelchair: asynchronous and non-invasive Brain–computer interfaces for continuous control of robots. *Clin. Neurophysiol.* 119, 2159–2169. doi: 10.1016/j.clinph.2008.06.001

Goldberger, A. L., Amaral, L. A. N., Glass, L., Hausdorff, J. M., Ivanov, P. C., Mark, R. G., et al. (2000). PhysioBank, physiotoolkit, and physionet components of a new research resource for complex physiologic signals. *Circulation* 101, 215–220.

Guan, C., Thulasidas, M., and Wu, J. (2005). "High performance P300 speller for brain-computer interface," in *Proceedings of the IEEE International Workshop on Biomedical Circuits and Systems 2004*, Vancouver, BC: IEEE.

Guger, C., Edlinger, G., Harkam, W., Niedermayer, I., and Pfurtscheller, G. (2003). How many people are able to operate an eeg-based brain-computer interface (bci)? *IEEE Trans. Neural Syst. Rehabil. Eng.* 11, 145–147. doi: 10.1109/tnsre.2003.814481

Herman, P., Prasad, G., Mcginnity, T. M., and Coyle, D. (2008). Comparative analysis of spectral approaches to feature extraction for EEG-based motor imagery classification. *IEEE Trans. Neural Syst. Rehabil. Eng.* 16, 317–326. doi: 10.1109/tnsre.2008.926694

Hsu, W. Y., and Sun, Y. N. (2009). EEG-based motor imagery analysis using weighted wavelet transform features. *J. Neurosci. Methods* 176, 310–318. doi: 10.1016/j.jneumeth.2008.09.014

Jin, C., Guan, M., Dong, M., Wu, J., He, Z., Chen, X., et al. (2018). Aberrant baseline brain activity in psychogenic erectile dysfunction patients: a resting state fMRI study. *Brain Imaging Behav.* 2, 1393–1404. doi: 10.1007/s11682-017-9805-9

Keng, A. K., Yang, C. Z., Chuanchu, W., Cuntai, G., and Zhang, H. (2012). Filter bank common spatial pattern algorithm on BCI competition IV datasets 2a and 2b. *Front. Neurosci.* 6:39. doi: 10.3389/fnins.2012.00039

Kingma, D. P., and Ba, J. (2014). Adam: a method for stochastic optimization. *arXiv* [preprint],

Krepki, R., Blankertz, B., Curio, G., and Müller, K.-R. (2007). The Berlin Brain-Computer Interface (BBCI) – towards a new communication channel for online control in gaming applications. *Multimedia Tools Appl.* 33, 73–90. doi: 10.1007/s11042-006-0094-3

Kumar, S., Sharma, A., Mamun, K., and Tsunoda, T. (2017). "A deep learning approach for motor imagery EEG signal classification," in *Proceedings of the 2016 3rd Asia-Pacific World Congress on Computer Science and Engineering (APWC on CSE)*, (Nadi: IEEE).

Lance, B. J., Kerick, S. E., Ries, A. J., Oie, K. S., and Mcdowell, K. (2012). Brain computer interface technologies in the coming decades. *Proc. IEEE* 100, 1585–1599. doi: 10.1088/1741-2560/5/1/P01

Lecun, Y., Bengio, Y., and Hinton, G. E. J. N. (2015). Deep learning. *Nature* 521, 436–444. doi: 10.1038/nature14539

Li, J., Struzik, Z. R., Zhang, L., and Cichocki, A. J. N. (2015). Feature learning from incomplete EEG with denoising autoencoder. *Neurocomputing* 165, 23–31. doi: 10.1016/j.neucom.2014.08.092

Lotte, F., Congedo, M., Lécuyer, A., Lamarche, F., and Arnaldi, B. (2007). A review of classification algorithms for EEG-based brain–computer interfaces. *J. Neural Eng.* 4, R1–R13.

Mcfarland, D. J., Anderson, C. W., Muller, K.-R., Schlogl, A., and Krusienski, D. J. (2006). BCI meeting 2005-workshop on BCI signal processing: feature extraction and translation. *Neural Inform. Process.* 14, 135–138. doi: 10.1109/tnsre.2006.875637

Meng, J., Zhang, S., Bekyo, A., Olsoe, J., Baxter, B., and He, B. J. S. R. (2016). Noninvasive electroencephalogram based control of a robotic arm for reach and grasp tasks. *Sci. Rep.* 6:38565. doi: 10.1038/srep38565

Miranda, R. A., Casebeer, W. D., Hein, A. M., Judy, J. W., Krotkov, E. P., Laabs, T. L., et al. (2015). DARPA-funded efforts in the development of novel brain–computer interface technologies. *J. Neurosci. Methods* 244, 52–67. doi: 10.1016/j.jneumeth.2014.07.019

Mullen, T., Kothe, C., Chi, M., Ojeda, A., Kerth, T., Makeig, S., et al. (2015). Real-time neuroimaging and cognitive monitoring using wearable dry EEG. *IEEE Trans. Biomed. Eng.* 62, 1–1.

Mullen, T., Kothe, C., Chi, Y. M., Ojeda, A., Kerth, T., Makeig, S., et al. (2013). Real-time modeling and 3D visualization of source dynamics and connectivity using wearable EEG. *Conf. Proc. IEEE Eng. Med. Biol. Soc.* 2013, 2184–2187. doi: 10.1109/EMBC.2013.6609968

Nicolas-Alonso, F. L., and Gomez-Gil, J. (2012). Brain computer interfaces, a review. *Sensors* 12, 1211–1279.

Ramoser, H., Muller-Gerking, J., and Pfurtscheller, G. (2000). Optimal spatial filtering of single trial EEG during imagined hand movement. *IEEE Trans. Rehabil. Eng.* 8, 441–446. doi: 10.1109/86.895946

Redmon, J., Divvala, S. K., Girshick, R., and Farhadi, A. (2016). "You only look once: unified, real-time object detection," in *Proceedings of the Conference on Computer Vision and Pattern Recognition*, (Las Vegas, NV: IEEE), 779–788.

Sakhavi, S., and Guan, C. (2017). "Convolutional neural network-based transfer learning and knowledge distillation using multi-subject data in motor imagery BCI," in *Proceedings of the International IEEE/EMBS Conference on Neural Engineering*, Shanghai: IEEE, 588–591.

Sakhavi, S., Guan, C., and Yan, S. (2015). "Parallel convolutional-linear neural network for motor imagery classification," in *Proceedings of the European Signal Processing Conference*, (Nice: IEEE), 2736–2740.

Saproo, S., Faller, J., Shih, V., Sajda, P., Waytowich, N. R., Bohannon, A., et al. (2016). Cortically coupled computing: a new paradigm for synergistic human-machine interaction. *IEEE* 49, 60–68. doi: 10.1109/mc.2016.294

Schirrmeister, R. T., Springenberg, J. T., Fiederer, L. D. J., Glasstetter, M., Eggensperger, K., Tangermann, M., et al. (2017). Deep learning with convolutional neural networks for EEG decoding and visualization. *Hum. Brain Mapp.* 38, 5391–5420. doi: 10.1002/hbm.23730

Schlögl, A., Lee, F., Bischof, H., and Pfurtscheller, G. (2005). Characterization of four-class motor imagery EEG data for the BCI-competition 2005. *J. Neural Eng.* 2, L14–L22.

Schmidhuber, J. (2015). Deep learning in neural networks: an overview. *Neural Netw.* 61, 85–117. doi: 10.1016/j.neunet.2014.09.003

Schwartz, A. B., Cui, X. T., Weber, D. J., and Moran, D. W. (2006). Brain-controlled interfaces : movement restoration with neural prosthetics. *Neuron* 52, 205–220. doi: 10.1016/j.neuron.2006.09.019

Simonyan, K., and Zisserman, A. (2014). Very deep convolutional networks for large-scale image recognition. *arXiv* [Preprint],

Stober, S., Cameron, D. J., and Grahn, J. A. (2014). "Using convolutional neural networks to recognize rhythm stimuli from electroencephalography recordings," in *Proceedings of the Neural Information Processing Systems*, Cambridge, MA, 1449–1457.

Suk, H. I., and Lee, S.-W. (2013). A novel bayesian framework for discriminative feature extraction in brain-computer interfaces. *IEEE Trans. Pattern Anal. Mach. Intell.* 35, 286–299. doi: 10.1109/tpami.2012.69

Sutskever, I., Vinyals, O., and Le, Q. V. (2014). Sequence to sequence learning with neural networks. *Adv. Neural Inform. Process. Syst.* 2, 3104–3112.

Szegedy, C., Ioffe, S., Vanhoucke, V., and Alemi, A. (2016). "Inception-v4, inception-resnet and the impact of residual connections on learning," in *Proceedings of the Thirty-First AAAI Conference on Artificial Intelligence*, San Francisco, CA, 4278–4284.

Tabar, Y. R., and Halici, U. (2017). A novel deep learning approach for classification of EEG motor imagery signals. *J. Neural Eng.* 14:016003. doi: 10.1088/1741-2560/14/1/016003

Thodoroff, P., Pineau, J., and Lim, A. (2016). Learning robust features using deep learning for automatic seizure detection. *Mach. Learn. Healthcare Conf.* 2016, 178–190. doi: 10.1016/j.clinph.2018.10.010

Van Erp, J., Lotte, F., and Tangermann, M. J. C. (2012). Brain-computer interfaces: beyond medical applications. *IEEE* 45, 26–34. doi: 10.1109/mc.2012.107

Vernon, L., Amelia, S., Nicholas, R. W. M., Gordon, S. M., Hung, C. P., and Lance, B. J. (2018). EEGNet: a compact convolutional neural network for EEG-based brain–computer interfaces. *J. Neural Eng.* 15:056013. doi: 10.1088/1741-2552/aace8c

Wang, Y., Gao, S., and Gao, X. (2005). Common spatial pattern method for channel selelction in motor imagery based brain-computer interface. *Conf. Proc. IEEE Eng. Med. Biol. Soc.* 5, 5392–5395.

Wang, Y., Zhang, Z., Li, Y., Gao, X., Yang, F., Gao, S., et al. (2004). BCI competition 2003-data set IV: an algorithm based on CSSD and FDA for classifying single-trial EEG. *IEEE Trans. Biomed. Eng.* 51, 1081–1086.

Yang, H., Sakhavi, S., Ang, K. K., and Guan, C. (2015). "On the use of convolutional neural networks and augmented CSP features for multi-class motor imagery of EEG signals classification," in *Proceedings of the International Conference of the IEEE Engineering in Medicine and Biology Society*, (Honolulu), 2620–2623.

Zagoruyko, S., and Komodakis, N. (2016). *Wide Residual Networks*. Paris: Université Paris-Est.

Zhu, X., Li, P., Li, C., Yao, D., Zhang, R., and Xu, P. (2019). Separated channel convolutional neural network to realize the training free motor imagery BCI systems. *Biomed. Sign. Process. Control* 49, 396–403.

Conflict of Interest: The authors declare that the research was conducted in the absence of any commercial or financial relationships that could be construed as a potential conflict of interest.

Copyright © 2019 Wu, Niu, Li, Li, Fu, Shi and Dong. This is an open-access article distributed under the terms of the Creative Commons Attribution License (CC BY). The use, distribution or reproduction in other forums is permitted, provided the original author(s) and the copyright owner(s) are credited and that the original publication in this journal is cited, in accordance with accepted academic practice. No use, distribution or reproduction is permitted which does not comply with these terms.

frontiers in Neuroscience

ORIGINAL RESEARCH
published: 27 November 2019
doi: 10.3389/fnins.2019.01282

Partial Least Squares Regression Performs Well in MRI-Based Individualized Estimations

*Chen Chen, Xuyu Cao and Lixia Tian**

School of Computer and Information Technology, Beijing Jiaotong University, Beijing, China

Estimation of individuals' cognitive, behavioral and demographic (CBD) variables based on MRI has attracted much research interest in the past decade, and effective machine learning techniques are of great importance for these estimations. Partial least squares regression (PLSR) is an attractive machine learning technique that can accommodate both single- and multi-label learning in a simple framework, while its potential for MRI-based estimations of CBD variables remains to be explored. In this study, we systemically investigated the performance of PLSR in MRI-based estimations of individuals' CBD variables, especially its performance in simultaneous estimation of multiple CBD variables (multi-label learning). We performed the study on the dataset included in the HCP S1200 release. Resting state functional connections (RSFCs) were used as features, and a total of 10 CBD variables (e.g., age, gender, grip strength, and picture vocabulary) were estimated. The results showed that PLSR performed well in both single- and multi-label learning. In fact, the present estimations were better than those reported in literatures, as indicated by stronger correlations between the estimated and actual CBD variables, as well as high gender classification accuracy (97.8% in this study). Moreover, the RSFCs that contributed to the estimations exhibited strong correlations with the CBD variable estimated, that is, PLSR algorithm automatically selected the RSFCs closely related to one CBD variable to establish predictive models for the variable. Besides, the estimation accuracies based on RSFCs among 100, 200, and 300 regions of interest (ROIs) were higher than those based on RSFCs among 15, 25, and 50 ROIs; the estimation accuracies based on RSFCs evaluated using partial correlation were higher than those based on RSFCs evaluated using full correlation. In addition to the aforementioned virtues, PLSR is efficient in model training and testing, and it is simple and easy to use. Therefore, PLSR can be a favorable choice for future MRI-based estimations of CBD variables.

Keywords: machine learning, multi-label learning, regression, classification, resting state fMRI, resting state functional connection, Human Connectome Project, partial correlation

OPEN ACCESS

Edited by:
Xi-Nian Zuo,
Institute of Psychology (CAS), China

Reviewed by:
Xin Di,
New Jersey Institute of Technology, United States
Veena A. Nair,
University of Wisconsin–Madison, United States

***Correspondence:**
Lixia Tian
lxtian@bjtu.edu.cn;
tian.bme@gmail.com

Specialty section:
This article was submitted to Brain Imaging Methods, a section of the journal Frontiers in Neuroscience

Received: *01 September 2019*
Accepted: *12 November 2019*
Published: *27 November 2019*

Citation:
Chen C, Cao X and Tian L (2019) Partial Least Squares Regression Performs Well in MRI-Based Individualized Estimations. Front. Neurosci. 13:1282. doi: 10.3389/fnins.2019.01282

Abbreviations: CBD, cognitive, behavioral and demographic; CSCC, composite score of crystallized cognition; CSFC, composite score of fluid cognition; CSOC, composite score of overall cognition; E-Net, elastic net; ICA, independent component analysis; PLSR, partial least squares regression; RMSE, root mean square error; ROI, regions of interest; RSFCs, resting state functional connections; RVR, relevance vector regression; SVR, support vector regression.

INTRODUCTION

Individual differences in brain structure and function exist even among persons with no diagnosable neurological or psychiatric diseases. Numerous studies have been performed to relate these differences to variability in CBD variables (for reviews, see Kanai and Rees, 2011; Parasuraman and Jiang, 2012). Besides these studies on the neural basis of individual differences in CBD variables using statistical techniques, there is a surge of interest in estimating individuals' CBD variables using machine learning techniques based on MRI-derived brain structural and functional measures (for reviews, see Arbabshirani et al., 2017; Rathore et al., 2017). These studies have taken an important step toward individualized estimations of CBD variables.

In the studies on individualized estimations of CBD variables, machine learning techniques play critical roles. A variety of machine learning techniques have been used to establish estimation models. The most frequently used techniques are support vector machine (SVR) (Feis et al., 2013; Ullman et al., 2014), elastic net (E-Net) (Tian et al., 2016; Cui and Gong, 2018), relevance vector regression (RVR) (Stonnington et al., 2010; Franke et al., 2012; Gong et al., 2014) and linear regression (Finn et al., 2015; Rosenberg et al., 2016). Each of these techniques is specialized for single-label learning; that is, the models built based on these techniques estimate one variable at a time. The extensive use of these techniques in MRI-based estimations benefit from three of their advantages: (1) being simple and easy to use; (2) offering high estimation accuracies; and (3) enabling later inferences of the biological significance underlying the estimations.

Besides the aforementioned single-label learning techniques, multi-label learning techniques have attracted widespread attention in the region of machine learning in recent years. For MRI-based estimations, multi-label learning enables simultaneously estimation of multiple CBD variables and thus can provide richer information as compared to single-label learning. For instance, for the case of the diagnosis of Alzheimer's disease (AD), multi-label learning enables simultaneous estimation of categorical variable (with value of either 'AD' or healthy control) and numerical variables such as Mini Mental State Examination (MMSE) and Alzheimer's Disease Assessment Scale-Cognitive Subscale (ADAS-Cog) (Zhang et al., 2012), while single-label learning can only estimate one variable at a time. Moreover, multi-label learning is expected to obtain equally high, or even higher, estimation accuracies by utilizing the correlation information among different labels (for a review, see Zhang and Zhou, 2014). To date, there have been several studies on MRI-based estimations of CBD variables using multi-label learning techniques (Zhang et al., 2012; Wan et al., 2014; Yu et al., 2016; Adeli et al., 2019). However, the complexity of the multi-label learning frameworks in these studies hampers their widely use in the region, even though relatively high estimation accuracies can be obtained. Moreover, complicated learning frameworks make it difficult to infer the biological significance underlying the estimations. In fact, effective, simple and convenient multi-label learning techniques for MRI-based estimations of CBD variables are lacking.

Partial least squares regression (PLSR) is a machine learning technique that can solve both single- and multi-label learning problems. Partial least squares models relationships between sets of observed variables with "latent variables" (Wold, 1982). By virtue of its computational efficiency (projecting 1000s of features into a very low-dimensional subspace), as well as its ability of achieving dimensionality reduction and model learning simultaneously, PLSR can be a valuable choice for prediction purpose. In fact, PLSR has been reported to perform well in such areas as computer vision (Guo and Mu, 2011), food science (Cozzolino et al., 2005), remote sensing (Hansen and Schjoerring, 2003), and geoinformation (Cho et al., 2007). Especially, it was reported to perform well in simultaneously estimating individuals' age and classifying their gender and ethnicity based on face images (Guo and Mu, 2011, 2013). In the neuroimaging region, Krishnan et al. (2011) foresaw the potential of PLSR in MRI-based estimations and described its main computational steps with a small artificial example. Afterward, PLSR has been used to estimate individuals' full scale IQ (Yang et al., 2013), motor skill acquisition (Wu et al., 2014), episodic memory performance (Meskaldji et al., 2016), long-term-memory scores (Meskaldji et al., 2016), clinical depression scores (Yoshida et al., 2017), attentional abilities (Yoo et al., 2018), gender (Zhang et al., 2018), and future processing speed (Kuceyeski et al., 2018) based on MRI data. To note, a single variable was estimated in most of these studies. That is, the potential of PLSR for MRI-based estimations of CBD variables remains to be explored, especially its potential for simultaneous estimations of individuals' multiple CBD variables.

In addition to machine learning techniques, appropriate brain structural and functional measures (features) are also important for MRI-based estimations. RSFCs have been one of the most commonly used features in MRI-based estimations of CBD variables (for a review, see Rathore et al., 2017). RSFCs measure the synchrony of resting state fMRI signals between brain regions and have been suggested to reflect the intrinsic architecture of the human brain (Biswal et al., 1995; Fox and Raichle, 2007). With the widespread availability of resting-state fMRI datasets of large sample sizes, RSFC has become one of the few most frequently used features for MRI-based estimations. To date, RSFCs have been reported to be effective for estimating a variety of CBD variables, such as sustained attention (Rosenberg et al., 2016; Yoo et al., 2018), intelligence quotient (Finn et al., 2015), creativity (Beaty et al., 2018), visual/verbal memory (Siegel et al., 2016), and temperament traits (Jiang et al., 2018), as well as age (Dosenbach et al., 2010) and gender (Feis et al., 2013; Zhang et al., 2018). These studies demonstrated the effectiveness of RSFCs for estimations of CBD variables.

In this study, we systemically investigated the performance of PLSR in MRI-based estimations of individuals' CBD variables (sometimes referred to as "labels" below), especially its performance in multi-label learning. We performed the study on the large sample resting state fMRI data from the HCP S1200 release. The RSFCs among the ROIs defined by ICA were used as features, and four sets of estimations were performed to make a full understanding of the performance of PLSR in MRI-based estimations. The first set was performed to test the

performance of PLSR on MRI-based multi-label learning. Here, we systemically analyzed the influences of ROI definition, RSFC evaluation strategies and the number of latent variables upon the estimations. In the second set, we simultaneously estimated another group of labels that have been estimated in other studies (Cui and Gong, 2018[1]), to provide an intuitive idea about the relative effectiveness of PLSR in MRI-based estimations. The third set was to test whether PLSR can accommodate more variables, by entering all CBD variables included in the aforementioned two groups into a single estimation model. The fourth set tested the performance of PLSR on single-label learning.

MATERIALS AND METHODS

Dataset

The publicly available dataset HCP S1200 release[2] was used in this study. For the current study, HCP data have two major advantages. First, the high quality of HCP data guarantees the reliability of RSFCs and CBD variables (Feinberg et al., 2010; Moeller et al., 2010; Setsompop et al., 2012; Xu et al., 2012), which are the basis for later PLSR model training. Second, the sample size of HCP S1200 is large enough to avoid any possible overfitting (Cui and Gong, 2018), which is often the case in estimations of CBD variables based on small sample MRI data.

The HCP S1200 release includes high quality multi-modal neuroimaging, behavioral and genotype data of nearly 1,100 healthy young adults (Van Essen et al., 2013; Glasser et al., 2016). Resting state fMRI data and several CBD variables were analyzed in this study. The following is a detailed description of the data we used.

Four resting state fMRI runs were acquired over 2 days for each subject. Each run lasted 15 min, with an isometric spatial resolution of 2 mm and a temporal resolution of 0.7 s. Details about data acquisition could be found in Smith et al. (2013). Based on rigorous quality control, the resting state fMRI data of 1,003 subjects were made available.

A total of 10 CBD variables were used in this study, and details about the variables can be found in **Table 1**. We used age, education, composite scores of fluid cognition (CSFC), crystallized cognition (CSCC), and overall cognition (CSOC) as the main estimation variables, and this group of variables will sometimes be referred to as "main labels" below. We chose to estimate age and intelligence for the consideration that they play important roles in human life. In fact, a number of studies have been performed on the estimations of age and intelligence based on MRI (Dosenbach et al., 2010; Finn et al., 2015). Age and education level were measured in years, and CSFC, CSCC, and CSOC were obtained based on the NIH Cognition Battery Toolbox. As age was also included as a label here, non-age-adjusted CSFC, CSCC, and CSOC (raw scores) were used in this study. The CSFC was designed to measure individuals' abilities to adapt to novel situations in everyday life, such as solving problems, thinking and acting quickly, and encoding new episodic memories. The CSCC was designed to measure the accumulated store of verbal knowledge and skills in individuals. The CSOC is derived from the CSFC and CSCC, and measures the overall intelligence level of an individual (see Akshoomoff et al., 2013 for more details about the three variables). Within the 1,003 subjects whose fMRI data were available, 13 subjects with missing labels were excluded. Thus, 990 subjects were included in the main analyses of this study, and their HCP IDs are provided in **Supplementary Table S1**.

To further provide an intuitive idea about the relative effectiveness of PLSR in MRI-based estimations, another group of CBD variables were used in this study, which will sometimes be referred to as "Supplementary labels" below. This group of variables includes gender, grip strength, reading recognition, picture vocabulary and VSPLOT, and raw scores (rather than age-adjusted scores) of these variables were used in this study. Cui and Gong (2018) previously estimated the latter four variables using six single-label learning methods, and we estimated these four variables here to provide an intuitive idea about the performance of PLSR. Gender was also included for the consideration that the estimation of individuals' gender is a typical classification problem. That is, it is convenient to test whether PLSR can solve classification and regression problems simultaneously by including gender as an additional variable. Four subjects with missing labels were further excluded in this analysis, and data of 986 subjects were analyzed. The HCP IDs of the four subjects further excluded here are also provided in **Supplementary Table S1**.

fMRI Data Pre-processing and RSFC Analyses

Resting state functional connections provided on the HCP website[2] were directly used as features in the current study, and no standardization or scaling was performed on the RSFCs before entering them into the PLSR-based estimation models. Before RSFC calculation, the resting state fMRI data of each subject underwent spatial and temporal pre-processing. The MRI data pre-processing pipelines of HCP were primarily built using tools from FSL (Jenkinson et al., 2012) and FreeSurfer (Fischl, 2012; Glasser et al., 2013).

Spatial pre-processing was designed to remove spatial artifacts from the data without removing other potentially useful information (Glasser et al., 2013). The spatial pre-processing steps include spatial distortion correction, head motion correction, B0 distortion correction, spatial registration to the T1w structural images and finally to the standard MNI template, resampling to 2 mm, global intensity normalization, and masking out non-brain voxels. More details about spatial pre-processing could be found in Glasser et al. (2013).

Temporal pre-processing was designed to eliminate artifacts and noise, while preserving neuro-biologically relevant fluctuations as much as possible (Smith et al., 2013). The temporal pre-processing steps include slow drift removal by weak high-pass temporal filtering, identification of artifactual

[1]https://db.humanconnectome.org/megatrawl/3T_HCP820_MSMAll_d200_ts2/megatrawl_1/

[2]https://db.humanconnectome.org/

TABLE 1 | Cognitive, behavioral and demographic variable information.

Label	Range (Mean ± std)	Description
Age	22–37 (28.721 ± 3.702)	Age of the participant in years
Education	11–17 (14.956 ± 1.773)	Years of education completed: 11- = 11; 12; 13; 14; 15; 16; 17 + = 17
Cognition score of fluid composite	86.680–145.170 (115.616 ± 11.500)	Measures individuals' abilities of adapting to novel situations in everyday life; Evaluated using the NIH Cognition Battery Toolbox.
Cognition score of crystallized composite	90.950–153.950 (118.053 ± 9.866)	Measures accumulated store of verbal knowledge and skills in individuals. Evaluated using the NIH Cognition Battery Toolbox.
Cognition score of total composite	88.950–153.360 (122.552 ± 14.454)	Measures the overall intelligence level of an individual. Evaluated using the NIH Cognition Battery Toolbox.
Gender*	F(0): 523/M(1): 463	Gender of the participant
Reading recognition*	84.200–150.710 (117.190 ± 10.594)	Measures the reading decoding skill. Evaluated using Oral Reading Recognition Test included in the NIH Cognition Battery Toolbox.
Picture vocabulary*	90.690–148.544 (116.998 ± 9.449)	Measures the general vocabulary knowledge. Estimated using Picture Vocabulary Test included in the NIH Cognition Battery Toolbox.
VSPLOT*	1–26 (15.015 ± 4.405)	Measures the abilities of spatial orientation. Estimated using Variable Short Penn Line Orientation Test included in the NIH Cognition Battery Toolbox.
Gripstrength*	55.290–154.010 (116.782 ± 11.288)	Measures the relative force the participant was able to generate using his/her dominant hand. Estimated using Grip Strength Dynamometry Test included in the NIH Cognition Battery Toolbox.

**The range and the mean (std) of the label were based on 986 subjects.*

components using FSL FIX, removal of artifacts and head motion based on linear regression. More details about temporal pre-processing could be found in Smith et al. (2013).

Regions of interest time-series were then extracted from the pre-processed resting state fMRI images based on ICA. Specifically, Group-ICA was first applied to the pre-processed resting state fMRI images at six dimensionalities (d = 15, 25, 50, 100, 200, 300). The time-series corresponding to the components for each subject were then estimated by multiple spatial regression of his/her pre-processed resting state fMRI image against the group-ICA spatial maps. The "components" will be referred to as "ROIs" for consistency with tradition. According to Smith et al. (2013), ICA-based ROI definition may provide "a more 'accurate' reflection of the connectivity structures in the data," may guarantee later network modeling "not to be rank deficient," and may "identify remaining artifactual process in the data." Later RSFC analyses were based on the time-series obtained above, which will be referred to as ROI time-series below.

The HCP website provided 12 variations of RSFCs, each of which was evaluated using one of six ROI definitions (15, 25, 50, 100, 200, and 300 ROIs) and one of two connectivity definitions (full correlation and partial correlation). Unlike full correlation, which is sensitive to both direct and indirect connections, partial correlation can theoretically provide a better approximation to direct connections (Marrelec et al., 2006; Smith et al., 2013). The partial-correlation-based RSFCs were evaluated using FSLNets[3], with *method* set to ridge regression, and *rho* set to 0.01[4]. Empirically, we performed the study based mainly on RSFCs among 200 ROIs evaluated using partial correlation, and the influences of ROI definitions and RSFC evaluation strategies were also analyzed (see section "Estimations Based on PLSR").

[3]https://fsl.fmrib.ox.ac.uk/fsl/fslwiki/FSLNets

[4]https://db.humanconnectome.org/megatrawl/HCP820_MegaTrawl_April2016.pdf

Estimations Based on PLSR

Partial least squares model the relationships between two sets of variables by projecting them into a low-dimensional subspace of latent variables (Wold, 1982; Guo and Mu, 2011; Krishnan et al., 2011). Let $X_{n\times N}$ denote the feature matrix, where n is the number of samples, and N is the number of features, and let $Y_{n\times M}$ denote the label matrix, where M is the number of labels; then PLS decomposes X and Y into the following form:

$$X_{n\times N} = T_{n\times d}(P_{N\times d})^{T} + E_{n\times N}$$

$$Y_{n\times M} = U_{n\times d}(Q_{M\times d})^{T} + F_{n\times M} \quad (1)$$

where T and U are matrices of the d extracted score vectors (latent variables), P and Q represent matrices of loadings, and E and F are the residual errors. Partial least squares decompose X and Y to obtain the maximized covariance between T and U. Based on X, Y, U, T, an explicit $N \times M$ matrix B that satisfies the following linear relationship can be obtained:

$$Y_{n\times M} = X_{n\times N}B_{N\times M} + F^{*}_{n\times M} \quad (2)$$

This linear relationship enables us to estimate the labels (here, the CBD variables) of unseen subjects based on their features (here, the RSFCs). PLSR was performed in this study using the *plsregress* function in MATLAB R2017b. There is only one hyper-parameter

for PLSR algorithm, and it is the number of latent variables (d-value in Eq. 1). In this study, d-value was empirically set to 50, and its influences on PLSR-based estimations were also analyzed.

A schematic overview of our estimation framework is shown in **Figure 1**. Four sets of estimations were performed to make a full understanding of the performance of PLSR in MRI-based estimations. The four sets were different only in the labels that were entered into the estimation model. Specifically, in the first set of estimations, all five main labels were entered into the model to evaluate the performance of PLSR on MRI-based multi-label learning; in the second set, we simultaneously estimated the five Supplementary labels. This set is expected to provide an intuitive idea about the relative effectiveness of PLSR in MRI-based estimations, as these labels have formerly been estimated using other machine learning techniques (e.g., SVR, elastic net) based on HCP resting state fMRI data (Cui and Gong, 2018[1]). In the third set, all 10 CBD variables were estimated simultaneously to test whether PLSR can accommodate more variables. In the fourth set, each of the five main labels was estimated separately, to evaluate the performance of PLSR on MRI-based single-label learning. For gender classification in the second and third sets, we set the label for male/female as 1/0, and the estimated gender was thresholded at 0.5 to make the final decision ($\geq$0.5 was classified as male, and $<$ 0.5 was classified as female).

In this study, three factors may influence the estimations based on PLSR, and these are the number of latent variables (d-value in Eq. 1), the ROI definition (15, 25, 50, 100, 200, and 300 ROIs) and RSFC evaluation strategies (full correlation and partial correlation). To test the influence of each of the three factors, further analyses were performed for the first set of estimations by fixing the other two factors to change the remaining one. First, the five main labels were simultaneously estimated with the number of latent variables (d-value) changed from 10 to 150 in steps of 10, based on partial correlation among 200 ROIs, to

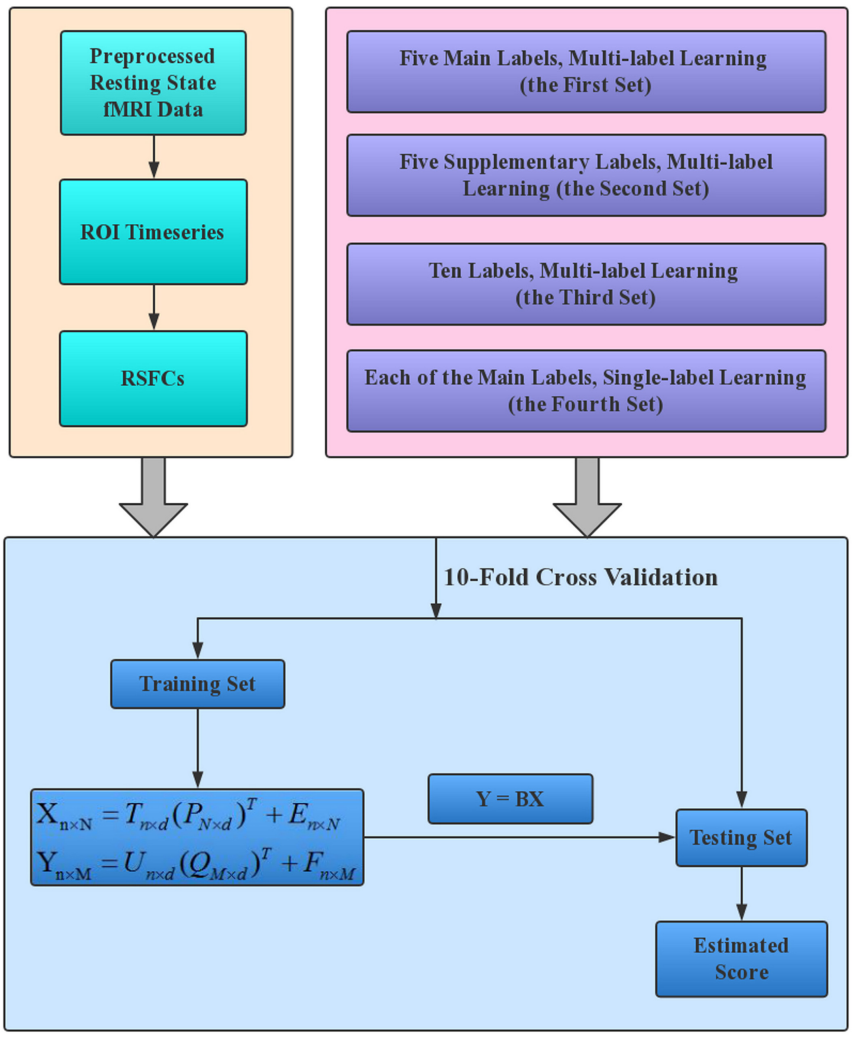

FIGURE 1 | The working flowchart of the proposed estimation framework. The resting state fMRI data of HCP 1200S release were analyzed in this study, and RSFCs provided on the HCP website (https://db.humanconnectome.org/) were directly used to establish the estimation models. Each of the four label sets in the upper right box corresponds to one set of estimations.

test the influence of the number of latent variables. Second, the five main labels were simultaneously estimated based on partial correlation among each of the other five sets of ROIs (15, 25, 50, 100, and 300 ROIs), with $d = 50$ for PLSR, to test the influence of ROI definition. Finally, the five main labels were simultaneously estimated based on full correlation among 200 ROIs, with $d = 50$ for PLSR, to test the influence of RSFC evaluation strategies.

A 10-fold cross-validation strategy was implemented to evaluate the performance of the PLSR. Specifically, all subjects were randomly divided into 10 subsets. In each loop of the 10-fold cross validation, one subset (99 subjects) was used as the testing set, and the other 9 subsets (891 subjects) were used as the training set. The estimation model was constructed (obtaining matrix B in Eq. 2) based on all training samples and then used to estimate the CBD variables of all testing samples. The training and testing procedures were repeated 10 times so that each of the 10 subsets was used as the testing set once.

The estimation performance was calculated with the Pearson correlation coefficient (R-value) between the actual and the estimated CBD variable and the RMSE between them. Permutation analysis was performed to test the significance of the R-values by randomly shuffling the CBD variables 5,000 times and repeating the estimation process. As the permutation analyses were time consuming, we performed permutation analyses only on the first and fourth sets of estimations. The P-values of the empirical correlation values, based on their corresponding null distributions, were computed as follows:

$$P = \frac{1 + N_{StrongerCorrelations}}{1 + N} \quad (3)$$

where N is the number of permutations (here, $N = 5,000$) and $N_{StrongerCorrelations}$ is the number of stronger correlations between the estimated and permuted CBD variable (as compared to that based on the non-permuted CBD variable).

Evaluating the Contribution of RSFCs

Based on Eq. 2, a linear relationship between the RSFCs and CBD variables can be established. This linear relationship may facilitate our evaluation of the contribution of the RSFCs to the estimations. In this study, as cross-validation was used to evaluate the performance of PLSR, slightly different linear models (as indicated by matrix B in Eq. 2) were built for each of the 10 loops. We averaged the 10 B matrices to obtain an average weight matrix ($\bar{B}$), and the contribution of the ith RSFC to the estimation of the j th CBD variable was evaluated as $\bar{B}_{ij}$. The significance of $\bar{B}_{ij}$ was again computed based on the aforementioned 5,000 permutations as follows:

$$P = \frac{1 + N_{Larger Absolute \bar{B}_{ij}}}{1 + N} \quad (4)$$

where $N_{Larger Absolute \bar{B}_{ij}}$ is the number of larger absolute $\bar{B}_{ij}$ in the 5000 permutations, as compared to that based on the non-permuted CBD variable. RSFCs whose weights satisfy $P < 0.05$ were regarded as making significant contributions to the estimation of a CBD variable.

We checked to what extent the RSFCs made significant contributions in multi-label learning overlapped those with significant weights for single-label learning (according to the P-values based on 5,000 permutations). Through this analysis, we meant to investigate whether the RSFCs would change if a few more CBD variables were entered into the PLSR model.

To investigate whether the RSFCs that made significant contributions to the estimation of a CBD variable were of biological significance, we directly correlated each RSFC with the CBD variable. Furthermore, we evaluated the contribution of the RSFCs from a network perspective. Specifically, we first clustered the ROIs into 10 functional networks based on their RSFCs using affinity propagation algorithm. The contribution of each network was then evaluated by summing up the contribution of all ROIs within it, and the contribution of each ROI was evaluated by the number of RSFCs (made significant contribution) associated with the ROI. We also evaluated the contribution of inter-network connections by the number of RSFCs (made significant contribution) between each pair of network.

RESULTS

Performances of PLSR in Multi- and Single-Label Learning

Partial least squares regression performed well in MRI-based estimations for both single- and multi-label learning purpose (**Figures 2**, **3** and **Tables 2**, **3**). For simultaneous estimation of the main labels (the first set of estimations), R-values of 0.627, 0.395, 0.369, 0.585, and 0.536 were obtained for age, education, CSFC, CSCC, and CSOC, respectively (**Figures 2A–E**). For each of the five variables, no stronger correlation was observed in the 5,000 permutations. That is, each of the five R-values corresponded to a P-value of 0.0002. In fact, the largest R-values in the 5,000 permutations were by far smaller than those based on actual CBD variables, which were 0.157, 0.146, 0.161, 0.142, and 0.161 for age, education, CSFC, CSCC, and CSOC, respectively.

The results regarding the simultaneous estimation of the five Supplementary CBD variables (the second set of estimations) are listed in **Table 2**. A gender classification accuracy of 97.6%, together with R-values of 0.701, 0.522, 0.555, and 0.376 for the estimations of grip strength, reading recognition, picture vocabulary and VSPLOT were obtained.

Table 2 also provided the results regarding the simultaneous estimations of 10 CBD variables (the third set of estimations). It can be seen that including five additional CBD variables into the model did not influence the estimations of the main labels. For instance, the R-value for age estimation changed from 0.627 to 0.625 here, and the gender classification accuracy changed from 97.6 to 97.8% here.

The current estimation accuracies of grip strength, reading recognition, picture vocabulary, and VSPLOT (R = 0.704, 0.519, 0.546, 0.382, respectively) were higher than those reported in Cui and Gong (2018) (not more than 0.55, 0.35, 0.35, 0.25, respectively), in which six commonly used machine learning algorithms were utilized. The estimation accuracies in this study

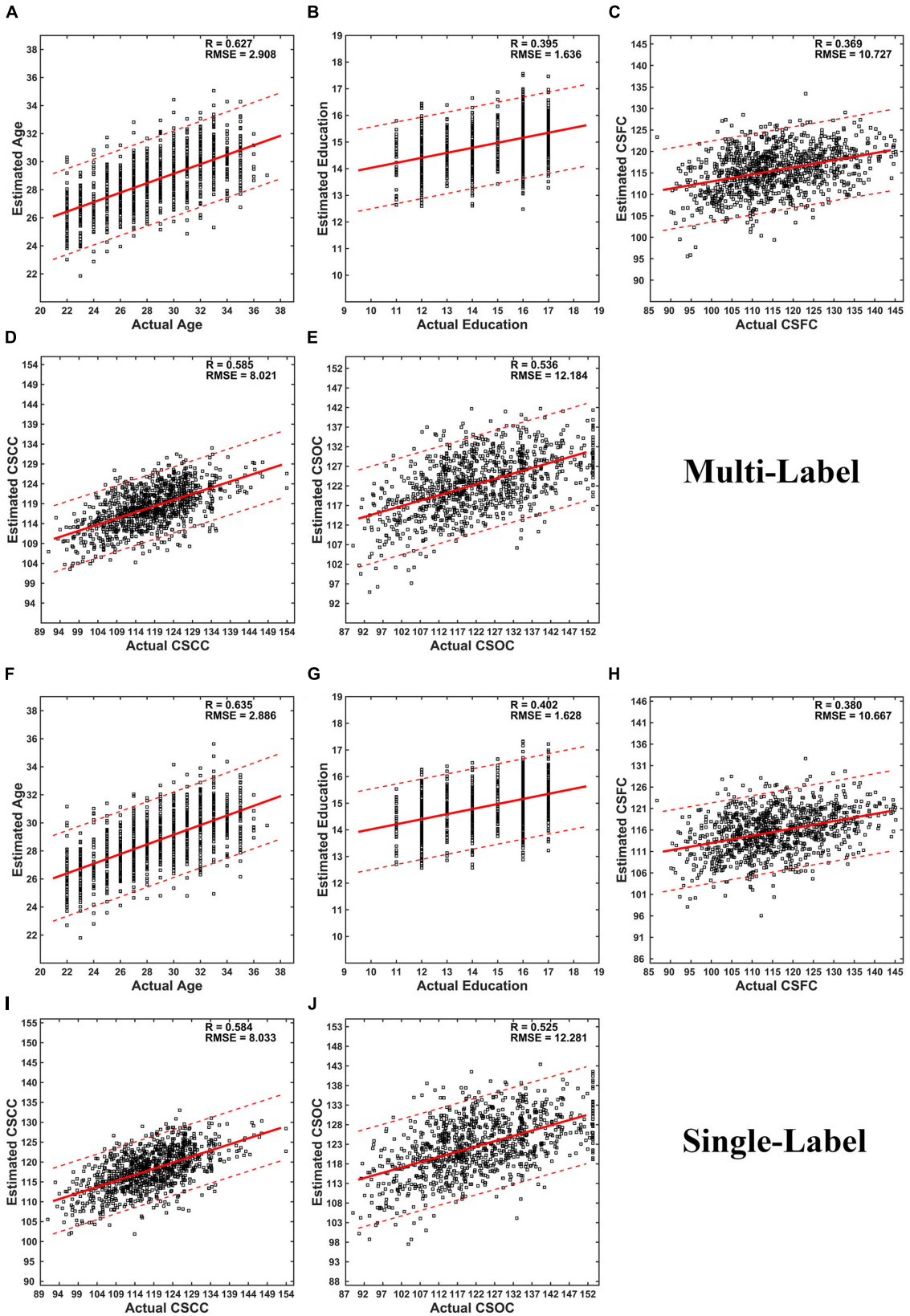

FIGURE 2 | Scatter plots of estimated vs. actual labels. **(A–E)** were based on the first set of estimations (multi-label learning), and **(F–J)** were based on the fourth set of estimations (single label learning). **(A,F)** Age; **(B,G)** Education; **(C,H)** CSFC; **(D,I)** CSCC; **(E,J)** CSOC.

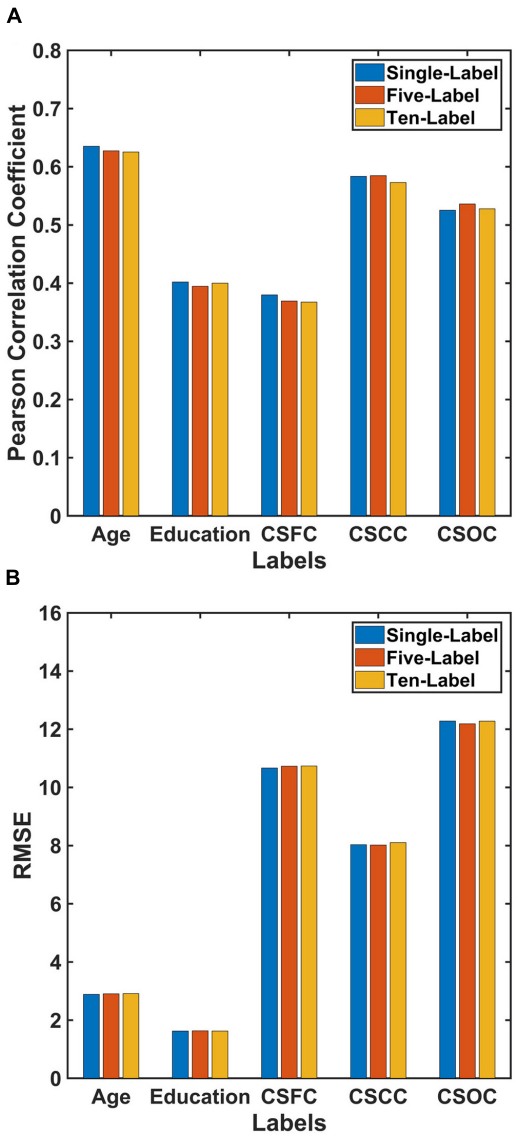

FIGURE 3 | Comparison of the performances of PLSR for single- and multi-label learning. The reported values were **(A)** Pearson correlation coefficient and **(B)** RMSE. The performances of the single-label PLSR were comparable to those of the multi-label PLSR, and adding additional five labels into the model had limited effect upon the estimation accuracies.

were also higher than those listed on the HCP website[5], which were based on the same RSFCs as were used in this study but obtained using elastic net, and **Table 3** is a direct comparison of our results and those listed on the HCP website. In fact, when we estimated the five main labels using three widely used single-label learning techniques, namely, SVR, E-Net and RVR, based on RSFCs among 200 ROIs evaluated using partial correlation, the estimation accuracies were much lower than those based on based on PLSR. For instance, the correlation between the estimated and actual ages were $R = 0.413, 0.392, 0.405$ for SVR, E-Net, and RVR, respectively, as compared to $R = 0.627$ for PLSR (for more details, please see **Supplementary Table S4**).

The performance of PLSR in MRI-based single-label learning (of the five main labels, the fourth set of estimations) can be found in **Figures 2F–J**, **3** and **Table 2**. There were only subtle differences between the accuracies of single- and multi-label learning. For instance, the estimation of age was slightly better based on single-label learning ($R = 0.635$, compared to $R = 0.627$ for multi-label learning), while the estimation of the CSOC was slightly better based on multi-label learning ($R = 0.536$, compared to $R = 0.525$ for single-label learning).

The number of latent variables (d-value) is an important factor for PLSR. On analyzing its influence, it was found that d-value had a limited effect on the estimations (**Figure 4**). Specifically, only subtle changes of the R-value and RMSE were observed, with d-values ranging from 10 to 150. This result indicated that PLSR was relatively robust to d-value selection.

Influences of ROI Definition and RSFC Evaluation Strategies

For the first set of estimations (multi-label learning of the five main labels), we further evaluated the influences of ROI definition and RSFC evaluation strategies. **Figure 5** illustrates the influence of ROI definition strategy on the estimations. The estimation accuracies based on 100, 200, and 300 ROIs were relatively higher than those based on 15, 25, and 50 ROIs. A comparison of the estimations based on RSFCs evaluated using full correlation and partial correlation can be found in **Figure 6**. Obviously, partial-correlation-based RSFCs generally outperformed full-correlation-based RSFCs.

RSFCs Made Significant Contributions to Estimations

Figure 7 demonstrates the extent to which the RSFCs with significant weights in the multi-label learning overlapped those with significant weights for the single-label learning. A large percentage of the RSFCs contributed to multi- and single-label estimations were common. For instance, among the 437 RSFCs with significant weights in the multi-label estimation of age, 396 RSFCs had significant weights in the single-label estimation (**Figure 7A**).

Figure 8 shows the percentage of RSFCs that made significant contributions to the estimations among the RSFCs that strongly correlated with the variable. It can be seen that quite a few RSFCs that made significant contributions to the estimation of a CBD variable had a strong correlation with that variable. For instance, among the 10 RSFCs that showed the strongest correlation with age, seven were observed to make a significant contribution to the estimation of age (**Figure 8F**). These strong correlations indicate that the RSFCs made significant contributions to estimations were of biological significance.

Figure 9 illustrates the contribution of the RSFCs from the perspective of functional networks. According to **Figure 9**, the network contribution was slightly different when estimating different variables. For instance, the medial visual network contributed relatively less in the estimation of age (**Figure 9A**),

[5]https://db.humanconnectome.org/megatrawl/

TABLE 2 | Performances of PLSR in the four sets of estimations.

The first set: multi-label learning, five main labels					
	Age	**Education**	**CSFC**	**CSCC**	**CSOC**
R	0.627	0.395	0.369	0.585	0.536
RMSE	2.908	1.636	10.727	8.021	12.184
The second set: multi-label learning, five Supplementary labels					
	Grip strength	**Reading recognition**	**Picture vocabulary**	**VSPLOT**	**Gender***
R	0.701	0.522	0.555	0.376	97.6%(ACC)
RMSE	8.066	9.038	7.871	4.109	0.996(AUC)
The third set: multi-label learning, ten labels					
	Age	**Education**	**CSFC**	**CSCC**	**CSOC**
R	0.625	0.400	0.367	0.573	0.528
RMSE	2.914	1.629	10.738	8.101	12.278
	Grip strength	**Reading recognition**	**Picture vocabulary**	**VSPLOT**	**Gender***
R	0.704	0.519	0.546	0.382	97.8%(ACC)
RMSE	8.033	9.059	7.920	4.093	0.996(AUC)
The fourth set: single-label learning, five main labels					
	Age	**Education**	**CSFC**	**CSCC**	**CSOC**
R	0.635	0.402	0.380	0.584	0.525
RMSE	2.886	1.628	10.667	8.033	12.281

**For gender classification, the classification accuracy (ACC) and the area under curve (AUC) were provided.*

TABLE 3 | Comparison of the estimations based on PLSR in this study to those based on elastic net listed on the HCP website*.

		Education	**Grip strength**	**Reading recognition**	**Picture vocabulary**	**VSPLOT**
PLSR	***R***	0.400	0.704	0.519	0.546	0.382
	CoD	0.156	0.494	0.269	0.297	0.136
Elastic net	***R***	0.28	0.65	0.16	0.27	0.25
	CoD	−0.05	0.34	−0.19	−0.18	−0.01

**https://db.humanconnectome.org/megatrawl/3T_HCP820_MSMAll_d200_ts2/megatrawl_1/. The estimation accuracies of the other five CBD variables (age, gender, CSFC, CSCC, and CSOC) were not available on the HCP website. Our results were based on the third set of estimations. The estimations based on PLSR in this study were better than those based on elastic net as listed on the HCP website. CoD stands for "coefficient of determination," which has been used to evaluate the performance of the predictive models together with the R-value on the HCP website. CoD is evaluated as follows: CoD = 1 – Variance of Estimation Error/Variance of the Variable, and higher CoD values indicate better estimations.*

as compared to the estimation of other variables (**Figures 9B–E**). The inter-network connections that contributed to the estimations of the five main labels were also slightly different. For instance, the RSFCs between the medial and lateral visual networks contributed relatively less to the estimation of education, as compared to the estimation of CSOC.

DISCUSSION

It is valuable to estimate individuals' CBD variables based on neuroimaging data, as these estimations may eventually lead to a better understanding of the neural basis that gives rise to individual differences in these variables, and may potentially assist in the clinical diagnosis of neuropsychiatric diseases. Machine learning techniques play critical roles in these estimations. Krishnan et al. (2011) foresaw the potential of PLSR in MRI-based estimations. Afterward, quite a few studies have been performed on MRI-based estimations using PLSR, but a majority of these studies estimated one CBD variable at a time. That is, the potential of PLSR for MRI-based estimations of CBD variables remains to be explored, especially its potential for multi-label learning. In this study, we systemically investigated the performance of PLSR in MRI-based estimations of individuals' CBD variables. The following is a detailed discussion of the results.

PLSR Performed Well in MRI-Based Estimations

In the current study, PLSR was observed to perform well in simultaneous estimations of individuals' multiple CBD variables

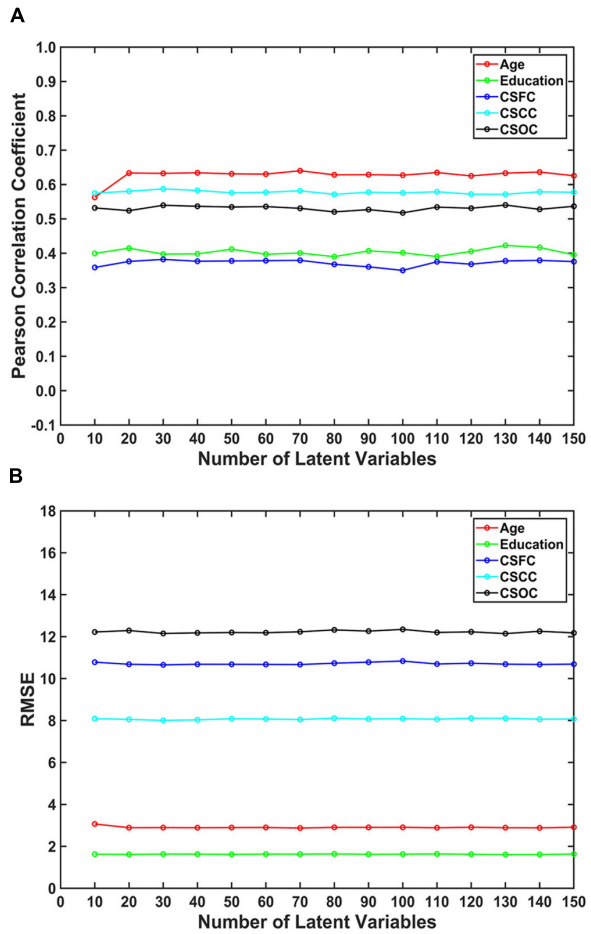

FIGURE 4 | The influence of the number of latent variables on the estimations. The reported values were **(A)** Pearson correlation coefficient and **(B)** RMSE. The number of latent variables ranged from 10 to 150. The results indicated that multi-label PLSR was relatively stable when the number of latent variables varied over a wide range (here, 10 ∼ 150).

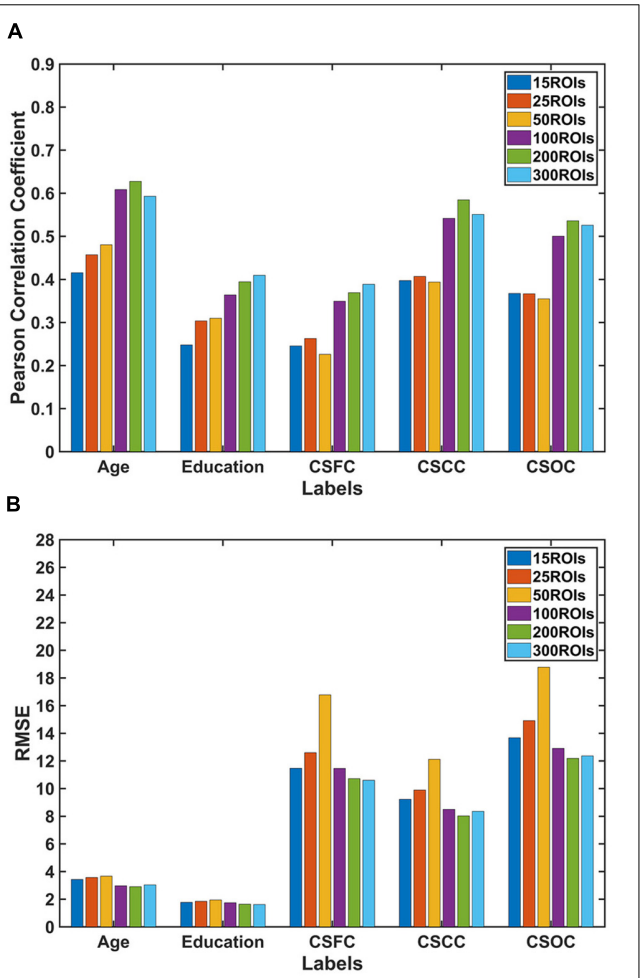

FIGURE 5 | Estimations based on different ROI definition strategies. The reported values were **(A)** Pearson correlation coefficient and **(B)** RMSE. The results indicated that estimations based on 100, 200, and 300 ROIs were better than those based on 15, 25, and 50 ROIs.

based on resting state fMRI (**Figures 2**, **3** and **Tables 2**, **3**). According to the Pearson correlations between the estimated and actual CBD variables (*R*-values, each corresponding to a $P = 0.0002$ in this study), the present estimations were better than those in two other studies based on the HCP resting state fMRI data but using single-label learning techniques (Cui and Gong, 2018) (see footnote 5). Specifically, the *R*-values for grip strength, reading recognition, picture vocabulary and VSPLOT obtained in this study (0.704, 0.519, 0.546, 0.382) was uniformly higher than those reported by Cui and Gong (2018) (not more than 0.55, 0.35, 0.35, 0.25), in which the four variables were estimated with six commonly used machine learning regression algorithms. The relatively higher estimation accuracy in the current study support the effectiveness of PLSR in MRI-based estimations, though better ROI definition and RSFC evaluation strategies (as will be discussed below) may also contribute to better estimations in this study. In fact, based on the same RSFC set (among 200 ROIs, and estimated using partial correlation), the current estimations were better than those listed on the HCP website, which was based on elastic net (**Table 3**). Moreover, when we estimated the five main labels using three widely used machine learning techniques, namely, SVR, E-Net and RVR, based on RSFCs among 200 ROIs evaluated using partial correlation, the estimation accuracies based on PLSR were uniformly higher than those based on the three techniques.

In addition to its relatively high estimation accuracy, PLSR exhibited four advantages in MRI-based estimations in this study. First, PLSR can solve both single- and multi-label learning problems. PLSR has been reported to perform well in estimating a variety of CBD variables (Yang et al., 2013; Wu et al., 2014; Meskaldji et al., 2016; Yoshida et al., 2017; Kuceyeski et al., 2018; Yoo et al., 2018; Zhang et al., 2018) based on MRI data. To note, a single variable was estimated in most of the studies. The current results indicate that, in addition to single label learning, PLSR can perform comparably well when multiple CBD variables were simultaneously estimated (**Figures 2**, **3** and **Table 2**).

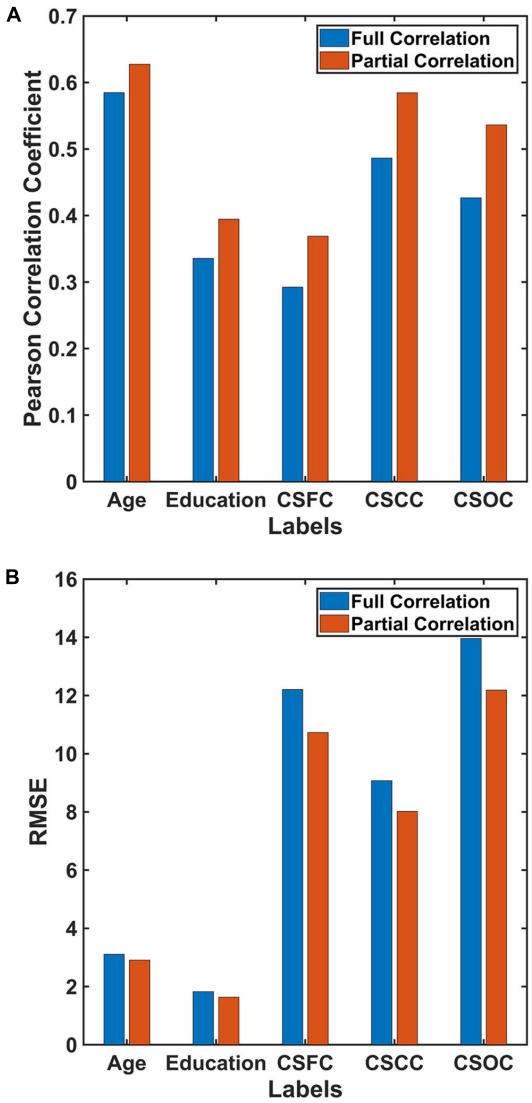

FIGURE 6 | Estimations based on different RSFC evaluation strategies. The reported values were **(A)** Pearson correlation coefficient and **(B)** RMSE. The results indicated that estimations based on RSFCs evaluated using partial correlation were better than those based on RSFCs evaluated using full correlation.

Second, PLSR can solve regression and classification problems simultaneously. In this study, an accuracy of 97.8% was obtained for gender classification, with the other nine CBD variables estimated simultaneously (**Table 2**). The present accuracy was slightly higher than that reported by Feis et al. (2013), and much higher than that reported by Zhang et al. (2018). Specifically, Zhang et al. (2018) reported a gender classification accuracy of 87% based on the resting state fMRI data of the HCP dataset. In the study by Feis et al. (2013), an accuracy of 96% was obtained based on MR images (T1-, T2-, and diffusion-weighted) using a linear support vector machine. The relatively higher gender classification accuracy in our study indicates that including the other nine CBD variables into the model may be helpful for gender classification in this study. In many cases, both continuous (e.g., MMSE score) and discrete (e.g., whether or not a subject had psychiatric disease) CBD variables are available (Zhang et al., 2012; Yoshida et al., 2017). The ability of solving classification and regression problems simultaneously enables PLSR to provide richer information and higher estimation accuracy in those cases.

Third, the estimations were relatively stable when the number of latent variables (d-value) changed over a wide range (**Figure 4**). This indicates that PLSR is not sensitive to the choice of d-value. It should be noted that the selection of d-values is not unlimited. In fact, when the d-value was set to larger than 200, the estimations deteriorate dramatically (**Supplementary Figure S1**). The reason for this deterioration is not known, and further studies are expected to address the issue.

Finally, PLSR is efficient in model training and testing, and it is simple and easy to use. PLSR is very fast in learning, and even faster in testing, capable of quickly reducing the original high-dimensional data into low dimensions. In this study, it took only 1.3729 s to reduce the original 19,900-dimensional RSFCs (based on 200 ROIs) into 50-dimensional latent variables on a PC with a 3.00 GHz Intel(R) Core(TM) i5-8500 CPU processor. Once the partial least squares decomposition is completed, the subsequent testing process involves only the linear product of matrices, which is even faster. A fast testing process is beneficial for practical applications of PLSR.

ROI Definition and RSFC Evaluation Strategies Had Obvious Influences Upon the Estimations

As has been mentioned, in addition to the advantages of PLSR, the relatively high estimation accuracies in this study may be partly due to better ROI definition and RSFC evaluation strategies. Proper ROI definition is critical for later RSFC evaluation, as a hidden hypothesis in the current study is that the ROIs for all subjects are same. This requirement of "same" ROI definition necessitates high-quality spatial normalization if a template were used. ICA itself can figure out subject specific ROIs that are more functionally "same" (Smith et al., 2013). The ICA-based ROI definition may be one reason for better estimations in this study, as compared to those in the study by Cui and Gong (2018), in which ROIs were defined based on the human brainnetome atlas.

Compared to estimations based on 15, 25 and 50 ROIs, the estimations based on 100, 200, and 300 ROIs were much better (**Figure 5**). This finding is consistent with that reported by Finn et al. (2015), in which the accuracy of individual identification based on 68 ROIs was much lower as compared to that based on 268 ROIs. Finn et al. (2015) suggest that "a relatively high-resolution parcelation contributes to the detection of individual variability and boosts identification rate." According to Yoshida et al. (2017), estimations of clinical scores deteriorate dramatically when the standard AAL template was further subdivided into 600 ROIs. It is still unknown whether more ROIs

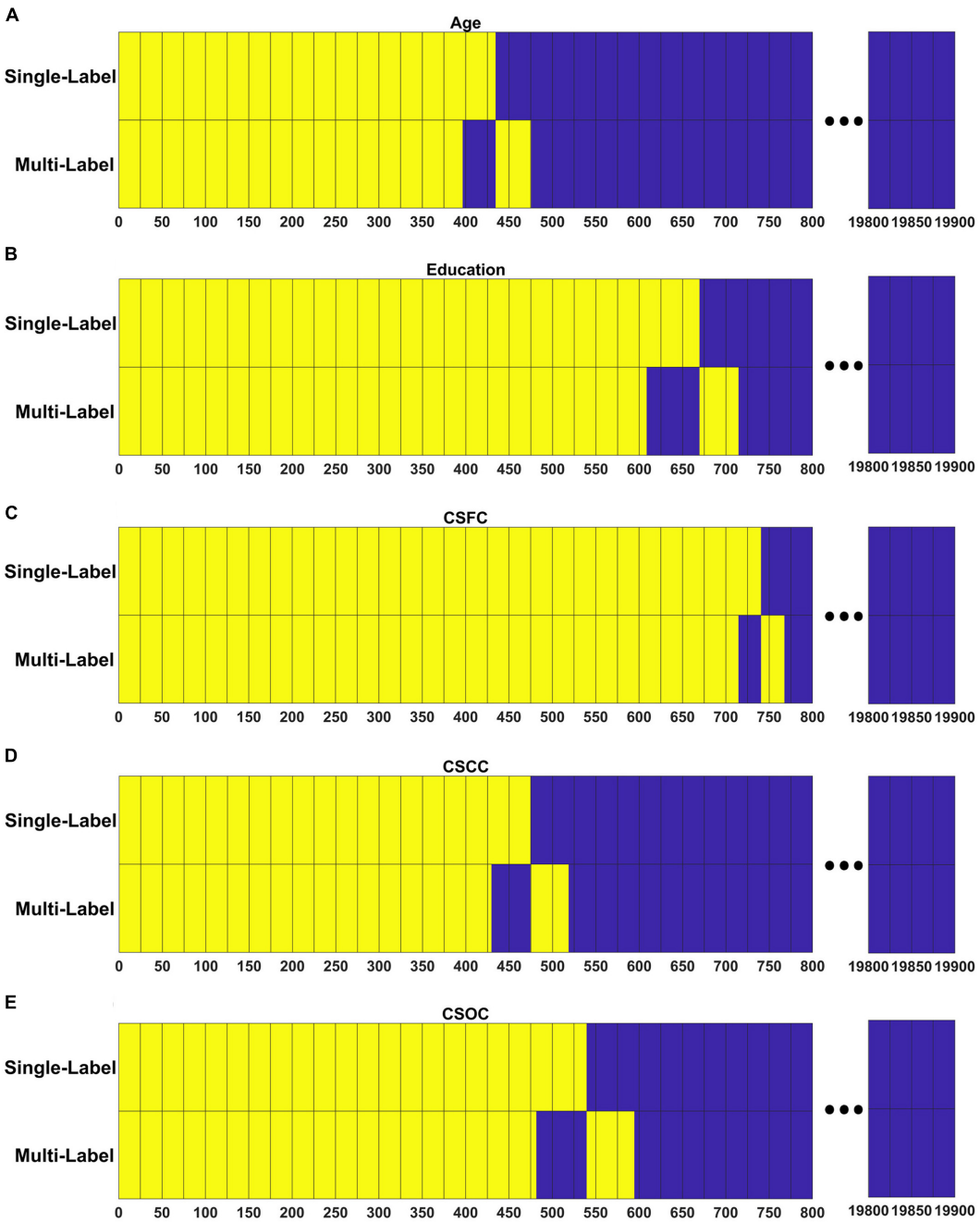

FIGURE 7 | Resting state functional connections made significant contributions shared across the PLSR models established in the first and fourth set of estimations. For each model, RSFCs made significant contributions are marked with yellow, RSFCs made non-significant contributions are marked with blue, and common features between the two models are vertically aligned. Respectively, among the 437, 653, 741, 473, and 536 RSFCs that made significant contributions to the simultaneous estimations of **(A)** age, **(B)** education, **(C)** CSFC, **(D)** CSCC, and **(E)** CSOC, 396, 608, 714, 429, and 481 were in common between the multi- and single-label learning.

(e.g., 600 or 1000) would impair the estimations based on PLSR. Further studies are needed to address this issue.

Estimations of all five CBD variables based on RSFCs evaluated using partial correlation were better than those based on RSFCs evaluated using full correlation (**Figure 6**). Partial correlation has been suggested to be a better approximation to direct connections in theory, while full correlation is more sensitive to both direct and indirect connections (Marrelec et al., 2006; Smith et al., 2013). If this were the case, the current results indicate that, by excluding the effects of indirect connections, the RSFCs evaluated based on partial correlation include less noise, and this is favorable for CBD variable estimations.

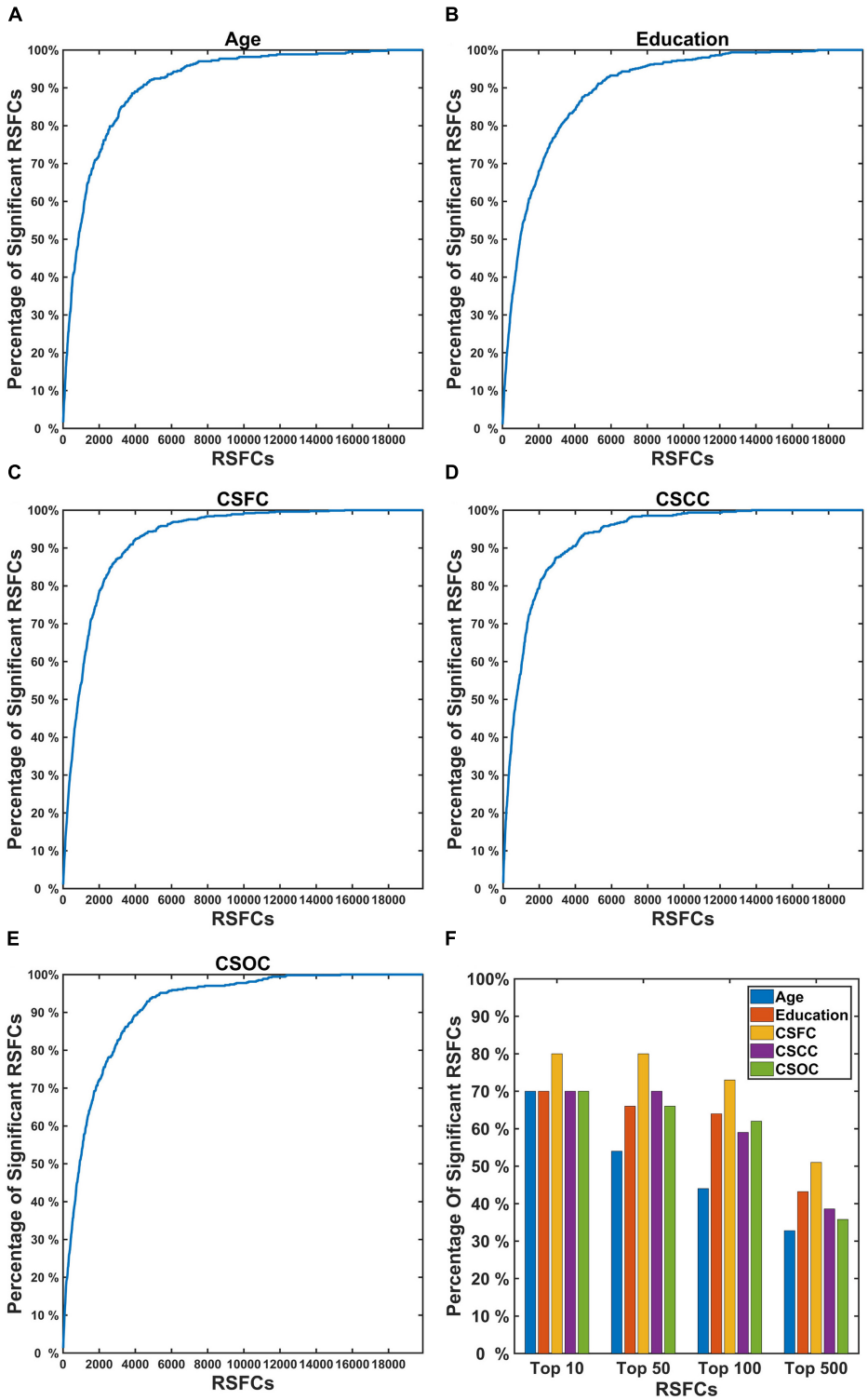

FIGURE 8 | Percentage of RSFCs that made significant contributions to the estimations of a CBD variable among the RSFCs that strongly correlated with that variable. In the first five subplots **(A–E)**, the X coordinate indicates the sequence number of the correlation (absolute value, sorted in descending order) between the RSFCs and the CBD variable [**(A)** for Age, **(B)** for Education, **(C)** for CSFC, **(D)** for CSCC, and **(E)** for CSOC]; the Y coordinate indicates the percentage of RSFCs that made significant contributions to that variable (among all RSFCs that made significant contributions to that variable). **(F)** Represents the percentage of RSFCs that made significant contributions to the estimations among the top 10, 50, 100, and 500 RSFCs that were most correlated with the CBD variable. The results were obtained based on the first set of estimations. A large percentage of the RSFCs that contributed to the estimation of a CBD variable were observed to have strong correlation with that variable.

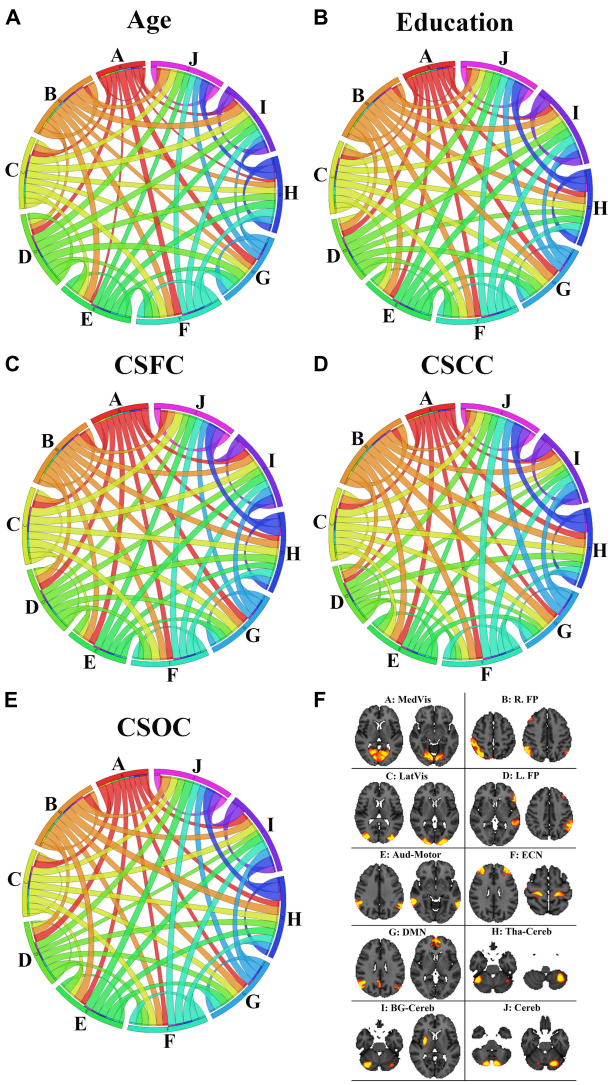

FIGURE 9 | The contribution of the RSFCs to the estimation of age **(A)**, education **(B)**, CSFC **(C)**, CSCC **(D)**, and CSOC **(E)**. The circular diagram indicates the relative contribution of the functional networks, with each functional network indicated by one color. The networks are the medial visual network (**A**: MedVis), the right fronto-parietal network (**B**: R. FP), the lateral visual network (**C**: LatVis), the left fronto-parietal network (**D**: L. FP), the auditory motor network (**E**: Aud-Mot), the executive control network (**F**: ECN), the default mode network (**G**: DMN), the thalamus cerebellum network (**H**: Tha-Cereb), the basal ganglia cerebellum network (**I**: BG-Cereb) and the cerebellum (**J**: Cereb). Two typical spatial maps of each network can be found in subfigure **(F)**. Each ribbon links two functional networks, and the ribbon size scales with the contribution of the RSFCs between the networks it linked.

RSFCs Made Significant Contributions to the Estimations Were of Biological Significance

Though all RSFCs were utilized to obtain the latent variables and finally to establish the linear relationship as given in Eq. 2, only a few RSFCs were observed to make significant contributions (**Figure 7**). Moreover, in the current study, the RSFCs that made significant contributions to multi-label estimations largely overlapped with those in single-label estimations (**Figure 7**). For instance, 396 of the 437 RSFCs that made significant contributions to age estimation based on the multi-label learning model were also found to make significant contributions based on a single-label learning model (**Figure 7A**). This result indicated that the RSFC sets utilized by PLSR were quite similar for single- and multi-label learning. We suggest that PLSR can automatically find out the RSFCs of biological significance for one CBD variable (e.g., age), irrespective of the influences of other CBD variables that were simultaneously estimated (e.g., education).

To investigate whether the RSFCs made significant contributions to the estimation of a CBD variable were of biological significance, we compared these RSFCs to those exhibited significant correlations with the variable. It was found that a majority of the RSFCs that made significant contributions to the estimation of a CBD variable also had strong correlation with the variable (**Figure 8**). For instance, nearly 90% of the RSFCs that made significant contributions to the estimation of age were among 4,000 (among 19,900) RSFCs that showed the strongest correlation with age (**Figure 8A**). This indicated that the estimations based on PLSR were largely dependent upon RSFCs of biological significance.

When the ROIs were clustered into 10 functional networks, each network contributed differently to the estimation of the five main labels (**Figure 9**). As has been mentioned, the medial visual network made relatively less contribution to the estimation of age (**Figure 9A**), as compared to the estimation of other variables (**Figures 9B–E**). The medial visual network is thought to be important for preliminary visual information processing. The present finding is consistent with the suggestion by Dosenbach et al. (2010), which indicates that the networks responsible for preliminary sensory functions mature early and aging late. That is, medial visual network may be relatively stable during early adulthood, so it contribute less to age estimation in this study (as subjects included in this study aged 22∼37 years). Inter-network connections were also observed to make slightly different contribution to the estimation of the five main labels (**Figure 9**). One example is that the connection between the medial and lateral visual networks contributed relatively less to the estimation of education (as compared to CSOC). The medial visual network plays an important role in preliminary visual information processing, and lateral visual network is critical for high-order visual information processing. the current finding may be consistent with the common sense that individuals' ability of visual information processing is less dependent on education, but the speed and quality of visual information processing (supported by the medial and lateral visual networks) may exert some influence upon individuals' cognitive abilities (as evaluated by CSOC).

Other Methodological Issues

Two methodological issues should be addressed. First, family structure was not considered in this study. Most subjects in this study had at least one blood relative, and many of them were twins (Van Essen et al., 2013). The homogeneity of the sample may make the estimation accuracies too optimistic, as many

families will be split across training and testing sets. To avoid over-optimistic estimation accuracies, we further performed 10-fold cross validation with family structure taken into account, by ensuring that no family was split across training and testing sets. The results indicated that whether or not considering family structure has limited influence on the final accuracies (**Supplementary Table S2**).

Another methodological issue is that the kernel trick was not considered in this study. The kernel trick has been widely used in the area of machine learning to capture the non-linear relationships between features and labels. According to Guo and Mu (2011), kernel PLSR resulted in a smaller error compared to linear PLSR. When we simultaneously estimated the five main labels using kernel PLSR, with the RBF function used as kernel and σ empirically set to 150, the estimation accuracies increased slightly (**Supplementary Table S3**). This result indicated that kernel PLSR can be a favorable choice for future MRI-based estimations.

CONCLUSION

In summary, we systemically investigated the performance of PLSR in MRI-based estimations of individuals' CBD variables. We found that PLSR performed well in both simultaneous estimation of multiple CBD variables and estimation of a single CBD variable. Furthermore, our study demonstrated five advantages of PLSR in MRI-based estimations, which are attractive to researchers in the field. First, PLSR can solve both single- and multi-label learning problems. Second, PLSR can solve regression and classification problems simultaneously. Third, the PLSR algorithm is relatively robust to the number of latent variables. Then, PLSR enables later inferences of the biological significance underlying the estimations. Finally, PLSR is efficient in model training and testing, and it is simple and easy to use. Besides, the choice of ROI definition and RSFC evaluation strategies are also critical for the estimations. Specifically, our results indicated that RSFCs evaluated using partial correlation had obvious advantages over those evaluated using full correlation, and the estimations based on RSFCs among 100, 200, and 300 ROIs were much better than those based on RSFCs among 15, 25, and 50 ROIs. This study used RSFCs as a test case, and it is obvious that PLSR can be easily extended to estimations based on other features (e.g., VBM evaluated based on MRI). Furthermore, PLSR is simple in principle and easy to use, so it can be widely used in future MRI-based estimations of CBD variables.

DATA AVAILABILITY STATEMENT

Publicly available datasets were analyzed in this study. This data can be found here: https://db.humanconnectome.org/.

ETHICS STATEMENT

The studies involving human participants were reviewed and approved by NIH. The patients/participants provided their written informed consent to participate in this study.

AUTHOR CONTRIBUTIONS

LT and CC designed the study and analyzed the data. CC, XC, and LT wrote the manuscript and approved the submitted version.

FUNDING

This work was supported by the National Natural Science Foundation of China (Grant Nos. 61773048 and 61272356) and National Key R&D Project (2017YFC1703506). The funding sources had no involvement in the preparation of the manuscript.

ACKNOWLEDGMENTS

Data were provided by the Human Connectome Project, WU-Minn Consortium (Principal Investigators: David Van Essen and Kamil Ugurbil; 1U54MH091657) funded by the 16 NIH Institutes and Centers that support the NIH Blueprint for Neuroscience Research; and by the McDonnell Center for Systems Neuroscience at Washington University.

SUPPLEMENTARY MATERIAL

The Supplementary Material for this article can be found online at: https://www.frontiersin.org/articles/10.3389/fnins.2019.01282/full#supplementary-material

REFERENCES

Adeli, E., Meng, Y., Li, G., Lin, W., and Shen, D. (2019). Multi-task prediction of infant cognitive scores from longitudinal incomplete neuroimaging data. *Neuroimage* 185, 783–792. doi: 10.1016/j.neuroimage.2018.04.052

Akshoomoff, N., Beaumont, J. L., Bauer, P. J., Dikmen, S. S., Gershon, R. C., Mungas, D., et al. (2013). VIII. NIH toolbox cognition battery (CB): composite scores of crystallized, fluid, and overall cognition. *Monogr. Soc. Res. Child Dev.* 78, 119–132. doi: 10.1111/mono.12038

Arbabshirani, M. R., Plis, S., Sui, J., and Calhoun, V. D. (2017). Single subject prediction of brain disorders in neuroimaging: promises and pitfalls. *Neuroimage* 145, 137–165. doi: 10.1016/j.neuroimage.2016.02.079

Beaty, R. E., Kenett, Y. N., Christensen, A. P., Rosenberg, M. D., Benedek, M., Chen, Q., et al. (2018). Robust prediction of individual creative ability from brain functional connectivity. *Proc. Natl. Acad. Sci. U.S.A.* 115, 1087–1092. doi: 10.1073/pnas.1713532115

Biswal, B., Yetkin, F. Z., Haughton, V. M., and Hyde, J. S. (1995). Functional connectivity in the motor cortex of resting human brain using echo-planar MRI. *Magn. Reson. Med.* 34, 537–541. doi: 10.1002/mrm.1910340409

Cho, M. A., Skidmore, A., Corsi, F., Wieren, S. E. V., and Sobhan, I. (2007). Estimation of green grass/herb biomass from airborne hyperspectral imagery using spectral indices and partial least squares regression. *Int. J. Appl. Earth. Obs.* 9, 414–424. doi: 10.1016/j.jag.2007.02.001

Cozzolino, D., Murray, I., Chree, A., and Scaife, J. R. (2005). Multivariate determination of free fatty acids and moisture in fish oils by partial least-squares regression and near-infrared spectroscopy. *LWT-Food Sci. Technol.* 38, 821–828. doi: 10.1016/j.lwt.2004.10.007

Cui, Z., and Gong, G. (2018). The effect of machine learning regression algorithms and sample size on individualized behavioral prediction with functional connectivity features. *Neuroimage* 178, 622–637. doi: 10.1016/j.neuroimage.2018.06.001

Dosenbach, N. U., Nardos, B., Cohen, A. L., Fair, D. A., Power, J. D., Church, J. A., et al. (2010). Prediction of individual brain maturity using fMRI. *Science* 329, 1358–1361. doi: 10.1126/science.1194144

Feinberg, D. A., Moeller, S., Smith, S. M., Auerbach, E., Ramanna, S., Gunther, M., et al. (2010). Multiplexed echo planar imaging for sub-second whole brain FMRI and fast diffusion imaging. *PLoS One* 5:e15710. doi: 10.1371/journal.pone.0015710

Feis, D. L., Brodersen, K. H., von Cramon, D. Y., Luders, E., and Tittgemeyer, M. (2013). Decoding gender dimorphism of the human brain using multimodal anatomical and diffusion MRI data. *Neuroimage* 70, 250–257. doi: 10.1016/j.neuroimage.2012.12.068

Finn, E. S., Shen, X., Scheinost, D., Rosenberg, M. D., Huang, J., Chun, M. M., et al. (2015). Functional connectome fingerprinting: identifying individuals using patterns of brain connectivity. *Nat. Neurosci.* 18, 1664–1671. doi: 10.1038/nn.4135

Fischl, B. (2012). FreeSurfer. *Neuroimage* 62, 774–781. doi: 10.1016/j.neuroimage.2012.01.021

Fox, M. D., and Raichle, M. E. (2007). Spontaneous fluctuations in brain activity observed with functional magnetic resonance imaging. *Nat. Rev. Neurosci.* 8, 700–711. doi: 10.1038/nrn2201

Franke, K., Luders, E., May, A., Wilke, M., and Gaser, C. (2012). Brain maturation: predicting individual BrainAGE in children and adolescents using structural MRI. *Neuroimage* 63, 1305–1312. doi: 10.1016/j.neuroimage.2012.08.001

Glasser, M. F., Smith, S. M., Marcus, D. S., Andersson, J. L. R., Auerbach, E. J., Behrens, T. E., et al. (2016). The human connectome project's neuroimaging approach. *Nat. Neurosci.* 19, 1175–1187. doi: 10.1038/nn.4361

Glasser, M. F., Sotiropoulos, S. N., Wilson, J. A., Coalson, T. S., Fischl, B., Andersson, J. L., et al. (2013). The minimal preprocessing pipelines for the human connectome project. *Neuroimage* 80, 105–124. doi: 10.1016/j.neuroimage.2013.04.127

Gong, Q. Y., Li, L. J., Du, M. Y., Pettersson-Yeo, W., Crossley, N., Yang, X., et al. (2014). Quantitative prediction of individual psychopathology in trauma survivors using resting-state fMRI. *Neuropsychopharmacology* 39, 681–687. doi: 10.1038/npp.2013.251

Guo, G., and Mu, G. (2011). "Simultaneous dimensionality reduction and human age estimation via kernel partial least squares regression," in *Proceedings of the Paper Presented at the CVPR 2011*, (Providence, RI: IEEE).

Guo, G., and Mu, G. (2013). "Joint estimation of age, gender and ethnicity: CCA vs. PLS," in *Proceedings of the Paper Presented at the 2013 10th IEEE International Conference and Workshops on Automatic Face and Gesture Recognition (FG)*, (Shanghai: IEEE).

Hansen, P. M., and Schjoerring, J. K. (2003). Reflectance measurement of canopy biomass and nitrogen status in wheat crops using normalized difference vegetation indices and partial least squares regression. *Remote Sens. Environ.* 86, 542–553. doi: 10.1016/s0034-4257(03)00131-7

Jenkinson, M., Beckmann, C. F., Behrens, T. E., Woolrich, M. W., and Smith, S. M. (2012). FSL. *Neuroimage* 62, 782–790. doi: 10.1016/j.neuroimage.2011.09.015

Jiang, R., Calhoun, V. D., Zuo, N., Lin, D., Li, J., Fan, L., et al. (2018). Connectome-based individualized prediction of temperament trait scores. *Neuroimage* 183, 366–374. doi: 10.1016/j.neuroimage.2018.08.038

Kanai, R., and Rees, G. (2011). The structural basis of inter-individual differences in human behaviour and cognition. *Nat. Rev. Neurosci.* 12, 231–242. doi: 10.1038/nrn3000

Krishnan, A., Williams, L. J., Mcintosh, A. R., and Abdi, H. (2011). Partial least squares (PLS) methods for neuroimaging: a tutorial and review. *Neuroimage* 56, 455–475. doi: 10.1016/j.neuroimage.2010.07.034

Kuceyeski, A., Monohan, E., Morris, E., Fujimoto, K., Vargas, W., and Gauthier, S. A. (2018). Baseline biomarkers of connectome disruption and atrophy predict future processing speed in early multiple sclerosis. *Neuroimage Clin.* 19, 417–424. doi: 10.1016/j.nicl.2018.05.003

Marrelec, G., Krainik, A., Duffau, H., Pelegrini-Issac, M., Lehericy, S., Doyon, J., et al. (2006). Partial correlation for functional brain interactivity investigation in functional MRI. *Neuroimage* 32, 228–237. doi: 10.1016/j.neuroimage.2005.12.057

Meskaldji, D.-E., Preti, M. G., Bolton, T. A., Montandon, M.-L., Rodriguez, C., Morgenthaler, S., et al. (2016). Prediction of long-term memory scores in MCI based on resting-state fMRI. *Neuroimage Clin.* 12, 785–795. doi: 10.1016/j.nicl.2016.10.004

Moeller, S., Yacoub, E., Olman, C. A., Auerbach, E., Strupp, J., Harel, N., et al. (2010). Multiband multislice GE-EPI at 7 tesla, with 16-fold acceleration using partial parallel imaging with application to high spatial and temporal whole-brain fMRI. *Magn. Reson. Med.* 63, 1144–1153. doi: 10.1002/mrm.22361

Parasuraman, R., and Jiang, Y. (2012). Individual differences in cognition, affect, and performance: behavioral, neuroimaging, and molecular genetic approaches. *Neuroimage* 59, 70–82. doi: 10.1016/j.neuroimage.2011.04.040

Rathore, S., Habes, M., Iftikhar, M. A., Shacklett, A., and Davatzikos, C. (2017). A review on neuroimaging-based classification studies and associated feature extraction methods for Alzheimer's disease and its prodromal stages. *Neuroimage* 155, 530–548. doi: 10.1016/j.neuroimage.2017.03.057

Rosenberg, M. D., Finn, E. S., Scheinost, D., Papademetris, X., Shen, X., Constable, R. T., et al. (2016). A neuromarker of sustained attention from whole-brain functional connectivity. *Nat. Neurosci.* 19, 165–171. doi: 10.1038/nn.4179

Setsompop, K., Gagoski, B. A., Polimeni, J. R., Witzel, T., Wedeen, V. J., and Wald, L. L. (2012). Blipped-controlled aliasing in parallel imaging for simultaneous multislice echo planar imaging with reduced g-factor penalty. *Magn. Reson. Med.* 67, 1210–1224. doi: 10.1002/mrm.23097

Siegel, J. S., Ramsey, L. E., Snyder, A. Z., Metcalf, N. V., Chacko, R. V., Weinberger, K., et al. (2016). Disruptions of network connectivity predict impairment in multiple behavioral domains after stroke. *Proc. Natl. Acad. Sci. U.S.A.* 113, E4367–E4376. doi: 10.1073/pnas.1521083113

Smith, S. M., Beckmann, C. F., Andersson, J., Auerbach, E. J., Bijsterbosch, J., Douaud, G., et al. (2013). Resting-state fMRI in the human connectome project. *Neuroimage* 80, 144–168. doi: 10.1016/j.neuroimage.2013.05.039

Stonnington, C. M., Chu, C., Klöppel, S., Jack, C. R. Jr., Ashburner, J., Frackowiak, R. S., et al. (2010). Predicting clinical scores from magnetic resonance scans in Alzheimer's disease. *Neuroimage* 51, 1405–1413. doi: 10.1016/j.neuroimage.2010.03.051

Tian, L., Ma, L., and Wang, L. (2016). Alterations of functional connectivities from early to middle adulthood: clues from multivariate pattern analysis of resting-state fMRI data. *Neuroimage* 129, 389–400. doi: 10.1016/j.neuroimage.2016.01.039

Ullman, H., Almeida, R., and Klingberg, T. (2014). Structural maturation and brain activity predict future working memory capacity during childhood development. *J. Neurosci.* 34, 1592–1598. doi: 10.1523/JNEUROSCI.0842-13.2014

Van Essen, D. C., Smith, S. M., Barch, D. M., Behrens, T. E. J., Yacoub, E., and Ugurbil, K. (2013). The WU-minn human connectome project: an overview. *Neuroimage* 80, 62–79. doi: 10.1016/j.neuroimage.2013.05.041

Wan, J., Zhang, Z., Rao, B. D., Fang, S., Yan, J., Saykin, A. J., et al. (2014). Identifying the neuroanatomical basis of cognitive impairment in Alzheimer's disease by correlation- and nonlinearity-aware sparse bayesian learning. *IEEE Trans. Med. Imaging* 33, 1475–1487. doi: 10.1109/TMI.2014.2314712

Wold, H. (1982). "Soft modeling: the basic design and some extensions," in *Proceedings of the Paper Presented at the Systems Under Indirect Observation*, eds K. G. Joreskog, and H. O. A. Wold, (Amsterdam).

Wu, J., Srinivasan, R., Kaur, A., and Cramer, S. C. (2014). Resting-state cortical connectivity predicts motor skill acquisition. *Neuroimage* 91, 84–90. doi: 10.1016/j.neuroimage.2014.01.026

Xu, J., Moeller, S., Strupp, J., Auerbach, E., Chen, L., Feinberg, D., et al. (2012). Highly accelerated whole brain imaging using aligned-blipped-controlled-aliasing multiband EPI. *Proc. Int. Soc. Mag. Reson. Med.* 20:2306.

Yang, J.-J., Yoon, U., Yun, H., Im, K., Choi, Y., Lee, K., et al. (2013). Prediction for human intelligence using morphometric characteristics of cortical surface: partial least square analysis. *Neuroscience* 246, 351–361. doi: 10.1016/j.neuroscience.2013.04.051

Yoo, K., Rosenberg, M. D., Hsu, W. T., Zhang, S., Li, C. R., Scheinost, D., et al. (2018). Connectome-based predictive modeling of attention: comparing different functional connectivity features and prediction methods across datasets. *Neuroimage* 167, 11–22. doi: 10.1016/j.neuroimage.2017.11.010

Yoshida, K., Shimizu, Y., Yoshimoto, J., Takamura, M., Okada, G., Okamoto, Y., et al. (2017). Prediction of clinical depression scores and detection of changes in whole-brain using resting-state functional MRI data with partial least squares regression. *PLoS One* 12:e0179638. doi: 10.1371/journal.pone.0179638

Yu, G., Liu, Y., and Shen, D. (2016). Graph-guided joint prediction of class label and clinical scores for the Alzheimer's disease. *Brain Struct. Funct.* 221, 3787–3801. doi: 10.1007/s00429-015-1132-6

Zhang, C., Dougherty, C. C., Baum, S. A., White, T., and Michael, A. M. (2018). Functional connectivity predicts gender: evidence for gender differences in resting brain connectivity. *Hum. Brain Mapp.* 39, 1765–1776. doi: 10.1002/hbm.23950

Zhang, D., Shen, D., and Alzheimer's Disease Neuroimaging Initiative (2012). Multi-modal multi-task learning for joint prediction of multiple regression and classification variables in Alzheimer's disease. *Neuroimage* 59, 895–907. doi: 10.1016/j.neuroimage.2011.09.069

Zhang, M.-L., and Zhou, Z.-H. (2014). A review on multi-label learning algorithms. *IEEE T. Knowl. Data En.* 26, 1819–1837. doi: 10.1109/tkde.2013.39

Conflict of Interest: The authors declare that the research was conducted in the absence of any commercial or financial relationships that could be construed as a potential conflict of interest.

Copyright © 2019 Chen, Cao and Tian. This is an open-access article distributed under the terms of the Creative Commons Attribution License (CC BY). The use, distribution or reproduction in other forums is permitted, provided the original author(s) and the copyright owner(s) are credited and that the original publication in this journal is cited, in accordance with accepted academic practice. No use, distribution or reproduction is permitted which does not comply with these terms.

frontiers in Neuroscience

ORIGINAL RESEARCH
published: 17 January 2020
doi: 10.3389/fnins.2019.01440

Differential tDCS and tACS Effects on Working Memory-Related Neural Activity and Resting-State Connectivity

*Kilian Abellaneda-Pérez[1,2], Lídia Vaqué-Alcázar[1,2], Ruben Perellón-Alfonso[1,2], Núria Bargalló[3,4], Min-Fang Kuo[5], Alvaro Pascual-Leone[6,7,8], Michael A. Nitsche[5,9] and David Bartrés-Faz[1,2,8]**

[1] Department of Medicine, Faculty of Medicine and Health Sciences, Institute of Neurosciences, University of Barcelona, Barcelona, Spain, [2] Institute of Biomedical Research August Pi i Sunyer, Barcelona, Spain, [3] Hospital Clínic de Barcelona, Magnetic Resonance Image Core Facility, Institute of Biomedical Research August Pi i Sunyer, Barcelona, Spain, [4] Hospital Clínic de Barcelona, Neuroradiology Section, Radiology Service, Centre de Diagnòstic per la Imatge, Barcelona, Spain, [5] Leibniz Research Centre for Working Environment and Human Factors, Dortmund, Germany, [6] Hinda and Arthur Marcus Institute for Aging Research, Hebrew SeniorLife, Boston, MA, United States, [7] Department of Neurology, Harvard Medical School, Boston, MA, United States, [8] Guttmann Brain Health Institute, Institut Universitari de Neurorehabilitació Guttmann, Autonomous University of Barcelona, Bellaterra, Spain, [9] Department of Neurology, University Medical Hospital Bergmannsheil, Bochum, Germany

OPEN ACCESS

Edited by:
Oscar Arias-Carrión, Hospital General Dr. Manuel Gea Gonzalez, Mexico

Reviewed by:
Silmar Teixeira, Federal University of Piauí, Brazil
Daniel Keeser, Ludwig Maximilian University of Munich, Germany

***Correspondence:**
David Bartrés-Faz
dbartres@ub.edu

Specialty section:
This article was submitted to Brain Imaging Methods, a section of the journal Frontiers in Neuroscience

Received: *13 September 2019*
Accepted: *20 December 2019*
Published: *17 January 2020*

Citation:
Abellaneda-Pérez K, Vaqué-Alcázar L, Perellón-Alfonso R, Bargalló N, Kuo M-F, Pascual-Leone A, Nitsche MA and Bartrés-Faz D (2020) Differential tDCS and tACS Effects on Working Memory-Related Neural Activity and Resting-State Connectivity. Front. Neurosci. 13:1440. doi: 10.3389/fnins.2019.01440

Transcranial direct and alternating current stimulation (tDCS and tACS, respectively) entail capability to modulate human brain dynamics and cognition. However, the comparability of these approaches at the level of large-scale functional networks has not been thoroughly investigated. In this study, 44 subjects were randomly assigned to receive sham (N = 15), tDCS (N = 15), or tACS (N = 14). The first electrode (anode in tDCS) was positioned over the left dorsolateral prefrontal cortex, the target area, and the second electrode (cathode in tDCS) was placed over the right supraorbital region. tDCS was delivered with a constant current of 2 mA. tACS was fixed to 2 mA peak-to-peak with 6 Hz frequency. Stimulation was applied concurrently with functional magnetic resonance imaging (fMRI) acquisitions, both at rest and during the performance of a verbal working memory (WM) task. After stimulation, subjects repeated the fMRI WM task. Our results indicated that at rest, tDCS increased functional connectivity particularly within the default-mode network (DMN), while tACS decreased it. When comparing both fMRI WM tasks, it was observed that tDCS displayed decreased brain activity post-stimulation as compared to online. Conversely, tACS effects were driven by neural increases online as compared to post-stimulation. Interestingly, both effects primarily occurred within DMN-related areas. Regarding the differences in each fMRI WM task, during the online fMRI WM task, tACS engaged distributed neural resources which did not overlap with the WM-dependent activity pattern, but with some posterior DMN regions. In contrast, during the post-stimulation fMRI WM task, tDCS strengthened prefrontal DMN deactivations, being these activity reductions associated with faster responses. Furthermore, it was observed that tDCS neural responses presented certain consistency across distinct fMRI modalities, while tACS did not. In sum, tDCS and tACS modulate fMRI-derived network dynamics differently. However, both effects seem to focus on DMN regions and the WM network-DMN shift, which are highly affected in

aging and disease. Thus, albeit exploratory and needing further replication with larger samples, our results might provide a refined understanding of how the DMN functioning can be externally modulated through commonly used non-invasive brain stimulation techniques, which may be of eventual clinical relevance.

Keywords: transcranial direct current stimulation (tDCS), transcranial alternating current stimulation (tACS), resting-state functional magnetic resonance imaging (rs-fMRI), task-based functional magnetic resonance imaging (tb-fMRI), working memory (WM)

INTRODUCTION

Working memory (WM) provides temporary storage and manipulation of information required for a variety of complex cognitive tasks (Baddeley, 1992, 2010). WM capacity plays a central role in daily life activities and is predictive for a wide-range of higher-level cognitive measures (Johnson et al., 2013; Unsworth et al., 2014). Impairments in WM entail functionally disabling symptoms in advanced age (Park et al., 2002; Park and Reuter-Lorenz, 2009; Anderson and Craik, 2017) and in several neuropsychiatric conditions (Lee and Park, 2005; Nakao et al., 2009).

The WM network (WMN) includes a fronto-parietal loop (Owen et al., 2005), where the dorsolateral prefrontal cortex (dlPFC) is of particular relevance (Curtis and D'Esposito, 2003; Barbey et al., 2013). This fronto-parietal circuit shows a negative correlation with the default-mode network (DMN; Fox et al., 2005; Buckner et al., 2008; Raichle, 2015). The DMN has been shown to be consistently activated during rest, while its nodes are inhibited during externally oriented tasks (Fox et al., 2005; Pfefferbaum et al., 2011). Thus, the brain may shift between two modes of information processing, one that puts the attentional focus on external stimuli and another one that relates to internally directed processing (Buckner et al., 2008). At the electrophysiological level, it has been shown that WM processes are mediated by synchronous firing of neural populations at distinct frequencies as well as via cross-frequency coupling (Sarnthein et al., 1998; Howard et al., 2003; Sauseng et al., 2005; Jensen and Colgin, 2007; Lisman and Jensen, 2013; Roux and Uhlhaas, 2014). A large body of literature indicates that the coupling of theta and gamma oscillations mediates communication within and between brain networks in general and during WM tasks in particular, possibly accounting for WM processing and capacity demands (for a review see Lisman and Jensen, 2013; Hanslmayr et al., 2019).

Despite the fact that neuroimaging and neurophysiological investigations have been providing relevant data on the anatomo-functional correlates of WMN and its anticorrelated systems (Nee et al., 2013; Roux and Uhlhaas, 2014; Eriksson et al., 2015; Raichle, 2015), the cognitive benefits derived from interventional approaches aimed to improve WM functioning have been limited. Notwithstanding, new methodologies, such as transcranial electrical stimulation (tES), have recently shown potential to enhance WM performance by targeting its critical network hubs, such as the dlPFC (Fregni et al., 2005; Ohn et al., 2008; Zaehle et al., 2011; Brunoni and Vanderhasselt, 2014; Meiron and Lavidor, 2014; Hoy et al., 2015; Alekseichuk et al., 2016; Dedoncker et al., 2016). Nevertheless, and despite this promising developments, data is still inconclusive, particularly in healthy populations (Tremblay et al., 2014; Hsu et al., 2015; Nilsson et al., 2015; Mancuso et al., 2016; Hill et al., 2017; Medina and Cason, 2017; Imburgio and Orr, 2018).

Among tES techniques, transcranial direct current stimulation (tDCS) and transcranial alternating current stimulation (tACS) are the most commonly used (Polanía et al., 2018). tDCS delivers weak tonic currents to the scalp. During tDCS, neural membrane potentials are depolarized under the anode, leading to an increase in cortical excitability, while neural membrane hyperpolarization develops under the cathode, thereby diminishing cortical excitability (Purpura and McMurtry, 1965; Nitsche and Paulus, 2000; Nitsche et al., 2008). On the other hand, tACS applies a sinusoidal current to the scalp at specific frequencies, exerting an exogenous modulation of ongoing brain oscillations (Zaghi et al., 2010a; Ali et al., 2013; Antal and Paulus, 2013; Herrmann et al., 2013; Reato et al., 2013; Antal and Herrmann, 2016; Moisa et al., 2016). Beyond their immediate impact, both techniques display after-effects that can outlast the period of stimulation, probably due to their capability to induce neuroplasticity-like processes (Nitsche and Paulus, 2001; Liebetanz et al., 2002; Nitsche et al., 2003; Monte-Silva et al., 2013; Vossen et al., 2015; Kasten et al., 2016; Wischnewski et al., 2019).

In this context, only two studies have explored the differential impact of tDCS and tACS on WM performance (Hoy et al., 2015; Röhner et al., 2018), indicating a more relevant effect of tACS as compared to tDCS. However, the physiological underpinnings of those protocols over large-scale neural systems supporting the WM function remain understudied. Further, to our knowledge, a direct comparison of the effects of these different stimulation protocols at the functional magnetic resonance imaging (fMRI)-derived network level has not been so far investigated. Since aging and various neuropsychiatric disorders show alterations in WM circuits and may benefit from their modulation, a better insight on tES impact on the brain's WMN and its linked neural systems, such as the DMN, would likely have clinical translational relevance.

MATERIALS AND METHODS

Participants

Forty-four healthy young subjects [age mean ± standard deviation (*SD*), 25.25 ± 4.22 years; age range, 19–37 years; 20 females; years of education mean ± *SD*, 21.11 ± 3.40 years;

36 right-handed] naive to tES were recruited from the general population and provided informed consent to participate in this study, in accordance with the Declaration of Helsinki (1964, last revision 2013). All study procedures were approved by the Institutional Review Board (IRB 00003099). None of the participants reported a diagnosis of a neurological or psychiatric disorder. For all participants, MRI images were examined by a senior neuroradiologist for any clinically significant pathology (none found).

Experimental Design

The present study was conducted in a randomized between-subjects placebo-controlled design. Online effects of prefrontal tDCS and tACS on resting-state fMRI (rs-fMRI) were assessed. Furthermore, the online and post-stimulation impact of these intervention protocols on WM-related neural activity and performance was explored, using a similar experimental setting as described elsewhere (i.e., Meiron and Lavidor, 2014; Brauer et al., 2018). Participants were randomly assigned to receive sham stimulation (N = 15), anodal tDCS (N = 15) or theta tACS (N = 14; **Figure 1A**) over the left dlPFC (l-dlPFC; **Figure 1B**; see also see section "Transcranial Electrical Stimulation (tES) Parameters"). A simple randomization procedure was used (Altman and Bland, 1999; Kang et al., 2008).

First, a brief cognitive assessment was conducted to obtain an estimation of the intelligence quotient (IQ) of the participants, using the vocabulary subtest of the Wechsler Adult Intelligence Scale-IV (WAIS-IV). Subsequently and within the same experimental day, tES was applied inside an MRI scanner. Here, an rs-fMRI sequence (∼8 min) was acquired before subjects underwent two sequential task-based fMRI (tb-fMRI) acquisitions while performing two identical verbal n-back tasks (∼11 min each one; Sala-Llonch et al., 2012). The rs-fMRI and the first tb-fMRI datasets were acquired during stimulation (i.e., online fMRI n-back task) and the second tb-fMRI sequence after stimulation delivery was turned off (i.e., post-stimulation fMRI n-back task). A high-resolution three-dimensional (hr-3D) structural image (∼8 min) was acquired at the end of the MRI session for co-registration purposes. A questionnaire of tES-related adverse events was administered at the end of the experimental session [adapted from Brunoni et al., 2011; **Figure 1C**; see also **Supplementary Material (SM)**].

Transcranial Electrical Stimulation (tES) Parameters

Stimulation was delivered using a battery-driven MRI-compatible DC-Stimulator Plus (neuroConn GmbH, Ilmenau, Germany) and was transferred by two MRI-compatible conductive rubber electrodes (7 cm × 5 cm) positioned in a room adjacent to the MRI scanner. The same montage was used in all groups, as applied in similar recent comparative studies (Lang et al., 2019). According to the international 10–10 system of measurement, the first electrode (anode in tDCS) was positioned over the F3 (l-dlPFC) and the second electrode (cathode in tDCS) was placed over the FP2 (right supraorbital area). This is one of the standard montages frequently employed to stimulate the l-dlPFC (Fregni et al., 2005; Nitsche et al., 2008; Ohn et al., 2008), the target area. In all groups, the current was initially increased and finally decreased in a ramp-like fashion of 15 s. In the sham condition, the current delivery was terminated after 30 s of stimulation with no further blinding processes. In the real stimulation groups, the current was supplied during 20 min, which covered the rs-fMRI acquisition and the first tb-fMRI sequence. tDCS was delivered with a constant current of 2 mA. tACS was fixed to 2 mA peak-to-peak in a 6 Hz frequency. We selected 6 Hz as this frequency has been widely used in recent tACS WM investigations (i.e., Polanía et al., 2012; Alekseichuk et al., 2016; Violante et al., 2017; Brauer et al., 2018; Röhner et al., 2018; Lang et al., 2019). All stimulation parameters adhered to safety criteria guidelines (Zaghi et al., 2010b; Fertonani et al., 2015; Bikson et al., 2016; Woods et al., 2016; Matsumoto and Ugawa, 2017; see SM for more details).

N-Back Task

Subjects performed a verbal n-back task, a commonly used paradigm to investigate WM in fMRI (Owen et al., 2005). The n-back task had different levels of memory load (from 1 to 3 letters to be retained) and a basic level of target stimulus identification that were randomly presented during the two

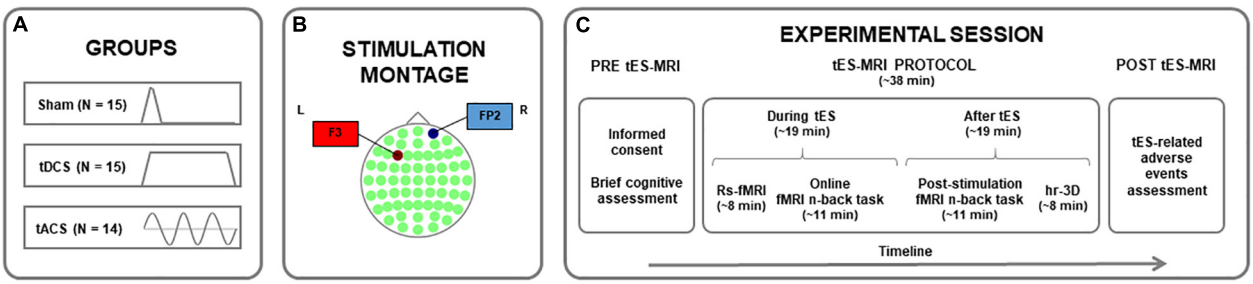

FIGURE 1 | Study protocol. **(A)** Assignment of participants to one of the experimental groups. **(B)** Stimulation montage for all groups, with the first electrode (anode for tDCS) centered over the F3 (in red) and the second electrode (cathode for tDCS) placed over the FP2 (in blue) in a 10–10 system map. **(C)** Timeline of the procedures accomplished before, during and after the tES-MRI protocol. tDCS, transcranial direct current stimulation; tACS, transcranial alternating current stimulation; tES, transcranial electrical stimulation; MRI, magnetic resonance imaging; rs-fMRI, resting-state functional MRI; hr-3D, high-resolution three-dimensional.

consecutive tasks achieved inside the MRI scan (Sala-Llonch et al., 2012; see SM for more information).

MRI Acquisition

All participants were scanned with a Siemens Magnetom Trio Tim Syngo 3 Tesla system using an 8-channel head coil at the Magnetic Resonance Image Core Facility (IDIBAPS) at the Hospital Clínic de Barcelona, Barcelona, Spain. The imaging sequences were acquired with the following parameters. First, a rs-fMRI dataset (T2*-weighted GE-EPI sequence; interleaved acquisition; repetition time [TR] = 2,700 ms; echo time [TE] = 30 ms; 40 slices per volume; slice thickness = 3.0 mm; interslice gap = 15%; voxel size = 3.0 mm × 3.0 mm × 3.0 mm; field of view [FOV] = 216 mm; 178 volumes) was acquired. Later, two identical fMRI n-back task datasets (T2*weighted EPI scans; interleaved acquisition; TR = 2,000 ms; TE = 28 ms; 34 slices per volume; slice thickness = 3.5 mm; interslice gap = 15%; voxel size = 3.5 mm × 3.5 mm × 3.5 mm; FOV = 238 mm; 336 volumes) were acquired, one during stimulation and another one after stimulation cessation. Lastly, a hr-3D structural dataset (T1-weighted magnetization-prepared rapid gradient-echo [T1-weighted MPRAGE]; sagittal plane acquisition; TR = 2,300 ms; TE = 2.98 ms; inversion time [IT] = 900 ms; slice thickness = 1.0 mm; voxel size = 1.0 mm × 1.0 mm × 1.0 mm; FOV = 256 mm; 240 slices) was acquired.

Image Analyses

The FMRIB Software Library (FSL; version 6.00[1]) and the Analysis of Functional NeuroImages (AFNI[2]) were used for preprocessing and analyzing neuroimaging data. Rs- and tb-fMRI preprocessing pipelines and head movement considerations are described in SM.

Functional Connectivity Analyses

Resting-state functional connectivity (rs-FC) analyses were performed using a seed-to-seed approach, following previous procedures in our group (i.e., Abellaneda-Pérez et al., 2019). Firstly, the concatenated fMRI dataset containing all rs-fMRI acquisitions from the entire sample was decomposed through independent component analysis (ICA) into 15 components using the Multivariate Exploratory Linear Optimized Decomposition into Independent Components (MELODIC; version 3.15) algorithm, part of the FSL (Smith et al., 2004; Beckmann et al., 2005; Jenkinson et al., 2012). The components related to the archetypical resting-state network, namely the DMN (Fox et al., 2005; Buckner et al., 2008; Raichle, 2015), along with the WM-related systems, the left and right fronto-parietal networks (lFPN and rFPN, respectively), were selected in a similar manner as described in previous reports from our group (i.e., Sala-Llonch et al., 2012). Furthermore, the executive-control network (ECN) was additionally considered due to its prefrontal nodes and its known relevance in cognitive functions (Smith et al., 2009). Moreover, two components that do not include the l-dlPFC and are not related to cognitive processing were used as control networks, namely the sensorimotor and visual-medial networks (SMN and VMN, respectively), as has been done in previous work of our group (i.e., Peña-Gómez et al., 2012). All components were identified using spatial correlations against previously defined maps (Smith et al., 2009). Secondly, the main regions of interest (ROIs) were selected based on the peak voxels of each network (**Figure 2** and **Table 1**). Next, spherical seeds with a 6-mm radius were placed over the identified regions, and ROI-specific time-series from the preprocessed and regressed data were extracted. Finally, to obtain an rs-FC measure for each seed-to-seed coupling in each subject, obtained ROI time-series were correlated with each other within every network using Pearson's correlation coefficients.

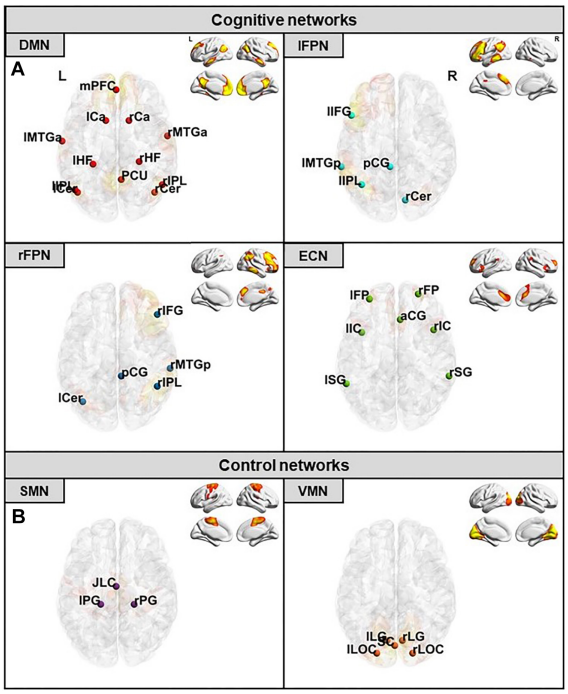

FIGURE 2 | Selected networks and their respective ROIs location. **(A)** Cognitive networks with their corresponding ROIs in red for the DMN, in light blue for the lFPN, in dark blue for the rFPN, and in green for the ECN. **(B)** Control networks with their corresponding ROIs in purple for the SMN and in orange for the VMN. DMN, default-mode network; lFPN, left fronto-parietal network; rFPN, right fronto-parietal network; ECN, executive-control network; SMN, sensorimotor network; VMN, visual-medial network. For ROI abbreviations see **Table 1**.

N-Back fMRI Data

Tb-fMRI data were analyzed with the FEAT-FSL software (Smith et al., 2004). At the first-level analysis, data were fit into a general linear model (GLM) containing the task time-series with a gamma convolution of the hemodynamic response function (Woolrich et al., 2001). In this GLM, four regressors and their first temporal derivatives were modeled: 0-back, 1-back, 2-back,

[1]http://fsl.fmrib.ox.ac.uk/fsl/fslwiki/

[2]https://afni.nimh.nih.gov/

TABLE 1 | Selected networks and their respective ROIs with associated coordinates in the Montreal Neurological Institute (MNI) system.

RSNs	MNI coordinates			ROI	ROI abbreviated
	X	*Y*	*Z*		
DMN	0	51	−15	Medial prefrontal cortex	mPFC
	6	−54	21	Precuneus cortex	PCU
	−48	−66	30	Left inferior parietal lobule	lIPL
	54	−60	27	Right inferior parietal lobule	rIPL
	−63	−9	−21	Left middle temporal gyrus (anterior division)	lMTGa
	60	−3	−24	Right middle temporal gyrus (anterior division)	rMTGa
	−12	15	3	Left caudate	lCa
	15	15	6	Right caudate	rCa
	−27	−36	−18	Left hippocampal formation	lHF
	27	−33	−15	Right hippocampal formation	rHF
	−45	−69	−42	Left cerebellum	lCer
	45	−69	−42	Right cerebellum	rCer*
lFPN	−51	21	21	Left inferior frontal gyrus	lIFG
	−39	−60	42	Left inferior parietal lobule	lIPL
	−63	−39	−9	Left middle temporal gyrus (posterior division)	lMTGp
	−6	−39	33	Cingulate gyrus (posterior division)	pCG
	12	−78	−30	Right cerebellum	rCer
rFPN	48	33	27	Right inferior frontal gyrus	rIFG
	48	−51	48	Right inferior parietal lobule	rIPL
	63	−30	−15	Right middle temporal gyrus (posterior division)	rMTGp
	6	−39	36	Cingulate gyrus (posterior division)	pCG
	−39	−69	−48	Left cerebellum	lCer
ECN	6	27	24	Cingulate gyrus (anterior division)	aCG
	−30	51	18	Left frontal pole	lFP
	27	57	18	Right frontal pole	rFP
	−39	12	−6	Left insular cortex	lIC
	45	15	−6	Right insular cortex	rIC
	−57	−48	30	Left supramarginal gyrus	lSG
	63	−39	33	Right supramarginal gyrus	rSG
SMN	0	−9	51	Juxtapositional lobule cortex	JLC
	−18	−30	63	Left precentral gyrus	lPG
	21	−30	60	Right precentral gyrus	rPG
VMN	0	−78	18	Supracalcarine cortex	SC
	−21	−87	27	Left lateral occipital cortex	lLOC*
	21	−87	27	Right lateral occipital cortex	rLOC
	−9	−72	0	Left lingual gyrus	lLG
	9	−72	0	Right lingual gyrus	rLG*

The asterisk (*) represents those ROIs that were not identified based on the functional peak voxels but selected for anatomo-functional reasons regarding the coordinates of the homologous region in the other hemisphere, being the two ROIs inside the network in the most anatomically plausible position. RSNs, resting-state networks; DMN, default-mode network; lFPN, left fronto-parietal network; rFPN, right fronto-parietal network; ECN, executive-control network; SMN, sensorimotor network; VMN, visual-medial network; MNI, Montreal Neurological Institute; ROI, region of interest.

and 3-back. We defined three contrasts of interest combining the distinct loads, as the difference of brain activity between 1-back, 2-back, and 3-back and the lowest load (0-back), namely: (1) lowest WM load: 1 > 0-back; (2) intermediate WM load: 2 > 0-back; and (3) highest WM load: 3 > 0-back. The results of the first-level analysis were further fit into higher-level or group-level statistics, performed using the FMRIB's Local Analysis of Mixed Effects (FLAME; Woolrich et al., 2004). We conducted GLM matrices modeling the different tES time-points (online and post-stimulation) and experimental groups (sham, tDCS, and tACS). Using this second-level GLM and the appropriate contrasts, we evaluated: (1) the group-mean activity maps of the three selected contrasts of interest in the first-level analysis (1 > 0-back, 2 > 0-back, and 3 > 0-back), in order to explore the WM-related neural patterns for each one in every tES time-point; (2) the interactions between tES time-point as a within-subject factor and group as a between-subject factor; (3) the patterns of time-related change within each group, as pairwise paired-samples *t*-tests; and (4) the group differences in each tES time-point separately, exploring neural changes in the following contrasts: tDCS vs. sham, tACS vs. sham and tDCS vs. tACS, as pairwise independent-samples *t*-tests. These analyses were performed voxel-wise and the statistical significance of the resulting maps was set at $p \leq 0.05$ and $z \geq 2.3$ (cluster-wise corrected).

Statistical Analyses

Non-imaging data analyses were performed using IBM SPSS (IBM, Corp., Released 2016. IBM SPSS Statistics for Windows, Version 24.0. Armonk, NY, United States: IBM, Corp.) and MATLAB (Version R2019a, The MathWorks, Inc., Natick, MA, United States). To evaluate differences between groups (sham, tDCS, and tACS) in seed-to-seed rs-FC connections, a one-factorial analysis of variance (ANOVA) was conducted, and all *post hoc* pairwise comparisons were subjected to Bonferroni correction. This statistical procedure was also used when considering tES-related adverse events. To evaluate differences in cognitive performance, a univariate ANOVA was conducted with tES time-point (online and post-stimulation) as a within-subject factor and group (sham, tDCS, and tACS) as a between-subject factor. Following this ANOVA, if there were significant interactions, two pairwise analyses were conducted. First, paired-samples *t*-tests were conducted to assess differences in performance over time in each group. Second, independent-samples *t*-tests were conducted to compare performance between groups for each tES time-point separately. Further, to obtain summary statistics, we extracted the mean values of the blood oxygen level dependent (BOLD) signal from the fMRI clusters derived from the significant neuroimaging results. These data were used to plot the fMRI findings and to corroborate the obtained results. Moreover, these data were used to associate the fMRI BOLD signal with cognitive performance estimates and rs-FC data using Pearson's correlations. All non-imaging statistical analyses were two-tailed and α was set at 0.05 (see SM for further details).

TABLE 2 | Demographics and neuropsychological data.

	Total (*N* = 44)	Sham (*N* = 15)	tDCS (*N* = 15)	tACS (*N* = 14)
Age	25.25 ± 4.22	25.40 ± 3.16	24.33 ± 4.12	26.07 ± 5.31
Gender (female/male)	20/24	8/7	7/8	5/9
Years of education	21.11 ± 3.40	21.00 ± 1.73	20.87 ± 4.50	21.50 ± 3.61
Laterality (right-/left-handed)	36/8	13/2	11/4	12/2
Vocabulary WAIS-IV	44.16 ± 4.40	43.60 ± 2.80	42.93 ± 5.86	46.07 ± 3.54

Data are presented as mean ± SD for the whole sample and considering the three experimental groups. WAIS-IV, Wechsler Adult Intelligence Scale-IV; tDCS, transcranial direct current stimulation; tACS, transcranial alternating current stimulation.

RESULTS

Demographics and N-Back Task Performance

No differences in age, gender, years of education, laterality and premorbid intelligence were found between groups (all p values > 0.05; see **Table 2**). Behaviorally, we did not observe any significant difference in n-back task performance between tES time-points and experimental groups (**Supplementary Figure S1**).

Effects of tDCS and tACS on rs-FC

Rs-FC was differentially modulated with respect to the specific tES protocol. An interaction between groups revealed different connectivity of distinct couplings within the DMN and the ECN. Comparing the real tES groups with sham we observed higher rs-FC in the tDCS group and lower connectivity in the tACS group. Contrasting across the two real tES groups, we observed higher rs-FC in the tDCS group as compared to the tACS group (**Figure 3** and **Table 3**). No differences between groups were found for left and right FPNs. Control networks also remained unmodified.

Effects of tDCS and tACS on WM-Related Neural Activity

An interaction between tES time-points and experimental groups was found in the precuneus (PCU) cortex and the posterior cingulate gyrus in the 2 > 0-back contrast (**Supplementary Figure S2A**). Further, another interaction was observed in the lateral occipital and the angular gyrus in the 3 > 0-back contrast (**Supplementary Figure S2B**). The group-mean activity maps obtained from each contrast (1 > 0-back, 2 > 0-back, and 3 > 0-back) in the sham group (considered as the 'reference' WM brain patterns) are additionally displayed in SM (**Supplementary Figure S3**). These maps show the characteristic fronto-parietal WM patterns and the expected task-deactivations, mainly placed within DMN-related areas, like the medial prefrontal cortex (mPFC) and the PCU.

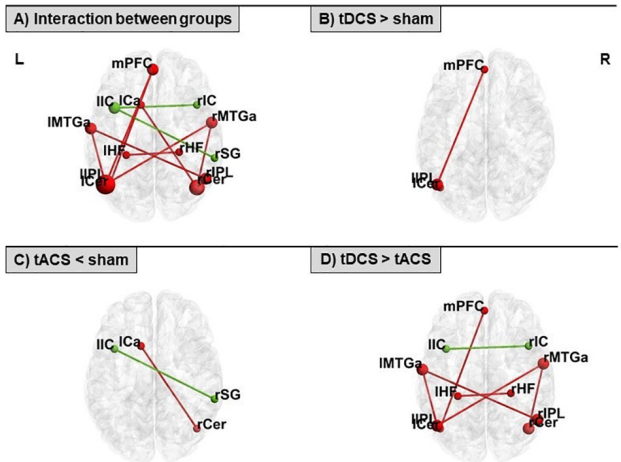

FIGURE 3 | Seed-to-seed statistically significant results within the DMN (in red) and the ECN (in green) for: **(A)** interaction between groups, **(B)** tDCS > sham, **(C)** tACS < sham, and **(D)** tDCS > tACS. tDCS, transcranial direct current stimulation; tACS, transcranial alternating current stimulation. For ROI abbreviations see **Table 1**.

Differential Effects Across tES Time-Points

The active stimulation groups showed differential changes in brain activity between both tES time-points. No time-related fMRI variances were found in sham participants. Specifically, neural modulations in the tDCS group were driven by clear decreases in brain activity post-stimulation as compared to online. These modulations were noticeable in view of the slight neural differences across time in the sham group within the observed significant areas. Anatomically, these changes were found in posterior midline structures during the lowest WM load and within medial frontal areas during the highest WM load (**Figure 4A**). Conversely, tACS effects appeared to be directed by manifest neural increases and robust lower deactivations online as compared to post-stimulation, in view of the minor brain activity changes in the sham group across time in the detected significant regions. At the anatomical level, increased neural activity was mainly evident during the intermediate WM load in the PCU, frontal and temporal regions, and the occipital lobe. Reduced deactivations were detected in the highest WM load in the medial frontal, posterior midline structures, and the left inferior parietal lobe (lIPL; **Figure 4B**). It is worth noticing that numerous of the detected fMRI clusters correspond to the main nodes of the DMN (i.e., those areas entailing typical task-deactivation processes).

Differential Online Effects

During the online fMRI n-back task performance, participants who received tACS exhibited larger brain activity compared to those who received sham in the three contrasts of interest. At the lowest and intermediate WM loads, more brain activity was found bilaterally in frontal regions, within the PCU, and in numerous widespread cortical (i.e., occipital) and subcortical (i.e., parahippocampal) regions. For the highest WM load, greater brain activity was only found bilaterally within the frontal pole

TABLE 3 | Seed-to-seed connections with statistically significant interactions and subsequent significant pairwise *post hoc* analyses within the DMN and the ECN.

RSNs	Seed-to-seed coupling	Interaction between groups	tDCS > sham	tACS < sham	tDCS > tACS
DMN	mPFC-lIPL	$F = 4.510$, $p = 0.017$	$p = 0.021$	–	–
	mPFC-lCer	$F = 5.089$, $p = 0.011$	–	–	$p = 0.009$
	lIPL-lMTGa	$H = 10.960$, $p = 0.004$	–	–	$p = 0.003$
	lIPL-rMTGa	$F = 5.569$, $p = 0.007$	–	–	$p = 0.008$
	lIPL-lCer	$F = 3.525$, $p = 0.039$	$p = 0.037$	–	–
	rIPL-lMTGa	$H = 6.904$, $p = 0.032$	–	–	$p = 0.033$
	rIPL-rCer	$F = 3.352$, $p = 0.045$	–	–	$p = 0.043$
	rMTGa-rCer	$F = 4.495$, $p = 0.017$	–	–	$p = 0.020$
	lCa-rCer	$H = 13.020$, $p = 0.001$	–	$p = 0.001$	–
	lHF-rHF	$F = 3.371$, $p = 0.044$	–	–	$p = 0.046$
ECN	lIC-rIC	$H = 8.502$, $p = 0.014$	–	–	$p = 0.013$
	lIC-rSG	$H = 7.875$, $p = 0.020$	–	$p = 0.016$	–

RSNs, resting-state networks; DMN, default-mode network; ECN, executive-control network; tDCS, transcranial direct current stimulation; tACS, transcranial alternating current stimulation. For ROI abbreviations see ***Table 1****.*

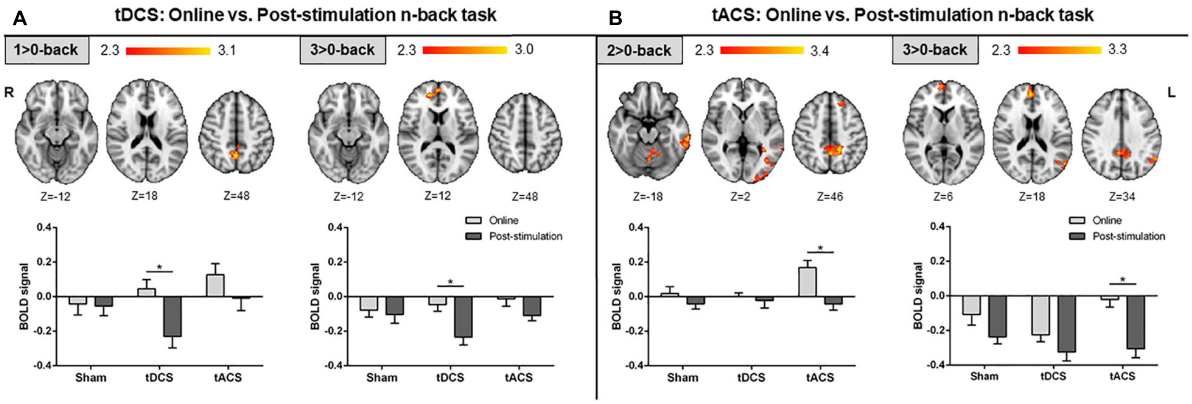

FIGURE 4 | Comparison between the online and post-stimulation fMRI n-back tasks in each group. **(A)** Online vs. post-stimulation results in the tDCS group. **(B)** Online vs. post-stimulation results in the tACS group. Top: statistically significant fMRI activity maps on the standard MNI for each contrast of interest. Results are shown in red-yellow for higher activations (or lower deactivations) online as compared to post-stimulation. Down: plots of mean BOLD signal values at the fMRI clusters considering sham, tDCS and tACS where significant differences between both fMRI n-back tasks were found. Data are presented as mean with standard error of the mean (*SEM*). tDCS, transcranial direct current stimulation; tACS, transcranial alternating current stimulation; BOLD, blood oxygen level dependent.

(**Figure 5A**). Furthermore, the tACS group exhibited larger brain activity in frontal areas, the PCU, and within the lIPL, when compared to the tDCS group, in the intermediate and highest WM loads (**Figure 5B**). No significant differences were found when comparing tDCS with sham at this tES time-point.

Differential Post-stimulation Effects

During the post-stimulation fMRI n-back task performance, differences in brain activity between tDCS and sham were detected. Specifically, in the intermediate WM load, the subcallosal cortex was found to be significantly more active in the tDCS than in the sham group. For the highest WM load, more fMRI signal was detected in a minor area of the right post-central gyrus in the tDCS group as compared to sham. Additionally, for the same WM load condition, the tDCS group showed significant lower brain activity within medial frontal structures when compared to sham (**Figure 6A**). When comparing tDCS vs. tACS, less brain activity was found in tDCS at the lowest WM load in distinct cortical (i.e., frontal and parietal) and subcortical (i.e., thalamic) areas. At the highest WM load, subjects who received tDCS showed lower activity as compared to tACS in right frontal areas only (**Figure 6B**). No significant differences were found when comparing tACS with sham at this tES time-point.

Associations Between WM-Related Neural Activity and Performance

At the highest WM load, those tDCS subjects with a greater reduction in brain activity post-stimulation compared to online within the fMRI cluster where tDCS showed less activity than sham post-stimulation (**Figure 6A**, blue-light blue fMRI cluster) showed faster reaction time (RT) post-stimulation as compared to online performance ($r = 0.540$, $p = 0.038$; **Figure 7**). Faster responses were not associated with lower accuracy (i.e., d′; $p > 0.05$). No significant associations were detected between brain activity and performance in the tACS group (all p values > 0.05).

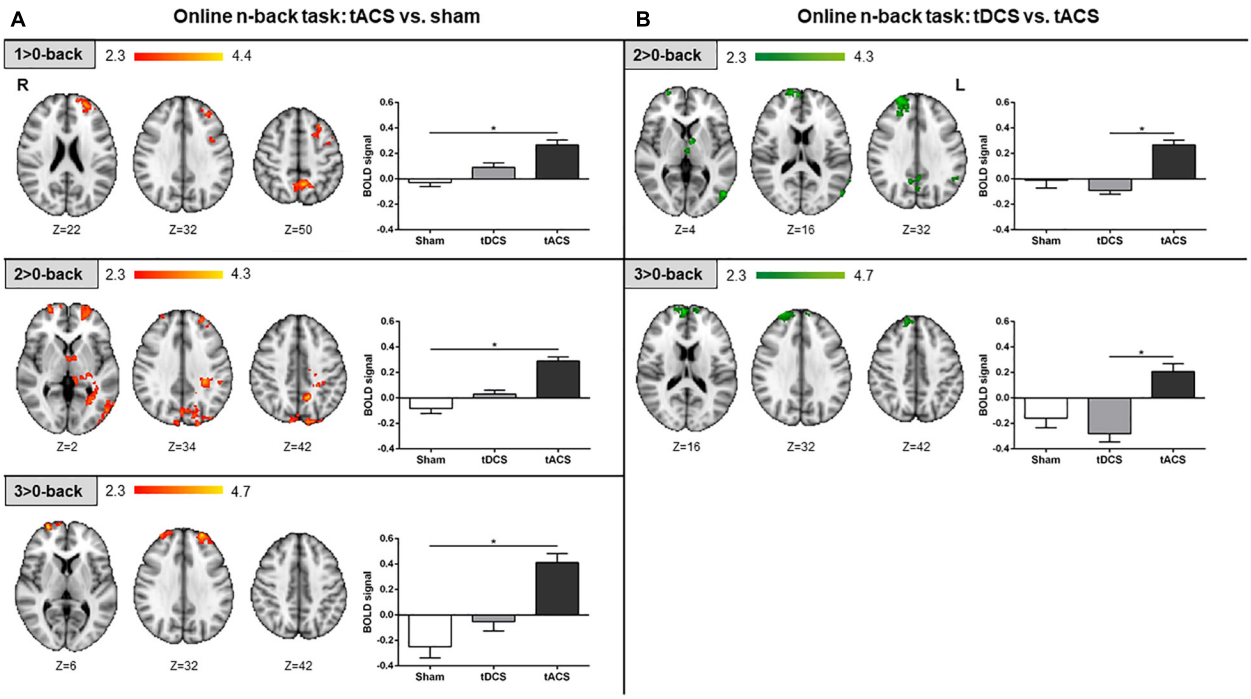

FIGURE 5 | Online fMRI n-back task results. **(A)** tACS vs. sham results are shown in red-yellow. **(B)** tDCS vs. tACS results are shown in green. Left: statistically significant fMRI activity maps on the standard MNI for each contrast of interest and group comparison. Right: plots of mean BOLD signal values at the fMRI clusters considering sham, tDCS and tACS where significant differences between groups were found. Data are presented as mean with *SEM*. tACS, transcranial alternating current stimulation; tDCS, transcranial direct current stimulation; BOLD, blood oxygen level dependent.

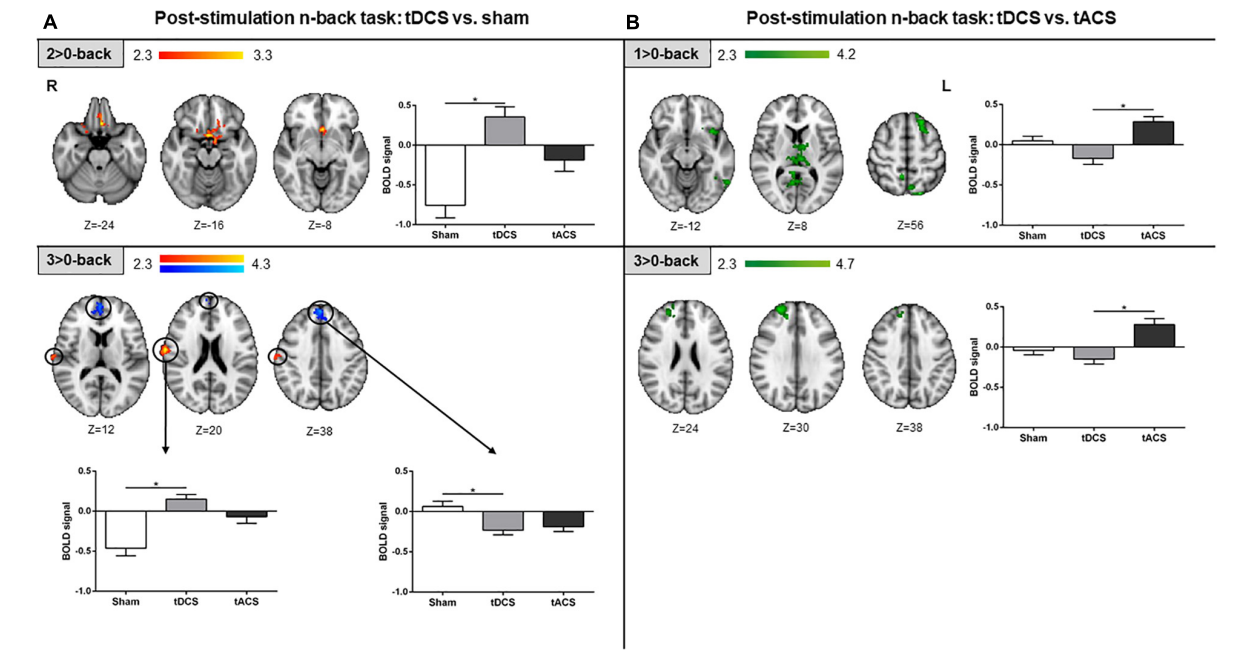

FIGURE 6 | Post-stimulation fMRI n-back task results. **(A)** tDCS vs. sham results are shown in red-yellow for higher activations and blue-light blue for lower activations. **(B)** tDCS vs. tACS results are shown in green. Left and up: statistically significant fMRI activity maps on the standard MNI for each contrast of interest and group comparison. Right and below: plots of mean BOLD signal values at the fMRI clusters considering sham, tDCS and tACS where significant differences between groups were found. Data are presented as mean with *SEM*. tDCS, transcranial direct current stimulation; tACS, transcranial alternating current stimulation; BOLD, blood oxygen level dependent.

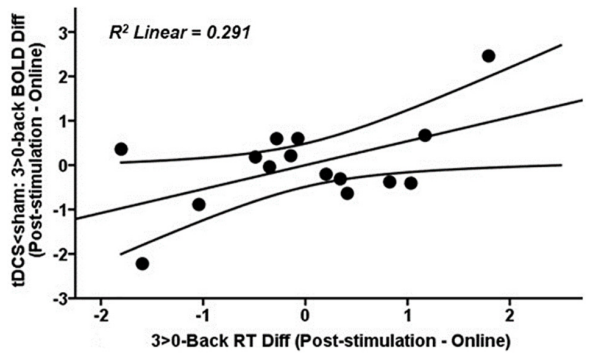

FIGURE 7 | Scatter plot showing the relationship at the highest WM load between tDCS-induced changes in BOLD signal post-stimulation when compared to online within the fMRI cluster where tDCS showed less activity than sham after stimulation (**Figure 6A**, blue-light blue fMRI cluster) and RT post-stimulation as compared to online. Data are presented with z scores. tDCS, transcranial direct current stimulation; BOLD, blood oxygen level dependent; Diff, difference; RT, reaction time.

tES-Related Individual Variability

Significant associations between rs-FC and brain activity were detected in the tDCS group. More precisely, those subjects of the tDCS group who exhibited higher mPFC-lIPL connectivity within the DMN also showed less BOLD signal at the highest WM load in the mPFC post-stimulation (**Figure 6A**; blue-light blue fMRI cluster; $r = -0.664$, $p = 0.007$; **Figure 8A**). Similarly, those subjects in the tDCS group displaying greater lIPL-left cerebellum connectivity within the DMN also showed a higher reduction in brain activity within the PCU at the lowest WM load post-stimulation as compared to online (**Figure 4A**; red-yellow fMRI cluster; $r = -0.643$, $p = 0.010$; **Figure 8B**). No significant relationships were observed between rs-FC and brain activity in the tACS group (all p values > 0.05).

tES-Related Adverse Events

An interaction between experimental groups was found as regards tingling ($H = 6.982$, $p = 0.030$). Pairwise *post hoc* analyses revealed more tingling estimates in the tACS group as compared to sham ($p = 0.025$). Another interaction was found regarding phosphenes occurrence ($\chi^2 = 11.360$, $p = 0.003$). Pairwise comparisons revealed a higher phosphenes occurrence in the tACS group in comparison to the tDCS group ($p = 0.002$, Fisher's exact test; see **Supplementary Table S1**).

DISCUSSION

Our study employed fMRI connectivity and activity analyses to investigate, in an exploratory manner, the effects of two commonly used tES protocols over the WMN and its major anticorrelated circuit, the DMN. Albeit the usage of the same neurophysiological readout (i.e., fMRI) is a critical condition to be able to directly compare the effects of distinct stimulation modalities, this approach has seldom been used. To the best of our knowledge, there have only been two studies that compared the effects of tDCS and tACS on WM performance (Hoy et al., 2015; Röhner et al., 2018). However, these studies did not explore the distinct impact of those protocols on fMRI network dynamics. Our main results showed that using our tES montage: (1) prefrontal tDCS is capable of increasing rs-FC, mainly within the DMN, while prefrontal theta tACS appears to disrupt rs-fMRI systems. (2) Comparing both fMRI WM tasks, tDCS seem to exert its neural effects through a reduction on neural activity after stimulation, whilst tACS increase neural activity during stimulation, occurring both modulations mainly within DMN areas. (3) In the online fMRI WM task, tACS induced distributed neural activity which was not accommodated within the WMN, but overlapping certain posterior DMN areas. (4) In the post-stimulation fMRI WM task, tDCS strengthened expected medial prefrontal DMN deactivations, which correlated with faster responses. (5) Lastly, we observed that tDCS showed certain consistency on their neural effects across rs- and tb-fMRI, which was not the case for tACS.

Effects of tDCS and tACS on rs-FC

We observed higher connectivity within the DMN in the tDCS group. This is in line with a previous investigation reporting rs-FC increases in this system after prefrontal tDCS (Keeser et al., 2011). This connectivity increase has been proposed to reflect augmented resources and higher readiness to facilitate cognition (Keeser et al., 2011). On the contrary, tACS appeared to reduce DMN and ECN rs-FC. Although relevant data about the tACS effects on rs-fMRI dynamics have recently been reported using distinct tES montages (i.e., Cabral-Calderin et al., 2016; Vosskuhl et al., 2016; Bächinger et al., 2017; Weinrich et al., 2017), prefrontal theta tACS impact on resting-state connectivity remains largely uninvestigated. The observed reduction in rs-FC for the tACS group could be explained as a disruption of the endogenous theta rhythm of the stimulated area. The theta frequency band mediates long-range connections in the brain through phase synchrony and cross-frequency coupling (for a review see Lisman and Jensen, 2013). Therefore, it is plausible that tACS at 6 Hz introduced an exogenous rhythm that disrupted phase synchrony on the DMN and ECN and thus decreased rs-FC.

Effects of tDCS and tACS on WM-Related Neural Activity

Differential Effects Across tES Time-Points

In the present investigation, tDCS effects were primarily driven by reductions in neural activity after stimulation (**Figure 4A**). This is in line with the notion that some of the tDCS effects might take place after the cessation of stimulation rather than during stimulation, as observed in the motor cortex (Santarnecchi et al., 2014). On the contrary, tACS effects appeared to be particularly driven by changes during stimulation (**Figure 4B**). This is coherent with the outcome obtained using a similar protocol to ours, where a significant tACS effect on WM accuracy was only observed online, but not post-stimulation (Meiron and Lavidor, 2014). At the neuroanatomical level, the effects of both tES protocols on fMRI brain activity were mainly observed within relevant DMN areas, such as the mPFC and the PCU, the main hubs of this network (Buckner et al., 2008).

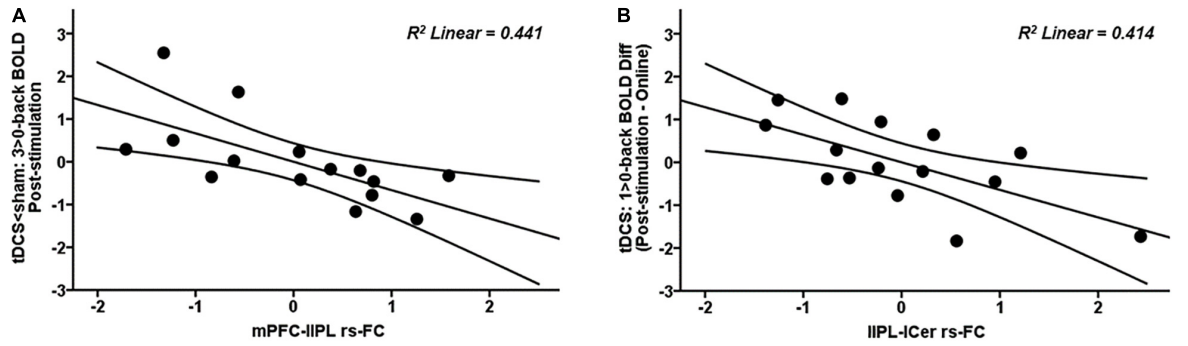

FIGURE 8 | Scatter plots showing the relationships in the tDCS group between **(A)** mPFC-lIPL rs-FC and post-stimulation 3 > 0-back BOLD signal (in the tDCS < sham fMRI cluster) and **(B)** lIPL-lCer rs-FC and 1 > 0-back difference in BOLD signal (in the post-stimulation – online fMRI cluster). Data are presented with z scores. tDCS, transcranial direct current stimulation; BOLD, blood oxygen level dependent; Diff, difference; mPFC, medial prefrontal cortex; lIPL, left inferior parietal lobule; rs-FC, resting-state functional connectivity; lCer, left cerebellum.

Differential Online Effects

In line with the abovementioned results, when exploring the neural modulations for each tES time-point, tACS effects were revealed to be different as compared to sham only in the online WM task (**Figure 5A**). Furthermore, neural activity changes were found in a cognitive load-dependent manner, were tACS engaged distributed neural resources in low load conditions, while at the highest demanding load, activity increases were only evident bifrontally. Notwithstanding, while the spatial distribution of the neuroimaging results did not completely overlap with the WM-dependent neural activity pattern, it plainly did meet some areas belonging to the DMN, such as the PCU. These tACS effects over the DMN were even more evident compared to tDCS (**Figure 5B**), where activity modulations in other DMN core areas also emerged, such as the lIPL. Altogether, prefrontal theta tACS during stimulation seemed to disrupt the characteristic WMN-DMN shift during externally oriented tasks (i.e., via a poorer DMN suppression, particularly within its posterior nodes). However, since no major significant behavioral differences were found between groups, this brain perturbation-like process (Paus, 2005) could have triggered compensatory overactivations in widespread regions regardless the WM-related areas, probably to allow a suitable response to the cognitive load required, and thus maintain cognition at an adequate level (i.e., such as the other experimental groups; see **Supplementary Figure S1**).

Differential Post-stimulation Effects

On the post-stimulation task, when compared to sham, we only detected brain activity changes in the tDCS group (**Figure 6A**). The most noteworthy outcome was a tDCS-induced activity reduction in a typically deactivated area corresponding to the anterior DMN node, namely the mPFC, in the highest WM load. It is worth noting that activity decreases are proportional to task difficulty (McKiernan et al., 2003). However, tDCS appeared to strengthen this characteristic medial prefrontal deactivation pattern. More interestingly, greater decreases in brain activity in this area were correlated with shorter response times (**Figure 7**). These results might be in line with the notion that tDCS increases neural efficiency on brain dynamics (Holland et al., 2011; Meinzer et al., 2012). In this case, neural efficiency may be operated via the inhibition of areas that need to be suppressed instead of an activity decrease in hyperactivated areas, as seen in normal and pathological aging (Meinzer et al., 2013, 2015). Thus, tDCS might be reinforcing the activation/deactivation WMN-DMN shift during the accomplishment of cognitive tasks, which is then associated with better performance.

Cognitive Performance

Despite the brain-behavioral associations previously mentioned (see section "Differential Post-stimulation Effects"), we were not able to detect any cognitive effects between tES time-points and experimental groups. In this sense, although some studies with the same tDCS montage have reported significant improvements on WM performance both online and post-stimulation (Fregni et al., 2005; Ohn et al., 2008), more recent investigations have revealed that a single session of prefrontal tDCS does not (or at best, modestly) induce cognitive improvements in WM performance in healthy subjects (Brunoni and Vanderhasselt, 2014; Nilsson et al., 2015; Mancuso et al., 2016; Hill et al., 2017; Medina and Cason, 2017; Imburgio and Orr, 2018). This may be due to ceiling effects in healthy populations (Hsu et al., 2015). Regarding the effects of our tACS montage on cognitive performance, certain improvements in fluid intelligence have been previously observed (Pahor and Jaušovec, 2014), but not on WM (Jaušovec and Jaušovec, 2014). However, using slightly different tACS montages, either targeting prefrontal regions (Meiron and Lavidor, 2014; Alekseichuk et al., 2016) or the fronto-parietal circuit (Polanía et al., 2012; Violante et al., 2017), WM improvements have been reported. Yet, data in these regards is likewise inconsistent to date (Pahor and Jaušovec, 2018).

tES-Related Individual Variability

Notable inter- and intra-individual variability has been seen in response to distinct non-invasive brain stimulation protocols (i.e., Hamada et al., 2013; López-Alonso et al., 2014; Martin-Trias et al., 2018). More specifically, López-Alonso et al. (2014) observed that only 45% of subjects responded as expected when

the motor cortex was targeted with anodal tDCS. However, whether individual responses to different stimulation techniques are consistent across distinct fMRI modalities has not yet been explored. Our study is the first to investigate this issue. Our results indicate that in the tDCS group, those subjects displaying higher rs-FC in specific couplings also exhibited greater tb-fMRI modulations (**Figure 8**). Therefore, subjects that received tDCS seem to display consistency on their neural effects across different fMRI modalities, which seems not to be the case for tACS.

Limitations

This investigation presents a number of limitations. First, although comparable to previous studies employing similar designs, the sample size was relatively modest. Second, an fMRI scan and a WM assessment at baseline (or using a cross-over design) could have permitted a more powerful analysis of the neural and cognitive effects of stimulation. Notwithstanding, to avoid practice effects, which previous WM studies have suffered (i.e., Röhner et al., 2018), a between-subjects design was selected. Further, in our study, methodological issues related to electrodes size or location might have underlie the absence of cognitive effects (for tDCS, see Imburgio and Orr, 2018; for tACS, see Mehta et al., 2015). Moreover, it is also worth noting that using individualized theta frequencies could have boosted cognitive performance in our experimental setting, although it does not guarantee any behavioral improvement by itself (Jaušovec and Jaušovec, 2014). Altogether, present data might provide a novel proof of concept of NIBS-fMRI effects for future research in the field. However, it is relevant to consider that our results should be interpreted in a cautious manner due to the stated limitations, which makes them exploratory and warranting further confirmation in larger studies.

CONCLUSION

In sum, in the present investigation we have shown that prefrontal tDCS and tACS appear to display different effects on rs- and tb-fMRI neural dynamics. However, both particularly would affect DMN functioning at rest as well as during WM performance. In fact, the DMN is known to be highly susceptible to alterations by means of transcranial stimulation (i.e., Antonenko et al., 2018). This is crucial given that this network supports basic cognitive processes (Buckner et al., 2008). In addition, it is negatively affected both by advancing age (Andrews-Hanna et al., 2007; Chen et al., 2016; Schultz et al., 2017; Staffaroni et al., 2018) and in distinct neuropsychiatric conditions (Beucke et al., 2014; Hu et al., 2017; Wise et al., 2017; Yan et al., 2019). Indeed, its capability to being deactivated during externally oriented tasks is a process strongly affected both in aging (Miller et al., 2008) and disease (Fryer et al., 2013). In this vein, present results, along with those of other investigations allowing a better understanding of how the distinct DMN mechanisms -and its relationships with other systems- can be extrinsically modulated might provide valuable knowledge for future applications in both basic research and clinical care.

DATA AVAILABILITY STATEMENT

The data that support the findings of this study are available from the corresponding author upon reasonable request.

ETHICS STATEMENT

The studies involving human participants were reviewed and approved by University of Barcelona's Bioethics Commission (IRB 00003099). The patients/participants provided their written informed consent to participate in this study.

AUTHOR CONTRIBUTIONS

KA-P, LV-A, and DB-F designed the research and wrote the manuscript. KA-P and LV-A analyzed the data. KA-P, LV-A, RP-A, NB, M-FK, AP-L, MN, and DB-F edited the manuscript.

FUNDING

This work was supported by grants from the Spanish Ministry of Economy and Competitiveness (MINECO/FEDER; PSI2015-64227-R) and the Spanish Ministry of Science, Innovation and Universities (MICIU/FEDER; RTI2018-095181-B-C21) to DB-F, which was also supported by an ICREA Academia 2019 grant award. KA-P was supported by a fellowship from the Spanish Ministry of Education, Culture and Sport (MECD; reference number, FPU14/02728). LV-A was supported by a fellowship associated with the MINECO/FEDER PSI2015-64227-R grant (reference number, BES-2016-077620). AP-L was supported by the Sidney R. Baer Jr. Foundation, the National Institutes of Health (NIH R01 MH100186, R01 NS073601, R01 HD069776, R21 MH099196, R21 NS082870, R21 NS085491, and R21 HD07616), Harvard Catalyst | The Harvard Clinical and Translational Science Center (NCRR and the NCATS NIH, UL1 RR025758), DARPA (via HR001117S0030), and the Football Players Health Study at Harvard University. The project that gave rise to these results also received the support of a fellowship from "la Caixa" Foundation (ID 100010434). The fellowship code is LCF/BQ/DI19/11730050. This research was furthermore supported by the Government of Catalonia (2017SGR748).

ACKNOWLEDGMENTS

We are indebted to the Magnetic Resonance Imaging Core Facility of the IDIBAPS for the technical help.

SUPPLEMENTARY MATERIAL

The Supplementary Material for this article can be found online at: https://www.frontiersin.org/articles/10.3389/fnins.2019.01440/full#supplementary-material

REFERENCES

Abellaneda-Pérez, K., Vaqué-Alcázar, L., Vidal-Piñeiro, D., Jannati, A., Solana, E., Bargalló, N., et al. (2019). Age-related differences in default-mode network connectivity in response to intermittent theta-burst stimulation and its relationships with maintained cognition and brain integrity in healthy aging. *Neuroimage* 188, 794–806. doi: 10.1016/j.neuroimage.2018.11.036

Alekseichuk, I., Turi, Z., Amador de Lara, G., Antal, A., and Paulus, W. (2016). Spatial working memory in humans depends on theta and high gamma synchronization in the prefrontal cortex. *Curr. Biol.* 26, 1513–1521. doi: 10.1016/j.cub.2016.04.035

Ali, M. M., Sellers, K. K., and Frohlich, F. (2013). Transcranial alternating current stimulation modulates large-scale cortical network activity by network resonance. *J. Neurosci.* 33, 11262–11275. doi: 10.1523/JNEUROSCI.5867-12.2013

Altman, D. G., and Bland, J. M. (1999). How to randomise. *BMJ* 319, 703–704. doi: 10.1136/bmj.319.7211.703

Anderson, N. D., and Craik, F. I. (2017). 50 years of cognitive aging theory. *J. Gerontol. B Psychol. Sci. Soc. Sci.* 72, 1–6. doi: 10.1093/geronb/gbw108

Andrews-Hanna, J. R., Snyder, A. Z., Vincent, J. L., Lustig, C., Head, D., Raichle, M. E., et al. (2007). Disruption of large-scale brain systems in advanced aging. *Neuron* 56, 924–935. doi: 10.1016/j.neuron.2007.10.038

Antal, A., and Herrmann, C. S. (2016). Transcranial alternating current stimulation and transcranial random noise stimulation: possible mechanisms. *Neural Plast.* 2016:3616807. doi: 10.1155/2016/3616807

Antal, A., and Paulus, W. (2013). Transcranial alternating current stimulation (tACS). *Front. Hum. Neurosci.* 7:317. doi: 10.3389/fnhum.2013.00317

Antonenko, D., Külzow, N., Sousa, A., Prehn, K., Grittner, U., and Flöel, A. (2018). Neuronal and behavioral effects of multi-day brain stimulation and memory training. *Neurobiol. Aging* 61, 245–254. doi: 10.1016/j.neurobiolaging.2017.09.017

Bächinger, M., Zerbi, V., Moisa, M., Polania, R., Liu, Q., Mantini, D., et al. (2017). Concurrent tACS-fMRI reveals causal influence of power synchronized neural activity on resting state fMRI connectivity. *J. Neurosci.* 37, 4766–4777. doi: 10.1523/JNEUROSCI.1756-16.2017

Baddeley, A. (1992). Working memory. *Science* 255, 556–559. doi: 10.1126/science.1736359

Baddeley, A. (2010). Working memory. *Curr. Biol.* 20, 136–140. doi: 10.1016/j.cub.2009.12.014

Barbey, A. K., Koenigs, M., and Grafman, J. (2013). Dorsolateral prefrontal contributions to human working memory. *Cortex* 49, 1195–1205. doi: 10.1016/j.cortex.2012.05.022

Beckmann, C. F., DeLuca, M., Devlin, J. T., and Smith, S. M. (2005). Investigations into resting-state connectivity using independent component analysis. *Philos. Trans. R. Soc. Lond. B Biol. Sci.* 360, 1001–1013. doi: 10.1098/rstb.2005.1634

Beucke, J. C., Sepulcre, J., Eldaief, M. C., Sebold, M., Kathmann, N., and Kaufmann, C. (2014). Default mode network subsystem alterations in obsessive-compulsive disorder. *Br. J. Psychiatry* 205, 376–382. doi: 10.1192/bjp.bp.113.137380

Bikson, M., Grossman, P., Thomas, C., Zannou, A. L., Jiang, J., and Adnan, T. (2016). Safety of transcranial direct current stimulation: evidence based update 2016. *Brain Stimul.* 9, 641–661. doi: 10.1016/j.brs.2016.06.004

Brauer, H., Kadish, N. E., Pedersen, A., Siniatchkin, M., and Moliadze, V. (2018). No modulatory effects when stimulating the right inferior frontal gyrus with continuous 6 Hz tACS and tRNS on response inhibition: a behavioral study. *Neural Plast.* 2018:3156796. doi: 10.1155/2018/3156796

Brunoni, A. R., Amadera, J., Berbel, B., Volz, M. S., Rizzerio, B. G., and Fregni, F. (2011). A systematic review on reporting and assessment of adverse effects associated with transcranial direct current stimulation. *Int. J. Neuropsychopharmacol.* 14, 1133–1145. doi: 10.1017/S1461145710001690

Brunoni, A. R., and Vanderhasselt, M. A. (2014). Working memory improvement with non-invasive brain stimulation of the dorsolateral prefrontal cortex: a systematic review and meta-analysis. *Brain Cogn.* 86, 1–9. doi: 10.1016/j.bandc.2014.01.008

Buckner, R. L., Andrews-Hanna, J. R., and Schacter, D. L. (2008). The brain's default network: anatomy, function, and relevance to disease. *Ann. N. Y. Acad. Sci.* 1124, 1–38. doi: 10.1196/annals.1440.011

Cabral-Calderin, Y., Williams, K. A., Opitz, A., Dechent, P., and Wilke, M. (2016). Transcranial alternating current stimulation modulates spontaneous low frequency fluctuations as measured with fMRI. *Neuroimage* 141, 88–107. doi: 10.1016/j.neuroimage.2016.07.005

Chen, G., Shu, H., Chen, G., Ward, B. D., Antuono, P. G., Zhang, Z., et al. (2016). Staging alzheimer's disease risk by sequencing brain function and structure, cerebrospinal fluid, and cognition biomarkers. *J. Alzheimers Dis.* 54, 983–993. doi: 10.3233/JAD-160537

Curtis, C. E., and D'Esposito, M. (2003). Persistent activity in the prefrontal cortex during working memory. *Trends Cogn. Sci.* 7, 415–423. doi: 10.1016/S1364-6613(03)00197-9

Dedoncker, J., Brunoni, A. R., Baeken, C., and Vanderhasselt, M. A. (2016). A systematic review and meta-analysis of the effects of transcranial direct current stimulation (tDCS) over the dorsolateral prefrontal cortex in healthy and neuropsychiatric samples: influence of stimulation parameters. *Brain Stimul.* 9, 501–517. doi: 10.1016/j.brs.2016.04.006

Eriksson, J., Vogel, E. K., Lansner, A., Bergström, F., and Nyberg, L. (2015). Neurocognitive architecture of working memory. *Neuron* 88, 33–46. doi: 10.1016/j.neuron.2015.09.020

Fertonani, A., Ferrari, C., and Miniussi, C. (2015). What do you feel if I apply transcranial electric stimulation? Safety, sensations and secondary induced effects. *Clin. Neurophysiol.* 126, 2181–2188. doi: 10.1016/j.clinph.2015.03.015

Fox, M. D., Snyder, A. Z., Vincent, J. L., Corbetta, M., Van Essen, D. C., and Raichle, M. E. (2005). The human brain is intrinsically organized into dynamic, anticorrelated functional networks. *Proc. Natl. Acad. Sci. U.S.A.* 102, 9673–9678. doi: 10.1073/pnas.0504136102

Fregni, F., Boggio, P. S., Nitsche, M., Bermpohl, F., Antal, A., Feredoes, E., et al. (2005). Anodal transcranial direct current stimulation of prefrontal cortex enhances working memory. *Exp. Brain Res.* 166, 23–30. doi: 10.1007/s00221-005-2334-6

Fryer, S. L., Woods, S. W., Kiehl, K. A., Calhoun, V. D., Pearlson, G. D., Roach, B. J., et al. (2013). Deficient suppression of default mode regions during working memory in individuals with early psychosis and at clinical high-risk for psychosis. *Front. Psychiatry* 4:92. doi: 10.3389/fpsyt.2013.00092

Hamada, M., Murase, N., Hasan, A., Balaratnam, M., and Rothwell, J. C. (2013). The role of interneuron networks in driving human motor cortical plasticity. *Cereb. Cortex* 23, 1593–1605. doi: 10.1093/cercor/bhs147

Hanslmayr, S., Axmacher, N., and Inman, C. S. (2019). Modulating human memory via entrainment of brain oscillations. *Trends Neurosci.* 42, 485–499. doi: 10.1016/j.tins.2019.04.004

Herrmann, C. S., Rach, S., Neuling, T., and Strüber, D. (2013). Transcranial alternating current stimulation: a review of the underlying mechanisms and modulation of cognitive processes. *Front. Hum. Neurosci.* 7:279. doi: 10.3389/fnhum.2013.00279

Hill, A. T., Rogasch, N. C., Fitzgerald, P. B., and Hoy, K. E. (2017). Effects of prefrontal bipolar and high-definition transcranial direct current stimulation on cortical reactivity and working memory in healthy adults. *Neuroimage* 152, 142–157. doi: 10.1016/j.neuroimage.2017.03.001

Holland, R., Leff, A. P., Josephs, O., Galea, J. M., Desikan, M., Price, C. J., et al. (2011). Speech facilitation by left inferior frontal cortex stimulation. *Curr. Biol.* 21, 1403–1407. doi: 10.1016/j.cub.2011.07.021

Howard, M. W., Rizzuto, D. S., Caplan, J. B., Madsen, J. R., Lisman, J., Aschenbrenner-Scheibe, R., et al. (2003). Gamma oscillations correlate with working memory load in humans. *Cereb. Cortex* 13, 1369–1374. doi: 10.1093/cercor/bhg084

Hoy, K. E., Bailey, N., Arnold, S., Windsor, K., John, J., Daskalakis, Z. J., et al. (2015). The effect of γ-tACS on working memory performance in healthy controls. *Brain Cogn.* 101, 51–56. doi: 10.1016/j.bandc.2015.11.002

Hsu, W., Ku, Y., Zanto, T. P., and Gazzaley, A. (2015). Effects of non-invasive brain stimulation on cognitive function in healthy aging and Alzheimer's disease: a systematic review and meta-analysis. *Neurobiol. Aging* 36, 2348–2359. doi: 10.1016/j.neurobiolaging.2015.04.016

Hu, M. L., Zong, X. F., Mann, J. J., Zheng, J. J., Liao, Y. H., Li, Z. C., et al. (2017). A review of the functional and anatomical default mode network in schizophrenia. *Neurosci. Bull.* 33, 73–84. doi: 10.1007/s12264-016-0090-1

Imburgio, M. J., and Orr, J. M. (2018). Effects of prefrontal tDCS on executive function: methodological considerations revealed by meta-analysis. *Neuropsychologia* 117, 156–166. doi: 10.1016/j.neuropsychologia.2018.04.022

Jaušovec, N., and Jaušovec, K. (2014). Increasing working memory capacity with theta transcranial alternating current stimulation (tACS). *Biol. Psychol.* 96, 42–47. doi: 10.1016/j.biopsycho.2013.11.006

Jenkinson, M., Beckmann, C. F., Behrens, T. E. J., Woolrich, M. W., and Smith, S. M. (2012). FSL. *Neuroimage* 62, 782–790. doi: 10.1016/j.neuroimage.2011.09.015

Jensen, O., and Colgin, L. L. (2007). Cross-frequency coupling between neuronal oscillations. *Trends Cogn. Sci.* 11, 267–269. doi: 10.1016/j.tics.2007.05.003

Johnson, M. K., McMahon, R. P., Robinson, B. M., Harvey, A. N., Hahn, B., Leonard, C. J., et al. (2013). The relationship between working memory capacity and broad measures of cognitive ability in healthy adults and people with schizophrenia. *Neuropsychology* 27, 220–229. doi: 10.1037/a0032060

Kang, M., Ragan, B. G., and Park, J. H. (2008). Issues in outcomes research: an overview of randomization techniques for clinical trials. *J. Athl. Train.* 43, 215–221. doi: 10.4085/1062-6050-43.2.215

Kasten, F. H., Dowsett, J., and Herrmann, C. S. (2016). Sustained aftereffect of α-tACS lasts up to 70 min after stimulation. *Front. Hum. Neurosci.* 10:245. doi: 10.3389/fnhum.2016.00245

Keeser, D., Meindl, T., Bor, J., Palm, U., Pogarell, O., Mulert, C., et al. (2011). Prefrontal transcranial direct current stimulation changes connectivity of resting-state networks during fMRI. *J. Neurosci.* 31, 15284–15293. doi: 10.1523/JNEUROSCI.0542-11.2011

Lang, S., Gan, L. S., Alrazi, T., and Monchi, O. (2019). Theta band high definition transcranial alternating current stimulation, but not transcranial direct current stimulation, improves associative memory performance. *Sci. Rep.* 9:8562. doi: 10.1038/s41598-019-44680-8

Lee, J., and Park, S. (2005). Working memory impairments in schizophrenia: a meta-analysis. *J. Abnorm. Psychol.* 114, 599–611. doi: 10.1037/0021-843X.114.4.599

Liebetanz, D., Nitsche, M. A., Tergau, F., and Paulus, W. (2002). Pharmacological approach to the mechanisms of transcranial DC-stimulation-induced after-effects of human motor cortex excitability. *Brain* 125, 2238–2247. doi: 10.1093/brain/awf238

Lisman, J. E., and Jensen, O. (2013). The theta-gamma neural code. *Neuron* 77, 1002–1016. doi: 10.1016/j.neuron.2013.03.007

López-Alonso, V., Cheeran, B., Río-Rodríguez, D., and Fernández-Del-Olmo, M. (2014). Inter- individual variability in response to non-invasive brain stimulation paradigms. *Brain Stimul.* 7, 372–380. doi: 10.1016/j.brs.2014.02.004

Mancuso, L. E., Ilieva, I. P., Hamilton, R. H., and Farah, M. J. (2016). Does transcranial direct current stimulation improve healthy working memory? a meta-analytic review. *J. Cogn. Neurosci.* 28, 1063–1089. doi: 10.1162/jocn_a_00956

Martin-Trias, P., Lanteaume, L., Solana, E., Cassé-Perrot, C., Fernández-Cabello, S., Babiloni, C., et al. (2018). Adaptability and reproducibility of a memory disruption rTMS protocol in the PharmaCog IMI European project. *Sci. Rep.* 8:9371. doi: 10.1038/s41598-018-27502-1

Matsumoto, H., and Ugawa, Y. (2017). Adverse events of tDCS and tACS: a review. *Clin. Neurophysiol. Pract.* 2, 19–25. doi: 10.1016/j.cnp.2016.12.003

McKiernan, K. A., Kaufman, J. N., Kucera-Thompson, J., and Binder, J. R. (2003). A parametric manipulation of factors affecting task-induced deactivation in functional neuroimaging. *J. Cogn. Neurosci.* 15, 394–408. doi: 10.1162/089892903321593117

Medina, J., and Cason, S. (2017). No evidential value in samples of transcranial direct current stimulation (tDCS) studies of cognition and working memory in healthy populations. *Cortex* 94, 131–141. doi: 10.1016/j.cortex.2017.06.021

Mehta, A. R., Pogosyan, A., Brown, P., and Brittain, J. S. (2015). Montage matters: the influence of transcranial alternating current stimulation on human physiological tremor. *Brain Stimul.* 8, 260–268. doi: 10.1016/j.brs.2014.11.003

Meinzer, M., Antonenko, D., Lindenberg, R., Hetzer, S., Ulm, L., Avirame, K., et al. (2012). Electrical brain stimulation improves cognitive performance by modulating functional connectivity and task-specific activation. *J. Neurosci.* 32, 1859–1866. doi: 10.1523/JNEUROSCI.4812-11.2012

Meinzer, M., Lindenberg, R., Antonenko, D., Flaisch, T., and Flöel, A. (2013). Anodal transcranial direct current stimulation temporarily reverses age-associated cognitive decline and functional brain activity changes. *J. Neurosci.* 33, 12470–12478. doi: 10.1523/JNEUROSCI.5743-12.2013

Meinzer, M., Lindenberg, R., Phan, M. T., Ulm, L., Volk, C., and Flöel, A. (2015). Transcranial direct current stimulation in mild cognitive impairment: behavioral effects and neural mechanisms. *Alzheimers Dement.* 11, 1032–1040. doi: 10.1016/j.jalz.2014.07.159

Meiron, O., and Lavidor, M. (2014). Prefrontal oscillatory stimulation modulates access to cognitive control references in retrospective metacognitive commentary. *Clin. Neurophysiol.* 125, 77–82. doi: 10.1016/j.clinph.2013.06.013

Miller, S. L., Celone, K., DePeau, K., Diamond, E., Dickerson, B. C., Rentz, D., et al. (2008). Age-related memory impairment associated with loss of parietal deactivation but preservd hippocampal activation. *Proc. Natl. Acad. Sci. U.S.A.* 105, 2181–2186. doi: 10.1073/pnas.0706818105

Moisa, M., Polania, R., Grueschow, M., and Ruff, C. C. (2016). Brain network mechanisms underlying motor enhancement by transcranial entrainment of gamma oscillations. *J. Neurosci.* 36, 12053–12065. doi: 10.1523/JNEUROSCI.2044-16.2016

Monte-Silva, K., Kuo, M. F., Hessenthaler, S., Fresnoza, S., Liebetanz, D., Paulus, W., et al. (2013). Induction of late LTP-like plasticity in the human motor cortex by repeated non-invasive brain stimulation. *Brain Stimul.* 6, 424–432. doi: 10.1016/j.brs.2012.04.011

Nakao, T., Nakagawa, A., Nakatani, E., Nabeyama, M., Sanematsu, H., Yoshiura, T., et al. (2009). Working memory dysfunction in obsessive-compulsive disorder: a neuropsychological and functional MRI study. *J. Psychiatr. Res.* 43, 784–791. doi: 10.1016/j.jpsychires.2008.10.013

Nee, D. E., Brown, J. W., Askren, M. K., Berman, M. G., Demiralp, E., Krawitz, A., et al. (2013). A Meta-analysis of executive components of working memory. *Cereb. Cortex* 23, 264–282. doi: 10.1093/cercor/bhs007

Nilsson, J., Lebedev, A. V., and Lovden, M. (2015). No significant effect of prefrontal tDCS on working memory performance in older adults. *Front. Aging Neurosci.* 7:230. doi: 10.3389/fnagi.2015.00230

Nitsche, M. A., Cohen, L. G., Wassermann, E. M., Priori, A., Lang, N., Antal, A., et al. (2008). Transcranial direct current stimulation: State of the art 2008. *Brain Stimul.* 1, 206–223. doi: 10.1016/j.brs.2008.06.004

Nitsche, M. A., Fricke, K., Henschke, U., Schlitterlau, A., Liebetanz, D., Lang, N., et al. (2003). Pharmacological modulation of cortical excitability shifts induced by transcranial direct current stimulation in humans. *J Physiol.* 553, 293–301. doi: 10.1113/jphysiol.2003.049916

Nitsche, M. A., and Paulus, W. (2000). Excitability changes induced in the human motor cortex by weak transcranial direct current stimulation. *J. Physiol.* 527, 633–639. doi: 10.1111/j.1469-7793.2000.t01-1-00633.x

Nitsche, M. A., and Paulus, W. (2001). Sustained excitability elevations induced by transcranial DC motor cortex stimulation in humans. *Neurology* 57, 1899–1901. doi: 10.1212/WNL.57.10.1899

Ohn, S. H., Park, C. I., Yoo, W. K., Ko, M. H., Choi, K. P., Kim, G. M., et al. (2008). Time-dependent effect of transcranial direct current stimulation on the enhancement of working memory. *Neuroreport* 19, 43–47. doi: 10.1097/WNR.0b013e3282f2adfd

Owen, A. M., McMillan, K. M., Laird, A. R., and Bullmore, E. (2005). N-back working memory paradigm: a meta-analysis of normative functional neuroimaging studies. *Hum. Brain Mapp.* 25, 46–59. doi: 10.1002/hbm.20131

Pahor, A., and Jaušovec, N. (2014). The effects of theta transcranial alternating current stimulation (tACS) on fluid intelligence. *Int. J. Psychophysiol.* 93, 322–331. doi: 10.1016/j.ijpsycho.2014.06.015

Pahor, A., and Jaušovec, N. (2018). The effects of theta and gamma tACS on working memory and electrophysiology. *Front. Hum. Neurosci.* 11:651. doi: 10.3389/fnhum.2017.00651

Park, D. C., Lautenschlager, G., Hedden, T., Davidson, N. S., Smith, A. D., and Smith, P. K. (2002). Models of visuospatial and verbal memory across the adult life span. *Psychol. Aging* 17, 299–320. doi: 10.1037/0882-7974.17.2.299

Park, D. C., and Reuter-Lorenz, P. (2009). The adaptive brain: aging and neurocognitive scaffolding. *Annu. Rev. Psychol.* 60, 173–196. doi: 10.1146/annurev.psych.59.103006.093656

Paus, T. (2005). Inferring causality in brain images: a perturbation approach. *Philos. Trans. R. Soc. Lond. B Biol. Sci.* 360, 1109–1114. doi: 10.1098/rstb.2005.1652

Peña-Gómez, C., Sala-Lonch, R., Junqué, C., Clemente, I., Vidal, D., Bargalló, N., et al. (2012). Modulation of large-scale brain networks by transcranial direct current stimulation evidenced by resting-state functional MRI. *Brain Stimul.* 5, 252–263. doi: 10.1016/j.brs.2011.08.006

Pfefferbaum, A., Chanraud, S., Pitel, A. L., Muller-Oehring, E., Shankaranarayanan, A., Alsop, D. C., et al. (2011). Cerebral blood flow in posterior cortical nodes of the default mode network decreases with task engagement but remains higher than in most brain regions. *Cereb. Cortex* 21, 233–244. doi: 10.1093/cercor/bhq090

Polanía, R., Nitsche, M. A., Korman, C., Batsikadze, G., and Paulus, W. (2012). The importance of timing in segregated theta phase-coupling for cognitive performance. *Curr. Biol.* 22, 1314–1318. doi: 10.1016/j.cub.2012.05.021

Polanía, R., Nitsche, M. A., and Ruff, C. C. (2018). Studying and modifying brain function with non-invasive brain stimulation. *Nat. Neurosci.* 21, 174–187. doi: 10.1038/s41593-017-0054-4

Purpura, D. P., and McMurtry, J. G. (1965). Intracellular activities and evoked potential changes during polarization of motor cortex. *J. Neurophysiol.* 28, 166–185. doi: 10.1152/jn.1965.28.1.166

Raichle, M. E. (2015). The brain's default mode network. *Annu. Rev. Neurosci.* 38, 433–447. doi: 10.1146/annurev-neuro-071013-014030

Reato, D., Rahman, A., Bikson, M., and Parra, L. C. (2013). Effects of weak transcranial alternating current stimulation on brain activity—a review of known mechanisms from animal studies. *Front. Hum. Neurosci.* 7:687. doi: 10.3389/fnhum.2013.00687

Röhner, F., Breitling, C., Rufener, K. S., Heinze, H. J., Hinrichs, H., Krauel, K., et al. (2018). Modulation of working memory using transcranial electrical stimulation: a direct comparison between TACS and TDCS. *Front. Neurosci.* 12:761. doi: 10.3389/fnins.2018.00761

Roux, F., and Uhlhaas, P. J. (2014). Working memory and neural oscillations: alpha-gamma versus theta-gamma codes for distinct WM information? *Trends Cogn. Sci.* 18, 16–25. doi: 10.1016/j.tics.2013.10.010

Sala-Llonch, R., Peña-Gómez, C., Arenaza-Urquijo, E. M., Vidal-Piñeiro, D., Bargalló, N., Junqué, C., et al. (2012). Brain connectivity during resting state and subsequent working memory task predicts behavioural performance. *Cortex* 48, 1187–1196. doi: 10.1016/j.cortex.2011.07.006

Santarnecchi, E., Feurra, M., Barneschi, F., Acampa, M., Bianco, G., Cioncoloni, D., et al. (2014). Time course of corticospinal excitability and autonomic function interplay during and following monopolar tDCS. *Front. Psychiatry* 5:86. doi: 10.3389/fpsyt.2014.00086

Sarnthein, J., Petsche, H., Rappelsberger, P., Shaw, G. L., and von Stein, A. (1998). Synchronization between prefrontal and posterior association cortex during human working memory. *Proc. Natl. Acad. Sci. U.S.A.* 95, 7092–7096. doi: 10.1073/pnas.95.12.7092

Sauseng, P., Klimesch, W., Schabus, M., and Doppelmayr, M. (2005). Fronto-parietal EEG coherence in theta and upper alpha reflect central executive functions of working memory. *Int. J. Psychophysiol.* 57, 97–103. doi: 10.1016/j.ijpsycho.2005.03.018

Schultz, A. P., Chhatwal, J. P., Hedden, T., Mormino, E. C., Hanseeuw, B. J., Sepulcre, J., et al. (2017). Phases of hyperconnectivity and hypoconnectivity in the default mode and salience networks track with amyloid and tau in clinically normal individuals. *J. Neurosci.* 37, 4323–4331. doi: 10.1523/JNEUROSCI.3263-16.2017

Smith, S. M., Fox, P. T., Miller, K. L., Glahn, D. C., Fox, P. M., Mackay, C. E., et al. (2009). Correspondence of the brain's functional architecture during activation and rest. *Proc. Natl. Acad. Sci. U.S.A.* 106, 13040–13045. doi: 10.1073/pnas.0905267106

Smith, S. M., Jenkinson, M., Woolrich, M. W., Beckmann, C. F., Behrens, T. E. J., Johansen-Berg, H., et al. (2004). Advances in functional and structural MR image analysis and implementation as FSL. *Neuroimage* 23(Suppl. 1), S208–S219. doi: 10.1016/j.neuroimage.2004.07.051

Staffaroni, A. M., Brown, J. A., Casaletto, K. B., Elahi, F. M., Deng, J., Neuhaus, J., et al. (2018). The longitudinal trajectory of default mode network connectivity in healthy older adults varies as a function of age and is associated with changes in episodic memory and processing speed. *J. Neurosci.* 38, 2809–2817. doi: 10.1523/JNEUROSCI.3067-17.2018

Tremblay, S., Lepage, J. F., Latulipe-Loiselle, A., Fregni, F., Pascual-Leone, A., and Théoret, H. (2014). The uncertain outcome of prefrontal tDCS. *Brain Stimul.* 7, 773–783. doi: 10.1016/j.brs.2014.10.003

Unsworth, N., Fukuda, K., Awh, E., and Vogel, E. K. (2014). Working memory and fluid intelligence: capacity, attention control, and secondary memory retrieval. *Cogn. Psychol.* 71, 1–26. doi: 10.1016/j.cogpsych.2014.01.003

Violante, I. R., Li, L. M., Carmichael, D. W., Lorenz, R., Leech, R., Hampshire, A., et al. (2017). Externally induced frontoparietal synchronization modulates network dynamics and enhances working memory performance. *eLife* 6:e22001. doi: 10.7554/eLife.22001

Vossen, A., Gross, J., and Thut, G. (2015). Alpha power increase after transcranial alternating current stimulation at alpha frequency (a-tACS) reflects plastic changes rather than entrainment. *Brain Stimul.* 8, 499–508. doi: 10.1016/j.brs.2014.12.004

Vosskuhl, J., Huster, R. J., and Herrmann, C. S. (2016). BOLD signal effects of transcranial alternating current stimulation (tACS) in the alpha range: a concurrent tACS–fMRI study. *Neuroimage* 140, 118–125. doi: 10.1016/j.neuroimage.2015.10.003

Weinrich, C. A., Brittain, J. S., Nowak, M., Salimi-Khorshidi, R., Brown, P., and Stagg, C. J. (2017). Modulation of long-range connectivity patterns via frequency-specific stimulation of human cortex. *Curr. Biol.* 27, 3061.e3–3068.e3. doi: 10.1016/j.cub.2017.08.075

Wischnewski, M., Engelhardt, M., Salehinejad, M. A., Schutter, D. J. L. G., Kuo, M. F., and Nitsche, M. A. (2019). NMDA receptor-mediated motor cortex plasticity after 20 Hz transcranial alternating current stimulation. *Cereb. Cortex* 29, 2924–2931. doi: 10.1093/cercor/bhy160

Wise, T., Marwood, L., Perkins, A. M., Herane-Vives, A., Joules, R., Lythgoe, D. J., et al. (2017). Instability of default mode network connectivity in major depression: a two-sample confirmation study. *Transl. Psychiatry* 7:e1105. doi: 10.1038/tp.2017.40

Woods, A. J., Antal, A., Bikson, M., Boggio, P. S., Brunoni, A. R., Celnik, P., et al. (2016). A technical guide to tDCS, and related non-invasive brain stimulation tools. *Clin. Neurophysiol.* 127, 1031–1048. doi: 10.1016/j.clinph.2015.11.012

Woolrich, M. W., Behrens, T. E., Beckmann, C. F., Jenkinson, M., and Smith, S. M. (2004). Multilevel linear modelling for FMRI group analysis using Bayesian inference. *Neuroimage* 21, 1732–1747. doi: 10.1016/j.neuroimage.2003.12.023

Woolrich, M. W., Ripley, B. D., Brady, M., and Smith, S. M. (2001). Temporal autocorrelation in univariate linear modeling of FMRI data. *Neuroimage* 14, 1370–1386. doi: 10.1006/nimg.2001.0931

Yan, C. G., Chen, X., Li, L., Castellanos, F. X., Bai, T. J., Bo, Q. J., et al. (2019). Reduced default mode network functional connectivity in patients with recurrent major depressive disorder. *Proc. Natl. Acad. Sci. U.S.A.* 116, 9078–9083. doi: 10.1073/pnas.1900390116

Zaehle, T., Sandmann, P., Thorne, J. D., Jäncke, L., and Herrmann, C. S. (2011). Transcranial direct current stimulation of the prefrontal cortex modulates working memory performance: combined behavioural and electrophysiological evidence. *BMC Neurosci.* 12:2. doi: 10.1186/1471-2202-12-2

Zaghi, S., Acar, M., Hultgren, B., Boggio, P. S., and Fregni, F. (2010a). Noninvasive brain stimulation with low-intensity electrical currents: putative mechanisms of action for direct and alternating current stimulation. *Neuroscientist* 16, 285–307. doi: 10.1177/1073858409336227

Zaghi, S., de Freitas Rezende, L., de Oliveira, L. M., El-Nazer, R., Menning, S., Tadini, L., et al. (2010b). Inhibition of motor cortex excitability with 15Hz transcranial alternating current stimulation (tACS). *Neurosci. Lett.* 479, 211–214. doi: 10.1016/j.neulet.2010.05.060

Conflict of Interest: AP-L serves on the scientific advisory boards for Starlab Neuroscience, Neuroelectrics, Axilum Robotics, Constant Therapy, NovaVision, Cognito, Magstim, Nexstim, and Neosync, and is listed as an inventor on several issued and pending patents on the real-time integration of transcranial magnetic stimulation with electroencephalography and magnetic resonance imaging. MN serves on the scientific advisory board for Neuroelectrics.

The remaining authors declare that the research was conducted in the absence of any commercial or financial relationships that could be construed as a potential conflict of interest.

Copyright © 2020 Abellaneda-Pérez, Vaqué-Alcázar, Perellón-Alfonso, Bargalló, Kuo, Pascual-Leone, Nitsche and Bartrés-Faz. This is an open-access article distributed under the terms of the Creative Commons Attribution License (CC BY). The use, distribution or reproduction in other forums is permitted, provided the original author(s) and the copyright owner(s) are credited and that the original publication in this journal is cited, in accordance with accepted academic practice. No use, distribution or reproduction is permitted which does not comply with these terms.

frontiers in Neuroscience

ORIGINAL RESEARCH
published: 14 February 2020
doi: 10.3389/fnins.2020.00109

Using Mobile EEG to Investigate Alpha and Beta Asymmetries During Hand and Foot Use

Julian Packheiser[1]†, Judith Schmitz[2†], Yaolu Pan[1], Yasmin El Basbasse[1], Patrick Friedrich[3,4], Onur Güntürkün[1] and Sebastian Ocklenburg[1,5]*

[1] Institute of Cognitive Neuroscience, Biopsychology, Department of Psychology, Ruhr-University Bochum, Bochum, Germany, [2] School of Medicine, University of St Andrews, St Andrews, United Kingdom, [3] Brain Connectivity and Behaviour Laboratory, Sorbonne Universities, Paris, France, [4] CNRS, Groupe d'Imagerie Neurofonctionnelle, Institut des Maladies Neurodégénératives, UMR 5293, CEA, University of Bordeaux, Bordeaux, France, [5] Department of Psychology, University of Duisburg-Essen, Essen, Germany

The Edinburgh Handedness Inventory (EHI) and the Waterloo Footedness Questionnaire (WFQ) are two of the most widely used questionnaires to assess lateralized everyday behavior in human participants. However, it is unclear to what extent the specific behavior assessed in these questionnaires elicit lateralized neural activity when performed in real-life situations. To illuminate this unresolved issue, we assessed EEG alpha and beta asymmetries during real-life performance of the behaviors assessed in the EHI and WFQ using a mobile EEG system. This methodology provides high ecological validity for studying neural correlates of motor behavior under more naturalistic conditions. Our results indicate that behavioral performance of items of both the EHI and WFQ differentiate between left- and right-handers and left- and right-footers on the neural level, especially in the alpha frequency band. These results were unaffected by movement parameters. Furthermore, we could demonstrate that neural activity elicited specifically during left-sided task performance provides predictive power for the EHI or WFQ score of the participants. Overall, our results show that these prominent questionnaires not only distinguish between different motor preferences on the behavioral level, but also on the neurophysiological level. Furthermore, we could show that mobile EEG systems are a powerful tool to investigate motor asymmetries in ecologically valid situations outside of the laboratory setting. Future research should focus on other lateralized behavioral phenotypes in real-life settings to provide more insights into lateralized motor functions.

Keywords: laterality, oscillations, asymmetry, EHI, WFQ, Edinburgh Handedness Inventory, Waterloo Footedness Questionnaire

OPEN ACCESS

Edited by:
Federico Giove, Centro Fermi – Museo Storico della Fisica e Centro Studi e Ricerche Enrico Fermi, Italy

Reviewed by:
Ulrich S. Tran, University of Vienna, Austria
Gareth Barnes, University College London, United Kingdom

***Correspondence:**
Julian Packheiser
julian.packheiser@rub.de

† These authors have contributed equally to this work

Specialty section:
This article was submitted to Brain Imaging Methods, a section of the journal Frontiers in Neuroscience

Received: *22 October 2019*
Accepted: *28 January 2020*
Published: *14 February 2020*

Citation:
Packheiser J, Schmitz J, Pan Y, El Basbasse Y, Friedrich P, Güntürkün O and Ocklenburg S (2020) Using Mobile EEG to Investigate Alpha and Beta Asymmetries During Hand and Foot Use. Front. Neurosci. 14:109. doi: 10.3389/fnins.2020.00109

INTRODUCTION

Most humans consistently prefer one hand or one foot over the other in everyday life (Porac and Coren, 1981; Güntürkün and Ocklenburg, 2017). Both human handedness and footedness are among the most well-studied lateralized behaviors. A recent meta-analysis involving a sample of over 2 million participants found that 81.9% of the population is right-handed using a non-right/right classification (Papadatou-Pastou et al., 2019). For footedness, the prevalence of

lateralized preferences in the population is less clear as no large-scale meta-analysis exists as of yet. A substantial sample of 3307 participants was investigated regarding their footedness by Coren (1993). He found that 86.7% of all participants were right-preferent, 7.1% were left-preferent, and 6.2% had no foot preference. This finding effectively demonstrates a similar distribution as was identified for handedness. These measures are generally positively correlated in individuals supporting this finding (Porac and Coren, 1981; Brown and Taylor, 1988; Reiss et al., 1999; Dittmar, 2002; Ocklenburg and Güntürkün, 2009).

A major interest in studying these lateral biases derives from the association between lateralized motor behavior with lateralized cognitive domains like language (Ocklenburg et al., 2014) and emotional processes (Elias et al., 1998) but also psychopathologies such as schizophrenia (Sommer et al., 2001; Dragovic and Hammond, 2005; Ocklenburg et al., 2015 for handedness; Tran et al., 2015 for footedness). In modern laterality research, handedness and footedness are usually assessed as continuous measures using questionnaires rather than dichotomous measures such as asking about the "writing hand" (as e.g., in Turnbull et al., 2001) or "kicking foot" (as e.g., in Brown and Taylor, 1988). Although dichotomous measures are seemingly plausible strategies to assess limb preferences, they come with certain disadvantages. Using for example "writing hand" as a measure for handedness results in a handedness mismatch of only about 0.4% for right-handers, but left-handers are falsely classified as right-handers in 13.5% of the cases because many left-handers use their right hand for writing (Papadatou-Pastou et al., 2013). Furthermore, the forced-choice nature of this assessment does not allow for mixed-handedness as a result. Therefore, continuous measures possess considerable advantages compared to dichotomous measures because they allow more accurate phenotyping and capture more individual variance, which is essential for understanding the underlying neural mechanisms of lateralized behavior (Kanai and Rees, 2011). Two questionnaires arose as the standard measures of human limb asymmetries:

For handedness, the most cited questionnaire is the Edinburgh Handedness Inventory (EHI, Oldfield, 1971) with well over 20,000 citations (Google Scholar). It has been identified to be the most widely used handedness questionnaire (Fazio et al., 2012). The EHI comprises 10 items of everyday tasks (writing, throwing a ball, drawing, using scissors, brushing teeth, using a knife, using a spoon, using a broom, striking a match and opening a box-lid/jar) and instructs the participants to assess their hand preference for each of them by entering a " + " sign either in a left or right preference column. If these hand preferences are so strong that the participants would never use the other hand for this task unless being absolutely forced to, they are instructed to enter a " + + ". If there is no preference for a specific task, the participants are instructed to enter a " + " in both the left and right preference column. For footedness, one of the most prominent questionnaires is the Waterloo Footedness Questionnaire (WFQ, Elias et al., 1998). Here, participants are asked to indicate whether they would rather perform everyday mobility and stability tasks (ball kicking, hopping on one leg, standing on one foot, smoothing sand, stepping onto a chair, weight-shifted relaxed standing, stepping on a shovel, grasping a marble, balancing on a rail and stepping on a bug) with the left or with the right foot/leg. Similar to the EHI, the answers can indicate the consistency of the foot/leg preference (whether they preferably use the left or right foot). Therefore, the EHI and WFQ are highly comparable as items in both questionnaires have five different outcomes (strong leftward preference, weak leftward preference, no preference, weak rightward preference, and strong rightward preference) and the evaluation of both questionnaires is represented in form of a laterality quotient.

While evaluative studies indicate both the EHI and WFQ to yield reliable measures that are relatively stable over time (Ransil and Schachter, 1994; Camargos et al., 2017), there has been some dispute about their validity to measure handedness or footedness respectively. Due to its broad usage, some studies have investigated the factorial validity of the EHI to determine how well its individual items measure handedness. Using exploratory factor analysis, Bryden (1977) identified that there were inconsistencies between three items of the questionnaire among right-handers, namely the opening of a box/jar, using a broom and the striking of a match. McFarland and Anderson (1980) found supporting results as using a broom and box/jar opening again poorly loaded on a converged handedness factor. Furthermore, they found the same result to be true for using a knife. This finding is contrasted by large-scale latent variable analysis that found the usage of a knife to be one of the best predictors for handedness (Tran et al., 2014).

The factorial validity was also investigated using confirmatory factor analysis. Here, it was again confirmed that broom usage and box/jar opening demonstrated considerable error variance rates indicating against their validity to assess handedness (Dragovic, 2004; Milenkovic and Dragovic, 2013). Veale (2014) even found that further removing items on scissor and knife usage as well as striking a match provided a better model fit indicating that these items do not load well on a single handedness factor. However, given its widespread use in the literature, the application of the EHI allows for comparability between studies, giving the EHI an advantage over other questionnaires.

Given the far less widespread prevalence of studies investigating footedness in general, it is unsurprising that the items of the WFQ have not been investigated with such rigor as is the case for the EHI. Up until now, factorial validity of the WFQ has only been compared between the mobility and the stability subscales of the questionnaire (Kapreli et al., 2015). Since the study found high correlations between the two subscales, it was concluded that the WFQ subscales measure a single footedness factor. While the two subscales seem to measure similar constructs of footedness, a specific investigation of individual items on the mobility subscale has not supported a one-dimensional measure of footedness. Tran and Voracek (2016) used psychometric measures in a well-powered sample and could show that a two-dimensional rather than a one-dimensional model provides a much better fit to the data for items that are also used in the WFQ. Thus, individual items of the WFQ do not seem to load on a single footedness factor on the behavioral level.

Both questionnaires have in common that their reliability and their factorial validity have been measured using the behavioral output of the participants. However, no study has so far investigated the validity of individual items of the EHI or the WFQ on the neural level. Therefore, the aim of the present study was to identify the neurophysiological validity of both questionnaires using mobile electroencephalography techniques. Mobile EEG systems enable to record brain activity during active movement thus allowing for the measurement of highly ecologically valid neurophysiological signals. Until recently, research on the neural correlates of motor behavior relied mostly on artificial settings investigating, e.g., finger tapping tasks with low ecological validity using stationary EEG or fMRI systems (e.g., Turesky et al., 2018; Schmitz et al., 2019). Mobile EEG systems tackle these shortcomings by allowing for more naturalistic behavior during physiological recordings (Gramann et al., 2014). However, only a handful of studies have been published so far using this novel technology (e.g., Griffiths et al., 2016). We used mobile EEG to identify how well-individual items of both the EHI and the WFQ differentiate between left and right body movements both in left- and right-handers and left- and right-footers on the neural level. It is well-established how the motor cortex controls behavioral output of the limbs (Kim et al., 1993; Hammond, 2002), namely that the left hemisphere dominantly controls the right body side and that the right hemisphere dominantly controls the left body side. Using stationary EEG systems, studies have reported increased asymmetries over sensorimotor electrodes in the alpha and beta frequency bands during unilateral movements (Pfurtscheller, 1981; Deiber et al., 2012). Therefore, we hypothesize that alpha and beta power asymmetries differentiate between left- and right-handers and left- and right-footers during task performance of EHI and WFQ items. Furthermore, we hypothesize that activity in these two frequency bands allows for a differentiation between left and right performance of these items.

MATERIALS AND METHODS

Participants

A total of 51 participants (32 females) took part in this study. The age range was between 18 and 34 years (mean age = 25.46 years, *SD* = 3.59 years). Handedness of the participants was assessed in a pre-screening using the EHI. 26 of the participants were consistently left-handed (EHI lateralization quotient < -40, mean = −87.42, *SD* = 15.84) and 25 of the participants were consistently right-handed (EHI lateralization quotient $> +40$, mean = 90.03, *SD* = 12.70). Mixed-handed participants were excluded during the pre-screening process. Lateralization quotients (LQs) were calculated using the following formula: LQ = [(R-L)/(R + L)]*100, with R indicating the number of right preferred tasks and L the number of left preferred tasks of the EHI items. The cut-offs for left-handedness and right-handedness (< -40 and $> +40$, respectively) were derived from previous studies (Li et al., 2003) based on findings linking handedness to cognitive abilities (Burnett et al., 1982). There were no sex differences in EHI scores [$t(50) = 1.13$, $p > 0.250$]. Furthermore, left- and right-handers did not differ in age [$t(50) = 0.06$, $p > 0.250$]. All participants had normal or corrected-to-normal visual acuity. Participants with known neurological or psychiatric disorders were excluded from the study. The study was conducted in accordance with the declaration of Helsinki and was approved by a local ethics committee of the psychological faculty at Ruhr-University Bochum. All participants gave written informed consent.

Experimental Task

The experimental paradigm consisted of two sessions, one for items of the EHI (conducted first) and one for items of the WFQ (conducted second):

In the EHI session, participants were instructed to perform the 10 tasks mentioned in the EHI both with the left and with the right hand. Each task was performed for 1 min per hand. Thus, the EHI session consisted of 20 trials (10 tasks, once per hand) and the trials were separated by an ITI of 30 s. After the ITI, participants were informed about the task of the following trial and with which hand it had to be performed via a standardized oral instruction. Left and right trials of the identical task were always conducted consecutively. The order of the tasks was randomized and counterbalanced across participants to exclude any serial order or exhaustion effects. Furthermore, we also randomized the starting side (left or right) for each individual task to exclude potential effects due to experience with the respective task. The experimenter assisted in handing the participants the necessary equipment for each specific trial. The tasks were executed as follows:

(1) Writing: the participants wrote down letters of the alphabet from a to z (restarting from the beginning of the alphabet after reaching z)
(2) Throwing: the participants threw a ball against a wall with the experimenter picking up and handing the ball to the participant
(3) Drawing: the participants drew along a pre-designed sketch
(4) Scissors: the participants cut out a spiral shape holding the scissor with one hand (instructed hand) and the piece of paper with the other
(5) Brushing teeth: the participants brushed their teeth
(6) Knife: the participants cut a piece of clay
(7) Spoon: the participants simulated eating soup from a bowl (the spoon was not put into the mouth)
(8) Broom: the participants used a broom as if they cleaned the floor
(9) Match: the participants continuously lit a match using the non-flammable side of the match box
(10) Opening a jar: the participants were handed jars and had to open them using only the instructed hand.

Whenever tasks had to be performed that could not be continuously executed without interruption (e.g., throwing the ball) or required picking up objects (e.g., opening a jar), the experimenter assisted the participant to ensure that only the instructed task was performed. While some tasks required the use of the hand that was not performing the task directly (e.g.,

holding the paper during cutting with the scissors), participants were instructed to move the other hand as little as possible under such circumstances.

For the WFQ session, the experiment followed the same procedure as for the EHI session. Again, the experiment consisted of 20 trials in total (10 tasks, once per foot) of 1 min duration during which the behavior had to be performed continuously. If the task could not be executed continuously without assistance (e.g., ball kicking), the experimenter assisted by placing, e.g., balls in front of the participant. Individual trials were separated by a 30 s ITI followed by a standardized oral instruction about the next trial. Task order and starting foot were randomized and counterbalanced across participants. The tasks were conducted as follows:

(1) Kicking a ball: the participants continuously kicked balls against the wall. The experimenter placed new balls in front of the instructed foot throughout the trial
(2) Jumping: the participants were asked to jump on the instructed foot for the duration of the trial
(3) Standing: the participants stood one-footed on the instructed foot
(4) Smoothing sand: the participants drew a prepared shape of the number eight with the instructed foot
(5) Stepping onto a chair: the participants continuously stepped onto a small chair (only with the instructed foot)
(6) Weight-shifted standing: the participants stood on the floor putting their weight onto the instructed foot
(7) Shovel: the participants simulated stepping onto a shovel by stepping onto the edges of a large broom
(8) Marble: the participants used their toes to move marbles from one bowl to another
(9) Balancing: the participants stood one-footed on a narrow wooden rail
(10) Bug: the participants continuously stepped onto a dot projected onto the floor by the experimenter.

EEG Recording, Preprocessing, and Analysis

EEG signals were recorded with a mobile recording system (LiveAmp 32, Brain Products GmbH, Gilching, Germany). The LiveAmp 32 comprises 32 Ag-AgCl electrodes arranged according to the international 10–20 system (C3/C4, FP1/FP2, F3/F4, F7/F8, FC1/FC2, FC5/FC6, FT9/FT10, T7/T8, CP1/CP2, CP5/CP6, TP9/TP10, P3/P4, P7/P8, and O1/O2). The FCz electrode served as primary reference during recording. Signals were amplified using a wireless amplifier (analog-to-digital conversion: 24-bit) and recorded using the Brain Vision analyzer software at a sampling rate of 1000 Hz. Impedances were kept below 10 kHz during the recording session to ensure good signal quality. The EEG system furthermore featured three acceleration sensors in the X, Y, and Z direction located at the backside of the skull that recorded movements of the head.

The signals were preprocessed offline using the *Brain Vision Analyzer* (Brain Products GmbH, Gilching, Germany). Raw data were filtered from 0.1 Hz (high pass filter) to 30 Hz (low pass filter) at a slope of 24 dB/octave. After filtering, all signals were manually inspected to exclude sections containing technical artifacts and to identify channels with poor recording quality. To remove systematic artifacts such as vertical and horizontal eye movements or pulse-related signals, we applied an infomax independent component analysis (ICA) to the remaining data. The FCz channel and channels of poor signal quality were then recalculated via topographic interpolation.

To analyze the data, tasks were first epoched as a whole (60 s duration) and baseline-corrected using a 500 ms window prior to trial onset as the baseline. These large epochs were segmented into 58 non-overlapping segments (1024 ms segment duration). Segments underwent automatic artifact rejection and were excluded if any of the following conditions applied: (1) voltage steps of 50 μV/ms, (2) value differences of more than 200 μV within a 200 ms interval and (3) signal strength below 0.5 μV within a 100 ms interval. We then applied a current source density (CSD; Peters and Servos, 1989) transformation to remove the reference potential from the processed data and finally used a Fast-Fourier transformation to decompose the oscillatory data into different frequency bands (Hammond window of 10%). Only alpha and beta frequencies were analyzed in the context of this study as these have been implicated in motor functioning (Klostermann et al., 2007). Alpha frequencies were defined as frequencies between 8 and 13 Hz and beta frequencies were defined in the range between 13 and 30 Hz. We then averaged the power density (power per unit bandwidth) and extracted it for all tasks individually and for all tasks pooled (all left – condition and all right – condition) per electrode pair (C3/C4, FP1/FP2, F3/F4, F7/F8, FC1/FC2, FC5/FC6, FT9/FT10, T7/T8, CP1/CP2, CP5/CP6, TP9/TP10, P3/P4, P7/P8, and O1/O2). Finally, asymmetry indices (AIs) were computed across the averaged power densities for each individual activity and for all left and all right tasks combined using the formula: AI = (power right – power left)/(power right + power left). The processing steps were identical for both the EHI session and the WFQ session.

Statistical Analysis

Statistical analyses were performed using SPSS (version 21, Chicago, IL, United States). For the alpha band analysis of the EHI session, asymmetric electrode sites were identified across all task conditions by applying a repeated-measures ANCOVA with the within-subjects factors side of task performance (left or right) and electrode pair as well as the between-subjects factor handedness. We used the X, Y, and Z acceleration sensor signals during the task segments as covariates to identify whether head movements during these behaviors had a significant influence on task-related variables in the recordings. Here, we used the raw signal of the accelerometers as covariate as we wanted to identify how actual rather than processed movement signals influence the physiological signal. Focusing on the most significantly asymmetric electrode pair, we conducted a 10 × 2 × 2 ANCOVA with all individual tasks of the questionnaire and side of the task performance as within-subjects factor and handedness as between-subjects factor. Again, X, Y, and Z acceleration sensor signals were used as covariates. Finally, we used multiple linear regression with all left-sided

tasks as predictors or all right-sided tasks as predictors to identify whether the neuronal signal could predict the EHI score of participants. Here, we repeated the analysis steps conducted for the EHI session. For the WFQ session, we used footedness as a between-subjects variable rather than handedness (identical cut-offs). These measures were strongly correlated indicating that lateral biases in handedness and footedness in individuals within our sample were associated [two-sided Pearson correlation: $r(50) = 0.689$, $p < 0.001$]. However, even though mixed-handers were excluded, a large fraction of participants ($n = 19$) exhibited mixed-footedness. The footedness analysis was therefore conducted in two steps. First, analogous to the handedness analysis, only left- and right-footed participants were compared. In a second step, participants with mixed foot preference were included into the analysis to identify whether they exhibited neurophysiological activity different from both left- and right-footed participants. All aforementioned analyses were conducted identically for alpha and beta frequency bands.

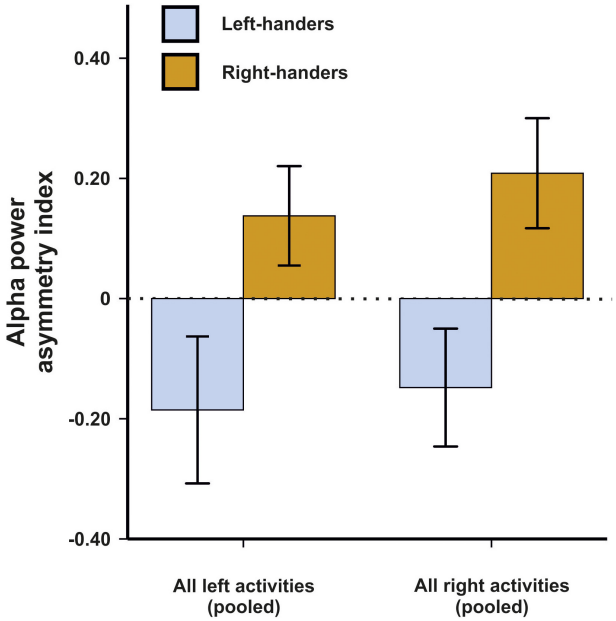

FIGURE 1 | Alpha power asymmetries between the left and right hemisphere during left and right task performance at the FC5/FC6 electrode pair. Error bars represent ± 1 SEM.

RESULTS

EHI

EEG Alpha Asymmetries

In a first analysis, we aimed to determine which electrode pair differentiated best between left- and right-handers in these motor tasks. While we expected that motor asymmetries demonstrate the strongest effects at fronto-central sites roughly overlapping with motor cortex or premotor cortex (Schmitz et al., 2019), we chose to use a non-biased approach due to the novelty of the used EEG system. We therefore performed a 14 × 2 × 2 ANCOVA with the within-subjects factors electrode pair (C3/C4, FP1/FP2, F3/F4, F7/F8, FC1/FC2, FC5/FC6, FT9/FT10, T7/T8, CP1/CP2, CP5/CP6, TP9/TP10, P3/P4, P7/P8, and O1/O2) and side of task performance (left and right) as well as the between-subjects factor handedness (left-handers and right-handers). Average movements in the X, Y and Z direction were included as covariates in the ANCOVA model to correct for potential movement effects. There was no main effect of electrode pair, side of task performance or handedness (all Fs < 1.44). The interaction between the factor electrode pair and handedness however reached significance in the ANCOVA indicating that some electrode pairs differentiated better between left- and right-handers than others [$F(9,414) = 2.27$, $p = 0.006$, $\eta^2 = 0.05$]. Bonferroni-corrected *post hoc* tests revealed that the best differentiation between left- and right-handers was found on electrodes FC5 and FC6 ($p = 0.011$). The FC electrodes correspond to supplementary motor and premotor areas (Puzzo et al., 2010). Here, left-handers had a negative asymmetry index indicating greater alpha power in the left hemisphere whereas right-handers had a positive asymmetry index indicating greater alpha power in the right hemisphere (**Figure 1**). We therefore decided to focus on this electrode pair throughout the manuscript in all further analyses. Importantly, neither the X, Y, or Z direction for movement signals exhibited a significant influence indicating that the behavioral tasks were unaffected by movement artifacts (all ps > 0.250). Thus, despite considerable movement during the experiment, they were no systematic effects on hemispheric asymmetries, likely because they are a relative measure and movement signals are found equally in both hemispheres.

In a next step, we investigated alpha power asymmetries for all individual tasks at the FC5/FC6 electrode site. We computed a 10 × 2 × 2 ANCOVA with the 10 tasks (writing, throwing a ball, drawing, using scissors, brushing teeth, using a knife, using a spoon, using a broom, striking a match and opening a box-lid/jar) and side of the task performance (left and right) as within-subject factors. Handedness was again used as a between-subjects factor and the X, Y, and Z direction movement accelerators were included as covariates. We found a significant main effect of handedness [$F(1,46) = 7.55$, $p = 0.009$, $\eta^2 = 0.14$]. There were no significant interactions with handedness or any of the movement parameters (ps > 0.087). Power spectra for the movement accelerometers of each individual task are depicted in **Supplementary Figure S1**. Alpha power asymmetries for all individual tasks are depicted in **Figure 2**.

Finally, we used multiple linear regression to identify whether tasks performed on the left and tasks performed on the right side could significantly predict the LQ of the participants. Using left-sided tasks as predictors, the model reached significance [$F(10,40) = 2.40$, $p = 0.024$, adjusted $R^2 = 0.22$]. Here, the only individual predictor reaching significance was writing ($p = 0.006$). For right-sided tasks, the model did not reach significance [$F(10,40) = 1.03$, $p > 0.250$, $R^2 = 0.05$].

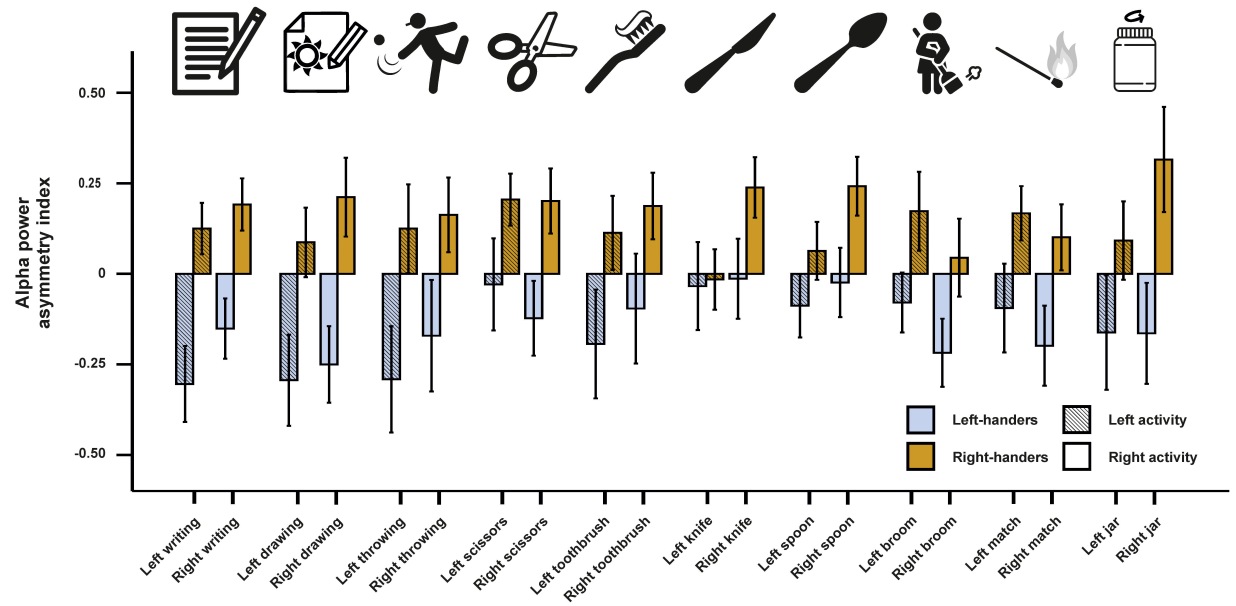

FIGURE 2 | Alpha power asymmetries between the left and right hemisphere at the FC5/FC6 electrode pair for all individual tasks of the Edinburgh Handedness Inventory (EHI). Tasks from left to right: writing the alphabet, drawing a sketch, throwing a ball, cutting a shape with scissors, brushing teeth, cutting clay with a knife, eating soup with a spoon, cleaning the floor with a broom, striking a match and opening jars. Error bars represent ± 1 SEM.

EEG Beta Asymmetries

For beta asymmetries, we repeated the analysis as for alpha asymmetries (10 × 2 × 2 ANCOVA with task and side of task performance as within-subjects factors and handedness as between-subjects factor). Again, we first checked whether movement artifacts as measured by the X, Y, and Z acceleration sensors had a significant influence on the signal. There were no significant results for any direction (all *p*s > 0.250). We could not detect any significant main effects of task, side of task performance or handedness (all *p*s > 0.135). However, there was a significant interaction between the side of the task performance and handedness [$F(1,45) = 4.33$, $p = 0.043$, $\eta^2 = 0.09$]. Bonferroni-corrected *post hoc* tests revealed that beta power asymmetries were significantly different between left- and right-sided tasks for both left- and right-handers ($p = 0.033$ and $p < 0.001$, respectively). The results for all tasks combined are depicted in **Figure 3**. The results for all individual tasks are shown in **Figure 4**.

Using the beta asymmetry indexes from left-sided tasks as predictors for the EHI score in a multiple linear regression model demonstrated a trend [$F(10,40) = 2.01$, $p = 0.058$, adjusted $R^2 = 0.17$]. Here, as for alpha asymmetries, the only significant predictor was the writing item of the EHI ($p = 0.002$). For right-sided tasks, the model was not significant [$F(10,40) = 1.15$, $p > 0.250$, adjusted $R^2 = 0.03$].

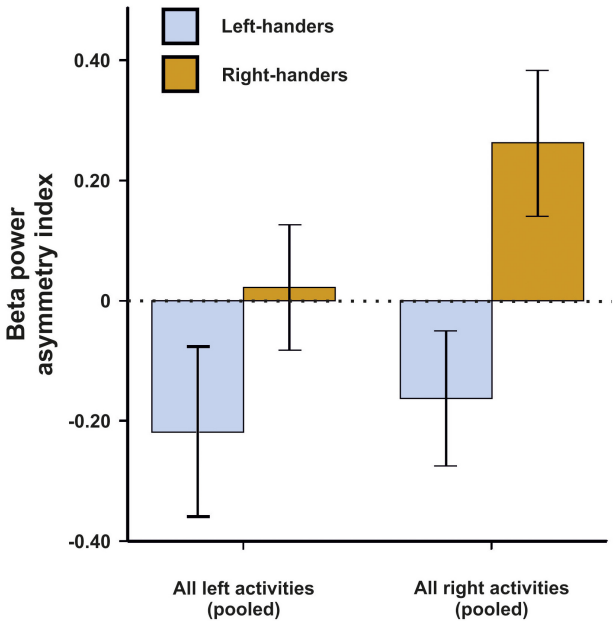

FIGURE 3 | Beta power asymmetry for both left- and right-handers during left- and right-sided tasks (pooled) of the EHI. Error bars represent ± 1 SEM.

WFQ

EEG Alpha Asymmetries

We first conducted a repeated-measures ANCOVA for the alpha power asymmetries using all left- and all right-sided tasks pooled as within-subjects variable and footedness as between-subjects variable. In a first step, only left- and right-footers were analyzed. We found that the FC5/FC6 electrode sites differentiated significantly between left- and right footers [$F(1,26) = 4.45$, $p = 0.045$, $\eta^2 = 0.15$, **Figure 5**]. However, there was no interaction between footedness and the side of the task performance ($F < 1$),

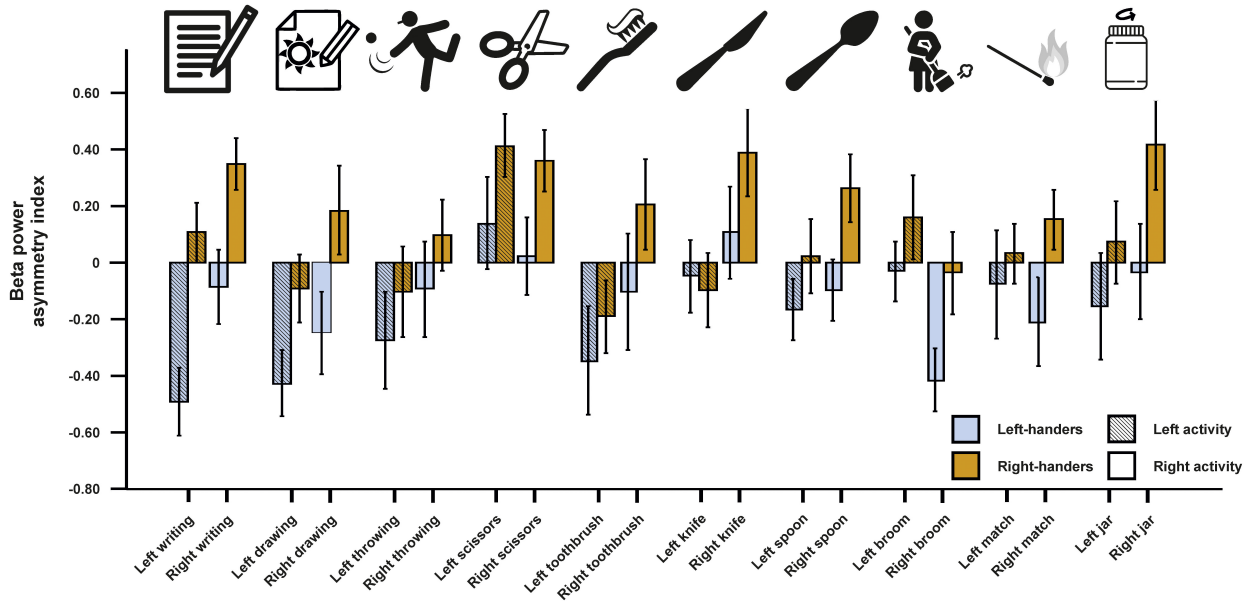

FIGURE 4 | Beta power asymmetry for all individual tasks of the EHI for left- and right-handers during left- and right-sided performance. Error bars represent ± 1 SEM.

nor with any of the acceleration sensors. We then conducted a 10 × 2 × 2 ANCOVA with the WFQ tasks (ball kicking, hopping on one leg, standing on one foot, smoothing sand, stepping onto a chair, weight-shifted relaxed standing, stepping on a shovel, grasping a marble, balancing on a rail and stepping on a bug) and side of task performance (left and right) as within-subjects variables and footedness as between-subjects variable. The ANCOVA for alpha power asymmetries demonstrated a significant main effect of footedness [$F(1,26) = 6.05$, $p = 0.021$, $\eta^2 = 0.20$]. No interaction with task, task side or any movement parameter reached significance (all $ps > 0.064$, **Figure 6**). Power spectra for the three movement accelerometers can be found in **Supplementary Figure S2**.

As before, multiple linear regression analysis was used to identify if the alpha power asymmetries in left- or in right-sided tasks could significantly predict the WFQ score. The model reached significance for left-sided tasks [$F(10,29) = 2.52$, $p = 0.040$, adjusted $R^2 = 0.343$], but not for right-sided tasks ($F < 1$). For left-sided tasks, only the beta-weight for grasping a marble was significant ($p = 0.006$).

Since a considerable number of our participants exhibited mixed-footedness ($n = 19$), we repeated the analysis including mixed-footers. There was again a main effect of footedness [$F(2,44) = 3.36$, $p = 0.044$, $\eta^2 = 0.13$]. *Post hoc* test revealed a significant difference between left- and mixed-footers in their alpha asymmetry levels ($p = 0.041$) whereas the difference between left- and right-footers did not reach significance ($p = 0.208$, see **Supplementary Figure S3**). No other main effect or interaction reached significance in this analysis (all $Fs < 1.06$). The 10 (task) × 2 (side) × 3 (footedness) ANCOVA demonstrated a significant main effect of footedness [$F(2,42) = 3.64$, $p = 0.035$, $\eta^2 = 0.15$, see **Supplementary Figure S4**]. Again, left-footers had significantly lower AIs compared to mixed-footers ($p = 0.035$), but not compared to right-footers ($p = 0.150$).

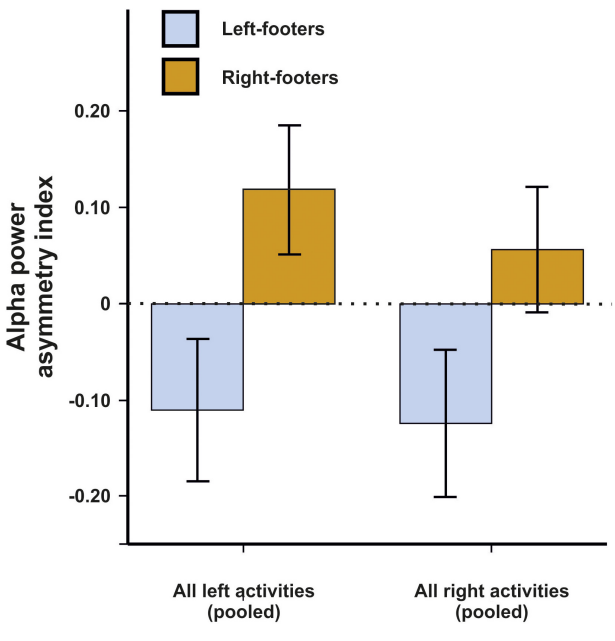

FIGURE 5 | Alpha power asymmetries between left- and right-footers at the FC5/FC6 electrode site for all pooled tasks of the WFQ. Error bars represent ± 1 SEM.

Both left- and right-sided task activity failed to significantly predict the WFQ score when mixed-footers were included in

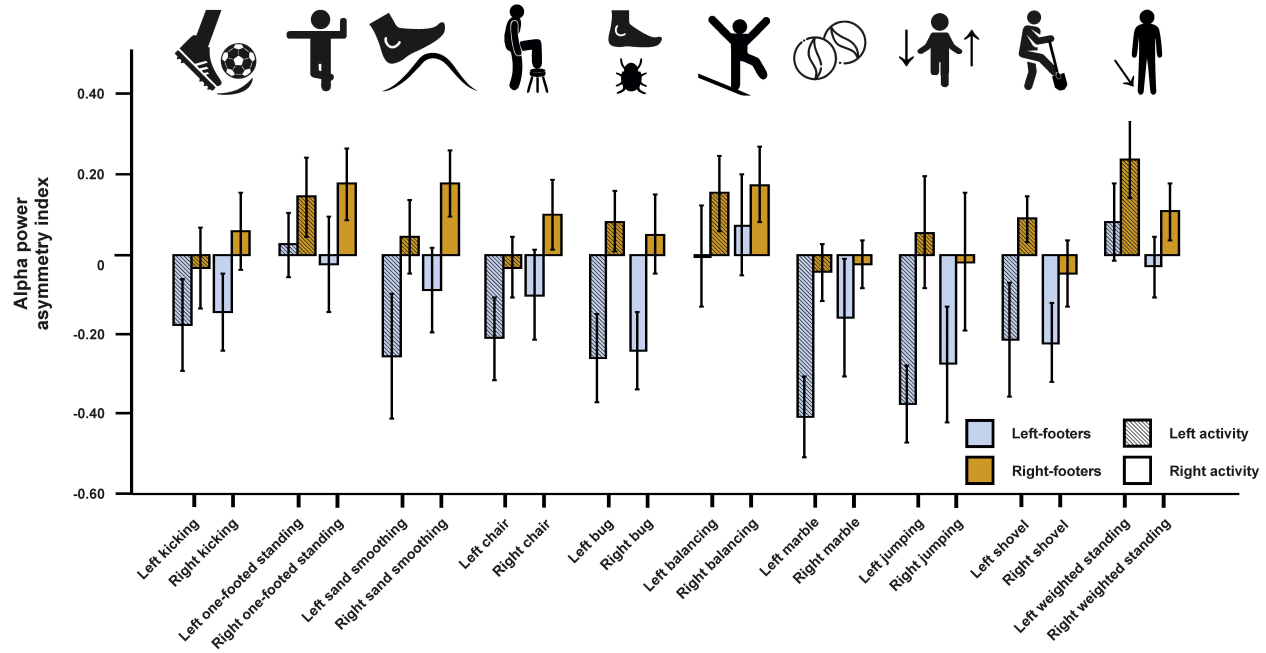

FIGURE 6 | Alpha power asymmetries for all individual tasks of the WFQ for left- and right-footers during left and right task performance. Individual tasks from left to right: kicking a ball, standing on one foot, simulated sand-smoothing, stepping onto a chair, stepping onto a bug (laser dot), balancing on a rail, grasping a marble, jumping one-footed, simulated step on a shovel (broom), weight-shifted relaxed standing. Error bars represent ± 1 SEM.

the analysis [$F(10,37) = 1.11$, $p = 0.382$, adjusted $R^2 = 0.022$ for left-sided tasks; $F(10,37) = 0.72$, $p = 0.699$, adjusted $R^2 = -0.06$ for right-sided tasks]. However, hopping on the left leg could significantly predict the WFQ score ($p = 0.029$) whereas no right-sided activity could predict WFQ scores.

EEG Beta Asymmetries

For beta asymmetries, the repeated-measures ANCOVA using all left- and all right-sided tasks pooled as within-subjects variable and footedness as between-subjects variable did not demonstrate any significant results (**Figure 7**). The same was true for the ANCOVA including all individual tasks (**Figure 8**) and the multiple linear regression for left- and right-sided task performance.

The inclusion of mixed-footers in the analysis did not change the result pattern as neither the ANCOVA for all left-sided and right-sided tasks (see **Supplementary Figure S5**), the ANCOVA including all individual items (see **Supplementary Figure S6**), nor the multiple linear regression for left- and right-sided tasks reached significance.

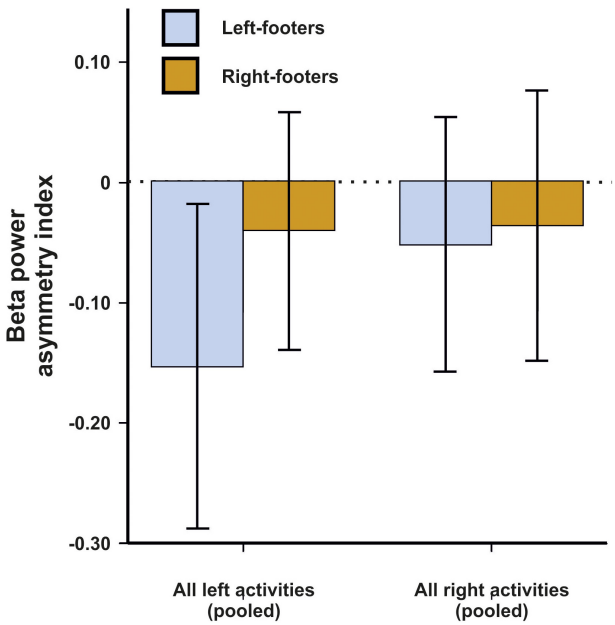

FIGURE 7 | Beta power asymmetries for all pooled tasks of the WFQ for left- and right-footers during left and right task performance. Error bars represent ± 1 SEM.

DISCUSSION

In the present study, we investigated the neurophysiological correlates of the most prominent handedness and footedness questionnaires—the EHI and the WFQ—in a real-life setting with high ecological validity. A mobile EEG system was used that allows for neural recording during active movement. We hypothesized that alpha and beta power asymmetries could differentiate both between left- and right-handers and between left- and right-footers during the performance of EHI and WFQ tasks. Furthermore, we hypothesized that these signals

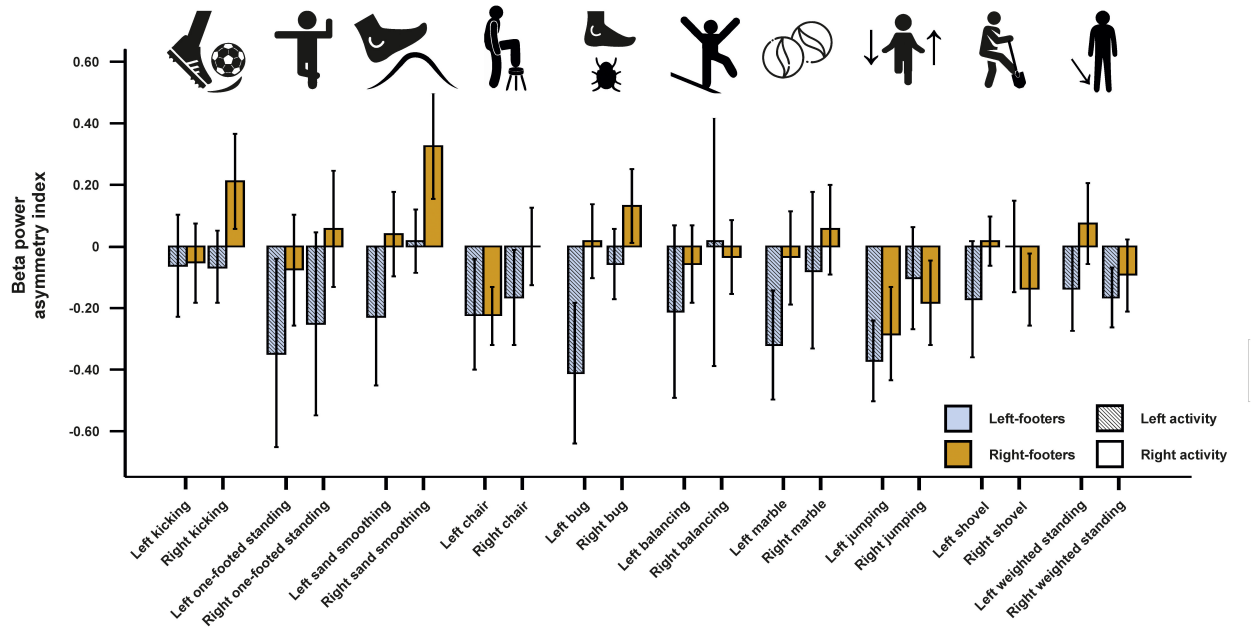

FIGURE 8 | Beta power asymmetries for all individual tasks of the WFQ for left and right-footers during left and right task performance. Error bars represent ± 1 SEM.

can distinguish between tasks performed on the left or on the right. Our results show that alpha power asymmetries at the FC5/FC6 electrode sites distinguished significantly between left- and right-handers for EHI items. The same was true for the distinction between left- and right-footers based on alpha power asymmetries during the performance of WFQ items. While we found no main effect of task side, we found significant interactions between task side and handedness in the beta frequency band for EHI items. These results were unaffected by movement artifacts since no analysis was significantly influenced by movement parameters as measured by the acceleration sensors. Finally, we could predict both the EHI and WFQ score based on alpha power asymmetries during tasks performed on the left side, but not on the right side using multiple linear regression analysis.

Edinburgh Handedness Inventory

For the EHI, results for the pooled tasks of all EHI items showed a significant difference between left- and right-handers in the alpha frequency band. Here, left-handers had negative alpha asymmetry power and right-handers had positive alpha power asymmetries. Oscillatory alpha activity has been associated with functional inhibition which has been demonstrated in visuospatial attention tasks (Worden et al., 2000; van der Werf et al., 2008; Kelly et al., 2009), but also during facial recognition (Jokisch and Jensen, 2007) and somatosensory working memory tasks (Haegens et al., 2010). This functional inhibition is hypothesized to be generated by rhythmic GABAergic input from local interneurons (Jensen and Mazaheri, 2010). Thus, the detected alpha power asymmetries in our study indicate that there was a stronger activation of the right hemisphere in left-handers (stronger left-hemispheric alpha power - > stronger left-hemispheric inhibition) and a stronger activation of the left hemisphere in right-handers (stronger right-hemispheric alpha power - > stronger right-hemispheric inhibition). These activation patterns are well in line with findings from fMRI and TMS studies demonstrating that movements of the dominant hand are generally associated with a stronger activation of the contralateral hemisphere (van den Berg et al., 2011; Grabowska et al., 2012). However, these studies also found that voluntary movements with the non-dominant hand are associated with more bilateral activation patterns indicating that the contralateral hemisphere to the dominant hand is generally implicated in the control of movement, regardless of the movement's body side. This result could explain why we found no significant interaction between the side of the task performance and handedness.

On the physiological level, we found no effects of individual tasks and their interactions with handedness. This finding contrasts studies investigating the factorial validity of the EHI questionnaire, which display that some items such as the usage of a broom or opening a box/jar load poorly on a single handedness factor (Dragovic, 2004; Milenkovic and Dragovic, 2013) probably due to the necessity of using the other hand as well for these tasks. A possible explanation for the discrepancy between behavioral and neurophysiological findings in our study might be attributed to a lack of power since item differences, if existing, are seemingly small in effect and therefore not easily detected by classical hypothesis testing.

While we did not find any differences between the items in the ANCOVA, we could find a significant prediction of the writing item in left-sided movements for the LQ in the alpha frequency band indicating that this item provides the best estimate for handedness on the neurophysiological

level. A corresponding finding was not evident for right-sided movements where no item could significantly predict the EHI score. A possible reason for the discrepancy between the predictive value of left vs. right task performance side can be found in differences in bilateral hand skill between left- and right-handers. Left-handers outperform right-handers in tasks involving a coordination between the left and the right hand (Judge and Stirling, 2003), perform almost equally well in fine-tuned motor task with the left and the right hand (Schmitz et al., 2019) and are better in faking right-handedness than right-handers faking left-handedness (McManus et al., 2018). Right-sided tasks are thus inadequate to differentiate between left- and right-handers as left-handers are usually very skilled in using their right hand. Therefore, neural activation patterns during tasks performed with the right hand are unlikely to provide substantial predictive value for the EHI score.

For the beta frequency band, we found comparable results to the alpha frequency analysis. Although an increase in beta power is not directly associated with functional inhibition, voluntary movements have been linked to decreases in beta power (Hammond et al., 2007). Therefore, our finding of higher beta power in the hemisphere that is not dominantly controlling the execution of the movement (i.e., higher beta power in the right hemisphere for right-sided movements and higher beta power in the left hemisphere for left-sided movements) fits into this framework. It has to be noted however that this hypothesis has been challenged and that the association between motor function and beta power still remains unclear (Jenkinson and Brown, 2011). Furthermore, a recent study of Ocklenburg et al. (2019) found strong correlations between asymmetries in the alpha and beta frequency band indicating that alpha and beta frequency bands might have functionally similar roles.

Notably, the interaction between task performance side and handedness was stronger in right-handers than left-handers, again indicating that right-handers are more lateralized compared to left-handers during motor tasks on the neural level. However, this finding could also be a result of our chosen cut-offs since the classification for left- and right-handers was symmetrical around 0 ($LQ < -40$ = left-handed, $LQ > 40$ = right-handed). A large-scale psychometric study has however demonstrated that cut-offs for left- and right-handers are not symmetrical around 0 for a refined 10-item scale based on the EHI ($LQ < -7$ = left-handed, $LQ > 72$ = right-handed; Tran et al., 2014). Unfortunately, the exclusion of mixed-handers from the analysis does not allow for definite conclusions on this matter as using the asymmetrical cut-offs as defined by Tran et al. (2014) only marginally changes the classification for left- and right-handers in our study. Future studies should therefore include mixed-handers to identify whether symmetrical or asymmetrical cut-offs significantly alter the neurophysiological result patterns as hinted at by extensive psychometric testing on the behavioral level (Tran et al., 2014). As for alpha asymmetries, no interaction between individual tasks of the EHI and handedness could be found indicating that there were no major differences between the items. However, multiple linear regression analysis again revealed a significant beta-weight for left-sided writing indicating that writing provides the best fit when estimating handedness based on neurophysiological activity.

Waterloo Footedness Questionnaire

For the WFQ session, we only found significant effects of footedness in the alpha frequency band indicating that items of the WFQ can differentiate between left- and right-footers on the neural level. As for handedness, there were no interactions with the side of the task performance. This lack of an interaction could again be attributed to bilateral activation patterns regardless of the side of execution. In fMRI studies, foot movements have been shown to be less lateralized than hand or finger movements (Kapreli et al., 2006; Rocca and Filippi, 2010). However, as for handedness, movement execution with the non-dominant foot displayed more bilateral activation patterns as compared to movements performed with the dominant foot (Rocca and Filippi, 2010). Comparable to the EHI, we found no interaction effects of individual tasks with footedness in the ANCOVA. However, multiple linear regression analysis indicated that grasping a marble is predictive of the participants' WFQ score, possibly due to the fine-tuned movement necessary in this condition. Since there has been no study investigating the factorial validity of the WFQ, this study provides a first insight into item-specific differentiation between left- and right-footers. Interestingly, the classically used item of kicking a ball did not reach significance here, possibly due to the necessity of stabilizing the body with the non-kicking foot resulting in bilateral activation patterns both in left- and right-footers.

Limitations

A shortcoming of the present study concerns the rather small sample size of the study. Low sample sizes heighten the probability for false negative results meaning that existing effects could not be detected due to low power (Button et al., 2013). Especially the non-significant differences between individual items both for the EHI and the WFQ could be attributed to a lack of power rather than a lack of differentiation between the items. Brysbaert (2019) noted that small effects can only be reliably detected if individual groups consist of at least 100 participants. Thus, our study only had the possibility to reveal medium to large effects, a problem that was increased in our footedness analysis due to the even smaller sample sizes per individual group. We want to stress however that the main effects between left- and right-lateralized participants were large indicating that the sample size was adequate to demonstrate the viability of mobile EEGs in neuroscientific research in general. Since these results are conform to a wide body of literature on motor asymmetries, we are confident in their validity. Nonetheless, it has to be noted that for example a large-scale imaging study on cortical asymmetry could for example not replicate effects found in previous studies with smaller sample sizes (Guadalupe et al.,

2014). Therefore, the results of the present study need to be replicated and extended in larger datasets to ensure the validity of our findings and to clarify whether the non-significant difference between items was a result of a lack in statistical power.

Another limitation of the study can be found in the *a priori* exclusion of mixed-handers as this group might have been informative regarding the specificity of our findings for left- and right-handers. We chose to exclude this group from the current study as we found very few mixed-handers according to the cut-offs used in this study during the pre-screening process. However, there was a considerable fraction of mixed-footers in the dataset that allowed for a comparison between left-, mixed-, and right-footers. We found that mixed-footers resemble right-footers in their neural activity patterns, a results that might have been due to the majority of mixed-footers being lateralized to the right rather than to the left ($n = 7$ for LQ < 0, $n = 12$ for LQ > 0). Interestingly, the mixed-footers seemed to be even stronger lateralized compared to right-handers. However, this result might have been due to variance in the signal and the reduced sample sizes per group.

Finally, it should be noted that we identified the electrode pair of interest by using the behavioral assessment of handedness. This induces a certain circularity into the analysis as we try to distinguish between left- and right-handers on the physiological level, but used the EHI score as a tool to find the strongest distinction between them. Since the multiple linear regression analyses indicate that the physiological signal can predict the EHI score (at least for individual items), a data driven approach to identify the handedness of the participants should however be possible using EEG. Future studies could use, e.g., machine learning tools to completely circumvent a behavioral assessment and try to identify handedness merely by the physiological activity.

Future Directions

This study is the first to use a mobile EEG system to investigate motor laterality during real-life motor behavior. Since we could replicate known result patterns from fMRI studies on motor laterality, this methodology seems to work appropriately. Therefore, it could be applied to other measures for handedness and footedness other than the EHI and the WFQ as recent studies have come up with new and more refined scales for both phenotypes (Tran et al., 2014; Tran and Voracek, 2016). Especially for footedness, Tran and Voracek (2016) could show that it is two-dimensional rather than a one-dimensional measure which could be reflected in different neurophysiological patterns in relation to the dimension of the specific items.

Furthermore, the mobile EEG could be used for studying motor laterality other than handedness and footedness. To fully understand the neural mechanisms of lateralized behavior, a large variety of lateralized phenotypes should be investigated. One recently highlighted field of research that could be studied using this novel approach are social touch behaviors. Prominent social touch phenomena such as embracing, kissing, and cradling have been shown to be lateralized on the population level (Ocklenburg et al., 2018). Several studies by our group have found that these biases are both determined by motor biases such as handedness or footedness, but also by the emotional context of the situation (Packheiser et al., 2019a,b). However, since all these studies used purely behavioral approaches, the underlying neurophysiology of social touch remains largely unknown. Mobile EEG as used in the present study could provide a powerful tool to study behavior in more ecologically valid real-life situations and thus could illuminate this field of research.

DATA AVAILABILITY STATEMENT

The datasets generated for this study are available on request to the corresponding author.

ETHICS STATEMENT

The studies involving human participants were reviewed and approved by Local ethics committee of the Faculty of Psychology, Ruhr-University Bochum. The patients/participants provided their written informed consent to participate in this study.

AUTHOR CONTRIBUTIONS

JP and JS conceived and supervised the experiment, analyzed the data, and wrote the manuscript. YP collected the data and reviewed the manuscript. YE and PF helped with data acquisition and data analysis and reviewed the manuscript. OG acquired funding and reviewed the manuscript. SO conceived the experiment, analyzed the data, acquired funding and reviewed the manuscript.

FUNDING

This study was funded by the Gefördert durch die Deutsche Forschungsgemeinschaft (DFG) – Projektnummer GRK-2185/1 (DFG-Graduiertenkolleg Situated Cognition) and by the Deutsche Forschungsgemeinschaft (DFG, German Research Foundation) – project number GRK-2185/1 (DFG Research Training Group Situated Cognition). We acknowledge the support by the DFG Open Access Publication Funds of the Ruhr-Universität Bochum.

ACKNOWLEDGMENTS

All icons of the pictograms were made by Freepik from www.flaticon.com.

SUPPLEMENTARY MATERIAL

The Supplementary Material for this article can be found online at: https://www.frontiersin.org/articles/10.3389/fnins.2020.00109/full#supplementary-material

FIGURE S1 | Power spectra for the **(A)** X-, **(B)** Y-, and **(C)** Z-head movement direction as measured by the accelerometers for the EHI tasks. Note that all individual activities demonstrate high delta power (oscillations between 0 and 4 Hz). All other frequency bands are almost absent in the signals. Movement in the Y-direction, i.e., back and forth movement of the head, exhibited the strongest amplitudes across all tasks.

FIGURE S2 | Power spectra for the **(A)** X-, **(B)** Y-, and **(C)** Z-head movement direction as measured by the accelerometers for the WFQ tasks. As for EHI tasks, delta power dominated the accelerometer signal strength in all individual tasks. Only jumping on one leg induced noticeable amplitudes in faster oscillating frequency bands.

FIGURE S3 | Alpha power asymmetries between left-, mixed-, and right-footers at the FC5/FC6 electrode site for all pooled tasks of the WFQ. Error bars represent ± 1 SEM.

FIGURE S4 | Alpha power asymmetries for all individual tasks of the WFQ for left-, mixed-, and right-footers during left and right task performance. Error bars represent ± 1 SEM.

FIGURE S5 | Beta power asymmetries for all individual tasks of the WFQ for left-, mixed-, and right-footers during left and right task performance. Error bars represent ± 1 SEM.

FIGURE S6 | Beta power asymmetries for all individual tasks of the WFQ for left-, mixed-, and right-footers during left and right task performance. Error bars represent ± 1 SEM.

REFERENCES

Brown, E. R., and Taylor, P. (1988). Handedness, footedness, and eyedness. *Percept. Mot. Skills* 66, 183–186. doi: 10.2466/pms.1988.66.1.183

Bryden, M. P. (1977). Measuring handedness with questionnaires. *Neuropsychologia* 15, 617–624. doi: 10.1016/0028-3932(77)90067-7

Brysbaert, M. (2019). How many participants do we have to include in properly powered experiments? A tutorial of power analysis with reference tables. *J. Cogn.* 2:16. doi: 10.5334/joc.72

Burnett, S. A., Lane, D. M., and Dratt, L. M. (1982). Spatial ability and handedness. *Intelligence* 6, 57–68. doi: 10.1016/0160-2896(82)90020-4

Button, K. S., Ioannidis, J. P. A., Mokrysz, C., Nosek, B. A., Flint, J., Robinson, E. S. J., et al. (2013). Power failure: why small sample size undermines the reliability of neuroscience. *Nat. Rev. Neurosci.* 14, 365–376. doi: 10.1038/nrn3475

Camargos, M. B., Palmeira, A. D. S., and Fachin-Martins, E. (2017). Cross-cultural adaptation to Brazilian Portuguese of the Waterloo Footedness Questionnaire-Revised: Wfq-R-Brazil. *Arq. Neuropsiquiatr.* 75, 727–735. doi: 10.1590/0004-282X20170139

Coren, S. (1993). The lateral preference inventory for measurement of handedness, footedness, eyedness, and earedness: norms for young adults. *Bull. Psychon. Soc.* 31, 1–3. doi: 10.3758/BF03334122

Deiber, M. -P., Sallard, E., Ludwig, C., Ghezzi, C., Barral, J., and Ibañez, V. (2012). Eeg alpha activity reflects motor preparation rather than the mode of action selection. *Front. Integr. Neurosci.* 6:59. doi: 10.3389/fnint.2012.00059

Dittmar, M. (2002). Functional and postural lateral preferences in humans: interrelations and life-span age differences. *Hum. Biol.* 74, 569–585. doi: 10.1353/hub.2002.0040

Dragovic, M. (2004). Towards an improved measure of the Edinburgh Handedness Inventory: a one-factor congeneric measurement model using confirmatory factor analysis. *Laterality* 9, 411–419. doi: 10.1080/13576500342000248

Dragovic, M., and Hammond, G. (2005). Handedness in schizophrenia: a quantitative review of evidence. *Acta Psychiatr. Scand.* 111, 410–419. doi: 10.1111/j.1600-0447.2005.00519.x

Elias, L. J., Bryden, M. P., and Bulman-Fleming, M. B. (1998). Footedness is a better predictor than is handedness of emotional lateralization. *Neuropsychologia* 36, 37–43. doi: 10.1016/S0028-3932(97)00107-3

Fazio, R., Coenen, C., and Denney, R. L. (2012). The original instructions for the Edinburgh Handedness Inventory are misunderstood by a majority of participants. *Laterality* 17, 70–77. doi: 10.1080/1357650X.2010.532801

Grabowska, A., Gut, M., Binder, M., Forsberg, L., Rymarzczyk, K., and Urbanik, A. (2012). Switching handedness: fMRI study of hand motor control in right-handers and converted left-handers. *Acta Neurobiol. Exp.* 72, 439–451.

Gramann, K., Ferris, D. P., Gwin, J., and Makeig, S. (2014). Imaging natural cognition in action. *Int. J. Psychophysiol.* 91, 22–29. doi: 10.1016/j.ijpsycho.2013.09.003

Griffiths, B., Mazaheri, A., Debener, S., and Hanslmayr, S. (2016). Brain oscillations track the formation of episodic memories in the real world. *NeuroImage* 143, 256–266. doi: 10.1016/j.neuroimage.2016.09.021

Guadalupe, T., Willems, R. M., Zwiers, M. P., Arias Vasquez, A., Hoogman, M., Hagoort, P., et al. (2014). Differences in cerebral cortical anatomy of left- and right-handers. *Front. Psychol.* 5:261. doi: 10.3389/fpsyg.2014.00261

Güntürkün, O., and Ocklenburg, S. (2017). Ontogenesis of lateralization. *Neuron* 94, 249–263. doi: 10.1016/j.neuron.2017.02.045

Haegens, S., Osipova, D., Oostenveld, R., and Jensen, O. (2010). Somatosensory working memory performance in humans depends on both engagement and disengagement of regions in a distributed network. *Hum. Brain Mapp.* 31, 26–35. doi: 10.1002/hbm.20842

Hammond, C., Bergman, H., and Brown, P. (2007). Pathological synchronization in Parkinson's disease: networks, models and treatments. *Trends Neurosci.* 30, 357–364. doi: 10.1016/j.tins.2007.05.004

Hammond, G. (2002). Correlates of human handedness in primary motor cortex: a review and hypothesis. *Neurosci. Biobehav. Rev.* 26, 285–292. doi: 10.1016/s0149-7634(02)00003-9

Jenkinson, N., and Brown, P. (2011). New insights into the relationship between dopamine, beta oscillations and motor function. *Trends Neurosci.* 34, 611–618. doi: 10.1016/j.tins.2011.09.003

Jensen, O., and Mazaheri, A. (2010). Shaping functional architecture by oscillatory alpha activity: gating by inhibition. *Front. Hum. Neurosci.* 4:186. doi: 10.3389/fnhum.2010.00186

Jokisch, D., and Jensen, O. (2007). Modulation of gamma and alpha activity during a working memory task engaging the dorsal or ventral stream. *J. Neurosci.* 27, 3244–3251. doi: 10.1523/JNEUROSCI.5399-06.2007

Judge, J., and Stirling, J. (2003). Fine motor skill performance in left− and right−handers: evidence of an advantage for left−handers. *Laterality* 8, 297–306. doi: 10.1080/13576500342000022a

Kanai, R., and Rees, G. (2011). The structural basis of inter-individual differences in human behaviour and cognition. *Nat. Rev. Neurosci.* 12, 231–242. doi: 10.1038/nrn3000

Kapreli, E., Athanasopoulos, S., Papathanasiou, M., van Hecke, P., Strimpakos, N., Gouliamos, A., et al. (2006). Lateralization of brain activity during lower limb joints movement. An fMRI study. *NeuroImage* 32, 1709–1721. doi: 10.1016/j.neuroimage.2006.05.043

Kapreli, E., Athanasopoulos, S., Stavridis, I., Billis, E., and Strimpakos, N. (2015). Waterloo footedness questionnaire (WFQ-R): cross-cultural adaptation and psychometric properties of Greek version. *Physiotherapy* 101(Suppl. 1):e721. doi: 10.1016/j.physio.2015.03.3577

Kelly, S. P., Gomez-Ramirez, M., and Foxe, J. J. (2009). The strength of anticipatory spatial biasing predicts target discrimination at attended locations: a high-density EEG study. *Eur. J. Neurosci.* 30, 2224–2234. doi: 10.1111/j.1460-9568.2009.06980.x

Kim, S. G., Ashe, J., Hendrich, K., Ellermann, J. M., Merkle, H., Uğurbil, K., et al. (1993). Functional magnetic resonance imaging of motor cortex:

hemispheric asymmetry and handedness. *Science* 261, 615–617. doi: 10.1126/science.8342027

Klostermann, F., Nikulin, V. V., Kühn, A. A., Marzinzik, F., Wahl, M., Pogosyan, A., et al. (2007). Task-related differential dynamics of EEG alpha- and beta-band synchronization in cortico-basal motor structures. *Eur. J. Neurosci.* 25, 1604–1615. doi: 10.1111/j.1460-9568.2007.05417.x

Li, C., Zhu, W., and Nuttall, R. L. (2003). Familial handedness and spatial ability: a study with Chinese students aged 14–24. *Brain Cogn.* 51, 375–384. doi: 10.1016/S0278-2626(03)00041-1

McFarland, K., and Anderson, J. (1980). Factor stability of the Edinburgh Handedness Inventory as a function of test-retest performance, age and sex. *Br. J. Psychol.* 71, 135–142. doi: 10.1111/j.2044-8295.1980.tb02739.x

McManus, I. C., Buckens, G., Harris, N., Flint, A., Ng, H. L. A., and Vovou, F. (2018). Faking handedness: individual differences in ability to fake handedness, social cognitions of the handedness of others, and a forensic application using Bayes' theorem. *Laterality* 23, 67–100. doi: 10.1080/1357650X.2017.1315430

Milenkovic, S., and Dragovic, M. (2013). Modification of the Edinburgh Handedness Inventory: a replication study. *Laterality* 18, 340–348. doi: 10.1080/1357650X.2012.683196

Ocklenburg, S., Beste, C., Arning, L., Peterburs, J., and Güntürkün, O. (2014). The ontogenesis of language lateralization and its relation to handedness. *Neurosci. Biobehav. Rev.* 43, 191–198. doi: 10.1016/j.neubiorev.2014.04.008

Ocklenburg, S., Friedrich, P., Schmitz, J., Schlüter, C., Genc, E., Güntürkün, O., et al. (2019). Beyond frontal alpha: investigating hemispheric asymmetries over the EEG frequency spectrum as a function of sex and handedness. *Laterality* 24, 505–524. doi: 10.1080/1357650X.2018.1543314

Ocklenburg, S., and Güntürkün, O. (2009). Head-turning asymmetries during kissing and their association with lateral preference. *Laterality* 14, 79–85. doi: 10.1080/13576500802243689

Ocklenburg, S., Güntürkün, O., Hugdahl, K., and Hirnstein, M. (2015). Laterality and mental disorders in the postgenomic age–a closer look at schizophrenia and language lateralization. *Neurosci. Biobehav. Rev.* 59, 100–110. doi: 10.1016/j.neubiorev.2015.08.019

Ocklenburg, S., Packheiser, J., Schmitz, J., Rook, N., Güntürkün, O., Peterburs, J., et al. (2018). Hugs and kisses – the role of motor preferences and emotional lateralization for hemispheric asymmetries in human social touch. *Neurosci. Biobehav. Rev.* 95, 353–360. doi: 10.1016/j.neubiorev.2018.10.007

Oldfield, R. C. (1971). The assessment and analysis of handedness: the Edinburgh Inventory. *Neuropsychologia* 9, 97–113. doi: 10.1016/0028-3932(71)90067-4

Packheiser, J., Rook, N., Dursun, Z., Mesenhöller, J., Wenglorz, A., Güntürkün, O., et al. (2019a). Embracing your emotions: affective state impacts lateralisation of human embraces. *Psychol. Res.* 83, 26–36. doi: 10.1007/s00426-018-0985-8

Packheiser, J., Schmitz, J., Berretz, G., Papadatou-Pastou, M., and Ocklenburg, S. (2019b). Handedness and sex effects on lateral biases in human cradling: three meta-analyses. *Neurosci. Biobehav. Rev.* 104, 30–42. doi: 10.1016/j.neubiorev.2019.06.035

Papadatou-Pastou, M., Martin, M., and Munafò, M. R. (2013). Measuring hand preference: a comparison among different response formats using a selected sample. *Laterality* 18, 68–107. doi: 10.1080/1357650X.2011.628794

Papadatou-Pastou, M., Martin, M., Munafo, M. R., Ntolka, E., Ocklenburg, S., and Paracchini, S. (2019). The prevalence of left-handedness: five meta-analyses of 200 studies totaling 2,396,170 individuals. *PsyArXiv* [Preprint]. doi: 10.31234/osf.io/5gjac

Peters, M., and Servos, P. (1989). Performance of subgroups of left-handers and right-handers. *Can. J. Psychol.* 43, 341–358. doi: 10.1037/h0084226

Pfurtscheller, G. (1981). Central beta rhythm during sensorimotor activities in man. *Electroencephalogr. Clin. Neurophysiol.* 51, 253–264. doi: 10.1016/0013-4694(81)90139-5

Porac, C., and Coren, S. (1981). *Lateral Preferences and Human Behavior*. New York, NY: Springer, doi: 10.1007/978-1-4613-8139-6

Puzzo, I., Cooper, N. R., Vetter, P., and Russo, R. (2010). Eeg activation differences in the pre-motor cortex and supplementary motor area between normal individuals with high and low traits of autism. *Brain Res.* 1342, 104–110. doi: 10.1016/j.brainres.2010.04.060

Ransil, B. J., and Schachter, S. C. (1994). Test-retest reliability of the Edinburgh Handedness Inventory and Global Handedness preference measurements, and their correlation. *Percept. Mot. Skills* 79(3 Pt 1), 1355–1372. doi: 10.2466/pms.1994.79.3.1355

Reiss, M., Tymnik, G., Kögler, P., Kögler, W., and Reiss, G. (1999). Laterality of hand, foot, eye, and ear in twins. *Laterality* 4, 287–297. doi: 10.1080/713754337

Rocca, M. A., and Filippi, M. (2010). Fmri correlates of execution and observation of foot movements in left-handers. *J. Neurol. Sci.* 288, 34–41. doi: 10.1016/j.jns.2009.10.013

Schmitz, J., Packheiser, J., Birnkraut, T., Hinz, N. -A., Friedrich, P., Güntürkün, O., et al. (2019). The neurophysiological correlates of handedness: insights from the lateralized readiness potential. *Behav. Brain Res.* 364, 114–122. doi: 10.1016/j.bbr.2019.02.021

Sommer, I., Ramsey, N., Kahn, R., Aleman, A., and Bouma, A. (2001). Handedness, language lateralisation and anatomical asymmetry in schizophrenia: meta-analysis. *Br. J. Psychiatry* 178, 344–351. doi: 10.1192/bjp.178.4.344

Tran, U. S., Stieger, S., and Voracek, M. (2014). Evidence for general right-, mixed-, and left-sidedness in self-reported handedness, footedness, eyedness, and earedness, and a primacy of footedness in a large-sample latent variable analysis. *Neuropsychologia* 62, 220–232. doi: 10.1016/j.neuropsychologia.2014.07.027

Tran, U. S., Stieger, S., and Voracek, M. (2015). Mixed-footedness is a more relevant predictor of schizotypy than mixed-handedness. *Psychiatry Res.* 225, 446–451. doi: 10.1016/j.psychres.2014.11.069

Tran, U. S., and Voracek, M. (2016). Footedness is associated with self-reported sporting performance and motor abilities in the general population. *Front. Psychol.* 7:1199. doi: 10.3389/fpsyg.2016.01199

Turesky, T. K., Olulade, O. A., Luetje, M. M., and Eden, G. F. (2018). An fMRI study of finger tapping in children and adults. *Hum. Brain Mapp.* 39, 3203–3215. doi: 10.1002/hbm.24070

Turnbull, O. H., Rhys-Jones, S. L., and Jackson, A. L. (2001). The leftward cradling bias and prosody: an investigation of cradling preferences in the deaf community. *J. Genet. Psychol.* 162, 178–186. doi: 10.1080/00221320109597959

van den Berg, F. E., Swinnen, S. P., and Wenderoth, N. (2011). Involvement of the primary motor cortex in controlling movements executed with the ipsilateral hand differs between left- and right-handers. *J. Cogn. Neurosci.* 23, 3456–3469. doi: 10.1162/jocn_a_00018

van der Werf, J., Jensen, O., Fries, P., and Medendorp, W. P. (2008). Gamma-band activity in human posterior parietal cortex encodes the motor goal during delayed prosaccades and antisaccades. *J. Neurosci.* 28, 8397–8405. doi: 10.1523/JNEUROSCI.0630-08.2008

Veale, J. F. (2014). Edinburgh Handedness Inventory – short form: a revised version based on confirmatory factor analysis. *Laterality* 19, 164–177. doi: 10.1080/1357650X.2013.783045

Worden, M. S., Foxe, J. J., Wang, N., and Simpson, G. V. (2000). Anticipatory biasing of visuospatial attention indexed by retinotopically specific alpha-band electroencephalography increases over occipital cortex. *J. Neurosci.* 20:RC63.

Conflict of Interest: The authors declare that the research was conducted in the absence of any commercial or financial relationships that could be construed as a potential conflict of interest.

Copyright © 2020 Packheiser, Schmitz, Pan, El Basbasse, Friedrich, Güntürkün and Ocklenburg. This is an open-access article distributed under the terms of the Creative Commons Attribution License (CC BY). The use, distribution or reproduction in other forums is permitted, provided the original author(s) and the copyright owner(s) are credited and that the original publication in this journal is cited, in accordance with accepted academic practice. No use, distribution or reproduction is permitted which does not comply with these terms.

frontiers in Neuroscience

ORIGINAL RESEARCH
published: 31 March 2020
doi: 10.3389/fnins.2020.00225

fMRI-Targeted High-Angular Resolution Diffusion MR Tractography to Identify Functional Language Tracts in Healthy Controls and Glioma Patients

Francesco Sanvito[1,2], Eduardo Caverzasi[3], Marco Riva[4,5], Kesshi M. Jordan[3], Valeria Blasi[6], Paola Scifo[7], Antonella Iadanza[1,2], Sofia Allegra Crespi[1,8], Sara Cirillo[1,2], Alessandra Casarotti[5], Antonella Leonetti[4], Guglielmo Puglisi[4], Marco Grimaldi[9], Lorenzo Bello[5,10], Maria Luisa Gorno-Tempini[3], Roland G. Henry[3], Andrea Falini[1,2†] and Antonella Castellano[1,2†]*

[1] Neuroradiology Unit and CERMAC, IRCCS San Raffaele Scientific Institute, Milan, Italy, [2] School of Medicine, Vita-Salute San Raffaele University, Milan, Italy, [3] UCSF Weill Institute for Neurosciences, Department of Neurology, University of California, San Francisco, San Francisco, CA, United States, [4] Department of Medical Biotechnology and Translational Medicine, Università degli Studi di Milano, Milan, Italy, [5] Neurosurgical Oncology Unit, Humanitas Clinical and Research Center – IRCCS, Rozzano, Italy, [6] IRCCS Fondazione Don Carlo Gnocchi, Milan, Italy, [7] Nuclear Medicine Unit, IRCCS San Raffaele Scientific Institute, Milan, Italy, [8] School of Psychology, Vita-Salute San Raffaele University, Milan, Italy, [9] Neuroradiology Unit, Humanitas Clinical and Research Center – IRCCS, Rozzano, Italy, [10] Department of Oncology and Hemato-Oncology, Università degli Studi di Milano, Milan, Italy

Background: MR Tractography enables non-invasive preoperative depiction of language subcortical tracts, which is crucial for the presurgical work-up of brain tumors; however, it cannot evaluate the exact function of the fibers.

Purpose: A systematic pipeline was developed to combine tractography reconstruction of language fiber bundles, based on anatomical landmarks (Anatomical-T), with language fMRI cortical activations. A fMRI-targeted Tractography (fMRI-T) was thus obtained, depicting the subsets of the anatomical tracts whose endpoints are located inside a fMRI activation. We hypothesized that fMRI-T could provide additional functional information regarding the subcortical structures, better reflecting the eloquent white matter structures identified intraoperatively.

Methods: Both Anatomical-T and fMRI-T of language fiber tracts were performed on 16 controls and preoperatively on 16 patients with left-hemisphere brain tumors, using a *q*-ball residual bootstrap algorithm based on High Angular Resolution Diffusion Imaging (HARDI) datasets (b = 3000 s/mm^2; 60 directions); fMRI ROIs were obtained using picture naming, verbal fluency, and auditory verb generation tasks. In healthy controls, normalized MNI atlases of fMRI-T and Anatomical-T were obtained. In patients, the surgical resection of the tumor was pursued by identifying eloquent structures with intraoperative direct electrical stimulation mapping and extending surgery to the functional boundaries. Post-surgical MRI allowed to identify Anatomical-T and fMRI-T non-eloquent portions removed during the procedure.

OPEN ACCESS

Edited by:
Itamar Ronen, Leiden University Medical Center, Netherlands

Reviewed by:
Yogesh Rathi, Harvard Medical School, United States
Shijie Zhao, Northwestern Polytechnical University, China

***Correspondence:**
Antonella Castellano
castellano.antonella@hsr.it

† These authors share senior authorship

Specialty section:
This article was submitted to Brain Imaging Methods, a section of the journal Frontiers in Neuroscience

Received: *05 November 2019*
Accepted: *02 March 2020*
Published: *31 March 2020*

Citation:
Sanvito F, Caverzasi E, Riva M, Jordan KM, Blasi V, Scifo P, Iadanza A, Crespi SA, Cirillo S, Casarotti A, Leonetti A, Puglisi G, Grimaldi M, Bello L, Gorno-Tempini ML, Henry RG, Falini A and Castellano A (2020) fMRI-Targeted High-Angular Resolution Diffusion MR Tractography to Identify Functional Language Tracts in Healthy Controls and Glioma Patients. Front. Neurosci. 14:225. doi: 10.3389/fnins.2020.00225

Results: MNI Atlases showed that fMRI-T is a subset of Anatomical-T, and that different task-specific fMRI-T involve both shared subsets and task-specific subsets – e.g., verbal fluency fMRI-T strongly involves dorsal frontal tracts, consistently with the phonogical-articulatory features of this task. A quantitative analysis in patients revealed that Anatomical-T removed portions of AF-SLF and IFOF were significantly greater than verbal fluency fMRI-T ones, suggesting that fMRI-T is a more specific approach. In addition, qualitative analyses showed that fMRI-T AF-SLF and IFOF predict the exact functional limits of resection with increased specificity when compared to Anatomical-T counterparts, especially the superior frontal portion of IFOF, in a subcohort of patients.

Conclusion: These results suggest that performing fMRI-T in addition to the 'classic' Anatomical-T may be useful in a preoperative setting to identify the 'high-risk subsets' that should be spared during the surgical procedure.

Keywords: tractography, high angular resolution diffusion imaging, brain tumor, fMRI, task-fMRI, language network, presurgical brain mapping

INTRODUCTION

The accurate identification of eloquent fiber tracts, such as language bundles, is a crucial step in the surgical work-up of brain tumors. In fact, the treatment goal for these neoplasms is the maximal safe resection (Sanai et al., 2008; Yordanova et al., 2011; Duffau, 2016), preserving eloquent structures underlying fundamental neurological functions such as language, vision, and motor skills (Duffau, 2012).

The gold standard technique to achieve the correct localization of these structures is the cortical and subcortical direct electrical stimulation (DES) performed during the surgical procedure (Ojemann, 1983; Berger et al., 1990; Berger and Ojemann, 1992). Nevertheless, DES is an invasive technique that requires the patient to perform language tasks while awake (awake-surgery) after craniotomy.

Currently, MR Tractography is the only method that can depict fiber tract localization and their relationship with the lesion *before* the craniotomy and non-invasively. Based on diffusion-weighted imaging that reflects water diffusion features in biological tissues, this technique allows to infer fiber trajectory, since water diffusion in the white matter is preferentially oriented along the direction of the axonal fibers (Mori and Zhang, 2006; Mukherjee et al., 2008). MR Tractography enables the *in vivo* non-invasive depiction of subcortical fascicles and it has thus rapidly become fundamental in the presurgical assessment of brain tumors (Bello et al., 2010; Riva et al., 2011; Castellano et al., 2012; Ulmer et al., 2014), in order to evaluate the displacement or modifications of the eloquent bundles before performing brain surgery (Bello et al., 2008; Bizzi, 2009; Essayed et al., 2017), to predict the extent of resection (Castellano et al., 2012), and to better tailor the extent of the craniotomy (Romano et al., 2009). In addition, MR Tractography reconstructions can be loaded onto the neuronavigational system in order to guide DES during awake surgery, thus decreasing the duration of surgery, patient fatigue, and intraoperative seizures (Bertani et al., 2009; Riva et al., 2011; Castellano et al., 2017).

Although the original Tractography approaches based on Diffusion Tensor Imaging (DTI) (Mori et al., 1999; Jellison et al., 2004; Stadlbauer et al., 2007) are still used in the clinics, new algorithms based on High Angular Resolution Diffusion Imaging (HARDI) acquisitions (Tournier et al., 2004; Tuch, 2004; Hess et al., 2006) – such as the residual-bootstrap q-ball algorithm – have brought several improvements to this technique in terms of sensibility and accuracy (Bucci et al., 2013) and have already been proven as clinically feasible (Caverzasi et al., 2015).

Nevertheless, Tractography provides information exclusively about the anatomical trajectory of white matter fascicles, regardless of their function. In fact, recent evidence has demonstrated that some components of language bundles identified with MR Tractography can be safely removed intraoperatively, since they do not elicit transient deficit when stimulated by means of DES (Mandonnet et al., 2007; Bello et al., 2008).

In the presurgical setting, data about brain functions can be provided by functional MRI (fMRI), that employs BOLD (blood oxygenation level dependent) contrast to map cortical activity (Bizzi, 2009; Castellano et al., 2017). However, this technique enables to identify exclusively cortical areas related with a given task, and cannot detect subcortical structures.

In this study, we hypothesized that combining Tractography (an anatomy-based technique) with fMRI (a function-based technique) will provide additional information about the subsets of the anatomical subcortical tracts that are more likely to be eloquent for the language function.

We develop a systematic pipeline to combine the "classic" Tractography of language bundles, based exclusively on anatomical landmarks (Anatomical-T), with language fMRI cortical activations, in order to achieve a fMRI-targeted

Abbreviations: AF, Arcuate Fasciculus; Anatomical-T, Anatomical Tractography; AVG, Auditory Verb Generation; DES, Direct Electrical Stimulation; ExC, External/Extreme Capsule; FAT, Frontal Aslant Tract; fMRI-T, fMRI-targeted Tractography; IFOF, Inferior Fronto-Occipital Fasciculus; ILF, Inferior Longitudinal Fasciculus; MNI, Montreal Neurological Institute; PN, Picture Naming; ROI, Region of Interest; SLF, Superior Longitudinal Fasciculus; SLF-II, II component of SLF; SLF-III, III component of SLF; SLF-tp, temporo-parietal (or vertical) component of SLF; UF, Uncinate Fasciculus; VF, Verbal Fluency.

Tractography (fMRI-T) that depicts the subsets of the anatomical tracts whose endpoints are located inside a fMRI activation.

In order to test this hypothesis, we performed Anatomical-T and fMRI-T and evaluated their relationship with the DES-based limits of surgical resection. By providing this additional functional information, fMRI-T may contribute to depict the physiological functional subcortical network underlying each task in the healthy controls' cohort, and the "high-risk subsets" of the subcortical bundles that should be spared during the surgical procedure in the patients' cohort.

MATERIALS AND METHODS

Subjects

Healthy controls' cohort included 16 right-handed native Italian speakers (7 men, 9 women; mean age, 29 years; range, 21-48 years). None of these individuals had a history of neurological disorders and their brain MRI scans presented no abnormalities.

Patients' cohort included 16 patients with left-hemisphere presumed gliomas (14 men, 2 women; mean age, 36 years; range, 18-68 years) retrospectively selected among those scanned at our Institution. Inclusion criteria were as follows: tumor resection based on awake-surgery guided by cortical and subcortical DES, availability of pre-surgical HARDI and language task-based fMRI datasets, availability of post-surgical conventional MRI, no history of other neurological disorders. Tumor histotypes included mainly grade II and grade III astrocytomas and oligodendrogliomas, none of these patients presented with glioblastoma. Surgical gross total resection (GTR, 100% extent of resection) had been achieved in 10 patients, whereas in 6 patients only a subtotal resection (STR) was possible, with extents of resection ranging from 81 to 98%.

All subjects gave informed consent to have their data used for research purpose.

MRI Acquisition Protocol

MRI acquisitions were performed at 3.0 T (Philips Achieva – Philips Healthcare, Best, Netherlands).

Conventional MRI protocol included axial T2-weighted Turbo-spin-echo (TSE) images (TR/TE 3000/85 ms; flip angle, 90°; Field of View [FOV], 230 mm; 22 slices; thickness, 5/1 mm gap; matrix, 512 × 512; SENSitivity-Encoding [SENSE] reduction factor, R = 1.5; acquisition time, 3 min 42 s), axial 3D Fluid Attenuated Inversion Recovery (3D-FLAIR) images (TR/TE/TI 10000/110/2750 ms; flip angle, 90°; FOV, 230 mm; 90 slices; thickness, 1.5/0 mm gap; matrix, 224 × 256; SENSE reduction factor R = 2; acquisition time 8 min 20 s), and axial T1-weighted Fast Field Echo (FFE) Multi-Shot images (TR/TE 8/4 ms; flip angle, 8°; FOV, 240 mm; 56 slices; thickness, 2.5/0 mm gap; matrix 256 × 256; SENSE reduction factor, R = 1; acquisition time, 1 min 46 s).

High Angular Resolution Diffusion Imaging (HARDI) data were obtained using an axial Single-Shot Spin-Echo Echo Planar Imaging (EPI) sequence and diffusion gradients were applied along 60 non-collinear directions (b-value, 3000 s/mm^2; TR/TE, 12000/74 ms; SENSE reduction factor, R = 2; in-plane resolution, 1.87 × 1.87 mm^2; 50 slices; thickness, 2.5/0 mm gap; FOV, 240 mm; matrix, 128 × 128; acquisition time, 13 min).

Three covert language tasks were employed for language fMRI: Picture Naming (PN), Verbal Fluency (VF), Auditory Verb Generation (AVG).

Picture Naming (PN): naming a series of common objects (i.e., "chair," "house," and "knife") presented on a screen; baseline consisted in looking at scrambled non-sense figures.

Verbal Fluency (VF): listing as many nouns starting with a given letter presented aurally (i.e., "fork," "field," "foot"; when the subject hears the letter "F"); baseline consisted in repeatedly counting from 1 to 10.

Auditory Verb Generation (AVG): generating an appropriate verb from a given noun presented aurally (i.e., "to eat"; when the subject hears the noun "bread"); baseline consisted in repeatedly counting from 1 to 10.

All healthy controls fulfilled all three tasks, patients' fMRI employed generally two tasks (with the exceptions of three patients, two of whom performed just one task, and one of whom performed all three tasks). For each patient, fMRI tasks were selected as follows: PN fMRI was acquired for every patient due to a neurosurgeons' preference (since intraoperative DES included a picture naming task), verbal VF fMRI was mainly reserved to patients with frontal tumors (in order to assess the relationship between fMRI activations and frontal phonological-articulatory areas, 9 patients), AVG fMRI was mainly applied to patients with temporal or parietal lesions (in order to map fMRI activations in the Wernicke area, 6 patients). In some cases, VF or AVG were not performed due to clinical scanning time constraints and/or suboptimal patient's collaboration.

Block-design task-based fMRI data were based on BOLD (blood oxygenation level dependent) contrast obtained using T2*-weighted Gradient-Echo EPI (GE-EPI) sequences (TR/TE, 3700/30 ms; TE, 30 ms; flip angle, 85°; FOV, 240 mm; matrix, 128 × 128; in-plane resolution 1.87 × 1.87 mm^2; 32 slices; thickness, 4 mm; SENSE factor R = 2; 80 dynamic scans for PN task, 100 for VF task, 100 for AVG task).

3.0 T post-surgical 3D-FLAIR images were acquired 24/48 h after the procedure.

fMRI Subject-Level Analysis

fMRI data obtained from both healthy controls and patients were analyzed with SPM8 (Wellcome Dept. Cogn. Neurol., London[1]) using MATLAB 7.1 (MathWork, Natick, MA, United States). Analyses were performed following a standard processing pipeline (Bizzi et al., 2008).

Images were corrected for motion, realigned to the mean image, and the estimated movement parameters were used as regressors in a single-subject statistical analysis. These realigned images were then spatially smoothed using a 8-mm full-width at half-maximum isotropic Gaussian kernel. The expected hemodynamic response function of the software package was modeled with a block design. In every subject, a t-contrast was defined according to the General Linear Model for each task: verbal fluency, auditory verb generation and picture naming.

[1]http://www.fil.ion.ucl.ac.uk/spm

Activations were considered significant if survived $P < 0.001$ uncorrected statistical threshold.

HARDI Preprocessing and Tractography Algorithm

Movement and eddy-current distortions were corrected using the FMRIB Software Library (University of Oxford[2]), then the original gradient table was consequently rotated using the FSL "fdt rotate bvecs" function. Diffusion tensor and fractional anisotropy (FA) maps were estimated using Diffusion imaging in Python (Dipy) software (Soares et al., 2013; Garyfallidis and Brett, 2014).

Tractography was based on a q-ball residual bootstrap algorithm (Berman et al., 2008; Caverzasi et al., 2014, 2015), following the steps described by Caverzasi et al. (2015) in order to fit the signal to spherical harmonics, to compute the Orientation Distribution Functions (ODFs), and to identify the primary and principal fiber orientations. The tracking was seeded from tract-specific seed-ROIs, as described in the following paragraph (2.5). Maximum turning angle of 60° (Caverzasi et al., 2015) and FA threshold of 0.10 (Bello et al., 2008) were used as stopping criteria. Seed density was set at 7^3 per voxel for healthy controls, and at 9^3 per voxel for patients, in order to compensate for streamline loss in the patients' cohort due to FA drops within the tissue affected by edema or tumor infiltration. Such compensation in the patients' cohort was necessary in order to obtain a sufficient number of streamlines that were able to survive the FA stopping criteria and reach the cortex, allowing the subsequent fMRI-targeting operation.

Anatomical-T

Anatomical-T approach was used to depict 8 left-hemisphere language tracts for each subject, including dorsal and ventral tracts (**Supplementary Figure 1**).

Dorsal tracts: Frontal Aslant Tract (FAT); Arcuate Fasciculus (AF) or long segment of the perisylvian language network; Superior Longitudinal Fasciculus component II (SLF-II), SLF component III (SLF-III), or anterior segment of the perisylvian language network; temporoparietal component of SLF (SLF-tp) or posterior segment of the perisylvian language network.

Ventral tracts: Inferior Fronto-Occipital Fasciculus (IFOF), Uncinate Fasciculus (UF), Inferior Longitudinal Fasciculus (ILF).

Anatomical-T for all tracts but FAT employed regions of interest (ROIs) placed exclusively referring to the anatomical seed-ROIs and target-ROIs landmarks reported by Caverzasi et al. (2015). As for FAT, a seed-ROI was placed on an axial plane including the subcortical voxels of the superior frontal gyrus corresponding to the supplementary motor area, and the inferior frontal gyrus was used as a target-ROI – these ROIs were chosen on the basis of the current knowledge regarding FAT trajectory (Dick et al., 2014).

Results were visualized using Trackvis[3] and carefully inspected in order to quality-check the tracts and to remove all the following: obvious artifacts, streamlines directed toward the basal ganglia, the pons, and the right hemisphere.

fMRI-T Tract Generation Pipeline

fMRI-targeted tractography tracts were generated by selecting the streamlines of Anatomical-T tracts that reached a task-specific fMRI-activated cortical area. Their generation was based on a two-step pipeline: the first step consisted in obtaining a fMRI-target-ROI that reflected the subject-specific task-specific activation areas; the second step consisted in generating fMRI-T tracts representing the subsets of the Anatomical-T tracts whose endpoints are located inside the fMRI-target-ROI.

Step 1

A binary fMRI-ROI was obtained for each subject's task by binarizing the subject-level fMRI results, and then registered to the corresponding subject's diffusion space using the FSL linear registration FLIRT tool (University of Oxford[2]). The relationship between this fMRI-ROI and the Anatomical-T tracts was evaluated using Trackvis[3] in order to decide whether or not some manual corrections (extension and/or reduction) were needed in order to obtain the definitive fMRI-target-ROI. These manual corrections were applied only in case certain criteria were met, which were strictly determined *a priori* by three of the authors (FS, AnC, EC) as follows.

A manual extension of the fMRI-ROI was performed exclusively when the endpoints of some streamlines were located within 3 voxels outside the fMRI-ROI and in the same anatomical area (same gyrus or sulcus) – a similar ROI-extension correction is also reported in other fMRI-based Tractography studies (Upadhyay et al., 2007; Zhu et al., 2014).

A manual reduction of the fMRI-ROI was performed exclusively when the endpoints of some streamlines were located in a non-cortical part of the fMRI-ROI (e.g., basal ganglia) or in a part of the fMRI-ROI belonging to a different lobe (e.g., temporal pole streamlines terminating in inferior frontal or insular part of the fMRI-ROI).

Step 2

The subject-specific task-specific fMRI-target-ROI obtained from the binary fMRI-ROI was used as a further target-ROI for each Anatomical-T tract to generate task-specific fMRI-T tracts. This latter operation consisted in a "either-end targeting" (a Trackvis built-in function), which allowed to include in the fMRI-T tract only the streamlines whose endpoints are located inside the corresponding fMRI-target-ROI. This pipeline (**Figure 1A**) produced, for each Anatomical-T tract, as many fMRI-T tracts as the fMRI tasks performed by the subject (**Supplementary Figure 2**).

Healthy Controls' Cohort: Anatomical-T and fMRI-T Atlases (Group Analysis)

For each healthy control, four subcortical networks (**Figure 1B**) were obtained (Anatomical, PN, VF, AVG) by merging the corresponding tracts (all Anatomical-T, PN fMRI-T, VF fMRI-T, AVG fMRI-T – respectively) using Trackvis built-in "merge" function. Dipy and FSL were then used to generate the four

[2]https://fsl.fmrib.ox.ac.uk/fsl/

[3]http://trackvis.org

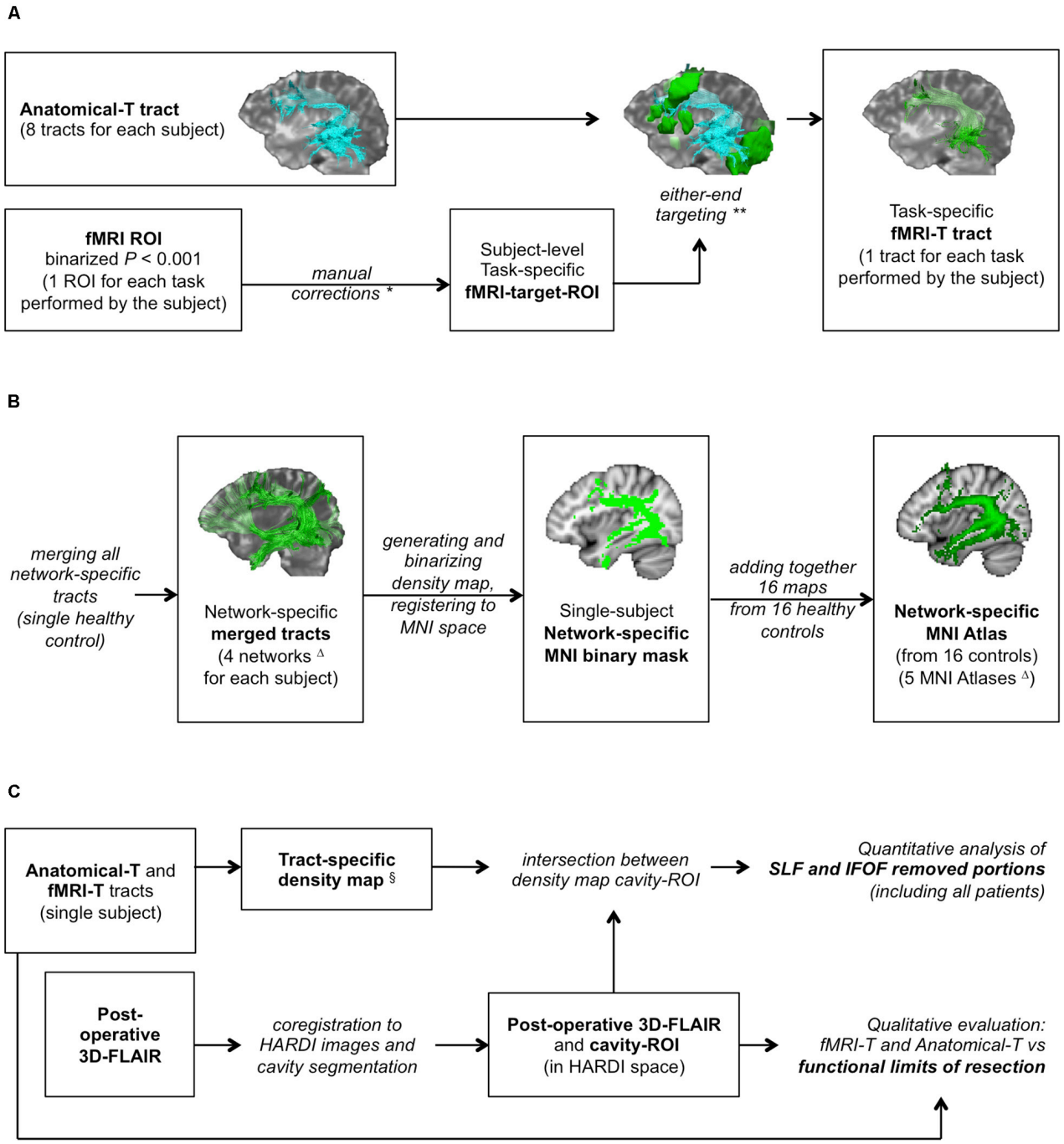

FIGURE 1 | Study design. **(A)** fMRI-targeted Tractography (fMRI-T) tracts generation pipeline (applied to both healthy controls and patients); **(B)** flow-chart to generate healthy controls' MNI Atlases (group study); **(C)** assessment method on patients' cohort. *Only if stated rules apply. **In some cases this operation yielded no results. ΔFour subcortical networks (Anatomical, Picture Naming, Verbal Fluency, Auditory Verb Generation) were used to generate four MNI Atlases; an additional MNI Atlas ("any-task" Atlas) was obtained from the sum of all fMRI-T networks. §Only for AF-SLF and IFOF.

corresponding network-specific density maps and to binarize them with a $\geq$ 2 threshold (to include only voxels with at least two streamlines). Binary masks were then registered to the MNI space using FSL linear and non-linear registration tools (FLIRT and FNIRT).

Four MNI network-specific Atlases (Anatomical-T, PN fMRI-T, VF fMRI-T, AVG fMRI-T Atlases) were obtained by adding together the binary masks of the corresponding network obtained from all 16 healthy controls, in order to compare the different subcortical networks.

An additional fMRI-T MNI Atlas representing *all* fMRI-T voxels was obtained by adding together the binary masks of all three tasks at the single subject level, and subsequently generating the corresponding MNI Atlas as described for the network-specific Atlases. This additional Atlas is composed by the subject-specific subcortical network underlying all fMRI tasks, and we will refer to it as "any-task" fMRI-T Atlas from now on.

In order to quantify the percentage of each Anatomical-T tract volume included in each fMRI-T tract, a voxel percentage index (VPI) was calculated for each task-specific fMRI-T density map (at the single subject level):

$$VPI = \frac{number\ of\ voxels\ in\ fMRI\ T\ tract}{number\ of\ voxels\ in\ corresponding\ Anatomical\ T\ Tract} * 100.$$

Patients' Cohort: Anatomical-T and fMRI-T Validation Method

For each patient, tumor resection was guided by cortical and subcortical DES evaluating the language function through neuropsychological testing employing naming and counting tasks during awake-surgery. Functional boundaries as intraoperatively identified by DES represented the limit of microsurgical resection. Post-operative 3D-FLAIR was registered to preoperative 3D-FLAIR and subsequently to preoperative B0 using FSL linear registration tool (FLIRT), and the volume of the cavity was segmented using FSL mask tools (cavity-ROI), in order to perform a qualitative analysis and a quantitative analysis (**Figure 1C**), as follows.

Qualitative Analysis

The relationship between the Tractography fascicle models, the limits of resection (corresponding to eloquent structures), and the cavity volume (corresponding to non-eloquent tissue) was evaluated by means of a 3D-rendering of those structures using Trackvis.

Quantitative Analysis

For fMRI-T and Anatomical-T AF-SLF and IFOF, a density map of those streamlines was obtained and binarized with a ≥ 2 threshold (to include only voxels with at least two streamlines). These binary masks were then intersected with the cavity-ROI, in order to obtain a ROI representing the voxels belonging to fMRI-T and Anatomical-T AF-SLF and IFOF located inside the surgical cavity. The components of the tracts corresponding to these voxels were considered removed during the procedure, therefore we will refer to them as "removed voxels" for brevity. Such removed voxels were considered as false positive results of Tractography, since they did not correspond to eloquent tissue at DES.

Patients' Cohort: Language Function Assessment

Patients' language function was assessed pre- and post-operatively at several time points using the Milano-Bicocca Battery (Papagno et al., 2012), that included the assessment of semantic and phonemic fluency, speech comprehension, picture naming, and the repetition of words, non-words, and sentences. Median follow-up time was 363 days (range, 6-1158 days), 14 patients out of 16 were evaluated at least for 2 months after surgery, 10 patients out of these 14 were evaluated for more than 12 months after surgery.

Statistical Analyses

Quantitative Analysis on Healthy Controls (VPI Analysis)

Voxel percentage indexes of all the tracts belonging to the same fMRI-T network were compared using Kruskal-Wallis tests and *post hoc* multiple comparisons (Dunn's tests).

Quantitative Analysis on Patients (AF-SLF and IFOF Removed Portions)

"Removed voxels" of AF-SLF and IFOF belonging to different networks (Anatomical-T, PN fMRI-T, VF fMRI-T, AVG fMRI-T) were compared using Kruskal-Wallis tests and Dunn's non-parametric comparison for *post hoc* testing and Bonferroni correction for multiple comparisons.

Clinical Outcome

We retrospectively distinguished patients with long-term (at 12 months) severe deficits and patients that had showed a long-term complete or partial clinical recovery, and compared clinical features of these two groups. Mann-Whitney test was employed to compare continuous numeric variables (age and extent of resection); Fisher's exact test was employed for categorical variables (sex category, tumor location, preoperative language deficits, and tumor grade – tumor grade was analyzed as a categorical variable, differentiating grade III tumors and tumors of lower grades).

In addition, a linear regression analysis was performed on patients that showed a complete clinical recovery in order to evaluate a correlation between the volume of AF-SLF and IFOF removed portions and the days necessary for the clinical recovery.

RESULTS

Healthy Controls' Tractography Atlases: PN vs VF vs AVG fMRI-T

The generation of the network-specific fMRI-T Atlases highlighted both task-specific components, and subsets shared by different tasks (**Figure 2**), as follows.

Picture Naming fMRI-T Atlas involves ventral tracts more than the other tasks. In particular, voxels belonging to ILF are depicted almost exclusively in this Atlas (dotted arrows in **Figures 2A,D**).

Verbal Fluency fMRI-T Atlas highlights the dorsal stream more than the ventral stream, and some dorsal branches belonging to AF-SLF and FAT are specific to this Atlas (arrowheads in **Figures 2B,D**).

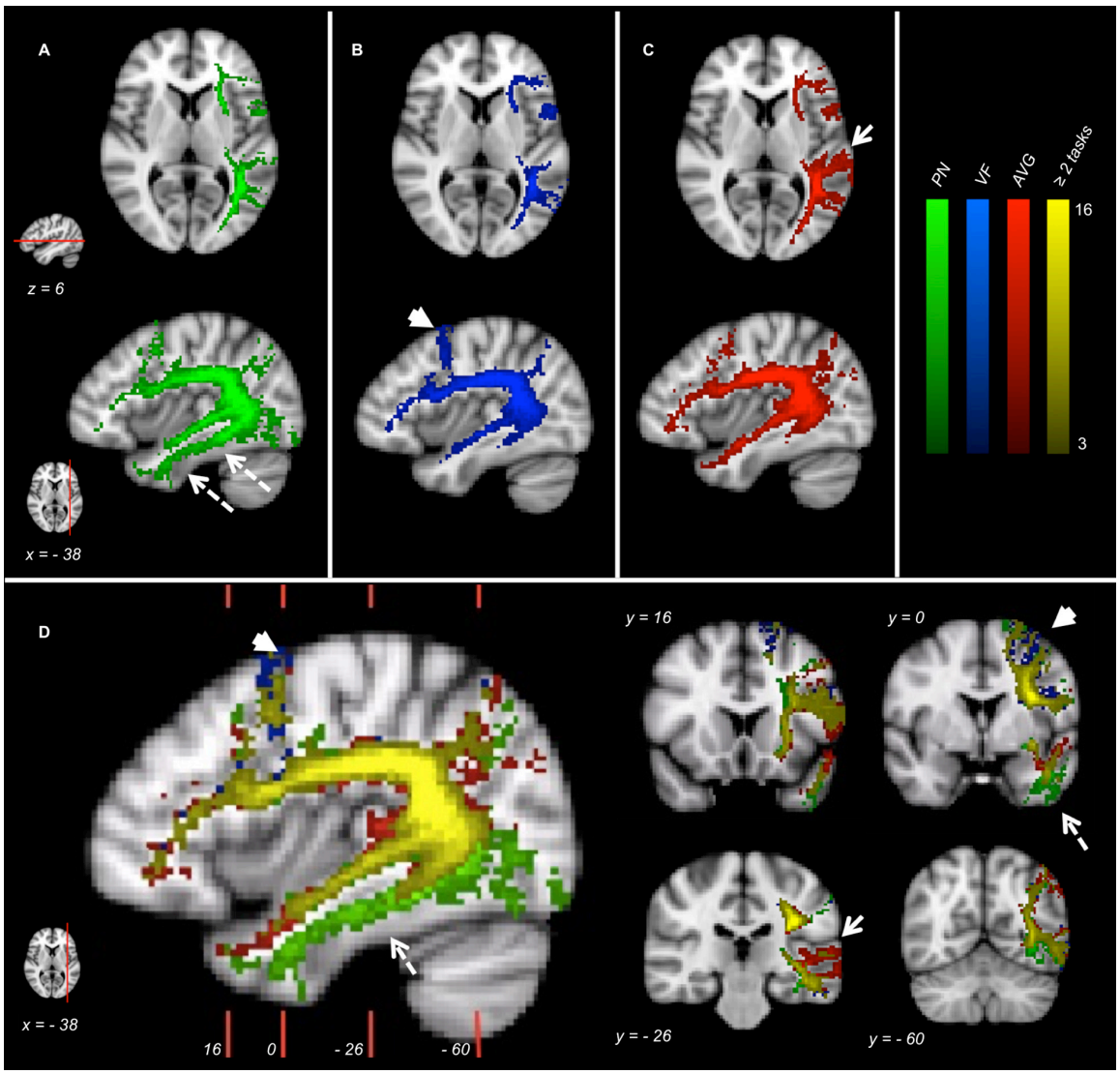

FIGURE 2 | fMRI-targeted Tractography Atlases (group analysis) of 16 healthy controls. **(A)** PN; **(B)** VF; **(C)** AVG; **(D)** Different tasks overlayed. Only voxels represented in at least three subjects are displayed. Color brightness of each voxel is proportional to the number of subjects in whom the voxel was represented. The reference axial and parasagittal MNI slices (MNI $z = 6$, $x = -38$, respectively) are shown on the left side of the figure. The reference coronal MNI slices (MNI $y = 16, 0, -26, -60$) are shown on the parasagittal figure in **(D)**.

Auditory Verb Generation fMRI-T Atlas involves temporal subcortical components belonging to AF-SLF more strongly than other tasks (arrows in **Figures 2C,D**).

A relevant part of the language pathway is shared by different tasks (yellow voxels in **Figure 2D**), specially the deepest white matter components belonging to AF-SLF and ExC.

Healthy Controls' Tractography Atlases: Anatomical-T vs fMRI-T

The comparison between the Anatomical-T Atlas and the "any-task" fMRI-T Atlas (**Figure 3**) showed that the fMRI-T network (all tasks included) is a subset of the Anatomical-T network, since several components of Anatomical-T Atlas were not included in the "any-task" fMRI-T one.

Healthy Controls' Tractography Quantitative Analysis: Voxel Percentage Index

Voxel Percentage Index analysis revealed that the number of voxels corresponding to each fMRI-T tract trajectory is constantly smaller than the respective Anatomical-T tract, as the mean VPI is always below 60% and, in most cases, is around 40% or even 20%.

When comparing VPIs from different tracts within the same task, this analysis showed that different task-specific fMRI-T

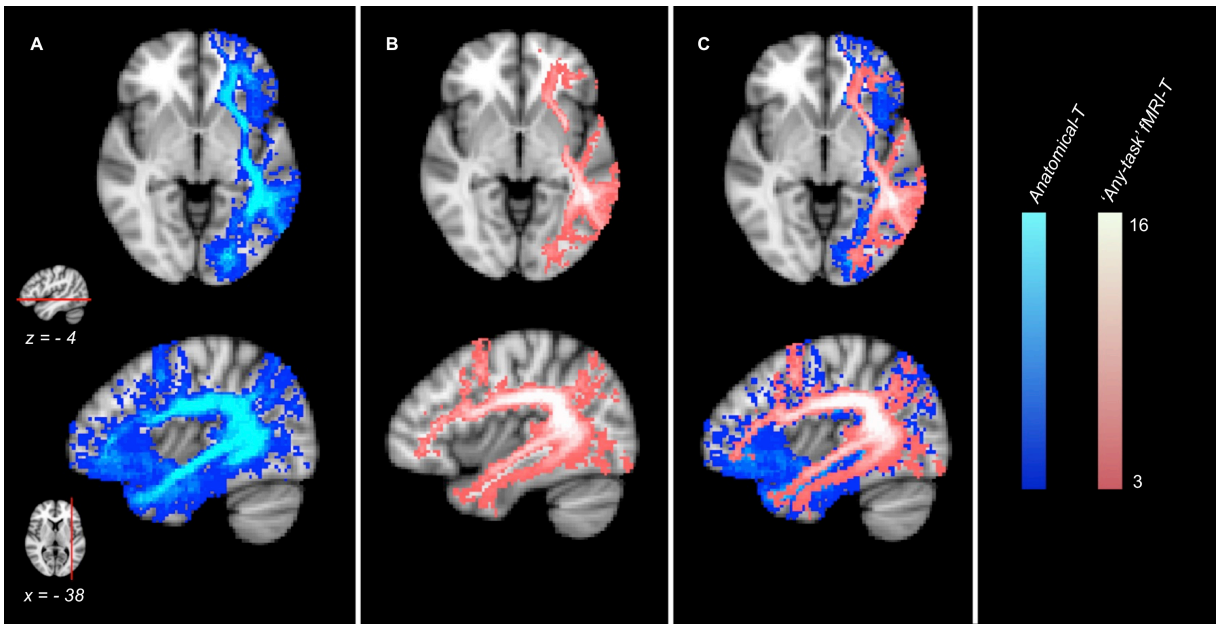

FIGURE 3 | Anatomical and fMRI-targeted Tractography Atlases (group analysis) of 16 healthy controls. **(A)** Anatomical Tractography; **(B)** "any-task" fMRI-targeted Tractography (all tasks included); **(C) (A)** and **(B)** overlayed. Only voxels represented in at least three subjects are displayed. Color brightness of each voxel is proportional to the number of subjects in whom the voxel was represented. The reference axial and parasagittal MNI slices (MNI $z = -4$, $x = -38$, respectively) are shown on the left side of the figure.

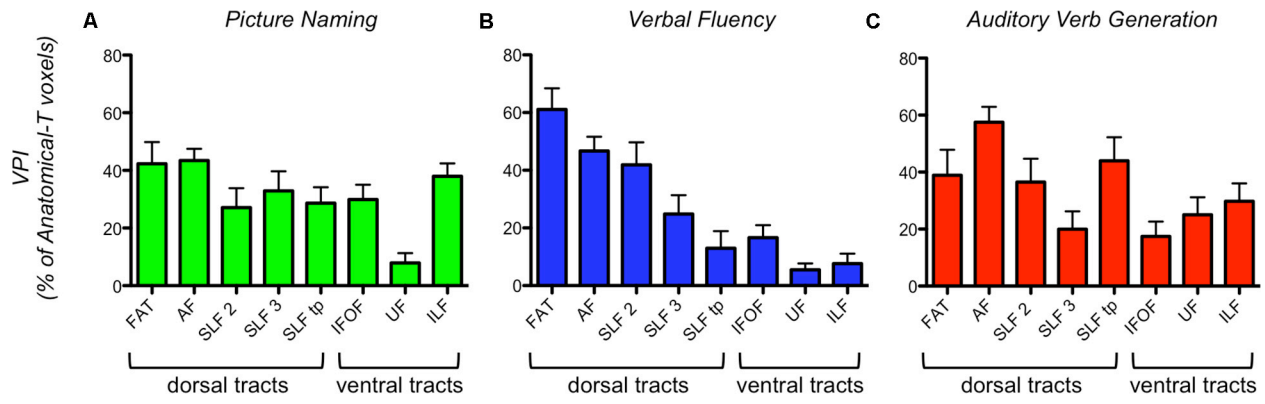

FIGURE 4 | Task-specific VPI (Voxel Percentage Index) of each fMRI-T fiber tract in 16 healthy controls. **(A)** PN; **(B)** VF; **(C)** AVG. The bar graph represents the mean and the standard error.

involve a different percentage of the Anatomical-T corresponding tract (**Figure 4**).

Verbal Fluency (VF) fMRI-T showed a strong difference between VPIs of dorsal frontal tracts (FAT, AF, SLF-II, SLF-III) and VPIs of ventral (IFOF, UF, ILF) and non-frontal tracts (SLF-tp). This means that a larger percentage of anatomical dorsal frontal tracts reaches VF-related activations, when compared to the percentage of ventral and non-frontal tracts. Kruskal-Wallis test highlighted a statistically significant difference among VPI from all tracts ($P < 0.0001$). *Post hoc* multiple comparisons (Dunn's tests) revealed that Kruskal-Wallis results are ascribable to a significant VPI difference: between FAT and all ventral and non-frontal tracts; between AF and SLF-tp, AF and UF, AF and ILF; between SLF-II and UF, SLF-II and ILF.

Picture Naming (PN) fMRI-T and Auditory Verb Generation (AVG) fMRI-T did not show a difference between VPIs of dorsal and ventral systems. For PN, Kruskal-Wallis test ($P = 0.0003$) and *post hoc* multiple comparisons (Dunn's tests) revealed that UF VPIs were significantly lower than VPIs of some other tracts (FAT, AF, ILF). For AVG, Kruskal-Wallis test ($P = 0.023$) and *post hoc* multiple comparisons (Dunn's tests) showed that AF VPIs were significantly higher than VPIs of some other tracts (SLF-III, IFOF).

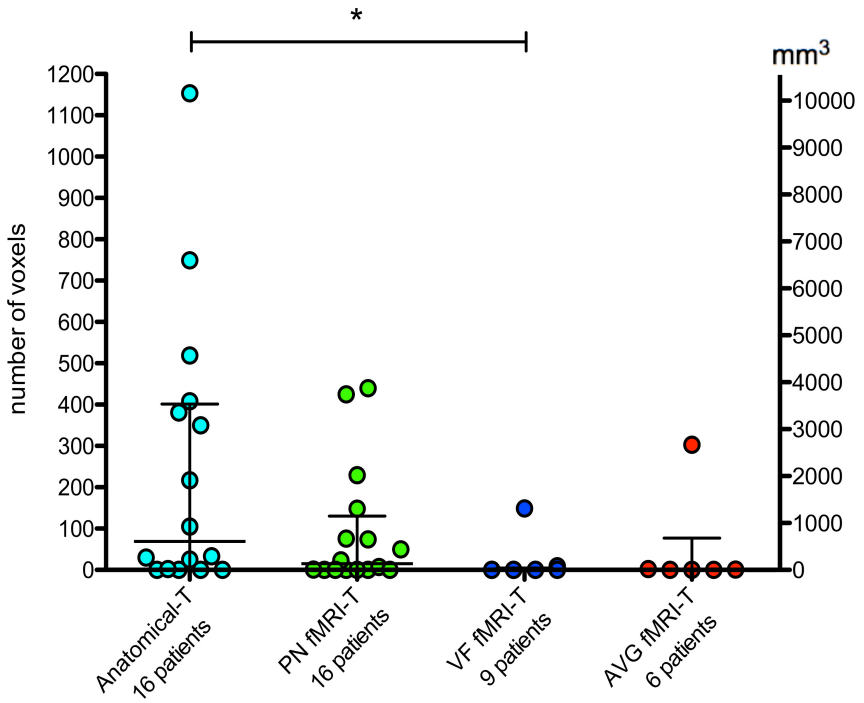

FIGURE 5 | Quantitative analysis of "removed voxels" belonging to AF-SLF and IFOF. The bars represent median and interquartile range. Statistical analysis refers to **Table 1**. *$P < 0.05$.

TABLE 1 | Statistical analysis of "removed voxels" belonging to AF-SLF and IFOF.

					p-value[a]		
	Anatomical-T (*n* = 16)	**PN fMRI-T (*n* = 16)**	**VF fMRI-T (*n* = 9)**	**AVG fMRI-T (*n* = 6)|**	**Anatomical-T vs PN fMRI-T**	**Anatomical-T vs VF fMRI-T**	**Anatomical-T vs AVG fMRI-T**
Number of voxels	69 (1-401)	15 (0-130)	0 (0-5)	1 (0-77)	> 0.05	0.033 *	> 0.05
Volume of removed voxels (mm^3)	606 (9-3524)	132 (0-1143)	0 (0-44)	9 (0-677)			

*Note: Data are interpatient median values, with interquartile range in parentheses. [a]Significant difference between groups. P-values were calculated using Kruskal-Wallis test with Dunn's non-parametric comparison for post hoc testing and Bonferroni correction for multiple comparisons. *P < 0.05*

Quantitative Analysis of AF-SLF and IFOF Removed Portions in Brain Tumor Patients

In patients with gliomas, the quantitative comparison between AF-SLF and IFOF removed portions obtained by means of Anatomical-T and task-specific fMRI-T (**Figure 5**) yielded statistically significant results (Kruskal-Wallis test $P = 0.035$) suggesting that fMRI-T is more specific than Anatomical-T, since fewer non-eloquent voxels (false positive results) belonging to AF-SLF and IFOF were depicted by the fMRI-T approach. *Post hoc* multiple comparisons (Dunn's non-parametric comparison for *post hoc* testing and Bonferroni correction for multiple comparisons) revealed that Kruskal-Wallis results are ascribable to the significant difference between Anatomical-T and VF fMRI-T (**Table 1**). Comparing each patient's removed voxels belonging to Anatomical-T and fMRI-T of AF-SLF and IFOF separately (**Supplementary Table 1**) reveals several cases for which significant portions of Anatomical-T tracts were resected while their fMRI-T counterparts were completely (or nearly completely) spared. In such cases, a significant number of voxels belonging to the Anatomical-T tract were removed, as opposed to a significantly lower amount of voxels belonging to fMRI-T tracts.

Qualitative Evaluation in Brain Tumor Patients: fMRI-T and Anatomical-T vs Limits of Resection

The qualitative evaluation was performed by subdividing the patients' cohort on the basis of their resection location: patients who underwent a superior frontal resection (eight patients, 50%), patients who underwent a lateral frontal resection (three patients, 18.75%), patients who underwent a temporal pole resection (two patients, 12.5% – in one case the resection also included the insular lobe), patients who underwent a parietal resection (two patients, 12.5% – in one case the resection also included a part of

the temporal lobe), one patient who underwent a fronto-parieto-insular resection (one patient, representative case in **Figure 6**).

Superior Frontal Resections

The functional limits of resection corresponded to the trajectory of AF-SLF (to AF in the majority of the cases), and to the trajectory of IFOF [in many cases, more specifically, to the fronto-opercular branch of IFOF – also known as IFOF superficial layer (Caverzasi et al., 2014)]. In a subgroup of these fascicles (four of eight IFOFs, and one out of eight AF-SLFs), VF fMRI-T tracts are aligned to the margins of the cavity, whereas portions belonging to Anatomical-T and PN fMRI-T are located inside the cavity (non-eloquent at DES). Interestingly, as far as IFOF is concerned, in such cases the superior portions of Anatomical-T IFOF and PN fMRI-T IFOF were removed during the procedure, whereas VF fMRI-T IFOF identified exclusively the fronto-opercular portion of IFOF that corresponded to the limits of resection. In all other fascicles but one (three of eight IFOFs, and seven out of eight AF-SLFs) both Anatomical-T and fMRI-T successfully predicted the functional limits of resection. In the remaining case (one IFOF)

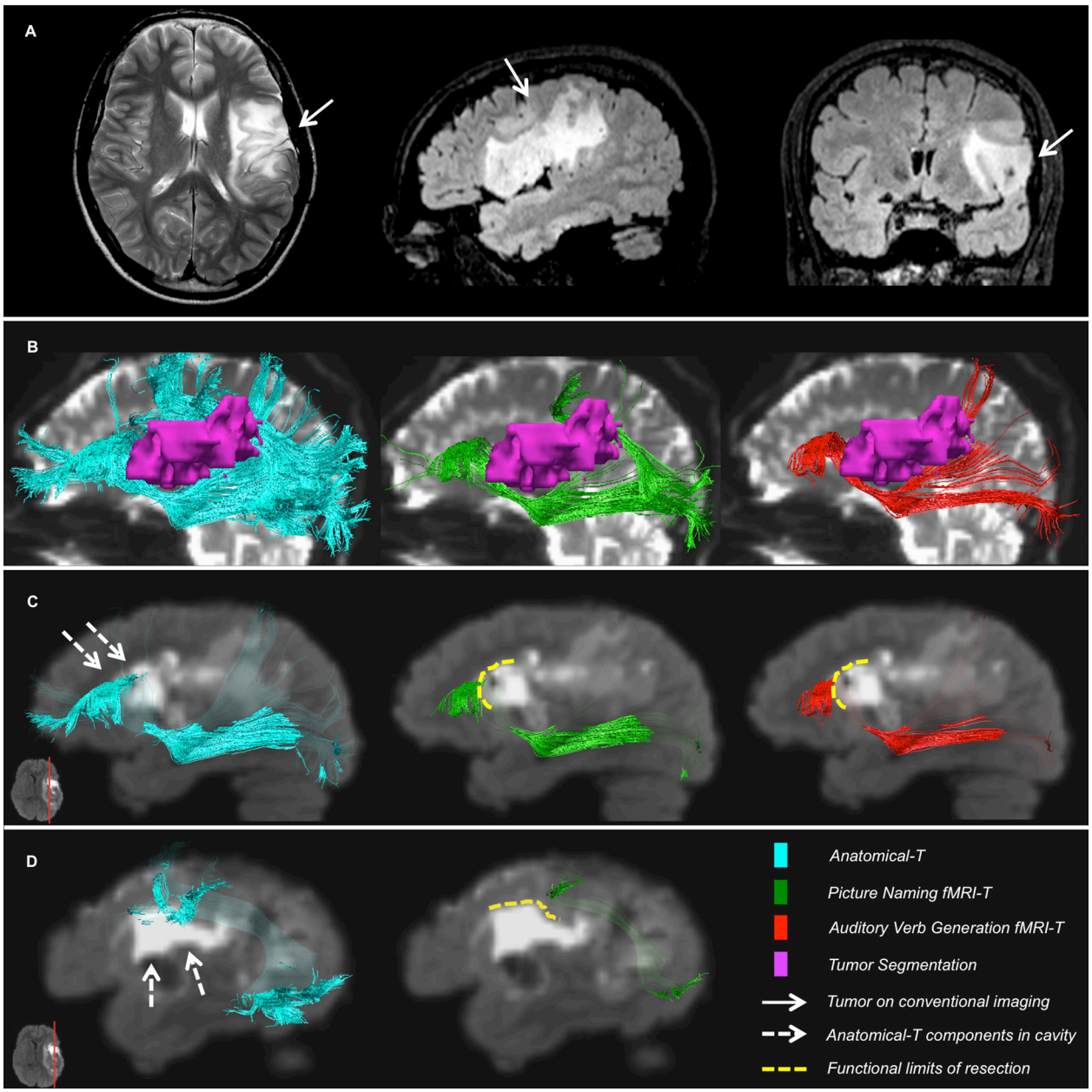

FIGURE 6 | Representative case of a patient. **(A)** T2-weighted and FLAIR images showing the tumor site; **(B)** Relationships between IFOF, AF and the tumor on preoperative B0; **(C,D)** Postoperative FLAIR registered to preoperative diffusion space shows components of Anatomical-T IFOF **(C)** and AF **(D)** located inside the surgical cavity, whereas fMRI-T IFOF **(C)** and AF **(D)** are aligned to the functional limits of resection.

the procedure removed a portion of IFOF that was common to both Anatomical-T and fMRI-T. As for FAT, different portions of this fascicle were involved by the resection, and there is no clear difference between Anatomical-T and fMRI-T.

Lateral Frontal Resections

The functional limits of resection corresponded to the trajectory of AF-SLF (more specifically AF and SLF-III). In one out of three cases, a branch of Anatomical-T SLF-III was involved by the surgery, whereas the trajectory of AVG and PN fMRI-T AF-SLFs were aligned to the margins of the surgical cavity. In two out of three cases, both Anatomical-T and fMRI-T AF-SLFs were able to identify the functional limits of resection.

Temporal Pole Resections

The surgical resection was pursued until the deep ExC portion of IFOF (medially) and the temporal components of AF-SLF (more specifically AF and SLF-tp, posteriorly) were encountered. In these two patients, Anatomical-T and fMRI-T equally depicted the eloquent components of these fascicles corresponding to the functional limits of resection. As for UF and ILF, both Anatomical-T and fMRI-T anterior components of these tracts are involved in the surgical resection.

Parietal Resections

In these two patients, portions of both Anatomical-T and fMRI-T tracts were removed during the procedure, including AF-SLF and IFOF.

Fronto-Parieto-Insular Resection

In this patient, the functional limits of resection are perfectly aligned to AF-SLF and IFOF depicted by PN fMRI-T and AVG fMRI-T, while considerable portions of Anatomical-T tracts are located within the cavity borders (**Figure 6**).

Neuropsychological Assessment of Patients' Language Function

Fourteen patients out of 16 presented with no presurgical language deficit, the remaining two patients presented with a mild deficit (one affecting non-word repetition, the other affecting phonemic fluency and sentence repetition).

Out of 16 patients: four (25%) never experienced post-surgical clinically relevant deficits, five (31.25%) recovered from relevant language deficits within 3 months from surgery day, one (6.25%) recovered within 6 months, one (6.25%) showed a mild language deficit at 12 months (a mild lexicon access and naming impairment), three patients (18.75%) showed severe language deficits at $>$ 12 months (all of the three showed severe lexicon access and comprehension impairment, two of them also showed a naming impairment). For the remaining two patients (12.5%), who showed a language deficit immediately after the procedure, the follow-up only lasted 1 week after surgery, and therefore we were not able to assess their long-term clinical outcome.

The three patients showing severe language deficits at $>$ 12 months were significantly older (Mann-Whitney test $P = 0.0195$) and underwent a less radical surgery in terms of EOR (Mann Whitney test $P = 0.0195$) when compared to the 11 patients showing a complete or partial long-term clinical recovery. A significant statistical association was found between preoperative deficits and long-term severe deficits (Fisher's exact test $P = 0.033$, positive predictive value 100%, negative predictive value 91.67%). No significant differences were found in tumor grade, tumor location, and sex category between these two groups.

In the 10 patients for whom a complete clinical recovery was documented, the number of days necessary to recover from relevant language deficits after surgery ranged from 0 to 101 days (mean, 42.5; median, 50). A linear regression analysis shows that the number of days necessary to recover from relevant language deficits is directly proportional to the number of AF-SLF and IFOF removed voxels ($P = 0.043$), both when considering Anatomical-T and PN fMRI-T. When considering VF fMRI-T, only two patients out of 10 had VF fMRI-T AF-SLF or IFOF portions removed by the procedure and the clinical recovery time was 78 days for both of them, whereas the mean recovery time for the remaining eight patients without VF fMRI-T AF-SLF or IFOF damage was 33.6 days (all 10 patients performed the VF task). As for AVG fMRI-T, only three patients out of these 10 performed the AVG task; two of them had a mild resection of AVG fMRI-T AF-SLF or IFOF ($<$ 0.02 cc) and experienced no postoperative deficits, the remaining patient had a major resection of AVG fMRI-T AF-SLF or IFOF ($\sim$ 2.67 cc belonging to these tracts) and his clinical recovery time was 78 days.

DISCUSSION

In this study, we developed a multiparametric pipeline combining Tractography (an anatomy-based technique) with fMRI (a function-based technique) in order to more specifically characterize the classic anatomical Tractography (Anatomical-T). This approach was applied to a healthy controls' cohort and yielded novel data regarding white matter tracts subserving different language tasks; the subsequent application to a patients' cohort was useful to highlight those "high-risk" subsets of the anatomical subcortical tracts that are more likely to be eloquent for the language function. This is the first study that systematically combines a HARDI-based Tractography with several language fMRI-tasks for this purpose.

Currently, MR Tractography is the only technique that non-invasively depicts subcortical fiber tracts *in vivo*, which is crucial in the presurgical planning for the resection of brain neoplasms (Bello et al., 2008; Castellano et al., 2012; Essayed et al., 2017). High Angular Resolution Diffusion Imaging (HARDI) acquisitions (Tournier et al., 2004; Tuch, 2004; Hess et al., 2006) have allowed to develop new algorithms that solve complex fiber orientation within the same voxel (Caverzasi et al., 2015), thus depicting subcortical tracts with higher sensitivity (Bucci et al., 2013) and allowing to perform the tracking through tumor-infiltrated areas (Mormina et al., 2016). In particular, the q-ball residual bootstrap probabilistic algorithm (Berman et al., 2008) has shown clinical feasibility, and has recently been employed to fulfill a fiber-tracking protocol that can be routinely applied

to depict all major language fascicles in the preoperative setting (Caverzasi et al., 2015).

Nevertheless, intraoperative subcortical direct electric stimulation (DES) remains the gold standard technique to identify fiber tracts trajectory (Berger and Ojemann, 1992; Duffau, 2012; Chang et al., 2015). Although DES and MR Tractography have shown a high degree of concordance (82-97%) (Bello et al., 2008; Leclercq et al., 2010; Castellano et al., 2017), the correspondence is not complete and the main reason is that MR Tractography is not able to provide information about tract functions. In particular, it is believed that some subsets of anatomical language-related fiber tracts may not have an essential function (Mandonnet et al., 2007; Bizzi, 2009). For instance, Bello et al. (2008) clearly reported that selected components of the AF-SLF complex (Superior Longitudinal Fasciculus-Arcuate Fasciculus) do not appear to be eloquent for language tasks when stimulated. This fiber bundle is considered the most relevant language tract; as a consequence, it is reasonable to hypothesize that also other language bundles may include some non-eloquent (or non-essential) subcomponents that can likely be safely removed during the surgical procedure. Providing new tools to preoperatively distinguish the functional core of the language subcortical network from these non-essential subcomponents could be crucial to optimize the presurgical planning of a maximal safe resection of gliomas.

While MR Tractography enables to identify subcortical anatomical structures, data regarding brain cortical structures associated with a specific function can be non-invasively provided by fMRI in the preoperative setting (Talos et al., 2003; Bizzi, 2009; Castellano et al., 2017). In this study, we combine these two techniques in order to achieve a fMRI-targeted Tractography. The possibility of employing Tractography and fMRI in a combined fashion has already been explored by several authors (Conturo et al., 1999; Guye et al., 2003; Dougherty et al., 2005; Smits et al., 2007; Upadhyay et al., 2007; Staempfli et al., 2008; Yang et al., 2009; Kleiser et al., 2010; Saur et al., 2010; Broser et al., 2012; Preti et al., 2012, 2014; Schmitt et al., 2014; Zhu et al., 2014; Figley et al., 2015; Liégeois et al., 2016; Reid et al., 2016). Nevertheless, those studies aimed at using fMRI to quickly and consistently identify the landmarks to be used as a seed for the Tractography algorithm, and the majority of them were performed via DTI-Tractography and exclusively on healthy controls. Conversely, the purpose of the present study is to synergistically combine the two techniques to provide additional information: the depiction of the subsets of the bundles that are connected to language-activated brain cortex. Moreover, this is the first study to develop a systematic pipeline to consistently perform fMRI-based Tractography both on healthy controls and patients with brain tumors, employing an advanced HARDI-based Tractography algorithm (q-ball residual bootstrap) and several tasks for language fMRI (picture naming, verbal fluency, auditory verb generation).

We applied this pipeline to a healthy controls' cohort to provide new data regarding the functional components of the tracts underlying different fMRI tasks.

The comparison among different MNI task-specific fMRI-T Atlases shows both task-specific portions (exclusively included in one Atlas) and common portions (shared by different tasks) of language tracts. Picture Naming fMRI-T Atlas specific voxels are preferentially located within the occipito-temporal ventral stream, and they correspond to ILF trajectory. Although the exact functions of this fascicle are not well defined, its putative role is consistent with this result, since ILF is believed to take part into semantic processing, visual processing, and face recognition (Grill-Spector et al., 2001; Yeatman et al., 2013). Verbal Fluency fMRI-T Atlas specific components belong to AF-SLF and FAT (that constitute the dorsal stream), and voxels belonging to this Atlas are more represented within the dorsal stream rather than the ventral stream. This evidence supports the well defined phonological-articulatory role of the dorsal stream (Rauschecker and Scott, 2009; Friederici, 2012), since Verbal Fluency involves phonological and articulatory capacities more than the other tasks employed, and does not require semantic processing. Auditory Verb Generation fMRI-T Atlas specific portions of the tracts are mainly located within the temporal branch of AF-SLF. As the posterior temporal lobe is crucial for semantic functions (Hickok and Poeppel, 2007), this result is likely due to the strong semantic processing required by Auditory Verb Generation, which is frequently employed to identify temporal areas (i.e., Wernicke area) (Deblaere et al., 2002). A considerable amount of fMRI-T Atlases network is shared by more than one task, and this is compatible with the notion that different tasks partly involve similar language domains: for instance, Picture Naming and Auditory Verb Generation require both semantic and articulatory capacities. More in detail, common voxels shared by several fMRI-T Atlases are preferentially located in the deep white matter, and they correspond to the trajectory of AF-SLF and ExC fascicles. In fact, the trajectories of different language pathway subsets are coherent and located within few voxels at those levels, and this is probably the reason why these deep white matter voxels are shared by two or more task-specific fMRI-T Atlases.

Comparing the Anatomical-T Atlas with the fMRI-T Atlas including all the tasks ("any-task" fMRI-T Atlas) allowed to demonstrate that fiber tracts components whose endpoints are located inside fMRI activations are indeed a subset of the anatomically defined tracts. This means that some other components of language-related tracts have no relationship with fMRI activations derived by any of the tasks, and can therefore be considered as portions of the tract that are not recruited by the language tasks empolyed. This result is consistent with the aforementioned hypothesis [already suggested by other Authors (Bello et al., 2008; Bizzi, 2009)] that some subsets of the language tracts may be redundant, or not strictly related to the language function.

This hypothesis is also supported by the quantitative analysis (VPI analysis) results, since the percentage of the anatomical tracts in relationship with a fMRI activation was always below 60% – and in most cases such percentage was around 40% or even 20%. In addition, VPI analysis clearly demonstrated that Verbal Fluency fMRI-T involved dorsal frontal tracts (FAT, AF, SLF-II, SLF-III) in a significantly higher percentage when compared to the other tracts. This result is consistent with the findings provided by the qualitative MNI fMRI-T Atlas

analysis, and supported by the well-defined language dual-stream hypothesis (Friederici, 2012) for the aforementioned reasons. The fact that PN fMRI-T and AVG fMRI-T VPI analysis did not reveal a similar trend is probably due to the fact that these tasks involve several language domains (phonological, articulatory, and semantic at least); whereas Verbal Fluency is almost purely phonological-articulatory.

The same pipeline developed on healthy controls was applied to patients with brain neoplasms, to assess the hypothesis that combining MR Tractography and language fMRI could identify the "high-risk" subsets of language fascicles that are more likely to be eloquent, and should be therefore spared by the surgical resection.

The quantitative comparison between Anatomical-T and task-specific fMRI-T AF-SLF and IFOF reveals that the number of removed voxels (corresponding to non-eloquent points at DES) belonging to Anatomical-T tracts was significantly greater than fMRI-T tracts, and multiple comparison *post hoc* analysis highlights that this difference is due to the difference between Anatomical-T and Verbal Fluency fMRI-T. This result supports our hypothesis that fMRI-T (and specifically VF fMRI-T) is more specific than Anatomical-T when depicting "high-risk" AF-SLF and IFOF components that are eloquent at DES, and therefore should not be removed during the surgical procedure. In fact, fewer non-eloquent voxels belonging to AF-SLF and IFOF were depicted by the VF fMRI-T approach when compared to the Anatomical-T approach, and those non-eloquent voxels are considered false-positive values yielded by the MR Tractography analysis.

The qualitative evaluation of the relationships between language tracts trajectory (Anatomical-T) and DES-defined functional limits of resection revealed a satisfying correspondence between MR Tractography and the limits of resection for AF-SLF and IFOF overall; conversely, some parts of FAT, UF, and ILF trajectories were often located inside the surgical cavity – meaning that those parts did not yield positive responses at DES for the specific intraoperative neuropsychological tests employed. AF-SLF and IFOF are known to be crucial for language function, since they are the fundamental components of the dorsal phonological stream and the ventral semantic stream, respectively (Friederici, 2012). In addition, the preservation of these two fascicles is a crucial objective of brain surgery, as their DES stimulation is known to yield major language disturbances: dysarthria, phonological paraphasias, speech arrest, repetition errors for AF-SLF; semantic paraphasias for IFOF (Bello et al., 2008; Chang et al., 2015). Our analyses indirectly confirm the already well-known match (Bello et al., 2008; Leclercq et al., 2010) between DES and classical Anatomical-T of AF-SLF and IFOF. On the other hand, the importance of preserving FAT, UF, and ILF is not concerted. FAT is a newly defined fascicle (Dick et al., 2014) and recent studies reported that patients experience stuttering (Kemerdere et al., 2016) and speech arrest (Kinoshita et al., 2015) when DES targets this tract. The findings of the present study seem not to confirm such evidences, since in our patients' cohort the surgical resection including portions of FAT did not lead to long-term language disturbances. UF is considered to participate in the semantic ventral stream (Friederici, 2012), but its role in language function is still not well defined and current literature advocates for no essential language-related functions, except for proper name retrieval (Papagno et al., 2011). As for ILF, recent evidence suggests that this fascicle can be safely removed during surgical procedures, as no language disturbances are evoked by applying DES to its trajectory (Mandonnet et al., 2007). However, some temporal portions of UF and ILF might contribute to some semantic functions (Chang et al., 2015) that were not specifically tested during DES in the present study, even though they were tested before and after surgery.

The qualitative comparison between Anatomical-T and fMRI-T AF-SLF and IFOF, and the evaluation of their relationship with the volume of the surgical cavity, illustrates that in a subset of patients (six out of 16 – 37.5%, in which the resection involved three AF-SLFs and five IFOFs) fMRI-T is able to predict the functional limits of resection *better* than Anatomical-T. In fact, in this subset Anatomical-T tracts are located inside the surgical cavity, whereas fMRI-T ones are perfectly aligned to its margins. In the majority of these cases (four IFOFs), the difference between Anatomical-T and fMRI-T (specifically VF fMRI-T) in predicting the limits of resection is due to the fact that Anatomical-T depicts IFOF superior and anterior frontal branches [also known as IFOF deep layer (Caverzasi et al., 2014)], whereas Verbal Fluency fMRI-T isolates only the component of the fronto-opercular branch (also called IFOF superficial layer) that terminates in a fMRI activated fronto-opercular area. This finding suggests that IFOF superficial layer, that terminates in fronto-opercular language-related cortex, could be the actual language-essential component of this tract. Nevertheless, it should be assessed whether fMRI-T is required to identify the eloquent component, or an anatomy-based target-ROI would be sufficient. In the remaining cases (three AF-SLFs and one IFOF), fMRI-T predicting the functional limits of resection was variously based on all tasks employed, and the surgical procedure involved frontal branches of Anatomical-T AF-SLF and IFOF. However, it should be noted that in a minority of cases some AF-SLF fronto-opercular terminations that were considered non-eloquent for the language function might have a role in praxia and subtle motor skills that were not investigated in the present study. In fact, such functions involve the ventral premotor areas and can be identified by dedicated DES tasks, which were not employed in the present study (Rossi et al., 2018).

Taken together, these analyses demonstrate our hypothesis that fMRI-T may provide additional information about "high-risk" subsets of AF-SLF and IFOF that are more likely to be eloquent, and that fMRI-T based on Verbal Fluency is the most specific for this purpose. Providing fMRI-T high-risk subsets of AF-SLF and IFOF could improve the presurgical planning and, above all, guide intraoperative DES at best, thus further shortening awake-surgery time. In addition, these results provide new data about IFOF, whose superficial layer may be the actual language-related functional core.

Language function assessment confirmed that DES-guided surgical resection succeeded in achieving a safe tumor resection in the majority of patients, who did not suffer from long-term language deficits. In these patients, time to recovery was generally longer when a higher number of voxels representing AF-SLF and

IFOF trajectory was involved in the surgical resection (both for Anatomical-T and fMRI-T). This result suggests that DES may be able to predict which fascicle subsets have a role that can be remapped onto other subsets with time, as also previously argued (Duffau, 2012).

As for the subset of patients affected by long-term language deficits, clinical and radiological evidences suggest that several factors may be held responsible of those deficits rather than the surgical resection itself, such as age, preoperative language deficits, disease progression and adjuvant treatment induced toxicity. Other factors possibly impacting the long-term clinical outcome in those three patients were: long-standing previous disease history with multiple surgical interventions (one out of three), preoperative major alterations of language fascicle Tractography (one out of three), postoperative status epilepticus (one out of three), post-operative radiation treatment for residual disease or disease progression (three out of three, one of whom also presented major radiation-induced alterations at MRI scans). Possible factors preventing the complete clinical recovery of the patient showing mild language deficits at 12 months include a long-standing previous disease history with one previous surgical intervention, radiation-toxicity, and a nodule of progressive disease in the territory of the arcuate fasciculus.

This study has some technical and clinical limitations. Firstly, the combination pipeline we developed relies on fMRI-derived binary ROIs. Task-based fMRI sensitivity and specificity strongly depend on the statistical threshold adopted (Roux et al., 2003) and eloquent areas individuation depends on the tasks employed (Black et al., 2017). In this study, we decided to adopt a $P < 0.001$ threshold, instead of a stricter threshold often adopted in the clinical setting (FWE), in order to keep false negative results to a minimum. As for the tasks employed, for the same purpose all but two enrolled subjects were asked to perform at least two different language fMRI tasks. Nevertheless, our battery lacked a syntax-specific task, and therefore this specific domain was not tested. Moreover, awake DES did not employ semantic (Chang et al., 2015), praxis (Rossi et al., 2018) or cognitive (Puglisi et al., 2018) testing. Not testing those specific functions might have contributed to the surgical resection of portions of nervous tissue that had a role in such functions, specifically in the temporal and frontal lobe. Nevertheless, semantic function was extensively tested before and after surgery, and, as already discussed, our results suggest that the surgical resection did not directly result in long-term language disturbances. More in detail, not testing praxis, fine motor skills and other cognitive functions other than language might have caused the surgical resection to include portions of nervous tissue that is non-eloquent for language, but eloquent for other tasks. For instance, praxis involves several cortical areas of the dominant hemisphere, including the oro-facial ventral premotor area (Rossi et al., 2018) that was shown to be adjacent to the language-related fronto-opercular areas (Fornia et al., 2018).

Other limitations are the relatively low number of enrolled patients (specifically, some tumor resection sites have a low number of items), and the fact that data analysis was performed retrospectively. In addition, the evaluation of the relationships between the fascicles and the cavity volume allowed to indirectly infer quantitative data about the specificity of the different Tractography approaches, but did not provide direct measures of their sensitivity – since DES-positive coordinates are not known.

Future studies willing to further assess the advantages provided by fMRI-T may try to overcome the aforementioned limits. Such studies should include both phonological-articulatory and semantic fMRI tasks, as it has also been recently suggested by the American Society of Functional Radiology guidelines (Black et al., 2017). For instance, Verbal Fluency task [which corresponds to Silent Word Generation (Zacà et al., 2013) task in these guidelines], and Verb Generation task [or the Sentence Completion (Zacà et al., 2013) task proposed in these guidelines] could be adopted, respectively. Similarly, a wider intraoperative language assessment, with refined tests for motor cognition and other cognitive functions, could provide a better depiction of functions underlying the tracts herein investigated. Furthermore, in order to obtain robust sensitivity and specificity quantitative data, a greater patients' cohort should be enrolled, and the exact sites of DES-tested positive and negative voxels should be compared to the trajectory of the fascicles.

Future tractography studies may also employ alternative tracking algorithms that have already been proven feasible on brain tumor patients, such as spherical deconvolution tractography (Mormina et al., 2016; Becker et al., 2019) and multi-fiber tractography (Chen et al., 2015; Gong et al., 2018). These methods, similarly to q-ball tractography, were shown to improve the depiction of complex fiber orientations (Tournier et al., 2007; Malcolm et al., 2010; Fillard et al., 2011; Dell'Acqua and Tournier, 2019). Besides, recent data illustrates how multi-tensor models can increase tracking sensitivity through tissue affected by edema or tumor infiltration by including an additional isotropic tensor reflecting the free water compartment (Gong et al., 2018). Similarly, other multi-compartimental models like NODDI may be employed to improve the tracking of complex fiber configurations (Reddy and Rathi, 2016). Finally, future studies may employ automated or semi-automated approaches for tract selections, such as fiber-clustering, which was shown to consistently group streamlines and assign them to a common cluster, basing on their trajectory similarity (O'Donnell et al., 2017). This approach could overcome the limits of the manual-ROI approach, that can be time-consuming and requires trained operators.

CONCLUSION

In this study we develop a systematic pipeline to combine the "classic" Tractography of language fascicles with language fMRI cortical activations in order to achieve a fMRI-targeted Tractography (fMRI-T). Our aim was to provide additional information regarding the functional components of subcortical language fascicles, and to apply this approach both on healthy controls and brain tumor patients.

In healthy controls' cohort, this approach provided novel insights regarding the subsets of white matter networks related to some fMRI language tasks commonly employed in the clinical setting (Bizzi et al., 2008; Bizzi, 2009). Furthermore,

these data are overall consistent with the current theories about language functional neuroanatomy (Hickok and Poeppel, 2007; Rauschecker and Scott, 2009; Friederici, 2012) – e.g., verbal fluency strongly involves dorsal frontal tracts, consistently with the phonogical-articulatory features of this task.

In the patients' cohort, quantitative and qualitative analyses revealed that this combined method provides additional useful information regarding the "high-risk" subsets of the fascicles that are more likely to be eloquent (specifically AF-SLF and IFOF). Indeed, in some cases fMRI-T predicted the functional limits of DES-guided surgical resection better than Anatomical-T. Employing this novel combined method in addition to the "classic" Anatomical-T could provide additional information to better plan the surgical approach with a refined patient-specific risk-assessment to ultimately guide intraoperative DES and thus resection.

DATA AVAILABILITY STATEMENT

The datasets for this study are avaliable from the authors upon request.

ETHICS STATEMENT

The studies involving human participants were reviewed and approved by Local ethical committee of Ospedale San Raffaele, Milan, Italy. All subjects provided signed informed consent prior to MR imaging.

AUTHOR CONTRIBUTIONS

FS designed the study, acquired, analyzed, and interpreted the imaging data, did the statistical analysis, and drafted the manuscript. EC designed the study, interpreted the diffusion imaging data, and drafted the manuscript. MR and LB acquired the neurostimulation data and drafted the manuscript. KJ designed the study and analyzed the diffusion imaging data. VB and SoC analyzed the fMRI imaging data. PS and AI acquired the imaging data. SaC analyzed the fMRI imaging data and drafted the manuscript. AlC acquired and interpreted the neuropsychological data. AL and GP acquired the data. MG acquired the post-surgical imaging data. MG-T interpreted the imaging data and drafted the manuscript. RH designed the study and interpreted the diffusion imaging data. AF designed the study and interpreted the data. AnC designed the study, acquired and interpreted the imaging data, and drafted the manuscript.

FUNDING

LB was supported by the AIRC (Associazione Italiana Ricerca sul Cancro) grant number 18482.

ACKNOWLEDGMENTS

The authors are grateful to Valentina Pieri and Gian Marco Conte for the useful discussion about the results of this study.

SUPPLEMENTARY MATERIAL

The Supplementary Material for this article can be found online at: https://www.frontiersin.org/articles/10.3389/fnins.2020.00225/full#supplementary-material

REFERENCES

Becker, D., Scherer, M., Neher, P., Jungk, C., Jesser, J., Pflüger, I., et al. (2019). Going beyond diffusion tensor imaging tractography in eloquent glioma surgery–high-resolution fiber tractography: Q-ball or constrained spherical deconvolution? *World Neurosurgery*. 134, e596–e609. doi: 10.1016/j.wneu.2019.10.138

Bello, L., Castellano, A., Fava, E., Casaceli, G., Riva, M., Scotti, G., et al. (2010). Intraoperative use of diffusion tensor imaging fiber tractography and subcortical mapping for resection of gliomas: technical considerations. *Neurosurgical. Focus* 28, :E6. doi: 10.3171/2009.12.FOCUS09240

Bello, L., Gambini, A., Castellano, A., Carrabba, G., Acerbi, F., Fava, E., et al. (2008). Motor and language DTI Fiber Tracking combined with intraoperative subcortical mapping for surgical removal of gliomas. *Neuroimage* 39, 369–382. doi: 10.1016/j.neuroimage.2007.08.031

Berger, M. S., and Ojemann, G. A. (1992). Intraoperative brain mapping techniques in neuro-oncology. *Stereotactic and. Functional. Neurosurgery.* 58, 153–161. doi: 10.1159/000098989

Berger, M. S., Ojemann, G. A., and Lettich, E. (1990). Neurophysiological monitoring during astrocytoma surgery. *Neurosurgery. Clinics of. North America.* 1, 65–80. doi: 10.1016/s1042-3680(18)30824-6

Berman, J. I., Chung, S. W., Mukherjee, P., Hess, C. P., Han, E. T., and Henry, R. G. (2008). Probabilistic streamline q-ball tractography using the residual bootstrap. *Neuroimage* 39, 215–222. doi: 10.1016/j.neuroimage.2007.08.021

Bertani, G., Fava, E., Casaceli, G., Carrabba, G., Casarotti, A., Papagno, C., et al. (2009). Intraoperative mapping and monitoring of brain functions for the resection of low-grade gliomas: technical considerations. *Neurosurgical. Focus* 27, :E4. doi: 10.3171/2009.8.FOCUS09137

Bizzi, A. (2009). Presurgical mapping of verbal language in brain tumors with functional MR imaging and MR tractography. *Neuroimaging. Clinics of. North America.* 19, 573–596. doi: 10.1016/j.nic.2009.08.010

Bizzi, A., Blasi, V., Falini, A., Ferroli, P., Cadioli, M., Danesi, U., et al. (2008). Presurgical functional MR imaging of language and motor functions: validation with intraoperative electrocortical Mapping. *Radiology* 248, 579–589. doi: 10.1148/radiol.2482071214

Black, D. F., Vachha, B., Mian, A., Faro, S. H., Maheshwari, M., Sair, H. I., et al. (2017). American society of functional neuroradiology–recommended fMRI paradigm algorithms for presurgical language assessment. *American. Journal of. Neuroradiology.* 38, E65–E73. doi: 10.3174/ajnr.A5345

Broser, P. J., Groeschel, S., Hauser, T.-K., Lidzba, K., and Wilke, M. (2012). Functional MRI-guided probabilistic tractography of cortico-cortical and cortico-subcortical language networks in children. *Neuroimage* 63, 1561–1570. doi: 10.1016/j.neuroimage.2012.07.060

Bucci, M., Mandelli, M. L., Berman, J. I., Amirbekian, B., Nguyen, C., Berger, M. S., et al. (2013). Quantifying diffusion MRI tractography of the corticospinal tract

in brain tumors with deterministic and probabilistic methods. *Neuroimage Clin.* 3, 361–368. doi: 10.1016/j.nicl.2013.08.008

Castellano, A., Bello, L., Michelozzi, C., Gallucci, M., Fava, E., Iadanza, A., et al. (2012). Role of diffusion tensor magnetic resonance tractography in predicting the extent of resection in glioma surgery. *Neuro-oncology* 14, 192–202. doi: 10.1093/neuonc/nor188

Castellano, A., Cirillo, S., Bello, L., Riva, M., and Falini, A. (2017). Functional MRI for surgery of gliomas. *Current. Treatment. Options in Neurology.* 19, :34. doi: 10.1007/s11940-017-0469-y

Caverzasi, E., Hervey-Jumper, S. L., Jordan, K. M., Lobach, I. V., Li, J., Panara, V., et al. (2015). Identifying preoperative language tracts and predicting postoperative functional recovery using HARDI q-ball fiber tractography in patients with gliomas. *Journal of. Neurosurgery.* 125, 33–45. doi: 10.3171/2015.6.JNS142203

Caverzasi, E., Papinutto, N., Amirbekian, B., Berger, M. S., and Henry, R. G. (2014). Q-ball of inferior fronto-occipital fasciculus and beyond. *PLoS One* 9:e100274. doi: 10.1371/journal.pone.0100274

Chang, E. F., Raygor, K. P., and Berger, M. S. (2015). Contemporary model of language organization: an overview for neurosurgeons. *Journal of. Neurosurgery.* 122, 250–261. doi: 10.3171/2014.10.JNS132647

Chen, Z., Tie, Y., Olubiyi, O., Rigolo, L., Mehrtash, A., Norton, I., et al. (2015). Reconstruction of the arcuate fasciculus for surgical planning in the setting of peritumoral edema using two-tensor unscented Kalman filter tractography. *Neuroimage: Clinical.* 7, 815–822. doi: 10.1016/j.nicl.2015.03.009

Conturo, T. E., Lori, N. F., Cull, T. S., Akbudak, E., Snyder, A. Z., Shimony, J. S., et al. (1999). Tracking neuronal fiber pathways in the living human brain. *Proceedings of the. National. Academy of. Sciences of the. United .States of. America.* 96, 10422–10427. doi: 10.1073/pnas.96.18.10422

Deblaere, K., Backes, W. H., Hofman, P., Vandemaele, P., Boon, P. A., Vonck, K., et al. (2002). Developing a comprehensive presurgical functional MRI protocol for patients with intractable temporal lobe epilepsy: a pilot study. *Neuroradiology* 44, 667–673. doi: 10.1007/s00234-002-0800-4

Dell'Acqua, F., and Tournier, J. D. (2019). Modelling white matter with spherical deconvolution: How and why? *NMR in Biomedicine.* 32, 1–18. doi: 10.1002/nbm.3945

Dick, A. S., Bernal, B., and Tremblay, P. (2014). The language connectome. *The Neuroscientist* 20, 453–467. doi: 10.1177/1073858413513502

Dougherty, R. F., Ben-Shachar, M., Bammer, R., Brewer, A. A., and Wandell, B. A. (2005). Functional organization of human occipital-callosal fiber tracts. *Proc. Natl. Acad. Sci. U.S.A.Proceedings of the National Academy of Sciences of the United States of America* 102, 7350–7355. doi: 10.1073/pnas.0500003102

Duffau, H. (2012). The challenge to remove diffuse low-grade gliomas while preserving brain functions. *Acta Neurochirurgica.* 154, 569–574. doi: 10.1007/s00701-012-1275-7

Duffau, H. (2016). Long-term outcomes after supratotal resection of diffuse low-grade gliomas: a consecutive series with 11-year follow-up. *Acta Neurochirurgica.* 158, 51–58. doi: 10.1007/s00701-015-2621-3

Essayed, W. I., Zhang, F., Unadkat, P., Cosgrove, G. R., Golby, A. J., and O'Donnell, L. J. (2017). White matter tractography for neurosurgical planning: a topography-based review of the current state of the art. *Neuroimage: Clinical.* 15, 659–672. doi: 10.1016/j.nicl.2017.06.011

Figley, T. D., Bhullar, N., Courtney, S. M., and Figley, C. R. (2015). Probabilistic atlases of default mode, executive control and salience network white matter tracts: an fMRI-guided diffusion tensor imaging and tractography study. *Frontiers in. Human. Neuroscience.* 9:585. doi: 10.3389/fnhum.2015.00585

Fillard, P., Descoteaux, M., Goh, A., Gouttard, S., Jeurissen, B., Malcolm, J., et al. (2011). Quantitative evaluation of 10 tractography algorithms on a realistic diffusion MR phantom. *Neuroimage* 56, 220–234. doi: 10.1016/j.neuroimage.2011.01.032

Fornia, L., Ferpozzi, V., Montagna, M., Rossi, M., Riva, M., Pessina, F., et al. (2018). Functional characterization of the left ventrolateral premotor cortex in humans: a direct electrophysiological approach. *Cerebral. Cortex* 28, 167–183. doi: 10.1093/cercor/bhw365

Friederici, A. D. (2012). The cortical language circuit: from auditory perception to sentence comprehension. *Trends in Cognitive. Sciences.* 16, 262–268. doi: 10.1016/j.tics.2012.04.001

Garyfallidis, E., and Brett, M. (2014). Dipy, a library for the analysis of diffusion MRI data. *Frontiers in. Neuroinformatics.* 8:8. doi: 10.3389/fninf.2014.00008

Gong, S., Zhang, F., Norton, I., Essayed, W. I., Unadkat, P., Rigolo, L., et al. (2018). Free water modeling of peritumoral edema using multi-fiber tractography: application to tracking the arcuate fasciculus for neurosurgical planning. *PLoS One* 13:e0197056. doi: 10.1371/journal.pone.0197056

Grill-Spector, K., Kourtzi, Z., and Kanwisher, N. (2001). The lateral occipital complex and its role in object recognition. *Vision Research.* 41, 1409–1422. doi: 10.1016/s0042-6989(01)00073-6

Guye, M., Parker, G. J. M., Symms, M., Boulby, P., Wheeler-Kingshott, C. A. M., Salek-Haddadi, A., et al. (2003). Combined functional MRI and tractography to demonstrate the connectivity of the human primary motor cortex in vivo. *Neuroimage* 19, 1349–1360. doi: 10.1016/s1053-8119(03)00165-4

Hess, C. P., Mukherjee, P., Han, E. T., Xu, D., and Vigneron, D. B. (2006). Q-ball reconstruction of multimodal fiber orientations using the spherical harmonic basis. *Magnetic. Resonance in. Medicine.* 56, 104–117. doi: 10.1002/mrm.20931

Hickok, G., and Poeppel, D. (2007). The cortical organization of speech processing. *Nature. Reviews. Neuroscience.* 8, 393–402. doi: 10.1038/nrn2113

Jellison, B. J., Field, A. S., Medow, J., Lazar, M., Salamat, M. S., and Alexander, A. L. (2004). Diffusion tensor imaging of cerebral white matter: a pictorial review of physics, fiber tract anatomy, and tumor imaging patterns. *AJNR. American. Journal of. Neuroradiology.* 25, 356–369.

Kemerdere, R., de Champfleur, N. M., Deverdun, J., Cochereau, J., Moritz-Gasser, S., Herbet, G., et al. (2016). Role of the left frontal aslant tract in stuttering: a brain stimulation and tractographic study. *Journal of. Neurology.* 263, 157–167. doi: 10.1007/s00415-015-7949-3

Kinoshita, M., de Champfleur, N. M., Deverdun, J., Moritz-Gasser, S., Herbet, G., and Duffau, H. (2015). Role of fronto-striatal tract and frontal aslant tract in movement and speech: an axonal mapping study. *Brain Structure and. Function.* 220, 3399–3412. doi: 10.1007/s00429-014-0863-0

Kleiser, R., Staempfli, P., Valavanis, A., Boesiger, P., and Kollias, S. (2010). Impact of fMRI-guided advanced DTI fiber tracking techniques on their clinical applications in patients with brain tumors. *Neuroradiology* 52, 37–46. doi: 10.1007/s00234-009-0539-2

Leclercq, D., Duffau, H., Delmaire, C., Capelle, L., Gatignol, P., Ducros, M., et al. (2010). Comparison of diffusion tensor imaging tractography of language tracts and intraoperative subcortical stimulations. *Journal of. Neurosurgery.* 112, 503–511. doi: 10.3171/2009.8.JNS09558

Liégeois, F. J., Butler, J., Morgan, A. T., Clayden, J. D., and Clark, C. A. (2016). Anatomy and lateralization of the human corticobulbar tracts: an fMRI-guided tractography study. *Brain Structure and. Function.* 221, 3337–3345. doi: 10.1007/s00429-015-1104-x

Malcolm, J. G., Shenton, M. E., and Rathi, Y. (2010). Filtered multi-tensor tractography. *IEEE Trans. Med. Imaging* 29, 1664–1675. doi: 10.1109/TMI.2010.2048121

Mandonnet, E., Nouet, A., Gatignol, P., Capelle, L., and Duffau, H. (2007). Does the left inferior longitudinal fasciculus play a role in language? A brain stimulation study. *Brain* 130, 623–629. doi: 10.1093/brain/awl361

Mori, S., Crain, B. J., Chacko, V. P., and van Zijl, P. C. (1999). Three-dimensional tracking of axonal projections in the brain by magnetic resonance imaging. *Annals of. Neurology.* 45, 265–269. doi: 10.1002/1531-8249(199902)45:2<265::aid-ana21>3.0.co;2-3

Mori, S., and Zhang, J. (2006). Primer principles of diffusion tensor imaging and its applications to basic neuroscience research. *Neuron* 51, 527–539. doi: 10.1016/j.neuron.2006.08.012

Mormina, E., Arrigo, A., Calamuneri, A., Alafaci, C., Tomasello, F., Morabito, R., et al. (2016). Optic radiations evaluation in patients affected by high-grade gliomas: a side-by-side constrained spherical deconvolution and diffusion tensor imaging study. *Neuroradiology* 58, 1067–1075. doi: 10.1007/s00234-016-1732-8

Mukherjee, P., Berman, J. I., Chung, S. W., Hess, C. P., and Henry, R. G. (2008). Diffusion tensor MR imaging and fiber tractography: theoretic underpinnings. *American. Journal of. Neuroradiology.* 29, 632–641. doi: 10.3174/ajnr.A1051

O'Donnell, L. J., Suter, Y., Rigolo, L., Kahali, P., Zhang, F., Norton, I., et al. (2017). Automated white matter fiber tract identification in patients with brain tumors. *Neuroimage: Clinical.* 13, 138–153. doi: 10.1016/j.nicl.2016.11.023

Ojemann, G. A. (1983). Brain organization for language from the perspective of electrical stimulation mapping. *Behavioral and. Brain Sciences.* 6, 189–206. doi: 10.1017/S0140525X00015491

Papagno, C., Comi, A., Riva, M., and Bello, L. (2012). Measuring clinical outcomes in neuro- oncology. A battery to evaluate low-grade gliomas (LGG). *J. Neurooncol*. 108, 269–275. doi: 10.1007/s11060-012-0824-5

Papagno, C., Miracapillo, C., Casarotti, A., Romero Lauro, L. J., Castellano, A., Falini, A., et al. (2011). What is the role of the uncinate fasciculus? Surgical removal and proper name retrieval. *Brain* 134, 405–414. doi: 10.1093/brain/awq283

Preti, M. G., Makris, N., Lagana, M. M., Papadimitriou, G., Baglio, F., Griffanti, L., et al. (2012). "A novel approach of fMRI-guided tractography analysis within a group: construction of an fMRI-guided tractographic atlas," in *Proceedings of the 2012 Annual International Conference of the IEEE Engineering in Medicine and Biology Society*, (Piscataway, NJ: IEEE), 2283–2286. doi: 10.1109/EMBC.2012.6346418

Preti, M. G., Makris, N., Papadimitriou, G., Laganà, M. M., Griffanti, L., Clerici, M., et al. (2014). A novel approach of Groupwise fMRI-guided tractography allowing to characterize the clinical evolution of Alzheimer's disease. *PLoS One* 9:e92026. doi: 10.1371/journal.pone.0092026

Puglisi, G., Leonetti, A., Cerri, G., and Borroni, P. (2018). Attention and cognitive load modulate motor resonance during action observation. *Brain and Cognition*. 128, 7–16. doi: 10.1016/j.bandc.2018.10.006

Rauschecker, J. P., and Scott, S. K. (2009). Maps and streams in the auditory cortex: nonhuman primates illuminate human speech processing. *Nature. Neuroscience.* 12, 718–724. doi: 10.1038/nn.2331

Reddy, C. P., and Rathi, Y. (2016). Joint multi-fiber NODDI parameter estimation and tractography using the unscented information filter. *Frontiers in. Neuroscience.* 10:166. doi: 10.3389/fnins.2016.00166

Reid, L. B., Cunnington, R., Boyd, R. N., and Rose, S. E. (2016). Correction: Surface-based fMRI-driven diffusion tractography in the presence of significant brain pathology: a study linking structure and function in cerebral palsy. *PLoS One* 11:e0162271. doi: 10.1371/journal.pone.0162271

Riva, M., Casaceli, G., Castellano, A., Fava, E., Falini, A., and Bello, L. (2011). Beautiful eyes guiding powerful hands - The role of intraoperative imaging techniques in the surgical management of gliomas. *European. Neurological. Review*. 6, 208–212. doi: 10.17925/ENR.2011.06.03.208

Romano, A., D'Andrea, G., Minniti, G., Mastronardi, L., Ferrante, L., Fantozzi, L. M., et al. (2009). Pre-surgical planning and MR-tractography utility in brain tumour resection. *European. Radiology.* 19, 2798–2808. doi: 10.1007/s00330-009-1483-6

Rossi, M., Fornia, L., Puglisi, G., Leonetti, A., Zuccon, G., Fava, E., et al. (2018). Assessment of the praxis circuit in glioma surgery to reduce the incidence of postoperative and long-term apraxia: a new intraoperative test. *Journal of. Neurosurgery*. 130, 17–27. doi: 10.3171/2017.7.JNS17357

Roux, F.-E., Boulanouar, K., Lotterie, J.-A., Mejdoubi, M., LeSage, J. P., and Berry, I. (2003). Language functional magnetic resonance imaging in preoperative assessment of language areas: correlation with direct cortical stimulation. *Neurosurgery* 52, 1335–1345.

Sanai, N., Mirzadeh, Z., and Berger, M. S. (2008). Functional outcome after language mapping for glioma resection. *New. England. Journal of. Medicine.* 358, 18–27. doi: 10.1056/NEJMoa067819

Saur, D., Schelter, B., Schnell, S., Kratochvil, D., Küpper, H., Kellmeyer, P., et al. (2010). Combining functional and anatomical connectivity reveals brain networks for auditory language comprehension. *Neuroimage* 49, 3187–3197. doi: 10.1016/j.neuroimage.2009.11.009

Schmitt, F. C., Kaufmann, J., Hoffmann, M. B., Tempelmann, C., Kluge, C., Rampp, S., et al. (2014). Case Report: practicability of functionally based tractography of the optic radiation during presurgical epilepsy work up. *Neuroscience. Letters.* 568, 56–61. doi: 10.1016/j.neulet.2014.03.049

Smits, M., Vernooij, M. W., Wielopolski, P. A., Vincent, A. J. P. E., Houston, G. C., and van der Lugt, A. (2007). Incorporating functional MR imaging into diffusion tensor tractography in the preoperative assessment of the corticospinal tract in patients with brain tumors. *American. Journal of. Neuroradiology.* 28, 1354–1361. doi: 10.3174/ajnr.A0538

Soares, J. M., Marques, P., Alves, V., and Sousa, N. (2013). A hitchhiker's guide to diffusion tensor imaging. *Frontiers in. Neuroscience.* 7:31. doi: 10.3389/fnins.2013.00031

Stadlbauer, A., Nimsky, C., Buslei, R., Salomonowitz, E., Hammen, T., Buchfelder, M., et al. (2007). Diffusion tensor imaging and optimized fiber tracking in glioma patients: histopathologic evaluation of tumor-invaded white matter structures. *Neuroimage* 34, 949–956. doi: 10.1016/j.neuroimage.2006.08.051

Staempfli, P., Reischauer, C., Jaermann, T., Valavanis, A., Kollias, S., and Boesiger, P. (2008). Combining fMRI and DTI: a framework for exploring the limits of fMRI-guided DTI fiber tracking and for verifying DTI-based fiber tractography results. *Neuroimage* 39, 119–126. doi: 10.1016/j.neuroimage.2007.08.025

Talos, I. F., O'Donnell, L., Westin, C. F., Warfield, S. K., Wells, W., Yoo, S. S., et al. (2003). "Diffusion tensor and functional MRI fusion with anatomical MRI for image-guided neurosurgery,". in *Proceedings of the Sixth International Conference on Medical Image Computing and Computer-Assisted Intervention - MICCAI'03: Lecture Notes in Computer Science*, Montréal,2878, 407–415. doi: 10.1007/978-3-540-39899-8_51

Tournier, J.-D., Calamante, F., and Connelly, A. (2007). Robust determination of the fibre orientation distribution in diffusion MRI: non-negativity constrained super-resolved spherical deconvolution. *Neuroimage* 35, 1459–1472. doi: 10.1016/j.neuroimage.2007.02.016

Tournier, J.-D., Calamante, F., Gadian, D. G., and Connelly, A. (2004). Direct estimation of the fiber orientation density function from diffusion-weighted MRI data using spherical deconvolution. *Neuroimage* 23, 1176–1185. doi: 10.1016/j.neuroimage.2004.07.037

Tuch, D. S. (2004). Q-ball imaging. *Magnetic. Resonance in. Medicine.* 52, 1358–1372. doi: 10.1002/mrm.20279

Ulmer, J. L., Klein, A. P., Mueller, W. M., DeYoe, E. A., and Mark, L. P. (2014). Preoperative diffusion tensor imaging. *Neuroimaging Clinics of. North America.* 24, 599–617. doi: 10.1016/j.nic.2014.08.002

Upadhyay, J., Ducros, M., Knaus, T. A., Lindgren, K. A., Silver, A., Tager-Flusberg, H., et al. (2007). Function and connectivity in human primary auditory cortex: a combined fMRI and DTI study at 3 Tesla. *Cerebral. Cortex* 17, 2420–2432. doi: 10.1093/cercor/bhl150

Yang, D. S., Hong, J. H., Byun, W. M., Kwak, S. Y., Ahn, S. H., Lee, H., et al. (2009). Identification of the medial lemniscus in the human brain: combined study of functional MRI and diffusion tensor tractography. *Neuroscience. Letters.* 459, 19–24. doi: 10.1016/j.neulet.2009.04.058

Yeatman, J. D., Rauschecker, A. M., and Wandell, B. A. (2013). Anatomy of the visual word form area: adjacent cortical circuits and long-range white matter connections. *Brain and Language.* 125, 146–155. doi: 10.1016/j.bandl.2012.04.010

Yordanova, Y. N., Moritz-Gasser, S., and Duffau, H. (2011). Awake surgery for WHO Grade II gliomas within "noneloquent" areas in the left dominant hemisphere: toward a "supratotal" resection. Clinical article. *Journal of. Neurosurgery.* 115, 232–239. doi: 10.3171/2011.3.JNS101333

Zacà, D., Jarso, S., and Pillai, J. J. (2013). Role of semantic paradigms for optimization of language mapping in clinical fMRI studies. *American. Journal of. Neuroradiology.* 34, 1966–1971. doi: 10.3174/ajnr.A3628

Zhu, D., Zhang, T., Jiang, X., Hu, X., Chen, H., Yang, N., et al. (2014). Fusing DTI and fMRI data: a survey of methods and applications. *Neuroimage* 102, 184–191. doi: 10.1016/j.neuroimage.2013.09.071

Conflict of Interest: The authors declare that the research was conducted in the absence of any commercial or financial relationships that could be construed as a potential conflict of interest.

Copyright © 2020 Sanvito, Caverzasi, Riva, Jordan, Blasi, Scifo, Iadanza, Crespi, Cirillo, Casarotti, Leonetti, Puglisi, Grimaldi, Bello, Gorno-Tempini, Henry, Falini and Castellano. This is an open-access article distributed under the terms of the Creative Commons Attribution License (CC BY). The use, distribution or reproduction in other forums is permitted, provided the original author(s) and the copyright owner(s) are credited and that the original publication in this journal is cited, in accordance with accepted academic practice. No use, distribution or reproduction is permitted which does not comply with these terms.

frontiers in Neuroscience

SYSTEMATIC REVIEW
published: 21 July 2020
doi: 10.3389/fnins.2020.00594

The Potential of Functional Near-Infrared Spectroscopy-Based Neurofeedback—A Systematic Review and Recommendations for Best Practice

Simon H. Kohl[1,2*], *David M. A. Mehler*[3], *Michael Lührs*[4,5], *Robert T. Thibault*[6,7], *Kerstin Konrad*[1,2] *and Bettina Sorger*[5]

[1] JARA-Institute Molecular Neuroscience and Neuroimaging (INM-11), Jülich Research Centre, Jülich, Germany, [2] Child Neuropsychology Section, Department of Child and Adolescent Psychiatry, Psychosomatics and Psychotherapy, Medical Faculty, RWTH Aachen University, Aachen, Germany, [3] Department of Psychiatry, University of Münster, Münster, Germany, [4] Brain Innovation B.V., Research Department, Maastricht, Netherlands, [5] Faculty of Psychology and Neuroscience, Department of Cognitive Neuroscience, Maastricht University, Maastricht, Netherlands, [6] School of Psychological Science, University of Bristol, Bristol, United Kingdom, [7] MRC Integrative Epidemiology Unit, University of Bristol, Bristol, United Kingdom

OPEN ACCESS

Edited by:
Jorge J. Riera, Florida International University, United States

Reviewed by:
Anuradha Godavarty, Florida International University, United States
Christian Paret, Heidelberg University, Germany

***Correspondence:**
Simon H. Kohl
si.kohl@fz-juelich.de;
simon.h.kohl@gmail.com

Specialty section:
This article was submitted to Brain Imaging Methods, a section of the journal Frontiers in Neuroscience

Received: *08 January 2020*
Accepted: *14 May 2020*
Published: *21 July 2020*

Citation:
Kohl SH, Mehler DMA, Lührs M, Thibault RT, Konrad K and Sorger B (2020) The Potential of Functional Near-Infrared Spectroscopy-Based Neurofeedback—A Systematic Review and Recommendations for Best Practice. Front. Neurosci. 14:594. doi: 10.3389/fnins.2020.00594

Background: The effects of electroencephalography (EEG) and functional magnetic resonance imaging (fMRI)-neurofeedback on brain activation and behaviors have been studied extensively in the past. More recently, researchers have begun to investigate the effects of functional near-infrared spectroscopy-based neurofeedback (fNIRS-neurofeedback). FNIRS is a functional neuroimaging technique based on brain hemodynamics, which is easy to use, portable, inexpensive, and has reduced sensitivity to movement artifacts.

Method: We provide the first systematic review and database of fNIRS-neurofeedback studies, synthesizing findings from 22 peer-reviewed studies (including a total of $N = 441$ participants; 337 healthy, 104 patients). We (1) give a comprehensive overview of how fNIRS-neurofeedback training protocols were implemented, (2) review the online signal-processing methods used, (3) evaluate the quality of studies using pre-set methodological and reporting quality criteria and also present statistical sensitivity/power analyses, (4) investigate the effectiveness of fNIRS-neurofeedback in modulating brain activation, and (5) review its effectiveness in changing behavior in healthy and pathological populations.

Results and discussion: (1–2) Published studies are heterogeneous (e.g., neurofeedback targets, investigated populations, applied training protocols, and methods). (3) Large randomized controlled trials are still lacking. In view of the novelty of the field, the quality of the published studies is moderate. We identified room for improvement in reporting important information and statistical power to detect realistic effects. (4) Several studies show that people can regulate hemodynamic signals from cortical brain regions with fNIRS-neurofeedback and (5) these studies indicate the feasibility of modulating motor control and prefrontal brain functioning in healthy

participants and ameliorating symptoms in clinical populations (stroke, ADHD, autism, and social anxiety). However, valid conclusions about specificity or potential clinical utility are premature.

Conclusion: Due to the advantages of practicability and relatively low cost, fNIRS-neurofeedback might provide a suitable and powerful alternative to EEG and fMRI neurofeedback and has great potential for clinical translation of neurofeedback. Together with more rigorous research and reporting practices, further methodological improvements may lead to a more solid understanding of fNIRS-neurofeedback. Future research will benefit from exploiting the advantages of fNIRS, which offers unique opportunities for neurofeedback research.

Keywords: real-time data analysis, functional near-infrared spectroscopy, neurofeedback, systematic review, clinical translation, self-regulation, brain-computer interfacing

INTRODUCTION

Functional near-infrared spectroscopy (fNIRS) is a growing functional neuroimaging technique that exploits the principles of near-infrared (NIR) spectroscopy and brain hemodynamics. Human tissues, including brain tissue, are relatively transparent to light in the NIR range (650–1,000 nm). If NIR light is directed onto the surface of the head most of the light scatters within the underlying tissue, while some of the light is absorbed by pigmented compounds (chromophores). The main chromophore hemoglobin (red blood cells transporting oxygen) absorbs and attenuates the NIR light, and the absorption spectrum of hemoglobin is dependent on the oxygenation level, i.e., oxy- (HbO) $>$ 800 nm and deoxyhemoglobin (HbR) $<$ 800 nm. This principle is utilized by fNIRS to detect relative changes of HbO and HbR levels and thereby indirectly estimating brain activation in the underlying brain tissue via optical sensors placed on the surface of the head (see Ferrari and Quaresima, 2012; Pinti et al., 2018b).

Compared to other neuroimaging modalities, such as functional magnetic resonance imaging (fMRI), electroencephalography (EEG), and magnetoencephalography (MEG), fNIRS shows both advantages and disadvantages. First, the spatial and temporal resolution of fNIRS lies between fMRI and EEG. It provides higher spatial resolution (between 2 and 3 cm) than EEG and potentially higher temporal resolution than fMRI, due to a higher sampling rate. The depth of fNIRS measurements is restricted to neocortical brain regions (Pinti et al., 2018b). FNIRS also has a lower spatial resolution and lower signal-to-noise ratio compared to fMRI (Cui et al., 2011). However, the practicability of fNIRS is a major advantage over fMRI: it is easier to use, portable, safe, nearly silent, inexpensive, and requires little setup time. Moreover, fNIRS measurements tolerate more head motion compared to EEG and fMRI measurements. This makes it possible to use fNIRS in more naturalistic environments/situations (e.g., allowing neural activity to be recorded during overt speech, movement, and direct interaction with another person). Furthermore, it permits populations to be investigated that are more likely to show head motion (e.g., neurological or psychiatric patients or infants) and situations that do not allow fMRI measurements (e.g., participants with ferromagnetic implants or claustrophobia). For recent reviews on the use of fNIRS in neuroscience see Pinti et al. (2018b) and Quaresima and Ferrari (2019).

Given the advantages of fNIRS over other neuroimaging modalities, this technique has been increasingly used as a tool for neurofeedback (Ehlis et al., 2018). During neurofeedback training, participants are trained to self-regulate their brain activity, generally with the ultimate goal of changing behavior or cognitive/emotional functions (for reviews see Thibault et al., 2016; Sitaram et al., 2017; Paret et al., 2019). **Figure 2** (upper part) shows a typical fNIRS-neurofeedback setup. Changes in HbO, HbR, or total hemoglobin (tHb) are assessed via optodes placed on the participants' heads covering a certain brain region of interest and are usually fed back to the subject in the form of visual representations. Individuals can then use this feedback information to learn successful self-regulation of brain activity and ideally transfer this skill to daily life. Successful neurofeedback training usually requires several neurofeedback sessions [1–5 sessions for fMRI-neurofeedback and up to 30 sessions for EEG-neurofeedback (see Thibault et al., 2016)], which is costly and difficult to perform with fMRI.

To date, there has been no comprehensive *systematic* review of fNIRS-neurofeedback studies. The available reviews are either not systematic or are *selective* (not covering all published fNIRS-neurofeedback work). Some reviews focus more on general aspects of fNIRS-based brain-computer interfacing (e.g., Naseer and Hong, 2015; Thibault et al., 2016; Ehlis et al., 2018). For example, a recent review by Ehlis et al. (2018) reviewed several of their own studies alongside a few other experiments. They concluded that fNIRS-neurofeedback training can enable participants to regulate their hemodynamic responses deliberately and that this training may induce changes in brain functions over time. Further, Ehlis et al. (2018) conclude that if future studies confirmed initial findings, fNIRS-neurofeedback may become a complementary or even alternative treatment option for neuropsychiatric disorders.

The present systematic review is divided into five stand-alone sections. We (1) synthesize information about training protocols; (2) provide an overview of the methods used for online

signal-processing to calculate the feedback signal; (3) critically evaluate the quality of published studies including experimental designs, reporting (Tufanaru et al., 2017; Ros et al., 2020), and statistical power; (4) assess and discuss the effectiveness of fNIRS-neurofeedback to regulate and induce pre-post changes in brain activity; and (5) assess and discuss its effectiveness in inducing changes in behavioral/cognitive/emotional[1] outcome measurements in healthy and pathological populations and also review the clinical potential of fNIRS-neurofeedback. We finish the review with a discussion arising from the findings of the five sections and also touch on the future of fNIRS-neurofeedback research.

METHODS

The study protocol for this systematic review was registered on *PROSPERO* and can be accessed at https://www.crd.york.ac.uk/PROSPERO/display_record.php?RecordID=141049. Data from this systematic review are available at the Open Science Framework (see https://osf.io/hnxfq/). We followed the Preferred Reporting Items for Systematic Reviews and Meta-Analyses (PRISMA) guidelines (Moher et al., 2009).

Search Strategy

We searched the following electronic bibliographic databases for studies published up until 3 July 2019: PubMed/MEDLINE, Web of Knowledge/Web of Science, Scopus, and EMBASE. Additional searches were conducted using the Real-time Functional Imaging and Neurofeedback (rtFIN) database (rtfin.org), Cochrane Reviews library database (cochranelibrary.com), Clinicaltrials.gov, scholar.google.de, and preprint servers: biorxiv.org, arxiv.org, psyarxiv.com, medrxiv.org, and osf.io. The following search terms were used: ("functional near infrared spectroscopy" OR "fNIRS" OR "near infrared spectroscopy" OR "NIRS") AND ("real-time" OR "real time" OR "neurofeedback" OR "biofeedback" OR "Brain-Computer Interface" OR "Brain computer interface" OR "BCI" OR "Brain-Machine Interface" OR "Brain Machine Interface" OR "BMI"). More details of the search strategy can be found in the protocol or via the following link: https://www.crd.york.ac.uk/PROSPEROFILES/141049_STRATEGY_20190703.pdf.

Study Selection

We included all published articles with study designs that applied fNIRS-neurofeedback training to regulate brain activity and/or *behavior* in healthy or patient populations. The field is very young and to date no randomized controlled trials have been published. Hence, we applied rather loose inclusion criteria, also including non-controlled, pilot, feasibility, and proof-of-concept studies involving at least four participants. Studies applying fNIRS only for the purpose of brain-based communication or control of devices were excluded. After removing duplicates, the titles and abstracts of 2,821 articles were screened and the full-text of the remaining 33 articles was retrieved and assessed for eligibility. Twenty-two studies met the inclusion criteria and were considered in the qualitative synthesis (see **Figure 1**), involving a total of 441 participants (337 healthy participants and 104 patients).

Data Extraction and Analysis

A spreadsheet was used to document data extracted from the studies. Extracted data included: information about study population and study design, details of the neurofeedback protocol and control conditions; methods used for online signal-processing to calculate the feedback information, and outcomes of the neurofeedback training categorized into behavioral and neural effects within and independent of targeted brain regions (see **Supplementary Material**). After finishing the data extraction, the spreadsheet was sent to all corresponding authors of the included studies to ask for corrections. Fifteen of 22 authors replied and either approved the data extraction or sent minor corrections. We also gave authors the opportunity to comment on a preprint version of the manuscript, which was uploaded at the Open Science Framework (see https://osf.io/hnxfq/) before submission. Further methodological details will be provided in the respective sections.

RESULTS AND DISCUSSION

We present and discuss the results of this systematic review in five sections (depicted in **Figure 2**).

1. Training Protocols

When designing a neurofeedback study and creating a new training protocol, there are a number of aspects to be considered. Some of these include: (1) population(s) to be studied (e.g., healthy or patients or both), (2) neural target for the neurofeedback training (e.g., a particular [set of] brain region(s) or a measure of connectivity), (3) control-group approach (see section 3.1), (4) duration of training, and (5) the neurofeedback procedure, including training conditions (e.g., regulation, rest, transfer), the kind of feedback presentation and task instructions. In this section of the review, we provide an overview of how previous fNIRS-neurofeedback studies established these protocol aspects. We also discuss implications and possible extensions for future studies. **Table 1** shows details of the training protocols used in the studies included in our review.

1.1. Target Populations

Figure 3A shows the different target populations investigated in the studies. Mostly healthy participants were investigated ($N = 337$), but also patients after stroke ($N = 20$), with social anxiety disorder ($N = 12$), autism spectrum disorder ($N = 6$), attention-deficit/hyperactivity disorder ($N = 27$ children and $N = 19$ adults), and adults with high impulsivity ($N = 20$).

1.2. Target Regions

Figure 3B shows the distribution of the neurofeedback target regions of the included studies. The bulk of the studies trained participants to regulate parts of the prefrontal cortex (PFC),

[1]To simplify the text, in the following we subsume the conceptually different behavioral, cognitive, and emotional outcome variables under the general term *behavior*.

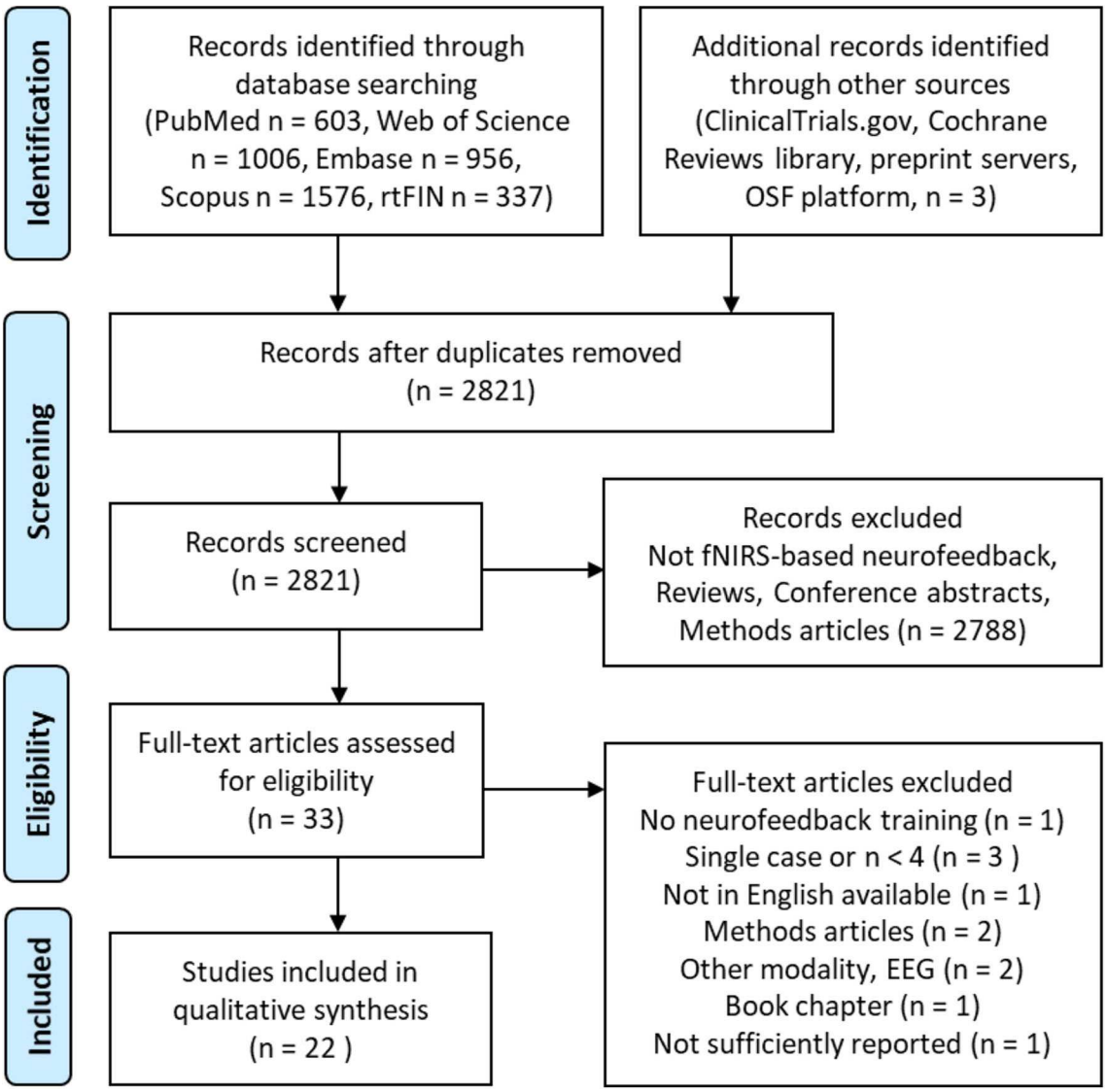

FIGURE 1 | Search decision flow diagram according to preferred reporting items for systematic reviews and meta-analyses (PRISMA; Moher et al., 2009).

i.e., dorsolateral prefrontal cortex (dlPFC), inferior frontal gyrus (IFG), frontal pole or orbitofrontal cortex (OFC). Some studies broadly targeted the PFC using eight to fourteen target channels (Barth et al., 2016; Hudak et al., 2017, 2018; Kimmig et al., 2018) and others targeted specific subregions of the PFC using only one target channel (Li et al., 2019). Another large proportion of the studies trained participants to regulate activation within sensorimotor regions and enhance motor imagery-related brain activation (e.g., Fujimoto et al., 2017). One study reinforced up-regulation of temporal and frontal face-processing regions, as individually defined by a functional localizer (Liu et al., 2016) and another aimed to train a broad affective network of frontal and occipital brain regions using a multivariate classifier approach (Trambaiolli et al., 2018). The signal-to-noise (SNR) ratio likely differs between target regions and depends on scalp-brain or source-detector distance. The SNR is dependent on individual physical features such as individual brain anatomy, head size, skull thickness, and hair properties (e.g., thickness, density, length and color; Orihuela-Espina et al., 2010). On average, the scalp-brain distance is higher in parietal regions and lower in frontal and temporal regions (Cui et al., 2011). These factors should be taken into account when selecting target regions/channels for a neurofeedback study [see also section Selection of Target Regions (Channels of Interest)]. It should be noted that to date no study has used fNIRS-neurofeedback training to target connectivity between specific brain regions.

1.3. Training Duration

The length of training varied broadly between studies and ranged from short one-session designs (nine studies) up to 30 sessions (Hudak et al., 2018), resulting in a total duration of regulation

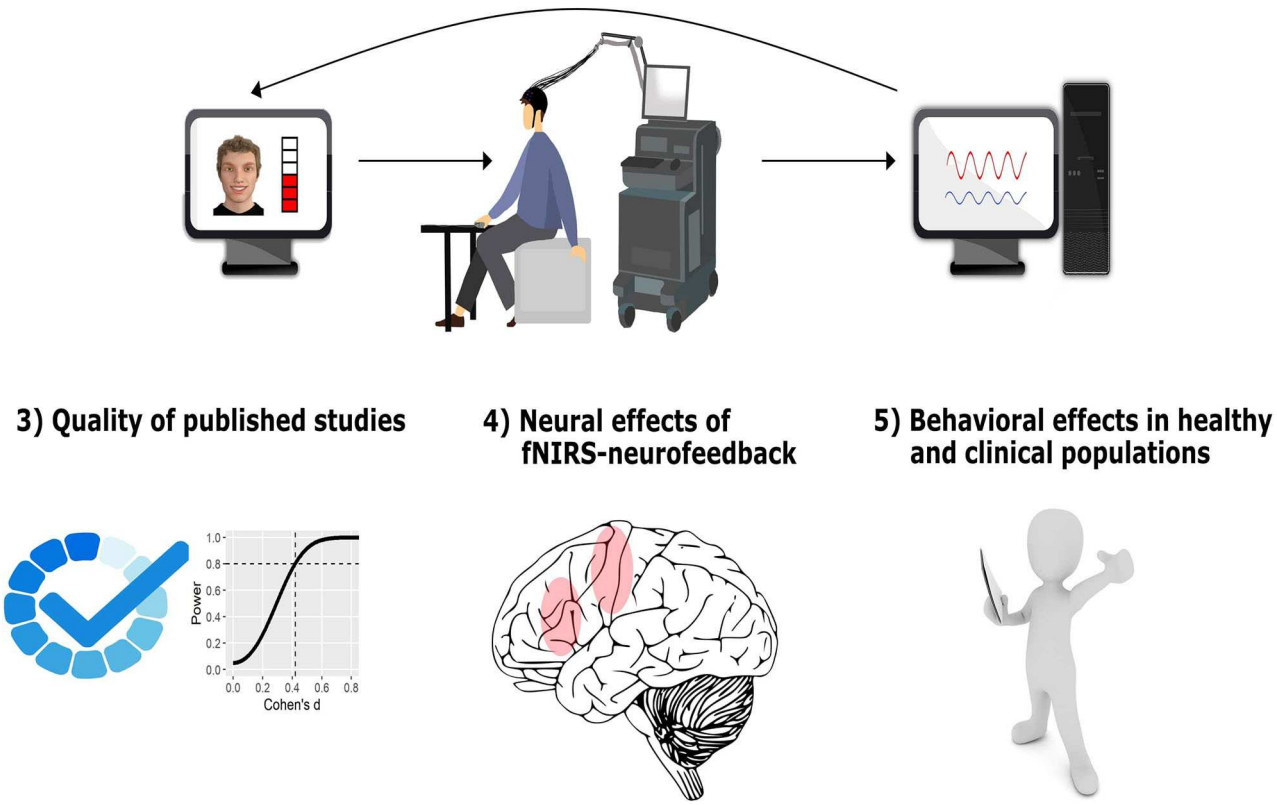

FIGURE 2 | Structure of results and discussion. In the first two sections, we provide a comprehensive overview of how fNIRS-neurofeedback training is implemented, describing and discussing important features of neurofeedback-training protocols (1) and of the real-time signal-processing methods applied (2). In the third section, we critically evaluate the quality of published studies including experimental design and reporting quality as well as statistical power/sensitivity as an indicator of reliability of the reported findings (3). In the fourth section, we assess and discuss the effectiveness of fNIRS-neurofeedback to regulate and induce pre-post changes in brain activity (4). Finally, we assess and discuss its effectiveness in changing behavioral outcomes and we review the clinical potential of fNIRS-neurofeedback (5). The fNIRS illustration was created by Laura Bell.

training that varied between 75 s and up to 8 h. In particular, clinical treatment studies used a higher number of training sessions (Marx et al., 2015; Hudak et al., 2018; Kimmig et al., 2018). The majority of studies applied five sessions or less. While the optimal number of sessions for acquiring self-regulation of hemodynamic brain responses via fNIRS needs to be determined, successful regulation after even a single session has been reported in sham-controlled studies (Fujimoto et al., 2017; Li et al., 2019). Similar to fMRI-neurofeedback, fNIRS-neurofeedback targets spatially specific brain hemodynamics and might therefore offer a faster pace of learning compared to EEG-neurofeedback with most studies involving 20–40 training sessions (see also Marx et al., 2015; Thibault et al., 2018). However, the data of studies by (Marx et al., 2015; Mayer et al., 2015) that directly compared fNIRS- with EEG-neurofeedback still need to be published to shed further light on different learning mechanisms.

1.4. Neurofeedback Procedure

A neurofeedback procedure consists of at least three different aspects: (1) within-run task periods and their timing, (2) feedback presentation (i.e., sensory modality employed, timing, and complexity of feedback information, and (3) instructions provided to participants.

1.4.1. Neurofeedback Run Periods and Their Timing

A neurofeedback run procedure consists of at least two different kinds of periods, i.e., a regulation period during which participants receive neurofeedback and try to change brain activity, and a resting period during which no feedback is provided that can also serve as a baseline-control condition. Most studies instructed participants to rest during the control condition, except for one study that instructed participants to engage in mental counting in an attempt to control for potentially confounding mental processes (Aranyi et al., 2016). Some protocols also included additional reward periods (e.g., smiling faces or points) presented after each regulation trial (Liu et al., 2016; Hudak et al., 2017, 2018; Kimmig et al., 2018), which is a form of additional delayed feedback. Two studies applied a combination of neurofeedback with (socio-)cognitive training and presented delayed feedback on activity during a

TABLE 1 | Neurofeedback training protocol details.

Study	Data for section 1.2 and Figure 3B	Data for section 1.3	Data for section 1.4			
	Target	**Training**	**Neurofeedback run periods and timing**	**Feedback**	**Instructed strategies**	**Regulation (total time)**
Aranyi et al. (2016)	Bilateral dlPFC asymmetry	1 session/1 practice run, 8 real runs/1 trial, 1 day of training	15 s rest/3 s instruction/40 s mental counting baseline/10 s rest/3 s instruction/40 s regulation/7 s rest	Immediate visual feedback, engagement (e.g., gaze, smile) of virtual agent	Express positive feelings toward the agent in order to capture its interest	6 min
Barth et al. (2016)	PFC	8 sessions/1 run/12 trials/ 30 s/8 days over 2 weeks	30 s relaxation (deactivation)/30 s regulation (activation)	Immediate visual feedback of all channels (color-coded)	Not reported	48 min
Fujimoto et al. (2017)	SMA	1 session real and 1 session sham NF/16 trials/5 s/2 days	8–15 s rest/5 s regulation	Immediate visual feedback, height and color of vertical bar	No strategies instructed	80 s
Hosseini et al. (2016)	dlPFC	4 sessions NF during verbal working memory task/1 run/80 trials/4 days over 2 weeks	8–10 s working memory trial (encoding and retention)/2 s test/6–8 s rest and feedback presentation	Delayed feedback, line plot displaying changes during previous ten trials	Meta-cognitive strategies	48 min
Hudak et al. (2017)	Bilateral dlPFC/IFG	8 sessions/2 runs NF/12 trials/1 run transfer/8 trials/session 1–4: 50/50%, session 5–8: 80/20% activation/deactivation trials/8 days over 2 weeks	20 s rest (5 s baseline)/30 s regulation/2 s reward	Immediate visual feedback, virtual classroom scenario: brightness of the lighting in the classroom, reinforcement after each trial	No strategies instructed	96 + 32 min transfer
Hudak et al. (2018)	Bilateral dlPFC/IFG	30 sessions/2 runs NF/12 trials/1 run transfer/8 trials/50/50% activation/deactivation trials/30 days over 12–49 weeks, 3 weeks intermission after session 15	30 rest (5 s baseline)/30 s regulation/2 s reward	Immediate visual feedback was presented via commercial EEG-NF system (moving objects and 2 s reinforcement)	Not reported	360 + 120 min transfer
Kanoh et al. (2011)	Left sensorimotor cortex	5 sessions/6 runs/5 trials/ 20 s/5 days of training	40–43 s rest/20 s up-regulation	Immediate visual feedback (length of white bar)	Motor imagery of right hand	50 min
Kimmig et al. (2018)	Bilateral dlPFC/IFG	15 sessions/2 runs NF/12 trials/1 run transfer/8 trials/75/25% up-/downregulation/15 days over 5–9 weeks, from 7th session: distractor background pictures with fear-related contents	30 s rest (5 s baseline)/30 s regulation/2 s reward	Immediate visual feedback, moving dot, and reinforcement "Well done!," anxiety-related or neutral background pictures from 7th session onwards	Not reported	180 + 60 min transfer
Kinoshita et al. (2016)	Bilateral frontal pole cortex	1 session/6 runs (2 runs real/2 runs sham NF/2 runs transfer) 18 trials/1 day of training	16 s rest/10 s up-regulation	Immediate visual feedback (blue bar)	Memory, executive functions, and verbal fluency strategies suggested	6 min real + 6 min transfer
Kober et al. (2014)	Motor cortex asymmetry	8 sessions/2 runs/40 trials/8 different days	7–11 s rest/6–8 s regulation	Immediate visual feedback, moving dot + numerical score continuously updated	Kinesthetic motor imagery	∼75 min
Kober et al. (2015)	Bilateral IFG	7 sessions/1 run/25 trials/7 different days	27–33 s rest/17–23 s up-regulation	Immediate visual feedback, moving dot + numerical score continuously updated	Motor imagery	∼58 min
Kober et al. (2018)	Bilateral IFG	1 session/1 run/20 trials/1 day (also NF during rest, but instructed to relax and bring signal back to baseline)	30 s rest/17–23 s regulation	Immediate visual feedback (color-coded on a schematic head model)	Kinesthetic motor imagery	∼7 min
Lapborisuth et al. (2017)	Left motor cortex	1 session/8 runs (motor imagery and execution)/4 runs with NF/4 runs without/6 trials	15 s rest/15 s up-regulation	Immediate visual feedback of all channels on a color-coded topographic image	Motor imagery/motor execution	6 min

(Continued)

TABLE 1 | Continued

Study	Data for section 1.2 and Figure 3B	Data for section 1.3	Data for section 1.4			
	Target	**Training**	**Neurofeedback run periods and timing**	**Feedback**	**Instructed strategies**	**Regulation (total time)**
Lee et al. (2015)	Sensory motor cortex	1 session, 2 runs, 1 run treadmill walking without NF, 1 run with NF	15 s rest/10 s up-regulation	Immediate visual feedback (red bar)	Not reported	100 s
Li et al. (2019)	Right lateral OFC	1 session, 1 run 6–10 trials to learn strategy, 4 real training runs/4 trials/one day/10–30 min break in between	25 s rest/25 s up-regulation	Immediate visual feedback, animation: "Lift a stone in front of a beach landscape"	No specific strategies instructed	∼9–11 min
Liu et al. (2016)	Frontal and temporal face processing regions	5 sessions/2 runs/1 run: functional localizer/4 trials morphing faces/1 run training/10 trials, 5 days over 5 weeks	30 s rest/house-matching 20 s/face-matching (up-regulation) 28 s/2s feedback/reward display	Delayed feedback, points displayed after each trial, points were later converted to cash	No specific strategies instructed	∼23 min
Marx et al. (2015)	Bilateral dlPFC/IFG	12 sessions/2 runs NF/12 trials/1 run transfer/8 trials, 50/50% activation/deactivation trials, 12 days within 4–6 weeks	25 s rest (5 s baseline)/30 s regulation/2 s reward	Immediate visual feedback was presented via commercial EEG-NF system (moving objects and 2 s reinforcement)	Not reported	144 + 48 min transfer
Mihara et al. (2012)	Left premotor cortex	1 session real/1 session sham NF/15 trials/1 day	8–15 s rest/5 s regulation	Immediate visual feedback, height and color of vertical bar	Kinesthetic motor imagery	75 s
Mihara et al. (2013)	Ipsilesional premotor cortex	6 sessions/32 trials/6 days over 2 weeks/10 min motor imagery training without NF before each session	8–15 s rest/5 s regulation	Immediate visual feedback, height and color of vertical bar	Kinesthetic motor imagery	16 min
Narita (2015)	Left PFC	2 sessions/7 runs/6 trials/2 days over 1 week? (but not clearly reported)	15 s rest/30 s regulation	Immediate visual feedback, color of monitor	Not reported	∼42 min
Trambaiolli et al. (2018)	Frontal and occipital networks	1 session/2 runs classifier training/2 runs NF/11 trials (5) trials real, 3 trials fixed, 3 trials random feedback (neutral and positive affect conditions)	5 s fixation cross/2 s instruction/30 s positive or neutral affect condition/self-paced self-evaluation	Immediate visual feedback, amorphous figure	Imagine positive personal experiences	5 min
Weyand et al. (2015)	Bilateral PFC	16 sessions/3 runs/20–22 trials (up- and down-regulation)/15 sessions within 3 weeks, last session 10 days later/session 1–5: select strategy/session 6–10: practice strategies/session 11–15: stop strategies, use desire to regulate/session 16: follow-up	20 s rest/17 s regulation	Immediate visual feedback, color-coded topographic image, ball that rises and falls, and game feedback	Yes, specific strategies instructed	277 min

dlPFC, dorsolateral prefrontal cortex; EEG, electroencephalography; IFG, inferior frontal gyrus; NF, neurofeedback; OFC, orbitofrontal cortex; PFC, prefrontal cortex; SMA, supplementary motor area.

cognitive task after a block (Hosseini et al., 2016; Liu et al., 2016). To ensure or assess the transfer of self-regulation skills beyond the neurofeedback sessions, a few studies employed transfer (no-feedback) periods (Marx et al., 2015; Hudak et al., 2017, 2018; Kimmig et al., 2018), where participants received the same instructions as in the neurofeedback task, but without receiving any feedback on their brain activity. Unfortunately, these studies did not report regulation success specifically for transfer periods. While most protocols either trained up- or downregulation, some also trained regulation in both directions, where activation and deactivation periods were randomly presented. The lengths of the regulation and baseline conditions varied broadly across studies from 5–40 to 6–43 s, with most studies varying between 20 and 30 s.

Transfer indicates that a skill is transferred to different situations or tasks. Depending on the contextual factors of the transfer situation, we can distinguish between *near* and *far transfer*, with the latter being more important for the success of training (see Barnett and Ceci, 2002). However, some studies (Marx et al., 2015; Hudak et al., 2017, 2018; Kimmig et al., 2018)

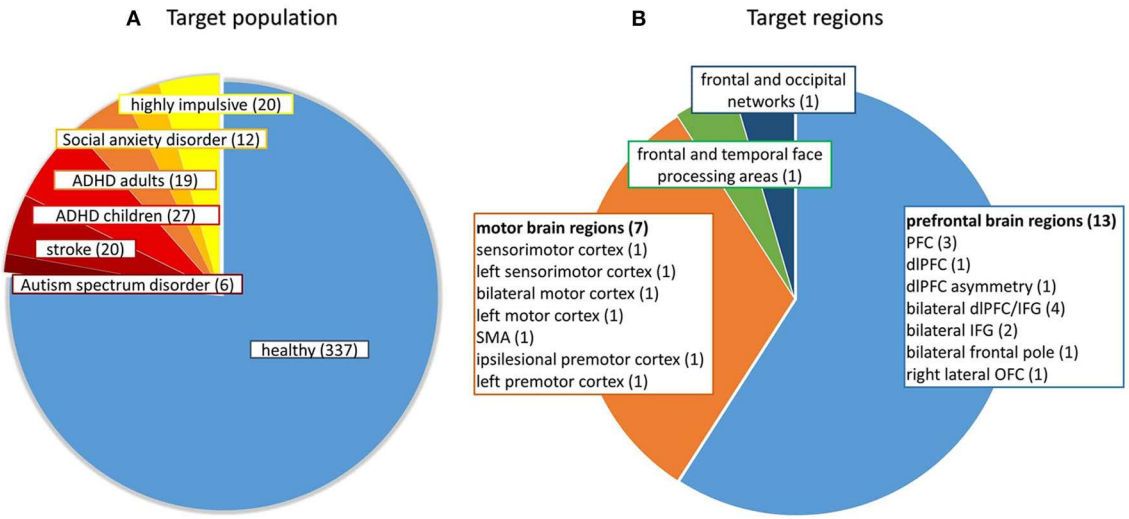

FIGURE 3 | (A) Number of participants from different target populations and **(B)** Number of studies targeting a certain brain region. ADHD, attention-deficit/hyperactivity disorder; dlPFC, dorsolateral prefrontal cortex; IFG, inferior frontal gyrus; OFC, orbitofrontal cortex; PFC, prefrontal cortex; SMA, supplementary motor area.

used the term *transfer* to describe task periods but presented a reward after each *transfer* trial. Hence, they switched from immediate to delayed neurofeedback training and are unable to ensure or demonstrate that participants are able to regulate brain activity without receiving feedback, i.e., to transfer the skill of brain regulation to a new situation and possibly beyond neurofeedback training (*far transfer*). When combining up- and down-regulation within a session, care should be taken to balance the randomization of up- and down-regulation periods in order to keep transition probabilities between periods equal. Otherwise, participants may anticipate and prepare for the following condition, i.e., regulate in the opposing direction during the baseline condition as demonstrated by Hudak et al. (2018). Similarly, anticipatory effects might be prevented by introducing variable onsets of the regulation conditions, as applied by some of the studies. This would render randomization of periods unnecessary and enable to present several up- and downregulation periods in a blocked fashion, which reduces cognitive demands and may facilitate shaping of individual strategies during the training. However, combining up- and downregulation in a single session might involve the risk of carry-over effects between periods, which may impede regulation performance. However, this speculation needs to be corroborated by a comparative study. The optimal trial structure for neurofeedback procedures needs further investigation. Since comparative studies including fMRI- and EEG-neurofeedback research are lacking, we mostly rely on theoretical considerations when designing neurofeedback tasks. Considering the time course of the hemodynamic response (Ogawa et al., 1992), which is delayed and peaks after 4–6 s, a reasonable duration of the regulation and baseline period is 20–30 s. Further research is needed to discover whether shorter or longer periods of up to 40 s (Aranyi et al., 2016) and above are beneficial. While a short duration of 5 s can be considered too short for a hemodynamic response to develop properly, these studies continue to show the feedback signal during a subsequent rest period (Mihara et al., 2012, 2013; Fujimoto et al., 2017). Moreover, we can assume that if feedback is presented immediately (a slowly developing hemodynamic signal), longer durations are required compared to delayed feedback, which is presented considering the activation of a whole previous trial.

1.4.2. Feedback Presentation

The presentation of feedback information may differ with regard to (1) sensory modality (visual, auditory, tactile), (2) timing (immediate vs. delayed), (3) complexity (simple vs. complex virtual environment), and (4) rewarding content (smiling faces or monetary reward). Most of the studies used a simple type of immediate visual feedback in the form of a bar (e.g., Fujimoto et al., 2017) or more complex animations of, for example, rising objects (e.g., Marx et al., 2015; Li et al., 2019), or smiling virtual agents (Aranyi et al., 2016). Others used color-coded topographic maps (Barth et al., 2016; Lapborisuth et al., 2017; Kober et al., 2018), displaying the signal change of all channels while instructing participants to focus on a certain region within the channel arrangement. Kimmig et al. (2018) started with a simple form of visual feedback (moving ball) and introduced neutral and anxiety-related pictures in the middle of the training period to provide a relevant context for patients with social anxiety disorder. Some studies presented delayed feedback in addition to immediate feedback in the form of a reward (e.g., smileys or points) after each trial (Hudak et al., 2017; Kimmig et al., 2018), or only delayed feedback in order to reduce distraction during the task/regulation period (Hosseini et al., 2016; Liu et al., 2016).

Whether immediate or delayed feedback is superior or whether they are equally effective is a matter of ongoing debate and there is only limited and as yet unclear evidence from a few comparative fMRI-neurofeedback studies (see Paret et al., 2019). In case of the noisier fNIRS-neurofeedback, feeding back mean or median activity at the end of each block may avoid confusing participants due to noisy fluctuations of the feedback signal and may also be beneficial with regard to timing (see above). The form of social neurofeedback used by Aranyi et al. (2016) may be experienced as more rewarding and may improve motivation, which is confirmed by preliminary evidence from an fMRI-neurofeedback study demonstrating that social neurofeedback outperforms simple visual feedback and leads to stronger activation of reward-related brain regions (Mathiak et al., 2015). In an effort to increase motivation and facilitate transfer to daily life or critical situations, neurofeedback has been embedded in a 3D virtual-reality environment. While the feasibility of this approach has been demonstrated in a subclinical adult population (Hudak et al., 2017), an ongoing clinical trial in children with attention-deficit/hyperactivity disorder (ADHD) is investigating whether virtual-reality-based neurofeedback is superior to simpler forms of feedback (Blume et al., 2017). Some researchers are opposed to complex feedback, arguing that neurofeedback should lead to knowledge of results and that gaming environments which are too complex may distract participants (Hinterberger et al., 2004; Sherlin et al., 2011). However, comparative studies provide evidence that the more engaging complex feedback embedded in a virtual environment may facilitate learning and is better received by users (Gruzelier et al., 2010; Cohen et al., 2016).

1.4.3. Instructions

In a neurofeedback study, participants are provided with general task instructions about the experiment and in most cases also instructions on how to regulate a certain brain region. Instructions can be very specific (e.g., use motor imagery to regulate motor brain regions) or rather loose (e.g., use mental strategies to change the feedback signal).

Twelve studies instructed participants to upregulate, one to downregulate, and six to up- and down-regulate a certain target region. Another study reinforced asymmetry, i.e., a difference between the activity of a target region and its homolog on the other hemisphere, and two used a multivariate analysis approach to calculate the feedback signal. While some studies provided explicit instructions about types of mental strategies to regulate brain activity, such as kinesthetic motor imagery (Kober et al., 2014) or affective strategies (Trambaiolli et al., 2018), others merely encouraged participants to learn self-regulation using a trial-and-error approach (e.g., Fujimoto et al., 2017; Hudak et al., 2017).

Even if no strategies are provided, study design and general instructions about the experiment may prime the use of certain strategies (Kohl et al., 2019). For example, in the study by Fujimoto et al. (2017), when participants were informed about the target region (supplementary motor area) they might have been tempted to use motor-imagery strategies. Therefore, care needs to be taken when giving task instructions and also when informing participants about the general purpose of the experiment. It is thus important that participants' strategies are documented thoroughly, ideally after each neurofeedback trial or run [see also section Experimental Design and Reporting Quality (CRED-nf Checklist)], although results need to be interpreted carefully, since retrospective self-reports may lack realiability (see Veenman, 2011), particularly in children (Stone and Lemanek, 1990). Whether explicit instructions are beneficial for neurofeedback learning or not remains an open question and may depend on the particular training protocol (see Paret et al., 2019). For instance, it has been suggested that explicit strategies are not necessary, and some work even indicated that they may be detrimental or at least not helpful in some cases (Birbaumer et al., 2013; Sepulveda et al., 2016; Shibata et al., 2019). This is also supported by a recent fNIRS-neurofeedback study (Weyand et al., 2015) where participants used two personalized mental strategies over ten sessions and were then instructed to stop using their strategies and instead to use only their desire to regulate brain activity. Interestingly, regulation performance remained the same after weaning off specific mental strategies and the majority of participants reported training to be less demanding and more intuitive. Nevertheless, strategy instruction may initially facilitate learning (Scharnowski et al., 2015) and may be helpful if successful strategies to regulate a certain brain region are clearly known, e.g., using motor imagery to regulate motor regions. Hence, the decision about instructions may depend on the targeted brain region, duration, and purpose of the neurofeedback-training experiment.

1.5. Conclusion—Training Protocols

FNIRS-neurofeedback has been applied in a variety of populations, including different patient populations, children, adolescents, and older adults. However, previous studies are heterogeneous in terms of (i) selected neurofeedback targets (mostly comprising prefrontal and sensory motor brain regions), (ii) duration of training, and (iii) design of the neurofeedback procedure, including timing, feedback display, and instructions. Generally, as fNIRS measures the same hemodynamic brain signal as fMRI, a large part of the fMRI-neurofeedback training procedures can be (and have already been) transferred to fNIRS-neurofeedback. Note, however, that also for neurofeedback in general there are a lot of open issues with regard to training protocol methods (see Paret et al., 2019). Further systematic research and discussion will help to achieve consensus and make neurofeedback training protocols more efficient.

2. ONLINE SIGNAL-PROCESSING METHODS AND HARDWARE

In this section, we give an overview of the different methods used for online signal-processing, including devices, selection of brain regions (fNIRS channels) of interest, online feature extraction (chromophores used), and preprocessing and artifact control (see also **Table 2**). Providing valid feedback of neural activity to the participant is a crucial component of successful neurofeedback applications. Therefore, methods have to be carefully selected to

TABLE 2 | Online signal-processing methods and hardware.

Study	Data for section 2.1	Data for section 2.2	Data for section 2.4		Data for section 2.3		Data for section 2.5
	Device	Selections of target regions [channel(s) of interest]	Online feature	Chromophore	Online preprocessing	Artifact control	Calculation of feedback signal
Aranyi et al. (2016)	fNIR400	8 channels positioned on subject's forehead	Asymmetry (left vs. right dlPFC amplitudes)	HbO	Low-pass filter (finite impulse response, order 20) 0.1 Hz, sliding-window motion artifact rejection, reference channel	Reference channels	Threshold of signal based on mean, SD, and signal variation of signal during counting (baseline)
Barth et al. (2016)	ETG-4000	14 channels aligned with positions of EEG 10–20 system, registered to MNI space (Tsuzuki et al., 2007)	Amplitude, PFC	HbO	Not reported	None	Change in HbO compared to 15 s baseline at beginning.
Fujimoto et al. (2017)	OMM-3000	4 channels aligned with positions of EEG 10–20 system. MNI positions estimated using individual structural MRI and digitizer measurements	Amplitude (*t*-values estimated by GLM), SMA	HbO	GLM analysis. 20 s sliding window. Linear term to correct drift. 4 short-distance channels (principal component included as regressor in GLM).	EMG, 4 short-distance channels	Contrast regulation vs. rest (adaptive GLM, 20 s sliding window), maximum *t*-value from the 4 channels. Primary principal component of short-distance channels as nuisance regressor
Hosseini et al. (2016)	ETG-4000	Channels aligned with positions of EEG 10–20 system (Okamoto et al., 2004). Functional localizer (working memory task)	Amplitude, dlPFC	HbO	Bandpass filter 0.01–0.5 Hz	No	Change in the average HbO signal over feedback channels (over 9 s window) relative to the calibration period
Hudak et al. (2017)	ETG-4000	8 channels aligned with positions of EEG 10–20 system, registered to MNI space (Tsuzuki et al., 2007)	Amplitude, dlPFC/IFG	HbO	Kalman filter with a 5 s sliding window, CAR of all channels	CAR	Change in HbO compared to 5 s baseline, CAR of all channels subtracted
Hudak et al. (2018)	ETG-4000	8 channels aligned with positions of EEG 10–20 system, registered to MNI space (Tsuzuki et al., 2007)	Amplitude, dlPFC/IFG	HbO	Bandpass filter: 0.01–0.1 Hz, 5 s moving average, CAR of all channels	CAR	Change in HbO compared to 5 s baseline, CAR of all channels subtracted
Kanoh et al. (2011)	ETG-4000	3 channels aligned with positions of EEG 10–20 system	Amplitude sensorimotor cortex	HbO	High-pass filter and 7-point moving average	None	Average of channels/no baseline before task (not explicitly reported)
Kimmig et al. (2018)	ETG-4000	10 channels aligned with positions of EEG 10–20 system, registered to MNI space (Tsuzuki and Dan, 2014)	Amplitude, dlPFC/IFG	HbO	5 s moving average filter, CAR of remaining channels	CAR	Average of channels, change in HbO compared to 5 s baseline. Standard deviation from previous trial used to scale maximum/minimum of feedback signal. CAR of remaining channels subtracted.
Kinoshita et al. (2016)	ETG-4000	6 channels aligned with positions of EEG 10–20 system, registered to MNI space (Tsuzuki et al., 2007).	Amplitude, frontopolar cortex	HbO	Not reported	Respiratory rate	Average of channels, moving baseline, last 10 s. Maximum display of the bar graph was +0.25 [mMmm]
Kober et al. (2014)	ETG-4000	8 channels aligned with positions of EEG 10–20 system registered to MNI space (Singh et al., 2005). Functional localizer to select channels with best signal quality during a motor task	Asymmetry (difference between left and right motor area)	HbO	0.01 HPF and 1.5 Hz LPF, 2 s moving average. Difference of right and left channels (also cancels out artifacts)	4 reference channels	HbO left vs. HbO right. No baseline period before trials

(Continued)

TABLE 2 | Continued

Study	Data for section 2.1	Data for section 2.2	Data for section 2.4		Data for section 2.3		Data for section 2.5
	Device	Selections of target regions [channel(s) of interest]	Online feature	Chromophore	Online preprocessing	Artifact control	Calculation of feedback signal
Kober et al. (2015)	ETG-4000	4 channels aligned with positions of EEG 10–20 system, positions assessed via individual digitizer measurements	Amplitude (difference between lFG and posterior regions)	HbO and HbR group	0.01 high- and 1.5 Hz low-pass filter, 2 s moving average. Difference of lFG and of posterior reference channels	EMG, 4 reference channels	HbO/HbR of FB channels vs. reference channels. No baseline period before trials
Kober et al. (2018)	NIRSport	4 channels, positions assessed via individual digitizer measurements, probably based on EEG 10–20 system	Amplitude, lFG	HbO and HbR group	Not reported	None	Not reported
Lapborisuth et al. (2017)	LABNIRS	14 channels aligned with positions of EEG 10–20 system, positions assessed via individual digitizer measurements	Amplitude, motor cortex	HbO	Detrending and normalization (last 10 s)	None	Difference of current sample divided by SD of previous 10 s and linear trend of previous 10 s
Lee et al. (2015)	FOIRE-3000	7 channels aligned with positions of EEG 10–20 system. Positions assessed via individual digitizer measurements	Amplitude, sensorimotor cortex	HbO	Not reported	None	*t*-values, probably GLM
Li et al. (2019)	NIRSport	1 channel aligned with positions of EEG 10–20 system. Position of channel validated by MRI scans in two independent participants	Amplitude, OFC	HbO	2 s moving average	None	Change in HbO compared to 2 s baseline, feedback scaled based on a pre-experiment ("difficulty coefficient")
Liu et al. (2016)	ETG-4000	Functional localizer at beginning of each session (channel with highest/lowest signal during face processing), positions assessed via individual digitizer measurements	Amplitude, frontal and temporal face processing regions	HbO	Reference channel (channel irrelevant for face-processing network identified during functional localizer)	Reference channel	HbO Percent signal change in feedback channel compared to reference channel (face matching compared to house matching)
Marx et al. (2015)	ETG-4000	8 channels aligned with positions of EEG 10–20 system, registered to MNI space (Tsuzuki et al., 2007)	Amplitude, dlPFC/lFG	HbO	Common average reference (CAR)	No	Change in HbO compared to 5 s baseline
Mihara et al. (2012)	OMM-3000	3 channels aligned with positions of EEG 10–20 system, positions estimated using structural MRI and digitizer measurements of representative participants	Amplitude (*t*-values estimated by GLM), premotor cortex	HbO	GLM analysis. 20 s sliding window, linear term to correct for drift. Autoregressive model order 1 to adjust autocorrelation, excluded 3 participants with finger movement	No, but reported offline control	Contrast regulation vs. rest (adaptive GLM, 20 s sliding window), maximum *t*-value from the 3 channels
Mihara et al. (2013)	OMM-3000	3 channels aligned with positions of EEG 10–20 system, positions estimated using individual MRI and digitizer measurements	Amplitude (*t*-values estimated by GLM), premotor cortex	HbO	GLM analysis, 20 s sliding window. Linear term to correct for drift, autoregressive model order 1 to adjust autocorrelation, EMG control	EMG	Contrast regulation vs. rest (adaptive GLM, 20 s sliding window), maximum *t*-value from the 3 channels
Narita (2015)	PocketNIRS, Dynasense	1 channel aligned with positions of EEG 10–20 system. No information about registration reported.	Amplitude, PFC	HbO	Not reported	None	Not reported

(Continued)

TABLE 2 | Continued

Study	Data for section 2.1	Data for section 2.2	Data for section 2.4		Data for section 2.3		Data for section 2.5
	Device	Selections of target regions [channel(s) of interest]	Online feature	Chromophore	Online preprocessing	Artifact control	Calculation of feedback signal
Trambaiolli et al. (2018)	NIRScout	32 channels aligned with positions of EEG 10–20 system. No information about registration reported	Output of classifier, frontal/occipital networks	HbO, HbR	1 Hz low-pass filter and 3 s moving average, normalization by average signal from the same channel during previous neutral condition	None	Output of linear discriminant classifier based on HbO and HbR of 32 channels, indicating neutral or positive affect
Weyand et al. (2015)	Imagent	9 channels aligned with positions of EEG 10–20 system. No information about registration reported	Classifier, PFC	HbO, HbR, tHb	Third-order Chebyshev IIR cascade filter with pass-band edge frequency of 0.1 Hz, stop-band edge frequency of 0.5 Hz, and pass band ripple of 0.1 dB	None	Session 1–5: weighted slope score. Session 6–16: output of classifier. LDA classifier using 8 features selected from 288 different temporal and spatiotemporal features from all channels and chromophores

CAR, common average reference; COI, channel(s) of interest; dlPFC, dorsolateral prefrontal cortex; EEG, electroencephalography; EMG, electromyography; IFG, inferior frontal gyrus; HbR, deoxyhemoglobin; LDA, linear discriminant analysis; HbO, oxyhemoglobin; PFC, prefrontal cortex; tHb total hemoglobin.

capture the neural activity of a target region and minimize strong extracranial artifacts, as are frequently present in the fNIRS signal (Caldwell et al., 2016).

2.1. Devices

Nine different devices were used in the studies: ETG-4000, OMM-3000, NIRSport, NIRScout, fNIR400, LABNIRS, FOIRE-3000, PocketNIRS, and Imagent. Some devices were used more frequently than others. However, this does not imply qualitative superiority, and it is beyond the scope of this review to judge the functionality of the devices used. Notably, other commercially available devices are used in cognitive neuroscience and custom-developed mobile fNIRS instrumentations (also available open-source: www.opennirs.org) are used for BCI applications (von Lühmann et al., 2015), and may be used for neurofeedback applications. For an overview of commercially available fNIRS systems and their features refer to Scholkmann et al. (2014) and Pinti et al. (2018a). Major differences between the devices are the wavelength used and the amount of wavelength exploited by the systems. Five of the devices used two wavelengths (ETG-4000, NIRSport, NIRScout, Imagent, fNIR400) whereas the other four devices support three wavelengths (OMM-3000, FOIRE-3000, LABNIRS, PocketNIRS). It should be noted that each of the devices used different wavelengths in the range from 690 to 860 nm and had different precisions (e.g., dynamic range or sensitivity, based on the hardware and its quality). These differences can potentially constitute confounds in the context of reproducibility of neurofeedback results. The use of more wavelengths can improve signal quality (Arifler et al., 2015) and might therefore be beneficial for fNIRS-neurofeedback applications.

2.2. Selection of Target Regions (Channels of Interest)

In order to target specific brain regions reliably, the studies applied different methods to verify appropriate channel selection for extracting the neurofeedback information. In fNIRS-neurofeedback studies, a certain number of optodes are placed on the participants' heads (general optode setup), then some of the channels ('channels of interest') are selected to extract the neurofeedback information. All the studies used *a priori* knowledge about the assumed location of specific brain regions involved in the regulation task. Additionally, most studies used the EEG 10–20 system (Jasper, 1958) as a reference to place the optodes (20 out of 22 studies; **Table 2**) and the methods of Okamoto et al. (2004), Singh et al. (2005), or Tsuzuki et al. (2007) to register channels to the MNI space. Alternatively (or in combination), the positions were either verified by an individual or reference structural MRI scan combined with a digitizer measurement (Fujimoto et al., 2017) or a functional localization procedure was performed. Eight studies used additional digitizer measurements to verify channel positions *post-hoc*. Three studies used a functional localizer before the training session to select task-relevant channel(s) with individually good signal quality (Kober et al., 2014; Hosseini et al., 2016; Liu et al., 2016). In one study, the optodes were placed on the forehead of the subject without describing the use of other reference points (Aranyi

et al., 2016). Three studies provided no further information about additional registration of the optodes. For the eight studies using digitizer measurements, the channels were positioned with respect to the neurofeedback target region based on MNI coordinates using virtual spatial registration or general head location in combination with a functional localizer (Liu et al., 2016). The input for the online feature was either a single channel or the average signal of channels covering the region of interest. The number of channels used for extracting the neurofeedback information ranged from 1 to 14 for studies using amplitude changes and 9 to 32 channels for studies using multivariate statistics as a feature for the feedback (see **Table 2**).

In sum, the selection of channels of interest relied mainly on the EEG 10–20 system in combination with MNI coordinates and *a priori* knowledge about specific brain regions that are involved in the regulation task, which is a suitable procedure for selecting target channels. A combination with functional localizers seems to be a more reliable solution (if applicable) for amplitude-based studies since it additionally takes subject-specific variance into account by selecting individualized channels. Additionally, using digitization of optode locations and alignment with (preferably individual) MRI scans allows even more details to be obtained on optimum placement of the optodes.

2.3. Online Pre-processing and Artifact Control

The fNIRS signal comprises different sources of noise. Most problematic in the context of real-time analysis seems to be the physiological noise that overlaps partly with task frequency, such as low-frequency oscillations of blood pressure (Mayer waves; Kamran et al., 2016). The studies applied different online preprocessing methods to deconfound the feedback signal from these sources of noise. Five studies did not report the online preprocessing methods they used and are thus not further considered in this review with respect to their preprocessing (Lee et al., 2015; Narita, 2015; Barth et al., 2016; Kinoshita et al., 2016; Kober et al., 2018). The majority of the studies which reported their online pre-processing steps applied different kinds of high- and low-pass filters (10 of 17; **Table 2**). Some studies did not use a high-pass filter (e.g., Aranyi et al., 2016; Kimmig et al., 2018; Li et al., 2019). For low-pass filtering, mainly finite impulse response (FIR) filters were used, most commonly a moving-average filter (window ranging from 2 to 5 s). Four studies (Marx et al., 2015; Hudak et al., 2017, 2018; Kimmig et al., 2018) used a common average reference (CAR) for data preprocessing, i.e., subtracting the average of all channels from the feedback channel, three of these in combination with additional filtering. Four studies used one or multiple reference channels (Kober et al., 2014, 2015; Aranyi et al., 2016; Liu et al., 2016). However, considering the lack of relevant information in other studies, it may be the case that some of these studies used additional filters but did not report them. Most of the studies did not use any explicit artifact control on top of the filtering methods (7 of 17). The studies that used artifact control to some degree most frequently employed either CAR or reference channels (8 out of 11) and one study (Kober et al., 2015) also included electromyography (EMG) measures for *post-hoc* artifact control. Only one of these eight studies used short-distance channels to control for artifacts (in combination with EMG measures, Fujimoto et al., 2017). Two studies used either only EMG (Mihara et al., 2013) or the respiration rate (Kinoshita et al., 2016) as a reference for *post-hoc* artifact control, which was implemented using, for example, visual inspection of the EMG signal or differences in the respiration rate. Aranyi et al. (2016) used a sliding-window motion artifact rejection (SMAR) procedure, which rejected motion-affected periods in the fNIRS signal. Other motion correction methods suitable for real-time applications, e.g., Cui et al. (2010), were not applied.

Surprisingly, only three out of the nine studies that targeted motor regions used EMG to control for subtle movements (Mihara et al., 2013; Kober et al., 2015; Fujimoto et al., 2017), which can confound the feedback signal, and details of the EMG analysis are rarely reported. Other studies did not control for this confound or only visually inspected movements of the participants (Mihara et al., 2012). It is important that future studies targeting motor regions control for this confound. To date, studies have only looked at motion artifacts *post-hoc*. Future studies could establish methods to control for EMG signals online, e.g., stop presenting feedback signal when movements occur or include the EMG signal as a nuisance regressor when using a general linear model (GLM) approach to calculate the feedback signal. Some studies did not apply high-pass filtering. It could be argued that if the feedback signal is compared to a preceding baseline in a short time frame, low-frequency drifts can be neglected, which would render high-pass filtering unnecessary. However, this remains to be confirmed by future research.

In general, the field would benefit from implementing more sophisticated artifact-control methods to account for potential confounding signals (Caldwell et al., 2016; Tachtsidis and Scholkmann, 2016; Pfeifer et al., 2018). Short-distance channels in combination with GLM seem to be the most efficient tool to correct for extracerebral physiological signal components (Brigadoi and Cooper, 2015; Tachtsidis and Scholkmann, 2016; von Lühmann et al., 2020). As already stated, only Fujimoto et al. (2017) used this technique, which may be because most of the fNIRS systems are not equipped with the appropriate hardware (Klein and Kranczioch, 2019). If this is the case, a potential alternative is the global component removal approach as introduced by Zhang et al. (2016). This technique seems to be promising to reduce global physiological signals from the fNIRS data and can be used for online artifact control as recently pointed out by Klein and Kranczioch (2019) specifically with respect to single-trial data. FNIRS-neurofeedback studies have not yet applied this method but have rather used CAR or other referencing to correct for evoked systemic cerebral and extracerebral components. However, referencing should be applied with care, as reference channels have to be independent of the target region and participants may modulate the feedback signal by regulating reference channels instead of feedback channels (Hudak et al., 2018). Therefore, the global component-removal approach could be a viable alternative. However, if none of those methods is available during the experiment it should

be checked *post-hoc* that these global signals did not drive the neurofeedback signal change.

2.4. Online Feature—Chromophores Used

For the online feature, either the amplitude or a derivative of the HbO or HbR was used, or a classifier was trained to discriminate specific states. Most studies (20 of 22) used a type of amplitude change. In examining the studies that used the amplitude, we found three studies (Mihara et al., 2012, 2013; Fujimoto et al., 2017) which used the maximum *t*-value of the selected channels. All other studies used the HbO or HbR amplitude as a direct source for the feedback, scaled to a certain level, and referenced to a specific period before the feedback. For the studies using a classifier, a linear discriminant analysis (LDA) classifier was trained to discriminate two classes (e.g., neutral or positive affect; Weyand et al., 2015; Trambaiolli et al., 2018).

Even though there are multiple options for the source of neurofeedback information using fNIRS, most of the studies used HbO. Only two of the 22 studies used both chromophores and only two used HbR and HbO for different study groups (Kober et al., 2015, 2018). It is important to note that two of the four studies that used both chromophores employed a classifier approach (Trambaiolli et al., 2018), and one also included tHb (Weyand et al., 2015). All other studies used the direct amplitude of HbO/HbR or a derivative of it. Kober et al. (2018) showed that people can regulate both chromophores with fNIRS-neurofeedback, but depending on the regulation strategy (in this case motor imagery to alter brain activation) regulation ability may be restricted to the natural course of the HbO and HbR signal changes related to this strategy.

The best-suited chromophore for neurofeedback (and other BCI) applications is still a matter of debate and has not been intensively investigated. Most studies use HbO since it displays larger amplitudes than HbR (Stangl et al., 2013; Sato et al., 2016). On the other hand, Kirilina et al. (2012) reported HbR to be less sensitive to artifacts. However, a recent study (Klein and Kranczioch, 2019) demonstrated that HbR is also affected by a global signal component. The contrast-to-noise ratio seems to be comparable for HbO and HbR across different tasks (Cui et al., 2011), but according to Naseer and Hong (2015) HbO signals were more discriminative for BCI applications than those of HbR signals.

In sum, although less frequently used, current evidence does not imply that HbR or tHb are less suitable for fNIRS-neurofeedback. While all three options (HbO, HbR and tHb) seem to be suitable, future research is still needed to ascertain whether one option outperforms the others in the context of neurofeedback applications.

2.5. Calculation of Feedback Information

The calculation of the feedback signal greatly depends on the type of display used for the presentation (see section 1.4.2). Generally, the amplitude of the HbO signal during the feedback/task block was used and either compared to a preceding baseline (e.g., Hudak et al., 2017, 2018), the fNIRS-system baseline (Barth et al., 2016), or a baseline of the GLM (e.g., Fujimoto et al., 2017). The signal of interest can additionally be compared to a different channel not covering the region of interest (Liu et al., 2016) or asymmetry scores can be calculated, e.g., difference between right- and left-hemispheric channels (Aranyi et al., 2016). For the two studies using a multivariate approach, the feedback was based on the output of the classifier identifying neutral or positive affect (Weyand et al., 2015; Trambaiolli et al., 2018). Two studies (Narita, 2015; Kober et al., 2018) did not report the methods used for feedback calculation. Using the system baseline instead of a preceding baseline before each trial seems risky, since low-frequency drifts may confound the signal if the applied preprocessing methods do not capture them properly.

Another important aspect is the selection of feedback thresholds, i.e., defining the amount of signal change necessary for change and setting a minimum and maximum of the presented feedback. For example, thresholds were defined based on signal variation during the preceding control condition (Aranyi et al., 2016; Kimmig et al., 2018) on the basis of *t*-values, which was also used for feedback (Fujimoto et al., 2017), or based on a certain HbO change (Kinoshita et al., 2016). Li et al. (2019) calibrated thresholds based on a pre-experiment conducted in an independent sample. However, some studies did not transparently report how the threshold used for feedback was defined [see also section 3.2].

2.6. Conclusion—Online Signal-Processing Methods and Hardware

While the studies reviewed applied a considerable diversity of online signal-processing methods, some similarities across the studies were also evident, e.g., regarding online-feature and chromophore selection. Unfortunately, crucial information regarding online signal-processing procedures was often missing. Since there are no established standards for online or offline processing methods (Kamran et al., 2016; Pinti et al., 2018b), future studies are encouraged to explore different methods and provide sufficient information so that other studies can easily replicate successful methods.

Assuring signal quality is crucial for neurofeedback applications, particularly for fNIRS-neurofeedback, which suffers from strong extracranial artifacts. A careful selection of online signal-processing methods is necessary to avoid the presentation of invalid feedback information. Further developments and more systematic research on fNIRS online signal-processing methods are definitely needed to overcome this specific shortcoming of the fNIRS technology.

3. QUALITY OF PUBLISHED STUDIES

In this section, we assess and discuss the quality of published studies including (1) features of experimental designs and methodological quality according to the JBI ratings, (2) design and reporting quality according to the CRED-nf checklist, and (3) analysis of statistical power/sensitivity as an indicator of reliability of the reported findings.

3.1. Quality of Experimental Designs

Table 3 shows important features of the experimental designs of the studies.

TABLE 3 | Study designs.

Study	Data for 1.2 and Figure 3B	Data for 1.2 and Figure 3A	Data for 3.1				
	Target	**Participants**	**Control group**	**Randomization**	**Blinding**	**Follow up**	**Transfer**
Aranyi et al. (2016)	dlPFC asymmetry	18 healthy	None	No	No	No	No
Barth et al. (2016)	PFC	13 healthy	None	No	No	No	Separate task
Fujimoto et al. (2017)	SMA	20 healthy	Sham (yoked feedback, within)	Yes	Single-blinded	No	No
Hosseini et al. (2016)	dlPFC	20 healthy	Sham (yoked feedback)	No	Not reported	No	No
Hudak et al. (2017)	Bilateral dlPFC/IFG	20 highly impulsive	EMG biofeedback	Yes	No	No	Separate tasks
Hudak et al. (2018)—excerpt from Mayer et al. (2015)	bilateral dlPFC/IFG	19 adults with ADHD	None	No	No	Not reported, but protocol included FU	No
Kanoh et al. (2011)	Left sensorimotor cortex	5 healthy	None	No	No	No	Separate task
Kimmig et al. (2018)	Bilateral dlPFC/IFG	12 SAD	None	No	No	No	Separate task
Kinoshita et al. (2016)	Bilateral frontal pole cortex	24 healthy	Sham feedback (artificially generated, within)	Yes	Single-blinded	No	Yes
Kober et al. (2014)	Motor cortex asymmetry	17 healthy	Sham (yoked feedback, within)	Yes	Single-blinded	No	No
Kober et al. (2015)	Bilateral IFG	20 healthy	HbO vs. HbR-group	Yes	Single-blinded	No	Separate task
Kober et al. (2018)	Bilateral IFG	48 healthy/12 per group	Bidirectional control for HbO and HbR	Yes	Single-blinded	No	No
Lapborisuth et al. (2017)	Left motor cortex	22 healthy	Motor imagery without feedback (within)	No	No	No	Yes
Lee et al. (2015)	Sensory motor cortex (S1, M1, SMA)	4 healthy	Motor task without feedback (within)	Unclear	No	No	No
Li et al. (2019)	Right lateral OFC	60 healthy	Sham (yoked feedback)	Yes	Single-blinded	No	No
Liu et al. (2016)	Frontal and temporal face processing regions	2 healthy, 2 ASD	Sham feedback (artificially generated)	Yes	Not reported	No	No
Marx et al. (2015)	Bilateral dlPFC/IFG	27 children ADHD/9 per group	EEG and EMG biofeedback	No	No	2 weeks and 6 months	Separate tasks
Mihara et al. (2012)	Left premotor cortex	21 healthy	Sham feedback (artificially generated, within)	Yes	Single-blinded	No	No
Mihara et al. (2013)	Ipsilesional premotor cortex	20 stroke patients	Sham feedback (artificially generated)	Yes	Double-blinded	2 weeks	No
Narita (2015)	Left PFC	4 ASD	None	No	No	1–3 months	No
Trambaiolli et al. (2018)	Frontal and occipital networks	33 healthy	Sham feedback (artificially generated, within)	Conditions presented in random order	Single-blinded? Not clearly reported	No	No
Weyand et al. (2015)	Bilateral PFC	10 healthy	None	No	No	10 days	No

ADHD, attention-deficit/hyperactivity disorder; ASD, autism spectrum disorder; ADHD dlPFC, dorsolateral prefrontal cortex; EEG, electroencephalography; EMG, electromyography; IFG, inferior frontal gyrus; HbR, deoxyhemoglobin; OFC, orbitofrontal cortex; HbO, oxyhemoglobin; PFC, prefrontal cortex; SAD, social anxiety disorder; SMA, supplementary motor area.

3.1.1. Control Conditions

Depending on the specific research aim, neurofeedback studies can make use of several different control conditions. Control conditions may include, treatment-as-usual, bidirectional-regulation control, feedback of an alternative brain signal, sham feedback, and mental-rehearsal control, and can be applied in a within- or between-subject design (see Sorger et al., 2019). Ideally, multiple control conditions are applied in order to disentangle neurofeedback-specific from unspecific processes. In this regard, Lubianiker et al. (2019) recently proposed an extension of established control conditions, in which participants of the control group are randomly assigned

to a subset of different neural control targets (randomized ROI control condition). In this way, specific effects related to the control targets and neurofeedback-unspecific processes that likely differ for different neurofeedback targets may average out across all subjects of this control group. For extensive discussions on different control conditions in neurofeedback research, see Lubianiker et al. (2019) and Sorger et al. (2019).

Seven of the studies did not use any control condition. Nine studies used a sham feedback based on either artificially created signals (five studies) or based on a brain signal of another participant (yoked feedback, four studies). Two studies compared the effects with other forms of biofeedback (EEG- or EMG-based). One study compared the effects of motor-imagery neurofeedback with mental rehearsal (motor imagery only) and another compared neurofeedback during a motor task with motor task only in a within-subject design. Also, the effects of neurofeedback based on HbO and HbR were compared in a between-subject design without an additional sham-feedback condition (Kober et al., 2015) and in a bidirectional-control approach, investigating four different groups (Kober et al., 2018).

3.1.2. Randomization and Blinding

Of the fifteen studies with a control group, eleven studies randomized assignment to groups or order of conditions. Seven studies blinded participants to conditions and only one applied double-blinding. However, in some situations blinding is not possible, e.g., when comparing neurofeedback to another treatment. These studies attempted to reduce bias by not informing participants about any other treatment than that which they received (Marx et al., 2015; Hudak et al., 2017), which may at least help to keep levels of expectation and motivation equal across groups. Assessments of motivation, expectation, or other unspecific factors can be included in future studies to check this assumption.

3.1.3. Assessment of Transfer

To assess a transfer effect, four studies made use of transfer trials or no-feedback conditions, where participants received the same instructions as in the neurofeedback task, but without receiving any neurofeedback information. As described in section 1.4, some studies used a very liberal definition of the term transfer (if at all a very *near transfer*; see Barnett and Ceci, 2002). Five studies (Mihara et al., 2012; Kober et al., 2015; Barth et al., 2016; Hudak et al., 2017; Kimmig et al., 2018) assessed transfer using other computerized tasks and investigated whether activation within the targeted brain region changes after neurofeedback training, and were able to demonstrate transfer beyond neurofeedback training (far transfer).

3.1.4. Follow-Up Measures

Only four of the studies investigated long-term effects of neurofeedback in a follow-up (10 days up to 6 months after neurofeedback training) in order to investigate whether participants were still able to regulate brain activity after a period without training (Weyand et al., 2015) or stability of observed behavioral effects (Marx et al., 2015). Evidence of delayed effects of neurofeedback emerging after the primary endpoint of a study has been reported. Particularly when investigating clinical populations, follow-up measures may boost statistical power and should be applied where possible (Rance et al., 2018; Van Doren et al., 2019).

3.1.5. Methodological Quality (JBI Critical Appraisal Tool)

To assess the methodological quality of the included studies, we used the checklist for quasi-experimental studies of the Joanna Briggs Institute (JBI) critical appraisal tools (Tufanaru et al., 2017). Two of the authors (SK and DM) independently rated studies according to the nine criteria of the checklist. These items include: *clarity of cause and effect (temporal relationship between variables), similar participants; similar treatment in compared groups; existence of a control group/condition; multiple measurement points of the outcome; completion of follow-up; similar outcome measurements in compared groups; reliability of outcome measurements; appropriate statistical methods*. Each study was allocated points based on the number of criteria fulfilled. Disagreements between the review authors were resolved by discussion. For further details about rating criteria, see **Supplementary Material**.

Table S1 shows the results of the ratings for each study. On average 5.55 ($SD = 2.15$) of 9 required quality criteria were rated "yes." It should be noted that only four studies used appropriate statistical methods according to this rating. Most of the studies were rated as not using appropriate statistical methods because they did not justify their sampling plan or omitted labeling their study a *pilot, feasibility* or *proof-of-concept* study.

3.2. Experimental Design and Reporting Quality (CRED-nf Checklist)

To assess experimental design and reporting quality we used the current version of the CRED-nf (Consensus on the reporting and experimental design of clinical and cognitive-behavioral neurofeedback studies) checklist (Ros et al., 2020). The CRED-nf checklist is designed to encourage best practice in terms of experimental designs and reporting of neurofeedback studies. It covers seven domains (*Pre-experiment, Control groups, Control measures, Feedback specifications, Outcome measures brain, Outcome measures behavior, and Data storage*), including 23 checklist items, fifteen of which are considered *essential,* and eight *encouraged*. In contrast to the JBI checklist, the CRED-nf checklist does not include subjective ratings. Instead, it assesses whether a study reports contents required by a respective item, e.g., "Report the feedback modality and content." One of the authors (SK) filled in a checklist for each study with page numbers identifying where each point was addressed. The number of addressed items of both categories *essential* and *encouraged* are reported for each study. For further details see **Supplementary Material**.

Table 4 and **Table S2** show detailed results of the CRED-nf checklist, including a short description of individual items of the respective CRED-nf domains. On average 63.03% (∼9 of 15) of the essential items and 10.23% (∼1 of 8) of encouraged items were reported. It should be noted that this best-practice checklist was published only very recently after all the included studies

TABLE 4 | Reporting and design quality according to the CRED-nf checklist.

CRED-nf domain	M ± SD (%)
Pre-experiment	20.45 ± 25.16
Control groups	25.45 ± 22.41
Control measures	42.73 ± 22.51
Feedback specifications	90.00 ± 13.45
Outcome measures—brain	53.03 ± 31.97
Outcome measures—behavior	18.18 ± 24.62
Data storage	0.00 ± 0.00
CRED-nf essential	63.03 ± 18.49
CRED-nf encouraged	10.23 ± 9.94
CRED-nf total	44.66 ± 13.56

Mean percentages and standard deviations of items rated "yes" for the different domains of the CRED-nf checklist. Detailed results for individual studies and items, including a description of the items of the respective domains, can be found in ***Table S2****. CRED-nf, consensus on the reporting and experimental design of clinical and cognitive-behavioral neurofeedback studies checklist (Ros et al., 2020).*

had been published. Hence, the authors of the included studies as well as ongoing studies could not make use of this resource in designing their experiments and publishing their results.

The domain *Pre-experiment* was not very well reported, on average only 20.45% of the items were included. Only one study reported a pre-registration of the experimental protocol (Hudak et al., 2018). However, this study deviated from the originally published registration (Mayer et al., 2015) and investigated a different research question including only a subsample of participants. None of the studies conducted a power analysis in order to justify sample size. Eight of the 22 studies were labeled as a *pilot*, *feasibility*, or *proof-of-concept* study, which renders a power analysis unnecessary.

On average only 25.45% of the items in the domain *Control groups* were reported, which is related to the fact that only a few clinical trials have yet been published and seven uncontrolled studies were included. Of the fifteen controlled studies, nine reported having used single- or double-blinding or at least discussed the fact that blinding was not possible (Marx et al., 2015; Hudak et al., 2017). Only one study reported having blinded raters of the outcomes or whether participants/experimenters remained blinded. Two of the clinical studies employed a standard-of-care intervention group as a benchmark for improvement (Mihara et al., 2013; Marx et al., 2015).

With respect to the domain *Control measures,* the studies reported on average 42.73% of the items. Six studies reported having used some measure of psychosocial or non-specific factors (e.g., motivation, expectation, effort). Since these measures are easy to implement and do not require much additional time, we recommend that future studies should make more use of this additional easy and low-cost method of controlling for non-specific effects. Almost a third of the studies did not report whether participants were provided with a strategy and only six studies reported strategies used by the participants. Even if no explicit strategies are provided, study design and general instructions about the experiment may prime the use of certain strategies. The use of mental strategies undoubtedly affects brain activity and may also induce behavioral effects on its own. Hence, better control and transparent and more detailed reporting of this factor is required, which may also contribute to solving outstanding issues of the utility of strategy instructions (see also section Neurofeedback Run Periods and Their Timing).

The domain *Feedback specifications* was well reported, on average 90% were included. All studies included feedback modality and content as well as the software and hardware used, and almost all studies reported the definition of the online-feature extraction. Sixteen of the studies also included at least some information about the reinforcement schedule, for example feedback-threshold criteria, but did not justify this in relation to the existing literature. Also, the amount of reward received by participants was rarely included. While most studies reported the essential contrast used for feedback, i.e., regulation *vs*. rest, only eight of the studies described both conditions of regulation and rest separately.

Studies reported on average 53.03% of the items related to *Outcome measures—Brain*. Most studies included neurofeedback regulation success based on the feedback signal. However, some studies did not report regulation success at all (Marx et al., 2015; Narita, 2015), while others only reported regulation success of representative participants or only based on significant channels and took surrounding channels that were not used for feedback calculation into account instead of reporting the average of all feedback channels (e.g., Mihara et al., 2012; Lapborisuth et al., 2017). This lack of transparency makes it difficult to conclude whether neurofeedback was at all effective on the brain level. Less than half of the studies plotted the feedback signal of within-session or between-session regulation blocks of the feedback signal, which would permit further insights into the dynamics of regulation performance over the course of the training period. Only seven of the studies statistically compared the experimental to the control condition or group. There were seven uncontrolled studies unable to make such a comparison. Hence, seven controlled studies did not undertake this comparison, but rather analyzed groups/conditions separately, which does not allow any conclusions to be drawn about group differences and makes it difficult to appraise the effectiveness of neurofeedback (Nieuwenhuis et al., 2011).

On average only 18.18% of items in the domain *Outcome measures—Behavior* were reported. However, this low rate can be explained by the fact that most studies were mainly interested in regulation performance, and behavioral variables did not represent the primary outcome or were not assessed at all. Of the 14 studies that actually assessed a behavioral variable, eight reported a correlation between regulation success and behavioral outcome. None of the studies included measures of clinical or behavioral significance, such as the minimal clinically important difference (MCID; Engel et al., 2018). However, there are only a few clinical studies in which such a measure is applicable.

None of the studies reported having uploaded materials, analysis scripts, code, or data to an open-access data repository.

3.2.1. CRED-nf Checklist—Conclusion

In sum, the reporting quality of published studies can be considered to be moderate to low in the light of current

consensus guidelines. While some domains such as *Feedback specifications* were well reported, other such as *Pre-experiment* or *Data Storage* were not. The CRED-nf checklist provides guidelines for best practice with regard to experimental design and reporting of neurofeedback studies. The field of fNIRS-neurofeedback is still very young and some of the standards set by the CRED-nf checklist do not yet apply at this early stage. For example, double-blinding or a measure of clinical or behavioral significance should be included at the stage of randomized controlled trials, but not necessarily in early proof-of-concept studies that primarily aim to test neural regulation performance. However, we note that we applied more lenient criteria for some of the items, which resulted in higher ratings than if we had applied the original items. This should be considered in future comparisons applying the CRED-nf checklist. As stated above, this best-practice checklist was not available when the studies included in this review were published. Hence, a lack of reporting for some items should be expected at this early stage. Nevertheless, the incomplete reporting identified in the domain *Outcome measures—Brain* gives reason for concern. Without this information, we cannot clearly identify whether participants learned to control the brain signal of interest. As is common across the published literature, findings that do not meet a threshold for statistical significance may remain underreported in the fNIRS-neurofeedback literature. Future studies could benefit from orienting toward these new guidelines, while also abiding by other guidelines for reporting clinical trials, such as CONSORT (Schulz et al., 2010). We encourage researchers to use the CRED-nf checklist as an orientation when designing new studies and suggest they make use of the CRED-nf web application (rtfin.org/CREDnf) when submitting results for publication. The web application helps authors to standardize the reporting of CRED-nf items, which will facilitate future systematic reviews.

3.3. Statistical Power/Sensitivity

To further assess study quality, we extracted information about the reported sample sizes and estimated statistical power/sensitivity of the included studies. Statistical power, the probability of detecting an effect size of a certain magnitude with a given sample size and accepted threshold for the probability of a false-positive finding, is an important indicator for the reliability of reported findings and will therefore be investigated here.

The majority of neuroscientific studies, including neuroimaging studies, feature relatively small sample sizes and hence remarkably low statistical power for detecting realistic (i.e., small to moderate) effect sizes (Button et al., 2013; Poldrack et al., 2017). Furthermore, small sample sizes imply higher variability around effect size estimates. In combination with publication bias (i.e., the tendency to publish mainly significant findings), reported effects thus tend to be overestimated (Algermissen and Mehler, 2018), rendering the scientific literature in psychology and neuroscience an unreliable basis for conducting power analyses for future studies (Szucs and Ioannidis, 2017; Allen and Mehler, 2019; Schäfer and Schwarz, 2019).

Computing statistical power requires knowledge of the effect size that is considered relevant and worth detecting, i.e., the smallest effect size of interest (SESOI). *Post-hoc* power analyses that are commonly not based on SESOIs represent mere transformations of the *p*-value. Such an approach cannot therefore provide any information about the *a priori* power of the included fNIRS studies. Since SESOIs are highly experiment-specific (Lakens et al., 2018) and unknown to us, it proved difficult to set an SESOI for (1) regulation performance and (2) behavioral outcomes for our purpose. First, we note that neurofeedback experiments represent complex interventions (Sitaram et al., 2017) during which various factors, or their interaction, may determine the outcome (see also section 1.4). We also note that neurofeedback studies vary greatly in how they define and quantify successful regulation (Paret et al., 2019) and different definitions may reveal different effect sizes. Second, SESOIs for behavioral outcomes will depend on the specific paradigm (e.g., motor imagery or emotion regulation), outcome variable (e.g., reaction times or self-rated measures of emotion regulation), and study population (i.e., healthy participants or patient populations, and for patient groups the type of clinical population, e.g., stroke or depressed patients). Therefore, we did not set an SESOI to calculate the *post-hoc* statistical power of fNIRS-neurofeedback studies, but instead used Cohen's conventions, covering a range of effect sizes that may be comparable to potential SESOIs ($d = 0.2$, 0.5, and 0.8; Cohen, 1992).

Additionally, we assessed the statistical sensitivity, calculating the smallest effect size that individual studies were able to detect with certain probabilities (0.8 and 0.95), given their reported sample size. We conducted separate analyses for regulation performance and for a behavioral outcome, where applicable. Several studies employed a repeated-measure analysis of variance (ANOVA) but did not provide details of the correlation among repeated measures or violation of the sphericity assumption. For pragmatic reasons, we thus assumed for all studies that there was no violation of sphericity and a correlation of 0.8, which is considered a good general estimate for test-retest correlations in neuropsychological assessments (Calamia et al., 2013). To simplify analyses, we also used uncorrected *p*-values and ANOVA/*t*-tests instead of non-parametric tests, if used by a specific study. Additionally, instead of mixed models or ANOVAs with more than one within factor, two-factorial mixed ANOVAs were used for the sensitivity analysis. Overall, these measures should lead to higher power estimation, and we can assume that we overestimated the statistical power of the studies. Analyses were carried out using G*Power (Faul et al., 2007).

Overall, sample sizes varied across studies from our minimum inclusion size, i.e., four (two per cell), up to 60 (30 per cell). One single group study included 33 participants. The median sample size of the studies was 20 (12 per cell). We calculated the median effect size that was detectable with 80 and 95% power. For the outcome regulation performance, we found a value of $d = 0.75$ and $d = 1$, respectively. For behavioral outcomes, this was value was $d = 0.52$ and $d = 0.69$, respectively. We further found that the median power to detect a small effect of $d = 0.2$ was low (0.16 and 0.22). Our results showed that the power was only sufficient to detect large effects of $d = 0.8$ regulation performance and 0.97 for behavioral effects, respectively (see **Table 5** and **Tables S3, S4**

TABLE 5 | Sensitivity and statistical power for reported analysis.

Study	*N*	Sensitivity		Power to detect		
		80% power	95% power	$d = 0.2$	$d = 0.5$	$d = 0.8$
REGULATION PERFORMANCE						
Mean	22.11	$d = 0.88$	$d = 1.15$	0.20	0.55	0.74
Median	20	$d = 0.75$	$d = 1$	0.16	0.48	0.8
BEHAVIORAL OUTCOMES						
Mean	22.1	$d = 0.66$	$d = 0.87$	0.20	0.68	0.87
Median	20	$d = 0.53$	$d = 0.69$	0.22	0.76	0.97

Note that in order to simplify the analysis for some studies, we performed the analysis for a different statistical test than originally reported, did not take into account correction for multiple comparisons, and assumed no sphericity violation and a high correlation among repeated measures for ANOVAs. Overall, these measures should have led to an overestimation of the statistical power/sensitivity of the studies.

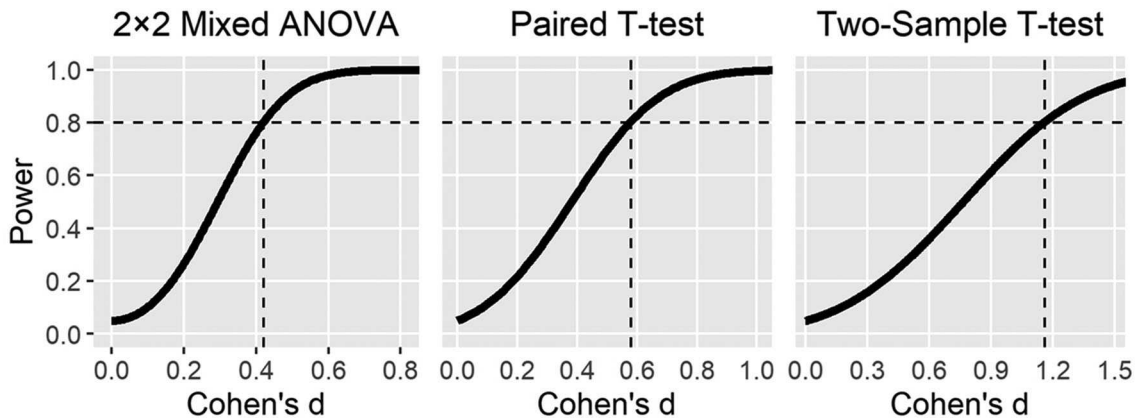

FIGURE 4 | Statistical power curves to detect different effect sizes with 20 participants (median sample size) for different statistical tests. Dashed lines indicate smallest effect sizes detectable at 80% power. Note that the power curve for the 2 × 2 mixed ANOVA was based on liberal statistical assumptions (e.g., high correlation among repeated measures, sphericity, and uncorrected *p*-value of 0.05).

for more details). **Figure 4** shows power curves for detecting different effect sizes with a sample size of 20 participants, which is equivalent to the median sample size of the studies included in this review, for different commonly used statistical tests.

Some studies that included control groups lacked a direct statistical comparison of regulation performance between the experimental and the control condition. Instead, these studies only reported the main effects within conditions and compared statistical significance between conditions instead of effect sizes. This statistical approach is erroneous for group comparisons (Nieuwenhuis et al., 2011) and makes it difficult to assess whether the experimental group outperformed the control group. If we assume that these studies found no statistically significant group effect, we note that due to insufficient statistical power we cannot come to valid conclusions about potential group effects. To check this assumption, we conducted sensitivity analyses for the respective group/interaction effects, using a statistical test that was appropriate for the respective study design (see **Supplementary Material**). While sensitivity for detecting a certain group/interaction effect size remained the same, it is reasonable to assume that interaction effects are smaller and, depending on the underlying assumptions, require four to sixteen times more participants to achieve similar *a priori* statistical power (Gelman, 2018). Therefore, studies were likely underpowered for reliably detecting group differences in neurofeedback effects, which are very likely smaller than within-effects.

As noted earlier, it remains difficult, if not impossible, to generalize these findings across paradigms because the smallest relevant effect sizes (SESOIs) may depend on the choice of the neurofeedback target region, population, control conditions, and other characteristics of the design. However, specific behavioral effects of neurofeedback, as assessed in placebo and motivation level-controlled designs, are possibly rather small (see **Supplementary Material**). This assumption is at least partly supported for the EEG-neurofeedback literature where well-controlled studies depending on population and rating report no specific group effect (e.g., Schabus et al., 2017; Schönenberg et al., 2017) or medium to small and non-significant effect sizes (Strehl et al., 2017).

Altogether, our results suggest the median sample size of published fNIRS-neurofeedback studies is relatively small at $N = 20$, which is comparable to sample sizes reported more broadly for neuroimaging (Poldrack et al., 2017). It is thus not surprising

that most studies lack sufficient statistical sensitivity to detect (realistic) SESOIs. In contrast, most studies were biased toward finding only relatively large effects (**Figure 4**). We further note that the analyses we present are based on rather liberal statistical assumptions (e.g., no application of multiple-testing correction) and thus likely still overestimate the true statistical sensitivity and power in the field.

Particularly with regard to specific behavioral effects, studies still lack statistical sensitivity and thus allow only very limited conclusions to be drawn about the feasibility of the paradigms and no conclusions about the specificity of fNIRS-neurofeedback effects. The field mainly consists of small feasibility, pilot, or proof-of-concept studies, which do not have to fulfill the same requirements with regard to sample size since their purpose is to explore the potential of fNIRS-neurofeedback in self-regulating a target brain signal and modulating behavior. However, as described above, most studies are not sufficiently transparent about this and hence risk overstating their findings. We thus reiterate previous concerns and recommend that authors appropriately label pilot, feasibility, and proof-of-concept studies, ideally in their manuscript title. Furthermore, we recommend a clear distinction between planned and exploratory analyses.

3.4. Conclusion—Quality of Published Studies

Altogether, the design and reporting quality of the studies can be considered to be moderate. There were a few studies of lower quality, but also some high-quality studies including sham-control conditions, randomization, and blinding (**Figure 5**). Sample sizes of the studies were small and thus their statistical power to detect realistic effects was low. While similar results have been reported for other fields within the neurosciences (Nieuwenhuis et al., 2011; Button et al., 2013; Szucs and Ioannidis, 2017), fNIRS-neurofeedback is still in its infancy and we thus still have the chance to tackle these issues early on and lay a more robust foundation to build upon in future work. As the field moves on, well-designed, sufficiently powered confirmatory studies are necessary to reach valid conclusions about the effectiveness of fNIRS-neurofeedback.

4. NEURAL EFFECTS OF NEUROFEEDBACK

In this section, we assess and discuss the effectiveness of fNIRS-neurofeedback for regulating and inducing pre-post changes in brain activity.

4.1. Neurofeedback Regulation Success

Before considering training effects in terms of changes in behavior or brain activity after neurofeedback, an essential question is whether neurofeedback training was successful, meaning was it effective for regulating the target brain signal. Unfortunately, no standard has been established so far, and there are a number of different ways to define and quantify neurofeedback regulation success. Paret et al. (2019) provide a taxonomy and discuss this issue in depth. In this section, we first discuss different success measures as applied by the studies and then systematically assess and critically discuss the effectiveness of fNIRS-neurofeedback for regulating a target brain signal, as reported by the studies (see **Table 6**).

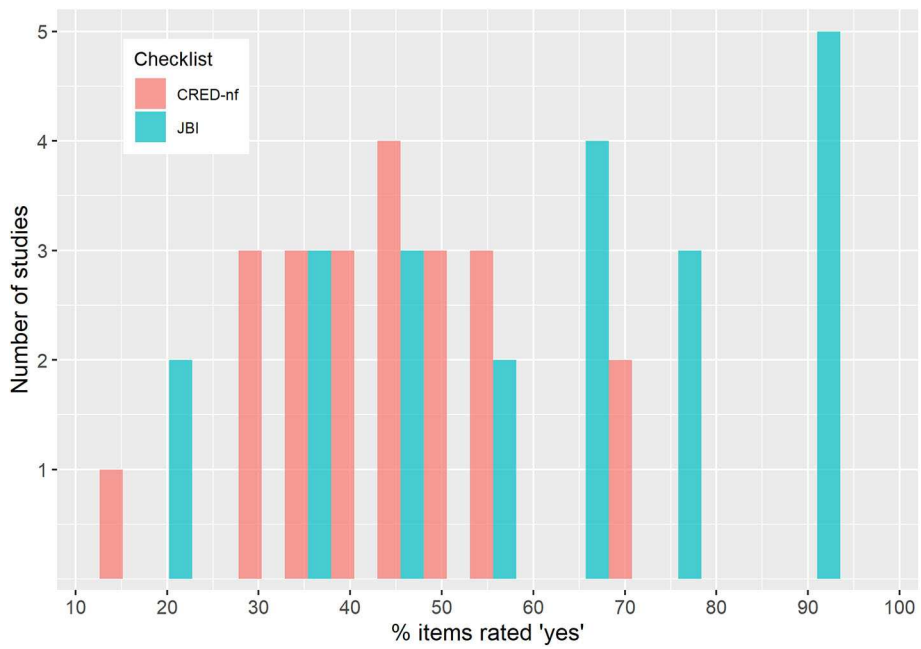

FIGURE 5 | Quality of studies according to the CRED-nf and JBI checklist.

TABLE 6 | Neurofeedback regulation success.

Study	Data for 1.2 and Figure 3B	Data for 1.2 and Figure 3A	Data for 4.1	Data for 4.1 and Figure 6			
	Target region	Target population	Success measure and analysis	Successful regulation as compared to			
				CTB	ECTL	Linear	CTC
Aranyi et al. (2016)	dlPFC asymmetry	18 healthy	*Success rate.* Successful trial = statistically significant increase in average asymmetry during NF compared to counting baseline (*t*-test)	Yes	NR	No	N/A
Barth et al. (2016)	PFC	13 healthy	*Fixed threshold.* Average increase of HbO over whole training course	Yes	NR	NR	N/A
Fujimoto et al. (2017)	SMA	20 healthy	*Fixed threshold.* Significant increase in HbO during late compared to early trials (time/condition interaction)	Yes	Yes	NR	Yes
Hosseini et al. (2016)	dlPFC	20 healthy	*Fixed threshold.* Linear regression over trials within and over sessions. Further group analysis offline (but overlap with feedback channels unclear)	No	No	No[a]	NR[b]
Hudak et al. (2017)	Bilateral dlPFC/IFG	20 highly impulsive	*Success rate.* Successful trial = at least 7 s of the last 15 s regulation in the desired direction. Average of all trials from first four sessions compared to last four sessions	NR	No	No	NR
Hudak et al. (2018) -	Bilateral dlPFC/IFG	19 adults with ADHD	*Success rate.* Successful trial = at least 7 s of the last 15 s regulation in the desired direction. Average of all trials from first half compared to last half of sessions	Yes	No	No	N/A
Kanoh et al. (2011)	Left sensorimotor cortex	5 healthy	*Fixed threshold.* Linear regression over sessions	NR	NR	No	N/A
Kimmig et al. (2018)	Bilateral dlPFC/IFG	12 SAD	*Success rate.* Successful trial = at least 7 s of the last 15 s regulation in the desired direction. Last three sessions compared to first three sessions.	NR	Yes	NR	N/A
Kinoshita et al. (2016)	Bilateral frontal pole cortex	24 healthy	*Fixed threshold.* Increased HbO in feedback channels compared to rest baseline	Yes	NR	NR	No
Kober et al. (2014)	Motor cortex asymmetry	17 healthy	*Fixed threshold.* Last three sessions vs. first three sessions	Yes	Yes	Yes	Yes
Kober et al. (2015)	Bilateral IFG	20 healthy	*Fixed threshold.* HbR increased over sessions in HbR group and HbO decreased. In HbO group HbR increased over session as well.	Yes/No[c]	NR	Yes/No[c]	NR
Kober et al. (2018)	Bilateral IFG	48 healthy/12 per group	*Fixed threshold.* Not compared to baseline, motor imagery and no group comparison	NR	NR	Yes/No[c]	NR
Lapborisuth et al. (2017)	Left motor cortex	22 healthy	*Fixed threshold.* Not clearly reported. Defined ROI based on motor execution task (overlap with feedback channels not clear) and analyzed HbR instead of HbO. No comparison between conditions and no effect for HbO reported	NR	NR	NR	NR
Lee et al. (2015)	Sensory motor cortex	4 healthy	*Fixed threshold.* Increased HbO in feedback channels. No statistical comparison between feedback and no feedback condition.	NR	NR	NR	NR

(Continued)

TABLE 6 | Continued

Study	Data for 1.2 and Figure 3B	Data for 1.2 and Figure 3A	Data for 4.1	Data for 4.1 and Figure 6			
	Target region	Target population	Success measure and analysis	Successful regulation as compared to			
				CTB	ECTL	Linear	CTC
Li et al. (2019)	Right lateral OFC	60 healthy	*Fixed threshold.* Significant increase in HbO over NF runs (time × group interaction). Regional specificity also confirmed by exploratory analysis of all channels	Yes	Yes	Yes	Yes
Liu et al. (2016)	Frontal and temporal face processing regions	2 healthy, 2 ASD	Not reported	NR	NR	NR	NR
Marx et al. (2015)	Bilateral dlPFC/IFG	27 children ADHD/9 per group	Not reported	NR	NR	NR	NR
Mihara et al. (2012)	Left premotor cortex	21 healthy	*Fixed threshold.* Increase in HbO compared to baseline for only one of the three feedback channels reported	Yes	NR	NR	No
Mihara et al. (2013)	Ipsilesional premotor cortex	20 stroke patients	*Fixed threshold.* Increased activation in one of the three FB channels compared to baseline. Timeline analysis and ROI analysis. Statistical details about timeline analysis missing	Yes	Yes	NR	Yes
Narita (2015)	Left PFC	4 ASD	Not reported	NR	NR	NR	N/A
Trambaiolli et al. (2018)	Frontal and occipital networks	33 healthy	*Success rate.* Successful trial = classifier. Percentage of successful trials for all conditions	Yes	NR	NR	No
Weyand et al. (2015)	Bilateral PFC	10 healthy	*Success rate.* Successful trial = classifier. Average classification accuracy for each session	Yes	NR	NR	N/A

ADHD, attention-deficit/hyperactivity disorder; ASD, autism spectrum disorder; CTB, compared to baseline; ECTL, early compared to late, trail(s); CTC, compared to control group or within control condition; dlPFC, dorsolateral prefrontal cortex; IFG, inferior frontal gyrus; HbR, deoxyhemoglobin; NF, neurofeedback; OFC, orbitofrontal cortex; HbO, oxyhemoglobin; PFC, prefrontal cortex; SAD, social anxiety disorder; SMA, supplementary motor area.

[a] *Marginal effects were considered "no," only significant effects were considered "yes".*

[b] *Effects were reported based on an offline analysis without clarifying whether significant effects overlapped with feedback channels and were therefore not considered in our analysis.*

[c] *Kober et al. (2015, 2018) trained regulation of HbO and HbR in separate groups.*

4.1.1. Neurofeedback Regulation Success—Measures

While most fNIRS-neurofeedback studies define regulation success based on the magnitude of a signal change, some also define it on the basis of time, i.e., on the amount of time in a trial during which the feedback signal exceeds a defined threshold (Hudak et al., 2017, 2018; Kimmig et al., 2018). Most studies apply a *fixed threshold* approach and compare the regulation statistically to a baseline condition over a session, while some also report *success rates*, i.e., a ratio of successful (as previously defined) trial per session (Weyand et al., 2015; Aranyi et al., 2016; Trambaiolli et al., 2018) or for a group of sessions (Hudak et al., 2017, 2018; Kimmig et al., 2018). None of the studies calculated *personal effect sizes*, i.e., divided average signal change by the standard deviation of a session or run to account for individual noise (cf. Paret et al., 2019). Finally, to judge the regulation success of neurofeedback training, effects over time should be assessed for potential learning curves, rather than merely assessing average signal change across all trials compared to the baseline. For instance, comparisons can be made between early [first session(s)/trial(s)] and late parts of the training period [last sessions(s)/trial(s)] (Kober et al., 2014; Fujimoto et al., 2017; Kimmig et al., 2018). Alternatively, assuming linear improvement, regulation success can be assessed over all trials or sessions via linear regression (Kober et al., 2018; Li et al., 2019). Ultimately, success measures should be compared with a control group or within control conditions. This is important since also sham feedback induces activations, particularly in frontal brain regions (Ninaus et al., 2013), which is the target of the majority of fNIRS-neurofeedback studies. Certain studies compared some of the first sessions with some of the last sessions (Kober et al., 2014; Kimmig et al., 2018), which seems arbitrary. If certain sessions or trials are selected for comparison, this should be theoretically or empirically justified. For example Fujimoto et al. (2017) compared the first six trials with the last ten trials, because according to the existing literature participants should reach a plateau after the first six trials during a motor-learning task (Hatakenaka et al., 2007).

It should be noted that, with a few exceptions in fMRI-neurofeedback (e.g., Goldway et al., 2019), variability measures have been neglected in most neurofeedback success definitions. According to learning theories, the probability of a certain behavior (brain activity) should increase after learning (Skinner, 1963), but variability (noise) should also be reduced. Some

theorists have compared neurofeedback learning to motor skill learning (Sitaram et al., 2017). From this perspective, it is assumed that in the course of learning a new skill variability is reduced to optimize performance (He et al., 2016).

4.1.2. Neurofeedback Regulation Success—Results

We assessed whether the studies reported an effect for each of the aforementioned comparisons (see **Table 6** and **Figure 6**). Overall, results show that fNIRS-neurofeedback can be used to regulate brain activity, with some of the studies also demonstrating a greater increase over time as compared to a control group (Mihara et al., 2013; Kober et al., 2014; Fujimoto et al., 2017; Li et al., 2019). Particularly these studies were all of higher quality according to our ratings, at least single- or double-blinded and applied a sham-feedback approach (see section 3.1). The other studies reported mixed results, lacked a control group, or did not report results sufficiently well, making it difficult to draw definite conclusions. For example, some studies did not report regulation success based on the feedback signal, but rather results from an offline analysis of all channels, and did not clarify whether significant effects overlap with channels used for feedback (e.g., Mihara et al., 2012; Lapborisuth et al., 2017). This impedes any judgement about the success of a neurofeedback protocol. We encourage authors to report regulation success based on all feedback channels. If more than one channel is used, the average of the channels or an ROI analysis only based on feedback channels can be reported. Furthermore, some of the studies used time-based binary success criteria and did not additionally report brain activation during regulation. These criteria require the definition of a threshold to be surpassed and neglect information about the signal amplitude. Some studies (Hudak et al., 2017, 2018; Kimmig et al., 2018) used a threshold of zero, i.e., spent at least half of the time of the last 15 s of a trial in the desired direction. This threshold is very liberal and it can be expected that random fluctuation (only noise) of a signal should be half of the time above and half of the time below zero. Hence, high success rates can be expected by chance and are not informative. When using time-based criteria, the amplitudes of the feedback signal should be reported as well.

4.2. Neural Changes Over Time and Neural Mechanisms

In addition to analyzing regulation success, some studies explored pre-post changes in neural outcomes or investigated neural mechanisms of neurofeedback as assessed during training. Hudak et al. (2017) found increased activation of the left dlPFC (part of the region trained) during NoGo trials after neurofeedback compared to an active control group, but there was also a baseline difference between groups, and decreased activity in the experimental group before neurofeedback training may explain the effect. No effect was reported for the working-memory task, which is in line with (Barth et al., 2016), who reported only marginal decreases for frontal and language-related brain regions during a working-memory task. Kimmig et al. (2018) found no change in social-threat processing-related brain activity after neurofeedback, but a change in the right inferior parietal sulcus, right inferior frontal gyrus, and supplementary motor cortex correlated positively with a change in social anxiety. Mihara et al. (2012) found increased activation of the left premotor cortex in channels not used for feedback, and decreased activity in the parietal association cortex, which was related to an increase in the sham-feedback group, speculatively related to switching to visual imagery strategies due to the incorrect feedback in this group. Kober et al. (2015) demonstrated transfer of neurofeedback training and showed that activity within the

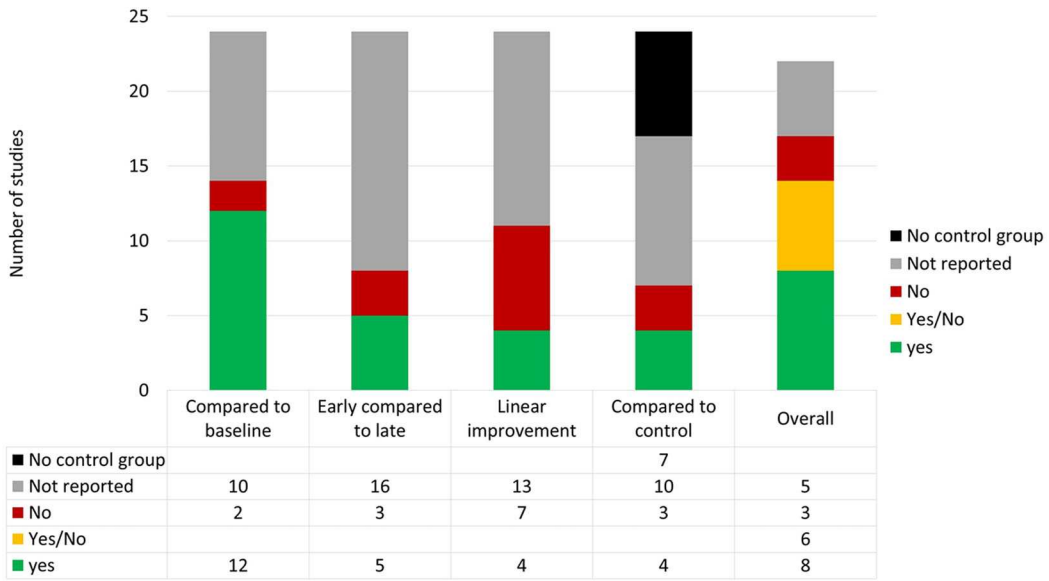

	Compared to baseline	Early compared to late	Linear improvement	Compared to control	Overall
No control group				7	
Not reported	10	16	13	10	5
No	2	3	7	3	3
Yes/No					6
yes	12	5	4	4	8

FIGURE 6 | Neurofeedback regulation success. Overall regulation was classified "Yes" if a significant effect for one or more of the four measures were reported and "No" if no significant effect was reported. If both were reported, the overall regulation was classified "Yes/No." Note that Kober et al. (2015, 2018) trained the regulation of HbO and HbR in different groups and found differential results for the groups. Therefore, the two studies were counted twice for the four measures. In overall regulation, the two studies were only counted once and were classified as "Yes/No".

IFG during motor imagery and motor execution of swallowing decreased (HbR increased) after neurofeedback training.

Some studies analyzed brain connectivity during neurofeedback training. Hudak et al. (2018) identified differential brain connectivity patterns for successful and failed regulation of the dlPFC, and demonstrated the importance of the fronto-parietal control network. Results may be specific to the training protocol and online analysis (i.e., influence of reference channels punishing activation in certain brain regions). However, Trambaiolli et al. (2018) found similar connectivity patterns for the random-, real-, and fixed-feedback (i.e., no-feedback) condition during an affective neurofeedback task.

4.3. Conclusion—Neural Effects of Neurofeedback

All in all, the results of some high-quality studies demonstrate the effectiveness of fNIRS-neurofeedback for regulating brain activation in motor regions (three of the successful studies) and in the OFC (one study). For other brain regions, such as the dlPFC, results are mixed and we cannot conclude whether fNIRS-neurofeedback is effective for regulating these regions as well. Moreover, a lacuna in reporting regulation success is evident as well, which, together with a high level of degrees of freedom on the part of the researchers as outlined above, raises suspicions of selectively reporting positive results (Simmons et al., 2011) and inflated effect sizes (Ioannidis, 2008). Furthermore, initial analyses provide preliminary evidence for potential neuroplastic effects of fNIRS-neurofeedback and further mechanistic insights. Future studies should follow up on such efforts and investigate neural mechanisms of neurofeedback. Neuroplastic effects may also be investigated in combination with other methods such as fMRI, which has higher spatial resolution and covers subcortical brain regions that contribute to neurofeedback learning (Emmert et al., 2016; Sitaram et al., 2017)

5. BEHAVIORAL EFFECTS OF fNIRS-NEUROFEEDBACK IN HEALTHY AND CLINICAL POPULATIONS

The ultimate goal of many neurofeedback applications is to induce significant effects in behavior as a prerequisite for developing clinical applications or neuroenhancing procedures. Because most studies have targeted prefrontal ($N = 13$) or motor brain regions ($N = 7$; see **Figure 3B**), we here review the effectiveness for improving executive functioning and motor rehabilitation across patient and healthy populations (see **Table 7**).

5.1. fNIRS-Neurofeedback to Improve Executive Functioning

Hosseini et al. (2016) found mixed effects on working memory after task-based neurofeedback training targeting down-regulation of the dlPFC. Performance improved in an n-back task as compared to the sham-feedback group, but no improvement was found in either group for the delayed verbal working-memory task used for the task-based neurofeedback paradigm. Additionally, a positive effect on task switching (analyzed exploratory) was reported. It should be noted that this study only reported marginal effects for regulation performance. Unfortunately, Barth et al. (2016) did not report the behavioral effects for working memory. In a subclinical sample, Hudak et al. (2017) found no effect in an n-back task but improved inhibitory control as assessed with a Go-NoGo task, and only a trend compared to an EMG-biofeedback control group. Stop-signal reaction-time variability also decreased (significant group effect). The latter study also does not show any indications of successful regulation. Li et al. (2019) found a trend for enhanced cognitive flexibility as assessed with an attentional set-shifting task, but they did not apply a pre-measurement and compared groups only at post. Moreover, OFC regulation correlated with reward experience in the neurofeedback group only.

Due to its potential to improve prefrontal brain functions, particularly inhibitory control, fNIRS-neurofeedback has been investigated as a potential treatment for children (Marx et al., 2015) and adults (Hudak et al., 2018) with ADHD. Indeed, Marx et al. (2015) found indications of improved inhibitory control after neurofeedback in children with ADHD as assessed with a Go-NoGo task, which was unfortunately not assessed in the control groups. Furthermore, this was accompanied by a decrease in ADHD symptoms, but similar improvements were also observed in the two active control groups. Therefore, while fNIRS-neurofeedback may improve attention and inhibitory control, leading to decreased ADHD symptoms, specificity has not been demonstrated yet and it remains open whether it offers any advantages over classical EEG-neurofeedback or other established treatments for ADHD. Larger clinical fNIRS-neurofeedback trials in children and adults with ADHD are currently under way (Mayer et al., 2015; Blume et al., 2017) and may shed further light on this issue.

Another potential clinical application for fNIRS-neurofeedback of the dlPFC is the treatment of social anxiety disorder. For example, it has been reported to reduce social threat-related attention bias and improve social and general trait anxiety as well as depressive symptoms (Kimmig et al., 2018). However, due to the absence of a control group, results are only preliminary. In addition, few indications of successful regulation were reported.

5.2. fNIRS-Neurofeedback for Motor Rehabilitation

Two studies demonstrated the modulation of swallowing-related motor regions (within the IFG) in healthy participants. HbR increased during motor imagery and execution of swallowing after training, though not compared to a control group. This training protocol might be investigated in patients with dysphagia in the future (Kober et al., 2015, 2018). fNIRS-neurofeedback of premotor regions improved self-assessed kinesthetic motor imagery during real neurofeedback as compared to a within sham-feedback condition in healthy participants (Mihara et al., 2012), but did not improve postural stability after one session (Fujimoto et al., 2017). The significant interaction was mainly driven by a decrease in postural stability

TABLE 7 | Behavioral effects of fNIRS-neurofeedback.

Study	Target region	Target population	Behavioral, cognitive/emotional effects
Aranyi et al. (2016)	dlPFC asymmetry	18 healthy	Alignment ratings (the subjective rating of how appropriate the virtual agent's facial expressions were to the subject's thoughts during NF) correlated with regulation success (within)
Fujimoto et al. (2017)	SMA	20 healthy	Significant time × group interaction for postural control, but no time effects for both groups—interaction was mainly driven by decreased performance in the sham feedback group
Hosseini et al. (2016)	dlPFC	20 healthy	Improved working memory (significant time × group interaction). Exploratory: improved task switching
Hudak et al. (2017)	Bilateral dlPFC/IFG	20 highly impulsive	Reduction in false alarms (Go-NoGo task, within effect, only trend for interaction). Reduction in stop-signal reaction times (SSRT) variability (between effect), but no effect on SSRTs
Kimmig et al. (2018)	Bilateral dlPFC/IFG	12 SAD	Decreased social and general trait anxiety as well as depressive symptoms and a reduced disturbance of daily life. Improved social threat-processing, i.e., reduction of social threat-related attention bias toward laughter, but not specifically for taunting vs. joyful laughter. No correlation of behavioral effects with regulation performance
Li et al. (2019)	Right lateral OFC	60 healthy	Trend for enhanced cognitive flexibility (but only group comparison at post). Shorter response times and higher rewarding experience were associated with stronger training-induced HbO increases in lOFC
Liu et al. (2016)	Frontal and temporal face processing regions	2 healthy, 2 ASD	Improved facial recognition in all participants (single case analysis, no statistic reported)
Marx et al. (2015)	Bilateral dlPFC/IFG	27 children ADHD/9 per group	Decreased ADHD scores (parent and teacher ratings) within group. No effect on associated behavioral symptoms (SDQ) and quality of life (child ratings). Go-NoGo RTs, RT variability and commission errors decreased within group. But RT effect only from post to follow up. TAP flexibility RTs and RT variability decreased within group. In the control groups, ADHD scores did not significantly decrease, but also no significant group effect was found. Baseline differences in quality of life and associated behavioral symptoms
Mihara et al. (2012)	Left premotor cortex	21 healthy	Increased self-assessed kinesthetic motor imagery scores
Mihara et al. (2013)	Ipsilesional premotor cortex	20 stroke patients	Improved recovery of sensorimotor function, as assessed by Fugl-Meyer assessment scale (significant time × group Interaction), no significant adverse effect
Narita (2015)	Left PFC	4 ASD	Improved working memory, performance in Stroop task, anxiety and mood (within-effect, only means, no statistic reported)
Weyand et al. (2015)	Bilateral PFC	10 healthy	Marginal decrease in task load comparing session 10 (strategy use) and 15 (voluntary self-regulation). Work load decreased and ease-of-use and perceived intuitiveness only increased over self-regulation sessions (11–15), not over mental task sessions (1–10)

ADHD, attention-deficit/hyperactivity disorder; ASD, autism spectrum disorder; dlPFC, dorsolateral prefrontal cortex; IFG, inferior frontal gyrus; OFC, orbitofrontal cortex; PFC, prefrontal cortex; SAD, social anxiety disorder; SMA, supplementary motor area.

after sham feedback. This missing effect might be attributed to the limited duration of training or to ceiling effects in the healthy participants, as a longer training period in patients after stroke was efficacious (Mihara et al., 2013). In this double-blind randomized sham-controlled design, patients underwent stroke rehabilitation and were trained to upregulate activation of the ipsilesional premotor cortex via motor imagery. The control group also practiced motor imagery but received artificially generated feedback. After six sessions specific effects were observed for the hand/finger subscale of the Fugl-Meyer assessment. Results are promising and indicate that fNIRS-neurofeedback may facilitate motor recovery in patients after stroke, but replications in a larger, controlled clinical trial are needed.

5.3. Other Potential Clinical Applications

FNIRS-neurofeedback was investigated as a potential treatment for autism spectrum disorder. Liu et al. (2016) applied a task-based neurofeedback approach to enhance the effects of facial-recognition training in adolescents with autism and found improved facial recognition which was also present in the patient receiving sham feedback. Given that these are only the initial data of a larger clinical trial which do not permit a statistical analysis, conclusions can be made only when all the data are published. Similarly, Narita (2015) trained four participants with autism to upregulate activity of the prefrontal cortex and reported improvements in working memory, inhibitory control as well as in anxiety and mood on a single-case level.

Furthermore, studies demonstrated successful classification of neutral and positive affective states (Trambaiolli et al., 2018) and regulation of asymmetric activation of the left dlPFC, a candidate neural mechanism of approach-avoidance motivation (Aranyi et al., 2016). These studies in healthy participants may pave the way for future applications in mood disorders.

Although not included in our review, it is worth mentioning a single-case study (Storchak et al., 2018) describing a new neurofeedback protocol to treat auditory verbal hallucinations in schizophrenia. A patient with paranoid schizophrenia

was trained for 47 sessions to regulate the activity of the bilateral posterior superior temporal gyrus. To counteract neural correlates of auditory hallucinations, the patient was instructed to upregulate when expecting and downregulate when experiencing hallucinations. She was successful in upregulation, but not downregulation. However, even though amplitudes did not differ significantly from zero over the sessions, a learning effect was reported for downregulation, i.e., a significant decrease in activation over the sessions. Throughout the training period hallucinations decreased and symptoms improved.

5.4. Conclusion—Behavioral Effects of fNIRS-Neurofeedback in Healthy and Clinical Populations

In sum, there is preliminary evidence for the effectiveness of fNIRS-neurofeedback for improving motor rehabilitation and executive functions, particularly for improved inhibitory control (Marx et al., 2015; Hudak et al., 2017) and cognitive flexibility (Hosseini et al., 2016; Li et al., 2019). Mixed results were reported for working-memory tasks, which may be attributable to ceiling effects (Hudak et al., 2017). This is in line with the EEG-neurofeedback literature where similar effects were observed for inhibitory control tasks (Bluschke et al., 2016; Mayer et al., 2016). However, non-specific factors (psychosocial/placebo effects) may explain a large proportion of the effect sizes found in neurofeedback studies (Thibault and Raz, 2016; Schönenberg et al., 2017; Ros et al., 2020). Hence, due to the limited evidence available and a lack of well-powered (see section 3.3) properly sham-controlled studies, it remains difficult to make any claims about the specificity of the reported effects. Regarding clinical potential, early pilot studies show the feasibility of fNIRS-neurofeedback in different patient populations such as ADHD, social anxiety disorder, autism, and stroke. The most promising data are found for stroke rehabilitation, where a double-blind sham-controlled study demonstrated beneficial effects (Mihara et al., 2013). It should be noted that most studies investigated effects in healthy populations and stronger effects may be expected in patient populations, displaying more room for improvement. Great optimism has been expressed with regard to future clinical applications (Ehlis et al., 2018), but larger well-controlled studies and clinical trials are needed to corroborate initial findings and demonstrate specificity before fNIRS-neurofeedback can be considered a viable complementary or even alternative treatment option.

THE POTENTIAL OF fNIRS FOR NEUROFEEDBACK RESEARCH—FUTURE DIRECTIONS

Neurofeedback research using fNIRS has just begun. Being more precise in targeting localized brain regions than EEG and much easier to use, and less expensive than fMRI, fNIRS may become an important tool for neurofeedback research and application. In this section, we outline our perspective on the future of fNIRS-neurofeedback and highlight its future potential.

Future research could benefit from exploiting the advantages of fNIRS to an even greater extent, since it offers unique opportunities for neurofeedback research. Compared to fMRI, it is easier to conduct a greater number of sessions and/or recruit more participants. This will help to solve the issue of low statistical power, which is a common problem in neuroscientific research (see section 3.3.4). Furthermore, this makes this technique more suitable than fMRI for larger multicenter studies. To our knowledge, no clinical multicenter fMRI-neurofeedback study has been published, while in EEG-neurofeedback research it has already been demonstrated that multicenter studies are possible (e.g., Strehl et al., 2017). Methods applied in studies are still quite heterogeneous and further agreements and standardization of protocols are necessary before this step can be taken. If the target is a region of the neocortex, it is also conceivable that methods may be combined, and successful fMRI-neurofeedback protocols transferred to fNIRS-neurofeedback to conduct a high-powered study employing many sessions and/or participants. Future studies could also compare fNIRS-based with fMRI-based neurofeedback protocols using simultaneous measures to reveal commonalities and differences or even combine both methods to exploit optimally their advantages. For example, in a first fMRI session the regions of interest could be precisely defined on the individual level to guide the placement of optodes (channels of interest) and improve the spatial specificity for the following (more economic) fNIRS-neurofeedback sessions.

FNIRS is particularly suited for and has been extensively and successfully used in developmental neuroscience (Lloyd-Fox et al., 2010; Pinti et al., 2018b). Future research may benefit from using fNIRS-neurofeedback particularly in children and older healthy and patient populations. These populations show more movement during experiments (e.g., Poldrack et al., 2002) and such movements are more tolerable with fNIRS. They also possess physical features that may be beneficial for fNIRS signal quality (e.g., skull thickness, hair thickness/pigmentation; Orihuela-Espina et al., 2010) and hence for neurofeedback applications.

Recently, portable and wireless fNIRS devices have been developed (Pinti et al., 2018b) that can be used outside the laboratory. Such portable devices could be used to conduct neurofeedback-training studies at home, in school, or any other place in the world, including also low-resource countries (Pinti et al., 2018b). If the ease-of-use of these devices were to be further developed participants could even conduct neurofeedback training on their own and thus train whenever they want. This would make it easy to conduct neurofeedback studies with long training times at low costs. Of course, before moving out of the laboratory, standard protocols have to be developed and proven to be effective.

Also, fNIRS may be particularly suitable for interactive hyperscanning neurofeedback approaches, which have already been introduced by Duan et al. (2013), who had two participants competing in a "tug-of-war" neurofeedback game. This competitive context may increase motivation. In the future, cooperative approaches may be introduced as well, where two or

more participants regulate a target brain signal together instead of competing.

Recent developments in fMRI-neurofeedback protocols could be transferred to fNIRS-neurofeedback. To date none of the fNIRS-neurofeedback studies used connectivity measures as a source of neurofeedback (other than support vector machine-based techniques). Connectivity-based neurofeedback has already been developed for fMRI-neurofeedback (Koush et al., 2015; Spetter et al., 2017; Yamashita et al., 2017; Zhao et al., 2019). Generally, some of these methods could be transferred to fNIRS since the sources and detectors can be freely positioned and might allow similar regions to those used in fMRI-neurofeedback studies to be covered. The high sampling of fNIRS allows stable correlations to be estimated in potentially shorter time windows, which is an advantage in this regard. However, these protocols should be established with caution and only with proper control of extracranial artifacts (e.g., using partial correlation and/or short-distance channels), which may easily produce spurious correlations. Future studies could also be oriented to recent methodological developments in fMRI-neurofeedback, such as implicit/covert neurofeedback protocols [i.e., neurofeedback without participants' awareness (e.g., Ramot et al., 2017) or decoded neurofeedback (Shibata et al., 2019)] and process-based neurofeedback, where protocols are designed to target disorder-specific processes (Lubianiker et al., 2019). Also, fMRI-informed approaches could be explored, as already applied in EEG-neurofeedback (e.g., Meir-Hasson et al., 2016), where fNIRS channels would predict the fMRI signal of a target region. Such approaches, if feasible with fNIRS, could result in improved spatial specificity and ideally make it possible to assess subcortical brain regions.

The problem of not reporting important information about signal-processing methods is also clearly visible in fMRI-neurofeedback studies and was addressed in a recent review by Heunis et al. (2020) recommending more rigorous reporting and development of methodological reporting standards. These recommendations can also be applied to fNIRS-neurofeedback research and similar default measures such as signal- or contrast-to-noise ratio calculations for evaluating fNIRS-signal quality could be established to make results more comparable across studies and to improve reproducibility (Heunis et al., 2020). Notably, fMRI-neurofeedback can already rely on a further developed field, and efforts with regard to standardization have already been made (Nichols et al., 2016). This is not the case for fNIRS research, where even standards for offline analysis methods are still lacking (Kamran et al., 2016; Pinti et al., 2018b). However, discussing this issue now will help to improve reporting quality and reproducibility at an early stage.

In general, the field will benefit from adopting more rigorous research and reporting practices as encouraged by a recent consensus (Aczel et al., 2019; Ros et al., 2020) to improve the likelihood of replicability and reproducibility (Mehler, 2019). These measures include sampling plans that are ideally based on adequate power analyses which render both positive and negative findings more informative (Mehler et al., 2019). We acknowledge that it remains challenging to define the smallest effect sizes of interest, which are context-specific. We thus recommend that researchers explore different approaches which have been established to define SESOIs (Lakens et al., 2018). We also acknowledge that neurofeedback studies are very resource-intensive requiring several training sessions and hence sampling plans that require relatively large sample sizes may be unrealistic to implement, particularly when working with patients. We therefore recommend considering ways of collaboration including multilab studies or multicenter trials and exploring alternatives such as sequential sampling methods with flexible stopping that can yield higher sensitivity (Schönbrodt and Wagenmakers, 2018) and encourage transparency in reporting sampling plans (e.g., mentioning practical constraints). Researchers can efficiently document design decisions, including the sampling and planned analyses, by publishing their protocols. These additional publishing formats include preregistration, where researchers document their methodology with a timestamp on a public platform such as the Open Science Framework before data acquisition starts (e.g., Mehler et al., 2017). An alternative approach is to publish trial protocols in dedicated journals, which may be undertaken in parallel to data acquisition (e.g., Cox et al., 2016). Moreover, the recently introduced publishing format Registered Reports includes an initial peer-review stage that can grant authors acceptance in principle for their work independent of the statistical outcome. We note that adopting such methods is challenging: they involve additional costs such as more time in the preparation phase of the study and less flexibility (Allen and Mehler, 2019). However, recent preliminary meta-research suggests that the chances of publishing findings that do not meet traditional statistical thresholds increases remarkably for studies published as Registered Reports (Allen and Mehler, 2019; Scheel et al., 2020) while citation counts are comparable to traditional papers (Hummer et al., 2019). Hence, increased transparency not only benefits the field, but likely also individual authors. We therefore recommend that researchers should consider these publishing formats for future studies.

Lastly, it will be crucial to further develop standards and agreements, particularly for neurofeedback success measures, in order to have comparable outcome variables in the future (Haugg et al., 2020). We repeat suggestions by Paret et al. (2019) that a basic science approach should be employed, systematically exploring and optimizing neurofeedback protocols and real-time signal-processing methods, which can then inform translational work in the field.

CONCLUSION

The present systematic review of fNIRS-neurofeedback studies suggests, although tentatively, that people can regulate hemodynamic signals from different cortical brain regions with fNIRS-neurofeedback indicating the feasibility of modulating normal behavior and psychiatric and neurological conditions. However, the field is at an early stage and consists mostly of feasibility, pilot, or proof-of-concept studies, so that the current systematic review might help to optimize future neurofeedback study designs but cannot provide recommendations on what

neurofeedback targets, populations, and training protocols have proven most beneficial. There is room for improvement in reporting important information and statistical power, which impedes valid conclusions about specific behavioral effects or potential clinical utility of the method.

Nevertheless, fNIRS is becoming a viable method for neurofeedback research and has the potential for clinical translation of neurofeedback. Along this avenue, further methodological improvements, particularly aiming at improving signal quality, are of crucial importance and, together with more rigorous research and reporting practices, may improve the chances of replicability and reproducibility. This will help to gain a more solid understanding of fNIRS-neurofeedback and move the field closer toward agreements and standardization. FNIRS-neurofeedback is still in its infancy, and we now have the chance to create a solid foundation to build upon in the future. With this systematic review, we hope to stimulate a discussion about methodological and reporting standards at this early stage.

DATA AVAILABILITY STATEMENT

Data from this systematic review are available in the **Supplementary Material** as well as at the Open Science Framework (see https://osf.io/hnxfq/), where we plan to update the database regularly in the future.

AUTHOR CONTRIBUTIONS

SK conceptualized the review with input from all other authors, selected the studies, extracted the data, conducted the analysis, assessed the quality of the studies, drafted, and revised the manuscript. DM assessed the quality of the studies and revised the manuscript. ML, RT, and KK revised the manuscript. BS supervised the drafting of the manuscript and revised it. All authors contributed to the article and approved the submitted version.

FUNDING

This work was supported by the International Research Training Group, The Neuroscience of Modulating Aggression and Impulsivity in Psychopathology (IRTG-2150) of the German Research Foundation (DFG). RT was supported by a post-doctoral fellowship from the Fonds de la recherche en santé du Québec. SK was supported by a fellowship from the Japan Society for the Promotion of Science (JSPS).

ACKNOWLEDGMENTS

We would like to thank Johannes Fendel for providing valuable input on systematic review methods, Laura Bell for her help in creating the figures, and Jenny Le for preparatory work for data extraction. We also thank Franziska Klein for comments on an earlier draft of the current manuscript. Lastly, special thanks are due to all the authors of the included studies, who made this systematic review possible and provided feedback on the data extraction.

SUPPLEMENTARY MATERIAL

The Supplementary Material for this article can be found online at: https://www.frontiersin.org/articles/10.3389/fnins.2020.00594/full#supplementary-material

REFERENCES

Aczel, B., Szaszi, B., Sarafoglou, A., Kekecs, Z., Kucharský, Š., Benjamin, D., et al. (2019). *A consensus-based transparency checklist*. *Nat. Hum. Behav.* 4, 4–6. doi: 10.1038/s41562-019-0772-6

Algermissen, J., and Mehler, D. M. A. (2018). May the power be with you: are there highly powered studies in neuroscience, and how can we get more of them? *J. Neurophysiol.* 119, 2114–2117. doi: 10.1152/jn.00765.2017

Allen, C. P. G., and Mehler, D. M. A. (2019). Open science challenges, benefits and tips in early career and beyond. *PLoS Biol.* 17:e3000246. doi: 10.1371/journal.pbio.3000246

Aranyi, G., Pecune, F., Charles, F., Pelachaud, C., and Cavazza, M. (2016). Affective interaction with a virtual character through an fNIRS brain-computer interface. *Front. Comput. Neurosci.* 10:70. doi: 10.3389/fncom.2016.00070

Arifler, D., Zhu, T., Madaan, S., and Tachtsidis, I. (2015). Optimal wavelength combinations for near-infrared spectroscopic monitoring of changes in brain tissue hemoglobin and cytochrome c oxidase concentrations. *Biomed. Opt. Express* 6:933. doi: 10.1364/BOE.6.000933

Barnett, S. M., and Ceci, S. J. (2002). When and where do we apply what we learn? A taxonomy for far transfer. *Psychol. Bull.* 128, 612–637. doi: 10.1037/0033-2909.128.4.612

Barth, B., Strehl, U., Fallgatter, A. J., and Ehlis, A. C. (2016). Near-infrared spectroscopy based neurofeedback of prefrontal cortex activity: a proof-of-concept study. *Front. Hum. Neurosci.* 10:633. doi: 10.3389/fnhum.2016.00633

Birbaumer, N., Ruiz, S., and Sitaram, R. (2013). Learned regulation of brain metabolism. *Trends Cogn. Sci.* 17, 295–302. doi: 10.1016/j.tics.2013.04.009

Blume, F., Hudak, J., Dresler, T., Ehlis, A.-C., Kühnhausen, J., Renner, T. J., et al. (2017). NIRS-based neurofeedback training in a virtual reality classroom for children with attention-deficit/hyperactivity disorder: study protocol for a randomized controlled trial. *Trials* 18:41. doi: 10.1186/s13063-016-1769-3

Bluschke, A., Broschwitz, F., Kohl, S., Roessner, V., and Beste, C. (2016). The neuronal mechanisms underlying improvement of impulsivity in ADHD by theta/beta neurofeedback. *Sci. Rep.* 6:31178. doi: 10.1038/srep31178

Brigadoi, S., and Cooper, R. J. (2015). How short is short? Optimum source–detector distance for short-separation channels in functional near-infrared spectroscopy. *Neurophotonics* 2:025005. doi: 10.1117/1.NPh.2.2.025005

Button, K. S., Ioannidis, J. P. A., Mokrysz, C., Nosek, B. A., Flint, J., Robinson, E. S. J., et al. (2013). Power failure: why small sample size undermines the reliability of neuroscience. *Nat. Rev. Neurosci.* 14, 365–376. doi: 10.1038/nrn3475

Calamia, M., Markon, K., and Tranel, D. (2013). The robust reliability of neuropsychological measures: meta-analyses of test–retest correlations. *Clin. Neuropsychol.* 27, 1077–1105. doi: 10.1080/13854046.2013.809795

Caldwell, M., Scholkmann, F., Wolf, U., Wolf, M., Elwell, C., and Tachtsidis, I. (2016). Modelling confounding effects from extracerebral contamination and systemic factors on functional near-infrared spectroscopy. *Neuroimage* 143, 91–105. doi: 10.1016/j.neuroimage.2016.08.058

Cohen, A., Keynan, J. N., Jackont, G., Green, N., Rashap, I., Shani, O., et al. (2016). Multi-modal virtual scenario enhances neurofeedback learning. *Front. Robot. AI* 3:52. doi: 10.3389/frobt.2016.00052

Cohen, J. (1992). A power primer. *Psychol. Bull.* 112, 155–159. doi: 10.1037/0033-2909.112.1.155

Cox, W. M., Subramanian, L., Linden, D. E. J., Lührs, M., McNamara, R., Playle, R., et al. (2016). Neurofeedback training for alcohol dependence versus treatment as usual: study protocol for a randomized controlled trial. *Trials* 17:480. doi: 10.1186/s13063-016-1607-7

Cui, X., Bray, S., Bryant, D. M., Glover, G. H., and Reiss, A. L. (2011). A quantitative comparison of NIRS and fMRI across multiple cognitive tasks. *Neuroimage* 54, 2808–2821. doi: 10.1016/j.neuroimage.2010.10.069

Cui, X., Bray, S., and Reiss, A. L. (2010). Functional near infrared spectroscopy (NIRS) signal improvement based on negative correlation between oxygenated and deoxygenated hemoglobin dynamics. *Neuroimage* 49, 3039–3046. doi: 10.1016/j.neuroimage.2009.11.050

Duan, L., Liu, W. J., Dai, R. N., Li, R., Lu, C. M., Huang, Y. X., et al. (2013). Cross-brain neurofeedback: scientific concept and experimental platform. *PLoS ONE* 8:e64590. doi: 10.1371/journal.pone.0064590

Ehlis, A. C., Barth, B., Hudak, J., Storchak, H., Weber, L., Kimmig, A. C. S., et al. (2018). Near-infrared spectroscopy as a new tool for neurofeedback training: applications in psychiatry and methodological considerations. *Jpn. Psychol. Res.* 60, 225–241. doi: 10.1111/jpr.12225

Emmert, K., Kopel, R., Sulzer, J., Brühl, A. B., Berman, B. D., Linden, D. E. J., et al. (2016). Meta-analysis of real-time fMRI neurofeedback studies using individual participant data: how is brain regulation mediated? *Neuroimage* 124, 806–812. doi: 10.1016/j.neuroimage.2015.09.042

Engel, L., Beaton, D. E., and Touma, Z. (2018). Minimal clinically important difference: a review of outcome measure score interpretation. *Rheum. Dis. Clin. North Am.* 44, 177–188. doi: 10.1016/j.rdc.2018.01.011

Faul, F., Erdfelder, E., Lang, A. G., and Buchner, A. (2007). G*Power 3: a flexible statistical power analysis program for the social, behavioral, and biomedical sciences. *Behav. Res. Methods* 39, 175–191. doi: 10.3758/BF03193146

Ferrari, M., and Quaresima, V. (2012). A brief review on the history of human functional near-infrared spectroscopy (fNIRS) development and fields of application. *Neuroimage* 63, 921–935. doi: 10.1016/j.neuroimage.2012.03.049

Fujimoto, H., Mihara, M., Hattori, N., Hatakenaka, M., Yagura, H., Kawano, T., et al. (2017). Neurofeedback-induced facilitation of the supplementary motor area affects postural stability. *Neurophotonics* 4:045003. doi: 10.1117/1.NPh.4.4.045003

Goldway, N., Ablin, J., Lubin, O., Zamir, Y., Keynan, J. N., Or-Borichev, A., et al. (2019). Volitional limbic neuromodulation exerts a beneficial clinical effect on fibromyalgia. *Neuroimage* 186, 758–770. doi: 10.1016/j.neuroimage.2018.11.001

Gruzelier, J., Inoue, A., Smart, R., Steed, A., and Steffert, T. (2010). Acting performance and flow state enhanced with sensory-motor rhythm neurofeedback comparing ecologically valid immersive VR and training screen scenarios. *Neurosci. Lett.* 480, 112–116. doi: 10.1016/j.neulet.2010.06.019

Hatakenaka, M., Miyai, I., Mihara, M., Sakoda, S., and Kubota, K. (2007). Frontal regions involved in learning of motor skill—a functional NIRS study. *Neuroimage* 34, 109–116. doi: 10.1016/j.neuroimage.2006.08.014

Haugg, A., Sladky, R., Skouras, S., McDonald, A., Craddock, C., Kirschner, M., et al. (2020). Can we predict real-time fMRI neurofeedback learning success from pre-training brain activity? *bioRxiv*. doi: 10.1101/2020.01.15.906388

He, K., Liang, Y., Abdollahi, F., Fisher Bittmann, M., Kording, K., and Wei, K. (2016). The statistical determinants of the speed of motor learning. *PLoS Comput. Biol.* 12:e1005023. doi: 10.1371/journal.pcbi.1005023

Heunis, S., Lamerichs, R., Zinger, S., Caballero-Gaudes, C., Jansen, J. F. A., et al. (2020). Quality and denoising in real-time functional magnetic resonance imaging neurofeedback: A methods review. *Hum. Brain Mapp*. doi: 10.1002/hbm.25010

Hinterberger, T., Neumann, N., Pham, M., Kübler, A., Grether, A., Hofmayer, N., et al. (2004). A multimodal brain-based feedback and communication system. *Exp. Brain Res.* 154, 521–526. doi: 10.1007/s00221-003-1690-3

Hosseini, S. M. H. H., Pritchard-Berman, M., Sosa, N., Ceja, A., and Kesler, S. R. (2016). Task-based neurofeedback training: a novel approach toward training executive functions. *Neuroimage* 134, 153–159. doi: 10.1016/j.neuroimage.2016.03.035

Hudak, J., Blume, F., Dresler, T., Haeussinger, F. B., Renner, T. J., Fallgatter, A. J., et al. (2017). Near-infrared spectroscopy-based frontal lobe neurofeedback integrated in virtual reality modulates brain and behavior in highly impulsive adults. *Front. Hum. Neurosci.* 11:425. doi: 10.3389/fnhum.2017.00425

Hudak, J., Rosenbaum, D., Barth, B., Fallgatter, A. J., and Ehlis, A. C. (2018). Functionally disconnected: a look at how study design influences neurofeedback data and mechanisms in attention-deficit/hyperactivity disorder. *PLoS ONE* 13:e0200931. doi: 10.1371/journal.pone.0200931

Hummer, L. T., Singleton Thorn, F., Nosek, B. A., and Errington, T. M. (2019). Evaluating Registered reports: a naturalistic comparative study of article impact short. *PsyArXiv*. 1–34.

Ioannidis, J. P. A. (2008). Why most discovered true associations are inflated. *Epidemiology* 19, 640–648. doi: 10.1097/EDE.0b013e31818131e7

Jasper, H. H. (1958). The ten-twenty electrode system of the international federation. *Electroencephalogr. Clin. Neurophysiol.* 10, 371–375.

Kamran, M. A., Mannan, M. M. N., and Jeong, M. Y. (2016). Cortical signal analysis and advances in functional near-infrared spectroscopy signal: a review. *Front. Hum. Neurosci.* 10:261. doi: 10.3389/fnhum.2016.00261

Kimmig, A.-C. S. C. S., Dresler, T., Hudak, J., Haeussinger, F. B., Wildgruber, D., Fallgatter, A. J., et al. (2018). Feasibility of NIRS-based neurofeedback training in social anxiety disorder: behavioral and neural correlates. *J. Neural Transm. (Vienna)* 126, 1175–1185. doi: 10.1007/s00702-018-1954-5

Kinoshita, A., Takizawa, R., Yahata, N., Homae, F., Hashimoto, R., Sakakibara, E., et al. (2016). Development of a neurofeedback protocol targeting the frontal pole using near-infrared spectroscopy. *Psychiatry Clin. Neurosci.* 70, 507–516. doi: 10.1111/pcn.12427

Kirilina, E., Jelzow, A., Heine, A., Niessing, M., Wabnitz, H., Brühl, R., et al. (2012). The physiological origin of task-evoked systemic artefacts in functional near infrared spectroscopy. *Neuroimage* 61, 70–81. doi: 10.1016/j.neuroimage.2012.02.074

Klein, F., and Kranczioch, C. (2019). Signal processing in fNIRS: a case for the removal of systemic activity for single trial data. *Front. Hum. Neurosci.* 13:331. doi: 10.3389/fnhum.2019.00331

Kober, S. E., Gressenberger, B., Kurzmann, J., Neuper, C., and Wood, G. (2015). Voluntary modulation of hemodynamic responses in swallowing related motor areas: a near-infrared spectroscopy-based neurofeedback study. *PLoS ONE* 10:e0143314. doi: 10.1371/journal.pone.0143314

Kober, S. E., Hinterleitner, V., Bauernfeind, G., Neuper, C., and Wood, G. (2018). Trainability of hemodynamic parameters: a near-infrared spectroscopy based neurofeedback study. *Biol. Psychol.* 136, 168–180. doi: 10.1016/j.biopsycho.2018.05.009

Kober, S. E., Wood, G., Kurzmann, J., Friedrich, E. V. C., Stangl, M., Wippel, T., et al. (2014). Near-infrared spectroscopy based neurofeedback training increases specific motor imagery related cortical activation compared to sham feedback. *Biol. Psychol.* 95, 21–30. doi: 10.1016/j.biopsycho.2013.05.005

Kohl, S. H., Veit, R., Spetter, M. S., Günther, A., Rina, A., Lührs, M., et al. (2019). Real-time fMRI neurofeedback training to improve eating behavior by self-regulation of the dorsolateral prefrontal cortex: a randomized controlled trial in overweight and obese subjects. *Neuroimage* 191, 596–609. doi: 10.1016/j.neuroimage.2019.02.033

Koush, Y., Meskaldji, D.-E., Pichon, S., Rey, G., Rieger, S. W., Linden, D. E. J., et al. (2015). Learning control over emotion networks through connectivity-based neurofeedback. *Cereb. Cortex* 27, 1193–1202. doi: 10.1093/cercor/bhv311

Lakens, D., Scheel, A. M., and Isager, P. (2018). Equivalence testing for psychological research: a tutorial. *Adv. Methods Pract. Psychol. Sci.* 1, 259–269. doi: 10.1177/2515245918770963

Lapborisuth, P., Zhang, X., Noah, A., and Hirsch, J. (2017). Neurofeedback-based functional near-infrared spectroscopy upregulates motor cortex activity in imagined motor tasks. *Neurophotonics* 4:021107. doi: 10.1117/1.NPh.4.2.021107

Lee, S. H., Jang, G. H., Jin, S. H., and An, J. (2015). "Neuro-feedback using real-time near infrared spectroscopy enhances brain plasticity during treadmill walking: a pilot study," in *IEEE/ASME International Conference on Advanced Intelligent Mechatronics, AIM* (Busan: IEEE), 437–440. doi: 10.1109/AIM.2015.7222572

Li, K., Kendrick, K. M., and Becker, B. (2019). Functional near-infrared spectroscopy-informed neurofeedback : regional-specific modulation of lateral orbitofrontal activation and cognitive flexibility. 6:025011. doi: 10.1117/1.NPh.6.2.025011

Liu, N., Cliffer, S., Pradhan, A. H., Lightbody, A., Hall, S. S., and Reiss, A. L. (2016). Optical-imaging-based neurofeedback to enhance therapeutic intervention in adolescents with autism: methodology and initial data. *Neurophotonics* 4:011003. doi: 10.1117/1.NPh.4.1.011003

Lloyd-Fox, S., Blasi, A., and Elwell, C. E. (2010). Illuminating the developing brain: the past, present and future of functional near infrared spectroscopy. *Neurosci. Biobehav. Rev.* 34, 269–284. doi: 10.1016/j.neubiorev.2009.07.008

Lubianiker, N., Goldway, N., Fruchtman-Steinbok, T., Paret, C., Keynan, J. N., Singer, N., et al. (2019). Process-based framework for precise neuromodulation. *Nat. Hum. Behav.* 3, 436–445. doi: 10.1038/s41562-019-0573-y

Marx, A.-M. M., Ehlis, A.-C. C., Furdea, A., Holtmann, M., Banaschewski, T., Brandeis, D., et al. (2015). Near-infrared spectroscopy (NIRS) neurofeedback as a treatment for children with attention deficit hyperactivity disorder (ADHD)–a pilot study. *Front. Hum. Neurosci.* 8:1038. doi: 10.3389/fnhum.2014.01038

Mathiak, K. A., Alawi, E. M., Koush, Y., Dyck, M., Cordes, J. S., Gaber, T. J., et al. (2015). Social reward improves the voluntary control over localized brain activity in fMRI-based neurofeedback training. *Front. Behav. Neurosci.* 9:136. doi: 10.3389/fnbeh.2015.00136

Mayer, K., Blume, F., Wyckoff, S. N., Brokmeier, L. L., and Strehl, U. (2016). Neurofeedback of slow cortical potentials as a treatment for adults with attention deficit-/hyperactivity disorder. *Clin. Neurophysiol.* 127, 1374–1386. doi: 10.1016/j.clinph.2015.11.013

Mayer, K., Wyckoff, S. N., Fallgatter, A. J., Ehlis, A.-C. C., and Strehl, U. (2015). Neurofeedback as a nonpharmacological treatment for adults with attention-deficit/hyperactivity disorder (ADHD): study protocol for a randomized controlled trial. *Trials* 16:174. doi: 10.1186/s13063-015-0683-4

Mehler, D. (2019). "The replication challenge: Is brain imaging next?," in *Casting Light on the Dark Side of Brain Imaging*, eds A. Raz and R. T. Thibault (London: Academic Press), 84–88. doi: 10.1016/B978-0-12-816179-1.00010-4

Mehler, D. M. A., Edelsbrunner, P. A., and Matić, K. (2019). Appreciating the significance of non-significant findings in psychology. *J. Eur. Psychol. Students* 10, 1–7. doi: 10.5334/e2019a

Mehler, D. M. A., Williams, A. N., Whittaker, J. R., Krause, F., Lührs, M., Wise, R. G., et al. (2017). *Study Pre-Registration: Gradual Real-Time fMRI Neurofeedback Training of Motor Imagery in Middle Cerebral Artery Stroke Patients*. Available online at: https://osf.io/7q68p/ (accessed April 22, 2020).

Meir-Hasson, Y., Keynan, J. N., Kinreich, S., Jackont, G., Cohen, A., Podlipsky-Klovatch, I., et al. (2016). One-class FMRI-inspired EEG model for self-regulation training. *PLoS ONE* 11:e0154968. doi: 10.1371/journal.pone.0154968

Mihara, M., Hattori, N., Hatakenaka, M., Yagura, H., Kawano, T., Hino, T., et al. (2013). Near-infrared spectroscopy-mediated neurofeedback enhances efficacy of motor imagery-based training in poststroke victims: a pilot study. *Stroke* 44, 1091–1098. doi: 10.1161/STROKEAHA.111.674507

Mihara, M., Miyai, I., Hattori, N., Hatakenaka, M., Yagura, H., Kawano, T., et al. (2012). Neurofeedback using real-time near-infrared spectroscopy enhances motor imagery related cortical activation. *PLoS ONE* 7:e32234. doi: 10.1371/journal.pone.0032234

Moher, D., Liberati, A., Tetzlaff, J., Altman, D. G., and Group, T. P. (2009). Preferred reporting items for systematic reviews and meta-analyses: the PRISMA statement. *PLoS Med.* 6:e1000097. doi: 10.1371/journal.pmed.1000097

Narita, N. (2015). Application of NIRS as a non-invasive and supportive tool for autism spectrum disorders. *Trans. Jpn. Soc. Med. Biol. Eng.* 53, S153_01. doi: 10.11239/jsmbe.53.S153_01

Naseer, N., and Hong, K.-S. S. (2015). fNIRS-based brain-computer interfaces: a review. *Front. Hum. Neurosci.* 9:3. doi: 10.3389/fnhum.2015.00003

Nichols, T. E., Das, S., Eickhoff, S. B., Evans, A. C., Glatard, T., Hanke, M., et al. (2016). Best practices in data analysis and sharing in neuroimaging using MRI. *bioRxiv* 054262. doi: 10.1101/054262

Nieuwenhuis, S., Forstmann, B. U., and Wagenmakers, E. J. (2011). Erroneous analyses of interactions in neuroscience: a problem of significance. *Nat. Neurosci.* 14, 1105–1107. doi: 10.1038/nn.2886

Ninaus, M., Kober, S. E., Witte, M., Koschutnig, K., Stangl, M., Neuper, C., et al. (2013). Neural substrates of cognitive control under the belief of getting neurofeedback training. *Front. Hum. Neurosci.* 7:914. doi: 10.3389/fnhum.2013.00914

Ogawa, S., Tank, D. W., Menon, R., Ellermann, J. M., Kim, S. G., Merkle, H., et al. (1992). Intrinsic signal changes accompanying sensory stimulation: Functional brain mapping with magnetic resonance imaging. *Proc. Natl. Acad. Sci. U.S.A.* 89, 5951–5955. doi: 10.1073/pnas.89.13.5951

Okamoto, M., Dan, H., Sakamoto, K., Takeo, K., Shimizu, K., Kohno, S., et al. (2004). Three-dimensional probabilistic anatomical cranio-cerebral correlation via the international 10–20 system oriented for transcranial functional brain mapping. *Neuroimage* 21, 99–111. doi: 10.1016/j.neuroimage.2003.08.026

Orihuela-Espina, F., Leff, D. R., James, D. R. C., Darzi, A. W., and Yang, G. Z. (2010). Quality control and assurance in functional near infrared spectroscopy (fNIRS) experimentation. *Phys. Med. Biol.* 55, 3701–3724. doi: 10.1088/0031-9155/55/13/009

Paret, C., Goldway, N., Zich, C., Keynan, J. N., Hendler, T., Linden, D., et al. (2019). Current progress in real-time functional magnetic resonance-based neurofeedback: methodological challenges and achievements. *Neuroimage* 202:116107. doi: 10.1016/j.neuroimage.2019.116107

Pfeifer, M. D., Scholkmann, F., and Labruyère, R. (2018). Signal processing in functional near-infrared spectroscopy (fNIRS): methodological differences lead to different statistical *results*. 11:641. doi: 10.3389/fnhum.2017.00641

Pinti, P., Aichelburg, C., Gilbert, S., Hamilton, A., Hirsch, J., Burgess, P., et al. (2018a). A review on the use of wearable functional near-infrared spectroscopy in naturalistic environments. *Jpn. Psychol. Res.* 60, 347–373. doi: 10.1111/jpr.12206

Pinti, P., Tachtsidis, I., Hamilton, A., Hirsch, J., Aichelburg, C., Gilbert, S., et al. (2018b). The present and future use of functional near-infrared spectroscopy (fNIRS) for cognitive neuroscience. *Ann. N. Y. Acad. Sci.* 1464, 5–29. doi: 10.1111/nyas.13948

Poldrack, R. A., Baker, C. I., Durnez, J., Gorgolewski, K. J., Matthews, P. M., Munafò, M. R., et al. (2017). Scanning the horizon: towards transparent and reproducible neuroimaging research. *Nat. Rev. Neurosci.* 18, 115–126. doi: 10.1038/nrn.2016.167

Poldrack, R. A., Paré-Blagoev, E. J., and Grant, P. E. (2002). Pediatric functional magnetic resonance imaging: progress and challenges. *Top. Magn. Reson. Imaging* 13, 61–70. doi: 10.1097/00002142-200202000-00005

Quaresima, V., and Ferrari, M. (2019). A mini-review on functional near-infrared spectroscopy (fNIRS): where do we stand, and where should we go? *Photonics* 6:87. doi: 10.3390/photonics6030087

Ramot, M., Kimmich, S., Gonzalez-Castillo, J., Roopchansingh, V., Popal, H., White, E., et al. (2017). Direct modulation of aberrant brain network connectivity through real-time neurofeedback. *Elife* 6:e28974. doi: 10.7554/eLife.28974.021

Rance, M., Walsh, C., Sukhodolsky, D. G., Pittman, B., Qiu, M., Kichuk, S. A., et al. (2018). Time course of clinical change following neurofeedback. *Neuroimage* 181, 807–813. doi: 10.1016/j.neuroimage.2018.05.001

Ros, T., Enriquez-Geppert, S., Zotev, V., Young, K. D., Wood, G., Whitfield-Gabrieli, S., et al. (2020). Consensus on the reporting and experimental design of clinical and cognitive-behavioural neurofeedback studies (CRED-nf checklist). *Brain*. doi: 10.1093/brain/awaa009

Sato, T., Nambu, I., Takeda, K., Aihara, T., Yamashita, O., Isogaya, Y., et al. (2016). Reduction of global interference of scalp-hemodynamics in functional near-infrared spectroscopy using short distance probes. *Neuroimage* 141, 120–132. doi: 10.1016/j.neuroimage.2016.06.054

Schabus, M., Griessenberger, H., Gnjezda, M.-T., Heib, D. P. J., Wislowska, M., and Hoedlmoser, K. (2017). Better than sham? A double-blind placebo-controlled neurofeedback study in primary insomnia. *Brain* 140, 1041–1052. doi: 10.1093/brain/awx011

Schäfer, T., and Schwarz, M. A. (2019). The meaningfulness of effect sizes in psychological research : differences between sub-disciplines and the impact of potential biases. *Front. Psychol.* 10:813. doi: 10.3389/fpsyg.2019.00813

Scharnowski, F., Veit, R., Zopf, R., Studer, P., Bock, S., Diedrichsen, J., et al. (2015). Manipulating motor performance and memory through real-time fMRI neurofeedback. *Biol. Psychol.* 108, 85–97. doi: 10.1016/j.biopsycho.2015.03.009

Scheel, A. M., Schijen, M., and Lakens, D. (2020). An excess of positive results: comparing the standard psychology literature with registered reports. *PsyArXiv* 1–14. doi: 10.31234/osf.io/p6e9c

Scholkmann, F., Kleiser, S., Metz, A. J., Zimmermann, R., Mata Pavia, J., Wolf, U., et al. (2014). A review on continuous wave functional near-infrared spectroscopy and imaging instrumentation and methodology. *Neuroimage* 85, 6–27. doi: 10.1016/j.neuroimage.2013.05.004

Schönbrodt, F. D., and Wagenmakers, E. J. (2018). Bayes factor design analysis: planning for compelling evidence. *Psychon. Bull. Rev.* 25, 128–142. doi: 10.3758/s13423-017-1230-y

Schönenberg, M., Wiedemann, E., Schneidt, A., Scheeff, J., Logemann, A., Keune, P. M., et al. (2017). Neurofeedback, sham neurofeedback, and cognitive-behavioural group therapy in adults with attention-deficit hyperactivity

disorder: a triple-blind, randomised, controlled trial. *Lancet Psychiatry* 4, 673–684. doi: 10.1016/S2215-0366(17)30291-2

Schulz, K. F., Altman, D. G., Moher, D., and CONSORT Group (2010). CONSORT 2010 statement: updated guidelines for reporting parallel group randomised trials. *BMJ* 340:c332. doi: 10.1136/bmj.c332

Sepulveda, P., Sitaram, R., Rana, M., Montalba, C., Tejos, C., and Ruiz, S. (2016). How feedback, motor imagery, and reward influence brain self-regulation using real-time fMRI. *Hum. Brain Mapp.* 37, 3153–3171. doi: 10.1002/hbm.23228

Sherlin, L. H., Arns, M., Lubar, J., Heinrich, H., Kerson, C., Strehl, U., et al. (2011). Neurofeedback and basic learning theory: implications for research and practice. *J. Neurother.* 15, 292–304. doi: 10.1080/10874208.2011.623089

Shibata, K., Lisi, G., Cortese, A., Watanabe, T., Sasaki, Y., and Kawato, M. (2019). Toward a comprehensive understanding of the neural mechanisms of decoded neurofeedback. *Neuroimage* 188, 539–556. doi: 10.1016/j.neuroimage.2018.12.022

Simmons, J. P., Nelson, L. D., and Simonsohn, U. (2011). False-positive psychology. *Psychol. Sci.* 22, 1359–1366. doi: 10.1177/0956797611417632

Singh, A. K., Okamoto, M., Dan, H., Jurcak, V., and Dan, I. (2005). Spatial registration of multichannel multi-subject fNIRS data to MNI space without MRI. *Neuroimage* 27, 842–851. doi: 10.1016/j.neuroimage.2005.05.019

Sitaram, R., Ros, T., Stoeckel, L., Haller, S., Scharnowski, F., Lewis-Peacock, J., et al. (2017). Closed-loop brain training: the science of neurofeedback. *Nat. Rev. Neurosci.* 18, 86–100. doi: 10.1038/nrn.2016.164

Skinner, B. F. (1963). Operant behavior. *Am. Psychol.* 18, 503–515. doi: 10.1037/h0045185

Sorger, B., Scharnowski, F., Linden, D. E. J., Hampson, M., and Young, K. D. (2019). Control freaks: towards optimal selection of control conditions for fMRI neurofeedback studies. *Neuroimage* 186, 256–265. doi: 10.1016/j.neuroimage.2018.11.004

Spetter, M. S., Malekshahi, R., Birbaumer, N., Lührs, M., van der Veer, A. H., Scheffler, K., et al. (2017). Volitional regulation of brain responses to food stimuli in overweight and obese subjects: a real-time fMRI feedback study. *Appetite* 112, 188–195. doi: 10.1016/j.appet.2017.01.032

Stangl, M., Bauernfeind, G., Kurzmann, J., Scherer, R., and Neuper, C. (2013). A haemodynamic brain-computer interface based on real-time classification of near infrared spectroscopy signals during motor imagery and mental arithmetic. *J. Near Infrared Spectrosc.* 21, 157–171. doi: 10.1255/jnirs.1048

Stone, W. L., and Lemanek, K. L. (1990). "Developmental issues in children's self-reports," in *Through the Eyes of the Child: Obtaining Self-Reports from Children and Adolescents*, ed A. M. La Greca (Boston, MA: Allyn and Bacon), 18–56.

Storchak, H., Hudak, J., Haeussinger, F. B., Rosenbaum, D., Fallgatter, A. J., and Ehlis, A. C. (2018). Reducing auditory verbal hallucinations by means of fNIRS neurofeedback–a case study with a paranoid schizophrenic patient. *Schizophr. Res.* 204, 401–403. doi: 10.1016/j.schres.2018.09.018

Strehl, U., Aggensteiner, P., Wachtlin, D., Brandeis, D., Albrecht, B., Arana, M., et al. (2017). Neurofeedback of slow cortical potentials in children with attention-deficit/hyperactivity disorder: a multicenter randomized trial controlling for unspecific effects. *Front. Hum. Neurosci.* 11:135. doi: 10.3389/fnhum.2017.00135

Szucs, D., and Ioannidis, J. P. A. A. (2017). Empirical assessment of published effect sizes and power in the recent cognitive neuroscience and psychology literature. *PLoS Biol.* 15:e2000797. doi: 10.1371/journal.pbio.2000797

Tachtsidis, I., and Scholkmann, F. (2016). False positives and false negatives in functional near-infrared spectroscopy: issues, challenges, and the way forward. *Neurophotonics* 3:031405. doi: 10.1117/1.NPh.3.3.031405

Thibault, R. T., Lifshitz, M., and Raz, A. (2016). The self-regulating brain and neurofeedback: experimental science and clinical promise. *Cortex* 74, 247–261. doi: 10.1016/j.cortex.2015.10.024

Thibault, R. T., MacPherson, A., Lifshitz, M., Roth, R. R., and Raz, A. (2018). Neurofeedback with fMRI: a critical systematic review. *Neuroimage* 172, 786–807. doi: 10.1016/j.neuroimage.2017.12.071

Thibault, R. T., and Raz, A. (2016). Neurofeedback: the power of psychosocial therapeutics. *Lancet Psychiatry* 3:e18. doi: 10.1016/S2215-0366(16)30326-1

Trambaiolli, L. R., Biazoli, C. E., Cravo, A. M., Falk, T. H., and Sato, J. R. (2018). Functional near-infrared spectroscopy-based affective neurofeedback: feedback effect, illiteracy phenomena, and whole-connectivity profiles. *Neurophotonics* 5:035009. doi: 10.1117/1.NPh.5.3.035009

Tsuzuki, D., Jurcak, V., Singh, A. K., Okamoto, M., Watanabe, E., and Dan, I. (2007). Virtual spatial registration of stand-alone fNIRS data to MNI space. *Neuroimage* 34, 1506–1518. doi: 10.1016/j.neuroimage.2006.10.043

Tufanaru, C., Munn, Z., Aromataris, E., Campbell, J., and Hopp, L. (2017). "Chapter 3: Systematic reviews of effectiveness," in *Joanna Briggs Institute Reviewer's Manual*, eds E. Aromataris and Z. Munn (The Joanna Briggs Institute). Available online at: https://reviewersmanual.joannabriggs.org/

Van Doren, J., Arns, M., Heinrich, H., Vollebregt, M. A., Strehl, U., and Loo, S. K. (2019). Sustained effects of neurofeedback in ADHD: a systematic review and meta-analysis. *Eur. Child Adolesc. Psychiatry* 28, 293–305. doi: 10.1007/s00787-018-1121-4

Veenman, M. V. J. (2011). Alternative assessment of strategy use with self-report instruments: a discussion. *Metacogn. Learn.* 6, 205–211. doi: 10.1007/s11409-011-9080-x

von Lühmann, A., Herff, C., Heger, D., and Schultz, T. (2015). Toward a wireless open source instrument: functional near-infrared spectroscopy in mobile neuroergonomics and BCI applications. *Front. Hum. Neurosci.* 9:617. doi: 10.3389/fnhum.2015.00617

von Lühmann, A., Ortega-Martinez, A., Boas, D. A., and Yücel, M. A. (2020). Using the general linear model to improve performance in fNIRS single trial analysis and classification: a perspective. *Front. Hum. Neurosci.* 14:30. doi: 10.3389/fnhum.2020.00030

Weyand, S., Takehara-Nishiuchi, K., and Chau, T. (2015). Weaning off mental tasks to achieve voluntary self-regulatory control of a near-infrared spectroscopy brain-computer interface. *IEEE Trans. Neural Syst. Rehabil. Eng.* 23, 548–561. doi: 10.1109/TNSRE.2015.2399392

Yamashita, A., Hayasaka, S., Kawato, M., and Imamizu, H. (2017). Connectivity neurofeedback training can differentially change functional connectivity and cognitive performance. *Cereb. Cortex* 27, 4960–4970. doi: 10.1093/cercor/bhx177

Zhao, Z., Yao, S., Li, K., Sindermann, C., Zhou, F., Zhao, W., et al. (2019). Real-time functional connectivity-informed neurofeedback of amygdala-frontal pathways reduces anxiety. *Psychother. Psychosom.* 88, 5–15. doi: 10.1159/000496057

Gelman, A. (2018). You need 16 times the sample size to estimate an interaction than to estimate a main effect. Retrieved from: https://statmodeling.stat.columbia.edu/2018/03/15/need-16-times-sample-size-estimate-interaction-estimate-main-effect/#comment-685111/

Kanoh, S., Susila, I., and Miyamoto, K. (2011). The Effect of neurofeedback training on cortical activity during motor imagery revealed by NIRS and fMRI. *Int. J. Bioelectromagn* 13, 82–83. Available online at: http://133.25.196.106/2006-/volume13/number2/2011_v13_no2_82-83.pdf

Tsuzuki, D., and Dan, I. (2014). Spatial registration for functional near-infrared spectroscopy: From channel position on the scalp to cortical location in individual and group analyses. *Neuroimage* 85, 92–103. doi: 10.1016/J.NEUROIMAGE.2013.07.025

Zhang, X., Noah, J. A., and Hirsch, J. (2016). Separation of the global and local components in functional near-infrared spectroscopy signals using principal component spatial filtering. *Neurophotonics* 3:015004. doi: 10.1117/1.NPh.3.1.015004

Conflict of Interest: ML is an employee of the research company Brain Innovation B.V., Maastricht, Netherlands. He was not involved in data extraction and quality assessments of the studies. He mainly contributed to the methodological section summarizing the current state of methods used for fNIRS real-time processing and discussing recent methodological developments in the field. RT has received payments to consult with neurofeedback start-up companies.

The remaining authors declare that the research was conducted in the absence of any commercial or financial relationships that could be construed as a potential conflict of interest.

Copyright © 2020 Kohl, Mehler, Lührs, Thibault, Konrad and Sorger. This is an open-access article distributed under the terms of the Creative Commons Attribution License (CC BY). The use, distribution or reproduction in other forums is permitted, provided the original author(s) and the copyright owner(s) are credited and that the original publication in this journal is cited, in accordance with accepted academic practice. No use, distribution or reproduction is permitted which does not comply with these terms.

frontiers in Neuroscience

METHODS
published: 22 July 2020
doi: 10.3389/fnins.2020.00728

Adaptive Wavelet Based MRI Brain Image De-noising

Noorbakhsh Amiri Golilarz[1], Hui Gao[1]*, Rajesh Kumar[1], Liaqat Ali[2], Yan Fu[1] and Chun Li[3]*

[1] School of Computer Science and Engineering, University of Electronic Science and Technology of China, Chengdu, China, [2] School of Information and Communication Engineering, University of Electronic Science and Technology of China, Chengdu, China, [3] The 54th Research Institute of China Electronics Technology Group Corporation, Shijiazhuang, China

This paper presents a unique approach for wavelet-based MRI brain image de-noising. Adaptive soft and hard threshold functions are first proposed to improve the results of standard soft and hard threshold functions for image de-noising in the wavelet domain. Then, we applied the newly emerged improved adaptive generalized Gaussian distributed oriented threshold function (improved AGGD) on the MRI images to improve the results of the adaptive soft and hard threshold functions and also to display, this non-linear and data-driven function can work promisingly even in de-noising the medical images. The most important characteristic of this function is that it is dependent on the image since it is combined with an adaptive generalized Gaussian distribution function.Traditional thresholding neural network (TNN) and optimized based noise reduction have good results but fail to keep the visual quality and may blur some parts of an image. In TNN and optimized based image de-noising, it was required to use Least-mean-square (LMS) learning and optimization algorithms, respectively to find the optimum threshold value and parameters of the threshold functions which was time consuming. To address these issues, the improved AGGD based image de-noising approach is introduced to enhance the qualitative and quantitative performance of the above mentioned image de-noising techniques. De-noising using improved AGGD threshold function provides better results in terms of Peak Signal to Noise Ratio (PSNR) and also faster processing time since there is no need to use any Least-mean-square (LMS) learning and optimization algorithms for obtaining the optimum value and parameters of the thresholding functions. The experimental results indicate that image de-noising using improved AGGD threshold performs pretty well comparing with the adaptive threshold, standard threshold, improved wavelet threshold, and the optimized based noise reduction methods.

Keywords: wavelet, MRI image de-noising, AGGD, adaptive threshold, PSNR

OPEN ACCESS

Edited by:
John Ashburner,
University College London,
United Kingdom

Reviewed by:
Zhifang Pan,
Wenzhou Medical University, China
Gulsher Ali Baloch,
Sukkur IBA University, Pakistan
Muhammad Aksam,
COMSATS University Islamabad,
Lahore Campus, Pakistan

****Correspondence:***
Noorbakhsh Amiri Golilarz
noorbakhsh.amiri@std.uestc.edu.cn
Hui Gao
huigao@uestc.edu.cn

Specialty section:
This article was submitted to Brain Imaging Methods, a section of the journal Frontiers in Neuroscience

Received: *28 March 2020*
Accepted: *18 June 2020*
Published: *22 July 2020*

Citation:
Amiri Golilarz N, Gao H, Kumar R, Ali L, Fu Y and Li C (2020) Adaptive Wavelet Based MRI Brain Image De-noising. Front. Neurosci. 14:728. doi: 10.3389/fnins.2020.00728

1. INTRODUCTION

Image de-noising is among the most important tasks in image and signal processing. Wide range of unwanted noises may affect the visual quality of images. The noise can affect an image during the processes of acquisition and transmission which can cause deflection from an original image. It is obvious that the image quality and resolution may be contaminated by these artifacts so that it is required to do image de-noising as the first step before any further analysis, such as super-resolution, classification and any qualitative and quantitative measurement.

One of the most crucial issues in image de-noising is keeping the most influential characteristics of the images and removing the non-important characteristics. Noise removal has become one of the critical pre-processing steps in many applications like remote sensing, satellite and biomedical image processing (Golilarz et al., 2019b). Some of these noises can affect the appearance and damage the attribute of an image. Others may not be continuous and they occur randomly. In this case, it is very difficult to get rid of these kinds of noises. However, many methods have been proposed for reducing the possible noises from the images and enhancing their quality.

Yuan and Ghanem (2015) introduced a new approach for image restoration in the presence of impulse noise. Weighted couple sparse representation has been introduced by Chen et al. (2015). To remove multimodal noise using semi-supervised learning on big data, Yin et al. (2018) introduced a highly accurate image reconstruction. Garnett et al. (2005) introduced a universal noise reduction algorithm combined with an impulse detector. Median- type noise detectors and detail-preserving regularization based noise removal are proposed by Chan et al. (2005). Moreover, impulse noise reduction with Gaussian curvature of image surface is proposed by Miura et al. (2013). Lin et al. (2010) introduced impulse noise suppression using a new adaptive center weighted median (ACWM) filter. A new impulse detector combined with weighted median filter is proposed by Dong and Xu (2007) to obtain the directional weighted median (DWM) filter. Universal noise reduction using a switching bilateral filter combined with a noise detector is utilized by Lin et al. (2010). The standard deviation to

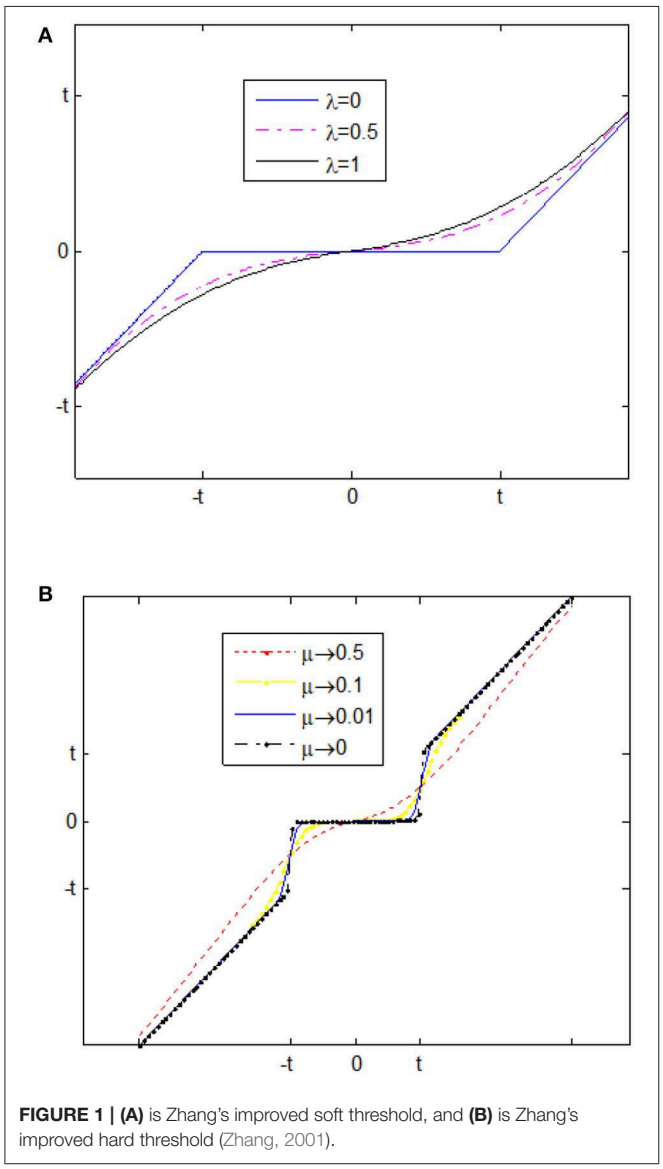

FIGURE 1 | (A) is Zhang's improved soft threshold, and **(B)** is Zhang's improved hard threshold (Zhang, 2001).

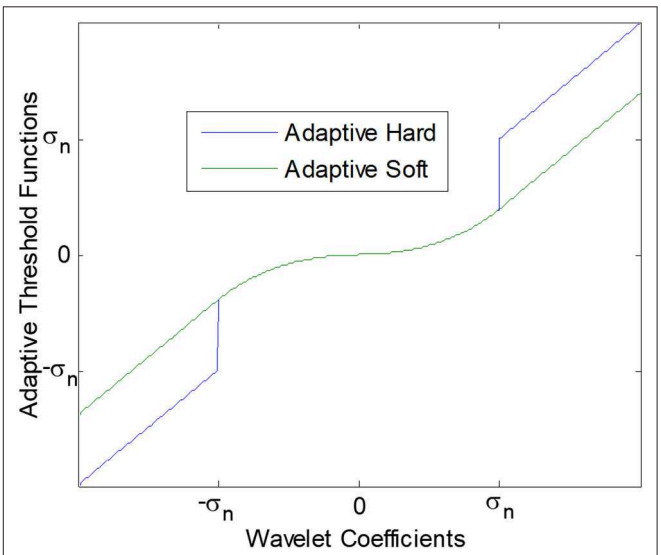

FIGURE 2 | Adaptive threshold functions.

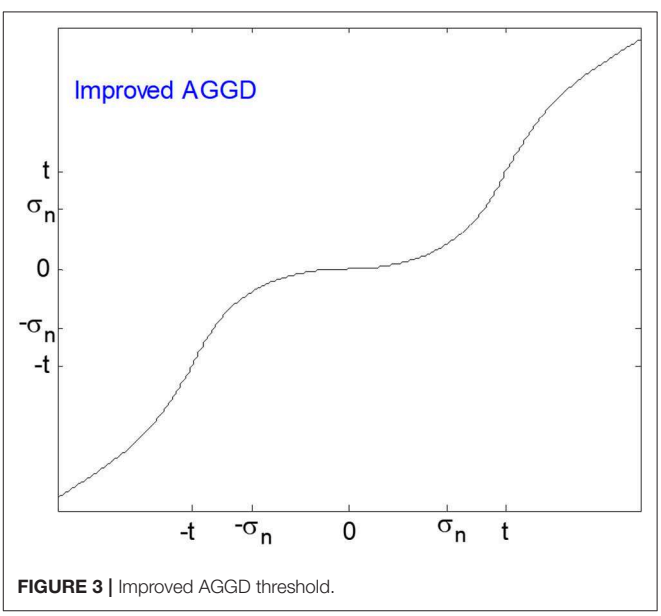

FIGURE 3 | Improved AGGD threshold.

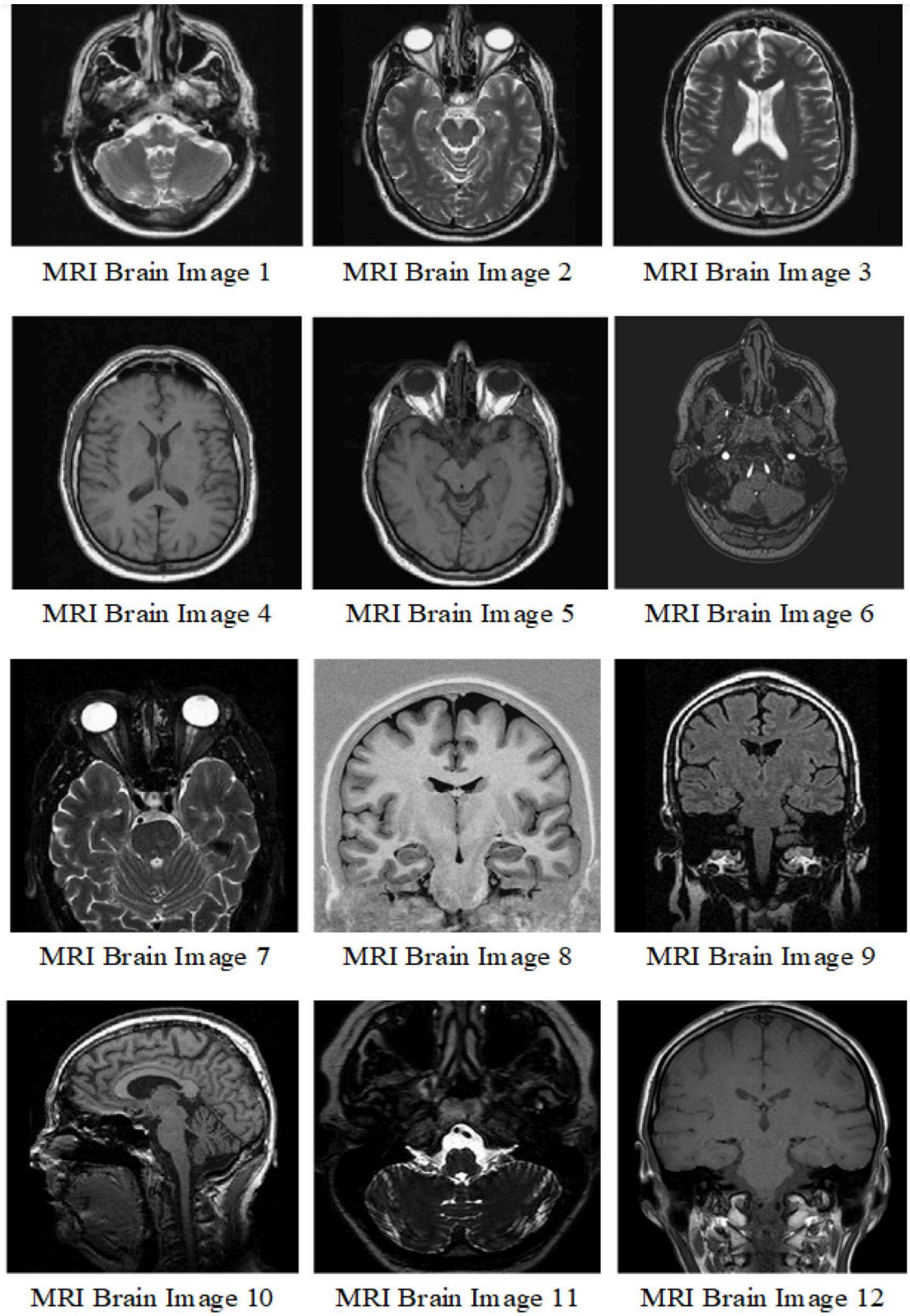

FIGURE 4 | Original MRI brain images.

acquire the optimal direction is proposed by Awad (2011) as a new technique to discard the noise from images influenced by random-valued impulse noise. In 2013, Lu et al. proposed sparse coding for noise removing with spike and slab prior (Lu et al., 2013). Noise reduction utilizing a scale mixture of Gaussians was presented by Portilla et al. (2003). In this technique, the components have been explained with a statistical model. Additionally, the estimation of mode in high-dimensional spaces using flat-top kernels has been proposed in a study conducted by De Decker et al. (2011). Recently, wavelet and thresholding based noise reduction has become very common among researchers in the field of image and signal processing. Many techniques have been introduced to discard the noises and keep the most significant characteristics of images in the wavelet domain.

Chang et al. (2000) proposed context modeling for parameter estimation of each component which is adaptive to wavelet thresholding. It is clear, this component is modeled as a random variable for GGD. Based on the obtained results, this method has better performance than orthogonal transform. Speckle noise reduction utilizing a Bayesian multiscale method is introduced by Achim et al. (2001). An empirical Bayes method with Jeffrey's non-informative prior is also a noise removal method based on wavelet transform proposed by Figueiredo and Nowak (2001). Şendur and Selesnick (2002) proposed bivariate shrinkage function for image denoising using wavelet transform. Image de-noising using joint inter- and interscale statistical model, translation invariant wavelet transformations, and Bayesian wavelet shrinkage based on heavy-tailed modeling have been proposed by Pizurica et al. (2002), Achim et al. (2003), and Sveinsson and Benediktsson (2003), respectively.

Starck et al. (2002) proposed the curvelet transform for noise reduction. Additionally, sparse and redundant representations over learned dictionaries for noise removing is proposed by Elad and Aharon (2006). The local adaptive wiener filter approach for noise suppression in wavelet domain is introduced by Li et al. (2011). Image de-noising with an un-decimated wavelet transform (UWT) utilizing soft thresholding function is introduced by Golilarz and Demirel (2018a). Furthermore, image de-noising based on translation invariant wavelet transform combined with smooth sigmoid based shrinkage (SSBS) function is introduced by Golilarz et al. (2017). Adapting to unknown smoothness via wavelet shrinkage is introduced by Donoho and Johnstone (1995).

To improve the quality and performance of the previous method, Coifman and Donoho (1995) proposed translation-invariant de-noising. Numerous literature has emerged for thresholding neural network (TNN) based noise suppression. Thresholding neural network (TNN) for adaptive noise reduction is proposed by Zhang (2001). In this study, new types of soft and hard threshold functions have been presented to be utilized as the activation function in TNN. These threshold functions are differentiable and non-linear. Moreover, thresholding neural network-based noise reduction with a smooth sigmoid based shrinkage and TNN using an improved threshold function have been proposed by Golilarz and Demirel (2017) and Golilarz and Demirel (2018b), respectively. Image denoising in the wavelet domain based on improved TNN and cycle spinning has been conducted in a study proposed by Sahraeian et al. (2007). In this study, the authors utilized a new adaptive improved threshold function combined with cycle spinning to enhance the results of TNN based image de-noising using adaptive thresholding. Besides, Nasri and Nezamabadi-pour (2009) presented a new adaptive thresholding function for wavelet based noise removal. In their research, they introduced a new TNN combined with a new type of adaptive function with three shape tuning parameters to improve the Zhang's approach (Zhang, 2001). Golilarz et al. (2018) introduced a new method for hyperspectral remote sensing image de-noising utilizing 3D un-decimated wavelet transform with a new improved soft thresholding function to improve the results of previous threshold based noise removal. Qian (2018) proposed an algorithm for image de-noising utilizing an enhanced thresholding and median filter. One of the drawbacks and limitations of utilizing TNN based noise reduction is that it is time-consuming. Gradient-based learning is used in TNN to attain the optimum threshold value. Therefore, to address this problem, Bhandari et al. (2016) proposed optimized adaptive thresholding based image de-noising which they used JADE optimization algorithm instead of the steepest descent gradient based LMS method to decrease the computational time for attaining the optimum threshold value and other parameters.

To improve the efficiency of de-noising based on JADE algorithm, Golilarz et al. (2019b) utilized Harris Hawks optimization (HHO) algorithm (Heidari et al., 2019) in the first stage, and then improved adaptive generalized Gaussian distribution (AGGD) threshold function (Golilarz et al., 2019a)

TABLE 1 | Performance analysis of adaptive and standard threshold for MRI image de-noising in terms of PSNR values.

Image	Variance	Hard	Soft	Adaptive hard	Adaptive soft
MRI image 1	0.01	20.56	21.46	23.52	25.74
	0.03	19.39	20.41	21.83	23.80
	0.05	18.71	19.63	21.01	22.69
MRI image 2	0.01	22.78	23.47	25.61	27.39
	0.03	20.14	21.31	24.5	26.51
	0.05	19.56	20.7	23.81	24.83

TABLE 2 | Performance analysis of adaptive and standard threshold for MRI image de-noising in terms of MSE.

Image	Variance	Hard	Soft	Adaptive hard	Adaptive soft
MRI image 1	0.01	571	465	289	173
	0.03	748	592	427	271
	0.05	875	708	515	350
MRI image 2	0.01	343	292	179	118
	0.03	630	481	231	145
	0.05	719	553	270	214

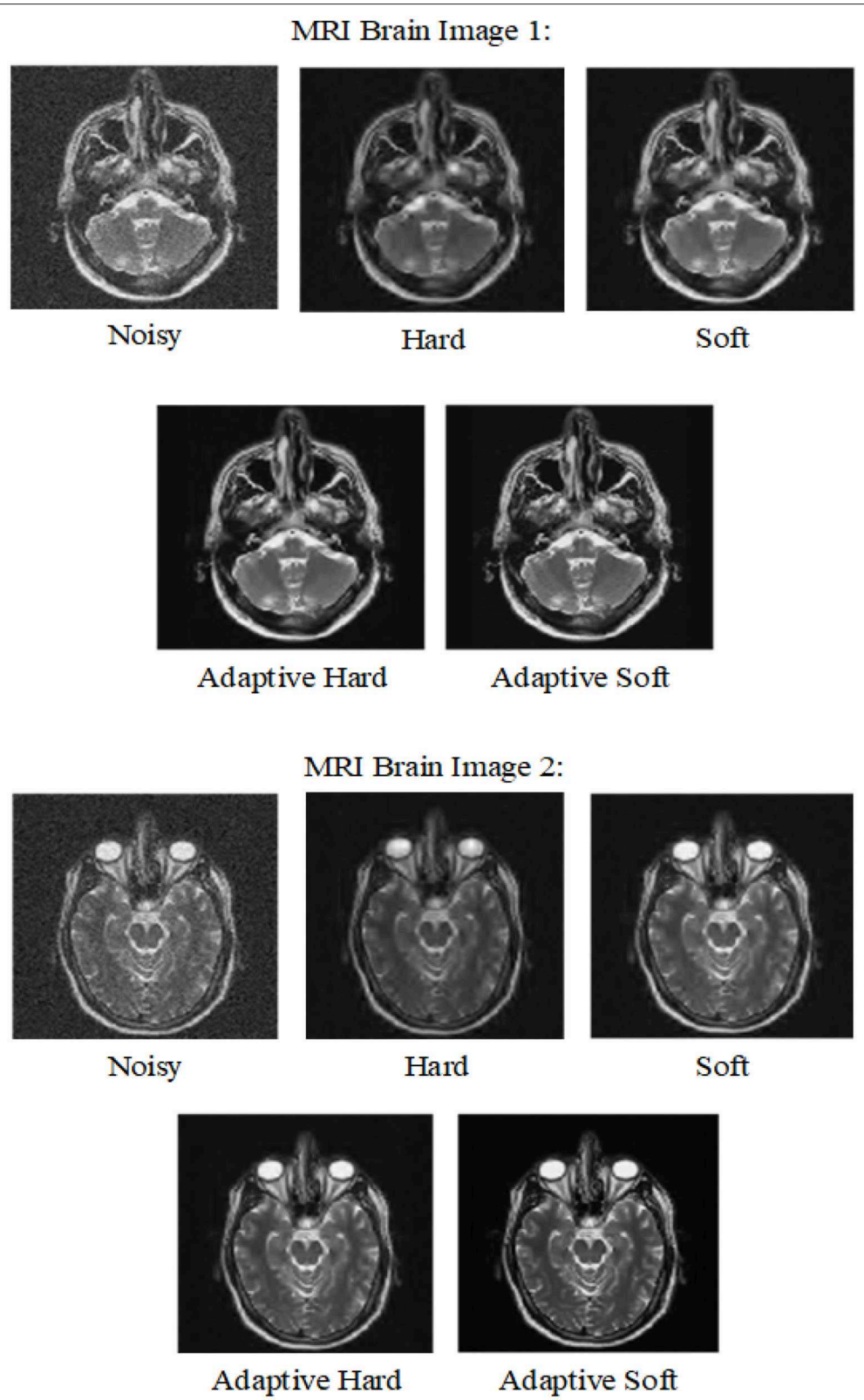

FIGURE 5 | Visual comparison between adaptive and standard thresholds for variance 0.03.

is used to enhance the quality of optimized based image de-noising approach, and lessen the computational time as well. The authors indicated that in improved AGGD based noise removal, the optimum value can be acquired without using any LMS learning and optimization algorithm. This advantage can save the processing time. In addition, the performance of wavelet thresholding can be enhanced using the adaptive GGD function because it provides us with more information about the image which the noisy constituents can be controlled well utilizing this adaptive function.

In this research, in the first stage we present adaptive soft and adaptive hard threshold to improve the results of standard hard and standard soft threshold function. In standard hard threshold, the small components are set to zero but adaptive soft and adaptive hard threshold can tune these coefficients using AGGD function in the interval $[-\sigma_n, \sigma_n]$. The results proved that adaptive threshold acts better than standard threshold in image de-noising. Additionally, to enhance the performance of image de-noising using optimization algorithms, improved adaptive generalized Gaussian distribution (AGGD) threshold is used for MRI brain image de-nosing. Moreover, we compared the proposed method with improved wavelet threshold proposed by Zhang et al. (2019). Experimental results prove the superiority of the proposed method over standard threshold, adaptive threshold, optimization (Golilarz et al., 2019b), and improved wavelet threshold (Zhang et al., 2019) based image de-noising methods.

2. WAVELET BASED IMAGE DE-NOISING

To get the output de-noised image in the wavelet domain, we can do as follows (Golilarz et al., 2019b). Firstly, by applying wavelet transform we will get wavelet coefficients. These components can be sorted in two main groups: those carrying the most significant features of images and those having the non-important characteristics, with the former is the detail coefficient and latter is the non-important coefficients or noisy constituents. Next, these wavelet coefficients which we got from the first step, should be tuned using a suitable threshold value to preserve the crucial features and attribute of the image and discard the non-important components. These tuned components are called as thresholded wavelet coefficients. Then, it is time to apply the inverse wavelet transform (IWT) on these tuned thresholded wavelet coefficients providing us with the noise free image. On this matter, it is an important task to use a suitable threshold function and a threshold value since it plays an important role in getting our desired output de-noised image.

2.1. Definition of Noise, Threshold, and Mean Square Error

Assume that the noisy vector is as: $f = \left[f_0, f_1, \ldots f_{N-1}\right]^T$ which is contaminated by additive white Gaussian noise (AWGN):

$$f_i = u_i + n_i, \quad i = 0, 1, 2, \ldots, N-1 \tag{1}$$

where, u_i represents the input noise-free wavelet constituents and n_i is the *iid* (independent and identically distributed) Gaussian noise.

Then, assume the data vector without noise as $U = [u_0, u_1, \ldots, u_{N-1}]^T$ and the thresholded output vector as $|\hat{U} = \left[\hat{u}_0, \hat{u}_1, \ldots, \hat{u}_{N-1}\right]^T$ Admittedly, the main goal in image de-noising is to minimize the Mean Square Error risk (Nasri and Nezamabadi-pour, 2009). The Mean Square Error (MSE) risk can be obtained as follows:

$$mse_{risk} = \frac{1}{2}E\|\hat{U} - U\|^2 = \frac{1}{2N}\sum_{i=0}^{N-1}(\widehat{u}_i - u_i)^2 \tag{2}$$

where, N is the size of the sub-band, (u_i) is the input coefficients and $\widehat{u}_i$ the thresholded wavelet coefficients (Nasri and Nezamabadi-pour, 2009).

Noise removal in the wavelet domain requires applying a proper threshold function and the threshold value. The universal threshold value (t_{uni}) can be obtained based on VisuShrink technique using the equation below (Donoho and Johnstone, 1994). VisuShrink applies a universal threshold to all of the wavelet detail constituents. This threshold is known to discard additive Gaussian noise with high probability tending to result in overly smooth image appearance due to the fact that the threshold may be big because of its dependancy to the number of samples, n.

$$t_{uni} = \sigma\sqrt{2\ln(n)} \tag{3}$$

where, n is the sample size and σ is the robust median estimator (Donoho and Johnstone, 1994) as follows:

$$\hat{\sigma} = Median\left(\left|G_{i,j}\right|\right)/0.6745 \tag{4}$$

where, $G_{(i,j)}$ is the components in the HH_1 sub-band (Donoho and Johnstone, 1994).

TABLE 3 | Comparison between different noise reduction methods in terms of PSNR values.

Image	Variance	Hard	Soft	Adaptive hard	Adaptive soft	HHO	Improved AGGD
MRI image 3	0.01	21.05	21.89	24.53	26.29	30.48	33.21
	0.03	19.69	20.43	22.48	24.46	29.11	32.14
	0.05	18.31	18.78	21.75	23.85	28.87	31.26

TABLE 4 | Comparison between different noise reduction methods in terms of MSE.

Image	Variance	Hard	Soft	Adaptive hard	Adaptive soft	HHO	Improved AGGD
MRI image 3	0.01	510	421	229	153	58	31
	0.03	698	589	367	233	79	40
	0.05	959	861	434	268	84	49

2.2. Thresholding Neural Network (TNN)

Thresholding neural network based (space scale adaptive) noise reduction is proposed by Zhang (2001). In this network, there is linear transform which is fixed, and activation function which can be adaptive. The input of TNN is noisy image in which the linear orthogonal transform can be applied on it to get noisy components. Note that η is the non-linear activation function. The noisy coefficients need to be passed through this function to get thresholded wavelet coefficients. Eventually, by applying inverse linear orthogonal transform, we will attain output de-noised image (Golilarz and Demirel, 2018b). Zhang introduced two types of the non-linear threshold, namely: improved soft, and improved hard threshold functions as follows (Zhang, 2001). These functions with different λ and μ values are shown in **Figure 1**.

$$\eta_{soft}(x,t) = x + \frac{1}{2}(\sqrt{(x-t)^2+\lambda} - \sqrt{(x+t)^2+\lambda}) \quad (5)$$

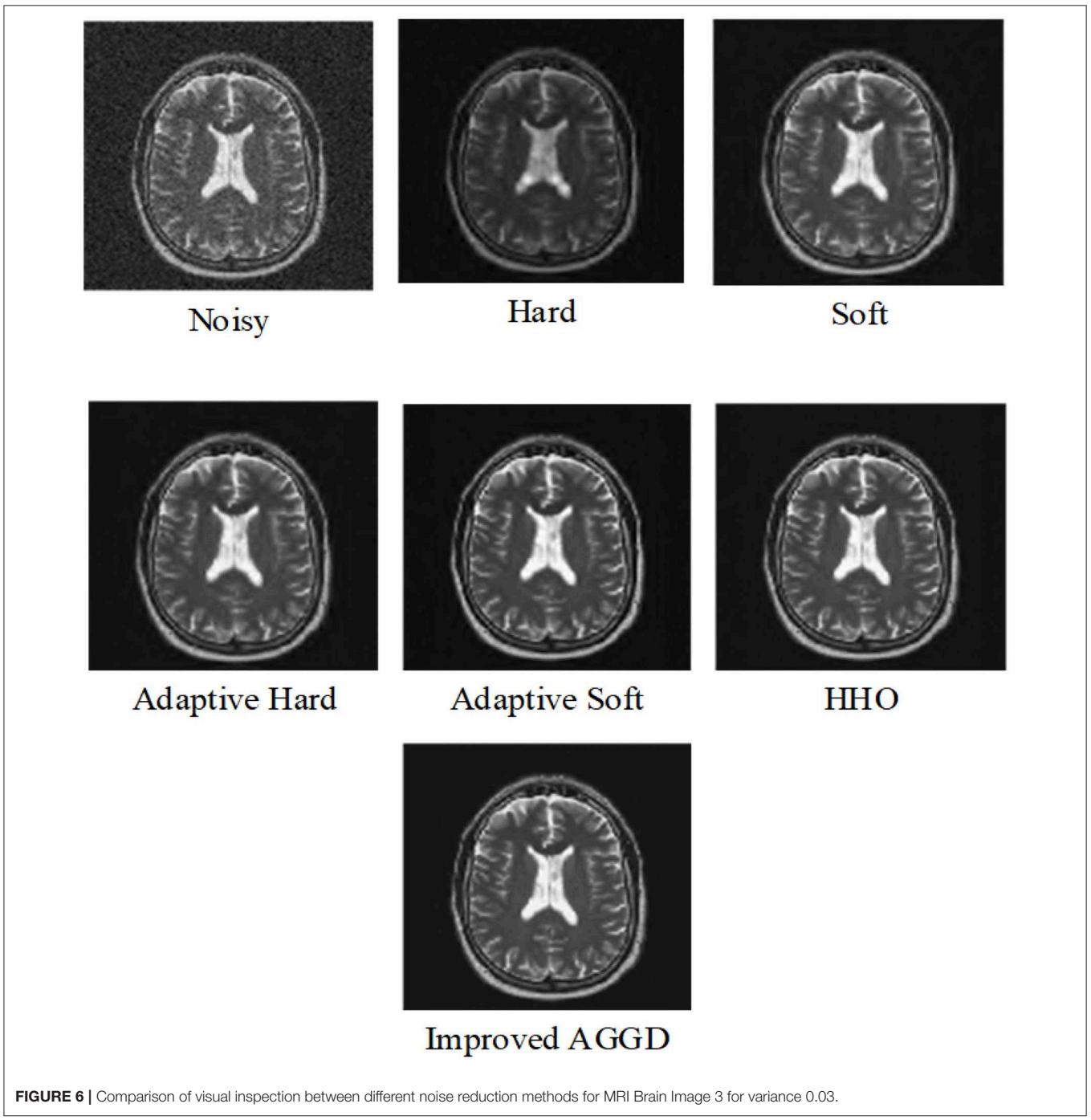

FIGURE 6 | Comparison of visual inspection between different noise reduction methods for MRI Brain Image 3 for variance 0.03.

where, η_{soft} is the improved soft threshold function. Here, x is the wavelet component, t is the threshold value and $\lambda > 0$ is a user-defined function parameter (Zhang, 2001).

$$\eta_{\text{hard}}(x,t) = \left(\frac{1}{1+\exp\left(\frac{-x+t}{\mu}\right)} - \frac{1}{1+\exp\left(\frac{-x-t}{\mu}\right)} + 1 \right) x \tag{6}$$

where, η_{hard} is the improved hard threshold function, x is the wavelet components, t is the threshold value and $\mu > 0$ is a user-defined function parameter (Zhang, 2001). In this network, the optimum threshold value in the step L is given below (Golilarz and Demirel, 2017):

$$t(L+1) = t(L) - \Delta t(L). \tag{7}$$

where, $\Delta t(L)$ is as:

$$\Delta t(L) = \theta(L)\frac{\partial J(t)}{\partial(t)}, t = t(L) \tag{8}$$

where θ is learning rate and $J(t)$ is the MSE risk function.

To improve the efficiency and speed of Zhang's proposed TNN, Nasri and Nezamabadi-pour (2009) introduced a new thresholding neural network in the wavelet domain. Despite the Zhang's network which is space scale adaptive, this network is sub-band adaptive noise reduction (Nasri and Nezamabadi-pour, 2009). Similarly, the activation function is also non-linear and data-driven. The whole procedure of acquiring the de-noised image is mentioned above. In adaptive wavelet-based noise removal techniques, the threshold functions are chosen to be non-linear and adaptive. In this case, to improve the capability of the threshold functions, instead of setting the noisy components (below the threshold value) to zero by standard threshold functions, we can adjust and control these small coefficients using polynomial functions (Bhandari et al., 2016).

2.3. Optimized Based Image De-noising

Noise reduction using an optimized adaptive threshold function combined with nature-inspired optimization algorithms is introduced by Bhandari et al. (2016). The authors presented several optimization algorithms for satellite image de-noising. It was proved that image de-noising using TNN with steepest descent learning is time-consuming so that utilizing the optimization instead of LMS learning algorithm not only can improve the quality but also can increase the speed remarkably. Bhandari et al. (2016), utilized several different evolutionary for image de-noising. In their study, they used Differential Evolution (DE) (Storn and Price, 1997), Particle Swarm Optimization (PSO) (Poli et al., 2007), Wind Driven Optimization (WDO) (Bayraktar et al., 2011), Firefly Algorithm (FA) (Yang, 2010), Cuckoo Search (CS) Algorithm (Yang and Deb, 2009), and JADE algorithm (Zhang and Sanderson, 2009) as the optimizers to obtain the optimized thresholded wavelet coefficients in the process of getting the de-noised image. At the end, it was shown that using JADE algorithm performs better than other optimization algorithms in terms of PSNR values and qualitative results. By getting motivation from this paper, Golilarz et al. (2019b) attempted to improve the cited results by proposing a new technique. Then, it is proposed to apply another meta-heuristic optimizer (Harris Hawks Optimizer introduced by Heidari et al., 2019) instead of using JADE algorithm in the optimization process. The results showed the superiority of HHO based image de-noising method.

The main steps of obtaining the desired de-noised image using an optimization algorithm are as follows (Bhandari et al., 2016):

1. Apply a discrete wavelet transform on input noisy image (AWGN with zero mean and standard deviation of) to get noisy coefficients. Then, we can set the parameters of the optimization algorithm (number of iterations, number of solutions, scale parameters, etc.).
2. The noisy coefficients can be passed through an optimization algorithm consisting of the adaptive function so that the solution for the optimization algorithm can be acquired.
3. After computing it through threshold function, the best fitness values for each solution can be obtained (Bhandari et al., 2016).
4. After passing these parameters through adaptive function, we can get optimized thresholded wavelet coefficients.
5. Inverse discrete wavelet transform (IDWT) can be applied to these coefficients to get output de-noised image.

TABLE 5 | Performance of improved AGGD compared with improved threshold in terms of PSNR values.

MRI images	Variance	Improved threshold	Improved AGGD
MRI image 4	0.01	27.68	33.39
	0.03	25.77	31.41
	0.05	24.35	30.36
MRI image 5	0.01	26.18	32.01
	0.03	25.73	30.76
	0.05	23.62	29.21
MRI image 6	0.01	27.07	32.79
	0.03	24.89	30.12
	0.05	23.51	29.03

TABLE 6 | Performance of improved AGGD compared with improved threshold in terms of MSE.

MRI images	Variance	Improved threshold	Improved AGGD
MRI image 4	0.01	111	30
	0.03	172	50
	0.05	239	60
MRI image 5	0.01	157	41
	0.03	174	54
	0.05	282	78
MRI image 6	0.01	128	34
	0.03	210	63
	0.05	290	81

3. ADAPTIVE THRESHOLD FOR $T = \sigma_N$

3.1. Adaptive Hard Threshold

This function consists of two main parts: in the interval $[-\sigma_n, \sigma_n]$, which is an AGGD oriented function, and behind the interval which is the identity function. As can be seen in **Figure 2**, since it is discontinuous, we call it an adaptive hard threshold function. We call this function as "tune and keep" since it keeps large coefficients behind the interval and unlike the standard hard threshold function, we can tune the small noisy coefficients instead of setting them to zero. This function is formulated below.

$$\chi(x) = \begin{cases} x & , x < -\sigma_n \\ s(x) - s(0), & |x| \leq \sigma_n \\ x & , x > \sigma_n \end{cases} \tag{9}$$

where $s(x) = \sigma_n \left(e^{\frac{x^2}{2\sigma_n^2} - \frac{1}{2}} \right)$, x is the coefficient, and $t = \sigma_n$ is the threshold value.

3.2. Adaptive Soft Threshold

The main difference between this function and the adaptive hard threshold is its continuity. As **Figure 2** adaptive threshold function which is given below. We call this function as "tune and shrink" since it shrinks large coefficients behind the interval by the threshold value but unlike the standard soft threshold function, it is possible to tune the small noisy coefficients instead of setting them to zero.

$$\beta(x) = \begin{cases} x + (t - s(t) - s(0))) & , x < -\sigma_n \\ s(x) - s(0) & |x| \leq \sigma_n \\ x - (t - s(t) - s(0))) & , x > \sigma_n \end{cases} \tag{10}$$

where, $\beta(x)$ is the adaptive soft threshold, $s(x) = \sigma_n \left(e^{\frac{x^2}{2\sigma_n^2} - \frac{1}{2}} \right)$, x is the coefficient, and $t = \sigma_n$ is the threshold value.

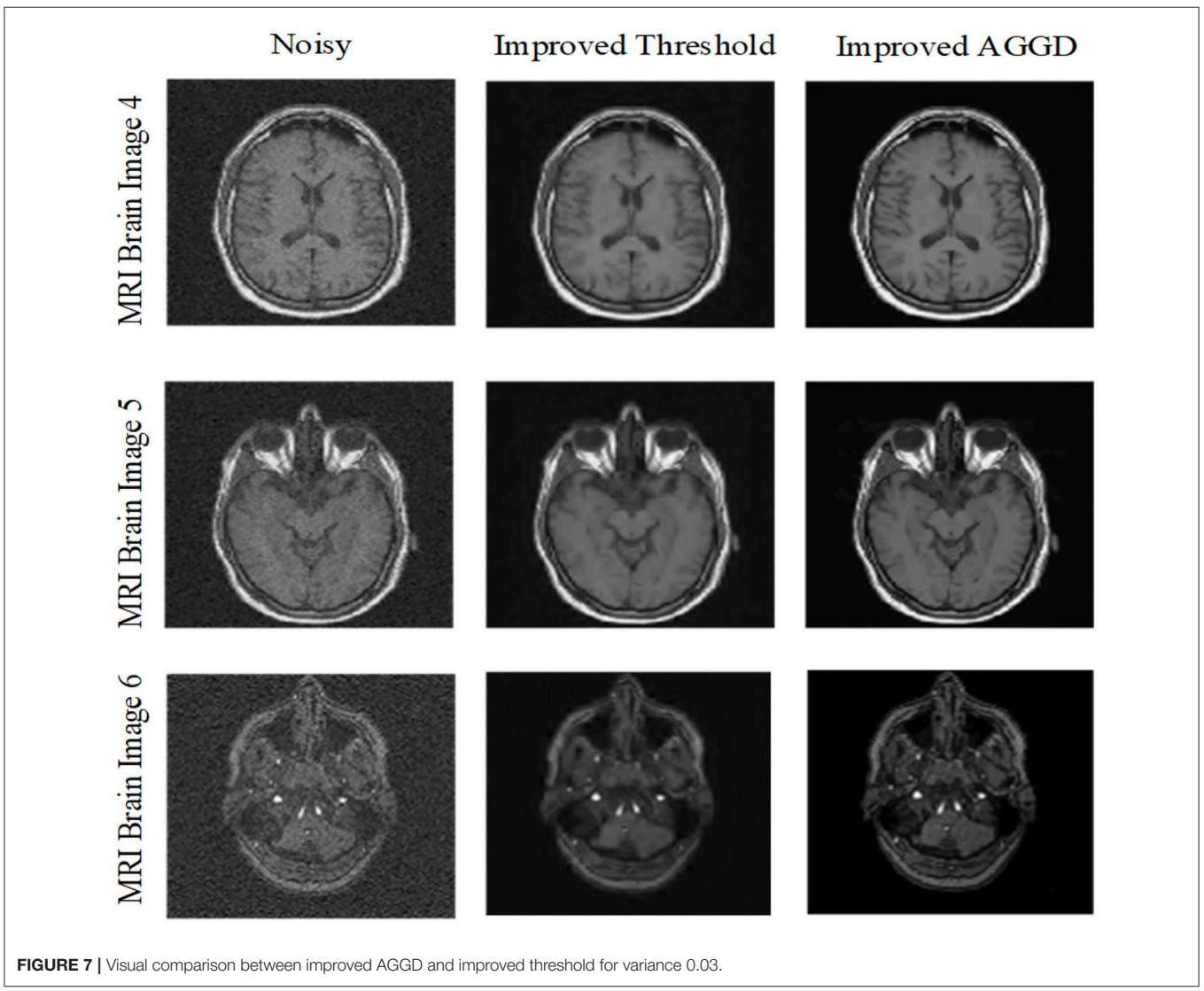

FIGURE 7 | Visual comparison between improved AGGD and improved threshold for variance 0.03.

4. IMPROVED AGGD THRESHOLD FOR $T > \sigma_N$

Golilarz et al., in 2019 proposed an adaptive generalized Gaussian distribution (AGGD) oriented threshold for image de-noising (Golilarz et al., 2019a). This function is data-driven, non-linear, and also flexible and fitted to any kind of images so that it can be shaped in various images. These are the most important characteristics of this function. It is proved that in the interval $[-t, t]$, this function tunes the non-important constituents using an adaptive GGD threshold function instead of setting these coefficients to zero. Admittedly, this characteristic enhances the capability and flexibility of this function. The AGGD threshold function is given as (Golilarz et al., 2019a):

$$\rho(x) = \begin{cases} x & ,x < -t \\ s(x) - s(0), & |x| \leq t \\ x & x > t \end{cases} \tag{11}$$

where, $s(x) = \sigma_n \left(e^{\frac{x^2}{2\sigma n^2} - \frac{1}{2}} \right)$, x is the coefficient, σ_n is the robust median estimator and t is the threshold value. This value is the inter section of x and $s(x)$.

Golilarz et al. (2019b) improved the capability, quality, and speed of their former method (AGGD) by proposing an improved version of AGGD threshold function which results in an enhancement in both qualitative and quantitative results. This function is completely non-linear and differentiable by an adaptive generalized Gaussian distribution function in the interval [−t, t], and another non-linear function behind the interval. Obviously, the whole coefficients can be tuned using non-linear and data-driven functions. Like the AGGD threshold function, the threshold value can be obtained without using any optimization and steepest descent learning algorithms. **Figure 3** shows improved AGGD function. This function is formulated as follows:

$$\mu(x) = \begin{cases} \left(\frac{1}{1+e^{x+t}} \right) x - \frac{t}{2}, & x < -t \\ s(x) - s(0), & |x| \leq t \\ \left(\frac{1}{1+e^{-x+t}} \right) x + \frac{t}{2}, & x > t \end{cases} \tag{12}$$

where, $\mu(x)$ is the improved AGGD threshold, $s(x) = \sigma_n \left(e^{\frac{x^2}{2\sigma_n^2} - \frac{1}{2}} \right)$, x is the coefficient, σ_n is the robust median estimator and t is the threshold value.

5. EXPERIMENTAL RESULTS

In this part we used four experiments to show the superiority of using improved AGGD method both qualitatively and quantitatively. In this research we used Peak Signal to Noise Ratio(PSNR) and MSE to evaluate the performance analysis of different de-noising techniques. MSE and PSNR (dB) can be obtained as follows:

$$MSE = \frac{1}{MN} \sum_{i=1}^{M} \sum_{j=1}^{N} [d(i,j) - \widehat{d}(i,j)]^2 \tag{13}$$

where d is the original image, $\hat{d}$ is the de-noised image and M, N are the size of image (Bhandari et al., 2016).

$$PSNR = 10 \log_{10} \left(\frac{255^2}{MSE} \right) \tag{14}$$

where MSE is the mean square error.

In this part, we analyzed the use of wavelet based noise reduction with adaptive GGD threshold to improve the visual quality of MRI brain images in clinical researches and investigation which may be affected to unwanted noises during receiving and transmitting procedures. Particularly, we applied improved AGGD threshold on brain images in the wavelet domain to evaluate the effectiveness and efficiency of the proposed method in de-noising the medical images in comparison with other techniques.

Here we utilized 12 MRI brain images which are shown in **Figure 4**. The dataset is available in Dataset (2020). The images are affected by additive white Gaussian noise AWGN with zero mean and different variance values. In these experiments we utilized Db4 wavelet with one level of decomposition. For HHO algorithm, the parameters are same with those in the original work of HHO (Heidari et al., 2019).

In the first experiment, as can be seen from **Tables 1**, **2**, we compare adaptive soft, adaptive hard with standard soft and

TABLE 7 | Performance analysis of proposed method compared with Sahraeian and Noorbakhsh's technique for MRI brain image de-noising in terms of PSNR values.

Image	Variance	Sahraeian	Noorbakhsh	Proposed
	0.01	29.54	29.95	33.26
MRI image 7	0.03	28.25	28.64	32.07
	0.05	25.69	26.12	29.65
	0.01	29.78	30.21	33.31
MRI image 8	0.03	27.95	28.51	32.04
	0.05	25.76	26.11	29.51
	0.01	30.42	30.89	34.52
MRI image 9	0.03	29.16	29.63	33.01
	0.05	27.55	27.95	31.51
	0.01	30.39	30.76	33.77
MRI image 10	0.03	29.12	29.68	32.48
	0.05	26.38	26.91	30.1
	0.01	28.62	29.17	32.05
MRI image 11	0.03	27.43	27.87	31.01
	0.05	26.1	26.61	29.59
	0.01	30.03	30.56	33.46
MRI image 12	0.03	28.81	29.15	32.5
	0.05	27.42	27.98	30.89

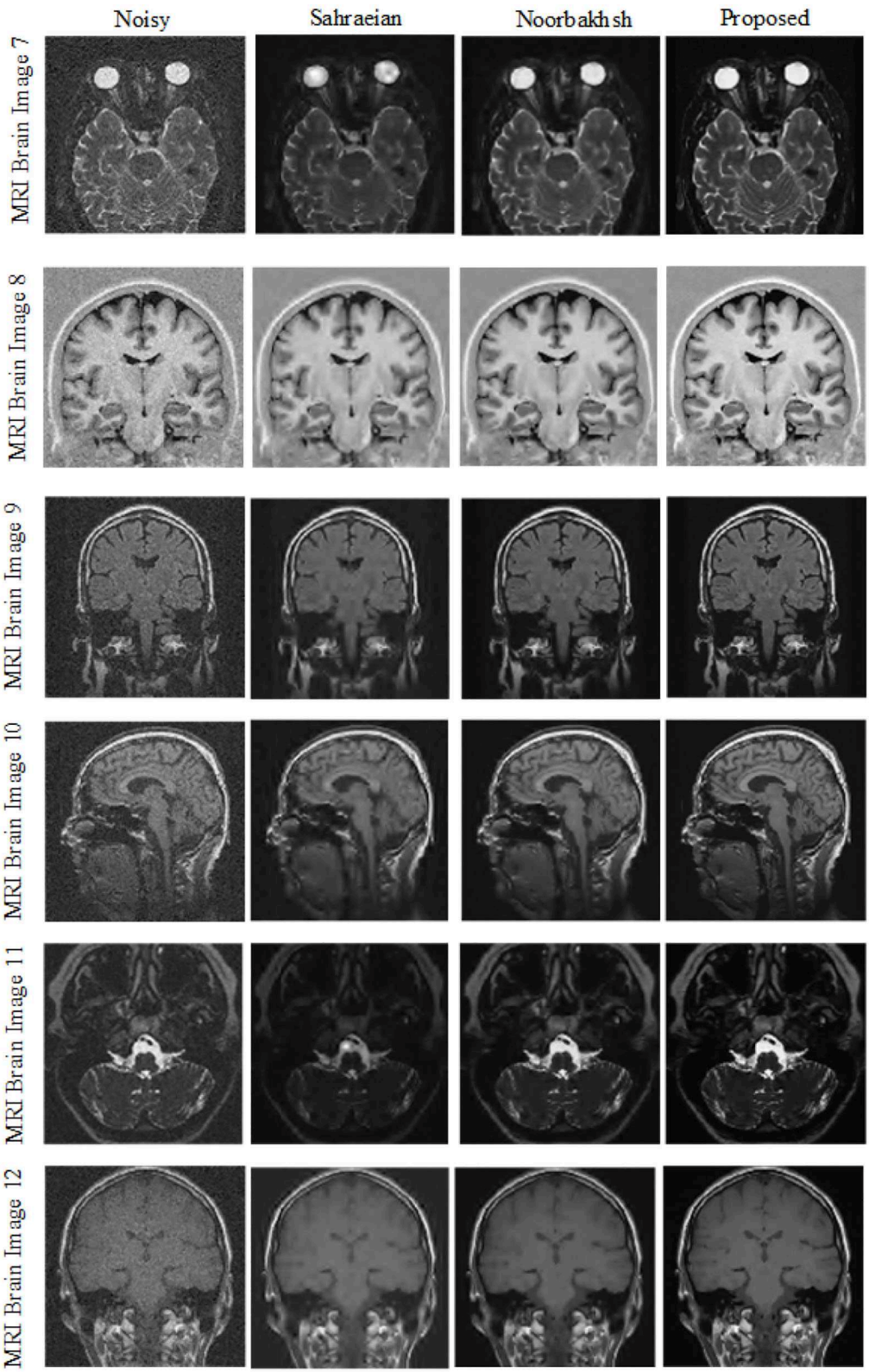

FIGURE 8 | Visual comparison between different noise suppression techniques for variance 0.03.

TABLE 8 | Processing time comparison among different techniques.

Methods	Hard	Soft	Adaptive hard	Adaptive soft	HHO	Improved threshold	Improved AGGD
Time (s)	4.2	4.6	3.5	3.2	4.4	2.6	1.8

standard hard threshold functions in terms of PSNR and MSE. In this experiment we used MRI images 1–2. In addition in **Figure 5**, we can see the visual comparison of these methods. It is obvious that adaptive soft threshold performs well comparing with adaptive hard, standard soft, and standard hard threshold function for image de-noising.

In the second experiment, in **Tables 3**, **4**, we compared improved AGGD with de-noising using Harris Hawks Optimization (HHO) based noise reduction (Golilarz et al., 2019b), adaptive soft, adaptive hard, standard soft, and standard hard thresholds. Note that we used MRI Brain Image 3. Additionally, in **Figure 6** we compared these techniques visually. It is obvious that improved AGGD performs better than other de-noising techniques.

In the third experiment we compared proposed improved AGGD with improved threshold (Zhang et al., 2019). Here we used MRI Brain Images 4–6. As can be seen from **Tables 5**, **6**, improved AGGD performs better than improved threshold function for MRI brain image de-noising. Moreover, **Figure 7** shows the superiority of the proposed technique over improved threshold function qualitatively.

In the fourth experiment we compared the proposed method with Sahraeian et al. (2007) and Noorbakhsh's technique (Golilarz et al., 2018) as well. Here we used MRI Brain Images 7–12. From **Table 7** we can conclude that improved AGGD performs better than Sahraeian and Noorbakhsh's proposed method for MRI brain image de-noising. Additionally, we can see this comparison visually in **Figure 8**.

The improved AGGD based image de-noising is presented to enhance both quality and the processing time. In the last experiment, we compared the processing time among various image de-noising methods. The computational cost of improved AGGD function is cheaper than improved threshold, HHO, adaptive soft, adaptive hard, standard soft and standard hard threshold functions. The speed and computational time among different noise suppression techniques has been compared in **Table 8** for MRI brain Image 1 for variance 0.01. For HHO, the time is the average of 10 runs. For all the implementations and experimental results, we used Matlab programming language on a computer with Intel core i7 and 16 GB RAM.

6. CONCLUSION

In this study, a new method for wavelet-based MRI image de-noising is presented. Firstly, adaptive soft and hard threshold functions are introduced to improve the performance of standard threshold functions in the wavelet domain. Secondly, we used the newly emerged improved adaptive generalized Gaussian distributed oriented threshold function (improved AGGD) on the MRI images to show that, this data driven and image dependent threshold function performs well comparing with adaptive soft and hard threshold functions. Recently, image de-noising in the wavelet domain attracts lots of attentions in image and signal processing. Previous TNN and optimized based noise removal methods have good results but still the quality of an image needs to be enhanced and improved. TNN and optimized based noise reduction methods, require to utilize Least-mean-square (LMS) learning and optimization algorithms, respectively for acquiring the value of the optimum threshold and the parameters of the threshold functions which this process was time consuming. The improved AGGD based image de-noising is presented to solve these drawbacks. The computational cost of improved AGGD method is quite cheaper than the above mentioned techniques because we are in no use of LMS learning and optimization algorithms. This approach has good results in terms of PSNR values. The experimental analysis proves the superiority of improved AGGD threshold over adaptive threshold, standard threshold, improved wavelet threshold, and the optimized based noise reduction methods. For the future work, we will extend this work to deal with other forms of noise like impulse noise and non-Gaussian noise as well.

DATA AVAILABILITY STATEMENT

Publicly available datasets were analyzed in this study. This data can be found here: https://www.mr-tip.com/serv1.php?type=db1&dbs=Brain%20MRI.

AUTHOR CONTRIBUTIONS

NA, HG, RK, LA, YF, and CL conceived and designed the research and wrote the paper. HG, LA, YF, and CL provided the data. HG supervised the study. NA, LA, YF, and CL analyzed the data. HG, RK, LA, YF, and CL revised the manuscript. All authors contributed to the article and approved the submitted version.

FUNDING

This research was supported by the National Natural Science Foundation of China under Grant No. 61673085.

REFERENCES

Achim, A., Bezerianos, A., and Tsakalides, P. (2001). Novel Bayesian multiscale method for speckle removal in medical ultrasound images. *IEEE Trans. Med. Imaging* 20, 772–783. doi: 10.1109/42.938245

Achim, A., Tsakalides, P., and Bezerianos, A. (2003). SAR image denoising via Bayesian wavelet shrinkage based on heavy-tailed modeling. *IEEE Trans. Geosci. Rem. Sens.* 41, 1773–1784. doi: 10.1109/TGRS.2003.813488

Awad, A. S. (2011). Standard deviation for obtaining the optimal direction in the removal of impulse noise. *IEEE Signal Process. Lett.* 18, 407–410. doi: 10.1109/LSP.2011.2154330

Bayraktar, Z., Turpin, J. P., and Werner, D. H. (2011). Nature-inspired optimization of high-impedance metasurfaces with ultrasmall interwoven unit cells. *IEEE Antennas Wireless Propagat. Lett.* 10, 1563–1566. doi: 10.1109/LAWP.2011.2178224

Bhandari, A. K., Kumar, D., Kumar, A., and Singh, G. K. (2016). Optimal sub-band adaptive thresholding based edge preserved satellite image denoising using adaptive differential evolution algorithm. *Neurocomputing* 174, 698–721. doi: 10.1016/j.neucom.2015.09.079

Chan, R. H., Ho, C. W., and Nikolova, M. (2005). Salt-and-pepper noise removal by median-type noise detectors and detail-preserving regularization. *IEEE Trans. Image Process.* 14, 1479–1485. doi: 10.1109/TIP.2005.852196

Chang, S. G., Yu, B., and Vetterli, M. (2000). Spatially adaptive wavelet thresholding with context modeling for image denoising. *IEEE Trans. Image Process.* 9, 1522–1531. doi: 10.1109/83.862630

Chen, C. L. P., Liu, L., Chen, L., Tang, Y. Y., and Zhou, Y. (2015). Weighted couple sparse representation with classified regularization for impulse noise removal. *IEEE Trans. Image Process.* 24, 4014–4026. doi: 10.1109/TIP.2015.2456432

Coifman, R. R., and Donoho, D. L. (1995). *Translation-Invariant De-Noising*, (New York, NY: Springer).

Dataset (2020). *Brain MRI*. Available online at: https://www.mr-tip.com/serv1.php?type=db1&dbs=brainmri

De Decker, A., François, D., Verleysen, M., and Lee, J. A. (2011). Mode estimation in high-dimensional spaces with flat-top kernels: application to image denoising. *Neurocomputing* 74, 1402–1410. doi: 10.1016/j.neucom.2010.12.013

Dong, Y., and Xu, S. (2007). A new directional weighted median filter for removal of random-valued impulse noise. *IEEE Signal Process. Lett.* 14, 193–196. doi: 10.1109/LSP.2006.884014

Donoho, D. L., and Johnstone, I. M. (1995). Adapting to unknown smoothness via wavelet shrinkage. *J. Am. Stat. Assoc.* 90, 1200–1224. doi: 10.1080/01621459.1995.10476626

Donoho, D. L., and Johnstone, J. M. (1994). Ideal spatial adaptation by wavelet shrinkage. *Biometrika* 81, 425–455. doi: 10.1093/biomet/81.3.425

Elad, M., and Aharon, M. (2006). Image denoising via sparse and redundant representations over learned dictionaries. *IEEE Trans. Image Process.* 15, 3736–3745. doi: 10.1109/TIP.2006.881969

Figueiredo, M. A., and Nowak, R. D. (2001). Wavelet-based image estimation: an empirical Bayes approach using Jeffreys' noninformative prior. *IEEE Trans. Image Process.* 10, 1322–1331. doi: 10.1109/83.941856

Garnett, R., Huegerich, T., Chui, C., and He, W. (2005). A universal noise removal algorithm with an impulse detector. *IEEE Trans. Image Process.* 14, 1747–1754. doi: 10.1109/TIP.2005.857261

Golilarz, N. A., and Demirel, H. (2017). Thresholding neural network (TNN) based noise reduction with a new improved thresholding function. *CRPASE* 3, 81–84.

Golilarz, N. A., and Demirel, H. (2018a). "Image de-noising using un-decimated wavelet transform (UWT) with soft thresholding technique," in *Proceedings–9th International Conference on Computational Intelligence and Communication Networks, CICN 2017* (Girne). doi: 10.1109/CICN.2017.8319347

Golilarz, N. A., and Demirel, H. (2018b). "Thresholding neural network (TNN) with smooth sigmoid based shrinkage (SSBS) function for image de-noising," in *Proceedings–9th International Conference on Computational Intelligence and Communication Networks, CICN 2017* (Girne). doi: 10.1109/CICN.2017.8319358

Golilarz, N. A., Demirel, H., and Gao, H. (2019a). Adaptive generalized gaussian distribution oriented thresholding function for image de-noising. *Int. J. Adv. Comput. Sci. Appl.* 10, 10–15. doi: 10.14569/IJACSA.2019.0100202

Golilarz, N. A., Gao, H., Ali, W., and Shahid, M. (2018). "Hyper-spectral remote sensing image de-noising with three dimensional wavelet transform utilizing smooth nonlinear soft thresholding function," in *2018 15th International Computer Conference on Wavelet Active Media Technology and Information Processing (ICCWAMTIP)* (Chengdu: IEEE), 142–146. doi: 10.1109/ICCWAMTIP.2018.8632597

Golilarz, N. A., Gao, H., and Demirel, H. (2019b). Satellite image de-noising with Harris Hawks meta heuristic optimization algorithm and improved adaptive generalized gaussian distribution threshold function. *IEEE Access* 7, 57459–57468. doi: 10.1109/ACCESS.2019.2914101

Golilarz, N. A., Robert, N., Addeh, J., and Salehpour, A. (2017). Translation invariant wavelet based noise reduction using a new smooth non-linear improved thresholding function. *CRPASE* 3, 104–108.

Heidari, A. A., Mirjalili, S., Faris, H., Aljarah, I., Mafarja, M., and Chen, H. (2019). Harris Hawks optimization: algorithm and applications. *Fut. Gen. Comput. Syst.* 97, 849–872. doi: 10.1016/j.future.2019.02.028

Li, D., Wang, Y., and Fang, T. (2011). "Wavelet image denoising algorithm based on local adaptive wiener filtering," in *Proceedings 2011 International Conference on Mechatronic Science, Electric Engineering and Computer, MEC 2011*, (Jilin).

Lin, C. H., Tsai, J. S., and Chiu, C. T. (2010). "Switching bilateral filter with a texture/noise detector for universal noise removal," in *ICASSP, IEEE International Conference on Acoustics, Speech and Signal Processing—Proceedings* (Dallas, TX). doi: 10.1109/ICASSP.2010.5495475

Lu, X., Yuan, Y., and Yan, P. (2013). Sparse coding for image denoising using spike and slab prior. *Neurocomputing* 106, 12–20. doi: 10.1016/j.neucom.2012.09.014

Miura, S., Tsuji, H., and Kimura, T. (2013). "Randomly valued impulse noise removal using Gaussian curvature of image surface," in *ISPACS 2013–2013 International Symposium on Intelligent Signal Processing and Communication Systems* (Naha). doi: 10.1109/ISPACS.2013.6704563

Nasri, M., and Nezamabadi-pour, H. (2009). Image denoising in the wavelet domain using a new adaptive thresholding function. *Neurocomputing* 72, 1012–1025. doi: 10.1016/j.neucom.2008.04.016

Pizurica, A., Philips, W., Lemahieu, I., and Acheroy, M. (2002). A joint inter-and intrascale statistical model for bayesian wavelet based image denoising. *IEEE Trans. Image Process.* 11, 545–557. doi: 10.1109/TIP.2002.1006401

Poli, R., Kennedy, J., and Blackwell, T. (2007). Particle swarm optimization: an overview. *Swarm Intell.* 1, 33–57. doi: 10.1007/s11721-007-0002-0

Portilla, J., Strela, V., Wainwright, M. J., and Simoncelli, E. P. (2003). Image denoising using scale mixtures of gaussians in the wavelet domain. *IEEE Trans. Image Process.* 12, 1338–1351. doi: 10.1109/TIP.2003.818640

Qian, Y. (2018). "Image denoising algorithm based on improved wavelet threshold function and median filter," in *2018 IEEE 18th International Conference on Communication Technology (ICCT)* (Chongqing: IEEE), 1197–1202. doi: 10.1109/ICCT.2018.8599921

Sahraeian, S. M., Marvasti, F., and Sadati, N. (2007). "Wavelet image denoising based on improved thresholding neural network and cycle spinning," in *ICASSP, IEEE International Conference on Acoustics, Speech and Signal Processing—Proceedings* (Honolulu, HI). doi: 10.1109/ICASSP.2007.365975

Şendur, L., and Selesnick, I. W. (2002). Bivariate shrinkage functions for wavelet-based denoising exploiting interscale dependency. *IEEE Trans. Signal Process.* 50, 2744–2756. doi: 10.1109/ICASSP.2002.1005979

Starck, J. L., Candès, E. J., and Donoho, D. L. (2002). The curvelet transform for image denoising. *IEEE Trans. Image Process.* 11, 670–684. doi: 10.1109/TIP.2002.1014998

Storn, R., and Price, K. (1997). Differential evolution–a simple and efficient heuristic for global optimization over continuous spaces. *J. Glob. Optim.* 11, 341–359. doi: 10.1023/A:1008202821328

Sveinsson, J. R., and Benediktsson, J. A. (2003). Almost translation invariant wavelet transformations for speckle reduction of SAR images. *IEEE Trans. Geosci. Rem. Sens.* 41, 2404–2408. doi: 10.1109/TGRS.2003.817844

Yang, X.-S. (2010). "Firefly algorithm, levy flights and global optimization," in *Research and Development in Intelligent Systems XXVI*, eds M. Bramer, R. Ellis, and M. Petridis (London: Springer), 209–218. doi: 10.1007/978-1-84882-983-1_15

Yang, X.-S., and Deb, S. (2009). "Cuckoo search via lévy flights," in *2009 World Congress on Nature & Biologically Inspired Computing (NaBIC)* (Coimbatore: IEEE), 210–214. doi: 10.1109/NABIC.2009.5393690

Yin, J. L., Chen, B. H., and Li, Y. (2018). Highly accurate image reconstruction for multimodal noise suppression using semisupervised learning on big

data. *IEEE Trans. Multimed.* 20, 3045–3056. doi: 10.1109/TMM.2018.2820910

Yuan, G., and Ghanem, B. (2015). "l0tv: a new method for image restoration in the presence of impulse noise," in *Proceedings of the IEEE Conference on Computer Vision and Pattern Recognition* (Boston, MA) 5369–5377.

Zhang, J., and Sanderson, A. C. (2009). JADE: adaptive differential evolution with optional external archive. *IEEE Trans. Evol. Comput.* 13, 945–958. doi: 10.1109/TEVC.2009.2014613

Zhang, X. P. (2001). Thresholding neural network for adaptive noise reduction. *IEEE Trans. Neural Netw.* 12, 567–584. doi: 10.1109/72.925559

Zhang, Y., Ding, W., Pan, Z., and Qin, J. (2019). Improved wavelet threshold for image de-noising. *Front. Neurosci.* 13:39. doi: 10.3389/fnins.2019.00039

Conflict of Interest: CL was employed by The 54th Research Institute of China Electronics Technology Group Corporation, Shijiazhuang, China.

The remaining authors declare that the research was conducted in the absence of any commercial or financial relationships that could be construed as a potential conflict of interest.

Copyright © 2020 Amiri Golilarz, Gao, Kumar, Ali, Fu and Li. This is an open-access article distributed under the terms of the Creative Commons Attribution License (CC BY). The use, distribution or reproduction in other forums is permitted, provided the original author(s) and the copyright owner(s) are credited and that the original publication in this journal is cited, in accordance with accepted academic practice. No use, distribution or reproduction is permitted which does not comply with these terms.

Advantages of publishing in Frontiers

OPEN ACCESS
Articles are free to read for greatest visibility and readership

FAST PUBLICATION
Around 90 days from submission to decision

HIGH QUALITY PEER-REVIEW
Rigorous, collaborative, and constructive peer-review

TRANSPARENT PEER-REVIEW
Editors and reviewers acknowledged by name on published articles

Frontiers
Avenue du Tribunal-Fédéral 34
1005 Lausanne | Switzerland

Visit us: www.frontiersin.org
Contact us: frontiersin.org/about/contact

REPRODUCIBILITY OF RESEARCH
Support open data and methods to enhance research reproducibility

DIGITAL PUBLISHING
Articles designed for optimal readership across devices

FOLLOW US
@frontiersin

IMPACT METRICS
Advanced article metrics track visibility across digital media

EXTENSIVE PROMOTION
Marketing and promotion of impactful research

LOOP RESEARCH NETWORK
Our network increases your article's readership